GSI Report 2005-1
June 2005

SCIENTIFIC REPORT 2004

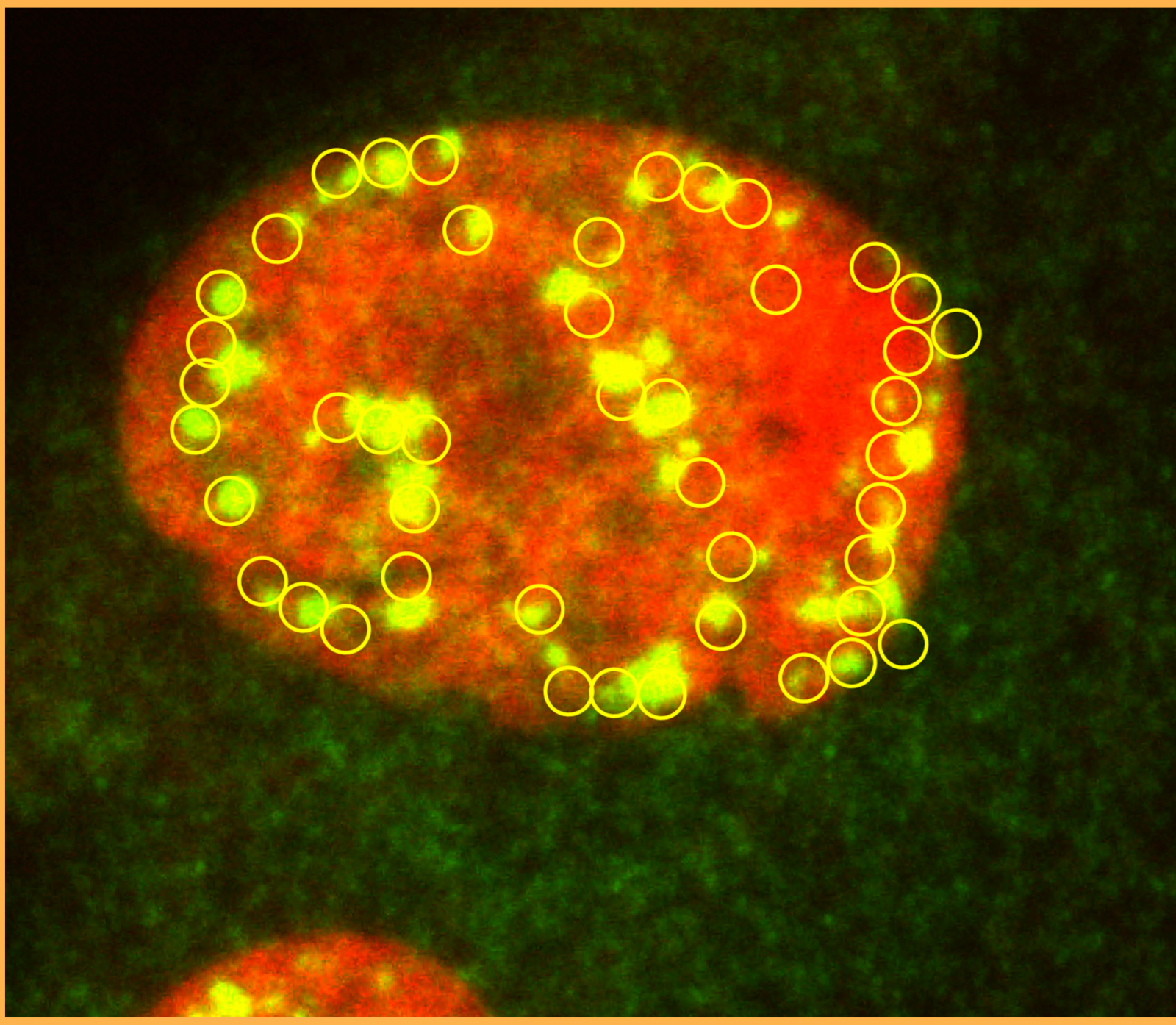

Gesellschaft für Schwerionenforschung mbH Darmstadt
Member of the Helmholtz Association

Cover illustration:

The nucleus of a human fibroplast cell (stained in red and about 15μm in diameter) is irradiated at the GSI microbeam facility, which allows irradiating of an individual cell with a given number of ions and with a spatial resolution of one micrometer. This is demonstrated here by delivering helium ions in a geometrical pattern representing the letters 'G S I'.
The actual positions of the ions are visualized by confocal microscopy on the basis of the biological response of the cell. This is achieved by staining a protein involved in the DNA damage repair, 53BP1, which accumulates at the position of the ion induced damage (bright yellow spots). For comparison, the intended targeted positions are indicated by yellow circles. At each of the 45 positions, four helium ions at 4.8 MeV/u were delivered. [See page 22/RADBIOPH-18 of this report.]

GSI Scientific Report 2004

GSI Report 2005-1
<http://www.gsi.de/library/GSI-Report-2005-1/>

ISSN: 0174-0814
and GSI Report 2005-1

Publisher: Gesellschaft für Schwerionenforschung mbH,
Planckstr. 1, 64291 Darmstadt, Germany, <http://www.gsi.de>
The GSI is a member of the Helmholtz Association of National Research Centres <http://www.helmholtz.de>.

Publication dates: June 2005 (online version), July 2005 (printed version)
Editor: Katrin Große
Technical Team for the printed and the Internet version: I. Giese, K. Große, U. Meyer, V. Schaa, and K. Schiebel.

Printed by: Frotscher Druck GmbH, 64295 Darmstadt, Germany

The complete scientific report is also available with supplementary colored figures and illustrations on the Internet: <http://www.gsi.de/library/GSI-Report-2005-1/>

Foreword

The photo on the cover page of this report shows the nucleus of a human cell that was irradiated with helium ions and then stained to reveal a repair protein assembling at the location of the ion track damages. The pattern inscribed by the individual ions traces the GSI acronym. It illustrates the precision and control achieved in ion irradiation – and it is an example of the fruitful interplay between research disciplines. Control of the ion irradiation down to individual ions and with high spatial precision was achieved by perfecting the ion-beam microprobe in the materials research group. Application in radio-biology extends these studies to the microscopic level.

This example is one of a number of developments in the different research areas pursued at GSI, some others are mentioned below. In addition, substantial effort was directed towards a range of developments for the FAIR project (Facility for Antiproton and Ion Research). Directly or indirectly, these dual tasks have required a special commitment from the staff, as well as from our guests and the many external collaborators involved in the present and/or future activities of the institute. This report reflects on their work. And this Foreword provides me with an opportunity to express my personal thanks and those of GSI to everybody involved.

In nuclear structure research, studies far from stability have continued with relativistic radioactive beams. New results were obtained, for example, in relativistic Coulomb excitation of the giant dipole resonance in heavy nuclei with up to eight neutrons (^{132}Sn) beyond the last stable isotope. They establish the low-energy excitation mode predicted for neutron-rich nuclei with excess neutrons at the nuclear surface oscillating against the core. The measurement also illustrates the sensitivity that can be achieved for selected reactions when carried out at relativistic energies. Orders of magnitude in event rate are gained from higher target thickness, favourable kinematics and resulting solid angle, as well as from substantially higher reaction cross section. Good-quality measurements are thus possible, as with the present example, for secondary beams with a few tens of ions per second.

Expected yields of radioactive beams follow from a comprehensive study carried out at GSI over several years, and recently completed, of cross sections and kinetic energies in the spallation of 1 AGeV ^{238}U with protons, measured in inverse kinematics with a uranium beam. Analysis of the masses of neutron-rich nuclei, previously measured in the ESR storage and cooler ring with isochronous mass spectroscopy, is nearing completion and will provide information on r-process components that would occur in a stellar environment of relativeley low neutron flux.

Proton elastic scattering of neutron-rich ^{6}He and ^{8}He in new detector geometry and now extending beyond the first diffraction minimum, provides new information on the respective nuclear matter distributions and facilitates a test of theoretical predictions within the Fermionic Molecular Dynamics model recently developed by the GSI theory group.

In the study of nucleus-nucleus collisions, new results are obtained at SIS energies on azimuthal angular emission patterns of kaons, providing important input to the understanding of the repulsive K^+N versus the attractive K^-N potential in the nuclear medium. At SPS energies, the analysis of pion to kaon yields reveals intriguing dependences on strangeness production in dense nuclear matter. Tantalizing evidence is also possibly seen in experiments at the FOPI detector for a deeply bound kaonic cluster state. A broad program to search for bound meson-nucleus states, both kaonic and with eta-mesons, is in preparation.

The study of di-lepton production in nucleus-nucleus collisions at SIS energies is entering an exciting phase with production runs and first results from proton-proton and heavy ion collisions from the HADES detector.

In addition to the experimental achievements in nuclear matter research, in hadron properties in nuclear matter, and in the dynamics of nucleus-nucleus collisions major progress has been made in the complementary theory work described in this report.

In atomic physics, advances in precision spectroscopy of highly charged ions are opening new opportunities. High-resolution dielectric recombination in few-electron heavy atoms promises excellent sensitivity to changes in nuclear charge radius between isotopes. A major step forward has been achieved experimentally by decoupling the dual functions of the ESR electron cooler namely, at the same time, beam cooling and electron target. By using stochastic cooling instead, one achieves a larger dynamic range and increased precision from dielectric-recombination transitions.

Proof of principle was made for laser cooling of beams of highly stripped atoms. Using the Lamb-shift transition in lithium-like carbon, a carbon beam in the 3^+ charge state was cooled in the ESR to a relative momentum spread of a few times 10^{-7}. Applying this to lithium-like heavy ions, laser cooling of highly relativistic beams in the future at FAIR, e. g. at energies of about 30 GeV per nucleon, might become reality.

Much of the effort in the area of plasma physics was directed towards the construction of the PHELIX petawatt laser. A major technological challenge is the damage threshold of various components, in particular of the compression gratings. Using a pulse from the PHELIX fs-frontend and compressing it in the existing terawatt compressor and down to a 300 micrometer spot size, a unique test bed for 500 femto-second laser-induced damage threshold measurements under vacuum was set up. This allowed extensive tests of gratings, in particular the ones of the emerging technology of multi-layer dielectric (MDL) gratings, from producers worldwide.

In the area of radiation biology, the research efforts were split again between an extensive program in microscopic studies of various aspects of cell responses to radiation on the one hand, and the efforts towards ion therapy on the other. The first involves the new development of live cell imaging at the beam target station of the UNILAC accelerator. The second involves the continued irradiation of patients at the GSI pilot facility, the construction of the dedicated clinical facility at Heidelberg, as well as technical developments such as the irradiation of moving organs.

Material science has continued its studies with the ion-microprobe and sample irradiation with high-energy ion beams in a pressure cell. Interesting ion-induced high-pressure phase transitions are observed. A major activity is directed towards investigations of the properties of nano-structures such as nano-wires of poly- and single-crystalline character, down to 20 nanometer diameter, and grown by electrochemical deposition in the nano-pores of etched ion-track polymer membranes.

For advancing the FAIR project, an International Steering Committee (ISC) was founded with representatives from 10 member countries that have signed on MoU for the preparatory and pre-contact phase, and also several observers. The Steering Committee has formed two major working groups, again with representatives from the partner states, one on scientific and technical issues (STI) and a second on administrative and financial issues (AFI), each with sub-working groups, in particular technical and scientific program advisory committees to evaluate and advise on accelerator issues and the scientific program. For the latter, letters-of-intent were solicited for June 2004 and, based on their evaluation, technical proposals (for the experiments) and technical reports (on accelerator sub-projects) were called for and collected at the beginning of 2005. These reports are the basis for establishing baseline cost and final project definition by the Steering Committee during 2005.

Walter F. Henning
Scientific Director

Contents

FAIR-EXP

Design and Development of Future Experiments at FAIR

The FAIR Project in 2004

Thomas W. Beier, Jürgen Eschke, Hans H. Gutbrod, and Ingo Augustin

GSI, FAIR Project-Coordination Group, Planckstr. 1, 64291 Darmstadt, Germany

1. Introduction

The proposal for the construction of an international *Facility for Antiproton and Ion Research* (FAIR) was presented by GSI in 2001. The scientific and technical concept for FAIR is based on extensive discussions about the long-term perspectives of research with beams of heavy highly charged ions. Based on these discussions, a first proposal for an 'International Accelerator Facility for Beams of Ions and Antiprotons' was proposed in 2000. One year later, in fall 2001, a 'Conceptual Design Report' [1] comprising more than 700 pages was presented. The 'Wissenschaftsrat der Bundesrepublik Deutschland' (Research Council of the Federal Republic of Germany) evaluated this proposal together with eight other applications of large-scale facilities for scientific research. The GSI proposal was recommended for funding to the BMBF (Bundesministerium für Bildung und Forschung, Federal Ministry for Education and Research), with the conditions (i) to present a staged plan for the realization of the project and (ii) to raise part of the required funds from foreign sources. The BMBF followed the recommendation of the Wissenschaftsrat and made the following decision in February 2003: The Gesellschaft für Schwerionenforschung (GSI) in Darmstadt shall build the new facilities together with European partners and become a leading European centre for physics. At least one quarter of the investments shall be raised by partners outside Germany.

Since then, considerable progress has been made in both the scientific-technical preparatory work as well as the legal and planning work. A call for letters of intent (LoI) was launched in October 2003. 25 LoIs have been submitted by more than 1750 authors in Spring of 2004 [2]. In June of 2004, three programme advisory committees, one on QCD physics (QCD-PAC), one on nuclear structure and astrophysics (NUSTAR PAC) and another one on atomic physics, plasma physics, applied physics (APPA PAC) have evaluated the 25 LoIs. The technical advisory committee (TAC) evaluated the ongoing accelerator and infrastructure plans. 23 experiment collaborations obtained the green light to present a Technical Proposal January 15th 2005, the accelerator groups were asked to present Technical Reports detailing the status of the design, planning and costs of the FAIR sub-projects. In close collaboration with the BMBF, a staged plan for the realization has been established.

2. Organization as an International Project

In February 2004, an international steering committee (ISC-FAIR, chaired by H. Schunck from the BMBF) was established for FAIR in order to coordinate the international involvement in the organizational and technical development of FAIR. Two working groups have been created to support the ISC FAIR: a) a working group for Scientific and Technical Issues (STI-FAIR), b) a working group on Administrative and Financial Issues (AFI-FAIR).

The FAIR member countries and a number of countries with observer status are represented in the ISC, and in the STI and AFI working groups, by delegates appointed by their research ministries or funding agencies.

The task of the AFI-FAIR working group includes the development of a suitable legal framework for the new company, the preparation of a Memorandum of Understanding (MoU) as a formal base for the cooperation during the so-called 'preparatory phase', i.e. up to the start of construction (expected in 2007), and the preparation of contracts between the partners for construction, commissioning and operation of the FAIR facility. For an estimate of construction costs, a further working group, the AFI-FCS (Full Cost Structure) working group has been established. Its task is the definition of contributions (deliverables) to the project, the accounting of in-kind contributions etc. After the mode for cost determination has been established, a fixed cost will be established for each work package which forms the base for calculating contributions by the partners. For the legal entity, the current legal status as a German limited liability company (GmbH), expanded by international shareholders, is favoured. The Convention, Articles of Association, and By-Laws are currently being worked out by the AFI-LFI working group (Legal Frame Issues). Up to January 2005, the MoU mentioned above has been signed by 10 countries (Finland, France, Germany, Greece, Italy, Poland, Russia, Spain, Sweden, United Kingdom). Some of the current formal observers (China, Hungary, India, United States of America) may also considering this step in the future. Other countries are invited to join.

The schedule for the different committees up to the final signature of the contract is shown in Fig. 1.

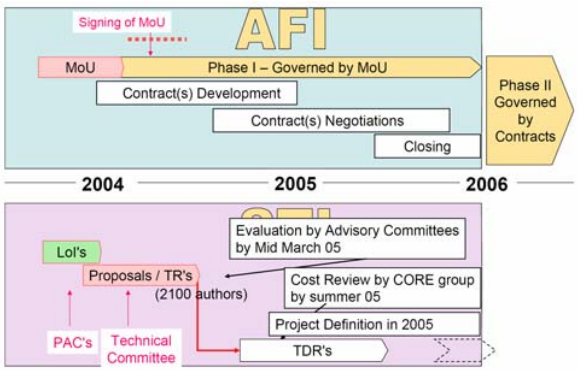

Fig. 1 Time schedule for AFI (top) and STI (bottom). The final project definition is expected in summer 2005, the signature of the contract is aimed for in mid 2006.

3. Time Schedule for the Stage Plan

A three-stage plan for the FAIR-project construction has been developed together with the BMBF. It follows from the following considerations: First, at the end of each stage, a major advance in research capabilities is achieved and allows the start-up of a corresponding partial research program. Second, civil construction of buildings will be carried

out as early as possible to minimize negative impact on facility progress and on the natural environment. In particular, it is aimed to perform all construction requiring considerable earthwork as early as possible, including the tunnels for SIS100/300 and the foundations for the storage-ring buildings as well as these buildings themselves. In this way, construction-caused vibration will be kept to a minimum when the experimental program starts at the end of stage 1. At the end of stage 1, the SIS18 upgrade will provide $2x10^{11}$ particles/pulse U^{28+} at 200 AMeV and $4x10^{10}$ particles/pulse U^{73+} at 1000 AMeV, a repetition rate of 4 Hz at up to 12 Tm and 1 Hz up to 18 Tm, and a bunch compression to 70 ns. Nomenclatures within the following figures are explained in detail in [1].

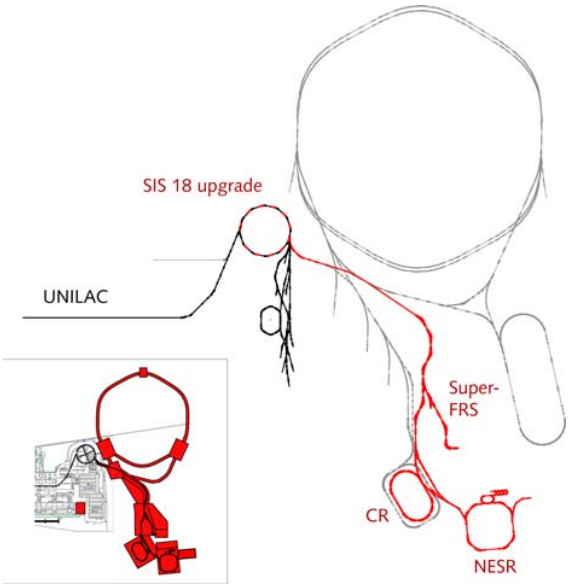

Fig 2. Components of Stage 1. Top: Accelerator and experiments, left buildings: Gray: Not yet in stage 1.

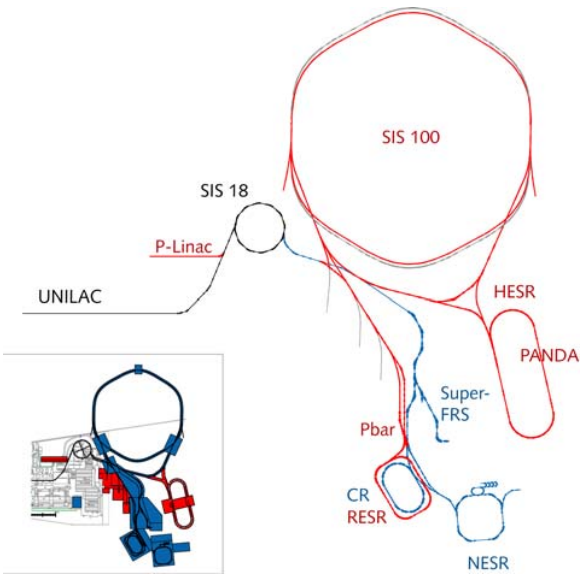

Fig 3. Components of Stage 2. Top: Accelerator and experiments, left buildings: Gray: not yet in stage 2.

After completion of Stage 1, nuclear structure investigations with a secondary beam of 100-fold increased intensity will be possible after the new superconducting fragment separator (Super-FRS), plasma physics in the existing target area with 200-fold improved power density and atomic physics with radioactive beams. In Stage 2, all buildings will be completed. After completion, the accelerator will deliver 10^{12} particles/pulse U^{28+} at 2.7 AGeV, 10^{11} particles/pulse U^{73+} at 8.3 GeV (or Ne^{10+} up to 14 AGeV), bunch compression up to 50 ns, $2.5x10^{13}$ protons/pulse up to 29 GeV, up to 10^{11} antiprotons accumulated, stored, and cooled in the HESR at up to 15 GeV, and antiprotons decelerated down to rest in the NESR and HITRAP. Nuclear structure physics will be possible with up to 10000-fold increased secondary-beam intensity, in addition QCD studies with protons and antiprotons and precision spectroscopy with antiprotons and antimatter at rest will form the anticipated research program.

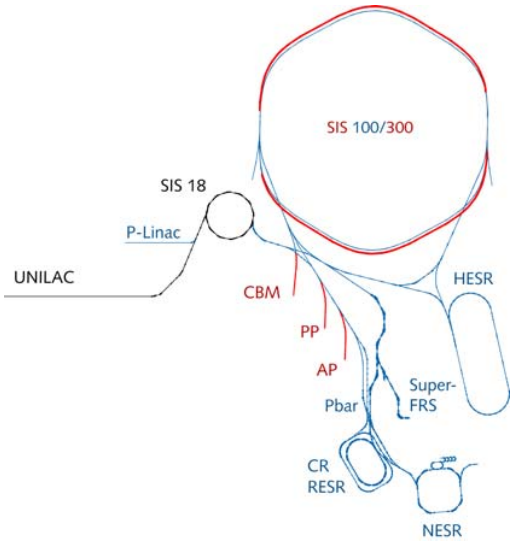

Fig. 4. Accelerator components to be completed during Stage 3: SIS300, AP, PP, CBM.

After completion of Stage 3, the full research programme will be possible with, in particular, parallel operation of up to four programmes. Beyond the parameters of Stage 2, plasma-physics research will benefit from up to 2500-fold increased power density. Atomic reaction studies will be possible with highly energetic beams. The accelerator is expected to deliver $2x10^{9}$ particles/pulse U^{92+} at up to 34 AGeV and stretcher possibility with extraction times of up to several minutes for the nuclear-matter program.

The planning for the construction work will take two more years, following the delivery of the TRs, so that beginning of construction work is anticipated for 2007. The legal procedure for the construction permit and the environmental compensation measures is ongoing. About 0.21 km^2 of forest have to be cleared, of which about 0.11 km^2 will be reforested within the GSI area. From the remaining area, about ½ will be reforested on adjacent fields. The operation of the FAIR facility has been approved by the Ministery of Environment of the State of Hessen following a thorough evaluation of the proposed radiation safety features worked out by the GSI Radiation Safety group.

[1] http://www.gsi.de/zukunftsprojekt/veroeffentlichungen.html

[2] http://www.gsi.de/zukunftsprojekt/loi.html

The CBM experiment at FAIR

P. Senger[1] for the CBM Collaboration
[1] GSI Darmstadt

The Compressed Baryonic Matter (CBM) experiment is designed to explore the QCD phase diagram in the region of moderate temperatures but very high baryon densities. Our current knowledge on the QCD phasediagram is illustrated in figure 1. The data points correspond to chemical freeze-out and result from a statistical analysis of particle ratios measured in Pb+Pb and Au+Au collisions at SIS, AGS, SPS and RHIC. The phase boundary between quark-gluon matter and hadronic and the location of the critical endpoint as shown in figure 1 is predicted by recent lattice QCD calculations which indicate that for values of μ_B larger than about 400 MeV the phase transition is first order, whereas for μ_B smaller than 400 MeV there is a smooth cross over from the hadronic to the partonic phase (dotted line).

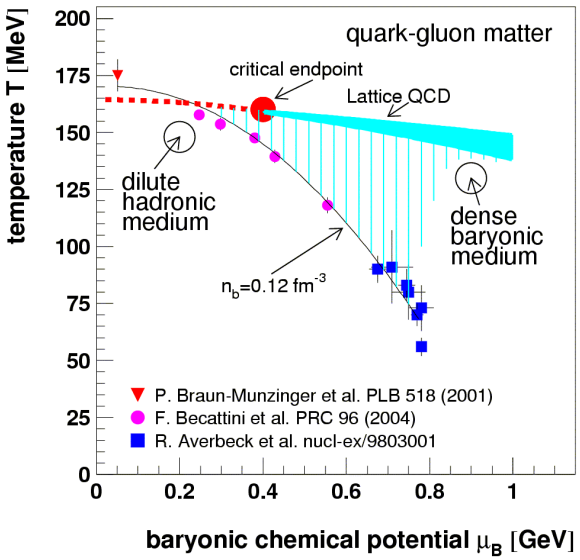

Figure 1: The phase diagram of strongly interacting matter.

The CBM research program includes the search for the deconfinement phase transition at high baryon densities, the study of chiral symmetry restoration in superdense baryonic matter, the search for the critical endpoint, and the study of the nuclear equation of state at high densities. The most promising diagnostic probes are particles with open and hidden charm, low-mass vector mesons decaying into dilepton pairs, (multi-)strange particles, event-by-event fluctuations, and collective flow.

The major experimental challenge is posed by the extremely high reaction rates of up to 10^7 events/second. These conditions require unprecedented detector performances concerning speed and radiation hardness. The detector signals are processed by a high-speed data acquisition and an online event selection system.

Simulations within the CBM software framework have been performed in order to study the feasibility of the planned measurements. Recent results of the simulations and of the detector R&D for CBM are presented in dedicated contributions to this Scientific Report.

1 Silicon Tracker System (STS)

The Silicon Tracking System (STS) serves for track measurement and for determination of primary and secondary vertices. The current STS layout consists of minimum 7 layers and is placed inside a magnetic dipole field which provides the bending power required for momentum determination with an accuracy of $\Delta p/p = 1$ %. The STS has to fulfill the following requirements: material budget below 0.3% radiation length per layer to reduce multiple scattering, hit resolution of about 10 μm to achieve a vertex resolution of about 50 μm along the beam axis, radiation hardness up to a dose of 50 MRad corresponding to the dose accumulated in ten years of running, and read-out times of about 25 ns to accommodate reaction rates of 10 MHz.

The first 2 stations (distance from the target 5 and 10 cm) will consist of pixel detectors in order to reduce the occupancy to about 1% (for a central Au+Au collision at 25 AGeV). Monolithic Active Pixel Sensors (MAPS) with a pixel size of 40x40 μm^2 and a thickness of 100 μm would perfectly fulfill our requirements concerning vertex resolution which is needed to measure the displaced vertices of D mesons. However, the radiation hardness and the read out speed of nowadays MAPS detectors have to be improved by 1 - 2 orders of magnitude in order to match our requirements. Moreover, we work on track reconstruction methods to resolve the tracks and vertices of up to 50 superimposed events in the MAPS detectors.

The ongoing development of low-mass hybrid pixel detectors for future LHC experiments may lead to a substantial reduction of their material budget. These detectors - which are fast and radiation hard - might then serve as a fall back solution for the CBM Vertex Tracker.

The next 5 Silicon layers (distance from the target 20, 40, 60, 80, and 100 cm) will consist of Silicon microstrip detectors. The current layout foresees a pitch of 25 μm and three different strip lengths of 20, 40 and 60 mm. The strips are arranged such that the occupancy is below 2% for a central Au+Au collision at 25 AGeV. The detectors will be double sided with a stereo angle between the strips which has to be optimized by simulations. The ambiguities due to double (or triple) hits having a distance smaller than the strip length result in 2 (or 6) ghost hits which pose a severe problem to the track reconstruction algorithms. It might be necessary to add more Silicon layers with a different orientation of the strips in order to minimize the ambiguities. Another possibility would be to reduce the length of the strips with the consequence of increasing the number of channels. The investigation of this problem is in progress.

2 Ring Imaging Cherenkov detectors

The RICH detector is designed to provide identification of electrons and suppression of pions in the momentum range of electrons from low-mass vector-meson decays. The actual layout of the RICH detector consists of a radiator (3 gases under study: N_2, 40% He + 60 %CH_4, and 50% N_2 + 50 %CH_4, length 2.2 m), a mirror (3 mm Be covered with 0.5 mm glass, radius 4.5 m), and a photon detector composed of about 100.000 photomultiplier (PM) channels (6 mm diameter, quantum efficiency 20 %). The glass window of the PMs is covered with wave-length shifter (WLS) films in order to increase the absorption of Cherenkov photons.

A crucial task is to match the rings to the charged particle tracks. If the track position at the mirror can be determined with an accuracy of 200 μm, and assuming a momentum resolution of 1%, the mismatch of pions to electron rings is less than 10^{-3} per event. This number will be considerably improved when taking into account particle identification by time-of-flight measurement and by the TRD. Performance studies are in progress, taking into account track reconstruction and more realistic detector properties, in order to optimize the detector layout.

3 Transition radiation detector(TRD)

Three Transition Radiation Detector stations will serve for particle tracking and for the identification of high energy electrons and positrons ($\gamma > 2000$) which are used to reconstruct J/ψ mesons. According to simulations which are based on the experience obtained with the development of the TRD for ALICE and of the TRT for ATLAS, pion suppression factors of up to 200 (for momenta above 2 GeV/c) at an electron efficiency of better than 90% can be achieved.

The major technical challenge is to develop highly granular and fast gaseous detectors which can stand the high-rate environment of CBM in particular for the inner part of the detector planes covering forward emission angles. For example, at small forward angles and at a distance of 4 m from the target, we expect particle rates of more than 100 kHz/cm^2 for 10 MHz minimum bias Au+Au collisions at 25 AGeV. In a central collision, particle densities of about 0.05/cm^2 are reached. In order to keep the occupancy below 5% the size of a single cell should be about 1 cm^2.

Within our R&D activities we investigate both the ALICE-TRD and the ATLAS-TRT concept. Both detector versions have to be modified in order to meet the CBM requirements. In the case of the ALICE-TRD, the rate capability of the read-out chambers has to be improved. Various prototypes of fast Multi Wire Proportional Chambers (MWPC) and Gas Electron Multipliers (GEM) have been tested with proton and pion beams up to intensities of 100 kHz/cm^2 and no major deterioration of the performance has been observed. The high-rate performance is required for less than 30% of the active TRD area (which is about 500 m^2 in total). A detector concept for CBM has been studied on the basis of straw tubes (ATLAS-TRT option). Here, the challenge is to build very small straw tubes which still provide a high efficiency in the regions of highest occupancy. A possible detector concept might be to use an MWPC-based TRD for the inner part of the detectors where the high rates occur, and a straw-based TRT for the outer regions.

4 Resistive plate chambers (RPC)

An array of Resistive Plate Chambers will be used for hadron identification via TOF measurements. The TOF wall is located about 10 m downstream of the target and covers an active area of about 120 m^2. The required time resolution is about 80 ps. For 10 MHz minimum bias Au+Au collisions the innermost part of the detector has to work at rates up to 20 kHz/cm^2. At small deflection angles the pad size is about 5 cm^2 corresponding to an occupancy of below 5% for central Au+Au collisions at 25 AGeV. With a small-size prototype a time resolution of about 90 ps has been achieved at a rate of 25 kHz/cm^2. Future R&D concentrates on the rate capability, low resistivity material, long term stability, and realization of large arrays with overall excellent timing performance.

5 Electromagnetic calorimeter

The electromagnetic calorimeter will be used to measure direct photons, neutral mesons decaying into photons, electrons and muons. Simulations and R&D have been started based on the shashlik type of detector modules as used in HERA-B, PHENIX and LHCb. Particular emphasis is put on a good energy resolution and a high pion suppression factor.

A sketch of the CBM detector is shown in figure 2.

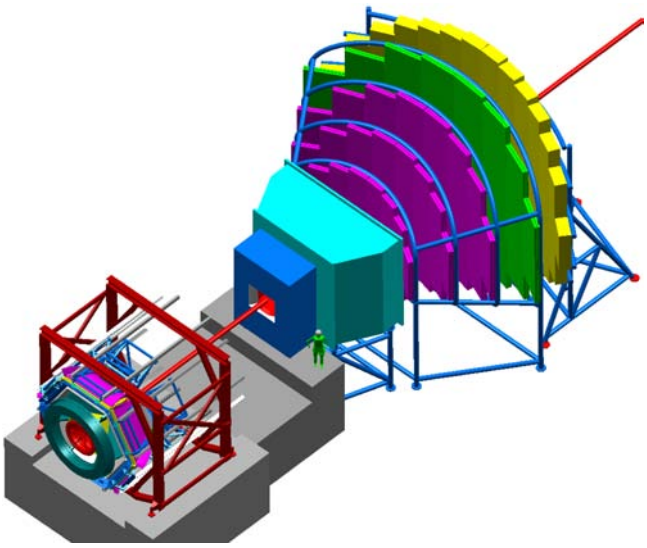

Figure 2: The CBM detector setup together with the HADES detector. HADES will be used for beam energies of up to 8 AGeV.

The CBM Technical Status Report can be found on

`www-linux.gsi.de/~hoehne/report/cbmtsr_public.pdf`

Recent progresses in the development of Monolithic Active Pixel Sensors

M.Deveaux[1,2], A.Besson[1], G.Deptuch[1], W.Dulinski[1], D.Grandjean[1], F.Rami[1], M.Winter[1]

[1] IReS, Strasbourg, France; [2] GSI, Darmstadt, Germany

Introduction

The ambitious physics goals of the CBM experiment call for unprecedented performances of its vertex detector, as well in terms of spatial resolution and material budget as for read-out speed and radiation hardness. Monolithic Active Pixel Sensors (MAPS) are considered as candidates for this application as they already demonstrated an excellent spatial resolution (~1.5 µm) and a low material budget (< 120 µm silicon). However, the high luminosities envisaged for CBM set stringent requirements in radiation hardness and readout speed, which impose further investigations in the detector design. Moreover, a model allowing to simulate MAPS within the CBM simulation framework is needed for feasibility studies.

The corresponding R&D project, involving IReS and GSI, was started in 2003 [1]. The progresses achieved in 2004 are summarised hereafter.

1. Investigation of a new fabrication process

The performances of MAPS depend quite dramatically from a few fabrication parameters. The thickness of the epitaxial layer (EL) is of prime importance, as it determines the active volume and therefore the signal magnitude. The modest signal charge (a few 100 e^- ENC) delivered by a standard, <10 µm thick EL, makes it difficult to drive the signal conditioning micro-circuits necessary for the fast, massively parallel read-out required for CBM.

By the end of 2003, the manufacturer AMS announced a new 0.35 µm fabrication process optimised for MAPS imaging applications. It was supposed to provide an EL of ~20µm thickness and very low leakage currents from the sensing diodes. MIMOSA-9 was designed, fabricated and tested on a 120 GeV/c pion beam at the CERN SPS in order to explore this process. Excellent performances (e.g. 1.5 µm spatial resolution, 99.5% detection efficiency) were achieved. However, in contrast to the foundry announcement, the total cluster charge observed (~800-900 e^- ENC) and visual checks by microscope suggest an EL thickness of ~10 µm - 11 µm. The leakage current was measured to be about one order of magnitude below the typical values of previous chips but increased by up to two orders of magnitude already after 20kRad integrated ionising radiation dose.

Nevertheless, the new fabrication process can be considered as the most effective tested up to now and solutions to its radiation sensitivity are very likely to be found soon.

2. Fast read-out architecture

The strategy of a massively, column parallel read-out architecture requires integrating advanced functionalities, like leakage current and pedestal subtraction, inside each pixel. Every column has to be equipped with a single discriminator handling the signal coming out sequentially from the pixels.

Three different sensors with column parallel read-out (MIMOSA 6-8) were prototyped and tested since 2003. The noise of MIMOSA-6 came out to be enhanced by large pixel-to-pixel signal dispersions. In contrast, preliminary test results on MIMOSA-8 show an individual pixel noise of 13-18 e^- ENC and a charge-to-voltage conversion gain of 50-110 µV/e^-, depending on architecture details [2]. Those performances, which are comparable to conventional MAPS, come together with a modest pixel-to-pixel dispersion. This architecture, which is still being characterised in detail, provides the path to follow in 2005 for the next R&D steps.

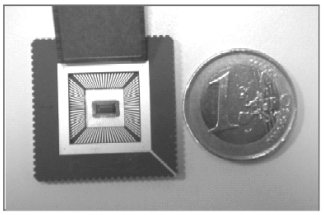

Fig 1: MIMOSA 8 developed with CEA/DAPNIA, on its read-out board. Made of 32 columns of 128 pixels each, it can be readout in ~20µs.

3. Radiation tolerance

The tolerance to ionising radiation was investigated in previous years with the MIMOSA-1, -2 and -4 sensors. It was found that ionising doses of about 200 kRad start degrading the detection performances, mainly due to leakage current and parasitic charge collection.

Within the SUCIMA collaboration (E.U. 5th Framework Programme), a dedicated radiation hard sensor, containing structures to reduce both of those unwanted effects, was designed and exposed to 1MRad so far. The sensor performances were found to be almost unaffected at an operating temperature around -15°C. While parasitic charge collection seems to be completely stopped, leakage currents lead to an increase of noise at higher temperatures [3].

In 2005, a next generation chip with several advanced radiation hard structures will be designed and tested in order to overcome this remaining weak point.

4. Detector simulation

A precise detector model is required for the ongoing studies of detection strategies for CBM. Of particular concern is the open charm detection relying on displaced vertex triggering in dense particle environments.

In order to allow the simulation of the consequences of future technology choices, an universal model of MAPS was provided, simulating the spatial resolution, detection efficiency and fake hit rate of the detector. Moreover, the expected pileup of several nuclear reactions within one read-out cycle of the vertex detector can be studied with this software [4].

References

[1] M.Deveaux et al., GSI annual report 2003

[2] Y.Degerli et al., Proc. of the IEEE NSS conference, Roma 2004. To be published in IEEE TNS.

[3] M.Deveaux et al., Proc. of the 5th RESMDD conference, Florence 2004. To be published in NIM A.

[4] M.Deveaux et al., CBM Internal Note (in preparation)

A Ring Imaging Cherenkov detector for CBM

C. Höhne[a], Yu. Kharlov[b], B. Polishchuk[b], V. Rykalin[b], S. Sadovsky[b], and the CBM collaboration
[a]GSI Darmstadt, Germany; [b]IHEP Protvino, Russia

The Ring Imaging Cherenkov Detector (RICH) for the CBM experiment is designed to provide electron identification in the momentum range of electrons from low-mass vector meson decays, $p \lesssim 10-12$ GeV/c. In addition, the RICH detector will be used for K/π separation at above 5-6 GeV/c, where the TOF capabilities quickly deteriorate. In the following, the overall design of the RICH detector, its main components and first simulation studies will be presented.

The overall design of the RICH detector is shown in Fig. 1. The detector will be positioned behind the dipole magnet about 1.5 m downstream of the target. It will consist of a 2.2 m long gas radiator with a beam pipe in the center, two arrays of spherical hexagonal Beryllium-glass mirrors, two photodetector planes and corresponding support structures. The total volume of the RICH detector will be about 60 m^3.

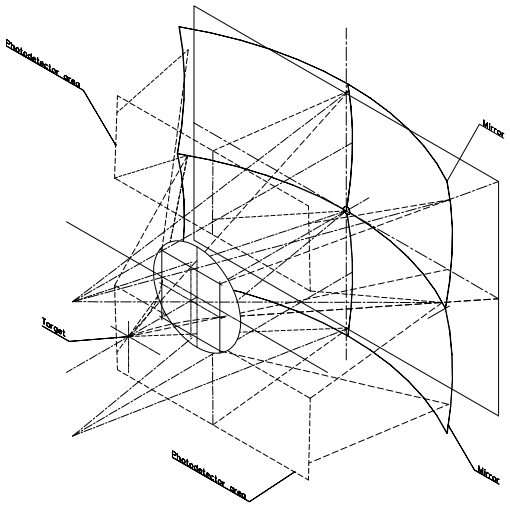

Figure 1: Overall design of the RICH detector.

The particle identification requirements introduced above restrict the choice of radiators to those with a threshold Lorentz factor $\gamma_{\rm th} \gtrsim 38$. Currently, several options are considered. Pure nitrogen as a radiator would fulfill all requirements, in addition it is non inflammable and a chemically passive gas. However, a disadvantage is that N_2 is a weak fluorescent gas in the UV region. Although the Omega RICH detector was successfully operated with nitrogen [1], its possible use in a high rate and high track density environment like at CBM has to be studied carefully. On the other hand, an admixture of e.g. 40% CH_4 or CO_2 can suppress the fluorescent light from N_2 [2]. A gas mixture difficult to cope with but with the aimed at $\gamma_{\rm th}$ and a long radiation length would be 40%He+60%CH_4.

The RICH mirrors will be made mainly of spherical hexagonal 3 mm thick Beryllium plates covered with 0.5 mm glass which forms an optically perfect mirror surface with a radius of 450 cm. The mirror plates will be assembled in two identical walls each having the overall dimensions of about 4.5×1.75 m^2. The measured optical surface roughness of a prototype after glass polishing, Al covering and SiO_2 coating is $\sigma_h = 1.6$ nm. These mirrors are chosen to provide excellent optics of the RICH detector with a low material budget at the same time.

The Cherenkov light produced by charged particles is focussed on two photodetector planes each covering an area of about 2.8×1.4 m^2. They will be positioned just after the dipole magnet yoke to reduce the background from particles crossing the photodetector plane. The main requirements for the photodetector are high granularity, high geometrical efficiency and high detection efficiency of photons, in particular in the near UV region, as well as a reliable operation. Currently, we concentrate on a design based on photomultipliers. IHEP Protvino in cooperation with Moscow Electrolamp Company (MELZ) has designed a small diameter photomultiplier tube with a bialkali photocathode (external $\varnothing = 6$ mm). The sensitivity in the UV range could be increased by covering the plain glass window of the photocathode with transparent wavelength shifter (WLS) films [3]. On the other hand, the readout of the RICH detector can as well be accomplished based on gaseous detectors with a suitable converter for UV photons.

Simulations have been started in order to study the layout of the RICH detector and to estimate the particle identification capabilities of the chosen setup. Size, position and orientation of the mirrors and the photodetector plane have to be optimized in order to improve the imaging properties of the setup, the adjustment of STS and RICH acceptance and the acceptance of high-momentum pions. The number of rings simulated per central Au+Au collision at 25 AGeV depends strongly on the material budget in front of the RICH detector and the mirror geometry and currently ranges between 40 and 80. The electron ring radius in the focal plane is about 5.5 cm. The number of photons detected per electron ring is determined by the wavelength dependent quantum efficiency of the chosen photodetector. A minimum of 10 photons is aimed at, with the photomultipliers developed at IHEP Protvino up to 35 photons could be detected. The high track density environment of CBM and the large number of electrons produced in secondary interactions complicate the ring-track matching and therefore diminish the purity of particle identification. Nevertheless, preliminary studies show that a pion rejection factor larger than 10^3 seems feasible.

References

[1] H.-W. Siebert et al., Nucl. Instr. and Meth. A 343 (1994) 60.
[2] H. Morii et al., Nucl. Instr. and Meth. A 526 (2004) 399.
[3] A. Kozhevnikov et al., Nucl. Instr. and Meth. A433 (1999) 164, A.M. Gorin et al., Nucl. Instr. and Meth. A 251 (1986) 461.

A Transition Radiation Detector for the CBM experiment at FAIR

A. Andronic[1], P. Braun-Munzinger[1], M. Kalisky[1], and the CBM Collaboration[1]
[1]GSI Darmstadt

A Transition Radiation Detector (TRD) was proposed for the CBM experiment [1] to provide electron identification and tracking of charged particles. It has to provide, in conjunction with the RICH detector and the electromagnetic calorimeter, sufficient electron identification capability for the measurements of charmonium and of low-mass vector mesons. The required pion suppression is a factor of about 100 and the required position resolution is of the order of 200-300 μm.

The gas mixture of the readout detectors has to be based on Xe, to maximize the absorption of transition radiation (TR) produced by the radiator. Because of the high rate environment expected in the CBM experiment, a fast readout detector has to be used. To ensure the speed and also to minimize possible space charge effects expected at high rates, it is clear that the detector has to have a thickness smaller than 1 cm. A multiwire proportional chamber (MWPC) with pad readout is the detector solution which we envisage to cope with the required granularity at small polar angles down to about 1 cm^2 cell size. The choice of the radiator type (regular or irregular) will be established after the completion of prototypes tests.

Currently, the whole detector is envisaged to be divided into 3 stations, positioned at distances of 4, 6 and 8 m from the target. A detailed study of the tracking performance in combination with all the CBM subdetectors is needed for a final decision on such a segmentation, as well as for the final requirements on position resolution within each of the planes. The total thickness of the detector in terms of radiation length has to be kept as small as possible to minimise multiple scattering and conversions.

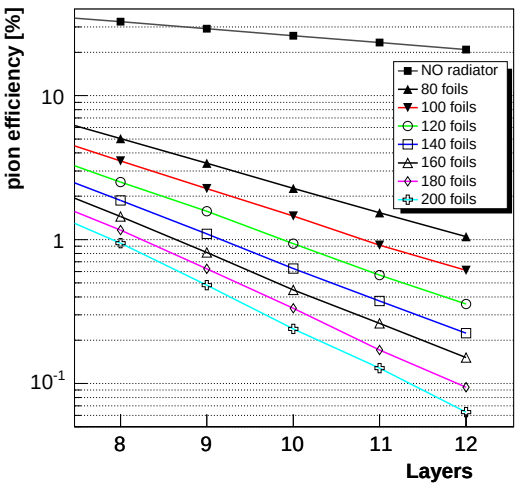

Figure 1: Pion efficiency as a function of the number of TRD layers for different number of foils. The pion efficiency based only on dE/dx (no TR included) is also shown. The detector thickness is 6 mm.

We present results on simulated electron/pion identification performance for a broad range of detector parameters. A standalone Monte Carlo C++ based simulation code was developed to perform the simulations. The basic ingredients of the simulations were validated in comparisons to measurements with ALICE TRD prototypes [2]. In Fig. 1 the pion efficiency as a function of number of layers is shown for different radiator thicknesses (number of foils, N_f). Also shown is the pion efficiency computed without radiator (only from dE/dx in case of electrons).

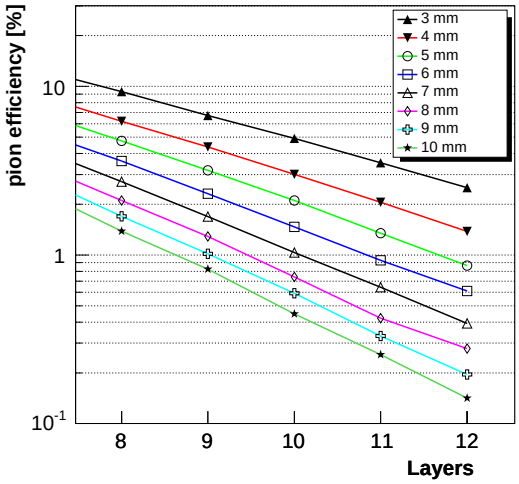

Figure 2: Pion efficiency as a function of the number of TRD layers for different detector gas thicknesses, for N_f=100.

Fig. 2 shows a similar dependence of the pion efficiency on the thickness of the gas readout chamber, for a fixed radiator thickness. The required pion efficiency can be reached with the proposed detector configuration of 9-12 layers. Different detector configurations will be further qualified. A lighter radiator (corresponding to less multiple scattering, which is more favorable for tracking) implies more layers (at higher costs for the extra electronics channels). A thicker readout chamber implies the benefit of fewer layers, but needs to be tested with prototypes concerning the rate capability and the position resolution performance. First investigations of detector prototypes in high rate conditions have already been performed and show promising results [3].

References

[1] Letter of Intent for the CBM Experiment at FAIR, Darmstadt, January 2004.
[2] A. Andronic et al., NIM A **522** (2004) 40.
[3] A. Andronic et al., this Report.

Hadron identification by TOF in the CBM experiment

T. Galatyuk[1], D. Kresan[2] and the CBM Collaboration
[1] GSI Darmstadt, [2]Univ. Kiev

The time-of-flight (TOF) detector system will serve for the identification of primary hadrons in CBM. The TOF system is located at approximately 10 m downstream from the target. For the results discussed below a time resolution of 80 ps is assumed.

The overall acceptances, calculated for central Au+Au events at 25 AGeV and p+A events at 80 AGeV with the UrQMD transport code, are listed in table 1. The values include decay-in-flight between STS and TOF. The acceptances do not vary strongly with beam energy even when calculated with a fixed magnetic field. By modification of the field, the acceptances can be optimized for different collision systems and beam energies.

Table 1: Acceptances of pions, kaons and protons for central Au+Au collisions at 25 AGeV and for p + Au collisions at 80 GeV including decay in flight.

	π^+	π^-	K^+	K^-	p
Au+Au 25 AGeV	0.40	0.40	0.34	0.35	0.54
p+Au 80 GeV	0.28	0.25	0.26	0.33	0.02

The particles are identified by a simultaneous measurement of momentum and velocity. Assuming that a track trajectory is reconstructed from the interaction vertex to the TOF system, the measured time-of-flight allows to calculate the velocity β of the particle. Together with the momentum p also following from track reconstruction, the (squared) mass of the particle can be calculated as $m^2 = p^2\left(\frac{1}{\beta^2} - 1\right)$. For fast particles the TOF resolution σ_t dominates the error in the squared mass over the contributions of momentum and track length inaccuracies. The two-dimensional distribution of m^2 as a function of transverse momentum is shown in the upper panel of figure 1 for positively charged particles as generated by UrQMD for central Au+Au collisions at 25 AGeV . The lower panel depicts the m^2 spectrum of positively charged particles at p_{lab} = 4 GeV/c. The solid line shows the fit to the spectrum, the dotted lines the contribution of the single particle species (π, K, p). By unfolding of the m^2 spectrum, kaon spectra can be determined up to a momentum of 8 GeV/c, provided that the shape of the single particle contribution to the spectrum (which is here taken as Gaussian) is known. The overall acceptance for pions and kaons in the plane rapidity versus transverse momentum is presented in figure 2.

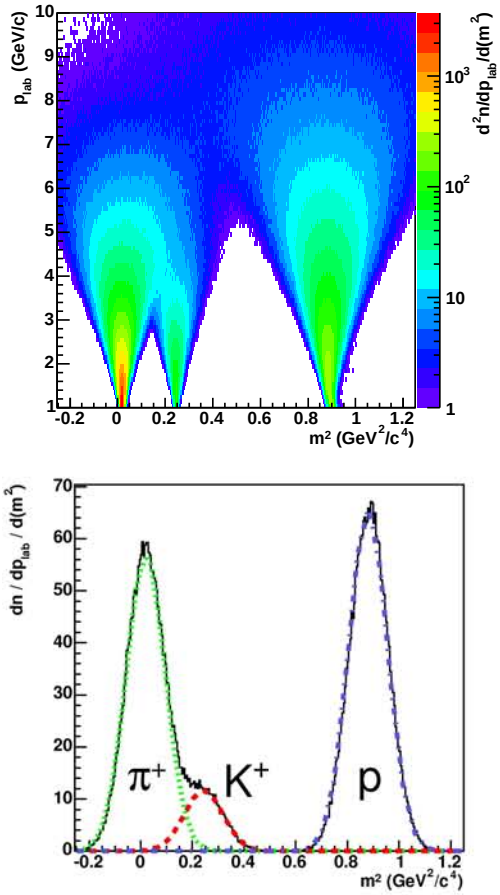

Figure 1: Upper panel: Distribution of m^2 versus momentum for positively charged hadrons. Lower panel: m^2 spectrum of positively charged particles at $p_{lab} = 4$ GeV/c. The distance between target and TOF detector is 10 m, the time resolution 80 ps.

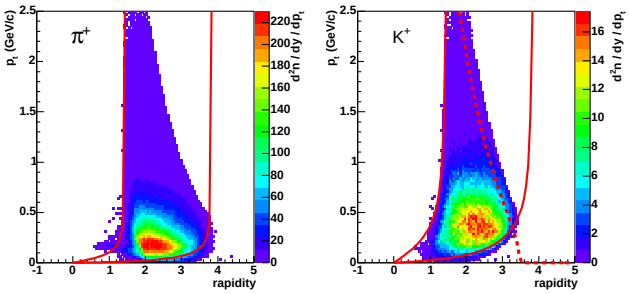

Figure 2: Phase space distribution of TOF-identified pions and kaons. The two solid lines show the geometrical acceptance of the STS and TOF and correspond to the polar angles 2.5 and 27 degrees. The dotted line shows the identification limit for K^+ at $p = 8$ GeV/c.

CBM Simulation and Analysis Framework

M. Al-Turany[1], D. Bertini[1], and I. Koenig[1]
[1]GSI

1 Introduction

The development of the current simulation and analysis framework has started at the end of 2003. The framework is completely ROOT [1] based. The modified HADES geometry interface used in this framework enables the user to select (on the fly) between the new ROOT Geometry Modeler and the Geant3 native geometry to describe the detectors. An Oracle database with a build-in versioning management is used to store efficiently the detector geometries, materials and parameters. Moreover the analysis is organized using the ROOT Tasks mechanism.

2 Design and implementation

The schematic design of the CBM framework (CbmRoot) is shown in Fig.[1].

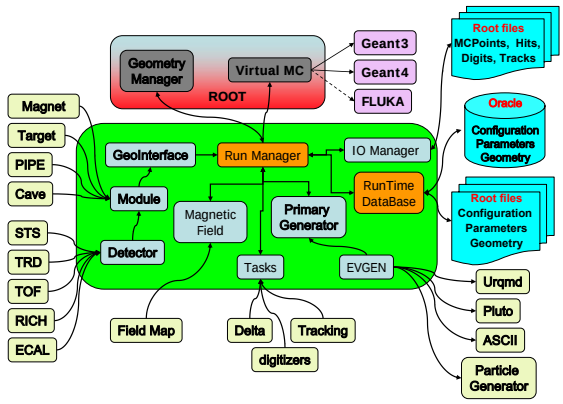

Figure 1: Schematic design of the CBM simulation and analysis framework

The CBM framework design follows some basic requirements:

- Fully based on the ROOT system.
- The user should have the possibility to create simulated data and also to perform data analysis using the same framework.
- Geant3 and Geant4 transport engine should be supported.
- The user code that creates simulated data should not depend on a particular monte carlo engine. For that purpose, the virtual monte carlo interface from the ROOT system has been used.

It should also provide some basic functionalities:

- Input/Output procedures.
- Parameters definition (geometry of the detectors, physic process definition, hit digitization, etc.)
- Implementation of the algorithms: the analysis should be organized in tasks.

The CBM Framework incorporates these requirements by defining the following set of classes:

2.1 The Run Manager class: CbmRun

This class controls the whole simulation and analysis program, providing methods to configure and add the different tasks which can be realized. For the simulation part, this includes methods to set the different:

- input / output files
- event generators
- monte carlo transport engines
- magnetic field map definitions
- material/medium definitions
- passive/active detector definitions

In the analysis case, the same class is used to organize the reconstruction process into a list of separated tasks, giving the user the possibility to switch on/off part of the reconstruction chain at run time.

2.2 The Monte Carlo Application: CbmMCApplication

This class uses the services of the ROOT Virtual Monte Carlo Application interface (class TVirtualMCApplication) to define the actions at each stage of the simulation run. These are:

- Geometry construction
- Geometry initialization
- Storage of primary track in an external stack container
- Pre-tracking action
- Stepping action and dispatching the hit processing to individual sensitive detectors
- Post-tracking action

2.3 The Input/Output Manager: CbmRootManager

This class is responsible of writing and reading all persistent data objects created in memory during a simulation run. The storage of all information collected by the different sensitive detectors is done on an event by event basis (an event means in this context one interaction between one beam particle and the target) . All persistent objects are serialized and stored into binary ROOT files. An

interface class (CbmMCPoint) is provided to define the structure of registered hit in a detector. Each detector can then provide a more specific implementation following the CbmMCPoint API. All registered hits will be collected into dedicated lists, one list corresponding to one detector entity. The ROOT class TTree is used to organize the output data into a "ntuple like" data structure . In the analysis case , the CbmRootManager provides methods to read this information. The user can select a subset of all registered list corresponding to his analysis tasks definition. A partial input/ouput mechanism is supported.

2.4 Parameter classes

Classes to contain and to manage all the numerical information needed to process the data (parameter).In order to analyse the simulated data, several numerical parameters are needed, as for example, calibration/digitization parameters or geometry positions of detectors. One common characteristic to most of these parameters is that they will go through several different versions corresponding, for example, to changes in the detectors definition or any other condition. This makes necessary to have a parameter repository with a well-defined versioning system. The runtime database (realized through the CbmRuntimeDb class) is such a repository. Different inputs are supported : Ascii format , ROOT binary format and Oracle Database input.

2.5 Tasks Classes (CbmTask)

For each event we need to accomplish various tasks or reconstruction algorithms The CbmTask is an abstract class defining a generic API allowing to execute one task and to navigate through a list of tasks. The user can create his own algorithm inheriting from CbmTask. Each task defines the relevant input data and parameter and creates its particular output data during the initialization phase. During the execution phase, the relevant input data and parameters are retrieved from the input file and the output data objects are stored in the output file.

3 Conclusion

The HADES simulation is now being adapted to the CBM framework, this will enable us to validate the ROOT navigation system (TGeoManager) against the native Geant3.

References

[1] R.Brun and F.Rademakers,"ROOT An object oriented Data Analysis Framework" ,Nucl. Inst. Method Phys. Res.,VolA389, P81-86,1997.

Event reconstruction in the CBM experiment

P. Akishin[1], E. Akishina[1], S. Baginyan[1], V. Friese[2], S. Gorbunov[3], J. Gläß[4], A. Ierusalimov[5], V. Ivanov[1], I. Kisel[6], B. Kostenko[1], E. Litvinenko[1], A. Malakhov[5], G. Ososkov[1], A. Soloviev[1], I. Vassiliev[2], P. Zrelow[1], and the CBM collaboration

[1]JINR-LIT, Dubna; [2]GSI, Darmstadt; [3]DESY, Zeuthen; [4]Univ. Mannheim; [5]JINR-LHE, Dubna; [6]Univ. Heidelberg

The CBM experiment will be designed to measure heavy-ion collisions at beam energies between 10 and 35 AGeV with unprecedentedly high interaction rates (up to 10^7 / s). Tracking will be provided by the Silicon Tracking System (STS) located inside the magnetic dipole field close to the target and several TRD detector layers outside of the field. In a central Au+Au collision at 25 AGeV, about 600 - 700 charged tracks are inside the STS acceptance (see figure 1). In this environment, the tracks have to be reconstructed with high efficiency ($> 90\%$) and good accuracy (required momentum resolution $< 1\%$). Moreover, the online event selection required to arrive at an estimated archival rate of 25 kHz calls for fast algorithms suitable to be implemented in programmable hardware.

Several approaches to both pattern recognition and determination of track parameters in the STS have been undertaken. The Hough transform method, transforming the hit coordinates into the three-dimensional Hough space and looking for peaks in this space, seems appropriate for fast tracking. The Cellular Automaton algorithm, which creates and links tracklets between the tracking stations, shows a comparable performance. 3D track following methods, either with or without a Conformal Mapping hit coordinate transformation, have been developed as well. All algorithms show a track finding efficiency above 90 % for $p > 2$ GeV/c (see figure 2). The efficiency decreases rapidly for lower momenta due to the lower number of measured points. For this track class, improvement of the algorithms is still needed.

As in the case of track finding, several methods for the determination of the track parameters have been investigated. These comprise global fitting methods using an approximate solution of the equation of motion in the inhomogeneous magnetic field as well as local methods, e. g. the Kalman filter. Figure 3 shows the momentum dependence of the relative momentum resolution obtained by a global fit method. A resolution of less than 1 % for momenta above 1 GeV/c is feasible. For low momentum tracks, the Kalman filter seems to be more appropriate. The momentum determination can possibly still be improved by combining the Kalman filter with the method of Orthogonal Polynomial sets, mapping the measured deflection angle to the momentum by simulation.

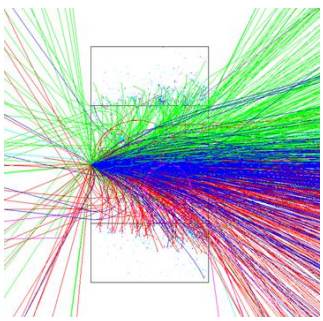

Figure 1: Visualisation of a simulated central Au+Au event at 25 AGeV in the STS system

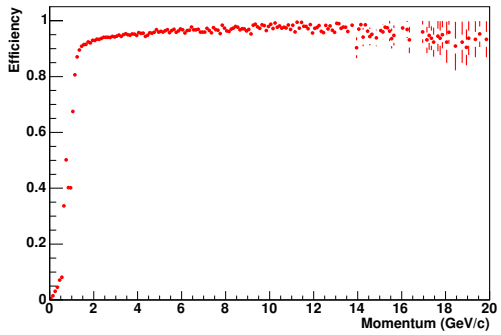

Figure 2: Track finding efficiency in central Au+Au at 25 AGeV for tracks with at least three hits in the STS, obtained with the Cellular Automaton method, as a function of momentum

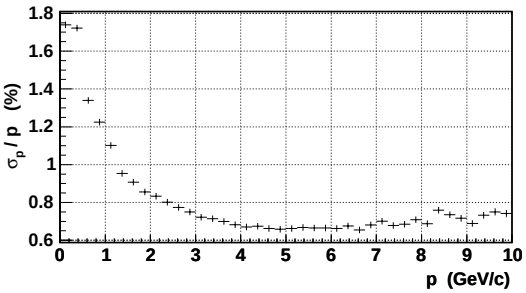

Figure 3: Relative momentum resolution as a function of momentum obtained with the Parabolic Approximation track fitter for tracks with at least three hits in the STS

Some of the algorithms developed for tracking in the STS have been applied to the TRD as well. Preliminarily, the track finding efficiency turns out to be similar to that found in the STS. Of particular interest in view of a fast event selection for the J/ψ measurement is the determination of the momentum from the TRD alone, assuming the track to originate from the target. By calculating an average field integral, the momentum can be reconstructed with an accuracy of about 8 % (see figure 4). Since the TRD delivers electron identification at the same time, this approximate momentum reconstruction is a candidate for the online selection of charmonium events, which necessi-

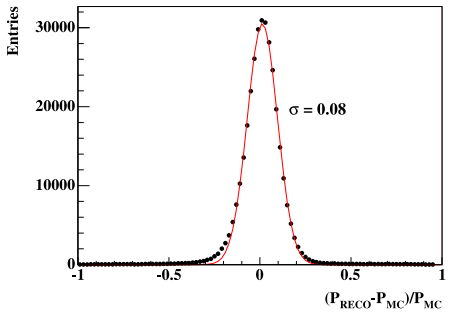

Figure 4: Relative momentum residuals of e^+ and e^- from J/ψ decay, using the fast momentum reconstruction in the TRD

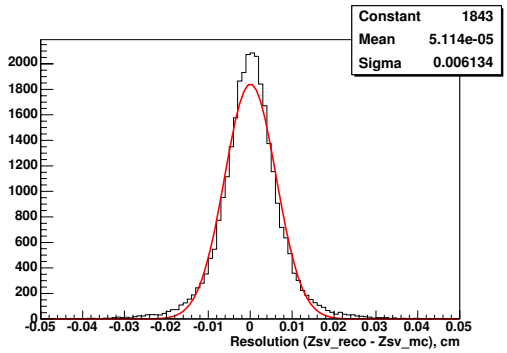

Figure 6: Residuals of the vertex z coordinate for track pairs from D^0 decays, reconstructed by the Kalman filter with topological and mass constraints

tates electron ID as well as a cut on the single track p_t.

The primary event vertex can be determined directly from the about 500 reconstructed tracks by minimisation of the track impact parameters or by use of the Kalman filter technique. The latter provides an accuracy of about 1 μm in the x and y positions and about 5 μm in beam direction. These values deteriote for events with lower multiplicity as demonstrated in figure 5.

The precise determination of secondary (decay) vertices is a prerequisite for open charm measurements. The Kalman filter has been applied to this problem as well. A geometrical fit with topological and mass constraints provides an accuracy of about 60 μm for the vertex coordinate in beam direction (see figure 6). This is well in range for an effective background suppression needed for the detection of D^0 mesons ($c\tau = 127\mu$m).

Rings in the RICH detector can be reconstructed using centre guidance by extrapolation of reconstructed tracks to the photodetector plane or by standalone methods. For the latter, a Hough transform method and the Elastic Net algorithm have been tested. Figure 7 shows a RICH event with rings reconstructed by the Elastic Net ring finder. The reconstruction efficiency for tracks originating from the target region and having at least 15 detected photons is 92 %. On average, 33 rings are found per central Au+Au

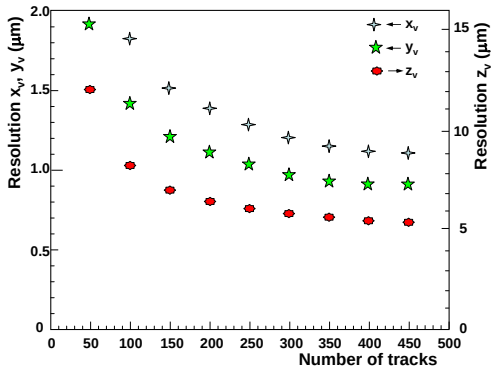

Figure 5: Resolution of the primary vertex coordinates as function of the number of tracks used for the fit

event at 25 AGeV. The ghost rate is about 15 %. These fake rings could be suppressed by matching found rings to reconstructed tracks in a next step. Due its good timing performance, the algorithm is also considered to be suited for online event selection.

First studies with a robust ring fitting algorithm similar to that used in the CERES experiment show that the radius of the rings can be determined with a precision of about 2 mm, the typical electron ring radius being 5 cm.

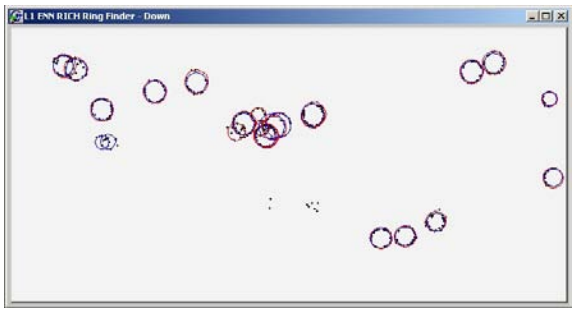

Figure 7: Example of a RICH event (lower photodetector plane) reconstructed by the Elastic Net ring finder. The reconstructed rings are shown in blue, the true ones in red.

This brief summary demonstrates that promising methods for event reconstruction in CBM are being developed. It should, however, be noted that most of the algorithms still work under idealised assumptions. In particular, the event pile-up associated with the rather long readout frame of the MAPS detectors (several μs compared to an average event spacing of 100 ns at the maximum interaction rate) has not been adressed so far. In addition, electronic noise and delta electrons originating from the target will have to be taken into account. The algorithms will be tested and improved under these more realistic conditions, using simulated detector response instead of pure transport data. These studies will also provide feedback for the design of the tracking devices. The final choice of algorithms will be based on efficiency and accuracy as well as on timing performance.

.

D^0 meson detection in $Au + Au$ collisions at 25 AGeV in the CBM experiment

Iouri Vassiliev[1], S. Gorbunov[2], V. Friese[1], I. Kisel[3], and the CBM Collaboration[1]

[1]Gesellschaft für Schwerionenforschung mbH, Darmstadt, Germany; [2]DESY, Zeuten, Germany; [3]Kirchhoff Institute of Physics, University of Heidelberg, Germany

One of the major experimental challenges of the CBM experiment is to trigger on the displaced vertex of the D-meson hadronic decay in the environment of a heavy-ion collision. This task requires fast and efficient track reconstruction algorithms and high resolution secondary vertex determination. Events without D-mesons have to be suppressed by a factor of more than 400 in order to reduce the envisaged reaction rate of 10 MHz down to the archiving rate of 25 kHz. Particular difficulties in recognizing the displaced vertex of the rare D meson decays are caused by: weak hyperon decays which produce displaced vertices between the target and first silicon tracking station, very low multiplicity of D^0 and $\bar{D}^0$ mesons production in central $Au + Au$ collisions at an energy of 25 AGeV, multiple scattering in detectors and beam pipe limiting the accuracy of track reconstruction and vertexing, lifetime of the D^0 mesons is $c\tau = 123.7$ μm.

To study the feasibility of a D^0 measurement in the CBM experiment 10^5 $Au + Au$ central UrQMD events at 25 $AGeV$ have been simulated. The K^- and π^+ pair from D^0 decay has been added as a signal to each event in order to simulate a signal in the environment of the background hadrons. The primary vertex was determined with high accuracy (few μm) from about 500 tracks fitted in the STS by the Kalman filter procedure. The secondary vertex resolution of 57μm without and 65μm with magnetic field is sufficient to separate detached vertices from the primaries [2].

The D^0 meson decays through a week process, consequently, in case of D^0 decaying to $K^- + \pi^+$ the two tracks have relatively large impact parameter and the distance between the primary vertex and decay point is measurable. Since the majority of the primary tracks have very small impact parameter, significant part of the combinatorial background could be rejected using the impact parameter cut.

The main background contributions are due to combinatorics (wrong vertex or track reconstruction) and due to hyperons decay, mainly K^0_S and Λ, $\Sigma^{+(-)}$, Ξ^- and Ω^-. One UrQMD event contains in average 7.6 K^0_S and 10.5 reconstructible Λs. The combinatorial background is suppressed mainly by track IP cut (lower value), z-vertex cut, as well by D^0 pointing cut (when one track from D^0 decay is combined with bad reconstructed track), p_t-cut, vertex χ^2 cut and p-cut. After applying all cuts background is suppressed by a factor of $2 \cdot 10^4$ in the signal mass region. The signal reconstruction efficiency is about 11%, the geometric acceptance is about 48%, resulting efficiency is about 5.3%. The optimized cut values together with the signal efficiency are shown on the table. In order to determine a signal to background ratio with such a large background suppression factor at least few times 10^7 MC events need to be simulated. The shape of the background in the signal IM region was estimated using so-called "MC super event" technique. One super event was equivalent to $3.6 \cdot 10^7$ UrQMD events. The multiplicity of $D^0 + \bar{D}^0$ mesons is $1.5 \cdot 10^{-4}$ per central $Au + Au$ event at 25 $AGeV$ according to the HSD model [1]. Taking into account the BR = 3.8 %, the signal efficiencies, the resulting background plus signal spectrum is shown in figure 1.

Table 1: cut parameters

cut	optimized value	signal efficiency %
track IP cuts	80 <IP< 500 μm	28
p-cut	1.0 GeV/c	72
pt-cut	0.5 GeV/c	61
z-vertex cut	250 μm	54
D^0 *pointing cut*	30 μm	99
vertex χ^2 *cut*	$\leq$5	91
all cuts	-	5.3

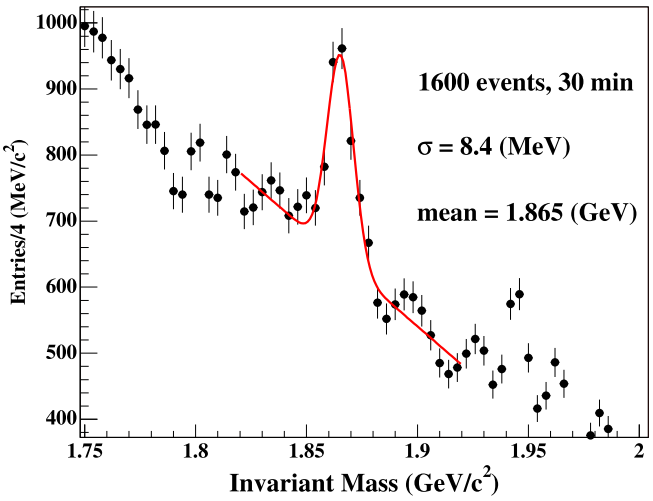

Figure 1: Invariant mass simulated signal plus background spectrum. The D^0 mass peak is clearly visible. Data taking time is about 30 minutes at 1 MHz central collision rate. No magnetic field is taken in to account

References

[1] W. Cassing and E. Bratkovskaya, Phys. Rep. 308 (1999) 165.

[2] Technical Status Report, CBM Collaboration, (2005), chapters: 13.2.1, 13.3.2, 13.4.

J/ψ detection via electron-positron decay in CBM

G.Kruzic[a], A.Maevskaya[c], E.L.Bratkovskaya[b], and the CBM collaboration

[a]GSI Darmstadt, Germany; [b]Institut für Theoretische Physik, Frankfurt, Germany; [c]Institute for Nuclear Research, Moscow, Russia

The measurement of open charm and charmonium production is one of the central aims of the CBM experiments at the future FAIR facility. The feasibility of detecting charmonia essentially depends on the J/Ψ signal relative to the background. In this contribution we investigate the possibility to identify the J/Ψ via the invariant mass spectrum of e^+e^- pairs which is a 7% decay branch of the lightest charmonium state. In order to ensure realistic J/ψ electron-positron decays in the CBM simulations the Hadron String Dynamics (HSD) transport approach [1, 2] has been used to predict the various particle multiplicities. The resulting J/Ψ multiplicities from these calculations are shown in Fig. 1 for the case of Au-Au collisions at impact parameter b=0.5 fm as a function of bombarding energy.

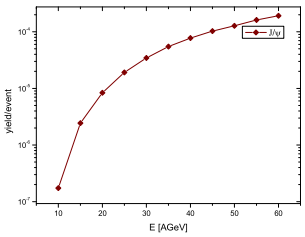

Figure 1: The J/ψ multiplicity from the HSD model for Au-Au at impact parameter b=0.5 fm as a function of the bombarding energy.

The J/ψ phase space distribution, furthermore, has been independently calculated by the PLUTO event generator assuming a thermal source of temperature T=170 MeV for the beam energy of 25 AGeV (normalized to the J/Ψ multiplicity from Fig. 1). To analyse the J/ψ electron-positron decay channel relative to the various sources the following background channels have been considered explicitly: e^+, e^- pairs from γ conversion in the target and detector materials, Dalitz decays of π^0 and η, direct decays of light vector mesons (ρ^0,ω and ϕ) as well as semileptonic decays of D-mesons. The semileptonic D-meson decays have been simulated by a newly developed thermal semileptonic fast event generator that adopts the particle multiplicities as predicted by the HSD model. The residual background sources have been, furthermore, simulated by transporting UrQMD events through the standard CBM detector simulation setup via GEANT3. As demonstrated in Ref. [3] the transport models HSD and UrQMD lead to almost identical results in the energy range from 20 - 30 AGeV for the light and strange hadrons. Additionally it has been assumed that 0.01% of electron-pion pairs might be misidentified as e^+e^- pairs. A finite momentum resolution of 1% has been incorporated, too.

At shown in Fig. 2 the contribution of e^+e^- background sources can be significantly reduced by a cut on the transverse momentum of the leptons, $P_T \geq 1$ GeV/c. When including the 1% momentum resolution and 0.01% electron-pion misidentification we end up with a visible J/ψ peak in the invariant mass spectrum of e^+e^- pairs (corresponding to $2 * 10^{10}$ events) as can be seen in Fig. 3. We conclude that the J/Ψ identification via the e^+e^- decay channel appears suitable in central collisions of Au+Au at 25 AGeV and above, however, becomes questionable at lower bombarding energies.

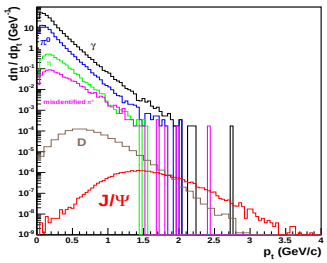

Figure 2: Transverse momentum spectrum of the e^- background contribution calculated for Au-Au at 25 AGeV within UrQMD. Black: γ conversion in the target; blue: π^0 Dalitz decay; green: η Dalitz decay; magenta: misidentified charged pions 0.01%; grey: open charm; red: J/ψ.

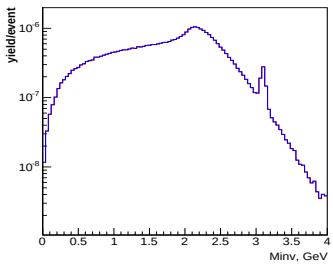

Figure 3: Invariant mass spectrum of e^+e^- pairs from $2 * 10^{10}$ events for Au-Au at 25 AGeV employing a cut $P_T \geq 1$ GeV/c and an electron-pion misidentification of 0.01%. The calculated signal to background ratio is S/B=1.

References

[1] E.L.Bratkovskaya, A.P.Kostyuk, W.Cassing, and H.Stöcker, Phys. Rev. C 69, 054903 (2004).

[2] W.Cassing, E.L.Bratkovskaya, S.Juchem, Nucl. Phys. A 674, 249 (2000).

[3] H. Weber et al., Phys. Rev. C 69, 014904 (2003).

J/ψ detection via $\mu^+\mu^-$ decay in CBM

V. Baublis[2], A. Khanzadeev[2], A. Kiseleva[1], Y. Riabov[2], V. Samsonov[2], P. Senger[1], and M. Zhalov[2]
[1]GSI Darmstadt; [2]PNPI, St. Petersburg

In addition to the measurement of J/ψ mesons via e^+e^- pairs in the future CBM experiment we have studied the possibility to detect J/ψ mesons via their decay into $\mu^+\mu^-$. This measurement would require a muon detector located after the TOF wall. It might be either a longitudinally segmented electromagnetic calorimeter (ECAL) or an additional dedicated device behind the ECAL. The study has been started recently and is still in a preliminary state.

The J/ψ signal decay was simulated with the PLUTO generator assuming a thermal source with a temperature of 130 MeV. The J/ψ multiplicity of 1.9×10^{-5} for central Au+Au collisions at 25 AGeV beam energy was taken from the HSD prediction [1]. The background, consisting mainly of decays of charged pions and kaons, was calculated with the UrQMD event generator for the same system. Both signal and background are transported through the detector setup with CBMROOT employing GEANT3. In this first step, the analysis is based on the following simplifying assumptions:

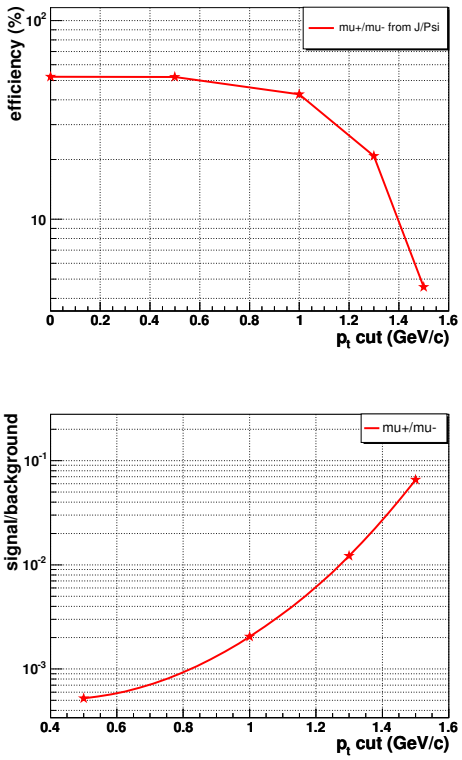

Figure 1: Efficiency for J/ψ meson detection (upper panel) and signal to background ratio (lower panel) as function of the transverse momentum cut p_t

- the muons are detected with 100% efficiency in a plane located 11 m downstream from the target,
- ideal track reconstruction is assumed. The momentum resolution was assumed to be 1%.

Taking into account the branching ratio of 6%, the multiplicity of J/ψ mesons decaying into a dimuon pair is only about 10^{-6} per central Au+Au collision at 25 AGeV. Figure 1 shows the efficiency for the J/ψ detection and the signal to background ratio, calculated in a $\pm 2\sigma$ window around the signal peak, as function of the minimal single muon p_t. For a cut at 1 GeV/c, the S/B ratio is about 0.2%, the efficiency being about 42%. Apparently, p_t cuts above 1.5 GeV/c are prohibitive because of the rapid drop in detection efficiency.

Further suppression of the background muons from pion or kaon decays can be achieved by measuring the kink angle between the trajectory of the meson and its decay muons. By a cut in this variable, most of the muon background originating from pion or kaon decay can be eliminated as shown in figure 2. The remaining background is almost exclusively due to misidentified pions, which cannot be suppressed by the kink angle cut. A measurement of J/ψ in the dimuon channel thus requires a charged pion supression of 10^3 or more and a measurement of the kink angle with a precision of a degree or better.

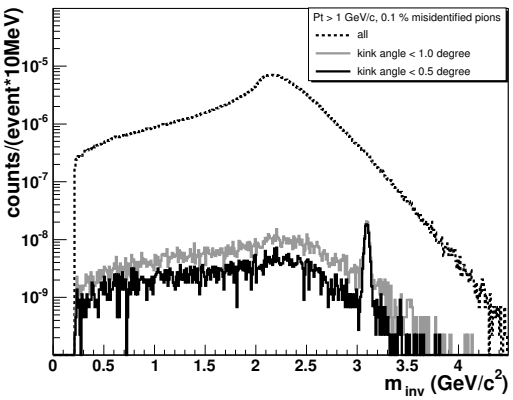

Figure 2: Invariant mass spectrum of muon pairs from central Au+Au collisions at 25 AGeV. The spectra include the combinatorial background, the J/ψ signal and a 0.1% contribution of misidentified π^+ and π^- mesons. The background is suppressed by the transverse momentum cut of $p_t > 1$ GeV/c, and by different kink angle cuts of 1.0^o (gray histogram), 0.5^o (black histogram). The black dotted histogram shows the spectrum without kink angle cut.

References

[1] W. Cassing, E. Bratkovskaya, A. Sibirtsev, Nucl. Phys. A 691 (2001) 74.

DAQ and Online Event Selection for CBM

Hans Essel[1], Joachim Gläß[2], Sergej Linev[1], Walter F.J. Müller[1], and the CBM Collaboration
[1]GSI, Darmstadt, Germany, [2]Mannheim University, Germany

The measurement of open charm is the key factor shaping the architecture of front-end electronics, data acquisition, and event processing in CBM. The D-mesons will be identified via the displaced vertices of their hadronic decays. The decision for selecting candidate events thus requires tracking, primary vertex reconstruction, and secondary vertex finding in the STS at the full interaction rate of 10 MHz. The execution time of such complex algorithms will vary strongly depending on the centrality of the interaction. This does not match well with the conventional system design using triggered front-end electronics, where the information of an event can be held for a limited time, usually only a few μs, in the front-end until a first level trigger decision prompts the data acquisition system to collect all data of an event and transport it to further processing stages.

CBM adopts a different approach. The front-end electronics of all detectors will be self-triggered. Each particle hit is autonomously detected and the measured hit parameters are stored with precise time stamps in large buffer pools. The event building, done by evaluating the time correlation of hits, and the selection of interesting events is then performed by processing resources accessing these buffers via a high speed network fabric. The essential performance factor is now computational throughput rather than decision latency, which results in a much better utilization of the processing resources especially in the case of heavy ion collisions with strongly varying multiplicities. Since there are no dedicated trigger data-paths, all detectors can contribute to the event selection from the first decision level on. The communication and processing resources can be configured to select relevant events for a wide range of physics signals, ranging from D and J/ψ detection in A-A collisions over low-mass dilepton detection in p-A collisions to Υ detection in p-p collisions at up to 500 MHz interaction rate.

This approach is very data intensive. In CBM the data flow from the front-ends to the processing resources will be about 1 TByte/sec. Fig. 1 shows a logical data flow diagram for an organization of the communication and processing needed between the front-end electronics and the archival storage, where the context of selected candidate events is recorded. The main components are:

- **Front-end electronics (FEE):** The front-end detects autonomously every particle hit and sends the hit parameters together with a precise timestamp and channel address information over the concentrator network (CNet) to a buffer pool.
- **Clock and time distribution (TNet):** Is a broadcast network, connecting a central controller logically with all front-end units, and distributes a low jitter clock (<25 ps sigma) and information about the absolute time.
- **Concentrator Network (CNet):** A rough estimate for the total data rate is 1 TB/sec, which requires about 1000 links with 10 Gbps each.

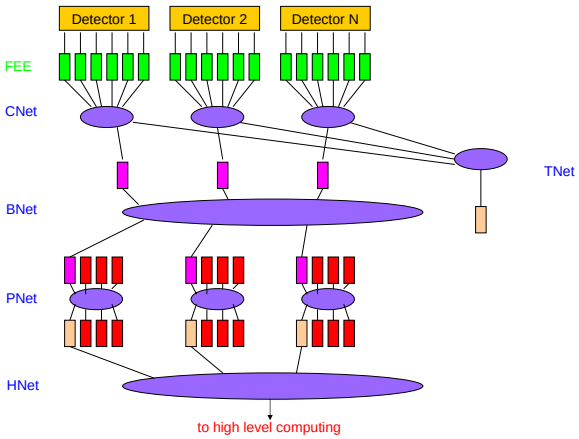

Figure 1: CBM overall data processing architecture

- **Active Buffers:** The next stage in the data flow is a large buffer pool, represented by magenta boxes in Fig. 1. They also separate the networks, allowing to use different technologies in CNet, BNet, and PNet.
- **Build Network (BNet):** For the event selection processing, the information of an event has to be assembled in a farm node. This data reorganization is performed by the build network and the active buffers.
- **Processing Resources:** A very rough estimate shows, that processing a data flow on the scale of a TByte/sec is likely to require a computational bandwidth on the scale of 10^{15} operations/sec. With todays technology, the most promising approach is a hybrid system using a combination of hardware processors, implemented with programmable logic components like FPGA's, and software processors, implemented with commodity PC's. The kernels of algorithms which allow highly parallel execution are done in hardware processors, the rest in software processors.
- **Processing Network (PNet):** The processing resources are grouped in farm nodes, each organized around a local processing network. The PNet is thus structured into many local networks.
- **High-level Network (HNet):** The HNet provides the connection to high-level event selection and reconstruction processing.

The key R&D areas for CBM are the development of self-triggered front-end electronics with adequate output bandwidth, of a data processing system which allows to combine the advantages of hardware processors build from programmable logic and software processors, and last but not least, of highly efficient feature extraction and event selection algorithms adapted to such a processing environment.

RPC development for CBM

A. Akindinov[7], V. Ammosov[8], E. Badura[3], M. Ciobanu[3], E. Cordier[4], F. Dohrmann[9], R. Ferreira Marques[2], P. Fonte[2], J. Garzon[10], D. Gonzalez-Diaz[10], Y. Grishuk[7], F. Guber[6], N. Herrmann[4], O. Karavichev[6], S. Kiselev[7], K. Koch[3], B. Kohlmeyer[5], R. Kotte[9], A. Kuznetsov[8], A. Maevskaia[6], A. Mangiarotti[4], A. Martemiyanov[7], M. Petrovici[1], A. Policarpo[2], V. Rasin[6], A. Schüttauf[3], A. Semak[8], A. Smirnitskiy[7], G. Stoicea[1], Y. Sviridov[8], V. Tiflov[6], K. Voloshin[7], V. Zaets[8], B. Zagreev[7], and the CBM Collaboration

[1] National Institute for Physics and Nuclear Engineering, Bucharest, Romania; [2] LIP, Coimbra, Portugal; [3] GSI, Darmstadt, Germany; [4] Physikalisches Institut, Universität Heidelberg, Germany; [5] Fachbereich Physik, Universität Marburg, Germany; [6] Institute for Nuclear Research, Moscow, Russia; [7] ITEP, Moscow, Russia; [8] IHEP, Protvino, Russia; [9] FZR, Institut für Kern- und Hadronenphysik, Rossendorf, Germany; [10] Universidad de Santiago de Compostela, Santiago de Compostela, Spain

The purpose of the TOF subdetector system of the CBM experiment is the identification of hadrons. The requirements imposed by the running conditions [1] are such that a time resolution better than 80 ps is necessary over the full acceptance and thus under different count rate loads ranging from 20 kHz near the beam axis to about 1 kHz at 28^o. The hit density changes significantly from 10^{-2}cm^{-2} to $6 \cdot 10^{-4}\text{cm}^{-2}$. In order to achieve a two to three sigma separation flight pathes in the order of 10 m are necessary. Therefore the full coverage of the same solid angle as the tracking system requires an area of the TOF system in the order of 150 m^2. The choice adopted by the CBM collaboration is to develop multigap timing RPCs.

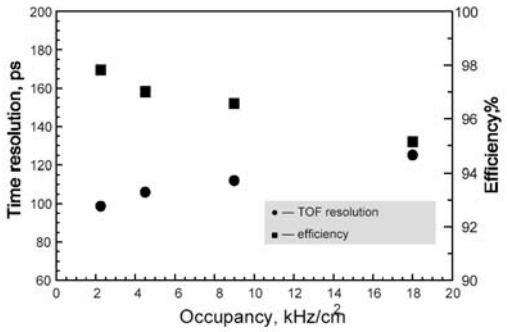

Figure 1: Time resolution and efficiency of an RPC prototype made of phosphate glass as a function of the beam rate

Semiconductive glass is one of the best candidate for electrode material to have very good time resolution for such high rates. Disadvantages are the absence of mass production and high prices of the prototype samples. Semiconductive glasses have been developed in Russia since the 60's of the last century. There are three known types of semiconductive glasses depending on the base material selected for their production: phosphate, silicate and borosilicate glasses. They are characterized by electron conductivity and contain the oxides of transition elements. INR started an R&D program about one year ago. Different samples from phosphate and silicate glasses [1] have been produced. A RPC prototype using phosphate glass has been produced and was tested at ITEP PS with MIPs. Results of the efficiency and time resolution measurements are shown in Fig. 1. Besides plastic materials are actively investigated at LIP [2].

The associated electronics must process the pulses with a minimum amount of supplementary time errors. The amplified and leading edge discriminated signal starts the time digitizer and the reference signal stops it. In our concept, the amplifier and discriminator blocks are included in the FEE TOF preamplifier unit [1]. Parasitic signals coupled from outside to the measurement channel increase the jitter. To decrease this influence, the CBM FEE should be oriented to differential coupling to the detector. A low cost solution would be to use twisted pair cables giving a moderate rejection of parasitic pick-up. The time over threshold walk correction can be favorable in the high integration case because it needs two time values instead of time and amplitude information. Based on experience from the FOPI experiment, we estimate the main technical parameters for the TOF preamplifier to be: gain >100, differential input impedance with 50 Ohms to ground of each line, bandwidth >1 GHz, noise related to input <20 μV rms, threshold 50-100 mV, time over threshold 1-10 ns, output Signal LVDS [1]. Fig. 2 shows a typical dependence of the Time Resolution to the input pulses amplitude, for the case of FEE TOF preamplifier made with discrete IC.

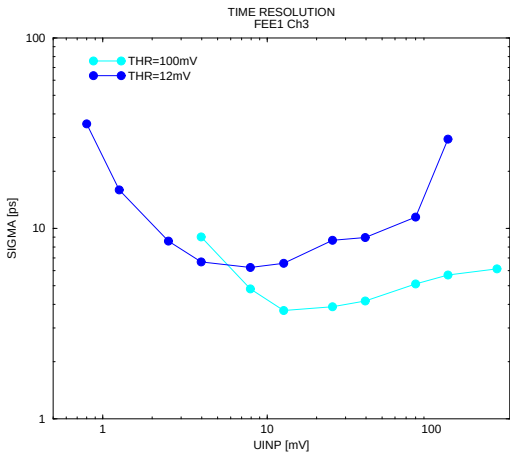

Figure 2: Time resolution as a function of signal amplitude

References

[1] CBM Collaboration, *Tech. Status Report CBM (2005)*
[2] L. Lopes et. al., *Nucl. Inst. and Methods A 533 (2004) 69-73*

Development of a Fast TRD Pre-Amplifier Shaper

Hans Kristian Soltveit, Johanna Stachel

Research and development for fast PASA suitable for MWPC-based detectors in future experiments (like TRD in CBM) has two challenges: i) low noise with short shaping time and high pulse rate. ii) low power consumption and small chip size. On the other hand, the use a state-of-the-art process that will bring less power and less area, and that will be the standard in few years is desireable. We have then decoupled the two open issues. First, one can check with a prototype that the requirements using standard technology (0.35 μm) can be fulfilled and tested with the prototype chambers give the expected physics performance. In a second step one needs to develop a completely new prototype in the state-of-the-art technology with close to final specifications (for example IBM 0.13 μm).

In order to achieve an overall noise of less than 1000 electrons per channel for a typical input capacitance of a total of 15-35 pF, the use of a low-noise circuit is required. A well proven topology to fulfil such a requirement is shown in fig. 1. Each channel consist of a low noise

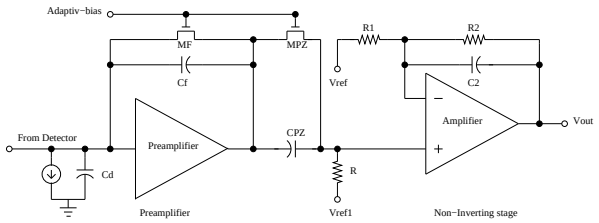

Figure 1: Schematics of the fast PASA done in 0.35μm technology

charge-sensitive amplifier, an active CR-RC pulse shaper, and a source follower buffer that can handle both polarities. The main noise contributor is the input transistor of the preamplifier that is based on the folded cascode topology. The cascode consist of a common-source stage followed by a common-gate stage. It combines two transistors (a wide input transistor and a narrower cascode transistor) to obtain: i) high transconductance and low noise of a wide transistor, ii) high output resistance and low output capacitance of a narrow transistor, and iii) reduced capacitance between output and input. In addition a Pole-Zero network is included to avoid undershoot that will strongly limit the counting rate behaviour. In the design a MOS transistor (MF) is used with a feedback capacitance Cf that is continously discharged with a decay time $td = Df \cdot Rds$ (MF). This continuously sensitive design is particularly suitable for a detector with high occupancy and high counting rate. To increase the gain and shape of the signal a shaper is built around a Miller OTA. By means of the external reference Vref, this part has in addition the capability of maximizing the dynamic range for a given polarity. The reference voltage is set closer to the positive rail so that its output swing towards the negative rail for positive input charges. For negative input charges the reference voltage is set closer to the negative rail such that its output swings toward the positive rail.

A first prototype using this design was submitted in October 2004 and has just been received back from foundry. First test has already been undertaken. Since the design was targeted for a slightly different type of detector the conversion gain is slightly higher (40mV/fC) in this prototype version compared to the requirement for the TRD. This can easily be lowered by adding a resistor of suitable size in series to the external reference voltage Vref . In this first prototype the peaking time is 30 ns (t0/100), and the FWHM is about 75 ns. It returns to the baseline after 270 ns. In terms of noise this circuit fulfil the requirement with an ENC of less than 850 electrons for an input capacitance of 35 pF. In terms of power consumption the circuit uses 8.5 mW/channel. The chip is fabricated in 0.35 μm standard CMOS technology, and has a pad pitch of 50 μm.

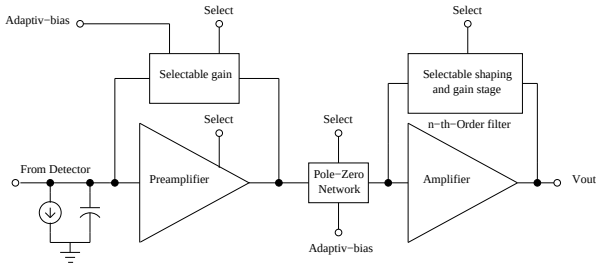

Figure 2: Schematics of the fast PASA under development in 0.13μm technology

The next step is to migrate from 0.35 μm technology to a smaller technology. A prototype development of a new circuit done in 0.13 μm IBM technology is already under way. The proposed schematic layout is shown in fig. 2. This circuit consist of a low noise, selectable gain, preamplifier that can detect both polarities. The choice of gain range in the preamplifier is made by switching the relevant range capacitors. The reason of choosing a selectable gain preamplifier is to provide a versatile preamplifier potentially suitable for several of the proposed CBM detectors (RICH, ECAL and TRD). The core preamplifier is based on the same topology as used in ALICE-TPC/TRD [1]. The change in decay time (due to change in gain range) also influence the P-Z network, that has to change to preserve to same relation to avoid undershoot. The shaper/gain circuit is also made selectable. The purpose of the selectable shaper/gain circuit is to amplify the input signal to the full scale voltage of the ADC ensuring that the maximum signal resolution is achieved. Several programmable shaper/gain topologies are under investigation to find the best candidate for the proposed detectors.

References

[1] H.K.Soltveit *et al.* GSI Annual Report 2003, p 244

The PANDA experiment at FAIR

The PANDA collaboration

Basel, Beijing, Bochum, Bonn, IFIN Bucharest, Catania, Cracow, Dresden, Edinburg, Erlangen, Ferrara, Frankfurt, Genova, Giessen, Glasgow, GSI, Inst. of Physics Helsinki, FZ Jülich, JINR Dubna, Katowice, Lanzhou, LNF, Mainz, Milano, Minsk, TU München, Münster, Northwestern, BINP Novosibirsk, Pavia, Piemonte Orientale, IPN Orsay, IHEP Protvino, PNPI St. Petersburg, Stockholm, Dep. A. Avogadro Torino, Dep. Fis. Sperimentale Torino, Torino Politecnico, Trieste, TSL Uppsala, Tübingen, Uppsala, Valencia, SINS Warsaw, TU Warsaw, AAS Wien

The PANDA collaboration plans to build a state-of-the-art universal detector for strong interaction studies at the high-energy storage ring HESR at the international FAIR facility. The detector is designed to take advantage of the extraordinary physics potential, which will be available utilizing high intensity, phase space cooled antiproton beams. In the year 2004, the collaboration submitted a Letter of Intent (LOI) to the appropriate FAIR committees and prepared for the submission of a Technical Progress Report.

Spectroscopy has been a prime tool for physics in the last century and has played a leading role in the development of quantum mechanics and the standard model of physics. Quantum Chromo Dynamics (QCD) is generally accepted to be the correct underlying theory of the strong interaction. However, our knowledge of the behavior at large distances is still rather primitive. Spectroscopy experiments within hadron physics are the tool to investigate both in the dynamics governing the interaction of fundamental particles and the existence of new forms of matter. The latter could consist of gluonic degrees of freedom, like glueballs and hybrids, previously undiscovered charmonium states, the extension of the nuclear chart into the strangeness dimension, or particles produced inside nuclear matter. Only when we can predict, confirm, and explain the physical states of the theory, we can hardly claim that we understand the strong interaction. Such a deep understanding might have farther- reaching implications in particle physics. For example, it is quite possible that the weak interactions becomes strong at high energies and field theories of the strong interaction may be relevant to the mechanism of the electroweak symmetry breaking. In strong-interaction studies based on QCD we have the ideal laboratory to test our understanding of theory against experimental results.

Significant progress beyond the present understanding can only be made if the statistics and precision of the data and their analysis exceeds past efforts by several orders of magnitude. The PANDA detector will be optimized for the physics goals as discussed above. At the same time, the detection system should be able to accommodate additional physics aspects, like Drell-Yan and CP-violating processes. The PANDA program carries outstanding discovery potential and excellent opportunities for the investigation of additional physics topics.

Placing a detector inside a storage ring allows for optimal use of precious antiprotons but poses severe experimental challenges. The number of antiprotons is limited and the required high-luminosity can only be achieved by an appropriately attuned target. Triggering on decaying charm particles requires precise micro vertex tracking close to the target or lepton identification, dependent on the final state. The PANDA detector has an advanced particle identification system. Charged particle tracking together with a high-resolution electromagnetic calorimeter are mandatory for spectroscopy experiments. The almost full coverage of the solid angle in PANDA is achieved by a combination of a target spectrometer with a forward spectrometer. The complex detector arrangement is to assure the measurement of complete sets of parameters and signatures. The procedure warrants a robust and redundant physics reconstruction which is considered particularly important in a high-luminosity environment.

The design of PANDA is based on previous experience in antiproton experiments and takes advantage of ongoing detector developments performed at the high-energy laboratories for experiments. The general layout of PANDA is based on two magnetic spectrometers and is shown in Fig. 1. The target spectrometer surrounds the interaction region and has a superconducting solenoid as momentum analyzer. A forward opening of 5–10 (depending on the respective axis) allows high momentum tracks to enter the forward spectrometer with a large-gap dipole magnet.

The superconducting solenoidal magnet has a length of 2.5 m, a diameter of 1.9m and provides an axial field of 2 T. It has to accommodate a gap for pipes of the target device. The target spectrometer is then made up of the following components:

The interaction point is surrounded by a micro vertex detector (MVD), which has five barrel shaped layers plus five disk-shaped detectors in forward direction. The three innermost layers are composed of pixel detectors to achieve best resolution and to be able to easily detect decay vertices displaced from the interaction point. The outer layers are composed of microstrip detectors which are easier to handle. The baseline technology chosen for the pixel detectors are hybrid active pixel sensors as used by several LHC experiments. The electronics still has to be modified to accommodate continuous readout. As alternatives to silicon pixels, GaAs based detectors are considered as well as much thinner monolithic pixel sensors where the problem of radiation hardness would have to be solved.

The MVD is surrounded by a cylindrical tracker. Two options are currently discussed, a straw tube tracker (STT) consisting of 15 double layers of self-supporting straws and a time projection chamber (TPC) with continuous readout. The TPC is the technically more challengingoption since it requires an ungated charge collection based on a GEM

readout. However it has the benefit of less material and offers in addition particle identification via dE/dx. On the other hand, the STT is seen as a safe fall-back solution which should still fulfil the basic tracking requirements.

In the forward direction circular or octagonal mini drift chambers are used to track particles with higher momenta before they enter the forward spectrometer.

The next detector is a Cherenkov counter based on the DIRC principle as used in BaBar at SLAC. It consists of quartz rods in which Cherenkov light is internally reflected to an array of photon detectors in the backwards direction. The readout can be either done by imaging a 2D pattern of reflections with a large number of PMTs or APDs or by measuring just one coordinate and the time of light propagation inside the quartz very precisely. In forward direction a disk-shaped Cherenkov counter with quartz radiator and detectors for internally reflected light similar as for the barrel DIRC is planned. Its readout should be located between the solenoid coil and the return yoke to allow the calorimeter end cap to be as close as possible.

An electromagnetic calorimeter is placed outside the DIRC. It consists of a barrel part with 11 360 crystals, a forward end cap with 6 864 crystals and a backward end cap with 816 crystals. As detector material $PbWO_4$ is foreseen, since it is fast and has a reasonable resolution. However, it might require cooling down to -25° C. As alternative BGO with still higher light yield albeit slower signals is considered.

Finally, outside the superconducting magnet and its iron return yoke, drift tubes track muons exiting the spectrometer. The necessity of a time-of-flight detector in the target spectrometer is still under discussion. Although the flight path is short, low momentum particles could still be identified.

The heart of the forward spectrometer is a dipole magnet with a large opening and a field integral of 2 Tm. This will provide the required momentum resolution for forward tracks with momenta up to 8 GeV/*c*. One problem of the dipole magnet is the deflection of the beam. If included in the beamline design it can be countered by a magnet chicane. Otherwise the beam could be shielded from the magnetic field, introducing some material in the acceptance.

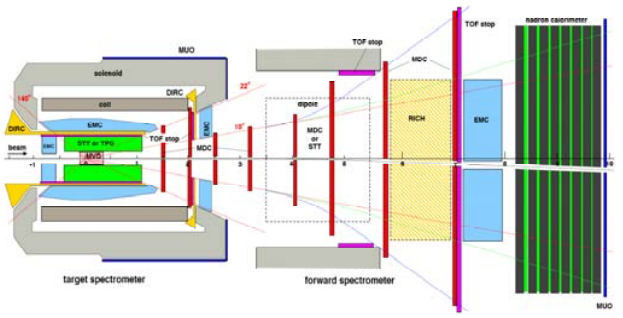

Figure 1: Layout of the PANDA detector.

The detector systems in the forward spectrometer are summarized in the following:

Tracking is provided by mini drift chambers. Before the magnet, they have the same octagonal shape as in the end cap of the target spectrometer. After the magnet, a rectangular shape matches is more suitable for the spread of tracks. The use of straw tube trackers inside the dipole field is considered for better momentum resolution.

The option of a third Cherenkov counter, based on gas or aerogel is still under investigation. In addition, a time-of-flight detector is considered for charged particle identification.

An electromagnetic calorimeter based on lead/scintillator sampling and WLS fibre readout (Shashlyk type) is foreseen in the forward spectrometer. It should have 276 channels to cover the acceptance and will reach a resolution in the range of 3–5%/√E[GeV].

After the electromagnetic calorimeter, the MIRAC detector from WA80 at CERN is under investigation as a hadron calorimeter after refurbishing its readout.

The last piece of equipment is a muon detector based on drift tubes.

The selected readout and trigger concept foresees continuous digitization of all detector channels. Special trigger hardware is not foreseen. The readout electronics has to be fully pipelined and has to perform autonomously the detection of valid hits as well as intelligent data reduction by clusterization, signal shape analysis, and time reconstruction to transfer only the physically relevant minimum of information. All data are marked by a synchronous timestamp by which event building can be performed at a later stage.

The data are fed into a configurable network. Attached computer nodes with the required bandwidth digest the full rate of certain sub-detectors used for the first selection level. Other detectors transfer data only for time slices selected on some level. Parallel selections are possible and several levels will bring the data rate down to the required 100–200 MB/s to mass storage. The clear advantage of this scheme is its flexibility: Any conceivable physics signature of an interesting process measurable by the PANDA detector could be converted into a sequence of selection algorithms. Typical signatures are the decays of J/ψ to leptons, decay vertices of charm or strange hadrons, identified kaons or electromagnetic showers, etc.. The level of complexity is only limited by the required processing power and can be scaled up by attaching more nodes.

The trigger system and the universality of the detector make PANDA a unique tool in hadron physics, ready for future challenges.

The PANDA collaboration itself consists of 350 physicists from 47 institutions and 15 countries.

The Micro-Vertex Detector of the $\bar{P}$ANDA Experiment[&]

The $\bar{P}$ANDA collaboration

$\bar{P}$ANDA at FAIR will use the antiprotons stored in the High-Energy Storage Ring HESR for a variety of experiments centered around the production of open and hidden charm degrees of freedom. The central issues of interest include charmonium spectroscopy, in particular of states with higher angular momenta and excitation energies, search for exotic states that cannot be associated with simple quark-model candidates, the study of charmed mesons and their properties in the nuclear medium, and the production and decay of hypernuclei. For most of these topics, a direct detection of the delayed decay of open charm is, if not a prerequisite for the decay channels under study, advantageous since the cross sections of the states which involve charm quarks are often predicted to be small.

Figure 1 shows a sketch of the micro-vertex detector system that is envisaged for the detection of delayed decays of charmed mesons into charged kaons and pions as well as displaced vertices that indicate the decay of kaons and hyperons. It consists of three barrel layers and two forward disk structures of pixel detectors (brown/grey; the innermost barrel is not visible) and two barrels as well as three disks of double-sided strips (green/blue). The radius of the largest barrel structure is 12 cm. The $\bar{p}$ beam enters from the right.

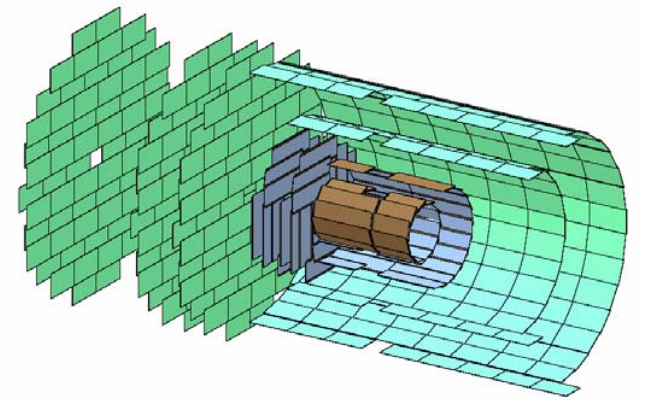

Fig. 1: *Layout of the $\bar{P}$ANDA MVD. See text for details.*

While the central task of the silicon tracker is the detection of charged-particle hits with a resolution that yields an overall spatial accuracy better than the characteristic decay lengths of the involved particles, which is of the order of 100 µm in case of D mesons, the energy loss measurement may also prove helpful with respect to the distinction of kaons, pions and other particle species. As can be inferred from Figure 2, which shows the momentum distributions of kaons and pions from the decay of D mesons according to $D^{\pm} \rightarrow K\pi\pi$, the energy of the detected mesons can become very small, so that Cherenkov radiation cannot be used for particle ID and must be substituted by energy loss and/or time-of-flight measurements.

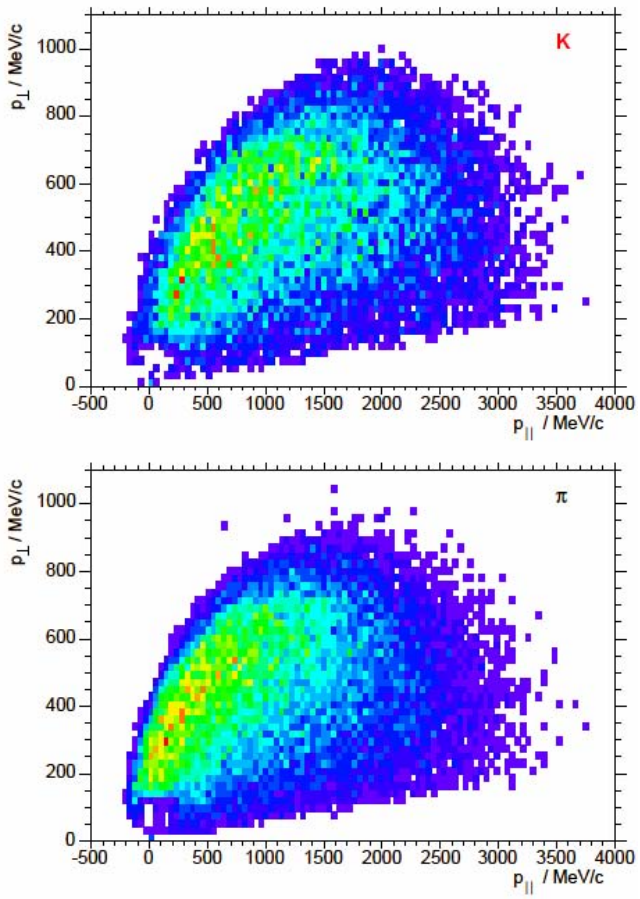

Fig. 2: *Momentum distributions of pions and kaons originating from D-meson decay after the $\bar{p}p \rightarrow \bar{D}D$ reaction at 6.7 GeV/c, where the D mesons decay according to $D^{\pm} \rightarrow K\pi\pi$..*

The small momenta also result in increased small-angle scattering, so that the resolution of the vertex detector is severely compromised. Therefore, the material budget of the vertex detector has to be minimized. Presently, the plans for the detector layout include three layers of hybrid pixel detectors similar to those in use for the LHC experiments for the innermost barrels and forward disks, and two layers of double-sided strip detectors.

At present, R&D for the MVD centers around standard-type pixel detectors. Alternative materials for the sensors and strip detectors are under investigation. Quite possibly, the present pixel size, e.g. 50·400 µm^2 for the ATLAS vertex detector, can be replaced by smaller cell sizes when technologies already available for microchips with feature sizes of .13 µm will be used for the hybrid readout chips.

& contact: K.-Th. Brinkmann, IKTP, TU Dresden
KT.Brinkmann@physik.tu-dresden.de

Pellet Target Development at the University of Uppsala

PANDA Collaboration

The antiproton-proton experiments, which form the major part of the physics programme of PANDA, require a high density hydrogen target. The approach of using frozen droplets of hydrogen, called pellets, is successfully in operation at the CELSIUS/WASA facility [1, 2]. In fact, the parameters achieved at that installation are already close to the requirements for the experiments at PANDA. In order to further improve this target and to evaluate whether such a target could be operated in PANDA, a second independent target (Pellet Test Station – PTS) has been build up at the The Svedberg Laboratory, Uppsala, Sweden.

This system is designed taking into account the experiences from the WASA system. However, a maximum of compatibility with this system is kept, such that an interchange of nozzles, capillaries, *etc* is feasible between the systems. The objective is to provide a set-up where tests and modifications are easily possible giving access for the measurement of all variables, like beam diameter, distribution, vacuum, *etc*. It may, however, be used in large parts for the installation at the future FAIR facility.

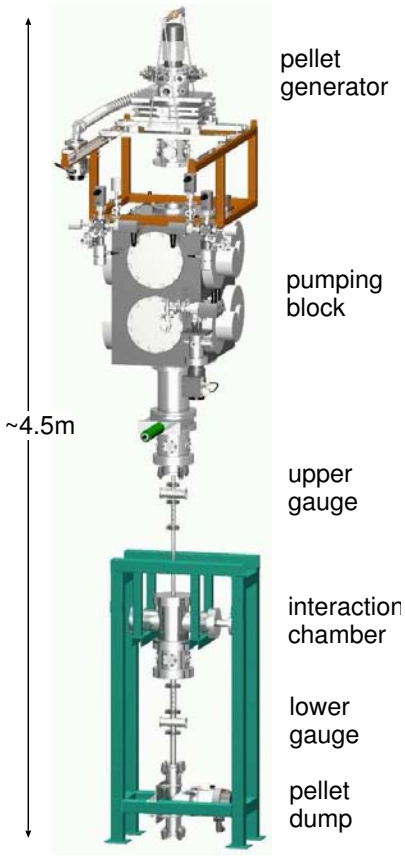

Figure 1: Pellet Test Station PTS designed for testing and further development of the target. On this drawing vacuum gauges, diagnostic tools, several pumps, and fittings are omitted.

Below the pumping block (see Fig. 1) an additional vacuum system has been designed and completed, which simulates the situation at PANDA. Furthermore, it also allows the monitoring of crucial variables like vacuum and beam shape, especially also at the so-called "interaction chamber", which is the point which simulates the beam intersection at PANDA.

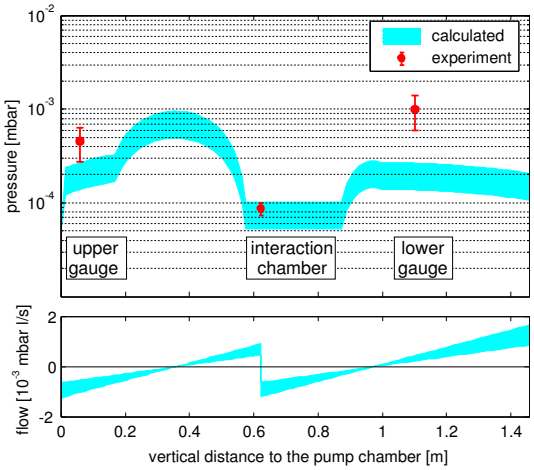

Figure 2: Comparison of experimental (red points) and calculated vacuum (light blue band) in the target pipe of the PTS. The errors indicate a 1σ uncertainty. The experimental points lie factors 2 to 4 above the calculated band but agree within 2σ. The lower part shows the calculated gas flow, which is below zero if the gas flows to the left the figure and positive if the flow is to the right, i.e. upwards and downwards respectively at the experiment.

Several test and measurements were performed using this system. The results of a vacuum measurement and its comparison to vacuum calculations using VAKLOOP [3] described in more detail in Ref. [4] are shown in Fig. 2. Applying the same calculations to the current PANDA design a vacuum of below than 2×10^{-5} mbar is expected inside the beam line around the interaction point. This is a value acceptable from the point of view of both the accelerator as well as the experiment.

Currently the system is equipped with a pellet tracking system and further tests on the divergence and pellet rate will follow.

References

[1] C. Ekström *et al.* [CELSIUS/WASA Collaboration], Phys. Scripta **T99** (2002) 169.

[2] J. Zabierowski *et al.* [CELSIUS/WASA Collaboration], Phys. Scripta **T99**, (2002) 159.

[3] V. Ziemann, SLAC-PUB-5962, (1992).

[4] Technical Progress Report for PANDA, [PANDA collaboration], (2005).

Development of a high-rate GEM-based TPC for PANDA

The PANDA Collaboration

1 Introduction

$\overline{\text{P}}$ANDA (Anti**P**roton **An**nihilations at **Da**rmstadt) [Pan05] is a universal detector to study fundamental questions of hadron physics at large distances using antiprotons. It is designed as an internal target detector at the antiproton storage ring HESR (**H**igh **E**nergy **S**torage **R**ing) to be built at FAIR (**F**acility for **A**ntiproton and **I**on **R**esearch). The rich physics program foreseen at $\overline{\text{P}}$ANDA requires an excellent 4π charged particle tracking system. Minimal material budget and a momentum resolution on the per cent level are mandatory. A possible solution for the central tracker of $\overline{\text{P}}$ANDA fulfilling these requirements is a TPC (**T**ime **P**rojection **C**hamber). In addition, such a detector would open the possibility for PID (**p**article **id**entification) via a measurement of the fractional energy loss $\mathrm{d}E/\mathrm{d}x$, in particular in the momentum range below 1 GeV/c. The continuous beam structure at the HESR in combination with interaction rates of the order of 10^7/s, however, constitute a big challenge for such a detector. Ions created in the amplification region have to be prevented from drifting back into the drift volume, where they would deteriorate the resolution. The use of GEM (**G**as **E**lectron **M**ultiplier) [Sau97] foils as charge amplifiers, with their intrinsic suppression of ion feedback could open the possibility to operate a TPC in an ungated mode without accumulating excessive space charge. Continuous operation of a TPC also requires the development of new algorithms for pattern recognition and for the reconstruction of tracks from hits that do not carry an absolute time stamp. This report summarizes the ongoing activities at Technische Universität München to study the feasibility of a GEM-based TPC for $\overline{\text{P}}$ANDA, both in simulations and prototype development.

2 Prototype Development

A small GEM-based TPC prototype with a drift length of $\sim$ 8 cm and an active area of 10×10 cm^2 has been designed and assembled (see Fig. 1). The layout has been adapted from a similar detector which was built and successfully operated with GEMs for studies of the TESLA TPC [Kam04]. It allows easy raplacement of the gas amplification stage, readout-PCB and front-end electronics. In particular the fieldcage can be exchanged by a longer one without major modifications. It is realized as a multilayer structure where the two major components are a 125 μm Kapton foil, which has a set of 18 μm thick copper strips on both sides to form the drift field, and a laminated honeycomb structure for mechanical stability. Aiming for a drift field of $\sim$ 400 V/cm, the cathode end cap has to be set to a potential of $\sim$ 8 kV (taking into account a voltage of $\sim$ 4 kV, which is needed to operate the GEM stack). The readout PCB, which also holds the GEM stack and the corresponding high voltage feedthroughs, is currently equipped with 2×6 mm^2 pads. For first tests, the front-end electronics developed for the ALICE TPC [Mus03] will be used.

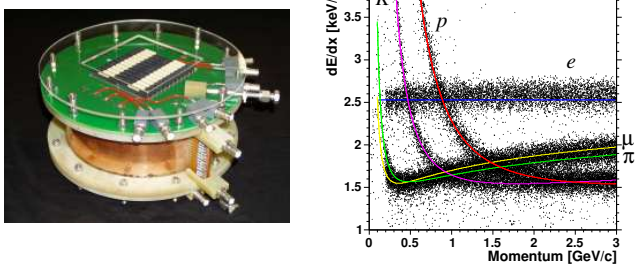

Figure 1: Left: Picture of the assembled TPC prototype. Right: Reconstructed energy loss per unit track length vs. momentum for p, K, π, μ and e; lines are fits of a parameterization.

The prototype design was chosen in a way that the chamber fits into a dipole magnet which is available at TU München. With this setup we intend to study systematically the detector performance in a magnetic field. In order to investigate the influence of field distortions due to space charge accumulation inside the drift volume of the TPC, an X-ray gun will be used. For this purpose, irradiation windows are foreseen in the prototype fieldcage. An open gas system has been designed to be able to test different gas mixtures for the TPC. At the moment Ar or Ne as counting gas, CO_2 as quencher, and possibly CH_4 as third admixture are foreseen.

3 Simulation Results

In order to simulate the TPC and its integration into the whole detector system it has been fully implemented into the $\overline{\text{P}}$ANDA simulation framework. This includes the simulation of charged particles traversing the gas volume, as well as the creation of signals and their reconstruction to tracks and vertices. With this tool the dependence of the tracking performance on certain design parameters like the pad size or the gas mixture have been studied. Especially the capability of the TPC to contribute to the particle identification of $\overline{\text{P}}$ANDA via $\mathrm{d}E/\mathrm{d}x$ measurements has been investigated. As can be seen from Fig.1 the TPC can provide valuable PID information for particle momenta below 1 GeV/c, where the Cerenkov detectors are not sensitive anymore. According to the simulations, a $\mathrm{d}E/\mathrm{d}x$ resolution of the order of 4 % can be achieved.

References

[Pan05] The $\overline{\text{P}}$ANDA Collaboration, *Technical Progress Report*, (2005).

[Sau97] F. Sauli, Nucl. Instr. Meth. **A386**, 531, (1997).

[Kam04] J. Kaminski et al., Nucl. Instr. Meth. **A535**, 201, (2004)

[Mus03] L. Musa et al., Proceedings of the IEEE Nucl. Sci. Symp., Portland, (2003).

$PbWO_4$ Scintillation Crystals for PANDA

PANDA Collaboration

Since the electromagnetic calorimeter of the PANDA detector aims for the detection of photons well below 20 MeV energy, the standard quality of the luminescence yield of $PbWO_4$ (PWO) had to be improved significantly to be considered as scintillator material to be read out with large area avalanche photo diodes (LAAPD). In close collaboration with M. Korzhik (RINP, Minsk) and the Bogoroditsk Technical Chemical Plant (BTCP) a new generation of bright crystals, referred as PWO-II, has been developed and manufactured.

Based on the R&D with respect to large-scale production for ECAL/CMS at LHC, CERN, the concentration of defects was significantly reduced to allow a lower concentration of the La- and Y-ions, leading to less quenching of the primary luminescence yield. PWO-II [1] delivers on average a light yield increased by almost 100%.

The thermal quenching of the scintillation light can be reduced by an operation of the crystals at low temperatures. The negative gradient of the light yield varies between 2 and 3%/K and leads to an increase of the scintillation light of > 300% at -25^0C compared to room temperature. The decay time of ~ 6ns at room temperature is only slightly changed allowing to integrate the complete detector response within 100ns.

The impact of both quality factors on the overall response function to high energy photons up to 520 MeV has been investigated for first test arrays using crystals of 20x20mm^2 cross section and 150 or 200 mm length, respectively.

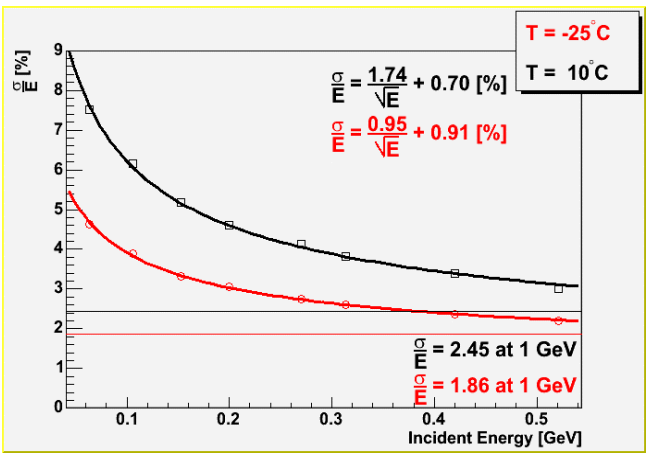

Fig. 1: Energy resolution of a 3x3 PWO-matrix obtained with photomultiplier read-out at two different operating temperatures.

The response functions have been measured at the tagged photon facility at MAMI, Mainz, using energy marked photons selected between 64 and 520 MeV, respectively. A 3x3 matrix of 200mm long crystals read out with photomultiplier tubes has been operated at temperatures of $+10^0$C and -25^0C, respectively, using commercial electronics. In spite of an insufficient active volume to contain the complete electromagnetic shower, the best ever measured energy resolution of

$$\sigma / E = 0.95\% / \sqrt{E / GeV} + 0.91\%$$

has been obtained at T = -25^0C as illustrated in Fig. 1.

In order to obtain a first estimate on the achievable performance using LAAPDs of 10x10mm^2 active surface as photo sensors, a 3x3 matrix of 150mm long crystals has been studied. A recently developed low noise preamplifier [2] has been used for charge integration to serve an energy and timing circuit after passive splitting. The deduced response function of the matrix for photons of similar energies delivers an excellent energy resolution at -25^0C of $\sigma / E = -0.26\% / E + 2.64\% / \sqrt{E} + 0.31\%$ (E in GeV) in spite of one not functioning module and not optimized shaping and digitizing electronics.

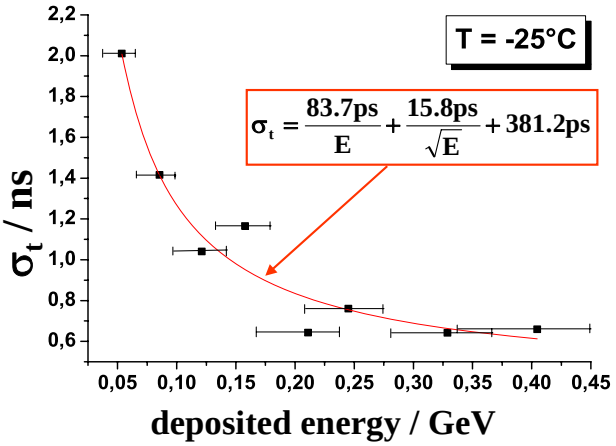

Fig. 2: Time resolution of a PWO detector read out with a LAAPD measured over a wide range of photon energies.

Using a commercial shaping and constant fraction discriminator circuit, the response time of the central module has been measured relative to the plastic scintillator for electron tagging. Fig. 2 illustrates the achieved preliminary time resolution, which drops below 1ns above 150 MeV photon energy and approaches 500 ps at 1 GeV.

The obtained first experimental data document the excellent time and energy response of PWO for both sensor concepts operating at low temperatures. The scintillator allows to handle extreme high count rates and remains sufficiently resistant to the expected radiation damage.

========

References

[1] A. Borisevich et al., Nucl. Instr. and Meth. in Phys. Res. A537 (2005) 101.

[2] M. Steinacher et al. , Physics Department, University Basel, Switzerland, private communication.

Development of Large Area APDs for the PANDA-EMC

Wilms, A.[1], Lewandowski, B.[1], and Peters, K.[2]
[1]Ruhr-Universität Bochum; [2]GSI Darmstadt

For the electromagnetic calorimeter (EMC) of the PANDA detector there are two different scintillator materials under investigation: lead tungstate (PWO) and bismuth germanate (BGO). The R&D of an optimized photosensor for the readout of those crystals has started in 2004.

The designated magnetic field of 1.5 T precludes the use of conventional photomultipliers as a readout of the EMC crystals. On the other hand is the signal generated by ionization in a PIN photodiode by a traversing charged particle too large for our applications. To solve these problems a photodevice with insensitivity to magnetic fields and a small response to ionizing radiation has to be used. In case of PWO, which has a relatively low light yield, an internal gain of the photosensor is required in addition.

Therefor we started the R&D of large area APDs (LAAPDs) with an active area of $(10 \times 10)\ mm^2$ based on the design of the APDs used for the readout of the PWO crystals of the ECAL of the CMS collaboration (active area: $(5 \times 5)\ mm^2$) in collaboration with Hamamatsu Photonics.

The essential parameters like quantum efficiency (QE), breakdown voltage (U_{br}), dark current (I_d) and terminal capacitance (Ct) of the first LAAPD prototypes (S8664-1010SPL) were measured at the CMS APD laboratory at CERN.

The results are listed in comparison to the corresponding values of a CMS-APD in table 1.

Prop.	Condition	CMS-APD	S8664-1010SPL
Area $[mm^2]$		(5×5)	(10×10)
QE [%]	$M = 1, \lambda = 420\ nm$	70	65
U_{br} $[V]$	$I_d = 100\ \mu A$	400	400
I_d $[nA]$	$M = 50$	5	10
Ct $[pF]$	$M = 50$	80	270

Table 1: Summary of APD properties measured at CERN.

In addition several tests concerning the radiation hardness of these photosensors have been done during the last year. The first test measurement took place at the PSI Villigen using a proton beam with an energy of $E_p = 70\ MeV$. During the irradiation the increase of the current was monitorized (see fig. 1). At an integrated fluence of nearly $5 \times 10^{12}\ p/cm^2$ the irradiation of the S8664-1010SPL type LAAPD was stopped, since no indication for a saturation of the measured current was observed. The maximum current measured at this value of fluence was $I \approx 200 \mu A$.

Due to this first irradiation test it turned out that the first delivered prototypes of the LAAPD were not radiation hard according to CMS standards. Therefor a new version of those APDs (S8664-1010) were ordered with a modified internal structure to reduce surface currents. The irradiation of those LAAPDs was done at the KVI Groningen using a proton beam of 90 MeV energy. The measurement at the KVI was done the same way as the measurements at PSI.

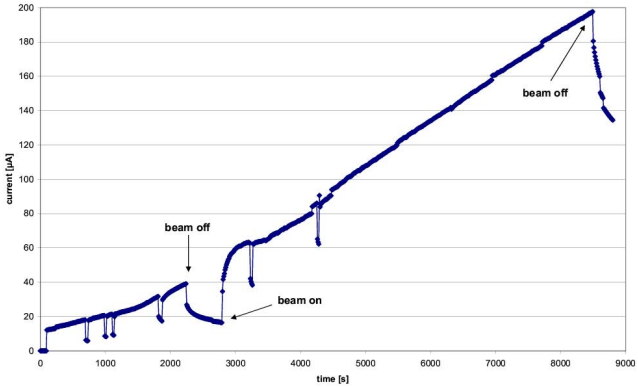

Figure 1: Increase of the current of LAAPD S8664-1010SPL during irradiation with 70 MeV protons at PSI.

The result of this test beam time is shown in fig. 2. After an integrated fluence of $1 \times 10^{12}\ p/cm^2$ was reached the beam current was increased by a factor of 10. The measurement was stopped after an integrated fluence of $\approx 1 \times 10^{13}\ p/cm^2$ was reached according to the estimated fluence for 10 years of operation.

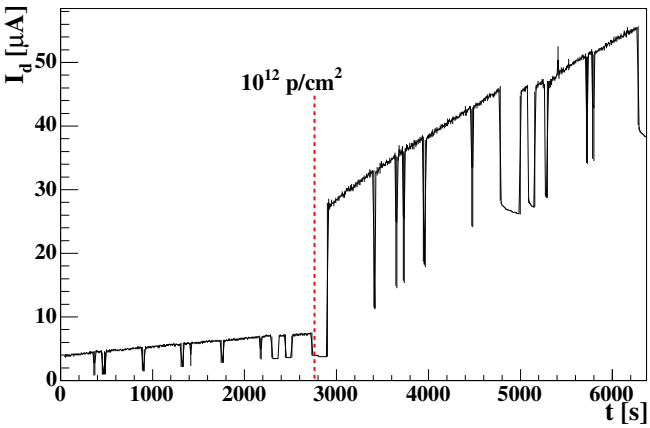

Figure 2: Increase of I_d of LAAPD S8664-1010 during irradiation with 90 MeV protons at KVI.

The maximum current measured at this value of fluence was $I_d \approx 55 \mu A$, which is nearly a factor of 4 lower than the value measured with the first prototypes at an integrated fluence of $5 \times 10^{12}\ p/cm^2$ at PSI.

Concerning the radiation hardness of the developed LAAPDs due to proton irradiation it turned out that the LAAPDs type S8664-1010 are radiation hard up to an integrated fluence of $10^{13}\ p/cm^2$.

Hypernuclei at PANDA: Hypernuclear Target

A. Sanchez-Lorente[1], P. Achenbach[1], M. Agnello[3], T. Bressani[4], A. Banu[1], D. Calvo[4], A. Feliciello[3], F. Ferro[3], F. Iazzi[3], J. Gerl[2], I. Kojouhavorv[2], J. Pochodzalla[1], G. Raciti[5], N. Saito[2], T.R. Saito[2], H. Schaffner[2], and C. Sfienti[2]

[1]U Mainz; [2]GSI; [3]Politecnico+INFN Torino; [4]INFN Frascati; [5]INFN Catania

The main purpose of the secondary, or hypernuclear, target is the stopping and absorption of the produced Ξ hyperon and the identification of the secondary reaction vertex by tracking of the incident Ξ and charged decay products from the weak decay of the $\Lambda\Lambda$ hypernuclei. Even with a moderate spatial resolution, this information will help to reduce the background in the offline analysis significantly.

The energy release of about 28 MeV during the conversion of the Ξ into two Λ hyperons may give rise to the emission of particles from the secondary target nucleus. As a consequence, a variety of double, single or twin hypernuclei as well as ordinary nuclei may be produced in excited states. In order to simplify the assignment of the various transitions to a specific nucleus four separated sections with up to four different main target materials are foreseen. The initial experiment will concentrate on light target materials like ^{9}Be, ^{10}B, ^{12}C and ^{13}C. In addition, the interactions in the material of the silicon detector can be studied. At the same time, the light elements help minimizing the absorption of γ-rays emitted by the excited hypernuclei.

The geometry of the solid-state micro tracker is mainly determined by the mean life time of the Ξ^- of only 0.164 ns. If the separation between the primary target and the secondary absorber is too big,low momentum Ξ^- will decay prior to stopping. On the other hand, energetic Ξ^- with momenta beyond approximately 500 MeV/c cannot be stopped prior to their decay. This limits the thickness of the active secondary target to a few cm (see Fig. 1).

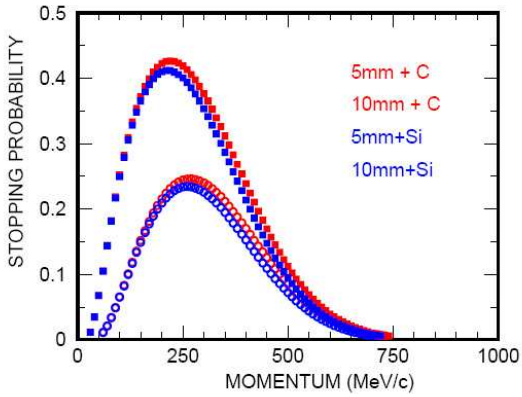

Figure 1: Stopping probability of Ξ^- hyperons in carbon and silicon as a function of the momentum. The upper and lower curves correspond to a gap between the primary target and the secondary absorber of 5 and 10 mm, respectively.

In order to determine the required sensitive region of the secondary target we investigated the distribution of the stopping points of the Ξ^- entering the secondary target. While the distance between the primary and secondary target should be minimal, the number of stopped Ξ^- is not very sensitive to this gap. For a safe operation of HESR we therefore foresee a beam pipe with a diameter of 15 mm. In order to track the Ξ^- (and the charged fragments resulting from the decay of the produced hypernuclei), it is planned to sandwich the secondary absorber with layers of silicon detectors. Outside of the beam pipe we projected in a first design a multi-layered structure of 1.5 mm thick carbon absorbers surrounded by 300 μm thick silicon layers. Fig. 2 shows the stopping points of Ξ^- hyperons, where the horizontal axis represents the beam direction and the vertical axis is the radial distance from the beam axis. The origin marks the primary target point. Consistent with the schematic calculations shown in Fig. 1 the stopping points are concentrated in an angular range from 40° to 90° and a radial thickness of about 20 mm. The free angular range between 0° and 40° is sufficiently large for the detection of the associated kaons emitted mainly in the forward region. The number of silicon detectors and the

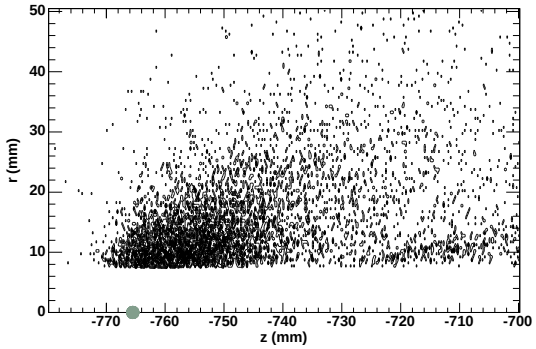

Figure 2: Stopping points of Ξ^- hyperons produced in $\bar{p}+X$ interactions at 3 GeV/c within an INC calculation [1]. The circle marks the position of the primary target.

thickness of the absorber will be a compromise between the necessary number of readout channels and the corresponding costs on one hand and a large stopping probability on the other hand. Furthermore, in order to keep the γ-ray absorption low, the overall thickness should be kept as low as possible.

References

[1] M. Agnello, F. Ferro, and F. Iazzi. hep-ex/0405061, 2004.

Production of Hypernuclei in PANDA: Hyperon production target

O.N. Hartmann[1,2], P. Achenbach[3], M. Agnello[4], T. Bressani[5], D. Calvo[5], A. Feliciello[5], F. Ferro[4], A. Galoyan[6], P. Gianotti[2], F. Iazzi[4], J. Pochodzalla[3], G. Raciti[7], A. Sanchez-Lorente[3], C. Sfienti[1], and V. Uzhinsky[6]

[1]GSI; [2]INFN-LNF; [3]U Mainz; [4]Politecnico+INFN Torino; [5]U+INFN Torino; [6]JINR Dubna; [7]U+INFN Catania

The study of double Λ hypernuclei is one of the major physics programs within the program of PANDA [1, 2]. The experimental setup, as described in [3], comprises a primary nuclear target which will be hit by the antiproton beam.

Double Hypernuclei are produced via the stopping and absorption of double strange baryons Ξ^- in a nucleus [4]. Thus, it's the task of the so-called primary target to produce $\Xi\overline{\Xi}$ pairs in a $\overline{p}$A reaction, while the stopping, absorption and hypernucleus production takes place in a secondary target. The primary reaction takes place close to the production threshold at an $\overline{p}$ momentum of 3 GeV/c, since the produced hyperons should not be too high in energy to be stopped furtheron.

The elementary reactions are $\overline{p} + n \rightarrow \overline{\Xi}^0 + \Xi^-$ and $\overline{p} + p \rightarrow \overline{\Xi}^+ + \Xi^-$.

Model studies in the framework of an Intranuclear Cascade Model (see [4]) were performed using a cross section of 2 μb, the mass number of the nucleus enters as $A^{2/3}$. The relevant quantity for the envisaged reaction is the number of stopped Ξ^- with respect to the total number of produced Ξ^-. This production factor depends on several parameters, namely the production rate, the distance between the primary target and the secondary target where the hyperons finally should be stopped and absorbed, the beam pipe diameter and the materials and geometry of the targets as well. The secondary target in the calculations was represented by a solid carbon block with a cylindrical hole (modelling the beam pipe).

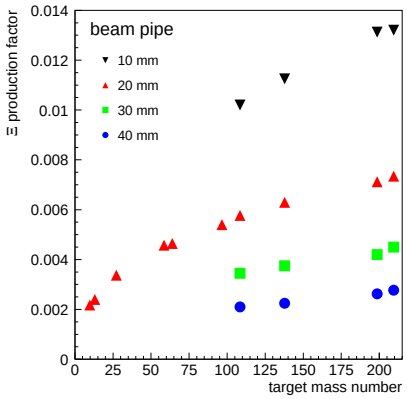

Figure 1: Ξ^- production factor as a function of the target mass number for different beam pipe diameters..

In Fig. 1 the result of this calculations is shown for four different beam pipe diameters. The ratio rises with increasing mass number of the target nucleus, and a smaller beam pipe diameter also leads to higher values.

These calculations suggest that a heavier target should be preferred because it gives a higher Ξ^- production factor, thus is more efficient in rescattering of the produced primary particles. However, there are also background particles from the annihilation present. A beam pipe diameter of 20 mm is envisaged.

To evaluate the background, the UrQMD [5] model together with an evaporation/multifragmentation part, as described in [2], chapter 12.3.1.3, has been used. In Fig. 2 the expected polar angle differential distributions for various target nuclei are shown.

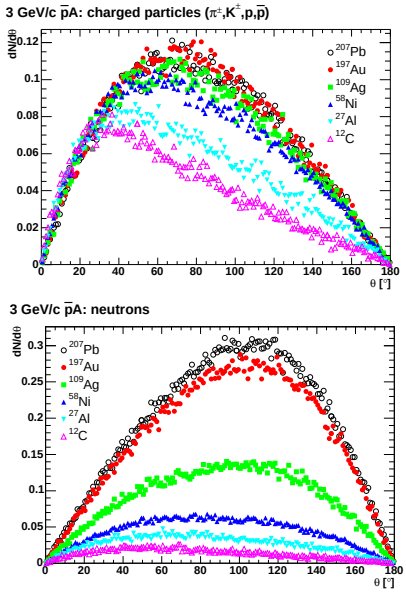

Figure 2: Differential polar angle distributions calculated with UrQMD+SMM for charged particles (above) and for neutrons (below) (3 GeV/c $\overline{p}$+A)

The neutron background at backward angles is the most critical issue (see [3]). Fig. 2 (below) suggests that for the heavier targets the neutron load at those angles increases significantly, while a lighter target gives less neutron flux at large polar angles. A good compromise between the Ξ^- production factor and the background would be a target in the region of $^{58}_{28}$Ni.

References

[1] http://www.gsi.de/panda/
[2] PANDA Technical Progress Report, 2005
[3] A. Sanchez Lorente, in this report
[4] F. Iazzi et al., hep-ex/0405061
[5] UrQMD coll., Prog.Part.Nucl.Phys. 41(98)225, JPG 25(99)1859

Performance of Germanium Detectors in High Magnetic Fields

A. Sanchez-Lorente[1], P. Achenbach[1], M. Agnello[3], A. Banu[1], T. Bressani[3], D. Calvo[3], A. Feliciello[3], F. Ferro[3], J. Gerl[2], P. Gianotti[4], O.N. Hartman[2,4], F. Iazzi[3], I. Kojouhavorv[2], J. Pochodzalla[1], G. Raciti[5], N. Saito[2], T.R. Saito[2], H. Schaffner[2], and C. Sfienti[2]

[1]U Mainz; [2]GSI; [3]Politecnico+INFN Torino; [4]INFN Frascati; [5]U+INFN Catania

Future experiments on hypernuclei γ-spectroscopy at FINUDA@DAFNE and PANDA@FAIR require the operation of germanium detectors in high magnetic fields ($B \approx 1\,\mathrm{T}$).
The performance of these detectors in such an environment has not been well investigated. In particular, one might expect three problems to arise: (i) break-down of FETs in the preamplifiers, (ii) discharging and sparking in the crystals, and (iii) deterioration of the vacuum enclosing the crystals.
Moreover since the PANDA and the FINUDA magnets will be a superconducting solenoid, the germanium detectors should survive possible events of magnet quenching without a deterioration of their functionality.
To verify that germanium detectors can be safely and efficiently operated in a high magnetic field two different kind of detectors have been tested: the EUROBALL cluster detector, being used by the RISING collaboration [1], and the VEGA detector [2].
The EUROBALL cluster detector consists of seven large hexagonal tapered germanium detectors closely packed in a common cryostat. The crystals have a length of 78 mm and a diameter of 70 mm at the cylindrical end.
The super-segmented-clover detector VEGA consists of four large, four-fold segmented germanium crystals.
Prior to the measurements the energy resolution of the detectors was measured with a ^{60}Co source to be 2.2 keV (FWHM) at 1.333 MeV. The detectors were then set up inside the ALADIN magnet and the VEGA as well as three of the seven crystals of the EUROBALL cluster detectors had full operating high-voltages.
Fig. 1 shows the energy resolution (FWHM) at 1.333 MeV

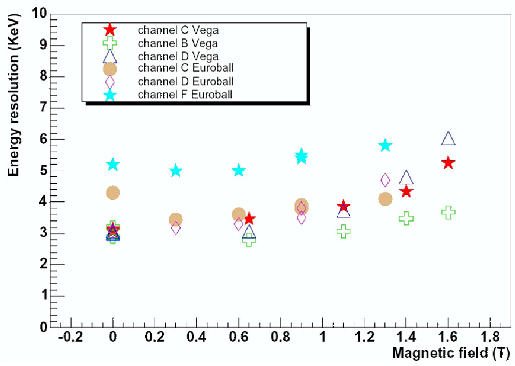

Figure 1: Measured energy resolution (FWHM) of EUROBALL cluster and VEGA detectors in a magnetic field.

of three crystals of each detector as a function of the magnetic field. The energy resolution of one of the EUROBALL crystals was found to be worse than the others because of pick-up noise in its electronic readout, whereas two other crystals of the same detector showed a similar behaviour in the magnetic field. Their energy resolution slightly exceeded 0.3 % at 1.2 T which, however, allows to perform γ-ray spectroscopy on hypernuclei. A similar behaviour was found for the VEGA detector.
The energy resolution of the VEGA detector was also measured for different angles between the detector's axis and the magnetic field in order to investigate a possible angular dependence in the energy resolution. In particular, the energy resolution has been measured for the maximum magnetic field value (1.6 T) and without magnetic field. For technical reasons, the sensible part of the detector had to be placed at a distance of about one meter from the center of the magnet, corresponding to a lower field ~ 0.3 T, at an angle of 30°.

channel C (keV)	channel D (keV)	channel B (keV)	mag. field (T)
3.2	3.03	2.99	0.3
3.17	3.13	2.74	0

Table summarises the results obtained. Differences are within the errors, indicating no deviation at 30° for a low magnetic field. Also for larger angles ($\sim 45°$) the magnetic field at the detector's position was too low to observe any dependence.
The measurements were performed over a period of two days without observing any problems with FETs, vacuum breaks or sparking of the crystals. After the measurements the original energy resolution was recovered. A pulse shape analysis with one data taken by a 100 MHz FADC system is in progress and details will be found in [3].
Finally, even though ALADIN being a resistive magnet it was not possible to reproduce a quencing situation, we monitored the behaviour of the VEGA detectors during a fast decrease of the current in the magnet from its maximum value (2400 A) to zero without observing any effect or detecting any damage.
Further tests to reach higher magnetic fields for different angles of the detectors will be performed in the near future.

This research is part of the EU integrated infrastructure initiative Hadronphysics project under contract number RII3-CT-2004-506078

References

[1] H.-J. Wollersheim et al. *Nucl. Instr. Meth.*, A. in print.
[2] J. Gerl, H. Grawe, and E. Roeckl, 1998. http://www-gsi-vms.gsi.de/eb/html/vegaproject.html.
[3] A. Sanchez-Lorente. PhD thesis, Institut für Kernphysik, Johannes Gutenberg-Universität Mainz.

FLAIR – a Facility for Low-Energy Antiproton and Heavy-Ion Research

A. Bräuning-Demian[1], M. Charlton[2], H. Danared[3], D. Grzonka[4], M. Holzscheiter[5], M. Hori[6], A. Källberg[3], H. Knudsen[7], W. Quint[1], A. Simonsson[3], M. Steck[1], T. Stöhlker[1], G. Testera[8], A. Trzcinska[9], J. Ullrich[10], L. Venturelli[11], J. Walz[12], C. Welsch[10], E. Widmann[13], Y. Yamazaki[6] for the FLAIR Collaboration
[1]GSI; [2]Swansea, UK; [3]Stockholm, Sweden; [4]Jülich, Germany; [5]Pbar Labs, USA; [6]Tokyo, Japan; [7]Aarhus, Denmark; [8]INFN Genova, Italy; [9]Warsaw, Poland; [10]Heidelberg, Germany; [11]Brescia, Italy; [12]Mainz, Germany; [13]Vienna, Austria

The proposed Facility for Low-energy Antiproton and Ion Research (FLAIR) will take advantage of the world highest antiproton flux available at FAIR. The planned complex of storage rings will produce beams of decelerated antiprotons with energy of 30 MeV and excellent phase space density in the NESR. This opens the possibility to further decelerate the beams to create low-energy antiprotons. As proposed in the Letter of Intent [1] submitted in 2004 by the FLAIR collaboration and positively evaluated by the international Project Advisory Committee, antiprotons of 20 keV can be produced using two additional storage rings, the Low-energy Storage Ring (LSR) and the Ultra-low energy Storage Ring (USR) [2]. Moreover using the LSR-HITRAP [3] tandem, antiprotons at ultra-low energies of few eV or even at rest will also be available. Cooled, fast or slow extracted, low-energy antiproton beams with high intensities will allow for unique experiments in nuclear physics, high-precision spectroscopy and atomic collisions [1].

The tasks of the planned LSR - deceleration of antiprotons from 30 MeV to 300 keV, cooling, and fast as well as slow extraction - can be successfully fulfilled by the storage ring CRYRING from Manne Siegbahn Laboratory in Stockholm [4] The ring is planned to be modified in the coming years and then moved to FLAIR.

At CRYRING, investigations of the operation of the ring for deceleration of (anti)protons have started. A very first result of these investigations is illustrated in Fig. 1. It shows the current of protons throughout an acceleration-deceleration cycle and the associated transmission. Before t=0, protons are stacked and continuously cooled at the injection energy of 300 keV, such that the stored current gradually increases. At t=0, 6.4 μA protons have been accumulated, and they are accelerated to 30 MeV in 1.6 s. The acceleration increases the velocity of the protons by a factor 10, and the current should thus also increase by a factor of 10. The observed factor is 9.3, indicating a 93% transmission during acceleration. After a flat top of 0.6 s, the deceleration starts, and it is seen that there is a loss of particles at this point in time. Of the current at the flat top, only 42% are transmitted, while the transmission during the deceleration back to the initial energy of 300 keV, which is reached at t=4 seconds, is 75%. The transmission through the entire cycle is thus 30%, and through the deceleration alone it is 32%. The current after deceleration, 1.9 μA, corresponds to 8×10^7 particles. This test shows that it is quite straightforward to operate CRYRING in a deceleration mode, and we expect to be able to eliminate the rather large particle loss after a few more days of development.

For the civil construction design of the FLAIR facility an optimisation of the required experimental areas and the annex facilities was performed. The proposed building covers an area of 3200 m^2 and has been designed to accommodate 9 different experimental areas, a hall for the LSR and additional areas for off-line mounting and testing, control and data acquisitions rooms, laser labs and storage rooms. Additional 700 m^2 will provide space for a workshop, and for storing and mounting of the experimental setups. There are 6 areas dedicated to low-energy antiproton physics, two for experiments with highly charged ions (HITRAP and the low-energy cave) and a third one, where both beams, highly charged ions and antiprotons, at extremely low energy will be provided.

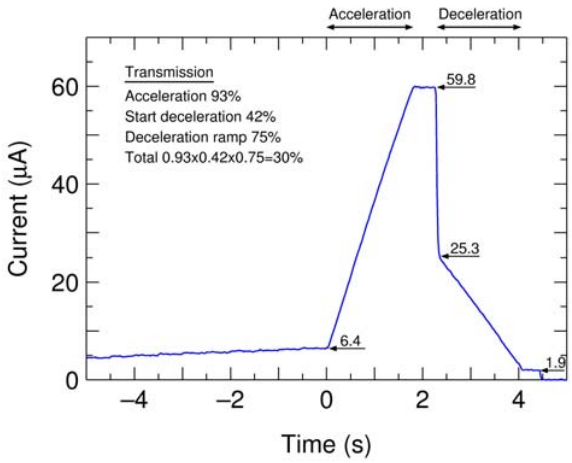

Fig. 1: Proton current throughout an acceleration–deceleration cycle in CRYRING.

The size of these areas has been adjusted to the size of the planned experimental setups. The general building layout is based on preliminary simulations for beam transport between the NESR, LSR, USR and the experimental areas and considers the beam parameters requested by the proposed experiments [4]. Also preliminary estimations of the needed concrete shielding have been performed by the GSI radiation protection group. The proposed shielding will permit parallel work in different areas independent of the presence of the beam at neighbouring locations. Technical details of the FLAIR facility have been discussed at a FLAIR Collaboration Meeting at GSI (September 2004) and at a workshop in Vienna (December 2004).

We acknowledge financial support by the European Union (RTD-Network HITRAP HPRI-CT-2001-50036).

References:

[1] FLAIR Letter of Intent, see www-linux.gsi.de/~flair
[2] TP C. Welsch et al., Proc. Part. Acc. Conf., Portland, 2004
[3] T. Beier *et al.*, HITRAP Technical Design Report, www.gsi.de/documents/DOC-2003-Dec-69-2.pdf
[4] FLAIR Technical Proposal, see www-linux.gsi.de/~flair

Technical developments for the R^{3}B experiment

The R^{3}B collaboration

A versatile reaction setup with high efficiency, acceptance, and resolution for kinematically complete measurements of Reactions with Relativistic Radioactive Beams (R^{3}B) is proposed. The setup will be located at the focal plane of the high-energy branch of the Super-FRS. The experimental configuration is based on a concept similar to the existing LAND reaction setup at GSI introducing substantial improvement with respect to resolution and an extended detection scheme, which comprises the additional detection of light (target-like) recoil particles and a high-resolution fragment spectrometer. The setup is adapted to the highest beam energies (corresponding to 20 Tm magnetic rigidity) provided by the Super-FRS capitalizing on the highest possible transmission of secondary beams. The experimental setup is suitable for a wide variety of scattering experiments, i.e., such as heavy-ion induced electromagnetic excitation, knockout and breakup reactions, or light-ion (in)elastic and quasi-free scattering in inverse kinematics, thus enabling a broad physics programme with rare-isotope beams to be performed. A technical proposal [1] describing the concept and the individual sub-systems was submitted by 15th of January 2005 and evaluated by the NUSTAR PAC in March.

A schematic drawing of the setup is shown in Figure 1. Although the secondary beams provided by the Super-FRS have a large momentum spread of ±2.5%, high-resolution scattering experiments are possible by individually tracking the ions starting from the middle focal plane of the separator. The heavy ions are identified and tracked on an event-by-event basis providing a momentum measurement with a relative precision of about 10^{-4}. The same precision will be reached for the outgoing fragments after the reaction target by tracking the beam through the dipole field of a large-acceptance dipole and a magnetic spectrometer ('High-resolution measurement', see Fig. 1). The design of the spectrometer will be close to that of the Super-FRS, i.e. providing the same angular and momentum acceptance. The relative momentum resolution of 10^{-4} will allow a precise measurement of the recoil momentum in knockout reactions and quasi-free scattering experiments even for heavy beams.

Alternatively, the fragments may be deflected to the other direction and detected by large-area detectors ('Large-acceptance measurement, see Fig. 1). In this case, the tracking results in a relative momentum resolution of about 10^{-3}.

The excitation energy of scattered projectiles is reconstructed from the measured momenta of the outgoing fragments and particles by using the invariant-mass method. In order to achieve good invariant-mass resolution (better than 1 MeV) even at high beam energies of around 1 GeV/u, a high-resolution ToF spectrometer for neutrons and a γ spectrometer with large sum-energy efficiency and high granularity is being developed. The γ calorimeter will consist of $LaBr_3$(Ce) crystals or cooled pure NaI or CsI crystals. The latter provide an intrinsic energy resolution of about 2%. $LaBr_3$ has a similar energy resolution without the need of cooling and has the additional advantage of higher density. This material, however, is at present rather expensive. In order to achieve small Doppler broadening in the order of the intrinsic resolution a very good angular resolution for the photons is demanded resulting in a high granularity of the array in the order of 10000 individual crystals with an entrance area of about 5×5 mm^2.

High-energy neutrons (~1 GeV) are detected in forward direction with high efficiency (close to 100 %) and their momenta are determined from position and time-of-flight measurements. The detector consists of alternating layers of converter material and charged-particles detectors. Resistive Plate Chambers (RPC) are considered providing excellent time resolution of σ_t<50 ps. Together with a position resolution of σ_x~1 cm, the neutron momentum can be measured with a relative resolution of about ~10^{-3}. For applications where the highest resolution is needed and cross section measurements at very low neutron-fragment relative energies, i.e. for astrophysical relevant reactions, the detector can be placed far away from the target (~35 m) resulting in an excellent resolution of better than 20 keV (at 100 keV relative energy).

References

[1] The R^{3}B Technical Proposal, http://www.gsi.de/nustar/

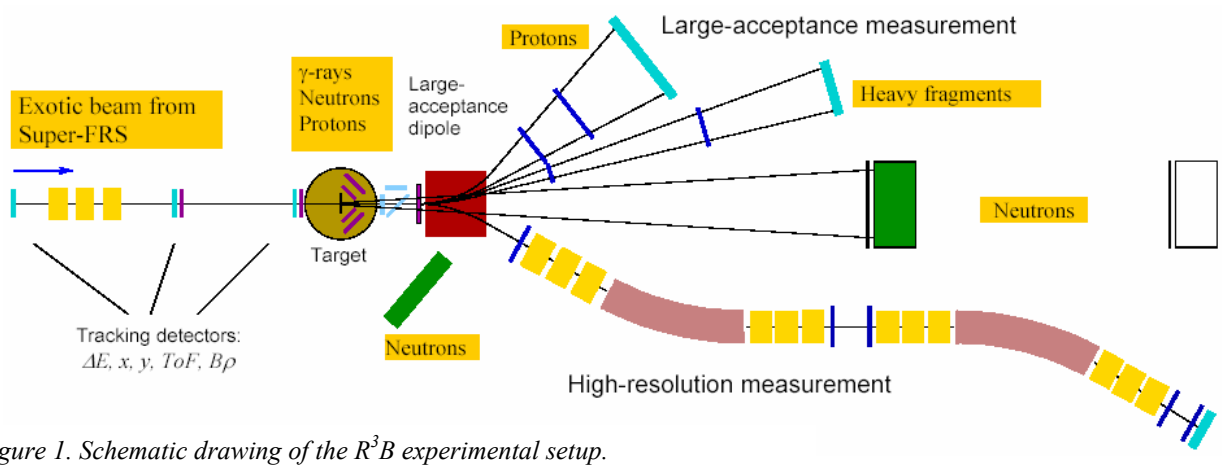

Figure 1. Schematic drawing of the R^{3}B experimental setup.

Simulations of a Liquid Jet Target Using a Fast Extraction Scheme for the Super-FRS

N. A. Tahir[1], H.Weick[1], H.Geissel[1], A.Kelic[1], B. Kindler[1], B.Lommel[1], G.Münzenberg[1], K.Sümmerer[1], A. Shutov[2], M.Winkler[1]*andD.H.H. Hoffmann*[1,3]

[1]GSI Darmstadt, [2]ICPR Chernogolovka, [3]*TUDarmstadt*

In addition to a rotating wheel shaped graphite target irradiated by an extended beam spot [1], a windowless liquid metal jet target may be considered for the high beam intensity of the order of 10^{12} ions of 1 GeV/u uranium delivered in a 50 ns long, single bunch to the Super-FRS. Different materials that can be used to construct the target include Li, Na, Ga, Hg and Pb. Lower-Z targets are preferable due to the higher nuclear cross section, for the same atomic energy loss, leading to much higher production rates of radioactive nuclides. Also activation will be much lower for these targets. It is important that the liquid does not become gaseous as a result of beam heating. From this point of view Li has an additional advantage as it has a wide operational range for temperature (melting temperature = 460 K and boiling temperature = 1643 K). However a definite decision about the choice of the material for a target will be made later.

This contribution presents first simulation results of a liquid lithium target that is irradiated by the above beam parameters. The simulations have been carried out using a two-dimensional hydrodynamic computer code, BIG-2 [2]. In practice one would use a free falling layer of liquid, but for the simlicity of the calculations we consider a cylinder of liquid lithium and the beam is incident on one of the faces of the target. The cylinder has a length of 7 cm so that the target line density is 3.7 g/cm^2 and the ions lose 27 % of their energy in the target and emerge from the opposite face with a reduced energy. In order to keep lithium in liquid state, an initial temperature of 460 K is assumed.

We consider two values for the beam focal spot. In practice one uses an elliptic focal spot with a Gaussian beam intensity profile in the transverse direction. However due to the limitation that BIG-2 is a two-dimensional model, we consider a circular focal spot that has the same area as the elliptic one. First we assume that the standard deviation , σ of the circular focal spot is 1.414 mm that corresponds to σ_x = 1 mm and σ_y = 2 mm for an equivalent elliptic focal spot. The results are plotted in Figs. 1, 2, 3 and 4.

In Fig. 1 we present the specific energy that is deposited in the target by the beam at t = 50 ns, the time when the beam has just delivered its total energy. At the maximum of the Gaussian intensity distribution at r = 0 mm, a maximum temperature of 6818 K and a maximum pressure of 7.25 GPa are created. The boiling temperature of lithium is 1643 K, therefore the material in the beam heated region will become gaseous. Simulations show that the gaseous material will move along the beam line with a high velocity of the order of 3.2 km/s. This will result in spilling of lithium in the beam line area which will be very difficult to remove. In Fig. 2 we plot the target density at t = 1000 ns and it is seen that the material has significantly expanded

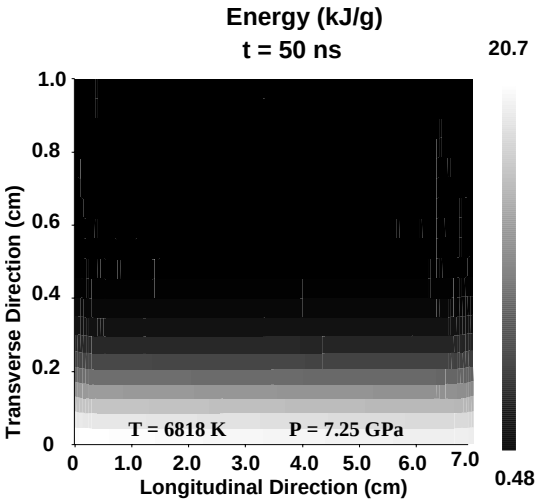

Figure 1: Specific energy deposition on a length-radius plane at t = 50 ns, N = 10^{12} ions, energy = 1 GeV/u, pulse duration = 50 ns, σ = 1.414 mm (equivalent to σ_x = 1 mm, σ_y = 2 mm, for an elliptic focal spot with the same area).

along the axial direction and the density in the expanded region has become 0.04 g/cm^3. Therefore with the considered beam parameters this design is not very attractive. Moreover, due to the high pressure in the heated region, a compression wave will be launched in the transverse direction. In Fig. 3 we plot the velocity of the material that moves outwards as a result of the compression wave along the transverse coordinate at different times. It is seen that at t = 350 ns the velocity has a maximum value of about 1 km/s, but due to cylindrical divergence the compression wave becomes weaker as it travels outwards and slows down. This is seen from Fig. 4 where we plot the density profiles along the transverse direction at different times. At t = 10 μs the velocity has been reduced to 145 m/s and by this time the wave amplitude has also been significantly reduced. The sound speed in the material is of the order of 5 km/s and it is seen that by this time the wave has traveled a distance of about 5 cm in the transverse direction. These calculations show that it may be possible that the compression wave will be damped before it reaches the nozzle of the jet.

Since the specific energy deposition is inversly proportional to the focal spot area, one can reduce the target heating by using a larger focal spot. We now consider a case where we assume a σ = 4.899 mm that has the same area as an elliptic focal spot with σ_x = 2 mm and σ_y = 12 mm. A focal spot of the primary beam with these di-

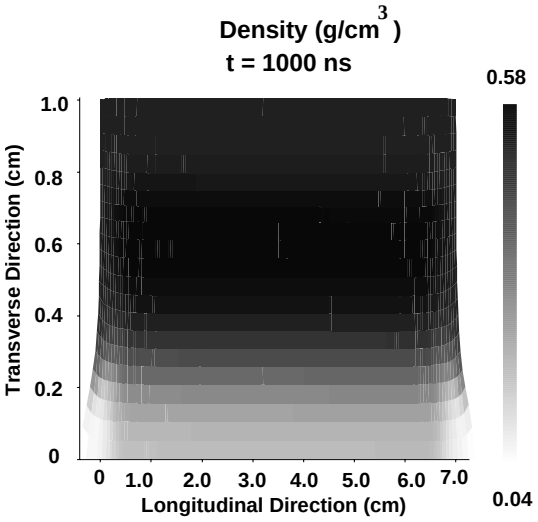

Figure 2: Target density at t = 1000 ns for the case presented in Fig. 1.

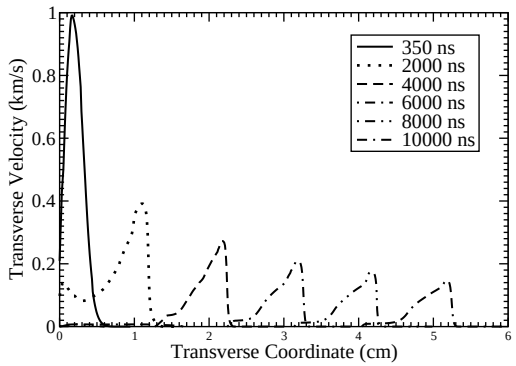

Figure 3: Material velocity in the transverse direction at different times after the irradiation.

mensions leads to an acceptable level of transmission and resolution of the radioactive isotopes. We note that this is an advantage of using a liquid lithium target because instead, if one uses a solid carbon target, one must use a focal spot with $\sigma_x = 4$ mm so that the target survives [3]. This larger value of $\sigma_x = 4$ mm will lead to a poorer resolution.

The results for this case are shown in Fig. 5 where we plot the target density at t = 1000 ns. In this case a specific energy of 1.66 kJ/g is deposited in the material at t = 50 ns at the maximum of the Gaussian distribution and the temperature increases to 1053 K from an initial value of 460 K. The corresponding pressure is of the order of 0.9 GPa. The material therefore remains in a liquid state and there will be no significant hydrodynamic expansion along the axial direction. However some liquid may splash from the surface due to the impact of the beam, but this effect cannot be studied with the present model.

The maximum velocity of the material moving outwards in the transverse direction is 106 m/s which occurs at t = 1200 ns, but at t = 10 μs it is reduced to 50 m/s.

It is seen from Fig. 5 that at t = 1000 ns, there is no sig-

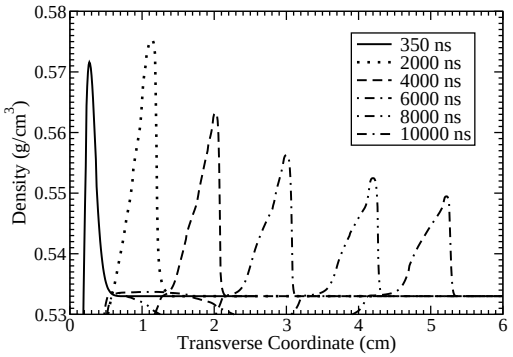

Figure 4: Density profiles along the transverse direction at different times after the irradiation.

nificant expansion along the longitudinal direction. In case of Fig. 2, on the other hand, there is substantial material expansion in longitudinal direction and the density of the expanded material has been reduced to 0.04 g/cm^3. These simulations therefore suggest that this target concept will work if one uses a larger focal spot.

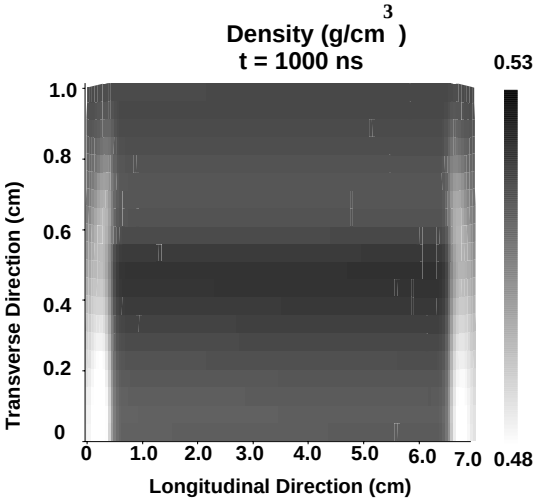

Figure 5: Target density at t = 1000 ns, N = 10^{12} ions, energy = 1 GeV/u, pulse duration = 50 ns, $\sigma = 4.899$ mm (equivalent to $\sigma_x = 2$ mm, $\sigma_y = 12$ mm, for an elliptic focal spot with the same area).

References

[1] N.A. Tahir et al., J. Phys. D (2005) In Print
[2] V.E. Fortov et al., Nucl. Sci. Eng. 123 (1996) 169.
[3] N.A. Tahir et al., J. Phys. D (2005) to be published.

Nuclear Structure Studies on Exotic Nuclei by Light-Ion Induced Direct Reactions with Stored Radioactive Beams

The EXL collaboration*

* see Annex for collaboration list

The experimental conditions at the future facility FAIR will provide unique opportunities for nuclear structure studies on nuclei far off stability, and will allow exploring new regions in the chart of nuclides of high interest for nuclear structure and astrophysics. In particular, the predicted luminosities will allow for the investigation of direct reactions with stored and cooled radioactive beams at internal H, He, etc. targets of the storage ring NESR. This technique enables high resolution measurements down to very low momentum transfer and provides a gain in luminosity from accumulation and recirculation of the radioactive beams.

The objective of the EXL-project (EXotic nuclei studied in Light-ion induced reactions at the NESR storage ring), which is part of the NUSTAR program, is to capitalise on light-ion induced direct reactions in inverse kinematics by using novel storage ring techniques, and a universal detection system providing high resolution and large solid angle coverage in kinematically complete measurements. During 2004 a Letter of Intent [1] was formulated, and the EXL collaboration was structured including the formation of several topical working groups, the first task of which was the preparation of a Technical Proposal [2] which was recently submitted to the FAIR-PAC.

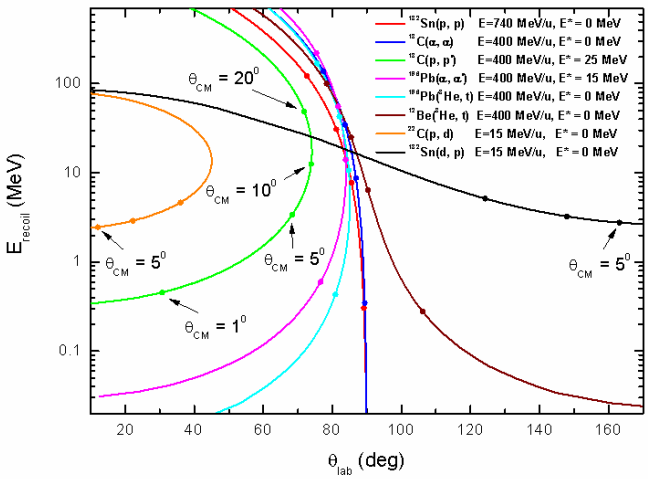

Fig. 1: Kinematics of target-recoil particles for selected reactions.

To address the key physics issues of the EXL project (formulated in details in [1, 2]), such as the investigation of:

- nuclear matter distributions near the neutron drip line (halo -, skin - structures, etc.),
- isospin-dependence of single-particle and shell structure (magic numbers, shell gaps, spectroscopic factors),
- nucleon-nucleon correlations, clusters,
- new collective modes (different deformations for protons and neutrons, giant resonance strengths),
- astrophysical r- and rp-processes (Gamow-Teller strength, neutron-capture),
- in-medium interactions in asymmetric and low-density nuclear matter,

a variety of light-ion induced direct reactions, such as for example elastic scattering (p, p), (α, α), etc., inelastic scattering (p, p'), (α, α'), etc., charge exchange reactions (p, n), (^{3}He, t), (d, ^{2}He), etc., quasi-free scattering (p, 2p), (p, pn), (p, pα), etc., and transfer reactions (p, t), (p, ^{3}He), (p, d), (d, p), etc., need to be investigated. Having in mind that for most of these reactions the relevant nuclear structure information is located in the region of moderate to very small momentum transfer, it becomes obvious from Fig. 1 that the use of cooled stored beams interacting with a thin internal gas target is mandatory for most of these investigations, as it provides

- high resolution detection of low energy recoil particles,
- high luminosities due to the continuous beam accumulation and recirculation,
- low-background conditions due to pure, windowless ^{1,2}H, ^{3,4}He, etc. targets.

Within the Technical Proposal [2] the design of a complex detection setup was investigated with the aim to provide a highly efficient, high-resolution universal detection system, applicable to a wide class of reactions. The apparatus foreseen being installed at the internal target of the NESR storage cooler ring is displayed in Fig. 2. It includes a Si-detector array for recoiling target-like reaction products, completed by gamma-ray and slow-neutron detectors, as well as forward detectors for fast ejectiles and an in-ring spectrometer for the detection of beam-like reaction products.

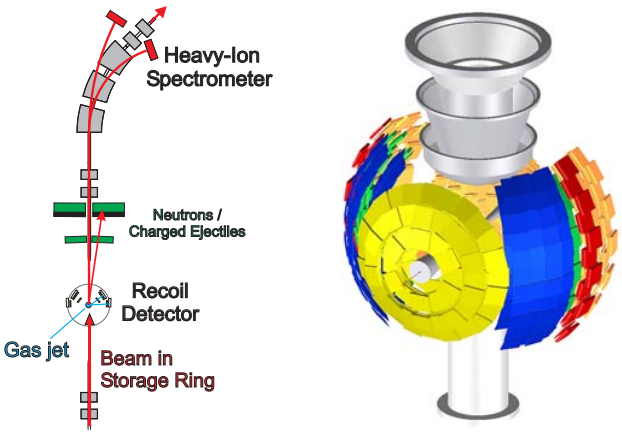

Fig. 2: Schematic view of the EXL detection systems. Left: Setup built into the NESR storage ring. Right: Target-recoil silicon detector surrounding the internal gas-jet target.

Whereas the design of the forward detectors and in ring spectrometers are based on technology already currently available at the LAND setup and at the ESR, respectively, the design and construction of a highly-efficient, universal recoil and gamma detector system will be one of the most challenging tasks of the present research project. In particular, the detector components need to fulfil strong demands concerning angular and energy resolutions, energy threshold, dynamic range, granularity, vacuum capability, etc., partly not available from standard detection systems. Consequently the detector design discussed in the Technical Proposal is only an initial study, which needs to be reconsidered and optimised in the framework of an extensive R&D program within the next three years.

A schematic view of the detector setup surrounding the internal gas-jet target is displayed in Fig. 3. It is foreseen to separate two regions of the setup with different vacuum conditions by a thin window. The inner "high vacuum" part will house the silicon particle array which will be bakeable to temperatures in the vicinity of 130 ºC in order to reach a vacuum of at least 10^{-8} – 10^{-9} mbar. The outer "low vacuum" part of the detector chamber will house the array of scintillation detectors, which is dedicated to detect the gamma-rays, as well as the residual energy of fast recoil particles, which punch through the silicon detectors. A vacuum of about 10^{-5} mbar will be sufficient for that part of the scattering chamber.

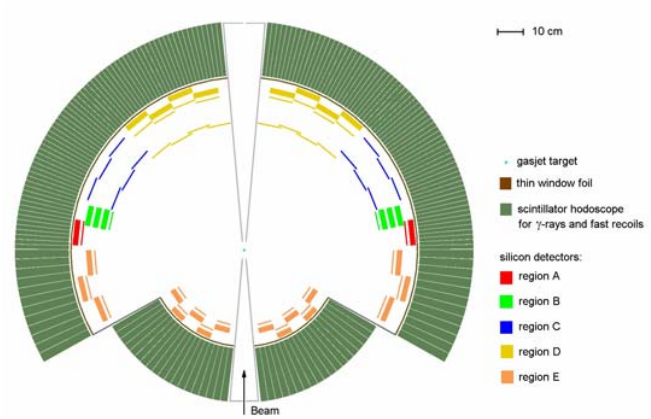

Fig. 3: Schematic view of the detector setup of the EXL recoil and gamma array (cross section through the mid plane).

Different regions A-E of the lab-angular range correspond to a colour code as defined in Fig. 3. Except for the regions C and D, where particle tracking is foreseen, the angular resolution will be determined in all other regions by the dimension of the gas-jet target and the distance of the detectors from the beam-target interaction point. The choice of the detector geometry and detector types for the different regions A-E are optimized with respect to the kinematical conditions and demands on energy and angular resolution for the various types of reactions to be studied (for details see [2]). For angular regions A, B and E telescopes consisting of double-sided silicon strip detectors, 300 µm thick, and 9 mm thick lithium-drifted silicon detectors behind are foreseen, whereas regions C and D will be equipped with tracking detectors consisting of double-sided silicon strip detectors, 100 (300) µm thick. To optimise the detection efficiency of the recoil detector, a maximum solid angle cover allowed by the installations needed for the gas-jet target is investigated. At angles close to Θ_{lab} = 90º a coverage of at least $\varphi = \pm 45º$ in azimuthal angle is foreseen, which can be increased in forward and backward directions. A first attempt at a possible 3D detector geometry is displayed in Fig. 2. It should be pointed out that this concept is subject to further detailed investigations in the near future to define a final optimum solution.

The scintillator hodoscope consisting of about 1500 individual crystals, built of scintillator material (CsI or others) is supposed to detect γ-rays emitted from excited beam-like reaction products, as well as the residual kinetic energy of fast target-like reaction products, which punch through the silicon detectors discussed above. Concerning the detection of γ-rays, aside of the γ-sum energy for missing-mass reconstruction in case the excited beam-like reaction product is particle unstable (for example after GR excitation), the detector has also to provide γ-multiplicities and individual γ-energies for spectroscopic purposes. By detecting the γ-rays from the decay of excited beam-like reaction products it also serves in separating elastic and inelastic reaction channels in cases of low-level spacing where the angular and energy resolution of the silicon detectors are not sufficient to resolve these reaction channels.

It is clear from these considerations that only a highly efficient, high-resolution device will satisfy the demands formulated above. An almost 4π coverage, sufficient detector thickness for ~ 80 % γ-detection efficiency at E_γ = 2 – 4 MeV and for stopping of up to 300 MeV protons, an energy and resolution of 2-3 % for γ-rays and 1 % for fast protons are required. In the case of γ-rays, the line broadening due to the Doppler shift, most substantial at highest beam energies, imposes a high detector granularity.

As already discussed above, an extended R&D program was recently started with the aim to

- continue the investigations concerning design studies for the several subsystems of the EXL setup,
- design and build prototype units of the different detector components, and to
- perform test experiments at the present ESR facility with the aim to explore the experimental conditions and to test prototype detectors under realistic beam conditions.

References

[1] http://www-w2k.gsi.de/superfrs/documents/NUSTAR/LoI/NUSTAR-LOI.pdf

[2] http://www-linux.gsi.de/~wwwnusta/tech_report/05-exl.pdf

Antiproton-Ion Collider

Peter Beller [1], Fritz Bosch [1], Michael Cargnelli [2], Laura Fabbietti [3], Thomas Faestermann [3], Bernhard Frankze [1], Hermann Fuhrmann [2], Ryugo S. Hayano [4], Albert Hirtl [2], Josef Homolka [3], Paul Kienle [2,3], Christophor Kozhuharov [1], Reiner Krücken [3], Horst Lenske [5], Yuri Litvinov [1], Johann Marton [2], Fritz Nolden [1], Peter Ring [3], Yuri Shatunov [6], Alexander N. Skrinsky [6], Ken Suzuki [3], Vladimir A. Vostrikov [6], Takayuki Yamaguchi [7], Eberhard Widmann [2], Slawomir Wycech [8] and Johann Zmeskal [2]

[1]Gesellschaft für Schwerionenforschung, Darmstadt, Germany; [2]Stephan Meyer Institut, Vienna, Austria; [3]Technische Universität München, Munich, Germany; [4]University of Tokyo, Tokyo, Japan; [5]Justus-Liebig Universität Giessen., Giessen, Germany; [6]Budker Institute of Nuclear Physics, Novosibirsk, Russia; [7]University of Saytama, Saytama, Japan; [8]Andrzej Soltan Institute for Nuclear Studies, Warsaw, Poland

An antiproton-ion collider is proposed to independently determine rms radii for protons and neutrons instable and short lived nuclei by means of antiproton absorption at medium energies[1]. The experiment makes use of the electron ion collider complex[2] with appropriate modifications of the electron ring to store, cool and collide antiprotons of 30 MeV energy with 740A MeV ions in the NESR (Fig. 1). Antiprotons are collected, in the RESR and will be cooled and slowed down to 30 MeV by an additional electron cooler. Hereafter the 30 MeV antiprotons are transferred to the electron storage ring using a new transfer line. Radioactive nuclei are produced by projectile fragmentation and projectile fission of 1.5A GeV primary beams and separated in the Super FRS. The separated beams are transferred to the collector ring (CR) and cooled at 740A MeV and transported via the RESR to NESR, in which especially short lived nuclei are accumulated continuously to increase the luminosity. The total absorption cross-section for antiprotons on the stored ions with mass A will be measured by detecting the loss of stored ions by means of the Schottky method[3]. Cross sections for the absorption on protons and neutrons, respectively, will be measured by the detection of residual nuclei with A-1 either by the Schottky method or by detecting them in recoil detectors after the first dipole stage of the NESR following the interaction zone. With a measurement of the A-1 fragment momentum distribution, one can test the momentum wave functions of the annihilated neutrons and protons, respectively. Furthermore by changing the incident ion energy the tails of neutron and proton distribution can be measured. Theoretical calculations clearly show that the absorption cross sections are directly proportional to the mean square radii[4]. Predicted cross sections and luminosities show that the method is applicable to nuclei with production rates down to about 10^5 s^{-1} or lower depending on the lifetime of the ions in NESR and half-lives of about down to 1 second (Table 1) [5].

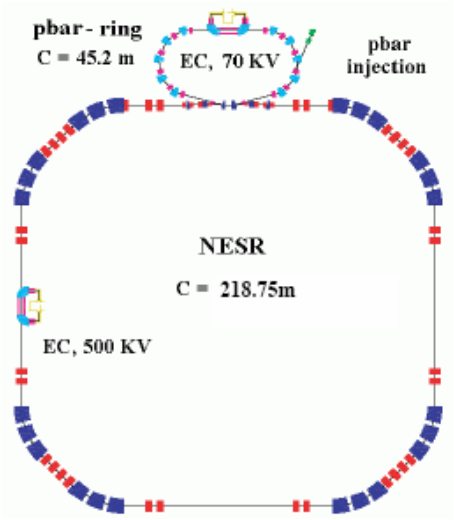

Figure. 1 Schematic layout of the antiproton-ion collider magnetic lattices.

References

[1] P. Kienle, Nucl. Instr. Meth. B 213 (2004) 191.

[2] ELISE Technical Proposal.

[3] B. Borer *et al*., Proc. IX Conf. on High Energy Accelerators, Stanford 1974.

[4] H. Lenske and P. Kienle, submitted to PLB, eprint-archiv; nucl-th/0502065.

[5] AIC Technical Proposal.

Table 1: Summary of luminosities, cross sections, event rate and related numbers for typical ions

Ion	Intensity	Life	Luminos	σ_{total}	σ_{N-1}	σ_{Z-1}	N_{event}(Total)	N_{event}(N-1)	N_{event}(Z-1)	Meas.Time
-	[1/s]	[s]	[1/(cm^{2}s)]	[barn]	[barn]	[barn]	[1/s]	[1/s]	[1/s]	[min/10k ev.]
^{40}Ar	*6E+08*	*20*	*1.2E+27*	*0.96*	*0.48*	*0.48*	*1151*	*173*	*173*	*0.14*
^{52}Ca	*4E+05*	*12*	*4.8E+23*	*1.14*	*0.64*	*0.51*	*0.55*	*0.09*	*0.07*	*304*
^{55}Ni	*8E+07*	*0.5*	*4.0E+24*	*1.2*	*0.60*	*0.60*	*4.80*	*0.72*	*0.72*	*34.7*
^{72}Ni	*9E+06*	*4.1*	*3.7E+24*	*1.3*	*0.80*	*0.50*	*4.80*	*0.89*	*0.55*	*34.7*
^{104}Sn	*1E+06*	*51*	*5.1E+24*	*1.81*	*0.94*	*0.87*	*9.25*	*2.40*	*2.22*	*18.0*
^{132}Sn	*1E+08*	*93*	*9.3E+26*	*2.13*	*1.32*	*0.81*	*1977*	*614*	*374*	*0.08*
^{134}Sn	*8E+05*	*2.7*	*2.2E+23*	*2.15*	*1.35*	*0.80*	*0.46*	*0.15*	*0.09*	*359*
^{187}Pb	*1E+07*	*34*	*3.4E+25*	*2.68*	*1.51*	*1.18*	*91.2*	*25.6*	*20.0*	*1.83*

The ELISe experiment at FAIR

The ELISe collaboration

The ELISe objective is to capitalize on elastic, inelastic, and quasi-free electron scattering on unstable, short-lived nuclei by using intersecting ion and electron storage rings and an electron spectrometer operating in conjunction with a detector system for reaction products, providing high resolution and large solid angle coverage. The experiment is foreseen to be installed at the New Experimental Storage Ring (NESR) at FAIR where cooled secondary beams of radioactive ions will collide with an intense electron beam circulating in a small electron storage ring.

The main two challenges in the foreseen experimental programme [1] are to reach sufficient luminosities for electron-ion scattering experiments in the ELISe setup and to build a in-ring spectrometer that combines a large solid angle coverage with a very high resolution of $\delta p/p$ 1.10^{-4} together with a angular resolution of 1 mrad. These requirements are given by the collider kinematics where angular and energy resolution gets coupled.

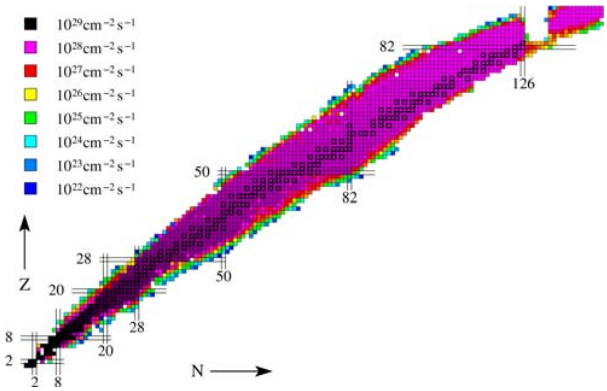

Figure1: Expected luminosities for the electron-ion collider in the interaction zone. A full simulation is done for each isotope, calculating optimized degrader settings for the separator and deducing losses due to transmission and nuclear and atomic lifetime.

We have a performed a full simulation of the production, transport and storage process in order to answer this question. The production yields have been already calculated for the conceptual design report by K.-H. Schmidt. This data together with another data set specifying the production method (i.e. fission or fragmentation), provided by the author, was used to estimate the ion optical transport through the separator, where a simple parameterisation could be used. The resolution for the ion-optical separation depends strongly on the total degrader thickness in units of the range of the ions through the separator. The range has been calculated and has been used to determine the degrader thickness in g/cm² for a given ratio. This ratio has been provided by the ion-optics group calculating the Super-FRS. The absolute thickness could now be used to compute degrader losses by electromagnetic and nuclear break-up reactions. Here the BCV parameterization has been used to calculate the nuclear interaction cross section. The electromagnetic has been simplified by assuming that the break-up process proceeds only through the GDR. The total cross section was computed using a parameterization for the GDR and folding it with the number of available equivalent photons. The injection limit into the ring system has been taken into account. The nuclear life times have been extracted from the Lund table of Isotope, the atomic life times in the NESR where calculated with a code provided by the atomic physics group. A result of these calculations is shown in Figure 1, where one can see that the reachable luminosities do not depend very much on neutron and proton number in a large range, and than drop down towards shorter lifetimes and lower production yields at the drip-lines. The featureless behaviour can be explained with the current injection limits into the storage rings. The expected luminosities allow for a viable experimental programme covering all proposed experiments for ELISe.

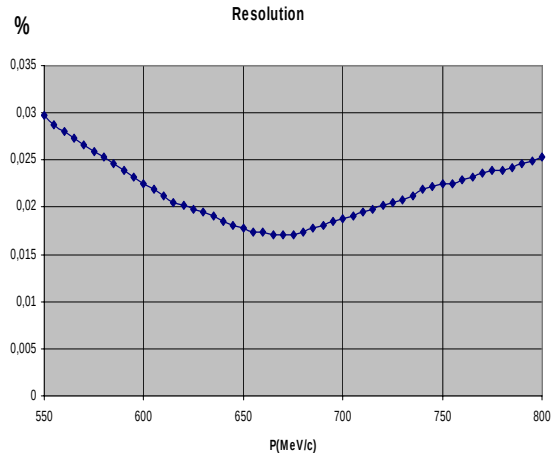

Figure 2: Final resolution of the non-optimized test-bench system. The nominal resolution of $\delta p/p=10^{-4}$ can almost be achieved. Necessary improvements are discussed in the text.

A test bench system has been defined for the spectrometer system, consisting of a in-ring pre-deflection system (the analogue of a septum magnet) and a dipole spectrometer stage with associated instrumentation. A design for the pre-deflection system has been determined. A tracking MC simulation has been performed for this system and the results are shown in Figure 2. Even with a non-optimized set-up – no higher order corrections to the magnetic systems have been introduced – the resolution meets almost the requirements, thus showing the feasibility of this core-component of the experimental setup.

In summary, two major issues for the electron-ion collider have been tackled. The next steps will be to sue the gathered information in order to come up with a full simulation of the foreseen experiments at the ELISe experiment.

References

[1] Technical Proposal and Letter of Intent for ELISe (see http://www.gsi.de/forschung/kp/kp2/nustar.html)

LAPLAS: Laboratory Planetary Science at Future FAIR Facility

N.A. Tahir[1], C. Deutsch[2], V.E. Fortov[3], B. Geil[4], D.H.H. Hoffmann[1,4], I.V. Lomonosov[3], A.R. Piriz[5], A. Shutov[3], M. Temporal[5], S. Udrea[4], and D. Varentsov[4]

[1]GSI Darmstadt; [2]LPGP Orsay; [3]IPCP Chernogolovka; [4]TU-Darmstadt; [5]UCLM Spain

Study of the structures of giant planets, Jupiter, Saturn, Uranus and Neptune is a very interesting subject as this knowledge could lead to clues about formation of the solar system and can also shed light on the early stages of evolution of life on earth. The first two planets are believed to be made mainly of hydrogen that exists under extreme conditions, while the latter two are expected to contain large quantities of water (ice) in very exotic states.

Development of high power lasers have made possible laboratory astrophysics. Recent advancements and planned future developments [1] in the technology of intense bunched beams of heavy ions have lead to the idea of laboratory planetary sciences using these beams. The proposed beam-target geometry is shown in Fig. 1. The target consists of a solid cylinder of hydrogen that is enclosed in a thick shell of a heavy material like lead or gold. One face of the target is irradiated by the beam so that the beam axis coincides with the target axis. The range of the particles is much larger than the target length so the energy deposition is uniform along the particle trajectory. Although the hydrogen will be heated by the beam, the pressure generated in the surrounding high density shell will be substantially higher than that of hydrogen, that will implode the target.

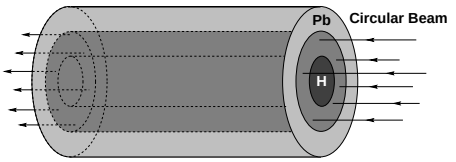

Figure 1: Beam-target configuration for LAPLAS (Laboratory Planetary Science) experiment.

The Gesellschaft für Schwerionenforschung (GSI), Darmstadt is in the process of building a new accelerator facility named FAIR (Facility for Antiprotons and Ion Research) that will generate a uranium beam with an intensity, N = 2 × 10^{12} ions that will be delivered in a single bunch. A wide range of particle energy (0.4 - 2.7 GeV/u) will be available and depending on the energy, the bunch length will lie between 20 - 100 ns. The beam intensity is expected to increase gradually, in steps, over a period of few years. It is therefore important to know if one can carry out useful experiments during the early stages of the facility when the beam intensity will be below the maximum value. To answer the above question we have carried out numerical simulations of the implosion of the target shown in Fig. 1 assuming a uranium beam with N = 10^{10} ions which are delivered in a single bunch that has a length, τ = 50 ns. The particle energy is assumed to be 1 GeV/u and the beam intensity in the transverse direction is considered to be uniform. These simulations have been carried out using a two-dimensional computer code, BIG-2 [2].

In Fig. 2 we plot the hydrogen density vs radius at the time of optimum compression for three different values of beam spot radius, r_b. These include r_b = 1, 1.5 and 2 mm respectively. It is seen that the density is higher for smaller beam spot because that leads to a higher specific energy deposition which in turn generates a higher driving pressure. It is also seen that the hydrogen is compressed to about 4 times the solid density. The corresponding temperature and pressure profiles are shown in Figs. 3 and 4 respectively. These figures show that with a beam intensity that is about two orders of magnitude less than the expected maximum intensity, one can implode hydrogen to achieve very interesting physical conditions.

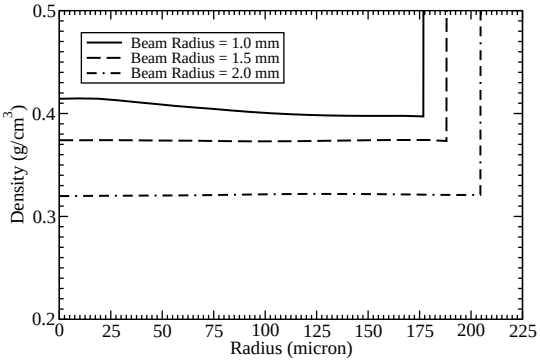

Figure 2: Hydrogen density vs radius at the time of maximum compression using three different values for the beam radius, beam intensity = 10^{10} uranium ions, pulse duration = 50 ns, particle energy = 1 GeV/u.

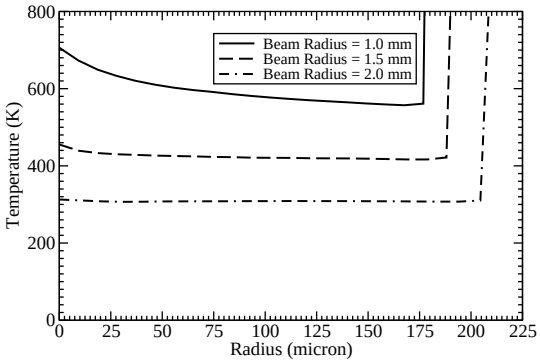

Figure 3: Temperature profiles corresponding to Figure 2.

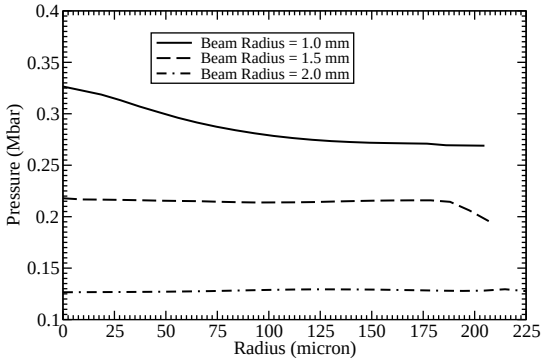

Figure 4: Pressure profiles corresponding to Figure 2.

We also carried out a parameter study of the target implosion using different values of the beam intensity over a wide range (10^{10} - 2×10^{12}). The pulse duration is considered to be 50 ns while three different values are used for the beam radius, assuming a uniform intensity profile in the transverse direction. Three different values are considered for the beam radius which include 0.7, 1 and 1.5 mm respectively. The results are plotted in Figs. 5, 6 and 7. It is seen from Fig. 5 that the maximum hydrogen density increases as the beam intensity increases and the curve with a smaller beam radius is the highest. This is because a smaller beam radius leads to a higher specific energy deposition in the material that generates a higher pressure in the gold shell which leads to a higher compression. However the density increase saturates around an intensity of 7.5×10^{11} ions. This is because if the beam intensity is increased further, the heating of the hydrogen by the beam becomes very strong that leads to a very high pressure and the material is therefore not compressed efficiently.

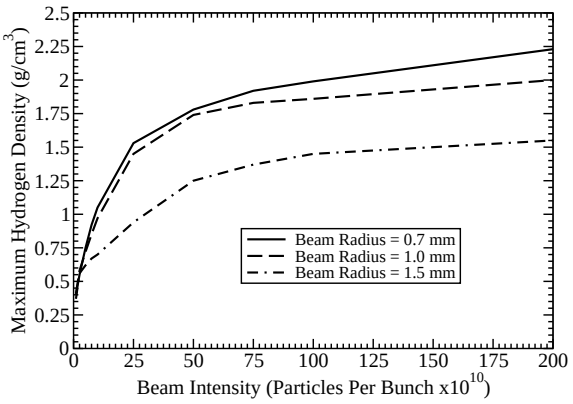

Figure 5: Maximum hydrogen density vs beam intensity using a bunch length = 50 ns, a particle energy of 1 GeV/u and three different values for the beam radius.

This is seen from Fig. 6 where we plot the corresponding temperature profiles. The temperature increases strongly with beam intensity and a maximum temperature of about 6 eV is created for the maximum beam intensity when one uses a beam radius of 0.7 mm. In case of a beam radius of 1.5 mm, the temperature is of the order of 2 - 3 eV. The corresponding pressure profiles are plotted in Fig. 7. It is seen that a wide range of physical parameters of hydrogen can be achieved using the LAPLAS scheme at the FAIR. The physical conditions that are expected in the interior of Jupiter and Saturn lie within this range. Similar calculations have been done using water as a sample material and we have found that one can easily achieve the exotic physical conditions that are predicted to exist in Uranus and Saturn.

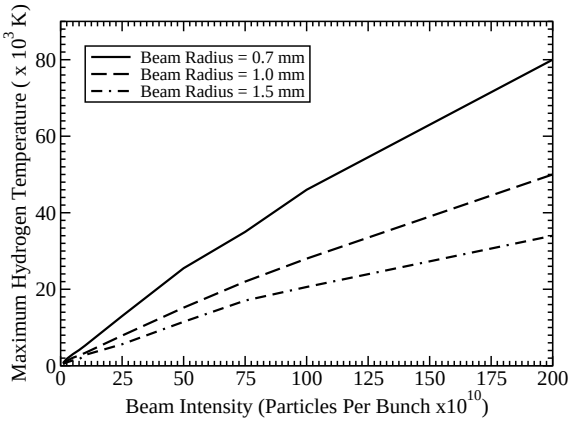

Figure 6:

We note that previously [3,4] we simulated the implosion of the same target, but using an annular focal spot so that the hydrogen was not directly heated by the beam. In that case the hydrogen temperature was much lower (a few thousand K) whereas the density was similar to that in the present case. The corresponding pressure in the previous case was also lower than that in the present one. The physical conditions reported in ref. [3,4] correspond to those needed to metallize hydrogen.

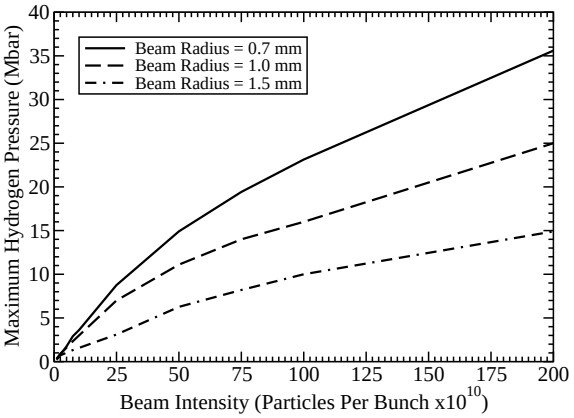

Figure 7:

References

[1] W.F. Hennimg, Nucl. Inst. Meth. A 214 (2004) 211.
[2] V.E. Fortov et al., Nucl. Sci. Eng. 123 (1996) 169.
[3] N.A. Tahir et al., Phys. Rev. E 63 (2001) 016402.
[4] A.R. Piriz et al., Phys. Rev. E 66 (2002) 056403.

HIHEX: Experiment Design to Study Equation of State Properties of High Energy Density Matter at Upgraded SIS18 and FAIR

N.A. Tahir[1], C. Deutsch[2], V.E. Fortov[3], V. Gryaznov[3], D.H.H. Hoffmann[1,4], M. Kulish[3], I.V. Lomonosov[3], V. Mintsev[3], P. Ni[4], D. Nikolaev[3], A. R. Piriz[5], N. Shilkin[3], A. Shutov[3], M. Temporal[5], V. Ternovoi[3], S. Udrea[4], and D. Varentsov[4]

[1]GSI Darmstadt; [2]LPGP Orsay; [3]IPCP Chernogolovka; [4]TU-Darmstadt; [5]Univ. Castilla-La Mancha

Currently, the uranium beam generated by the SIS18 has an intensity of 4×10^9 ions with a particle energy of up to 1 GeV/u that are delivered in a single bunch, a few hundred ns long. It is expected that when the SIS18 upgrade is completed, the beam intensity will increase to 2×10^{11} ions while the bunch length will be reduced to about 100 ns. A new synchrotron SIS100, that will be built at the future FAIR facility, will be able to provide a much more powerful uranium beam with an intensity of 2×10^{12} ions per bunch. The particle energy will be in the range of 400 MeV/u - 2.7 GeV/u and depending on the energy, the bunch length will be in the range 20 - 100 ns.

The beam intensity at the above two facilities is expected to increase gradually and the respective maximum beam intensities will be achieved over a period of several years. It is therefore important to investigate if one can perform useful experiments during the intermediate stages of the facility upgrades. For this purpose we have carried out extensive numerical simulations of thermodynamic and hydrodynamic response of a sample material employing a two–dimensional computer code, BIG-2 [Fortov et al., Nucl. Sci. Eng. 123 (1996) 169], using a wide range of beam intensities (10^{10} - 10^{11} ions/bunch). The design of the proposed experiment showing the beam-target configuration is presented in Fig.1.

The target consists of a number of circular discs of a sample material, each having a diameter, d and a thickness x_1. Separation between two neighboring discs is x_3 and these are enclosed in a cylindrical shell of a strong transparent material like LiF or sapphire. This transparent wall will allow one to perform diagnostics during the experiment. On either side of the cylindrical target, a thin disc of W is placed. The separation between the sample material and the W is denoted by x_2. The ion beam is incident on one face of the target. A thick cylindrical shell of a high density material is used as a beam blocker that stops the ions from irradiating the transparent wall. The ions which are allowed to proceed, penetrate through the W disc, subsequently pass through the elements of the test material and finally emerge from the second W disc. The energy of the incident ions is chosen in such a way that the ion range is much larger than the line density of the target. This allows for a uniform energy deposition along the particle trajectory. In order to ensure a uniform energy deposition along the transverse direction, we assume that the full width at half maximum (FWHM) of the Gaussian intensity profile along the beam radius is much larger than the diameter, d, of the test material.

In one of the simulation cases we use a 500 MeV/u uranium beam with an intensity $N = 7.5 \times 10^{10}$ ions that are delivered in a 100 ns long bunch. The FWHM of the

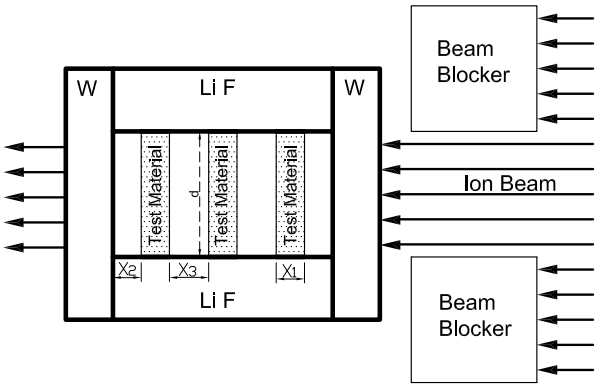

Figure 1: Beam-target geometry for the proposed experiment.

Gaussian beam intensity profile along the radial direction is assumed to be 3 mm. For the sample material we use lead and consider d = 0.8 mm, $x_1 = 200$ μm, $x_2 = 100$ μm and $x_3 = 200$ μm respectively, using three pieces of the test material which is lead. Each of the W discs has a thickness of 50 μm and thickness of the LiF shell is 3 mm. In Figs. 2, 3 and 4 we plot the temperature, pressure and density profiles respectively along the the target length at different times in the lead region. The simulations show that a specific energy of 1.3 kJ/g is deposited in lead.

It is seen from Fig. 2 that at t = 100 ns, the lead region is uniformly heated and the material has already been set in motion. This is also seen from the corresponding pressure and density curves in Figs. 3 and 4 respectively. At t = 150 ns, the counter expanding material from the different pieces of the sample collides and one sees a peak in temperature, pressure and density correspondingly. Multiple reflections take place that tend to homogenize the physical conditions in the sample material (see the corresponding curves at t = 1000 ns).

In Fig. 5 we plot the density, temperature and pressure along the radius in the sample material at t = 5000 ns that shows fairly homogeneous physical conditions in this regions. It is seen that the density is about 5.6 g/cm^3, pressure is of the order of 20 kbar while the temperature is of the order of 8800 K that correspond to conditions of an expanded hot liquid state.

In Fig. 6 we present the same parameters as in Fig. 5, but using $N = 5 \times 10^{10}$, $x_1 = 100$ μm, $x_2 = 100$ μm and $x_3 = 200$ μm. It is seen that the density is about 3.5 g/cm^3, pressure is 6 kbar while the temperature is 7400 keV. These represent physical conditions of a super critical state. The critical point parameters for lead are expected to be a den-

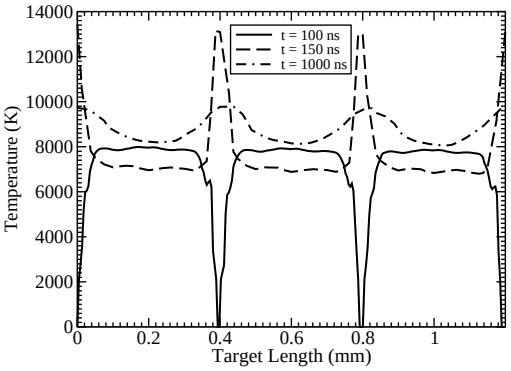

Figure 2: Temperature along target length at different times; 7.5 × 10^{10} uranium ions, 500 MeV/u particle energy, 100 ns long bunch, FWHM = 3 mm; thickness of W = 50 μm, thickness of LiF shell = 3 mm, x_1 = 200 μm, x_2 = 100 μm and x_3 = 200 μm.

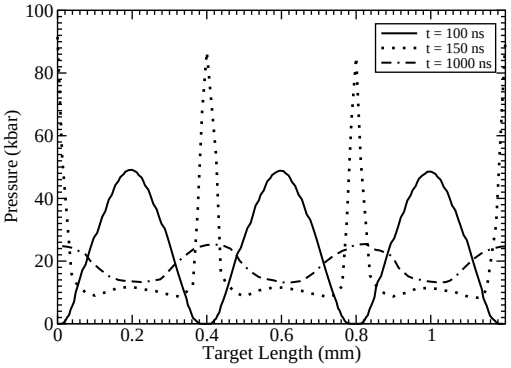

Figure 3: Pressure profiles corresponding to Fig. 2

sity of 3.1 g/cm^3, a pressure of 2.3 kbar and a temperature of 5500 K. The above simulation results show that by changing the dimensions, x_1, x_2 and x_3 of the target, one can control the final density and pressure achieved in the sample material thereby accessing different physical states.

This study suggests that by using beam intensities that are much lower than the maximum expected intensities at the upgraded SIS18 and FAIR, it will be possible to access very interesting regions of the phase diagram. This includes state of an expanded hot liquid, two-phase liquid-gas region and critical as well as supercritical states. However strongly coupled plasma states can only be accessed by much higher beam intensities that will be available at the FAIR when it will be working at its full capacity.

In the HIHEX scheme the equation of state properties will be determined by direct measurement of the physical parameters, density, temperature and pressure. The maximum pressure that LiF can withstand is of the order of 100 kbar, Therefore the target will be stable to the physical conditions achieved in these experiments. The sample pressure will be measured using laser interferometry techniques while the density will be determined using ion beam and proton radiography. The ions for this purpose will be provided from a second beam (imaging beam) that will be incident on the target perpendicular to the main beam. In addition to that, knowing the initial volume of the target, one can easily determine the final density of the sample material. The temperature will be measured by analyzing the thermal radiation emitted from the sample material through the transparent wall of LiF with a pyrometer.

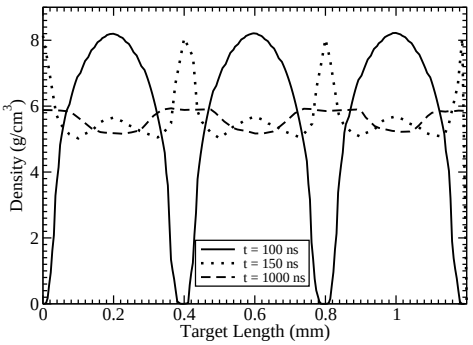

Figure 4: Density profiles corresponding to Fig. 2

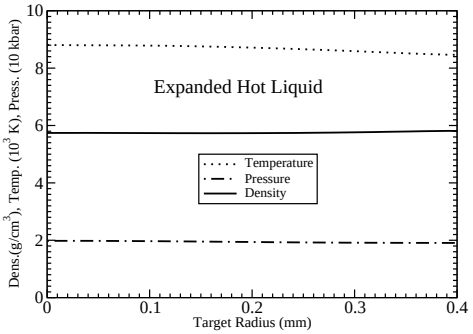

Figure 5: Density, Temperature and pressure vs target radius at t = 5000 ns corresponding to the the case presented in Fig. 2.

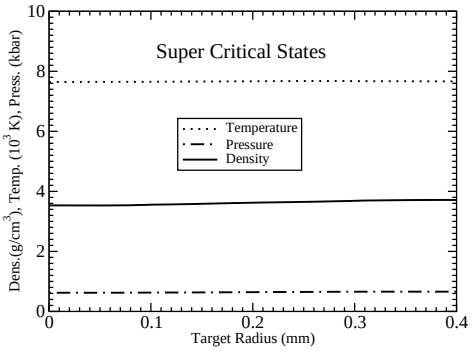

Figure 6: Same as in Fig.7, but using N = 5 × 10^{10} ions, x_1 = 100 μm, x_2 = 100 μm and x_3 = 200 μm at t = 5000 ns.

SPARC Collaboration: A Status Report

R. Schuch[1] and Th. Stöhlker[2] for SPARC

[1]Stockholm University, Sweden; [2]GSI-Darmstadt, Germany

SPARC Collaboration

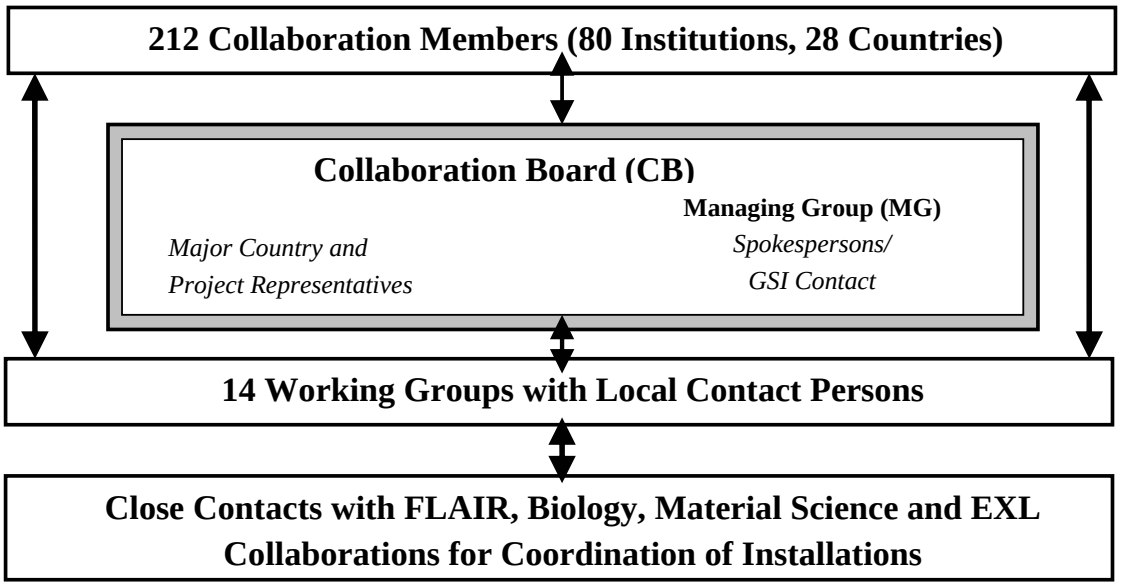

At present the SPARC collaboration consists of 212 members of 80 institutions from 28 countries. On the first SPARC collaboration meeting, Oct. 28.-30. 2004 the collaboration elected a Collaboration Board (CB). This Board takes decisions on physics cases and the collaboration priorities. An election mechanism that guarantees a reasonable country, institute, or research subject representation was defined by the present CB. A spokesperson and a deputy have been proposed by the collaboration board and elected by the collaboration. In addition, the GSI atomic physics division names contact persons responsible for different SPARC subprojects. This group is called the Managing Group (MG) and is part of the CB.

In order to guarantee the construction and set-up of the various components of the project, the collaboration formed 12 experimental working groups responsible for the different technical parts of the project and two theoretical groups [1]. During the first collaboration meeting, the working groups have identified and agreed upon responsibilities for the various tasks. External expert advice will be asked for when deemed necessary by the CB. For each working group, one person, located at GSI or at an institute nearby GS, serves as coordinator with a deputy supporting the coordinator. These persons are named here responsible/contact persons. It is foreseen that the working groups work on the various tasks assigned to them, meet periodically and report to the CB. Written internal reports will be regularly requested by the CB.

Coordination of the financial issues of the project (EU applications, national funding, and additional financial contributions) is another task of the CB. Working group issues, manpower issues, time-plans, and internal financing are handled by the Managing Group and reported regularly to the whole collaboration. Critical decisions on these issues will be taken with the help of the CB.

In 2004 R&D activities and design studies were started within SPARC. At the ESR a first laser cooling experiment was conducted for C^{3+} ions [2]. A dielectronic recombination (DR) experiment, performed with U^{91+} at the ESR electron cooler addressed the KLL resonances in highly charged ions [3]. Also beam lifetime and cross-section studies for low-charged Xe^{18+} ions were performed. The results of this experiment have high relevance for the future FAIR accelerator development activities.

Further on, a two dimensional position sensitive germanium detector prototype was designed and constructed. The detector is now available at GSI for test experiments [4]. This type of detector is needed for high resolution atomic spectroscopy, as presented in the Technical Proposal prepared by the collaboration [5].

Design studies for the electron target as well as for the chamber layout at the internal target proposed to be installed at New Experimental Storage Ring (NESR) were started.

In close collaboration with the FLAIR group, the design of the experimental areas dedicated to low-energy highly charged ions was also started.

References

[1] http://www.gsi.de/sparc

[2] U. Schramm et al., in this report

[3] C. Brandau et al., in this report

[4] D. Protic et al., in this report

[5] SPARC Technical Proposal, see http://www.gsi.de/sparc

FAIR-ACC

Development of the New Accelerator Complex FAIR

Geometrical optimisation of the 70 mA, 70 MeV CH-Proton Injector Cavity for the FAIR Project

G. Clemente[1], M. Droba[1], H. Podlech[1], U. Ratzinger[1], R. Tiede[1,] K. Dermati[2]
[1]Institut für Angewandte Physik der Johann-Wolfgang-Goethe-Universität, Germany
[2] Gesellschaft für Schwerionenforschung, Germany

The FAIR project needs a new injector for the SIS-12, namely a 352 MHz CH proton linac with an output energy of 70 MeV and a beam current of 70 mA[1]. The single cell geometry has been investigated extensively in order to improve the electrical and mechanical properties at the low energy side. A cell geometry with a length of 40 mm (equivalent to β=0.09) was chosen and studied with the program Microwave Studio (see Fig.1).

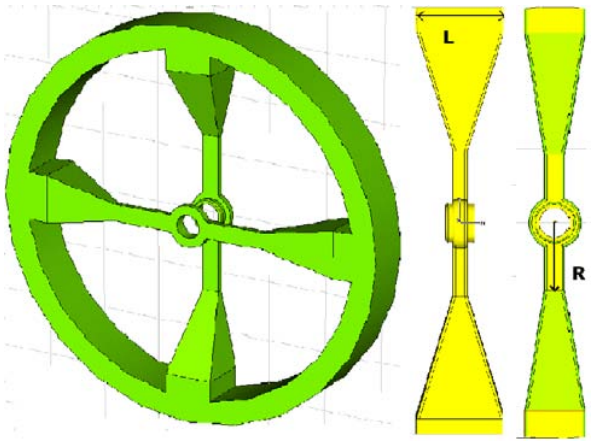

Fig**. 1: The new proposed single-cell design as simulated with Microwave Studio.**

The shunt impedance of the single cell shows a strong dependency on the longitudinal width *L* of the stem: this dependency is plotted for different heights *R* of the parallelepipedal stem part. The effect occurs because of the reduction of the inductivity obtained by decreasing this length towards the beam axis.

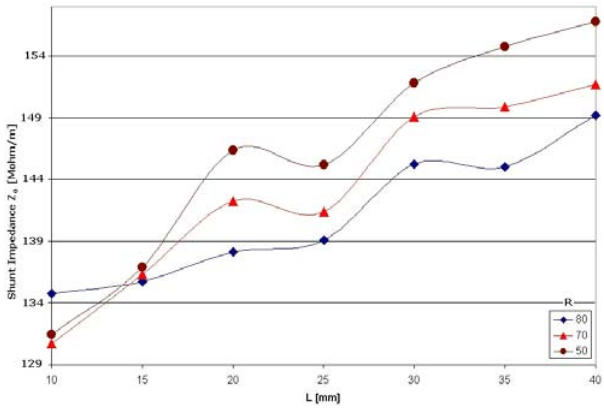

Fig. **2**: **Influence of the cavity geometry on the shunt impedance Z_0 obtained by Microwave Studio simulations by variation of R and L.**

Together with the electrical optimisation we started also to investigate the mechanical properties at the low energy side. At present, several proposals for the design and assembly of this novel type of cavity are under investigation (see fig. 3). In particular, our attention is focused on the mounting of the drift tubes inside the stem.

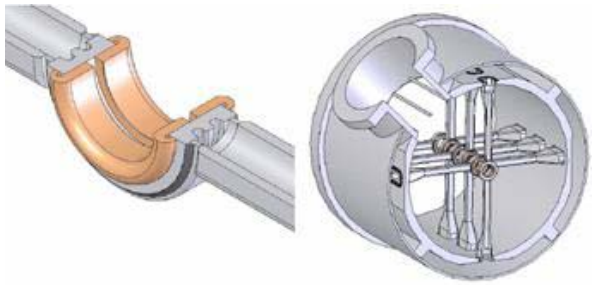

Fig. **3: A detail of the proposed geometry for the drift tubes and for a cavity modeule.**

As shown in Figure 4, a good result could be achieved by press-fitting the half tube from massive copper into the stainless steel stem: it is exspected that this technique will provide both good rf-contacts and mechanical stability.

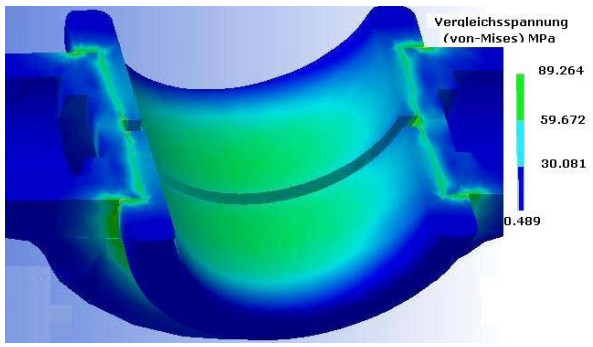

Fig. **4: Mechanical Tensions distribution as simulated by the ANSYS code around the press-fitted drift tubes.**

In the next months the IAP will start the construction of a full size model to investigate in detail all the aspects related to the assembly and mounting of one short module.

References

[1] U.Ratzinger et al. Design Status of the 70 mA, 70 MeV Proton DTL for the FAIR Project, GSI ANNUAL REPORT 2003 p. 262
[2] IAP ARBEITSNOTIZ IAP-ACCC-230704

Development of superconducting magnets for FAIR

Egbert Fischer, Guenther Hess, Juris Kaugerts, Marion Kauschke, Gebhard Moritz, Carsten Muehle, Pierre Schnizer, Claus Schroeder, Gertrud Walter, Yu Xiang

GSI Darmstadt, Germany

SIS100

Substantial progress in reduction of AC losses has been achieved with new model dipole and quadrupole magnets [1,2]. Compared with the original Nuclotron the experimental obtained losses in the new designed 4K test dipole (yoke at liquid helium temperatures) were reduced from 53 W to 24 W (standard cycle 2T, 4T/s, 1Hz). The measured AC losses in the 50K yoke quadrupole and improved 4K yoke quadrupole were 7 W and 15.6 W respectively, i.e. about the factor of 5 and 2.2 less compared to the reference Nuclotron quadrupole [3]. FEM calculations on detailed 3D-models have shown very good agreement with the experimental results [4]. The calculated theoretical limits provide also the quantitative information to design a prototype with minimized AC loss and optimal field quality. This result allows us to estimate a possible loss reduction in the SIS100 dipoles to 6+/-1 W/m (coil) and 7+/-2 W/m (yoke). So the dynamic losses at cryogenic temperatures will be reduced by a factor of 3 and the corresponding overall AC loss in the dipoles will not exceed 7 W/m at intended operating cycles. The final design and operation parameters of the SIS100 magnets depend on additional decisions as the definition of the SIS100 aperture size, the beam pipe design and the coil restrain. The R&D to find a long time reliable and optimal mechanical coil design, allowing also an effective production technology was intensified and is the central part of a EU-FP6 task in close collaboration with industry. In parallel an alternative approach to design and manufacture a hollow tube high current superconducting cable was realized [5]. The new technology, based on superconducting keystoned wires, was developed. From that cable a first single-layer dipole model coil was manufactured and tested. The experimental results have shown the feasibility to build the SIS100 model dipole with a single–layer superconducting coil.

SIS 300

The conceptual design report for the SIS 300 dipole was completed by the Institute for High Energy Physics (IHEP) and a new contract was awarded to IHEP for the technical design of this magnet, including drawings from which model magnets can be constructed [6]. A technique to measure magnetic field harmonics during a fast ramp has been developed at BNL and has been used to measure the field harmonics of the SIS 200 model dipole GSI 001 [7]. Work is continuing to refine the measurement technique. A collaboration was begun with CERN to jointly design the SIS 300 dipoles with IHEP and GSI and then to build and test model dipoles at CERN.

Wire & Cable Development for SIS 100& SIS 300

120 kg of wire was made by European Advanced Superconductors (EAS) for use in the first SIS 300 model magnets. The conductor development was begun before the upgrade from SIS 200 to SIS 300, so that the wire is not well optimized for the SIS 300 application. A more advanced low loss CuMn interfilamentary matrix fine filament strand will be obtained. A cored cable with the dimensions required for SIS 300 has been made by Alstom for coil winding tests and interstrand loss reduction R&D. A fine filament (4 microns) wire was made by EAS to minimize the AC losses.

Collector Ring (CR) and Super Fragment Separator (SFRS)

The bending dipole magnets of the CR, SFRS Pre-Separator 2nd stage and SFRS Main Separator will be superferric because of the high operational costs of resistive solutions in consequence of their very large apertures. A supporting study was made by Al Zeller [8]. The parameters of the SFRS dipoles are very similar to those of the CR. For synergy reasons, the SFRS dipoles will be built to be almost identical to the CR dipoles.

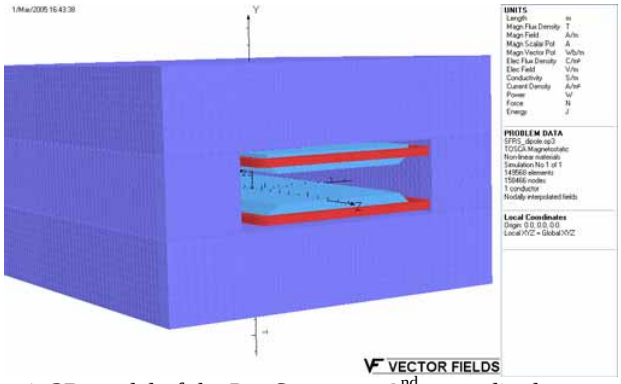

Fig. 1: 3D model of the Pre-Separator, 2nd stage dipole.

A. Kalimov et al. [9] investigated the C-shaped, D-shaped and straight magnet options for the iron design. The straight version is by far the version simplest to calculate and fabricate. Due to the short length of 2.1 m the sagitta is only 70 mm. This leads only to a small increase of iron costs of 11 % compared to the curved version. Therefore we decided for the stacked straight version. A design satisfying all requirements for the superferric CR and SFRS dipoles was made by A. Kalimov [10] and is shown in Fig. 1. An appropriate cryostat structure for the CR dipole was designed by Q. Wang [11]. A. Kalimov also finished a preliminary design of the superferric SFRS wide quadrupole that meets the conditions for the wide CR quadrupole, too.

Cryogenics

The proposal to use two cryoplants with different sizes (7 kW at stage 1, 15 kW at stage 2) for the FAIR project has been technically justified. A general layout for helium distribution from the central cryoplants to individual facilities has been proposed. For the individual facilities, e.g. SIS 100, SIS 300, HEBT, Super-FRS, CR, RESR and NESR, the cryogenic transfer line, the feed- and end-boxes, including the current leads have been specifically quantified. Based on the conceptual design of the cryogenic system for FAIR,

R&D working packages for the individual subprojects have been outlined according to the priority and the risk. In addition, the costs and the personnel required for the R&D and the construction have been projected.

Test facility

For testing fast-ramped superconducting magnets for the FAIR project a test facility is set up at GSI to test model and prototype superconducting magnets for the different planned machines (SIS100, SIS300, SFRS and the storage rings). The following magnet tests are planned: measurements of losses, quenches and training, magnetic measurements and long-term stability tests. The facility accommodates forced-flow cooled model and prototype magnets with a maximum length of 2.6 m, and bath-cooled magnets for the planned CR, SFRS, and NESR/RESR. The facility will consist of a refrigerator (400 W at 4 K) with a distribution box for the different cooling schemes (supercritical for the RHIC-/UNK-type magnets and two-phase helium for the Nuclotron-type window-frame magnet) which were already commissioned. In addition, the 2 feedcans providing electrical and cryogenic supply for the magnets and an all-purpose horizontal magnet cryostat for all kinds of different magnets were already delivered. An AC power supply including the quench protection system is partly commissioned and most components of a quench detection system adapted from the LHC-series test facilities are also delivered. The completion of the test facility is planned for spring 2005. For magnetic measurements of the superconducting magnets at 4 K a non-metallic prototype warm bore is under construction and a mole is in the design phase.

Fig. 2: The prototype test facility for fast-ramped superconducting magnets. Left hand side: feedcan, right hand side: rectangular all-purpose cryostat.

References

[1] A.D.Kovalenko et al. “Design and study of a superferric model dipole and quadrupole magnets for the GSI fast-pulsed synchrotron” in Proc. 9ht European Particle Accelerator Conference, Lucerne, 2004, to be published

[2] E. Fischer et al, "Minimization of AC Power Losses in Fast Cycling Window Frame 2T Superferric Magnets with the Yoke at 4.5 K", ASC 2004: 3LR04, to be published

[3] Report on R&D contract Nr.5; GSI Darmstadt – JINR Dubna, 2005

[4] R. Kurnyshov, P. Shcherbakov, E. Fischer, Report on FEM-R&D contract Nr.1; GSI Darmstadt, 2004

[5] H. Khodzhibagiyan, et.al.,. " Design and Test of a Hollow Superconducting Cable based on Keystoned NbTi Composite Wires " ASC 2004: 1LX03, to be published

[6] J. Kaugerts et al, “Design of a 6 T, 1 T/s Fast-Ramping Synchrotron Magnet for GSI’s Planned SIS 300 Accelerator“, to be published, Proceedings of the 2004 Applied Superconductivity Conference, held in Jacksonville, Florida

[7] A. Jain et al, “Magnetic Field Measurements for Fast-Changing Magnetic Fields”, to be published, Proceedings of the 2004 Applied Superconductivity Conference, held in Jacksonville, Florida

[8] Al Zeller, Study on "Possibilities for using superferric magnets for the proposed GSI upgrade", 2002

[9] A. Kalimov, G. Moritz, and A. Zeller, "Design of a Superferric Dipole Magnet With High Field Quality in the Aperture", IEEE Trans. Appl. Superconductivity, 14 (2004) 271

[10] A. Kalimov, "Comparison of the CR- and SFRS-dipole and quadrupole superferric magnets", Internal Note, MT-INT-Kalimov-2005-001-CRandSFRSDipoleQuadrupole, 2005

[11]Q. Wang, "Cryostat Structure for CR", Internal Note, MT-INT-Wang-2004-001-CRDipoleCryostat, 2004

3D Simulation of the Eddy-Current Losses in the Laminated, Ferromagnetic Nuclotron Yoke

H. De Gersem[1], S. Koch[2], T. Weiland, TEMF, TU Darmstadt

1 Introduction

For the SIS-100 synchrotron planned in FAIR, superconductive magnets with a laminated, ferromagnetic yoke are designed. During the ramping of the magnets, substantial eddy-current losses are generated in the yoke, especially at the end parts [1].

2 Eddy-current model

The eddy-current losses are simulated using a 3D magnet model (Fig. 1). The magnetoquasistatic subset of the Maxwell equations is formulated in terms of line-integrated magnetic vector potential using the Finite Integration Technique for geometrical discretisation. The model is linearised by a successive-approximation technique with relaxation based on backtracking. A single-diagonal implicit Runge-Kutta method is used for time stepping.

The ferromagnetic yoke is laminated along the axis of the magnet, here denoted by z. A non-conductive coating prevents currents to migrate between laminations. The individual laminations can not be resolved by the grid. Instead, an anisotropic conductivity tensor $\bar{\kappa} = \mathrm{diag}(\kappa, \kappa, 0)$ with κ the conductivity of iron, and an anisotropic reluctivity tensor $\bar{\nu} = \mathrm{diag}(\nu_\parallel, \nu_\parallel, \nu_\perp)$ is used. The parallel and perpendicular reluctivities are computed from

$$\nu_\parallel = 1/\left(\frac{\gamma}{\nu_{\mathrm{Fe}}} + \frac{1-\gamma}{\nu_0}\right) ; \quad (1)$$

$$\nu_\perp = \gamma\nu_{\mathrm{Fe}} + (1-\gamma)\nu_0 \quad (2)$$

with γ the stacking factor, ν_0 the reluctivity of the coating and $\nu_{\mathrm{Fe}}(|\mathbf{B}|)$ the reluctivity of the nonlinear ferromagnetic material which is updated for every grid cell separately according to the local, instantaneous magnetic flux density $\mathbf{B}$ at every transient and nonlinear simulation step.

3 Simulation results

The eddy-current losses are simulated for a slightly simplified geometry of the SIS-100 magnet generating a sawtooth magnetic flux density in the aperture (Fig. 2). At the beginning of the cycle, eddy currents are generated in small layers at the ends of the magnet yoke. The corresponding losses increase quadratically with the aperture field. At higher flux densities, the saturated ferromagnetic material results in higher reluctivities and accordingly larger skin depths which results in lower losses. At the decreasing part of the cycle, a maximum for the losses is obtained as well, albeit lower as for the increasing part. The axial distribution of the eddy-current losses is shown in Fig. 3. The energy loss per cycle amounts to 25.8 Watt. The results are in agreement with measurements and numerical results obtained independently [1].

[1]Supported by GSI, Darmstadt
[2]Supported by DFG under contract GraKo 410.

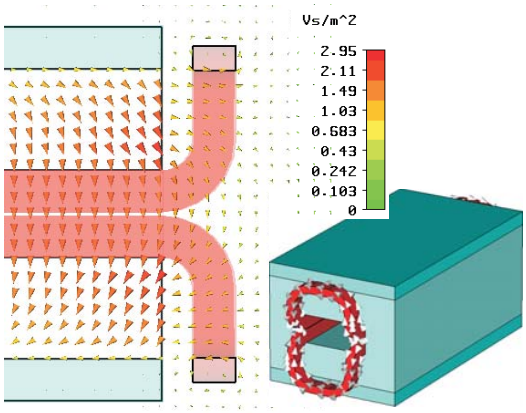

Figure 1: Magnetic field at the end parts of the yoke.

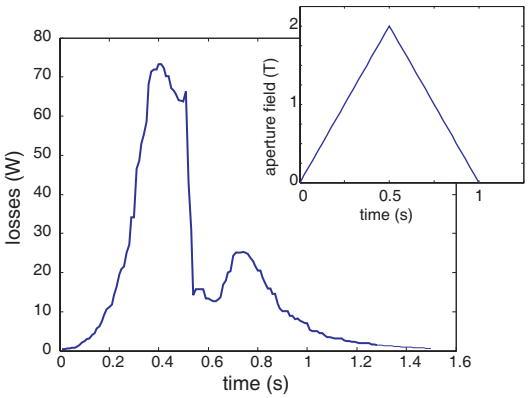

Figure 2: Eddy-current losses during the ramping.

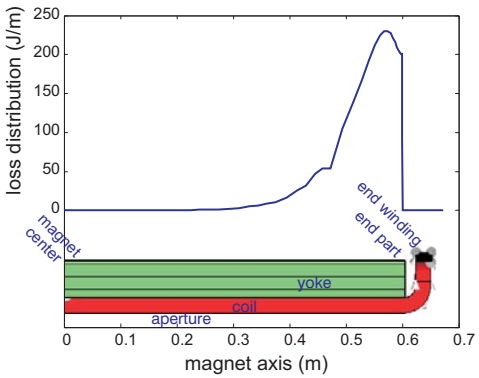

Figure 3: Eddy-current loss distribution along the magnet axis (for both end parts together).

References

[1] A. Kalimov, E. Fischer, G. Hess, G. Moritz, and C. Mühle. Investigation of the power losses in a laminated dipole magnet with superconductive coils. *IEEE Trans. Appl. Superconduct.*, 14(2):267–270, June 2004.

Studies on Maximum RF Voltages in Ferrite-tuned Accelerating Cavities

Klaus Kaspar, Hans Guenter Koenig, Thomas Winnefeld

GSI Darmstadt

1. General

In the main synchrotron of the FAIR project, SIS100, accelerating voltages up to 450 kV are required. [1,2]. In parallel with the studies on MA cavities conventional ferrite-loaded cavities are studied as an alternative for the needed accelerating system.

2. Q-Loss Effect Limitations

In ferrite-tuned cavities, the maximum accelerating voltage is most often strongly restricted by the Q-Loss-effect (QLE) [3, et al.] as illustrated in Fig.1. When a square pulse of rf power with constant frequency is applied to the ferrite cavities, above a certain level, the rf voltage follows the pulse shape only for about 5-10 ms and then drops to a lower level. In GSI the lowest Q-loss threshold (QLT) is about 16 kV in the SIS18 and 5 kV in the ESR cavities.

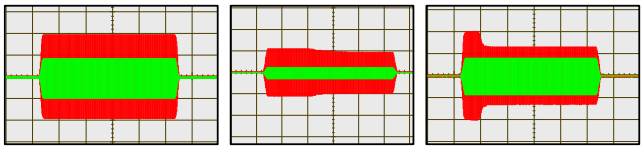

Fig.1: Example of the Q-Loss-Effect in the ESR cavity
Outer signal: Cavity gap voltage, Inner: grid 1 drive voltage
Left: 0.8 MHz, low dc bias field, 10 ms/div
Middle: 2.0 MHz, medium bias, beginning of QLE
Right: Same as middle, strong QLE with more power

3. Measurements and results

Measurements have been carried out on small sample rings of Philips FXC 4L2, 4M2, and 8C12 m. FXC 8C12 m, used in the GSI cavities, turned out as most adequate for SIS100 as well and has been studied in more detail [5].

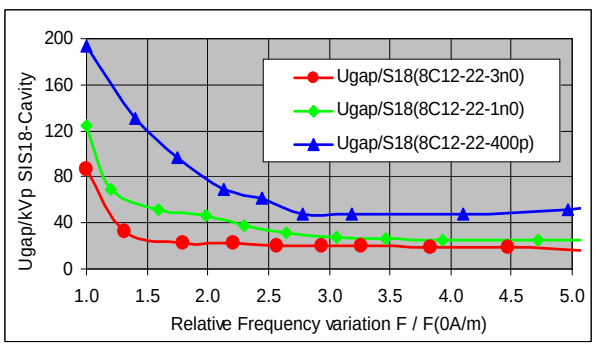

Fig. 2: Q-Loss thresholds as scaled to a full-size SIS18 cavity from measurements on small ferrite sample rings of the material FXC 8C12 m. Measuring conditions are:
8C12-22-3n0: 22 rf wdgs/ring, C1=3.0 nF, 0.33-1.7 MHz
8C12-22-1n0: 22 rf wdgs/ring, C1=1.0 nF, 0.64-3.2 MHz,
8C12-22-400p: 22 rf wdgs/ring, C1=0.4 nF, 0.94-4.7 MHz,

Fig.2 summarizes the typical results. The x-axis shows the relative frequency variation with dc bias of 0-550 A/m. The ordinate shows the QLT gap voltages scaled up to a SIS18 cavity from the measurements on small ring samples.

The important point is the relative variation of the curves. At zero and very low bias fields, the ferrites can be driven up to a factor of 4-5 above the lowest QLT value appearing at higher bias fields. Here it is possible to drive ferrite cavities to such high voltage levels and rf flux densities where other technical limitations are predominant, like ferrite cooling, high voltage problems, etc., but no longer the QLE.

The improvements on the gap voltage measured on the small samples could be verified in several tests on the original size GSI cavities as well [5].

4. Studies with dynamic tuning of the cavities

With the frequency variation during normal synchrotron acceleration, the QLTs usually move to considerably higher levels [4]. This effect could be verified also in a SIS18 cavity. With a tuning rate of df/dt>1 MHz/s and closed loop amplitude and frequency control, up to 24 kV over the full SIS18 tuning range of 0.85-5.4 MHz were reached then.

5. Applications for SIS18 and SIS100

Due to both effects, the high voltage capabilities of ferrites at low bias fields and their dynamic tuning properties, it seems now possible to raise the gap voltages of the SIS18 cavities up to at least 20 kV. The condition df/dt>1 MHz needed to overcome the 16 kV QLT above 2 MHz, is fulfilled for all accelerating modes used in SIS18 by now.

Furthermore, the design of the existing SIS18 accelerating stations can be taken over very well as a base for the future SIS100 and SIS300 accelerating systems. Due to the different operating conditions of SIS100, and with only some minor technical changes, like measures for higher voltage stability, and larger output power of the anode supplies, it seems possible to realize up to 25 kV per cavity with a relatively high degree of reliability.

REFERENCES

[1] An International Accelerator Facility For Beams of Ions and Antiprotons, Conc. Design Report, GSI (2001)

[2] The Future GSI Facility: Beams of Ions and Antiprotons, W. F. Henning, GSI, PAC03

[3] Notes on 'High Loss Effect" in RF cavity Tuning Ferrite, J. E. Griffin, FERMILAB-TM-0655, 1976. 20pp.

[4] J. Griffin, G. Nicholls, A Review of Some Dynamic Loss Properties of NI-Zn Accelerator RF System Ferrite, IEEE Trans. Nucl. Sci., NS-26,p3965-7, June 1979

[5] Studies on Maximum RF Voltages in Ferrite-tuned Accelerating Cavities, K.Kaspar, H.G.König, T. Winnefeld, GSI, EPAC 2004

Barrier Bucket Experiments at the ESR

G. Schreiber, P. Hülsmann, M. Steck, K. Beckert, P. Beller

First experiments with barrier buckets in the ESR have been performed in 2003. The RF setup has now been improved to achieve higher voltages to capture uncooled beams. New experimental low level electronics have been installed, providing the signal generation for moving barriers to longitudinally compress a coasting beam as proof of principle experiment for the SIS100 bunch-precompression scheme and the longitudinal stacking schemes in the new storage rings NESR and RESR.

RF Setup and Cavity

One of the two ESR ferrite cavities without any additional rf load is used for barrier bucket purposes. To keep the ferrite bias current as low as possible the gap capacitors have to be removed to reach the necessary resonant frequency of 5 MHz, corresponding to a barrier pulse width of 200 ns. With its high Q-value of ~10 the cavity requires a special offset pulse generation with short rise times below 10 ns together with the single sine pulse to avoid an unwanted overshooting voltage of the cavity. This results in high bandwidth requirements for the signal generation and amplification. Using the 80 kW tube amplifier driven by a 500 W broadband solid state preamplifier a maximum gap voltage of 1.4 kV is achievable. The necessary driving signal and the resulting gap voltage is shown in Fig 1.

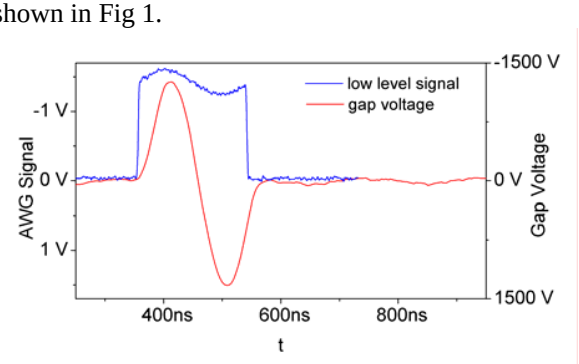

Fig. 1 Low level signal generation: single sine with offset pulse. Resulting gap voltage: 5 MHz single sine pulse with maximum amplitude of 1.4 kV.

The low level signal generation is realized by a 300 MS/s arbitrary waveform generator. Segmented memory tables offer the possibility to create stationary and moving barrier pulses.

Experiments with a C^{6+} beam

For the barrier bucket experiments, a C^{6+} beam at an energy of 120 MeV/u was injected. A small gap in the beam was generated by adiabatically increasing the voltage of a stationary barrier pulse so that particles with a momentum spread lower than $\Delta p/p = +/- 9.2\ 10^{-4}$ could be captured into the barrier bucket. This allows first experiments to compress an uncooled beam, which has been done by generating a moving and a stationary barrier pulse. Fig. 2 shows the bunch profile during the bunch compression with barrier buckets at GSI. First of all, the voltage of the two barriers at a position of t = 0 ns and t = 600 ns is adiabatically increased. One long and one short bunch are formed out of the coasting beam. After 25 ms, the barrier at t = 0 s starts to move linearly in time towards the second barrier. The bunch in-between is compressed from a length of 400 ns to less than 200 ns within 50 ms without some measurable increase of longitudinal emittance. The short bunch around t = 700 ns is simultaneously decompressed.

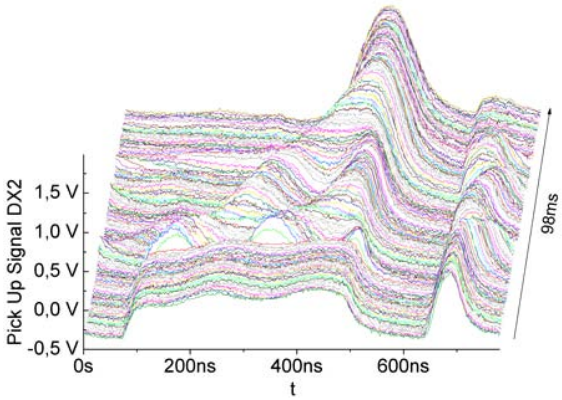

Fig. 2 Bunch profiles during barrier bucket compression within 50 ms by two pulses illustrated over one revolution period (780 ns).

Generating a stationary barrier together with a moving barrier in one cavity causes some overshooting voltage and ringing between the signals during phase movement (see Fig. 2). This results in a nonlinear distribution of the particles in the barrier bucket during the compression. Furthermore, to avoid the short bunch at the beginning of the process, an overlap of the barrier potential would be necessary, which could not be realized with the use of a single cavity. Therefore, experiments with two cavities, each producing a single barrier pulse, are planned.

The experiments presented were done within the framework of a PhD thesis. Further work will be concentrated on the development of the final low-level electronics solution which allows two-cavity operation and control by a centralized control system.

Advances in dynamic aperture and loss calculations for the SIS100

G. Franchetti, I. Hofmann, P. Spiller, GSI

This report describes our progress in dynamic aperture (DA) calculations and beam loss, in particular a scaling law with error strength. The new lattice of the SIS100 [1] has magnet apertures larger than in those used in [2]: semi-axes 60×32.5 mm in quadrupoles and 65×32.5 mm in bending magnets. The modeling of the lattice nonlinearities for the lower magnet excitation is as in [3]. To choose a working point we first inspect the tune diagram including all the systematic resonances up to 5^{th} order, and random error resonances up to the 3^{rd} order (Fig. 1a). We choose

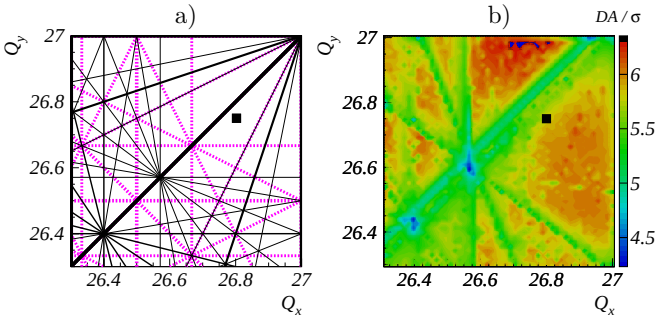

Figure 1: a) Tune diagram with systematic (black) and error resonances (pink-dotted). b) Dynamic Aperture for 10^4 turns. The marker shows in both pictures the preliminary working point.

the preliminary working point $Q_{x0/y0} = 26.8/26.75$ which allows an ideal tunespread of $\Delta Q_y = 0.25$. The effective DA limitation is, however estimated performing a scan of DA with $\Delta p/p = 0$ over the tune diagram (Fig. 1b). The definition of DA is as in [3]. The DA is here rescaled as usual to a beam of equal rms emittances of $\epsilon = 8.75$ mm-mrad. The DA shrinks in correspondence of the coupling resonance $Q_x = Q_y$. A cluster of 7^{th} order resonances is found at the point $Q_x = Q_y = 26.57$ and a trace of 5^{th} order resonances is found at $Q_x = Q_y = 26.4$. For $Q_{x0/y0}$ we find a DA of 5.4σ. The influence of quality of magnetic field on this result is estimated as follow: we consider as working ansatz a rescaling of the bend multipoles b_n^0 reported in Fig. 2a according to $b_n = f b_n^0$. The DA is computed for 10^4 turns with a scaling factor $0.1 < f < 10$ (Fig. 2b), we also plot a fit of the function $D = D_1 f^c$; the

a)

n	b_n^0(fit)
3	1.65
5	-1.41×10^{-1}
7	2.43×10^{-2}
9	6.67×10^{-4}
11	7.7×10^{-4}
13	1.75×10^{-4}

units 10^{-4}, $R_{ref} = 25$ mm

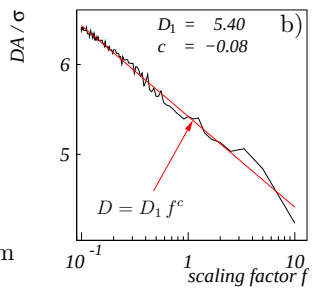

Figure 2: a) Multipoles used in the bending magnet; b) DA vs scaling of multipoles for the chosen working point.

parameters D_1, c for $Q_{x0/y0}$ are given in Fig. 2b). This scaling holds only for values of DA inside the magnet aperture. This fit law suggests how the magnet quality should be improved in order to improve the DA. For example, an improvement of 10% of DA requires $f = 0.3$. By constrast an extension of the scaling law in [4] shows that the DA induced **only** by the nonlinear component of order $n+1$ is $D = D_1 f^{-1/(n-1)}$. We infer that the high order components are responsible for DA correction. The effect of random errors in the strength of the nonlinear component on DA at 10^4 turns for $Q_{x0/y0}$ has been studied as well. To each magnet a strength $b_n = b_n^0(1 + 0.1\xi)$ has been given [5]. Here ξ is a Gaussian random variable with unitary variance. The study of random error effects has been made using 400 error sets. The distribution of DA is peaked at 5σ with width 0.42σ. The impact of a DA of 5.4σ on beam loss has been evaluated by tracking for 10^5 turns a 2D Gaussian beam of 2000 macroparticles with $\epsilon_x = 50$ mm-mrad, $\epsilon_y = 20$ mm-mrad (at 2σ). The local pipe aperture has been consistent with each lattice element aperture. We found an initial loss of 1% which is consistent with the acceptance 161/47 mm-mrad. We finally explored the space charge induced effects for this lattice and working point. The simulation with only systematic error [3] was made with a frozen space charge modeling of a Gaussian bunch with 2000 macroparticles. A synchrotron oscillation takes 1000 turns. The detailes of this method and its benchmark versus an experiment are discussed in [6]. The maximum tuneshift for this test bunch is $\Delta Q_{x/y} = 0.41/0.26$. In

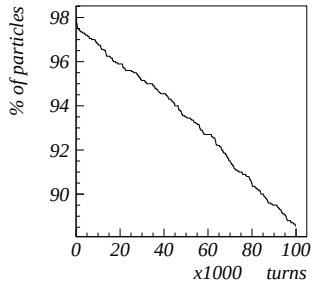

Figure 3: Bunch intensity vs storage time.

Fig. 3a we plot the beam intensity vs storage time, 12% of the ions are lost in 10^5 turns. With respect to the loss prediction reported in [7] we find a substantial increase of beam loss. For minimizing beam loss a careful choice of the working point and a scraping of the distribution tails in a system with collimations is required.

[1] GSI Technical Design Report.
[2] C. D. R. http://www.gsi.de/GSI Future/cdr/.
[3] G. Franchetti, GSI Scientific Report 2003.
[4] E. Todesco and W. Scandale, LHC-Project-Report-135, CERN, 1997.
[5] G. Moritz, private comunication.
[6] G. Franchetti *et al.*, PRST-AB **6**, 124201 (2003).
[7] G. Franchetti, I. Hofmann, EPAC 2004.

Development of Multistage Pseudospark Switches

Isfried Petzenhauser[1], Klaus Frank[1] and Udo Blell[2]

[1] Univ. Erlangen, Germany; [2]GSI Darmstadt, Germany

The fast injection/extraction kicker magnet system of the projected SIS100/300 accelerator complex will demand a pulse forming network that meets the following requirements:

Peak voltage:	100 kV
Peak current:	10 kA
Pulse duration:	≤ 9 µs
Charge transfer:	~ 0,1 C
Repetition rate:	4 Hz
Energy/shot:	~ 10 kJ
Peak Power/shot:	~ 1 GW

The kicker rise time has to be 250 ns or less. Therefore the current rise rate has to be higher than $4*10^{10}$ A/s.

Within this pulse forming network a high-power switch is necessary. One possible switch type is the pseudospark switch, also known as cold-cathode thyratron. This switch combines a high current rise rate (>10^{11} A/s), a reasonable lifetime (typ. 10^6 to 10^8 shots, depending on application), 100% current reversal capability and its low power consumption.

Single stage pseudospark switches have been produced commercially and the results are promising. These switches can withstand a voltage of about 35 kV. To meet the given requirements a multistage system is necessary. To reach the 100 kV with a reasonable low faulty shot probability a four gap system will be necessary.

As first step of development this year two different designs of two-gap pseudospark switches have been set up.

The two types are shown in Fig. 1 and Fig. 2. Type one is a single gap switch with an additional flat electrode in the middle of the gap.

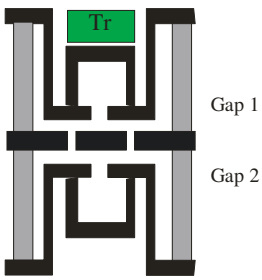

Fig. 1: Doublegap switch (Type 1)

Type 2 is a stack of two single gap switches. Charges can travel between the two switches across the drift-space ('DR'). To obtain acceptable delay and jitter values, the coupling between the two gaps has to be optimized. The design of the drift-space is therefore crucial for the switch performance. Both systems have a single trigger unit to initiate the breakdown. At the moment one trigger unit seems to be enough to realize jitter values that meet the projected requirements. This still has to be proven. If the jitter values should be worse than estimated, there is still the possibility of a multi-trigger system. But these systems are more complicated and therefore it's better to go for a single trigger setup.

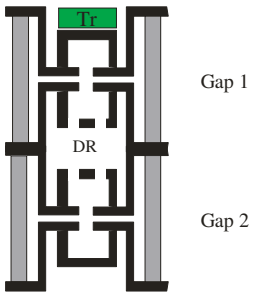

Fig. 2: Doublegap switch (Type 2)

First measurements of the hold-off voltage and the overall switching behaviour have been done. First results are shown in Fig. 3.

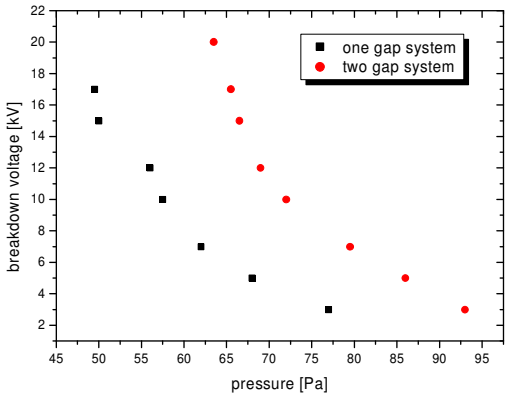

Fig. 3: Breakdown voltage of different switches

Already the first results show the positive effect of a doublegap system. The difference in the breakdown voltage is bigger with lower pressure, but the voltage probes that have been used are limited to a d.c. voltage of 20 kV. At the moment different external voltage dividers are tested at the switches to improve the overall performance of the switch.

Shielding of SIS 100/300

G. Fehrenbacher, F. Gutermuth, and T. Radon
Gesellschaft für Schwerionenforschung, Darmstadt, Germany

Introduction

The loss of primary beam particles in accelerator structures leads to the production of different kinds of secondary radiation. With respect to the radiation exposure of the staff and the public neutrons and gamma rays are the most important radiation components as they dominate the radiation field behind thick shielding layers. Muons may also contribute significantly but can be neglected when looking at the radiation exposure in lateral direction to the beam line.

Dose rate on public ground

The new synchrotron SIS100/300 is foreseen to be built under ground in shaft construction. Also for ecological reasons, this choice is rather obvious. The tunnel will be several meters below ground level in order to assure that the dose rate on ground level will not exceed $8 \cdot 10^{-8}$ Sv/h which is the limit for public ground according to the German Radiation Protection Ordinance. For the following

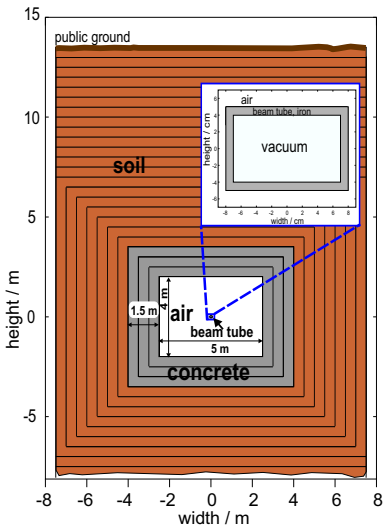

Figure 1: Geometry of SIS 100/300 tunnel used for the Monte Carlo input.

considerations a beam-loss of 10 % is assumed. The operation of three different beam parameters is discussed. The first scenario describes a uranium beam with an intensity of $1 \cdot 10^{12}$ particles per second with an energy of 1.5 GeV/u. For the second and third scenario proton beams of 29 GeV and 90 GeV are investigated with an intensity of $5.6 \cdot 10^{12}$ particles per second. The beam losses are simulated in such a way that the ions leave the reference orbit with an angular spread of ±5 degrees. The beam tube was chosen to have a rectangular cross section 140×80 mm^2 with a wall thickness of 10 mm. As the beam tube is curved all ions have to penetrate the beam tube after a certain flight path in the vacuum. The cross section of the accelerator tunnel is 5×4 m^2, see Fig. 1. A concrete layer of 1.5 m in

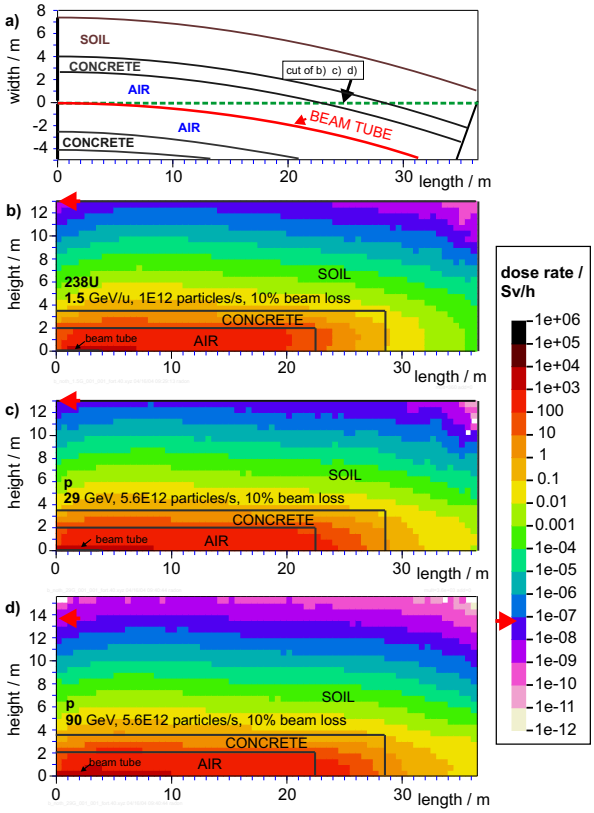

Figure 2: Dose pattern computation of the SIS 100/300 accelerator. The upper panel a) shows a cross section of the underground accelerator at the height of the beam tube. A layer of concrete (1.5m) is used to shield the accelerator in all directions. Another 10 m of soil is needed to sufficiently reduce the dose rate on the ground level for the three sets of beam parameters, see panels b) c) and d).

all directions serves as a first shield and prevents the soil from higher activation levels. It can be seen from Fig. 2 that approximately 10 m of soil is needed in addition to the concrete to reduce the dose rate to $\approx 1 \cdot 10^{-7}$ Sv/h on ground level for the three parameter sets. All simulations were done with the Monte Carlo code FLUKA [1]. For this example the lately published version of FLUKA was used which is able to treat the transport of heavy ions by employing a RQMD-model [2].

References

[1] A. Fassò, A. Ferrari, and P. R. Sala. Electron-photon transport in FLUKA: status. *Proceedings of the MonteCarlo 2000 Conference, Lisbon, October 23–26 2000, A.Kling, F.Barao, M.Nakagawa, L.Tavora, P.Vaz - eds., Springer-Verlag Berlin*, pages 159–164, 2001.

[2] H. Sorge. Flavor production in Pb(160A GeV) on Pb collisions: Effect of color ropes and hadronic rescattering. *Physical Review C*, 52(6):3291–3314, 1995.

Progress Report on the Collector Ring (CR) for the FAIR project

A. Dolinskii, P. Beller, K. Beckert, B. Franzke, I. Nesmiyan, F. Nolden, M. Steck

GSI, Darmstadt, Germany

In 2004 further detailed investigations on various layouts of the CR took place and external studies on critical items were performed. The CR is a special storage ring, which is designed to provide fast cooling of rare isotope (RI) and antiproton beams (Pbars). The required emittance reduction is shown in Table 1.

Table 1. Beam parameters in the CR.

	Pbar		RI	
	$\delta p/p$ [%]	ε_{xy} [mm mrad]	$\delta p/p$ [%]	ε_{xy} [mm mrad]
At injection	6	240	3.5	200
After debunching	1.5	240	0.8	200
After SC*	0.2	5	0.1	0.5
Total cool. time	5 s		1 s	

*SC – Stochastic cooling

The linear optimisation served to derive a lattice solution with good dynamic behaviour simultaneously meeting the demands for very fast stochastic cooling for two optical modes (for RI and Pbar). Additionally, a quite different quadrupole setting is required to fulfill the isochronicity condition ($\gamma_{tr}=\gamma$). In the first-order layout of the CR the required local phase advances between pick-ups and kickers for stochastic cooling for each quadrupole setting have been achieved. There is room for the insertion of rf-cavities for bunch rotation, injection/extraction devices and the stochastic cooling system. The results of those considerations were presented in [1,2]. The present layout of the CR is shown in Fig.1 and some major parameters are given in Table 2.

Table 2. Major CR parameters.

Max.mag.rigidity	13 Tm	
Circumference	206.05 m	
	Pbar	RI
Max. Energy	3 GeV	740 MeV/u
Betatron tunes, Q_x/Q_y	4.42/4.18	3.18/3.17
Transition, γ_{tr}	3.55	2.8

Chromaticity control is a very important ingredient at the large acceptance operation. Stronger focussing (especially at Pbar optics) results in higher chromaticities and, hence, stronger sextupoles are required for chromaticity correction. Previous solutions of the CR lattice were considered on the basis of a superconducting quadrupole magnet, which includes sextupole fields. It could reduce the sextupole field and save space in the ring. But it seems that such a type of quadrupole requires special R&D and takes too much time to be developed. The present layout of the CR has been designed considering normalconducting quadrupole magnets with a number of separate sextupoles (Fig.1). Calculations with the MAD code show that for chromaticity correction in RI optics one needs to use 24 sextupole magnets. But in Pbar optics, where the momentum spread is much higher and quadrupole focusing stronger, 32 sextupole magnets are necessary. In Fig.2 the tune spread of the Pbar beams as a function of momentum spread after chromaticity correction with 24 and 32 sextupole magnets is shown. The side effect of using of such large number of sextupoles is the introduction of additional non-linearities in the ring.

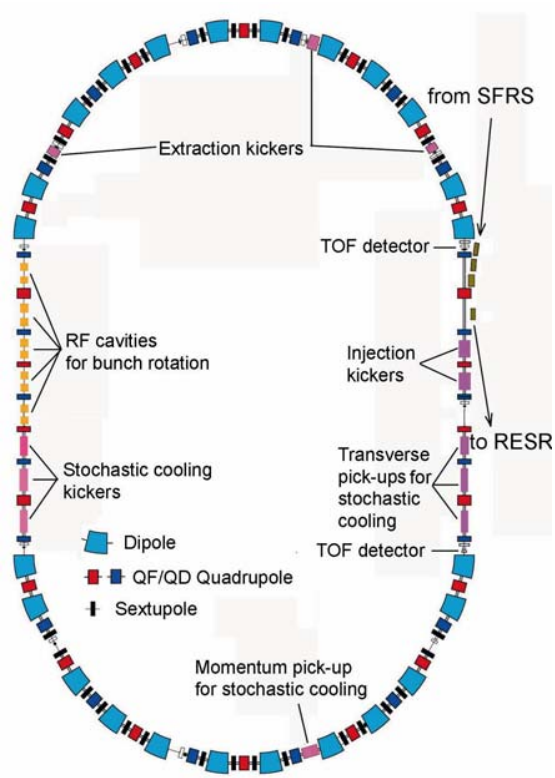

Fig.1 Layout of the CR with main insertions in the ring.

Effects due to non-linear field contributions of the magnet field in dipoles and quadrupoles are very critical in this ring. Using a single particle dynamics approach, the major magnetic non-linearities of the CR have been studied and some results are presented in [2,3].

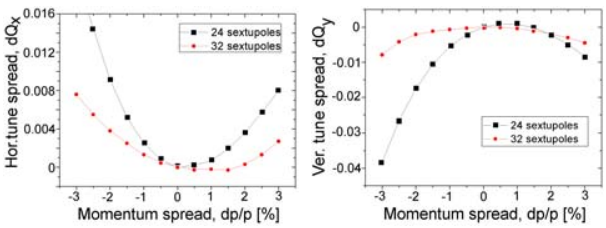

Fig.2 Chromaticity correction with separated sextupoles.

References

[1] A.Dolinskii, et al, EPAC'02, Paris, June 2002, p.572.

[2] A.Dolinskii, et al, "Optimized lattice for the Collector Ring CR", NIMA, A532 (2004), p. 483-487

[3] A.Dolinskii, et al, EPAC'04, Lucerne, Juli 2004, p.1177-1179

Study of Antiproton Stochastic Cooling for the CR Project

F.Nolden, I.Nesmiyan

GSI, Darmstadt

In the Collector Ring CR [1] stochastic cooling is required for antiproton beams with velocities β≈0.97 and with very large transverse emittances $\varepsilon_{x,y}$ up to 240 π mm rad and momentum spreads Δp/p up to ±3%.

We have made simulation calculations for coasting beams based on the Fokker-Planck equation and analytical calculations for a stochastic cooling system for antiprotons to be installed in the CR.

The cooling rates for momentum and emittance are given by,

$$\frac{1}{\tau} = \frac{2W}{N}\left(2Bg - g^2(M+U)\right) \qquad (1)$$

where W is the cooling band, N is the number of particles, g is the co called "system gain", U is the noise to signal ratio. The mixing factor M from kicker to pick-up (good mixing) is

$$M \approx \left((m_2 - m_1)|\eta|\,\Delta p / p\right)^{-1} \qquad (2)$$

where η is the frequency slip factor, m_1 and m_2 are the harmonic mumbers at the lower and upper limits of the cooling band. The mixing factor B from pick-up to kicker (bad mixing) is

$$B \approx \cos\left(\overline{m}\,\omega_{rev}\eta_{p-k}\frac{\Delta p}{p}T_{p-k}\right) \qquad (3)$$

Here $\overline{m}$ is the central harmonic number of the cooling band; ω_{rev} is the revolution frequency of the reference particle, T_{p-k} is the nominal time of flight between pick-up and kicker. The local slip factor η_{p-k} is $\eta_{p-k} = 1/\gamma_{p-k} - 1/\gamma$, where γ_{p-k} is the transition energy from pick-up to kicker and γ is the relativistic Lorenz factor.

In order to realize rapid cooling, it is important to have highly sensitive electrodes. In our calculations we have used the new type of slot-line structures [2] that have been designed at GSI. Simulation calculations for momentum cooling with notch-filter and analytical calculation for transverse direction have been performed. The parameter set typically used here are listed in Table 1. The symbols L/T in this table refer to longitudinal and transverse directions.

Table 1: Parameter set used in the calculation

Cooling band [GHz] (L/T)	1-2/1-3
Number of electrode pairs (L/T)	48/64
Length of electrode [mm]	25
Electrode characteristic Impedance[Ω]	100
System gain [dB]	136-160
Pick-up effective noise temperature [K]	80
Pick-up and kickers maximal sensitivity	1.75

One of the important results from the study is that this calculation leads us to a lattice design with $\gamma_t \approx 3.5$ for the CR. In our calculation for the case of transverse cooling we have assumed that Δp/p changes linearly from 0.7% to 0.35% in 2 seconds. Besides the good mixing and bad mixing, we have also optimized the noise-to-signal ratio for different γ_t.. Fig.1 gives a quantitative view of the features discussed above.

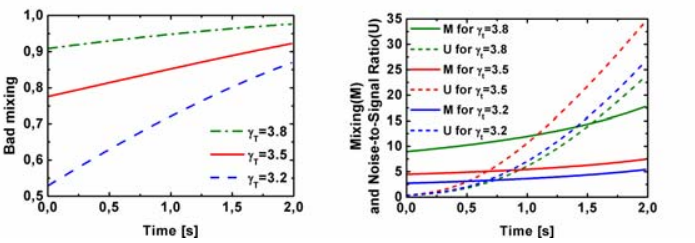

Figure 1. Mixing parameters for different γ_t.

As expected from Fig.2 (a), in the case of $\gamma_t \approx 3.5$ the cooling time is minimized. We have also investigated the requirements on average power for momentum cooling. The effect on cooling time is shown in Fig.2 (b).

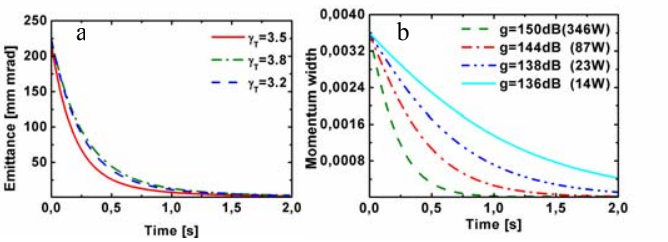

Figure 2 a) Evolution of the emittance for different γ_t; b) Evolution of the momentum width for different system gains(electrical power).

References

[1] A.Dolinskii, et al, this report.

[2] C.Peschke, this report.

Performance Studies of Planar Electrodes for Stochastic Beam Cooling

M. Balk*[1], T. Weiland[1], F.Nolden[2]; [1]TU-Darmstadt, [2]GSI

Stochastic cooling will be an important issue in the new GSI project. Crucial to the efficiency of stochastic cooling is an ideal coupling to the beam. The main coupling elements are pickup/kicker electrodes. These electrodes have to be analysed and optimised extensively. The optimisation is performed by a three dimensional numerical electromagnetic field simulation package "CST MicrowaveStudio" [1].
The structure to be investigated is described in [2]. Basically, it consists of a countersunk slotline on a substrate coupling to the beam. The signal is extracted by microstrip lines on the lower side of the substrate. In practice, several electrodes in series are needed. Additionally, these electrodes are mounted with a certain offset, to cover the whole range of the beam. Therefore, the structures are investigated with respect to the transversal offset *d* and the longitudinal distance *a* of two electrodes (see Figure 1). Furthermore, the combination of three electrodes is analysed.

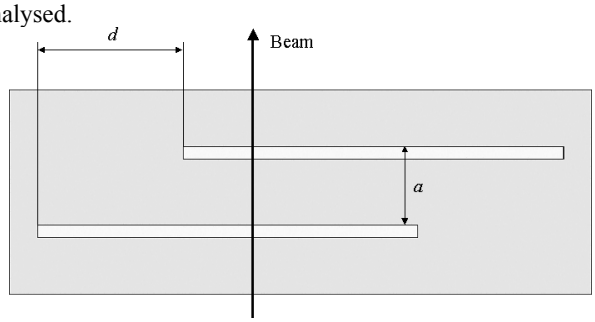

Figure 1: Schematic drawing of a of 2 electrode configuration.

The electrodes are analysed regarding the sensitivity [3]

$$S(x,y,\omega)=\frac{U_K(x,y,\omega)}{U_{in}(\omega)}, U_K(x,y,\omega)=\int_S \vec{E}(x,y,s,\omega)\cdot e^{j\frac{\omega}{v}s}\,d\vec{s}$$

or —in case of the combination of two electrodes— concerning a scaled sensitivity [2] $S/\sqrt{L}$ which accounts for the fact, that a lower sensitivity per electrode can be more efficient if a larger number of electrodes per length L can be applied. For all cases the trajectory of the beam coincides with the centre of the structure and the velocity of the beam is 0.83*c*. The sensitivity results for an offset *d=0*, but for different distances *a*, are shown in Figure 2.

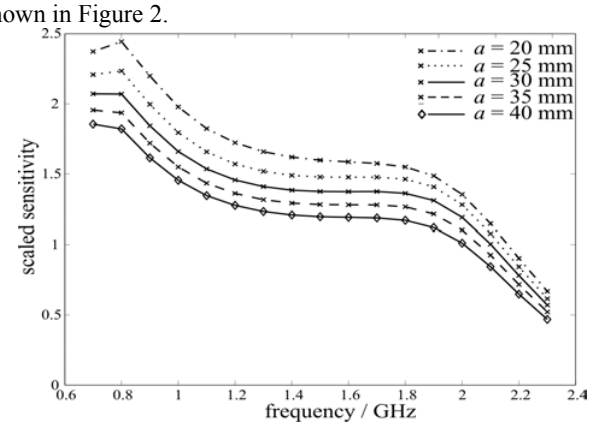

Figure 2: Sensitivity for different distances *a* of 2 electrodes.

In principle, the sensitivity increases with decreasing distance between the electrodes. There is a practical limit: There has to be some space for signal lines. So, the distance of the electrodes is chosen to 25 mm in further simulations.
The analysis of the electrodes for different offsets is shown in Figure 3. The offset is measured in terms of the structure's size. With increasing offset, the absolute height of the sensitivity decreases, but the covered area increases as expected.

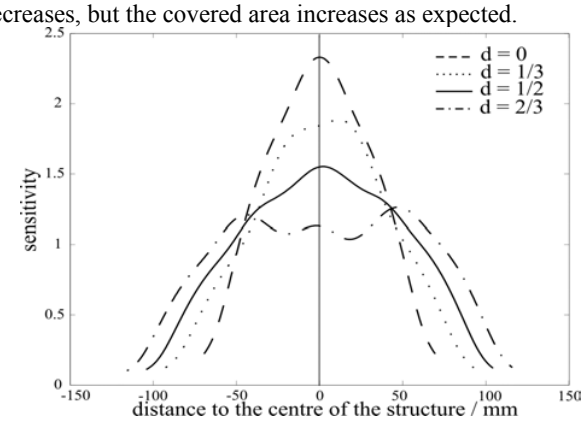

Figure 3: Sensitivity for 2 electrodes for different offsets.

Finally, the combination of three electrodes is simulated. The sensitivity results are shown in Figure 4. The sensitivity does not increase linearly due to coupling effects, as explained already in [2]. We expect a stagnating influence of the coupling effect, for an increasing number of electrodes, because the coupling effect is limited in space.

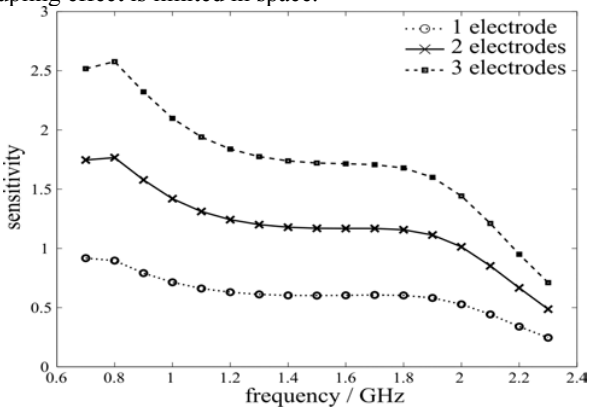

Figure 4: Sensitivity for a combination of 1-3 electrodes.

In future studies, combinations of 4 electrodes or different particle velocities could be considered.
The authors acknowledge the intensive collaboration with Claudius Peschke (GSI) and Stephan Koch (TEMF).

References

[1] CST GmbH, Bad Nauheimer Str. 19, 64289 Darmstadt

[2] M. Balk, T. Weiland, F. Nolden, GSI Report 2003

[3] G. Lambertson, AIP Conference Proceedings, 153, 1987, pp. 1414-1442

* Supported in part by DFG under contract GraKo 410 and GSI, Darmstadt

Pick-Up and Kicker Electrodes for Stochastic Cooling at FAIR

F. Nolden[a], C. Peschke[a], and L. Thorndahl[b]
[a]GSI, Darmstadt; [b]CERN, Geneva

The main task of the FAIR collector ring (CR) is stochastic cooling of rare isotope beams (RIBs) with $\beta = 0.83$ and antiprotons ($\bar{p}$) with $\beta = 0.97$. The CR should achieve a phase space volume reduction of $1.6 \cdot 10^4$ in 5 s for $\bar{p}$ and $1.3 \cdot 10^6$ in 1 s for RIBs. To fulfill this, the pick-ups must have a large bandwidth and a high S/N ratio in spite of the large aperture of $120 \cdot 120$ mm^2. A new planar electrode is developed [2] to meet these requirements.

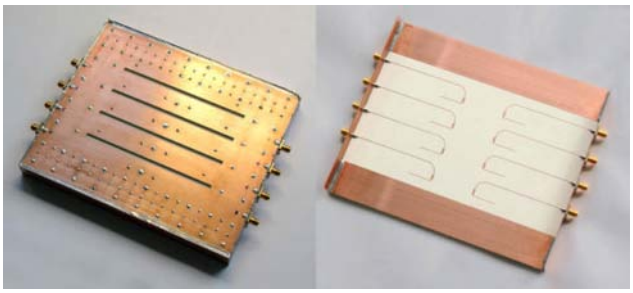

Figure 1: Test array of the new slotline pick-up electrode.

Fig. 1 shows a test structure 1-2 GHz. This band is used for notch filter cooling of $\bar{p}$, horizontal and vertical cooling of $\bar{p}$ and RIBs and probably Palmer cooling of RIBs. For horizontal and vertical cooling, a second band from 2-4 GHz is proposed. An array of these electrodes is mounted with the slotlines (Fig. 1 left) orthogonally to the beam. The mirror current has to cross the slots and induces travelling waves in both directions of the slotline. These signals are coupled out to microstrip lines on the back side (Fig. 1 right). The remaining $\lambda/4$-slotline is a virtual open and the $\lambda/4$ at the beginning of the microstrip line is a virtual short to one slotline conductor. The signals from both ends will be combined using Wilkinson combiners.

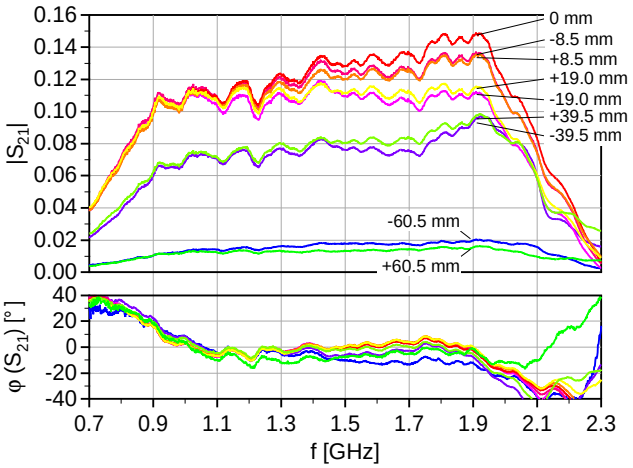

Figure 2: Transmission from a E-field probe above a slotline pick-up to the output of the combiner.

For field measurements, a computer controlled E-field mapper has been built. Fig. 2 shows the transmission from the near field probe 5 mm above the slot to the output of the combiner versus frequency and transverse position. This value is proportional to the output amplitude of a pick-up and the square root of the coupling impedance. The position 0 mm is the center of the slotline, ±19 mm is the position of the microstrip line and ±60.5 mm is the end of the slotline. In agreement with equivalent network calculations, the measurement shows a relatively flat response over one octave and a nearly constant phase over frequency and position.

To analyse the behavior of this electrode type in large arrays and to compare the performance with other possible designs, two reports have been elaborated [1]. A major result is that the novel electrodes are superior to both the $\lambda/4$-superelectrodes and the slow-wave couplers. Fig. 3 shows the square root of the longitudinal impedance (for a beam in chamber center, and longitudinal kicker mode) of a 2 m long array of 80 slotline electrodes, a 2 m long array of 23 CERN AC band 1 superelectrodes and a scaled FNAL slow-wave structure with 80 cells with a length of 32.5 cm without coupler [1].

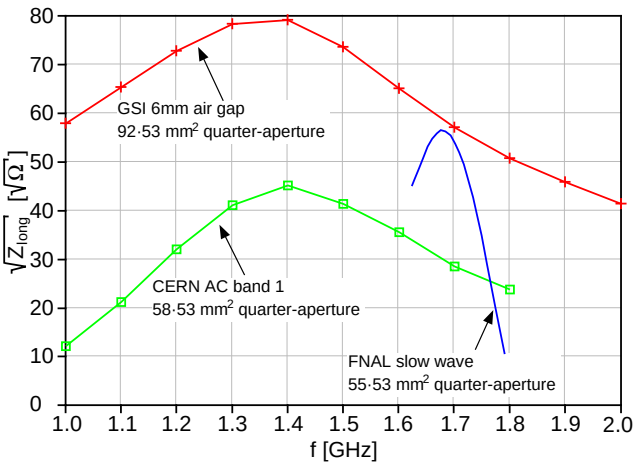

Figure 3: Comparison between different longitudinal kicker electrodes.

The $\lambda/4$-superelectrodes have a similar bandwidth, but a lower impedance. The advantage of the slow-wave structure is simplicity without combiners and β-switches. The disadvantages are the necessity of five sub-bands with signal processing per octave and the dependance of the center frequencies from β and plunging position. Plunging is necessary due to the large phase space reduction.

References

[1] L. Thorndahl: "Comparison between 3 Types of Longitudinal Kickers for Stochastic Cooling in the GSI CR"; private communication; Oct. 2004

[2] C. Peschke, F. Nolden and M. Balk: "Planar Pick-Up Electrodes for Stochastic Cooling"; Nuclear Instruments and Methods A 532 (2004) 459-464

Design of the Electron Cooling System for the NESR

V. Panasiuk[1], V. Parkhomchuk[1], V. Reva[1], M. Vedenev[1], P. Beller[2], B. Franzke[2], and M. Steck[2]
[1]BINP Novosibirsk; [2]GSI Darmstadt

The storage ring NESR of the FAIR project will serve various kinds of experiments. Many modes of operation are considered employing stable and radioactive ion beams and antiprotons. For radioactive ions the cooling time is crucial for short-lived nuclei. These ions will be pre-cooled in the CR storage ring by stochastic cooling at an energy of 740 MeV/u. The cooling time in the NESR should not exceed the projected cooling time in the CR which is below 1 s, in order to make radioactive ions with lifetimes in the range of seconds available for experiments. For stable ions the cooling time requirements are more relaxed, but beams of highest phase space density will be required for precision spectroscopy. Antiprotons will be pre-cooled and accumulated in the CR-complex and transferred to the NESR at an energy of 3 GeV. For the low energy complex behind the NESR the antiprotons will be decelerated in the NESR to 30 MeV. Electron cooling at an antiproton energy of about 800 MeV will compensate diffusion due to imperfections of the deceleration process and increase the efficiency of deceleration. Finally electron cooling will provide high quality decelerated beams of ions and antiprotons. After deceleration the electron cooling system should provide cooling at a minimum energy of 30 MeV for antiprotons and of 4 MeV/u for ions.

The electron cooling system must be able to provide electrons up to an energy of about 450 keV, which is beyond the energy range of existing electron cooling systems. Deceleration with a ramping time of 2 s will be applied to short-lived nuclei. The electron energy must be varied from the maximum energy needed for cooling after injection down to the lowest energy of 4 MeV/u which is the design energy for further deceleration in a linac in front of a trap system. A cooling system (Table 1) has been designed which is capable to provide the cooling power and to achieve the required cooling performance.

Table 1: Parameters of the NESR electron cooling system.

energy range	2-450 keV
maximum electron current	2 A
cathode radius	10 mm
electron beam radius in cooling section	2.5-14 mm
maximum magnetic field strength	
in gun section	0.4 T
in collector section	0.23 T
in cooling section	0.2 T
magnetic field straightness in cooling section	$\leq 5 \times 10^{-5}$
cooling section length	5 m
maximum power in collector	15 kW

Special attention must be paid to the fast ramping of the accelerating voltage which is required for cooling at injection energy and cooling after deceleration. A ramp rate of 250 kV/s corresponds to a 1 T/s ramp rate of the magnetic field. Standard highly stabilized high voltage power supplies would need huge charging currents and consequently an output power of several 10 kW. As an alternative solution a power supply with two rectifiers operated with opposite polarity is proposed. This should allow fast ramping with an output power below 1 kW. The voltage of up to 500 kV will be achieved by cascading 25 capacitive plates which are excited by an rf generator and rectification of the excited voltage. The maximum voltage of 500 kV is a moderate extension of existing technology and can be realized employing a SF_6 filled pressurized container. The auxiliary high voltage power supplies for the generation of the electron beam will be operated on the high potential inside the pressure vessel. A collector power supply of 15 kW power will be needed to recuperate the electron beam with high efficiency.

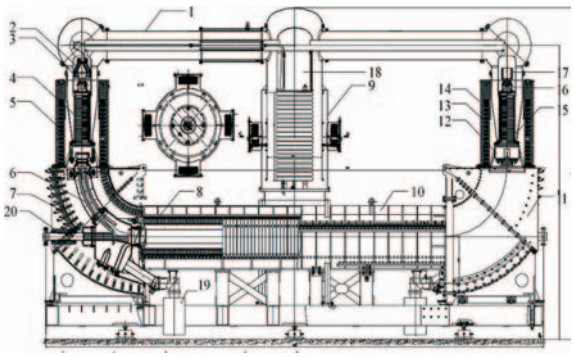

Figure 1: Sketch of the NESR electron cooling system.

The magnetic system of the electron cooler will be operated with a field strength around 0.2 T. Because of the energy of the electron beam a good field straightness in the cooling section will be mandatory, a level of field straightness of a few times 10^{-5} should be reached. The choice of the magnetic field strength is guided by considerations to operate the system in the regime of magnetized cooling. A magnetic field of up to 0.2 T is estimated to provide sufficient cooling rate.

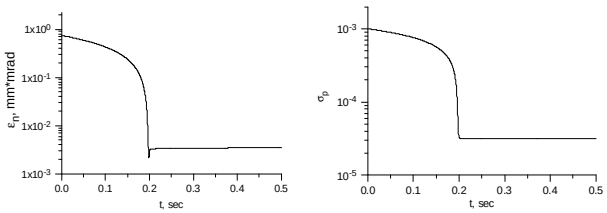

Figure 2: Cooling of the emittance and the momentum spread of a bare uranium beam by an electron current of 1 A after stochastic pre-cooling in the CR.

The cooling process has been simulated for the typical conditions with rare isotope beams at 740 MeV/u after stochastic pre-cooling in the CR storage ring (Fig. 2) and for antiprotons after stochastic pre-cooling and deceleration to 800 MeV. Cooling times of 0.2 s for the heaviest bare ions can be expected with an electron current of 1 A, the expected cooling time for the antiprotons with an electron current of 2 A is 30 s. In both cases the electron beam radius was optimized for the fast cooling of the respective beam.

References

[1] Electron Cooling for NESR, design study, BINP Novosibirsk, November 2004.

Advanced beam dynamics for storage rings

O. Boine-Frankenheim[1], A. Dolinskii[1], R. Hasse[1], I. Kadenko[2], A. Lehrach[3], I. Meshkov[4], Th. Weiland[5], P. Zenkevich[6], and V. Ziemann[7]

[1]GSI, Darmstadt; [2]Uni. of Kiev, Ukraine; [3]FZ Jülich, Germany; [4]JINR, Dubna, Russia; [5]TU Darmstadt; [6]ITEP, Moscow, Russia; [7]TSL, Uppsala, Sweden

The challenging storage ring and beam cooling projects at high energies [1] are the driving force behind new efforts in beam dynamics modeling and experimental verification. Optimization of the proposed cooling scenarios, including studies on rf manipulations, stochastic and electron cooling, intrabeam scattering, internal target scattering, as well as other processes, requires not only accurate but also fast numerical models. The main target of the studies performed within the INTAS project "Advanced beam dynamics for storage rings" is the high energy storage ring HESR as part of the FAIR project at GSI. For the HESR, that is presently being designed at FZ Jülich, electron cooling up to 8 MeV is proposed. Electron cooling at very high energies (55 MeV) is proposed for the RHIC upgrade (RHIC-II). At FNAL a 4.3 MeV electron cooler is presently being installed in the Recycler. An important question is the predictive power of the theoretical models, especially for high energy. For example, in case of RHIC-II cooling dynamics must be known with an accuracy better than a factor of 2. We categorize the topics into four sections: intrabeam scattering, electron cooling modeling, internal target scattering, and resulting cooling equilibria.

Intrabeam scattering:

A number of different approximations are used to obtain IBS rates for Gaussian beams. The different approximations can differ by factors of 2, depending on the application. In order to describe the detailed evolution of the bunch density profile and also the beam loss, direct analytical or numerical solutions of the Landau collision term, which has a Fokker-Planck structure, must be obtained. Two alternative simulation approaches (Langevin equation and collision map) have been worked out in Ref. 1. The nonlinear electron cooling forces result in non-Gaussian beam distribution functions. A kinetic treatment of IBS is therefore essential for accurate simulations.

Electron cooling forces:

The cooling force estimations for the HESR and for the RHIC-II projects are based on the Parkhomchuk formula, which is an empirical generalization of the theoretical friction force for unmagnetized electrons. Magnetized electron cooling will be crucial for RHIC-II and for the HESR in order to achieve the required cooling rates. For magnetized cooling theoretical complications arise e.g. from the small Coulomb logarithm. Experimentally, the correction of field misalignments is a challenging technical problem. The precise knowledge of the residual field errors is required for accurate simulations of beam cooling. All these complication will make predictions (within a factor of 2) for magnetized cooling very difficult. A comparison of theoretical models with accurate experimental results obtained at low energy is presently being performed: Longitudinal cooling forces have been measured in the CELSIUS ring using the very accurate phase shift method. Transverse cooling forces have been measured for the first time using a kicked pencil beam in CELSIUS [1].

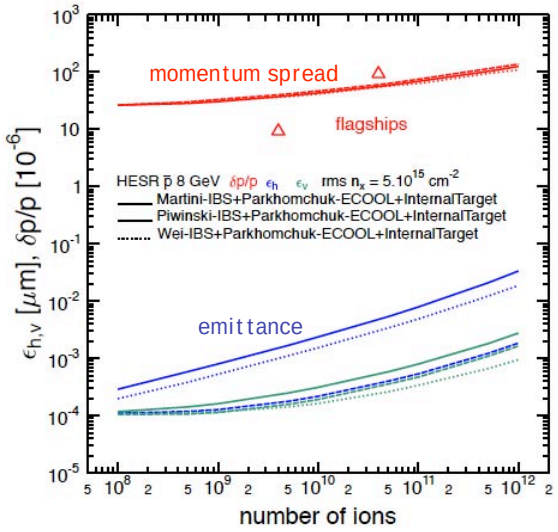

Figure 1: Equilibrium momentum spread and emittance obtained with "betacool" using different IBS models.

Internal target scattering:

A hydrogen pellet target is presently the only possible candidate for high luminosity experiments with antiprotons in the HESR. Compared to the more conventional low density gas targets the main questions are related to the high density and to the granularity of the pellets. First theoretical results show that the energy loss straggling in the pellets can result in strongly non-Gaussian momentum spread distributions [1].

Electron cooling equilibrium:

Extensive simulations of the cooling dynamics have been performed using different models. As an example Fig. 1 shows the rms equilibrium momentum spread together with the emittances obtained with the "betacool" code for the proposed "flagship" experiments in the HESR. It can be seen that the "high resolution" mode (lower triangle) cannot be achieved, whereas the "high luminosity" experiments seem to be possible.

Outlook:

The experiments at COSY, ESR and CELSIUS on cooling forces, target scattering and equilibrium beam distributions will be intensified. Ongoing efforts focus on the 3D kinetic modeling of cooling dynamics and on the stability of cooling equilibria with regard to collective instabilities.

References

[1] R.Hasse, I. Hofmann (ed.), AIP proceedings of the 33rd ICFA advanced beam dynamics workshop, Bensheim, Germany, Oct. 2004

Status report on beam diagnostics developments for the FAIR project

A.Peters [1], J.Belleman[2], P.Forck [1], A.Galatis [1], T.Giacomini [1], M.Häpe[3], P.Kowina[1], D.Liakin [4], H.Reeg [1], U.Raich [2], W.Ricken [2], V.Skachkov [5], A.Zoubir [6]

[1]GSI, Germany, [2]CERN, Switzerland, [3]University of Kassel, Germany, [4]ITEP, Russia, [5]Moscow State University, Russia, [6]Technical University of Darmstadt, Germany

This status report will give an overview about the research and development activities of the GSI beam diagnostics group in collaboration with other European partners for the instrumentation in the FAIR project.

Alternative concept of a DC/AC current measurement device for 100 A peak with better than 1mA resolution based on MR sensors

For most beam parameters the stored current is monitored by a commercially available dc-transformer offering a dynamic range from 1 µA to 20 A maximum. Its bandwidth of 10 kHz allows determination of the beam lifetime with ms time resolution. But it is known, that these types of transformers have severe problems by a high current bunched beam passage [1]. Even though an improved version is available, no test with beams has been performed so far and scalability from other machines might be doubtful due to the resonance nature of the severe distortion. Therefore investigations of a different type of sensitive magnetic field sensor in collaboration with the University Kassel (Germany) have been started. The idea consists in taking the scheme of a clamp-on ammeter and using a high-effective magnetic sensor in the core gap. Usually Hall-sensors are installed in such measurement devices, but due to the larger core diameter needed in beam diagnostics and the high dynamics of the beam currents to be monitored other sensors have to be investigated like AMR (Anisotrope MagnetoResistance), GMR (Giant MagnetoResistance) or GMI (Giant Magneto-Impendance) and tailored for this application [2]. The scheme of such a device and a first simulation of the magnetic flux concentrator are shown in Fig. 1.

First results show that the GMI effect would be the most interesting candidate for the sensor, but no commercial element is available until today [3]. For GMR the situation looks better [4] and the further development will concentrate on this sensor type.

Signal processing and analysing electronics for beam position monitors

Beam Position Monitors (BPM) serve as the main diagnostic tool at many facilities. For the closed orbit determination a high precision of less than 100 µm of the beam position reading is required, which is difficult to achieve due to the large beam tube diameter of 100 mm. For the control of the injection matching and manipulations during the acceleration or bunch compression a fast turn-by-turn (or even a bunch-by-bunch) readout is mandatory. Advanced investigations to determine e.g. linear couplings or higher order magnet strength can be performed by this fast readout within one cycle [5]. In addition, a closed orbit feedback uses the position readings from all BPMs to calculate magnetic corrector setting on a ms time scale.

For the analogue signals precise, automatically calibrating pre-amplifiers, capable to span an exceptional large dynamic range of 160 dB, are under development containing a precise amplification/attenuation chain with flat frequency characteristic [6]. The amplified signal will then be digitised on a special designed electronic board using latest 12 bit ADCs with at least 125 MS/s and a storage capability of about 500 MB/channel for e.g. a full SIS 100 cycle. For the data handling and reduction a powerful FPGA (Field Programmable Gate Array) will be used, which is embedded in a commercial product, see Fig. 2. Versatile algorithms for the beam position calculation will be implemented on this FPGA ena-

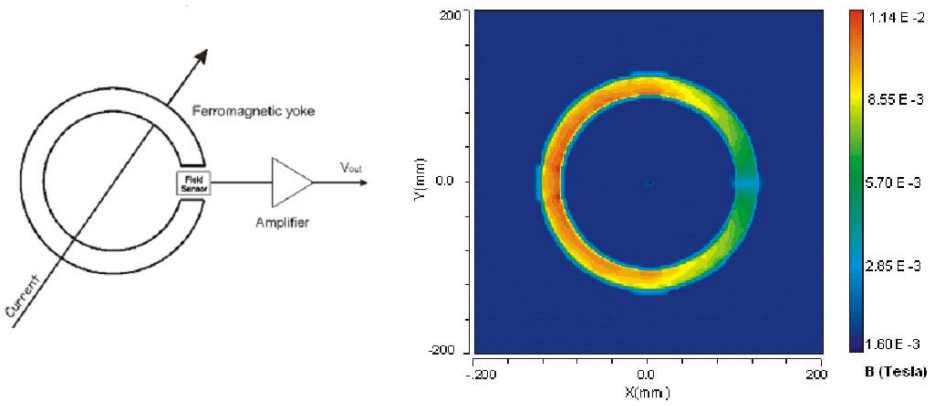

Figure 1: Scheme of the novel current monitor device and a first simulation of the magnetic flux concentrator

bling a real time processing [7]. Depending on the user application the results can be evaluated on the short time scale on a bunch-by-bunch basis as well as in a time average- or narrowband-mode for precise closed orbit measurements. The error signal generation for a closed orbit feedback system must be implemented on this board. This development is part of the approved EU FP6-Design Proposal and is worked out in cooperation with CERN, FZ-Jülich, Technical University of Darmstadt and the Slovenian company Instrumentation Technology [8].

Figure 2: Preliminary prototype of the BPM front-end digitisation and evaluation board

New set-up for a residual gas monitor with high resolution and turn-by-turn measurement capability

By monitoring of the transverse beam profile in a synchrotron or storage ring the emittance and its evolution during the acceleration can be determined. The influence on planned changes of the beam settings, like changes of the tune or various rf-manipulations can be monitored, as well as emittance enlargements by intra-beam scattering or impedance influence. Moreover, the matching of the injected

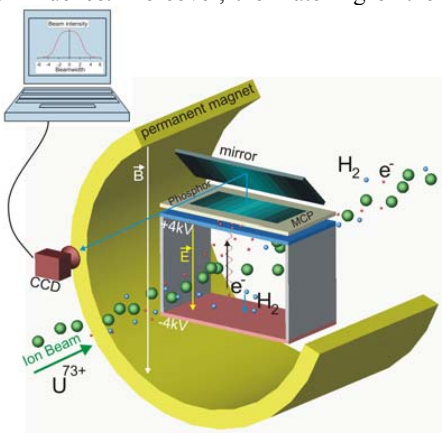

Figure 3: Scheme of an IPM

beam emittance and dispersion with respect to the acceptance can be controlled on a turn-by-turn basis [9]. Fast changes of the transverse profile by any beam manipulation can be also monitored on a turn-by-turn time scale.

The scheme of an Ionization Profile Monitor (IPM) used for this purpose is shown in Fig. 3. Here secondary electrons for the residual gas are created by the beam's energy loss and accelerated by an electric field toward an MCP-detector, where the particle hit is detected with a CCD camera for the high resolution mode or an array of photo-diodes for the turn-by-turn mode. A magnetic field of 100 mT is required field for the guidance of the electrons toward the MCP and to overcome the beam's space charge. Within the separately funded INTAS project Ref. Nr. 03-54-3931 the design work is done in collaboration between ITEP (Moscow), MSU (Moscow), MSI (Stockholm) and COSY (Jülich). It contains the design of the mechanics, the electric and magnetic fields, the detectors, the fast multi-channel electronics and the software [10] [11]. The insertion length will be around 2.5 m including corrector magnets to compensate the kick of the detector magnets. Experiences are gained from the existing installation at SIS18. As an example Fig. 4 shows an application of the SIS 18 device for the transverse beam size evolution, where a transition for the high current working point is changed to a working point required for slow extraction.

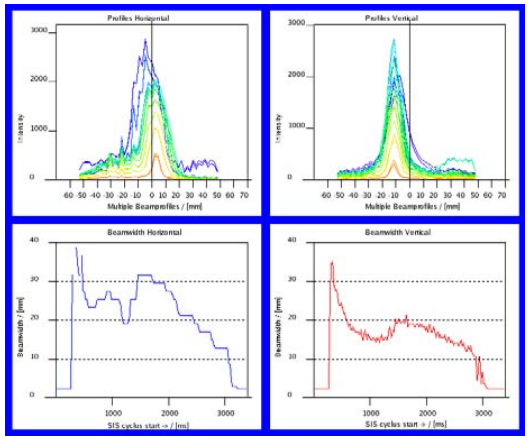

Figure 4: The beam profile evolution during a tune resonance crossing from Q_h =4.15 → 4.31 for a high current Kr-beam .

References

[1] Technical Report SIS18 upgrade

[2] M. Häpe, CARE meeting Lyon, see http://desyntwww.desy.de/mdi/CARE/Lyon/ABI-Lyon.htm

[3] M. Häpe, diploma work, University of Kassel

[4] J.Marien, MR Symposium 2005, see http://www.sensitec.com

[5] A. Franchi, R. Tomas, *Magnet Strength Measurement in a Circular Accelerator from Beam Position Data using a kicked Beam*, Phys. Rev Spec. Topic Acc. and Beams, submitted (2005)

[6] J. Schölles, DIPAC 2005, in preparation

[7] A. Galatis, DIPAC 2005, in preparation

[8] http://www.i-tech.si

[9] G. Ferioli, DIPAC03, see http://www.jacow.org

[10] P. Forck, DIPAC03, see http://www.jacow.org

[11] S. Barabin, EPAC04, see http://www.jacow.org

First Steps towards FAIR Controls

P. Schütt, U. Krause, R. Bär, B. Franczak, L. Hechler, A. Redelbach, S. Richter, V. Schaa, W. Schiebel

GSI Darmstadt

1. Introduction

In 2004 the work on FAIR controls has started. Among the core requirements is parallel handling of different beams, so that FAIR accelerators will be able to serve up to 4 experiments independently. To this end, the system architecture is crucial as well as the design of the timing system. Moreover, effective set-up procedures and surveillance mechanisms are needed to operate the accelerators with a small operator crew.

2. Design Concepts

The system will be designed as a decentralized distributed system. A sketch of the architecture of the control system is shown in Figure 1, specifying the structure of three layers of applications, device presentation and equipment control.

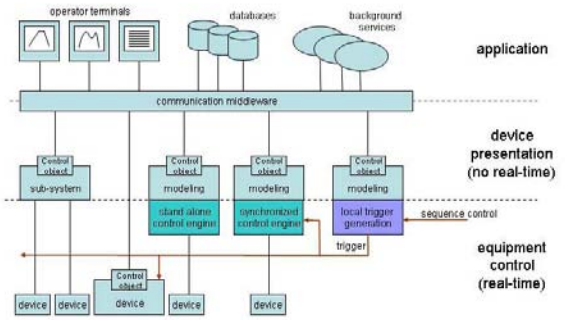

Figure 1: Architecture of the Control System

The timing system foresees a central sequencing unit for the coordination of the local timing generators. Information about the next beam to be handled and timing events for the actual accelerator cycle will be distributed by the local timing generators; see also Figure 2, where the interplay in this hierarchical timing structure is illustrated.

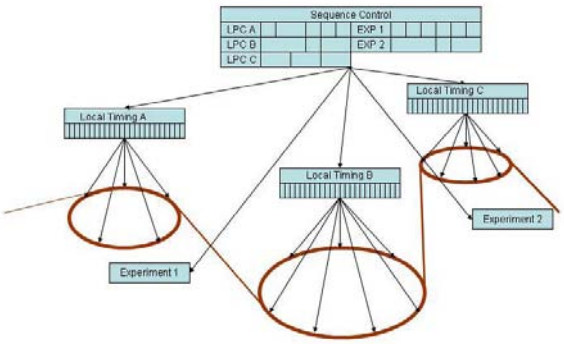

Figure 2: Hierarchical Timing Structure

The development of the system core and front-end side will be twofold: On the one hand an evaluation of recent technologies is in progress, including control systems, e.g. ACS, and also timing components or interfacing technology. First steps in the evaluation of embedded processors have been done and will be followed up by FireWire technologies. Since, on the other hand the requirements for FAIR controls are being gathered; a combination of both sides will lead to the development of a general layout of the system in a modern way.

Operating FAIR will require efficient operation tools to support set-up and optimization of set-values for the equipment. Services will be provided to help both operators and equipment specialists in understanding the many complex situations which will arise during commissioning or operation of the FAIR accelerators.

3. SIS18 Upgrade

Since SIS18 will serve as injector for FAIR, its upgrade to higher repetition rates and intensities is crucial [1]. In order to increase the SIS18 repetition rate via 1 Hz up to 4 Hz, not only the ramp rate must be increased, but also the logistics of the SIS cycle must be overhauled with the goal to overlap the different phases: e.g. extraction must be prepared during the acceleration phase.

Furthermore, a number of machine experiments and technical studies have been performed to study and improve the behavior of the synchrotron during faster ramping. While the technical equipment is capable of running the full design ramp rate of 10 T/s, the beam cannot be accelerated so far.

4. Summary and Outlook

Preliminary concepts for the FAIR control system have been developed[2]. Due to the complexity of the system, it is crucial to discover potential weak points as soon as possible, in particular by checking critical parts in a running environment. Since the present GSI facility is in many aspects similar to FAIR, it provides an outstanding test environment.

An early completion of consolidation of the control system will help to free resources for the FAIR project. As emphasized above, it will also serve as a 'real-life' test bench of controls to analyze the present status of GSI accelerators and to shed more light on necessary measures to fulfill the various requirements for an efficient operation of the FAIR facility.

References

[1] P. Schütt, R. Bär, B. Franczak, U. Krause, A. Redelbach, S. Richter, V.R.W. Schaa, W. Schiebel: "Schneller Pulsbetrieb am SIS", GSI internal Report, 2004.

[2] P. Schütt, U. Krause, W. Schiebel, R. Bär, B. Franczak, L. Hechler, A. Redelbach, S. Richter, V.R.W. Schaa: "Technical Report on Controls, Commissioning and Operation of the Accelerators of FAIR", GSI, 2005.

NUSTAR-E

Experimental Nuclear Structure, Astrophysics and Reactions

DECAY SPECTROSCOPY

EXOTIC BEAMS AND REACTIONS

New results on synthesis of Hs isotopes

J. Dvorak[1], R. Krücken[1], F. Nebel[1], Z. Novackova[1], A. Türler[1], B. Wierczinski[1], A. Yakushev[1], W. Brüchle[2], E.Jäger[2], E. Schimpf[2], M. Schädel[2], A. Semchenkov[1,2], A. Kuznetsov[3], M. Chelnokov[3], A. Yeremin[3], Ch. E. Düllmann[4], Y. Nagame[5], K. Eberhardt[6], P. Thörle[6], R. Dressler[7], Z. Qin[2,8],M. Wegrzecki[9]

[1]TUM Garching; [2]GSI Darmstadt; [3]JINR Dubna; [4]LBNL Berkeley and UC Berkeley; [5]JAERI Tokai; [6]Universität Mainz; [7]PSI Villigen; [8]IMP Lanzhou, [9]ITE Warsaw

Synthesis and investigation of heavy nuclei close to the deformed nuclear shells at Z=108 and N=162, especially of the even-even nucleus ^{270}Hs, provide important data for comparison with theoretical predictions. Relatively long half-lives for alpha decay and spontaneous fission were predicted for these nuclei [1,2]. The first chemical identification and the study of nuclear decay properties of Hs isotopes was accomplished in 2001 [3,4]. Gas phase chemical separation of Hs isotopes in the form of volatile HsO_4 provides a highly selective and very efficient method of isolation. Here we report preliminary results of a recent Hs chemistry experiment performed at the GSI UNILAC accelerator to measure the excitation function of the reaction ^{26}Mg(^{248}Cm, xn)$^{274-xn}$Hs and to obtain additional information on the decay properties of Hs isotopes and their daughters. Based on calculated excitation functions, experiments at beam energies of E_{lab} = 135 MeV and E_{lab} = 145 MeV in the center of the target were carried out. The resulting excitation energies of 40 MeV and 49 MeV correspond to the predicted maxima of the 4n and 5n evaporation channel, respectively. The experimental procedure is decribed in [5]. Beam integrals of 1.46×10^{18} (145 MeV) and 2.02×10^{18} (135 MeV) ^{26}Mg ions were accumulated. A first, preliminary analysis of the data at 145 MeV revealed 7 decay chains attributed to the decay of Hs isotopes. These decay chains with observed α-particle or fission fragment energies in MeV, decay times, as well as detector number, top (T) or bottom (B) position and gas flow rates are presented in Figure 1. The probabilities that the observed decay chains are of random origin are low and comparable to the values given in [3,4]. The data accumulated at 135-MeV is currently being analyzed.

References

[1] I. Muntian et al., Acta Phys. Pol. B **32**, 691 (2001).
[2] R. Smolańczuk et al., Phys. Rev. C, **52**, 1871 (1995).
[3] Ch.E. Düllmann et al., Nature **418**, 859 (2002).
[4] A. Türler et al., Eur. Phys. J. A **17**, 505 (2003).
[5] J. Dvorak et al., this Annual Report, p.

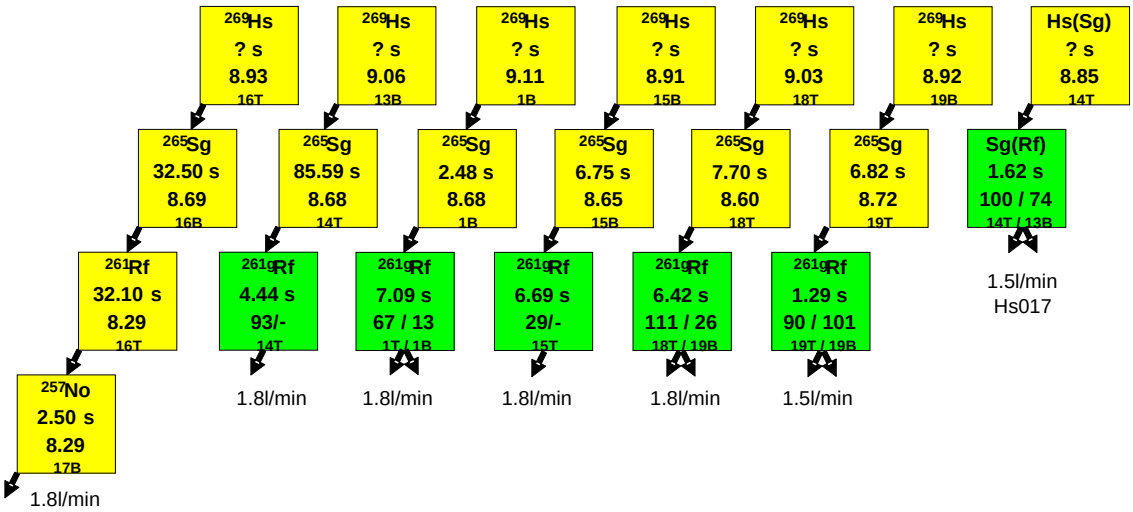

Figure 1. Correlated decay chains observed in the 145-MeV run.

Nilsson Levels in Odd Mass Odd Z Nuclei in the Region Z = (99 – 105)

F.P.Heßberger[1], S. Hofmann[1,2], D. Ackermann[1,3], S. Antalic[4], I. Kojouharov[1],P. Kuusiniemi[1], R. Mann[1], K. Nishio[1,5], S. Saro[4], B. Streicher[4], B. Sulignano[1,3] and M. Venhart[4]

[1]GSI, Darmstadt, Germany, [2]Johann Wolfgang Goethe – Universität, Frankfurt, Germany, [3]Johannes Gutenberg – Universität, Mainz, Germany, [4]Comenius University, Bratislava, Slovakia, [5]JAERI, Tokai, Japan

Similarities in nuclear structure are observed for isotopes of odd-Z elements with even neutron numbers. These can be used to explain the α-spectra and to construct partial level schemes. Vice versa changes in the α-decay pattern may reveal a change of the ground-state (gs) configuration in the daughter nuclei. Results of previous studies were presented in the last year GSI Scientific Report [1]. In 2004 for two more Md-isotopes α-γ-coincidence measurements were performed: ^{249}Md was produced via the reaction ^{209}Bi(^{50}Ti,2n)^{257}Db – α → ^{253}Lr – α → ^{249}Md. In coincidence with α-decays of the latter isotope we measured a γ-line of 253 keV. A so far unknown α-γ-coincidence pair of (E_α = 7092 keV, E_γ = 352 keV) was observed in an irradiation of ^{207}Pb with ^{48}Ca at 4.60 AMeV. In this reaction predominantly the isotope ^{253}No was produced. As a control we performed irradiations of ^{206,208}Pb and ^{209}Bi where mainly the isotopes ^{252,254}No and ^{255}Lr were produced. In these reactions the above mentioned activity was not observed. Thus it is seemingly connected to the production of ^{253}No. However it cannot be attributed to ^{253}No itself or any known daughter product of which α-decay has been reported so far. Since an EC branch of ≈30 % is reported for ^{253}No [2], it is straightforward to assign the unknown activity (tentatively) to a so far not reported α-branch in the EC-daughter ^{253}Md.

The E_γ = 295 keV line in coincidence with α-decays of ^{251}Md [1] has been confirmed by Theisen et al. [3] (although they give a somewhat different energy of 290 keV), who in addition observed one more line at 235 keV, which was confirmed by us in a recent experiment, however, our energy of E = 243 keV is slightly different. We measured an intensity ratio of I(295) : I(243) = 1 : 0.13.

As discussed in [1] the strongest γ-lines may be attributed to the transition 7/2$^-$[514] → 7/2$^+$[633] in the Es daughter isotopes, where the final state may be regarded as the ground- or a low lying state.

The new results allow for a complete systematics of the 7/2$^-$[514] Nilsson level in odd mass einsteinium isotopes in the mass range A=243 to A=253. The experimental data are shown in fig. 1b. Evidently an increase of the level energies with increasing neutron numbers is observed until the maximum is reached at ^{251}Es, whereas it drops from ^{251}Es to ^{253}Es by about 90 keV.

The experimental results can be compared with theoretical calculations shown in fig. 1a. The calculations of Cwiok et al. [4] qualitatively represent the trend, although they predict a more smooth increase and locate the maximum at ^{249}Es. Energies are, however, higher by several hundred keV. The energies according to the calculations of Parhomenko and Sobiczewki [5] are in general closer to the experimental values, but locate opposite the experimental trend the maximum already at ^{245}Es.

Both calculations predict the 7/2$^-$[633] level as ground states and locate the 3/2$^-$[521] – level above 100 keV, while from experimental side, as discussed in [1], the situation is not clear so far.

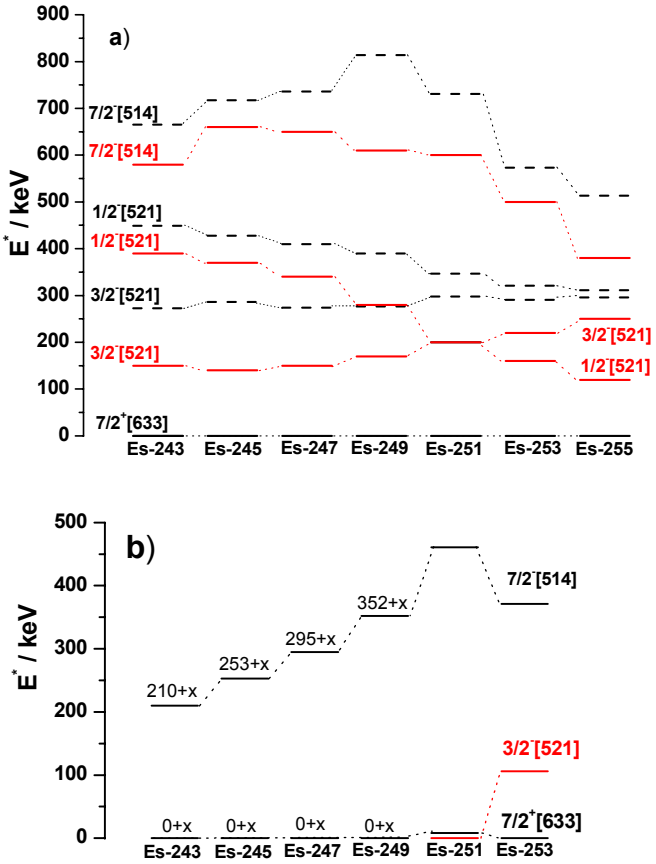

Fig1: a) Theoretical predictions of low lying Nilsson levels In odd – mass Es-isotopes. Dashed line: calculations of Cwiok et al.[4], full line: calculations of Parkhomenko and Sobiczewki [5]
b) Experimental level energies

References:

[1] F.P. Heßberger et al., GSI Scientific Report 2003, GSI-2004-1, 3 (2004)
[2] F.P. Heßberger, GSI Report GSI-85-11 (1985)
[3] Ch. Theisen et al. Proceedings ENAM 04 and private communication
[4] S. Cwiok, W. Nazarewicz, S. Hofmann, Nucl. Phys. A 573, 356 (1994)
[5] A. Parkhomenko, A. Sobiczewski, Acta Phys. Pol. B35, 2447 (2004)

Decay spectroscopy of ^{255}No

F.P.Heßberger [1], S. Hofmann [1,2], D. Ackermann [1,3], S. Antalic [4], I. Kojouharov [1], P. Kuusiniemi [1], R. Mann [1], K. Nishio [1,5], S. Saro [4], B. Streicher [4], B. Sulignano [1] and M. Venhart [4]

[1]GSI Darmstadt, Germany, [2] Johann Wolfgang Goethe − Universität Frankfurt, Germany, [3]Johannes Gutenberg − Universität Mainz, Germany, [4]Comenius University Bratislava, Slovakia, [5]JAERI, Tokai, Japan

Within our experiments on nuclear structure investigation of superheavy elements we also investigated ^{255}No. A detailed α-decay study of this nuclide was performed by Eskola et al. [1] more than thirty years ago. On the basis of observed α-intensities and derived hindrance factors a partial level scheme for the daughter nucleus ^{251}Fm (see fig. 1) was suggested. Later on Dittner et al. [2] identified the 5/2$^+$[622] level at $E^* \approx 190$ keV as an isomeric state with $T_{1/2} = 15.5$ μs. In table works [3] two γ-lines of E = 192 keV and 187.2 keV are found, representing the decay of the $E^* \approx 190$ keV level into the ground state and the transition ($E^* \approx 397$ keV) → ($E^* \approx 190$ keV). (The numbers here are taken from [1,2.3]).

We investigated the decay of ^{255}No using the production reactions ^{208}Pb(^{48}Ca,n)^{255}No (E = 4.40, 4.45 AMeV) and ^{209}Bi(^{48}Ca,2n)^{255}Lr – EC → ^{255}No (E = 4.55, 4.60, 4.65 AMeV). α-particles were measured using the standard detector system behind SHIP [4], γ-rays were measured using an unshielded four-fold segmented Clover detector. Besides prompt α-γ - coincidences also delayed (Δt(α − γ) = (15 – 100) μs) coincidences were searched for. Concerning the latter the production via EC – decay of ^{255}Lr turned out to be more favourable than by the reaction ^{208}Pb(^{48}Ca,n)^{255}No, since in the latter one the 8.10 MeV α-line of ^{254}No (2n channel) having about a factor of ten higher intensity than the 8.10 MeV α-line of ^{255}No and was source of disturbing random α-γ – coincidences.

In the 'prompt' spectum (fig. 2a) besides the strong line at E = 192.2 keV, two weaker ones at E = 358.2 keV and E = 165.0 keV were observed. α-particles in coincidence with the 358.2 keV and the 192.2 keV lines show 'narrow' peaks at $E_\alpha = (7745 \pm 15)$ keV and (7910 ± 19) keV. In the latter case in addition a second, broad one at $E_\alpha \approx 7780$ keV was observed. This energy is roughly equal to the result of energy summming of E = 7745 keV – α-particles and K-conversion electrons from a ΔE(358.2 −192.2) keV transition, indicating that the level emitting the 192.2 keV line is also fed by internal conversion decay of the level emitting the 358.2 keV γ-rays. The 165.0 keV line, which fits also to this energy difference may represent a weak γ-transition between the two levels. Fig. 2b shows the spectrum of γ-rays emitted in delayed coincidence with ^{255}No α–decays. Besides x-rays a line at E = 199.7 keV is observed, representing γ-decay into the ground state. From the time distances between α- and γ/x-ray a half-life of $T_{1/2} = (23 \pm 15)$ μs was measured in agreement with the result of [2] .

References:
[1] P. Eskola et al. Phys. Rev. C 2, 1058 (1970)
[2] P.F. Dittner et al. Phys. Rev. Lett. 26,1037 (1971)
[3] R.F. Firestone et al. (eds.) Table of Isotopes (1996)
[4] S. Hofmann et al. Z. Phys. A 350, 277 (1994)

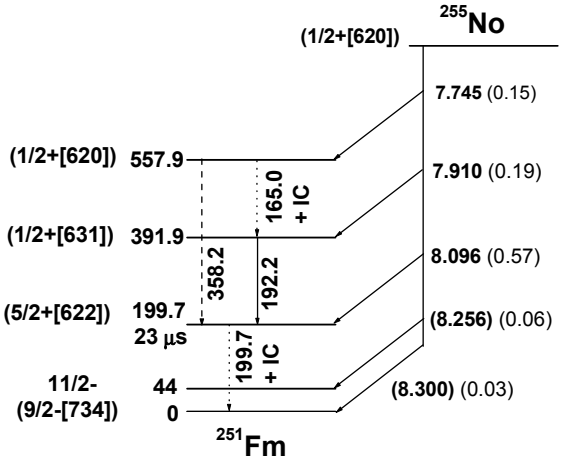

Fig 1: Partial level scheme of ^{251}Fm derived from α-decay of ^{255}No. Levels (except 1/2+[631]) and relative intensities of α-lines are shown as suggested by [1]. Energies are taken from this experiment.

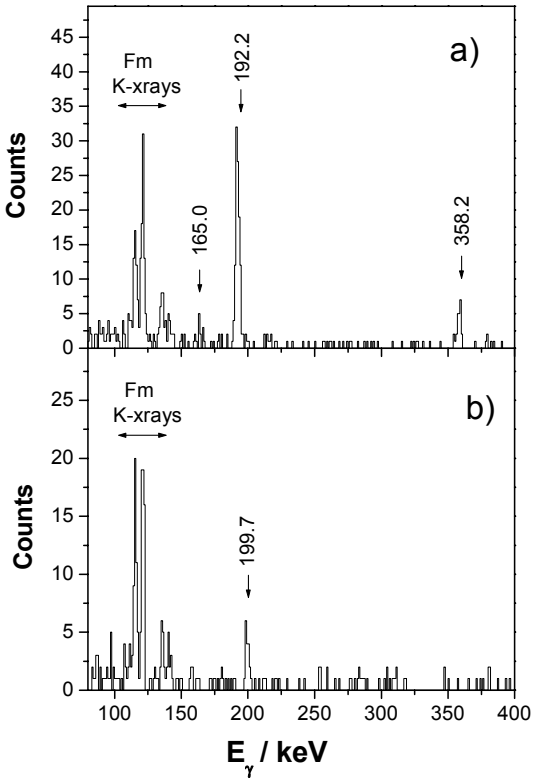

Fig 2: a) γ-ray spectrum measured in prompt coincidence with α-deccays of ^{255}No (7.7 − 8.0 MeV)
b) γ-ray spectrum measured in delayed coincidence with α-decays of ^{255}No (7.7 − 8.15 MeV

Evidence for an Isomeric State in ^{251}No

B. Sulignano[1,3], F.P.Heßberger[1], S. Hofmann[1,2], D. Ackermann[1,3], S. Antalic[4], I. Kojouharov[1], P. Kuusiniemi[1], R. Mann[1], K. Nishio[1,5], S. Saro[4], B. Streicher[4] and M. Venhart[4]

[1]GSI, Darmstadt, Germany, [2]Johann Wolfgang Goethe−Universität, Frankfurt, Germany, [3]Johannes Gutenberg−Universität, Mainz, Germany, [4]Comenius University, Bratislava, Slovakia, [5]JAERI, Tokai, Japan

Investigation of isomeric states deliver valuable information about nuclear structure. In the region of transfermium nuclei isomeric states decaying by α-emission is a wide spread phenomenon. Although the energy of the isomeric levels is not well established in general, most of them are believed to be located at rather low energies ($E^* < 500$ keV). Most of them are attributed to a low spin state, typically of spin ½ ħ; just for ^{257}Rf a high spin state is more likely (see e.g. [1] for further details). Solely in ^{270}Hs an isomeric state, interpreted as a K-isomer with spin and parity 9^- or 10^- at around $E^* = 1100$ keV has been identified [2].

Information on γ-isomers at $E^* > 500$ keV is scarce. A 7^- K-isomeric state at $E^* = 1425.2$ keV is known in ^{256}Fm [3]. There is also indication for K-isomers in ^{250}Fm and ^{254}No from γ-recoil measurements, but direct decay by γ-ray emission or internal conversion has not been observed so far.

In a recent investigation of the radioactive decay of ^{251}No and its daughter product ^{247}Fm, produced in the reaction ^{206}Pb(^{48}Ca,3n)^{251}No, in coincidence with evaporation residues (ER) followed by an α-decay of ^{251}No within 6.5 s, at least four γ-lines of $E_\gamma = 142.4 \pm 0.5$ keV (15 events), 203 ± 0.5 keV (31 events), 713.6 ± 0.5 keV (9 events) and 782.5 ± 0.5 kev (16 events) were observed (preliminary data). The complete spectrum is shown in fig. 1b. A half-life of ≈2 μs was obtained from the time distances between the ER and the γ-events using a TAC range of 5 μs..

Notably the energies of the two low energetic γ – lines agree with those of the γ-events observed in coincidence with α-decays of ^{255}Rf. These lines have been attributed to the transitions $9/2^-$ [734] → $7/2^+$ [624] (ground-state) (203.6 keV) and $9/2^-$ [734] → $9/2^+$, where the $9/2^-$ [734] is populated by α-decay of ^{255}Rf [4]. These data were confirmed and improved in a recent SHIP experiment. The result is shown in fig. 1a. It is therefore tempting to ascribe the two low energy lines in coincidence with ER correlated to α-decays of ^{251}No to the decay of the $9/2^-$ [734] level in ^{251}No. Although this interpretation is straightforward we presently hesitate to draw a final conclusion: the intensity ratio I(143)/I(203) is roughly 1:1 in the case of ^{255}Rf decay, but 1:2 in the case of coincidence with ^{251}No ER. This difference could be due to statistical fluctuations with respect to the low number of counts, but it also cannot be excluded that the agreement is fortituous. On the other hand, taking into account a decrease of the efficiency of the Clover – detector used for the γ-measurements by a factor of about two from 200 keV to 800 keV the intensity of the 782.5 keV line is significantly lower than that of the sum of the 142.4 and 203.1 keV lines, which could mean that the lines at 713.6 keV and 782.5 keV are rather emitted from the same level than forming a cascade. Present rates are, however, too small to prove (or disprove) this asumption by γ-γ- coincidence measurements. Also spin and parity assignments cannot be given presently. Nevertheless it seems to be evident that an isomeric state of at least $E^* \approx 925$ keV exists in ^{251}No.

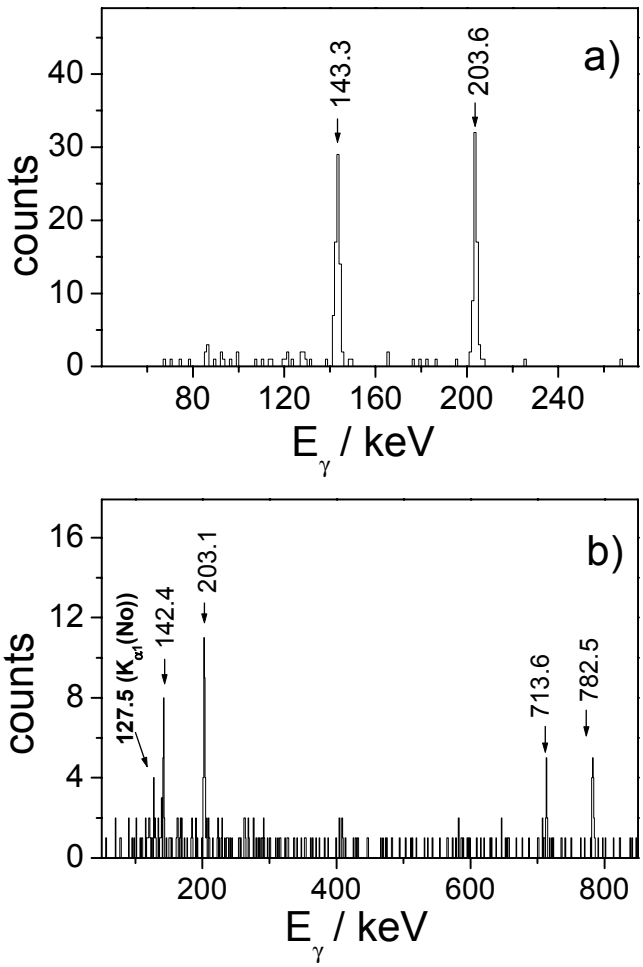

Fig. 1: a) γ - spectrum observed in coicidence with α-particles of ^{255}Rf, produced by the reaction ^{207}Pb(^{50}Ti,2n)^{255}Rf at E = 4.84 AMeV.
b) γ – spectrum observed in coincidence with ER followed by α-decays of ^{251}No, produced in the reaction ^{206}Pb(^{48}Ca,3n)^{251}No (preliminary data).

References:
[1] M. Leino, F.P. Heßberger ARNPS 54, 175 (2004)
[2] S. Hofmann et al. EPJ A 10, 5 (2001)
[3] R.S. Firestone et al. (eds) Table of Isotopes (1996)
[4] F.P. Heßberger et al. EPJA 12, 57 (2001)

Search for the "missing" α-decay branch in ^{239}Cm

Z. Qin [1,2], D. Ackermann[1,3], W. Brüchle[1], F.P. Hessberger[1], E. Jäger[1], P. Kuusiniemi[1], G. Münzenberg[1], D. Nayak[1,4], E. Schimpf[1], M. Schädel[1], B. Schausten[1], A. Semchenkov[1,6], B. Sulignano[1,3], K. Eberhardt[3], J.V. Kratz[3], D. Liebe[3], P.Thörle[3],Yu.N. Novikov[1, 5]

[1]GSI, Darmstadt, Germany, [2]Institute of Modern Physics, Chinese Academy of Science, Lanzhou, P.R. China,

[3]Johannes Gutenberg-Universität, Mainz, Germany, [4]Saha Institute of Nuclear Physics, Kolkata, India,

[5]Petersburg Nuclear Physics Institute, Gatchina, Russia, [6]Technical University of Munich, Germany

It is of special interest to search for those unknown α-emitters in the transuranium region which (i) are located along the path of α-decay chains that start in the superheavy element region, and (ii) establish a link to nuclides with known masses. The knowledge of all Q_α values in an α-decay chain provides direct information on strongly desired mass values of SHE [1]. A search for the α-decay of ^{239}Cm was carried out at JAERI applying nuclear chemistry techniques [2]. Three α-events with an energy of 6.43±0.14 MeV were assigned to ^{239}Cm and the α/EC branching ratio was estimated as $(6.2 \pm 1.4)\times10^{-5}$. However, due to this poor statistics, not only the α-energy was determined with an insufficient precision but also the isotope assignment remained questionable.

In our experiment, curium isotopes were produced in the reaction ^{232}Th(^{12}C,xn)$^{244-x}$Cm. Banana-shaped ^{232}Th targets were prepared by molecular plating at the University of Mainz. As a backing material, 5 μm thick Ti and 15 μm thick Be foils were used. Th target thicknesses were ≈ 700 μg/cm^2 on Ti and ≈ 900 μg/cm^2 on Be. $^{12}C^{2+}$ beams from the UNILAC were chosen such that after passing through a 20 μm Be vacuum window, He cooling gas of 200 mbar, and the backing material, the ^{12}C projectile energy was 74 MeV in the middle of the target. According to HIVAP calculations, this energy corresponds to the maximum of the excitation function for the reaction ^{232}Th(^{12}C,5n)^{239}Cm. Irradiations were performed with the rotating target wheel ARTESIA. Reaction products recoiling out of the target were implanted into 3.9 μm Cu catcher foils mounted 4 mm behind the rotating target wheel. Most fission fragments passed through the catcher because of their high TKE. To avoid overheating of the target and catcher material by the intensive ion beam, irradiations were carried out in a He atmosphere at 200 mbar. Each irradiation lasted ≈6 to 8 hours, and typical (particle) beam intensities varied between 0.3 μA during daytime and 0.85 μA at night. After irradiation, the copper catcher wheel was dismounted and was transported to a chemistry laboratory. The radiochemical separation procedure to prepare a purified Cm sample for α-spectroscopy was finished within 1.5 h or less. This procedure is described in a separate contribution to this report [3].

Two separate runs were carried out at the beginning and end of November. During the first run, targets with Th on Ti were used. They failed because of massive losses of target material from the Ti backing during the irradiation. Furthermore, ^{48,49,51}Cr, $^{43,44,46-48}$Sc, and ^{55,56}Co were produced from ^{12}C on Ti reactions with very high β- and γ-activities masking complementary γ-spectroscopic measurements. During the second run, targets with Th on Be foil were used which did not show significant Th losses. β and γ activities were about ten times lower than in the first run, and the nuclides mentioned above were not present.

In attempts to identify ^{239}Cm by γ-spectroscopic measurements, some samples were measured with a γ-x-detector and with a Ge-clover detector. γ-ray spectra dominantly showed lines from the decay of ^{153}Sm, ^{150,151}Pm and ^{147}Nd originating from fission of the compound nucleus. Cross sections for these isotopes are about 5 mb [4]. These activities from chemically not separated homologous rare earth elements did not allow identifying ^{239}Cm in the (single) γ-spectra or any Cm by characteristic x-rays. A further evaluation of coincidences is under way.

Samples were assayed for α-activities by 450 mm^2 PIPS detectors. The energy resolution of the evaporated samples was 60 keV. The α-events together with detector numbers and associated times were recorded and stored in list mode. Fig. 1 shows, for the first 10 h measuring time, the sum spectrum of five samples. As expected, ^{240}Cm (4n-channel, ≈100% α-decay) with α-energies of 6.29 and 6.24 MeV is dominant. Interestingly, there are some events around 6.5 MeV, close to the energy of ^{238}Cm (6n-channel). Data analysis and search for ^{239}Cm with a reported energy of 6.43 MeV [2] are in progress.

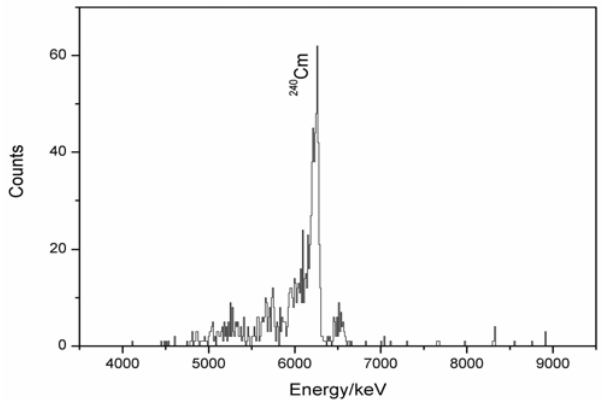

Fig.1 Sum α-spectrum of five samples (t_m =10 h each).

[1]G. Münzenberg. FRS Berichte, GSI (1995) (unpublished)

[2] N. Shinohara et al., JAERI-Review 2002-029, p. 45

[3] Z. Qin et al., GSI Scientific Report 2004

[4] A. Ramaswami et al., J. Radiochem. Nucl. Chem. 246 (2000) 225

α - Decay Fine Structure of ^{213}Ra to ^{209}Rn

P. Kuusiniemi[1,2], F.P. Heßberger[1], D.Ackermann[1,3], S. Hofmann[1,4],
K. Nishio[1,5], B. Sulignano[1,3], I. Kojouharov[1] and R. Mann[1]

[1] Gesellschaft für Schwerionenforschung mbH, Darmstadt, Germany;
[2] University of Jyväskylä, Jyväskylä, Finland; [3] Johannes Gutenberg Universität Mainz, Mainz, Germany;
[4] Institut für Kernphysik, Johann Wolfgang Goethe-Universität, Frankfurt/M, Germany; [5] JAERI, Tokai, Japan

So far decay data for ^{213}Ra [1] are already well established (fig. 1). Furthermore, the 110, 105 and 215 keV transitions are assigned to E2 and two E2(+M1) mixtures [2], respectively. However, on the basis of the N = 123 even-Z isotones [1,3] the $3/2^-$ and the $5/2^-$ g.s. as well as the $3/2^-$ and $1/2^-$ states are expected to be connected by M1 transitions. To clarify this we produced ^{213}Ra using the ^{50}Ti + ^{170}Er → ^{220}Th* reaction at SHIP (for experimental details, see e.g. [4,5]). Our results are listed in table 1.

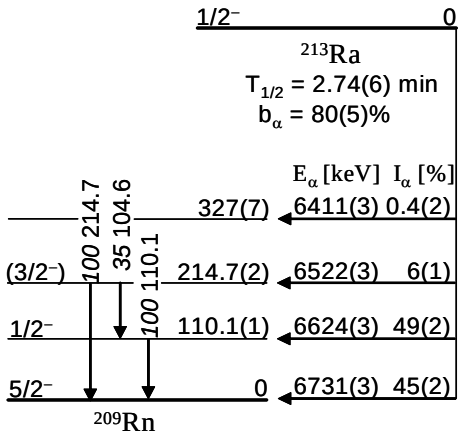

Figure 1: Decay scheme of ^{213}Ra [1].

Total conversion coefficients α_{tot} for the 105, 111 and 215 keV transitions were extracted using the ratio of the observed numbers of α-γ-coincidences (the γ-decay rate) and the calculated number of α-γ-coincidences expected for a given α-line (the total decay rate). The expected numbers of α-γ-coincidences were calculated using the absolute efficiency of the Ge-detector [4,5].

For the 111 keV transition the measured α_{tot} = 5.1(9) is consistent with the theoretical value of α_{E2} = 5.4 [6] while $\alpha_{E1} < 0.5$, $\alpha_{M1} = 11$ and $\alpha_{E3} = 124$ are excluded. Thus we conclude that the 111 keV transition is E2. This is further supported by α-energies observed in α-γ-coincidences gated by radon K X-rays and by radon K X-ray and γ-ray intensities gated by ^{213}Ra α-decays. The relative γ-ray intensities for 105, 111, 215 and 328 keV (normalized to 111 keV γ-rays) are 4(1):100(7):10(2):0.9(4) and the relative intensity ratio between radon K X-rays and 111 keV γ-rays is 87(6):100(3), respectively. Since the ratio of radon K X-rays and 111 keV γ-rays corresponds to an upper limit of the K-conversion coefficient $\alpha_K < 1.0$, we can exclude magnetic transitions for which $\alpha_K > 8.5$ [6].

A situation for the 105 and 215 keV transitions is more complex since they both depopulate the 215 keV level. Using the absolute efficiency, α-intensity to the level at 215 keV and γ-ray intensities depopulating it we were able to limit possible multipolarities to E1, M1 or E2 for the 105 keV transition and to E1, M1, E2 or E3 for the 215 keV transition by demanding that the total decay rate for a given transition has to be less than that of the number of α-decays populating the level at 215 keV. Furthermore, on the basis of radon K X-rays we concluded that in order to explain the number of radon K X-rays in the γ-ray spectrum gated by ^{213}Ra α-decays and subtracted by those resulting from the 111 keV E2 transition both the 105 and 215 keV transitions ($\alpha_{K,E2}$ = 0.34 and $\alpha_{K,E3}$ = 0.35 [6] for 105 and 215 keV, respectively) cannot be electric since such a small conversion coefficients would only explain < 10% of radon K X-rays observed in the subtracted γ-ray spectrum. Thus we concluded that both the 105 and 215 keV transitions have an M1 character with a very small (< 10%) if any admixture of E2.

Due to poor statistics we were not able to reliably extract the total conversion coefficient for the weak ($I_{\alpha,rel.}$ = 0.4(2)%) transition at 328 keV fed by 6413 keV α-decay but only a rough value ≈ 4 could be estimated. However, α-energies gated by 111 and 215 keV γ-rays indicate that the 328 keV level also populates the levels at 111 and 215 keV. Therefore our estimated value should be considered as an upper limit rather than a real value which together with multipolarity assignments are left for further studies.

Table 1: The α-γ data attributed to the α-decay of ^{213}Ra.

E_α [a]	E_{level} [a]	E_γ [a]	$I_{\gamma,rel.}$ / %	Mλ	I^π
6733(2)	0	–			$5/2^-$ [b]
6625(2)	110.5(1)	110.5(1)	100	E2	$1/2^-$ [b]
6521(2)	214.9(2)	214.8(2)	100(9)	M1	$3/2^-$ [c]
		104.7(3)	30(7)	M1	
6413(4)	328.2(3)	328.2(3)	100 [d]		

[a] Energy in keV. [b] Ref. [1]. [c] M1 to $5/2^-$ and $1/2^-$. [d] Tentative.

References:

[1] R.B. Firestone *et al*., *Table of Isotopes*, Wiley 1996
[2] D.G. Raich *et al*., Z. Phys. A **279**, 301 (1976)
[3] P. Kuusiniemi *et al*., to be published
[4] P. Kuusiniemi *et al*., EPJ A **22**, 429 (2004)
[5] F.P. Heßberger *et al*., EPJ A **22**, 253 (2004)
[6] F. Rösel *et al*., ADNDT **21**, 291 (1978)

New isotopes ^{186,187}Po and ^{192}At

A.N. Andreyev[1], S. Antalic[2], D. Ackermann[3,8], S. Franchoo[4], F. P. Heßberger[3], S. Hofmann[3,9], M. Huyse[5], I. Kojouharov[3], B. Kindler[3], P. Kuusiniemi[3], S. R. Lesher[5], B. Lommel[3], R. Mann[3], G. Münzenberg[3,8], K. Nishio[3], R.D. Page[6], J. Ressler[7], B. Streicher[2], B. Sulignano[3], P. Van Duppen[5], and D. Wiseman[6]

[1]TRIUMF, 4004 Wesbrook Mall, Vancouver BC, Canada, V6T 2A3; [2]Department of Nuclear Physics, Comenius University, Bratislava, SK-84248, Slovakia; [3]Gesellschaft fur Schwerionenforschung, Planckstrasse 1, D-64291 Darmstadt, Germany; [4]IPN Orsay, F-91406 Orsay Cedex France; [5]Instituut voor Kern- en Stralingsfysica, University of Leuven, B-3001 Leuven, Belgium; [6]Department of Physics, Oliver Lodge Laboratory, University of Liverpool, Liverpool L69 7ZE, UK; [7]Dept. of Chemistry, Simon Fraser University, Burnaby BC Canada V5A-1S6; [8]Inst. f. Physik, Johannes Gutenberg-University, D–55099 Mainz, Germany; [9]Physikalisches Institut, J.W. Goethe-Universität, D–60054 Frankfurt, Germany

The new nuclides ^{186,187}Po and ^{192}At were identified in experiments at the velocity filter SHIP. The ^{186,187}Po isotopes were produced in the 4n and 3n evaporation channels, respectively, of the ^{46}Ti+^{144}Sm→^{190}Po* reaction, while ^{192}At was produced in the 3n channel of the ^{51}V+^{144}Sm→^{195}At* reaction. The ^{46}Ti and ^{51}V beams were provided by the UNILAC with a typical intensity of about 150-200 pnA on target. Eight 400 μg/cm^2 thick ^{144}Sm targets (96.47% enriched) were mounted on a target wheel rotating synchronously with the UNILAC macro-pulsing.

The evaporation residues were separated in-flight by SHIP and implanted in a position-sensitive silicon detector to measure subsequent particle decays. A large-volume 4-fold segmented Clover-type germanium detector was installed behind the silicon detector for the α-γ (ΔT(α-γ)$\leq$5 μs) coincidence measurements. The nuclei were identified on the basis of the recoil-α, recoil-α-α and recoil-α-γ analysis. Preliminary data for all three new isotopes are reported in this contribution, while the full account will be given elsewhere [1].

^{186,187}Po

Figure 1 shows an example of a four-member α-decay correlation chain measured for ^{187}Po. In addition about 40 two-member and three-member correlated events were also assigned to ^{187}Po, allowing a rather detailed analysis to be performed. In particular, the observation of the α(7528 keV)-γ(285 keV) coincidences for the parent ^{187}Po (see Fig.1) establishes a low-lying excited state at E*=285 keV in the daughter ^{183}Pb. Based on the preferential decay to the 285 keV state versus the strongly hindered α decay to the ground state in ^{183}Pb, we conclude that the E*=285 keV state should be a low-lying deformed intruder state. This pattern is very similar to the decay of ^{189}Po previously identified and studied in detail at the SHIP, in which a low lying excited state at E*=278 keV in ^{185}Pb was observed [2] and interpreted as an intruder state [2,3]. These conclusions are supported by the potential energy surface calculations for odd-mass Pb and Po isotopes [4].

We note that the preliminary data analysis shows the presence of two isomeric states in ^{187}Po.

Four four-member correlations were observed for the new isotope ^{186}Po along with a number of double and triple correlations. The preliminary estimated half-live of ^{186}Po is about 40(10) μs.

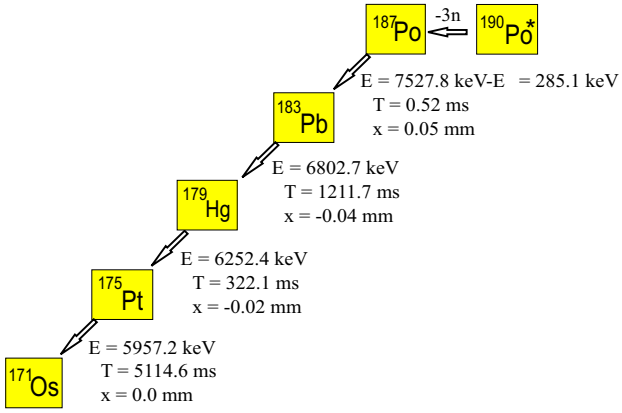

Figure 1: An example of the decay chain for ^{187}Po. Shown are α decay energies along with time and position difference between each member of the decay chain. Note that the first α decay at 7528(15) keV in this chain was observed in prompt coincidence with the γ decay at 285 keV.

Isomeric states in the new isotope ^{192}At

Figure 2 shows a part of the two-dimensional α1-α2 correlation spectrum deduced for the reaction ^{51}V+^{144}Sm→^{195}At*. The figure clearly shows the α1 decays in the energy range of 7200-7600 keV situated mainly in the regions marked by the rectangles 'A', 'B' and 'C' in Fig.2.

The measured half-life T$_{1/2}$=280(20) ms and energy E$_{\alpha 2}$=6815(10) keV for the α_2 decay in rectangle 'A' of Fig.2 are in a good agreement with the decay properties of the I$^\pi$=(10$^-$) α-decaying isomer ^{188m1}Bi (T$_{1/2}$=265(10) ms, E$_\alpha$=6813(5) keV [5]). The group in rectangle 'C' at E$_{\alpha 2}$=7305(15) keV corresponds to the 7302(5) keV decay of ^{188m1}Bi with the intensity of I$_{\alpha 2}$=3.6(1.0)% relative to the 6813 keV decay [5].

Similarly, the measured half-life T$_{1/2}$=66(6) ms and energy E$_{\alpha 2}$=6995(10) keV for the strongest group of the α_2 decays in the rectangle 'B' of Fig.2 are in a good agreement with decay properties of the (3$^+$) ^{188m2}Bi isomeric state (T$_{1/2}$=60(3) ms and E$_\alpha$=6992(5) keV [5]). A weaker group at E$_{\alpha 2}$=7110(15) keV in Fig.2 corresponds to the 7106(5) keV decay of ^{188m2}Bi with the intensity of I$_{\alpha 2}$=2.1(2)% relative to the 6992 keV decay [5]. Based on above evi-

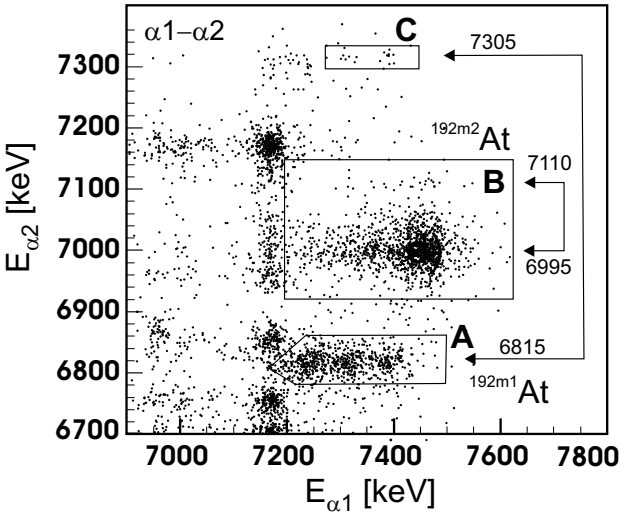

Figure 2: a) A part of the two-dimensional α1-α2 correlation spectrum from the reaction ^{51}V+^{144}Sm$\rightarrow^{195}$At*. The following conditions were applied: ΔT(recoil-α1) $\leq$400 ms, ΔT(α1 $-$ α2) $\leq$1.5 s. Events in rectangles marked by 'A','B','C' correspond to the decays originating from ^{192}At.

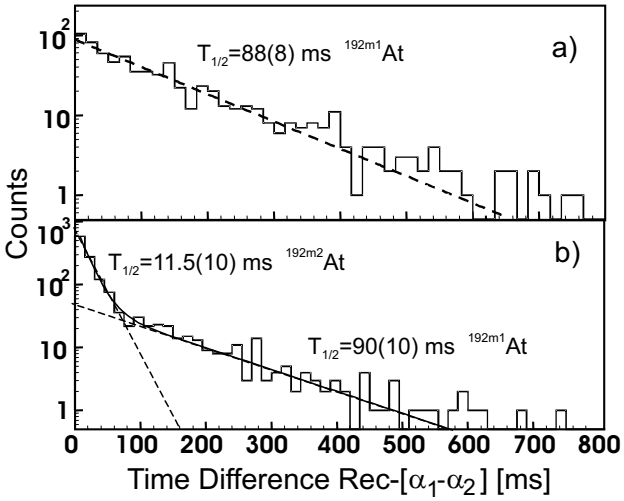

Figure 3: Time distributions between the recoil and subsequent pair of correlated α_1-α_2 decays for the events from the regions marked 'A' (^{192m1}At) - panel a), and 'B' (^{192m2}At) - panel b) of Fig.2. The continues line in part b) shows the result of the simultaneous fit by two exponential curves, shown separately by the dashed lines. The deduced half-lives and isotope assignments for the different components are given.

dence, the events inside rectangles 'A', 'B' and 'C' were attributed to the decay of the parent nucleus ^{192}At to two isomeric states in the daughter ^{188}Bi nucleus.

Figure 3a,b show the time distributions between the recoil implantation and a pair of subsequent correlated α_1-α_2 decays for the events from the rectangles 'A' and 'B', respectively. Two different half-life values of 88(8) ms for the events from rectangle 'A' and 11.5(10) ms for the events from rectangle 'B' were deduced.

Therefore, two different half-live values for the α1 decays of ^{192}At together with two distinct decay paths toward two isomeric states in the daughter nucleus ^{188}Bi allows us to distinguish two isomeric states in ^{192}At. The detailed decay scheme will be presented in [1].

Finally, we mention that in study [6], dealing with the identification of ^{191,193}At, a brief comment on the identification of ^{192}At was made, but no data on the half-life, α decay or decay scheme were given.

We thank the UNILAC staff for providing the stable and high intensity ^{46}Ti beam. This work was supported by the Access to Large Scale Facility programme under the Training and Mobility of Researchers programme of the European Union within the contract HPRI-CT-1999-00001, by the EXOTAG contract HPRI-1999-CT-50017, by the FWO-Vlaanderen and by the Interuniversity Attraction Poles Programme - Belgian State - Federal Office for Scientific, Technical and Cultural Affairs (IAP grant P5/07) and UK EPSRC. A.N.A. and J.R. were partially supported by the NSERC of Canada.

References

[1] A.N. Andreyev *et al.*, in preparation (2005)
[2] A.N. Andreyev *et al.* Eur. Phys. J. **A6**, 381 (1998)
[3] K. Van de Vel *et al.* Eur. Phys. J., A (2005), DOI: 10.1140/epja/i2004-10124-7 Issue: Online First
[4] R. Wyss, private communication
[5] A.N. Andreyev *et al.* Eur. Phys. J. **A18**, 39 (2003)
[6] H. Kettunen *et al.* Eur. Phys. J. **A18**, 537 (2003)

Direct Mass Measurements of Stored Exotic Nuclei

Yu.A. Litvinov[1,2], D. Boutin[1,2], L. Chen[1,2], H. Geissel[1,2], E. Kaza[1], C. Kozhuharov[1], S.A. Litvinov[1,2], M. Matos[1], Yu.N. Novikov[12], W. Plass[2], C. Scheidenberger[1], G. Vorobjev[1,12], H. Weick[1], F. Attallah[1], K. Beckert[1], P. Beller[1], F. Bosch[1], L. Caceres[1], J.J. Carroll[4], R.S. Chakrawarthy[5], D. Cullen[6], B. Franczak[1], B. Franzke[1], J. Gerl[1], E. Greda[1], M. Hausmann[3], G. Jones[8], A. Kishada[6], O. Klepper[1], H.-J. Kluge[1], R. Knöbel[2], R. Koyama[9], K.L. Kratz[10], E. Kulich[1], N. Kuzminchuk[1], Z. Liu[7], S. Mandal[1], F. Montes[11], G. Münzenberg[1,10], F. Nolden[1], T. Ohtsubo[9], A. Ostrowski[10], A. Ozawa[13], Z. Patyk[14], B. Pfeiffer[10], Z. Podolyak[8], M. Portillo[1], R. Propri[4], T. Radon[1], S. Rigby[6], N. Saito[1], T. Saito[1], H. Schatz[11], M. Shindo[15], J. Stadlmann[1], M. Steck[1], K. Sümmerer[1], T. Suzuki[9], P. Ugorowski[4], D. Vieira[3], P.M. Walker[8], S. Watanabe[9], S. Williams[8], M. Winkler[1], T. Winkler[1], H.-J. Wollersheim[1], H. Wollnik[2], and T. Yamaguchi[16]

[1]GSI, Darmstadt; [2]JLU, Giessen; [3]LANL, Los Alamos; [4]Uni. Youngstow; [5]TRIUMF, Vancouver; [6]Uni. Manchester; [7]TU München; [8]Uni. Surrey; [9]Uni. Niigata; [10]JGU, Mainz; [11]MSU, East Lansing; [12]PNPI, St. Petersburg; [13]RIKEN, Saitama; [14]SINS, Warsaw; [15]Uni. Tokyo

1 Schottky Mass Spectrometry (SMS)

As a continuation of the very successful experimental program on direct mass measurements of cooled neutron-deficient projectile fragments [1] we applied Schottky mass spectrometry to neutron-rich ^{238}U projectile fragments. A new data acquisition (DAQ) system was tested in this run and the masses of three nuclides were obtained for the first time (see Ref. [2]). The achieved sensitivity and accuracy required improvements.

The DAQ system was improved and a new experiment was performed in autumn of 2004. New masses and half-lives measurements of neutron-rich nuclides in the element range of ytterbium-uranium were the main goal. Part of the run was devoted to search for new long-lived isomeric states in the A=180 mass region.

A 670 MeV/u ^{238}U primary beam with intensities of up to $2 \cdot 10^9$ particles/spill impinged on a 4 g/cm^2 ^{9}Be production target in front of the fragment separator FRS. The neutron-rich projectile fragments were separated in flight and injected into the storage ring ESR, where they were stored and electron cooled. A thin 0.5 mm plastic energy degrader ($B\rho - \Delta E - B\rho$ separation) was used in the FRS to separate the ions of interest.

The revolution frequencies of stored ions were measured with the time-resolved SMS [3]. A large frequency bandwidth of 320 kHz was applied to cover the entire frequency acceptance of the ESR at 30^{th} harmonics of the revolution frequency. Although, the analysis is still progress, the identification of several spectra was already performed, as illustrated in Fig. 1. In the figure, the prominent lines are labelled with the corresponding identification. In the insert, a zoom on the ^{228}Fr and ^{228}Ra frequency peaks is shown. The mass value of ^{228}Fr is presently unknown [4].

About 1000 GB of raw data were stored after about 20 days of experiment. The analysis is underway at the universities of Giessen and Surrey, and at GSI.

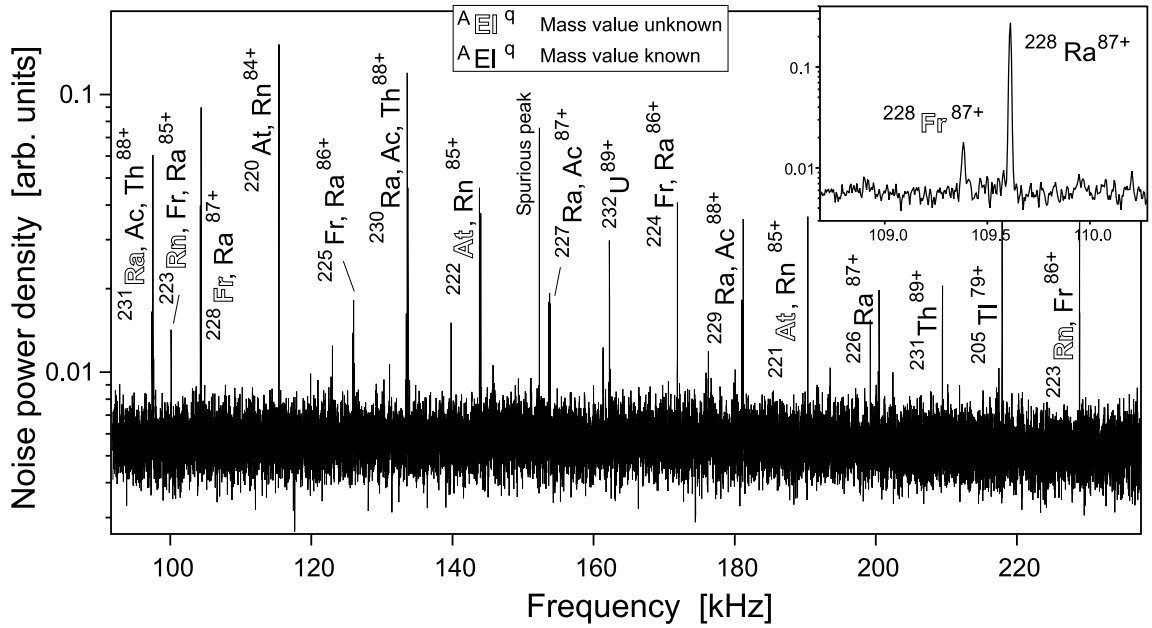

Figure 1: Part of the Schottky frequency spectrum measured in the new experiment. Only the prominent identified lines are marked. The labelling of known and unknown masses is done according to the AME'03 [4].

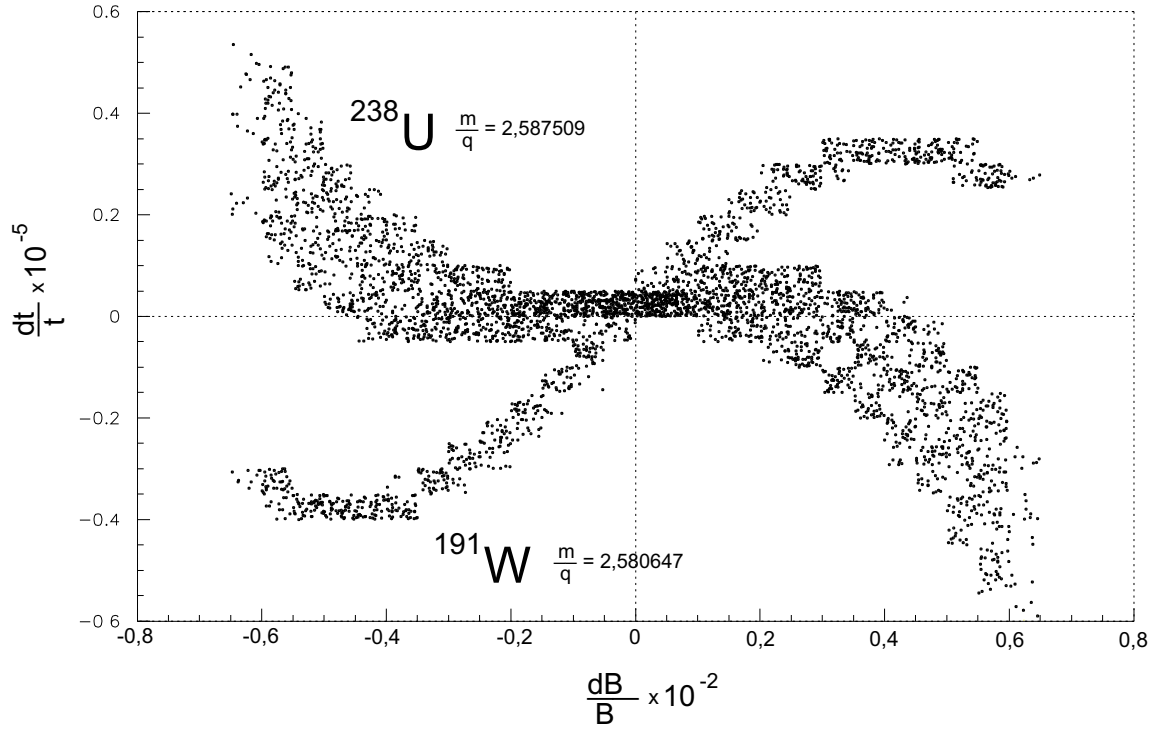

Figure 2: MOCADI simulation of the ESR in the isochronous mode for two ion species with different mass-over-charge ratios. The relative difference in the revolution times is plotted as function of the corresponding magnetic rigidity deviations. It is clearly seen that the isochronicity condition depends on the mass-over-charge ratio of stored ions.

2 Isochronous Mass Spectrometry (IMS)

IMS was developed to measure masses of nuclides with lifetimes down to sub-millisecond range, because it does not require cooling.

Neutron-rich zinc projectile fragments [5] and uranium fission fragments [6] were recently measured and provided about 40 new mass values which are important for nuclear structure and astrophysics [5]. Only a region of the measured time-of-flight spectra was analyzed yet. The reason is that the isochronous condition is only fulfilled for a restricted mass-over-charge range in the recorded spectrum. This is a disadvantage since the ESR in the isochronous mode can accept a large mass-over-charge range of about 13%. Moreover, the restriction may cause systematic uncertainties.

In order to enlarge the restricted range an additional correlation, like the measured velocity, position, or the magnetic rigidity is needed for each circulating ion. The data from an earlier experiment with ^{84}Kr projectile-fragments are being investigated to find such correlations. This data set contains about 60 stable and long-lived neutron-deficient nuclides with precisely (less than 10 keV) known mass values.

Moreover, a simulation program is under development which describes the production of exotic nuclei, their separation in the FRS, injection into the ESR, and its isochronous operation. The atomic and nuclear interactions of the ions penetrating through matter, including the carbon foil of the time-of-flight detector in the ESR, are taken into account. This program is based on the MOCADI code [7]. First results are presented in Fig. 2 where the relative difference in the revolution times is plotted as function of the corresponding magnetic rigidity deviations. The isochronicity condition is set and fulfilled for uranium ions whereas for different mass-over-charge ratios a larger spread of revolution times is obtained. This is illustrated for tungsten ions in the figure.

In future experiments additional detectors can be installed in the FRS, inside the ESR lattice, or after extraction from the ESR for independent velocity measurements of each ion.

References

[1] T. Radon et al., Nucl. Phys. A677 (2000) 75.
[2] E. Kaza, PhD Thesis, JLU Giessen, 2004.
[3] Yu.A. Litvinov et al., Nucl. Phys. A, in press.
[4] A.H. Wapstra et al., Nucl. Phys. A729 (2003) 129.
[5] M. Matoš, et al. in Proc. EXON2004, in press.
[6] C. Scheidenberger et al., GSI Report 2003-1, 6.
[7] N. Iwasa et al., NIM B126 (1997) 284.

Study of production and decay of long-lived isomeric states using time-resolved Schottky Mass Spectrometry

D. Boutin[a], Yu.A. Litvinov[a], C. Scheidenberger[a], K. Beckert[a], P. Beller[a], F. Bosch[a], T. Faestermann[b], B. Franczak[a], B. Franzke[a], H. Geissel[a,c], E. Kaza[a], A. Kelic[a], P. Kienle[b], O. Klepper[a], C. Kozhuharov[a], L. Maier[b], M. Matoš[a,d], G. Münzenberg[a,e], F. Nolden[a], Yu.N. Novikov[f], T. Ohtsubo[g], W. Plass[c], M. Portillo[a,d], K.-H. Schmidt[a,h], J. Stadlmann[a], M. Steck[a], H. Weick[a], M. Winkler[a], and T. Yamaguchi[a,i]

[a]GSI Darmstadt; [b]TU München; [c]JLU Giessen; [d]MSU, East Lansing, USA; [e]JGU Mainz; [f]NPI St Petersburg, Russia; [g]Niigata University, Japan; [h]TU Darmstadt; [i]Saitama University, Japan

During the past years, experiments at GSI permitted to study the production and the decay of isomeric states with half-lives ranging from seconds to hours [1], [2]. These isomeric states were produced by projectile fragmentation of (100-1000) MeV/u beams on a Be target, separated by the FRS , and injected into the ESR. The decay of the ions was studied via time-resolved Schottky Mass Spectrometry (SMS), which yielded information about their mass and lifetime.

We report new results from an experiment dedicated to the study of the bound-state β-decay of $^{207}Tl^{81+}$ [3]. The application of the stochastic precooling system [4], for the first time for fragments, permitted the observation of the isomeric state of ^{207}Tl ($T_{1/2}$(neutral) = 1.33(11) s) and to evaluate its decay to the ground state. Fig. 1 displays the intensities of ions as a function of storage time for one injection into the ESR.

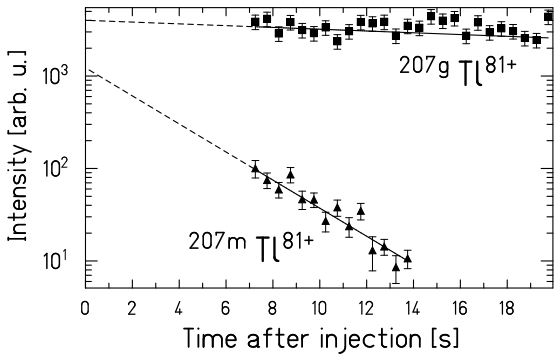

Figure 1: Decay curves of isomeric (m) and ground (g) states of bare $^{207}Tl^{81+}$. The lines represent a least-square fit to the data, starting from 7.5 s due to uncomplete cooling of fragments.

The half-life, deduced from 3 different injections, yields $T_{1/2}$ = 1.47(32) s, which is in very good agreement with the calculated value $T_{1/2}$(bare) = 1.52(13) s, derived from the vanishing of the electron conversion channel, in the case of a fully-ionized ion. From the ratio of the intensities at the injection I(t=0), we extract an isomeric production ratio defined as $R = I_m(0)/(I_g(0)+I_m(0)) = 0.15(4)$.

The results obtained from this experiment and the previous ones have been compared to calculations based on the abrasion-ablation model [5], where important parameters are the masses of both projectile and fragment (including the difference $\Delta A = A_p - A_f$) and the spin of the fragment. Two examples are shown in Fig. 2 for fragments with small and large ΔA.

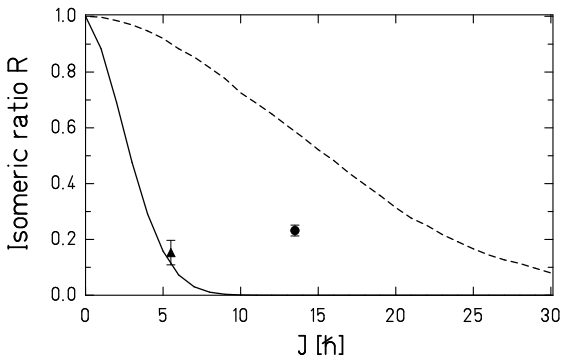

Figure 2: Isomeric production ratio R as a function of spin, for ^{207}Tl (triangle: experiment, solid line: calculation) and ^{149}Dy (circle: experiment, dashed line: calculation).

The calculations and experimental results are compiled in Table 1. We note an overestimation of the ratio for the case of fragments with masses far from the projectile mass, which is slightly different from the observations made by Pfützner *et al.* [6]. For fragments close to the projectile, the calculations seem to underestimate the isomeric state production (^{52}Mn is a particular case where the spin of the isomeric state is lower than the one of the ground state).

Projectile	Fragment	ΔA	J^π	$T_{1/2}$ (s)	R_{meas}	R_{calc}
^{58}Ni [1]	^{52}Mn	6	2^+	1380(180)	0.38(2)	0.65
^{58}Ni [1]	^{53}Fe	5	$19/2^-$	149(3)	0.10(1)	0.004
^{209}Bi [2]	^{149}Dy	60	$27/2^-$	11(1)	0.23(2)	0.58
^{209}Bi [2]	^{151}Er	58	$27/2^-$	19(3)	0.21(3)	0.57
^{208}Pb	^{207}Tl	1	$11/2^+$	1.47(32)	0.15(4)	0.11

Table 1: Compilation for the different isomeric states evaluated in [1], [2] and this work.

More detailed calculations are planned to improve the predictions on the production of isomeric states by projectile fragmentation.

References

[1] H. Irnich *et al.*, Phys. Rev. Lett. **75** (1995) 4182.
[2] Yu.A. Litvinov *et al.*, Phys. Lett. **B573** (2003) 80.
[3] D. Boutin *et al.*, GSI Report **2004-1** (2004) 18; D. Boutin, PhD Thesis, in preparation.
[4] F. Nolden, Nucl. Instr. Meth. **A441** (2000) 219.
[5] M. de Jong *et al.*, Nucl. Phys. **A613** (1997) 435.
[6] M. Pfützner *et al.*, Phys. Lett. **B444** (1998) 32.

Lifetimes of excited states in ^{113}I measured by the particle - X-ray coincidence technique

Z. Janas[1], L. Batist[2], R. Borcea[3], J. Döring[3], M. Gierlik[1], R. Kirchner[3], M. La Commara[4], S. Mandal[3], C. Mazzocchi[3,5], F. Moroz[2], S. Orlov[2], A. Płochocki[1], E. Roeckl[3], and J. Żylicz[1]

[1]Warsaw University, Poland; [2]St. Petersburg Nuclear Physics Institute, Russia; [3]GSI Darmstadt, Germany; [4]University "Federico II" and INFN, Italy; [5]University of Tennessee, USA

It has been demonstrated that the particle - X-ray coincidence technique (PXCT) [1] can be used to get information on lifetimes of excited nuclear states in the time range of 10^{-15}–10^{-17} s, such data being difficult to access by other methods. The PXCT technique uses an "atomic clock" (filling of the atomic shell vacancy) to measure the time scale of the nuclear deexcitation process. The β-delayed proton emission following electron capture decay (ECp) is ideally suited for this type of measurements. In this case the PXCT method is based on the following principle: A nucleus (with atomic number Z) decaying, e.g., by K-electron capture to excited state in the daughter (Z–1) produces an atomic K-shell vacancy. If this level decays by proton emission, the X-rays related to the filling process are characteristic for (Z–1) or (Z–2) element, depending on whether the vacancy is filled before or after the proton emission, respectively. For a single proton transition the relative intensity of the (Z–2) and (Z–1) KX-ray peaks observed in coincidence with protons is related to the total widths of the nuclear level (Γ_{nucl}) and the K-shell vacancy state (Γ_K) via formula: I_{KX}(Z–2)/I_{KX}(Z–1)=Γ_{nucl}/Γ_K. Since the total width of the K-shell vacancy states are known, the I_{KX}(Z–2)/I_{KX}(Z–1) ratio is a direct measure of the total decay width of the excited daughter state.

In this paper we report on the PXCT measurement which provides information on the lifetimes of ^{113}I proton-unstable states populated in the ECp decay of ^{113}Xe.

The ^{113}Xe nuclei were produced in reactions of a 4.74 MeV/u ^{58}Ni beam impinging on a 3.7 mg/cm^2 thick ^{58}Ni target. Reaction products were stopped in a niobium/tantalum catcher and ionized in the FEBIAD-B2C ion source of the GSI on-line mass separator. The ions extracted from the source were accelerated to 55 keV, mass-separated and implanted into a tape which periodically moved the collected activity into the center of the total absorption spectrometer (TAS) [2]. The radioactive sources were positioned between an X-ray detector and a telescope for β-delayed proton registration.

The PXCT measurement for the ^{113}Xe decay was performed by selecting ECp transitions to the ^{112}Te 2$^+$ state. This decay mode was identified by setting a gate on the 689 keV line visible in the proton-gated TAS spectrum. The inset in Fig. 1 shows the X-ray spectrum registered in coincidence with protons (unrestricted in energy) and the 689 keV line observed in the TAS. The tellurium and iodine KX-ray peaks are clearly visible, their intensity ratio being (5.2±0.5)%. This value is 3–5 times lower than the typical PXCT ratio measured for isotopes in the A=65–80 region [1, 3]. Figure 1 shows the measured $I_{KX}(Te)/I_{KX}(I)$ ratio as a function of ^{113}I excitation energy. The latter was calculated as a sum of the energy of emitted protons, the excitation energy of the ^{112}Te 2$^+$ state and the proton separation energy of 0.74(18) MeV in ^{113}I.

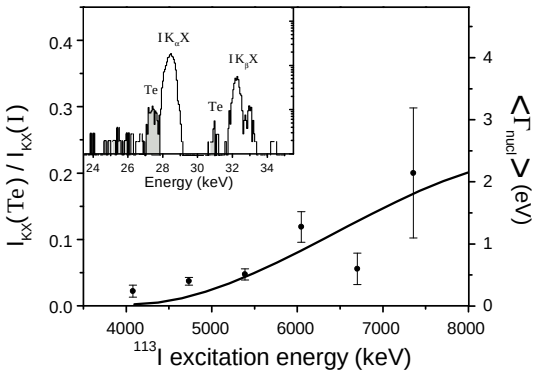

Figure 1: The I_{KX}(Te)/I_{KX}(I) ratio for proton transitions to the ^{112}Te 2$^+$ state plotted as a function of ^{113}I excitation energy. The solid line shows the result of the statistical model calculations. The inset shows the X-ray spectrum gated by protons and the 689 keV γ transition registered in the TAS.

Knowing that the total width of the K-shell vacancy state in the iodine atom is 10.7 eV one can determine the corresponding average total widths of the ^{113}I states. As shown on the scale at the right side of Fig. 1, in the excitation energy range of 4–7.5 MeV the total widths of ^{113}I states populated in the ECp decay of the ^{113}Xe 5/2$^+$ state increase from ∼0.25 to ∼2 eV. The corresponding lifetimes range from $2.6\cdot10^{-15}$ to $3.3\cdot10^{-16}$ s. We note, that the indicated widths (lifetimes) must be regarded as averages over ^{113}I states with spins that are allowed to be populated in the decay of ^{113}Xe.

The solid line in Fig. 1 shows the energy dependence of the $I_{KX}(Te)/I_{KX}(I)$ ratio resulting from a statistical model calculations [4] of the total decay widths of the ^{113}I states. The back-shifted Fermi gas level density formula and the standard γ-strength function and optical model parameters were used in the calculations. The model reasonably well reproduces the measured excitation energy dependence of the PXCT ratio. The best agreement was obtained for the level density parameters value a=14.9 MeV^{-1} and Δ=1.1 MeV, which follow the systematic trends in the A=110–130 mass region.

References

[1] J.C. Hardy *et al.*, Phys. Rev. Lett. **37**, 133 (1976).
[2] M. Karny *et al.*, Nucl. Instr. Meth. B **126**, 411 (1997).
[3] J. Giovinazzo *et al.*, Nucl. Phys. A **674**, 394 (2000).
[4] P. Hornshøj *et al.*, Nucl. Phys. A **187**, 609 (1972).

Measurements of α decay half-lives of ^{110}Xe and ^{106}Te

Z. Janas [1], C. Mazzocchi [2,3], L. Batist [4], A. Blazhev [2,5], M. Górska [2], M. Kavatsyuk [2,6], O. Kavatsyuk [2,6], R.- Kirchner [2], A. Korgul [1], M. La Commara [7], K. Miernik [1], I. Mukha [2,8,9], A. Płochocki [1], E.- Roeckl [2] and K. Schmidt [2]

[1]Warsaw University, Poland; [2]GSI, Darmstadt, Germany; [3]University of Tennessee, Knoxville, USA; [4]St. Petersburg Nuclear Physics Institute, Russia; [5]University of Sofia, Bulgaria; [6]T. Shevchenko National University, Kyiv, Ukraine; [7]University Federico II and INFN, Napoli, Italy; [8]University of Leuven, Belgium; [9]RRC Kurchatov Institute, Moscow, Russia

When exploring the island of α emitters above ^{100}Sn, it is particularly interesting to probe whether such nuclei undergo superallowed α-decay due to enhanced correlations of valence protons and neutrons occupying the same single-particle orbitals in N ≅ Z nuclei [1]. Based on this motivation, we re-investigated the α-decays of ^{110}Xe and ^{106}Te.

Neutron-deficient trans-tin isotopes, produced in the ^{58}Ni(^{58}Ni,xpyn) reaction, were stopped and ionized in the FEBIAD-B2C ion source of the GSI on-line mass separator. Since ^{106}Te nuclei are too short-lived (< 100 μs) to be efficiently released from the ion source, they were produced as α-decay products of mass-separated ^{110}Xe. Two different detector arrays were used. Firstly, the mass-separated A = 110 beam was periodically implanted (1 s beam-on / 1 s beam-off) in a thin carbon foil placed in front of a silicon surface-barrier detector telescope. The grow-in and decay observed for the collected activity was used to determine the decay half-life. Figure 1 shows the result of this measurement which yields a half-life of 105^{+35}_{-25} ms for ^{110}Xe, which considerably improves the previous result [2]. Secondly, the A = 110 beam was continuously implanted into a thin carbon foil placed between two silicon detectors, thus minimizing the loss due to the ^{106}Te recoil escape and efficiently registering ^{110}Xe-^{106}Te α-α correlations. A DGF-4C module was used for digitally registering amplitude and time stamp of α-decay signals occurring within less than 100 μs after each other. The known [3] half-life of ^{106}Te was redetermined with improved accuray to be 80^{+25}_{-15} μs.

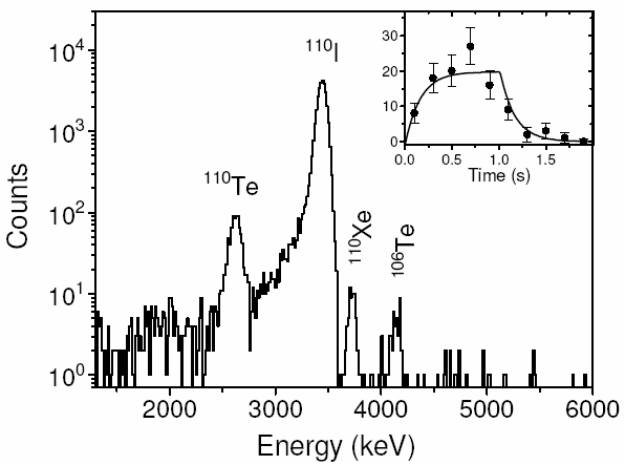

Fig. 1. Energy spectrum of α-particles registered in the ΔE detector in anticoincidence with the E detector of the telescope. The inset shows the time distribution of the summed intensities of the 3737 keV (^{110}Xe) and 4160 keV (^{106}Te) α lines; the solid curve represents the best fit of a grow-in and decay characteristic to the experimental data.

Figure 2 diplays the systematics of reduced α decay widths for even-even α emitters above ^{100}Sn and ^{208}Pb, plotted as a function of $N_pN_n/(N_p+N_n)$. Here N_p and N_n denote the number of valence protons and neutrons with reference to the ^{100}Sn and ^{208}Pb core, respectively. A weak, even though statistically insignificant indication is observed for an increase of the reduced α-decay widths of trans-tin isotopes over those of trans-lead nuclei. However, improved half-life and α branching-ratio data are clearly needed. The results of this work have been published recently [5].

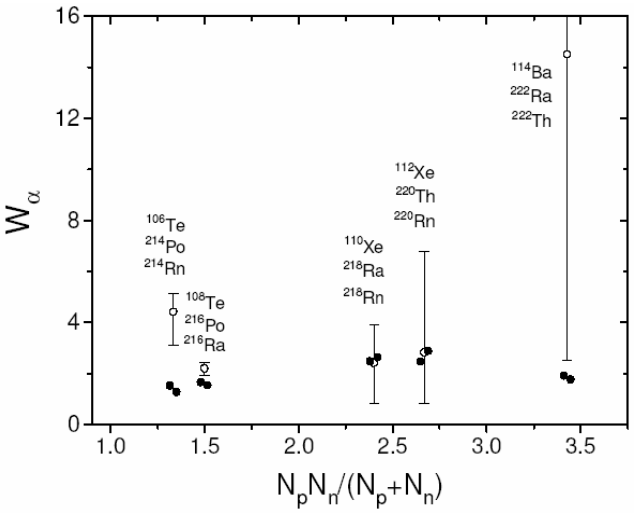

Fig. 2. Experimental reduced α-decay widths for even-even emitters plotted as a function of parameter $N_pN_n/(N_p+N_n)$. Data points for trans-tin and trans-lead isotopes are marked by open and full circles, respectively. Experimental data for ^{108}Te, ^{112}Xe and trans-lead isotopes were taken from [4] whereas those for ^{114}Ba, ^{106}Te and ^{110}Xe stem from [2] and from the present work.

[1] R.D. Macfarlane, A. Siivola, Phys. Rev. Lett. 14, 114 (1965)

[2] C. Mazzocchi et al., Phys. Lett. B 532, 29 (2002).

[3] D. Schardt et al., Nucl. Phys. A 368, 153 (1981)

[4] Y. A. Akovali, At. Data Nucl. Data Tables 84, 1 (1998)

[5] Z. Janas et al., Eur. Phys. J. A 23, 197 (2005)

Beta decay studies of ^{106}Sb and ^{107}Sb

K. Miernik[1], L. Batist[2], A. Blazhev[3,4], T. Faestermann[5], M. Górska[3], H. Grawe[3], Z. Janas[1], M. Karny[1], M. Kavatsyuk[3,6], O. Kavatsyuk[3,6], R. Kirchner[3], M. La Commara[7], C. Mazzocchi[8], I. Mukha[9], C. Plettner[10], A. Płochocki[1], E. Roeckl[3], K. Rykaczewski[11], and K. Schmidt

[1]Warsaw University, Poland; [2]St. Petersburg Nuclear Physics Institute, Russia; [3]GSI Darmstadt, Germany; [4]University of Sofia, Bulgaria; [5]Technical University, Munich, Germany; [6]T. Shevchenko Kiev National University, Ukraine; [7]University "Federico II" and INFN Napoli, Italy; [8]University of Tennessee, USA; [9]K.U. Leuven, Belgium; [10]Yale University, New Haven, USA; [11]Oak-Ridge National Laboratory, USA

The decay studies of neutron-deficient antimony nuclei provide information on low-spin states in light tin isotopes which is complementary to the high-spin structure data already available. The β-decay of nuclei in the ^{100}Sn region is dominated by the Gamow-Teller (GT) transformation of a $g_{9/2}$ proton into a $g_{7/2}$ neutron. In the decays of odd-odd isotopes one expects the population of 4-quasiparticle (qp) states at an excitation energy of 5–6 MeV in the daughter, whereas in the decays of odd-even nuclei one should observe substantial feeding of 3-qp configurations at an excitation energy of 4–5 MeV.

In this contribution we report on the first observation of the β-decay of ^{106}Sb and present new data on the decay properties of ^{107}Sb. The ^{106,107}Sb nuclei were produced in reactions induced by a ^{58}Ni beam on a 3.7 mg/cm^2 thick ^{58}Ni target. The reaction products were stopped and ionized in the FEBIAD-B2C ion source of the GSI on-line mass separator. The source was operated with an addition of CS_2 vapour which decreased the sticking time of antimony atoms at the source surfaces and thus improved their overall separation efficiency [1]. The intensities of mass-separated ^{106}Sb$^+$ and ^{107}Sb$^+$ beams amounted to >10 and 600 atoms/s, respectively. The latter value was a factor of 4 higher than the previously reported ^{107}Sb beam intensity [2]. The mass-separated ions were implanted into a tape placed in the center of an array of germanium γ-ray and silicon β-particle detectors. Alternatively, the beam was stopped on a tape which periodically moved the collected activity into the center of the total absorption spectrometer (TAS) [3]. Figure 1 shows the β-gated spectrum of γ-rays registered by the germanium detectors during the mass A=106 measurement. The inset shows the grow-in and decay of the intensity of the 1207 keV line identified as the $2^+ \rightarrow 0^+$ transition in ^{106}Sn. The least-square fitting procedure yielded a value of 1.1(1) s for the half-life of ^{106}Sb. Several other γ lines, among them the known 811 keV $4^+ \rightarrow 2^+$ transition in ^{106}Sn, were assigned to the decay of ^{106}Sb on the basis of the half-life and/or coincidence relations. These data were used to construct a partial decay scheme of ^{106}Sb.

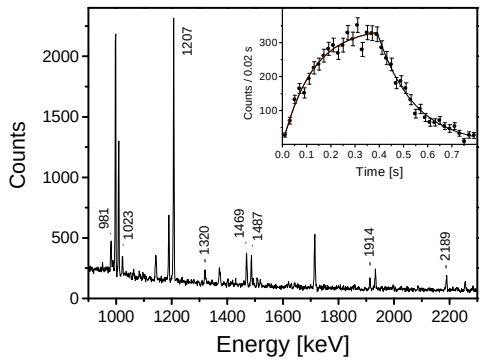

Figure 1: Part of the spectrum of γ-rays measured in coincidence with positrons during the mass A=106 measurement. Lines assigned to ^{106}Sb decay are marked by their energies. The inset shows the time dependance of the 1207 keV line.

The high-resolution measurement of ^{107}Sb decay allowed us to identify several new transitions in the daughter nucleus and substantially extend the existing decay scheme [2, 4]. More than 20 new γ transitions were assigned to the decay of ^{107}Sb and ^{107}Sn levels up to the excitation energy of 2 MeV were established on the basis of the observed γ-γ coincidence relations. However, qualitatively new information on the decay properties of ^{107}Sb was revealed by the TAS measurement. Figure 2 shows the energy spectrum of the TAS signals registered in coincidence with the Sn K_αX-rays. This condition selects the electron capture decay of ^{107}Sb. Feeding of two groups of states is clearly observed: At low excitation energies 1-qp states are populated by the $\pi d_{5/2} \rightarrow \nu d_{3/2}$ GT transformation whereas the 3-qp states at an excitation energy of 4–5 MeV are fed by the $\pi g_{9/2} \rightarrow \nu g_{7/2}$ GT transitions. We note that the 3-qp states were completely missing in the decay schemes based on the high-resolution, low-efficiency measurements.

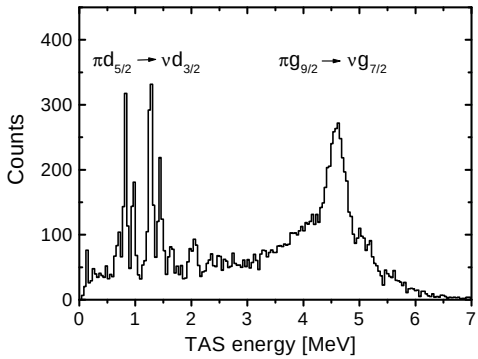

Figure 2: TAS energy spectrum observed in coincidence with the Sn K_αX-rays during the mass A=107 measurement.

References

[1] R. Kirchner, Nucl. Instr. Meth. B **204**, 179 (2003).
[2] M. Shibata *et al.*, Phys. Rev. C **55**, 1715 (1997).
[3] M. Karny *et al.*, Nucl. Instr. Meth. B **126**, 411 (1997).
[4] J.J. Ressler *et al.*, Phys. Rev. C **65**, 044330 (2002).

Reinvestigation of direct proton decay of ^{105}Sb

Z. Liu[1], P.J. Woods[1], K. Schmidt[1], H. Mahmud[1], P.S.L. Munro[1], A. Blazhev[2], J.Döring[2], H. Grawe[2], M. Hellström[2], R. Kirchner[2], Z.K. Li[2], C. Mazzocchi[2], I. Mukha[2], C. Plettner[2], E. Roeckl[2], and M. La Commara[3]

[1] University of Edinburgh, Edinburgh, EH9 3JZ, United Kingdom; [2]GSI, Planckstrasse 1, D-64291 Darmstadt, Germany; [3]Department of Physical Sciences, University "Federico II" and INFN, I-80126, Napoli, Italy

The isotope ^{105}Sb is known as the lightest ground state proton emitter [1]. In an experiment performed at Berkeley [2], a 478±15 keV proton line was reported and assigned to the the proton emission from the spherical $\pi d_{5/2}$ orbital in ^{105}Sb. As the experimental technique used in this experiment, namely a helium-jet system, did not allow for background suppression, the proton energy spectrum contained a large number of unidentified proton lines. A branching ratio of approximately 1% was estimated for the 478 keV proton line. However no half-life measurement was obtained. In an FRS experiment the half-life of ^{105}Sb was determined to be 1.12±0.16 s [3]. One proton-like event was found (with an 85% confidence level) at an energy of 550±30 keV, in disagreement with the Berkeley value. A confirmation of the proton radioactivity in ^{105}Sb remained imperative. A previous attempt to clarify the situation was made at the GSI on-line mass separator using two thin ΔE Si detectors [5], but did not yield a clear result, as the detection system was not able to suppress β-radiation background in the energy region of interest. It has been demonstrated that the background caused by β-emission can be suppressed well below a threshold of 400 keV with a thin DSSD detector [4]. This is due to the fact that the range of the direct decaying protons in silicon is much shorter than the pixel size of DSSD detector, i.e. the protons mostly deposit all energy in one single pixel. While the range of β particles is much longer and the energy loss process much more complicated. Beta background will be suppressed effectively by restricting events to those with single strip multiplicity conditions (M=1) for the front and back DSSD signals, and require equal energies for these signals. The proton decay of ^{105}Sb of was reinvestigated on the GSI on-line mass separator by combining the tape transport system and a thin DSSD detector.

^{105}Sb was produced in the ^{50}Cr(^{58}Ni,1p2n) reaction. The beam energies on the surface and in the middle of the ^{50}Cr target corresponded to 255 and 222 MeV, respectively, covering the energy range at which the proton line was reported at Berkeley [2]. The average beam intensity was 36 particle nA. A FEBIAD-E type ion source was used with improvements in efficiency made for antimony isotopes [5]. The total separation efficiency between production and collection was expected to be higher than 2% for ^{105}Sb. The mass separated A=105 activity was collected on a transport tape, and then moved to the counting position every 2.8 s. A 67 μm thick 48×48 DSSD, with an active area of 16×16 mm^2 was used for proton spectroscopy. The solid angle covered by the DSSD is around 10% of 4π. The energy responses of the 96 channels were carefully studied with precision pulser signals. The whole system was tested and calibrated with the well known proton emmiter ^{147}Tm. The energy resolution obtained for the 1.051 MeV ^{147}Tm ground-state proton peak is ∼30 keV in FWHM.

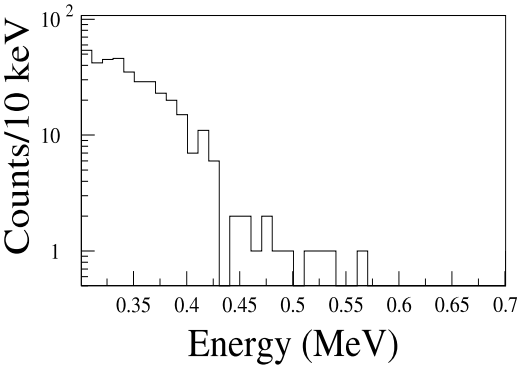

Figure 1: Decay energy spectrum (lower energy part only) obtained with the condition of multiplicity M=1 and energy difference of less than 3σ (40 keV) on both sides of the DSSD.

The run for ^{105}Sb lasted for 60 hours. The accumulated data are presented in Fig. 1 and show no indication of a peak at the energy of 478(15) keV measured in the Berkeley experiment [2]. Assuming a production cross section of 30 μb estimated in [6], a beam intensity of around 2.0 atoms/s was expected for ^{105}Sb. Assuming a similar yield rate of the 478 keV proton line measured in the Berkeley experiment [2], a peak with ∼ 150 counts should appear. The present data are therefore in strong disagreement with the Berkeley result. In fact the present data would rule out all proton decays from ^{105}Sb with energies > 430 keV and branching ratios > 0.1% (see Fig. 1). A simple WKB calculation assuming a spherical $d_{5/2}$ proton orbital and a spectroscopic factor ∼1 would give a branching ratio ∼ 0.1% for a 430 keV proton energy using the known beta-decay half-life of 1.12 s [3].

References

[1] A.A. Sonzogni, Nucl. Data Sheets **95**, 1 (2002).
[2] R.J. Tighe *et al.*, Phys. Rev. **C49**, R2871 (1994).
[3] J. Friese, in *Proceedings for the International Workshop XXIV on Gross Properties of Nuclei and Nuclear Excitations, Hirschegg, austria, 1996*, edited by H. Feldmeier, J. knoll, and W.Nörenberg (GSI, Darmstadt, 1996), p. 123.
[4] R.D. Page *et al.*, Phys. Rev. Lett. **73**, 3066 (1994).
[5] M. Shibata *et al.*, Phys. Rev. **C55**, 1715 (1997).
[6] M. Lipoglavšek *et al.*, Nucl. Phys. **A682**, 399c (2001).

Observation of direct proton decay of the high-spin isomer ^{94}Ag (21$^+$)

I. Mukha[1,2,3], E. Roeckl[1], J. Döring[1], L. Batist[4], A. Blazhev[1,5], H. Grawe[1], C. Hoffman[6], M. Huyse[2], Z. Janas[7], R. Kirchner[1], M. La Commara[8], C. Mazzocchi[1], C. Plettner[1,9], S. L. Tabor[6], P. Van Duppen[2], and M. Wiedeking[6]

[1]Gesellschaft für Schwerionenforschung mbH, Darmstadt, Germany; [2] KU Leuven, Belgium; [3]RRC "Kurchatov Institute", Moscow, Russia; [4]St. Petersburg Nuclear Physics Institute, Gatchina, Russia; [5]University of Sofia, Bulgaria; [6]Florida State University, Tallahassee, USA; [7]Warsaw University, Warsaw, Poland; [8]Universita di Napoli "Federico II", Napoli, Italy; [9]Yale University, New Haven, USA

Direct proton decay of the (21$^+$) isomer was observed in ^{94}Ag, the heaviest odd-odd N=Z nucleus with known decay properties. This isomer features a high excitation energy of 6.7(5) MeV with remarkably long half-life of 0.39(4) s, and is open to at least five decay modes, i.e. β-delayed γ ray, proton and two-proton [1, 2, 3], as well as direct proton and two-proton radioactivity [4]. Here we report on the observation of direct proton decay of ^{94m}Ag(21$^+$) to two excited states in ^{93}Pd. The measurements were performed at the GSI on-line mass separator [5]. The ^{94}Ag nuclei were produced by ^{58}Ni(^{40}Ca,p3n) fusion-evaporation reactions and ionized by a FEBIAD-B2C ion source [6], which provided a beam intensity of 2 s^{-1} for the (7$^+$) and (21$^+$) isomers in ^{94}Ag while suppressing the ^{94}Pd contamination. The mass-separated A=94 beam was implanted into a tape surrounded by an array of charged-particle and γ-ray detectors. Three large-area silicon (Si) multi-strip detectors were used for measurements of charged particles and 17 germanium (Ge) crystals for γ rays. Direct proton decay of the (21$^+$) isomer was observed by demanding coincidences between single-hit events recorded in the silicon and γ-γ coincidence events registered in the Ge detectors [7]. The applied γ gates were based on the known ^{93}Pd levels [8].

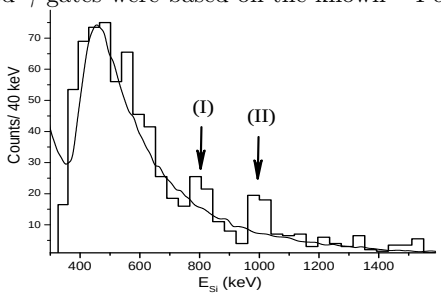

Figure 1: Spectrum of Si detectors selected with Si+γ+γ coincidence and with γ gates on ^{93}Pd* (histogram). The 0.8 and 1 MeV peaks indicate the direct proton decay of ^{94}Ag (21$^+$). Solid line is the single Si spectrum.

The proton spectrum shown in Fig. 1 has a fine structure with two proton peaks at 0.79(3) and 1.01(3) MeV. Therefore two proton transitions were assigned with branching ratios of 1.9(5) and 2.2(4) %, respectively. They are marked as (I) and (II) in Fig. 1. The protons (I) are coincident with all γ rays following de-excitation of the known (33/2$^+$) state in ^{93}Pd [8], and the protons (II) are coincident with the same γ rays except the 1132 keV one. In addition, new 614 and 403 keV γ rays were observed in coincidence with the protons (II).

The resulting decay scheme is shown in Fig. 2. From these data, the excitation energy of the (21$^+$) isomer was found to be 6.7(5) MeV, assuming a proton separation energy of 0.9(5) MeV for ^{94}Ag [9]. Orbital momenta $\ell_{(I)}$=4 and $\ell_{(II)}$=5 were tentatively assigned to the decay branches. The respective reduced widths $\Theta_p^2 = \gamma_p^2/\gamma_W^2$.

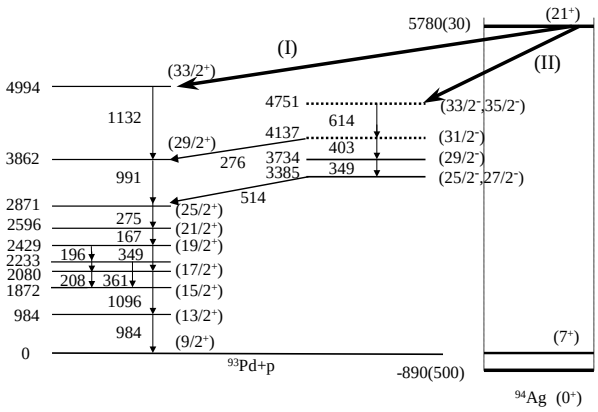

Figure 2: Direct proton decay of the ^{94}Ag(21$^+$) isomer to excited states in ^{93}Pd. Energies of known γ transitions and levels in ^{93}Pd [8] are indicated in keV and are given respective to the ^{93}Pd+p threshold.

are estimated to be $1\cdot10^{-6}$ and $4\cdot10^{-6}$, the reduced proton width γ_p^2 being obtained from the R-matrix partial width $\Gamma_p = 2\gamma_p^2 \cdot P_{\ell_p}(E_p)$, and γ_W^2 being the respective Wigner estimate of a reduced width due to single-proton ℓ_p configuration in mother state. These widths are very small in comparison with those derived from shell-model calculations. For example, a spectroscopic factor of 0.044 is found for the $\ell_{(I)}$=4 branch as an overlap of the single-proton $g_{9/2}$ configuration in the (21$^+$) isomer with the daughter ^{93}Pd(33/2$^+$) state in spherical shell-model calculations made in $\pi\nu(p_{1/2}, g_{9/2})$ space with the empirical Gross-Frenkel interaction. The small reduced widths of direct proton decays might reflect dominant collective configurations in (21$^+$), and the fine structure in the proton spectrum might indicate a strong deformation of the (21$^+$) isomer like in the proton decay of ^{141m}Ho [10].

References

[1] M. La Commara et al., Nucl. Phys. A **708**, 167 (2002).
[2] C. Plettner et al., Nucl. Phys. A **733**, 20 (2004).
[3] I. Mukha et al., Phys. Rev. C **70**, 044311 (2004).
[4] I. Mukha et al., Nucl. Phys. A **746**, 66 (2004).
[5] E. Roeckl et al., NIM in Phys. Res. B **204**, 53 (2003)
[6] R. Kirchner, NIM in Phys. Res. B **70**, 186 (1992).
[7] I. Mukha et al., Eur. Phys. J. A Direct, accepted.
[8] C. Rusu et al., Phys. Rev. C **69**, 024307 (2004).
[9] G. Audi et al., Nucl. Phys. A **729**, 337 (2003).
[10] K. Rykaczewski et al., AIP Conf.Proc. **681**,11 (2003).

Two-proton radioactivity of ^{94m}Ag (21^+)

I. Mukha[1,2,3], E. Roeckl[1], L. Batist[4], A. Blazhev[1,5], J. Döring[1], H. Grawe[1], L. Grigorenko[6,3], C. Hoffman[7], M. Huyse[2], Z. Janas[8], R. Kirchner[1], M. La Commara[9], C. Mazzocchi[1], C. Plettner[1,10], S. L. Tabor[7], P. Van Duppen[2], and M. Wiedeking[7]

[1]GSI, Darmstadt, Germany; [2] KU Leuven, Belgium; [3]RRC "Kurchatov Institute", Moscow, Russia; [4]St. Petersburg Nuclear Physics Institute, Gatchina, Russia; [5]University of Sofia, Bulgaria; [6]JINR, Dubna, Russia; [7]Florida State University, Tallahassee, USA; [8]Warsaw University, Warsaw, Poland; [9]University "Federico II" and INFN, Napoli, Italy; [10]Yale University, New Haven, USA

The (21^+) isomer in the N=Z nucleus ^{94}Ag is a high-spin nuclear trap with the largest spin ever observed for β-decaying nuclei. It has a remarkably long half-life of 0.4 s, its high excitation energy of 6.7(5) MeV making three direct-particle decay modes possible [1], i.e., proton, α and two-proton emission. Here we present evidence of direct two-proton (2p) decay of this isomer to the excited (11^+) state in ^{92}Rh. This result was obtained by analyzing the same experimental data that already yielded evidence for direct proton radioactivity of ^{94m}Ag (21^+) [2, 3]. The measurements were performed at the ISOL facility in GSI. A mass-separated ^{94}Ag beam was produced by ^{58}Ni(^{40}Ca,p3n) fusion-evaporation reactions with an intensity of 2 s^{-1}. Arrays of silicon (Si) charged-particle and germanium (Ge) γ-ray detectors measured energies of charged particles and γ rays following the decay of ^{94m}Ag [3, 4].

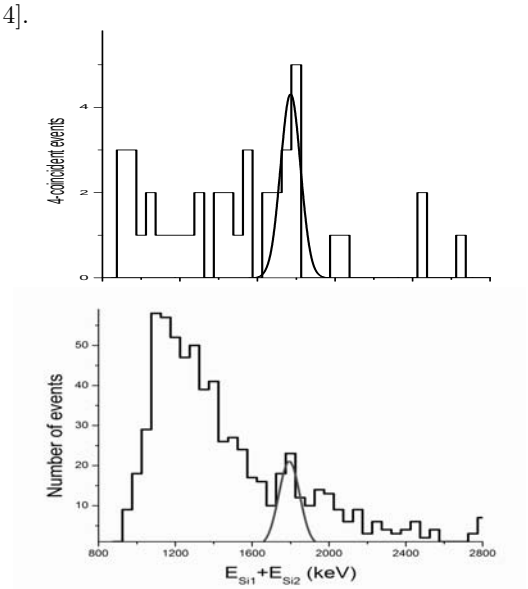

Figure 1: Sum-energy spectra of two Si detectors obtained with Si_1-Si_2-γ-γ coincidence condition and with one or two γ gates on ^{92}Rh* transitions (upper and lower histograms, respectively). The 1.8 MeV peaks indicate the two-proton decay ^{94}Ag(21^+)$\rightarrow$^{92}Rh(11^+)+p+p.

Direct two-proton decay of the (21^+) isomer was searched for by measuring coincidences between double-hit events recorded by the Si detectors and γ-γ events registered by the Ge detectors [2]. The γ gates were based on the known ^{92}Rh level scheme [5] and are shown in Fig. 2. The sum-energy (E_{Si1}+E_{Si2}) spectra derived from such coincidences are shown in Fig. 1. Both spectra indicate a two-proton decay with the E_{Si1}+E_{Si2} energy amounting to 1.77(5) MeV and the branching ratio of 0.5(3) % [2]. For a cross-check, E_{Si1}+E_{Si2} spectra were generated by shifting the γ ray gates away from the energies of the ^{92}Rh γ transitions. They reveal no peak in the 1.8 MeV region. The γ-ray spectrum projected from the Si_1+Si_2+γ+γ events and gated by the 1.8 MeV peak shows evidence for all known γ rays following de-excitation of the (11^+) state in ^{92}Rh while no indication of a population of the higher-energy states in ^{92}Rh is obtained. Cross-check γ-ray spectra made with E_{Si1}+E_{Si2} conditions shifted below and above of the 1.8 MeV region show no sign of ^{92}Rh γ rays. On this basis, a 2p-decay scheme has been tentatively established as shown in Fig. 2. A 2p-orbital momentum ΔL=10 was tentatively assigned, and the proton separation energy in ^{93}Pd was determined to be 2.42(5) MeV, which is to be compared with the predicted value 3.63(57) MeV [1].

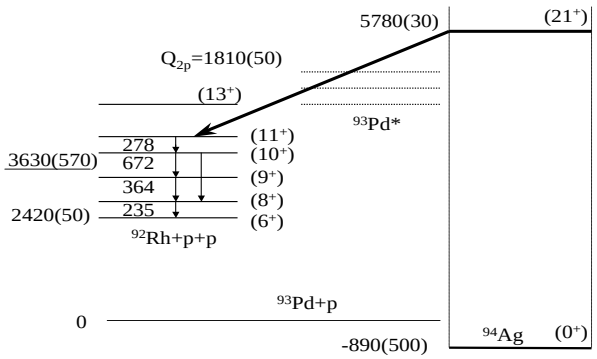

Figure 2: Direct two-proton decay of the ^{94}Ag (21^+) isomer to excited state in ^{92}Rh. Energies of levels and γ transitions are given in keV.

Two mechanisms of 2p-decay are possible, a sequential emission via intermediate states in ^{93}Pd and a genuine three-particle decay. The E_{Si1}-E_{Si2} correlations obtained for the 1.8 MeV 2p-decay, show no sign of population of states in ^{93}Pd, as well as no indication of a correlated ^{2}He emission. The three-particle decay mechanism can describe the E_{Si1}-E_{Si2} spectrum, but predicts the 2p-decay branching ratio smaller than the observed one by a factor 10^8. Nuclear deformation can increase the probability of 2p-decay. Calculations of 2p-decay intensity of a prolate deformed nucleus agree with the data, only assuming a strong deformation of $\beta \sim$0.5 for the (21^+) isomer.

References

[1] G. Audi et al., Nucl. Phys. A **729**, 337 (2003).
[2] I. Mukha et al., EPJ A Direct, in print.
[3] I. Mukha et al., GSI Scientific Report 2004.
[4] I. Mukha et al., Phys. Rev. C **70**, 044311 (2004).
[5] D. Kast et al., Z. Phys. **356**, 363 (1997).

Hindered E4 decay of the ^{52}Fe 12^+ yrast trap

A. Gadea [1], S. M. Lenzi [2], D. R. Napoli [1], C. A. Ur [2,3], G. Martínez-Pinedo [4], M. Górska [5], E. Roeckl [5], E. Caurier [6], F. Nowacki [6], G. de Angelis [1], M. Axiotis [1], L. Batist [7], R. Borcea [5], F. Brandolini [2], D. Cano-Ott [8], J. Döring [5], C. Fahlander [9], E. Farnea [2], H. Grawe [5], M. Hellström [5], Z. Janas [5,10], R. Kirchner [5], M. La Commara [5], C. Mazzocchi [5,11], E. Nácher [8], C. Plettner [5], A. Płochocki [10], B. Rubio [8], K. Schmidt [5], R. Schwengner [12], J. L. Tain [8] and J. Żylicz [10]

[1]Laboratori Nazionali di Legnaro, Italy; [2]Dipartimento di Fisica and INFN, Padova, Italy; [3]H. Hulubei NIPNE, Bucharest, Romania; [4]University of Aarhus, Denmark; [5]GSI, Darmstadt, Germany; [6]IReS, Strasbourg, France; [7]PNPI, Gatchina, Russia; [8]IFIC, Valencia, Spain; [9]Lund University,Sweden; [10]University of Warsaw, Poland; [11]Universitá degli Studi di Milano, Italy; [12] FZ Rossendorf, Germany

High multipole moments of nuclei can yield information on nuclear structure, in particular that connected with shape phenomena. Based on this motivation, we searched for the hitherto unobserved internal de-excitation of the 12^+ spin-gap isomer in ^{52}Fe to the low-lying 8^+ states, which allows one to determine the corresponding B(E4) values. In-beam studies [1] have identified the high-spin structure of ^{52}Fe up to the 10^+ state at 7.4 MeV, lying above the yrast 12^+ level, thereby confirming the predicted inversion of the yrast 10^+ and 12^+ states. However, the excitation of the latter state, known from β-decay work [2] to be isomeric, was only determined with an uncertainty of the order of hundred keV.

The ^{52m}Fe activity, produced by bombarding a ^{nat}Si target by a ^{36}Ar beam, was ionized in the FEBIAD-E2 ion source of the GSI on-line mass separator. The mass-52 beam was implanted in a tape which moved every 80 s, taking away the long-lived isobaric contaminants. The implantation position was surrounded by a plastic scintillator for β-ray and a germanium array for γ-ray detection. The analysis of the γ - γ coincidences, including a veto condition derived from the scintillator, allowed us for the first time to observe the internal de-excitation of the 12^+ isomer to the 8^+_1 and 8^+_2 states at 6360 and 6493 keV via E4 transitions of 597 and 465 keV, respectively [4]. This yields an excitation energy of 6958(1) keV for the isomeric 12^+ level. The intensities of these transitions per isomer decay amount to $1.2(4)\times10^{-4}$ and $0.9(3)\times10^{-4}$, corresponding to B(E4) values of 1.1(4) and 8(4) e^2fm^8 or $5(2)\times10^{-4}$ and $3(2)\times10^{-3}$ W.u., respectively.

The newly determined B(E4) values are considerably smaller than those of other fp-shell nuclei, which range from 0.14 W.u. for the $2^+ \rightarrow 6^+$ transitions in ^{52}Mn to 1.4 W.u. for the $6^+ \rightarrow 2^+$ transitions in ^{44}Sc. The experimental B(E4) values of fp-shell nuclei are confronted in Fig. 1 to shell-model predictions obtained with the code ANTOINE [5] in the full pf model space. Three different residual interactions have been used, namely the FPD6 [6] and the KB3G [7] interactions, which are known to very well reproduce the spectroscopy of $f_{7/2}$ shell nuclei, and the recently introduced GXPF1 [8] interaction. The effective charges used to calculate the B(E4) reduced transition probabilities are the same as those used in [1]. As can be seen from Fig. 1, all three interactions reproduce the experimental B(E4) data for ^{44}Sc, ^{46}Ti, ^{52}Mn, ^{53}Fe and ^{54}Fe with good accuracy. However, it is evident that both the KB3G and GXPF1 interactions fail in the case of ^{52}Fe. This discrepancy is interpreted on the basis of the predicted occupation numbers for protons and neutrons in the shell-model orbits involved in the E4 decay. While all interactions yield quite similar occupation numbers for the 12^+ state, they are very different for the 8^+_1 and 8^+_2 levels. The 8^+_1 state calculated with FPD6 is apparently more collective than that predicted by KB3G. Further insight into the origin of the E4 hindrance in ^{52}Fe is obtained by taking not only the overlaps between the 8^+ states and the 12^+ one into account, but also the distribution of the hexadecapole strength originating from the 12^+ isomer to all 8^+ states in the fp shell-model space. The latter calculation indicates that most of the E4 strength is located at excitation energies higher than that of the 12^+ isomeric state. All in all, it is clear that measurements of hexadecapole transition probabilities constitute a sensitive tool for discriminating the correct structure of the wavefunctions involved.

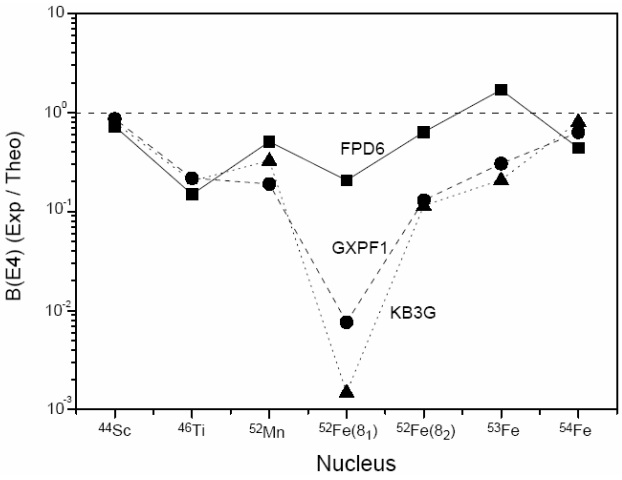

Fig. 2. Ratio between the experimental and theoretical B(E4) values for nuclei in the $f_{7/2}$ shell. Data corresponding to the FPD6 interaction are shown by squares (full line), while GXPF1 and KB3G predictions are given by full circles (dashed-line) and triangles (dotted-line) respectively.

[1] C. A. Ur et al., Phys. Rev. C **58**, 3163 (1998)
[2] D. F. Geesaman et al., Phys. Rev. C **19**, 1938 (1979)
[4] A. Gadea et al., Proc. Int. Workshop on Selected Topics on N=Z Nuclei, Lund, June 2000, Report LUIP 003 (2000), p. 118
[5] E.Caurier, Code ANTOINE, Strasbourg, 1989; E. Caurier and F. Nowacki, Acta Phys. Pol. **30**, 705 (1999)
[6] W. A. Richter et al., Nucl. Phys. A **523**, 325 (1991)
[7] A. Poves, E. Caurier and F. Nowacki, xxx
[8] M. Honma et al., Phys. Rev. C **65**, 061301(R) (2002)

Breakup of relativistic halo nuclei (i)

P. Adrich[a,h], T. Aumann[a,e], O. Bochkarev[b], M.J.G. Borge[f], L.V. Chulkov[a,b], D. Cortina[a], Th.W. Elze[g], J. Fernandez-Vazquez[a], U. Datta-Pramanik[a], H. Emling[a], H. Fynbo[j], H. Geissel[a], L.V. Grigorenko[a,b], M. Hellström[a], H. Johansson[a,d], A. Klimkiewicz[a,h], K. Jones[a], B. Jonson[d], J.V. Kratz[e], R. Kulessa[h], Le Hong Khiem[a], E. Lubkiewicz[h], K. Markenroth[d], M. Meister[a,d], G. Münzenberg[a], F. Nickel[a], T. Nilsson[i,k], G. Nyman[d], M. Pantea[a,k], R. Palit[a], V. Pribora[b], W. Prokopowic[h], A. Richter[k], K. Riisager[j], C. Scheidenberger[a], G. Schrieder[k], H. Simon[a], K. Sümmerer[a], O. Tengblad[f], I.J. Thomson[c], W. Walus[h], and M.V. Zhukov[d]

[a]GSI Darmstadt; [b]Kurchatov Institute, Moscow; [c]University of Surrey, Guilford; [d]Chalmers Tekniska Högskola, Göteborg; [e]Johannes-Gutenberg-Universität, Mainz; [f]CSIC, Madrid; [g]Johann-Wolfgang-Goethe-Universität, Frankfurt; [h]Universytet Jagiellonski, Krakow; [i]CERN, Geneva; [j]Aarhus Universitet, Aarhus; [k]Technische Universität, Darmstadt

In the studies of the breakup of relativistic halo nuclei, the complete kinematics data as well as the energy and angular correlations have given new insight concerning the ground-state structure of the Borromean nuclei.

For the analysis of experimental data, we propose an effective method based on a series expansion of the transition amplitude into hyperspherical functions. The expansion coefficients are determined from the fit to the experimental distributions. The method makes possible the determination of the relative contribution of different partial waves. The comparison with the theoretical partial amplitudes allows either to choose between different models or to specify changes in the model that would be needed to describe the experimental data.

This was demonstrated with the example of ^{6}He. The dissociation of ^{6}He on a lead target, where the main contribution is expected from the electromagnetic dissociation, has been studied at 240 MeV/u.

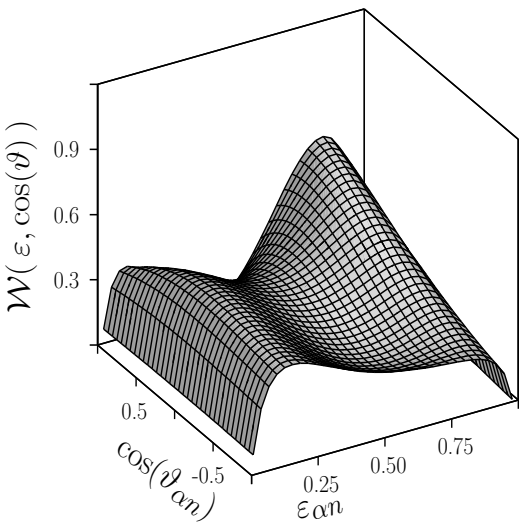

Figure 1: Two-dimensional correlation spectrum reconstructed from the fit to the experimental distributions in the continuum energy region 3-6 MeV.

The experimental continuum energy spectrum and the angular distributions for breakup of the 240 MeV/u ^{6}He nucleus on a lead target are well described under the assumption of pure electromagnetic dipole dissociation without involving any other reaction mechanisms, while using different theoretical approaches(see Refs. [1, 2]). The inclusion in the analysis of the three-body correlation distributions results in more strict and quantitative conclusions.

The three-body correlation distributions have, for the first time, been used in the analysis. The distributions have been directly compared with the results of calculations using the hyperspherical harmonics method while assuming a dipole mode for the electromagnetic dissociation [1]. The experimental data have also been analyzed by using a series expansion of the final transition amplitude into hyperspherical functions.

Besides the orientation of the whole system, the three-body configuration is determined by the angle $\vartheta_{\alpha n}$ between Jacobi momenta $\mathbf{q}_{\alpha n}$ and $\mathbf{q}_{n-\alpha n}$, by the total energy of the three-body system E, and by the energy shared in a selected pair of particles, e.g. fractional energy in the subsystem α-n, $\varepsilon_{\alpha n} = q^2_{\alpha n}/E$. The dependence of $\vartheta_{\alpha n}$ on $\varepsilon_{\alpha n}$ reconstructed from experimental data in the region $3 < E < 6$ is shown in Fig. 1. Two distinct ridges of the distribution in Fig. 1 correspond to the αn interaction forming the ^{5}He($3/2^-$) resonance. The role of this resonance is more important than expected from the hyperspherical harmonics method [1], but is in line with the results of the calculations made in the framework of the complex scaling method [2]. The analysis has shown that the transition of one neutron from the p-shell to the s-shell dominates. This statement is consistent with the calculations [1, 2] at low energies, but in the energy region 3-6 MeV, theoretical considerations predict a larger contribution from the p- to d-shell transition. The analysis points out the existence of a ^{6}He resonant state with a $p_{3/2}s_{1/2}$ structure at continuum energy 3 - 6 MeV.

Thus, the new experimental observables pose new questions to the theoretical models for the dissociation of the Borromean nucleus ^{6}He at high energy, and give interesting insight in the development of the theory.

References

[1] B.V. Danilin *et al.*, Nucl. Phys. **A 632** (1998) 383

[2] T. Myo *et al.*, Phys. Rev.**C63** (2001) 054313

Investigation of nuclear matter distribution of the neutron-rich He isotopes by proton elastic scattering at intermediate energies

F. Aksouh[1], A. Bleile[1], O.V. Bochkarev[2], L.V. Chulkov[2], D. Cortina-Gil[1,a], A.V. Dobrovolsky[1,3], P. Egelhof[1], H. Geissel[1], M. Hellström[1], N.B. Isaev[3], O.A. Kiselev[1,3,b], B.G. Komkov[3], M. Mátos[1], F.V. Moroz[3], G. Münzenberg[1], M. Mutterer[4], V.A. Mylnikov[3], S.R. Neumaier[1], V.N. Pribora[1,2], D.M. Seliverstov[3], L.O. Sergueev[3], A. Shrivastava[1,c], K. Sümmerer[1], H. Weick[1], M. Winkler[1], and V.I. Yatsoura[3]

[1]GSI Darmstadt; [2]Kurchatov Institute, Moscow; [3]PNPI, St. Petersburg; [4]IKP TU Darmstadt; [a]Present address: Depto. de Fisica de Particulas, Universidade de Santiago de Compostela, Spain; [b]Present address: Institut für Kernchemie, Johannes Gutenberg Universität Mainz, Germany; [c]Present address: Bhabha Atomic Research Centre, Mumbai, India

The method of elastic proton scattering at beam energies close to 700 MeV/u in inverse kinematics has been proven to be very effective for deriving from the measured differential cross sections the nuclear matter distributions in the halo nuclei, such as ^{6}He, ^{8}He [1],[2] and ^{11}Li [3], with the aid of the Glauber multiple scattering theory. Previous measurements performed in the small momentum transfer region have yielded valuable information on the nuclear sizes and radial structure of the overall nuclear matter density distributions. Recently, a novel experimental approach has been accomplished with the aim to deduce the differential $p^{6,8}$He cross sections at a higher momentum transfer close to the first diffraction minimum. The major difference with respect to the previous experiments was that instead of the active gaseous target a liquid hydrogen target was used, combined with a proton recoil detector [4].

The differential cross sections obtained in both experiments have been evaluated using several phenomenological parameterizations for the nuclear matter distribution. The formalism used for this part of the analysis is described in [2]. In addition, a model-independent analysis with the help of a Sum-Of-Gaussians (SOG) method has been performed, which is a standard method for the investigation of nuclear charge distributions from electron scattering data [5]. Figure 1 shows the radial shape of the total nuclear matter distribution in ^{6}He and ^{8}He derived from the SOG analysis. The deduced values of the nuclear matter radii R_m of ^{6}He 2.37(5) fm and ^{8}He 2.49(4) fm are consistent with the results of the phenomenological analysis and confirm the existence of an extended neutron halo in these nuclei. The nuclear charge radius of ^{6}He has been recently measured for the first time using the method of isotope shift based on laser spectroscopy technique [6]. It was found to be 2.054(14) fm, and the corresponding value for the point-proton radius is 1.912(18) fm. The deduced value is in good agreement with the present value of R_{core} = 1.97(9) fm (obtained from the phenomenological analysis when assuming an α-particle core + 2n halo structure for ^{6}He) which assures the consistency of both measurements. The analysis of the experimental cross sections confirms the structure of ^{6}He as a three-body system. The core size of ^{8}He has been found to be R_{core} = 1.86(8) fm. In addition, within the phenomenological approach, the nuclear matter density has been parameterized alternatively as an α-particle core and four valence neutrons and a ^{6}He core and two valence neutrons. Both parameterizations permit the same quality of description of the experimental cross sections. A possible explanation is that a ground state of ^{8}He may be a mixture of these two configurations. This fact is supported by the analysis of inelastic scattering of ^{8}He on protons, measured also in the present experiment [7].

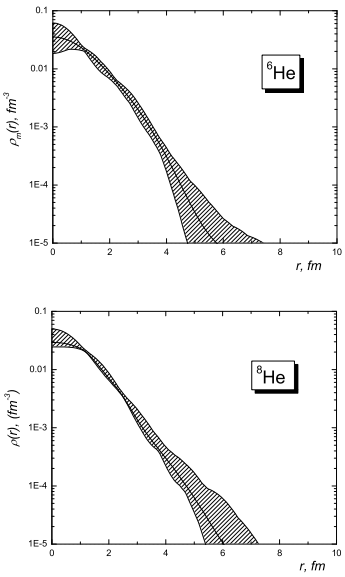

Figure 1: Nuclear matter density distributions deduced from the experimental cross sections for ^{6}He and ^{8}He using a Sum-of-Gaussian analysis. The shaded areas represent the resulting error band.

References

[1] S.R. Neumaier et al., Nucl. Phys. A, **712**, (2002) 247.
[2] G.D. Alkhazov et al., Nucl. Phys. A, **712**, (2002) 269.
[3] P. Egelhof et al., Eur. Phys. J. **A15**, (2002) 27.
[4] O.A. Kisselev et al., procedings of ENAM2001, Springer Verlag, (2003) 186; F. Aksouh, PhD thesis, Université de Paris XI, Orsay, France, 2002.
[5] I. Sick, Nucl. Phys. A, **218**, (1974) 509.
[6] L.-B. Wang et al., Phys. Rev. Lett. Vol. **93**, (2004) 142501.
[7] L.V. Chulkov et al., to be published in Nucl. Phys. A.

Breakup of relativistic halo nuclei (ii)

P. Adrich[a,h], T. Aumann[a,e], O. Bochkarev[b], M.J.G. Borge[f], L.V. Chulkov[a,b], D. Cortina[a], Th.W. Elze[g], J. Fernandez-Vazquez[a], U. Datta-Pramanik[a], H. Emling[a], H. Fynbo[j], H. Geissel[a], L.V. Grigorenko[a,b], M. Hellström[a], H. Johansson[a,d], A. Klimkiewicz[a,h], K. Jones[a], B. Jonson[d], J.V. Kratz[e], R. Kulessa[h], Le Hong Khiem[a], E. Lubkiewicz[h], K. Markenroth[d], M. Meister[a,d], G. Münzenberg[a], F. Nickel[a], T. Nilsson[i,k], G. Nyman[d], M. Pantea[a,k], R. Palit[a], V. Pribora[b], W. Prokopowic[h], A. Richter[k], K. Riisager[j], C. Scheidenberger[a], G. Schrieder[k], H. Simon[a], K. Sümmerer[a], O. Tengblad[f], I.J. Thomson[c], W. Walus[h], and M.V. Zhukov[d]

[a]GSI Darmstadt; [b]Kurchatov Institute, Moscow; [c]University of Surrey, Guilford; [d]Chalmers Tekniska Högskola, Göteborg; [e]Johannes-Gutenberg-Universität, Mainz; [f]CSIC, Madrid; [g]Johann-Wolfgang-Goethe-Universität, Frankfurt; [h]Universytet Jagiellonski, Krakow; [i]CERN, Geneva; [j]Aarhus Universitet, Aarhus; [k]Technische Universität, Darmstadt

The quasi-free scattering (QFS) is the dominant reaction mechanism in the nuclear beakup at several hundred MeV/nucleon and provide quite precise information concerning clustering effects in nuclei. In QFS, a probe particle scatters off a bound cluster inside a nucleus. The process leads to a separation of the cluster from the nucleus, the rest of the nucleus acts as a spectator. The transition amplitude may be separated into a reaction term and a nuclear structure term, this property is a prerequisite for nuclear-structure investigations. In the past, QFS studies have provided a wealth of nuclear structure information for stable nuclei. The application of this method to experiments with radioactive beams is very promising. The QFS method has been used in investigations of the cluster structure of drip-line nuclei Refs. [1, 2]. However, these experiments were restricted mainly to the valence-neutron knockout by a complex particle (^{9}Be or ^{12}C). Here we describe a complete-kinematics experiment with

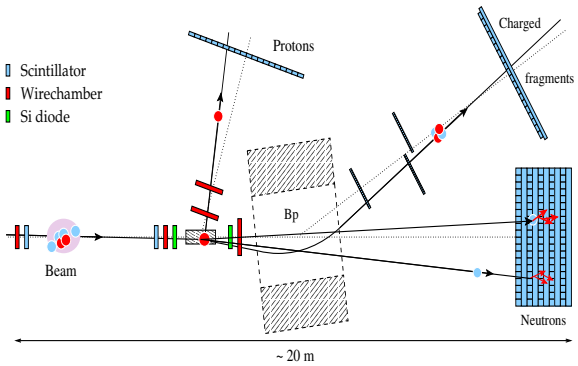

Figure 1: Experimental setup.

a proton as a probe particle and present preliminary results. The experiment was performed at GSI, Darmstadt, where radioactive beams were produced by fragmentation of ^{18}O (308 MeV/nucleon and 362 MeV/nucleon) beams from the heavy-ion synchrotron, SIS, on a beryllium production target. The secondary ^{8}He, ^{11}Li and ^{14}Be beams with energies of 230 MeV/nucleon, 265 MeV/nucleon and 290 MeV/nucleon, respectively, were selected by magnetic analysis in the fragment separator, FRS, and directed towards the liquid-hydrogen target which was placed in front of the large-gap magnetic dipole spectrometer, ALADIN. The experimental setup is shown in Fig. 1. A detection of the recoil proton allows the separation of different QFS channels [3], while a registration of neutrons in coincidence with fragments makes possible the usage of an invariant-mass method.

Table 1: Preliminary cross sections (mb) for different reaction channels.

Channel	^{8}He	^{11}Li	^{14}Be
$-2n$	20.6 ^{6}He	42.4 ^{9}Li	56.4 ^{12}Be
$-3n$	-	28.5 ^{8}Li	24.1 ^{11}Be
$-4n$	6.5 ^{4}He	15.6 ^{7}Li	-
$-p2n$	-	4.9 ^{8}He	5.9 ^{11}Li
$-p3n$	-	-	-
$-p4n$	0.5 ^{3}H	10.4 ^{6}He	8.7 ^{9}Li
$-p5n$	-	-	7.8 ^{8}Li
$-p6n$	-	9.2 ^{4}He	7.1 ^{7}Li

Estimated cross sections for the breakup of ^{8}He, ^{11}Li and ^{14}Be resulting in different fragments in the final state are shown in Table 1. The neutron knockout has largest cross section. Note, that for Borromean nuclei this channel leads to neutron unstable states. Large cross section is observed for channels which might be associated with the proton knockout. Proton knockout channels will lead to the nuclear-unstable resonances ^{7}H, ^{10}He and ^{12,13}Li. The α-particle knockout from ^{8}He is of special interest in connection with recently renewed discussions of a bound tetra-neutron nucleus [4]. Besides, the spectroscopic factors for neutrons, protons α clusters, and momentum distributions of knocked-out particles and of the spectators are among the main goals of the present experiment.

References

[1] B. Jonson, Phys. Rep. **389** (2004) 1.

[2] B.A. Brown, P.G. Hansen, B.M. Sherrill, J.A. Tostevin, Phys. Rev. **C 65** (2001) 061601(R).

[3] L.V. Chulkov *et al.*, submitted to Nucl. Phys. A.

[4] F.M. Marqués *et al.*, Phys. Rev. **C 65** (2002) 044006.

Investigation of proton elastic scattering on ^{70}Zn in inverse kinematics using a stored ESR beam interacting with an internal CH_4 target

A. Bleile[1], F. Bosch[1], K. Beckert[1], P. Beller[1], C. Brandau[1], P. Egelhof[1], S. Ilieva[1], O.A. Kiselev[2,3], C. Kozhuharov[1], J.P. Meier[1], F. Nolden[1], U. Popp[1], M. Steck[1], and T. Stöhlker[1]

[1]GSI Darmstadt; [2]Institut für Kernchemie, Johannes Gutenberg Universität Mainz; [3]PNPI, St. Petersburg

The investigation of light-ion induced direct reactions in inverse kinematics, using stored and cooled radioactive beams, interacting with internal H, He, etc. gas-jet targets, bears a large potential for nuclear structure and astrophysics studies on exotic nuclei. In particular, this technique enables, as compared to investigations at external targets, high resolution measurements down to very low momentum transfer. It also provides in many cases a gain in luminosity from accumulation and recirculation of the radioactive beams [1]. Consequently an extended research project was recently proposed to the FAIR-PAC by the EXL collaboration (EXotic nuclei studied in Light-ion induced reactions at the NESR storage ring) [2]. In order to explore the experimental conditions for measurements planned at FAIR, performance tests with a prototype detector setup, installed at the internal target of the ESR have been recently performed with stored stable beams.

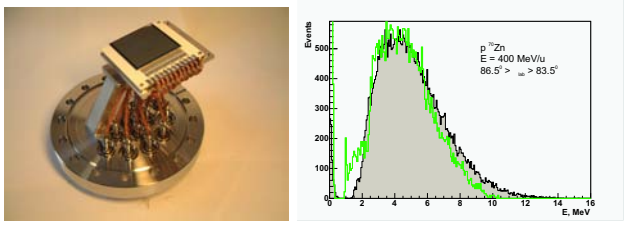

Figure 1: Left side - UHV compartible Si-strip detector for recoil protons; right side - comparison of the experimental energy spectrum obtained from detector-group 2 (green histogram) and the result of a Monte Carlo simulation (filled gray histogram).

The experimental setup consisted of a 40 x 40 mm^2 Si-strip detector (Fig. 1, left), mounted on the 90^0 flansch of the existing ESR vacuum chamber surrounding the internal target, which was supposed to measure the target-like recoil particles from the interaction of the circulating beam with the internal target in a single mode, or, alternatively, in coincidence with the scattered beam particles, detected in a standard scintillation detector located downstream from the target after the first dipole magnet. The Si detector, provided by MICRON, was specially designed to meet the strict UHV conditions required at the ESR. The 1 mm thick Si wafer is mounted on a ceramic support structure, and the connectors including the readout scheme (collective readout by charge division of 5 groups of 8 channels each) have been made without soldering, thus allowing baking of the detector up to 200^0 C. The excellent detector performance (energy resolution of ΔE = 40 keV for 5 MeV α-particles, and position resolution of Δx = 1 mm) was maintained after several baking cycles. UHV capable cables with glass pearls for providing isolation from the shielding were used, and a 1 μm thick Ni foil was mounted in front of the detector to suppress δ-electrons. The detector was mounted at a distance of 16 cm from the gas-jet target, thus covering an angular range $89^0 \geq \theta_{lab} \geq 74^0$.

In a first test experiment data were taken with a 400 MeV/u ^{70}Zn beam, interacting with a CH_4 gas-jet target. The average luminosity was estimated to be of the order of 10^{27}cm^{-2}s^{-1}. An energy spectrum obtained in coincidence with the scattered projectiles from the detector-group 2 ($86.5^0 \geq \theta_{lab} \geq 83.5^0$), is displayed in Fig. 1, right. The good agreement with the result of a Monte Carlo Simulation for ^{70}Zn proton scattering demonstrates that the measured spectra are well understood, and that background reactions are well discriminated by the coincidence requirement.

The differential cross section dσ/dt, extracted from the present data is displayed in Fig. 2. The solid line represents a Glauber calculation assuming a Gaussian-like matter distribution for ^{70}Zn. The results are interpreted as follows: for the data taken without coincidence condition (red dots), a good agreement with the predicted cross section is obtained for $t \leq 0.025$ (GeV/c)^2, whereas for higher momentum transfer the measured cross section is enhanced, most probably due to a considerable background contribution from ^{70}Zn + ^{12}C reactions. For the data taken in coincidence with the scattered projectiles (blue dots), the data for $t \geq 0.025$ (GeV/c)^2 are in excellent agreement with the predicted t-dependence of the cross section, thus demonstrating that the coincidence condition provides an efficient discrimination against background. For the low momentum transfer region the measured cross section in the coincidence mode is drastically reduced, most probably due to the lack in coincidence capability of the scintillation detector for very small momentum transfer.

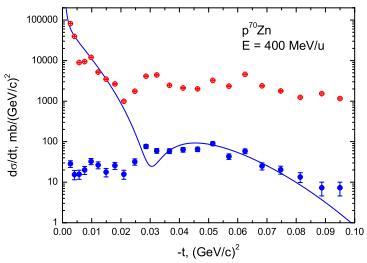

Figure 2: p^{70}Zn elastic scattering differential cross section versus the four momentum transfer squared -t (for discussions see test).

References

[1] P. Egelhof et al., Physica Scripta, **T104**, (2003) 151.
[2] The EXL collaboration, GSI Annual Report 2004.

Even-odd structural phenomena in the cooling down of excited nuclear systems

M. V. Ricciardi [1], P. Napolitani [1,2], C. Villagrasa[3] for the CHARMS collaboration

[1]GSI, Damrstadt, Germany; [2]GANIL, Caen, France, [3]DAPNIA/SPhN CEA/Saclay, France

Recently, a complex even-odd structure was observed in the production cross sections from the projectile fragmentation of 1 *A* GeV ^{238}U nuclei in a titanium target, measured at the FRS at GSI [1]. Although in the past the even-odd effect was already observed in the charge distributions of several nuclear reactions at high energies, it was with the reaction 1*A* GeV ^{238}U on Ti that for the first time the staggering phenomena could be systematically investigated with full nuclide identification over an extended area of the chart of the nuclides. In subsequent experiments, the formation cross sections of all the produced nuclides of four other systems, ^{56}Fe and ^{136}Xe on proton and on titanium at several energies were determined [2,3]. Part of the results is presented in Figure 1. The data are filtered according to the *N*-*Z* value. As it was found for the system ^{238}U+Ti, the data reveal a complex structure. All even-mass nuclei present a visible even-odd effect, which seems particularly strong for *N*=*Z* nuclei. Odd-mass nuclei show a "reversed" even-odd effect, with enhanced production of odd-*Z* nuclei. This enhancement is stronger for nuclei with larger values of *N*-*Z*. However, for nuclei with *N*-*Z*=1 the reversed even-odd effect vanished out at about *Z*=16, and again an enhanced production of even-*Z* nuclei can be observed.

All the above mentioned reactions can be quite violent and are expected to introduce a large range of excitation energies in the nucleus. Although the initial steps of the interaction can be rather different form one reaction to the other, all the reactions have in common that the excited nucleus will later cool down through the evaporation of particle. Therefore, we tested the hypothesis that the even-odd staggering is produced at the end of the evaporation cascade due to the influence of nuclear structure on the properties of excited levels and on the masses. Applying a statistical evaporation model, where pairing was introduced both in the masses and in the level densities in a consistent way, the yields were determined. In Figure 2, the calculation for the system ^{238}U+Ti is presented. All the features of the complex staggering behaviour are reproduced, with the remarkable exception of the *N*=*Z* chain, whose peculiarity could be connected to phenomena that go beyond pairing (as e.g. alpha clustering). The vanishing of the effect with increases mass of the fragment was also reproduced considering the competition between the particle-decay and gamma-emission channels.

In the past, the even-odd effect in the production yields in specific nuclear reactions at low energies, e.g. low-energy fission, was explained by means of the theory of nuclear superfluidity. However, the nucleus is expected to exit the superfluid phase and enter into the normal liquid phase at about 10 MeV of excitation energy. Above 10 MeV, any structural effect should be lost. So, we cannot assume that structural effects are preserved in the spectator nuclei. But the results of the statistical model show that the structural properties can be restored. We interpreted our results as the manifestation of the liquid-superfluid phase transition. The structure appears as a result of the condensation process of the heated nuclear matter while cooling down in the evaporation process. Our results could have consequences on the evaluation of the nuclear temperature using isotopes ratios.

This work was supported by the European Commission in the frames of the EURISOL and the HINDAS projects.

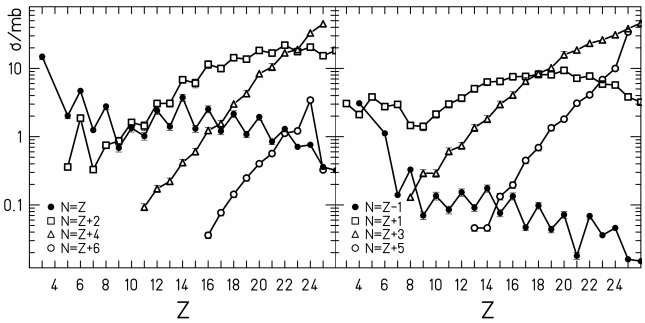

Figure 1: Experimental production cross sections for the residues of 1 *A* GeV ^{56}Fe on ^{1}H (data are from ref. [2]).

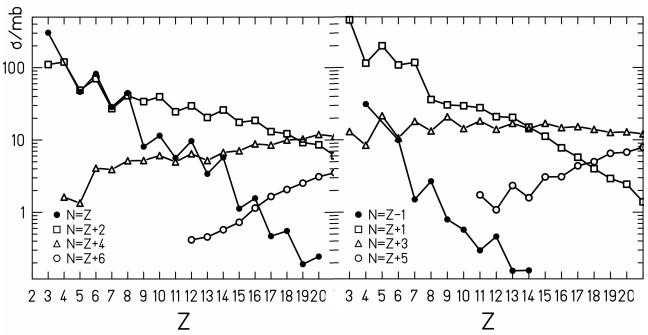

Figure 2: Experimental production cross sections for the residues of 1 *A* GeV ^{136}Xe on Ti (data are from ref. [3]).

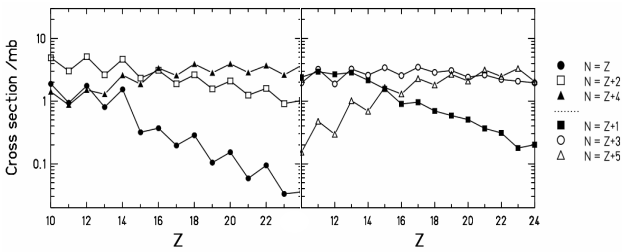

Figure 3: Production cross sections for the reaction 1 *A* GeV ^{238}U on Ti calculated with a statistical model. Details on the calculation are presented in ref. [1].

References

[1] M. V. Ricciardi et al., Nucl. Phys. A 733 (2004) 299-318

[2] C.Villagrasa-Canton, PhD Thesis, Université de Paris XI, France (December 2003)

[3] P. Napolitani, PhD Thesis, Université de Paris XI, France (September 2004)

Pygmy and Giant Dipole Resonances in $^{130-132}$Sn

P. Adrich[a,d], T. Aumann[a], K. Boretzky[b], D. Cortina-Gil[f], U. Datta Pramanik[a], Th.W. Elze[c], H. Emling[a], M. Fallot[a], H. Geissel[a], M. Hellström[a], K.L. Jones[a], A. Klimkiewicz[a,d], J.V. Kratz[b], R. Kulessa[d], Y. Leifels[a], C. Nociforo[b], R. Palit[c], H. Simon[a,e], G. Surowka[d], K. Sümmerer[a], and W. Walus[d]

[a]GSI Darmstadt; [b]Univ. Mainz; [c]Univ. Frankfurt; [d]Univ. Kraków, Poland; [e]TU Darmstadt; [f]Univ. Santiago de Compostela, Spain

We report on first results from dipole-strength measurements in the region of unstable nuclei around ^{132}Sn; experimental details were presented earlier [1]. In brief, such studies are motivated by theoretical predictions of multipole distributions in exotic nuclei differing much from that observed in stable nuclei; aditional strength near the neutron separation threshold, moreover, may have consequences for astrophysical models of the r-process nucleosynthesis [2]. One of the most exciting prediction concerns a new mode of collective excitation in medium and heavy neutron-rich nuclei at energies below the giant dipole resonance (GDR). This so-called Pygmy or Soft Dipole mode (PDR), being interpreted as an oscillation of the neutron skin against the core of the nucleus, is at present very lively discussed, e.g., see [3, 4, 5].

Measurements of the dipole strength in ^{132}Sn and a number of neighboring isotopes of similar A/Z ratio have been performed at the LAND-FRS facility. The secondary, radioactive beam was produced via in-flight fission of a primary ^{238}U beam at 550 MeV/u. Isotopes of interest were selected with the FRS and identified on an event-by-event basis. From the electromagnetic excitation of the projectiles in a 0.5 g/cm^2 Pb target, energy differential cross sections were obtained by means of the invariant-mass analysis. To allow for the reconstruction of the invariant mass momenta of all the decay products (neutrons, γ-rays, heavy fragment) remaining after (Coulomb) dissociation in the target were measured.

The left-hand panels in fig. 1 show the measured cross sections for ^{130}Sn and ^{132}Sn, the right-hand panels show the deduced photo-neutron cross sections. An excess cross section over that of the giant dipole resonance at energies close to 10 MeV is evident in both isotopes.
In order to extract quantitative information a function composed as the sum of a lorentzian distribution (to account for the GDR) and a gaussian distribution (to account for the enhancement at low energy) was adopted describing the measured photo-neutron cross sections. This function was then translated into energy-differential Coulomb-excitation cross section (by means of the virtual-photon method) and folded with the detector response obtained from an elaborated Monte-Carlo simulation. The parameters of both components were found by a χ^2-minimization procedure. The solid line in the figure indicates the fitted function; the lorentzian and gaussian contributions are shown separately as dash-dotted and dashed lines, respectively.

The low-energy peak is found at excitation energies of $10.1^{+1.1}_{-0.3}$ MeV in ^{130}Sn and of 9.8±0.7 MeV in ^{132}Sn. Their integrated cross sections correspond to 7(3)% and 4(3)% of the respective values of the Thomas-Reiche-Kuhn energy-weighted sum rule ($S_{TRK} = 60\frac{NZ}{A}$ mb·MeV). Such an amount of strength appears too large to be interpreted in terms of a single-particle excitation and indicates a coherent motion of part of the nucleons. The experimental findings are rather close to the results of calculations within a (Q)RPA-phonon-coupling [3] and a relativistic RPA approach [4].

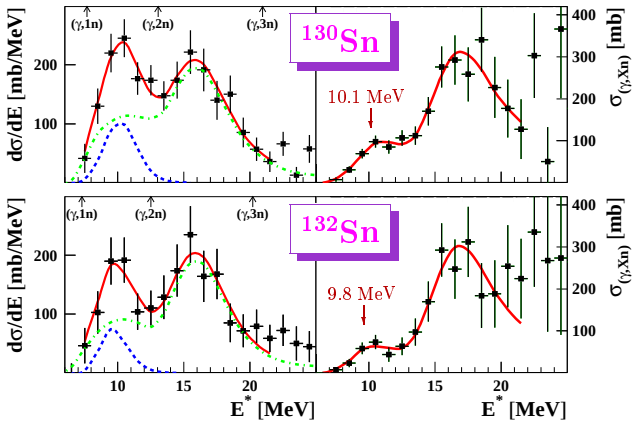

Figure 1: Experimental Coulomb-excitation cross sections and deduced photo-neutron cross sections.

The parameters deduced from the lorentzian distributions adopted for the giant dipole resonance are found not to deviate significantly from that of the systematics known from photo-absorption measurements in stable nuclei. For instance, the maxima of the GDR peaks are located at 15.9±0.5 MeV in ^{130}Sn and at $16.1^{+0.9}_{-0.6}$ MeV in ^{132}Sn.

A more complete report of the experimental results obtained so far is presently being prepared for publication. The analysis of remaining data collected for neutron-rich isotopes of In, Sb, and Te is in progress and will be reported later.

References

[1] LAND-FRS Collaboration, GSI Scientific Report 2003, ISSN 0174-0814, p. 26
[2] S. Goriely, Phys. Lett. **B436** (1998) 10-18
[3] D. Sarchi, P. F. Bortignon and G. Colò, Phys. Lett. **B601** (2004) 27-33
[4] N. Paar, et al., Phys. Rev. **C67** (2003) 34312
[5] N. Tsoneva, H. Lenske and Ch. Stoyanov, Phys. Lett. **B586** (2004) 213-218

Velocity distributions of Bi produced in charge-pickup reactions of ^{208}Pb

A. Kelić [1], K.-H. Schmidt [1], T. Enqvist [1], A. Boudard [2]

[1]GSI, Germany; [2]CEA/Saclay, France

In nuclear charge-pickup reactions at projectile energies well above the Fermi energy there are two processes mostly responsible for the increase of the nuclear charge of the projectile [1]: A quasi-elastic collision between a target proton and a projectile neutron, and the excitation of a target or a projectile nucleon into the Δ(1232)-resonance state and its subsequent decay. These two mechanisms populate different regions of velocity distributions of charge-pickup products [1]: While the quasi-elastic (QE) component is situated at the velocities close to that of the beam, the deexcitation of Δ(1232)–resonance state populates a broader peak at lower velocities. At relativistic energies charge-exchange reactions involve the formation of Δ–particles and pions, therefore, they can be used as a tool for studying the in-medium behaviour of these particles [2]. These reactions can also give some insight into the neutron density distribution in the nucleus [3].

The charge-pickup reactions of 1 *A* GeV ^{208}Pb with ^{1}H, ^{2}H and Ti were studied [4] at the FRS. As a magnetic spectrometer, the FRS allows one to measure the kinematical properties of the reaction residues with high resolution. Details on the experiment can be found in Ref. [4].

The experimental velocity distributions in the projectile frame are shown in Fig. 1. In the same figure, on the upper axis is shown the energy transfer in the laboratory frame, which was calculated applying two-body kinematics. For ^{208}Bi, events with negative energy transfer reflect the finite resolution of the experiment. In the cases A < 208 the two-body kinematics applied for calculating the energy transfer is not strictly valid, which additionally contributes to the events with apparent negative energy transfer. In case of ^{208}Bi one can see a clear presence of both components. Going from the ^{1}H to the ^{2}H target, the QE contribution leading to the production of ^{208}Bi decreases by a factor 1.4. The QE component of a charge-pickup reaction can occur only on the target proton, and, consequently, it is expected to be about two times weaker in the ^{2}H case. Distortion effects of the ^{2}H target could influence this ratio. On the other hand, the contribution of the Δ–resonance excitation to the formation of ^{208}Bi is larger for the ^{2}H target than for the ^{1}H target. In case of the ^{1}H target a process leading to the production of ^{208}Bi is p(^{208}Pb, ^{208}Bi)Δ^{0}, while in case of the ^{2}H target, depending on the orientation of a deuteron with respect to the projectile, one can excite the Δ–resonance either on the target proton or on the target neutron via n(^{208}Pb, ^{208}Bi)Δ^{-} reaction. As the isospin Clebsch-Gordan coefficient for neutrons is three times larger than for protons [5], one would expect the Δ-resonance component to be about two times stronger in case of the ^{2}H target as compared to the ^{1}H target. A distortion of the ^{2}H could also influence this ratio. From the fits to the measured velocity distributions of ^{208}Bi, we obtain that the Δ–resonance contribution for the ^{2}H target is by a factor of 1.7 larger as compared to the ^{1}H target. From the same fit, we have obtained that the mean energy transfer corresponding to the Δ–resonance contribution is equal to (293 ±12) MeV and (274±12) MeV for ^{1}H and ^{2}H target, respectively, which is in agreement with other data [2].

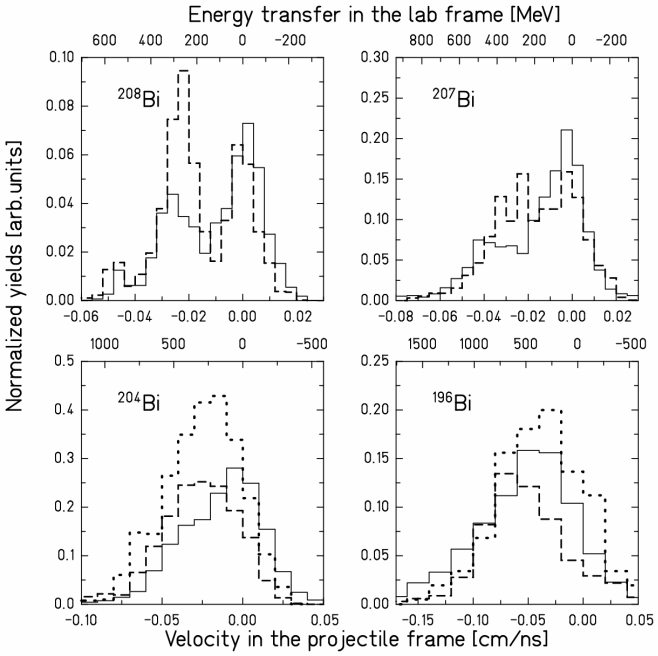

Fig 1. Longitudinal velocities (lower scale) of several bismuth isotopes produced in the interaction of 1 *A* GeV ^{208}Pb with the ^{1}H- (full line), ^{2}H- (dashed line) and Ti-target (dotted line). The upper scale represents the energy transfer in the laboratory frame.

An interesting finding is that for the isotopes $^{204\text{-}207}$Bi produced on the ^{1}H target, the QE component is stronger as compared to the ^{2}H or the Ti target. For the lightest bismuth isotopes (A < 204) the overall shape and mean value of the velocity distributions are very similar for all three targets. The velocity distributions of the bismuth residues were calculated with INCL4+ABLA code and were found to be in qualitative agreement with the measured distributions [4]. It was also shown that these kind of experimental data can help to improve the treatment of the Pauli blocking in the intra-nuclear cascade model.

References

[1] C. Gaarde, Annu. Rev. Nucl. Part. Sci. 41 (1991) 187

[2] T. Udagawa *et al.*, Phys. Rev. C 49 (1994) 3162

[3] V.P. Koptev *et al.*, Yad. Fiz. 31 (1980) 1501

[4] A. Kelić *et al.*, Phys. Rev. C 70 (2004) 064608

[5] E. Oset *et al.*, Phys. Lett. B224 (1989) 249

Measurement of a complete set of nuclides, cross sections, and kinetic energies in the spallation of ^{238}U 1 *A* GeV with protons

M. Bernas[1], M. V. Ricciardi[2], J. Taieb[1,2], P. Armbruster[2], J. Benlliure[2,3], A. Boudard[4], E. Casarejos[3], S. Czajkowski[5], T. Enqvist[2], S. Leray[4], P. Napolitani[1,2], J. Pereira[3], F. Rejmund[1,2], K.-H. Schmidt[2], C. Stephan[1], L. Tassan-Got[1], and C. Volant[4]

[1]IPN, Orsay, France; [2]GSI, Darmstadt, Germany; [3]Universidad de Santiago de Compostela, Spain; [4]DAPNIA/SPhN, CEA, Saclay, France; [5]CEN Bordeaux-Gradignan, France

In 1996, in view of the future technological applications, a European collaboration started a dedicated experimental program, devoted to reaching a full comprehension of the proton-induced spallation reactions. The experiments, carried out at the FRagment Separator at GSI, were performed in inverse kinematics at relativistic energies, making the high-energy nuclear beams impinge into liquid-hydrogen and liquid-deuterium targets. Results from the experiments on several systems (Au+ ^{1}H, Pb + ^{1,2}H, U + ^{2}H, Fe + ^{1}H, Xe + ^{1,2}H) in the energy range 0.3-1.5 GeV per nucleon were already published or are still being analyzed. Here we report on the nuclide production cross sections in ^{238}U+^{1}H [1] at 1 GeV per nucleon, presented in Figure 1, which were completed very recently.

The fully stripped reaction products were identified at the FRS by detecting their nuclear charge, *Z*, with a ionization chamber and their mass, *A*, from the *A/Z* ratio deduced from the magnetic rigidity and from the time-of-flight between the mid plane and the exit of the spectrometer. Once the nuclides were identified, so *A* and *Z* were integer numbers, their velocity was precisely evaluated by the magnetic rigidity. By the known beam intensities, target properties and transmission ratios the production cross sections were calculated on the basis of the measured yields. The measured velocity spectra allowed deducing the reaction mechanism in which the residues were formed. In this way, fission events (producing fragments with Z<74 approximately) could be disentangled from the evaporation residues (Z>74 approximately). Details of the experimental technique and of the physical meaning of the results can be found in ref. [1-5].

With the above method, for 1385 nuclides, production cross sections down to values of 10 μb with a mean accuracy of 15%, velocities in the uranium rest frame, and kinetic energies were determined. This is the first ever complete investigation on nuclide production cross sections and kinematics in ^{238}U+^{1}H.

Financial support by EU Contract No.ERBCHBCT940717 for J. B., T. E., and F. R. and by GSI for P. N., M.V. R., and J.T. is gratefully acknowledged. This work was partially supported by the European Union in the HINDAS project (Contract No. FIKW-CT-2000-00031) and by the project Access to Large Facilities (Contract No. EC-HPRI-CT-1999-00001).

References

[1] P. Armbruster et al., Phys. Rev. Lett. 93 (2004) 212701

[2] J. Taieb,et al., Nucl. Phys. A 724 (2003) 413-430

[3] M. Bernas et al., Nucl. Phys. A 725 (2003) 213-253

[4] M. V. Ricciardi et al., to be published.

[5] M. Bernas et al., to be published.

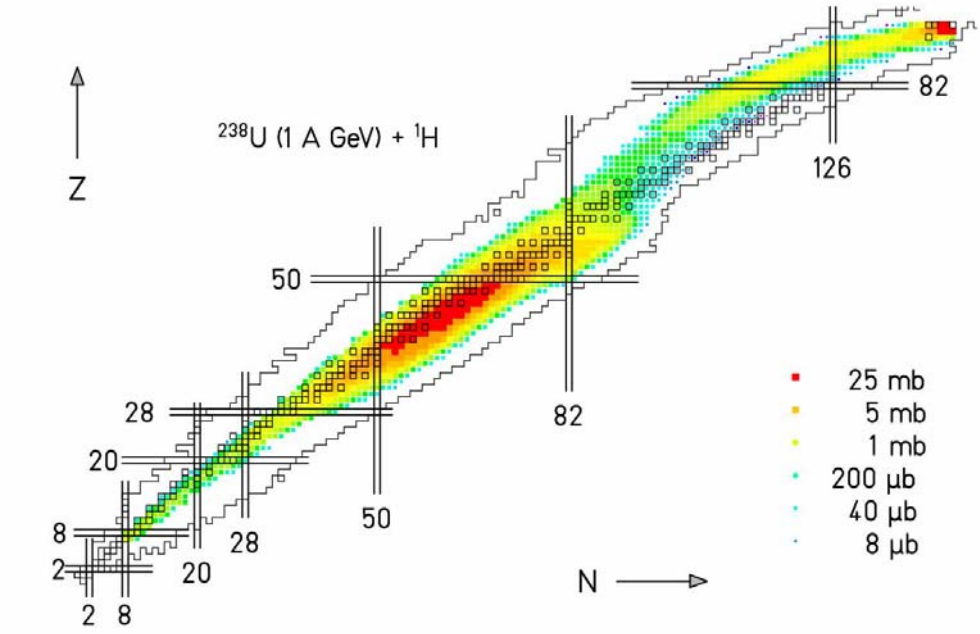

Figure 1: The identified nuclides are shown on a chart of nuclei. Numerical values are available on http://www-w2k.gsi.de/charms/data.htm. The experimental cross sections are indicated by a logarithmic color scale.

Neutron yields from 1 GeV/u ^{238}U beams on Fe target

O. Yordanov, K. Gunzert-Marx, P. Adrich, T. Aumann, K. Boretzky, H. Emling, G. Fehrenbacher, F. Gutermuth, H. Iwase, H. Johansson, K.L. Jones, A. Kovalov, T. Radon, D. Schardt
GSI Darmstadt, Germany

Radiation protection issues at heavy-ion accelerator facilities operated at beam energies of about hundred MeV to a few GeV per nucleon are dominated by neutron radiation produced in nuclear reactions when ion beam losses occur. Data on neutron production are necessary for the radiation protection planning of the next generation of Rare-Isotope-Beam (RIB) facilities, like the FAIR facility at GSI, which will have considerably higher beam intensities than available at present.

Experimental data on neutron emission from the interaction of heavy-ion beams with matter are scarce. Recently, neutron spectra in the angular range from 0° to 90° for various targets and ion beams with energies up to 800 MeV/u were measured by Kurosawa et al. [1]. No experimental data are available for neutrons produced by very heavy beams such as uranium beams. Here, double differential (energy and angle) neutron distributions in the angular range from 0° to 20° were measured at GSI for ^{238}U beams of 1 GeV/u kinetic energy which are stopped in an massive iron target.

During the measurement, the detector system was arranged in two different geometries.

Setup I: The ion beam was passed through an active collimator limiting the beam spot size to 2 cm x 2 cm, subsequently impinging on a thin organic scintillator. Downstream, an iron target of 20 cm depth and of 10 cm x 10 cm lateral dimensions was placed with its centre at a distance of 22 cm to the scintillator. Behind the target, a large-gap dipole magnet served to deflect charged particles. Neutrons were detected in LAND (active area of 2 m x 2 m) located at 10.85 m to the centre of the target; neutron polar angles up to 7.8^{o} were covered. In front of LAND, an array of organic scintillators was installed enabling charged particle discrimination.

Setup II: In a second setup, collimator, scintillation detector, and target were moved into a position behind the dipole magnet, reducing the distance between target and LAND to 7.06 m. Both, the neutron detector and the charged-particle detector in front of it were horizontally displaced with the centre of LAND at 1.65 m distance to the axis of the incident beam; neutron polar angles were covered in a range between 5.2^{o} and 20.5^{o}.

The neutron events were sorted into bins of 10 MeV kinetic energy and of 1^{o} in polar angle. The data were corrected for detection efficiency, divided by the covered solid angle, and normalized to the number of incident uranium ions. Results are shown in Fig. 1; statistical errors are small compared to the systematic ones which are shown. Fig.2 displays the neutron angular distribution, i.e., integrating the neutron yield over a range from 50 MeV to 2 GeV in neutron kinetic energy.

Neutron spectra from heavy-ion beams caused by nucleus-nucleus interactions can now be calculated by means

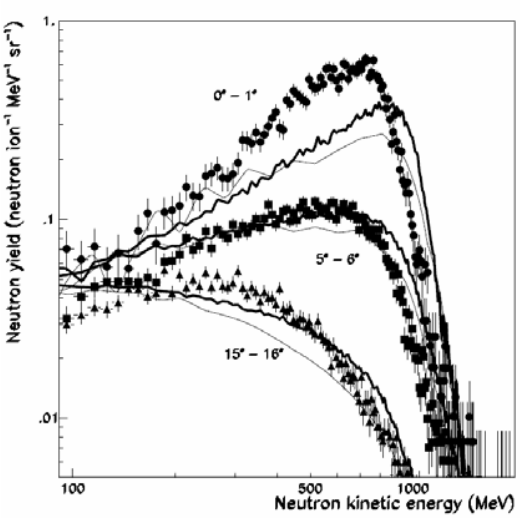

Fig.1. Measured neutron yields for three angular bins. The experimental data are compared to calculations with the FLUKA (heavy curves) and PHITS code (thin curves).

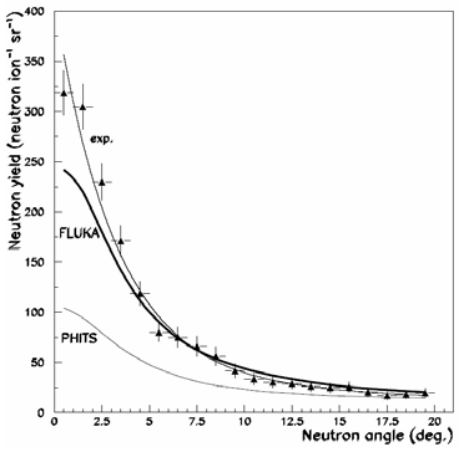

Fig.2. Neutron angular distribution.

of a new generation of Monte Carlo transport codes; a comparison with results from the latest versions of the FLUKA [2] and the PHITS code [3] is shown in Figs. 1 and 2. The experimentally observed integrated (0^{o} – 20^{o}; 50-2000 MeV) yield of 15.5(3.5) neutrons per incident uranium ion is reproduced by FLUKA which delivers 16 neutrons; PHITS delivers a lower value of 12 neutrons, presumably due to the fact that Coulomb fission and dissociation is not incorporated. The present data are considered as a bench mark in testing transport codes under conditions relevant for radioprotection issues at high-current heavy-ion accelerators.

[1] T. Kurosawa et al., Phys. Rev. **C62** (2000) 044615
[2] www.fluka.org
[3] H. Iwase, J. of Nucl. Sci. and Tech., **39** (2002) 1142

How doubly-magic is the nucleus $^{78}_{28}Ni_{50}$?

B. Pfeiffer[1,2] and K.-L. Kratz[1,2]

[1]Institut für Kernchemie, Universität Mainz, Germany; [2]HGF VISTARS

Doubly-magic nuclei play an important role in nuclear structure theory as testbeds for shell model calculations. Data on neutron-rich nuclei in the regions of doubly-magic nuclei such as $^{78}_{28}Ni_{50}$ and $^{132}_{50}Sn_{82}$ have a decisive influence on nucleosynthesis calculations. These "longer-lived" waiting-point nuclei determine the duration of the r-process and the matter flow through the abundance maxima at the magic neutron numbers [1]. Remaining deficiencies prior to the abundance maxima in r-process calculations have been interpreted as signatures of new nuclear structure effects near the neutron drip-line, for example overestimation of the shell strength far from stability in global mass models such as FRDM and ETFSI-1. A

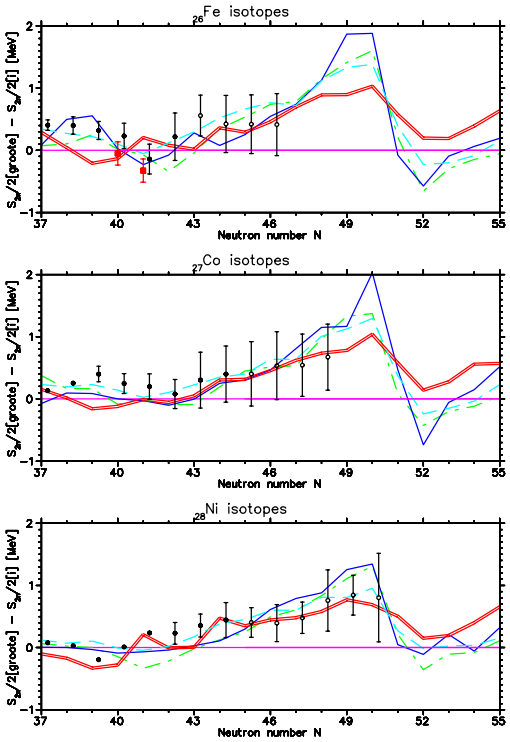

Figure 1: Deviations of experimental [black dots: 2003 mass evaluation [7], red squares: FRS/ESR measurements [8]] and theoretical S_{2n} values from the smoothly varying Groote mass formula [2] across the shell gap at N=50 are shown for $_{26}$Fe (upper part), $_{27}$Co (middle part) and $_{28}$Ni (lower part) isotopes. [Theoretical masses: Groote: magenta, FRDM: red [3], ETFSI-1: cyan [4], HFB-2: green [5], HFB-8: blue [6]]

weakening ("quenching") of spherical shells with increasing isospin, resulting in a gradual setting in of collectivity, has been predicted by recent HFB calculations, and is well established for the lower neutron-magic numbers N=20 and N=28.

In this context, it is of interest to determine the mutual influence of the proton and neutron magic numbers far from stability. The shell strength can be derived from the differences of the two-neutron separation energies S_{2n} prior and behind a magic neutron number. Fig. 1 displays differences between experimental and theoretical S_{2n} values relative to the smoothly varying mass formula of Groote et al. [2] for Fe, Co and Ni isotopes.

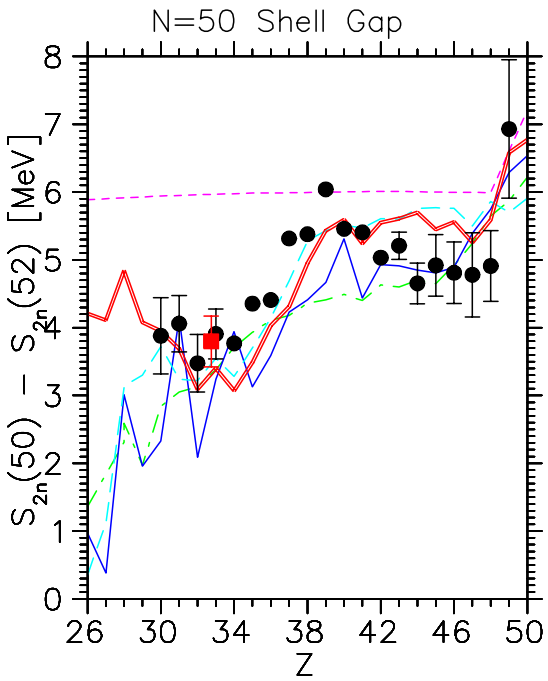

Figure 2: The N=50 shell gap as a function of Z. Experimental and extrapolated values from the 2003 mass evaluation [7] (black circles) and experimental values from direct mass measurements at ESR/FSR [red square] are compared to theoretical mass models. [Same colour coding for the mass models as in Fig. 1.]

Fig. 2 shows the N=50 shell gap over a wide Z range. Most global mass models predict a local maximum for doubly-magic ^{78}Ni. So far, below Z=30 no experimental masses have been determined, so that this prediction cannot be verified. With upgraded U-beams, direct mass measurements at the FRS-ESR of GSI will in future extend the range of experimental masses in this region to more neutron-rich isotopes.

References

[1] K.-L. Kratz et al., Ap. J. **403**, 216 (1993).
[2] H. von Groote et al., ADNDT **17**, 418 (1976).
[3] P. Möller et al., ADNDT **66**, 131 (1997).
[4] Y. Aboussir et al., ADNDT **61**, 127 (1995).
[5] S. Goriely et al., ADNDT **77**, 311 (2001).
[6] M. Samyn et al., Phys. Rev. **70**, 044309 (2004).
[7] G. Audi et al., Nucl. Phys. **A729**, 3 (2003).
[8] M. Matos, PhD thesis, Giessen (2004).

Influence of mass measurements at FSR-ESR on r-process calculations

B. Pfeiffer[1,2], K.-L. Kratz[1,2], K. Beckert[3], P. Beller[3], F. Bosch[3], D. Boutin[3], T. Faestermann[5], B. Franczyk[3], B. Franzke[3], H. Geissel[3,6], M. Hausmann[7], E. Kaza[3], O. Klepper[3], H.-J. Kluge[3], C. Kozhuharov[3], Yu. A. Litvinov[3], L. Maier[4], M. Matos[3], G. Münzenberg[3], F. Nolden[3], Yu. N. Novikov[4], T. Ohtsubo[8], A.N. Ostrowski[10], Z. Patyk[9], M. Portillo[3], C. Scheidenberger[3], J. Stadlmann[3], M. Steck[4], D. Vieira[7], H. Weick[3], M. Winkler[3,6], H. Wollnik[6], and T. Yamaguchi[3]

[1]Institut für Kernchemie, Universität Mainz, Germany; [2]HGF VISTARS; [1]GSI, Darmstadt, Germany; [3]GSI, Darmstadt, Germany; [4]St. Petersburg Nuclear Physics Institute, Gatchina, Russia; [5]TU München, Garching, Germany; [6]Justus-Liebig-Universität, Gießen, Germany; [7]LANL, Los Alamos, USA; [8]Riken, Saitama, Japan; [9]Institute for Nuclear Studies, Warsaw, Poland; [10]Dekanat Physik, Universität Heidelberg, Germany

The influence of nuclear data input on r-process calculations can be studied within the "waiting-point" concept. The r-process abundances $N_{r,\odot}$ originate from a high-density and high-temperature environment, which supports an equilibrium between neutron captures and photodisintegrations. The reaction rates for these processes are related by detailed balance. The main nuclear physics input data are 1) the β-decay properties half-lives $T_{1/2}$ and β-delayed neutron emission probabilities P_n and 2) neutron separation energies S_n, which enter into the nuclear Saha equation. For a given stellar temperature T_9 and neutron density n_n, the S_n determine the distance of the r-process path from the valley of β-stability; and the β-decay half-lives are proportional to the abundances of the precursor nuclei in the path [1].

The r-process involves very neutron-rich nuclei, for most of them only scarce or no experimental data are available. Hence, data from global mass models have to be applied. Remaining deficiencies in calculated abundances have been interpreted by our group as signatures for new nuclear structure patterns for unstable nuclei [1]. The ETFSI-Q mass model [2] has incorporated heuristically such new structure effects as "quenching" of magic neutron numbers far from stability. It is important to verify these theoretical concepts experimentally [3]. The direct mass measurements on neutron-rich nuclei performed at the FRS-ESR [4] are compared to different mass models in two contributions to this Annual Report [5]. In addition, they offer an opportunity to study the influence of the nuclear physics input on r-process calculations.

Fig. 1 shows differences of S_n values derived from mass measurements and from the ETFSI-Q model in the range $80 < A < 105$. These neutron-rich nuclei are situated beyond the ^{81}Ga break-out point of the r-process matter flow from the first $N_{r,\odot}$ maximum related to the magic neutron number N=50.

The measured isotopes are moderately neutron-rich, therefore they influence r-process components with quite low neutron number densities. Fig. 2 displays the r-process path for the stellar conditions $n_n=3\times10^{19}$ cm^{-3} and $T_9=1.35$, for which the (n,γ)$\leftrightarrow$(γ,n) equilibrium condition still holds. The most neutron-rich isotopes for Z around 40 measured at GSI are situated just at the edge of this path. Slight shifts of the path occur for isobars of Kr and Zr according to the differences observed in Fig. 1.

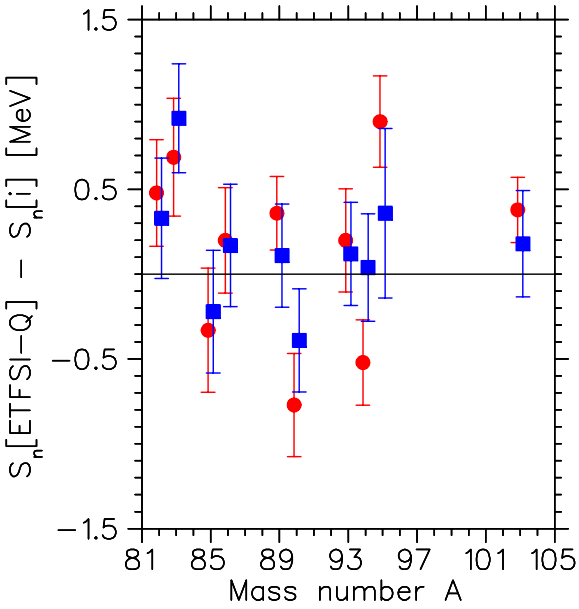

Figure 1: Differences between experimental neutron separation energies (S_n) [blue squares: 2003 mass evaluation [6], red dots: FRS-ESR measurements [7]] and the theoretical values from ETFSI-Q mass model [2] are shown for ^{82}Ga, ^{83}Ge, ^{85,86}As, ^{89,90}Se, ^{93}Br, ^{94,95}Kr and ^{103}Y.

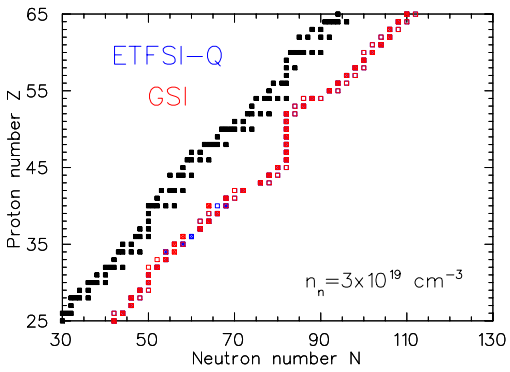

Figure 2: The r-process path is shown for stellar parameters $T_9=1.35$ and neutron number density $n_n=3\times10^{19}$ cm^{-3} as compared to the valley of stability [black squares]. Relative abundances in each isotopic chain are displayed as open squares if greater than 10% and the maximal value is represented by a crossed square. The path applying only theoretical masses from the ETFSI-Q [2] is shown in blue. Combined theoretial and experimental values from the direct mass measurements at GSI are displayed in red.

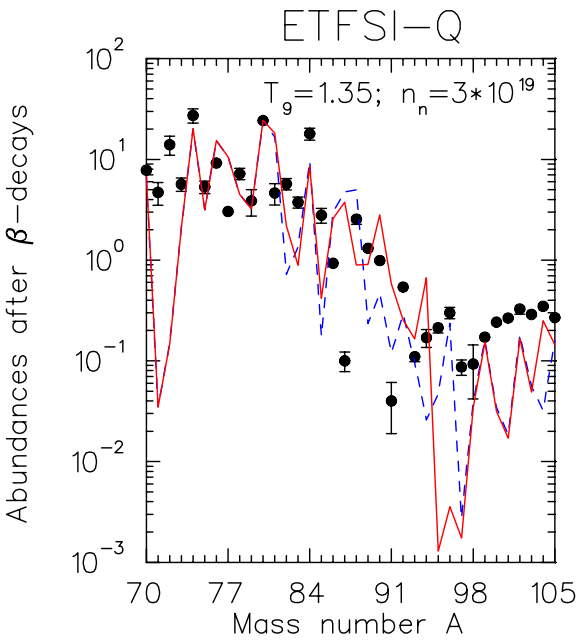

Figure 3: Isotopic r-process abundances calculated in the "waiting-point" approximation are compared to the Solar system r-process residuals $N_{r,\odot}$ [black dots] from [8]. The calculation applying theoretical mass values from the ETFSI-Q model is shown as dashed blue line. The red line shows the theoretical abundances when including the new experimental data from FRS-ESR. The abundances have been normalized to the solar value at A=80.

Fig. 3 shows isobaric r-process abundances calculated for these stellar parameters. Under these conditions, the first abundance peak at A≃80 related to the magic neutron number N=50 can be formed. The abundances obtained when replacing the theoretical masses from the ETFSI-Q model [dashed blue line] with the measured ones from FRS-ESR whenever available [red line] are in general in better agreement with the Solar system values. The pronounced "hole" around A=95 reflects the deviations of the S_n values of ^{94,95}Kr obtained at FSR-ESR from the ETFSI-Q predictions.

An appreciable influence of measured masses on r-process calculations requires data on more neutron-rich nuclei than measured so far at GSI. Fig. 4 shows r-process paths for neutron number densities of 3×10^{19} cm^{-3} [blue squares] and 3×10^{22} cm^{-3} [red squares], respectively. The path for the higher neutron number density, which forms the second abundance peak at A≃130 related to the magic number N=82, lies about 5 neutrons further away from the valley of β-stability. These isotopes will be reached by the future SuperFRS Facility at GSI.

But the mass values of the not so extremely neutron-rich nuclei measured uptill now at GSI nevertheless will have an indirect influence on the r-process calculations. Especially in the mass region around A=115 with refractory elements not accessible to classical ion sources, only scarce experimental mass data exist. The new measured

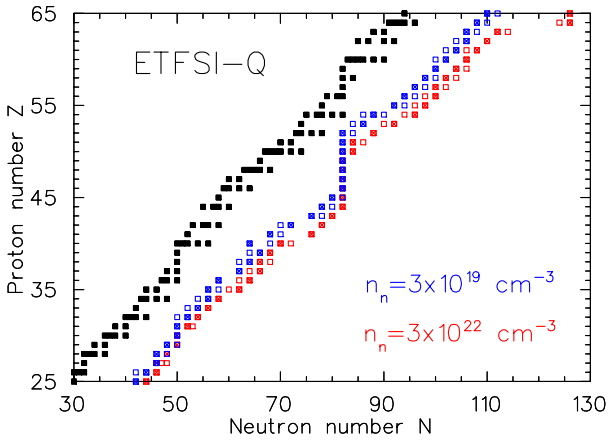

Figure 4: Comparison of r-process paths for neutron number densities of 3×10^{19} cm^{-3} [blue squares] and 3×10^{21} cm^{-3} [red squares], respectively. In both cases the theoretical masses from the ETFSI-Q model have been substituted by the values measured at GSI whenever available. [The same notatons apply as in Fig. 2]

masses will extend the knowledge of the mass surfaces and allow to expand the near-range extrapolations as in Ref. [6] into the region of very neutron-rich nuclei. The extended experimental basis should make theoretical mass predictions more reliable, as it should not be forgotten that the r-process paths for very high neutron number densities will rest unavailable for experiments still for some time.

References

[1] K.-L. Kratz et al., Ap. J. **403**, 216 (1993).
[2] J.M. Pearson et al., Phys. Lett. **B387**, 455 (1996).
[3] K.-L. Kratz et al., AIP Conf. Ser., in print
[4] C. Scheidenberger, Nucl. Phys. **A751**, 209 (2005).
[5] B. Pfeiffer and K.-L. Kratz, Ann. Rep. 2004, GSI.
[6] G. Audi et al., Nucl. Phys. **A729**, 3 (2003).
[7] M. Matos, PhD thesis, Giessen (2004).
[8] F. Käppeler et al., Rep. Prog. Phys. **52**, 945 (1989).

N=82 shell gap above $^{132}_{50}Sn_{82}$

B. Pfeiffer[1,2] and K.-L. Kratz[1,2]

[1]Institut für Kernchemie, Universität Mainz, Germany; [2]HGF VISTARS

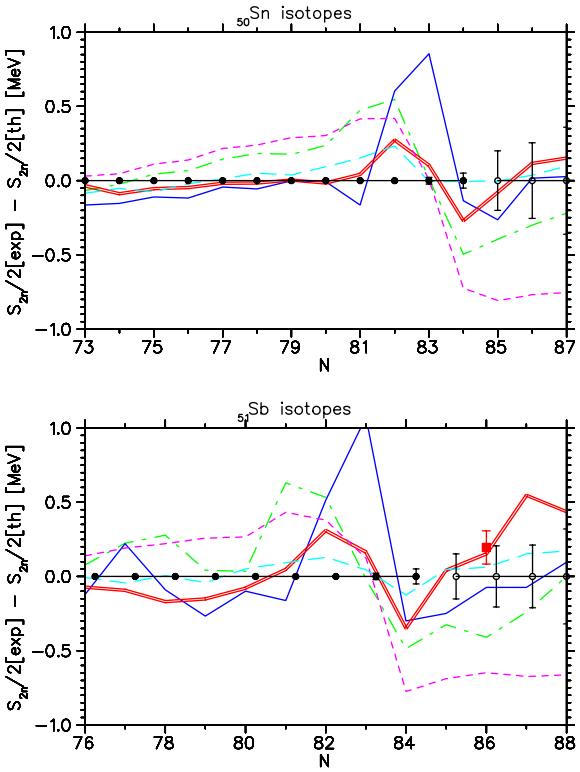

Figure 1: Differences between experimental two-neutron separation energies (S_{2n}) [black dots: 2003 mass evaluation [3], red squares: FRS/ESR measurements [4]] and theoretical values across the shell gap at N=82 are shown for $_{50}$Sn (upper part) and $_{51}$Sb isotopes (lower part). [Theoretical masses: Groote: magenta, FRDM: red, ETFSI-Q: cyan, HFB-2: green, HFB-8: blue]

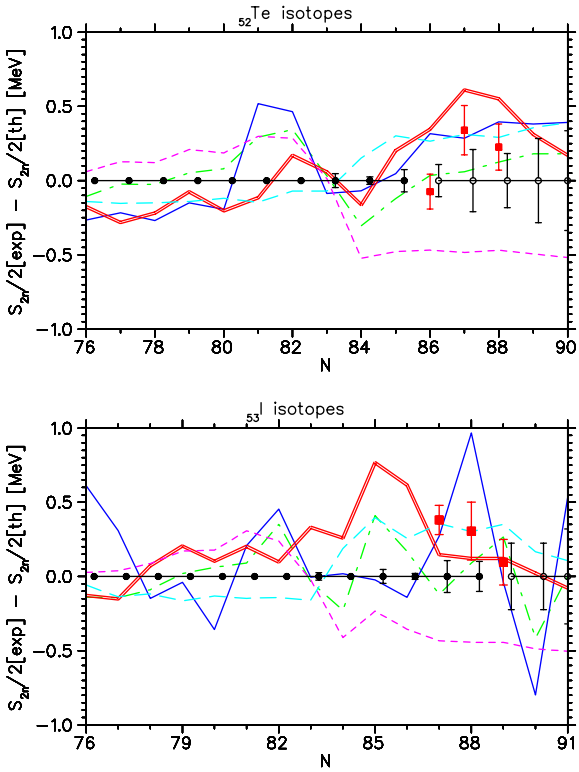

Figure 2: Same notation as for Fig. 1 for $_{52}$Te (upper part) and $_{53}$I isotopes (lower part).

The influence of nuclar structure on the r-process nucleosynthesis can be studied within the"waiting-point" concept [1]. The successful reproduction of the global isotopic abundances ($N_{r,\odot}$) as well as remaining deficiencies have been interpreted by our group as signatures for new nuclear structure patterns for unstable nuclei [1]. One such effect is an overestimation of the N=82 and 126 shell strength in global mass models such as FRDM and ETFSI-1. A weakening ("quenching") of spherical shells with increasing isospin, resulting in a gradual setting in of collectivity, is well established for the lower neutron-magic numbers and has been predicted by HFB calculations for the spherical shells at N=82 and 126 [2].
Signatures for a "quenching" of the shell strength can be derived from two-neutron separation energies (S_{2n}) across a magic neutron number. Studies of the N=82 nuclide ^{130}Cd at CERN-ISOLDE yielded a surprisingly high Q_β value, which is only in agreement with recent mass models that include the phenomenon of N=82 shell "quenching" [5, 6]. First direct mass measurements on neutron-rich isotopes at FRS-ESR yielded data on isotopes beyond the double-magic nucleus ^{132}Sn. Together with the experimental and short-range extrapolated masses from the 2003 mass evaluation [3], a meaningful comparison with theoretical approaches is now possible. As an example, Figs. 1 and 2 display S_{2n} values for $_{50}$Sn, $_{51}$Sb, $_{52}$Te and $_{53}$I isotopes. Surprisingly, the "old" models ETFSI-Q and FRDM perform better than recent self-consistent HFB approaches as the HFB-2 and especially HFB-8 from the Brussels-Montreal group. But, the discrepancies increase with distance to the magic proton number Z=50 for all models.
Direct mass measurements with upgraded U-beams at FRS-ESR will extend the range of experimental masses at N=50 , 82 and 126 closer to the r-process "boulevard".

References

[1] K.-L. Kratz et al., Ap. J. **403**, 216 (1993).
[2] B. Pfeiffer et al., Acta Physica Polonica **27**, 475 (1996).
[3] G. Audi et al., Nucl. Phys. **A729**, 3 (2003).
[4] M. Matos, PhD thesis, Giessen (2004).
[5] I. Dillmann et al., Phys. Rev. Lett. **91**, 162503 (2003).
[6] B. Pfeiffer and K.-L. Kratz, Ann. Rep. 2003, GSI, p. 28.

NUSTAR-T

Theoretical Nuclear Structure, Astrophysics and Reactions

UCOM-Hartree-Fock with Realistic NN-Interactions

H. Hergert[a,b], R. Roth[b], P. Papakonstantinou[b], and N. Paar[b]
[a]GSI Darmstadt; [b]Institut für Kernphysik, TU Darmstadt

The Unitary Correlation Operator Method (UCOM) provides a powerful means of combining numerically affordable many-body Hilbert spaces with the precision of current realistic NN-interactions [1, 2, 3]. Variational calculations in the mass range $A \lesssim 60$ using the Gaussian basis states of Fermionic Molecular Dynamics (FMD) have been reported previously.

Within the UCOM-Hartree-Fock scheme, it is possible to perform calculations using a realistic NN-interaction over the *whole* nuclear chart. Like in FMD, we employ a correlated version of the Argonne V18 interaction. We perform calculations in a configuration space approach, using a basis of spherical harmonic oscillator (HO) eigenstates, which allows us to implement central and tensor correlations in the two-nucleon system exactly. For HO states, one can also separate center-of-mass and relative motion exactly by means of a *Talmi transformation*. The interaction matrix elements are calculated once and stored for subsequent use in Hartree-Fock, No-Core Shell Model, RPA calculations, etc.

Bare realistic interactions usually feature both a strong repulsive core and a strong tensor force, causing a coupling of states of different momentum and energy scales. Converged results can then only be achieved by performing calculations in a Hilbert space of very large dimension, e. g., a spherical HO configuration space with excitations as high as several hundred $\hbar\omega$. The correlation procedure reduces this coupling and effectively pre-diagonalizes the interaction in momentum space. As a direct result, the convergence of self-consistent calculation schemes is improved notably.

In the case of Hartree-Fock calculations, the use of bare interactions does not yield bound systems at all — the treatment of correlations by UCOM techniques is *crucial*. Fig. 1 shows results for the binding energies of closed shell nuclei up to ^{208}Pb. The correlated interaction already reproduces the trends in the experimental binding energies very well.

By construction, the correlation operators are used to describe short-range correlations only. Long-range correlations should be treated by an appropriate choice of the model space. Thus, as a first step, we have used many-body perturbation theory to investigate the effect of the leading non-zero correction to the UCOM-HF results. The relevant term originates at the second order of the Goldstone expansion:

$$\Delta E^{(2)} = -\frac{1}{4} \sum_{i,j}^{\text{occ.}} \sum_{a,b}^{\text{unocc.}} \frac{|\langle ab| v_{\text{UCOM}} |ij\rangle|^2}{\epsilon_a + \epsilon_b - \epsilon_i - \epsilon_j} \,. \qquad (1)$$

It should be emphasized that the 'standard' Goldstone expansion can be applied because a Brueckner resummation is no longer necessary due to the correlation procedure. The lower line in Fig. 1 displays the improved results obtained with $\Delta E^{(2)}$ included, using HO shells up to $N_{\max} = 10$.

The treatment of long-range correlations can be further improved by performing RPA and coupled cluster calculations. Preliminary results from RPA are in agreement with the trend set by the perturbative treatment. We also plan to include pairing effects by performing Hartree-Fock-Bogoliubov calculations with the correlated interaction.

Work supported by the DFG (SFB 634).

References

[1] H. Feldmeier, T. Neff, R. Roth, and J. Schnack, Nucl. Phys. **A632**, 61 (1998).
[2] T. Neff and H. Feldmeier, Nucl. Phys. **A713**, 311 (2003).
[3] R. Roth, T. Neff, H. Hergert, and H. Feldmeier, Nucl. Phys. **A745**, 3 (2004).

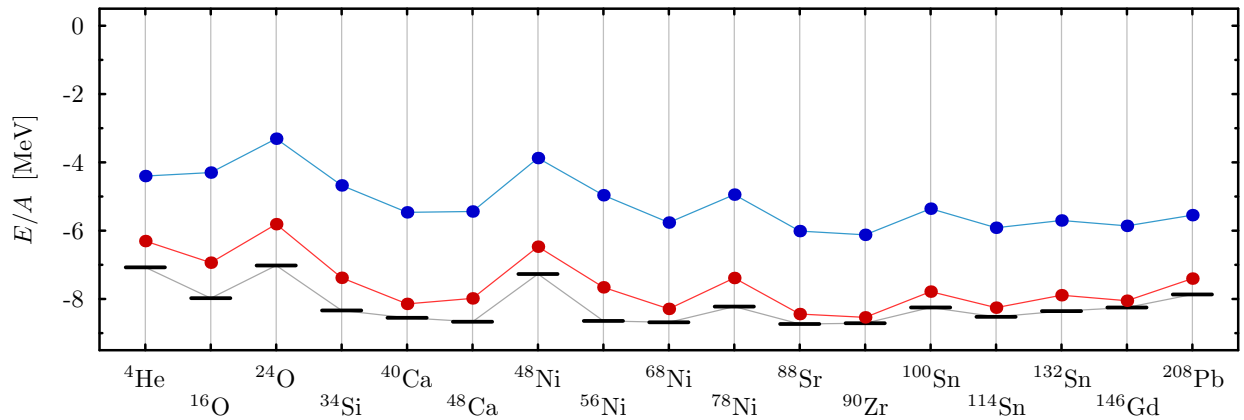

Figure 1: Binding energy per nucleon of closed shell nuclei. The results were obtained using the correlated Argonne V18 interaction alone (upper line), and including the perturbative correction (1) (lower line). Experimental values are indicated by black bars. HO shells up to $N_{\max} = 10$ were included.

Neutron-Rich Helium Isotopes in FMD

T. Neff and H. Feldmeier
GSI Darmstadt

The A-body basis states in Fermionic Molecular Dynamics [1] are parity and angular momentum projected Slater determinants $\left| Q \right\rangle$

$$\left| Q^{J^\pi}_{MK} \right\rangle = P^{J^\pi}_{MK} \left| Q \right\rangle \qquad (1)$$

of single particle states $\left| q \right\rangle$ that are described by Gaussian wave packets localized in phase-space

$$\left\langle \vec{x} \middle| q \right\rangle = \sum_i c_i \exp\left\{ -\frac{(\vec{x} - \vec{b}_i)^2}{2a_i} \right\} \left| \chi_i \right\rangle \otimes \left| \xi \right\rangle . \qquad (2)$$

A FMD state $\left| Q \right\rangle$ is obtained by minimizing the intrinsic energy of the parity projected Slater determinant with respect to the parameters of all single-particle states. The projection on angular momentum is done after the minimization (PAV$^\pi$). In the often deformed or clustered nuclei of the p-shell the correlation energies can be very large. We therefore use additional intrinsic configurations that are obtained by minimizing the energy under constraints on collective variables like the radius or the quadrupole moment. In a multiconfiguration calculation the Hamiltonian is then diagonalized in this set of projected Slater determinants.

For our calculations we use an effective interaction that is derived from the realistic Argonne V18 interaction by means of the Unitary Correlation Operator Method (UCOM) [2, 3, 4]. The correlated interaction includes the short-range central and tensor correlations induced by the repulsive core and the tensor force. The correlated interaction no longer connects to high momenta. Thus it can be used directly with simple many-body states of a Hartree-Fock or FMD approach.

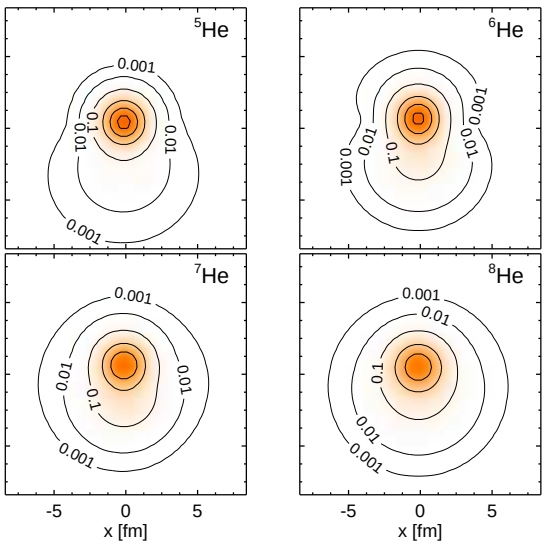

Figure 1: Intrinsic shapes of Helium isotopes corresponding to the minima in a variation after parity projection (PAV$^\pi$) calculation. Shown are cuts through the nucleon density calculated with the intrinsic state before parity projection. Densities are given in units of nuclear matter density $\rho_0 = 0.17\text{fm}^{-3}$.

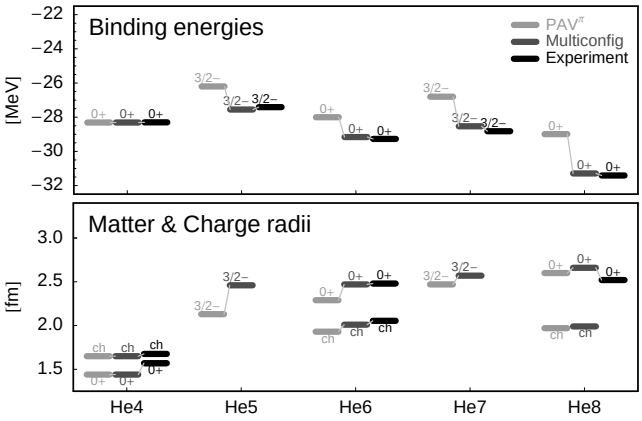

Figure 2: Binding energies and matter and charge radii for the Helium isotopes. Charge radii are indicated by ch. Results are given for the PAV$^\pi$ and the multiconfiguration calculations. Experimental matter radii are taken from [5]. The experimental charge radius of ^{6}He is given in [6].

Fig. 1 shows the intrinsic states obtained by minimizing the energy of the Helium isotopes. In all nuclei a dipole deformation caused by a displacement of the neutrons against the α-core is found. In ^{6}He the configuration with two neutrons on the same side of the core is preferred to configurations with the two neutrons located at opposite sides of the core. In ^{8}He one approaches the $p_{3/2}$ neutron shell closure with an almost spherical neutron distribution.

In Fig. 2 the binding energies and matter radii obtained after angular momentum projection (PAV$^\pi$) are compared to the experimental binding energies and radii. To improve the many-body states we create additional configurations using the dipole moment as a generator coordinate. The multiconfiguration calculations (Multiconfig) reproduce the experimental binding energies and radii very well. This illustrates the importance of the soft-dipole mode, that is realized in the form of groundstate correlations, for the understanding of the borromean nature of ^{6}He and ^{8}He. The increase of the charge radii compared to ^{4}He is mainly due to the motion of the α core against the center of mass of the nucleus. For ^{6}He we calculate a charge radius of 2.01 fm that has to be compared to the recently measured value of 2.054 ± 0.014 fm [6], for ^{8}He we predict a value of 1.99 fm.

References

[1] H. Feldmeier, J. Schnack, Rev. Mod. Phys. **72** (2000) 655
[2] R. Roth, T. Neff, H. Hergert, H. Feldmeier, Nuc. Phys. **A745** (2004) 3
[3] T. Neff, H. Feldmeier, Nuc. Phys. **A738** (2004) 357
[4] T. Neff, H. Feldmeier, Nuc. Phys. **A713** (2003) 311
[5] A. Ozawa, T. Suzuki, I. Tanihata, Nuc. Phys. **A693** (2001) 32
[6] L.-B. Wang et al, Phys. Rev. Lett **93** (2004) 142501

`http://theory.gsi.de/~tneff/`

Relativistic nuclear density functional constrained by QCD and chiral symmetry

Paolo Finelli[1], Norbert Kaiser[1], Dario Vretenar[2], and Wolfram Weise[1]

[1]Physik-Department, Technische Universität München, D-85747 Garching, Germany; [2]Physics Department, Faculty of Science, University of Zagreb, 10 000 Zagreb, Croatia

A new relativistic energy density functional has been derived in [1], where the many-body dynamics is constrained by in-medium QCD sum rules [2] and chiral symmetry [3]. The basic assumptions at the origin of our approach are:

1. Large scalar and vector fields of approximately equal magnitude and opposite sign, arising from the in-medium changes of the chiral condensate and the quark density, act as background fields (BG). They are parametrized by local four-point interactions with constant couplings G_i^{BG} $(i = S, V)$.

2. In-medium chiral pion-nucleon dynamics, calculated according to the rules of chiral perturbation theory, is consistently encoded in density dependent couplings $G_i^{\pi}(\rho)$ $(i = S, V, TS, TV)$ and D_i^{π} $(i = S, V)$.

Inspired by the success of Density Functional Theory (DFT) [4], we have identified the following pattern in the expression of the energy ground-state[1]:

$$\mathcal{E}_0[\rho] = \mathcal{E}_{\rm kin}[\rho] + \mathcal{E}_{\rm BG}[\rho] + \mathcal{E}_{\pi}[\rho] + \mathcal{E}_{\rm coul}[\rho] \,, \qquad (1)$$

where $\mathcal{E}_{\rm kin}$ is the kinetic energy of the free system and

$$\mathcal{E}_{\rm BG}[\rho] = \frac{1}{2}\int d^3x \, [G_S^{BG}\rho_S^2 + G_V^{BG}\rho^2] \,, \qquad (2)$$

$$\begin{aligned}\mathcal{E}_{\pi}[\rho] = \frac{1}{2}\Big\{ & \int d^3x \, [G_S^{\pi}(\rho)\rho_S^2 + G_V^{\pi}(\rho)\rho^2] \\ & + \int d^3x \, [G_{TS}^{\pi}(\rho)\rho_{S3}^2 + G_{TV}^{\pi}(\rho)\rho_3^2] \\ & - \int d^3x \, [D_S^{\pi}(\vec{\nabla}\rho_S)^2 + D_V^{\pi}(\vec{\nabla}\rho)^2] \Big\} \,, \qquad (3)\end{aligned}$$

$$\mathcal{E}_{coul}[\hat{\rho}] = \int d^3x \; A^0 e \frac{1+\tau_3}{2}\rho \,. \qquad (4)$$

The overall structure of $\mathcal{E}_0$ is reminiscent of what is commonly introduced for relativistic atomic systems, where $\mathcal{E}_{\pi}$ plays the role of the exchange correlation term ($\mathcal{E}_{exc}$) and $\mathcal{E}_{BG}$ is the nuclear counterpart of the usual Hartree term. The philosophy behind DFT [4] is to isolate the (in principle) tractable dominant contribution from the many-body correlations. The success relies, of course, on whether approximations for the exchange correlation term could be found. Calculations performed in Ref. [3] are a good starting point. Minimization of the ground-state energy with respect to orbital wavefunctions leads to our "Kohn-Sham" equations of motion:

$$[-i\beta\boldsymbol{\alpha}\cdot\boldsymbol{\nabla} + M_N + \gamma_0\Sigma_V^0 + \Sigma_S]\psi_k = \epsilon_k\psi_k \,, \qquad (5)$$

where Σ_V^0 and Σ_S are respectively the vector and scalar potentials. This approach has been tested in the analysis of symmetric and asymmetric nuclear matter and in bulk properties of finite nuclei. As an example we show in Fig. 1 binding energies and charge radii predictions along the Sn isotope chain. The agreement with experimental data is indeed very good. Our "QCD-inspired" model is a first step towards estabilishing connections between the structure of finite nuclei and underlying principles of low-energy QCD. Work supported in part by BMBF, GSI and MURST.

[1]for notation and details we refer the reader to [1]

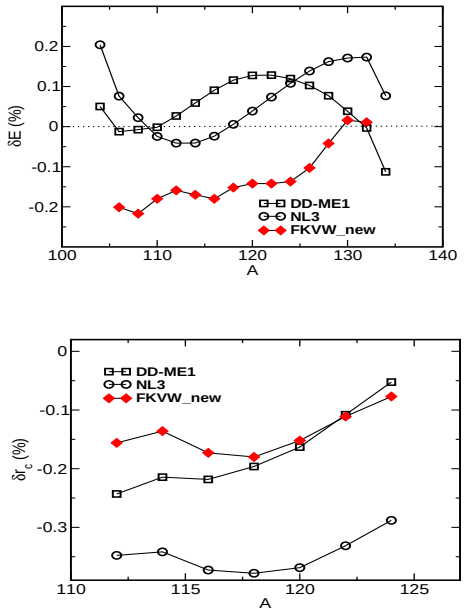

Figure 1: The deviations of the theoretical masses and the charge radii of Sn isotopes from the empirical values, in comparison with phenomenological approaches [5].

References

[1] P. Finelli, N. Kaiser, D. Vretenar and W. Weise, Eur. Phys. J. A**17** (2003) 573; Nucl. Phys. A **735** (2004) 449; in preparation.

[2] T.D. Cohen, R.J. Furnstahl and D.K. Griegel, Phys. Rev. Lett. **67** (1992) 1507; X. Jin, M. Nielsen, T.D. Cohen, R.J. Furnstahl and D.K. Griegel, Phys. Rev. C**49** (1994) 464.

[3] N. Kaiser, S. Fritsch, and W. Weise, Nucl. Phys. A**697**, (2002) 255; [nucl-th/0406038].

[4] R. M. Dreizler and E. K. U. Gross, Density Functional theory, Spinger-Verlag, 1990; R. M. Dreizler, Lect. Notes Phys. **620** (2003) 123.

[5] G. A. Lalazissis, J. Konig and P. Ring, Phys. Rev. C **55** (1997) 540; T. Niksic, D. Vretenar, P. Finelli and P. Ring, Phys. Rev. C **66** (2002) 024306

Relativistic *ab initio* Theory for Nuclear Matter and Nuclei

H. Lenske[1], U. Badarch[1], C. Keil[1], and P. Konrad[1]
[1]Institut für Theoretische Physik, Universität Giessen

Field theoretical approaches to nuclear dynamics are most promising for understanding the interplay of strong interactions and nuclear many-body dynamics. Such a program, allowing to calculate in-medium interactions *ab initio* from the free space baryon-baryon (BB) interactions is the aim of the Density Dependent Relativistic Hadron (DDRH) field theory. In DDRH theory we consider meson exchange processes as the relevant and dominant degrees of freedom for interactions in free space and nuclear matter. This picture is well established and impressively confirmed by the good description of NN phase shifts and other on-shell observables with the existing relativistic one-boson NN potentials. Since we are interested also in extensions of the theory to hypernuclei we include the pseudo-scalar and vector meson multiplets and also the experimentally less well established nonet of scalar mesons. However, nuclear matter calculations obviously probe the meson spectrum only in the t- and u-channels without direct reference to s-channel meson spectral functions.

We obtain the in-medium interactions by solving the in-medium Bethe-Salpeter (BS) equation [1, 2], including modifications from the self-energies $\Sigma(k, k_F)$ and, as the main contribution, the two-particle Pauli-projector $Q_F(k_1, k_2) \sim \Theta(k_1^2 - k_F^2(1))\Theta(k_2^2 - k_F^2(2))$ which inhibits scattering into the occupied states inside the Fermi spheres. Such a description requires knowledge of the off-shell behavior of interactions over a range of momenta up to $\sim 2k_F$. Hence, the medium imposes an additional scale which is defined purely by many-body dynamics and varying with density and the proton-to-neutron ratio. As such, the Fermi-scale k_F introduces additional density dependent constraints on the momentum structure of the interaction. At normal nuclear density this implies to cover adequately a momentum range of at least 600 MeV/c. Correspondingly larger ranges are required in high density systems like neutron stars and highly compressed matter as envisioned in the CBM proposal for FAIR. In using the full spectrum of mesons below 1 GeV we account for these constraints.

In DDRH theory we apply a systematic approach allowing to identify the diagrammatic content of interactions at each stage of the calculation. Infinite nuclear matter at varying asymmetry is described by Dirac-Brueckner Hartree Fock (DBHF) theory. We separate the medium dependent Fermi-scale from the fundamental interaction scales by means of density dependent meson-baryon vertex functionals $\Gamma_{mB}(\hat{\rho})$ [1, 2, 3]. The functionals are introduced at the level of the Lagrangian such that the basic requirements as Lorentz invariance and the covariance of the field equations are retained which constrains the density dependent arguments of the vertices to Lorentz scalars. In addition, the Hugenholtz-van Hove theorem is fulfilled. For practical purposes we obtain in a first step the $\Gamma_{mB}(\hat{\rho})$ y expanding the half off-shell solutions $K(q, q_s)$ of the BS equation in terms of meson-exchange kernels D_m with masses m and express correlation effects by susceptibilities $\chi_m(q_s, k_F)$ [1]. Inserting this *ansatz* into the BS equation we find

$$\sum_m (D_m(q, q_s) - C_m(q, q_s|k_F))\chi_m(q_s|k_F) = V(q, q_s) \quad (1)$$

where q_s denotes the on-shell momentum, $V(q, q_s)$ is the full set of half off-shell tree-level amplitudes and correlation effects are contained in $C_m(q, q_s)$ [2].

A significant advantage of the approach sketched above is that we have full access to the analytic structure of interactions in nuclear matter. The medium-dependence of the susceptibilities is found to be given primarily in terms of the dimensionless variables $z = k_F/m$. The functional form is given by known transcendental functions but will not be displayed here. More interesting is that numerically the shapes resemble Lorenz distributions. Thus, the functional forms assumed previously [1] and also applied in phenomenological approaches [4] are confirmed *a posteriori*.

The DBHF vertices include by definition only contributions from the fully iterated series of ladder diagrams and the corresponding self-energies. A logical next step is to extend the approach by additional classes of diagrams and to investigate their contributions to the properties of nuclear matter and finite nuclei. As a first step towards such theory we have considered dynamical correlations in asymmetric nuclear matter [5]. A (non-relativistic) transport theoretical approach is chosen by which correlation effects are treated self-consistently [6]. Dynamical correlations lead to energy and momentum dependent self-energies, giving rise to spectral functions with a non-vanishing width Γ and finite life time $\tau \sim 1/\Gamma$. In neutron-rich matter the spectral functions are determined by a delicate balance of static isovector mean-field effects and the genuine dynamical correlation effects from the coupling to intermediate excitations of the background medium. The calculations show that the dynamical correlations are of universal character. Their origin are short range interactions mediated by processes on the scale of the vector meson masses [5, 6]. In [5] Landau-Migdal theory is used to separate the relevant short-range components of the interactions.

References

[1] H. Lenske, Springer Lecture Notes 641 (2004) 147.
[2] C. Keil, Dissertation, Universität Giessen, Dez. 2004.
[3] H. Lenske, C. Keil, Phys.Rev. C (submitted).
[4] S. Typel, H.H. Wolter, Wolter, Nucl. Phys. A656 (1999) 331; D. Vretenar, T. Niksic, P. Ring, Phys.Rev. C 68 (2003) 024310.
[5] P. Konrad, H. Lenske, U. Mosel, Nucl.Phys. A(2005) (in print);nucl-th/0501007.
[6] F. Frömel, H. Lenske, U. Mosel, Nucl.Phys. A723 (2003) 544.

Effective nuclear forces and low lying collective excitations in Sn

P. Fleischer[1], P. Klüpfel[1], P.-G. Reinhard[1], J.A. Maruhn[2]

[2] Institut für Theoretische Physik, Universität Erlangen / Germany

[3] Institut für Theoretische Physik, Universität Frankfurt / Germany

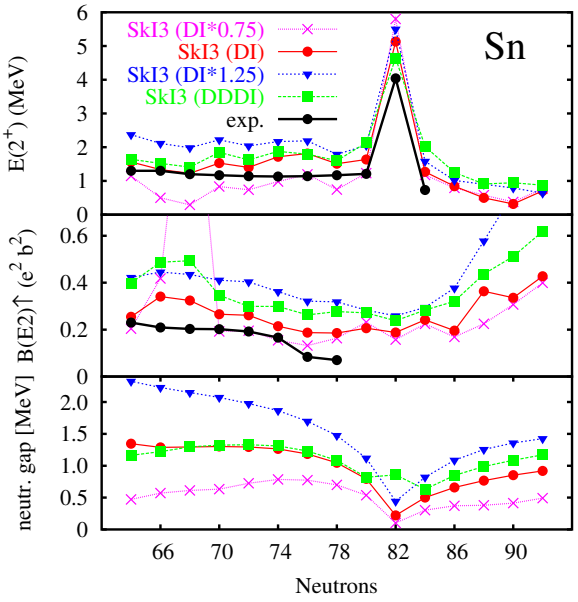

Figure 1: Excitation energies $E(2^+)$ and corresponding $B(E2)\uparrow$ values for the lowest quadrupole excitation along the chain of Sn isotopes. The lowest panel shows the average neutron-pairing gaps at spherical shape. The results are calculated with the Skyrme force SkI3 [6] and different pairing recipes as indicated. The experimental results are taken from [7].

A key feature of nuclear excitations are the low-lying 2^+ states. At first glance, they suggest the collective picture of the nucleus as a liquid drop which can undergo global quadrupole oscillations. This picture leads to the Bohr-Hamiltonian which describes a collective dynamics in the five quadrupole degrees of freedom. The connection to the microscopic description is established by the concept of a deformed mean field. The link is formalized by the generator-coordinate method which provides closed expressions to derive the Bohr-Hamiltonian from a given mean-field theory [1]. We have used that scheme to explore the ability of self-consistent nuclear mean-field models to describe low lying quadrupole spectra. We do that here for the Skyrme-Hartree-Fock mean field [2]. As test cases, we consider the lowest 2^+ state in the chain of Sn isotopes. For reasons of space, we concentrate here on the effect of the pairing field. We compare the volume pairing (= delta interaction = DI) with surface pairing (= density-dependent delta interaction = DDDI). And for the case of DI, we also check the sensitivity to variations of pairing strength. A more extensive study, discussing also in detail the effect of the Skyrme mean field, is found in [3, 4]. Formal and technical details of the solution of the collective Schrödinger equation are found in [3, 5].

Figure 1 shows the collective spectra along the Sn chain for SkI3 computed with different pairing prescriptions. We have added in the lowest panel some information about the internal pairing structure, namely the average neutron-pairing gaps $\bar{\Delta} = \sum_\alpha u_\alpha v_\alpha \Delta_{\alpha\alpha} \big/ \sum_\alpha u_\alpha v_\alpha$. Variation of pairing strengths (25% enhanced and reduced) has an obvious effect. The pairing gap is increased or reduced and the $E(2^+)$ energies change in the same direction. The effect is most pronounced in the pairing dominated regions sufficiently far from the neutron shell closure $N = 82$. Small changes in pairing strength cause large changes in excitation energies. Thus the low-energy spectra in soft vibrators provide valuable information about the pairing strengths if the contributions from the underlying mean field are carefully disentangled [8]. The DDDI pairing stays in most cases close to the results of DI pairing because it was tuned to the same average pairing gap. However, DDDI pairing reacts differently to shell effects as can be seen in the vicinity of the shell closure $N = 82$ and for the weak shell closure which the Skyrme force SkI3 produces at $N = 72$. The $B(E2)\uparrow$ values show generally smooth trends, except for $N \geq 86$ where an increase sets on which is related to the increasing softness of these neutron rich isotopes. The sensitivity to varying pairing recipes is small for $N \leq 82$. Somewhat more significant differences appear in the far exotic regime $N > 82$.

Altogther, while the excitation energies come out fairly well, the $B(E2)\uparrow$ values are still to larger as compared to data. We have indications that this is due to the simple choice of the deformed mean field by quadrupole constrained Skyrme-Hartree-Fock. More elaborate models for the collectively deformed mean fields are still required to improve the agreement.

Acknowledgment: This work was supported by the BMBF, projects 06 ER 124 and 06 F 131.

References

[1] P.-G. Reinhard, K. Goeke, Rep.Prog.Phys. **50** (1987) 1

[2] M. Bender, P.-H. Heenen, P.-G. Reinhard, Rev.Mod.Phys. **75** (2003) 121

[3] P. Fleischer, PhD thesis, Erlangen 2003

[4] P. Fleischer, P. Klüpfel, P.-G. Reinhard, and J. A. Maruhn, Phys.Rev. C **70** (2004) 054321

[5] P. Klüpfel, diploma thesis, Erlangen 2004

[6] P.-G. Reinhard, H. Flocard, Nucl.Phys. A **584** (1995) 467

[7] `www.nndc.bnl.gov/nndc/nudat/levform.html`

[8] J. Dobaczewski *et al*, Phys.Rev. C **63** (2001) 024308

Neutron-rich isotopes in the outer crust of neutron stars

Stefan Rüster, Matthias Hempel, Matthias Hanauske, Jürgen Schaffner-Bielich
Institut für Theoretische Physik, J. W. Goethe Universität, Frankfurt am Main, Germany

Neutron stars are the remnants of core collapse supernovae with typical sizes of about 10 km but a mass comparable to the mass of our sun. The outermost layer of a (cold) neutron star consist of a thin atmosphere of atoms for mass densities up to about 10^4 g/cm^3. For larger densities, a lattice of nuclei forms which is surrounded by free electrons — the so called outer crust of the neutron star. With increasing (electron) density, the nuclei in the lattice become more and more neutron-rich. The equation of state in this region of the neutron star was originally calculated by Bethe, Pethick and Sutherland (BPS) in a classic paper in 1971 [1].

The inner crust of the neutron star begins at the neutron-drip density of $\rho \sim 4.3 \cdot 10^{11}$ g/cm^3, when the density gets so high that neutrons start to drip out of the nuclei. The liquid interior of the neutron star is finally reached when all nuclei are melted away, which happens around $\rho \sim 1.4 \cdot 10^{14}$ g/cm^3, i.e. at about half normal nuclear density as calculated by Negele and Vautherin in 1973 [2]. The equation of state of BPS and of Negele and Vautherin is still used in the community as a standard for calculating the global properties of neutron star by matching with various high-density equations of state.

Here, we report on first results from an ongoing project to study the inner and outer crust of non-accreting cold neutron stars focusing here on the outer crust [3]. The properties of the outer crust can be described by the model laid out in detail by BPS [1]. Here, we utilise this approach but use modern nuclear data in order to update the results of BPS and Haensel et al. [4]. In particular, we use the most recent compilation of the experimental nuclear data from the atomic mass table of Audi, Wapstra, and Thibault from 2003 [5]. As the sequence of nuclei in the outer crusts extends to the drip-line, atomic masses are needed beyond the nuclear data tables. We compare different nuclear models to check their differences with respect to the neutron drip-line, magic numbers and occurrences of nuclei in the outer crust. In particular, we compared about 16 mass tables generated by relativistic field theoretical models including the chiral nuclear model of the Frankfurt group and by non-relativistic Hartree-Fock-Bogoliubov models with Skyrme force parametrisations. In addition, mass calculations for spherical as well as for deformed nuclei are studied for the nuclear sequence in the outer crust of neutron stars.

The figure shows the sequence of proton and neutron numbers of nuclei in the outer crust for a few selected nuclear models. With increasing density, the nuclei become more neutron rich and heavier in mass number. The detailed sequence is listed in the table for the models shown in the figure. We stress, that the old BPS parametrisation using a liquid-drop model starts to deviate from the more modern nuclear models already quite early in the nuclear sequence! Note, that there are distinct neutron numbers populated by the nuclear model calculations shown, which are just the neutron magic numbers 50 and 82. It is interesting to see, that the nuclei show rather moderate proton numbers even when reaching the neutron-drip density, i.e. Z is always between 26 and 44. Also, there appears dramatic differences between the models in the sequence for large neutron numbers.

We thank Thomas Bürvenich, Thomas Cornelius, and Stefan Schramm for providing some of the nuclear mass tables used in this research project. This work is support by GSI via the program "Fremde F&E-Mittel" in the research project OF/SAF "Struktur von neutronenreichen, exotischen Kernen in der Kruste von Neutronensternen".

References

[1] G. Baym, C. Pethick, and P. Sutherland, Ap. J. **170**, 299 (1971).
[2] J. W. Negele and D. Vautherin, Nucl. Phys. **A207**, 298 (1973).
[3] manuscript in preparation.
[4] P. Haensel and B. Pichon, Astron. Astrophys. **283**, 313 (1994).
[5] G. Audi, A. H. Wapstra, and C. Thibault, Nucl. Phys. **A729**, 337 (2003).

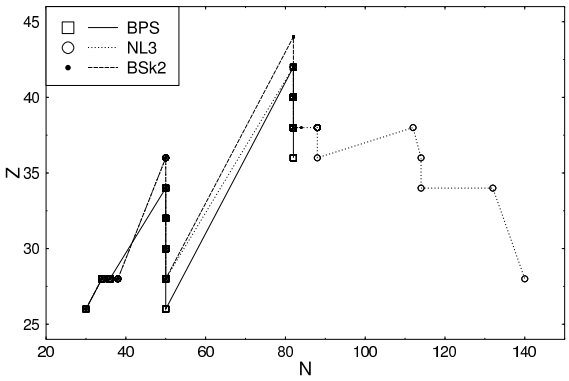

Figure 1: The sequence of proton and neutron numbers of nuclei in the outer crust for the models BPS, NL3 (Relativistic Mean-Field) and BSk2 (Hartree-Fock-Bogoliubov).

BPS	^{56}Fe, ^{62}Ni, ^{64}Ni, ^{84}Se, ^{82}Ge, ^{80}Zn, ^{78}Ni, ^{76}Fe, ^{124}Mo, ^{122}Zr, ^{120}Sr, ^{118}Kr
NL3	^{56}Fe, ^{62}Ni, ^{64}Ni, ^{66}Ni, ^{86}Kr, ^{84}Se, ^{82}Ge, ^{80}Zn, ^{78}Ni, ^{124}Mo, ^{122}Zr, ^{120}Sr, ^{126}Sr, ^{124}Kr, ^{150}Sr, ^{150}Kr, ^{148}Se, ^{166}Se, ^{168}Ni
BSk2	^{56}Fe, ^{62}Ni, ^{64}Ni, ^{66}Ni, ^{86}Kr, ^{84}Se, ^{82}Ge ^{80}Zn, ^{78}Ni, ^{126}Ru, ^{124}Mo, ^{122}Zr, ^{120}Sr, ^{122}Sr

Table 1: Sequence of nuclei in the outer crust of a neutron star (see figure).

Relativistic quasiparticle RPA with applications to exotic nuclei

T. Nikšić[1], N. Paar[2], J. Daoutidis[1], D. Pena Arteaga[1], P. Ring[1], and D. Vretenar[3]

[1]Physik Department, Technische Universität München, 85748 Garching, Germany; [2]Institut für Kernphysik, Technische Universität Darmstadt, 64289 Darmstadt, Germany; [3]Physics Department, Faculty of Science, University of Zagreb, 10000 Zagreb, Croatia

Studies of the structure and stability of nuclei with extreme isospin values provide new insights into every aspect of the nuclear many-body problem. In neutron-rich nuclei far from the valley of β-stability, in particular, new shell structures occur as a result of the modification of the effective nuclear potential. Neutron density distributions become very diffuse and the phenomenon of the evolution of the neutron skin and, in some cases, the neutron halo have been observed. The weak binding of outermost neutrons gives rise to soft excitation modes. In particular, the pygmy dipole resonance (PDR), i.e. the resonant oscillation of the weakly-bound neutron mantle against the isospin saturated proton-neutron core, have important implications on theoretical predictions of the radiative neutron capture rates in the r-process nucleosynthesis, and consequently to the calculated elemental abundance distribution. Furthermore, the detailed knowledge of the structure of low-energy modes of excitation would also place stringent constraints on the isovector channel of effective nuclear interactions. An interesting problem is the isotopic dependence of the PDR, and especially the behavior of the PDR in the vicinity of major spherical shell gaps.

We have solved the relativistic RPA [1], and corresponding QRPA equations in the canonical basis of the Relativistic Hartree-Bogoliubov model [2, 4]. In general, the dipole response of very neutron-rich isotopes is characterized by the fragmentation of the strength distribution and its spreading into the low-energy region, and by the mixing of isoscalar and isovector modes. In relatively light nuclei the onset of dipole strength in the low-energy region is due to non-resonant independent single particle excitations of the loosely bound neutrons. However, the structure of the low-lying dipole strength changes with mass. As we have shown in the RRPA analysis of Ref. [1], in heavier nuclei low-lying dipole states appear that are characterized by a more distributed structure of the RRPA amplitude. Among several peaks characterized by single particle transitions, a single collective dipole state is identified below 10 MeV, and its amplitude represents a coherent superposition of many neutron particle-hole configurations.

In Fig. 1 we plot the calculated PDR peak energies and the one-neutron separation energies for the Ni and Pb isotopic chains. The density-dependent effective interaction DD-ME1 [3] is used. In the pairing channel we worked with the finite range Gogny interaction D1S. The RHB results for the neutron separation energies are compared with the experimental values. For both chains the RQRPA calculation predicts a very weak mass dependence of the PDR peak energies. In the sequence of Ni isotopes the crossing between the theoretical curves of one-neutron separation energies and PDR peak energies is calculated already at $A = 64$. In heavier, neutron-rich Ni nuclei the PDR is expected to be located high above the neutron emission threshold. For the Pb isotopes the crossing point is calculated at $A = 208$, in excellent agreement with very recent experimental data on the PDR in ^{208}Pb [5]. Future (γ, γ') experiments on Pb nuclei could confirm the predictions of the present analysis.

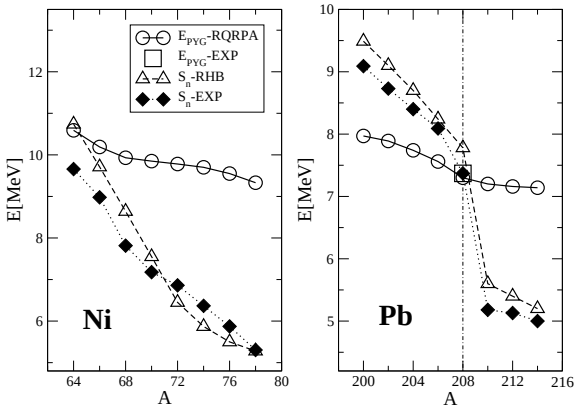

Figure 1: The calculated PDR peak energies and the one-neutron separation energies for the sequence of chain of Ni and Pb isotopes, as functions of the mass number. The open square denotes the experimental position of the PDR in ^{208}Pb [5].

In addition two important technical improvements of the computer code for solving the relativistic QRPA equations have been developed this year, (i) we are implementing full relativistic continuum RPA calculations and (ii) we developed a computer code for the solution of the deformed relativistic QRPA equations. It has been successfully tested for the correct treatment of the spurious mode connected with the rotational motion and shall be used for the investigation of the low lying $K = 1^+$ resonance in deformed nuclei far from stability.

References

[1] D. Vretenar, N. Paar, P. Ring, and G. A. Lalazissis, Nucl. Phys. **A692**, 496 (2001).

[2] N. Paar, P. Ring, T. Nikšić, and D. Vretenar, Phys. Rev. **C67**, 034312 (2003).

[3] T. Nikšić, D. Vretenar, P. Finelli, and P. Ring, Phys. Rev. **C66**, 024306 (2002).

[4] D. Vretenar, A. V. Afanasjev, G. A. Lalazissis, and P. Ring, Phys. Rep. 409, 101 (2005).

[5] N. Ryezayeva et al., Phys. Rev. Lett. **89**, 272502 (2002).

Deformation systematics of giant resonances

T. Cornelius[1], J.A. Maruhn[1], V. Nesterenko[2], P.-G. Reinhard[2]

[3] Institut für Theoretische Physik, Universität Frankfurt / Germany

[2] Institut für Theoretische Physik, Universität Erlangen / Germany

The giant dipole resonance (GDR) is a most pronounced feature in the nuclear excitation spectrum giving crucial clues to nuclear structure and dynamics. The upcoming possibility to measure GDR in exotic nuclei [1] challenges theorists to scrutinize the predictive value of their models. Of particular interest are self-consistent mean field approaches which describe the ground state and the excitation spectrum within one and the same parameterization, for a recent review see e.g. [2]. The additional information from GDR probes otherwise loosely fixed aspects of effective mean-field models. It is the aim of this paper to present an exploration of the GDR in deformed nuclei, computing the excitation spectra using the time-dependent Skyrme-Hartree-Fock (SHF) method. The deformation removes the degeneracy of the resonance peaks in spatial x-, y,- and z-directions, leading to a collective splitting of the resonance. A competing mechanism which also spreads the resonance peak to some extent is Landau fragmentation, due to a coupling of the resonance with energetically close $1ph$ states. The interplay of these two mechanisms was studied recently for the case of deformed metal clusters and it was found that Landau fragmentation can mask deformation splitting under certain conditions [3]. We will address this question here for the chain of Nd isotopes where a transition from spherical to deformed nuclei takes place. The GDR spectra are computed from symmetry unrestricted time-dependent mean-field theory and subsequent spectral analysis [4].

Figure 1 shows dipole strengths for the separate modes and in total as computed with the Skyrme force SLy6. The modes are degenerate as they should be for a spherical nucleus ^{142}Nd. The spectrum, however, shows strong fragmentation with a well developed side peak. This is due to Landau fragmentation. The deformation grows up gradually when moving from ^{142}Nd to ^{150}Nd. The separate strengths show the expected collective shifts. However, in the transitional region is the width of the peaks larger than the shift. This inhibits a clear identification of weak deformations from the GDR spectra. And that holds the more so as Landau fragmentation distracts strength from the apparent peaks and produces sometimes separate side-peaks which which can give misleading visual impressions. It is only for the heaviest and most strongly deformed nucleus in the sample that deformation splitting safely outweighs Landau fragmentation. Still, the mix of the effects inhibits a simple one-to-one relation between peaks and deformation. One has to analyze the strengths by elaborate peak fitting assisted with theoretical estimates from time-dependent mean-field theory.

Acknowledgment: This work was supported by the BMBF, projects 06 F 131 and 06 ER 124.

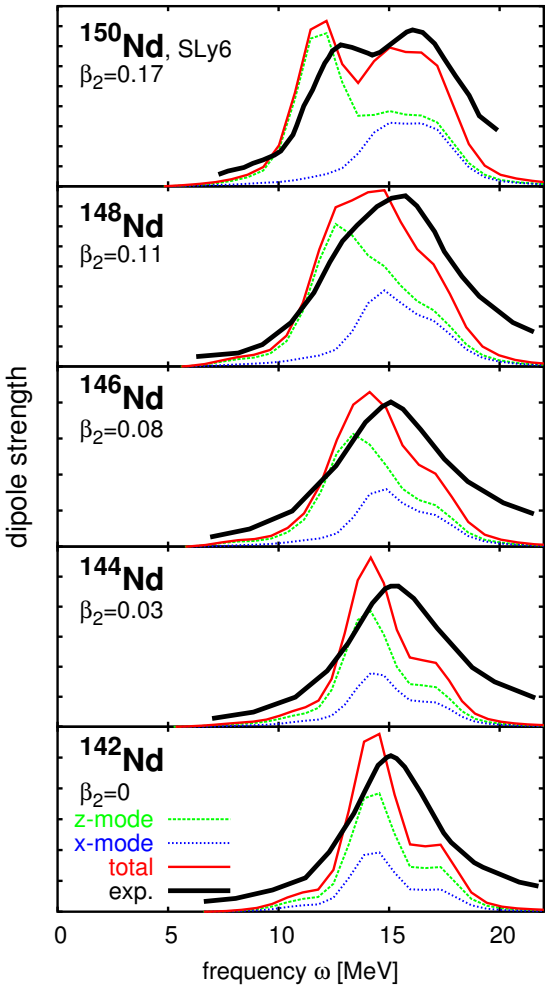

Figure 1: Dipole strengths for Nd isotopes computed with SLy6: dashed green line = modes along z-direction, dotted blue line = mode along x+y-direction, solid red line = total computed strength, heavy black line = experimental data [5]. The dimensionless quadrupole deformation β_2 of the ground state is indicated in each panel.

References

[1] A.L. Leistenschneider *et al*, Phys.Rev.Lett. **86** (2001) 5442

[2] M. Bender *et al*,Rev.Mod.Phys. **75** (2003) 121

[3] V.O. Nesterenko *et al* Eur.Phys.J. D **19** (2002) 57

[4] P.-G. Reinhard, E. Suraud, *Introduction to Cluster Dynamics*, Wiley, Berlin 2003

[5] S. S. Dietrich, B. L. Bermann, At.Data Nucl.Data Tab. **38** (1988) 199

Scaling laws and effective-range approach for electromagnetic strength in single-particle halo nuclei

S. Typel[1] and G. Baur[2]
[1]GSI Darmstadt; [2]IKP, Forschungszentrum Jülich

Electromagnetic strength functions of single-particle halo nuclei exhibit universal features that can be described in terms of characteristic scale parameters [1, 2]. These exotic nuclei are often well described assuming a simple nucleon+core structure. They have been studied extensively in recent years by electromagnetic excitation with the help of the Coulomb breakup method. A large electromagnetic strength is observed at low excitation energies [3, 4].

Neutron halo nuclei are characterized by a small separation energy $S_n = \hbar^2 q^2/(2\mu)$ of the least bound neutron in a s or p state with reduced mass μ. For larger orbital angular momenta the strong centrifugal barrier prevents the formation of a halo. The relevant matrix elements for electric transitions to continuum states with energy E are essentially determined by the asymptotics of the bound and scattering wave functions with orbital angular momenta l_i and l_f. The reduced transition probability for an $E\lambda$ excitation can be expressed as

$$\frac{dB}{dE}(E\lambda, l_i \to l_f) = \left[Z_{\rm eff}^{(\lambda)} e\right]^2 \frac{2\mu}{\pi\hbar^2} D_{l_i}^{l_f}(\lambda) \frac{|C_{l_i}|^2}{q^{2\lambda+3}} \mathcal{S}_{l_i}^{l_f}(\lambda) \quad (1)$$

with a characteristic shape function $\mathcal{S}_{l_i}^{l_f}(\lambda)$ that can be calculated analytically. $Z_{\rm eff}^{(\lambda)} = Z_c\,[m_n/(m_n+m_c)]^\lambda$ is the effective charge number and $D_{l_i}^{l_f}(\lambda)$ is an angular momentum coupling factor (neglecting spins). The parameter q determines the asymptotic slope of the ground state wave function and the factor C_i represents the asymptotic normalization coefficient (ANC).

Considering the $q^{2\lambda+1}$ factor and the scaling $C_0 \propto \sqrt{q}$ and $C_{l_i} \propto \sqrt{q}\gamma^{l_i-1/2}$ for $l_i \geq 1$ of the ANC, the large excitation strength in halo nuclei is obvious. The shape function $\mathcal{S}_{l_i}^{l_f}(\lambda)$ only depends on the dimensionless parameters $\gamma = qR$ with the nuclear interaction radius R, $x = \sqrt{E/S_n}$, and the phase shifts δ_{l_f} of the scattering wave function that quantify the final-state interaction (FSI) between the neutron and the core. At low energies the phase shift can be parametrized by the effective-range expansion. In the lowest-order approximation we have $\tan(\delta_l) = -(xc_l\gamma)^{2l+1}$ with the scattering length $a_l = (c_l R)^{2l+1}$. The FSI distorts the shape function. This effect is reduced for halo nuclei with a small γ.

The approach can be generalized to proton halo nuclei. The nucleon-core interaction affects the determination of the astrophysical S factor at zero energy in the ANC method. It is also relevant for the extrapolation of radiative capture cross sections to low energies.

The integrated excitation strength is directly related by the non-energy weighted sum rule

$$B(E1, l_i) = \left[Z_{\rm eff}^{(\lambda)} e\right]^2 \frac{3}{4\pi} \langle r^2 \rangle_{l_i} \quad (2)$$

to the root-mean-square radius of the halo nucleon with orbital angular momentum l_i. In contrast, the energy-weighted sum rule (in form of a cluster sum rule) gives a result independent of l_i. The characteristic scaling $\langle r^2\rangle_0 \propto R^2/\gamma^2$, $\langle r^2\rangle_1 \propto R^2/\gamma$, $\langle r^2\rangle_{l_i} \propto R^2$ for $l_i \geq 2$ is found. The radius of halo states with $l_i = 0, 1$ and the total excitation strength diverge in the limit $\gamma \to 0$.

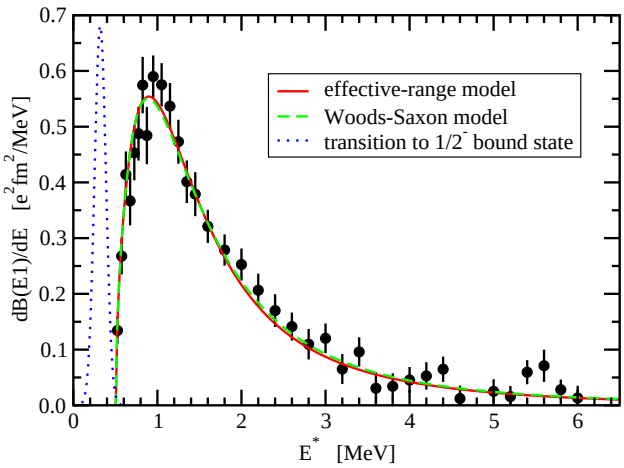

Figure 1: Reduced transition probability $dB(E1)/dE$ for the breakup of ^{11}Be into ^{10}Be+neutron as a function of the excitation energy $E^* = E + S_n$ compared to experimental data extracted from the Coulomb breakup of ^{11}Be [3].

The theoretical approach was applied to the analysis of the $E1$ strength in the neutron-halo nucleus ^{11}Be ($S_n = 503$ keV) that was determined from relativistic Coulomb excitation at GSI [3], see Fig. 1. It was possible to extract the ANC of the $1/2^-$ s-wave ground state wave function and the scattering lengths in the $3/2^-$ and $1/2^-$ p-wave continuum states [1]. The ANC was converted to a spectroscopic factor of 0.704(15) that is consistent with values determined in other approaches. The scattering length of the $1/2^-$ appeared to be unnaturally large. This result reflects the existence of a bound $1/2^-$ state close to the excitation threshold. Correspondingly, the total transition strength to the continuum is reduced.

Another recent application of the method is the Coulomb dissociation of ^{23}O [4] where a strongly distorted excitation spectrum was observed. The analysis of experimental shape functions in our approach allows to extract information on the spectroscopic factor and the FSI without the need for optical potentials.

References

[1] S. Typel and G. Baur, Phys. Rev. Lett. 93, 142502 (2004).

[2] S. Typel and G. Baur, preprint nucl-th/0411069.

[3] R. Palit et al., Phys. Rev. C 68, 034318 (2003).

[4] C. Nociforo et al., Phys. Lett. B 605, 79 (2005).

Antiproton-Nucleus Interactions as a Probe for Neutron Skins

H. Lenske[1] and P. Kienle[2,3]

[1]Institut für Theoretische Physik, Universität Giessen (Germany); [2]Physik Department, TU München, Garching (Germany); [3]Stefan Meyer Institut, Wien (Austria)

A highly interesting question of modern nuclear structure physics is to understand the evolution of nuclear shapes and sizes well into the regions far off $\beta-$ stability. Experimentally, a variety of efforts is undertaken or in planning to investigate properties of neutron-rich exotic nuclei, e.g. also at FAIR. An interesting alternative is to use antiprotons to probe nuclear sizes of stable and unstable nuclei in a systematic way.

Investigations of radii and, deduced from those measurements, of density distributions in stable nuclei are by itself a long discussed and applied method, e.g. at BNL and LEAR, respectively. Hitherto, the experiments have been performed with secondary antiproton beams on a variety of stable nuclei in fixed target geometry and standard kinematics. Obviously, such experimental configurations are not applicable for reactions on short-lived isotopes which are available for obvious reasons only as secondary beams, produced either by fragmentation or isotope separation on line. A solution dissolving these constraints are measurements in colliding beam geometry. Such a setup was recently proposed in [2] is part of the AIC proposal for FAIR [3]. With moderate modifications on an acceptable level the NESR/e^- setup can be converted into a $\overline{p}A$ collider facility.

Theoretically, the physics of $\overline{p}A$ interactions is by itself an interesting topic. The various aspects range from the unique way of introducing an anti-baryon into a nuclear environment and observing the subsequent evolution of the system over the use of antiprotons for in-medium meson spectroscopy to nuclear structure studies, The usefulness of $\overline{p}+A$ scattering for studies of the neutron skins of stable medium and heavy nuclei was realized already rather early in an experiment at BNL [4]. As for the elementary antiproton nucleon ($\overline{p}N$) vertex the $\overline{p}A$ reactions are dominated by processes in which the incoming antiproton annihilates on a target nucleon into a variety of particles producing typically and preferentially a shower of pions as the final result. Here, we utilize the strong $\overline{p}A$ absorption for nuclear structure investigations without paying particular attention to the hadron physics aspects.

In the present context the very details of $\overline{p}N$ annihilation in a nuclear medium are not of our primary interest. We are satisfied to know that the elementary annihilation processes result in a strong suppression of the incoming flux. In the elementary elastic scattering amplitude $f_{\overline{p}N}$ the annihilation channels are observed as a strong imaginary part and a small, almost vanishing, real part. Taking this observation as a starting point we derive from the elementary $\overline{p}N$ scattering amplitude the free space T-matrix $t_{\overline{p}N}(q,\sqrt{s}) \sim V_{\overline{p}N}(\sqrt{s})F(q)$ where the energy dependent on-shell amplitude $V_{\overline{p}N}$ is obtained from the antiproton-proton scattering data and $F(q)$ is an off-shell form factor of gaussian shape and depending on the momentum transfer q. The on-shell amplitudes are complex. The imaginary part is fixed by the optical theorem and the real part is calculated by dispersion theory [1]. We assume isospin independence, hence $t_{\overline{p}p} \equiv t_{\overline{p}n}$. The antiproton-nucleus interaction is then obtained in impulse approximation by folding t_{pbarN} with HFB densities. The resulting optical potentials are dominated by large imaginary parts, in agreement with empirical parameterizations. From the $\overline{p}A$ Schroedinger equation one finds the absorption cross section in closed form as

$$\sigma_{abs} = -\frac{2\widetilde{m}}{k\hbar^2}\int d^3r \Psi^{(+)\dagger}(\mathbf{k},\mathbf{r}) \Im U_{opt}(\mathbf{r}) \Psi^{(+)}(\mathbf{k},\mathbf{r}) \quad , \quad (1)$$

where $\widetilde{m}$ is the reduced mass and k the wave number. Since $\Im U_{opt} = W_p + W_n$ is given by the sum of proton and neutron components which, in turn, are directly determined by the corresponding densities, the close relationship of the absorption process to the nuclear density distributions is apparent [1]. However, U_{opt} is also contributing to all orders to the optical model wave functions $\Psi^{(\pm)}$, leading to a strong suppression of the incoming flux in the nuclear interior. Results for the annihilation of antiprotons on the Ni isotopes at $T_{Lab} = 400$ MeV are shown in Fig.1 and compared to the HFB rms radii by normalizing the curves at $A = 58$. The remarkable agreement in the mass dependence shows that antiproton absorption is indeed an ideal tool for neutron skin measurements.

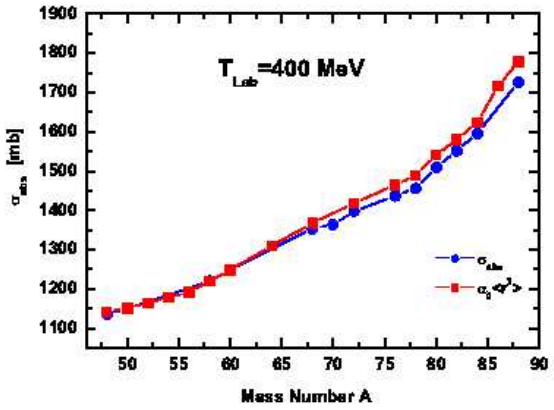

Figure 1: Antiproton absorption cross sections on Ni isotopes at $T_{Lab} = 400$ MeV are compared to the HFB rms-radii. The curves are normalized at $A = 58$.

References

[1] H. Lenske, P. Kienle, Phys.Lett. B (2005) submitted.
[2] P.Kienle, NIMB **214** (2004) 193.
[3] The AIC Proposal at FAIR, GSI, Jan. 2005.
[4] W. M. Bugg et al., Phys. Rev. Lett. **31** 475 (1973).

NQMA-EXP

Nuclear & Quark Matter Experiments

Probing the Coulomb field in relativistic collisions

P.Napolitani[1,2,*] for the CHARMS collaboration

[1]GSI, Darmstadt, Germany; [2]IPN, Orsay, France

Two main questions determine the recent directions of the research in nuclear dynamics. One is the role of the Coulomb field in diluted nuclear matter: in cosmological objects (e.g. neutron stars, supernovae) theoretical studies relate it to the formation of crystalline structures by frustration effects [1]. The Coulomb field can be probed experimentally at the nuclear scale, where it rules the mechanism of disintegration in multifragmentation reactions. Another question is the research of the conditions (density and excitation) that determine the appearing of a bimodal behaviour of the heaviest-residue distribution, which can be related to the order parameter of a liquid-gas phase transition [2].

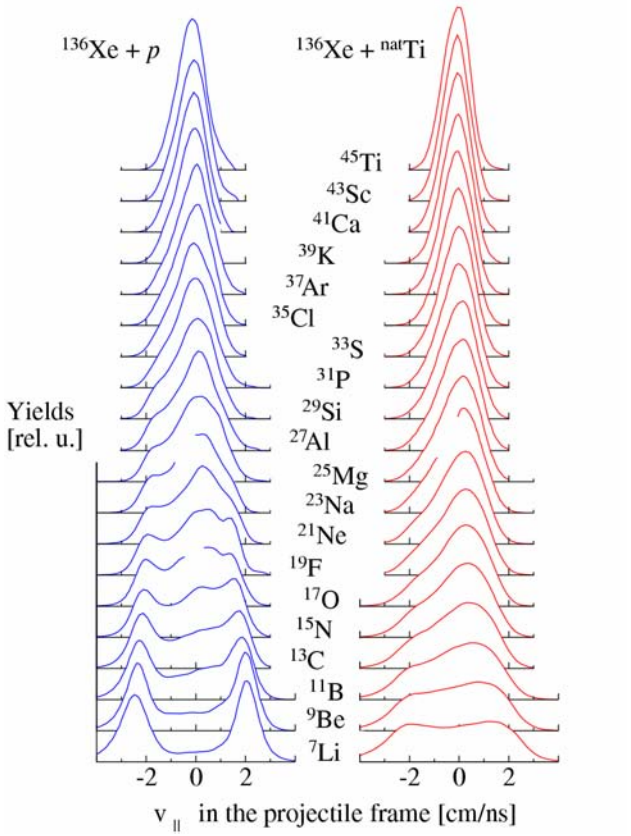

Fig. 1. Normalized experimental velocity spectra, measured for a series of isotopes having $N = Z + 1$ in the systems ^{136}Xe+^{1}H (left) and ^{136}Xe+Ti (right) at 1 *A* GeV.

Among the inclusive measurements, the FRS operated in inverse kinematics provides unique experimental information about the reaction kinematics. The high resolution and absence of energy thresholds in the detection of ejectiles allow for extracting the full longitudinal-velocity spectrum of each nuclide formed as a reaction fragment [3]. Moreover, the possibility of employing liquid-hydrogen and heavy targets allows for studying the largest variation of excitation energy at a given incident energy in relativistic collisions. In Fig. 1, a series of longitudinal-velocity spectra recently measured for the ^{136}Xe+^{1}H, Ti systems [4], is shown for twenty isotopes having N=Z+1. The velocities are shown in the reference frame of the projectile. For both reactions, each spectrum can be decomposed in a double-humped shape and a wide Gaussian-like component. The widths and the relative weights of these components vary as a function of the isotope. Two wide humps are mostly evident in the lightest isotopes produced in ^{136}Xe+^{1}H. Also the system ^{136}Xe+Ti manifests the presence of a two-humped component for isotopes lighter than ^{15}N. As the two humps are largely spaced, the system ^{136}Xe+^{1}H shows clearly the superposition of the Gaussian-like and the two-humped contribution. The high resolution of the spectra even shows that the central Gaussian-like component is shifted in forward directions with respect to the two-humped component.

Multifragmentation reactions are characterised by the simultaneous disintegration of the nuclear system into several fragments. The concept of simultaneity is related to the Coulomb field: the nucleus disassembles so rapidly (10^{-22}-10^{-21}s) that the fragments can exchange mutual interactions while they are accelerated by the Coulomb field of the system. For this reason, the shape of the velocity distributions is directly associated to the multiplicity and size of fragments. Two-humped shapes reflect an asymmetric split: we observe one light fragment repelled by the heavy partner at velocities that even exceed fission velocities [4]. The central component is associated with more complex emission mechanisms such as a volume emission of several light fragments. The forward shift of the central shape with respect to the two-humped component is rather surprising. The central component is related to more violent collisions resulting in volume emission. If we associate more violent collisions only to larger frictional effect, we would expect a shift of the central component in the opposite direction that we observe. The forward peaking of the emission was also measured in ion-ion collisions at the FRS and related to “blast” effects induced on the spectator by the fire-ball [5]. A similar ‘highly unusual feature’ was observed in proton-induced collisions at high-energy and interpreted as the effect of shock waves [6]. In our experiment such a feature was observed for the first time in proton-induced collisions in the 1 *A* GeV incident-energy range.

** Present addr.: GANIL, Blvd. H. Becquerel, Caen, France*

References

[1] Horowitz et al., Phys. Rev. C69 (2004) 045804

[2] Ph. Chomaz et al., Phys. Rev. E64 (2001) 046114

[3] P. Napolitani et al., Phys. Rev. C70 (2004) 054607

[4] P. Napolitani, PhD Thesis, Univ. Paris XI, Sept. 2004

[5] M.V. Ricciardi et al., Phys. Rev. Lett. 90 (2003) 212302

[6] N.T. Porile et al., Phys. Rev. Lett. 43 (1979) 918

Investigation of isotopic composition of heavy residues produced in the fragmentation of ^{124}Xe and ^{136}Xe beams

D.Henzlova[a,*] for the CHARMS collaboration

[a]GSI, Germany

The isotopic compositions of the residues produced in the heavy-ion collisions attain an increasing interest since they provide information on the nuclear equation of state. The range of the isotopes presently available for similar investigations is, however, constrained by the mass resolution of the majority of the large-acceptance experimental devices. This corresponds to the mass range generally not exceeding $A \sim 20$. With the use of a high-resolution magnetic spectrometer, such as the Fragment Separator (FRS) at GSI, mass identification may be extended over the whole mass range up to the mass of the heavy projectile.

Two dedicated experiments on the investigation of the isotopic composition of the residues produced in the fragmentation of ^{124}Xe and ^{136}Xe beams in a lead target at 1 *A* GeV have been performed at the FRS. The main focus was to provide fully isotopically identified residues in the whole mass range to study the dependence of the final isotopic composition on the *N/Z* of the projectile. The experiments have been performed using the standard FRS set-up with several settings of magnetic fields to cover fragments with different *N/Z*. More details on the experimental technique may be found in [1].

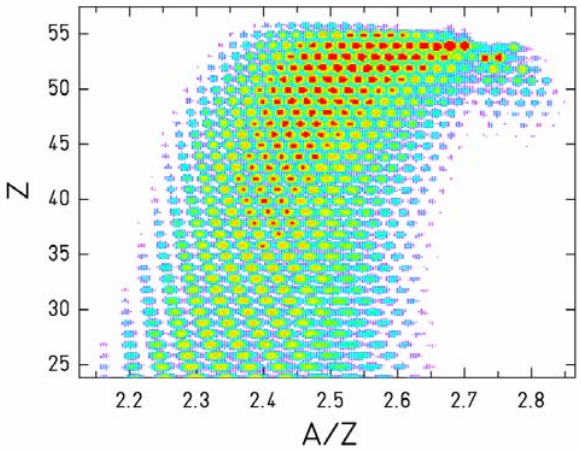

Figure 1: The identification pattern for the reaction ^{136}Xe+Pb at 1 *A* GeV, in logarithmic color scale. Yields of different isotopes are not normalized to the beam doses.

Figure 1 displays the residues identified in the charge range $25<Z<56$ in the fragmentation of ^{136}Xe. A clear separation between the single isotopes is observed together with a broad range of isotopes measured for each element.

Figure 2 shows the mean N-over-Z ($<N>/Z$) ratio deduced from the measured isotopic distributions. The $<N>/Z$ of the residues close to the projectile decreases rather steeply with charge as a consequence of the dominating neutron evaporation. For lower charges (higher excitation energies) the $<N>/Z$ changes more moderately and surprisingly the difference between the final $<N>/Z$ is preserved over the whole charge range. It has been shown [2] that the isotopic composition of the final residues after the long sequential evaporation gradually approaches the region of equilibrium probabilities of proton and neutron emission, known as the evaporation-attractor line (EAL). For high excitation energies, the final isotopic composition should therefore no longer depend on the *N/Z* of the initial system. The difference between the $<N>/Z$ of residues from ^{136}Xe and ^{124}Xe projectiles preserved in the whole nuclear-charge range may be interpreted as an indication for the break-up of a highly excited nucleus. In the break-up process part of the initial excitation energy is consumed in the formation of smaller fragments, reducing thus the excitation energy available for further evaporation.

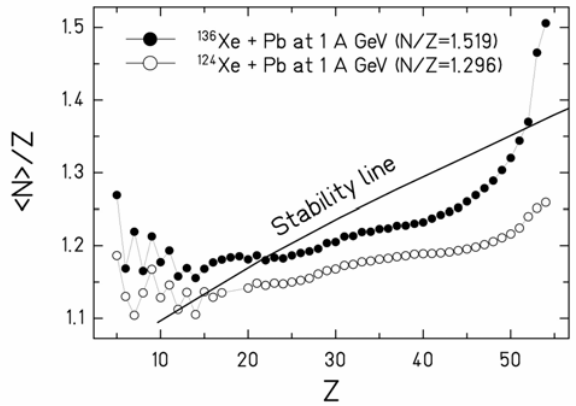

Figure 2: Comparison of the $<N>/Z$ of the fragmentation residues from ^{136}Xe and ^{124}Xe at 1 *A* GeV.

Thanks to the full isotopic identification available with the FRS, the connection between the $<N>/Z$ of the final residues and the *N/Z* of the fragmenting projectile is followed over the full nuclear-charge range. Provided the *N/Z* evolution in the dynamical stage of the reaction is known, this is particularly well suited to study the sensitivity of the final isotopic composition to the conditions at the freeze-out of the break-up stage as proposed in [3].

* on leave from NPI, Rez, Czech Republic

References

[1] T. Enqvist *et al.*, Nucl. Phys. A 658, 47 (1999)

[2] R.J. Charity, Phys. Rev. C 58 (1998) 1073

[3] K.-H. Schmidt *et al.*, Nucl. Phys. A 710 (2002) 157

Spectroscopy of η-mesic nuclei using recoilless (d,^{3}He) reaction

Hans Geissel[A], Albrecht Gillitzer[B], Kenji Gomikawa[C], Ryugo S. Hayano[C], Satoru Hirenzaki[D], Kenta Itahashi[E], Masahiko Iwasaki[E], Paul Kienle[F,G], Karl Lindberg[H], Yuri Litvinov[A], Gottfried Münzenberg[A], Haruhiko Outa[E], Miki Shindo[C], Ken Suzuki[F], Per-Erik Tegnér[H], Agnieszka Trzcińska[I], Helmut Weick[A], Toshimitsu Yamazaki[J], and Irina Zartova[H]

[A]Gesellschaft für Schwerionenforschung, Darmstadt, Germany; [B]Institut für Kernphysik, Forschungszentrum Jülich; [C]Department of Physics, University of Tokyo; [D]Department of Physics, Nara Women's University; [E]Advanced Meson Science Laboratory, RIKEN; [F]Physik-Department, Technische Universität München; [G]Stefan Meyer Institut für subatomare physik of the Austrian Academy of Sciences; [H]Department of Physics, Stockholm University; [I]Heavy Ion Laboratory, Warsaw University ; [J]RI Beam Science Laboratory, RIKEN

Deeply bound pionic atoms were for the first time produced and discovered in 1996 at GSI by a novel technique of using the ^{208}Pb(d,^{3}He) reaction at T_d=600MeV [1]. In contrast to the conventional method to produce exotic atoms, the pion is directly produced in the nuclear reaction and substitutes one of the valence neutrons in the target nucleus. Fulfilling the zero-momentum transfer condition additionally delivers two unique features, namely the enhancement of the cross section to form such deeply bound states, and the selective population of the substitutional state, both of which are important for a precision determination of the binding energy and the width of the states. We performed subsequently a series of experiments for a precise measurement of the deeply bound pionic 1s state, from which we determined the s-wave pion-nucleus optical potential [2, 3, 4]. With their uniqueness and precision, the data on deeply bound pion-nucleus states initiated an exploration of their sensitivity to the partial restoration of chiral symmetry in the nuclear medium [4, 5].

We extended the program to the spectroscopy of even more exotic systems, namely η meson-nucleus bound states. Since the η meson is a neutral particle, the system is bound solely by the strong interaction. Such a system should not be seen as an exotic atom but as a new kind of exotic nucleus. We use the ^{12}C(d,^{3}He) reaction with T_d=3.5GeV provided from SIS. The experimental feasibility and the impact on chiral models are discussed in Refs. [6, 7] (Fig.1). A serious problem is the very high rate of protons from the break-up of the incident deuterons reaching up to 10^8/s. We have developed a new type of Cherenkov counter (TORCH) [8], which is only sensitive to the slow ^{3}He nuclei ($\beta \simeq 0.87$) while being totally blind to the fast background protons ($\beta \simeq 0.94$) even at a rate of 10^8/s. This indispensable background suppression capability of the experiment is realized by making use of the different total reflection conditions of the photons at the radiator surface which are created at different Cherenkov emission angles for ^{3}He and protons selected by the Fragment Separator (FRS). To achieve this, the proper refractive index of the Cherenkov radiator has to be chosen. Simultaneously a good position resolution is ensured by measuring the photon intensity distribution as a function of the x coordinate with PMTs (Fig.2). TORCH detectors are placed at the central and final focal plane of the FRS in order to do Time-of-Flight measurements.

Although ready in the beginning of 2004, the TORCH detector was further improved to have better rejection capability for delta-electrons produced from background protons by increasing the quality of the radiator.

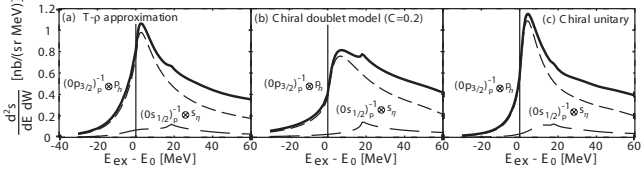

Figure 1: The theoretical spectra of ^{12}C(d,^{3}He)^{11}B$\otimes\eta$ reaction at T_d=3.5 GeV calculated by (a) the t-ρ approximation, (b) the chiral doublet model with C=0.2, and (c) the chiral unitary approach. From Ref. [7]

Figure 2: View inside the TORCH detector.

References

[1] T. Yamazaki *et al.* Z. Phys. A **355** (1996) 219
[2] H. Gilg, K. Itahashi *et al.* Phys. Rev. C **62** (2000) 025201-025202.
[3] H. Geissel *et al.* Phys. Rev. Lett. **88** (2002) 122301.
[4] K. Suzuki *et al.*, Phys. Rev. Lett. 94 (2004) 072302.
[5] E.E. Kolomeitsev, N. Kaiser and W. Weise, Phys. Rev. Lett. **90** (2003) 092501.
[6] R.S. Hayano, S. Hirenzaki and A. Gillitzer, Eur. Phys. J. **A6** (1999) 99.
[7] H. Nagahiro, D. Jido and S. Hirenzaki, Phys. Pev. C. **68** (2003) 035205.
[8] T. Yoneyama, Master thesis, Tokyo Institute of Technology.

Au+Au around the Balance Energy

J. Łukasik and W. Trautmann for the INDRA-ALADIN Collaboration
Gesellschaft für Schwerionenforschung mbH, D-64291 Darmstadt, Germany

The study of the directed flow for the Au + Au reactions, measured with the 4π detector INDRA at the GSI facility [1], has been continued and revealed new observations [2]. The excitation function of the directed flow has been found to increase monotonically with incident energy, contrary to [3], and to change its sign between 50 and 60 AMeV. The observed anti-flow has been linked to the strong Coulomb effects in Au + Au system.

Values for the balance energy in Au + Au, at which the directed flow vanishes, have previously been determined by extrapolating from higher energies [4, 5, 6], and also by searching for the minimum of flow [3]. The extrapolations yielded values between 47 and 56 AMeV. The parabolic excitation function of flow reported in [3] showed a minimum at $E_{\rm bal} = 42 \pm 4$ MeV per nucleon. Contrary to this measurement, the present data yield a monotonic excitation function with the zero-crossing energy at 54 ± 4 MeV for Z=2 particles (solid symbols in Fig. 1).

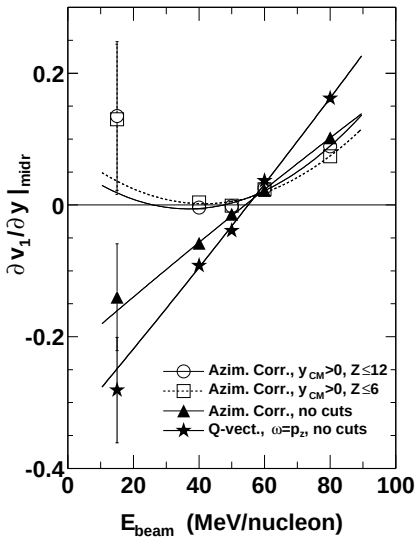

Figure 1: Excitation functions of the mid-rapidity slopes of the v_1 parameter for $Z = 2$ particles and impact parameters 0-4 fm. The symbols correspond to the indicated methods and conditions used to define the reaction plane. The lines represent parabolic fits.

The parabolic excitation function of the flow parameter could be qualitatively reproduced, provided the same upper limits $Z \leq 12$ as in [3] or $Z \leq 6$ were used in the analysis (Fig. 1, open symbols).

The origin of the observed anti-flow in the present data is illustrated in Fig. 2. For peripheral collisions at high incident energy (top panels) the deflections of the projectile and target, as represented by the three-dimensional Q-vector, are small. The Coulomb repulsion from the heavy residues leads to the apparent depression of helium yields near the entrance-channel rapidities and to maximum intensities at lower absolute rapidity, as discussed in [7]. The stronger deflection of mid-rapidity particles is evident from the rapid rise of v_1 with $y_{\rm cm}$ which, at $y_{\rm cm} \approx 0.2$, starts to be modified by the effect of the spectators. The resulting pattern appears similar to the two-component flow obtained in QMD calculations [8].

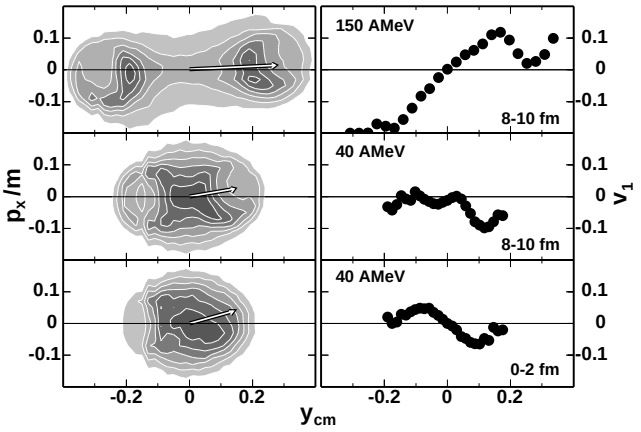

Figure 2: Contour plots (in linear scale) of the in-plane component of the transverse velocity (p_x/m) versus the center-of-mass rapidity $y_{\rm cm}$ (left column) and the coefficient v_1 as a function of $y_{\rm cm}$ (right column) for $Z = 2$ particles and three selected cases of incident energy and impact parameter as indicated. The arrows represent the directions of the three-dimensional Q-vector.

At 40 AMeV, and the same peripheral impact-parameters (middle panels), the structure of v_1 as a function of $y_{\rm cm}$ is qualitatively the same as at 150 AMeV but compressed into a smaller range of absolute rapidity. In central collisions, at this energy, the distributions are even more compact (bottom left). This concentration of mass and charge, apparently, causes the $Z = 2$ particles to be preferentially deflected to the opposite side. The resulting flow, evaluated around mid-rapidity, is negative (anti-flow). Clearly, Q-vectors that do not contain the momenta of the heavier fragments causing this deflection or shadowing will have different directions, and the flow measured relative to them may appear positive, leading to parabolic excitation functions.

The commonly invoked picture of the attractive mean field globally balancing the repulsive effect of the collisions around the balance energy seems to be too simple here to explain the observed inversion of flow. The main difference, as compared to lighter reaction systems for which this picture may hold, is the enlarged Coulomb field which not only has a strong impact on the entrance and exit channel trajectories [8] but also manifests itself in large recoil effects (larger Coulomb rings).

References

[1] J. Łukasik, W. Trautmann et al., GSI Scientific Report 2003.
[2] J. Łukasik et al., nucl-ex/0410030, Phys. Lett. B, In Press.
[3] D.J. Magestro et al., Phys. Rev. C 61 (2000) 021602.
[4] W.M. Zhang et al., Phys. Rev. C 42 (1990) 491.
[5] M.D. Partlan et al., Phys. Rev. Lett. 75 (1995) 2100.
[6] P. Crochet et al., Nucl. Phys. A 624 (1997) 755.
[7] J. Łukasik et al., Phys. Lett. B 566 (2003) 76.
[8] S. Soff et al., Phys. Rev. C 51 (1995) 3320.

Isotopic Scaling and the Symmetry Energy in Spectator Fragmentation

A. Le Fèvre[a], A. Botvina[a,l], W. Trautmann[a], and the ALADIN-INDRA Collaboration[a,b,c,d,e,f,g,h,i,j,k]

[a]GSI Darmstadt, Germany; [b]GANIL Caen, France; [c]IPN Orsay, France; [d]LPC Caen, France; [e]DAPNIA Saclay, France; [f]IPN Lyon, France; [g]INFN Napoli, Italy; [h]INFN Catania, Italy; [i]SINS Warsaw, Poland; [j]IFJ Kraków, Poland; [k]CNAM Paris, France; [l]INR Moscow, Russia

The growing interest in isospin effects in nuclear reactions is motivated by an increasing awareness of the importance of the symmetry term in the nuclear equation of state, in particular for astrophysical applications. Supernova simulations or neutron star models require inputs for the nuclear equation of state at extreme values of density and asymmetry [1, 2, 3]. The demonstration in the laboratory of the effects of the symmetry term at abnormal densities is, therefore, an essential first step within a program aiming at gaining such information experimentally [4, 5].

Isotopic scaling, or "isoscaling", a phenomenon common to many different types of heavy ion reactions [6, 7, 8, 9]. is observed by comparing product yields from otherwise identical reactions with isotopically different projectiles or targets. It is constituted by an exponential dependence of the measured yield ratios $R_{21}(N,Z)$ on the neutron number N and proton number Z of the considered product, following the relation:

$$R_{21}(N,Z) = Y_2(N,Z)/Y_1(N,Z) = C \cdot exp(\alpha N + \beta Z) \quad (1)$$

The data were obtained with INDRA at GSI, for the collisions of ^{12}C at 300 and 600 A.MeV on enriched targets of ^{112}Sn and ^{124}Sn [10]. Selected light isotopes ($Z \leq 5$) were identified over the range of polar angles $45° \leq \theta_{\rm lab} \leq 176°$. For impact-parameter selection, the charged-particle multiplicity $M_{\rm C}$ measured with the full detector was used. To reduce preequilibrium contributions, upper limits were set for hydrogen and helium isotopes. The ratios of the fragment yields measured for the two reactions obey the law of isoscaling, as illustrated in Fig. 1. It shows the scaled isotopic ratios $S(N) = R_{21}(N,Z)/\exp(\beta Z)$ (the indices 1 and 2 denote the neutron poor and neutron rich system, respectively). Their slope parameters change considerably with impact parameter, extending from $\alpha = 0.62$ to values as low as $\alpha = 0.25$ for the most central event group at 600 MeV per nucleon (Fig. 2, top).

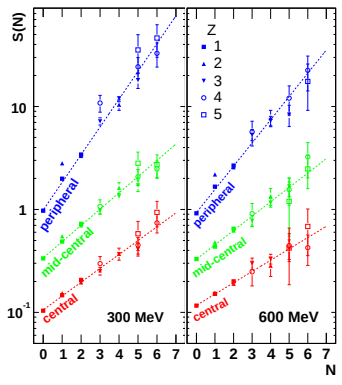

Figure 1: Scaled isotopic ratios $S(N)$ for ^{12}C + ^{112,124}Sn at E/A = 300 MeV (left panel) and 600 MeV (right panel) for 3 intervals of reduced impact parameters $b/b_{\rm max}$ (0-0.4-0.6-1) and with offset factors of multiples of three. The dashed lines are exponential fits according to Eq. (1).

In the grand-canonical approximation, assuming that the temperature T is about the same, the scaling parameters α and β are proportional to the differences of the neutron and proton chemical potentials for the two systems, $\alpha = \Delta\mu_{\rm n}/T$ and $\beta = \Delta\mu_{\rm p}/T$. As shown e.g. in [6], their connection with the symmetry term coefficient follows the relation

$$\alpha T = \Delta\mu_{\rm n} = \mu_{\rm n,2} - \mu_{\rm n,1} \approx 4\gamma\left(\frac{Z_1^2}{A_1^2} - \frac{Z_2^2}{A_2^2}\right) \quad (2)$$

where Z_i and A_i are the charges and mass numbers of the two systems. Hence, with the knowledge of the temperature and the isotopic compositions, the coefficient γ of the symmetry term can be determined from isoscaling.

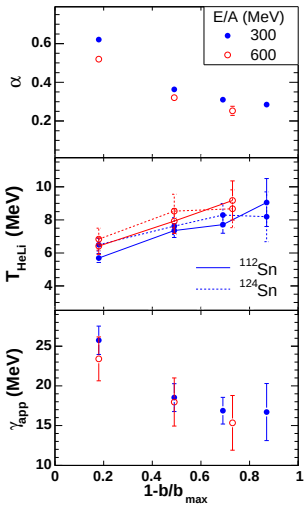

Figure 2: Isoscaling coefficient α (top), double-isotope temperatures $T_{\rm HeLi}$ (middle) and resulting $\gamma_{\rm app}$ (bottom) for E/A = 300 MeV (full symbols) and 600 MeV (open symbols), as a function of the centrality parameter $1 - b/b_{\rm max}$. The temperatures for the ^{112}Sn and ^{124}Sn targets are distinguished by full and dashed lines, respectively.

Temperature estimates were obtained from the yields of ^{3,4}He and ^{6,7}Li isotopes, and the deduced $T_{\rm HeLi}$ contains a correction factor 1.2 for the effects of sequential decay. The temperatures are quite similar for the two target cases and increase with centrality from about 6 MeV to 9 MeV (Fig 2, middle). This rise does not compensate for the decrease of the isoscaling parameter α with centrality, which implies a decreasing symmetry term coefficient γ (Eq. (2)). Deduced symmetry term coefficients are near $\gamma = 25$ MeV for peripheral and $\gamma < 15$ MeV for central collisions.

References

[1] J.M. Lattimer *et al.*, Phys. Rev. Lett. **66**, 2701 (1991).
[2] J.M. Lattimer and M. Prakash, Phys. Rep. **333**, 121 (2000).
[3] A.S. Botvina and I.N. Mishustin, Phys. Lett. B **584**, 233 (2004).
[4] Bao-An Li, Phys. Rev. Lett. **88**, 192701 (2002).
[5] V. Greco *et al*, Phys. Lett. B **562**, 215 (2003).
[6] A.S. Botvina, O.V. Lozhkin, and W. Trautmann, Phys. Rev. C **65**, 044610 (2002).
[7] M.B. Tsang *et al.*, Phys. Rev. Lett. **86**, 5023 (2001).
[8] G. A. Souliotis *et al.*, Phys. Rev. C **68**, 024605 (2003).
[9] W. A. Friedman, Phys. Rev. C **69**, 031601(R) (2004).
[10] A. Le Fèvre *et al.*, nucl-ex/0409026.

Gross Properties of Multifragment Decay at Relativistic Energies

C. Sfienti and the *ALADiN2000* Collaboration

P. Adrich, T. Aumann, C.O. Bacri, T. Barczyk, R. Bassini,S. Bianchin, C. Boiano, A.S. Botvina, A. Boudard, J. Brzychczyk, A. Chbihi, J. Cibor, B. Czech, M. De Napoli, J.-E. Ducret, H. Emling, J. Frankland, M. Hellström, D. Henzlova, K. Kezzar, G. Immé, I. Iori, H. Johansson, A. Lafriakh, A. Le Fèvre, E. Le Gentil, Y. Leifels, W.G. Lynch, J. Lühning, J. Łukasik, U. Lynen, Z. Majka, M. Mocko, W.F.J. Müller, A. Mykulyak, H. Orth, A.N. Otte, R. Palit, P, Pawłwoski A. Pullia, G. Raciti, E. Rapisarda, H. Sann, C. Schwarz, C. Sfienti, H. Simon, A. Sokolov, K. Sümmerer, W. Trautmann, M.B. Tsang, G. Verde, C. Volant, M. Wallace, H. Weick, J. Wiechula, A. Wieloch and B. Zwieglinski

A systematic study of isospin effects in the breakup of projectile spectators at relativistic energies has been performed with the ALADiN spectrometer. Four different beams, ^{107}Sn, ^{124}Sn, ^{124}La and ^{197}Au, all with an incident energy of 600 AMeV, have been used. The two proton-rich secondary beams ^{107}Sn and ^{124}La were produced at the FRS by fragmentation of a primary ^{142}Nd beam. The measurement of the charge and the momentum vector of all projectile fragments with $Z \geq 2$ has been performed with high efficiency and high resolution with the TP-MUSIC IV detector [1].
In order to investigate to which extent the isotopic composition of the excited spectator affects the gross properties of the multifragmentation pattern, charge partitions and multiplicity distributions have been analyzed and the results have been compared with the SMM prediction [2]. In

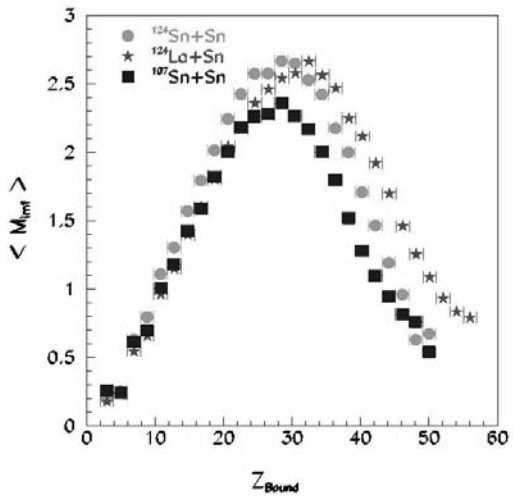

Figure 1: Experimental Rise and Fall of multifragmentation correlating the mean multiplicity of intermediate-mass fragments and $Z_{\rm bound}$.

Fig. 1, the obtained correlation between the mean multiplicity of intermediate-mass fragments, $< M_{IMF} >$, and the variable $Z_{\rm bound}$ for the ^{107}Sn, ^{124}Sn and ^{124}La systems is shown. The global universality of the Rise and Fall behavior [3] is preserved, but already some distinct differences can be observed. At small excitation energies (large $Z_{\rm bound}$ values) the curves end, as expected, approximately at the charge of the original projectiles. However, the slope of the curve is steeper in the case of the ^{124}Sn. This effect can be understood by considering that in the case of the neutron-rich system, heavy residues with low excitation energy will predominantly emit neutrons, a channel that is suppressed in the case of the two neutron-poor nuclei. In these latter cases, peripheral collisions are more spread out towards smaller values of $Z_{\rm bound}$, thus leading to a slower rise of $< M_{IMF} >$. This effect, as well as the corresponding difference in the $Z_{\rm bound}$ distribution, is in good agreement with the SMM predictions.

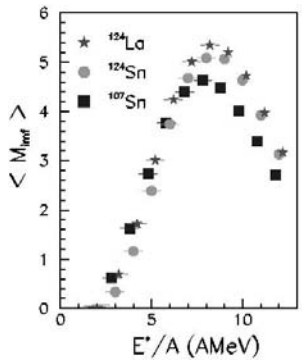

Figure 2: Prediction of the Statistical Multifragmentation Model for the mean IMF multiplicity as a function of the excitation energy for excited ^{124}La, ^{124}Sn and ^{107}Sn nuclei.

Towards more central collisions, we observe a lower maximum in $< M_{IMF} >$ for the lighter Sn isotope, whereas the two A=124 systems exhibit the same value for the maximum mean multiplicities. This mass effect, reproduced by SMM calculations (Fig. 2) is unexpected since the definition of IMF ($3 \leq Z \leq 20$) is based on the charge. Therefore, the partition space should be primarily a function of the charge of the source. In the rise, up to 6 or 7 MeV per nucleon, the number of fragments is just given by the excitation energy. The ^{107}Sn bends over more quickly towards vaporization: less neutrons are available and we may have more alpha-type fragments (like ^{8}Be, ^{12}C) that decay easily into alpha particles. Note that the absolute multiplicities are overpredicted because the calculations are performed for sources of fixed mass and not for the ensemble of spectator systems produced in the collision.
Very specific isotopic effects which support the idea of overall equilibrium at breakup have also been extracted from the mean N/Z of medium-size fragments [2].

References

[1] C. Sfienti et al., GSI Scientific Report 2003, p.232.
[2] C. Sfienti et al., nucl-ex/0410044.
[3] A. Schüttauf et al., Nucl. Phys. A 607 (1996) 457.

Flow and stopping in Ni+Ni and Pb+Pb at 0.4, 0.8 and 1.16AGeV

Z.G.Xiao,[1,4], A. Andronic[1], O.N. Hartmann[1], N. Herrmann[2], K.D. Hildenbrand[1], B. Hong[3], Y.J. Kim[1,3], M. Kirejczyk[1], P. Koczoń[1], Y. Leifels[1], W. Reisdorf[1], A. Schüttauf[1], and Z. Tymiński[1]

[1]GSI, Darmstadt; [2]Universität Heidelberg; [3]Korea University; [4]IMP, Lanzhou

This report present a systematic study on transverse flow and nuclear stopping in the central symmetric collisions of Ni+Ni and Pb+Pb at 0.4, 0.8 and 1.16AGeV. The transverse flow is extracted from the dependence of the mean kinetic energy on the mass of light charged particles(LCP) at midrapidity. The degree of stopping is obtained from their rapidity spectra.

Figure 1 shows $\langle E_{\rm kin}\rangle$ of the LCP at midrapidity as a function of the mass in Ni+Ni and Pb+Pb at three beam energies. The "slope" of the linear fit,κ, expresses the flow velocity β_r via $\kappa = 1/\sqrt{1-\beta_r^2} - 1$, and the "intercept", $E_{\rm th}$, reflects the temperature of the fireball approximately by $E_{\rm th} = 3T/2$. Both κ and $E_{\rm th}$ increase with the beam energy. The linear extrapolation of $\langle E_{\rm kin}\rangle$ to zero mass, i.e. the freeze-out temperature shows no dependence on the system size. The slope, however, exhibits a larger value in the Pb+Pb than in Ni+Ni, indicating that heavier system expands with a higher velocity.

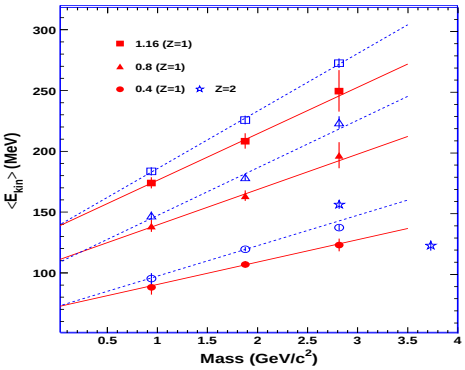

Figure 1: Dependence of $\langle E_{\rm kin}\rangle$ on the mass of LCP for Ni+Ni(solid) and Pb+Pb(open) at three beam energies

Figure 2 presents the rapidity spectra of p, d and t. The differential yield, $dN/dy^{(0)}$ is scaled to a constant system size of 100 nucleons by multiplying with $(100/A_{sys})$, where A_{sys} is the system mass. The curves are the predictions of the blast model, where β_r and T are taken from the $\langle E_{\rm kin}\rangle$ analysis as shown in fig. 1. The area of the curve is normalized to the total measured yield for each particle individually. It is shown that the scaled yield of proton is much higher in Ni+Ni than in Pb+Pb, while that of deuteron exhibits smaller difference, for tritons, however, the scaled yield becomes higher in Pb+Pb than in Ni+Ni. Heavier particles are more favored in heavier system. This is consistent with our earlier results[1], where the charge resolved cluster with $Z > 2$ is found to follow this law.

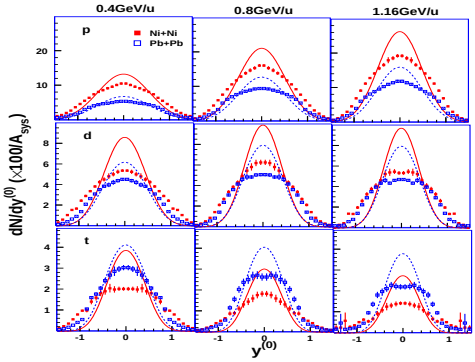

Figure 2: Reduced $dN/dy^{(0)}$ distribution of p,d and t for Ni+Ni(solid) and Pb+Pb(open). The lines are the prediction of blast model.

Another globe feature is that the measured distribution is broader than the prediction of the blast model and hence contradicts the picture of isotropic expansion of a fully stopped fireball. Considering the rapidity distribution of the light particles is insensitive to the form of the β_r profile [2], we could conclude that full stopping is not achieved in the collision. Figure 3 depicts the ratio of the RMS value of the $dN/dy^{(0)}$ spectra predicted by the blast model over the RMS of the measured $dN/dy^{(0)}$ distribution for the hydrogen isotopes. For p, the difference betwen two reaction systems is small. For d and t, however, the ratio, which reflects the degree of stopping, is much lower in Ni+Ni than in Pb+Pb, indicating higher partial transparency in lighter system. The same conclusion is drawn from the observation of "*vartl*" defined in [3].

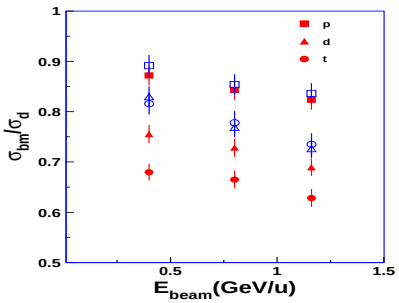

Figure 3: (a) Ratio of the RMS of $dN/dy^{(0)}$ spectra extracted from the blast model over the RMS of the measured $dN/dy^{(0)}$ spectra.

References

[1] W. Reisdorf et al., Phys. Lett. B595,118(2004).
[2] W. Reisdorf et al., Nucl. Phys. A612,493(1997).
[3] W. Reisdorf et al., Phys. Rev. Lett. 92,232301(2004).

Strangeness production with π^- beam at 1.15 GeV/c

M.L. Benabderrahmane[1], E. Cordier[1], N. Herrmann[1], Y. Leifels[2], A. Mangiarotti[1], M. Merschmeyer[1], and the FOPI Collaboration

[1]Physikalisches Institut, Universität Heidelberg, Germany; [2]GSI, Darmstadt, Germany

First measurements with a π^- beam of 1.15 GeV/c at GSI were performed with the FOPI detector. In August 2004 five different targets: Carbon, Aluminum, Copper, Tin and Lead, were irradiated with an intensity of up to $2 \cdot 10^4$ pions per spill. The aim is to investigate the strangeness production and possible in-medium modifications of the production cross section at normal nuclear matter density ($\rho = \rho_0 = 0.17$ fm^{-3}). Theoretical calculations [1] predict a dramatic change of the thresholds and cross sections for the elementary reaction $\pi^- + N \rightarrow K^0 + \Lambda, \Sigma$, when in-medium effects are taken into account.

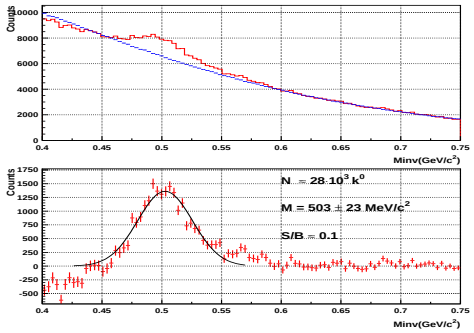

Figure 1: Invariant mass distribution for $(\pi^+\pi^-)$ pairs measured with the carbon target.

K^0_S and Λ particles can be reconstructed in the FOPI detector acceptance by combining $(\pi^+\pi^-)$ pairs detected in the central drift chamber (CDC), and $(p\pi^-)$ pairs in the forward wall (p) and CDC (π^-), respectively.

As a first preliminary result, we present the inclusive production cross sections of K^0_S meson. Figure 1 shows the invariant mass spectrum of $(\pi^+\pi^-)$ pairs for the Carbon target. In the top panel the red curve represents the the invariant mass fromm all $(\pi^+\pi^-)$ pairs found in an event, and in blue the combinatorial background from a mixed event analysis is given. In the bottom panel the signal distribution after background subtraction is shown. K^0_S mesons are clearly visible at a signal-to-background ratio of 1:10.

The inclusive cross section for the reaction: $\pi^- + X \rightarrow K^0_S + Y$ is calculated via: $N_{K^0{}_s}/(N_{\pi^-} \cdot N_{targ} \cdot \varepsilon)$. N_{π^-} is the number of incident pions, N_{targ} is the number of nuclei per cm^{-2} in the target, and ε is the efficiency for the detection of the K^0_S. The contributions to the efficiency ε are: branching ratio, geometrical acceptance, tracking efficiency and angular distribution. To estimate the efficiency ε, we used MC - simulations based on IQMD [2]. For the reaction $\pi^- + {}^{12}C \rightarrow K^0_S + Y$ we find an efficiency of 41% for the reconstruction of $(\pi^+\pi^-)$ pairs originating from K^0_S decays. This number is used to estimate the inclusive cross section for all targets. In Table 1 the preliminary results of reconstructed K^0_S, the number of recorded events and the inclusive cross section for each target assuming the same efficiency is given.

Target	$N_{k^0_s}$	N_{eve}	σ (mb)
^{12}C	$28 \cdot 10^3$	10^7	3.52±0.24
^{27}Al	10^3	$3.5 \cdot 10^5$	6.77±2.80
^{63}Cu	$6 \cdot 10^3$	$19 \cdot 10^5$	11.82±2.00
^{118}Sn	$2.3 \cdot 10^3$	10^6	17.82±4.50
^{208}Pb	$29 \cdot 10^3$	$1.4 \cdot 10^7$	22.37±1.50

Table 1: Statistics and preliminary results for the inclusive cross section for the various targets.

To compare the cross section of $(\pi^- + A)$ reactions to that of the elementary reaction $(\pi^- + p)$, we have to scale the cross section to account for the proton number of the target nuclei. To resolve the scaling parameter we show in Fig. 2 the inclusive cross section as function of the charge number Z of the nucleus in a logarithmic representation. The error bars are statistical only. The data were fited by a power law, which has the form: $\sigma_{inc} = a \cdot Z^b$. The result of the fit is shown in the figure 2. Within errors the parameter "b" is close to 2/3, indicating that the cross section scales with the surface ($\sigma \propto Z^{2/3}$). The second parameter "a" gives the averaged scaled inclusive cross section and amounts to about $1mb$. This has to be compared to the theoretical predictions, e.g. a cross section of 1.3 mb that is expected when disregarding all medium effects [1].

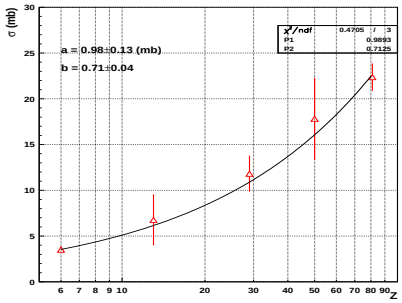

Figure 2: Inclusive cross section of the K^0_S as function of the target charge Z

A more reliable view of the in-medium reduction of the cross section will be obtained from an individual efficiency correction for the various target that is currently being evaluated. Further constraints of the reaction kinematics can be obtained from the analysis of the $K^0_S - \Lambda$ coincidences of which about 1000 are contained in the presently available data samples for the carbon and lead targets.

References

[1] K.Tsushima et al. Phys.Rev.C62(2000)064904
[2] C.Hartnack et al. Eur.Phys.J.,A1:151-169,1998

Neutral strange particle production in Ni+Ni collisions at 1.93 AGeV

X. Lopez[1], M. Merschmeyer[2], and the FOPI Collaboration
[1]LPC Clermont-Ferrand, France; [2]Physikalisches Institut, Universität Heidelberg, Germany

Strangeness production in heavy ion collisions is an intense field of experimental and theoretical researches since it is expected to provide insight into possible changes of hadron properties in a hot and dense nuclear medium [1]. The SIS energy range is best suited to investigate the in-medium properties of strange particles because the latter are produced below threshold or close-to-threshold. Indications for in-medium modifications of charged kaon properties at SIS energies have been already observed experimentally [2]. We present here recent experimental results [3] on the production of K^0_S and Λ in Ni+Ni collisions at 1.93 AGeV measured with the FOPI detector. The data were taken in a high statistics experiment, with about 110 millions of central ($\sigma_{geo} = 760$ mb) events recorded.

The neutral strange particles are identified by reconstruction of the invariant mass of their charged decay products measured in the FOPI Central Drift Chamber. K^0_S and Λ are reconstructed via $K^0_S \to \pi^+\pi^-$ (branching ratio 68.6 %) and $\Lambda \to p\pi^-$ (branching ratio 63.9 %), respectively[1]. Conditions on track quality and on geometrical and kinematic properties are applied in order to suppress the combinatorial background.

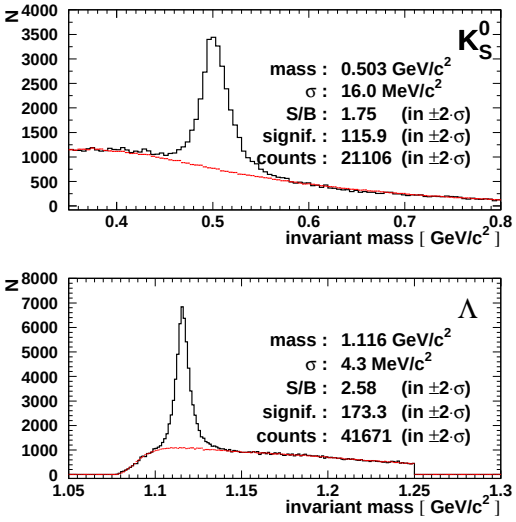

Figure 1: Invariant mass spectra of $\pi^+\pi^-$ (top) and $p\pi^-$ (bottom) pairs. The solid and dashed histograms show the combinatorics and mixed-events background respectively.

Figure 1 shows the invariant mass spectra of $\pi^+\pi^-$ and $p\pi^-$ pairs fulfilling the reconstruction requirements for central ($b_{geo} < 3.3$ fm, $\sigma_{geo} = 350$ mb) reactions. The combinatorial background (dashed histograms) is estimated by using the event-mixing technique. In the present analysis, a total of $\sim 34 \cdot 10^6$ events were analyzed. After background subtraction, more than $2 \cdot 10^4$ K^0_S and $4 \cdot 10^4$ Λ are reconstructed with signal-to-background ratios of 1.8 and 2.6, respectively. The widths of the peaks of 16.0 MeV/c^2 (K^0_S) and 4.3 MeV/c^2 (Λ) are due to the detector resolution.

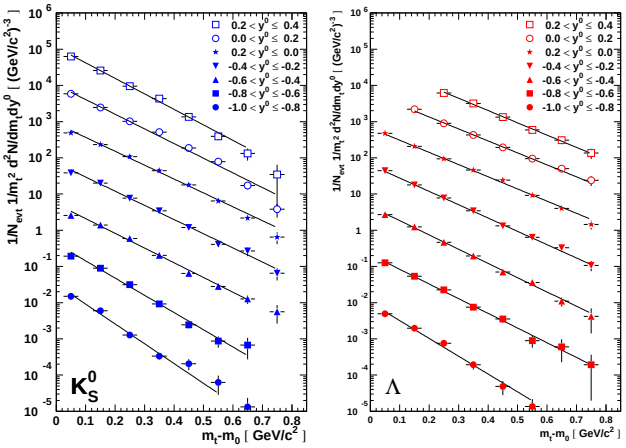

Figure 2: Transverse mass spectra of K^0_S (left) and Λ (right) for several rapidity bins ($y^0 = y/y_{cm} - 1$).

Figure 2 shows the transverse mass spectra ($m_t = \sqrt{p_t^2 + m_0^2}$) of K^0_S and Λ particles for several rapidity bins indicated on the figure. The spectra are corrected for the detector efficiency by means of a complete simulation of the FOPI detector using the GEANT package. In order to compile all spectra in one plot they are multiplied by 10^n starting from the lowermost spectrum ($n = 0$) to the uppermost spectrum ($n = 6$). If particles are emitted by a thermal Boltzmann-like source, their behaviour is then described by the following simple function:

$$\frac{1}{m_t^2}\frac{d^2N}{d(m_t - m_0)dy^0} = A \cdot \exp\frac{-(m_t - m_0)}{T_B} \qquad (1)$$

within a narrow window of rapidity dy^0. Both the inverse slope parameter (T_B) and the integration constant (A) are functions of rapidity. Each spectrum is adjusted with this function and the results are displayed by the solid lines. This allows to extract the rapidity distributions of the inverse slope parameter T_B and the rapidity density distributions dN/dy^0 by integrating the fitting function from $m_t - m_0 = 0$ to ∞.

For a thermalized system, the inverse slope parameter corresponds to the particle temperature at freeze-out. For an isotropically emitting source, the Boltzmann temperature T_B has a simple dependence on rapidity:

$$T_B = \frac{T_0}{\cosh y} \qquad (2)$$

where T_0 is the effective temperature at mid-rapidity.

In the following figures the circles indicate measured data points for K^0_S and Λ while the squares denote points

[1]Λ from $\Sigma^0 \to \Lambda\gamma$ are also included in the Λ signal.

reflected with respect to mid-rapidity. The results include only statistical errors. The stars correspond to previously measured distributions of K^+ [4] and protons [5] in the same reaction. The upper plot in Fig. 3 shows the T_B rapidity distribution for the K^0_S. A good agreement is found between K^0 and K^+. An effective temperature of 111±1 MeV is extracted from the fit using equation 2. The lower plot of the figure depicts the corresponding results for the Λ with an effective temperature of 125±1 MeV. The comparison to protons shows that both measurements roughly agree around mid-rapidity but differ significantly at projectile and target rapidities. This difference can be attributed to the presence of cold spectator matter.

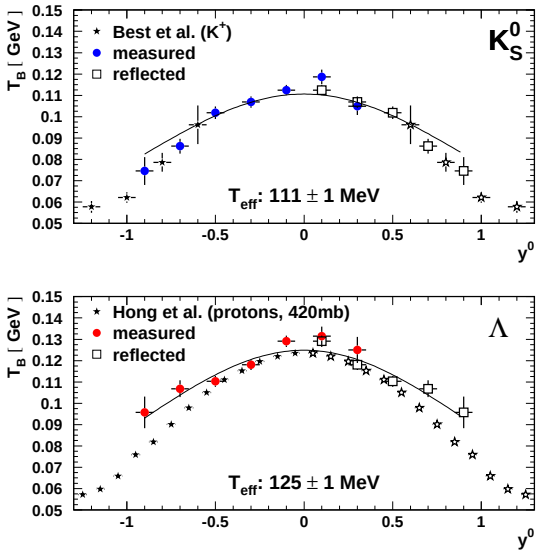

Figure 3: Inverse slope parameter distributions of K^0_S (upper plot) and Λ (lower plot). The stars correspond to previously measured K^+ [4] and protons [5].

The rapidity density distributions are presented in Fig. 4. The distributions for K^0_S and Λ particles are corrected for the corresponding branching ratios. In addition the original yields of K^0_S are multiplied by a factor 2 in order to take into account K^0_L. The upper plot shows a comparison between K^0 and K^+ distributions which are found very similar in the overlap regions around target/projectile rapidities. The total K^0 production yield per collision of 0.074±0.005 is obtained from a Gaussian fit to the data.

The dN/dy^0 distribution of Λ is displayed in the lower panel of Fig. 4 and is compared to the one of protons (down-scaled in order to have the same integral as the Λ data). One observes a pronounced longitudinal spread of the proton distribution which could be an indication for a large degree of transparency in the Ni+Ni system. Unlike protons, Λ are produced in the fireball and scatter with the surrounding nuclear medium leading to a more narrow distribution. The Λ production yield per collision is 0.120±0.004.

The curves in both plots denote the Siemens-Rasmussen distributions [6] for two different sets of temperature T and radial expansion velocity β_r. The dashed (solid) line corresponds to T =92 (100) MeV and β_r = 0.32 (0.23). While kaons are insensitive to a change of the two parameters and fully agree with the Siemens-Rasmussen distribution, a difference is visible for Λ. This confirms that despite the fact that their yield distribution is significantly different from that of protons, even Λ are not fully thermalized.

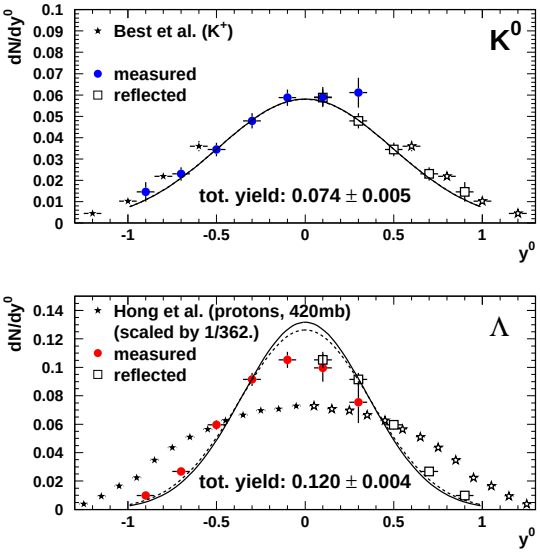

Figure 4: Rapidity density distributions of K^0 (upper plot) and Λ (lower plot). The stars correspond to previously measured K^+ [4] and protons [5].

The large statistics of reconstructed K^0_S and Λ allows for more detailed studies on e.g. the centrality dependence of the production yield and flow [3, 7] as it has been already investigated at the AGS [8]. This should help to improve our understanding of production mechanisms for strange particles close to threshold.

References

[1] For reviews, see e.g. W. Cassing and E. Bratkovskaya, Phys. Rep. 308 (1999) 65; C.M. Ko, V. Koch, G. Li, Ann. Rev. Nucl. Part. Sci. 47 (1997) 1, and ref. therein.

[2] N. Herrmann, K. Wisniewski, Acta Phys. Polon. B 35 (2004) 1091; P. Senger, Prog. Part. Nucl. Phys. 53 (2004) 1, and ref. therein.

[3] X. Lopez, PhD thesis, Clermont-Ferrand University (2004); M. Merschmeyer, PhD thesis, Heidelberg University (2004).

[4] D. Best et al., Nucl. Phys. A 625 (1997) 307.

[5] B. Hong et al., Phys. Rev. C 57 (1998) 244.

[6] P.J. Siemens, J.O. Rasmussen, Phys. Rev. Lett. 42 (1979) 880.

[7] FOPI collaboration, in preparation.

[8] M. Justice et al., Phys. Lett. B 440 (1998) 12; P. Chung et al., Phys. Rev. Lett. 85 (2000) 940; P. Chung et al., Phys. Rev. Lett. 86 (2001) 2533.

Analysis of Λ-Deuteron Correlations in Ni + Ni reactions

N. Herrmann[1], M.L. Benabderrahmane[1], E. Cordier[1], A. Mangiarotti[1], M. Merschmeyer[1], and the FOPI Collaboration

[1]Physikalisches Institut, Universität Heidelberg, Germany

The two body final state Λ - hyperon + deuteron represents one of the possible decay channels of the kaonic cluster state ppnK$^-$ proposed in [1]. Heavy ion collisions at beam energies close to the strangeness production threshold could offer an alternate way to produce these exotic states that have been observed so far only in kaon induced reactions [2, 3].

The FOPI data set of 10^8 recorded events of Ni+Ni collisions at an incident energy of 1.93 AGeV was analyzed. About 65k Λ - baryons were found under selection criteria that give a signal - to - background ratio of about 5:1. The events containing those Λ were inspected for the existence of Λ-d correlations. The deuterons were identified by their specific energy loss in the central drift chamber and their momentum, their purity is about 70%.

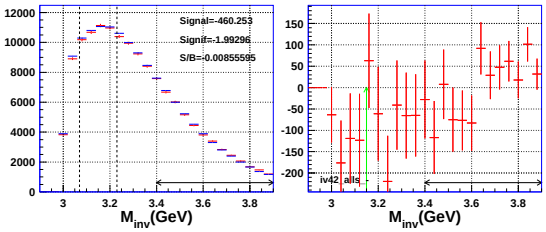

Figure 1: Distribution of invariant mass for Λ-d pairs. On the left side the correlated pairs within one event (red) are compared to mixed pairs from different events (blue). The distributions are normalized in the range indicated by the horizontal arrow. The right panel shows the difference of both distributions. The color code and the layout is kept for all following figures.

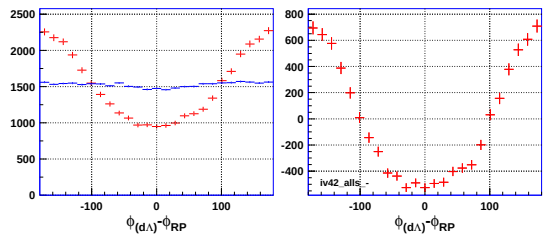

Figure 2: Distribution of azimuthal angle of Λ-d pairs with respect to the reaction plane (RP).

The reconstructed invariant mass distribution of Λ-d pairs is compared in Fig. 1 to the mixed event distribution where Λ candidates are combined with deuterons measured in different events of the same charged particle multiplicity (registered in FOPI's forward wall). The shape of the invariant mass distribution is not well reproduced by the event mixing. The main reasons for this mismatch were identified as: 1) Deuterons and Λ hyperons are emitted preferentially into the reaction plane. Therefore also the pairs show this preferred direction (Fig. 2). Hence, the events were rotated in a way that the reaction planes are aligned. 2) The difference of the azimuthal angles of a given pair is shown in Fig. 3. At small difference angles a deficit is found with respect to the mixed event sample. This is caused by the particle reconstruction efficiency that is lower for intercepting and close-by tracks, an effect that is not present when tracks from different events are combined. The distortions can be avoided by eliminating all track pairs from the analysis, where the deuteron track crosses any of the daughter tracks of the Λ hyperon.

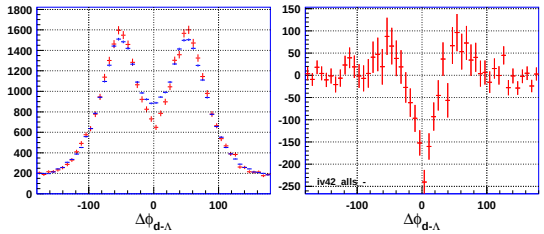

Figure 3: Distribution of difference of azimuthal angle.

The final result after removing the artificial correlations and additionally requiring a pair rapidity of $y < 0.65$ is shown in Fig. 4 in comparison to MC simulations where the same procedures and selection criteria were employed for data and simulations. It was verified that a resonance introduced into IQMD Ni+Ni events can be reconstructed correctly (middle row) while no resonance like structure is generated due to the method (lower row). The remaining excess in the data has a mean mass of 3.16 GeV, a width of $\Gamma \approx 100$ MeV and a statistical significance of 4.7. To which extent this finding is compatible with [2] is subject to further investigations.

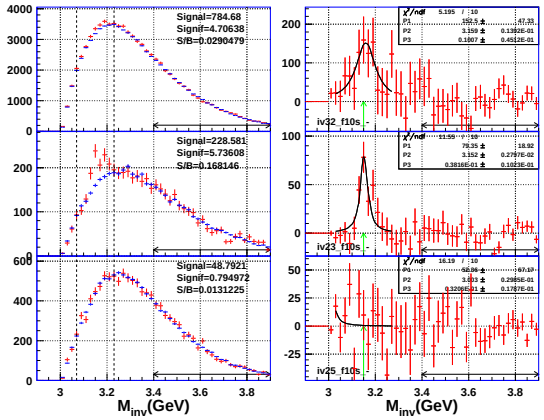

Figure 4: Distributions of invariant mass of Λ-d pairs in data (top), signal - MC (middle) and background - MC (bottom).

References

[1] Y. Akaishi, T. Yamazaki, Phys. Rev. **C 65** (2002) 044005.
[2] M. Iwasaki *et al.*, submitted to PLB (nucl-ex/0310018).
[3] T. Suzuki *et al.*, Phys.Lett .**B 597** (2004) 263.

Search for K Nuclear Clusters in Nuclear Collisions with FOPI

L.Fabbietti [1], N. Herrmann [2], P.Kienle [1, 3], K. Suzuki [1], T. Yamazaki [4] and J. Zmeskal [3]

[1] Physik Department, Technische Universität München,Germany ,[2] Physikalisches Institut der Universität Heidelberg, Germany, [3]Stefan Meyer Institut für subatomare Physik, Wien, Austria, [4] Heavy-Ion Nuclear Physics Laboratory, RIKEN, Japan

We propose to search for $\overline{K}$ nuclear clusters (ppK^-, $ppnK^-$, $pppK^-$, $pppnK^-$ and $ppnnK^-$) as residues in nuclear collisions. These kaonic nuclei have recently been predicted by [1] to be narrow discrete bound states with large binding energies of about 100 MeV, so that their main decay channels to $\Sigma\pi$ are energetically forbidden. Due to the strong K^-p attraction these $\overline{K}$ nuclei are expected to be enormously condensed systems with an average nucleon density as much as 0.5 fm^{-3} and thus are called $\overline{K}$ *clusters*. Very recently, experimental evidences [2] for T=0 $ppnK^-$ and T=1 $pnnK^-$ clusters have been obtained at KEK from ^{4}He(stopped-K^-,n) and ^{4}He(stopped-K^-,p) reactions, respectively. The observed $\overline{K}$ binding energies are substantially larger than the predicted ones.

We propose to produce and identify $\overline{K}$ clusters in nuclear collisions by making use of the excellent capability of the FOPI [3]detector at GSI in identifying both K^0 mesons and Λ hyperon. Using 3.5 – 4.5 GeV protons on a *d* target the $\Lambda^*(=\Lambda(1405)= pK^-)$ particle serves as a doorway to form ppK^- clusters as follows:

$$p+d \rightarrow [\Lambda^* p]+K^0+p \rightarrow ppK^-+K^0+p.$$

In this reaction a missing-mass (MM) spectrum of ppK^- can be constructed using p and K^0 and according to the decay pattern:

$$ppK^- \rightarrow \Sigma^{+,-} + \pi^{+,-} + p \text{ or } \Lambda + p,$$

an invariant mass (IM) spectrum can also be built. Detailed simulation studies have been carried out for the reaction *p+d @ 4.5GeV* to check the feasibility of the measurement of the ppK^- signal. The formation cross section for the Λ^* at this energy was estimated [4] to be of about 20 μb, the probability that it combines with a proton to form a ppK^- cluster depends on the relative momentum of the two and is about *1% (P_{rel}<300 MeV/c).*

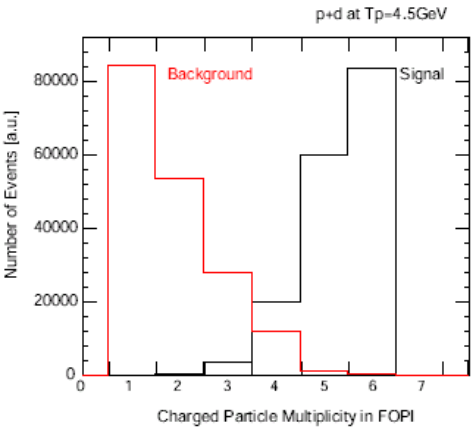

Fig 1: Charged particle multiplicity distribution for the signal and the background in p+d collisions. The multiplicity shown refers to the particles emitted in the FOPI acceptance. The formation probability for the cluster is hence about *0.2 μb* and it has to be compared with the total reaction cross-section of 78 mb. All the p+d output channels have been simulated and an online multiplicity trigger has been investigated using the FOPI plastic wall and the Barrel. Fig 1 shows tha charged particles distribution in the FOPI geometrical acceptance, requiring at least 4 charged particles in the acceptance the background is reduced of a factor 8000 respect to the signal.

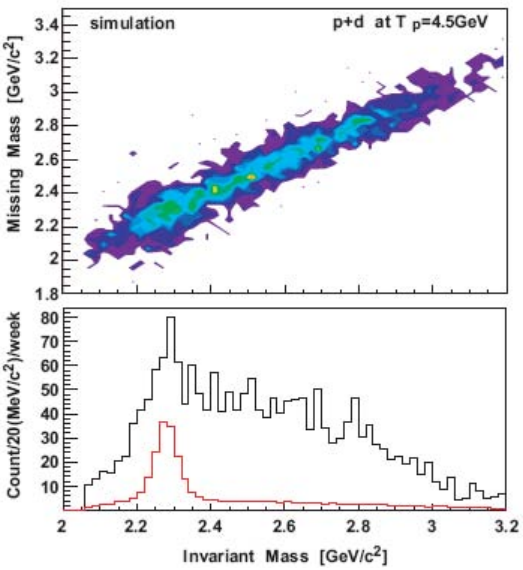

Fig 2: (upper) Correlation plot of the IM versus MM and (lower) projection along the IM axis. The red line in the lower histogramm represents the signal, the black line the sum of the signal and background.

Applying this trigger condition and assuming for the ppK^- a mass of *2279 MeV/c^2* and a width of *20 MeV/c^2*, the combination of the MM and IM analysis, together with energy and momentum conservation condition, delivers the plot shown in fig. 2. The projection on the IM axis shows that a signal to background ratio of 1/3 is achieved. This hypothesys will be verified by the scheduled beam-time at the end of 2005.

References:

[1] Y. Akaishi and T. Yamazaki, Phys. Rev. **C 65** (2002) 044005.

[2] M. Iwasaki *et al.*. submitted to Phys. Lett. B (ArXiv-nucl-ex/0310018).

[3] J.L. Ritman *et al.*, FOPI Collaboration, Nucl. Phys. Proc. Suppl. **44** (1995) 708.

[4] J.Ritmann, private comunication.

Azimuthal angular emission patterns of K^+ and K^- from Au+Au at 1.5 AGeV

M. Płoskoń[a], E.Grosse[f,g], A.Förster[b], P.Koczoń[a], B.Kohlmeyer[d], S.Lang[b], L.Naumann[f], H.Oeschler[b], W.Scheinast[f], A.Schmah[b], T.Schuck[c], E.Schwab[a], P.Senger[a], Y.Shin[c], H.Ströbele[c], C.Sturm[b], F.Uhlig[b], A.Wagner[f], and W.Waluś[e]

[a]GSI; [b]TU Darmstadt; [c]Univ. Frankfurt; [d]Univ. Marburg; [e]Univ. Cracow; [f]FZ Rossendorf; [g]TU Dresden

Relativistic heavy-ion collisions provide an opportunity to study modifications of particles properties in the hot and dense nuclear medium. Especially strange mesons and their features are expected to be influenced by the in-medium meson-baryon potential. Theoretical calculations show that the superposition of the scalar and vector constituents leads to a small repulsive K^+N and a strong attractive K^-N potential.

Additionally, the interaction of kaons and antikaons with nuclear matter is different. The strangeness conservation law inhibits the absorption probability of K^+ as they contain an $\bar{s}$-quark. K^-, however, interacting with a nucleon are easy to be converted into a Λ or Σ and a pion. Moreover, the reverse process is the dominant production mechanism of K^- (*strangeness-exchange*) at SIS energies [1].

The azimuthal angular emission patterns of kaons are expected to be sensitive observables for their in-medium properties [2]. Previous observations have confirmed the influence of the repulsive force on K^+ emerging from the hot and dense phase of the collision. An enhanced out-of-plane emission of K^+ was observed in Au+Au reactions at 1.0 AGeV and 1.5 AGeV, and also in Ni+Ni at 1.93 AGeV [3, 4]. Recent measurements presented here confirm these results (see figure 1).

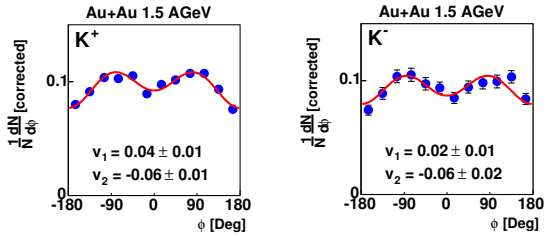

Figure 1: *Azimuthal angular emission patterns of K^+ (left) and K^- (right) measured close to mid-rapidity ($0.25 < y/y_{beam} < 0.6$) with centrality selection $b > 6.4fm$ and transverse momenta $0.2 < p_t < 0.8GeV/c$.*

Up to now the emission pattern of K^- was studied only in Ni+Ni collisions at 1.93 AGeV and it has been found to be very different than the one of K^+ [4]. The elliptic flow of K^- revealed a slight in-plane emission. In contrast to that, recent measurement of the emission pattern of K^- from non-central Au+Au at 1.5 AGeV collisions performed with the KaoS spectrometer [5] close to mid-rapidity shows an enhanced out-of-plane emission (fig. 1, right).

The predictions concerning K^-, however, suggest an almost isotropic emission pattern as a consequence of the attractive K^-N potential balancing large rescattering and absorption probability of K^- in the spectating fragments [6]. On the other hand, the observed in-plane flow of K^- from Ni+Ni at 1.93 AGeV collisions has been explained with a scenario where the strangeness-exchange reaction ($\pi Y \leftrightarrow K^-N$, with $Y = \Lambda, \Sigma$) plays a crucial role in delaying the antikaon emission from the fireball, and thus minimizing their interaction with the spectators [1, 7].

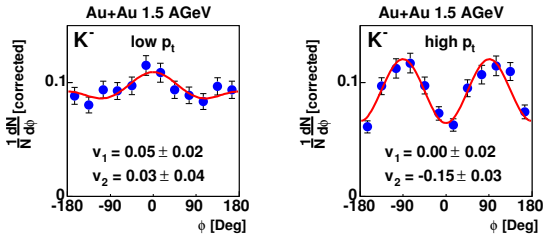

Figure 2: *Azimuthal angular emission pattern of K^- mesons with low ($0.2 < p_t < 0.5GeV/c$ - left) and high ($0.5 < p_t < 0.8GeV/c$ - right) transverse momentum measured close to mid-rapidity ($0.25 < y/y_{beam} < 0.6$) with non-central events ($b > 6.4fm$).*

Analysis of the azimuthal emission pattern as a function of the transverse momentum has revealed that K^+ show the out-of-plane emission independent of the p_t, but this is not the case for K^-. The antikaons registered with $p_t < 0.5$ GeV/c are preferentially emitted in the reaction plane and the particles with $p_t > 0.5$ GeV/c show strong out-of-plane enhancement (see fig. 2). The emission patterns of K^- can be explained in terms of two competing phenomena: one of them is indeed the influence of the attractive K^-N potential, however, the second one originates from the strangeness-exchange process. If one relates the transverse momentum of the particle to its emission time it becomes clear that the low momenta K^- are mostly influenced by the strangeness-exchange mechanism being retarded and thus emitted preferentially in-plane (no spectator shadowing). On the other hand high p_t K^- emerge early from the fireball with the spectators shadowing their flight path, causing an out-of-plane emission. It is very much required to verify this picture with detailed transport model calculations.

References

[1] A. Förster, F. Uhlig et al., PRL **91** (2003) 152301.
[2] G.Q.Li et al., Phys. Lett. B 381 (1996)
[3] Y. Shin et al., PRL **81** (1998) 1576.
[4] F. Uhlig, A. Förster et al., nucl-ex/0411021
[5] P. Senger et al., NIM **A327** (1993) 393.
[6] Z.S. Wang et al., Eur. Phys. J. A 5 (1999) 275
[7] C. Hartnack et al. PRL 90 (2003) 102302.

Dielectron production in C+C and *pp* collisions

The HADES collaboration

1 Introduction

In 2004 the HADES collaboration concentrated on completing the first experimental proposal S262 focused on dielectron production in C+C and *pp* collisions. Two dedicated production runs using carbon and proton beams of 1 *A*GeV and 2.2 *A*GeV kinetic energy, respectively, were successfully conducted. Based on experiences gained in a first commissioning run using the liquid hydrogen target built at Orsay in late 2003, effective data taking in the proton production run was possible. Since 2004 the spectrometer is fully equipped with all detector sub-systems with the exception of two outermost drift chambers (MDCIV). The main goal of the *pp* production run is to experimentally determine the detection efficiency of electron pairs. To this end, η production in both a hadronic and a leptonic decay channel is studied. We like to note that the reaction $pp \rightarrow pp\eta$ can be determined unambiguously using the missing mass technique. Detailed information on the reconstruction efficiency for electron and positron tracks, an important ingredient in the analysis of dielectron production in heavy ion collisions, can be deduced.

In the second run in August 2004, dielectron production was measured in the C+C collisions at 1 *A*GeV. In this measurement, we took data for a system in which a substantial excess of electron pairs above the pion Dalitz region was found by the DLS collaboration [2]. The analysis of these data will permit a substantial assessment of the results published by the DLS collaboration. In the meantime, we continued construction of the last two missing drift chambers (MDCIV) in IPN Orsay. Both chambers will be completed by end of 2005. Moreover, substantial progress was achieved in the design of the new inner time-of-flight system, which is based on single cell RPC detector elements. This system will replace the preliminary TOFINO detector which does not provide sufficient granularity and is achieving moderate time resolution only.

2 Dielectron production in $C+C$ collisions

In our previous status report [1] we presented preliminary results on dielectron production from C+C at 2 *A*GeV obtained in a commissioning run in 2001. Here, we show preliminary results obtained from the analysis of the high-statistics experiment performed in the end of 2002. The analysis procedure was similar to the one used for the first experiment and is described in [1, 3, 4]. The experimental set-up, however, was more advanced in the 2002 run as compared to the one realized in 2001. All six sectors were fully equipped with RICH, inner tracking chambers (MDCI/II) and time-of-flight/PreShower (META) detectors. In two sectors two outer tracking planes (MDCIII and MDCIV) were installed, for two additional sectors the third tracking plane was equipped. However, in the first instance, the data analysis concentrated on a symmetric six sector configuration not making use of detector information provided by the outer drift chambers. This allowed a direct comparison to the results obtained in the 2001 commissioning run. The two sectors with complete tracking system were utilized for tracking studies focusing on the purity and efficiency of track reconstruction. This allowed to better estimate tracking errors of the low-resolution configuration.

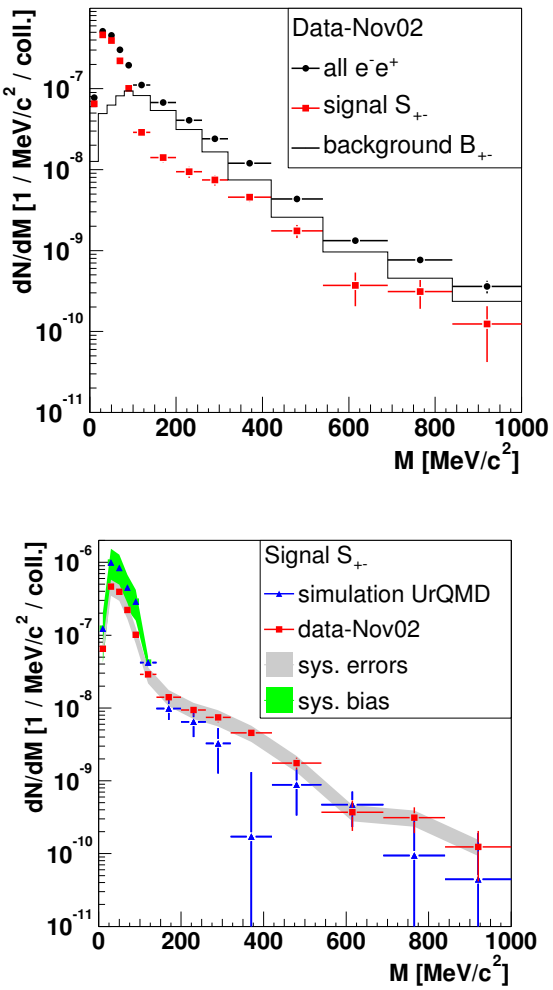

Figure 1: **Top**: Invariant-mass distributions of unlike-sign pairs (black symbols), combinatorial background (CB, solid histogram) and signal pairs (full red symbols) normalized to the number of LVL1 events from C+C collisions at 2 *A*GeV. **Bottom**: Signal (red points) after CB substraction The grey shaded area displays variations due to the pair cuts used in the analysis and the green shaded area depicts systematic bias (see text for more details). Blue symbols represent simulated signal based on events from the UrQMD transport code analyzed and normalized as the experimental data.

In the C+C experiments data acquisition is triggered by a first level trigger (LVL1) based on the hit multiplicity in the time-of-flight wall with a condition requiring 4 or

more charged particles in the acceptance. In the production run in 2002 the second level trigger (LVL2) was successfully used for the first time. It on-line selects events with at least one electron candidate inside the HADES acceptance by requiring correlated electron hits in the RICH and META detectors. With this trigger setting a pair efficiency of 92% was realized reducing at the same time the accepted event rate by a factor of 12. The recorded statistics of pairs could thus be increased by almost one order of magnitude as compared to the commissioning run in 2001. The LVL2 trigger bias was studied carefully by examination of electron distributions in events taken with and without positive LVL2 trigger. The later events were recorded applying a proper scale down to LVL1 triggered events. Besides overall scaling no significant effect was found [5].

For the analysis a total statistics of 6×10^7 LVL2, corresponding to more than 6×10^8 LVL1 events, was used. In the first stage of the analysis single electron tracks were reconstructed requiring charged tracks matched to a ring in the RICH detector as well as to a hit in the META detectors. The candidates are further cleaned by requiring a velocity $\beta \simeq 1$. From the identified single electron (and positron) tracks unlike and like-sign pair distributions were derived. Only those combinations were accepted, which contain separated tracks in all detectors, i.e. with no common hit in either the RICH, the inner MDC or the META detector. Furthermore, only tracks with an opening angle $\theta_{e+e-} > 9^0$ and with a good χ^2 from the track fitting in the inner MDCs were accepted as a valid pair. The χ^2 condition was found to represent a powerful tool to reject close pairs originating from external photon conversion and π^0-Dalitz decays which account for most of the combinatorial background. Such pairs to a large extent do not appear as separated tracks in the inner drift chambers but rather constitute single track candidates. From detailed Monte-Carlo studies we have deduced that this cut rejects more than 90% of close pairs with opening angles $\theta_{e+e-} < 3°$, still achieving an efficiency of 95% for single electron track reconstruction.

The upper panel in Fig. 1 shows the unlike-sign invariant mass distributions together with the corresponding combinatorial background. The combinatorial background N_{CB} was calculated from like-sign pairs N_{++}, N_{--} using the sum $N_{CB} = N_{++}+N_{--}$. We checked via Monte-Carlo calculations that this prescription describes our combinatorial background reasonably well. The signal pair distributions (red symbols) were obtained subtracting the combinatorial background from the unlike-sign distribution and by normalizing it to the number of accepted LVL1 triggers. The total pair statistics, after subtraction of combinatorial background and analysis cuts described above, amounts to $\sim$ 16k. The data are neither corrected for the reconstruction efficiencies nor spectrometer geometrical acceptance.

The lower panel in Fig. 1 shows a comparison of the reconstructed dielectron invariant-mass distribution with simulations. In the simulation we used 1×10^8 events obtained from the UrQMD transport model (Version 1.3) which were transported through the spectrometer using GEANT and digitized applying realistic detector response

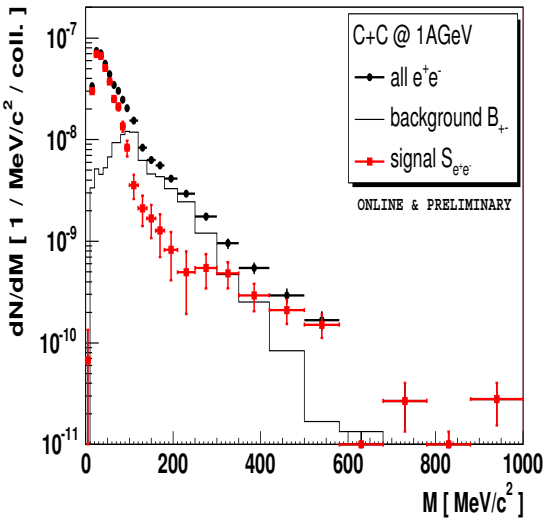

Figure 2: Invariant-mass distributions of unlike-sign pairs (black symbols), combinatorial background (solid histogram) and signal pairs (full red symbols) from C+C collisions at 1 AGeV.

functions. The data obtained in that way was processed through exactly the same analysis procedure as it was used for the experimental data. Finally, the simulation events were normalized to the number of UrQMD events passing the LVL1 trigger condition used for the real data. We would like to point out that the simulated spectra contain contributions from π^0 and η decay only. It is apparent that in the low-mass region (dominated by π^0 Dalitz pairs) the simulation overestimates the data but in the higher-mass region the simulation and data agree rather well. The presented results are fully consistent with our first analysis presented in the previous report [1]. The systematic errors of the comparison were studied in detail and are shown in Fig. 1 by two colored bands. The grey shaded area shows the variation of the experimental dielectron signal due to the effect of various selection criteria imposed on pair tracks. It was obtained by switching off one cut in the experimental data analysis but keeping the others active. As it can be seen, variations of the signal yield are rather small. However, a systematic difference between the simulation and the experimental data was found in the reaction of the pair yields to the analysis cuts at low invariant masses. Its magnitude (green shaded area) was obtained by comparing the relative reduction of the unlike sign and like sign pair yields due to the action of all cuts in the data and the simulation. In a perfect case these reductions should be identical. However, we observe a systematic difference (bias) which leads to smaller reduction of unlike sign and larger reduction for like sign pairs, and as a consequence larger signal yield, in the simulation. The reason for this difference is presently under investigation.

In order to complete the investigations of the C+C collision system another production run at 1 AGeV was performed in the end of 2004. The experimental set-up with full coverage in the outer MDCIII and four chambers in the

MDCIV layers were achieved as compared to the 2 AGeV run. Using the same trigger setting as for the previous run 9×10^7 LVL2 events, corresponding to almost 2×10^9 LVL1 events were accumulated. An online, and hence very preliminary, dielectron analysis was performed in parallel to the data taking using on-line detector calibration. Fig. 2 shows the invariant mass distributions of unlike-sign, combinatorial background and signal pairs normalized to the number of LVL1 triggers. A statistics equivalent to $5.4k$ signal pairs was obtained from the analysis of 75% of the collected statistics. It is expected that better detector calibration and analysis of all available data will further improve the pair statistics. Nevertheless, one may already conclude that the data quality is sufficient to determine a spectrum with experimental uncertainties substantially smaller than the current discrepancies between theoretical and experimental (DLS) results. Data analysis is in progress and the final spectra are expected in this year.

3 pp collisions at 2.2 A GeV

The main goal of the pp experiment was to collect data for pp elastic scattering to be used for tracking and alignment studies, and to identify exclusively reaction channels of the type $pp \rightarrow pp(\pi^0, \eta)$. The reaction channels with a single meson were selected as a means to verify the dielectron reconstruction efficiency needed for an absolute normalization of the C+C data. A proton beam with an intensity of 2×10^7 protons/s and a 5 cm long liquid hydrogen target was used in this experiment. Typical ratios of trigger rates for the full and empty target of 10 : 1 were achieved during data taking. We collected around 4×10^8 events with two main LVL1 trigger settings: (1) $MUL \geq 2$ in opposite META sectors for pp elastic scattering and (2) $MUL \geq 4$ in the META for exclusive meson identification. In the latter case we also used a LVL2 trigger setting as for C+C collisions to enhance events with electron pairs.

The prerequisite for the identification of a reaction channel with a single neutral meson is missing mass resolution. In order to achieve it, precise MDC calibration and detector alignment is mandatory. For this purpose several alignment procedures are being pursued. One is based on straight track reconstruction from runs without magnetic field and the second one uses the advantage of the pp elastic scattering kinematics. Fig. 3 shows the current state of the art of our tracking precision (status end of 2004). In the upper panel we present the angular correlation between two tracks using the relation $\tan(\theta_1) \times \tan(\theta_2) = 1/\gamma^2_{CM}$ reconstructed for the trigger type (1). The prominent peak indicating elastic pp events is centered around the expected $1/\gamma^2_{CM} = 0.46$. The lower figure shows the total center of mass energy reconstructed from two tracks fulfilling the elastic scattering condition imposed on the polar $(tan(\theta_1) \times tan(\theta_2) \sim 1/\gamma^2_{CM}$ and the azimuthal angles (coplanarity). The width of the peak is equivalent to a mass resolution of 4% and is still a factor 2 lower than the one expected assuming ideal detector calibration and geometry. However, it is already sufficient for a single neutral meson channel identification and therefore processing of all collected data has been started.

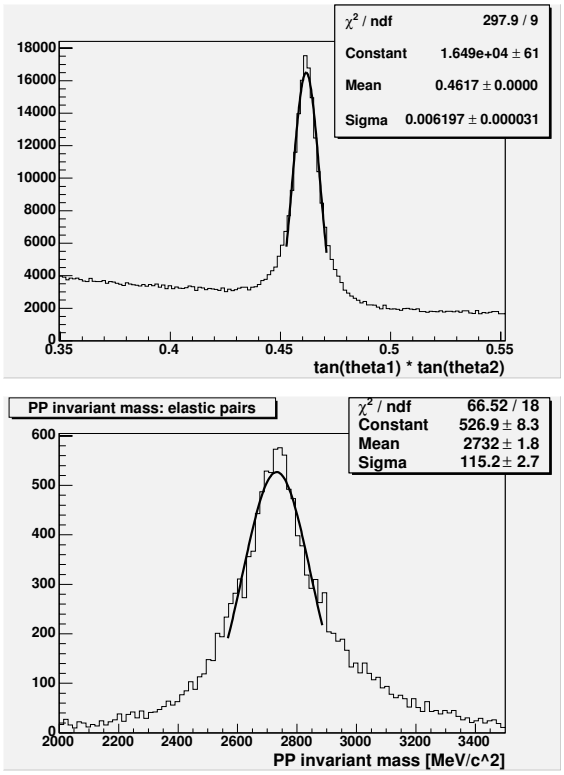

Figure 3: **Top**: Polar angular correlation of two tracks reconstructed in pp collisions at 2.2 GeV. A prominent peak centered at $\tan(\theta_1) \times \tan(\theta_2) = 0.46$ indicates elastic scattering events. **Bottom**: Invariant mass of two tracks fulfilling elastic scattering kinematics. The total center of mass energy is $E_{\rm cm} = 2.767$ GeV.

The collaboration gratefully acknowledges the support by BMBF and GSI, GA CR 202/00/1668 and GA AS CR IAA1048304 (Czech Republic), KBN 5P03B 140 20 (Poland), INFN (Italy), CNRS/IN2P3 (France), MCYT FPA2000-2041- C02-02 and XUGA PGID T02PXIC20605PN (Spain), INTAS 03-51-3208 (EU).

References

[1] Hades collaboration, GSI annual report 2003
[2] R. J. Porter *et al.* [DLS Collaboration], Phys. Rev. Lett. **79** (1997) 1229
[3] P. Tlusty, J.Otwinowski for HADES collaboration, Proceedings of XLII International meeting on Nuclear Physics, Bormio 2004, Vol 120.
[4] P. Salabura et al., Nucl. Phys. A 749(2005) 150c
[5] A. Toia, PHD thesis, University of Giessen, 2005

Pion and kaon production in A+A collisions at low SPS energies

C. Alt[1], C. Blume[1], P. Dinkelaker[1], D. Flierl[1], V. Friese[2], M. Gaździcki[1], C. Hoehne[2], S. Kniege[1], I. Kraus[2], M. Kliemant[1], B. Lungwitz[1], C. Meurer[2], M. Mitrovski[1], R. Renfordt[1], A. Richard[1], A. Sandoval[2], T. Schuster[1], R. Stock[1], C. Strabel[1], H. Ströbele[1], and the NA49 Collaboration

[1]Fachbereich Physik der Universität Frankfurt [2] GSI Darmstadt

The results from the NA49 energy scan programme at the SPS have revealed an anomalous behavior of the energy dependence of the $\langle K^+\rangle/\langle\pi^+\rangle$ ratio in central Pb+Pb collisions [1] which is absent in p+p interactions. Here we report the results on charged kaon and pion production in central collisions at 20 and 30 A·GeV as well as their system size dependence at 40 A·GeV. The former data extend the energy range of the NA49 data to a region well below the observed structure. The latter studies the onset of the anomalous behavior by comparing particle ratios obtained in p+p, C+C, Si+Si, and minimum bias Pb+Pb collisions.

In order to identify kaons, an analysis of the energy loss dE/dx in the NA49 time projection chambers is performed. Raw K^+ and K^- yields were extracted from fits of the distributions of dE/dx and tof (where available) in narrow bins of momentum and transverse momentum. The yields at mid-rapidity are obtained using the combined dE/dx and tof information ($tof + dE/dx$ analysis).

To obtain the π^- yields, all negatively charged particles were binned in rapidity (calculated assuming the π–mass) and p_T. The contamination from K^-, $\overline{p}$ and e^- from the interaction vertex as well as non–vertex hadrons originating from strange particle decays and secondary interactions was subtracted.

The resulting $K^\pm$ and π^- yields were corrected for geometrical acceptance, losses due to in–flight decays, inefficiencies of the tracking algorithms and quality cuts. The details on the correction procedure can be found in [1].

Spectra of transverse mass $m_T = \sqrt{p_T^2 + m^2}$ (m is the rest mass of the particle) for K^+, K^- ($tof + dE/dx$ analysis) and π^- mesons produced near mid-rapidity in central Pb+Pb collisions (0-7.2%) at 20 and 30 A·GeV (Fig. 1 left) and in C+C, Si+Si, and Pb+Pb with different centrality selections (Fig. 1 right) are fitted by Eq. 1 in the range 0.2 GeV $< m_T - m <$ 0.7 GeV:

$$\frac{dn}{m_T dm_T dy} = C \cdot \exp\left(-\frac{m_T}{T}\right). \qquad (1)$$

The five centrality selected event samples were obtained from minimum bias Pb+Pb collisions on the basis of the energy deposited by the projectile spectator nucleons in the forward calorimeter [2]. The resulting fractions of the total inelastic cross–section are 0-5%, 5-12.5%, 12.5-23.5%, 23.5-33.5%, and 33.5-43.5%.

The rapidity distributions dn/dy plotted in Fig. 2 were obtained by summing the measured m_T spectra and using the fitted exponential function (Eq. 1) to extrapolate to full m_T. For most bins the necessary correction is small ($\cong$ 5%). The rapidity spectra were parameterized by the sum of two Gaussian distributions placed symmetrically with respect to mid-rapidity. The results of the fits are indicated by the full lines in Fig. 2. The mean multiplicities were obtained by integration of the fitted curves.

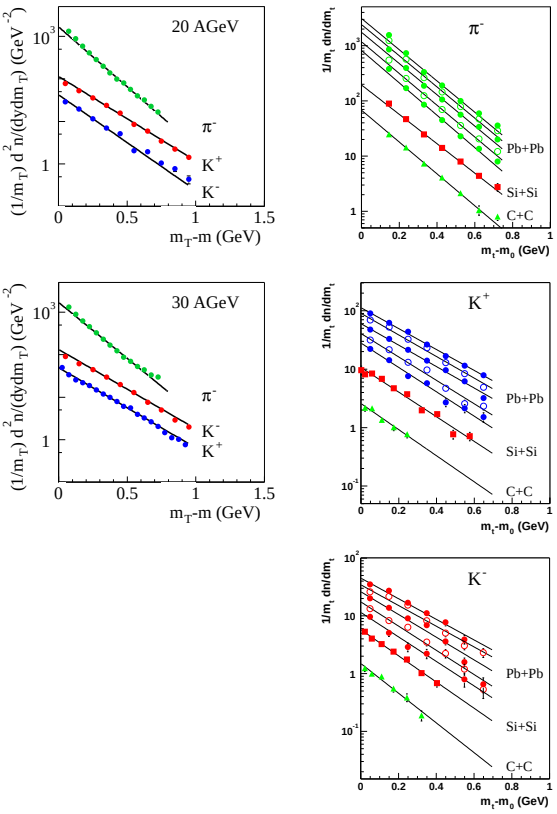

Figure 1: left: Transverse mass spectra of π^-, K^+ and K^- mesons produced at mid-rapidity ($|y| < 0.1$ for kaons in the $tof + dE/dx$ analysis, and $0 < y < 0.2$ for pions) for central Pb+Pb collisions at 20 and 30 A·GeV.
right: 40 A·GeV transverse mass spectra of π^-, K^+, and K^- at midrapidity ($-0.5 < y < 0.5$) for C+C, Si+Si, and minimum bias Pb+Pb collisions.

Figure 3 shows the system size dependence of the $\langle\pi^-\rangle/\langle N_W\rangle$, $\langle K^+\rangle/\langle N_W\rangle$, $\langle K^-\rangle/\langle N_W\rangle$, $\langle K^+\rangle/\langle K^-\rangle$, $\langle K^+\rangle/\langle\pi^+\rangle$, and $\langle K^-\rangle/\langle\pi^-\rangle$ ratios. $\langle N_W\rangle$ is the mean number of wounded nucleons calculated within a Glauber model. For p+p interactions no measurements of these ratios exist at this energy, therefore an interpolation of measurements at other energies is used [3]. To ease the comparison to the isospin symmetric light nuclei, the π yield in isospin averaged nucleon-nucleon interactions (N+N) was estimated as $\langle\pi^-\rangle_{(NN)} = 0.5 \cdot (\langle\pi^+\rangle_{(pp)} + \langle\pi^-\rangle_{(pp)})$ and the ratios which use this yield are also shown in the figures.

The $\langle\pi^-\rangle/\langle N_W\rangle$ ratio shows a fast rise for the smaller

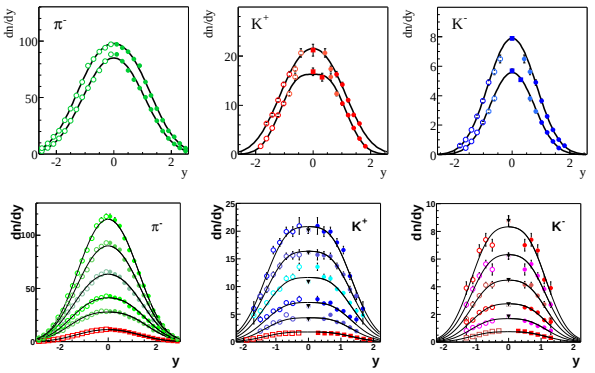

Figure 2: Top: Rapidity distributions of π^-, K^+ and K^- mesons produced in central Pb+Pb collisions at 20 and 30 A·GeV. For kaons squares and circles indicate the results of *tof* and dE/dx only analyzes, respectively. The closed symbols indicate measured points, open points are reflected with respect to mid-rapidity. The lines indicate double Gaussian fits to the spectra. The plotted errors, which are mostly smaller than the symbol size, are statistical only, the systematic errors are ±5%.
Bottom: rapidity spectra for Si+Si (squares) and the five centrality bins of minimum bias Pb+Pb collisions (circles) at 40 A·GeV beam energy. The triangles illustrate the mid-rapidity TOF measurements. The solid lines represent the fits described in the text.

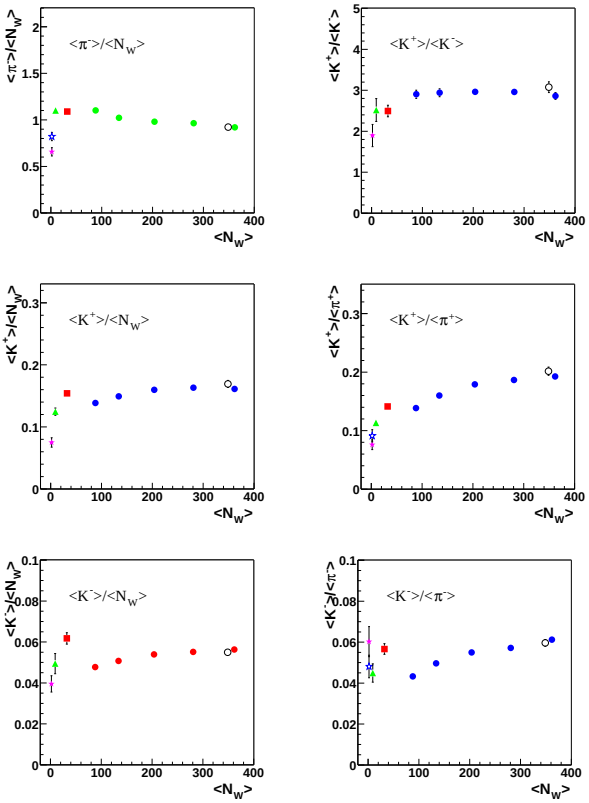

Figure 3: System size dependence of various ratios at 40 A·GeV. The p+p (full stars) and N+N (open stars) data points result from an interpolation of measurements at other energies (see text). C+C (triangles), Si+Si (squares), and minimum bias Pb+Pb (circles) are displayed at their corresponding $\langle N_W \rangle$.

systems and decreases slowly from there on to central Pb+Pb collisions. The $\langle K^+ \rangle / \langle N_W \rangle$ ratio rises fast with system size for the small systems. The value for central Si+Si reactions is slightly higher than the measurement for peripheral Pb+Pb collisions. The dependence on centrality seen in the minimum bias Pb+Pb data, on the other hand, is weak. A qualitatively similar behaviour is observed for the $\langle K^- \rangle / \langle N_W \rangle$ ratio.
The $\langle K^+ \rangle / \langle K^- \rangle$ ratio rises at small numbers of wounded nucleons with the system size and remains almost constant from peripheral to central Pb+Pb collisions. A similar behaviour is observed by the E802 Collaboration at AGS energies [4].
The $\langle K^+ \rangle / \langle \pi^+ \rangle$ ratio is constructed by scaling the $\langle \pi^- \rangle$ yield with the π^+/π^- ratio, as measured at mid-rapidity with the time-of-flight detectors. For the isospin symmetric systems C+C and Si+Si the ratio π^+/π^- is unity. Again, a steep rise of the $\langle K^+ \rangle / \langle \pi^+ \rangle$ ratio is observed for the small systems with the ratio in Si+Si collisions being higher than in peripheral Pb+Pb collisions. However, the centrality dependence of this ratio in minimum bias collisions is more pronounced than the one of the $\langle K^+ \rangle / \langle N_W \rangle$ ratio. The system size dependence of the $\langle K^- \rangle / \langle \pi^- \rangle$ ratio resembles the one of the $\langle K^+ \rangle / \langle \pi^+ \rangle$ ratio. The observed $\langle K^- \rangle / \langle \pi^- \rangle$ ratio in Si+Si collisions is close to the measurement in central Pb+Pb collisions.

The new results on π and K production at 20 and 30 A·GeV will now be discussed together with published measurements at lower (AGS) and higher (SPS, RHIC) energies. The dependence of basic hadron production properties on the collision energy, expressed by Fermi's measure F [5] ($F \equiv (\sqrt{s_{NN}} - 2m_N)^{3/4} / \sqrt{s_{NN}}^{1/4}$, where $\sqrt{s_{NN}}$ is the c.m.s. energy per nucleon–nucleon pair and m_N the rest mass of the nucleon) is plotted in Fig. 4 for central Pb+Pb (Au+Au) collisions and p+p($\overline{\text{p}}$) interactions (see references in [6, 7]).

The top panel of the figure shows that the total number of pions ($\langle \pi \rangle = 1.5 \cdot (\langle \pi \rangle + \langle \pi \rangle)$) produced per wounded nucleon increases with energy as expected in both reactions. However, the rate of increase in nucleus–nucleus collisions becomes larger within the SPS energy range and then stays constant up to the RHIC domain. Below 40 A·GeV the ratio $\langle \pi \rangle / \langle N_W \rangle$ in A+A collisions is lower than in p+p interactions (pion suppression), while at higher energies $\langle \pi \rangle / \langle N_W \rangle$ is larger in A+A collisions than in p+p($\overline{\text{p}}$) interactions (pion enhancement). The transition from pion suppression to pion enhancement (the "kink") is demonstrated more clearly in the insert of Fig. 4, where the difference between $\langle \pi \rangle / \langle N_W \rangle$ for A+A collisions and the straight line parameterization of the p+p($\overline{\text{p}}$) data is plotted as a function of F up to the highest SPS energy.

The energy dependence of the ratio $\langle K^+ \rangle / \langle \pi^+ \rangle$ of the mean multiplicities of K^+ and π^+ mesons produced in

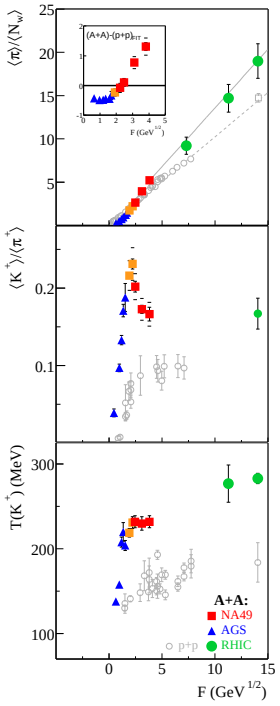

Figure 4: Energy dependence of the mean pion multiplicity per wounded nucleon, the $\langle K^+\rangle/\langle\pi^+\rangle$ ratio and the inverse slope parameter T of the transverse mass spectra of K^+ mesons measured in central Pb+Pb (Au+Au) collisions (solid symbols) compared to results from p+p($\overline{\text{p}}$) reactions (open dots). The changes in the SPS energy range (solid squares) suggest the onset of the deconfinement phase transition.

central Pb+Pb (Au+Au) collisions is plotted in the middle panel of Fig. 4. Following a fast rise from threshold, the ratio passes through a maximum (the "horn") in the SPS range and then seems to settle to a lower plateau value at higher energies. Kaons are the lightest strange hadrons and $\langle K^+\rangle$ counts for about half of all the anti-strange quarks produced in the collisions at AGS and SPS energies, the other half being contained in K^0 (isospin symmetry). Thus, the relative strangeness content of the produced matter passes through a sharp maximum at the SPS in nucleus–nucleus collisions. This feature is not visible in p+p($\overline{\text{p}}$) reactions.

The energy dependence of the inverse slope parameter T of transverse mass spectra of K^+ mesons produced in central Pb+Pb (Au+Au) collisions is presented in the bottom panel of Fig. 4. The plateau at the SPS energies (the "step") is preceeded by a steep rise of T measured at the AGS and followed by a further increase indicated by the RHIC data. Although the scatter of data points is large, T appears to increase smoothly in p+p($\overline{\text{p}}$) interactions [7].

The system size dependence of the yields of negatively charged pions and charged kaons are presented for C+C, Si+Si, and minimum bias Pb+Pb collisions at 40 A·GeV beam energy. The nearly constant $\langle K^+\rangle/\langle K^-\rangle$ ratio from C+C interactions up to central Pb+Pb collisions indicates that there are no significant changes in the respective production mechanisms of K^+ and K^-. The slow decrease of the $\langle\pi^-\rangle/\langle N_W\rangle$ ratio for centrality selected Pb+Pb collisions could be an effect of the increased pion absorption probability in the extended hot and dense nuclear matter of the larger systems.

The results on the $\langle K\rangle/\langle N_W\rangle$ and the $\langle K\rangle/\langle\pi\rangle$ ratios suggest that the mean number of wounded nucleons $\langle N_W\rangle$ is not the appropriate scaling parameter for the system size dependence of the yields of charged kaons [8, 9].

New results on charged pion and kaon production in central Pb+Pb collisions at 20 and 30 A·GeV are presented and compared to measurements at lower and higher energies. A change of energy dependence is observed around 30 A· for the yields of pions and kaons as well as for the shape of the transverse mass spectra. Of the available model explanations [10, 11, 12, 13] a reaction scenario with the onset of deconfinement best reproduces the measurements.

References

[1] S V Afanasiev et al., (NA49 Collaboration), Phys. Rev. **C66** (2002) 054902.

[2] S. Afanasiev et al. (NA49 Collab.), Nucl. Instrum. Meth. **A430**, 210 (1999).

[3] A M Rossi et al., Nuclear Physics **B84** (1975) 269.

[4] Ahle et al., (E802), Phys. Rev. **C60** (1999) 044904.

[5] E. Fermi, Prog. Theor. Phys. **5**, 570 (1950).

[6] M. Gaździcki and D. Röhrich, Z. Phys. **C65**, 215 (1995); **C71**, 55 (1996) and references therein.

[7] M. Kliemant, B. Lungwitz and M. Gazdzicki, Phys. Rev. C **69**, 044903 (2004) [arXiv:hep-ex/0308002].

[8] C Höhne for the NA49 Collaboration, Nucl. Phys. A715 (2003) 474c.

[9] C Alt et al., (NA49 Collaboration), nucl-ex/0406031.

[10] M. Gazdzicki, M. I. Gorenstein, F. Grassi, Y. Hama, T. Kodama and O. . J. Socolowski, Braz. J. Phys. **34**, 322 (2004) [arXiv:hep-ph/0309192].

[11] S. A. Bass *et al.*, Prog. Part. Nucl. Phys. **41**, 225 (1998) [arXiv:nucl-th/9803035],

[12] H. Sorge, H. Stocker and W. Greiner, Nucl. Phys. A **498** (1989) 567C.

[13] W. Cassing, E. L. Bratkovskaya and S. Juchem, Nucl. Phys. A **674**, 249 (2000) [arXiv:nucl-th/0001024].

NQMA-THE

Nuclear & Quark Matter Theories

The relativistic Brueckner approach and asymmetric nuclear matter

E.N.E. van Dalen, C. Fuchs, and Amand Faessler
Institut für Theoretische Physik, Universität Tübingen

Symmetric nuclear matter has been studied extensively. However, investigations of asymmetric nuclear matter are rather rare. The investigation of asymmetric matter is important for astrophysical studies and for physics related to neutron-rich nuclei. The interest for physics related to neutron-rich nuclei is only of recent date, because data for asymmetric nuclei were scarce in the past. However, this situation is changing with a new generation of high-intensity radioactive beam facilities, e.g. the future GSI facility.

In Ref. [1] we describe asymmetric matter at zero temperature in the relativistic DBHF approach using the Bonn A potential. In here, the representation scheme is an important issue due to the fact that ambiguities arise, because pseudoscalar (ps) and pseudovector (pv) components can not uniquely be disentangled for on-shell scattering. However, with a pseudoscalar vertex the pion couples maximally to negative energy states, which is inconsistent with the potentials used and leads to spurious contributions in the nuclear self-energies. The conventional pv representation used to cure this problem fails. Finally, new and reliable methods, the complete pv representation [2] and the subtracted T matrix representation [3], were proposed to remove these spurious contributions from the T matrix for symmetric nuclear matter. In contrast, only the conventional pv representation has been applied for asymmetric nuclear matter [4]. In our work [1] the optimal representation scheme for the T matrix, the subtracted T matrix representation, is applied and compared with other representation schemes.

In the limit of symmetric nuclear matter our results agree with those of Ref. [3]. The binding energy shows the expected quadratic dependence on the asymmetry parameter. The density dependence of the symmetry energy is shown in Fig. 1. The symmetry energy $E_{\rm sym}$ is found to be 34 MeV at saturation density in the subtracted T matrix representation scheme. The value of 34 MeV is in remarkable agreement with a recent approach to the nuclear many-body problem based on chiral dynamics in combination with QCD sum rules [5]. In the complete pv representation scheme $E_{\rm sym}$ is found to be 37 MeV, which is probably too high. Furthermore, $E_{\rm sym}$ is stiff, particularly at high densities. In Fig. 1 $E_{\rm sym}$ is also compared to parameterizations from density dependent relativistic mean-field (RMF) theory [6] where the asymmetry parameter a_4 varies from 30 to 38 MeV. The dependence of $E_{\rm sym}$ at moderate densities is qualitatively similar to the RMF parameterizations using $a_4 = 32 - 34$ MeV. However, at high densities $E_{\rm sym}$ shows a non-linear and a more pronounced increase than in RMF theory.

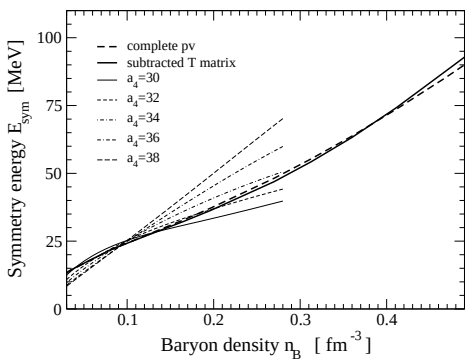

Figure 1: Symmetry energy as a function of the baryon density.

With increasing proton fraction the neutron effective mass increases in both representations. In addition, the density is stronger than the asymmetry dependence on the neutron effective mass.

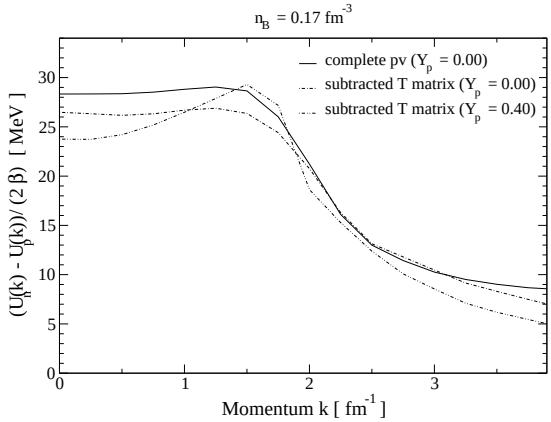

Figure 2: Strength of the isovector potential at $n_B = 0.17$ fm^{-3} as a function of momentum $\mathbf{k}$.

A quantity which is sensitive on the momentum dependence of $\Sigma_{s,0,v}$ is the optical potential. The optical potential is given by

$$U(|\mathbf{k}|, \mathbf{k^0}) = \mathbf{\Sigma_s}(|\mathbf{k}|) - \frac{\mathbf{1}}{\mathbf{M}}\mathbf{k}^\mu \mathbf{\Sigma}_\mu(|\mathbf{k}|) + \frac{\mathbf{\Sigma_s^2}(|\mathbf{k}|) - \mathbf{\Sigma_\mu^2}(|\mathbf{k}|)}{\mathbf{2M}}. \quad (1)$$

The calculated isovector nucleon optical potentials are shown in Fig. 2. In these cases the isovector optical potential in neutron rich matter stays roughly constant up to a momentum of 1.5 fm^{-1} and then decreases strongly with energy. Furthermore, at zero momentum it is in good agreement with the empirical value of 22 - 34 MeV. The DBHF model thereby predicts neutron-proton effective mass splitting of $m_n^* < m_p^*$.

The results have also been analyzed in terms of mean-field Dirac scalar-vector isoscalar-isovector quantities. By this way the DBHF results can be parameterized and applied to finite nuclei within the framework of density dependent relativistic Hartree (DDRH) theory.

References

[1] E. N. E. van Dalen, C. Fuchs, and Amand Faessler, Nucl. Phys. **A744** (2004) 227.
[2] C. Fuchs, T. Waindzoch, A. Faessler, and D. S. Kosov, Phys. Rev. C **58** (1998) 2022.
[3] T. Gross-Boelting, C. Fuchs, and Amand Faessler, Nucl. Phys. **A648** (1999) 105
[4] F. de Jong and H. Lenske, Phys. Rev. C **58** (1998) 890.
[5] P. Finelli, N. Kaiser, D. Vretenar, and W. Weise, Nucl. Phys. **A735** (2004) 449.
[6] D. Vretenar, T. Nikšić, P. Ring, Phys. Rev. C **68** (2003) 024310.

Kaon slopes from SIS to lower SPS energies

A.B. Larionov[1,2], U. Mosel[1], and M. Wagner[1]

[1]Institut für Theoretische Physik, Universität Giessen, D-35392 Giessen, Germany; [2]RRC "I.V. Kurchatov Institute", 123182 Moscow, Russia

The inverse slope parameters of the kaon spectra are being discussed extensively in literature [1, 2, 3, 4], since they are related to the kaon properties in nuclear matter. Moreover, a constancy of the inverse slope parameter of the kaon transverse mass spectra at the SPS energy region could be a signal of the phase transition to the QGP [5].

With an eye on the planned CBM experiment we have performed a BUU study of the kaon production in heavy-ion collisions at SIS [6] and AGS to lower SPS energies [7]. The upper Figure shows the inverse slope parameter T of the K^+ c.m. kinetic energy spectrum vs the number of participating nucleons A_{part} for the system Au+Au at 1.5 A GeV in comparison to the data [1]. The dashed line with open triangles shows the calculation without kaon potential. The dotted line with open squares and the solid line with open circles correspond to the calculations with so called "Ko-Li" (KL, $U^{KL}_{K^+}(\rho_0) = 6$ MeV) and "Brown-Rho" (BR, $U^{BR}_{K^+}(\rho_0) = 32$ MeV) parameterizations of the kaon potential defined in Ref. [8], respectively. In peripheral collisions there is, practically, no influence of the potential due to a relatively weak compression. In central collisions the data can be only reproduced by a calculation with the kaon potential. The KL parameterization describes the inverse slope parameter better than the BR one, however, the kaon multiplicity is better reproduced by the BR parameterization.

The lower Figure shows the inverse slope parameter T of the K^+ transverse mass spectra as a function of the laboratory energy for central Au+Au (AGS) and Pb+Pb (SPS) collisions in comparison to the data from Refs. [2, 3, 4]. The calculation was done in the cascade mode, i.e. by neglecting potentials for all particles. We understimate the data by 30-40 %. A similar problem has been reported before in Ref. [9] and ascribed to the lack of pressure due to missed nonhadronic degrees of freedom in the transport models. We speculate here that also the inclusion of multi-baryon collisions would tend to make the spectrum harder. The probability for such processes naturally increases with a high power of baryon density.

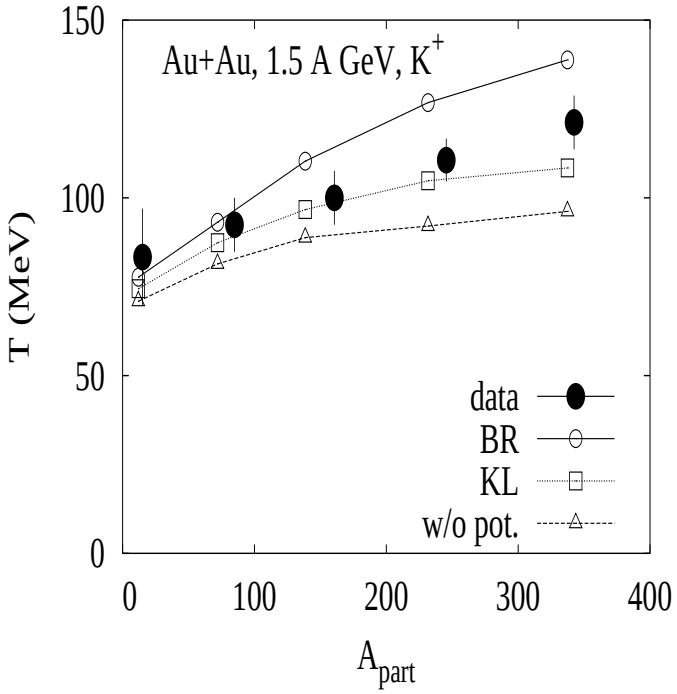

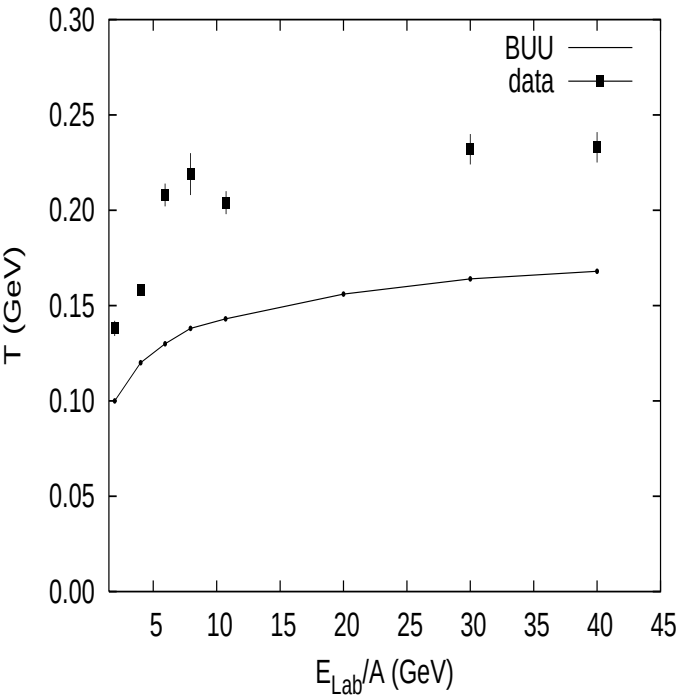

References

[1] A. Förster et al., Phys. Rev. Lett. **91**, 152301 (2003).
[2] L. Ahle et al., Phys. Lett. B **490**, 53 (2000).
[3] S. Afanasiev et al., Phys. Rev. C **66**, 054902 (2002).
[4] V. Friese, J. Phys. G **30**, 119 (2004).
[5] M.I. Gorenstein, M. Gaździcki and K. Bugaev, Phys. Lett. B **567**, 175 (2003).
[6] A.B. Larionov and U. Mosel, in preperation.
[7] M. Wagner, A.B. Larionov and U. Mosel, nucl-th/0411010, to be published in Phys. Rev. C.
[8] Y.-M. Zheng et al., Phys. Rev. C **69**, 034907 (2004).
[9] E.L. Bratkovskaya et al., Phys. Rev. Lett. **92**, 032302 (2004).

Spectral function of the omega meson in nuclear matter

Pascal Mühlich[1], Vitaliy Shklyar[1], Marcus Post[1], Stefan Leupold[1], and Ulrich Mosel[1]
[1]Institut für Theoretische Physik, Universität Giessen, Germany

An exciting aspect of hadron physics is the question how a hadron changes its properties once it is put in a strongly interacting environment. Here, the vector mesons deserve special attention as they couple directly to (virtual) photons. The latter can decay into dileptons which leave the strongly interacting system untouched. Via that process information about possible in-medium modifications of the vector mesons can be carried to the detectors.

In the following we concentrate on the ω-meson and its change of properties at finite baryon densities. Such information is encoded in the spectral function $\mathcal{A}$ which is basically the imaginary part of the (retarded) propagator. The latter is related to the (retarded) self energy Π of the ω-meson. Neglecting Lorentz indices for the simplicity of presentation, one has (cf. [1] for details)

$$\mathcal{A}(q) = -\frac{1}{\pi}\,\mathrm{Im}D_\omega(q) = -\frac{1}{\pi}\,\mathrm{Im}\,\frac{1}{q^2 - m_\omega^2 - \Pi(q)}\,. \qquad (1)$$

Hence the key quantity is the self energy which we determine in linear-density approximation [2]

$$\Pi(q) = \rho T(q) \qquad (2)$$

with the nucleon density ρ and the nucleon-ω forward scattering amplitude T. To be precise, $T(q)$ is the in general offshell forward scattering amplitude of an ω-meson with arbitrary mass $\sqrt{q^2}$ which scatters on one of the nucleons which form the medium. To determine T we have extended the K-matrix approach of [3, 4] to allow for an arbitrary four-momentum of the incoming/outgoing ω-meson.

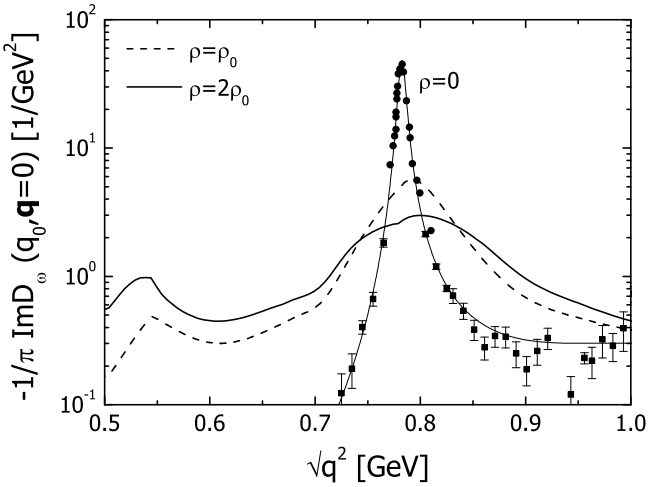

Figure 1: Spectral function of the ω-meson for different densities. Here the ω-meson is at rest with respect to the medium. ρ_0 denotes normal nuclear matter density.

The K-matrix approach is capable of dealing with the coupled-channel problem for elementary scattering reactions including on equal footing (π, N), (γ, N), (η, N), (K, Λ), (K, Σ) and also (ω, N). Due to inelastic rescattering effects these channels should not be treated separately. Baryonic resonances are included as intermediate states in this approach. For the case at hand the coupling of resonances to the ω-nucleon system are of special interest.

Results of our calculations are shown in figs. 1 and 2. Most noticable we observe collisional broadening of the ω-peak and the appearance of a second peak. The latter is a collective resonance-hole branch caused by the coupling to the $N^*(1535)$. The collisional broadening amounts to about 60 MeV for an ω at rest at normal nuclear matter density. It will be interesting to see what these in-medium changes imply for the dilepton spectra which will be measured by the HADES collaboration.

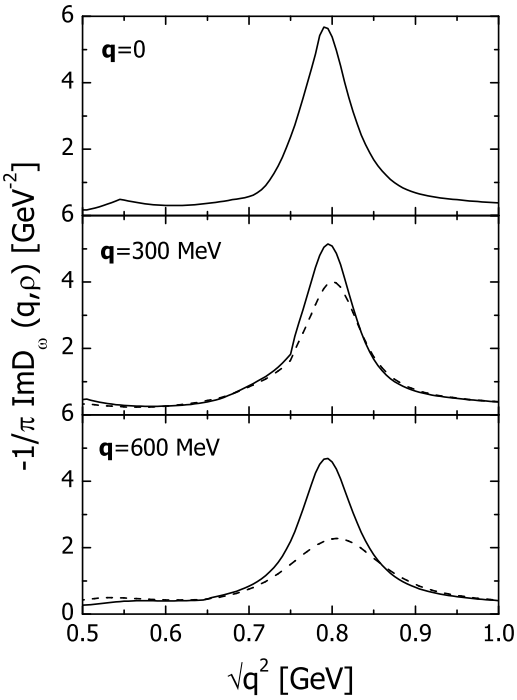

Figure 2: Spectral function of the ω-meson for normal nuclear matter density for different three-momenta $\mathbf{q}$ of the ω relative to the medium and for different polarizations. The full (dashed) lines show the spectral functions of the longitudinal (transversal) modes.

References

[1] P. Mühlich, V. Shklyar, M. Post, S. Leupold and U. Mosel, in preparation.
[2] C.B. Dover, J. Hüfner and R.H. Lemmer, Ann. Phys. 66 (1971) 248.
[3] G. Penner and U. Mosel, Phys. Rev. C 66 (2002) 055211, 055212.
[4] V. Shklyar, H. Lenske, U. Mosel and G. Penner, submitted to Phys. Rev. C, arXiv:nucl-th/0412029.

Strangeness Production in Expansion Dynamics

V.D. Toneev[1,2], E.G. Nikonov[1,2], B. Friman[1], W. Nörenberg[1], K. Redlich[1,3], and A.S. Parvan[2]
[1]GSI; [2]JINR Dubna; [3]University of Wroclaw

The quest for the deconfinement transition, the phase transition from a confined hadronic phase to a deconfined quark–gluon phase, remains a major challenge in strong interaction physics. Enhanced production of strangeness relative to that from proton–proton and proton–nucleus collisions was one of the conjecture signals of the quark–gluon plasma formation in heavy ion collisions. In [1] we explore global effects of strangeness production in hot and dense nuclear matter within a collective thermodynamic approach. Thermodynamical properties of excited systems are analyzed with various phenomenological models for the equation of state (EoS), which differ in the order of the deconfinement phase transition: a first order transition (the two–phase bag model), a crossover–type transition (the statistical mixed–phase model) and no phase transition (pure hadronic models). The consequences of strangeness separation (strangeness distillation effect) and softening of the (EoS) are discussed. It is expected generally that these characteristics of the deconfinement phase transition may manifest themselves in observables through the expansion dynamics [1].

As an illustration, we show in Fig.1 the influence of the EoS and the order of phase transition on the K^+/π^+ excitation function evaluated in a longitudinally expanding fireball model [1]. The calculated curves are rather smooth (similar results are available for other strange hadrons [1]), in contrast to the results of a very simple statistical model of the early stage [5] which predicts a peaked structures in these excitation functions at a bombarding energy of $E_{lab} \approx 30\ A \cdot GeV$ as a signal for the onset of a first order deconfinement phase transition. As is seen from the figure, low-energy SPS measurements indeed exhibit some anomalous strangeness enhancement just in the expected energy range $E_{lab} = 20 - 40\ A \cdot GeV$.

In our model the scenario of Ref. [5] has been worked out in more detail. In particular, strange hadrons formed in the initial stage may interact with each other in the course of subsequent hydrodynamic evolution of the system. As seen in Fig.1, the resulting strangeness excitation functions do not reproduce the anomalous enhancement of the NA49 Collaboration on [4] mentioned above. A striking result of this calculation is, furthermore, that bulk properties of strangeness production in A–A collisions depend only weakly on the particular form of the EoS: hydrodynamics, with the assumption of a shock–like freeze–out in heavy-ion collisions, practically washes out differences in the EoS.

Consequently a new scenario based on the strangeness distillation idea has been proposed [6] where the anomalous strangeness enhancement is related to the passage of the evolving system near the critical end-point rather than the latent heat emerging from the onset of the first order deconfinement phase transition. Lattice calculations indicate the existnce of a critical end-point is found in the QCD phase diagram. At this point the first order phase transition at high densities turns into a crossover transition at low densities. If, at freeze-out, there is no chemical equilibrium between different components of the mixed phase, the strangeness distillation effect at the critical end-point may result in such a peaked behavior in strangeness excitation functions [6]. This effect should be most sizeable for the n_{K^+}/n_{π^+} ratio, because in the case of a crossover transition the dominating hadronic component at freeze out will be enriched by strange quarks due to strangeness distillation. Model calculations suggest that dynamical trajectories in the phase diagram pass near the critical end-point for $E_{lab} \sim 30\ A \cdot GeV$.

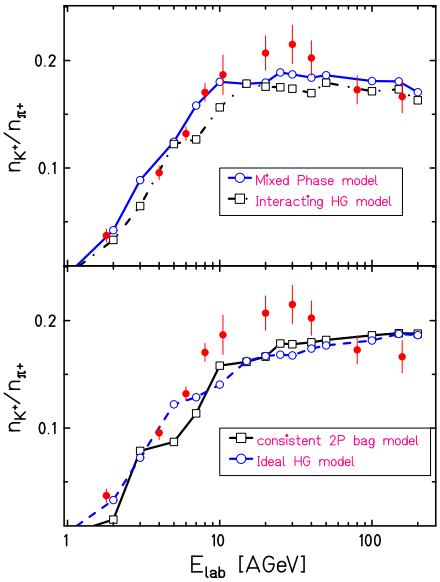

Figure 1: The ratios of 4π–integrated strange particle yields per pion yields for central Au–Au collision as a function of beam–energy. The compilation of experimental data is taken from [2, 3]. Preliminary results at $E_{lab} = 20$ and 40 $A \cdot GeV$ [4] are plotted as well. The calculated excitation functions are given for different EoS with the canonical suppression factor.

References

[1] V.D. Toneev, E.G. Nikonov, B. Friman, W. Nörenberg, K. Redlich, Eur. Phys. J. **C32** (2004) 399.
[2] R. Stock, hep-ph/0204032; The NA49 Collaboration, *Phys. Rev.* **C66** (2002) 054902; M. van Leeuwen for the NA49 Collaboration, *Nucl. Phys.* **A715** (2003) 161.
[3] K. Redlich, *Nucl. Phys.* **A698**, 94 (2002).
[4] M. Gazdzicki et al. (NA49 Collaboration) J. Phys. **G 30** (2004) S701.
[5] M. Gazdzicki and M.I. Gorenstein, Acta Phys. Pol. **B 30** (1999) 2705.
[6] V.D.Toneev and A.S.Parvan, nucl-th/0411125.

Self consistent and covariant propagation of pions, nucleon and isobar resonances in cold nuclear matter

C.L. Korpa[1] and M.F.M. Lutz[2]
[1]University of Pecs, [2]GSI,

The study of pion propagation in dense nuclear matter is of central importance when addressing the in-medium modifications of nucleon and delta resonances. There are strong hints from the empirical photon nucleus absorption cross section as well as from pion-nucleus scattering data that the low-lying nucleon and delta resonances do change their properties in nuclear matter substantially already at nuclear saturation density [1]. Since most nucleon and isobar resonances have a substantial decay fraction into one nucleon and one pion, the in-medium resonance structure reflects to a large extent the medium modified propagation properties of pions. The pion self energy in nuclear matter is quantitatively constrained by pionic atom data. Most exciting are the recently established states where a negatively charged pion is bound by a heavy nucleus in an s-wave or p-wave state [2]. It is still an open problem to find a quantitative and microscopic derivation in particular for the large absorptive part in the nuclear optical potential needed in the phenomenological description of pionic atom data [3]. The problem requires a non-perturbative many-body approach, since the low-density expansion ceases to converge rapidly at the relevant nuclear densities even when chiral correction terms are considered.

In this work we generalize the covariant framework of [4], which was recently proposed for the self consistent propagation of antikaons and hyperon-resonances in nuclear matter, to the problem of pion, nucleon- and isobar-resonance propagation incorporating short range correlation effects [5]. The merit of the scheme is that it is formulated entirely in terms of the two-body scattering phase-shifts properly extrapolated to subthreshold energies. Given the empirical πN phase shifts and values for the Migdal parameters describing important short range correlations the scheme is parameter free. We expect self consistency to lead to a broadening of the pion spectral function which may help to establish a microscopic understanding of pionic atom data and also offer an improved understanding of the expected broadening of nucleon and isobar resonances in nuclear matter. Our present approach constitutes a significant progress as compared to previous self consistent calculations which were based on p-wave pion-nucleon dynamics only. Moreover this work is the first attempt to consider the effects of the in-medium mixing of partial wave amplitudes. In particular the feedback effect of the in-medium modified s-wave $N(1520)$ and $N(1650)$, the p-wave $N(1440)$ and the d-wave $N(1535)$ resonances to the propagation properties of pions is evaluated in this work.

Using reasonable values for the Migdal parameters we find that the nucleon resonances $N(1535)$ and $N(1650)$ are basically unaffected by the nuclear environment. Contrasted results were obtained for the p-wave $N(1440)$ and d-wave $N(1520)$ resonances for which we predict considerable broadening already at nuclear saturation density. Our result for the isobar resonance are not satisfactory at this stage, due to a significant overestimate of its in-medium decay width. Improved results are obtained by incorporating a soft phenomenological form factor into the πNN vertex. The latter does not affect the broadening of the $N(1440)$ and $N(1520)$ resonances. Whereas the properties of slow isobars in nuclear matter are changed significantly, a soft form factor has rather moderate effects on the pion spectral function. These results show that further detailed investigations of the effects of vertex modifications in the medium are required to arrive at a fully microscopic understanding of the properties of isobars in nuclear matter.

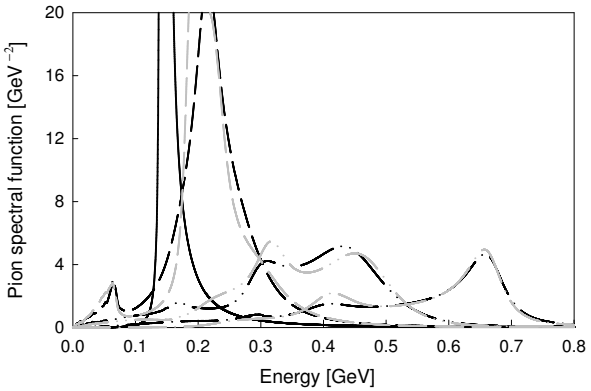

Figure 1: In-medium pion spectral function at nuclear saturation density, for different values of pion momentum: 0 (solid line), 200 MeV (long dash), 400 MeV (short dash), 600 MeV (dot-dash line). The Migdal parameters are $g'_{11} = g'_{12} = g'_{22} = 0.8$. The black line corresponds to calculation without form factors, while the gray lines are obtained with $\Lambda_{\pi NN} = 0.5$ GeV, $\Lambda_{\pi N\Delta} \to \infty$. For zero momentum the change is marginal and not shown.

References

[1] J.H. Koch, E.J. Moniz and N. Ohtsuka, Ann. Phys. **154** (1984) 99.
[2] H. Gilg et al., Phys. Rev. **C 62** (2000) 025201.
[3] E.E. Kolomeitsev, N. Kaiser and W. Weise, Phys. Rev. Lett. **90** (2003) 092501.
[4] M.F.M. Lutz and C.L. Korpa, Nucl. Phys. **A 700** (2002) 309.
[5] C.L. Korpa and M.F.M. Lutz, Nucl. Phys. **A 742** (2004) 305.

The associated photoproduction of positive kaons and $\pi^0\,\Lambda$ or $\pi\,\Sigma$ pairs in the region of the $\Sigma(1385)$ and $\Lambda(1405)$ resonances

M.F.M. Lutz[1] and M. Soyeur[2]

[1]GSI, Darmstadt, [2]Commissariat à l'Energie Atomique, Saclay

The $\gamma p \to K^+\pi^0\Lambda$ and $\gamma p \to K^+\pi\Sigma$ reactions are studied in the kinematic region where the $\pi^0\Lambda(1116)$ and $\pi\Sigma(1192)$ pairs originate dominantly from the decay of the $\Sigma(1385)$ and $\Lambda(1405)$ resonances [1]. We consider laboratory photon energies around 2 GeV, significantly above the threshold for producing the $K^+\,\Sigma(1385)$ and $K^+\,\Lambda(1405)$ final states.

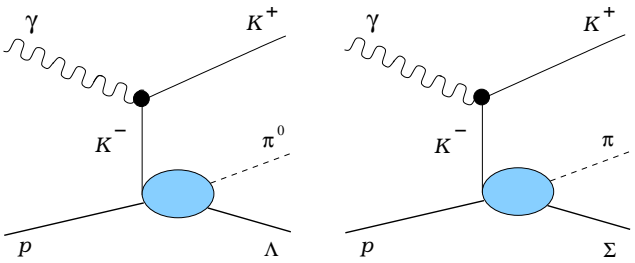

We compute for both reactions the process in which the ingoing photon dissociates into a real K^+ and a virtual K^-, the off-shell K^- scattering subsequently off the proton target to produce the $\pi^0\,\Lambda$ or $\pi\,\Sigma$ pair. The $K^-p \to \pi^0\Lambda$ and $K^-p \to \pi\Sigma$ amplitudes are calculated in the framework of a chiral coupled-channel effective field theory of meson-baryon scattering [2]. The structure of the amplitudes reflects the dominance of the $\Lambda(1405)$ in the $\pi\Sigma$ channel and of the $\Sigma(1385)$ in the $\pi\Lambda$ channel. The full pion-hyperon final state interaction is included in these amplitudes. We extract from the calculated cross section the gauge-invariant double kaon pole term. We find this term to be large and leading to sizeable cross sections for both the $\gamma p \to K^+\pi^0\Lambda$ and $\gamma p \to K^+\pi\Sigma$ reactions, in qualitative agreement with the scarce data presently available. Accurate measurements of these cross sections should make it possible to extract the contribution of the double kaon pole and hence to assess the possibility of studying kaon-nucleon dynamics just below threshold through these reactions. Such accurate data are expected in the near future from experiments in progress or planned at ELSA and SPring-8.

We recall that the $\pi\,\Sigma$ channel is dominated by the $\Lambda(1405)$ and the $\pi\,\Lambda$ channel by the $\Sigma(1385)$. The properties of the spectral functions of the $\Sigma(1385)$ and $\Lambda(1405)$ resonances are very apparent. The shape of the resonant behaviour of the $K^-\,p \to \pi^0\,\Lambda$ cross section below threshold is quite symmetric and close to a Breit-Wigner form. The s-wave contribution is small as expected for a process dominated by a p-wave resonance. In contrast, the spectral form of the $K^-\,p \to \pi\,\Sigma$ cross sections for the three possible $\pi\,\Sigma$ channels is asymmetric and largely given by s-wave dynamics, reflecting the $\Lambda(1405)$ dominance. The grey histograms show (in arbitrary units) the empirical shape of the $\Lambda(1405)$ resonance extracted from the $p\,(\gamma, K^+\pi)\,\Sigma$ reaction at 1.5-2.4 GeV photon energy [3]. It should be

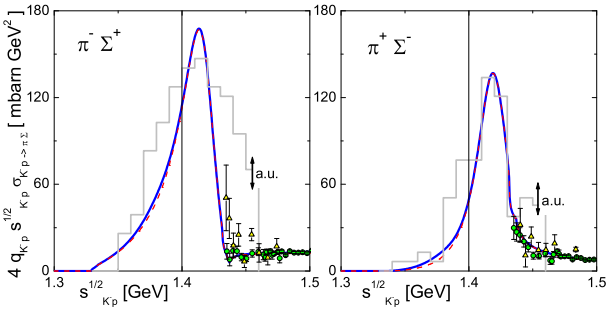

emphasized that strictly speaking the comparison implied by the figure is not yet justified. Only after extracting the double kaon pole contribution from the cross section by a detailed study of t-distributions can this comparison become legitimate. The result of such an analysis is expected to resolve the discrepancy of the histograms and the K^-p scattering data, at least above threshold. Nevertheless, the different line shapes of [3] seem to confirm the prediction of chiral coupled-channel dynamics that the spectral shape of the $\Lambda(1405)$ resonance depends crucially on the initial and final states it is probed with [2]. We note that the available K^-p scattering data close to threshold have large error bars, emphasizing the interest of being able to determine from experiment the subthreshold K^-p scattering amplitudes by extracting the double kaon pole contributions to the $\gamma p \to K^+\pi Y$ reactions calculated in this work.

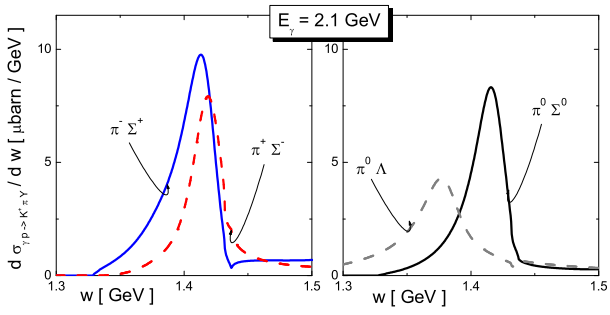

References

[1] M.F.M. Lutz and M. Soyeur, Nucl. Phys. A 748 (2005) 499.

[2] M.F.M. Lutz, E.E. Kolomeitsev, Nucl. Phys. A 700 (2002) 193.

[3] K. Ahn, Nucl. Phys. A721 (2003) 715c and private communication from T. Nakano.

Relativistic Mean-Field Models with Effective Hadron Masses and Coupling Constants, and ρ^- Condensation

E.E. Kolomeitsev[1] and D.N. Voskresensky[2]
[1]University of Minnesota USA; [2]GSI; MEPhI Moscow

We study [1] generalized relativistic mean field (RMF) models that include in-medium field dependent changes of meson masses and coupling constants. We demonstrate equivalence of a certain class of the models. Practically we show that the energy density for homogeneous matter depends only on three independent combinations of mass and coupling scaling functions. Often this equivalence is not realized and one considers some models as different, whereas in reality they are identical for the description of homogeneous matter on the mean field level.

Then, following the Brown-Rho suggestion we discuss a possibility to incorporate a concept of a universal decrease of hadron masses with a density increase into an RMF model. We show that a naive modification of solely boson masses would lead to severe drawbacks, like discontinuous changes of mean fields and hadron masses with the density. To get rid off these problems the mass scaling should be essentially compensated by the scaling of the corresponding coupling constants. For linear RMF models, i.e., without a non-linear σ potential U, we demonstrate equivalence of the models with universal scaling $g_i^* m_i/g_i m_i^* \simeq 1$, $i=\sigma,\omega,\rho$, and the models without any scaling of those masses and couplings. For non-linear RMF models ($U\neq 0$) the above equivalence would require a certain relation between corresponding non-linear potentials.

Then we demonstrate the efficiency of the generalized RMF models based on the modified Walecka (MW) model with a non-universal scaling of meson masses and couplings (MW(nu)). It allows to enlarge the threshold density for the extremely efficient direct Urca process $n\to pe\bar\nu$ and produces a stiffer equation of state of the neutron star (NS) matter at large densities without any changes of the equation of state near the saturation density. These possibilities are favored by "the nuclear medium cooling scenario" for the NS cooling, cf. [2], and by recent measurements of heavy NSs. All standard RMF models yield the threshold density for the direct Urca reaction in NSs $n_{\rm crit}^{\rm DU} < (2\div 3)\ n_0$. If one used a standard RMF model fitted to reproduce the Urbana-Argonne EoS for $n<4n_0$, but, producing a low DU threshold ($n_{\rm crit}^{\rm DU}\simeq (2.6\div 2.7)\, n_0$), one would conclude that the majority of the NSs seen in soft X rays are low mass objects with the mass $M<1.3\,M_\odot$. Objects with $M>1.3\,M_\odot$ are then not seen in soft X rays being very cold due to the permitted direct Urca process. However the value $1.3\,M_\odot$ is below the averaged value of the NS mass ($M\simeq 1.35\pm 0.04\,M_\odot$) measured in the NS binaries. The microscopic Urbana-Argonne model (A18+δv+UIX*) [3] produces $n_{\rm crit}^{\rm DU}\simeq 5\ n_0$, that is reached in the center of the NS with $M=M_{\rm crit}^{\rm DU}\simeq 2\,M_\odot$.

Authors of many RMF models (e.g., cf. NLZ model) being applied for the description of finite nuclei and heavy ion collisions do not care about the problem with low threshold density for the direct Urca reaction and obtain so low values $n_{\rm crit}^{\rm DU}$ that the process would occur already in low mass NSs, $M<1\,M_\odot$. However according to the standard mechanisms only the NSs with $M\gtrsim 1\,M_\odot$ can be formed in supernova explosions.

We also demonstrated an example of the MW(nu) model that fits well the mentioned Urbana-Argonne equation of state (more precisely, the fit [4] that cures the causality problem) including the symmetry energy, thus yielding the same threshold density for the direct Urca process.

Our generalized RMF models with a non-universal scaling of meson masses and couplings might be useful in discussion of possibilities of different phase transitions in NS interiors, since they allow to compensate a softening of the equation of state due to a phase transition by a stiffening due to a stronger decrease of masses compared to a decrease of couplings.

If one introduces a rho-meson field as a non-Abelian gauge boson in a RMF model which supports the decreasing ρ-meson mass, one should take care of the possibility of the charged rho meson condensation in the neutron enriched matter. We demonstrated that in the framework of our MW(nu) models the novel phase arises in NSs by a second order phase transition. The critical density $n_{\rm c}^{\rho,\rm II}$ is rather low (typically $\sim 3\div 4\,n_0$). If one used a model assuming a smaller nucleon mass at the saturation, one could get a still smaller value of the critical density. Charged ρ condensation slightly softens the equation of state. In the neutron-enriched matter the charge of the ρ-meson condensate is negative. We evaluated the emissivity of the direct Urca-like processes on the condensate ρ^- meson. The resulting rate behaves similar to that for the π^- condensate. The analysis of the cooling data indicates that the value $n_{\rm c}^{\rho,\rm II}$ should be not too small, $n_{\rm c}^{\rho,\rm II}\gtrsim (2.5\div 2.7)\ n_0$.

The MW(nu) models can be useful for the description of properties of finite nuclei. It would be interesting to apply them to the description of heavy-ion collisions. Recent studies of the collective isospin flow [5] extracted the density dependence of the symmetry energy but did not introduce any astrophysical constraints and a possible soft mode contribution. It is therefore a challenge to fit the corresponding data using the constructed above models with inclusion of thermal contribution from soft modes.

References

[1] E.E. Kolomeitsev and D.N. Voskresensky, arXiv: nucl-th/0410063.
[2] D. Blaschke, H. Grigorian, and D.N. Voskresensky, Astron. Astrophys. **424**, 979.
[3] A. Akmal, V.R. Pandharipande and D.G. Ravenhall, Phys. Rev. **C58** (1998) 1804.
[4] H. Heiselberg and M. Hjorth-Jensen, Phys. Rep. **328** (2000) 237.
[5] K. Tuchitani et al., arXiv:nucl-th/0407004.

Strange and charm resonances in a hot pion gas

C. Fuchs, Amand Faessler, M.I. Krivoruchenko, B.V. Martemyanov
Institut für Theoretische Physik, Universität Tübingen

In heavy-ion reactions at RHIC energies the medium is baryon dilute but meson rich. Since by far the most abundant particles are pions, one can speak about pion matter. In [1, 2] we investigated medium modifications of mesons with open strangeness (K) and open charm (D) and the consequences of the corresponding resonances (ϕ and charmonia $J/\Psi, \Psi', \ldots$) which are considered as promising probes for the fireball formed in ultra-relativistic reations.

The in-medium mass operator of kaons can be expressed in terms of the πK forward scattering amplitudes. At the on-shell point the kaon self-energy, $\Sigma(M_K^2, M_K)$, the mass shift δM_K, and the vector potential V_K can be expressed in terms of the s- and p-wave scattering lengths and the s-wave effective ranges:

$$\begin{aligned} \Sigma(M_K^2, M_K) &= -4\pi n_v \frac{M_\pi + M_K}{M_\pi} a_0^+ \\ V_K &= -\frac{2\pi n_v}{M_\pi + M_K}\left(a_0^+ + 2M_\pi M_K (b_0^+ + 3a_1^+)\right) \\ \delta M_K + V_K &= \frac{\Sigma(M_K^2, M_K)}{2M_K} \quad . \end{aligned} \tag{1}$$

The self-energy operator for kaons has in isotopically symmetric pion matter the same form as for antikaons due to C-parity and the same holds for δM_K and V_K, distinct from nuclear matter where SU(3) symmetry breaking leads to a $K^\pm$ mass splitting. The on-shell πK amplitudes have been calculated

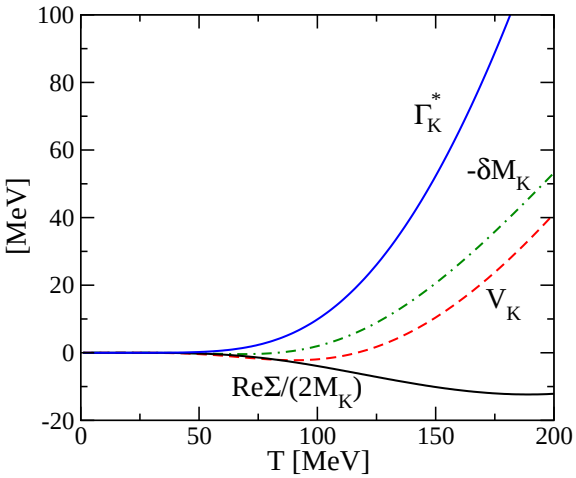

Figure 1: Kaon self-energy $\Re\Sigma/(2M_K)$, mass shift $-\delta M_K$, and vector potential V_K, and collision width Γ_K^* versus temperature T in isotopically symmetric pion matter.

in ChPT to the order p^4 by several authors, Ref. [3] gives $a_0^+ = (0.023 \pm 0.012)/M_\pi$ and $b_0^+ + 3a_1^+ = (0.054 \pm 0.008)/M_\pi^3$. The representation (1) is valid when the amplitudes are expanded near threshold and provide the complete results in ChPT to one loop. However, ChPT is applicable at temperatures $T \leq M_\pi$. To go to higher T we used a more phenomenological approach which satisfies unitarity, fits the experimental πK scattering phases and matches smoothly with one-loop ChPT in the low-temperature limit. The result can be seen from Fig.1. The in-medium ϕ-meson width increases, since the Breit-Wigner distribution allows an effective reduction of the kaon masses and, as a consequence, an effective increase of the available phase space. At $T = 170$ MeV, we obtain a medium width of $\Gamma_\phi^{\rm med} \sim 12$ MeV.

In [2] the approach was extended to the charm sector. The D-meson self-energies in pion matter have been determined to leading order in density taking thereby resonances in the $D\pi$ amplitude into account. The resonances in $s-$, $p-$ and $d-$ waves of D-meson-pion system were represented by low lying scalar, vector and tensor D^*-mesons which have been observed experimentally. For the forward resonance amplitude $A_{1/2}$ we use the relativistic Breit-Wigner form

$$A_{1/2} = \sum_{j=0,1,2} \frac{8\pi\sqrt{s}}{k} \frac{(2j+1)}{(2j_1+1)(2j_2+1)} \frac{-\sqrt{s}\Gamma_j^{D\pi}}{s - M_j^2 + i\sqrt{s}\Gamma_j^{tot}} \ , \tag{2}$$

where $j = 0, 1, 2$ corresponds to the $s-, p-$ and $d-$ wave resonances D_0^*, D^* and D_2^* in the $D\pi$ system with masses M_j, partial and total widths $\Gamma_j^{D\pi}$ and Γ_j^{tot} , respectively; $j_1 = j_2 = 0$ are the spins of the D and the pion, respectively, and k is the c.m. momentum. This allows to determine the D self-energy in a model independent way. At a temperature around 200MeV the D-meson mass is reduced by about 60MeV and the scattering width is also about 60MeV. Similar medium modifications were found for D^*- vector mesons. Consequently, the widths of

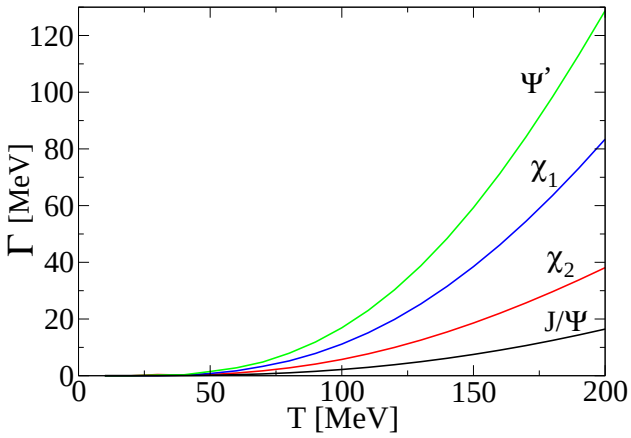

Figure 2: In-medium width of J/Ψ, χ_1, χ_2 and Ψ' mesons.

the decay and dissociation channels of the charmonium states Ψ', χ_c and J/Ψ to $D\bar{D}$, $D^*\bar{D}$, $D\bar{D}^*$, $D^*\bar{D}^*$ pairs are significantly enhanced (from $\Gamma_{J/\Psi} \simeq 16$ MeV to $\Gamma_{\Psi'} \simeq 130$ MeV at $T \simeq 200$ MeV). As a consequence, feeding of J/Ψ states from excited charmonium states ceases almost in a hot pion gas which characterizes the hadronic final state in high energetic heavy ion reactions in good approximation.

References

[1] B.V. Martemyanov, A. Faessler, C. Fuchs, M.I. Krivoruchenko, Phys. Rev. Lett. **93** (2004) 052301.
[2] C. Fuchs et al., nucl-th/0410065.
[3] V. Bernard et al., Nucl. Phys. **B357** (1991) 129.

Phase Space Considerations for High-Energetic Heavy-Ion Collisions

W. Deinet, D. H. Rischke
Institut für Theoretische Physik der Universität Frankfurt

The influence of the kinematics on the shape of transverse mass spectra and rapidity spectra was studied using data for Pb-Pb collisions at 158AGeV taken by the NA49-Collaboration [1]. In a first step, the quantum mechanical transition matrix element was put to 1, which has the effect that interactions between the particles are neglected. This leads to the relativistic invariant phase space integral, which describes the kinematics of the process. Depending on the total energy of the reaction some thousands of secondary particles can appear.

A Fortran routine by Kajantie and Karimäki, available at the CPC-library, based on a statistical method using the saddle-point procedure [2] to calculate phase space integrals up to about 100 particles, was modified to handle more than 2000 particles. Besides the total energy of the reaction, input parameters of the program are the mass and the multiplicity of the secondaries.

The multiplicity table published by the NA49-Collaboration contained data of measured particles only. The model however needs data for all secondaries. By symmetry considerations, conservation laws, a simple quark model, and an empirical rule multiplicity values of further particles were reconstructed. By this totally 2611 secondary particles were obtained. The extended multiplicity table was used for most of the model calculations. Tests with 200 additional particles showed that the results of the study do not change significantly.

Transverse mass spectra and rapidity spectra are derived from the phase space integral and compared in detail with the measured spectra of π^-, K^+ and K^--mesons. The model predicts transverse mass spectra of exponential shape, which are different from those derived by the thermal model, respectively the Cooper-Frye model with freeze-out at some time $t = const$ [3]. The experimental transverse mass spectra are approximately straight lines in a lin-log plot. The phase space integral model predicts a larger slope value than the measured one. This means that in the experiment high transverse momenta are suppressed beyond simple phase space considerations in the reaction.

The rapidity spectra of the thermal and the phase space model are very similar and have a gaussian-like shape. The distributions obtained by the phase space model are a little wider than those of the thermal model. The experimental rapidity spectra are considerably wider than those of both models.

To improve the agreement between the measurements and the phase space integral model a matrix element was simulated by a simple function that performs the suppression of high transverse momentum values. For this an exponentially decaying function of the transverse mass and a free parameter a was introduced into the phase space integral. The positive parameter a has the consequence that the transverse mass spectra are decaying faster as well as the rapidity spectra getting wider. Fortran- and Maple-programs were developed to calculate the modified phase space integral. This extended model describes the experimental spectra of pions and kaons fairly well by adjusting the free parameter a. The best fits were obtained by choosing different parameters a for each kind of particle or when fitting transverse mass spectra and rapidity spectra separately.

The relativistic invariant phase space integral defines a distribution function for the momenta which is different from the distribution functions obtained in thermodynamics. The system defined by the relativistic invariant phase space integral is not described in terms of thermodynamics and the model does not yield a value for the temperature in agreement with basic thermodynamic rules.

References

[1] The NA49 Collaboration, S.V. Afanasiev et al., *Energy Dependence of Pion and Kaon Production in Central Pb+Pb Collisions*, arXiv:nucl-ex/0205002v2, 2002

[2] K.Kajantie, V.Karimäki, *The Evaluation of the Volume of the Phase Space of N Particles*, Computer Physics Communications 2, North Holland Publishing Company, p. 207, 1971

[3] F.Cooper, G. Frye, E. Schonberg, *Landau's hydrodynamic model of particle production and electron-positron annihilation into hadrons*, Phys. Rev. D, Vol.11, N.1, 1975

Transport analysis of K^+ production in p+A collisions

Z. Rudy[1], W. Cassing[2], A. Kowalczyk[2]
[1]University of Cracow, [2] University of Giessen

The production of heavy mesons in $p + A$ reactions at bombarding energies far below and close to the free nucleon-nucleon threshold is of specific interest as one hopes to learn about cooperative nuclear phenomena and the meson interaction potential at normal nuclear matter density. Especially K^+ mesons are considered as promising hadronic probes due to the rather moderate final state interaction, which is a consequence of strangeness conservation.

Experiments on $K^{\pm}$ production from nucleus-nucleus collisions at SIS energies of 1– 2 A· GeV have shown that in-medium properties of the kaons are seen in the collective flow pattern of K^+ mesons both, in-plane and out-of-plane, as well as in the abundancy of antikaons [1]. Thus in-medium modifications of the mesons have become a topic of substantial interest in the last decade triggered in part by the early suggestion of Brown and Rho [2], that the modifications of hadron masses should scale with the scalar quark condensate $< q\bar{q} >$ at finite baryon density.

In this study on K^+ production in p+A reactions we use the coupled-channel (CBUU) transport model that has been developed first for the description of nucleus-nucleus collisions and later on employed for the simulation of pion- and proton-nucleus reactions, too. In this model the effects of momentum-dependent self energies for all hadrons can be studied explicitly as well as their production and propagation in the nuclear medium. The actual version of the CBUU transport model used in our present analysis is identical to that described in Ref. [3] where the explicit momentum-dependent potentials employed for the nucleon and hyperon degrees of freedom are given.

As demonstrated in Ref. [4] these calculations compare well to the data from the ANKE collaboration [5] for p + ^{12}C and p+^{197}Au reactions from 1.0 to 2.3 GeV laboratory energy. Moreover, we recall that the variation in the low K^+ momentum spectrum in the laboratory is a consequence of i) the different acceleration of the charged kaon in the Coulomb field of the target and ii) an additional acceleration in the repulsive kaon potential in the nuclear medium (target nucleus). The combined effect of both the Coulomb and nuclear repulsion is most easily seen when comparing the K^+ spectra from different targets. To this aim we show in Fig. 1 the ratio of the spectra from Au to C targets at 1.5 and 2.3 GeV, where this effect is most pronounced (cf. Ref. [5]). The different solid lines in Fig. 1 correspond to calculations employing different nuclear kaon potentials of magnitude 0, 10 and 20 MeV at normal nuclear density ρ_0 (starting from the left).

It is seen that the ratio for (Au/C) is approximately independent on the bombarding energy and shows a maximum at about 230 MeV/c. When neglecting kaon repulsion from nuclear forces – including only Coulomb repulsion – this maximum shows up slightly below 200 MeV/c, which is clearly too low in comparison to the data (cf. [5]). We recall that the relative strength of the momentum shift in the forward K^+ spectra is proportional to the square root of the sum of Coulomb and nuclear potentials, $\Delta p \approx \sqrt{2M_K(U_{Coul} + U_K)}$, which implies that an additional repulsive nuclear K^+ potential is needed to describe the data. Since the strength of this potential – linear in the nuclear density at the K^+ production point – is a 'parameter' in the transport calculations, we may in turn determine the strength of this potential in comparison to the data. A χ^2-fit gives $U_K(\rho_0) \approx 20 \pm 5$ MeV for the ratio of $p + Au$ to $p + C$ reactions which is compatible with the result from the scattering length approximation and the analysis of A+A reactions [1].

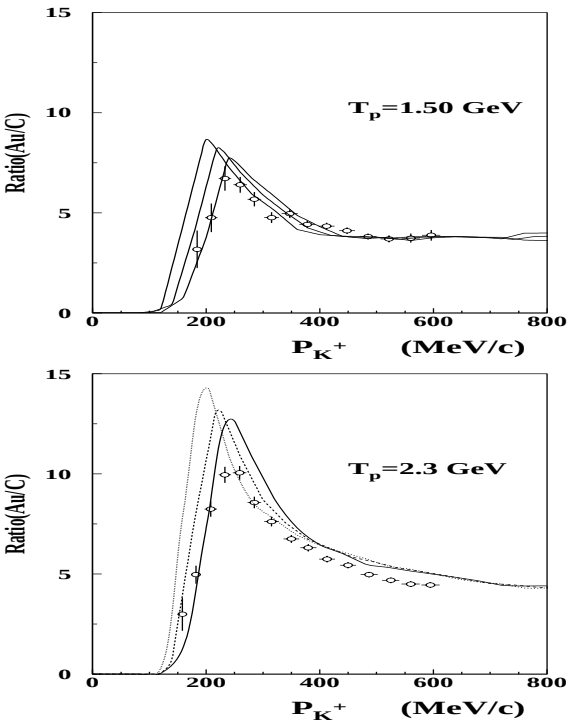

Figure 1: The ratio of the calculated differential K^+ spectra from $p + Au$ to $p + C$ reactions at 1.5 and 2.3 GeV in comparison to the data from Ref. [5]. The different solid lines correspond to calculations employing different kaon potentials at normal nuclear density ρ_0. Starting from the left the results correspond to repulsive kaon potentials of 0, 10 and 20 MeV at ρ_0.

References

[1] P. Senger, Prog. Part. Nucl. Phys. **53**, 1 (2004)
[2] G. E. Brown, M. Rho, Phys. Rev. Lett. **66**, 2720 (1991)
[3] Z. Rudy *et al.*, Eur. Phys. J. A **15**, 303 (2002)
[4] Z. Rudy *et al.*, Eur. Phys. J. A **23**, 379 (2005)
[5] M. Büscher *et al.*, Eur. Phys. J. A **22**, 301 (2004)

Relativistic Heavy-Ion Collisions within 3-Fluid Hydrodynamics

I. Hadronic Scenario

Yu.B. Ivanov[1,2], V.N. Russkikh[1,2], and V.D. Toneev[1,3]
[1]GSI; [2]Kurchatov Inst., Moscow; [3]JINR, Dubna

A 3-fluid hydrodynamic model for relativistic heavy-ion collisions is a joint project of GSI, Kurchatov Inst. and JINR. It is primarily aimed to study physics related to the future GSI facility, i.e. relativistic nucleus-nucleus collisions at incident energies $E_{\rm lab} \simeq 10 - 40$ A·GeV. In this energy range the highest baryon densities and highest relative strangeness at moderate temperatures are expected to be achieved. A brief account of this model has been already reported in ref. [1]. The developed code allows calculations with various equations of states (EoS). We have started with the simplest, purely hadronic EoS which involves only a simple density dependent mean field, providing saturation of cold nuclear matter at normal nuclear density $n_0 = 0.15$ fm^{-3} with the proper binding energy -16 MeV. This EoS is a natural reference point for any other more elaborate EoS. Much to our surprise, this trivial EoS turned out to be able to reasonably reproduce a great body of experimental data. These results are reported below. The quality of data reproduction is illustrated in Figs 1 and 2. Predictions of transport HSD and UrQMD models [2] are also shown for comparison. Since particles are not isotopically distinguished in the 3-fluid model, the proton spectrum is estimated as Z/A fraction of the nucleon one, where Z and A are the proton and mass numbers, respectively, in the colliding (identical) nuclei. This estimate is quite reasonable at incident energies of few A·GeV. However, at higher energies, when abundant particle production starts, this recipe somewhat underestimates the proton number, because newly produced particles tend to restore the isotopic symmetry. The $(p-\bar{p})$ quantity, which is usually measured at higher incident energies, is much less sensitive to the effect of newly produced particles, since their contribution is essentially canceled in the difference $(p - \bar{p})$. Therefore, the Z/A scaling of the nucleon-antinucleon difference is a reasonable approximation for it. Due to the same reason, numbers of pions of each charge are approximately assumed to be equal, i.e. $N_{\pi^+} = N_{\pi^-} = N_{\pi^0} = N_\pi/3$, where N_π is the calculated total number of pions. Of course, this is a rough estimate of π^+ and π^- yields, since N_{π^-} always exceeds N_{π^+} because of the initial isotopic asymmetry of colliding nuclei. Therefore, "a good agreement" with pion data means that calculated $N_\pi/3$ complies with experimental $(N_{\pi^+} + N_{\pi^-})/2$. A similar reproduction is also achieved for proton transverse-mass distributions, rapidity spectra of Λ and $\bar{\Lambda}$ hyperons and antiprotons [3]. With this EoS there are problems with description of proton and pion directed flow at $E_{\rm lab} \gtrsim 40$ A·GeV.

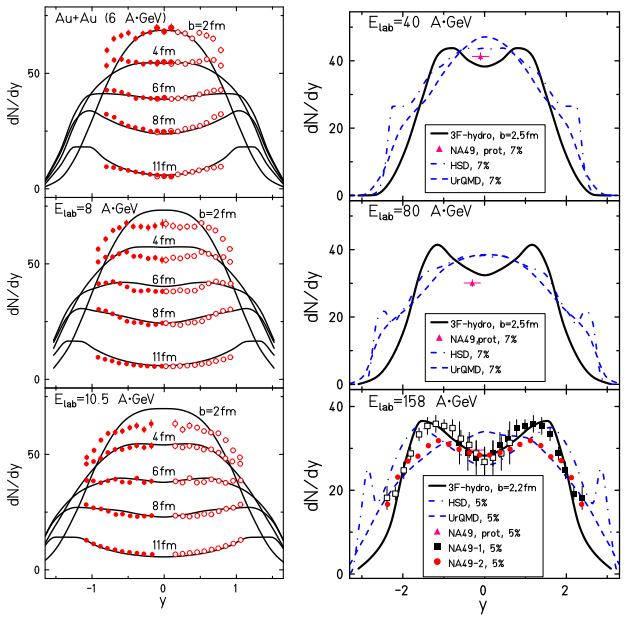

Figure 1: Proton rapidity spectra at AGS energies for various impact parameter (left panel) and $(p-\bar{p})$ rapidity distribution from central $Pb+Pb$ collisions at SPS energies (right panel). Solid lines are 3-fluid calculations, dashed-dotted and dashed lines are the corresponding predictions of the HSD and UrQMD models [2], respectively. Experimental data are from E895 Collaboration (left panel) and NA49 Collaboration (right panel).

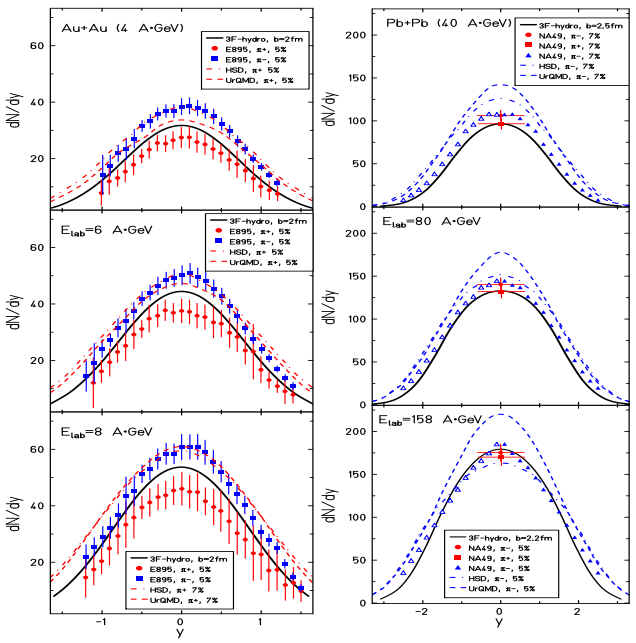

Figure 2: The same as in Fig.1 but for pion rapidity spectra from central collisions.

References

[1] V.N. Russkikh et al., Phys. At. Nucl. **67** (2004) 199.
[2] H. Weber et al., Phys. Rev. C **67** (2003) 014904.
[3] Yu.B. Ivanov, V.N. Russkikh, V.D. Toneev, in preparation.

Relativistic Heavy-Ion Collisions within 3-Fluid Hydrodynamics

II. Global Evolution

Yu.B. Ivanov[1,2], V.N. Russkikh[1,2], and V.D. Toneev[1,3]
[1]GSI; [2]Kurchatov Inst., Moscow; [3]JINR, Dubna

It was shown that the 3-fluid hydrodynamic model with the simplest, purely hadronic EoS is able to reasonably reproduce a great body of experimental data on relativistic heavy-ion collisions [1]. With thus fixed parameters of the model, it is possible to address to the question of global evolution of nuclear collisions, i.e. to the values of baryon densities and temperatures achieved in the course of them. An important question also is how long and in which volume these achieved values survive. A conventional way to address to these questions is in terms of dynamic trajectories in the temperature–baryon-density (T, n_B) plane, see Fig. 1. The transition (mixed-phase) region from the hadronic phase to the QGP one is displayed just for orientation, since the actual EoS is purely hadronic. The 3-fluid nonequilibrium is quite strong at the initial stage of the collision. Therefore, the mean values of T and n_B are calculated by means of averaging of these quantities corresponding to either separate fluids, if their mutual stopping has not occurred, or the unified fluid, if the stopping has happened, with the weight of baryon charge. This convention has been chosen in order to map the nonequilibrium configuration in terms of equilibrium quantities, avoiding unphysical contributions of the Lorentz contraction and collective motion into thermodynamic quantities $\langle T \rangle$ and $\langle n_B \rangle$. In addition to the uncertainties of mapping of nonequilibrium on equilibrium, the displayed time instants correspond to the cm frame of colliding nuclei and hence are noninvariant. Therefore, Fig. 1 does not tell us (in invariant way) how long the dense matter survives and in which volume.

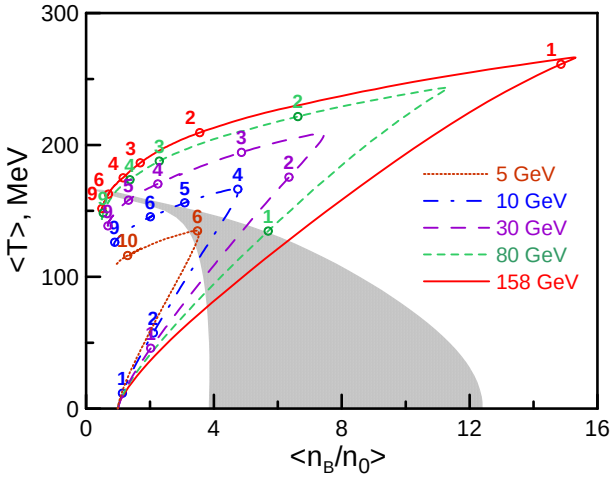

Figure 1: Dynamic trajectories in the (T, n_B) plane for central $Pb+Pb$ collisions at different energies. The transition (mixed-phase) region from the hadronic phase to the QGP one, estimated by means of the standard EoS based on the MIT bag model [2], is displayed by shaded area. Numbers near the dynamical trajectories show the evolution time instants.

The way to overcome the above difficulties was proposed in [3]. It consists in calculation of an invariant 4-volume V_4 in which a quantity q exceeds a given value Q

$$V_4(Q) = \int d^4x \, \Theta(q - Q). \qquad (1)$$

This quantity provides a Lorentz invariant measure of the space–time region, where the quantity q keeps high value $q \geq Q$. In Fig.2 this 4-volume is shown for two cases: $q = n_B^{(\mathrm{eq.})}$, i.e. with 4-volume summed only over those regions where stopping (i.e. equilibration) has occurred and thermalized n_B exceeds certain value, and $q = n_B^{(\mathrm{noneq.})}$, i.e. with 4-volume summed over all regions, including those where stopping has not occurred. To get an impression of the scale of these quantities, we draw a short-dashed line presenting the Lorentz-contracted 4-volume $\Delta t \cdot \pi R^2 \cdot 2R/\gamma_{cm}$ composed of Lorentz-contracted cylindrical space volume of radius $R = 5$ fm and time interval $\Delta t = 3$ fm/c, here γ_{cm} is the γ-factor of colliding nuclei in their cm frame. In particular, it is seen that incident energies 10–40 A·GeV are favorable for production equilibrated matter with baryon densities higher $6n_0$.

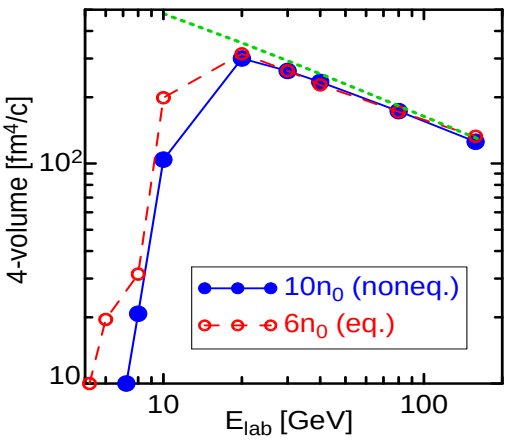

Figure 2: Invariant 4-volumes corresponding to conditions $n_B^{(\mathrm{noneq.})} > 10n_0$ (solid line) and $n_B^{(\mathrm{eq.})} > 6n_0$ (long-dashed line) for central $Pb + Pb$ collisions as functions of the incident energy.

References

[1] V.N. Russkikh et al., Phys. At. Nucl. **67** (2004) 199; Yu.B. Ivanov et al., in preparation.
[2] V.D. Toneev et al., Eur. Phys. J. **C32** (2004) 399.
[3] B. Friman et al., Eur. Phys. J. **A3** (1998) 165.

Collective flow of open and hidden charm in the hadron/string picture

E.L. Bratkovskaya[a], W. Cassing[b], A. P. Kostyuk[a], H. Stöcker[a], and N. Xu[c]
[a]Institut für Theoretische Physik & FIAS, Univ. Frankfurt; [a]Institut für Theoretische Physik, Univ. Giessen;
[c]LBNL, Berkeley, CA 94720, USA

The $c, \bar{c}$ quark degrees of freedom are of particular interest in context with the phase transition to the quark-gluon plasma (QGP) since $c\bar{c}$ meson states (J/Ψ, χ_c, Ψ') might no longer be formed due to color screening as suggested by Matsui and Satz [1]. However, more recent calculations within lattice QCD (LQCD) have shown that at least the J/Ψ should survive up to $\sim 2\,T_c$ ($T_c \approx 0.17$ GeV) such that the lowest $c\bar{c}$ states remain bound up to energy densities of about 5 GeV/fm^3, which is well within the anticipated QGP phase [2]. In the recent years it been pointed out, furthermore, that at top RHIC energies the charmonium formation from open charm and anticharm mesons might become essential or even exceed the yield from primary nucleon-nucleon (NN) collisions.

Indeed, a previous analysis within the HSD transport model [3] has demonstrated that the charmonium production from open charm and anticharm mesons ($D + \bar{D} \to J/\Psi$ + meson) should become essential in central Au+Au collisions at RHIC while these backward channels – relative to charmonium dissociation with comoving mesons – should be practically negligible at SPS energies. Furthermore, at SPS energies the differences between the results of various statistical models and the HSD transport approach are found to be rather moderate due to a fit of the model parameters to the available data. This situation changes substantially at RHIC energies of $\sqrt{s} = 200$ GeV where the comover absorption model as well as the threshold absorption model by Blaizot *et al.* [4] lead to an almost complete suppression of J/Ψ's in central collisions. As argued in Ref. [3] this large suppression is essentially due to a neglect of the backward channels $D + \bar{D} \to$ charmonia + meson in the latter models. On the other hand the HSD calculations – that include the various backward channels – lead only to a moderate J/ψ suppression roughly compatible with the result of the statistical coalescence model and the PHENIX data (cf. Ref. [5]). This finding suggests that the J/Ψ and open charm degrees of freedom reach approximate chemical equilibrium for mid-central and central Au+Au collisions at RHIC.

Apart from the total and relative abundancies of charmonia and open charm mesons also their collective properties are of interest. Here the transverse momentum (or mass) spectra are expected to provide valuable insight to the dynamics in the very early phase as well as the in-plane flow (v_1) and elliptic flow (v_2). The central question is: will the charmonia and open charm mesons with their substantially higher mass also show the strong flow of the light hadrons – composed of $u, d, s, \bar{u}, \bar{d}, \bar{s}$ quarks – as expected from hydrodynamics?

The HSD predictions are shown in Fig. 1 for the directed flow v_1 and elliptic flow v_2 of $D + \bar{D}$-mesons and J/Ψ from Au + Au collisions at $\sqrt{s} = 200$. Whereas the flow v_1 of $D, \bar{D}$ and charmonia is comparable with that of the light mesons [6] the elliptic flow v_2 of $D, \bar{D}$ and charmonia stays on a rather low level ($\sim$ 3 %) and is limited (at midrapidity) in transverse momentum p_T by 4%. This low elliptic flow in the hadron/string dynamical picture is a consequence of small (or moderate) interaction rates with the light hadrons [6]. The preliminary data from PHENIX and STAR, however, suggest an elliptic flow of $\sim 15\%$ for $p_T \geq 1.5$ GeV/c – comparable to the elliptic flow of light hadrons – which is large compared to the HSD predictions. We interpret this failure of the hadron/string picture to early and strong interactions in a partonic plasma phase. Note, however, that this early phase is incompatible with a weakly interaction plasma and shows the dynamical properties of a almost ideal colored liquid.

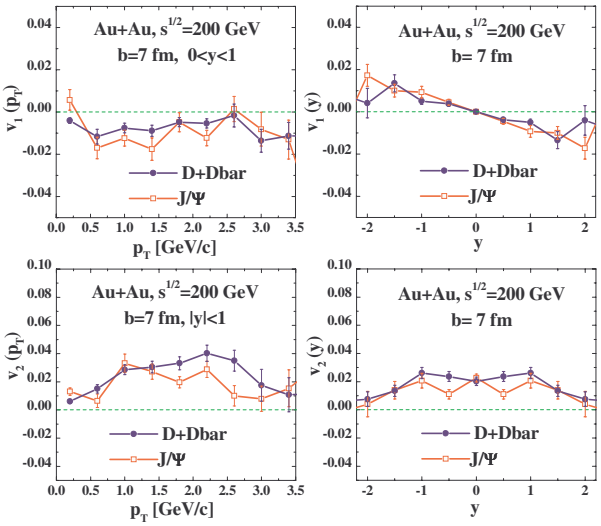

Figure 1: The directed flow v_1 (upper part) and elliptic flow v_2 (lower part) of $D + \bar{D}$-mesons (solid lines with full dots, color: blue) and J/Ψ (solid lines with open squares, color: red) from Au + Au collisions at $\sqrt{s} = 200$ GeV for $b = 7$ fm versus p_T for $0 < y < 1$ (left part) and rapidity y (right part) integrated over p_T.

References

[1] T. Matsui and H. Satz, Phys. Lett. B **178**, 416 (1986).
[2] S. Datta, F. Karsch, P. Petreczky, and I. Wetzorke, J. Phys. G **30**, S1347 (2004).
[3] E. L. Bratkovskaya, W. Cassing, and H. Stöcker, Phys. Rev. C **67**, 054905 (2003).
[4] J. P. Blaizot, P. M. Dinh and J. Y. Ollitrault, Phys. Rev. Lett. **85**, 4012 (2000).
[5] E.L. Bratkovskaya, A.P. Kostyuk, W. Cassing, and H. Stöcker, Phys. Rev. C **69**, 054903 (2004).
[6] E.L. Bratkovskaya, W. Cassing, H. Stöcker, and N. Xu, nucl-th/0409047, Phys. Rev. C, in press.

Inhomogeneous freeze-out in heavy-ion collisions

A. Dumitru[a], L. Portugal[a,b] and D. Zschiesche[a]
[a]Institut für Theoretische Physik, Universität Frankfurt a.M., Germany
[b]Instituto de Fisica, Universidade Federal do Rio de Janeiro, Brazil

Lattice QCD finds that a line of first-order phase transitions in the (μ_B, T) plane ends in a critical point at $T \approx 160$ MeV, $\mu_B \approx 360$ MeV [1]. There is an ongoing experimental effort to detect that critical point in heavy-ion collisions at high energies. It is hoped that by varying the beam energy, for example, one can "switch" between the regimes of first-order transition and cross over, respectively. If the particles decouple shortly after the expansion trajectory crosses the line of first order transitions one may expect a rather inhomogeneous (energy-) density distribution on the freeze-out surface [2] (similar, say, to the CMB photon decoupling surface observed by WMAP [3]). On the other hand, collisions at very high energies ($\mu_B \simeq 0$) may cool smoothly from high to low T and so pressure gradients tend to wash out density inhomogeneities. Similarly, in the absence of phase-transition induced non-equilibrium effects, the predicted initial-state density inhomogeneities [4] should be strongly damped.

Here, we investigate the properties of an inhomogeneous fireball at (chemical) decoupling. Note that if the scale of these inhomogeneities is much smaller than the decoupling volume then they can not be resolved individually, nor will they give rise to large event-by-event fluctuations. Because of the nonlinear dependence of the hadron densities on T and μ_B they should nevertheless reflect in the *event-averaged* abundances. Our goal is to check whether the experimental data show any signs of inhomogeneities on the freeze-out surface.

Perhaps the simplest possible *ansatz* is to employ the grand canonical ensemble and to assume that the intensive variables T and μ_B are distributed according to a Gaussian. This avoids reference to any particular dynamical model for the formation and the distribution of density perturbations on the freeze-out surface. Also, in this simple model we do not need to specify the probability distribution of volumes V. Then, the average density of species i is computed as

$$\overline{\rho}_i\,(\overline{T}, \overline{\mu}_B, \delta T, \delta\mu_B) = \int_0^\infty dT\; P(T; \overline{T}, \delta T) \int_{-\infty}^{\infty} d\mu_B\; P(\mu_B; \overline{\mu}_B, \delta\mu_B)\; \rho_i(T, \mu_B)\;, \tag{1}$$

with $\rho_i(T, \mu_B)$ the actual "local" density of species i, and with $P(x; \overline{x}, \delta x) \sim \exp\left(-\frac{(x-\overline{x})^2}{2\,\delta x^2}\right)$ the distribution of temperatures and chemical potentials on the freeze-out surface. Feeding from (strong or weak) decays is included by replacing $\overline{\rho}_i \to \overline{\rho}_i + B_{ij}\;\overline{\rho}_j$. The implicit sum over $j \neq i$ runs over all unstable hadron species, with B_{ij} the branching ratio for the decay $j \to i$. For the present analysis we computed the densities $\rho_i(T, \mu_B)$ in the ideal-gas approximation.

We perform a χ^2 fit to both the midrapidity and 4π data obtained by NA49 for central Pb + Pb collisions at $\sqrt{s_{NN}} = 17.3$ GeV (compiled in [5]). A similar analysis for lower and higher energies is underway. Error estimates for the parameters (confidence intervals) are obtained from the projection of the regions in parameter space defined by $\chi^2 \leq \chi^2_{min} + 1$ onto each axis. This corresponds to a confidence level of 68.3% if the errors are normally distributed.

Table 1 shows the resulting best fits with and without finite widths of the T and μ_B distributions. The fits improve (lower χ^2/dof) substantially in both cases when δT, $\delta\mu_B$ are not forced to zero. The inhomogeneous fits return significantly lower mean temperature $\overline{T}$. However, this is *not* the "mean" temperature of the particles, which instead is given by $\langle T\rangle_i = \int dT\; TP(T) \int d\mu_B\; P(\mu_B)\; \rho_i(T, \mu_B)/\overline{\rho}_i$, cf. table 2. We see that e.g. the bulk of the particles originates from different density and temperature regions than the corresponding anti-particles. Hence, our results suggest that the decoupling surface might not be very well "stirred".

$\overline{T}$	$\overline{\mu}_B$	δT	$\delta\mu_B$	χ^2/dof
		SPS-158 (mid)		
155 ± 5	200 ± 10	0	0	40.4/8
105 ± 5	230 ± 15	35 ± 5	80 ± 40	11.2/6
		SPS-158 (4π)		
145 ± 5	210 ± 15	0	0	40.0/11
100 ± 5	260 ± 15	30 ± 5	190 ± 35	5.7/9

Table 1: Fit results. Lines with $\delta T = \delta\mu_B = 0$ correspond to a forced homogeneous fit.

SPS 158	p	$\bar{p}$	K^+	K^-	Ω	$\bar{\Omega}$
$< T >$ [MeV] (mid)	157	170	152	150	164	180
$< \mu_B >$ [MeV] (mid)	268	191	237	222	234	225
$< T >$ [MeV] (4π)	136	153	140	139	151	165
$< \mu_B >$ [MeV] (4π)	487	22	306	213	277	206

Table 2: Mean temperature and chemical potential of various particle species for the inhomogeneous freeze-out.

References

[1] Z. Fodor and S. D. Katz, JHEP **0404** (2004) 050.
[2] K. Paech, H. Stöcker and A. Dumitru, Phys. Rev. C **68** (2003) 044907; K. Paech and A. Dumitru, in preparation; O. Scavenius, A. Dumitru and A. D. Jackson, arXiv:hep-ph/0103219, figs. 5,6.
[3] `http://map.gsfc.nasa.gov/m_mm.html`
[4] M. Gyulassy, D. H. Rischke and B. Zhang, Nucl. Phys. A **613**, 397 (1997); M. Bleicher *et al.*, Nucl. Phys. A **638** (1998) 391; O. J. Socolowski, F. Grassi, Y. Hama and T. Kodama, Phys. Rev. Lett. **93** (2004) 182301.
[5] F. Becattini, M. Gazdzicki, A. Keranen, J. Manninen and R. Stock, Phys. Rev. C **69** (2004) 024905.

Transverse mass spectra in Heavy Ion Collisions from AGS to RHIC

M. Reiter[1], M. Bleicher[1], E. Bratkovskaya[1], S. Schramm[1], and H. Stöcker[1]
[1]Institut für Theoretische Physik, Johann Wolfgang Goethe-Universität Frankfurt am Main

Transverse mass spectra of hadrons are presently in the center of interest of the experimental study of relativistic heavy ion collisions. The significant suppression of high transverse momentum hadrons in Au+Au collisions compared to *pp* observed at RHIC energies [1] is often attributed to the energy loss of highly energetic particles in a hot colored medium (QGP) [2]. On the other hand, the measured transverse mass spectra of hadrons $(1/m_T)dN/dm_T \sim \exp(-m_T/T)$ at AGS, SPS and RHIC energies show a substantial *hardening* in central Au+Au collisions relative to *pp* interactions (cf. [3]). This hardening of the spectra for low transverse mass or momentum is commonly attributed to strong collective flow, which is absent in the respective *pp* or *pA* collisions.

We have investigated [4] the inverse slope parameter of transverse hadron spectra from *pp*, *pA* and *AA* collisions from AGS to RHIC energies within the HSD and UrQMD transport approaches, both based on quark, diquark, string and hadronic degrees of freedom. We have, furthermore, included various hadronic scenarios not present in the default versions of the models, to explore their potential effects on the $K^{\pm}$ spectra. These include the incorporation of PYTHIA [5] in UrQMD, denoted here as UrQMD 2.0, as well as the inclusion of additional high mass resonances, denoted as UrQMD 2.1. In HSD, the experimentally established initial state enhancement of transverse momentum spectra with increasing target mass A, known as the Cronin effect [6], has been implemented using an effective approach [7]. Our results are shown in Fig. 1, where the dependence of the inverse slope parameter T on $\sqrt{s}$ is compared to experimental data.

The slope parameters from *pp* collisions (r.h.s. in Fig. 1) are seen to increase smoothly with energy both in the experiment and in the HSD calculations. The UrQMD 1.3 results are systematically lower than the slopes from HSD at all energies. When including jet production and fragmentation via PYTHIA in UrQMD 2.0 the results become similar to HSD above $\sqrt{s} = 10$ GeV demonstrating the importance of jets in *pp* reactions at high energy.

Regarding the slope parameters of $K^{\pm}$ mesons for central Au+Au/Pb+Pb collisions (l.h.s. of Fig. 1), we find that the Cronin initial state enhancement indeed improves the description of the data at RHIC energies, however, does not give any sizeable enhancement at AGS energies. Here UrQMD 2.1 with the high mass resonance states performs better for K^+ mesons, but overestimates the K^- slopes at AGS as well as upper SPS energies.

Both models thus fail to give a complete description of the experimental data, both in their default versions and incorporating the alternative scenarios presented. Our analysis therefore suggests that the additional pressure - as expected from lattice QCD calculations at finite μ_q and T - should be generated by strong interactions in the early pre-hadronic/partonic phase of central Au+Au (Pb+Pb) collisions because hadronic interactions don't produce it in the later stages. These pre-hadronic/partonic degrees of freedom seem to play a substantial role in central Au+Au collisions already at AGS energies above ~ 5 A·GeV.

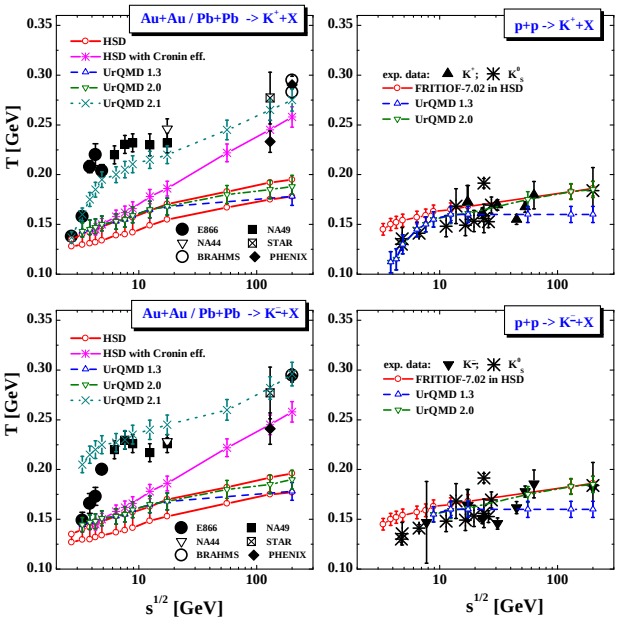

Figure 1: Comparison of the inverse slope parameters T for K^+ and K^- from central AA (l.h.s.) and *pp* collisions (r.h.s.) at midrapidity as a function of $\sqrt{s}$ from HSD, UrQMD 1.3, 2.0 and 2.1 with data. For references cf. [4].

Acknowledgements

We gratefully acknowledge support by the Frankfurt Center for Scientific Computing.

References

[1] J. L. Nagle and T. S. Ullrich, (2002); S. S. Adler *et al.*, Phys. Rev. Lett. **91**, 072303 (2003); J. Adams *et al.*, Phys. Rev. Lett. **91**, 072304 (2003); I. Arsene *et al.*, Phys. Rev. Lett. **91**, 072305 (2003).

[2] X.-N. Wang, Phys. Rev. **C58**, 2321 (1998); R. Baier, D. Schiff, and B. G. Zakharov, Ann. Rev. Nucl. Part. Sci. **50**, 37 (2000).

[3] C. Alt *et al.*, J. Phys. **G30**, S119 (2004); M. I. Gorenstein, M. Gazdzicki, and K. A. Bugaev, Phys. Lett. **B567**, 175 (2003).

[4] E. L. Bratkovskaya *et al.*, Phys. Rev. **C69**, 054907 (2004).

[5] H.-U. Bengtsson and T. Sjostrand, Comput. Phys. Commun. **46**, 43 (1987).

[6] J. W. Cronin *et al.*, Phys. Rev. **D11**, 3105 (1975); D. Antreasyan *et al.*, Phys. Rev. **D19**, 764 (1979).

[7] W. Cassing, K. Gallmeister, and C. Greiner, Nucl. Phys. **A735**, 277 (2004).

Simulation of hadronic collisions with the MC event generator SHERPA*

T. Gleisberg, S. Höche, F. Krauss, A. Schälicke, S. Schumann, J. Winter, and G. Soff
Institute for Theoretical Physics, D-01062 Dresden, Germany

Hadron colliders, such as the Tevatron at Fermilab or the Large Hadron Collider (LHC), which is under construction at CERN, provide an excellent opportunity to test whether the observed dynamics of collision products coincide with the predictions made by the Standard Model and its possible extensions. In such an environment, the accurate description of QCD effects is a major challenge. In particular, the composite nature of the beam particles leads to new calculational complications, which are absent in the case of leptonic initial states.

For the prediction of exclusive quantities, Monte Carlo (MC) event generators are the appropriate tool. Such programs rely on the approach to decompose the overall event into different stages. The main part is constituted by a hard scattering, which can be perturbatively calculated from first principles. Partons entering this hard scattering are found in the beam particles according to a Parton Distribution Function (PDF), and outgoing partons fragment into primary hadrons according to a Fragmentation Function (FF). Factorization guarantees the core process independence of these distributions. Several MC algorithms exist, which allow for an interpretation of the PDF and the FF through the parton shower picture. These algorithms can be employed to generate a realistic multiparton final state.

However, since parton showers resum the leading logarithmic terms of soft and/or collinear parton splittings, they fail in predicting wide angle and/or hard parton emissions. Such configurations are adequately described by hard matrix elements, which take all interference effects into account. On the other hand, since the calculational work increases roughly factorially with the order, the matrix element approach is insufficient for multiple parton emission. Thus, it is desirable to combine both approaches, thereby collecting their advantages and removing their weaknesses. In order to avoid double counting of equivalent phase space regions, the multijet phase space is divided into two regimes employing a jet resolution scale Q_{cut}. Given an appropriate definition of a jet measure Q, jet production is described by the tree-level matrix elements, whereas the intrajet evolution is given by the parton shower. Technically, this is realized as follows. The hard matrix elements are reweighted by a combined coupling and Sudakov weight, which accounts for a corresponding parton shower history. In turn, parton shower configurations already included by higher order matrix elements are vetoed. In doing so, the overall dependence on the separation cut is minimized. The entire algorithm is known as the CKKW merging procedure [1]. It is fully implemented in the new MC event generator `SHERPA` [2] for leptonic and pure hadronic initial states.

`SHERPA`'s matrix elements are provided by the built-in automatic tree-level matrix element generator `AMEGIC++`, while the parton shower algorithms are implemented in the module `APACIC++`. Their interplay is appropriately set up for the CKKW merging procedure by `SHERPA` itself. During the past year, the `SHERPA` implementation of the CKKW approach has been extensively tested, see [5]. In Fig. 1 and 2, results for W and Z boson production at the Tevatron are shown. They emphasize that the CKKW approach yields an improved LO prediction; the total rate can then be obtained through a constant K factor.

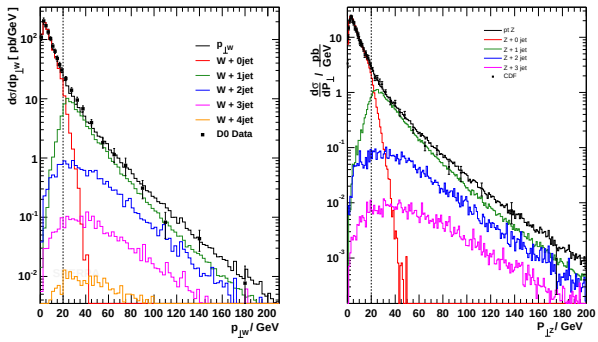

Figure 1: Transverse momentum spectra of the W and Z boson at Tevatron Run I compared to DØ and CDF data [3], respectively ($Q_{cut} = 20$ GeV). The coloured lines indicate the contributions from the different jet samples.

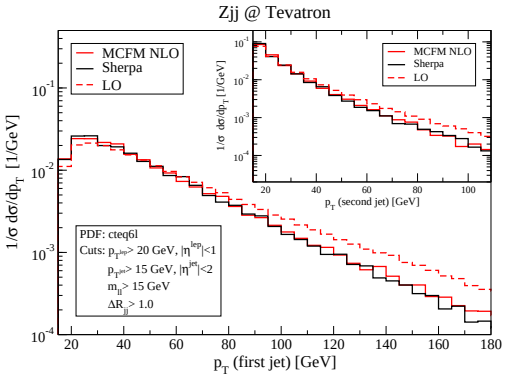

Figure 2: Parton level P_T distribution of the 1st and the 2nd jet in exclusive $Z + 2jet$ production at the Tevatron Run II compared to the naive LO result and the NLO QCD prediction obtained with MCFM [4].

References

[1] S. Catani, F. Krauss, R. Kuhn and B. R. Webber, JHEP **0111** (2001) 063.

[2] T. Gleisberg, S. Höche, F. Krauss, A. Schälicke, S. Schumann and J. Winter, JHEP **0402** (2004) 056.

[3] B. Abbott *et al.* [DØ collaboration], Phys. Lett. B **513** (2001) 292, T. Affolder *et al.* [CDF collaboration], Phys. Rev. Lett. **84** (2000) 845.

[4] J. Campbell and R. K. Ellis, Phys. Rev. D **65** (2002) 113007.

[5] F. Krauss, A. Schälicke, S. Schumann and G. Soff, Phys. Rev. D **70** (2004) 114009.

* Dedicated to the memory of Gerhard Soff, teacher and friend.

Hadron Structure from Lattice QCD

A. Ali Khan[1], D. Brömmel[2], M. Göckeler[3,4], P. Hägler[5], T. Hemmert[6], R. Horsley[7], A. Manashov[3], H. Perlt[3,4], D. Pleiter[8], P. Rakow[9], A. Schäfer[3], G. Schierholz[2,8], A. Schiller[4], S. Solbrig[3], H. Stüben[9], N. Warkentin[3], and J. Zanotti [QCDSF-Collaboration][8]

[1]Institut für Physik, Humboldt Universität zu Berlin, D-10115 Berlin; [2]DESY, D-22603 Hamburg; [3]Institut für Theoretische Physik, Universität Regensburg, D-93040 Regensburg; [4]Institut für Theoretische Physik, Universität Leipzig, D-04109 Leipzig; [5]Department of Physics and Astronomy, Vrije Univeriteit, 1081 HV Amsterdam, NL; [6]Physik-Department, Theoretische Physik, TU München, D-85747 Garching; [7]School of Physics, University of Edinburgh, Edinburgh EH9 3JZ, UK; [8]DESY, D-15738 Zeuthen; [9]Konrad-Zuse-Zentrum für Informationstechnologie Berlin, D-14195 Berlin

Most questions of interest in hadron physics can be cast in a form such that they are related to specific matrix elements of the form

$$\langle \text{Hadron}(\vec{p})|\text{quark/gluon operators}|\text{Hadron}'(p')\rangle \qquad (1)$$

where also the (non-trivial) QCD-vacuum can take the place of one of the hadronic states. Typically the precise relation between an experimental observable and matrix elements of type (1) is given by **O**perator **P**roduct **E**xpansion, for which the range of applicability is continuously extended. Lattice QCD allows to systematically calculate such so called 3-point-functions and thus to relate experimental information directly to the fundamental theory of quarks and gluons, QCD. In practice, however, this task is much facilitated by the introduction of a comprehensive parametrization which reduces the problem to the calculation of a limited number of well defined parameters. For many obervables **G**eneralized **P**arton **D**istributions provide such a parametrization. The great potential of GPDs lies in the fact that they allow to relate on a firm QCD level different experimental results, which so far could only be related within models. Furthermore they provide information which can not be extracted directly from any experimental measurement, most notably the total angular momentum of quarks and gluons and the transverse spatial distribution of e.g. spin and energy in a fast hadron. Some results we obtained with quenched improved Wilson fermions for moments of GPDs, like e.g. $H_q(x,\xi,t)$ which are generalized form factors, like e.g. $A_{q,2}(t)$ are shown in Fig. 1, [1].

$$\int_{-1}^{1} dx\; x\; H^q(x,\xi,t) \;=\; A^{q,2}(t) \qquad (2)$$

From calculations with dynamical Wilson fermions and a chPT [2] fit to these data we got e.g. very good agreement with the experimental nucleon mass, see Fig.2, [3]. This work was supported by DFG, BMBF and LRZ.

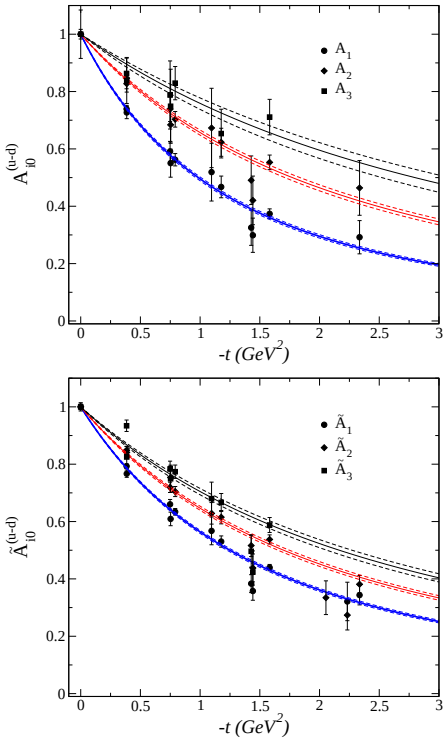

Figure 1: Generalized form factors A_{10}^{u-d}, A_{20}^{u-d}, A_{30}^{u-d} (left), and $\widetilde{A}_{10}^{u-d}$, $\widetilde{A}_{20}^{u-d}$, $\widetilde{A}_{30}^{u-d}$ (right), together with a dipole fit. All form factors have been normalized to unity.

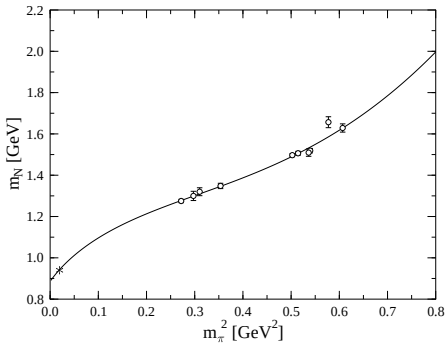

Figure 2: Nucleon mass results (open symbols), their chPT extrapolation [2] and the experimental value (asterix).

References

[1] M. Göckeler *et al.*, hep-lat/0501029.
[2] M. Procura *et al.*, Phys. Rev. D **69** (2004) 034505.
[3] A. Ali Khan *et al.*, Nucl. Phys. B **689** (2004) 175

Hadron Resonances and Topological Modes from Lattice-QCD with Chiral Fermions

T. Burch[1], C. Gattringer[1], M. Göckeler[2,1], C. Hagen[1], P. Hasenfratz[3], D. Hierl[1], C.B. Lang[4], F. Niedermayer[3], A. Schäfer[1], and S. Solbrig [BGR-Collaboration][1]

[1]Institut für Theoretische Physik, Universität Regensburg, D-93040 Regensburg, Germany; [2]Institut für Theoretische Physik, Universität Leipzig, D-04109 Leipzig, Germany; [3]Institut für Theoretische Physik, Universität Bern, CH-3012 Bern, Switzerland; [4]Institut für Theoretische Physik, Universität Graz, A-8010 Graz, Austria

Lattice QCD calculations are performed with various actions, which are different discretizations of the same continuum QCD action with specific advantages and disadvantages. Basically, one wants to minimize the various systematic errors due to finite lattice spacing, finite lattice volume, unphysically large quark masses, quenching, etc. for a given physics problem. In the future, the presently used actions will be superseded by actions with Dirac operators fulfilling the Ginsparg-Wilson equation

$$\gamma_5 D_E + D_E \gamma_5 = a D_E \gamma_5 D_E \quad , \qquad (1)$$

where D_E is the discretized (Euclidean) Dirac operator on the lattice. The much larger computational costs of such operators are compensated by their distinctive advantages. They do not only respect chiral symmetry, which makes them, e.g., especially useful to study topological properties of QCD, but they also allow to use smaller, more physical quark masses: To calculate hadronic properties on the lattice one needs the quark propagator, which is just the inverse of the matrix D_E+m_0. In principle D_E+m_0 has only positive (non-vanishing) eigenvalues and thus is invertable. Computationally, however, this is only true if m_0 is larger than the numerical noise in D_E. This is why lattice calculations are usually done with unphysically large quark (or equivalently pion) mass. The quadratic eigenvalue equation following from (1) forces the eigenvalues onto a circle and thus eliminates this problem. Fig. 1 illustrates this for one of the Dirac operators (CI-fermions) we use.

We have calculated masses for hadron ground states as well as higher resonances, quantities like the pion scattering length and properties of topological modes in the quenched approximation. We have also developed algorithms which hopefully might allow for calculations with dynamical chiral quarks already with existing computer resources on a (1.8 fm)$^3\times$ (3.6 fm/c) lattice with 2+1 flavours; these runs are just starting. Figs. 2 and 3 show results for hadron resonance masses and the pion scattering length. For other results see [1]. For GSI our studies of the link between confinement and chiral symmetry breaking are probably especially interesting [2]. This work was supported by DFG, BMBF, LRZ, HLRZ-Juelich, SNF (Swiss) and WFW (Austria).

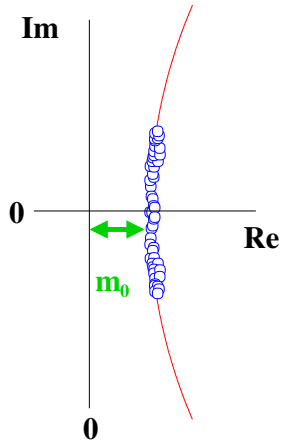

Figure 1: The smallest 50 eigenvalues (symbols) and the Ginsparg-Wilson circle (curve).

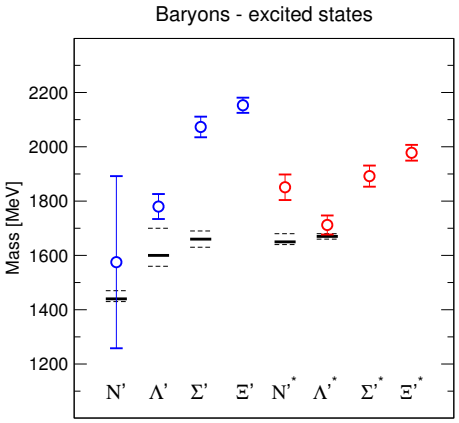

Figure 2: Some results for excited hadron masses.

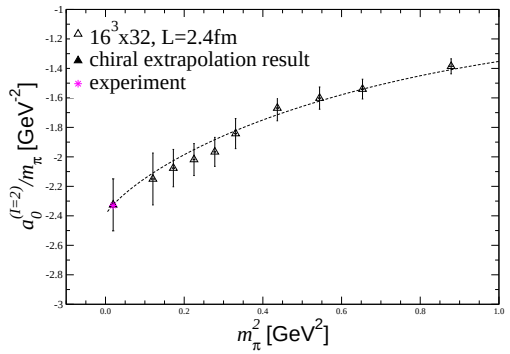

Figure 3: The pion scattering length $a_0^{I=2}$, Dotted line: behaviour predicted by chiral perturbation theory.

References

[1] C. Gattringer *et al.*, Nucl. Phys. B **677** (2004) 3; T. Burch *et al.*, Phys. Rev. **D70** (2004) 054502.

[2] J. Gattnar *et al.*,hep-lat/0412032; C. Gattringer *et al.*, Phys. Rev. D **69** (2004) 094510, Nucl. Phys. Proc. Suppl. **129** (2004) 653.

Heavy Quark Physics in Lattice QCD

A. Ali Khan[1], V. Braun[2], T. Burch[2], M. Göckeler[3,2], G. Lacagnina[2], A. Schäfer[3], G. Schierholz[4,5], and H. Stüben[6]

[1]Institut für Physik, Humboldt Universität zu Berlin, D-10115 Berlin; [2]Institut für Theoretische Physik, Universität Regensburg, D-93040 Regensburg; [3]Institut für Theoretische Physik, Universität Leipzig, D-04109 Leipzig; [4]DESY, D-22603 Hamburg; [5]DESY, D-15738 Zeuthen; [6]Konrad-Zuse-Zentrum für Informationstechnik Berlin, D-14195 Berlin

One of the research activities of the antiproton program at FAIR will be high precision studies of hadrons with open and hidden charm, including their decay properties and branching fractions. As the charm quark is neither 'light' nor 'heavy' on the hadronic mass scale, meaning that it is equally unjustified to neglect the charm mass and to approximate it by infinity, charmed systems pose a real challenge for QCD. This is reflected by the fact that recently charm-strange bound states have been found experimentally which did not fit the theoretical expectations. While lattice QCD should in principle allow us to determine the properties of such systems this turns out to be highly non-trivial in practice because the charm Compton wave length requires the usage of a very small lattice constant resulting in the need for a huge number of lattice points to cover a physically sensible total volume. However, with the recent progress in computer performance such calculations become possible. On the other hand, because of their special kinematic region charmed systems are of special interest to hadron physics.

We perfom lattice simulations for a variety of observables, especially concentrating on spectroscopy and the determination of specific QCD transition matrix elements and form factors, e.g. the matrix elements for the decays of heavy-light mesons ($B^{(*)} \to D^{(*)} l\nu_l$ and $D^{(*)} \to K^{(*)} l\nu_l$). The differential decay rate for $D^{(*)} \to K^{(*)}$ is, e.g., determined by the QCD matrix element

$$\langle K(p')|V_{cs}^{\mu}|D(p)\rangle \qquad (1)$$

and other matrix elements of the same form. Our code uses quenched non-perturbatively improved Wilson fermions, and the production runs have just started. (All calculations are done for a variety of masses simultaneously.)

In a completely different sub-project we analyse excited heavy quark states with chirally improved fermions. Here a special method is used (wall sources) to simultaneously obtain the full mass correlation matrix and thus the complete spectrum. First results are shown in Fig.1 and Tab. 1 for a small number of configurations [1, 2]. Obviously the method works in principle, but still has to be improved. Fig.2 shows that our results are very stable with respect to the quark/η_c mass and do in fact agree with the experimental values. The dashed line in this figure corresponds to the charm quark mass as extracted from the η_c mass. (The precise value of m_c to be used is debatable.)

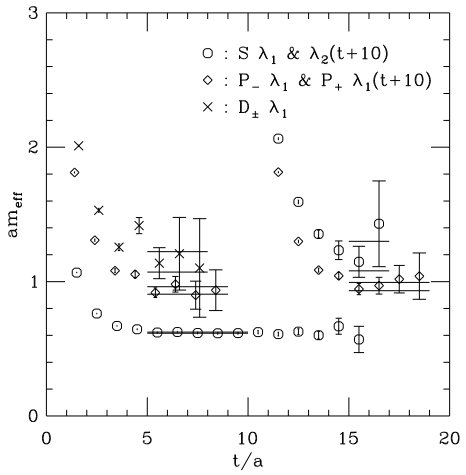

Figure 1: Effective masses for heavy-light mesons near B_s ($am_q = 0.08$, $am_Q = 3.0$).

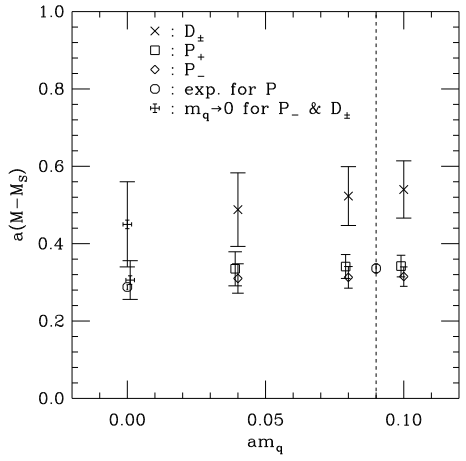

Figure 2: Mass splitting between the D,P and the S-state heavy-light meson as a function of the quark mass, respectively η_c-mass.

Table 1: Lattice results for the mass splittings of the $B_s^{(*)}$ system.

$\mathcal{O}$	$a(M-M_S)$	$M-M_S$ (MeV)	exp. [1]
S'	0.58(11)	770(150)	-
P_-	0.314(28)	419(37)	448(16)
P_+	0.341(31)	455(41)	448(16)
$D_\pm$	0.530(76)	710(100)	-

References

[1] S. Eidelman *et al.*, Phys. Lett. B592 (2004) 1.

[2] T. Burch, C. Gattringer, & A. Schäfer, contribution to Lattice 2004, hep-lat/0408038.

Volume dependence of the pion mass

J. Braun[1], B. Klein[1,2], and H.-J. Pirner[1]
[1]University of Heidelberg; [2]GSI Darmstadt

Volume effects on meson masses are important for understanding the results of QCD lattice simulations, which are still limited to large meson masses and small volumes. Such finite volume effects have been studied in different approaches [2, 3, 4], mainly using chiral perturbation theory (chPT) . Since quark effects involving higher momentum scales also seem to play a role [5], we study the pion mass volume dependence in a model involving quark effects with renormalization group (RG) methods, which provides a way to account for these effects in the low-energy theory.

We consider the quark-meson-model, as an effective low-energy model of QCD, in a finite three-dimensional volume, using the Schwinger proper-time renormalization group. We use a local potential approximation of the effective action, which incorporates fermionic as well as bosonic fluctuations to the potential density U [1]. In order to break chiral symmetry in the finite volume, we introduce a small current quark mass. The corresponding effective meson potential breaks chiral $O(4)$ symmetry explicitly and depends on σ and $\vec{\pi}$ fields separately. Therefore the following ansatz for the mesonic potential is justified:

$$U(\sigma,\vec{\pi}^2)=\sum_{i=0}^{N_\sigma}\sum_{j=0}^{[\frac{1}{2}(N_\sigma-i)]} a_{ij}(\sigma-\sigma_0)^i(\sigma^2+\vec{\pi}^2-\sigma_0^2)^j$$

The scale dependence is introduced by an infrared cutoff function. By replacing the bare couplings a_{ij} with the scale-dependent running couplings $a_{ij}(k)$, we obtain an RG flow equation for the effective potential, which reads:

$$k\frac{\partial}{\partial k}U_k(\sigma,\vec{\pi}^2)=\frac{3}{16}\frac{k^6}{L^3}\sum_{\{\vec{n}\}}\left\{-\frac{4N_cN_f}{(k^2+p_F^2+M_q^2(\sigma,\vec{\pi}^2))^{5/2}}+\sum_{i=1}^{N_f^2}\frac{1}{(k^2+p_B^2+M_i^2(\sigma,\vec{\pi}^2))^{5/2}}\right\}$$

$$\text{where}\quad p_F^2=\frac{4\pi^2}{L^2}\sum_{i=1}^{3}\left(n_i+\frac{1}{2}\right)^2\ \text{and}\quad p_B^2=\frac{4\pi^2}{L^2}\sum_{i=1}^{3}n_i^2\,.$$

We apply periodic boundary conditions for bosons and anti-periodic boundary conditions for fermions in timelike and spatial directions. The sums run from $-\infty$ to $+\infty$, where the vector $\vec{n}$ denotes (n_1,n_2,n_3). The meson masses are the eigenvalues of the second derivative matrix of the meson potential $U_k(\sigma,\vec{\pi}^2)$, whereas the quark mass is given by $M_q^2=g^2[(\sigma+m_c)^2+\vec{\pi}^2]$.

In fig. 1 we show the relative shift of the pion mass from its infinite volume limit as a function of the volume L. The relative change of the pion mass decreases with the volume size L and the pion mass $m_\pi(\infty)$. Fig. 1 also contains the results of chPT from the exact one-loop calculation in finite volume [2] and also the "best estimate" from [4]. To calculate this "best estimate", the difference between the results of Lüscher's formula [3] for the mass shift, which uses as input $\pi\pi$-scattering in the one-(*lo*) and three-(*nnlo*) loop order, is used as a correction to the *exact* one-loop mass shift from [2]. Our RG results have the same slope as the chPT results, but are consistently above them, including even those results with corrections to three loops. The difference between the RG result and the loop expansion decreases with higher loop order.

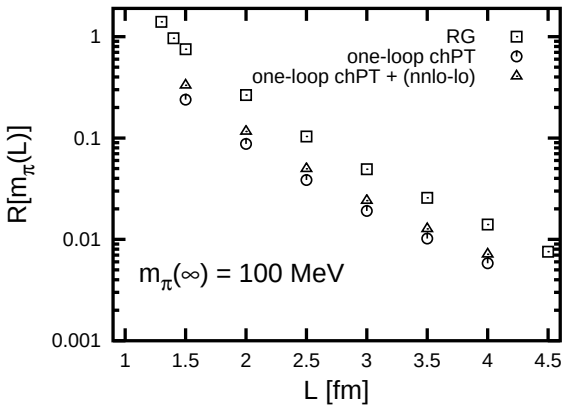

Figure 1: Volume dependence of the pion mass. We plot the relative shift of the pion mass from its infinite volume limit $R[m_\pi(L)]=(m_\pi(L)-m_\pi(\infty))/m_\pi(\infty)$ as a function of the size of the volume L for $m_\pi(\infty)=100$ MeV.

For large volumes, the pion mass drops as $\exp(-m_\pi L)$, therefore the slopes of the RG and the chPT results are the same. The RG calculation can be extended to smaller box sizes than chPT. It remains valid even beyond the regime dominated by chiral symmetry breaking, well into the region with restored chiral symmetry. There the chiral expansion can no longer be considered reliable and is thus no longer applied.

While the relative difference between the exact one-loop result and the RG results remains approximately constant for different pion masses, the relative difference between the RG results and the chPT results of Colangelo and Dürr [4] decreases when the mass of the pion is increased. This difference is consistent with the error estimate of Lüscher's approximation formula.

Next, we plan to investigate the influence of the choice of spatial boundary conditions for the fermions, since in QCD lattice calculations different behavior of the mass shift is seen for periodic and antiperiodic boundary conditions [5].

References

[1] J. Braun, B. Klein, and H.-J. Pirner, to appear in Phys. Rev. D [arXiv:hep-ph/0408116].
[2] J. Gasser and H. Leutwyler, Phys. Lett. B **184** (1987) 83.
[3] M. Lüscher, Commun. Math. Phys. **104** (1986) 177.
[4] G. Colangelo and S. Dürr, Eur. Phys. J. C **33** (2004) 543 [arXiv:hep-lat/0311023].
[5] S. Aoki, *et al.*, Phys. Rev. D **50**, 486 (1994).

Chiral excitations of baryons with charm

M.F.M. Lutz[1] and E.E. Kolomeitsev[2]
[1]GSI, [2]University of Minnesota

The ground states of charmed baryons form an anti-triplet and sextet representations of the SU(3) group. The s-wave interaction of the latter with the octet of Goldstone bosons is predicted by the chiral properties of QCD. The Clebsch-Gordon coefficients that describe the relative interaction strength of the various channels reflect the SU(3) multiplet structure of the hadron the Goldstone bosons are scattered off [1]. In the SU(3) limit the decomposition follows

$$8 \otimes \bar{3} = \bar{3} \oplus 6 \oplus \overline{15}\,, \quad 8 \otimes 6 = \bar{3} \oplus 6 \oplus \overline{15} \oplus 24\,.$$

For $8 \otimes \bar{3}$ scattering the leading order chiral Lagrangian predicts attraction in the anti-triplet and sextet sectors, but repulsion for the anti-15plet. For $8 \otimes 6$ scattering there is attraction in the anti-triplet, sextet but also in the anti-15plet sectors. The interaction is repulsive in the 24plet sectors. Chiral SU(3) symmetry predicts a hierarchy of strengths with the strongest attraction in the triplet channels, which is five times as strong as the attraction in the anti-15plet. In the sextet sector the attraction is reduced by a factor 3/5 only. It is also rewarding to compare the amount of attraction in the anti-triplet channels as they result from the reduction of $8 \otimes \bar{3}$ versus $8 \otimes 6$. Chiral symmetry predicts stronger binding in the latter case. The amount of attraction is larger by a factor 5/3 as compared to the former case

We confront the empirical spectrum with the spectrum of chiral molecules. The latter are formed as a consequence of coupled-channel interactions of the Goldstone bosons with the baryon states. The interaction strength is unambiguously determined by the well-known value of the pion decay constant. Consider the chiral excitations of the triplet states manifest in the first and third rows of the figures. According to our discussion those states form a strongly bound anti-triplet and a weakly bound sextet. The $(I,S) = (0,0)$ resonance is identified with the $\Lambda_c(2880)$ being a member of the anti-triplet [2]. It is in fact a bound state at this leading order computation. The isospin doublet of that multiplet, a $(1/2,-1)$ state, is a much broader object so far unobserved. The chiral sextet excitations of the anti-triplet is visible in the $(1,0), (1/2,-1)$ and $(0,-2)$ sectors. Most spectacular would be the exotic and bound $\bar{K}\,\Xi_c(2470)$ system, if it survives chiral correction terms.

An even richer spectrum is formed by the chiral excitations of the sextet states as shown in the second and fourth rows of the figures. Chiral SU(3) symmetry predicts attraction with decreasing strength in the triplet, sextet and anti-15plet. The triplet states are identified with the $\Lambda_c(2593)$ and $\Xi_c(2790)$ resonances [2]. The sextet manifests itself most clearly as a bound $\bar{K}\,\Xi_c'(2580)$ system. The existence of the anti-15plet is clearly seen in the $(0,0), (1,0)$ and $(1/2,-1)$ sectors where it leads to narrow resonance structures around 3 GeV. Additional signals of the anti-15plet in the exotic sectors $(1/2,1), (3/2,-1)$ and $(1,-2)$ are weaker and are not shown in the figures.

The properties of the chiral excitations depend crucially on the values of the current quark masses of QCD. An SU(3) limit where the pion mass is as heavy as the empirical kaon mass leads to a bound state spectrum, typically. The SU(3) limit where the kaon mass is as light as the empirical pion mass implies the disappearance of the resonance signals. This is a striking prediction of chiral dynamics which should be verified by unquenched lattice QCD simulations.

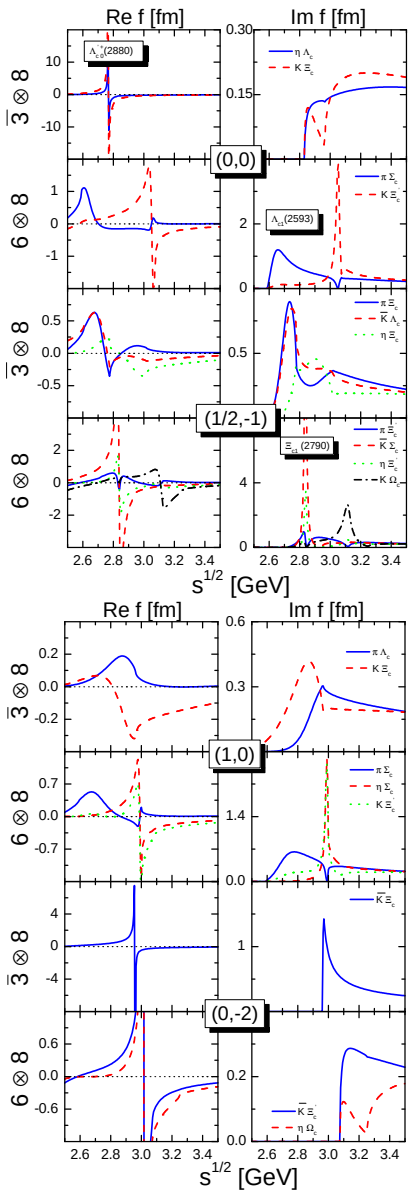

References

[1] M.F.M. Lutz and E.E. Kolomeitsev, Nucl. Phys. **A 730** (2004) 110.
[2] S. Eidelman et al., Phys. Lett. **B 592** (2004) 1.

Bethe-Salpeter Description of Light Mesons

P. Watson, and W. Cassing
University of Giessen

The Bethe-Salpeter equation (BSE) is the framework for a Poincaré covariant treatment of the two-body bound state problem. Within the context of Quantum Chromodynamics (QCD) it provides for a description of mesons. In conjunction with the Dyson-Schwinger equations (DSEs) for the propagators of QCD, the BSE naturally contains information about chiral symmetry and its explicit, dynamical and anomalous breaking and so is ideally suited to studying the properties of light mesons. The key observation is that the truncation schemes applied to the BSE and DSEs (necessary to form a tractable analysis) must be in accordance with the axial-vector Ward-Takahashi identity (AXWTI). Contemporary studies have been so far largely restricted to the rainbow-ladder approximation in which the kernels of both sets of equations are consistently replaced by their lowest order perturbative form supplemented by a phenomenologically motivated dressing to generate the required degree of dynamical chiral symmetry breaking. For recent reviews on this subject, see for example [1, 2, 3].

Our work has been focused on three different but related aspects to the BSE approach to light mesons. The first aspect is the comparison of results for the pseudoscalar and vector meson masses with lattice data at intermediate quark masses [4]. The rainbow-ladder truncated vector meson masses are plotted in Fig. 1 as a function of pseudoscalar mass and compared to unquenched lattice data; the BSE results agree well with the CP-PACS data.

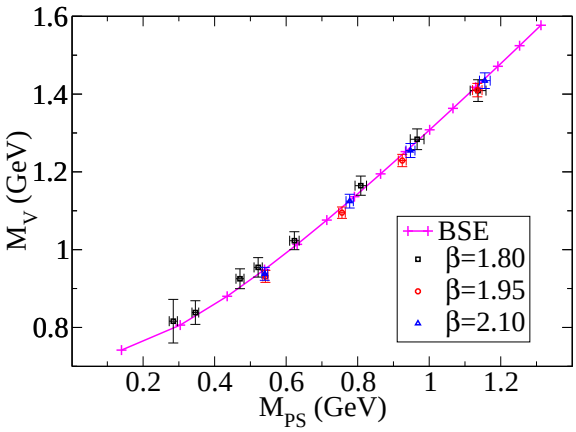

Figure 1: Comparison of BSE vector and pseudoscalar meson masses with CP-PACS lattice results [5, 6].

An immediate extension is to consider the effect of unquenching the gluon propagator [7]. This will provide an initial scheme within the BSE framework to study the effects of sea-quark masses and extrapolate (unquenched) lattice results to the chiral limit.

The second aspect of our work was to consider a more sophisticated truncation scheme employed in the BSE and quark DSE to include corrections to the quark-gluon vertex [8]. The aim was specifically to investigate the ground state axial-vector meson masses which in the rainbow-ladder truncation are $\sim 300MeV$ too light. By modeling the correction to the vertex with an Abelian type one-loop graph characterized by exchange of a single gluon – dressed with a δ-function – the system is tractable and the truncated kernels of the BSE and DSEs can be made consistent with the AXWTI. The net result was that the 1^{+-} (b_1) axial-vector channel was found to be sensitive to this type of vertex correction and the mass was raised by $\sim 300MeV$ in qualitative accordance with experiment, all other light meson channels being insensitive to the vertex corrections [8].

The third aspect of our work was to consider the effects of unquenching the kernels of the BSE and DSEs (again consistently in accordance with the AXWTI) in order to describe meson decay and coupled channel effects [9]. The inclusion of quark loops in the kernel of the BSE gives a mechanism by which internal resonant mesonic correlations (in particular the pion) contribute to the imaginary component of the meson mass and hence describe its decay. A suitable (ie., tractable) scheme for this has been developed and the internal quark-antiquark correlations have been studied in [9]. The evaluation of the self-consistent decay $\rho \to \pi\pi$ is in progress [10].

References

[1] P. Maris and C. D. Roberts, Int. J. Mod. Phys. E **12** (2003) 297 [arXiv:nucl-th/0301049].
[2] C. D. Roberts and S. M. Schmidt, Prog. Part. Nucl. Phys. **45** (2000) S1 [arXiv:nucl-th/0005064].
[3] R. Alkofer and L. von Smekal, Phys. Rept. **353** (2001) 281 [arXiv:hep-ph/0007355].
[4] P. Watson, arXiv:hep-ph/0411032.
[5] A. Ali Khan *et al.* [CP-PACS Collaboration], Phys. Rev. D **65** (2002) 054505 [Erratum-ibid. D **67** (2003) 059901] [arXiv:hep-lat/0105015].
[6] Y. Namekawa *et al.* [CP-PACS Collaboration], Phys. Rev. D **70** (2004) 074503 [arXiv:hep-lat/0404014].
[7] P. Watson, C. S. Fischer, and W. Cassing, work in progress.
[8] P. Watson, W. Cassing and P. C. Tandy, Few Body Syst. **35** (2004) 129 [arXiv:hep-ph/0406340].
[9] P. Watson and W. Cassing, Few Body Syst. **35** (2004) 99 [arXiv:hep-ph/0405287].
[10] P. Watson, and W. Cassing, work in progress.

Exotic hadrons from quark clustering at FAIR

Stefan Scherer[1] and Marcus Bleicher[1]

[1]Institut für Theoretische Physik, Johann Wolfgang Goethe-Universität, D-60054 Frankfurt am Main, Germany

The CBM experiment at FAIR will probe nuclear matter at high densities and comparatively low temperatures, giving access to a region of the phase diagram of QCD not yet studied in detail. One expects to find highly compressed hadronic matter and, at higher energies, deconfined quark matter, possibly subject to strong correlations.

These conditions could be favourable to the production of exotic hadronic states, such as the recently discovered pentaquark Θ^+ and the conjectured Ξ^{--} [1]. The possible creation of pentaquark states in ultrarelativistic heavy ion collisions has been studied so far using statistical and dynamical models [2]. However, experimental searches at RHIC and SPS energies have not yet identified any pentaquark candidates.

We have applied the fully dynamical, classical quark dynamics model qMD [4] to investigate the formation of hadronic clusters made up of up to six quarks and/or anti-quarks in the hadronization stage of a ultrarelativistic heavy ion collision going through a state of deconfined quark matter. We look at collisions of Pb+Pb @ 30 GeV/N in the target frame ($\sqrt{s} = 7.7$ GeV). The initial stage of the collision is described by the hadronic transport model UrQMD. At full overlap of the colliding nuclei, all nucleons which have undergone at least one scattering are decomposed into their (valence) quark content, which is used as initial state for the subsequent time evolution with qMD. Here, quarks are propagated as classical point particles which carry a colour charge and are subject to a confining, linear pair potential. The dynamical evolution yields colourless quark clusters which can be mapped to hadrons, if stable hadronic states exist.

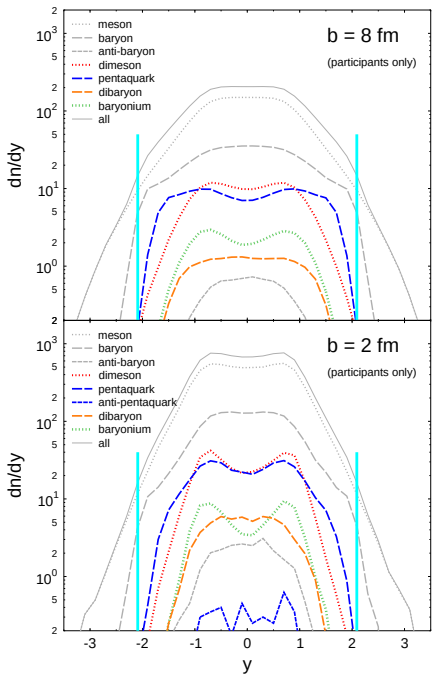

Figure 1: Rapidity distribution of hadronic clusters for central (top) and peripheral (bottom) collisions of Pb+Pb @ 30 GeV/N ($\sqrt{s} = 7.7$ GeV.)

Figure 1 shows the rapidity distribution of hadronic clusters formed from up to six (anti-)quarks for peripheral (bottom) and central (top) collisions. There is a considerable production of dimeson and pentaquark clusters. Figure 2 scales the rapidity distribution of pentaquark clusters to baryon and meson clusters for different impact parameters. This ratio is highest for peripheral collisions at roughly 0.7 units of rapidity inwards of projectile and target. It is also higher at this FAIR energy than at upper SPS and RHIC energies [5].

One has to keep in mind that the quark clustering procedure populates the whole multiplet structure of pentaquark states. Since almost none of these states correspond to stable hadrons, these clusters will decay into baryons and mesons. Thus, to obtain an estimate for the production of Θ^+, one has to scale down the pentaquark curves in figures 1 and 2 by a factor of the order 400 [5], taking into account spin and (uncomplete) flavour SU(3).

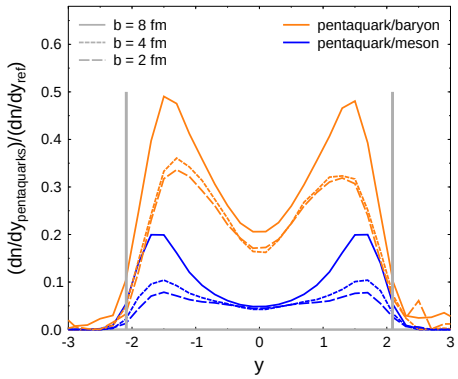

Figure 2: Yield of pentaquark clusters scaled to baryons (upper curves) and mesons (lower curves). Note that the complete SU(3) multiplet is populated. This lowers Θ^+ estimates by a factor of the order 400.

References

[1] T. Nakano *et al.*, Phys. Rev. Lett. **91** (2003) 012002; C. Alt *et al.*, Phys. Rev. Lett. **92** (2004) 042003; summary in K. Hicks, arXiv:hep-ph/0408001;

[2] J. Randrup, Phys. Rev. C **68** (2003) 031903; J. Letessier *et al.*, Phys. Rev. C **68** (2003) 061901; L. W. Chen *et al.*, Phys. Lett. B **601** (2004) 34.

[3] S. Kabana [STAR Collaboration], hep-ex/0406032; S. Kabana, hep-ph/0501121.

[4] M. Hofmann *et al.*, Phys. Lett. B **478** (2000) 161; S. Scherer *et al.*, New J. Phys. **3** (2001) 8.

[5] S. Scherer, hep-ph/0411296; to appear in J. Phys. G

Resonance Production and Absorption at SIS-300 Energies

Sascha Vogel, Marcus Bleicher
Institut für Theoretische Physik, Johann Wolfgang Goethe-Universität, Frankfurt am Main

We present predictions for the yields and spectra of Δ_{1232} and ρ_{770} resonances produced in Pb+Pb collisions at the SIS-300 energy of 30 AGeV. The rapidity spectra of all decaying resonances and of reconstructable resonances for this FAIR project energy are investigated. From the comparison of the yields in the the leptonic and hadronic decay channel one can obtain information on the duration of the hadronic rescattering stage.

Recently, detailed experimental studies of hadron resonances became available for SPS and RHIC energies. For the first time ρ, Δ and K_0^* resonances have been reconstructed from hadron correlations in heavy ion reactions at full SPS and the highest RHIC energies [1, 2, 3, 4, 5]. In contrast to the SPS and RHIC experiments that probe hot and meson dominated systems, the new accelerator SIS-300 allows to test resonance dynamics at high baryonic densities. In this case mass modifications and rescattering effects might be drastically altered. Especially the reconstruction of the resonance in the hadronic channel will be modified because the daughter particles of decayed resonances will now interact with a dense baryonic medium and the baryonic absorption channel become more important than at higher energies. For recent studies within the present transport approach see e.g. [6].

The experiment can detect resonances only via the hadronic or leptonic decay products reconstructing the resonance properties from the invariant mass spectrum of the decay (daughter) particles. Thus, if a resonances daughter particle scatters after the decay, the resonance cannot be seen by the experiment. This suppression effect is especially interesting for resonances which have decay branchings into leptonic and hadronic channels (e.g. the ρ and ϕ mesons): The dilepton channel yields information about the integrated ρ^0 yield and is mostly sensitive to the early stage of the collision, because the electrons or muons do not rescatter after their creation. Thus, one can explore the evolution of the system by comparing the yields and spectra from both the leptonic and hadronic channels.

For our studies we apply the UrQMD model, which provides the full space time dynamics for hadrons and strings. It is a non-equilibrium model based on the covariant propagation of hadrons and strings. All cross sections are fitted to available data or calculated by the principle of detailed balance. For further details of the model the reader is referred to [7, 8].

Figure 1 shows rapidity spectra for the Δ_{1232} resonance. The dashed line denotes all resonances that decay, the solid line shows the reconstructable resonances.

Figure 2 shows the rapidity densities for ρ^0_{770} meson resonances. Comparing the numbers at midrapidity one observes for the Δ_{1232} a suppression to a level of about 20% and for the ρ_{770} to about 10-15%.

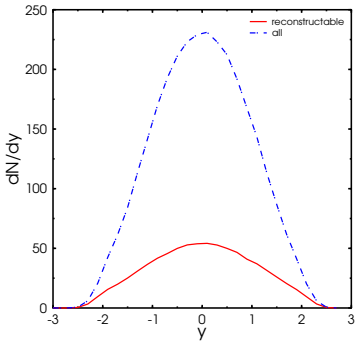

Figure 1: Rapidity densities of Δ_{1232} resonances for Pb+Pb collisions at $E_{beam} = 30$ AGeV, $b \leq 3.4$ fm. The dashed lines depicts all decaying resonances, while the full lines show the calculation for the experimentally reconstructable resonances from the hadronic invariant mass spectrum.

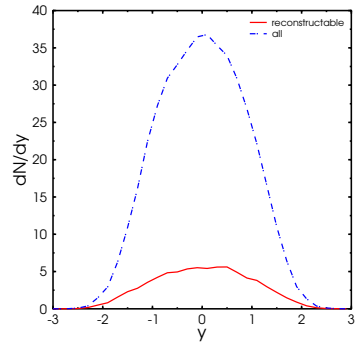

Figure 2: Rapidity densities of ρ^0_{770} resonances for Pb+Pb collisions at $E_{beam} = 30$ AGeV, $b \leq 3.4$ fm. The dashed lines depicts all decaying resonances, while the full lines show the calculation for the experimentally reconstructable resonances from the hadronic invariant mass spectrum.

References

[1] C. Markert [STAR Collaboration], J. Phys. G **30** (2004) S1313 [arXiv:nucl-ex/0404003].
[2] C. Markert [STAR Collaboration], arXiv:nucl-ex/0308029.
[3] P. Fachini [STAR Collaboration], J. Phys. G **30** (2004) S565 [arXiv:nucl-ex/0305034].
[4] P. Fachini, J. Phys. G **30** (2004) S735 [arXiv:nucl-ex/0403026].
[5] S. S. Adler *et al.* [PHENIX Collaboration], dE(T)/d arXiv:nucl-ex/0409015.
[6] M. Bleicher and J. Aichelin, Phys. Lett. B **530** (2002) 81 [arXiv:hep-ph/0201123].
[7] S. A. Bass *et al.*, Prog. Part. Nucl. Phys. **41** (1998) 225 [arXiv:nucl-th/9803035].
[8] M. Bleicher *et al.*, J. Phys. G **25** (1999) 1859 [arXiv:hep-ph/9909407].

The quark propagator for small chemical potential in Landau gauge

D. Nickel[a], R. Alkofer[b,c], and J. Wambach[a,d]
[a]TU Darmstadt; [b]U Tübingen; [c]U Graz; [d]GSI

Since the quark propagator contains information about the phase structure of quark matter, especially about dynamically broken symmetries, it is of particular interest. Due to asymptotic freedom, it can be systematically studied at high densities in a weak coupling expansion [1]. At low densities, i.e. in the non-perturbative regime, such an expansion is lacking. Therefore non-perturbative methods such as truncated Dyson-Schwinger equations have to be applied here [2]. In our approach, we extend the scheme proposed in [3], which is in quantitative and qualitative agreement with lattice calculations for the vacuum, to finite densities. The renormalised Dyson-Schwinger equation for the quark propagator then reads

$$S^{-1}(p) = Z_2 S_0^{-1}(p) - \frac{Z_2}{3\pi^3}\int d^4q\,\frac{\alpha(k^2)}{k^2}\,\gamma_\mu S(q) V_\nu^{abel}\left(\delta_{\mu\nu}-\frac{k_\mu k_\nu}{k^2}\right), \quad (1)$$

where $\alpha(k^2)$ is the running coupling constant and V_ν^{abel} is an abelian vertex construction (see [3]).

For the chirally broken phase, we work in quenched approximation, i.e. neglect the backreaction of the quarks on the Yang-Mills sector. This is justified, since the quarks are massive and their contribution to the gluon self-energy is small [3]. Fig. 1 shows numerical results for the mass function of the quark propagator at various quark chemical potentials compared to lattice results for the vacuum [3, 7]. The Pennington-Curtis vertex construction is used here. We stress, that there are no parameters in our truncation.

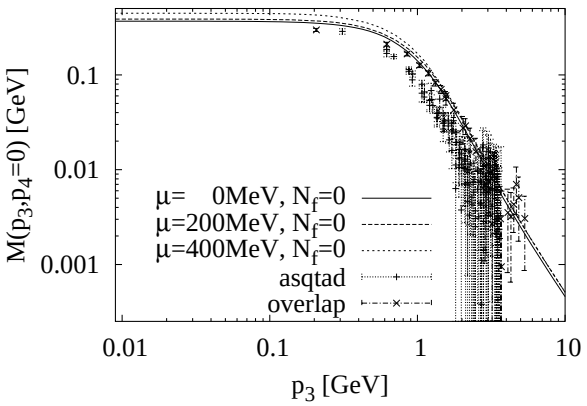

Figure 1: Numerical results for the mass function of the quark for three quark chemical potentials compared to quenched lattice results for the vacuum [4, 5].

For the chirally symmetric and for the superconducting 2SC/CFL phases (see [6]), the medium polarisation of undressed quarks is added to the inverse gluon propagator for describing screening and damping effects by particle-hole excitations in a first step. Eq.(1) is then changed by

$$\frac{\alpha(p^2)}{p^2}P_{\mu\nu} \rightarrow \frac{\alpha(p^2)}{p^2+G(p)}P^T_{\mu\nu}+\frac{\alpha(p^2)}{p^2+F(p)}P^L_{\mu\nu},$$

$$G(p) = m(p)^2\frac{ip_4}{|\vec{p}|}\left[\left(1-\left(\frac{ip_4}{|\vec{p}|}\right)^2\right)Q\left(\frac{ip_4}{|\vec{p}|}\right)+\frac{ip_4}{|\vec{p}|}\right],$$

$$F(p) = 2\,m(p)^2\frac{p_4^2+\vec{p}^2}{\vec{p}^2}\left[1-\frac{ip_4}{|\vec{p}|}Q\left(\frac{ip_4}{|\vec{p}|}\right)\right],$$

$$Q(x) = \frac{1}{2}\ln\frac{x+1}{x-1},$$

$$m(p)^2 = \frac{N_f\mu^2\alpha(p^2)}{\pi},$$

where the transversal projector of the momentum $P_{\mu\nu}$ is split into transversal $P^T_{\mu\nu}$ and longitudinal $P^L_{\mu\nu}$ part with respect to the medium. The results for the gaps in the 2SC and CFL phase with a bare vertex on the Fermi surface and in the chiral limit are shown in Fig. 2. By calculating the action difference within the CJT formalism we find, that the CFL phase is always favored compared to the unbroken and 2SC phase [7].

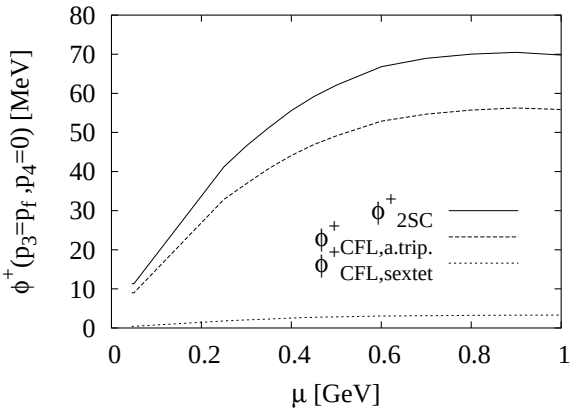

Figure 2: Gaps in 2SC and CFL phase on the Fermi surface as a function of the chemical potential.

References

[1] T. Schäfer and F. Wilczek, Phys. Rev. D60, 114033(1999), hep-ph/9906512.
[2] C.D. Roberts, S.M. Schmidt, Prog. Part. Nucl. Phys. 45(2000) 1-103, nucl-th/0005064.
[3] C.S. Fischer and R. Alkofer, Phys. Rev. D67, 094020(2003), hep-ph/0301094.
[4] F.D. Bonnet *et al.*, Phys. Rev. D65, 114503(2002), hep-lat/0202003.
[5] P.O. Bowman, U.M. Heller and A.G. Williams, Phys. Rev. D66, 014505(2002), hep-lat/0203001.
[6] D.H. Rischke, Prog. Part. Nucl. Phys. 52(2004) 197-296, nucl-th/0305030.
[7] D. Nickel, R. Alkofer, J. Wambach, in preparation.

The High-Temperature Phase of Landau Gauge Yang-Mills Theory

Axel Maas[1], Jochen Wambach[1,2], and Reinhard Alkofer[3,4]
[1]GSI, Darmstadt; [2]Darmstadt University of Technology; [3]University of Tübingen; [4]University of Graz

The high-temperature phase of QCD is an enigma. Although its equation of state is close to that of an ideal gas, perturbation theory fails in describing it. Indeed, the problems encountered are similar to those in the vacuum, like infrared divergences. A possible way towards understanding the origin of this discrepancy is presented here.

In a first step only Yang-Mills theory is treated, i.e. QCD without quarks, to reduce the complexity of the problem. For many technical reasons it is advantageous to choose Landau gauge. In equilibrium the theory is then governed by the Euclidean Lagrangian [1]

$$\begin{aligned} \mathcal{L} &= \frac{1}{4}F^a_{\mu\nu}F^a_{\mu\nu} + \bar{c}^a\partial_\mu D^{ab}_\mu c^b \qquad (1)\\ F^a_{\mu\nu} &= \partial_\mu A^a_\nu - \partial_\nu A^a_\mu - g f^{abc} A^b_\mu A^c_\nu \\ D^{ab}_\mu &= \delta^{ab}\partial_\mu + g f^{abc} A^c_\mu \ . \end{aligned}$$

Herein A denotes the gluon field and c and $\bar{c}$ the Faddeev-Popov ghost and anti-ghost fields. The latter are a convenient way to describe the quantum fluctuations of the gluon field and additionally ensure the correct number of degrees of freedom.

From (1), the corresponding Dyson-Schwinger equations have been derived and solved in an approximation scheme for the propagators at temperatures above the phase transition [2, 3]. The propagators are described by three independent scalar functions as

$$\begin{aligned} D_G(q) &= -\frac{G(q_0^2,q_3^2)}{q^2} \ , \\ D_{\mu\nu}(q) &= P^T_{\mu\nu}(q)\frac{Z(q_0^2,q_3^2)}{q^2} + P^L_{\mu\nu}(q)\frac{H(q_0^2,q_3^2)}{q^2} \ . \end{aligned}$$

Here G denotes the ghost dressing function, and Z and H the ones for gluons transverse or longitudinal w.r.t. the heat bath. $q = (q_0, q_3)$ is the four-momentum with q_0 the Matsubara frequency $q_0 = 2\pi n T$ with n integer.

The infrared properties of the propagators can be directly linked to confinement and the presence of long-range forces. Especially a ghost dressing function G which diverges at $q^2 = 0$ indicates the presence of long-range forces and signals confinement according to the Kugo-Ojima and Gribov-Zwanziger scenarios. Furthermore, if a propagator vanishes at $q^2 = 0$, the corresponding particle is confined. This is clear for a massless particle, as this is just the statement that the on-shell propagator vanishes (for a brief introduction to confinement in covariant gauges see [4]).

As visible from figure 1, displaying the soft modes $q_0 = 0$, G diverges. Furthermore, Z vanishes, in accordance with lattice results. Thus at least gluons transverse to the heat bath are confined. Propagators for gluons longitudinal w.r.t. the heat-bath are not shown. They exhibit screening, although they are not entirely trivial [2]. This behavior is not changed even in the infinite temperature

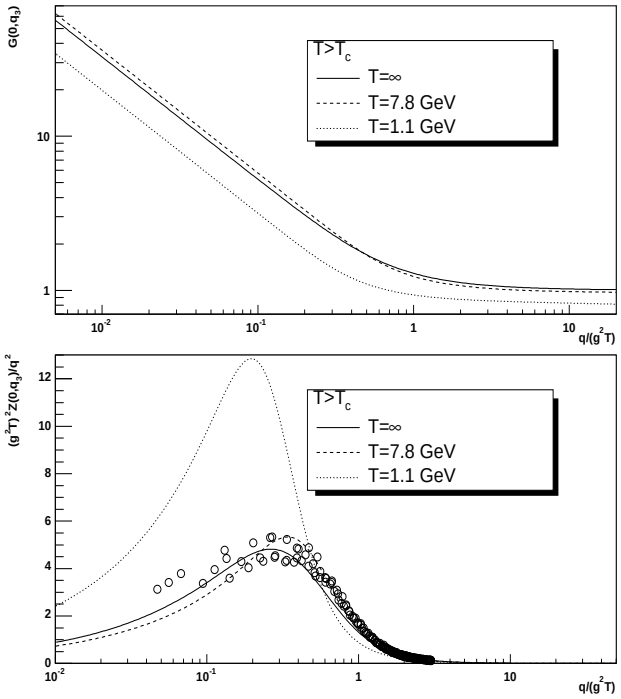

Figure 1: The dressing function of the ghost and the propagator of the gluon transverse w.r.t. the heat-bath are displayed from top to bottom for soft modes. The infinite temperature lattice data in the lower panel are from [5].

limit. Therefore the high-temperature phase is microscopically never purely perturbative and at least a residual confinement is present. Investigations of the thermodynamic potential, however, indicate that the potential is dominated by the hard modes. The latter are not not shown, but are essentially tree-level like, up to perturbative corrections [3]. Therefore the equation of state is nearly that of an ideal gas. This indicates how the discrepancy mentioned in the beginning could be resolved, but it has to be studied in more detail before a firm conclusion can be drawn.

References

[1] R. Alkofer and L. von Smekal, *Phys. Rept.* **353**, 281 (2001) and references therein.

[2] A. Maas, J. Wambach, B. Grüter and R. Alkofer, Eur. Phys. J. C **37** (2004) 335 [arXiv:hep-ph/0408074].

[3] A. Maas, PhD thesis, Darmstadt University of Technology, 2004.

[4] W. Schleifenbaum, A. Maas, J. Wambach and R. Alkofer, arXiv:hep-ph/0411060 and references therein.

[5] A. Cucchieri, T. Mendes and A. R. Taurines, *Phys. Rev.* **D67**, 091502 (2003); A. Cucchieri, F. Karsch and P. Petreczky, *Phys. Rev.* **D64**, 036001 (2001).

The ghost-gluon vertex in Landau gauge Yang-Mills theory

Wolfgang Schleifenbaum[1,2], Axel Maas[3], Jochen Wambach[1,3], and Reinhard Alkofer[2,4]
[1]TU Darmstadt; [2]U Tübingen; [3]GSI; [4]U Graz

The infrared properties of strong interaction, such as confinement, require a non-perturbative treatment. One possibility to approach this challenging task is to employ the Dyson-Schwinger technique to derive an infinite tower of mutually coupled equations for the Green functions of Yang-Mills theory. The Landau gauge has the intriguing feature that the ghost-gluon vertex $\Gamma_\mu(k;q,p)$ reduces to its tree-level value in the limit of vanishing incoming ghost momentum p [1]. In the ultraviolet, this vertex is expected to yield the perturbative behavior. Therefore, one might be tempted to choose the ghost-gluon vertex bare for all momentum variables. The bare vertex approximation has been applied to Landau gauge Dyson-Schwinger studies to arrive at a gluon propagator that is suppressed in the infrared and an enhanced ghost propagator in the infrared, thus satisfying criteria for confinement in pure Yang-Mills theory [2]. An investigation of the non-perturbative ghost-gluon vertex will test this assumption and, moreover, provide insight into this interesting and non-trivial object.

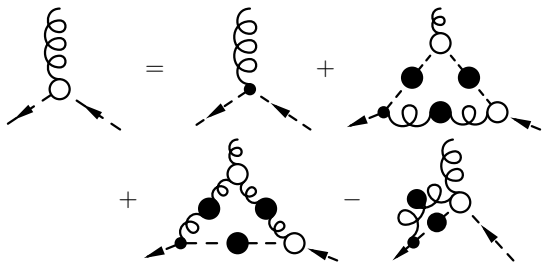

Figure 1: Complete DSE for the ghost-gluon vertex. Curly lines are gluons, dashed lines are ghosts, blobs represent dressed objects.

The complete Dyson-Schwinger equation for the ghost-gluon vertex in the Landau gauge has been derived [3], see Fig. 1. This non-linear equation can be solved by iteration for both four and three Euclidean spacetime dimensions d, employing the non-perturbative propagators calculated in [4, 5]. The contribution of the four-point interaction is neglected in accordance to the truncation applied for the propagators. For the reasons mentioned above, the bare ghost-gluon vertex is a good starting point for the iteration. The three-gluon vertex is set to its tree-level value. After one iteration step the ghost-gluon vertex shows a behavior [3, 6] which is quite close to the input for all momentum variables. The infrared behavior of the result satisfies the constraint imposed by gauge invariance, i.e. the Slavnov-Taylor identity of the vertex. In the ultraviolet asymptotic freedom is observed. The previously unknown limit of vanishing gluon momentum k is shown for $d = 4$ and $SU(2)$ in Fig. 2, where

$$1 + A(k^2;q^2,p^2) = \frac{k^2 q_\mu t_{\mu\nu}(k)}{i g_d (q^2k^2 - (q\cdot k)^2)} \Gamma_\nu(k;q,p)$$

with the gauge coupling g_d and the transverse projector $t_{\mu\nu}(k) = \delta_{\mu\nu} - k_\mu k_\nu / k^2$. Choosing $d = 3$ and/or $SU(3)$ does not significantly change the results [3, 6]. The deviations from tree-level are in the range of 20%, indicating that the input of the iteration is quite close to the fixed point. The comparison to recently obtained lattice data [7] shows good agreement. Other inputs for the ghost-gluon vertex, motivated by its Slavnov-Taylor identity, have also been used and yielded similar results [3, 6].

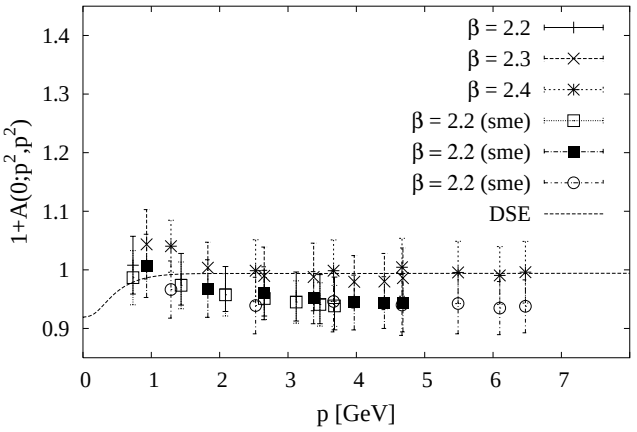

Figure 2: The $d = 4$ ghost-gluon vertex in the limit of vanishing gluon momentum compared to lattice data [7].

These calculations justify the bare vertex approximation a posteriori and provide a more profound confirmation of the features of the propagators, in particular gluon confinement in the four-dimensional vacuum theory [4]. For the three-dimensional investigations, support is given for remnant long-range interactions in the high-temperature phase of Yang-Mills theory [5]. Moreover, the results corroborate the hypothesis that the Green functions of Yang-Mills theory are dominated by ghosts in the infrared and thus strengthen the evidence for the Gribov-Zwanziger confinement scenario [8].

References

[1] J. C. Taylor, Nucl. Phys. B **33** (1971) 436; W. J. Marciano and H. Pagels, Phys. Rept. **36** (1978) 137.
[2] R. Alkofer and L. von Smekal, Phys. Rept. **353** (2001) 281 [arXiv:hep-ph/0007355].
[3] W. Schleifenbaum, diploma thesis, TU Darmstadt, 2004;
[4] C. S. Fischer and R. Alkofer, Phys. Lett. B **536** (2002) 177 [arXiv:hep-ph/0202202].
[5] A. Maas, J. Wambach, B. Grüter and R. Alkofer, Eur. Phys. J. **C37** (2004) 335 [arXiv:hep-ph/0408074].
[6] W. Schleifenbaum, A. Maas, J. Wambach and R. Alkofer, arXiv:hep-ph/0411052.
[7] A. Cucchieri, T. Mendes and A. Mihara, JHEP **0412** (2004) 012 [arXiv:hep-lat/0408034].
[8] D. Zwanziger, Phys. Rev. D **69** (2004) 016002 [arXiv:hep-ph/0303028]; D. Zwanziger, Nucl. Phys. B **412** (1994) 657; V. N. Gribov, Nucl. Phys. B **139** (1978) 1.

Nonperturbative approach to SU(2)/SU(3) Yang-Mills thermodynamics

Ralf Hofmann[1]

[1]Institut für Theoretische Physik, Universität Frankfurt, Johann Wolfgang Goethe - Universität, Robert-Mayer-Str. 10, 60054 Frankfurt, Germany

Motivation

The objective is a nonperturbative and analytical approach to SU(2)/SU(3) Yang-Mills thermodynamics. This is motivated by the failure of unsummed perturbation theory to provide for a converging loop expansion of thermodynamical quantities (Linde 1980) due to the problem of weakly screened, soft magnetic gluons at arbitrarily high temperature, various pathologies of various resummation schemes, such as the temperature dependence of ultraviolet divergences (Blaizot, Iancu Rebhan 2003 for a review), and by the fact that lattice gauge theory observes nonperturbative effects deep inside the deconfining phase, such as a linearly in temperature rising spatial string tension (Philipsen 1998). Moreover, a quantitative understanding of the confining phase(s) is aimed at. On the experimental side, an analytical understanding of why a hydrodynamical description of the elliptic flow in ultra-relativistic heavy-ion collisions, at least for not too large p_T, is so successful and also answers to various cosmological questions are aimed at with the approach.

Results

We have derived the phase and the modulus of a composite and adjoint Higgs field ϕ, which is quantum mechanically and statistically inert, for the deconfining (or electric) phase of a pure SU(2) Yang-Mills theory. This field is defined as an incomplete integration over the moduli space of a single trivial-holonomy (anti)caloron with the integrand being a series of n-point functions of the field strength. The existence of the field ϕ implies, in the physical unitary-Coulomb gauge, a cutoff for the off-shellness of topologically trivial gauge-field fluctuations - a so-called compositeness constraint. No ultraviolet divergences occur in loop integrals and thus no renormalization program is needed. On the other hand, off-diagonal gauge-field fluctuations become temperature-dependently massive ($m \propto 1/\sqrt{T}$). This resolves the problem of infrared instabilities in the loop expansion of thermodynamical quantities. Thermodynamical quantities, such as the pressure or the entropy density have a convergent loop expansion (much in contrast to naive perturbation theory where the series breaks down at order g^6). We have calculated the two-loop correction to the pressure for SU(2) in the deconfining phase which turned out to be smaller than 0.1% of the one-loop result. In an earlier work we have investigated the phase structure of SU(2)/SU(3) Yang-Mills theory. The theory turns out to be in either of the following three phases: electric (deconfining; quick, that is, power-like approach to the Stefan-Boltzmann limit), magnetic (confinement of fundamental test charges by a monopole condensate but asymptotically propagating, massive 'photons'), center (confinement of test charges; no propagating gauge mode; fermionic excitations with exponentially rising density of states). While the center-phase thermodynamics needs heavy numerical machinery (lattice simulations) to simulate the effective theory the two other phases are accessible in a near-to analytical way. The critical exponent ν for the electric-magnetic transition, which goes with the restoration of a global Z_2 electric symmetry in a three dimensional field theory, was computed for the SU(2) case. We have found a value of $\nu = 0.61 + 0.02 - 0.01$ which is compatible with the exponent of the 3D Ising model $\nu_{IS} \sim 0.63$ - a result expected from universality arguments. For the SU(3) case an ambiguity in determining ν was observed. This proves that the electric-magnetic phase transtion can not be second order. We have shown deconfinement and confinement by investigating the Polyakov loop in the respective effective theories. We have also shown that the transition from the magnetic to the center phase is of the Hagedorn type, and thus nonthermal, for both SU(2) and SU(3). A computation of the pressure, the energy density, and the entropy density was carried out for the electric and the magnetic phase. The pressure quickly approaches its Stefan-Boltzmann limit for $T \to \infty$ while it starts to be negative shortly above the electric-magnetic transition and reaches its maximal negative value at the magnetic-center transition. Negative pressure has been seen on the lattice by Christ et al. 1988 when computing it with the so-called differential method. This result was considered unphysical (on the contrary, we have discussed why it is physical in hep-th/0411214) and has led the lattice community to compute the pressure with the so-called integral method which assumes the thermodynamical limit (volume$\to \infty$) on a finite-size lattice. We have discussed in hep-ph/0404265 why this method fails to describe infrared sensitive quantities such as the pressure. Since the magnetic phase has an infinite correlation length (inverse mass of a BPS monopole) infrared sensitive quantities are not described properly on a finite-size lattice. However, infrared insensitive quantities, such as the entropy density, are. Our result for the entropy density in SU(3) Yang-Mills theory coincides with that obtained on the lattice using the differential method.

Outlook

We are in a position to compute the equation of state of an SU(2)/SU(3) Yang-Mills theory before 'hadronization' (Hagedorn transition) up to corrections on the 0.1% level. It remains to be seen how one can extend this to QCD. The central question here is whether quarks should be viewed as fundamental or as center-vortex crossings of additional dual and pure SU(3) Yang-Mills theories. If this can be assumed a computation of the equation of state for QCD light is straight-forward. The above assumption can be tested by using the so-obtained equation of state as an input for perfect-fluid hydrodynamical simulations to describe the low-p_T elliptic flow in URHIC.

Hot QCD at finite quark chemical potential: lattice thermodynamics and field theoretic models

Claudia Ratti, Michael A. Thaler, and Wolfram Weise
Physik-Department, Technische Universität München, D-85747 Garching, Germany

The study of QCD thermodynamics at finite chemical potential μ via lattice simulations is a formidable challenge, due to problems related to the non-reality of the euclidean Dirac operator when going to finite chemical potential. A lot of progress has recently been made, and the first lattice data at finite μ are now available. At the same time alternative strategies have been proposed, in order to improve our understanding of the QCD phase diagram. One of these is the study of two-colour QCD, a theory which has additional symmetries that guarantee the reality of the fermion determinant even at finite chemical potential.

We have investigated two- and three-colour QCD thermodynamics at finite μ by means of an extended Nambu Jona-Lasinio model including the scalar diquark channel. A background temporal gauge field couples the chiral and diquark condensates to the Polyakov loop via the gauge-covariant derivative. The Lagrangian of the model has the following form:

$$\mathcal{L}_{NJL}=\bar{\psi}\left(i\gamma_\mu D^\mu - m_0\right)\psi + G\left[\left(\bar{\psi}\psi\right)^2+\left(\bar{\psi}\gamma_5\tau\psi\right)^2\right] + \frac{H}{2}\left(\bar{\psi}i\gamma_5\tau_2 t_2 C\bar{\psi}^T\right)\left(\psi^T C i\gamma_5\tau_2 t_2\psi\right) - V\left(\Phi\right), \quad (1)$$

where $V(\Phi)$ is the effective potential for the Polyakov loop field Φ. $V(\Phi)$ is a polynomial in Φ whose powers differ between the two- and three-color model, according to the different centre symmetries Z_2 and Z_3, and

$$D^\mu = \partial^\mu + igA^\mu, \qquad A^\mu = \delta^{\mu 0}A_0. \quad (2)$$

The Polyakov loop is related to A_0 by $\Phi = tr_c \exp\left[i\beta g A_0\right]$. The parameters of the Polyakov loop potential are fixed to lattice results in the pure gauge sector, while the NJL model parameters are fixed by reproducing the pion mass, pion decay constant and quark condensate at $T < T_c$.

From the Lagrangian (1), we can evaluate the thermodynamic potential of the system. Minimizing it, we can find the behaviour of the Polyakov loop and the chiral (σ) and diquark (Δ) condensates as functions of temperature and chemical potential. In the two-colour case, lattice data exist for the chiral and diquark condensates as functions of μ, at zero temperature. We show a comparison between our results [2] and the lattice data in the left panel of Fig. 1. We confirm that a second order phase transition occurs, from the vacuum to a state with finite baryonic density, at a critical chemical potential equal to half the mass of the Goldstone modes (pions and scalar diquarks). Another interesting quantity that can be evaluated in our model, and compared to the existing lattice data, is the pion mass as a function of the chemical potential, at zero temperature. Our results are shown in the right panel of Fig. 1 in comparison to the corresponding lattice data.

In the three-colour case, lattice data at small chemical potential are available for two interesting quantities. The first one is the (scaled) quark number density which can be

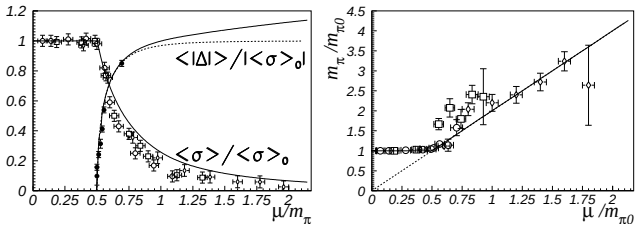

Figure 1: Left panel: comparison between our results for the chiral and diquark condensates as functions of the chemical potential at zero temperature, and the corresponding lattice data taken from Ref. [1]; right panel: comparison between our results for the pion mass as a function of $\mu/m_{\pi 0}$ and the lattice data taken from Ref. [1].

obtained from the thermodynamic potential of the system, $\Omega(T,\mu)$, through the relation

$$\frac{n_q}{T^3} = -\frac{1}{T^3}\frac{\partial\Omega(T,\mu)}{\partial\mu}. \quad (3)$$

The second one is the (scaled) pressure difference, defined as $\Delta p(T,\mu)/T^4 = (p(T,\mu) - p(T,\mu=0))/T^4$. We show our results [4] for these quantities in Fig. 2 in comparison with the corresponding lattice data. From our results

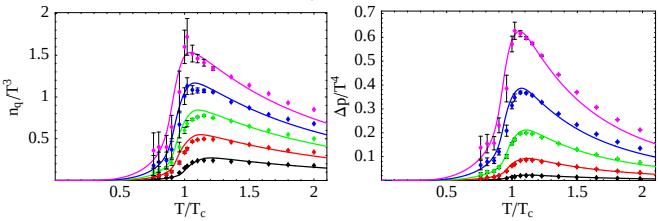

Figure 2: Left panel: comparison between our results for the scaled quark number density as a function of T/T_c, and the corresponding lattice data taken from Ref. [3]. Right panel: comparison between our results for the scaled pressure difference as a function of T/T_c and the lattice data taken from Ref. [3]. In both panels, the different curves correspond to different quark chemical potentials: from bottom to top: $\mu = 0.2T_c$, $\mu = 0.4T_c$, $\mu = 0.6T_c$, $\mu = 0.8T_c$, $\mu = T_c$, with $T_c \simeq 170$ MeV.

we can conclude that an NJL-type quasiparticle model, in which a coupling to a background temporal gauge field has been introduced, can reproduce successfully the existing lattice simulations of QCD thermodynamics at finite chemical potential, both for $N_c = 2$ and $N_c = 3$.

Work supported in part by BMBF, GSI and INFN.

References

[1] S. Hands *et al.*, Eur. Phys. J **C22**, 451 (2001).
[2] C. Ratti and W. Weise, Phys. Rev. **D70**, 054013 (2004).
[3] C. R. Allton *et al.*, Phys. Rev. **D68**, 014507 (2003).
[4] C. Ratti, M. A. Thaler and W. Weise, in preparation.

Hadron Liquid with a Small Baryon Chemical Potential at Finite Temperature

D.N. Voskresensky[1,2]
[1]GSI; [2]MEPhI Moscow

The description of the hadron system with a small baryon chemical potential, $|\mu_{\rm bar}| \ll T$, at the finite temperature is essentially different from the description of the dense baryonic system $|\mu_{\rm bar} - m_{\rm bar}| \gg T$. The former regime might be relevant for heavy ion collisions at RHIC and LHC, whereas the latter one, for SIS energies. In [1] we discuss general properties of a system of heavy fermions interacting with effectively rather light bosons. The fermion chemical potential is supposed to be small, $\mu_f \lesssim T$. We further assume that fermions are coupled to bosons with the help of a two-fermion – one-boson interaction. Then, the Φ-functional is given by the series of diagrams

$$i\,\Phi = \frac{1}{2} \quad + \quad \frac{1}{4} \quad + \ldots \qquad (1)$$

where the bold solid line corresponds to the fermion (or antifermion) full Green function and the bold wavy line, to the boson (or antiboson) full Green function, small dots denote free vertices. More specifically, we consider scalar σ, vector ω, isovector ρ and pseudovector π mesons interacting with nucleons and other baryons.

We start with the treatment of the first diagram of eq. (1) for the system of one species fermion and one species boson. We show that already for the low temperature, $T \ll \min(T_{\rm bl.f}, m_b)$, the fermion mass shell proves to be partially blurred due to multiple fermion rescatterings on virtual bosons, m_b is the boson mass, $T_{\rm bl.f}$ ($\ll m_f$) is the typical temperature corresponding to a complete blurring of the gap between fermion-antifermion continua, m_f is the fermion mass. As the result, the ratio of the number of fermion-antifermion pairs to the number provided by the ordinary Boltzmann distribution becomes larger than unity ($R_N > 1$). Quasiparticle approximation for fermions fails already in regime of *a warm hadron liquid* ($m_b^2/m_f \lesssim T \ll \min\{m_b, T_{\rm bl.f}\}$), if this limit is indeed realized for the given particle species. The effect is known as Urbach rule in the condensed matter physics.

For $T \gtrsim m_b^*(T)$ (hot hadron liquid), $m_b^*(T)$ is the effective boson mass that decreases with increase of the temperature, the abundance of all particles dramatically increases. Bosons behave as quasi-static impurities, on which heavy fermions undergo multiple rescatterings. Blurred fermions play a role of a glue for bosons. The hadron liquid comes to the state of *a hadron porridge*. The soft thermal loop approximation (it uses that typical thermal boson momenta are much smaller than the fermion ones) solves the problem. The effective fermion mass $m_f^*(T)$ decreases with the temperature increase. For $T \gtrsim T_{\rm bl.f}$ fermions are essentially relativistic particles.

Due to the interaction of the boson with fermion-antifermion pairs, $m_b^*(T)$ decreases leading to the possibility of the "hot Bose condensation" for $T > T_{\rm cb}$. The phase transition might be of the second order or of the first order depending on the species under consideration. For σN system correlation effects of higher order diagrams of Φ produce a suppression of vertices for $T \gtrsim m_b^*(T)$. Further we discuss the system of heavy fermions interacting with more light vector bosons (e.g., $N\omega$ and $N\rho$) and then, with pseudo-scalar bosons (e.g., $N\pi$). For the fermion – vector boson system correlation effects are incorporated by keeping the Ward identity. In case of the fermion – pseudo-scalar boson system correlation effects are rather small. Fig. 1 illustrates the ratio of the fermion (nucleon) density to the quantity calculated for the Boltzmann pseudoscalar boson (pion) gas as function of the temperature. This ratio becomes essentially larger than unity already for rather low temperature.

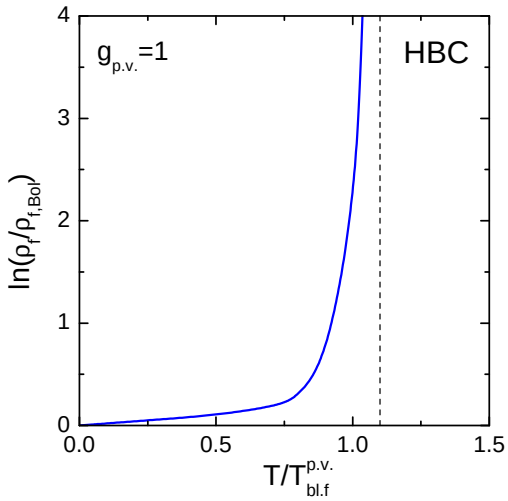

Figure 1: Logarithm of the ratio of the fermion density to the corresponding Boltzmann one for πN sub-system (pseudo-vector coupling) as function of T in units of $T_{\rm bl.f}^{p.v.}$. The vertical dash-line indicates the area of the HBC.

Finally, we allow for all interactions. We estimate $R_N \sim 1.5$ for $T \sim m_\pi/2$; $T_{\rm bl.f}$ proves to be near $T_{\rm cb}$; both values are in the vicinity of the pion mass m_π. The abundance of some high-lying baryon resonances proves to be of the same order, as the nucleon-antinucleon abundance.

We described the system in terms of only hadron degrees of freedom. In realistic situation quark-gluon degrees of freedom are also excited for $T \gtrsim m_\pi$. These effects may yield an additional diminishing of effective hadron masses due to the decrease of the quark condensate.

References

[1] D.N. Voskresensky, Nucl. Phys. **A744** (2004) 378.

The progress and the crisis in understanding QCD phase diagram

S. B. Rüster[1], I. A. Shovkovy[1,2], and D. H. Rischke[1,2]

[1]Institut für Theoretische Physik, J.W. Goethe-Universität, 60054 Frankurt am Main, Germany

[2]Frankfurt Institute for Advanced Studies, J.W. Goethe-Universität, 60054 Frankurt am Main, Germany

Theoretical studies predict that baryonic matter at asymptotic densities is a color superconductor. In nature, the highest densities of matter are reached in central regions of compact stars. There, the density might be as large as $10\rho_0$ where $\rho_0 \approx 0.15$ fm^{-3} is the saturation density. It is possible that baryonic matter is deconfined under such conditions and, perhaps, it is color superconducting. It is of great interest, therefore, to address physical implications of such a possibility.

In theoretical studies, many different color superconducting phases were proposed, which may appear inside compact stars, for reviews see Ref. [1]. In order to decide which phases are most favorable, one needs to know the phase diagram of strongly interacting matter obtained under the specific conditions realized in stars: (i) electric and color charge neutrality, and (ii) β-equilibrium.

The first attempt to obtain the phase diagram of dense, locally neutral three-flavor quark matter as a function of the strange quark mass, the quark chemical potential, and the temperature was made in Ref. [2]. It was shown that, at zero temperature and small values of the strange quark mass, the ground state of matter corresponds to the color-flavor-locked (CFL) phase. At some critical value of the strange quark mass, this is replaced by the recently proposed gapless CFL (gCFL) phase. In addition, several other phases were found as well. For instance, it was shown that there should exist a metallic CFL (mCFL) phase, a so-called uSC phase, as well as the standard two-flavor color-superconducting (2SC) phase and the gapless 2SC (g2SC) phase [3].

In Ref. [2], the effect of the strange quark mass was incorporated only approximately through a shift of the chemical potential of strange quarks, $\mu_s \to \mu_s - m_s^2/(2\mu)$. Such an approach is certainly reliable at small values of the strange quark mass. To go beyond this limitation, the study of the phase diagram [2] was further developed in Refs. [4, 5] where the strange quark mass was properly taken into account.

The phase diagram of dense, locally neutral three-flavor quark matter in the plane of temperature and m_s^2/μ, obtained in Ref. [5], is shown in Fig. 1. Here, the results are plotted for a fixed value of the quark chemical potential, $\mu = 500$ MeV. The three solid lines denote the three phase transitions between phases with different ground state symmetries. In the mean-field approximation used in the study, all three transitions are second order phase transitions. The two dashed lines mark the appearance of gapless modes in the metallic CFL (mCFL) and 2SC phases. In addition, there is also an insulator-metal crossover transition between the CFL and mCFL phase. This is marked by the dotted line on the phase diagram in Fig. 1.

It turns out that the phase diagram in Fig. 1, as well as the analogous diagrams in Refs. [2, 4], cannot be completely correct. The reason is that some of the phases that

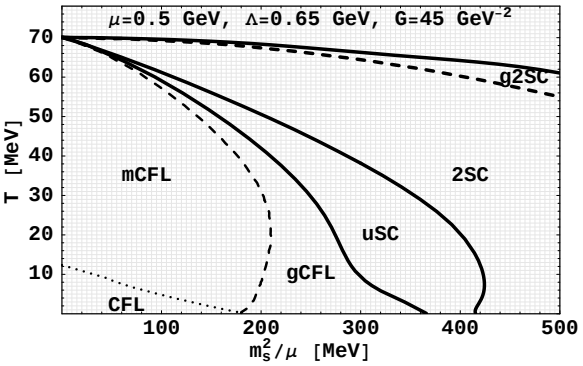

Figure 1: The phase diagram of neutral three-flavor quark matter in the plane of temperature and m_s^2/μ at a fixed value of the quark chemical potential, $\mu = 500$ MeV. By definition, $G \equiv g^2/\Lambda^2$.

appear in such phase diagrams are known to possess a so-called chromomagnetic instability [6]. This is seen from the fact that the Meissner screening masses are imaginary in the corresponding ground states of matter. It appears that all recently proposed gapless two- and three-flavor color superconducting phases share this problem.

Therefore, the regions in the phase diagram in Fig. 1, labelled "g2SC", "gCFL" and possibly even "uSC" should be modified. Unfortunately, it is not known unambiguously which stable phases would replace them. Therefore, there exists a fundamental crisis in the present understanding of the phase diagram of neutral dense quark matter. Of course, it is of primary importance to resolve this crisis.

In the future, the phase diagram should be studied within a framework that takes dynamically generated quark masses consistently into account. In order to understand the properties of matter in the interior of protoneutron stars, it is also of great interest to study the phase diagram in the plane of temperature and neutrino chemical potential.

References

[1] D. H. Rischke, Prog. Part. Nucl. Phys. **52**, 197 (2004); I. A. Shovkovy, nucl-th/0410091.

[2] S. B. Rüster, I. A. Shovkovy and D. H. Rischke, Nucl. Phys. A **743**, 127 (2004).

[3] I.A. Shovkovy and M. Huang, Phys. Lett. B **564** (2003) 205; M. Huang and I.A. Shovkovy, Nucl. Phys. A **729** (2003) 835.

[4] K. Fukushima, C. Kouvaris and K. Rajagopal, hep-ph/0408322.

[5] I. A. Shovkovy, S. B. Rüster and D. H. Rischke, nucl-th/0411040.

[6] M. Huang and I. A. Shovkovy, Phys. Rev. D **70**, 051501 (2004); Phys. Rev. D **70**, 094030 (2004).

A General Effective Theory for High-Density Quark Matter

Philipp T. Reuter, Qun Wang, Dirk H. Rischke
Institut für Theoretische Physik, Johann Wolfgang Goethe-Universität, D-60054 Frankfurt, Germany

Quark matter at small temperature T and large quark chemical potential μ is a color superconductor [1, 2]. In a color superconductor, there are several energy scales: the quark chemical potential μ, the inverse gluon screening length $m_g \sim g\mu$, and the superconducting gap parameter ϕ. In weak coupling these three scales are naturally ordered, $\phi \ll g\mu \ll \mu$. The ordering of scales implies that the modes near the Fermi surface, which participate in the formation of Cooper pairs, can be considered to be independent of the modes deep within the Fermi sea. This suggests that the most efficient way to compute properties such as the color-superconducting gap parameter is via an *effective theory for quark modes near the Fermi surface*. Such an effective theory has been originally proposed by Hong [3] and was subsequently refined by others [4, 5].

In order to construct such an effective theory, we pursue a different venue and introduce cut-offs in momentum space for quarks, Λ_q, and gluons, Λ_g. These cut-offs separate relevant from irrelevant quark modes and soft from hard gluon modes. We then explicitly integrate out irrelevant quark and hard gluon modes and derive a general effective action for hot and/or dense quark-gluon matter [6].

We show that the standard HTL and HDL effective actions are contained in our general effective action for a certain choice of the quark and gluon cut-offs Λ_q, Λ_g. We also show that the action of the high-density effective theory derived by Hong and others is a special case of our general effective action. In this case, relevant quark modes are located within a layer of width $2\Lambda_q$ around the Fermi surface.

The two cut-offs, Λ_q and Λ_g, introduced in our approach are in principle different, $\Lambda_q \neq \Lambda_g$. We show that in order to produce the correct result for the color-superconducting gap parameter to subleading order in weak coupling, we have to demand $\Lambda_q \leq g\mu \ll \Lambda_g \leq \mu$, so that $\Lambda_q/\Lambda_g \sim g \ll 1$. Only in this case, the dominant contribution to the QCD gap equation arises from almost static magnetic gluon exchange, while subleading contributions are due to electric and non-static magnetic gluon exchange.

The color-superconducting gap parameter is computed from a Dyson-Schwinger equation for the quark propagator. In general, this equation corresponds to a self-consistent resummation of all one-particle irreducible (1PI) diagrams for the quark self-energy. A particularly convenient way to derive Dyson-Schwinger equations is via the Cornwall-Jackiw-Tomboulis (CJT) formalism. In this formalism, one constructs the set of all two-particle irreducible (2PI) vacuum diagrams from the vertices of a given tree-level action. The functional derivative of this set with respect to the full propagator then defines the 1PI self-energy entering the Dyson-Schwinger equation. Since it is technically not feasible to include all possible diagrams, and thus to solve the Dyson-Schwinger equation exactly, one has to resort to a many-body approximation scheme, which takes into account only particular classes of diagrams. The advantage of the CJT formalism is that such an approximation scheme is simply defined by a truncation of the set of 2PI diagrams. However, in principle there is no parameter which controls the accuracy of this truncation procedure.

The standard QCD gap equation in mean-field approximation studied in Refs. [7, 8, 9, 10, 11] follows from this approach by including just the sunset-type diagram which is constructed from two quark-gluon vertices of the QCD tree-level action. We also employ the CJT formalism to derive the gap equation for the color-superconducting gap parameter. However, we construct all diagrams of sunset topology from the vertices of the general *effective* action derived in this work. The resulting gap equation is equivalent to the gap equation in QCD, and the result for the gap parameter to subleading order in weak coupling is identical to that in QCD, provided $\Lambda_q \leq g\mu \ll \Lambda_g \leq \mu$. The advantage of using the effective theory is that the appearance of the two scales Λ_q and Λ_g considerably facilitates the power counting of various contributions to the gap equation as compared to full QCD. We explicitly demonstrate this in the course of the calculation and suggest that, within this approach, it should be possible to identify the terms which contribute beyond subleading order to the gap equation. Of course, for a complete sub-subleading order result one cannot restrict oneself to the sunset diagram, but would have to investigate other 2PI diagrams as well. This shows that an *a priori* estimate of the relevance of different contributions on the level of the effective action does not appear to be feasible for quantities which have to be computed self-consistently.

References

[1] K. Rajagopal and F. Wilczek, arXiv:hep-ph/0011333.
[2] D.H. Rischke, Prog. Part. Nucl. Phys. **52**, 197 (2004).
[3] D.K. Hong, Phys. Lett. B **473**, 118 (2000); Nucl. Phys. B **582**, 451 (2000).
[4] T. Schäfer, Nucl. Phys. A **728**, 251 (2003); eConf **C030614**, 038 (2003).
[5] G. Nardulli, Riv. Nuovo Cim. **25N3**, 1 (2002).
[6] P. T. Reuter, Q. Wang and D. H. Rischke, Phys. Rev. D **70**, 114029 (2004).
[7] T. Schäfer and F. Wilczek, Phys. Rev. D **60**, 114033 (1999).
[8] R.D. Pisarski and D.H. Rischke, Phys. Rev. D **61**, 051501, 074017 (2000).
[9] D.K. Hong, V.A. Miransky, I.A. Shovkovy, and L.C.R. Wijewardhana, Phys. Rev. D **61**, 056001 (2000) [Erratum-ibid. D **62**, 059903 (2000)].
[10] Q. Wang and D. H. Rischke, Phys. Rev. D **65**, 054005 (2002).
[11] A. Schmitt, Q. Wang and D. H. Rischke, Phys. Rev. D **66**, 114010 (2002).

Lattice QCD Constraints on Hybrid and Quark Stars

Yu.B. Ivanov[1,2], A.S. Khvorostukhin[3], E.E. Kolomeitsev[4], V.V. Skokov[1,3], V.D. Toneev[1,3], and D.N. Voskresensky[1,5]

[1]GSI; [2]Kurchatov Inst. Moscow; [3]JINR Dubna; [4]University of Minnesota; [5]MEPhI Moscow

Nowadays it is commonly accepted that the quark-gluon phase of the matter can be formed in the course of heavy-ion collisions at ultrarelativistic energies. On the other hand, many papers are devoted to the possibility of quark matter existence either in interiors of some stars or as a new family of pure quark stars. A straightforward calculation of properties of strongly interacting matter and, in particular its equation of state (EoS), is possible on the lattice. So far, the main body of lattice results concerns the case of zero baryon chemical potential ($\mu = 0$) and finite temperatures. Recently new lattice predictions on the EoS at finite but small baryon chemical potentials became available [1]. Nevertheless, they are still far from the astrophysically relevant domain. Therefore, a theoretical modeling is needed for their extrapolation.

In [2] we would like to draw "lattice QCD motivated" predictions on possible existence of hybrid and quark stars, as well as their properties. To do this, we extrapolate the existing lattice results to the region of cold electroneutral baryon matter relying on the phenomenological QCD motivated dynamical-quasiparticle (DQ) model recently proposed in Ref. [3]. At high temperatures the DQ model complies with the quasiparticle picture of the hard thermal loop approach, whereas at lower temperatures it simulates the confinement of the QCD. Two sets of parameters of this model (below denoted as "1-loop" and "2-loop") were fitted to reproduce lattice data at finite baryon chemical potentials [1]. To have a reference point for the DQ model, we also consider three versions of the MIT bag model. Two "light-bag" models ("light-bag-155" and "light-bag-200") with conventional current quark masses, zero gluon mass and different bag constants ($B^{1/4} = 155$ MeV and 200 MeV) covering broad range of EoS's are usually applied to the treatment of hybrid and quark stars. We also consider a "heavy-bag" model, quark/gluon masses and bag constant of which are fitted to reasonably reproduce lattice results of Ref. [1]: $m_u = m_d = 330$ MeV, $m_s = 450$ MeV, $m_g = 600$ MeV and $B^{1/4} = 183$ MeV.

Both versions of the DQ model perfectly fit the lattice data (see Fig. 1) As is seen, the "heavy-bag" model also reasonably well covers the lattice data. Values of the effective bag parameter B prove to be very high in the DQ model. Whereas in the "heavy-bag" model B is in the range of ordinarily used values. The "light-bag" models do not follow lattice predictions. This failure can be associated with small values of quark and gluon masses used in the calculation.

In application to electroneutral β-stable matter we demonstrate that all lattice-QCD-motivated models (DQ and "heavy-bag") of quark phase matched with the realistic relativistic mean-field models of the hadronic phase predict onset of the phase transition at very high critical densities (typically $n_c^h \gtrsim 10\, n_0$) which are higher than those reachable within these models in neutron star interiors (see Fig.2) and thereby do not allow existence of hybrid (quark-hadron) stars. Pure quark stars are possible and have low masses, small radii and very high central densities. "Light-bag" models result in critical densities in the range which is usually considered in papers devoted to hybrid stars that allow for their existence.

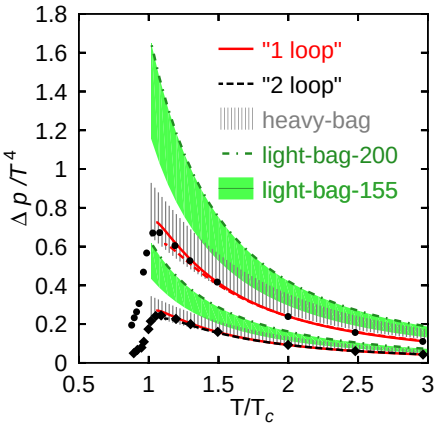

Figure 1: $\Delta P = P(T,\mu) - P(T,\mu=0)$ scaled by T^4 as functions of T/T_c at nonzero baryon chemical potentials $\mu = 330$ and 530 MeV (from bottom to top). The results for bag models are displayed by bands accounting for uncertainity associated with the perturbative correction [2]. Lattice data are from [1].

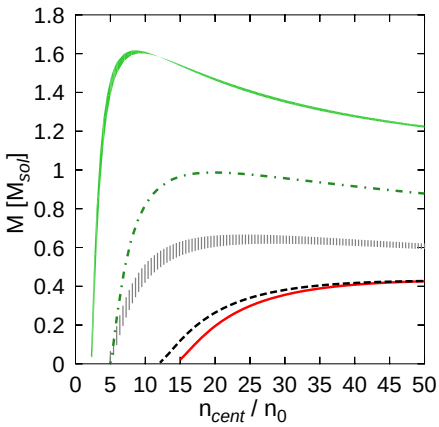

Figure 2: Quark star mass – central density relation. Notation is the same as in Fig. 1.

References

[1] Z. Fodor, Nucl. Phys. A **715** (2003) 319; F. Csikor *et al.*, JHEP **405** (2004) 46.

[2] Yu.B. Ivanov, A.S. Khvorostukhin, E.E. Kolomeitsev, V.V. Skokov and D.Voskresensky, astro-ph/0501254.

[3] Yu.B. Ivanov, V.V. Skokov, and V.D. Toneev, Phys. Rev. **D71** (2005) 014005.

Equation of State of Deconfined Matter within Quasiparticle Description

Yu.B. Ivanov[1,2], V.V. Skokov[1,3], and V.D. Toneev[1,3]
[1]GSI; [2]Kurchatov Inst., Moscow; [3]JINR Dubna

Motivated by lowest-order perturbative QCD, a simple dynamic-quasiparticle (DQ) model of the quark–gluon matter is proposed [1]. It is applied to interpret the lattice QCD equation of state [2, 3]. The effective Lagrangian of the DQ model [1] treats transverse gluons ϕ_a and quarks ψ_{fc} of $N_f = 3$ flavors and $N_c = 3$ colors. For this model it is essential that $N_f = N_c$. These constituents interact via mean fields $\vec{\zeta} = \{\zeta_u, \zeta_d, \zeta_s\}$:

$$\begin{aligned}\mathcal{L} &= \frac{1}{2}\sum_{a=1}^{N_g}\left[(\partial_\mu\phi_a)^2 - m_g^2(\vec{\zeta})\phi_a^2\right] \\ &+ \sum_{c=1}^{N_c}\sum_{f=1}^{N_f}\bar{\psi}_{fc}[i\gamma_\mu\partial^\mu - m_f(\vec{\zeta})]\psi_{fc} - B(\chi), \quad (1)\end{aligned}$$

where $N_g = 2(N_c^2 - 1)$ is the number of transverse gluons, $\chi^4 = \sum_{f=1}^{N_f}\zeta_f^4$,

$$m_g^2 = \frac{2}{N_g}\sum_{f=1}^{N_f}\zeta_f^2 g^2(\chi), \quad m_f^2 - m_{f0}^2 = \frac{1}{2N_c}\zeta_f^2 g^2(\chi). \quad (2)$$

Here m_{f0} is the current f-quark mass, m_g and m_f are effective masses of gluons (g) and quarks, respectively. The masses and the coupling constant $g^2(\chi)$ depend on mean fields $\vec{\zeta}$. The potential of the mean-field self-interaction

$$B(\chi) = B_C - \left[\frac{\chi_1^4 g^2(\chi_1)}{N_g}\right]_{\chi_C}^{\chi} + \frac{2}{N_g}\int_{\chi_C}^{\chi} d\chi_1\chi_1^3 g^2(\chi_1)\,, \quad (3)$$

has a meaning of an effective bag parameter. Here B_C and χ_C are parameters of the model. The solution of equations of motion for the mean fields gives

$$\zeta_f^2 = \eta^2 + \frac{N_g}{4N_c}\xi_f^2, \quad (4)$$

$$\eta^2 = \frac{N_g}{2\pi^2}\int_0^\infty \frac{k^2\,dk}{(k^2+m_g^2)^{1/2}} f_g(k), \quad (5)$$

$$\xi_f^2 = \frac{N_c}{\pi^2}\int_0^\infty \frac{k^2\,dk}{(k^2+m_f^2)^{1/2}}[f_{q,f}(k) + \bar{f}_{q,f}(k)], \quad (6)$$

Here η^2 and ξ_f^2 are scalar densities of gluons and quarks (divided by the mass), respectively, and f_g, $f_{q,f}$ and $\bar{f}_{q,f}$ are occupation numbers of gluons, quarks and antiquarks. In equilibrium these are conventional Bose and Fermi occupation numbers in terms of the temperature T and chemical potential μ. With this solution the effective masses of gluons and quarks, cf. Eq. (2), reproduce the hard-thermal-loop results in the high-temperature limit, provided the coupling constant $g^2(\chi)$ is appropriately defined. The appropriate choice of the coupling constant is

$$g^2(\chi) = \frac{16\pi^2}{\beta_0\ln[(\chi^2+\chi_0^2)/\chi_C^2]} f(\chi)\,, \quad (7)$$

where $\beta_0 = \frac{1}{3}(11N_c - 2N_f^{\rm eff})$. $N_f^{\rm eff}$ is the effective number of quark flavors at the energy scale χ, which may be $N_f^{\rm eff} < N_f$, and χ_0^2 is another parameter of the model. An auxiliary function $f(\chi)$, satisfying the condition $f(\chi \to \infty) \to 1$, helps us to choose between the 1-loop ($f \equiv 1$) and 2-loop perturbative limits of the coupling constant.

A reasonable fit of the quark–gluon sector can be obtained with different sets of phenomenological parameters, listed in the Table (the critical temperature, T_C, and χ_C are presented in MeV, "f" is the effective value of f-function, and $\chi_0^2 = 0.01\chi_C^2$). The "1-loop" version of the model certainly looks more natural, since it does not involve an "exotic" auxiliary function f. The only problem is that it overestimates all lattice quantities by approximately 10% (therefore, the normalization $N_{\rm norm} = 0.9$ is used). However, since the overall normalization of the lattice data is somewhat uncertain due to the poor extrapolation to the continuum limit, this misfit is quite acceptable. The quality of reproduction of lattice data is demonstrated in Fig. 1. Similar reproduction is obtained at nonzero μ for $\Delta P = P(T,\mu) - P(T,\mu=0)$, interaction measure $(\varepsilon - 3P)$ and baryon density [1].

Version	$N_f^{\rm eff}$	T_C	χ_C	B_C/χ_C^4	"f"	$N_{\rm norm}$
1-loop	2+1	195	141.3	-97.5	1	0.9
1-loop	2	175	141.3	-97.5	1	0.9
2-loop	2+1	195	119.6	-267.5	2.6	1
2-loop	2	175	119.6	-262.0	2.6	1

The presented model simulates the confinement of the QCD. The solution to the model equations simply does not exist below certain combination of the temperature and the chemical potential. This is the reason why we are able to fit the lattice quantities only above T_C.

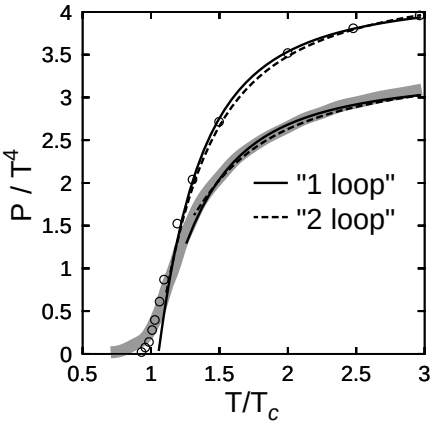

Figure 1: Pressure scaled by T^4 as a function of T/T_C at $\mu = 0$. The (2+1)-flavour lattice data [2] are displayed by open circles, and the 2-flavour data [3] – by grey band.

References

[1] Yu.B. Ivanov, V.V. Skokov, and V.D. Toneev, Phys. Rev. D **71**, 014005 (2005).
[2] F. Csikor, et al., JHEP **405**, 46 (2004).
[3] F. Karsch, Lect. Notes in Phys. **583**, 209 (2002).

Restoration of Scale Invariance and Chiral Symmetry at Finite Temperatures

Gebhard Zeeb[1], Detlef Zschiesche[1], and Stefan Schramm[2]

[1]Institut für Theoretische Physik, J.W. Goethe Universität, Max-von-Laue-Str. 1, D-60438 Frankfurt am Main;
[2]Center for Scientific Computing, J.W. Goethe Universität, Max-von-Laue-Str. 1, D-60438 Frankfurt am Main

Due to the non-perturbative properties of QCD at low energies, lattice gauge calculations represent the most direct approach to investigate the QCD phase diagram of strongly interacting matter. However, upto now lQCD alone does not seem to be able to completely disentangle the physics of the QCD phase transition and give an explanation of the phase diagram structure. Hence, effective lagrangians are studied, representing a complementary approach to gain understanding and intuition of the physics of the QCD phase transition (see e.g. [1, 2]).

We use a relativistic field theoretical model of baryons and mesons built on chiral $SU(3)_L \times SU(3)_R$ symmetry and broken scale invariance, introduced in Ref. [3]. The model has been shown to describe successfully hadronic vacuum masses as well as properties of nuclear matter, finite nucleii and neutron stars [3, 4]. At high temperatures the model predicts a transition to a chirally restored hadronic phase. In Ref. [5] we have studied the parameter dependence of this chiral phase transition for the case that the gluon condensate χ, which represents the order parameter of the broken scale invariance [1, 6], does not couple to the baryons. In this case the T-dependence of the χ-field is small and no restoration of scale invariance occurs. Then keeping the gluon condensate to its vaccum value ($\chi \equiv \chi_0$) is a reasonable approximation.

However, this situation changes substantially if the χ-field couples strongly to the baryons. We consider such a scenario by modelling the mass difference between nucleon and Δ by exchange of instantons [7]. Then this mass difference ($\approx$ 300 MeV for the vaccuum case) is generated by the coupling of the gluon condensate to the baryon decuplet. The upper panel of Fig. 1 shows that with this

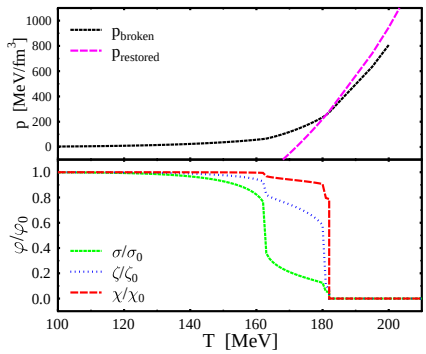

Figure 1: The pressure (upper panel) and the order parameter fields (lower panel) vs. T ($\mu = 0$).

strong coupling the phase with vanishing order parameters for breaking of chiral symmetry (σ, ζ) *and* scale invariance (χ), respectively, becomes stable for $T > T_{\rm p.t.} \approx 182$ MeV (larger pressure than the broken phase). The lower panel depicts the behaviour of the different fields (condensates). All of them show large sudden drops, but at different temperatures. The sudden drops in the chiral condensates signal the (partial) chiral restoration. As discussed in [5], the T-dependence of the chiral restoration depends on the couplings of the baryons to the chiral fields. A change in these couplings would also shift the pressure curve of the phase with spontaneously broken scale invariance (large χ). This will alter the characteristics of the transition to the completely restored phase. However, as long as the gluon condensate couples strongly to the baryons, the phase with restored chiral symmetry and scale invariance will be stable above $\approx$ 180 MeV. I.e., the chiral restoration happens before *or* simultaneously with the restoration of scale invariance. Such a phase transition behavior was expected in [1]. There the vanishing of all order parameters was identified with gluon- and quark-deconfinement.

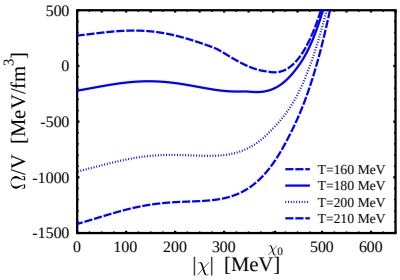

Figure 2: The grand canonical potential vs. the χ-field for different T ($\mu = 0$).

The transition to the completely restored phase can be illustrated by the grand canonical potential as a function of χ (Fig. 2). Near $T_{\rm p.t.}$ ($T = 180$ MeV), the two minima are almost degenerate. For higher T the minimum at $\chi = 0$ is below the one corresponding to the restored phase. And for $T > 200$ MeV the restored phase vanishes at all.

The investigation for $\mu > 0$ and the implementation of further hadronic resonances is in progress. Then both the comparison to the latest lQCD results and the application of the resulting equation of state to simulations of relativistic heavy-ion collisions will be possible.

We gratefully acknowledge support by the Frankfurt Center for Scientific Computing.

References

[1] B. A. Campbell, J. R. Ellis and K. A. Olive, Nucl. Phys. B **345** (1990) 57.
[2] M. A. Stephanov, Prog. Theor. Phys. Suppl. **153** (2004) 139.
[3] P. Papazoglou et al., Phys. Rev. C **59** (1999) 411.
[4] S. Schramm & D. Zschiesche, J. Phys. G **29** (2003) 531.
[5] D. Zschiesche et al., arXiv:nucl-th/0407117.
[6] J. Schechter, Phys. Rev. D **21** (1980) 3393.
[7] G. 't Hooft, Phys. Rev. D **14** (1976) 3432.

Gapless Hartree-Fock Resummation Scheme for the $O(N)$ Model

Yuri B. Ivanov[1,2], Felix Riek[1], and Jörn Knoll[1]
[1]GSI; [2]Kurchatov Institute, Moscow

We present a modified selfconsistent Hartree-Fock approximation [1] at the example of the ϕ^4 $O(N)$-model. The modification complies a) with all the desireable features of selfconsistent Dyson resummation schemes base on the 2PI functional formalism (Φ-derivable approximation) like conservation laws and thermodynamical consistency, while b) it simultaneously respects the Nambu-Goldstone theorem in the chirally broken phase. The Lagrangian of our model is given by

$$\mathcal{L} = \frac{1}{2}(\partial_\mu \phi_a)^2 - \frac{1}{2}m^2\phi^2 - \frac{\lambda}{4N}(\phi^2)^2, \qquad (1)$$

where ϕ is a N-dimensional vector and the summation over repeated indices is implied. The normal Hartree Approximation to this model leads to an unphysical behaviour of the pion mode at finite temperatures, where we find a massive pion instead of a massless Goldstone Boson [2]. This can be corrected in so called gapless Approximations [3] which however are not Φ-derivable and therefore are neither thermodynamicly consistent nor conserving. Our Approximation deals with this problem by adding a phenomenological correction term

$$\Delta\Phi = -\frac{(N-1)\lambda}{2N}(Q_\pi - Q_\sigma)^2 \qquad (2)$$

directly to the Φ-functional which restores the Goldstone behaviour. The functions Q_a represent the Tadpole self-energies where we set all divergent parts to zero. Note that this correction term is zero for the case that both masses are equal, meaning that the normal Hartree Approximation is unchanged in the chiraly restored phase. A Variation of the CJT effective potential with respect to the Propagators and the Meanfield now leads to the following set of Gap-Equations

$$\begin{aligned} M_\sigma^2 &= m^2 + \frac{\lambda}{N}\left[3\phi^2 + (5-2N)Q_\sigma + 3(N-1)Q_\pi\right] \\ &= M_\pi^2 + \frac{\lambda}{N}\left[2\phi^2 + 2(N-1)(Q_\pi - Q_\sigma)\right], \qquad (3) \\ M_\pi^2 &= m^2 + \frac{\lambda}{N}\left[\phi^2 + 3Q_\sigma + (N-1)Q_\pi\right], \qquad (4) \\ 0 &= \phi\left[m^2 + \frac{\lambda}{N}\left(\phi^2 + 3Q_\sigma + (N-1)Q_\pi\right)\right], \qquad (5) \end{aligned}$$

where the temperature dependence enters through the Tadpoles. The parameters m and λ are determined form the requirement that the vacuum masses of the pion and sigma-meson are 0 and 600 MeV respectively. From Equations (5) and (4) one can directly see that we indeed managed to keep the pion-mass equal to zero in the broken phase where we have nonzero meanfield ($\phi \neq 0$). In the following we restrict the discussion to the case of $N = 4$. The solution of the Gap-Equations turned out to reveal an even more complex phase structure than we expected. In the Fig. 1 and 2 we present the results for the temperature dependence of the masses and the meanfield. In order to

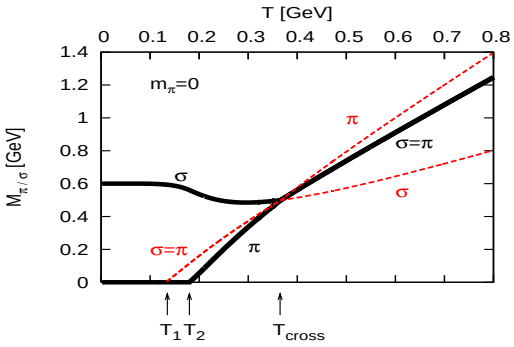

Figure 1: Meson masses as functions of temperature. Stable and unstable branches are presented by solid and dashed lines respectively

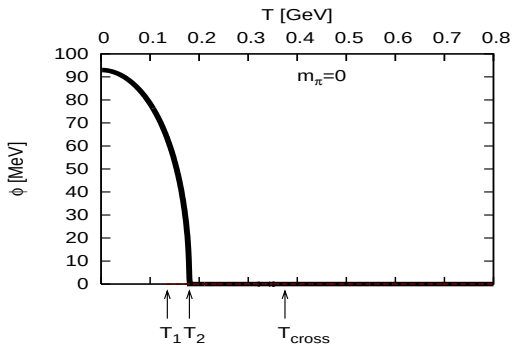

Figure 2: σ-Meanfield ϕ as a function of temperature. Stable and unstable branches are presented by solid and dashed lines respectively

determine the most stable solution one has to calculate the value of the effective potential [1]. Here we only indicate the most stable one by a solid line. Doing so we find three different phases which are connected by second order phase transitions. Phase 1 is the chiraly broken phase starting from the vacuum. Above $T = T_1$ we find a second solution to the Gap-Equations which has equal masses but which is only metastable. At $T = T_2$ the meanfield becomes zero and we enter Phase 2 where we have zero meanfield but still different masses. The pion mass becomes finite and increases with temperature. If we go even higher in temperature we reach $T = T_{cross}$ where the up to now metatstable solution with equal masses becomes the most stable one and we enter the chiraly restored phase.

References

[1] Yu. B. Ivanov et al. hep-ph/0502146
[2] Lanaghan and Rischke, J.Phys. G26 (2000) 431
[3] Hohenberg and Martin, Ann. Phys. (NY) 34 (1965) 291

Cooling of Color Superconducting Hybrid Stars

H. Grigorian[1,2], D. Blaschke[3,4], and D.N. Voskresensky[5,6]

[1]Institut für Physik, Universität Rostock, D-18051 Rostock, Germany; [2]Department of Physics, Yerevan State University, Alex Manoogian Str. 1, 375025 Yerevan, Armenia; [3]Fakultät für Physik, Universität Bielefeld, D-33615 Bielefeld, Germany; [4]Joint Institute for Nuclear Research, RU-141980, Dubna, Russia; [5]Theory Division, GSI mbH, D-64291 Darmstadt, Germany; [6]Moscow Institute for Physics and Engineering, RU-115409 Moscow, Russia

Recently, we have reinvestigated the cooling of neutron stars within a purely hadronic model [1] and demonstrated that the modern neutron star cooling data can be well explained within the *nuclear medium cooling scenario* [2], including a suppression of the $3P_2$ neutron gap [3]. Since in this scenario the direct Urca (DU) process once occuring would cool the star very fast, we have formulated the requirement that the critical neutron star mass above which the DU process is allowed should be larger than that of a typical neutron star [4], $1.05\ M_\odot < M_{\rm typ} < 1.78\ M_\odot$. This puts a tight constraint on the asymmetry energy in the nuclear equation of state (EoS) which determines the proton fraction and thus the threshold for the onset of the DU process. The latter dependence is an important issue for the analysis of heavy ion collisions especially within the new program for the investigation of compressed baryon matter (CBM) to be realized at the future accelerator facility FAIR at the GSI Darmstadt.

Our assumption about the mass distribution can be developed into a more quantitative test of cooling scenarios when these are combined with population synthesis models [4]. Ref. [5] argued that the presence of quark matter in massive compact star cores is a most reliable hypothesis since within their model hyperons appear at sufficiently low densities and the equation of state becomes too soft to carry neutron star masses in the range of $M_{\rm BRP}$.

We demonstrated [6] that within a recently developed nonlocal, chiral quark model (see [7] and Refs. therein) the critical densities for a phase transition to color superconducting quark matter can be low enough for these phases to occur in compact star configurations with masses below 1.3 $M_\odot$. For the choice of the Gaussian formfactor the 2SC - normal quark matter mixed phase arises at $M \simeq 1.21\ M_\odot$. We have shown that without a residual pairing the 2SC quark matter phase could describe the cooling data only if compact stars had masses in a very narrow band around the critical mass for which the quark core can occur. Since there are observations of neutron stars with higher and essentially different masses such a scenario should be disfavored.

Then we assumed that formally unpaired quarks can be paired with small gaps $\Delta_X < 1$ MeV (2SC+X pairing), which are density dependent according to $\Delta_X(\mu) = \Delta_c\ \exp[-\alpha(\mu-\mu_c)/\mu_c]$, where the parameters are chosen such that at the critical quark chemical potential $\mu_c = 330$ MeV for the onset of the deconfinement phase transition the X-gap has its maximal value of $\Delta_c = 1.0$ MeV and at the highest attainable chemical potential $\mu_{\rm max} = 507$ MeV, i.e. in the center of the maximum mass hybrid star configuration it falls to a value of the order of 10 keV. We choose the value $\alpha = 10$ for which $\Delta_X(\mu_{\rm max}) = 4.6$ keV.

We show in Fig. 1 that the present day cooling data could be well explained by hybrid stars, however, when assuming a complex pairing pattern, where quarks are partly strongly paired within the 2SC channel, and partly weakly paired with density dependent gaps $\Delta_X < 1$ MeV.

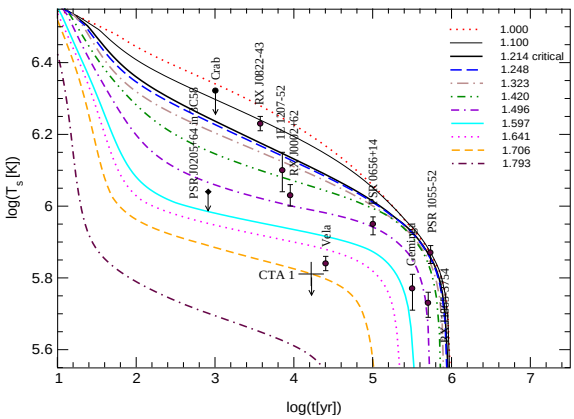

Figure 1: Cooling curves for hybrid star configurations with quark matter core in the 2SC+X phase. The weak diquark pairing gap Δ_X is density dependent [6], the neutron $3P_2$ gap is taken from [8] but then is suppressed by factor 0.1. The labels correspond to the gravitational masses of the configurations in units of the solar mass.

H.G. has been supported in part by the Virtual Institute of the Helmholtz Association under grant No. VH-VI-041 and by DAAD University partnership program; D.V. has been supported in part by DFG grant No. 436 RUS 17/117/03.

References

[1] D. Blaschke, H. Grigorian, and D.N. Voskresensky, A & A **424**, 979 (2004).

[2] D.N. Voskresensky, in "Physics of Neutron Star Interiors", Springer LNP **578** (2001) 467.

[3] H. Grigorian and D. N. Voskresensky, arXiv:astro-ph/0501678.

[4] S. Popov, H. Grigorian, R. Turolla, and D. Blaschke, arXiv:astro-ph/0411618.

[5] M. Baldo, G. F. Burgio and H. J. Schulze, arXiv:astro-ph/0312446.

[6] H. Grigorian, D. Blaschke and D. Voskresensky, arXiv:astro-ph/0411619.

[7] H. Grigorian, D. Blaschke, and D.N. Aguilera, Phys. Rev. **C 69**, 065802 (2004).

[8] T. Takatsuka, and R. Tamagaki, Prog. Theor. Phys. **112**, 37 (2004).

Direct Urca process constraint and DBHF - CSL hybrid stars

D.B. Blaschke[1,2], T. Klähn[3], H. Grigorian[3,4], E.N.E. van Dahlen[5], C. Fuchs[5], and A. Faessler[5]

[1]Fakultät für Physik, Universität Bielefeld, D-33615 Bielefeld, Germany; [2]Joint Institute for Nuclear Research, RU-141980, Dubna, Russia; [3]Institut für Physik, Universität Rostock, D-18055 Rostock, Germany; [4]Department of Physics, Yerevan State University, Alex Manoogian Str. 1, 375025 Yerevan, Armenia; [5]Institut für Theoretische Physik, Universität Tübingen, D-72076 Tübingen

The cooling of compact stars depends on a multitude of different processes. A very efficient one is the direct Urca process (DU) which occurs above a proton fraction of $Y_p \approx 1/9$ and leads to a very fast cooling. In the case of hadronic matter the onset of this process is determined by the density dependence of the asymmetry energy. While stars with a central density ρ_c slightly below the DU threshold (ρ_{DU}) still cool rather slow, a small increase of ρ_c above this threshold fastens the cooling dramatically. Let's make the very conservative assumption that the range of measured masses of binary radio pulsars (BRP) $M_{BRP} = 1.35 \pm 0.04\, M_\odot$ [1] is an indication for the unknown range of masses of isolated compact stars in the temperature-age diagram. Then the DU should occur at high enough densities that $M_{\rho_{DU}} > M_{BRP}$ since otherwise the surface temperatures of stars inside the BRP mass region would be far below the known X-ray data points (DU problem [2]).

In this work we describe the hadronic equation of state in a relativistic Dirac-Brueckner-Hartree-Fock (DBHF) framework, using the Bonn A potential [3]. As typical for relativistic mean field equations of state, the DU threshold is crossed already for rather light stars in the vicinity of M_{BRP} (see Fig. 1) and the DU problem occurs. Here we suggest that this problem can be solved provided a phase transition to quark matter occurs for $\rho < \rho_{DU}$ in the stars interior.

The DU in normal quark matter would be allowed at all densities but in the case of a two-flavor color superconducting (2SC) phase this process is suppressed. However, as has been discussed in [4], this phase is most unlikely in compact stars. If 2SC does not occur, this excludes the 2SC+X phase which has been discussed for hybrid star cooling [5, 6] and other patterns of diquark pairing satisfying color and charge neutrality can become energetically more favorable than normal quark matter. As a viable alternative we suggest the color-spin-locking (CSL) phase [7], for which the pairing gaps are small enough that the EoS is well described by a bag model [6].

In Fig. 1 we show that a hadronic description of stars would result in the DU problem for all stars with masses above 1.3 $M_\odot$, as denoted by the white circle. A phase transition to quark matter in the CSL phase, here modeled by a Maxwell construction as sketched in Fig. 2, takes place before the critical proton fraction is reached. The same result would hold by applying a Gibbs construction.

In conclusion we suggest that the existence of a CSL quark matter phase could explain the cooling behavior of compact stars even for a DBHF hadronic equation of state with a DU onset for small densities.

This work has been supported by the Virtual Institute of the Helmholtz Association under grant No. VH-VI-041.

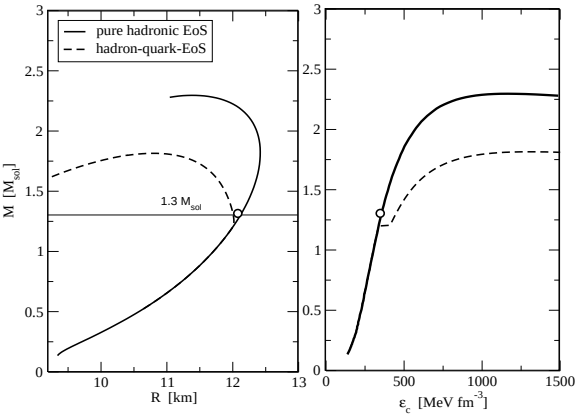

Figure 1: Direct Urca in pure hadronic matter (solid line) would occur for a star mass of $\approx 1.3 M_\odot$. In a mixed hadron–CSL-quark-phase this process will be blocked.

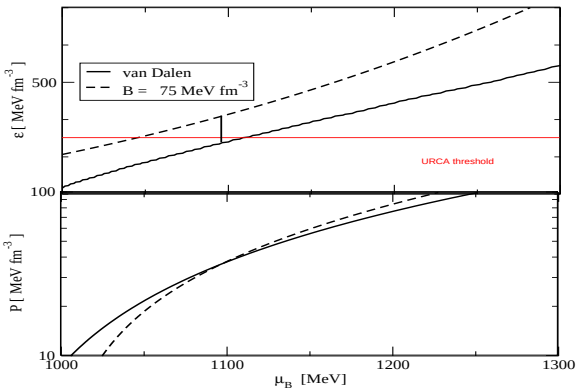

Figure 2: DBHF and CSL equations of state with phase transition. The horizontal line denotes the phase transition takes place just before the Urca-process threshold.

References

[1] S. E. Thorsett and D. Chakrabarty, Astrophys. J. **512**, 288 (1999)

[2] D. Blaschke, H. Grigorian, and D. Voskresensky, Astron. Astrophys. **424**, 979 (2004)

[3] E.N.E. van Dalen, C. Fuchs, and A. Faessler, Nucl. Phys. A **744**, 227 (2004).

[4] D. N. Aguilera, D. Blaschke, and H. Grigorian, arXiv:hep-ph/041266 (2004).

[5] H. Grigorian, D. Blaschke and D. Voskresensky, arXiv:astro-ph/0411619 (2004).

[6] H. Grigorian, D. Blaschke and D. Aguilera, Phys. Rev. C **69**, 065862 (2004).

[7] D. N. Aguilera, D. Blaschke, M. Buballa, and V. L. Yudichev, in preparation

High $p_\perp$ suppression in URHICs: (pre–)hadronic FSI and radiative energy loss

K.Gallmeister*

*Institut für Theoretische Physik, Universität Giessen, Germany

Ultrarelativistic heavy ion collisions (URHICs) are supposed to build up a new phase of matter, the "quark-gluon-plasma" (QGP). In order to extract information of this new matter, the spectra of particles at high transversal momenta at midrapidity are thought to be messengers. Hadrons with high transversal momenta fragment from partons built in a hard collision. Since these partons have to travel through the strongly interacting matter built in the collision, they loose energy. The most popular mechanism here is energy loss by induced (gluon) radiation.

On the other hand one knows, that hadrons stemming from high energy collisions suffer final state interactions among each other. This could lead to the same observation as above: hadrons with high transversal momenta are shifted to lower transversal momenta by inelastic hadronic interactions [1]

With an eye on planned experiments at LHC, we analyze ongoing experiments at RHIC in order to estimate the effect of hadronic interactions by performing transport calculations based on BUU equations [2]. The most prominent feature of these calculations is the fact, that hadrons including partons from the hard interaction (so called "leading hadrons") can interact immediately after the hard interaction. (In order to take care of the fact, that huge energy densities are produced in the $A+A$ collision, interactions are postponed to times where local energy is less than 1 GeV/fm^3.) Since these "leading" hadrons can interact immediately, we call this "interaction of pre–hadronic states". Results for most central collisions are shown in fig. 1. One observes drastic suppression effects in

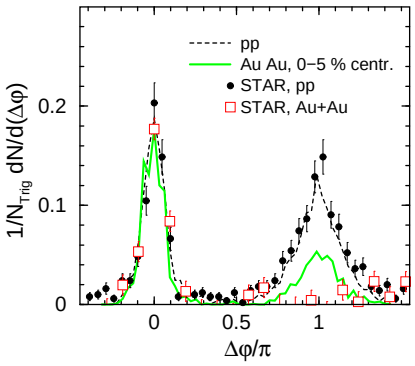

Figure 1: The angular correlation of high $p_\perp$ attenuation by (pre–)hadronic interactions for most central collisions compared with data. See [2] for details.

the calculations, which are however not able to explain the full hadron attenuation: high $p_\perp$ hadrons are suppressed in the single hadron spectra, the far side peak in correlations spectra is also reduced by same amount, while the near side peak is hardly affected. The same prescription explains suppression effects seen in cold nuclear matter in $\gamma^* A$ reactions at HERMES [3]

In order to circumvent all problems mentioned above, better messengers than "hadrons" are needed. Here leptons offer an additional source of information. Disregarding all information one could get from thermal distributions at intermediate energies [4], leptons and dileptons especially from the decay of open charm mesons have to be observed. Fig. 2 shows some calculations [5] estimating the size of radiative energy loss on the single lepton spectra stemming from mesons with open charm. Unfortunately

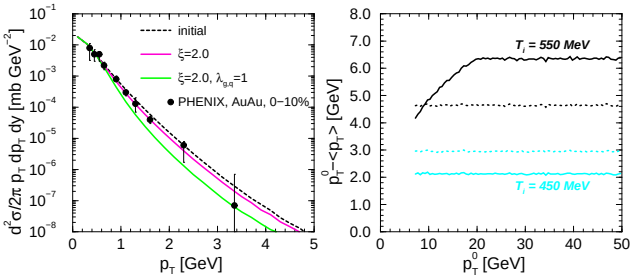

Figure 2: Left: Influence of partonic energy loss on single leptons from open charm at RHIC [5]. Right: Energy dependence of partonic energy loss [6].

the quality of data up to now does not allow any conclusive answer about the size of suppression.

Also the up to now used description of "high $p_\perp$" is insufficient, since interesting features of radiational energy loss (cf. Fig. 2) may occur at energies not covered by the experiments today [6] Higher energies, as planned for LHC, would offer the possibility to study all the effects mentioned above. In addition, ALICE measuring dileptons in the full azimuthal coverage and going higher than scales obtained by now is necessary to answer open questions about the properties of particles traversing a strong interacting zone and their fragmentation into hadrons

[1] K.Gallmeister, C.Greiner, Z.Xu, Phys. Rev. C67, 044905 (2003)

[2] W.Cassing, K.Gallmeister, C.Greiner, Nucl. Phys. A735, 277 (2004); K.Gallmeister, W.Cassing, Nucl. Phys. A748, 241 (2005)

[3] T.Falter, W.Cassing, K.Gallmeister, U.Mosel, Phys. Rev. C70, 054609, (2004).

[4] R.Thomas, K.Gallmeister, S.Zschocke, B.Kämpfer, hep-ph/0501202

[5] K.Gallmeister, B.Kämpfer, S.Zschocke, nucl-th/0410035

[6] K.Gallmeister, B.Kämpfer, O.Pavlenko, Phys. Rev. C66, 014908 (2002)

CHEM-SHE

Chemistry and Superheavy Element Research

On the production and chemical separation of Hs (element 108)

J. Dvorak[1], R. Krücken[1], F. Nebel[1], Z. Novackova[1], A. Türler[1], B. Wierczinski[1], A. Yakushev[1], W. Brüchle[2], E.Jäger[2], E. Schimpf[2], M. Schädel[2], A. Semchenkov[1,2], A. Kuznetsov[3], M. Chelnokov[3], A. Yeremin[3], Ch. E. Düllmann[4], Y. Nagame[5], K. Eberhardt[6], P. Thörle[6], R. Dressler[7], Z. Qin[2,8],M. Wegrzecki[9]

[1]TUM Garching; [2]GSI Darmstadt; [3]JINR Dubna; [4]LBNL Berkeley and UC Berkeley; [5]JAERI Tokai; [6]Universität Mainz; [7]PSI Villigen; [8]IMP Lanzhou, [9]ITE Warsaw

Chemical separation of Hs in the form of HsO_4 provides an excellent tool to study the formation reactions and nuclear structure of nuclei close to the deformed nuclear shells at Z=108 and N=162 due to a high overall efficiency and a very high purification factor. The first chemical identification of Hs as HsO_4 was performed by Düllmann et al. [1] at GSI in 2001. Seven decay chains were detected in a thermogradient detector and were attributed to the decay of ^{269}Hs and ^{270}Hs. Deposition temperatures of -44 ± 6^{o}C and -82 ± 7^{o}C and adsorption enthalpies of -46 ± 2 kJ/mol and -39 ± 1 kJ/mol were reported for HsO_4 and OsO_4, respectively.

Here we report on preliminary results of a recent Hs chemistry experiment performed at the GSI Darmstadt in December 2004. A rotating ^{248}Cm target wheel consisting of three arc-shaped segments with a target thickness of 788, 743 and 244 μg/cm^2 on 15-μm Be backing foils was irradiated with $^{26}Mg^{5+}$ ions to produce Hs isotopes. The third segment contained 2 % in weight of ^{152}Gd (30% enrichment) for the simultaneous production of α-decaying Os isotopes. A total beam integral of 3.48×10^{18} ^{26}Mg particles was accumulated during 12 days: 1.46×10^{18} at E_{lab} = 145 MeV and 2.02×10^{18} at E_{lab} = 135 MeV in the middle of the target. The experimental setup (Fig. 1) was similar to the one described in [1]. Recoil products were thermalized in a He/O_2 (10% of O_2) gas mixture in a recoil chamber heated to 400°C. The chemical reaction was completed at 650-700°C in a quartz column directly connected to the exit of the recoil chamber. Volatile Hs and Os tetroxides were formed and transported with the gas flow at room temperature to a detector setup. Two different gas flow rates of 1.8 l/min and 1.5 l/min were applied. The transport time through a Teflon™ capillary, 8 m in length, with an inner diameter of 2 mm was less than 2 s. The new detection system COMPACT (Cryo On-line Multidetector for Physics And Chemistry of Transactinides) was used. A temperature gradient from +20°C to -142°C was established along the detector channel which consisted of 2×32 single PIPS detectors (1×1 cm^2 in size). The distance between top and bottom arrays was 0.6 mm. The active detector surface covered 70% of the inner surface of the detector assembly The overall efficiency of the experimental apparatus was about 50%. Decay chains detected in the 145-MeV run are presented in [2].

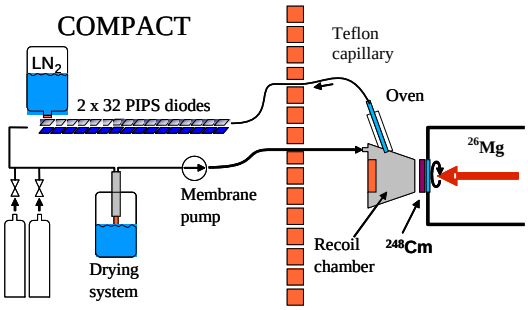

Fig. 1. Schematic of the experimental setup.

Figure 2 depicts the distribution of α-events with E_α = 4-5.1 MeV attributed to ^{172,173}Os along the detector as measured in the 145-MeV run. Seven events attributed to Hs isotopes are added to this plot (Fig. 2). The data are still being evaluated.

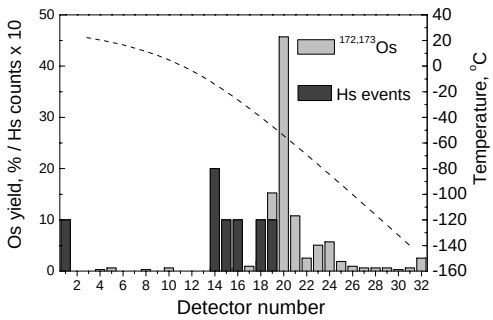

Fig. 2. Distribution of ^{172,173}Os and Hs isotopes in COMPACT.

References

[1] Ch.E. Düllmann et al., Nature **418**, 859 (2002).
[2] J. Dvorak et al., this Scientific Report, p.

Theoretical Investigations of the Reactivity of MO_4 and the Electronic Structure of $Na_2[MO_4(OH)_2]$, where M = Ru, Os, and Hs (element 108)

V. Pershina* and J. V. Kratz**
*GSI, Darmstadt
**Institut für Kernchemie, Universität Mainz

Recent experiments on the chemical identification of element 108, Hs, have delivered straightforward evidence that it belongs to group 8 of the Periodic Table [1]. In the presence of oxygen, Hs formed HsO_4 which was deposited in a gas-phase chromatography column at a temperature somewhat higher than that of OsO_4, thus confirming its chemical similarity with the latter and the high volatility. In more recent experiments [2] with volatile tetroxides, HsO_4 was shown to react with moisturized NaOH forming very probably the sodium hassate (VIII), $Na_2[HsO_4(OH)_2]$, by analogy with $Na_2[OsO_4(OH)_2]$ according to the reaction

$$2\ NaOH + HsO_4 \rightarrow Na_2[HsO_4(OH)_2]. \qquad (1)$$

In the present work, we study the reactivity of RuO_4, OsO_4, and HsO_4 with NaOH on the basis of results of the fully relativistic calculations for the components of the reaction of type (1) using the 4-component Density-Functional Theory method [3]. A model [4] was used to determine the free energy change ΔG^r of a reaction via changes in the ionic (ΔE^C) and covalent (ΔE^{OP}) contributions to the total binding energy. The latter are calculated using Mulliken effective charges Q_M and overlap populations, OP. It was shown that relative values of ΔG^r could be reliably predicted via the ΔE^C. The bond lengths (R_e) of the Os complex were taken from the experiment [5], and those of the Ru and Hs complexes were estimated using R_e for RuO_4 and HsO_4 with respect to $R_e(OsO_4)$ [6].

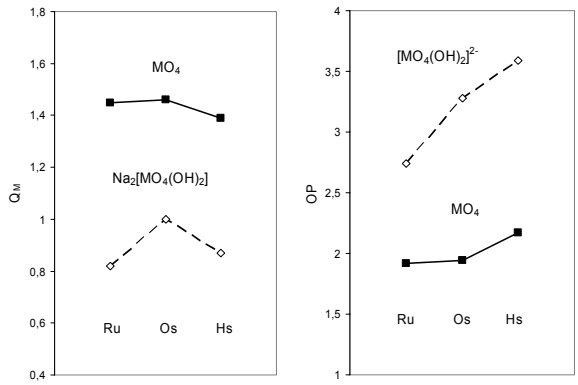

Fig. 1. Effective metal charges, Q_M, and overlap populations, OP, in MO_4 [6] and $[MO_4(OH)_2]^{2-}$ [this work] (M = Ru, Os, and Hs).

The values of Q_M and OP obtained for $[MO_4(OH)_2]^2$ and MO_4 are depicted in Fig. 1. They show $[HsO_4(OH)_2]^{2-}$ to be more covalent than the Os homolog, similarly to MO_4. Both Q_M and OP in $[RuO_4(OH)_2]^{2-}$ are significantly smaller than Q_M and OP of the Os and Hs anions, which is indicative for the fact that the Ru anion is not stable due to the weak ionic and covalent constituents of the bond strength. This is not the case with MO_4, where Q_M and OP of RuO_4 are very similar to those of OsO_4 (Fig. 1).

Table 1. Coulomb binding energies, E^C, for complexes of Ru, Os, and Hs and their differences, ΔE^C (in eV), for reactions of the complex formation

Complex/reaction	Ru	Os	Hs	Ref.
E^C: MO_4	-13.74	-13.86	-12.04	6
E^C: $[MO_4(OH)_2]^{2-}$	-3.58	-7.64	-5.26	this
E^C: $Na_2[MO_4(OH)_2]$	-5.70	-8.77	-6.41	this
ΔE^C: MO_4 ⇔ $[MO_4(OH)_2]^{2-}$	10.16	6.23	6.78	this
ΔE^C: MO_4 ⇔ $Na_2[MO_4(OH)_2]$	8.04	5.09	5.63	this

The obtained E^C for the species and ΔE^C for the complex formation reactions are given in Table 1. The values are similar for reactions of HsO_4 and OsO_4: HsO_4 should be slightly less reactive than OsO_4. We can give the upper limit of the difference in ΔG^r between HsO_4 and OsO_4 of 52 kJ/mol defined by the difference in their ΔE^C. (The slightly larger $\Delta OP=1.42$ for the Hs reaction than $\Delta OP=1.34$ for the Os reaction should slightly decrease this value). The values of ΔE^C for the reactions of RuO_4 are about 300 kJ/mol more positive than ΔE^C of the OsO_4 and HsO_4 reactions. The reason for that is the too low stability of the Ru complex anion manifested in its low E^C (low Q_M) and low E^{OP} (low OP) (Fig. 1). Thus, the so much more positive ΔG^r of the complex formation reaction of Ru compared to those of Os and Hs explains why $[RuO_4(OH)_2]^{2-}$ is not known. Finally, on the basis of these calculations, we predict the following trend for the formation of $[MO_4(OH)_2]^{2-}$, or $Na_2[MO_4(OH)_2]$ in group 8:

$$Os > Hs >> Ru.$$

The predicted slightly lower reactivity of HsO_4 as compared to that of OsO_4 has so far not clearly been revealed experimentally [2].

References

[1] C. Düllmann *et al.* Nature (Letters) **418**, 859 (2002).
[2] A. von Zweidorf, *et al*. A. Radiochim. Acta **92**, 855 (2004).
[3] S. Varga *et al*. Phys. Rev. A **59**, 4288 (1999).
[4] V. Pershina, Radiochim. Acta **92**, 455 (2004).
[5] N. N. Nevskii, *et al*. Dokl. Akad. Nauk. **266**, 628 (1982).
[6] V. Pershina, *et al.* J. Chem. Phys. **115**, 792 (2001).

Relativistic Effects on Volatility of Element 112

V. Pershina,[*] T. Bastug,[**] B. Fricke,[***] C. Sarpe-Tudoran,[***] J. Anton[***]
[*]GSI, Darmstadt
[**] School of Physics, University of Sydney, Australia
[***] Theoretische Physik, Universität Kassel

Investigation of influence of relativistic (rel.) effects on properties of the heaviest elements, especially on volatility of element 112, is one of the most fundamental and interesting tasks. Volatility is usually measured as the adsorption temperature, T_{ads}, in a chromatography column from which the adsorption enthalpy, ΔH_{ads}, is deduced. The only way to "detect" rel. effects is to compare measurements with rel. *vs.* nonrelativistic (nr.) predictions. The aim of the present study is to show the influence of rel. effects on volatility of element 112 in comparison with that of Hg as adsorption on inert and metal surfaces.

Adsorption on inert surfaces. For adsorption on inert surfaces (a quartz column, or a metal column covered with ice), a trend in volatility of the group-12 elements could be predicted using the following equation for the dispersion interaction energy [2]

$$E(x) = -\frac{3}{16}\left(\frac{\varepsilon-1}{\varepsilon+2}\right)\frac{\alpha_{at}}{\left(\frac{1}{IP_{slab}}+\frac{1}{IP_{at}}\right)x^3}, \quad (1)$$

where IP_{slab} is the ionization potential of the surface atom, ε is the dielectric constant of the surface (slab) substance and x is the interaction distance. Substituting calculated rel. and nr. values of α and IP of Hg and element 112 into eq. (1) gives results of Fig. 1.

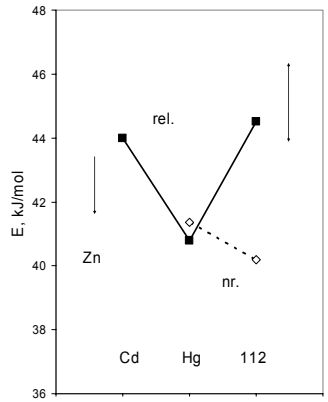

Fig. 1. Rel. and nr. dispersion interaction energies of the group-12 elements with quartz surface.

Thus, upon adsorption on an inert surface, element 112 will have the largest $E = -\Delta H_{ads}$ in group 12 and, hence, will be the least volatile. Non-relativistically, the trend is opposite.

Adsorption on metal surfaces. For the case of adsorption of element 112 and Hg on metal surfaces, e.g., Au(100), the influence of rel. effects on ΔH_{ads} could be different depending on the adsorption position – on-top, bridge or hollow – with respect to the surface atoms. In the on-top position, the main stereochemically active orbitals of Hg and element 112 are the ns and $np_{1/2}$, whose nr. and rel. R_{max} change in opposite ways in group 12. In the hollow position, the (n-1)d valence orbitals of these elements should be predominantly involved in bonding, whose rel. and nr. R_{max} change in the same way in the group. Present fully rel. and nr. 4c-DFT calculations for Hg and element 112 interacting with Au clusters of 14 and 9 atoms helped to elucidate this effect quantitatively. The results are summarized in Table 1 and Fig. 2.

Table 1. Rel. and nr. binding energies (D_e= -ΔH_{ads}, eV) and optimized bond lengths (R_e, a.u.) for M-Au_{14} in the on-top and for M-Au_9 in the hollow positions (M = Hg and element 112)

Case	top		hollow	
	R_e	D_e	R_e	D_e
		Hg-Au_{14}		Hg-Au_9
rel.	5.0	0.86	3.8	0.85
nr.	5.5	0.64	4.6	0.41
		112-Au_{14}		112-Au_9
rel.	5.2	0.71	4.2	0.79
nr.	5.8	0.70	4.9	0.52

Thus, upon adsorption on the Au (100) surface, element 112 will be more volatile than Hg. Rel. effects do not increase $-\Delta H_{ads}$ of element 112 when adsorbed in the on-top position, while for the hollow position, rel. effects strongly increase the interaction energy, so that, relativistically, element 112 will be less volatile than nonrelativistically. The rel. and nr. ΔH_{ads} show opposite trends from Hg to element 112.

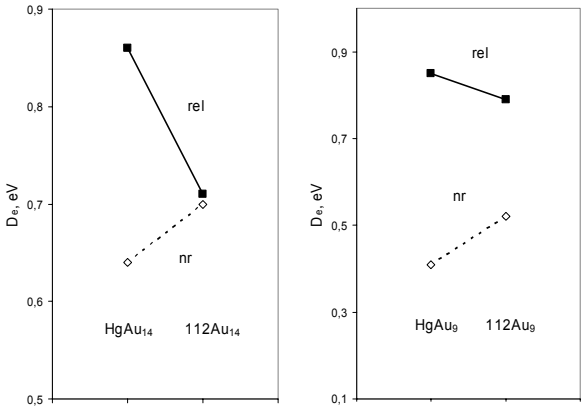

Fig. 2. Rel. and nr. binding energies (D_e, eV) for M-Au_{14} in the on-top position and for M-Au_9 in the hollow position (M = Hg and element 112).

Calculations of the adsorption energies of element 112 and its homolog Hg on the Au(100) surface with improved basis sets

C. Sarpe-Tudoran,* V. Pershina,** B. Fricke,* J. Anton*, W.-D. Sepp*
* Theoretische Physik, Universität Kassel
**GSI, Darmstadt

Within the framework of the theoretical study of the adsorption of element 112 and its homolog, Hg, on surfaces of transition-element metals [1-3], results of the improved calculations for ad-atom-gold cluster systems are reported here. The fully relativistic, 4-component Density Functional Theory (DFT) method [4] in its embedded cluster approximation was used for that purpose. For exchange-correlation effects, the Relativistic Local Density (RLDA) and General Gradient (BP88/P86), a higher level of theory, approximations were used. According to the embedding technique, the surface was simulated by a metal cluster embedded into an environment. This enables one to take effects of the environment explicitly into account and to achieve converged results with clusters of a moderate size.

In the calculations, inner clusters Au_m of m=14, 16, 22 and 29 atoms embedded in outer clusters of 112, 110, 92 and 156 atoms, respectively, were used to simulate the Au(100) surface. Hg and element 112 were considered in the on-top, bridge and hollow adsorption positions with respect to the surface atoms. The calculations were performed with two types of basis set: the set of type B includes the filled 1s through ns orbitals and virtual np and (n-1)f orbitals, while a more extended basis set of type B' includes the virtual nd, (n-2)g and nf orbitals in addition to those of the basis set B. Binding (adsorption) energies E_b of Hg and element 112 with clusters of various size and the different adsorption positions, calculated with the basis sets B and B', are shown in Fig. 1 and Table 1 (for the basis set B').

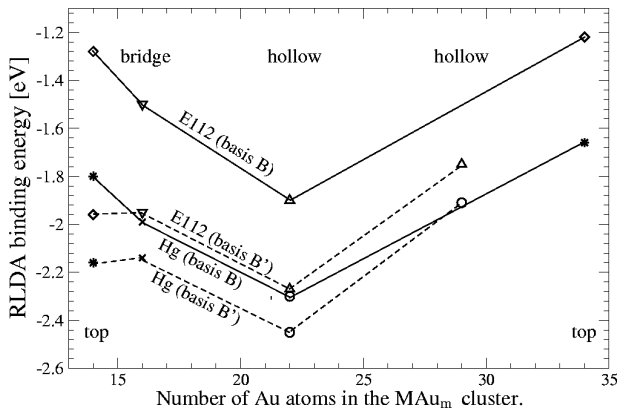

Fig. 1. The RLDA binding energies of element 112 and Hg with Au_m calculated for the basis set of types B and B'.

The results show that using the basis set B' improves E_b. Thus, E_b(B88/P86) for Hg in the preferential hollow position approaches the experimentally measured ΔH_{ads} = 101 kJ/mol (1.04 eV) [5].

Table 1. The RLDA and GGA(B88/P86) binding energies E_b and bond lengths r of Hg and element 112 with Au_m calculated for the basis set of type B'

m posit.	Approx.	$HgAu_m$		$112Au_m$	
		E_b, eV	r, a.u.	E_b, eV	r, a.u.
14 top	RLDA	2.16	4.82	1.96	5.10
	B88/P86	1.64	4.97	1.47	5.32
16 bridge	RLDA	2.14	4.30	1.95	4.50
	B88/P86	1.26	4.30	1.07	4.50
22 hollow	RLDA	2.45	3.50	2.27	3.80
29 hollow	RLDA	1.91	3.51	1.75	3.80
	B88/P86	0.86	4.11	0.72	4.37

The difference in the binding energies between Hg and element 112, E_b^{Hg}-E_b^{112}, stays almost the same for the basis set of type B or B', independently of m and the adsorption position (Fig. 2). Using the extended basis set B' instead of B brings this difference from ~0.4 eV down to 0.15 eV. A slight decrease in ΔE_b is also observed with increasing m.

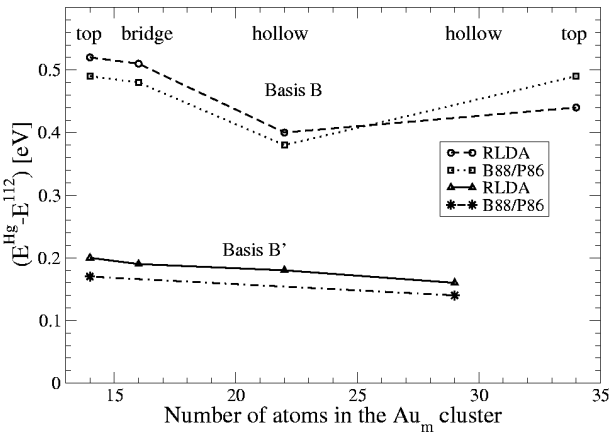

Fig. 2. The difference in the binding energies, E_b^{Hg}-E_b^{112}, between Hg and element 112 interacting with Au_m.

Thus, results of these calculations with the more extended basis set show that element 112 should be about 0.15 eV (15 kJ/mol) weaker adsorbed on the (100) Au surface than Hg, in agreement with our earlier conclusions made on the basis of the calculations for the Hg and 112 dimers [1,2].

References

[1] V. Pershina *et al*. *Chem. Phys. Lett*., **365**, 176 (2002).
[2] V. Pershina, *et al*. *Nucl. Phys*. A **734**, 200 (2004).
[3] C. Sarpe-Tudoran, Doctoral Thesis, Kassel, 2004.
[4] T. Jacob, *et al*. *Surf. Sci.* **536**, 45 (2003).
[5] J.-P. Niklaus, *et al.* PSI Annual Report 2002, p. 8.

Relativistic Density Functional Calculations for (E114)X and PbX, where X = O, Pd, Pt, Au

C. Sarpe-Tudoran*, V. Pershina**, B. Fricke*, J. Anton*, and W.-D. Sepp*

* Universität Kassel, D-34109 Kassel; **Gesellschaft für Schwerionenforschung, D-64291 Darmstadt

The production of element $^{290}114$ with the half-life of 21 s [1] was reported by JINR, Dubna, Russia. Presently, chemical experiments are planned at GSI to prove the existence of E114 by its deposition on surfaces of transition-element metals. Element 114 is a closed-shell atom with an electronic configuration $7s^2 7p_{1/2}^2$. Due to the relativistic stabilization of the $7s$ and the $7p_{1/2}$ orbitals and the closed shell it is expected to be very inert. By now, only few calculations were done for element 114 and its compounds [2–6]. In the present work we consider some diatomic systems, with metal-metal ones serving as models for future cluster calculations.

In order to describe the molecular systems we use the 4-component non-collinear RDFT, in which the ground state energy is a unique functional of both electronic $[\rho]$ and magnetization density $[\vec{m}]$. The total energy of a molecular system is:

$$E = \sum_{i=1}^{M} n_i \left\langle \psi_i \right| \hat{t} \left| \psi_i \right\rangle + \int V^N \rho \, d^3\vec{r} + \frac{1}{2} \int V^H \rho \, d^3\vec{r} + E^{xc}[\rho, \vec{m}] + \sum_{p>q} \frac{Z_p \, Z_q}{|\vec{R}_p - \vec{R}_q|} \, .$$

Details of the method are given by Anton *et al.* [5].

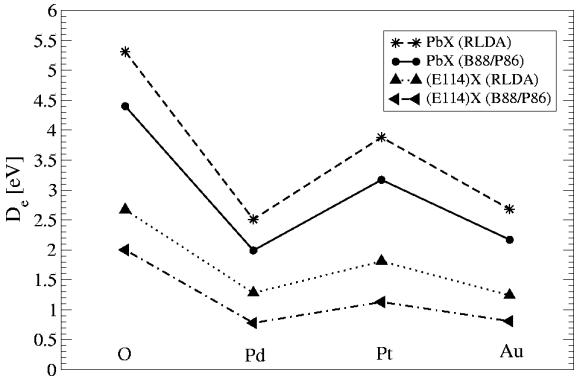

Figure 1: Dissociation energies for PbX and (E114)X, where X=O, Pd, Pt and Au.

Results of the calculations for PbX and (E114)X, where X = O, Pd, Pt and Au, as well as for Pb_2 and $(E114)_2$ are shown in Table 1. The obtained values for D_e, r and ω are in agreement with those obtained by Liu *et al.* for M_2 and MO [3]. By comparing with the experiment, one should keep in mind that spectroscopic constants are dependent on the experimental method. Thus, generally, agreement with experiment is quite satisfactory. The binding energies for the E114 compounds are all smaller than for the Pb compounds, showing that, indeed, element 114 is more inert than Pb. As the trend, $D_e^{MO} > D_e^{MPt} > D_e^{MAu} > D_e^{MPd}$ is predicted, where M = Pb and element 114. The bond lengths, r, increase from the Pb to E114 compounds.

Table 1: Binding energies (D_e), bond lengths (r) and vibrational frequencies (ω) for the PbX and (E114)X dimers, where X=O, Pd, Pt and Au.

		$D_e[eV]$	$r[a.u.]$	$\omega[cm^{-1}]$
Pb_2	RLDA	1.53	5.48	121.11
	B88/P86	1.16	5.62	108.58
	Exp. [6]	0.88	5.53	110.09
PbO	RLDA	5.31	3.62	747.08
	B88/P86	4.40	3.66	721.50
	Exp. [7]	3.87	3.63	721.00
PbPd	RLDA	2.50	4.62	222.61
	B88/P86	1.93	4.73	201.77
PbPt	RLDA	3.88	4.55	229.56
	B88/P86	3.17	4.63	213.49
PbAu	RLDA	2.68	4.88	167.17
	B88/P86	2.17	4.99	152.73
$(E114)_2$	RLDA	0.37	6.12	41.75
	B88/P86	0.13	6.60	25.85
(E114)O	RLDA	2.67	3.82	591.04
	B88/P86	2.00	3.89	536.34
(E114)Pd	RLDA	1.28	4.88	168.88
	B88/P86	0.78	5.07	137.82
(E114)Pt	RLDA	1.81	4.72	181.57
	B88/P86	1.13	4.83	157.37
(E114)Au	RLDA	1.24	5.17	116.44
	B88/P86	0.81	5.38	96.70

References

[1] Yu. Ts. Oganessian et al., *Phys. Rev. Lett.*, **83**, 3154, (1999); S. Hofmann, *et al.*, *Nucl. Phys. News*, **14**, 5-13, (2004).

[2] P. Schwerdtfeger, M. Seth, *J. Nucl. Radiochim. Sci.*, **3-1**, 133-136, (2002).

[3] W. Liu, C. van Wüllen, Y. K. Hahn, Y. J. Chi, and Y. S. Lee, *Adv. Quant. Chem.* **39**, 325 (2001).

[4] K. Balasubramanian, *J. Chem. Phys.*, **117**, 7426, (2002).

[5] J. Anton *et al.*, *Chem.Phys.*, in press.

[6] M. Heaven, T. Miller, V. E. Bondybey, *J. Phys. Chem.*, **87**, 2072-2075, (1983).

[7] K. P. Huber and G. Herzberg, *Molecular spectra and molecular structure* (Van Nostrand Reinhold, New York, 1979),Vol. 4.

The electrochemical deposition of Hg on various metal electrodes

H. Hummrich, F. Feist, J.V. Kratz

Institut für Kernchemie, Johannes Gutenberg-Universität Mainz, Germany

Recently, attempts were undertaken to chemically characterize element 112 in gas phase experiments [1].

A different approach involves experiments in the liquid phase. If we assume that element 112 is a noble metal (like its homolog Hg), a separation by electrochemical deposition on a metal electrode should be possible. Furthermore, this would result in an ideal sample for α-spectrometry.

In our experiments, we investigated the electrochemical deposition of Hg on various metal electrodes. A solution of $Hg(NO_3)_2$ in 0.1M HNO_3 was irradiated at the TRIGA reactor of the Mainz for 6h at a neutron flux of $7 \cdot 10^{11}$ n/s·cm² . The isotope ^{197g}Hg with a half live of 64,1h was produced with a specific activity of 70 kBq/mg, and its γ-line at 77 keV was evaluated in the experiments.

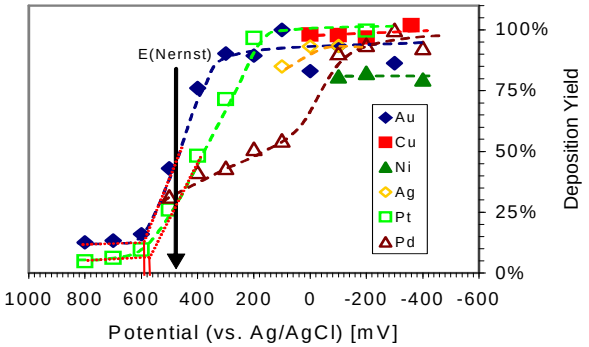

Fig.1: Electrodeposition yield vs. electrode potential for the deposition of ^{197g}Hg on various metal electrodes. In the experiments with Ag, Au, and Cu, 0.1M HNO_3 and with Pt, Pd, and Ni, 0.1M HCl was used as electrolyte

A heatable electrolysis cell with two working electrodes (total area 2 cm²), a Pt counter electrode and a Ag/AgCl reference electrode was used. The electrolyte volume of 1-2 ml was stirred with a high volume magnetic stirrer at 1000-1400 rpm. The total Hg concentration in each experiment was $5 \cdot 10^{-6}$ mol/l. This was low enough, so that the deposition still took place in the sub-monolayer region. 0.1 M HCl and 0.1 M HNO_3 were used as the electrolyte. The electrolysis time was 10 min. This should result in the maximum possible deposition for the given potential.

The electrodeposition yield was measured vs. the electrode potential (Fig. 1). The experiments, in which Ag, Cu, and Ni electrodes were used, were started at the potential that occured when the electrode is immersed into the solution (rest potential). At the rest potential, no current is applied. An increase of the potential beyond this rest potential would lead to a dissolution of the electrodes. For the deposition of Hg on Pt and Au, a critical potential at which a significant deposition starts, was deduced. For Pd, no well defined critical potential was found. For Cu, Ni, and Ag, the deposition is already nearly complete at the rest potential (spontaneous deposition).

In table 1, the critical potentials are compared with $E_{50\%}$-values, which were calculated with a microscopic-macroscopic model proposed by Eichler and Kratz [2] using thermodynamic properties of Hg and of the electrode material.

Table 1: Critical potentials for the deposition of Hg on various metal electrodes compared with theroetically predicted $E_{50\%}$ -values (all potentials vs. Ag/AgCl)

Electrode	E_{crit} [mV]	$E_{50\%}$ calc.
Au	+ 600	+ 710
Ni	> +50	+ 660
Ag	> +100	+ 620
Cu	> -100	+ 630
Pt	+ 580	+ 970
Pd	-	+ 1140

The electrodeposition speed was investigated for the deposition on Pd (20° and 80°) and Cu electrodes. Fig. 2 shows the decrease in activity vs. the electrolysis time. The $t_{50\%}$ - value is the time at which 50% of the activity is deposited. The electrodeposition seems to be faster on Cu electrodes than on Pd electrodes at room temperature. An increase in temperature lead to an increase in electrodeposition speed, in analogy to previous experiments with Pb [3].

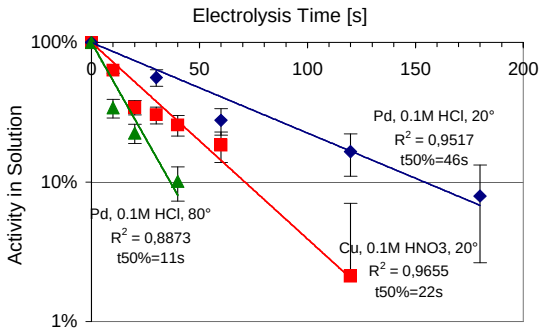

Fig.2: Electrodeposition speed vs. electrolysis time for the deposition of ^{197g}Hg on Pd and Cu. Electrolytic systems: Pd / 0.1M HCl / 20° / -500mV; Cu / 0.1M HNO_3 / 20° / -300mV; Pd / 0.1M HCl / 80° / -500mV

The obtained results will be taken into account in a beam time at GSI, where carrier-free Hg isotopes are produced via the reaction of ^{40}Ar with Sm. The transport of Hg with a KCl gas jet, the transfer into the liquid phase with the ALOHA system [4] and a subsequent electrodeposition will be investigated.

References

[1] S. Soverna et al, GSI, *Scientific Report 2003*, p. 187

[2] B. Eichler, J.V. Kratz, Radiochimica Acta **88,** 475 (2000)

[3] H. Hummrich et al., GSI, *Scientific Report 2003*, p. 199

[4] H. Hummrich et al, *this report*

Separation of ^{211}Pb with ALOHA and subsequent electrochemical deposition

H. Hummrich , F. Feist, D. Liebe, J.V. Kratz

Institut für Kernchemie, Johannes Gutenberg-Universität Mainz, Germany

To achieve a fast and (quasi)-continuous transfer of recoil atoms from the recoil chamber into the liquid phase, the ALOHA system was constructed and successfully used in chromatography experiments [1].

To prepare liquid phase experiments with element 114, the separation of its homolog Pb with ALOHA and its subsequent electrochemical deposition was investigated. A ^{219}Rn-emanating source was prepared by co-precipitation of ^{227}Ac with $Fe(OH)_3$. The source was placed in a 300 ml glass chamber where the 3,96s ^{219}Rn was allowed to decay. The daughter nuclides ^{211}Pb and ^{211}Bi were attached to KCl-clusters and transferred with a He flow of 2 l/min to ALOHA and deposited by impaction on a Ta disc. After impaction, the activity was stepped to the dissolution position and transferred to the electrolytic cell by continuously cyclic pumping of the electrolyte (0.1M HCl) with a low dead-volume HPLC pump. Fig. 1 shows the experimental set-up.

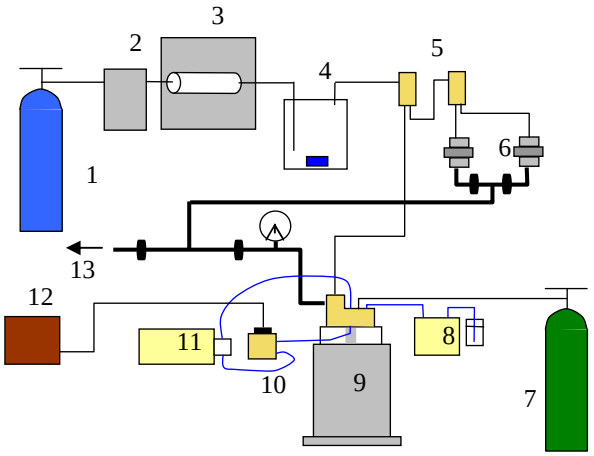

Fig.1: Experimental set-up. 1 Helium, 2 mass-flow-controller, 3 KCl cluster oven, 4 ^{227}Ac emanating source, 5 gas-jet switches, 6 direct catch and waste unit, 7 Nitrogen, 8 Acetone pump, 9 ALOHA, 10 electrodeposition cell, 11 electrolyte pump, 12 potentiostat, 13 to the ventilation sysem. Gas jet flow: black line, vacuum system: thick black line, liquid flow: blue line

The yield of impaction and dissolution in ALOHA (compared to a direct catch on a glassfiber filter) was measured via γ-spectrometry at different stepping times. Fig.2 shows that about 75 to 90% of the activity was successfully transferred from the gas-jet into the liquid phase using stepping times of 5s and longer. At lower stepping times, activity is lost due to the low dissolution volume.

For electrodeposition experiments with ^{211}Pb, a heatable electrolytic cell was attached to the ALOHA system. Pd was chosen as electrode material, 0.1M HCl as electrolyte. The deposition potential was –500 mV vs. Ag/AgCl.

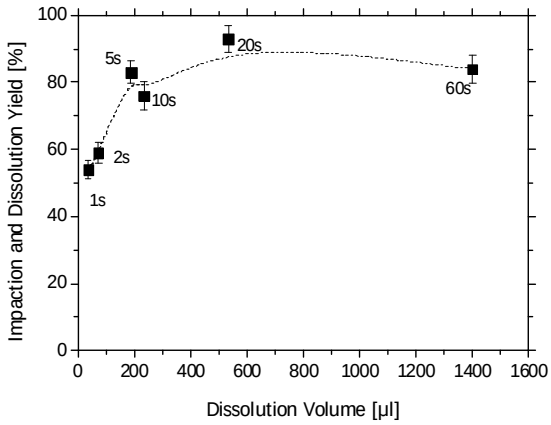

Fig.2: Impaction and dissolution yield for ^{211}Pb/^{211}Bi vs. dissolution volume (stepping time) with the ALOHA system, solvent 0.1M HCl

The activity was impacted for 10 min in the collection position, transferred to the dissolution position and dissolved. The deposition experiments were carried out at a temperature of ca. 75° and under vigorous stirring. At $t_{50\%}$=20s, 50% of the activity was deposited, as can be seen in Fig.3.

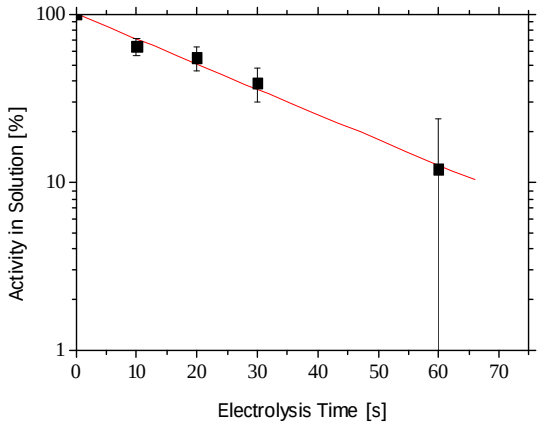

Fig 3: Electrodeposition of ^{211}Pb on Pd electrodes from 0.1M HCl at –500mV vs. electrolysis time.

The deposited activity could also be measured via α-spectrometry after the radioactive equilibrium between ^{211}Pb and ^{211}Bi was reached. Here, a 0.1 µm polycarbonate filter was used for the direct catch. In both cases, a FWHM of 60 keV for the 6,2 MeV line of ^{211}Bi was achieved

The presented system will be tested in a beam time at GSI with short lived Pb-isotopes in the reaction ^{40}Ar on Gd.

References

[1] A. Kronenberg et al., Annual Report, Institut für Kernchemie, Universität Mainz 2001, A4

Development of a separation scheme to search for ^{239}Cm
Part I: The overall separation scheme

Z. Qin[1,2], W. Brüchle[1], E. Jäger[1], D. Nayak[1,3], E. Schimpf[1], B. Schausten[1], M. Schädel[1]
[1]GSI, Darmstadt, Germany, [2]Institute of Modern Physics, Chinese Academy of Science, Lanzhou, P.R. China,
[3]Saha Institute of Nuclear Physics, Kolkata, India

As radiochemical techniques have an unsurpassed sensitivity, they are best apt to search for, to identify and to determine very small α-decay branches of longer-lived transuranium nuclides. Therefore, we have developed a chemical separation scheme to search for the "missing" α-decay branch in ^{239}Cm ($T_{1/2} \approx 3$h). Details of the motivation for this experiment and preliminary results from the first experiments are given elsewhere in this report [1].

We decided to use Cu foils of 3.9 µm thickness, prepared by the GSI target laboratory, as a catcher material for ^{239}Cm. These Cu foils are thick enough to provide good mechanical stability and to catch all recoiling ^{239}Cm from the ^{232}Th (^{12}C, 5n) reaction. But they are thin enough to let large amounts of unwanted species, like the light fission products, pass through and to minimize the energy loss and heating from the passage of the ^{12}C beam. Cu also provides numerous advantages for the start of our chemistry to separate and prepare a clean Cm sample for a sensitive search for a very small α-branch.

Radiotracers of ^{153}Gd, ^{170}Tm, ^{153}Sm, ^{149,151}Pm and ^{147}Nd were obtained by irradiation of lanthanide (Ln) oxides or nitrates at the Mainz TRIGA reactor (thermal neutron flux ~ 10^{12} n cm^2/ s). They were used to develop the chemical separation scheme for actinides (An) consisting of a liquid-liquid extraction, a precipitation and a liquid chromatography (see Fig. 1), and to determine chemical yields.

The Cu catcher (≈ 20 mg Cu) was dissolved in 6 M HCl adding 2 drops of H_2O_2. To remove major activities produced in nuclear reactions with the Cu catcher, Ga and Ge were extracted quantitatively with 2,6-Dimethyl-4-heptanone. After adding 1 mg of La carrier Ln^{3+} and An^{3+} were precipitated with conc. NH_4OH while Cu remained in solution. The precipitate was dissolved in 500µl of 0.4 M HNO_3 which was fed into the sample loop of the liquid chromatography column. Details of the chromatographic separation of a Cm fraction, modeled with Nd, Pm, Sm and Gd tracer, can be found in Part II of this contribution.

The separated Cm fraction (Sm-Pm-fraction in Fig. 1) was rapidly evaporated on a Ta disk, which was heated from below by a hot plate. In addition, flowing hot He gas and an intensive IR-lamp were applied. This sample was suitable for α-particle pulse-height analysis to search for the α-decay of ^{239}Cm.

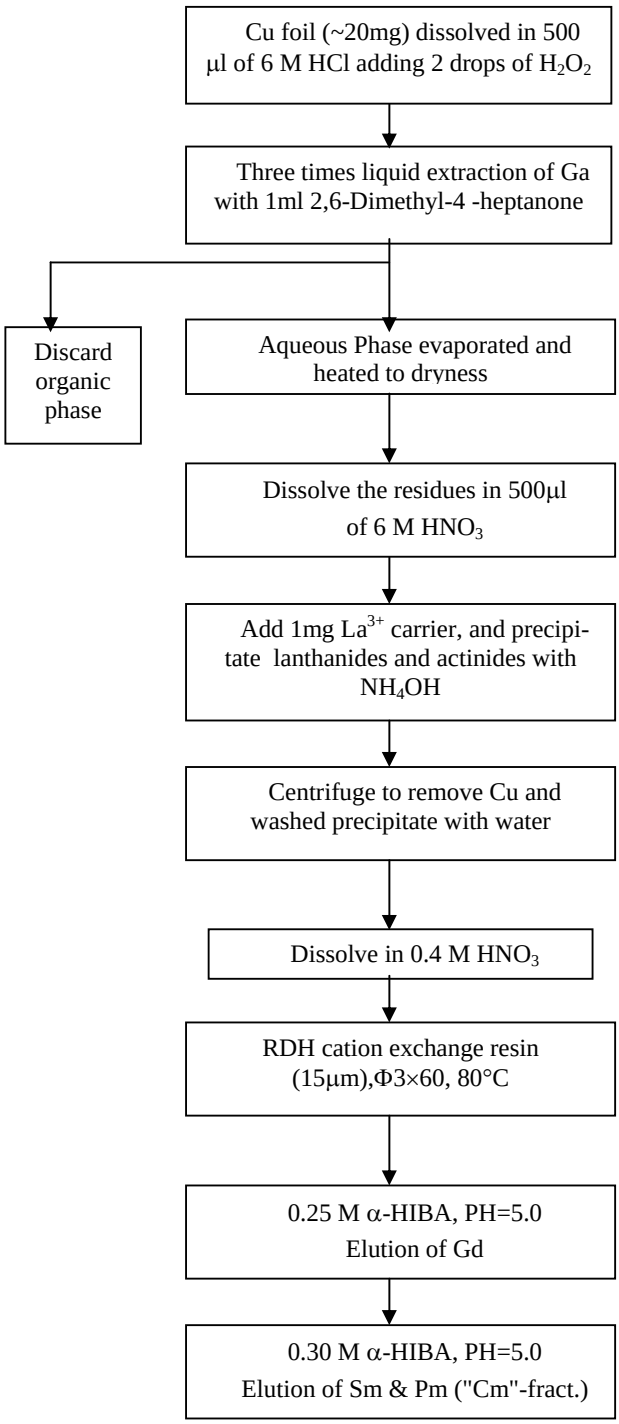

Fig. 1: The radiochemical separation procedure of a Cm fraction (Sm-Pm) from a Cu catcher foil.

Reference

[1] Z. Qin et al., GSI Scientific Report 2004.

Development of a separation scheme to search for ^{239}Cm
Part II: The Cm separation modeled with lanthanide radiotracers

Z. Qin[1,2], W. Brüchle[1], E. Jäger[1], D. Nayak[1,3], E. Schimpf[1], B. Schausten[1], M. Schädel[1]
[1]GSI, Darmstadt, Germany, [2]Institute of Modern Physics, Chinese Academy of Science, Lanzhou, P.R. China,
[3]Saha Institute of Nuclear Physics, Kolkata, India

The overall separation scheme to obtain a chemically purified Cm sample for the search of an α-decay branch in ^{239}Cm (see [1] for preliminary results) is described in Part I of this contribution. This Part II describes details of the liquid chromatographic separation of a Cm fraction – modeled with lanthanide (Ln) tracers. The main goal of the scheme was to produce fast, reliably and with a high and controllable yield Cm fractions which are free from unwanted α-activities. This separation scheme was not optimized to separate elements which may strongly interfere in γ-spectroscopic studies.

One of the best known and most frequently applied separations of actinides (An) from each other is performed on cation exchange resin (CIX) utilizing differences in the complex formation of An^{3+} (Ln^{3+}) ions with (buffered) ammonium α-hydroxyisobutyrate (α-HIB) [2-4]. In comparative studies of the Ln and An separation [4] usually the elution position of Cm is taken as a reference and is normalized to 1. Elution positions for all other elements are, for a given system, given relative to Cm. For elutions with α-HIB from the CIX Dowex 50x12 at 87^{0}C literature [4] values for the trivalent actinides Bk, Cm and Am are 0.45, 1.0 and 1.4. As the trivalent lanthanides Gd, Eu, Sm, Pm, and Nd elute at position 0.28, 0.39, 0.71, 1.2, and 2.1 they are ideal tracers not only to develop but also to monitor a Cm separation.

Our separation was performed by High Performance Liquid Chromatography (HPLC). The HPLC set-up consisted of six chemical inert pumps that pumped various solutions through tubing (i.d. 0.3 mm) to the chromatography column. Pneumatic slider valves, controlled by a PC computer, were used to direct the flow of conditioning solutions to the column, to load the sample solution onto the column, and to apply the eluents for the separation. In test experiments, see Fig. 1, five drops per fraction were collected and were assayed for γ-ray activity with a shielded HPGe detector.

A water-jacketed chromatographic column (3 mm i.d., 60 mm long) was packed with a 15 µm particle size CIX (8% cross-linked from Riedel-de Haen, Seelze-Hannover) and was heated to 80^{0}C. The hydroxide precipitation of Ln and An (see Part I) was dissolved in 500 µL 0.4 M HNO_3, transferred into a sample loop and loaded onto the column. With a flow rate of 0.3 mL/min, used throughout the experiment, all lanthanides and actinides were strongly adsorbed on top of the column after 2 min. Thereafter, for conditioning, the column was washed (i) with water for 6 min (1.8 mL), (ii) with 0.5 M NH_4NO_3 (pH = 5) for 15 min (4.5 mL) to convert the resin into the NH_4^+ form, and (iii) with water again for 6 min (1.8 mL). Subsequently, the mobile phase was changed to 0.25 M α-HIB at pH=5 to clean the column from unwanted species before starting the Cm elution. A typical behavior of Tm and Gd in test separations is shown in Fig. 1. From the elution position of the ^{170}Tm tracer (K_d = 0.026) a column dead volume of 20 drops (0.46 mL) was determined.

After 8 min (100 drops) - the major part of ^{153}Gd was eluted at that time - the mobile phase was changed to 0.3 M α-HIB at pH=5. Fig. 1 shows elution curves of ^{153}Sm, ^{151}Pm and ^{147}Nd tracers from test experiments. Curium is expected to peak at about drop number 160. Cm fractions (80 drops) were collected starting from drop 120 (20 drops after changing to 0.3 M α-HIB). The overall chemical yield for Cm should be 70% or higher as determined from lanthanide tracers. It should be noted that no Cm-Am-separation was planned. The Cm fraction would contain relatively large amounts of Am if present. For sample preparation, the Cm fraction was evaporated to dryness (see Part I).

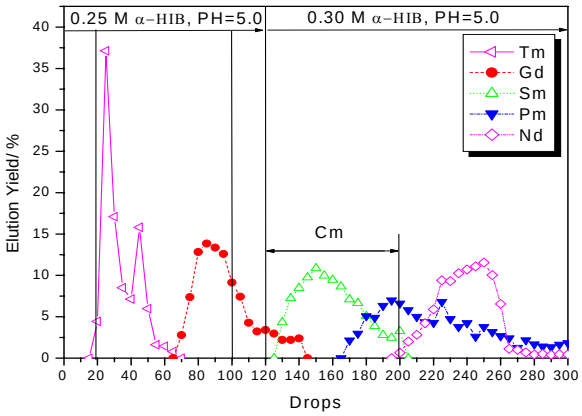

Figure 1. Elution curve of Gd, Tm, Sm, Pm, Nd with α-HIB.

After the Cm elution was finished, the column was stripped with 0.5 M α-HIB at pH=5 to remove the La^{3+} carrier, which was used for the precipitation described in Part I, from the resin. Subsequently, the column was regenerated by rinsing it with water and 0.4 M HNO_3 to prepare it for the next separation.

Reference

[1] Z. Qin et al., GSI Scientific Report 2004.

[2] G.R. Choppin et al., J. Inorg. Nucl. Chem. 2 (1956) 66.

[3] H.L. Smith and D.C. Hofmann J. Inorg. Nucl. Chem. 3 (1956) 243.

[4] G.H. Higgins, The Radiochemistry of the Transcurium Elements, U.S. National Academy of Science, Nuclear Science Series, NAS-NS-3031 (1960).

Approaches to estimate the ionic radius of hydrated Po^{2+}

K. Lyczko [1], A. Bilewicz[1], W. Brüchle [2], B. Schausten[2], and M. Schädel [2]

[1]Institute of Nuclear Chemistry and Technology, Warsaw, Poland; [2]GSI, Darmstadt, Germany

Due to the relativistic stabilisation of $6p_{1/2}$ electrons polonium – usually present in the 4+ oxidation state – can be reduced to the 2+ oxidation state. This cation has – outside it's filled $[Xe]4f^{14}5d^{10}$ electron shells - two electron pairs: $6s^2$ and $6p_{1/2}{}^2$. No information is available about the ionic radius of Po^{2+} and about it's coordination number of water molecules in aqueous solutions. The measurement of the ionic radius could be one first step towards a better understanding of the contribution of Po^{2+} electron orbitals to the chemical bonding.

The goal of our studies was to estimate the ionic radius of hydrated Po^{2+} from a comparison of the distribution coefficients (K_d) for Po^{2+} with K_d values of divalent metal cations of the second group of the Periodic Table (Ca^{2+}, Sr^{2+} and Ba^{2+}). This is based upon a well established linear correlation between reciprocal ionic radii (known for Ca^{2+}, Sr^{2+} and Ba^{2+}) and K_d values. This correlation is valid for ions with similar coordination numbers. K_d values can be obtained from the maxima of elution peaks in liquid-chromatography experiments. Earlier a cation exchange study of Po^{4+} in acid solutions ($HClO_4$, H_2SO_4, H_3PO_4, CH_3COOH and oxalic acid) has been reported [1].

We eluted polonium from the cation exchange resin Dowex 50W-X8, 200-400 mesh, with 3 M $HClO_4$ and 3.3 M CF_3SO_3H (triflic acid), both in SO_2 water solution. Perchloric acid and triflic acid were used because of their non-complexing properties for metal cations [2]. In order to reduce Po(IV) to Po(II) SO_2 was applied. It is commonly known that sulfur dioxide and hydrazine reduce polonium to oxidation state +2 in acidic solutions [3]. As we were using low-level radioactive tracer solutions of ^{210}Po the measurement of α-activity from these samples was mandatory. Therefore, we were only able to use SO_2 as a reducing agent. Using hydrazine was impossible due to white salt residues which appeared during the evaporation step for α-sample preparation.

The used radiotracers ^{47}Ca (40 Bq/mg) and ^{85}Sr (3.3 kBq/mg) were produced at the Mainz TRIGA reactor. While the Ca tracer had a very low specific activity, commercially available ^{133}Ba was carrier free. Tracer solutions were prepared by dissolving the irradiated oxides in perchloric acid and aliquots were loaded onto the column (46 mm length and 3.2 mm inner diameter). Elutions were performed at a rate of about 3.3 mL/min.

From the maxima of the elution position in 3M $HClO_4$ we determined K_d values of 2, 7 and 24 for $^{47}Ca^{2+}$, $^{85}Sr^{2+}$, and $^{133}Ba^{2+}$, respectively. The corresponding literature [4] values are 10.4, 13.4 and 25.1. Presumably, lower K_d values for Ca and Sr in comparison with values from [4] result from the use of relatively large amounts of carrier material in our experiment. It should also be noted here that our Ca and Sr elution curves were rather wide and exhibited considerable tailings. For the elution with 3.3 M CF_3SO_3H the K_d values were 11 for Sr and 37 for Ba.

Then we studied the behaviour of polonium during the elution using 3 M $HClO_4$ with and without SO_2. The elution curves for both solutions were similar. Peaks were very broad with maxima appearing only after 65-75 mL giving incomprehensibly large K_d values (~ 450-550). As an additional surprise, we measured a (too) large elution maximum of about 25 mL, corresponding to a K_d of ~ 150, with 3.3 M CF_3SO_3H in SO_2 water. One would not expect a large or any difference in the elution of Po^{2+} with 3.3 M CF_3SO_3H and 3 M $HClO_4$.

We interpret the large K_d values for polonium in both systems such that we were not able to reduce polonium effectively to the +2 oxidation state by SO_2. The observation of the different elution position in the two acids can possibly be explained by the oxidizing properties of $HClO_4$. In perchloric acid solution we most likely could not reduce Po(IV) to the lower oxidation states at all.

The next step in these experiments will be the application of hydrazine as a reductant when using γ-emitting ^{206}Po, or liquid scintillation counting to measure α-active ^{210}Po in solution.

References

[1] Ampelegova N. I., *Soviet Radiochem.* **17**, 52 (1974)

[2] Cotton F. A. et al., *Advanced Inorganic Chemistry*, 6-th Edition, J. Wiley & Sons (1999), Chapter 2

[3] Gmelin Handbook: *Po* Suppl. Vol. 1, part 11

[4] M.Marhol, *Ion Exchangers in Analytical Chemistry*, Czechoslovak Academy of Sciences, Prague (1981), p.493

APHYSEXP

Experimental Atomic Physics with Heavy Ions

SPECTROSCOPY AND ATOMIC PROPERTIES

ATOMIC COLLISION PROCESSES

DEVELOPMENTS

PHELIX

The nuclear charge radii of the radioactive lithium isotopes

R. Sánchez[1], D. Albers[2], J. Behr[2], P. Bricault[2], B. Bushaw[3], A. Dax[1], J. Dilling[2], M. Dombsky[2], G. Drake[4], G. Ewald[1], S. Götte[1], R. Kirchner[1], H.-J. Kluge[1], Th. Kühl[1], J. Lassen[2], C. D. P. Levi[2], W. Nörtershäuser[1,5], M. Pearson[2], E. Prime[2], V. Ryjkov[2], A. Wojtaszeck[1], Z.-C. Yan[6], and C. Zimmermann[5]

[1]GSI, Darmstadt; [2]TRIUMF, Vancouver BC, Canada; [3]PNNL, Richland, USA; [4]Univ. Windsor, Canada; [5]Univ. Tübingen; [6]Univ. New Brunswick, Canada

^{11}Li exhibits a large nuclear matter radius in comparison to other lithium isotopes. The discovery of this exciting phenomenon [1] started many investigations and soon the picture of two loosely bound neutrons orbiting a core of ^{9}Li was established. The two neutrons form a long tail in the matter distribution, which these days is known as a "halo". Not only ^{11}Li shows this intriguing behavior; many other short-lived and neutron rich isotopes, especially those close to the neutron drip line, form halo nuclei.

Important information about the interaction between the neutrons and the core protons can be obtained from the nuclear charge radius. We have performed isotope shift measurements of an electronic transition of all accessible lithium isotopes to determine the root mean square (rms) nuclear charge radii in a model-independent manner. The isotope shift (IS) can be expressed as the sum of two contributions, the mass shift (MS) and the field shift (FS). The mass shift is proportional to the relative change of the nuclear mass, while the field shift is proportional to the difference between the mean squared charge radii of the isotopes. For light elements like lithium, the extraction of the field shift, which is 10^4 times smaller than the mass shift, is only possible if an accurate calculation of the mass shift can be performed. Recently this has been accomplished for the $2S \rightarrow 3S$ transition in lithium [2]. Taking the rms nuclear charge radius of the ^{7}Li isotope measured by electron scattering as reference, $\overline{r}_c(^7\mathrm{Li}) = \langle r_c^2\rangle^{1/2}(^7\mathrm{Li}) = 2.39(3)$ fm [3], the rms nuclear charge radius of the other lithium isotopes can be obtained from the measured isotope shift and the calculated mass shift [2]:

$$\langle r_c^2\rangle(^{\mathrm{A}}\mathrm{Li}) = \langle r_c^2\rangle(^7\mathrm{Li}) + \frac{\mathrm{IS}^{\mathrm{A,7}}_{2S\rightarrow 3S} - \mathrm{MS}^{\mathrm{A,7}}_{2S\rightarrow 3S}}{-1.5661\ \mathrm{MHz\ fm}^{-2}} \quad . \qquad (1)$$

The isotope shift, $\mathrm{IS}^{\mathrm{A,7}}_{2S\rightarrow 3S}$ was determined experimentally using high resolution Doppler-free two-photon spectroscopy as described in [4], [5] and [6]. First measurements on ^{8,9}Li were performed at GSI in 2003 [6], which were repeated in 2004 and extended to ^{11}Li at the ISAC facility at TRIUMF, Vancouver BC, Canada. In the latter, the isotopes were produced using an ISOL technique where a tantalum target was bombarded with cw 500 MeV protons at a current of 40 μA. Reaction products were mass separated and the relevant Li-isotope was delivered to our experiment at an energy of 30 keV. Yields of about 10^9 ions/s, 10^8 ions/s, and 50 000 ions/s were usually obtained for ^{8}Li, ^{9}Li, and ^{11}Li, respectively. The lithium ions were stopped in a hot thin carbon foil and thermally released as an atomic cloud. These atoms were resonantly ionized with laser light at 735 nm (provided by a Ti:Sa laser) and 610 nm (generated by a dye laser) using the ionization scheme $2S_{1/2} \xrightarrow{2\mathrm{x}735\mathrm{nm}} 3S_{1/2} \overset{\tau\approx 30\mathrm{ns}}{\rightsquigarrow} 2P_{3/2,1/2} \xrightarrow{610\mathrm{nm}} 3D_{3/2,5/2} \xrightarrow{735\mathrm{nm}/610\mathrm{nm}} \mathrm{Li}^+$. The created photo ions were then mass analyzed with a quadrupole mass spectrometer and detected with a channeltron. The isotope shift in the $2S \rightarrow 3S$ transition was measured by tuning the 735 nm light across the lithium resonances. For ^{8}Li and ^{9}Li examples of individual spectra are shown in Fig. 1. The spectrum of ^{11}Li is a sum of 7 single scans over the transition. All spectra were recorded at different laser intensities to determine the AC Stark shift of the resonance positions. Reference spectra for ^{6}Li were regularly taken among the other scans. From the data analysis the $\mathrm{IS}^{8,6}_{2S\rightarrow 3S} = 20089.75(4)$ MHz and $\mathrm{IS}^{9,6}_{2S\rightarrow 3S} = 26787.26(4)$ MHz were obtained, which, taking into account the IS between ^{6}Li and ^{7}Li, correspond to $\overline{r}_\mathrm{c}(^8\mathrm{Li}) = 2.30(4)$ fm and $\overline{r}_\mathrm{c}(^9\mathrm{Li}) = 2.21(4)$ fm. These results agree with previous measurements at GSI [6]. Analysis of the ^{11}Li data is still ongoing, but preliminary results indicate that the rms nuclear charge radius of ^{11}Li is as large as the rms nuclear charge radius of ^{6}Li, $\overline{r}_\mathrm{c}(^6\mathrm{Li}) = 2.55(4)$ fm [3].

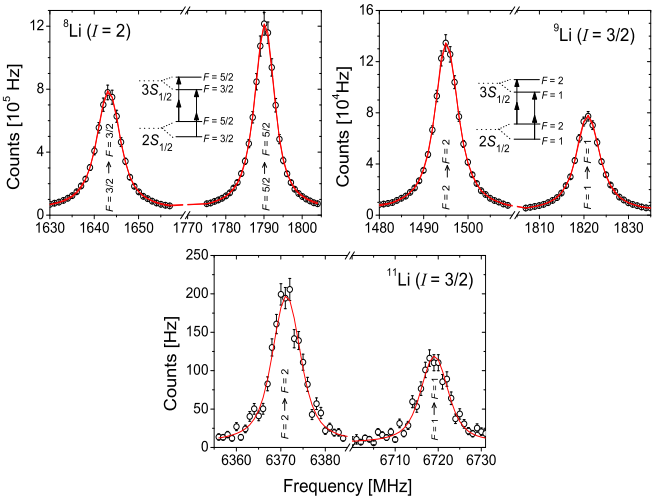

Figure 1: Examples of the $2S \rightarrow 3S$ transitions in the lithium isotopes. The accumulation time per frequency channel are 15, 11 and 70 s for ^{8}Li, ^{9}Li and ^{11}Li respectively.

References

[1] I. Tanihata *et. al.*, PRL **55**, 2676 (1985).
[2] Z.-C. Yan, G. W. F. Drake, PRA **66**, 042504 (2002).
[3] C. W. de Jager *et. al.*, Atom. Data Nucl. Data Tab., **14**, 479 (1974).
[4] W. Nörtershäuser *et. al.*, NIMB **204**, 644 (2003).
[5] W. Nörtershäuser *et. al.*, GSI **2004-1**, 97 (2004).
[6] G. Ewald *et. al.*, PRL **93**, 113002 (2004).

Laser Cooling and Spectroscopy of Relativistic C^{3+} Beams at the ESR[1]

U. Schramm, M. Bussmann, D. Habs[1], M. Steck, T. Kühl, K. Beckert, P. Beller, B. Franzke, J. Kluge, F. Nolden, T. Stöhlker[2], G. Saathoff, S. Reinhard[3], and S. Karpuk[4]

[1]Department für Physik, LMU München, D-85748 Garching; [2]GSI, D-64291 Darmstadt; [3]Max-Planck-Institut für Kernphysik, D-69029 Heidelberg; [4]Institut für Physik, Universität Mainz, D-65128 Mainz

We report on the first laser cooling of a bunched beam of multiply charged carbon ions at the ESR. For a beam energy of $E = 1.47\,\mathrm{GeV}$ ($\beta = 0.47$) the $2S_{1/2} - 2P_{3/2}$ transition of the Li-like C^{3+} ion ($\lambda \sim 155\,\mathrm{nm}$) is Doppler-shifted into resonance with a frequency doubled line of the Ar-ion laser. Concerning beam energy and charge state, the experiment represents an intermediate step toward the unique laser cooling scheme proposed for relativistic beams of highly charged heavy ions at SIS 300 (FAIR) [1].

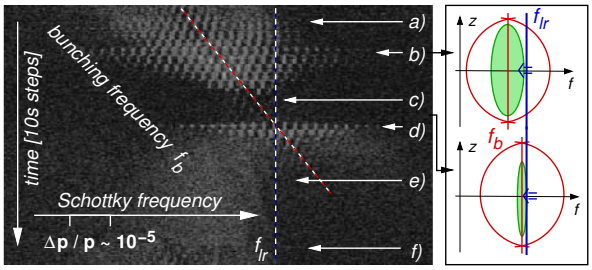

Figure 1: Schottky noise spectra (47^{th} harmonic) of the laser cooled bunched beam with rising bunching frequency f_b (diagonal dashed line). The decelerating laser beam is operated at fixed frequency and resonant with ions at f_{lr} (vertical dashed line). The frequency $f_b = hf_{rev} = 10 \times 1.295\,\mathrm{MHz}$ is increased in steps of 10 Hz every 10 s.

Bunched beam laser cooling [2] relies on the damping of the synchrotron motion by the strong but narrow-band (decelerating) laser force. Its width corresponds to $\Delta p/p \approx 5 \times 10^{-8}$. For matching the initial momentum distribution, the center frequency of the bucket was continuously tuned as depicted in Fig. 1. Starting at a low frequency f_b where ions close to the separatrix come into resonance, the ion beam is cooled into the bucket (a). Within the harmonic range, the number of synchrotron sidebands increases (b) interpreted as a laser cooled bunched beam where individual ions perform synchrotron oscillations with $f_{sync} \sim 100\,Hz$. From the synchrotron frequency (the sideband spacing) a momentum acceptance of about $\Delta p/p \sim 2 \times 10^{-5}$ can be deduced that corresponds to the observed momentum spread (roughly the number of sidebands). Closer to resonance the sidebands suddenly vanish (c) when the beam enters the space-charge dominated regime. When the laser beam comes into resonance with ions at the bucket center (d) the synchrotron motion is driven. Ions are decelerated (e) out of the bucket until the cycle restarts (f).

Fig. 2 (left) shows the transition into the space-charge dominated regime in real space, where the bunch length does not decrease any further with increasing cooling strength. This point corresponds to the situation c) in Fig. 1. The right graph depicts the fluorescence as a function of the relative momentum deviation. For a frequency detuning corresponding to $\Delta p/p = 6 \times 10^{-7}$ at $h = 10$ a momentum spread of $\Delta p/p = 4 \times 10^{-7}$ is measured for a cold fraction of the beam. For an ion number of about 1.5×10^6 it corresponds to a plasma parameter of $\Gamma \sim 1$.

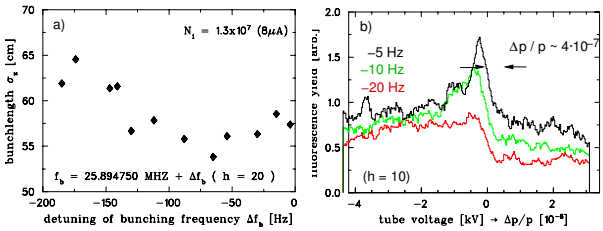

Figure 2: Bunch length as a function of the detuning of the bucket center with respect to the laser resonance, i.e., the cooling strength (left), and momentum distribution close to optimum cooling (right).

A more efficient cooling technique is presently under development, where a dedicated broad band laser system addresses the whole ion bunch.

The cooling experiment incorporates the spectroscopy of the $2S - 2P$ transitions of Li-like C^{3+} at a precision limited by the knowledge of the ion energy $\Delta\omega_0/\omega_0 = (1-\beta^2)^{-1}\,\Delta\beta = \beta^{-1}\,\Delta\gamma/\gamma$. This energy has been measured via the electron energy of the cooler at the ion revolution frequency corresponding to the laser resonances [3]. The following transition wavelengths can be deduced, where the first error denotes the calibration accuracy of the electron energy and the second the statistical error.

ref.	$\lambda(2S_{1/2} - 2P_{1/2})$ [nm]	$\lambda(2S_{1/2} - 2P_{3/2})$ [nm]
Exp.	155.0705(39)(3)	154.8127(39)(2)
Th.[4]	155.0739(26)	154.8173(53)

Thus, the accuracy given by theory (second line) can be reached. With an improvement of the voltage calibration or measurements at different ion energies and laser wavelength on the same transition, theory could be readily challenged. At the ESR the method could be extended up to O^{5+} ions while, at FAIR, every element can be reached.

References

[1] U. Schramm, et al., LoI#18 FAIR APPA–PAC (2004) and GSI annual report, 275 (2004)
[2] U. Schramm, D. Habs, Prog. Part. Nucl. Phys.**53**, 583–677 (2004)
[3] U. Schramm et al., Proc. LASER 2004 Poznan
[4] I.I. Tupitsyn and V.M. Shabaev, priv. com. (2004)

[1]supported by BMBF (06ML183)

First mass measurements of radionuclides at SHIPTRAP

M. Block[1], D. Ackermann[1], D. Beck[1], K. Blaum[1,2], M. Breitenfeldt[3], A. Chauduri[3], A. Doemer[4], S. Eliseev[1], D. Habs[5], S. Heinz[5], F. Herfurth[1], F.P. Heßberger[1], S. Hofmann[1], H. Geissel[1,6], H.-J. Kluge[1], V. Kolhinen[5], G. Marx[3], J.B. Neumayr[1], M. Mukherjee[1], M. Petrick[6], W. Plass[6], W. Quint[1], S. Rahaman[1], C. Rauth[1], D. Rodríguez[7], C. Scheidenberger[1,6], L. Schweikhard[3], M. Suhonen[8], P.G. Thirolf[5], Z. Wang[6], C. Weber[1,2], and the SHIPTRAP collaboration[1]

[1]GSI; [2]Universität Mainz; [3]Universität Greifswald; [4]NSCL, Michigan State University; [5]Ludwig-Maximilians-Universität München; [6]Universität Gießen; [7]LPC Caen; [8]Stockholm University

The ion-trap facility SHIPTRAP [1] at GSI Darmstadt will allow various precision experiments on heavy elements produced in fusion-evaporation reactions at the velocity filter SHIP [2]. SHIPTRAP focuses on mass measurements of nuclei not available at ISOL or fragmentation facilities with a Penning-trap mass spectrometer. Especially the region of transuranium elements is very attractive since the majority of masses in this region is only known from extrapolations. From the measured mass values the nuclear binding energy can be deduced which is an important parameter for nuclear structure theories. Systematic measurements along isotopic and isotonic chains covering shell closures are planned. For the elements heavier than uranium the very low production rates, only about one ion per second in the case of nobelium (Z=102), are very challenging.

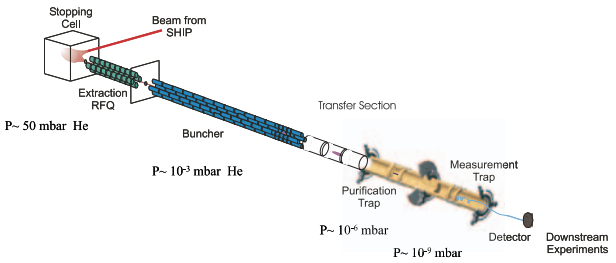

Figure 1: Schematic overview of the SHIPTRAP facility.

A schematic drawing of the setup is shown in Fig. 1. The reaction products from SHIP with energies in the order of a few 100 keV/u are stopped in a buffer-gas-filled cell. For an efficient injection into the Penning traps an RFQ cooler and buncher is utilized where the ions are cooled within a few milliseconds and extracted as a low-emittance bunched beam. A system of two cylindrical Penning traps in one superconducting magnet of 7-T field strength allows for high-precision mass measurements. The first trap, where a mass resolving power of about 85,000 for ^{133}Cs has been achieved, is used for isobaric purification. In the second trap mass measurements are performed by the time-of-flight ion cyclotron resonance method [3]. A mass resolving power of 10^6 is routinely achieved for an excitation time of the order of 1 s.

Mass measurements of radionuclides, e.g. in the rare earth region with production rates of some thousand ions per second, are already feasible as demonstrated in July 2004 when the first on-line mass measurements at SHIPTRAP were performed. Holmium and erbium radionuclides around A=147 produced at SHIP via the reaction ^{92}Mo(^{58}Ni, xpxn) were studied. The area close to ^{147}Ho is of interest because of the phenomenon of ground-state proton radioactivity, discovered at SHIP [4] several years ago. The key parameter is the proton separation energy, which can be derived from atomic masses. Furthermore, important data for nuclear structure studies are obtained, in particular for the two-neutron separation energies around the neutron shell closure at N=82. At present, many masses in this region are experimentally unknown. During the run the masses of ^{147}Ho, ^{147}Er, and ^{148}Er were measured with the masses of the two erbium nuclides being experimentally determined for the first time. The data are currently analyzed in detail. As an example, a time-of-flight resonance of ^{147}Ho is shown in Fig. 2. The present overall efficiency of SHIPTRAP is dominated by the total efficiency of the gas cell of 5-8%, including the extraction RFQ, and the detection efficiency of the micro-channel plate detectors of 10-30%. In order to understand the stopping-cell efficiency studies with a ^{223}Ra source were performed [5].

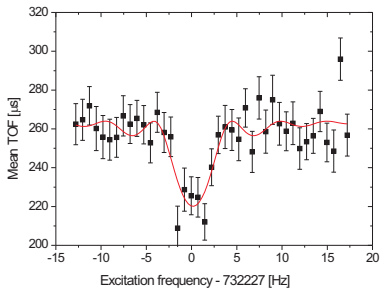

Figure 2: Time-of-flight resonance of ^{147}Ho$^+$ obtained with an excitation time of 200 ms. The solid line is a fit of the theoretical line shape to the data points.

We acknowledge financial support by the GSI F&E program and the EU (contracts HPRI-CT-2001-50034 and HPRI-CT-2001-50022)).

References

[1] J. Dilling et al., Hyperfine Interactions **127**, 491 (2000).

[2] S. Hofmann and G. Münzenberg, Rev. Mod. Phys. **72**, 733 (2000).

[3] G. Gräff, H. Kalinowski, and J.Traut, Z. Phys. A **297**, 35 (1980).

[4] S. Hofmann et al., Z. Phys. **A305**, 111-123 (1982).

[5] S. Eliseev et al., GSI Jahresbericht 2004.

Accurate mass measurements with ISOLTRAP for fundamental tests

G. Audi[a], S. Baruah[b], D. Beck[c], K. Blaum[c,d], G. Bollen[e], P. Delahaye[f], J. Dilling[g], S. George[d], C. Guénaut[a], F. Herfurth[c], A. Herlert[b,f], A. Kellerbauer[f], H.-J. Kluge[c], D. Lunney[a], M. Mukherjee[c], D. Rodriguez[c], S. Schwarz[e], L. Schweikhard[b], C. Weber[c,d], and C. Yazidjian[c,f]

[a]CSNSM Orsay, France; [b]Universität Greifswald, Germany; [c]GSI, Germany; [d]Universität Mainz, Germany; [e]NSCL, USA; [f]CERN, Switzerland; [g]TRIUMF, Canada

With the Penning trap mass spectrometer ISOLTRAP at ISOLDE/CERN close to 300 masses of radionuclides have been measured to date. In 2004 the masses of 21 nuclides have been determined, in many cases direct mass measurements have been performed for the first time. In addition to the mass determination of neutron rich krypton isotopes, $^{84-95}$Kr, the research interest was focused on mass measurements for fundamental tests.

The experimental setup comprises three ion traps. The first linear radiofrequency ion trap cools and bunches the continuous radioactive ion beam coming from the ISOLDE target. The ion bunches are sent to the second ion trap, a cylindrical Penning trap in a helium buffer-gas environment, for removal of isobaric contaminants and further cooling of the ion bunch. The short-lived ions are finally transferred to the precision Penning trap, where the mass m is determined via the measurement of the cyclotron frequency, $\nu_c = qB/(2\pi m)$, by the application of a time-of-flight cyclotron-resonance detection technique. The magnetic field B is calibrated with the measurement of ν_c of a reference nuclide with well-known mass.

The atomic mass of a nuclide not only reveals information on the nuclear binding energy. It is also important for a wide range of physics branches, especially for fundamental tests, where the mass needs to be known with a relative uncertainty of $\delta m/m = 1 \cdot 10^{-8}$ or smaller. One example is the test of the Standard Model with respect to the conserved-vector-current hypothesis of the weak interaction and the unitarity of the Cabibbo-Kobayashi-Maskawa quark-mixing matrix, where the mass of superallowed β-decaying nuclides is required [1]. Succeeding the recent mass determination of ^{74}Rb [2], the mass of ^{22}Mg was measured with a relative mass uncertainty of $1.3 \cdot 10^{-8}$ [3]. In addition, the masses of ^{21}Na and ^{22}Na were improved [3], which contribute to a test of an astrophysical model of nova explosions, where the rate of the proton capture reaction ^{21}Na$(p,\gamma)^{22}$Mg is needed (see Fig. 1).

Another application of mass measurements is the test of the quadratic form of the isobaric-multiplet mass equation (IMME). This equation is used to predict level energies and unknown masses. From the mass values of the nuclides $^{35-38}$K and $^{43-46}$K determined in 2004, the mass of ^{35}K is of special interest for the test of the IMME for the isospin $T = 3/2$ quartet ^{35}S,^{35}Cl,^{35}Ar, and ^{35}K. The preliminary analysis shows a deviation from the quadratic form, i.e. a non-zero coefficient of the cubic term. However, further analysis is needed for the lowest lying excited state of ^{35}Cl, which is currently dominating the overall uncertainty.

The mass measurement of ^{17}Ne in the last beamtime of ISOLTRAP in 2004 was a highlight in many respects. It is the lightest short-lived nuclide measured so far in a Penning trap. It is also of interest for the test of the IMME

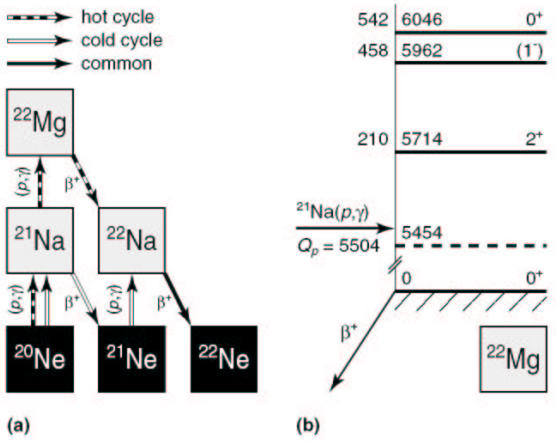

Figure 1: (a) "Hot" and "cold" reaction paths of the NeNa cycle. The bottom row (black boxes) are stable nuclides. (b) Level scheme of ^{22}Mg, showing the levels with astrophysical relevance. The level energies E_x (center) are shown along with the center-of-mass energies $E_x - Q_p$ (left; both in keV) and the spin parity (right). (From [3]).

for the isospin $T = 3/2$ quartet ^{17}N,^{17}O,^{17}F, and ^{17}Ne, where the mass uncertainty of ^{17}N still needs to improved. Thus a mass measurement of ^{17}N is scheduled in 2005.

In addition to the intense physics program, the further development of the experimental setup was pursued. A new conversion-electrode detector has been constructed in order to increase the detection efficiency to access nuclides with a production yield below 100 ions/s. With a new ion source more stable nuclides will be available to serve as reference masses in addition to carbon clusters from a new carbon-cluster ion source. In order to lower the systematic relative mass uncertainty, a temperature and pressure stabilization of the superconducting magnet of the precision trap is being commissioned. Finally, a new method has been tested to access nuclides, that are not delivered from ISOLDE: in-trap-decay mass spectrometry of short-lived nuclides, demonstrated for ^{37}Ar which was produced by in-trap decay of ^{37}K in the preparation Penning trap [4].

References

[1] I.S. Towner and J.C. Hardy, Phys. Rev. C (2005), submitted

[2] A. Kellerbauer *et al.*, Phys. Rev. Lett. 93, 072502 (2004)

[3] M. Mukherjee *et al.*, Phys. Rev. Lett. 93, 150801 (2004)

[4] A. Herlert *et al.*, New J. Phys., in press

First Dielectronic Recombination Measurements with H-Like Uranium

C. Brandau[a,b], C. Kozhuharov[a], A. Müller[b], K. Beckert[a], P. Beller[a], F. Bosch[a], S. Böhm[b], F.J.Currell[d], B. Franzke[a], A. Gumberidze[a], Z. Harman[c], J. Jacobi[b], P.H. Mokler[a], F. Nolden[a], W. Scheid[c], S. Schippers[b], E.W. Schmidt[b], U. Spillmann[a], Z. Stachura[e], M. Steck[a], and Th. Stöhlker[a]

[a]Gesellschaft für Schwerionenforschung (GSI), 64291 Darmstadt; [b]Institut für Atom-und Molkülphysik, Justus-Liebig-Universität, 35392 Gießen; [c]Physics Department, Queen's University, Belfast BT7 1NN, U.K.; [d]Institut für Theoretische Physik, Justus-Liebig-Universität, 35392 Gießen; [e]Instytut Fizyki Jądrowej, 31-342 Kraków, Poland

In this report we present first results on dielectronic recombination (DR) measurements with H-like uranium U^{91+}. The experiments were conducted in December 2004 at the storage ring ESR.

DR of H-like ions is of fundamental interest in particular for the heaviest atomic species, i.e., in the domain of highly relativistic systems. In addition to precision information on the atomic structure, the measurement of rate coefficients on an absolute scale enables one to access Auger rates and radiative transition matrix elements and, hence, the dynamics of the recombination process. Numerous theoretical studies can be found in the literature, e.g. about the Breit interaction in such heavy systems [1] or about interferences between DR with its none resonant counterpart, radiative recombination (RR) [2], to name only a few. It is worth noting, that DR measurements of very heavy H-like ions open up a new field of QED studies, namely, QED interference effects of overlapping DR resonances [3].

For H-like ions a resonant dielectronic capture of a free electron involves a simultaneous $\Delta n \geq 1$ excitation of the bound K-shell electron. Accordingly, the minimum energy for DR of H-like ions, i.e., an excitation K→L and capture into the L-shell, KLL, is of the order of half of the binding energy of the K-shell electron. With increasing electron-ion collision energies, resonance series with KLn configurations are formed. The corresponding high-energy transitions, expected to be beyond 64 keV for uranium, cannot be accessed with the well-established technique (e.g.[4, 5]) of alternately switching the cooler between cooling and measurement. It is not possible to swiftly and precisely ramp the cooler voltage up and down between potentials that have to differ by more than 170 kV in the lab frame. In a first successful series of experiments with H-like Xe^{53+} ions [6], this problem was solved by cooling the ion beam continuously with the stochastic cooling and using the cooler as an electron target only. For the present measurements a slightly modified scheme was applied: U^{91+} ions were injected into the ESR at an energy of $\sim$ 400 MeV/u and then stochastically cooled. The ion-optical settings for the stochastic cooling of the uranium beam prohibit the detection of the recombined ions with the particle detectors at their present position in the bending magnet. Therefore, subsequent to cooling, the beam was rebunched and HF-shifted to lower momentum, i.e., to a more central orbit. The bunching was retained during the measurement phase in order to preserve a constant beam energy.

Owing to the excellent vacuum conditions we could achieve a good signal-to-noise ratio even with the small cross sections of the KLn-DR processes. Fig. 1 shows preliminary experimental data for the photorecombination of U^{91+} in the region of the $KL_jL_{j'}$ resonances. The fine structure of the individual j-j' groups is clearly resolved. The measurement is compared to a fully relativistic DR/MCDF calculation which is convoluted with a 120 eV Gaussian. For an easier comparison, the preliminary calibrated experimental data are shifted to lower energies and normalized to the theory. In addition, the same theory is displayed unconvoluted, i.e., with the natural line widths only. The large natural widths of about 50 eV are caused by the fast radiative decay of the intermediate doubly excited states. It can be seen that the resolution of the online data is close to the natural widths.

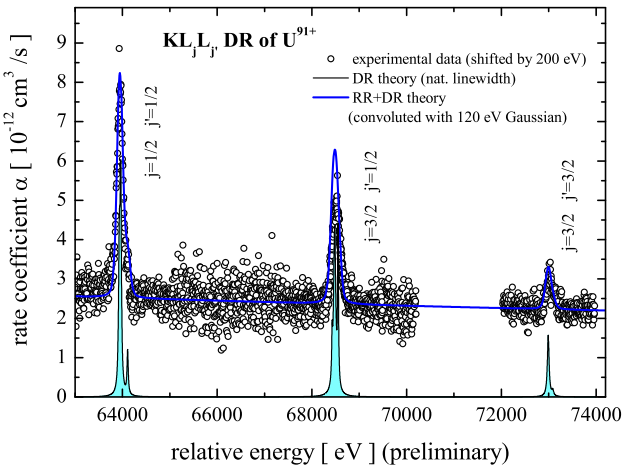

Figure 1: Photorecombination of U^{91+} in range of the KLL-DR resonances: ESR measurements (dec 2004 online data, preliminary, open circles). The experimental data are shifted by 200 eV to lower energies and normalized to the theory (full blue line). The offline analysis will yield energies and absolute rate coefficient independent from any theory. The smooth background is due to contributions of the non-resonant radiative recombination (RR). In addition, the theoretical DR cross section is displayed with natural line widths only (thin black line)

Not shown in this report are data for KLM and KLN resonances which were also measured. Normalization to the electron and the ion current will yield the recombination rate coefficient on an independent absolute scale which then will allow for a detailed comparison with the calculations.

These new results herald a new era of DR experiments, i.e., high precision measurements at high electron-ion collision energies.

References

[1] P. Zimmerer, et al., J. Phys. B **24**, 2633 (1991).
[2] M. Zimmerman, et al., J. Phys. B **30**, 5259 (1997).
[3] A. V. Nefiodov, et al., Phys. Rev. A **60**, 2069 (1999).
[4] W. Spies, et al., PRL **69**, 2768 (1992).
[5] C. Brandau, et al., PRL **91**, 073202 (2003).
[6] C. Brandau, et al., GSI Report 2002, GSI 2003-1, 91.

Radiative Recombination into Bare and H-like Uranium Ions

R. Reuschl[1,2], A. Gumberidze[1,2], S. Fritzsche[3], C. Kozhuharov[1], U. Spillmann[1,2], Th. Stöhlker[1,2], A. Surzhykov[3], and S. Tashenov[1,2]

[1]GSI, Darmstadt, Germany; [2]IKF, Univ. of Frankfurt, Germany; [3]University of Kassel, Germany

Radiative Recombination (RR) is the time inversed process of photo ionization and therefore one of the well known and fundamental processes in physics. Here an electron undergoes a direct transition into a bound state of the stationary ion via the emission of a photon carrying away the energy difference between the initial and final electron states, i.e. $\hbar\omega = E_{kin} + E_B$. In this report we present an investigation of the RR transitions into the bound states of bare and H-like uranium ions.

The experiment was performed at the electron cooler device of the ESR storage ring [1]. There the x-rays emitted via RR of the cooler electrons into the bound states of the bare and H-like uranium ions (forming H- and He-like systems respectively) were detected by a solid state detector which viewed the interaction region at an observation angle close to 0°. In figure 1 we present a x-ray spectrum recorded for RR into bare uranium at the beam energy of 43.95 MeV/u [2]. The most intense lines observed in the spectrum can be attributed to the direct recombination into K- and L-shells and to characteristic transitions. In the following we concentrate on two major aspects: 1) a detailed analysis of RR into the K- and L-shell of bare and H-like uranium; 2) an investigation of recombination into highly-excited levels of bare ions followed by subsequent cascades and emission of characteristic x-ray radiation.

Due to the applied deceleration mode it was possible for the first time to observe the Balmer radiation as well as the capture into the L-shell sublevels L-RR$_{j=\frac{1}{2}}$ and L-RR$_{j=\frac{3}{2}}$, what enabled us to perform state selective investigations. The accumulated data contain no absolute number of events and therefore the ratios of the different lines had to be analyzed. In figures 2 and 3 the results of the data analysis are shown. Figure 2 depicts the ratios of the L-RR$_{j=\frac{1}{2}}$:K-RR and L-RR$_{j=\frac{3}{2}}$:K-RR lines for capture into bare uranium. The results are compared with a non-relativistic (dotted line) and a relativistic (solid line) theory. In the case of capture into bare uranium data at the ion beam energy of 20.74 MeV is also available.

In order to compare the ratios of L-RR and K-RR for bare and H-like uranium the K-RR intensity had to be normalized on the number of vacancies in the K-shell of the initial ion. Therefore, the number of counts in the K-RR line for bare uranium had to be divided by two.

From figure 2 we can state that the fully relativistic theory describes quite well the experimental data in contrast to the results of the non-relativistic approach. Although the relativistic theoretical ratio L-RR$_{j=\frac{1}{2}}$:K-RR differs slightly from the experimental results it is considerably closer than the one from the non-relativistic theory. At this point it should be mentioned that the error bars assumed are of pure statistic origin.

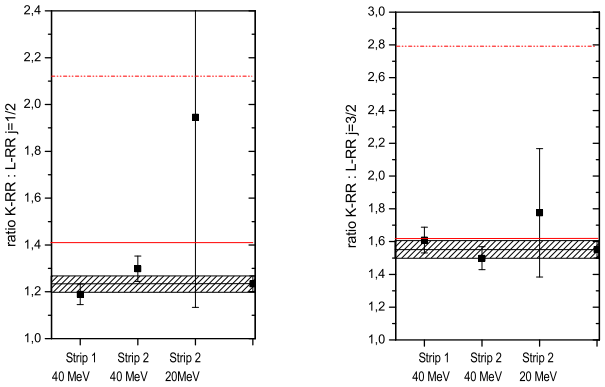

Figure 2: Results for capture into bare uranium ions (compare text).

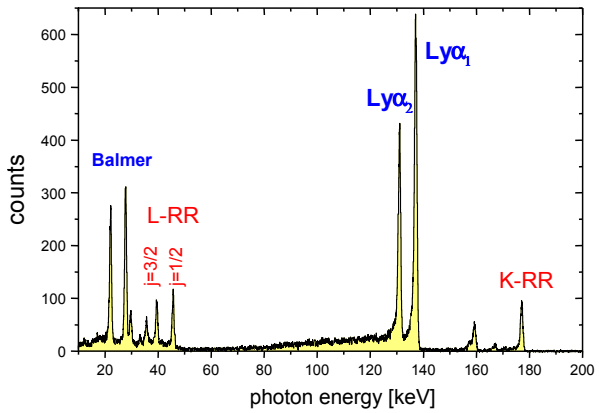

Figure 1: Coincident x-ray spectrum for initially bare uranium as observed for decelerated ions at the electron cooler of the ESR storage ring.

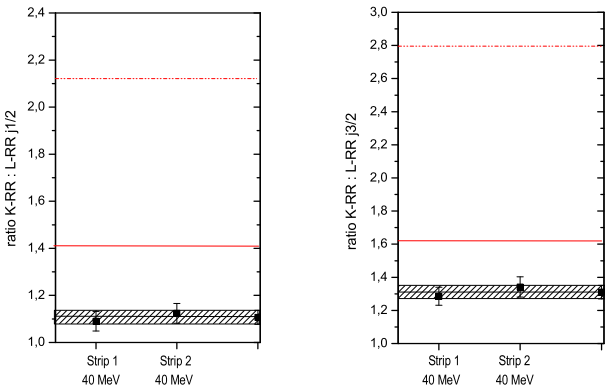

Figure 3: Results for capture into H-like uranium ions

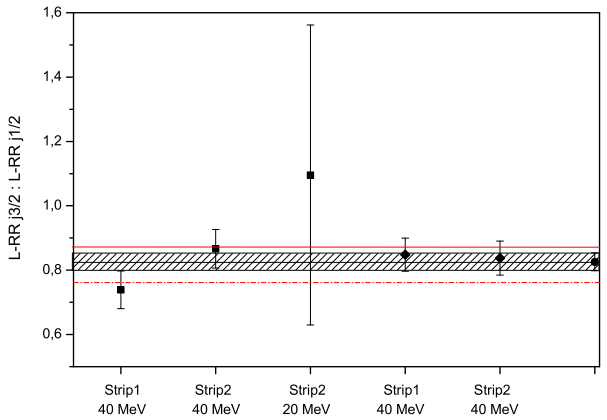

Figure 4: Comparison of the capture into the L-shell sublevels in bare and H-like uranium ions.

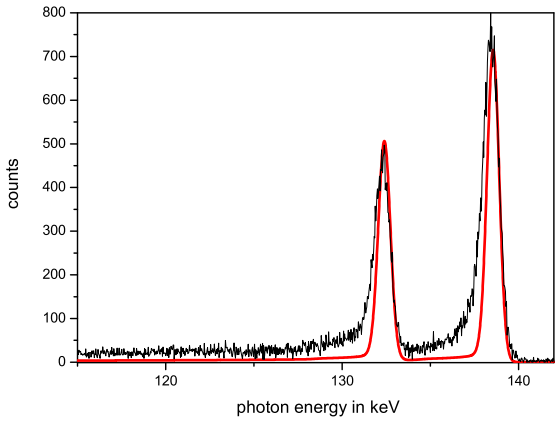

Figure 5: Simulation of the energy spectrum including states up to a principal quantum number n=130. The simulation differs markedly from the experimental results.

Figure 3 shows the data for capture into H-like uranium. It is obvious that the theoretical approach is not describing the experimental results well. Since the theory used here is the one-electron approach strictly valid only for recombination into initially bare ions one may conclude that the already present K-shell electron plays an important role in the population mechanism.

While figures 2 and 3 show the ratios of L-RR and K-RR lines, figure 4 depicts the results for the ratio L-RR$_{j=\frac{1}{2}}$:L-RR$_{j=\frac{1}{2}}$. The squares represent the ratio for capture into bare and the diamonds the capture into H-like uranium. All data points -independent from the capturing ion- are consistent within the error bars what suggests that the presence of the K-shell electron gives a negligible effect on the recombination into the L-shell states.

Besides the direct RR and characteristic transitions, the tails of the Lyman-α lines, caused by cascade feeding of the L-shell levels and subsequent delayed Lyman transitions are of particular interest for the current study [3]. Due to the low β-value of 0.29 and the experimental time resolution of about 20 ns, photo events which occurred inside the cooler section could be distinguished from events where the emission took place in front of the x-ray detector. For the latter x-ray events, the set-up possesses a comparably large solid angle and the photon energy appears markedly shifted leading to the low-energy tails of the Lyman radiation [3, 1].

In order to investigate the origin and shape of these tails in detail simulations of the RR into highly excited states followed by de-excitation cascades were performed. In the electron cooler the relative energy between electrons and ions is close to zero. Therefore the initial population (via the RR) of bound-states up to very high principal quantum numbers n has to be taken into account. In the simulation transitions between bound-states up to n=7 were calculated by a complete relativistic theory whereas higher transitions were described by a non-relativistic electric dipole approximation. The values for the initial population of the levels via the RR process were taken from a complete relativistic theory [4] for states up to n=5 and a non-relativistic theory [5] for all higher states. States with relatively high quantum numbers n and angular momentum l (preferably populated by the RR) mainly decay via the so called Yrast-Cascades ($\Delta n = -1$, $\Delta l = -1$) which have comparably long lifetimes and they contribute to the delayed Lyman emission.

In figure 5 the results of the simulation including states with quantum number n up to 130 are shown in comparison with the experimental spectrum. It is obvious that even taking into account levels with such a high quantum number the tails can not be reproduced quantitatively. This means that the simulation considerably underestimates the intensity of the delayed characteristic transitions. The highest quantum number considered in our simulation was limited on one hand by the computation time and on the other hand by the fact that no further considerable increase of the delayed emission was observed when going above n=130. Also, the cutoff due to the time of flight of the ions from the electron cooler to the x-ray detector lies in the same region. This disagreement is currently subject of detailed investigations (crosschecks) with respect to the theoretical data used, assumptions (approximations) made in the simulations etc. Besides, this deviation could originate from the so-called "rate enhancement" phenomenon observed for the RR at the electron cooler devices which is not completely understood up to now. Therefore, the x-ray spectroscopic investigations of this kind may provide an additional information and sensitivity concerning the mechanism of this process.

References

[1] A. Gumberidze et al., Phys. Rev. Lett. **92**, 203004-1 (2004).
[2] A. Gumberidze et al., GSI, Annual Report, 89 (2001).
[3] H. F. Beyer et al., Z. Phys. D **35**, 169 (1995).
[4] J. Eichler et al., Phys. Rev. A **51**, 3027 (1995).
[5] A. Burgess, Mem. Roy. Ast. Soc. **69**, 1 (1964).

Optical Spectroscopy of Trans-Fermium Elements at SHIPTRAP

H. Backe[1], A. Dretzke[1], R. Horn[1], T. Kolb[1], P. Kunz[1], W. Lauth[1], P. Thörle[2], and N. Trautmann[2]
[1]Institut für Kernphysik, Universität Mainz, Germany; [2]Institut für Kernchemie, Universität Mainz, Germany

An ultra sensitive laser spectroscopic method is being developed for the investigation of the completely unknown atomic structure of the elements No and Lr. Such experiments aim in the investigation of relativistic effects. These, roughly speaking, originate from a shrinkage of the wave functions of inner shell electrons which, in turn, influence the binding energy of the valence electrons and thus the chemical properties. A direct approach to investigate relativistic effects may be to study first ionization potentials (IP) or even better, the atomic level schemes [1].

First experiments will be performed within the SHIPTRAP collaboration at No which will be produced via the fusion reaction ^{208}Pb(^{48}Ca,2n)^{254}No. The reaction products, separated by SHIP, will be stopped in a buffer gas cell in which Resonance Ionization Spectroscopy (RIS) is performed with detection of the ionization process by the α-decay of ^{254}No. The technique is similar to that developed for RIS at fission isomers [2]. The experimental setup is shown in Fig. 1. The reaction products with an energy of 40 MeV are injected into the argon buffer gas trap and stopped in the gas at an pressure of 100-300 mbar. The neutral part of about 15% will be ionized resonantly and guided by electric fields onto a detector which registers the α-decay radiation. After each detuning of the laser frequency of the first excitation step one has to wait for the decay of the accumulated ions. The symmetric construction offers the opportunity to collect on one detector ions, that are resonantly ionized while counting with the other one the activity collected at a different wavelength.

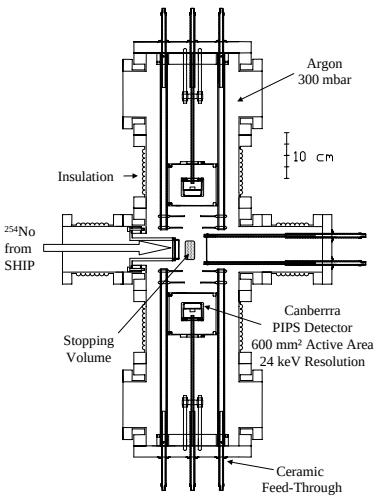

Figure 1: *Experimental set-up. The separated fusion product from SHIP is injected into a buffer gas trap. About 10% of these ions neutralize in the slowing down process and are thus available for laser spectroscopic investigations.*

A first on-line test experiment at GSI was carried through with the radioactive isotopes ^{152,153}Er (half-lives of 10.3 s and 37.1 s, α-decay) which were produced by the nuclear reaction ^{40}Ar(^{116}Sn,xn)^{152,153}Er with the relatively large reaction cross sections of about 100 mb. The atomic level scheme of erbium is well known, and this reaction thus provides an ideal test case. The longitudinal and transversal distribution of the recoils has been measured with the aid of a semiconductor strip detector. For the resonance ionization spectroscopy experiments a mixture of approx. 150 mbar Ar and approx. 40 mbar N_2 was chosen. The pressure was optimized in such a way that the stopping distribution was located in the middle of the cell, where the overlap with the laser beams (λ_1 = 472 nm, 100 μJ and λ_2 = 351 nm, 2 mJ) is maximal. A slight but significant increase of the α-events in the detector was observed. A dependency on the laser frequency λ_1 could not be observed, meaning that the ionization is a non-resonant process. A possible reason for the non-resonant low ion signal could be that erbium compounds, such as ErN, are formed.

The second on-line experiment was performed on ytterbium, the chemical homolog of nobelium. It was produced by the fusion reaction ^{40}Ca(^{118}Sn,xn)^{154,155}Yb. The gas cell was filled with 150 - 250 mbar argon. Wave lengths λ_1 = 398.9 nm and λ_2 = 399.6 nm were chosen for the first and second level, respectively. The second level is a Rydberg state, which should provide a higher efficiency as excitation into the continuum. Results of these measurements are shown in Fig. 2. Although the apparatus could be proven in this experiment to be operational, the efficiency for resonance ionization turned out to be only 2-4·10^{-5}·. An increase of the efficiency by a large gain factor may be obtained if the 85% fraction of the thermalized ions are collected by and reevaporated from a filament as atoms by a high temperature pulse. The this way localized atom cloud would also improve the overlap with the laser beams.

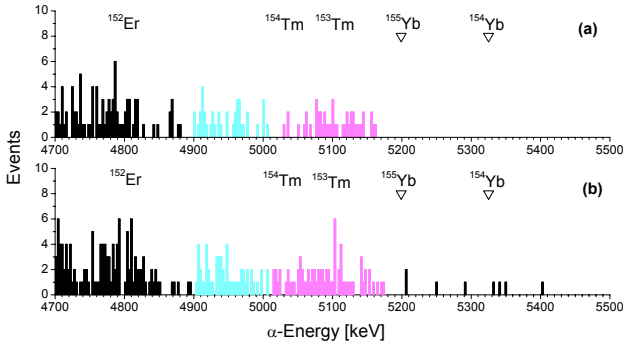

Figure 2: *Resonance ionization signals of ^{154}Yb and ^{155}Yb. (a) α-energy spectrum off-resonant and (b) at resonance ($\bar{\nu}_1$ = 25068.24 cm^{-1}, $\bar{\nu}_2$ = 25025.84 cm^{-1}). The α-lines of the ^{154,155}Yb decay are marked with $\triangledown$.*

Work supported by the Bundesministerium für Bildung und Forschung under contract 06 MZ 959I.

References

[1] M. Sewtz et al., Phys. Rev. Lett. 90, 163002-1 (2003)
[2] H. Backe et al., Phys. Rev. Lett. 80, 920 (1998)

Study of the intra-L shell transitions in Be-like uranium

J. Rzadkiewicz[3], A. Gumberidze[1,2], Th. Stöhlker[1,2], C. Brandau[1], H. F. Beyer[1], S. Fritzsche[5], S. Hagmann[1,2], C. Kozhuharov[1], R. Reuschl[1,2], T. Nandi[1], D. Sierpowski[4], U. Spillmann[1,2], A. Surzhykov[5], S. Tashenov[1,2], A. Wilk[4]

[1]GSI, Darmstadt, Germany; [2]IKF, Univ. of Frankfurt, Germany
[3]The Soltan Institute for Nuclear Studies, Swierk, Poland
[4]Jagiellonian University, Krakow, Poland
[5]Universität Kassel, Kassel, Germany

In collisions of few electron heavy ions with low-Z target atoms, the projectile may loose or capture an electron into a bound state. While the K-shell ionization of high-Z Li-like ions in fast collisions turned out to be a highly selective mechanism for the population of the 1s2s $^1S_0$ and 1s2s $^3S_1$ states [1], the electron capture into the $2p_{3/2}$ orbital can populate the $2s2p_{3/2}$ $^1P_1$ and $2s2p_{3/2}$ $^3P_2$ magnetic substates of Be-like uranium. Only the first one (J=1) can deexcitate to the $1s^22s^2$ ground state of the berylliumlike uranium by the E1 transition (see Fig.1).

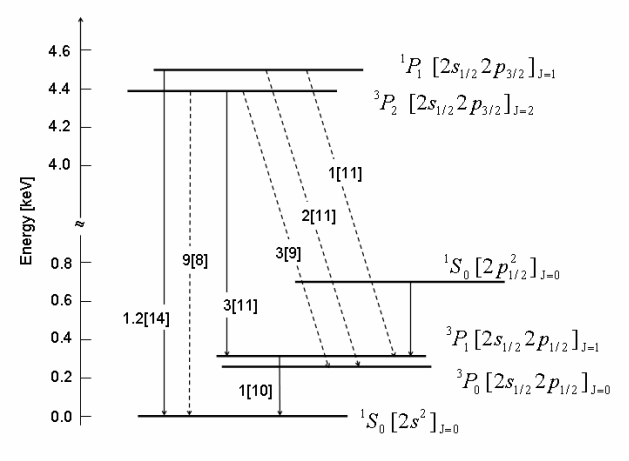

Figure 1: Diagram of the levels of berylliumlike U^{88+}. The dominant deexcitation channels for each state are presented by solid arrows. For the radiative decay rates the following notation is used: x[y] corresponding to $x \times 10^y\, s^{-1}$.

However if the $[2s2p_{3/2}]_{J=2}$ state is formed, the de-excitation to the $1s^22s^2$ ground state is not dipole-allowed. Such a state can decay via a $2p_{3/2}$ - $2p_{1/2}$ M1 transition. The intensities of the other deexcitation channels (E2 and M2) are two orders of magnitude smaller than the M1 decay rate.

The studies of the E1 $2p_{3/2}$-$2s_{1/2}$ and M1 $2p_{3/2}$-$2p_{1/2}$ transitions are interesting in several respects. First, x-ray transitions in berylliumlike ions are sensitive to both intrashell and innershell interactions. For the $\Delta n = 0$ transitions the relative QED contributions to the total transition energy are much higher (~10%) than for the K x-ray transitions (0.5%) [2]. Therefore in recent years the $\Delta n = 0$ transitions in few electron ions were subject of intensive studies [2-4]. Finally, the $2p_{3/2}$-$2s_{1/2}$ and $2p_{3/2}$-$2p_{1/2}$ transitions give direct quantitative information of the magnetic sublevel production in the electron capture process.

In order to investigate the intra-L shell decays of the magnetic substates $^1P_1$ and $^3P_2$ produced via electron capture, a measurement of the x-ray spectra produced in collisions of 100-MeV/u Li-like uranium with gaseous N_2 target have been performed. In this experiment, the projectiles having captured one electron were registered in a particle detector. The emitted x-rays were registered in coincidence with down-charged Be-like uranium ions by an array of germanium detectors mounted at observation angles in the range from 35^o to 120^o with respect to the beam direction. The x-ray spectrum recorded by the Ge(i) detector placed at 35 degree is shown in Fig. 2.

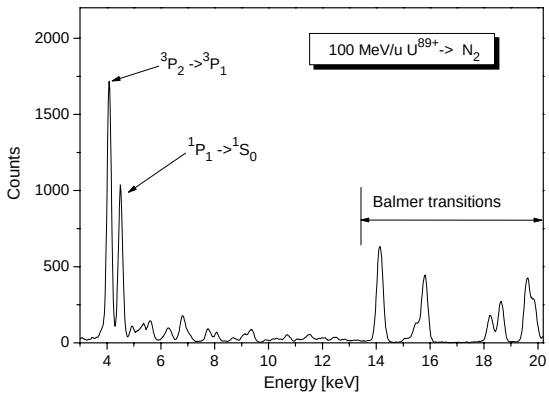

Figure 2: The x-ray spectrum of Be-like uranium ions measured in coincidence with electron capture in 100-MeV/u U^{89+} on a N_2 target collisions.

In the low energy region of the spectrum one can see well separated x-ray lines which correspond to intra-L shell transitions. These $\Delta n = 0$ transitions correspond to the deexcitation of the $2s2p_{3/2}$ $^1P_1$ and $2s2p_{3/2}$ $^3P_2$ magnetic sublevels to the $1s^22s^2$ $^1S_0$ ground state and $2s2p_{1/2}$ $^3P_1$ excited state of berylliumlike uranium, respectively. Note that the lifetimes of these two states differ by two orders of magnitude. Currently, a detailed analysis of all recorded spectra is in progress.

References

[1] D. Banas et al., GSI Scientific Report, 88 (2002).
[2] M. S. Safronova et al., Phys. Rev. A **53**, 4036 (1996).
[3] P. Beiersdorfer et al., Phys. Rev. A **58**, 1944 (1998)
[4] P. Beiersdorfer et al., Phys. Rev. A **71**, 3939 (1993).

g-Factor experiments on hydrogen-like highly charged ions

J. Alonso[1,2], T. Beier[2], K. Blaum[1], S. Djekic[1], H.-J. Kluge[2], W.Quint[2], S. Stahl[1], T. Valenzuela[1], J. Verdú[1], M. Vogel[1], and G. Werth [1]

[1]Johannes Gutenberg Universität, D-55099 Mainz, [2]GSI, D-64291 Darmstadt

The magnetic moment of the electron bound in hydrogen-like systems, expressed by the g-factor, differs from that of the free electron by different contributions: The binding to the nucleus leads to relativistic shifts, which are analytically known, bound state quantum-electrodynamic (BSQED) corrections are 3 orders of magnitude smaller, finally nuclear structure and recoil corrections are small for low values of the nuclear charge Z but become comparable in size to the BSQED part for higher Z. Our experiments aim at a determination of these corrections and a comparison to BSQED theory.

After a determination of the g factor in hydrogen-like carbon $^{12}C^{5+}$ in 2000 [1], we completed a similar experiment on oxygen $^{16}O^{7+}$. A single O^{7+} ion was confined in a Penning trap and its motional frequencies were measured for accurate calibration of the trap's magnetic field. A superimposed B-field inhomogeneity serves for determination of the electron´s spin direction [2]. From a measurement of the induced spin flip frequency we derived the g-factor to g=2.000 047 025 4 (15)(44), where the first error is our combined statistical and systematical error, while the second one reflects the uncertainty of the electron´s mass [3]. The result agrees within the limits of error to a theoretical calculation: g_{theo}=2.000 047 020 2 (6) [4].

Attempts to reduce the experimental uncertainty have led to a new method of detecting the cyclotron resonance of the stored ion: An additional radio-frequency field at the difference of the axial and cyclotron oscillation frequencies leads to coupling of the two motional modes and a splitting of the ion´s axial resonance into two components. From a measurement of the split frequency the cyclotron frequency can be determined. Compared to our previous method of direct excitation of the cyclotron mode, now the ion's radial energy is much smaller and reduces the linewidth of the g-factor resonance. Test measurements have demonstrated that this method has the potential for further improvement in accuracy [5].

Preparations have started to extend the experiments to hydrogen-like ions with larger values of Z, particularly for Ca^{19+}. Extension to heavier masses, however, is limited by our method of detecting induced electron spin flips. It relies on the observation of small frequency differences in the ion´s axial oscillation. For Ca^{19+} it would require detection of 0.2 Hz frequency changes in a total oscillation frequency of 370 kHz. This is below the present limit of sensitivity. Therefore a new method has been developed which determines phase differences between the axial oscillation frequencies [6]. The present limit of sensitivity corresponds to a frequency difference of 0.09 Hz and thus is sufficient for the planned experiments on Ca^{19+} (fig. 1). Further improvements may increase the sensitivity to a level where g-factor experiments on single protons are possible. Future plans to perform similar experiments on single stored antiprotons may represent a test of CPT invariance [7].

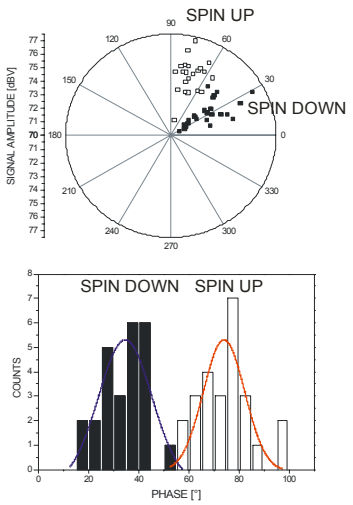

Figure 1: Phase measurement of the axial oscillation frequencies of a single stored ion for the two electron spin directions. Measurement time is 1 s (from [6]).

At the HITRAP facility preparations are under way to extract hydrogen-like ions of high Z, particularly U^{91+}, from the ESR storage ring, to decelerate them to low energies, to capture and cool them in a cooler Penning trap, and to confine them in a Penning trap for g-factor determinations on heavy highly charged ions. Simulations have been carried out for electron and positron cooling of U^{91+} which indicate that low ion energies can be obtained without significant particle loss by recombination or annihilation [8].

We acknowledge financial support by the European Union (Network HITRAP HPRI-CT-2001-50036) and the BMBF (Project 06MZ180). J.A. gratefully acknowledges a Marie-Curie fellowship.

References

[1] H. Häffner et al., Phys. Rev. Lett. **85**, 5308 (2000)

[2] G. Werth et al., Adv. At. Mol. Phys. **48**, 191 (2002)

[3] J. Verdú et al., Phys. Rev. Lett. **92**, 093002 (2004)

[4] V.A. Yerokhin et al., Phys. Rev. Lett. **89**, 143001 (2002)

[5] J. Verdú et al., Physica Scripta **T112**, 68 (2004)

[6] S. Stahl et al., submitted to J. Phys. B

[7] W. Quint et al., Nucl. Instr. Meth. B **214**, 207 (2004)

[8] J. Bernard et al., Nucl. Instr. Meth. A **532**, 224 (2004)

Double Ionization of He by Proton Impact

D. Fischer[1], R. Moshammer[1], A. Dorn[1], J. R. Crespo López-Urrutia[1], B. Feuerstein[1], C. Höhr[1], C. D. Schröter[1], S. Hagmann[2,4], H. Kollmus[2], R. Mann[2], B. Bapat[3], J. Ullrich[1]

[1]MPIK-Heidelberg, [2]GSI Darmstadt, [3]Ahmedabad India, [4]Uni-Frankfurt

Double ionization of helium by charged particle impact belongs to the most simple and therefore fundamental, unsolved dynamical many-electron problems in atomic physics. At medium to small perturbations (Z/v < 1; Z, v projectile charge and velocity) mainly two mechanisms contribute to the double ionization cross section: First, one electron can be ionized directly by the interaction with the projectile, and the second one is ejected due to the rearrangement of the remaining target ion. Second, the target electrons can be emitted subsequently by two independent interactions with the projectile. These two contributions can essentially be assigned to first and second order amplitudes in a perturbative Born expansion. Since the First Born Approximation (FBA) is independent of the sign of the projectile charge, in numerous previous studies the interest was focussed on the projectile charge-sign dependence of the ionization process by exploring the total double ionization cross sections. By comparing the results for electron and positron respectively proton and antiproton impact, differences have been observed which were explained by an interference between first and second order contributions (for details see [1]).

In the present contribution, we report on the first experimental fully differential cross sections (FDCS) for double ionization by positively charged particle impact [2]. The experiment was performed using a multi-electron recoil-ion momentum spectrometer ("reaction microscope"), which has been described in detail elsewhere [3]. A beam of protons was used as projectiles, which was provided by the Tandem accelerator of the MPI-K. An intermediate projectile velocity (15.5 a.u. i.e. 6 MeV) was chosen, since in this range a strong charge-sign dependence has been observed in total cross section measurements. The experimental cross sections were compared to previous results of electron impact double ionization [4] for a similar velocity regime (12 a.u., i.e. 2 keV).

In figure 1, fully differential cross sections for proton (a) and for electron impact (b) are shown. A coplanar geometry is chosen, i.e. the momentum vectors of all particles are in the same plane, the so called scattering plane. The density plots represent the angular distribution of the two outgoing electrons with respect to the projectile beam direction for a momentum transfer to the target system of 0.8-1.5 a.u. and for an equal sharing of the excess energy ($\Delta E_{e1,e2}$ < 2.5 eV). For these conditions the angle of the momentum transfer vector ranges from 60 to 70 degrees, which is denoted by the thick bar in the centre of the plots.

This representation elucidates some general properties of the FBA which are independent of the target description: The FBA and the experimental data both feature a four peak-structure, which is a consequence of selection rules in a dipole approximation, prohibiting emission along the broken lines (for details see [2, 4]). Moreover, since for an equal energy sharing the two electrons are indistinguishable, no emission along the diagonal line (lower left to upper right) occurs and the spectra are mirror-symmetrical along this line making the two peaks in the upper left equivalent to those in the lower right. In addition, FBA results have to be symmetric with respect to the momentum transfer direction. The corresponding symmetry axis is shown as a solid line in the graphs. Here a clear difference for electron and proton impact emerges. Whereas for proton impact the symmetry enforced by the FBA is closely fulfilled, for electron impact a strong asymmetry appears.

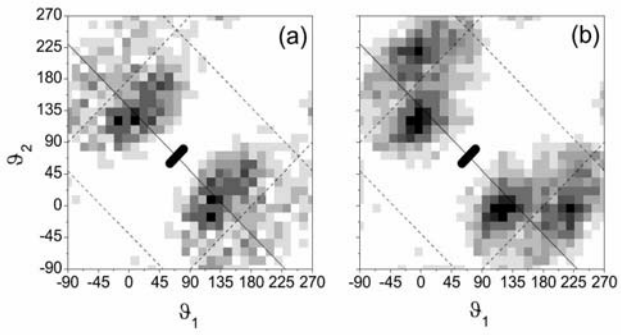

Figure1: *Angular distribution of the ejected electrons (ϑ_1, ϑ_2: polar angle with respect to the forward beam direction) in coplanar geometry for proton (a) and electron (b) impact (from [2]).*

In the framework of the Born theory, any asymmetry as observed for electron impact double ionization has to be assigned to higher order contributions, which are not present for positively charged particle impact. However, it is surprising that the higher order terms, which evidently result for negatively charged particle impact in a significant contribution, play a minor role for positively charged particle impact. A similar behaviour has already been observed for the total cross sections [1]. The cancellation of the higher order terms not only for the integrated cross section, but also for the fully differential data, would be an indication that, in general, all contributions beyond the first Born approximation are of less importance in collisions with positively charged projectiles.

In order to rule out the projectile mass dependence, further experiments for antiproton impact double ionization are planned. These experiments can be performed at the planned antiproton storage ring at GSI, where due to the high beam luminosity data with a unprecedented statistical quality will be obtained.

References

[1] J. H. McGuire, Phys. Rev. Lett. 49, 1135 (1982)
[2] D. Fischer, et al., Phys. Rev. Lett. 90, 243201 (2003)
[3] R. Moshammer, et al., Nucl. Instr. Methods Phys. Res. B 108, 425 (1996)
[4] A. Dorn, et al., Phys. Rev. Lett. 86, 3755 (2001)

State-selective x-ray study of the enhancement effect in recombination of U^{92+} bare ions with cooling electrons

M. Pajek[1], Th. Stöhlker[2,3], D. Banaś[1], S. Boehm[4], F. Bosch[2], C. Brandau[2,4], M. Czarnota[1], S. Chatterjee[2], J.-Cl. Dousse[5], A. Gumberidze[2,3], S. Hagmann[2], C. Kozhuharov[2], A. Müller[4], R. Reuschl[2,3], E. W. Schmidt[4], D. Sierpowski[6], U. Spillmann[2,3], J. Szlachetko[1,5], S. Tashenov[2,3], S. Trotsenko[2], P. Verma[2], M. Wałek[1], A. Warczak[6], and A. Wilk[6]

[1]Institute of Physics, Świętokrzyska Academy, Kielce, Poland; [2]Gesellschaft für Schwerionenforschung, Darmstadt, Germany; [3]Institut für Kernphysik, Universität Frankfurt, Germany; [4]Institut für Kernphysik, Justus-Liebig Universität, Giessen, Germany; [5]Department of Physics, University of Fribourg, Switzerland; [6]Institute of Physics, Jagiellonian University, Cracow, Poland

The recombination experiments performed so far show that the measured recombination rates for the RR process agree with the theoretical predictions only for higher relative energies exceeding transverse electron beam temperature $kT_\perp$, while for the lower energies, below the longitudinal temperature $kT_\parallel$, a substantial increase of the measured rates with respect of the RR predictions is observed. This, so-called, "enhancement" effect, first observed at the dense electron target experiment at the GSI [1], was well evidenced for a number of experiments performed in ion storage rings using different ions, up to bare U^{92+} [2].

In the recombination experiments performed up to now the recombination events were detected with a particle detector counting the recombined ions separated in the bending magnet of the ring. Such a technique, when applied to the recombination experiment at zero relative energy, i.e. the cooling condition, is thus not state-selective and gives no information on the ionic final state of the ion. On the other hand, in the recombination experiments performed earlier in the electron cooler of the ESR storage ring with U^{92+} ions the x-rays from RR were detected, demonstrating thus a possibility to perform the state-selective measurements of RR rates [3].

The first state-selective x-ray recombination experiment aiming to explain the the enhancement effect has been performed at the ESR storage ring in September 2004. In this experiment the uranium ions accelerated in the UNILAC/SIS complex, which were stripped to U^{92+} and then stored and decelerated in the ESR storage ring to an energy of 23 MeV/amu, were used. The x-rays emitted from recombination process between ions and electrons in the electron cooler, for several fixed relative energies, were measured by two germanium detectors placed nearly at 0° and 180° with respect to the ion beam direction. This allowed to measure the photons originating from radiative recombination to low n-states, namely K-RR, L-RR, as well as the Lyman and Balmer x-ray photons from radiative cascades following a recombination to high n-states. From the K-RR and L-RR intensities recombination rates for $1s_{1/2}$, $2s_{1/2}$, $2p_{1/2}$ and $2p_{3/2}$ can be obtained in a state-selective way. Moreover, the intensities of the Lyman and Balmer x-rays, originate mainly from capture into highly-excited states and subsequent development of the deexcitation cascades in a recombined ion, are a sensitive tool for studying of the recombination processes for a wide range of states, including the Rydberg states. In the first part of the experiment performed a dependence of the recombination enhancement on the electron detuning energy was investigated by selecting one value of B-field and measuring the recombination rates for six off-cooling electron cooler voltage settings, corresponding to the relative electron energies of about 69 meV, 190 meV and 930 meV, with the highest relative energy measurement (about 1 eV) for a determination of the transverse electron beam temperature. The measurements were performed by changing the effective cooler voltage by modifying the voltage of cooler drift tubes with a time-pattern shown in Fig 1.

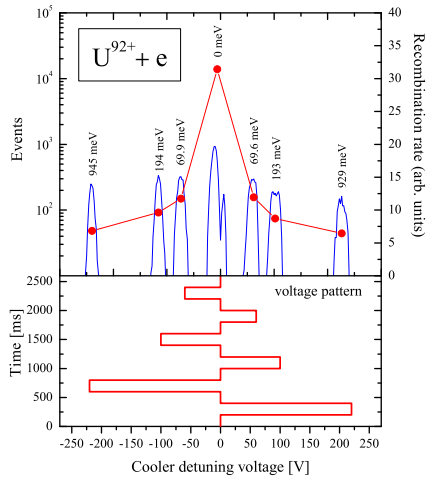

Figure 1: The radiative recombination K-RR events measured for the cooler detuning voltage pattern shown in the lower panel. The measured recombination rate for the K-shell is also shown in the upper panel (the data are preliminary).

The measured dependence of the radiative recombination rate on the relative electron energies, shown in Fig. 1 for the K-RR case, will be interpreted (work in progress) in terms of the theoretical calculations of the radiative recombination effect. In particular, a role of the recombination to high Rydberg states for the enhancement effect as well as an influence of the relativistic effects on the angular distributions of photons will be addressed.

References

[1] A. Müller et al., Phys. Scripta T37, 62 (1991).
[2] W. Shi et al., Eur. Phys. J. D 15, 145-154 (2001)
[3] A. Gumberidze et al., Phys. Rev. Lett. 92, 203004-1 (2004)

Charge state dependence of vacancy transfer in heavy-ion heavy-atom collisions

P. Verma[1, 3, 4], P.H. Mokler[1, 2], A. Bräuning-Demian[1], H. Bräuning[2], E. Berdermann[1], S. Chatterjee[1], A. Gumberidze[1], S. Hagmann[5], C. Kozhuharov[1], A. Orsic-Muthig[1], R. Reuschl[5], M. Schöffler[5], U. Spillmann[1], Th. Stöhlker[1], Z. Stachura[6], S. Tashenov[1] and M.A. Wahab[3].

[1]GSI Darmstadt, [2]University Giessen, [3]JMI (India), [4] Vaish College (India), [5]University Frankfurt, [6]IFJ Krakow (Poland)

Heavy-ion heavy-atom collisions with highly charged projectiles at moderate collision velocities give access to couplings in the inner-most shells of transiently formed superheavy quasimolecules and, hence, also to the region of supercritical fields [1,2 and references therein].

The electron/vacancy transfer in inner shells of superheavy quasimolecules is elucidated by the charge state (q) evolution and charge exchange cross sections of relativistic heavy ions penetrating through very thin solid foils [cf. 3] as well as by corresponding x-ray emission cross sections. Thin Au targets of 21 to 225 μg/cm^2 thicknesses were bombarded by a SIS beam of 70 MeV/u Bi^{q+} [77≤q≤82]. For the investigated system the adiabaticity factor η for the K-shells [$\eta = (v/u)^2$] ≤ 0.5 and hence, the inner shell vacancy transfer in close collisions can be considered within the quasi-molecular picture.

The emerging projectile charge states were analyzed by the magnetic spectrometer in Cave A and detected by a one-dimensional position-sensitive CVD-diamond detector [4]. The emitted x-rays were detected by two in-plane intrinsic Ge detectors.

Fig.1a shows two examples of "composite" charge state distributions [2] obtained for Bi^{82+}-ions incident on Au targets (21 μg/cm^2 and 225 μg/cm^2). The charge state fractions $f_q = (N^{q+}/N_{tot})$ for incoming Bi^{82+}-ions are shown, as function of the Au target thicknesses, in Fig.1b (N^{q+} is the number of projectiles for a particular charge state q+ and N_{tot} is the total number of projectiles). From the decrease of the Bi^{82+}-fraction f_{82} with target thickness the total electron capture cross section is deduced to be in the order of 3.10^{-18} cm^2 [2]. This value is in agreement with estimates using the semi-empirical non-relativistic scaling formula from ref. [5]. In distant collisions, electron capture into outer shells prevails. For Bi^{82+}-ions carrying a projectile K vacancy, this yields to an enhancement of the projectile K x-ray emission. From this we obtained a corresponding capture cross section which concurs with the above value and indicates a predominant electron capture at collision distances around 12600 fm.

For collisions with Bi^{82+} projectiles also the Au K x-ray emission increases substantially. This is explained by the K-K vacancy sharing in the collision molecules. From the increase of the Au K x-ray emission we deduced that the sharing region is located, in close collisions, at around 2300 fm.

Fig.2 shows a diabatic correlation diagram for the neighbouring Pb-Pb collision system [6]. The above given estimates for the interaction distance for electron capture and the coupling distance for K-K vacancy sharing conform to the calculated SCF-DFS multi-electron level diagram. The capture distance concurs with the region where the atomic levels turn towards molecular ones, whereas the K-K sharing takes place where the quasimoleular 1sσ and 2pσ levels start to diverge towards the united atom system.

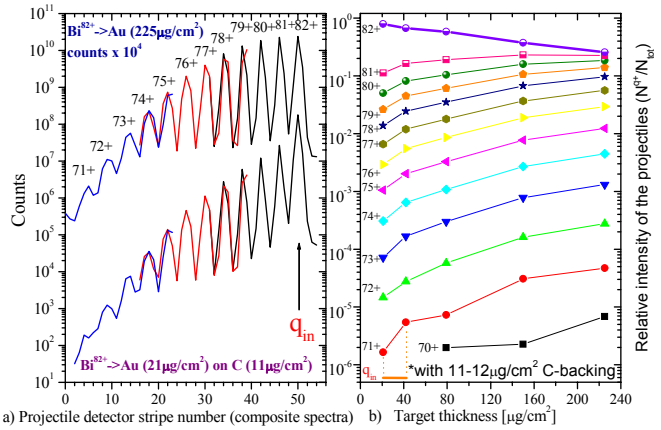

Fig.1a Projectile charge state distribution for Bi^{82+} on 21 μg/cm^2 and 225 μg/cm^2 Au targets

Fig.1b Charge state fraction f_q for incoming Bi^{82+}-ions as function of Au target thickness.

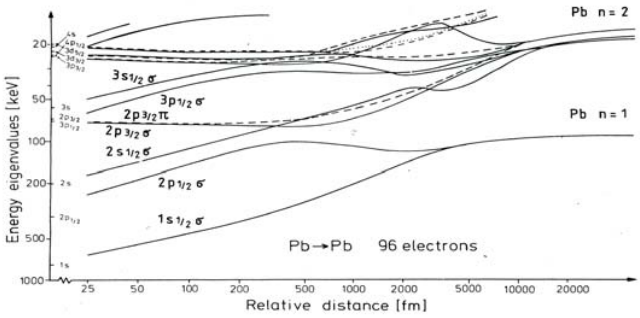

Fig.2 Diabatic correlation diagram for a Pb-Pb collision system [6].

References:

[1] P.H. Mokler et al., GSI Scientific Report'03, p 105.

[2] P. Verma et al., NIM B (2005), in print.

[3] S. Datz et al., Phys. Rev. A 2 (1970) 430.

[4] A. Braeuning-Demian et al., in this report.

[5] A.S. Schlachter et al., Phys. Rev. A 27 (1983) 3372.

[6] M. Mann et al., J. Phys. B 15 (1982) 4199.

Gas-Solid Difference in Mean Charge and Stopping Force of Uranium Ions

A. Fettouhi[1,2], M. Portillo[1,3], H. Ogawa[1,4], H. Geissel[1,2], C. Scheidenberger[1,2], H. Weick[1,2], K.-H. Behr[1], F. Becker[1], D. Boutin[1], A. Brünle[1], K. H. Burkard[1], K. Dermati[1], D. Henras[1], B. Kindler[1], R. K. Knöbel[2], J. Kurcewicz[5], W. Kurcewicz[5], J. Kurpeta[5], Yu. Litvinov[1,2], R. J. Liversay[6], B. Lommel[1], D. J. Morrissey[3], G. Münzenberg[1], J. A. Nolen[7], N. Sakamoto[4], J. Stadlmann[1], J. Steiner[1], H. Tsuchida[4], M. Winkler[1], and N. Yao[1,2]

[1] *Gesellschaft für Schwerionenforschung, Darmstadt, Germany*; [2] *II. Physikalisches Institut, Justus-Liebig-Universität Gießen, Gießen, Germany*; [3] *National Superconducting Cyclotron Laboratory, Michigan State University, East Lansing, MI, USA*; [4] *Department of Physics, Nara Women's University, Nara, Japan*; [5] *Institute of Experimental Physics, Warsaw University, Warsaw, Poland*; [6] *Colorado School of Mines, Golden, CO, USA*; [7] *Argonne National Laboratory, Argonne, IL, USA*

The gas-solid effect in the stopping power was discovered over 20 years ago [1] at beam energies varying from 1 to 10 MeV/u using the UNILAC at GSI Darmstadt. Later similar experiments in Orsay and with the LISE spectrometer at GANIL, with 22 MeV/u uranium ions, were performed and verified this effect. The gas-solid effect for partially ionized projectiles is caused by a higher frequency of those collisions, which lead to projectile excitation and charge exchange, in solids compared to gases. This results in a higher mean charge inside solids due to lifetimes of excited states which are longer than the time between collisions.

At the Fragment Separator at GSI we have measured charge state distributions (CSDs) and energy losses of uranium ions in gases and solids at 58 MeV/u. A gas-cell target with N_2, Ne, Ar, Kr, Xe and ethylene and solid targets of Be, C, Al, Ti, Cu, Ag, Au and polypropylene were used. The charge-state distribution and the energy loss were measured by analysis of the magnetic rigidity in focal plane of the FRS with a position sensitive detector.

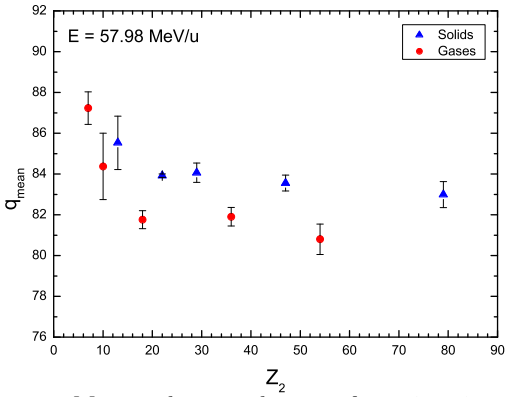

Figure 1: Measured mean charges of uranium ions at 58 MeV/u as a function of the atomic number of the target.

Figure 1 shows the preliminary results of the mean charge (at equilibrium) of uranium ions in the different materials. The mean charge in the gases is about 2 % lower than in the solids. The corresponding preliminary stopping cross sections are shown in figure 2. For light targets higher values are observed in solids whereas for the heavier targets the difference is within the experimental uncertainties. The uranium ion has on average its K-shell completely and its L-shell almost completely filled. Bohr's

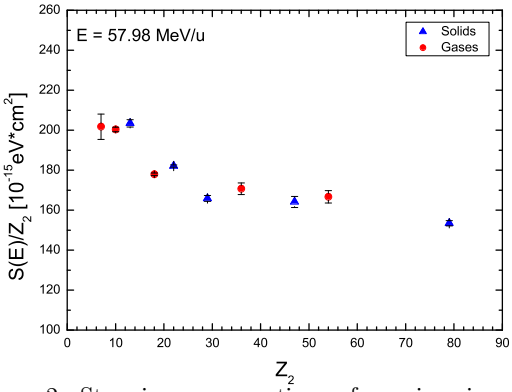

Figure 2: Stopping cross sections of uranium ions at 58 MeV/u as a function of the atomic number of the target.

$\kappa = 2Z_1 v_0/v$ parameter [3] is roughly 14.6 at this energy. In this region a classical orbit picture may be used [3]. The L-shell radius of uranium is $a_L = a_0/23 \simeq 0.025$Å, beyond a screening radius ($a_{sc} \simeq 0.012$Å) based on Thomas-Fermi theory [4] can be applied. The smallest possible diameter is roughly $b = 2Z_1 e^2/mv^2 \simeq 0.046$Å, then most collisions happen for $b > a_L$ and the stopping force is expected to scale like q_1^2.

A 2% gas-solid effect in mean charge should then yield about 4% gas-solid effect in the stopping force. A detailed investigation of the error of the target thickness is on the way which presents the main contribution to the uncertainty of the measured stopping force.

References

[1] H. Geissel *et al.*, Phys. Lett. A 99 (1983) 77.

[2] R. Bimbot *et al.*, Nucl. Instr. and Meth. B 107 (1991) 9.

[3] N. Bohr, K. Dan. Vidensk. Selsk., Mat. Fys. Medd. 18, 71 (1948).

[4] P. Sigmund, Phys. Rev. A **56** (1997) 3781.

Coulomb fragmentation of CO in collisions with fast highly charged Xe-ions

B. Siegmann*, U. Werner* and R. Mann†

*Universität Bielefeld, Fakultät für Physik, Universitätsstr. 25, D-33615 Bielefeld, Germany; †Gesellschaft für Schwerionenforschung (GSI), D-64291 Darmstadt, Germany

We studied the multiple ionization and fragmentation of CO in collisions with 3.6MeV/u Xe^{21+} and Xe^{38+}-ions provided by the UNILAC at GSI using a position- and time-sensitive multi-particle detector [1] which allows the coincident measurement of the momenta of correlated fragment ions. If all fragments from a particular fragmentation are detected, a kinematically complete study of the molecular break-up process is possible [2, 3]. In the present experiment we observed complete fragmentations into $C^{p+}+O^{q+}$ with a total charge $p+q$ of at least up to 12, and the kinetic energy release (KER) and orientation of the molecule axis could be analyzed for $p+q \leq 9$.

At low degrees of ionization several potential curves of the formed molecular ion have a non-coulombic shape and the measured KER spectra show some projectile dependend structures (Fig. 1) due to different electronic excitations. At higher degrees of ionization the potential curves behave mostly coulombic and the KER spectra have a simple shape, which may be approximately described by the position of the maximum and the width of the distribution. In collisions with fast highly charged MeV/u projectiles the most probable kinetic energy of the two fragments is (for q>3) quite well described by the Coulomb explosion (CE) model while the measured width of the distributions is much larger than predicted by this simple model (Fig. 2). We therefore developed a more elaborate model, the Average Bunch Statistical (ABS) model, of Coulomb fragmentation, which is based on a statistical description of the individual potential energy curves of the molecular ion[4]. In this model the manifold of potential curves is approximated by an average bunch of curves around the screened Coulomb potential

$$V_{AB}^{0} = \frac{Z_A Z_B}{R}\zeta(R) + \frac{q_1 q_2}{R}(1-\zeta(R)) \qquad (1)$$

where $\zeta(R) = e^{-r/\alpha_B}$ is the Bohr screening function.

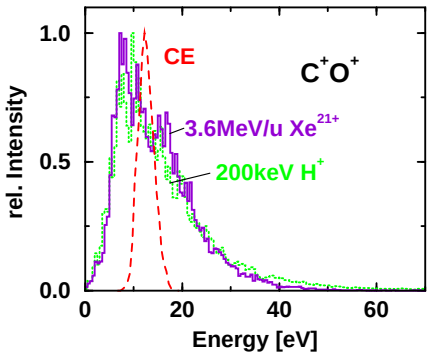

Figure 1: Total kinetic energy distribution of coincident $C^+ + O^+$ fragment ions in collisions with 3.6MeV/u Xe^{21+} (brown) and 200keV He^+-projectiles (green). The dashed line is the prediction of a point charge CE-model.

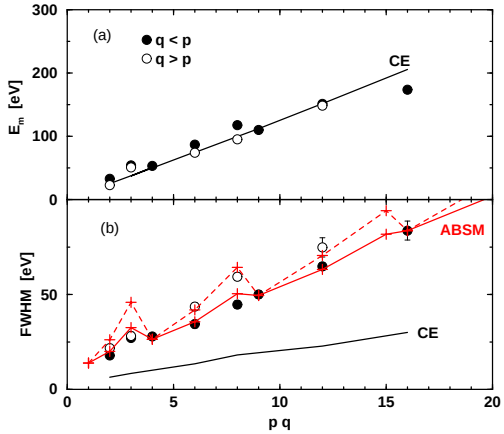

Figure 2: Most probable kinetic energy (a) and width (FWHM) (b) of the $C^{p+} + O^{q+}$ KER distributions as a function of p·q from collisions with 3.6 MeV/u Xe^{21+}.

The final width W of the observed KER distribution is caused by two contributions. The first contribution W_c is the width associated with each individual potential curve which amounts only to a small fraction of the total width. The main contribution comes from the spreading width W_{sp} which describes the spread of the potential curves in the bunch. Our analysis [5] shows that it may be approximated as

$$W_{sp} = \tilde{V}_{AB}(R_e) + V_{AB}^{(2)}(R_e) \qquad (2)$$

where $\tilde{V}_{AB}$ is the contribution of the monopole–quadrupole interaction of ions A and B and $V_{AB}^{(2)}$ is the contribution of the dispersion interaction. The model contains two parameters which were fitted to the measured energy distributions. The calculated widths are shown in Fig. 2 connected by the red lines. Evidently, for fast HCI impact the model calculations can satisfactorily reproduce not only the position of the experimental maximum but also the width of the KER distribution.

This work was supported by the Deutsche Forschungsgemeinschaft (DFG) in the project “Strahlungswechselwirkungen”.

References

[1] J. Becker, K. Beckord, U. Werner and H.O. Lutz, Nucl. Instrum. Methods **A 337**, 409 (1994).

[2] U. Werner, K. Beckord, J. Becker, and H.O. Lutz, Phys. Rev. Lett. **74**, 1962 (1995).

[3] B. Siegmann U. Werner, H.O. Lutz, and R. Mann, J. Phy. B **35**, 3755 (2002)

[4] B. Siegmann, U. Werner, R. Mann, N.M. Kabachnik, and H.O. Lutz, Phys. Rev. **A62**, 022718 (2000).

[5] U. Werner, B. Siegmann, R. Mann, N.M. Kabachnik, and H.O. Lutz, Physica Scripta. **T92**, 244 (2001).

Highly-charged ions at rest: the status of the HITRAP project

J. Alonso [1], W. Barth [2], A. Bechtold [3], T. Beier [2], K. Blaum [1], M. Block [2], G. Bollen [4], L. Dahl [2], S. Djekic [1], P. Forck [2], G. Gruber [2], F. Herfurth [2], C. Kitegi [3], H.-J. Kluge [2], C. Kozhuharov [2], A. Krämer [2], S. Minaev [3], W. Quint [2], U. Ratzinger [3], H. Reich-Sprenger [2], D. Rodríguez [2], A. Schempp [3], S. Schwarz [4], S. Stahl [1], T. Valenzuela [1], J. Verdu [1], W. Vinzenz [2], M. Vogel [1], C. Weber [2], G. Werth [1]

[1]Univ. Mainz, [2]GSI, [3]Univ. Frankfurt, Germany; [4]NSCL/MSU, USA

HITRAP is a planned ion-trap facility for low-energy experiments with heavy, highly-charged ions at the ESR storage ring [1]. Ions up to U^{92+} at 4 MeV/u will be delivered by the ESR and decelerated in the HITRAP facility down to 6 keV/u by an IH structure followed by an RFQ structure (Fig. 1). Afterwards, the ions will be trapped and cooled down to cryogenic temperatures by electron and resistive cooling. From the cooler trap, they will be extracted and delivered to experiments. Further details can be found in the technical design report[2].

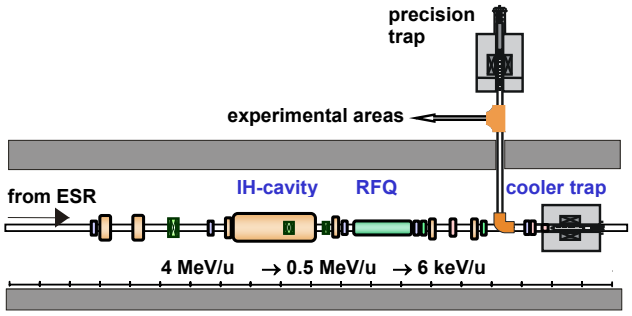

Fig. 1: Scheme of the HITRAP facility with decelerator tanks and cooler trap in the reinjection channel between ESR and SIS.

After the presentation of the technical design report in 2003 a committee of international experts rated the project very positively in January 2004. Many detailed design aspects of the IH structure, the low energy transfer line between RFQ and cooler trap and the cooler trap itself have been addressed and solved in 2004.

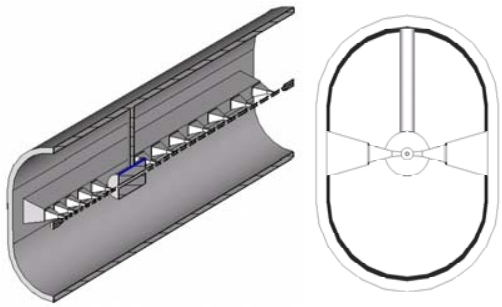

Fig. 2: Preliminary design of the IH-decelerator tank

For the IH structure the detailed calculations of the beam dynamics have been continued. A second harmonic prebuncher operating at 216 MHz has been included. A major improvement of transmission efficiency is expected from this device. Finally the ion optical calculations have been finished and the cavities for the IH structure have been conceived (Fig. 2).

In order to decrease the energy spread of the decelerated beam after the RFQ decelerator a debuncher has been included in calculations of the RFQ. This reduces the energy spread by about 30%. The radio -frequency power of the debuncher will be coupled out from the main radio-frequency amplifier for the RFQ only connected via a phase shifter since the electrical power needed for the rebuncher is only a few Watt.

To improve the transition between the different sections a more detailed ion beam simulation was performed. Single particles have been tracked through the prebunchers, the IH structure, the RFQ, and the low energy beamline until the injection into the cooler trap. A dedicated scheme of operation of the cooler trap would allow capturing all the four in the ESR circulating ion pulses consecutively without requiring a very long magnet. It seems also possible to rebunch the ions circulating in the ESR into one single bunch using the backup cavity bench. Both measures would improve the efficiency considerably compared to the originally foreseen efficiency. A design based on electrostatic lenses for the low energy beam line between RFQ and cooler trap has been simulated. It seems feasible and is considerably shorter than the previously foreseen beam line based on magnetic elements.

Detailed simulations are the prerequisites for the definition of the parameters of the cooler trap magnet. The emerging technique of cryogen-free superconducting magnets seems now feasible to use for the HITRAP cooler trap magnet. This has the advantage of much easier operation, an important issue since the access to the re-injection tunnel of the SIS will be limited. Different suitable trap electrode arrangements have been compared to select the optimal setup with regard to the maximal ion intensity, minimal cooling time and best vacuum conditions.

HITRAP will later be an integral and central part of the facility for low-energy experiments with antiprotons and heavy ions (FLAIR) within the future international accelerator facility for research with ions and antiprotons (FAIR). Therefore, all components of the setup are designed in a way that also antiprotons can be decelerated, accumulated and delivered to experiments at low energy.

We acknowledge financial support by the GSI F&E program, the EU (HPRI-CT-2001-50036) and the BMBF.

References

[1] W. Quint *et al.*, Hyp. Int. 132, 457 (2001).

[2] T. Beier *et al.*, HITRAP Technical Design Report, www.gsi.de/documents/DOC-2003-Dec-69-2.pdf.

The TSR electron target and preparations for the NESR electron target

Frank Sprenger[1], Michael Lestinsky[1], Dimitri Orlov[1], Udo Weigel[1], Andreas Wolf[1], Dirk Schwalm[1], Carsten Brandau[2], and Christophor Kozhuharov[2]

[1]Max-Planck-Institut für Kernphysik, Heidelberg, Germany; [2]GSI, Darmstadt, Germany

The future storage ring NESR will have an ultracold electron target for precise electron-ion collision studies. Within the SPARC collaboration [1] an *Electron Target Working Group* was formed towards the realization of this project. The storage ring TSR at the Max-Planck-Institute for Nuclear Physics in Heidelberg is equipped with such a dedicated electron target section [2]. The experiences which are gained at this set-up as well as the development of novel techniques provide significant contributions for the design of the NESR electron target.

At the TSR the phase-space cooling is separated from the target operation which improves the ion beam quality by continuous cooling and suppression of beam dragging. In the electron target, a cold electron beam is prepared by adiabatic magnetic expansion and adiabatic acceleration. Two electron sources are available, a high intensity thermionic cathode and a cryogenic photocathode [3]. For very low electron temperatures, the latter has been integrated into the electron target this year. In recent experiments, the excellent energy resolution in dielectronic and dissociative recombination measurements could be demonstrated. The temperatures (transverse and longitudinal with respect to the beam direction) of the electron beam are strongly anisotropic, being much colder in the longitudinal direction. For collision experiments, the energy resolution at low relative energies (at the TSR typically $< 10\,\mathrm{meV}$) is limited by the transverse temperature. At high energies the longitudinal temperature is dominating. In order to reduce the transverse temperature (initially given by the cathode temperature $k_BT_C \approx 110\,\mathrm{meV}$ for a thermionic source and $k_BT_C \approx 8\,\mathrm{meV}$ for a cryogenic source) adiabatic magnetic expansion is applied. The electrons are produced in a strong magnetic field ($B_{gun} \leq 3.5\,\mathrm{T}$). Subsequently the field is reduced to typically $B_{guide} = 0.04\,\mathrm{T}$ along the electron beam trajectory. The reduction of the temperature is given by the ratio of final and initial magnetic field. The longitudinal temperature is strongly reduced by the acceleration of the electrons to their final energy (typically 0.5–8 keV). The final longitudinal temperature is limited by potential energy relaxation during the acceleration. This effect is suppressed using a long acceleration section allowing for an adiabatic acceleration by properly shaping the potential over a length of 1.5 m. In the interaction section of the TSR electron target (length $\approx 1.5\,\mathrm{m}$), a precision solenoid magnet is used, which was designed to ensure minimal field angles of $B_\perp/B_0 < 10^{-4}$ necessary for an energy resolution $< 0.1\,\mathrm{meV}$.

With respect to high interaction energies, Fig. 1 shows dielectronic recombination spectra of helium-like $B^{3+}(1s^2)+e^- \rightarrow B^{2+}(1s\,2l\,3l')$ in the $\Delta N = 1$ region obtained with the electron cooler (thick line) and with the electron target (thin line). The strongly improved resolution obtained with the electron target is clearly visible. Longitudinal

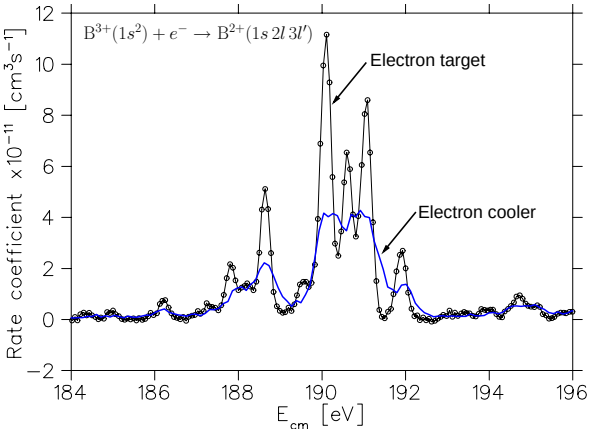

Figure 1: $\Delta N = 1$ resonances of helium-like B^{3+} measured with the TSR electron target and a continuously cooled beam (thin line) and the electron cooler only (thick line). In the latter experiment the cooler serves alternately as a cooler and as a target.

temperatures for target and cooler were derived from an isolated resonance at $E_{cm} = 161\,\mathrm{eV}$ and were found to be $k_BT_\parallel = 40\,\mu\mathrm{eV}$ and $k_BT_\parallel = 180\,\mu\mathrm{eV}$, respectively. At low relative energies, measurements have been performed among others on F^{6+}, Sc^{18+} and HD^+. For HD^+ a transverse temperature as low as 0.5 meV has been observed with the photocathode. With atomic ions, the measured transverse temperatures were found to be higher ($\gtrsim 1\,\mathrm{meV}$). The influence of the target electron beam on the energy of the stored ion beam has been studied with Si^{11+} using Schottky analysis. For an electron density ratio $n_e^{target}/n_e^{ecool} = 0.36$ – even at small cm energies of $E_{cm} \approx 10\,\mathrm{meV}$ – energy shifts ΔE_{cm} due to drag force effects were found to be $< 5 \cdot 10^{-5}\,\mathrm{eV}$.

Further investigations to optimize the properties of the electron target, e.g. studies of heating processes in the toroid sections, of the mutual influence of the cooling forces of cooler and target, and of the influence of the magnetic guiding field on the electron temperatures are currently being performed. The recent recombination studies at the TSR electron target show strong improvements with respect to precision and resolving power in electron-ion collision experiments and exemplify the potential of a dedicated electron target for novel and unique experiments with unsurpassed sensitivity at the future storage ring NESR.

References

[1] http://www.gsi.de/zukunftsprojekt/experimente/sparc/index_e.html.
[2] F. Sprenger, et al., NIM A **532** (2004), 289.
[3] D.A. Orlov, et al., NIM. A **532** (2004), 418.

An Imaging Forward Electron Spectrometer in the ESR

M.Nofal[1], S. Hagmann[1], Th. Stöhlker[2], Chr. Kozhuharov[1], J. Ullrich[3], R. Moshammer[3], R. Dörner[1], F. Bosch[2], H. Rothard[4], M. Steck[2], F. Nolden[2], B. Franczak[2], P.Beller[2], K. Becker[2], N. Lineva[2], A. Gumberidze[2], R. Reuschl[1], C. Brandau[2], S. Tachenov[2], U. Spillmann[2], R. Dubois[5]

[1]Inst.f. Kernphysik, Univ. Frankfurt, Germany; [2]GSI-Darmstadt,Germany, [3]Max Planck Inst. f. Kernphysik, Heidelberg, Germany, [4]CIRIL-GANIL,Caen, France [5]U.of Missouri, Rolla, Mo, USA

We present first 0^0 electron spectra taken with the ESR imaging forward electron spectrometer. The azimuthal distribution of the electron loss to continuum (ELC) Cusp electrons emitted by the projectile in the target zone is imaged onto the new 2D position sensitive detector

For studying the dynamics of fundamental atomic collision processes in the realm of relativistic collision velocities and strong perturbing fields an extended reaction microscope (ERM) has been built which consists of a standard longitudinal reaction microscope combined with an imaging forward electron spectrometer. The new instrument in the ESR will serve to measure complete differential cross sections, e.g. for the mechanism of atomic fragmentation (projectile and target Multiple Ionization MI), kinematically complete measurements of electron impact ionization of ions and the short wavelength limit of the electron nucleus-Bremsstrahlung process (BS).

The imaging forward electron spectrometer part of the ERM consists of a 60^0 dipole 900 mm downstream of the ESR jet target which deflects electrons with $\Delta\Theta \leq \pm 1.5^0$ around the beam axis from the coasting beam, followed by a large aperture quadrupole triplet and another 60^0 dipole. The new 2D position sensitive electron detector (PSD) is positioned downstream of the 2^{nd} dipole magnet behind momentum defining slits. The small deflection experienced by the coasting beam in the magnetic B-field of the first 60^0 dipole is compensated by two correction coils which are ramped tracking the 60^0 dipole field. Sample trajectories for electrons in the spectrometer are given in Fig.1.

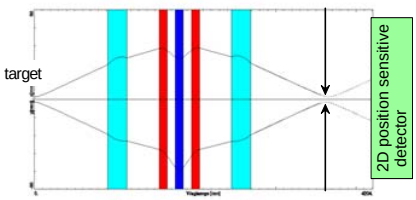

Fig.1 Trajectory of electrons in the spectrometer

The imaging forward electron spectrometer has been successfully tested previously in the ESR target zone with a Ge(i) detector in the focal plane (instead of the 2D electron detector which by itself is not energy sensitive) in order to assess its ability to separate electrons from background particles with the same momentum. In the 2^{nd} half of 2004 it has been equipped with a multihit capable 2D position sensitive electron detector replacing the Ge(i) detector.

In a first experiment with the 2D position sensitive electron detector we have measured forward electrons from Li-like 100AMeV U^{89+} + N_2 for electron energies between 16 keV and 280 keV, e.g. from well below the Cusp (at 53 keV) to beyond the Binary Encounter. The spectrometer is operated in a quasi multi-scaling mode: for each measurement cycle minimum and maximum momentum of electrons [p_{min}, p_{max}] to be transmitted from the target zone to the 2D electron detector (see Fig.2) are chosen. Then corresponding dipole B-field values B_{min} and $B_{max,}$, the quadrupole lens currents, the number of steps from B_{min} to B_{max} used to execute one cycle and the two correction coil currents are set.

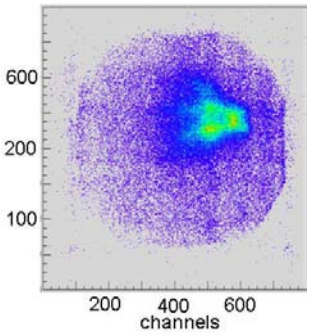

After each measurement for a pass-momentum p_n certain number of fillings of the ESR all spectrometer parameters are stepped to the next setting p_{n+1} in accordance with the procedure given above. This stepping is to be initiated manually every time before a new series of fillings of the ESR is requested.

Fig. 2 Image of electrons mapped onto 2D PSD; the active diameter is 80 mm; no coincidence condition is applied.

In Fig. 3 an electron loss to continuum ELC cusp spectrum measured for Li-like 98.2 AMeV $U^{89+}(1s^22s)$ + N_2 is shown; the electron spectrum was taken in coincidence with the single projectile electron loss channel U^{90+}. The spectrum is dominated by electrons ionized from the projectile into its low energy continuum by interactions with either the target nucleus or target electrons. These two contributing channels are currently not distinguishable but can be separated once the reaction microscope for analyzing the vector momenta of low energy electrons and recoil ions is implemented in the ESR as well. The currently observed width of the cusp is compatible with that expected from continuum momentum transfer during projectile 2s ionization. A detailed analysis of the coincident 2D electron images (providing the transverse momentum width) and comparison with images due to electron capture to the continuum ECC cusp is in progress.

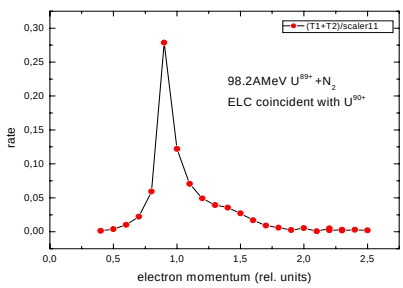

Fig. 3 ELC Cusp coincident with U^{90+} in 98.2 AMeV U^{89+} + N_2 collisions.

The FOCAL Project for Accurate X-Ray Spectroscopy

H.F. Beyer[1], Th. Stöhlker[1], D. Liesen[1], D. Banas[2], S. Chatterjee[1], D. Protić[3], K. Beckert[1], P. Beller[1], J. Bojowald[3], F. Bosch[1], W. Brüchle[1], E. Förster[4], B. Franzke[1], A. Gumberidze[1], S. Hagmann[1], J. Hoszowska[5], P. Indelicato[6], H.-J. Kluge[1], B. Kindler[1], Chr. Kozhuharov[1], B. Lommel[1], X. Ma[1], B. Manil[7], I. Mohos[3], A. Oršić-Muthig[1], F. Nolden[1], U. Popp[1], A. Simionovici[8], D. Sierpowski[2], U. Spillmann[1], Z. Stachura[2], M. Steck[1], S. Tachenov[1], M. Trassinelli[6], N. Trautmann[9], A. Warczak[2], O. Wehrhan[4], and E. Ziegler[5]

[1]GSI, Planckstraße 1, D-64291 Darmstadt, Germany; [2]Institute of Physics, Jagiellonian University, PL-30059 Cracow, Poland; [3]FZ Jülich, Institut für Kernphysik, Germany; [4]Inst. für Optik und Quantenelektronik, F. Schiller-Universität, D-07743 Jena, Germany; [5]ESRF, F-38043 Grenoble, France; [6] Lab. Kastler Brossel, Université P. et M. Curie, F-75252 Paris Cédex 05, France; [7]CIRIL-GANIL, rue Claude Bloche, F-14070, Caen, France; [8]Laboratoire de Sciences de la Terre, ENS, F-69007 Lyon, France; [9]Institut für Kernchemie, Universität Mainz, D-55128 Mainz, Germany

A system of two crystal spectrometers is presently being completed for accurate wavelength measurements of hard x rays emitted from heavy ions in flight. The motivation for this development is the measurement of the 1*s* Lamb shift in hydrogen-like heavy ions as a test of the QED in the strong-field domain. The present crystal optics, set up in the FOcusing Compensated Asymmetric Laue (FOCAL) geometry[1], overcome serious resolution limitations of previous experiments conducted with Ge(i) detectors. In a recent test experiment with a prototype of the FOCAL spectrometer installed at the gas jet of the ESR it was demonstrated that such an experiment is feasible. In order to make complete use of the Doppler-compensation capabilities inherently built into FOCAL it is necessary to operate *two* spectrometers in concert as schematically shown in figure 1.

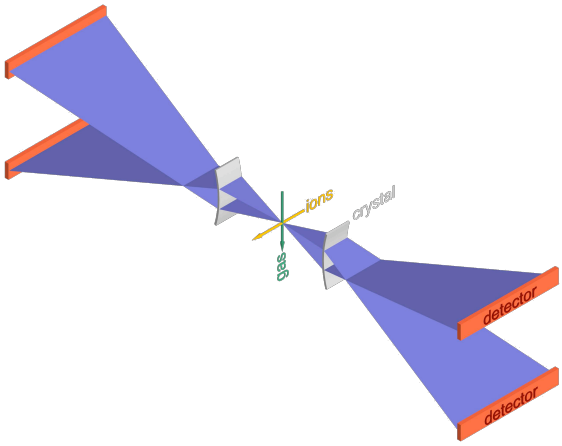

Figure 1: The twin crystal-spectrometer arrangement, Bi-FOCAL, at the gas jet of the ESR.

For calibration and alignment purposes, the x-ray spectra dispersed symmetrically in the vertical direction are recorded by step-scanning a conventional Germanium detector equipped with a narrow horizontal slit. In figure 2 we compare scanned spectra of a ^{169}Yb source with those obtained by a newly developed Germanium strip detector [2] covering an extended spectral region. The latter is superior in terms of measurement speed and low background mandatory for a production run.

During the last year extended tests of the spectrometer have been performed securing quantitatively spectral resolving

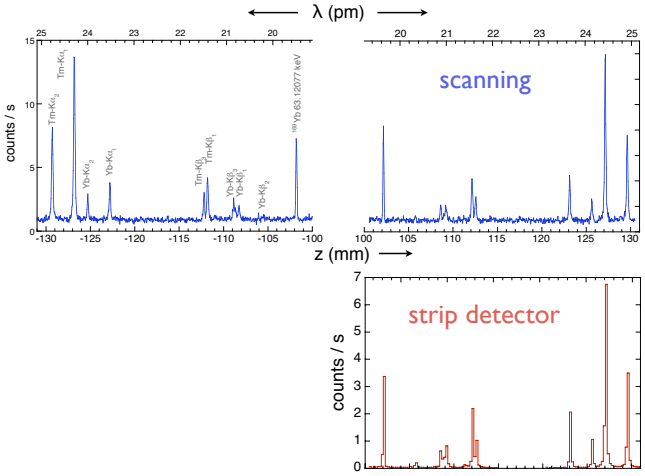

Figure 2: X-ray spectra of a ^{169}Yb source recorded by scanning a Ge(i) detector over a lower and upper portion along the dispersive (i.e. vertical) direction of the spectrometer or with the Ge strip detector.

power and efficiency predicted by numerical simulations. Detailed performance figures are summarized elsewhere [3]. The spectrometer mechanics have been redesigned to meet the requirements at the ESR gas jet for a convenient installation procedure. Most of the mechanical components are fabricated so that the final assembly and the test operation can start soon.

For the present application nearly perfect Silicon single crystals need to be bent cylindrically close to the limits where they start to break. We further refined our bending mechanism and our procedures for measuring the curvature. A new two dimensional position-sensitive strip detector fabricated at FZ Jülich is being tuned and optimized for starting operation as part of the FOCAL spectrometer.

Supported by a Marie Curie Fellowship of the European Community Programme IHP under contract number HPMT-CT-2000-00197.

References

[1] H. F. Beyer, Nucl. Instrum. Methods. A**400** (1997) 137.
[2] D. Protić *et al.* IEEE Trans. Instr. Meas. **48** (2001) 1048.
[3] H.F. Beyer *et al.*, Spectrochimica Acta **B 59** (2004) 1535.

Calorimetric Low Temperature Detectors for High Resolution X-Ray Spectroscopy on Stored Highly Stripped Heavy Ions

V. Andrianov [1], A. Bleile [1,2], P. Egelhof [1,2], O. Kiselev [2], A. Kiseleva [1], J. Kluge[1], S. Kraft-Bermuth [1,2], D. McCammon [3], H. J. Meier [1], J. P. Meier [1,2], C. Stahle [4], and T. Stöhlker[1]

[1]GSI Darmstadt, Germany; [2]Institut f. Physik, Univ. of Mainz, Germany; [3]Dept. of Physics, Univ. of Wisconsin, Madison, USA; [4]NASA/Goddard Space Flight Center, Greenbelt, USA

The precise determination of the Lamb shift in hydrogen-like heavy ions provides a sensitive test of quantum electrodynamics in very strong Coulomb fields, not accessible otherwise. For increasing accuracy on the 1s Lamb shift in $^{238}U^{91+}$ in measurements performed at the ESR, high resolving X-ray detectors for hard X-rays ($E \leq 100$ keV) are required to precisely determine the Lyman-α transition energies. As one option to replace the presently used conventional semiconductor detectors, the concept of calorimetric low temperature detectors was proposed [1], and consequently such a detector system, optimized for high resolution detection of hard X-rays, was developed and recently tested at the ESR under running conditions. In contrast to conventional semiconductor detectors, calorimetric low temperature detectors measure the temperature rise of an absorber due to the energy deposited by the incident X-ray. The potential advantage of this detection concept is due to a more complete detection of the deposited energy and a better counting statistics of the detected quanta (phonons). Therefore, such detectors promise a considerable improvement in energy resolution in combination with a still reasonable detection efficiency.

The detector modules for the present setup are designed on the basis of silicon microcalorimeters which were developed by the Goddard / Wisconsin groups for astrophysical applications. Each detector pixel consists of a silicon thermistor and of an X-ray absorber glued on top of it by means of an epoxy varnish. Thermistor arrays, consisting of 36 pixels each, are provided from the collaborating group from Goddard Space Flight Center. For the Lamb shift measurement, the experimental setup was optimized with respect to energy resolution and detection efficiency for hard X-rays at the experimental area of the storage ring ESR. The final detector concept foresees three calorimeter arrays, the active area of one pixel being about 0.5 – 1 mm^2. In order to reach sufficient photopeak efficiency, the absorber should be a high-Z material and have a volume of at least $V \geq 0.5$ mm^2 x 40 μm. To obtain a reasonable detection solid angle, the detector arrays have to be located as close as possible to the interaction zone at the internal target of the ESR. To realize this concept, a special ^{3}He/^{4}He-dilution refrigerator with a side arm which fits to the internal target geometry was designed. The cryostat is prepared to read out a total of 100 detector channels. The operating temperature of the detectors can be chosen between 50 mK and 100 mK.

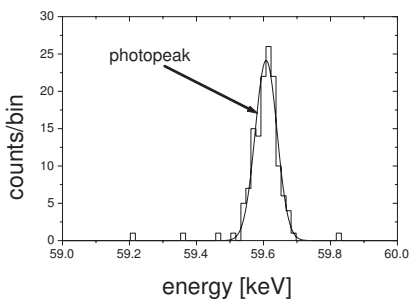

Fig. 1: Energy spectrum observed with a calorimetric low temperature detector with a 0.2 mm^2 x 47 μm Pb absorber for 59.6 keV photons. For the photopeak an energy resolution of $\Delta E = 65$ eV is obtained.

The detector performance was first tested with single detector pixels. The best results were obtained with Sn and Pb as absorber materials. The energy spectrum obtained for a detector with a 0.2 mm^2 x 47 μm Pb absorber for 59.6 keV photons, provided by an ^{241}Am source, is displayed in Fig. 1. For the photopeak, an energy resolution of $\Delta E = 65$ eV is obtained. This result may be compared to the theoretical limit of the energy resolution for a conventional semiconductor detector of about $\Delta E \approx 380$ eV for 60 keV photons.

As a further step in direction of setting up the full detector system, a prototype array, consisting of 8 pixels equipped with Sn and Pb absorbers with a total active area of 2.9 mm^2, was built and installed at the ESR, and was already subject to tests under realistic experimental conditions. The detector geometry and the performance obtained, again for 60 keV X-rays from an ^{241}Am source, is summarized in Table 1. No substantial change in performance was observed under ESR running conditions, i.e. with circulating beam and internal gas-jet operation.

Very recently, the detector performance was also tested with 60 keV Lyman-α X-rays produced by a 140 MeV/u ^{238}U beam interacting with a N_2 internal gas-jet target. The detector, covering a total solid angle of 1.9 x 10^{-5} sr, thus reaching an overall K_α detection efficiency of 2 x 10^{-7}, was positioned at $\theta_{lab} = 145°$. At present, data analysis is still in progress.

References

[1] P. Egelhof et al., NIM A **370** (1996) 263

pixel Nr.	absorber material	absorber mass, μg	active area, mm^2	ΔE, eV @ 60 keV
11	Pb	220	0.42	100
13	Sn	159	0.29	75
15	Pb	220	0.44	130
16	Sn	182	0.31	90
31	Pb	200	0.41	82
32	Sn	244	0.41	190
35	Sn	182	0.27	100
36	Pb	209	0.39	300

Table 1: Detector geometry and results of a performance test for an 8-pixel prototype array.

Two-Dimensional Microstrip Germanium Detector for X-Ray Spectroscopy of Highly-Charged Heavy Ions

D. Protić[1], T. Krings[1], I. Mohos[1], U. Spillmann[2] , Th. Stöhlker[2]

[1]IKP, FZ-Jülich, Germany; [2]GSI-Darmstadt, Germany

New possibilities are opened utilizing position-sensitive germanium detectors in the X-ray spectroscopy of highly charged heavy ions at GSI-Darmstadt [1]. The recent experiments revealed the need for two-dimensional strip detectors with their inherent advantages concerning spectroscopy and imaging capabilities as well as polarization sensitivity. Very recently a new method for producing position-sensitive structures on germanium detectors having amorphous Ge contacts (a-Ge contacts) has been presented [2, 3]. The method is based on the well established technique for manufacturing position-sensitive germanium and silicon detectors by means of photolithography and subsequent plasma etching of grooves by implanted contacts [4, 5]. Using this technique a one-dimensional 200 strip detector [6] and a 4x4 planar pixel detector [1], both made of high-purity germanium, were manufactured in the Laboratory for Semiconductor Detectors at IKP and successfully applied at GSI for the spectroscopy of atomic transitions in the hard X-ray regime above 15 keV and for polarization studies [1].

For the first prototype, a germanium diode (70 mm x 41 mm, 11 mm thick) with a boron implanted p^+-contact on the junction side and a blocking a-Ge-contact on the other side has been prepared. A 128 strip structure on an area of 32 mm x 56 mm with a pitch of 250 μm, surrounded by a guard-ring, was defined by means of photolithography on the implanted p^+-contact. On the a-Ge-contact only 48 strips with a pitch of 1167 μm, also surrounded by a guard-ring, were created using the same techniques as for the p^+-contact.

The detector is mounted in a cryostat (Fig. 1) which will enable any orientation of the detector with respect to a photon source. A view of the detector holder and the connection to the preamplifiers placed outside the vacuum system is shown in Fig. 2.

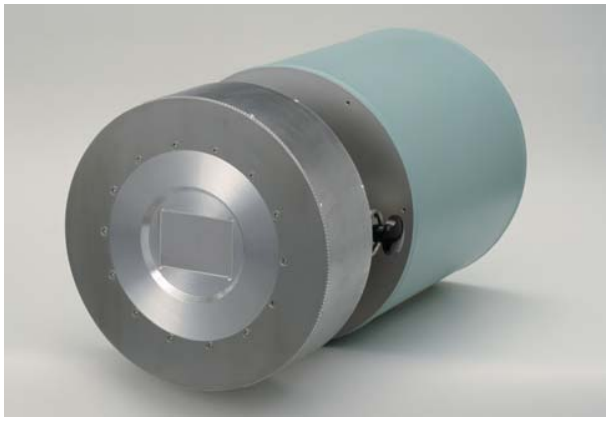

Fig. 1: *View of the detector system. The detector is placed behind a 0.5 mm thick Be-window. The LN_2-dewar allows operation of the detector in any orientation without LN_2 spillage even when the dewar is full.*

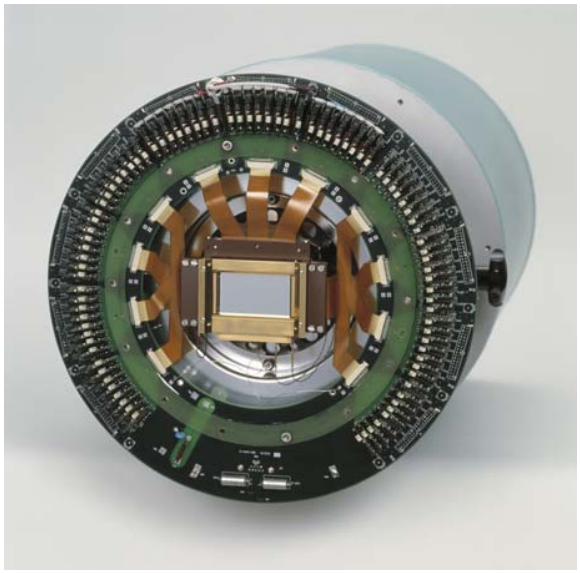

Fig. 2: View of the Ge-detector and one half of the preamplifiers with open cryostat cap.

In June 2004 the detector system was delivered to GSI. There it will be used to perform:

High resolution X-ray spectroscopy for precise tests of quantum electrodynamics (QED) in the heaviest one-and two-electron systems such as hydrogen- and helium-like uranium

Polarization studies for hard X-rays exploiting 3D capability of the detector and the Compton effect

References:

[1] Th. Stöhlker et al., "Applications of Position Sensitive Germanium Detectors for X-ray Spectroscopy of Highly-Charged Heavy Ions", NIM B 205, pp. 210-214, 2003

[2] D. Protić and T. Krings, "Detection characteristics of Ge detectors with microstructured amorphous Ge contacts", IEEE Trans. Nucl. Sci., vol. 51, pp. 1129-1133, June 2004.

[3] D. Protić and T. Krings, "Microstructures on Ge detectors with amorphous Ge contacts", IEEE Trans. Nucl. Sci., vol. 50, pp. 998-1000, August 2003.

[4] D. Protić and G. Riepe, "Thick silicon strip detectors", Nucl. Instrum. Methods, vol. 226, pp. 103-106, 1984.

[5] D. Protić and G. Riepe, "Position-sensitive germanium detectors", IEEE Trans. Nucl. Sci., vol. NS-32, pp. 553-555, February 1985.

[6] D. Protić et al., "A micro-strip germanium detector for position sensitive X-ray spectroscopy", IEEE Trans. Nucl. Sci., vol. 48, pp. 1048-1052, August 2001.

Digital processing of Ge-detector signals

M. Kajetanowicz[1], S. Samek[1], D. Sierpowski[1], Th. Stöhlker[2], A. Warczak[1], A. Wilk[1]

[1]Jagiellonian University, Krakow, Poland; [2]GSI Darmstadt, Germany

Nowadays, advanced experiments concerning investigation of atomic processes in heavy-ion atom collisions require simultaneous running of many complex solid state detectors, in particular for registration of x-ray photons [1], [2]. In order to simplify both, detectors signal processing and data acquisition a new electronic system for multi-channel read out of Ge strip detectors is developed. The read out is based on the continuous signal sampling. All the channels are sampled, digitized and the digital values are stored in the FIFO [First In First Out] memory. The sampling frequency is 64 MHz. The number of samples collected in the FIFO memory, related to a given trigger, is defined by the length of the user selectable time window. The length of the time window is in the range of 200 ns to 3.98 μs. The number of samples collected before and after the trigger is defined by the user. Only samples from channels which had the input signal above the threshold are sequentially read from the memory and sent to the VME module for further processing. The goal is to get, for all the channels, the energy information and the time information referred to the trigger stamp.

The read-out electronics is split into 16-channel boards. Each channel on the read-out board contains the input amplifier, the ADC [Analog to Digit Converter] and the FIFO memory. The logic controller on the board controls the operation of the input channels and the data transmission to the VME module. The boards are read sequentially. The digital data from all the boards are transmitted with one 50-way cable to the VME crate. Possible distance between the detector and the crate is up to 100 meters.

This new solution aims for placing all the front-end electronics on the detector or at a small distance (less than 1m) from that. The final solution depends on the available space. All the data will be transmitted out of the detector in the digital form with only one cable in the event by event mode. The data packets will be further on-line processed in the VME module and will be accessible to the user via the VME crate controller.

The main advantages of this new read out electronics are: reduced noise pick-up, low channel to channel cross talk, improved signal to noise ratio, high reliability, modular structure (easy to upgrade), fast on-line data processing.

In order to obtain, from the digitalized data stream, information on the energy and time of the detected photon, special algorithms have been developed and prepared. Recently, the first tests of the read-out board and the algorithms used were performed in Krakow.

First, as a testing input signal, the differentiated step voltage signal from a generator was used. The shape of such a signal is similar to the one of a Ge-detector. Signals were filtered and cleaned by the DSP algorithms [3] , [4].

Fig. 1 shows an example spectrum of the amplitude of the signal.

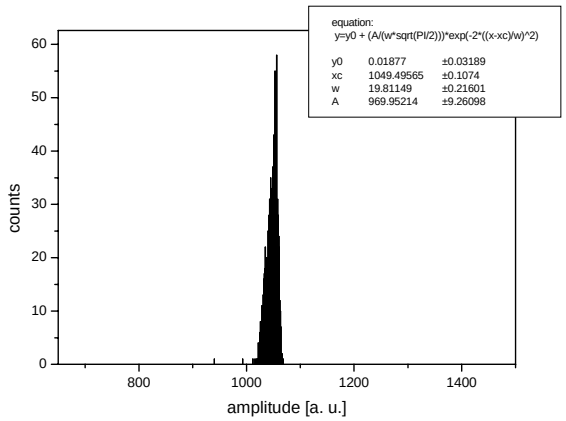

Figure 1. Amplitude spectrum

Here, one observes a good amplitude resolution of about 1.5%, apart from the rather high noise to signal ratio of about 5%.

Next, measurements of the time difference between trigger and signal were performed. In Fig. 2 an example of the time spectrum is shown.

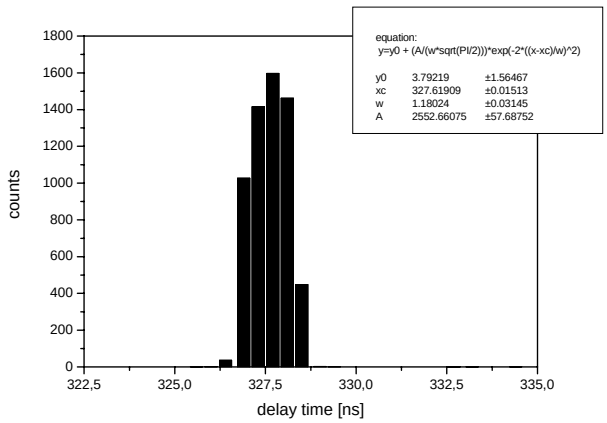

Figure 2. Time spectrum

The achieved very good time resolution is of about 1ns.

Additional tests with Ge detectors are in progress.

References

[1] Th. Stoehlker et al., Phys. Rev. Lett. 86, 983(2001)

[2] X. Ma et al., Phys Rev A68, 042712(2003)

[3] "Understanding Digital Signal Processing" Richard G. Lyons (Prentice Hall, 2004)

[4] "Digital Filters" R.W. Hamming (Prentice Hall, 1983)

Position sensitive CVD-diamond detector for intermediate energy heavy ions

A. Bräuning-Demian[1], E. Berdermann[1], P. Verma[1, 2, 3] and P.H. Mokler[1, 4]

[1]GSI Darmstadt, Germany; [2]Vaish College, India, [3]Jamia Millia Islamia, New Delhi, India, University Giessen, Germany

For charge dependent, coincident measurements a fast, large area detector with position resolution below 1 mm and high detection efficiency over large energy and intensities ranges is needed. Ion beams, from ESR and SIS 18, with energies between 10 MeV/u and 500 MeV/u and intensities between few times 10^4 part/s and 10^7 part/s must be detected. For most of the experiments the detector 'sees' the whole beam intensity. Especially for the heavier ions at lower energies, the energy deposition in the detector is tremendous: U^{92+} at 10 MeV/u loses all his kinetic energy in a 56 µm thick Diamond layer. The polycrystalline chemical vapour deposited diamond (CVD-diamond) emerged during the last years as the best solution for radiation hard detectors [1]. For the detection of highly charged ions at the focal plane of the magnetic spectrometer installed in cave A for atomic physics experiments a one dimensional position sensitive Diamond-based detector has been developed [2].

The detector has a 40 x 60 mm active area and is 200 µm thick. The position decoding is made by 32 vacuum deposited, thin gold strips, 2 mm wide with individual read-out. Previous measurements attested high detection performance for heavy ions of few hundred MeV/u [1]. The available information about the radiation hardness, detection efficiency and time resolution of CVD-detectors have been obtained with minimum ionizing particles (mip). The goal of the present measurements was to test the detector performance with highly charged heavy ions at intermediate energies (E_{ion} < 100 MeV/u). Due to the large amount of primary charge created by the incoming ions, polarization effects inside the Diamond can induce variations of the pulse height of signals which may finally end in losses of detection efficiency.

For these measurements a Bi^{81+} beam at 68.4 MeV/u have been used. The measurements have been performed using Au and C foils, with different thicknesses t (12 µg/cm^2 < t < 225 µg/cm^2) as target. To determine the detection efficiency of the Diamond detector, measurements of its total count rate have been performed and compared to the count rate of a SEcondary Electron TRAnsmission Monitor (SEETRAM) [3]. The configuration of the experimental arrangement is schematically presented in Fig.1. The Diamond detector was placed in the focal point, at the 14.5 deg. exit of the analysing magnet. After the interaction with the target, the emerging ion beam was separated in different charge states which were created in the interaction with the targets. The SEETRAM detector was installed at the zero deg. exit of the dipole and during the measurements has seen the whole beam intensity.

Fig. 2 presents the diamond detector pulse shape distribution obtained with the broad band preamplifiers DBA III developed at GSI [4]. The large separation between noise and real signals is remarkable and practically no real events are lost due to the later electronic level discrimination.

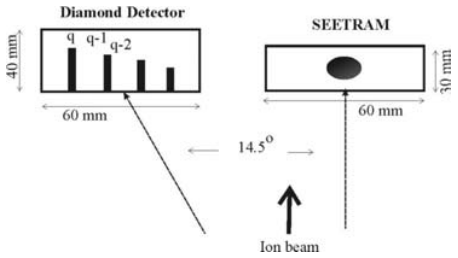

Fig 1: Schematics of the experimental set-up (cave A)

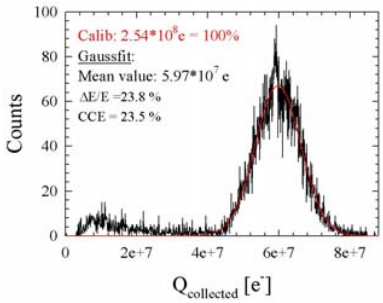

Fig. 2: Pulse shape distribution of the CVD-Detector

Fig. 3 shows the ratio of the detectors count rate to the number of ions per spill stored in SIS (Det_CR / I_spill). The real detection efficiency of both detectors is higher than the values indicated in this graph and is close to unity. The real beam intensity reaching the target is lower than the number of ions extracted from SIS due to the fact that, using the stripper foil placed behind the SIS special charge states for the projectile ions were bred but only one was selected. Therefore only a fraction of the extracted SIS beam reaches the target. However, assuming that the beam extraction from the SIS is constant (over 90% of the stored particles) one can use this number for normalization purposes.

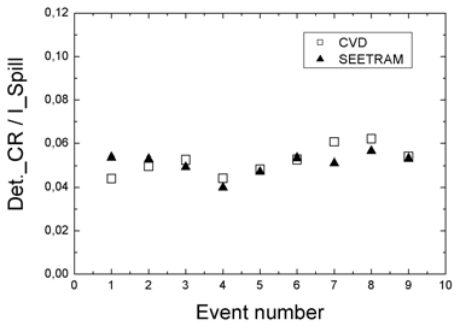

Fig.3 Detection efficiency of the CVD-detector compared to the SEETRAM detector.

References

[1] W. Adam et al.. Int. Conf. Rad. Eff., Florence 2000.

[2] S. Toleikis, Ph. D. Thesis, GSI Diss.2002-11.

[3] F.P. Hessberger, GSI report, GSI-85-11.

[4] P. Moritz et al. DIPAC III, Frascati (1997).

Recent results on the efficiency and the extraction times of the SHIPTRAP gas-filled stopping cell

S. Elisseev[1], M. Block[1], Z. Di[2], W.R. Plaß[2], Z. Wang[2], and the SHIPTRAP collaboration

[1]GSI, [2]Univ. Giessen

The SHIPTRAP facility [1] was designed for mass measurements of heavy nuclides, produced in fusion-evaporation reactions at SHIP. The energy of the reaction products ranges from 20 to 500 keV/u. To stop them and transfer them to an ion trap system for precision experiments, a gas stopping cell was designed and built in Munich [2]. An investigation of the properties of the cell was started with online experiments in 2003 at Garching [3] and at GSI. Further tests that were performed to determine the extraction efficiency are presented here.

In order to produce ions in a well-defined point-like region of the gas cell, a ^{223}Ra ion source was used. In the α-decay into ^{219}Rn the recoil ions from the source were stopped in the gas cell and extracted. For the measurements of the efficiency and extraction times from the cell, a Si-detector was mounted behind the extraction RF quadrupole (RFQ) of the cell. For the investigation of contaminants extracted from the cell, mass spectra were recorded using a time-of-flight mass spectrometer with orthogonal extraction [3]. It was coupled directly to the extraction RFQ of the gas cell.

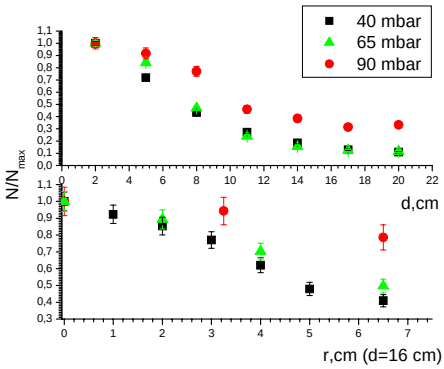

Figure 1 Relative efficiency of the gas cell vs the axial distance d of the ^{223}Ra-source from the exit of the cell (top) and vs the radial distance (bottom) from the axis.

The dependence of the relative gas cell efficiency on the position of the ion source in the cell was measured at three different He pressures between 40 and 90 mbar. The electrical field applied along the axis was set to 5 V/cm. The axial distance *d* of the source from the exit of the cell was varied from 2 cm to 22 cm. The radial distance *r* from the axis of the cell was varied from 0 cm to 7 cm for a fixed value of d = 16 cm. The preliminary results are shown in Fig. 1. With increasing distance from the exit of the cell the efficiency decreases. For higher pressures in the gas cell, a less steep drop in the efficiency curves is observed. This indicates that diffusion of the ions towards the electrodes of the gas cell strongly affects the efficiency.

The extraction time of the ions from the cell was measured at a pressure of 40 mbar (c.f. Fig.2). Depending on the distance from the nozzle it ranges from 4 to 25 ms in agreement with earlier measurements at the MLL [2] using laser created ions.

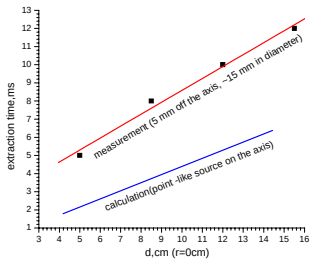

Figure 2. Extraction times at 40 mbar vs the distance *d* of the ^{223}Ra-source from the nozzle for a radial position of r = 0.

Fig. 3 shows a typical mass spectrum of ions extracted from the gas cell after a typical bake-out duration of 20 hours. The dominant peaks in the spectrum are due to ^{219}Rn and its decay products. In addition, Xe impurities, originating from the He gas supply line, were present. The Xe isotopes could be successfully removed from the cell using a cold trap at the gas inlet to the gas cell.

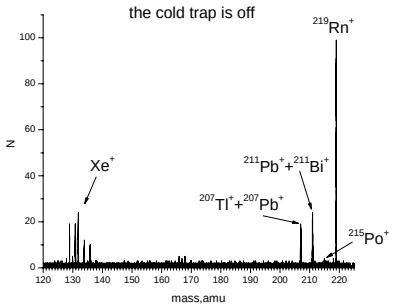

Figure 2. Typical mass spectrum of ions extracted from the gas cell.

The estimated total efficiency of the gas cell is on the order of 10%, determined by the product of calculated stopping and measured extraction efficiencies. Factors limiting the efficiency are quantitatively understood. Under proper conditions, ion-molecule reactions do not seem to limit the efficiency of the gas cell significantly. The effect of neutralization and charge-exchange still needs to be investigated.

References

[1] J.Dilling and al., *Hyp. Int. 127, 491 (1999)*
[2] J.Neumayr, *PhD Thesis, Univ. München (2004)*
[3] S.Eliseev, *PhD Thesis, Univ. Giessen (2004)*

A new detection scheme for high-precision mass measurements

R. Ferrer[1], K. Blaum[1,2], S. George[1], S. Stahl[1], C. Weber[1,2], and the SHIPTRAP Collaboration.
[1]Institute of Physics, Johannes Gutenberg-University, D-55099 Mainz
[2]GSI, Plankstr. 1, D-64291 Darmstadt

The development of storing, cooling, and detection techniques for ions and, thereby, realisable precision experiments with these particles has rapidly become more important within the last few years. The experiments and their applications are not only in the center of the modern atomic physics, but also in lots of other areas of the natural sciences. At the Johannes Gutenberg-University of Mainz and the Gesellschaft für Schwerionenforschung (GSI) in Darmstadt, precision experiments with stored and cooled ions are performed, generally using Penning traps for the three dimensional confinement of ions.

Recently, a Helmholtz research group for young investigators [1] with the subject ``Experiments with stored and cooled ions´´ was initiated at the University of Mainz with strong support from the Helmholtz-Gemeinschaft and GSI. The research group serves as a link between the University of Mainz and GSI with the aim to develop new cooling and detection techniques for high-precision Penning trap experiments, *e.g.* at SHIPTRAP at GSI.

The SHIPTRAP facility [2] is designed to deliver very clean and cooled beams of singly charged recoil ions produced at the SHIP velocity filter [3] at GSI. The SHIPTRAP setup consists of a gas cell for stopping and thermalizing recoil ions from SHIP, a radiofrequency (RF) quadrupole ion guide for extraction of the ions from the gas cell, a linear RF trap for accumulation and bunching of the ions, and a double Penning trap system for isobaric purification and precision measurement. One of the scientific goals of SHIPTRAP is mass spectrometry experiments on heavy transuranium nuclides produced at the velocity filter. Within the group of young researchers, it is intended to investigate alternative methods of cyclotron resonance measurements to perform mass spectrometry on radionuclides.

Nowadays the destructive time-of-flight ion cyclotron resonance (TOF-ICR) detection method is exclusively used for the mass determination of radionuclides in a Penning trap. For a single resonance, several hundred ions are required with minimum yield of about 100 ions per second due to the overall efficiency in the order of 10^{-2}. So far microchannel-plate detectors with typical efficiencies of only 30% have been used to record the TOF resonance. To increase the detection efficiency in order to access nuclides with production yields of a few tens per second, a new conversion electrode Channeltron detector has been developed and will be implemented in on-line Penning trap experiments. A sketch of the new detector setup is shown in Fig. 1.

To access radionuclides with production rates well below one per second, as *e.g.* in the superheavy element region, a different detection scheme has to be developed. Here, we propose the employment of the non-destructive and highly-sensitive Fourier Transform FT-ICR technique. The signals of charged particles stored in a hyperbolically shaped Penning trap with a segmented ring electrode, see Fig. 2, are picked up by means of an attached narrow-band electronic resonance circuit working under cryogenic conditions (T = 4 K). It enables the detection of a single ion as well as further successive measurements with the same ion. Since many superheavy nuclides have lifetimes of more than a second, this detection technique is ideally suited.

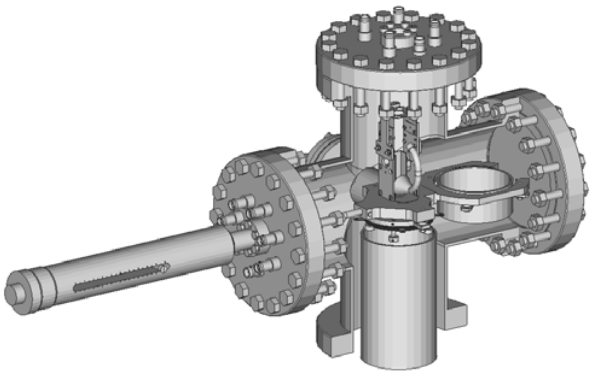

Figure 1: For the destructive detection technique either a microchannel plate detector (center) or a Channeltron (top) will be used. The linear feedthrough enables the exchange of the two detector types.

An FT-ICR setup is presently under construction in the Helmholtz research group at Mainz. The recent installation of a superconducting magnet (B = 7 T) with a relative field inhomogeneity of less than 0.5 ppm (within a volume of 1 cm^3) together with the newly designed ion traps will allow the first attempt for an application of this technique to radionuclides.

Figure 2. Compensated hyperboloid trap.

References.

[1] http://www.physik.uni-mainz.de/quantum/mats/
[2] J. Dilling et al., Hyp. Int. **127**, 491 (2000).
[3] S. Hofmann and G. Münzenberg, Rev. Mod. Phys. **72**, 733 (2000).

Status of PHELIX

S. Borneis[1], R. Bock[1], E. Brambrink[1, 2], H. Brand[1], C. Bruske[1], J. Caird[3], R. Fuchs[1], S. Götte[1], T. Hahn[1], H.-M. Heuck[1,4], D. H. H. Hoffmann[1,2], D. Javorkova[1], H. - J. Kluge[1], Th. Kühl[1], S. Kunzer[1], R. Lotz[1], T. Merz[1,2], P. Neumayer[5], E. Onkels[1], D. Reemts[1], M. Roth[1,2], G. Schaumann[1,2], F. Schrader[1], C. Spielmann[5], R. Stenner[1], A. Tauschwitz[1], R. Thiel[1], U. Thiemer[1], D. Ursescu[1], P. Wiewior[5], U. Wittrock[4], B. Zielbauer[1,6]

[1]Gesellschaft für Schwerionenforschung mbH; [2]TU Darmstadt; [3]Lawrence Livermore National Laboratory, USA; [4]Fachhochschule Münster; [5]Julius-Maximilians Universität Würzburg; [6]Max-Born-Institut Berlin

We report the major achievements of the physics/engineering design effort and the construction of the PHELIX laser, which will be capable of producing pulses up to a peak power of one PW (10^{15} W) in 500 fs and 400 GW in 10 ns.

One of the main technological challenges in the production of high-energy petawatt (HEPW) pulses is the reduction of the peak power on today's highest damage threshold laser components (some GW/cm^2). The enabling technological advancement which reduces the intensity in the high-energy laser amplifier of PHELIX by a factor of 30,000 and thus avoids catastrophic damage as well as deleterious nonlinear effects is chirped pulse amplification (CPA) [1, 2]. In the front-end section of PHELIX, a low-energy (~nJ), 15 nm bandwidth seed-pulse is passed through a positive-dispersion delay line (grating stretcher). This produces out of the 110 fs oscillator pulse a three ns duration chirped pulse which is then amplified at an irradiance well below the self-focusing threshold. After amplification in the main amplifier to ~650 J, the high-energy chirped pulse will be recompressed by a pair of parallel diffraction gratings to ~500 fs. The emerging technology of multi-layer dielectric (MLD) gratings is believed to offer a substantial improvement of the laser induced damage threshold (LDT) compared to the traditional meter size gold coated gratings [3, 4]. In cooperation with LLE Rochester in the US and LULI in France, we spent significant effort for the investigation of the LDT of MLD gratings produced by Horiba Jobin Yvon, Lawrence Livermore National Laboratory, and General Atomics. We designed and built a vacuum test bed for 500 fs LDT measurements. The set-up used 45 mJ pulses from the PHELIX fs-front-end which were compressed in our 10 joule terawatt compressor and then focused to a 300 micron diameter spot onto the test sample. With this set-up a large number of measurements were conducted during the course of the year with grating samples ranging from 2 inch to 480 x 330 mm^2 in size. Uniquely so far, the measurements are fully conducted in vacuum. This avoids nonlinear pulse distortion as well as providing the actual environment in which the gratings will finally be operated.

In 2004 the physics design of the PW compressor was completed. We developed a ray tracing and beam propagation model that allowed us to evaluate the performance of different geometries. Our model predicts that a single pass is the optimum solution for our requirements. This geometry offers the highest possible throughput and the most efficient/economic use of the available grating surface. However, the output beam exhibits a considerable amount of uncompensated spatial chirp. Our beam propagation calculations model the impact of the chirp onto the focused intensity as well as the effect of spectral clipping on the limited size gratings. In addition we studied the near-field propagation effects that could potentially lead to damage of the final optics behind the compressor. The simulations show a shear of the pulse front in the focus (Fig. 1) which results in an increase in the duration of the energy deposition across the focus by 5% (~20 fs). However, the pulse stays locally short and the peak intensity remains unchanged. The code should be extendable to also simulate the alignment and wave front tolerances for a tiled grating compressor which should allow to go beyond one PW in the future.

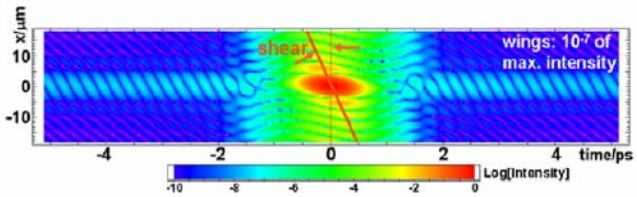

Fig. 1: Calculated focused log. intensity in the focal region showing a pulse front shear (5% pulse width broadening) due to the spatial chirp after compression. The 10^{-7} intensity wings result from spectral clipping on the gratings.

Important for the final layout of the compressor was the assessment of the alignment tolerances. This analysis shows that an angle of incidence of 72° instead of the original 62° is beneficial for relaxing the incidence angle tolerance by a factor of ~20. The high line density (1740 lines/mm) permits still a relatively compact setup with a grating separation of only 4 m resulting in the required group delay dispersion of 194 ps/nm. A 3D model of the geometrical arrangement is shown in Fig. 2. It may be housed in a vacuum chamber of about 5.5 x 2.5 x 0.7 m^3. A finite-element analysis was performed by GSI's design department to optimize the shape and wall thickness of this chamber in order to minimize costs and the total weight.

The MLD grating based petawatt compressor necessitates a new pulse stretcher using the same groove density as the compressor gratings. For the design of the new stretcher a detailed ray trace modelling was performed taking into account the acceptable spatial and temporal dispersion. The stretcher will transmit a full bandwidth of 16 nm and incorporates a small compressor that allows compression of pulses from the short pulse front-end. This will be used to validate pulse compression, to test diagnostics equipment and also for short-pulse damage testing. The stretcher optics has been delivered and setup will be completed in spring 2005.

The work on the PHELIX pulsed power system concentrated on the rebuilding of the power supplies for the 19 mm and 45 mm preamplifier heads. These activities were mainly

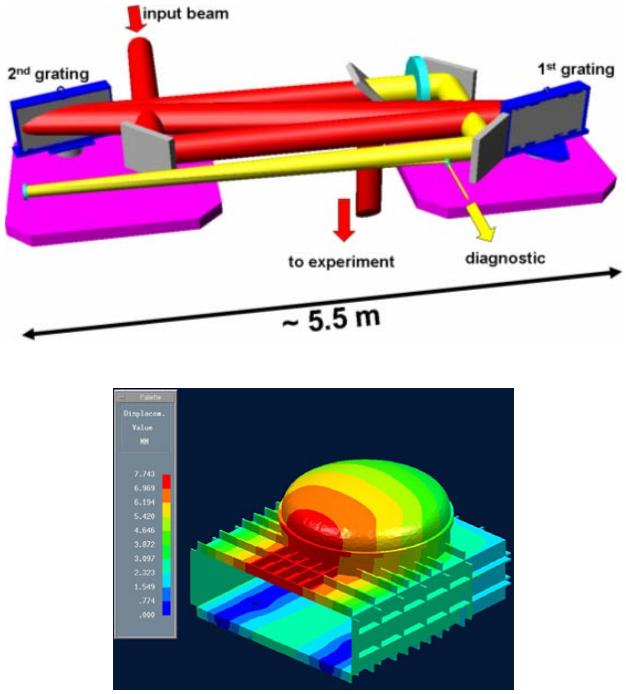

Fig 2. Beam path through the petawatt pulse compressor (top); finite-element analysis of part of the PW vacuum chamber (bottom)

driven by safety issues and the desire to change the control hardware to the same profibus system that is used to operate the main capacitor bank. The test and monitoring capabilities of the system were extended by adding the capability of using internal dummy loads instead of the flash lamps. Circuits were integrated which allow to measure the charging voltage and flash lamp current. Furthermore the grounding and cable connections to the amplifier heads including the high voltage cable connections were improved. Screening boxes were installed around the laser heads to minimize high voltage hazards.

A major step forward in the set-up of the beam transportation to the experiments was the start of the installation of our 315 mm diameter Faraday isolator (FI) required to protect the 2-pass main amplifier system from potential target back-reflections and subsequent catastrophic damage. In addition to the design and the start of the construction of the mechanical support structure of the FI, the capacitor bank for the 315 mm diameter FI was connected to the power transmission cables. The setup of the PFN required the modelling of the ignitron and capacitor protection circuit which has to avoid the reversal of voltage and current. In addition to the FI, most of the control electronics for the main amplifier capacitor bank was refurbished and adapted to fiber optics readout systems.

The scheme for timing and synchronization of PHELIX with the different accelerators at GSI was finalized and extended to include different operation modes of the laser. All necessary hardware as gate and delay generators and wide-band fiber optical transmission lines were purchased. About 8 km of predominantly fast coaxial cables were used to ensure a synchronization of the laser hardware with the UNILAC, SIS, and ESR with sub-nanosecond precision. Within the PHELIX building the trigger and timing signals are mainly distributed by fiber optics.

In close collaboration with the ECOS group of the DVEE department of GSI the PHELIX Interlock System (PILS) was set-up as part of the PHELIX Control System (PCS). The system is fully hard-wired in accordance with our safety regulations and protects the operators and users from safety hazards arising from intense laser light and high voltage. An important milestone was the successful safety audit of the German VDE and the approval of the conformity with the required safety standards. The system is in daily operation and has proven its reliability. The PCS is based on a framework which is in-house developed by the ECOS group [5]. Parts of the PCS have been implemented and tested until now while others are under commissioning.

The control system needs to monitor all essential operational and beam parameters of PHELIX with various diagnostics and to provide the ability to adjust parameters as needed. Particularly important is the beam diagnostics of the output beam of the PHELIX main amplifier. The concept of the beam diagnostics was developed and the set-up started. Among the most important parameters are energy, power, near and far field distributions, spectrum and wavefront. To fit the 280 mm beam of the main amplifier onto the sensors of the diagnostics package it is de-magnified by telescopes in three steps. The telescopes have been designed and optimized with the optical design software ZEMAX for lowest aberrations. A first, corrected Galileo-telescope at the entrance collimates the beam to 50 mm diameter, significantly lowering cost of subsequent optics. The non-focussing design prevents gas breakdown at nominal output beam energy. A calibrated energy sensor picks up a constant fraction of the incoming beam in the input section of the diagnostics, at the same time the beam is attenuated to 10% of the incoming energy. Following, the energy density is low enough to allow a further telescopic (Galilean type) beam diameter reduction to 20 mm, which enables the employment of cost-efficient off-the-shelf 2"-diameter optics in the subsequent attenuator section of the diagnostics setup. Stepped attenuation of the beam is achieved by either a fine meshed hole-array in front of the entrance lens and/or by a 5-stepped attenuator comprised of various optics of different transmissions. A third telescope (Keppler type) reduces the beam size to 10 mm and generates a first real image of the incoming beam. The beam is split, transformed and directed to individual chains of the beam diagnostic, i.e. near and far field diagnostics, spectral intensity and phase measurement as well as wave front analysis.

References

[1] D. Grischkowsky et al., Appl. Phys. Lett. **41**, 1 (1982)
[2] D. Strickland et al., Opt. Comm. **56**, 219 (1985)
[3] B. W. Shore et al., J. Opt. Soc. Am. **A 14**, 1124 (1997)
[4] C. P. J. Barty et al., Nucl. Fusion **44**, 266 (2004)
[5] D. Beck et al., Nucl. Instrum. Meth. **A 527**, 567 (2004)

Interaction of Strong Short Pulsed Laser Fields with Confined Charged Particle Plasmas

D. Ursescu[1,2], B. Zielbauer[1,2,3], S. Borneis[1], A. Gumberidze[1], T. Kühl[1,2], J. McDonald[4], P. Neumayer[1,5], D. Schneider[4], R. Schuch[6], U. Spillmann[1], Th. Stöhlker[1], and S. Trotsenko[1]

[1]GSI-Darmstadt; [2]Universität Mainz; [3]Max-Born-Institut Berlin; [4]Lawrence Livermore Nat. Laboratory, USA; [5]Universität Würzburg; [6]University of Stockholm, Sweden

Multiple ionization of **atoms** [1], using intense optical fs lasers, is studied experimentally and theoretically [2]. Studies on **ions** are up to now scarce and mostly qualitative.

We report on the temporary set-up of a low density plasma target facility from the University of Stockholm for the investigation of the interaction of short pulsed strong electromagnetic fields with electromagnetically confined plasmas at GSI. Strong oscillating short electromagnetic fields ($> 10^{11} V/cm$) are provided by intense lasers such as the PHELIX laser at GSI and by the upcoming "Free Electron Laser (FEL)" facilities (e.g. VUV FEL at DESY). The laser experiments are aimed to gain understanding of ionic ionization/excitation, the plasma ionization balance, as well as photon polarization processes caused and effected by the strong electromagnetic fields [3].

The plasma target device comprises of a "Refrigerated Electron Beam Ion Trap (REBIT)" [4] and has the advantage that one can breed charge states and study multiple ionization/excitation starting from different initial charge states [5]. The REBIT relies on a closed cycle refrigerator for the cooling of the superconducting magnet, making it especially suited for this type of experiments due to the compactness of the set-up. The REBIT resembles an open cylinder Penning trap geometry, where an electron beam passes through three axial drift tubes as trap electrodes inside a cryogenic super-conducting 3T magnet. The low density ($< 10^{12}/cm^3$) plasma is produced and confined in the center drift tube. The ions are confined radially by the space-charge of the compressed ($\approx 60\mu m$), high density electron beam ($\approx 150 mA$) and by the magnetic field while axial confinement is provided by appropriate biasing the trap drift tubes; the trap biases are superimposed on a high voltage potential which determines the electron beam impact energy. The electron beam energy, intensity and the ionization time determine the achievable charge state distribution via successive electron impact. A sketch of the set-up is shown in Fig. 1.

The laser beam taken out from the x-ray laser target chamber is focused into the ion plasma target by a 90^o off-axis parabola (350 mm focal length, 75 mm diameter)

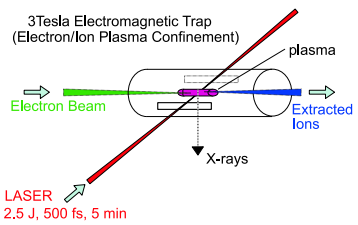

Figure 1: Set-up sketch for laser plasma interaction studies

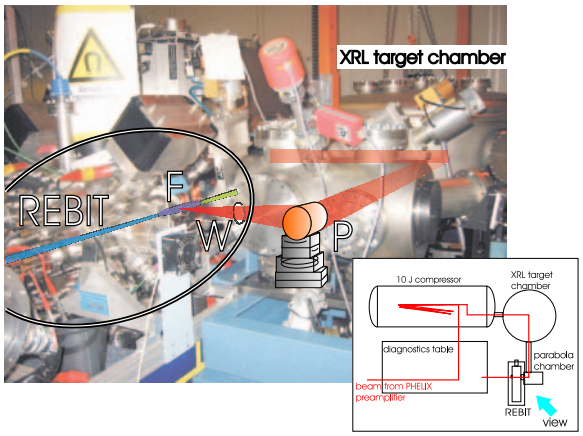

Figure 2: Low density plasma target set-up at the PHELIX laser with focus (F), $0.3mm$ window (W) and parabola (P) positions; inset: x-ray laser laboratory overview

mounted on a step-motor driven 5-axis actuator under high vacuum. A 50 mm diameter, thin (0.3 mm, $\frac{\lambda}{6}$) window with a 7^o tilt separates this vacuum from the cryogenic UHV section of the REBIT and allows the high power photon beam to interact with the plasma without distorting the vacuum or causing background effects. Fig. 2 shows the apparatus as it was set-up in the PHELIX x-ray laser laboratory.

The laser focus of $\approx 20\mu m$ diameter matches the ion volume in the REBIT of nominal $75\mu m$ diameter at 3T. Laser beams of 400 fs pulse length and of typical 1-5 J energy at 1054 nm wavelength are envisioned for these experiments. In the proposed experiments it will be possible to observe the x-ray emission from the confined ion plasma. The gated extracted ion charge state distribution as function of the laser power, electron energy and time delay from ion production to extraction can also be analyzed.

References

[1] A. l'Huillier, L. A. Lompre, G. Mainfray, and C. Manus, Phys. Rev. A 27, 2503 (1983), D. N. Fittinghoff, P. R. Bolton, B. Chang, and K. C. Kulander, Phys. Rev. Lett. 69, 2642 (1992), P. B. Corkum, Phys. Rev. Lett. 71, 1994 (1993)

[2] J. B. Greenwood, I. M. Johnston, P. McKenna, and I. D. Williams, Phys. Rev. Lett. 88, 233001 (2002)

[3] The Science and Applications of Ultra-fast, Ultra-intense Lasers: Opportunities in Science and Technology Using the Brightest Light Known to Man (Report on the SAUUL Workshop, June 17-19, 2002)

[4] http://atomlx04.physto.se/~rebit/

[5] D. Schneider et al., Phys. Rev. A 44, 3119 (1991)

APHYSTHE

Theory for Atomic Physics with Heavy Ions

Radiative electron capture into heavy, lithium–like ions

Stephan Fritzsche[1], Andrey Surzhykov[1], and Thomas Stöhlker[2]
[1]Institut für Physik, Universität Kassel, Germany; [2]Gesellschaft für Schwerionenforschung, Darmstadt, Germany

During the last decade, relativistic collisions of highly–charged ions with electrons and low–Z target atoms have been studied intensively at the GSI storage ring in Darmstadt. In such collisions, one of the dominant processes is the radiative electron capture (REC) of either a target or cooler electron into a bound state of the projectiles which is accompanied by the emission of photons. So far, however, most experimental REC studies concerned the capture of electrons by *bare* projectile ions, including measurements of the total and angular–differential cross sections [1]. Usually, good agreement is found when the cross sections are compared with computations based on Dirac's theory [2]. Less attention, in contrast, was paid to the electron capture by *few–electron* projectiles owing to the fine–structure effects for ions with (initially) open shells which arise from the interaction among the electrons. A first step towards the study of *interelectronic* effects has been done only recently by Bednarz and co–workers [3], who measured the angular distributions of the x–ray photons following the REC by *hydrogen–like*, *helium–like* and *lithium–like* uranium ions. In this experiment, rather high collision energies ($T_p > 200$ MeV/u) was employed for which the radiative recombination is not sensitive to the electron–electron repulsion. However, further studies on the REC angular distributions are planned at the GSI storage ring, and will be focused on the use of *decelerated* ions, for which one expects more pronounced effects from the interaction of the electrons.

In this contribution, we report about detailed calculations of the angle–differential REC cross sections for the capture into *few–electron* heavy ions, performed for a wide range of collision energies. In order to explore the influence of the interelectronic–interaction on the angular distributions of the emitted photons, two theoretical approaches were applied: In the independent–particle model (IPM), we first made use of hydrogenic functions and proper set of Slater determinants to account for the Pauli principle in the capture of (additional) electron. Apart from this simple "one–electron" model, the angular distributions of the recombination photons have been also calculated by means of the Multi–configuration Dirac–Fock (MCDF) approach which allows to incorporate the electron–electron interaction effects in a more systematic fashion. Within the MCDF approach, both the initial and the final ionic states with angular momentum and parity $\left(J^P\right)$ are approximated by a linear combination of the so–called configuration state functions (CFS) of the same symmetry:

$$|\psi_\alpha(PJM)\rangle \;=\; \sum_r^{n_c} c_\gamma(\alpha)\; |\gamma_r(PJM)\rangle \;, \qquad (1)$$

where n_c is the number of CSF and $c_r(\alpha)$ denotes the representation of the ionic state in this basis. As usual, the CFS are antisymmetrized products of a common set of *orthonormal* orbitals which are optimized on the basis of the Dirac–Coulomb Hamiltonian.

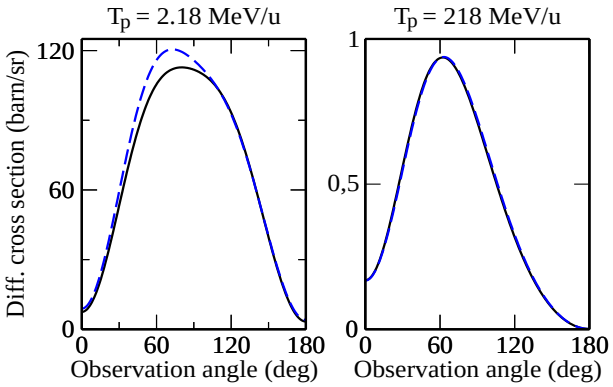

Figure 1: Angle–differential cross sections for the radiative electron capture into the $1s^2\ 2s^2$ state of (initially) lithium–like uranium ions U^{89+} with projectile energies of 2.18 and 218 MeV/u. Results are presented within the independent particle model (- - -), and Multi–configuration Dirac–Fock approach (—).

The MCDF method is implemented, for instance, in the RATIP [4] program and has been utilized to calculate the *bound–free* transition amplitude and, hence, the angular distributions of the recombination x–ray photons [5]. Figure 1 shows the angle–differential cross sections for the radiative capture of electrons into the $1s^2\ 2s^2$ state of (initially) lithium–like uranium ions U^{89+} with projectile energies $T_p = 2.18$ and 218 MeV/u and compares them with the cross section data as obtained in the IPM. For sufficiently large projectile energies, such as $T_p = 218$ MeV/u, both, the "one–electron" and "many–electron" approximations yield virtually identical results, which shows that the electron–electron interaction effects become negligible for high collision energies. For *decelerated* ions with an energy $T_p = 2.18$ MeV/u, in contrast, the electron–electron correlation alters the angular distribution of the recombination photons considerably with a rather strong effect around the angle $\theta = 70°$ in the laboratory system [5].

In the present work, we explored the influence of the electron–electron correlations on the *angle–differential* REC cross sections. More pronounced effects due to the interelectronic–interactions are expected, however, for the (linear) *polarization* of the emitted radiation for which a first analysis is currently performed by combining the MCDF approach with the density matrix theory [6].

References

[1] Th. Stöhlker, Phys. Scr. **T80**, 165 (1999).
[2] J. Eichler *et al.*, Phys. Rev. A **54**, 4954 (1996).
[3] G. Bednarz *et al.*, Hyperfine Int. **146**, 29 (2003).
[4] S. Fritzsche, JESRP **114–116**, 1155 (2001).
[5] S. Fritzsche *et al.*, Phys. Rev. A (2005) submitted.
[6] A. Surzhykov *et al.*, Phys. Rev. A **68**, 022710 (2003).

Excitation of heavy nuclei by electron capture

Adriana Pálffy[1], Zoltán Harman[1,2], and Werner Scheid[1]
[1]Institut für Theoretische Physik, Justus-Liebig-Universität Giessen, Heinrich-Buff-Ring 16, 35392 Giessen;
[2]Max-Planck-Institut für Kernphysik, Saupfercheckweg 1, 69117 Heidelberg

In the resonant process of nuclear excitation by electron capture (NEEC) a free electron is captured into a bound shell of an ion with the simultaneous excitation of the nucleus. This is the time-reversed process of the internal conversion. The excited nuclear state can then decay radiatively by the emission of a photon or by internal conversion. The process is similar to the dielectronic recombination (DR) in which the captured electron transfers its energy to the excitation of a bound electron. This electronic excitation is now replaced by the excitation of the nucleus.

The investigation of NEEC opens the possibility to explore the spectral properties of heavy nuclei through atomic physics experiments.

Considering the analogy with DR we have extended the formalism developed in [1] for calculating the DR cross section, so that it accounts for nuclear transitions. Zimmerer [1] has applied a relativistic formalism for expanding the transition operator introducing Feshbach projector operators to clearly separate the different subspaces involved in this process.

In the following we consider that the electron is captured to a bound state in the Coulomb field of a bare nucleus, so that no competition with the DR process occurs. The cross section for the NEEC process, followed by the radiative deexcitation of the nucleus, reads:

$$\sigma = \frac{2\pi}{p^2}\frac{A_r Y_n}{\Gamma_d} L_d(E - E_d). \qquad (1)$$

Here, $L_d(E-E_d)$ is the Lorentz resonance profile, centered on the resonance energy E_d and having the total natural width Γ_d of the excited nuclear state. Further, p and E are the momentum and the energy of the continuum electron, respectively, A_r is the radiative decay rate of the excited nuclear state and Y_n the NEEC rate, which was calculated in the Coulomb gauge according to the formula

$$Y_n = \frac{8\pi^2 e^2}{(2L+1)^3} R_0^{-2(L+2)}$$

$$\times \sum_\kappa |R_{L,j_f,j_i}|^2 B(EL)(2j_f+1) C\left(j_f\ L\ j_i; \frac{1}{2}\ 0\ \frac{1}{2}\right)^2 . \qquad (2)$$

For describing the nucleus we have used a nuclear collective model [3] which assumes irrotational flow of the nuclear currents. This model accounts only for the excitation of low lying nuclear levels by electric multipole transitions. Here, L denotes the multipolarity of the nuclear transition, $B(EL)$ is the reduced electric nuclear transition probability and R_0 the nuclear radius. In the numerical calculations we have used experimental values for $B(E2)$ and A_r taken from [2]. The electronic state is labelled by $\kappa = (-1)^{j+l+1/2}(j+1/2)$, with the total angular momentum j and the orbital angular momentum l. The indices

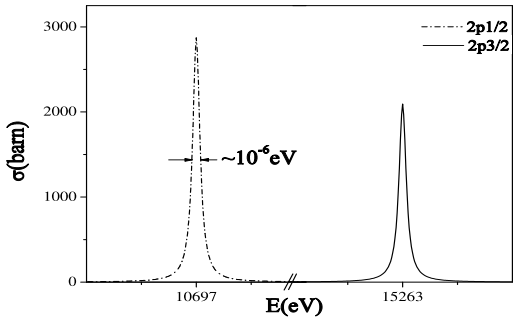

Figure 1: NEEC cross section for ^{238}U with excitation of the first nuclear 2^+ state

i and f stand for the initial, respectively final electronic states. R_{L,j_f,j_i} is the radial integral given by

$$R_{L,j_f,j_i} = \frac{1}{R_0^{L-1}} \int_0^{R_0} dr r^{L+2} \left[f_f(r) f_i(r) + g_f(r) g_i(r)\right]$$
$$+ R_0^{L+2} \int_{R_0}^{\infty} dr r^{-L+1} \left[f_f(r) f_i(r) + g_f(r) g_i(r)\right], \quad (3)$$

where $g(r)$ and $f(r)$ are the large and small radial components of the relativistic electron wavefunction, respectively. These integrals were calculated numerically.

For the numerical calculation we have considered the case of ^{238}U with its $E2$ transition from the ground state to the first 2^+ state at the excitation energy of 44.913 keV. This energy value allows the excitation of the nucleus by capturing a continuum electron into the L atomic shell. The transition rate of capturing the free electron into the $2p_{1/2}$ or $2p_{3/2}$ orbitals is $\sim 10^{10} s^{-1}$, two orders of magnitude larger than that for the capture in the $2s_{1/2}$ orbital, which is $\sim 5 \cdot 10^8 s^{-1}$. Calculations for ^{236}U produced very similar results.

Figure 1 shows the NEEC cross sections for the $E2$ transitions in ^{238}U, with the capture of the free electron in the $2p_{1/2}$ and $2p_{3/2}$ orbitals of the L shell, followed by the radiative decay of the excited nuclear state. The resonance energies of the continuum electron are 10.697 and 15.263 keV, respectively. The resonance strength is 10^{-2} barn·eV in the case of the $2p_{1/2}$ capture and $7 \cdot 10^{-3}$ barn·eV in the case of the $2p_{3/2}$ capture. These values are 5-6 orders of magnitude smaller than the resonance strength for DR, making NEEC challenging to be observed experimentally. Calculations of magnetic nuclear transitions induced by the current of the electron are in progress.

References

[1] P. Zimmerer, Dissertation, Univ. Giessen (1992)
[2] S. Raman et al., At. D. Nucl. D. Tabl. **78** (2001) 1
[3] T. deForest, J. D. Walecka, Adv. Phys. **15** (1966) 1

Angular correlations in the two–photon decay of highly–charged ions

Andrey Surzhykov[1], Stephan Fritzsche[1], and Peter Koval[2]
[1]Universität Kassel; [2]Max–Planck–Institut für Kernphysik, Heidelberg

During recent years, a number of experiments have been performed at the GSI facilities in Darmstadt in order to explore the two–photon decay in medium and heavy ions [1, 2]. When compared to theoretical predictions, the outcome of these measurements provides a unique possibility to probe the influence of relativistic as well as quantum electrodynamical (QED) effects on the electronic structure of ions (atoms). Until now, most of the experimental and theoretical studies focused on the total decay rates as well as the energy distributions of the emitted photons. In contrast, less attention, has been paid so far to the effects of relativity on the photon–photon *angular correlation* function, that is if the angular distribution of one of the photons is observed relative to the emission of the second one in a two–photon transition. However, with the recent progress in x–ray detector design, measurements on the angular correlations in the two–photon decay of heavy atomic systems are likely to be become possible within the next few years.

To understand the details of the two–photon decay, we analyzed the photon–photon angular correlation function for highly–charged, hydrogen–like ions in the framework of second–order perturbation theory and Dirac's equation [3, 4]. Within this framework, the photon–photon angular correlation function can be traced back to the evaluation and computation of the second–order transition amplitude:

$$M_{fi} = \sum\!\!\!\!\!\!\int_{\nu} \frac{\langle \psi_f |\mathbf{A}_1^*| \psi_\nu \rangle \langle \psi_\nu |\mathbf{A}_2^*| \psi_i \rangle}{E_\nu - E_i + E_{\gamma_2}} + \frac{\langle \psi_f |\mathbf{A}_2^*| \psi_\nu \rangle \langle \psi_\nu |\mathbf{A}_1^*| \psi_i \rangle}{E_\nu - E_i + E_{\gamma_1}} , \quad (1)$$

where $(\psi_i,\ E_i)$, $(\psi_\nu,\ E_\nu)$ and $(\psi_f,\ E_f)$ refer to the *relativistic* wavefunctions and the energies of the initial, intermediate and final atomic states, respectively. In this expression, as usual, the electron–photon interaction is described in terms of the transition operator $\mathbf{A} = \boldsymbol{\alpha}\, \mathbf{u}_\lambda\, e^{i\boldsymbol{k}\cdot\boldsymbol{r}}$ which includes the unit vector $\mathbf{u}_\lambda$ in order to describe the polarization of the emitted photons.

As indicated in equation (1), the summation over the intermediate states refers to the *complete* one–particle spectrum (ψ_ν, E_ν), including a summation over the discrete part of the spectrum as well as the integration over the continuum. Since such a summation over the *complete* spectrum is not feasible in practice, a number of alternative methods has been proposed for calculating second–order amplitudes. In our work, for example, we first express the transition amplitude (1) by means of relativistic Coulomb–Green's functions [3] in order to avoid an explicit summation over the spectrum. For the hydrogen–like ions, the Coulomb–Green's functions are known *analytically* and allow for an accurate and fast computation of the transition amplitude (1) and, hence, of the photon–photon angular correlation function.

Apart from the summation over the complete hydrogen spectrum (ψ_ν, E_ν), the transition amplitude (1) includes formally also the – infinite – summation over (the products of) the multipole photon fields, E1E1, E1M2, M1M1, E2M2, ... which arise from the decomposition of the photon plane wave $\mathbf{u}_\lambda\, e^{i\boldsymbol{k}\cdot\boldsymbol{r}}$ into its multipole components. However, often, this summation can be restricted to the 'leading' term which usually dominates the two–photon transitions for any given pair of initial and final bound states. For example, the $2s_{1/2}$ and $3d_{5/2}$ levels decay into the $1s_{1/2}$ ground state primarily by the emission of two electric–dipole (E1E1) photons, while all the higher multipoles contribute with less than 0.5 % to the total decay rate. Nevertheless, a significant effect from the higher multipoles is expected for the *angular* distributions of the emitted photons. Figure 1 displays this (higher multipole) effect for the $2s_{1/2} \to 1s_{1/2}$ and $3d_{5/2} \to 1s_{1/2}$ two–photon decay of hydrogen–like uranium U^{91+} ions. As seen from this Figure, the photon–photon angular correlation function, which is found to be symmetric with respect to the angle $\theta = 90°$ in the electric dipole (E1E1) approximation, becomes asymmetric due to the higher (non–dipole) components of the radiation filed, and this effect is even more pronounced for the decay of the $3d_{5/2}$ state.

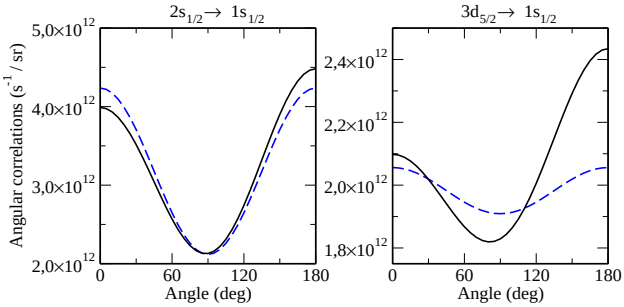

Figure 1: Photon–photon angular correlations in the $2s_{1/2} \to 1s_{1/2}$ and $3d_{5/2} \to 1s_{1/2}$ (two–photon) decay of hydrogen–like uranium U^{91+} ions. Results are presented for the exact relativistic theory (—) and the relativistic electric dipole approach (– –) for two emitted photons with energies $E_{\gamma_1} = E_{\gamma_2}$.

Until now, we have restricted our calculations of the photon–photon angular correlations to *hydrogen–like* ions. However, the Green's function approach which has been successfully applied for these (one–electron) ions, can also be extended for the study of the two–photon decay in many–electron heavy ions. First investigations of the $2^1S_0 \to 1^1S_0$ (two–photon) decay in the helium–like ions are currently under way.

References

[1] H. W. Schäffer *et al.*, Phys. Lett. A **260**, 489 (1999).
[2] P. H. Mokler *et al.*, Phys. Rev. A **70**, 032505 (2004).
[3] A. Surzhykov *et al.*, Phys. Rev. A (2005) in press.
[4] J. Santos *et al.*, Eur. Phys. J. D **3**, 43 (1998).

Angular distribution of the cascade photons in the radiative electron capture

E. G. Drukarev

Petersburg Nuclear Physics Institute, Gatchina, St. Petersburg 188300, Russia

Recent experiments on the cascade photon distribution in the collisions of uranium ions with light targets for the bare uranium nuclei U^{92+} and the one-electron ions U^{91+} in the ground states provided different results. In the former case distributions of the photons emitted in the decay of intermediate $2p_{3/2}$ state exhibit strong angular dependence. In the latter case the angular dependence of the superposition of the emission of the corresponding 2^1P_1 and 2^3P_2 states is very weak [1, 2]. In this note I present a theoretical explanation of this phenomena.

In the case of bare nucleus U^{92+} all the electron states can be described by the relativistic Coulomb field functions (RCFF). There are different forms for presentation of the RCFF. In [3] the RCFF are presented as a fast converging $(\alpha Z)^2$ series. We carried out the calculations by using several lowest terms of the expansion [3]. This confirmed previously obtained experimental and theoretical results on the angular distribution. The latter is shown to vary by about 50% in the whole interval of the values of angles.

In the case of capture by a single-electron ion U^{91+} we must build the two-electron wave functions. Since the electromagnetic interaction between the electrons is $1/Z \sim 10^{-2}$ times smaller then their interaction with the nucleus, the asymmetric combination of the single-electron RCFF functions is a reasonable approximation. In other words, we neglect the electromagnetic interaction between the electrons, while the spin correlations are included (Pauli principle is respected).

By using presentation [3] for RCFF we obtain an analytical expression for the amplitude. The distribution of the photons emitted in the decays of the intermediate states 2^1P_1 and 2^3P_2 treated separately still exhibit strong angular dependence. However there is a large cancellation of their angular dependent contributions to the superposition of the distributions which is detected in the experiment. The final result is that the angular dependence should not vary by more then 10% in the observable superposition of the decays of the two states.

Thus we conclude that the observed difference of the angular distributions for the capture by bare nucleus of U and by its single-electron ion is due to the Pauli principle.

I thank P. Mokler for fruitful discussions and for the hospitality during my visit to GSI.

References

[1] Th. Stöhlker *et al.*, Phys. Rev. Lett. **85**, 3109 (2000).

[2] X. Ma *et al.*, Phys. Rev. A **68**, 04712 (2003).

[3] V.G. Gorshkov, ZhETP, **40**, 1481 (1961).

QED Calculations of Bound-Electron g Factors in Highly-Charged Ions

O. Yu. Andreev[1,2], I. Bednyakov[1], T. Beyer[1], J. Winter[1], G. Plunien[1], G. Soff[1], D. A. Glazov[2], D. L. Moskovkin[2], I. I. Tupitsyn[2], V. A. Yerokhin[2], L. N. Labzowsky[2], and V. M. Shabaev[2]

[1]Institut für Theoretische Physik, TU Dresden; [2]Department of Physics, St. Petersburg State University

Highly-charged ions or simple atoms offer an opportunity for high-accuracy calculations of atomic properties within the ab-initio framework of bound-state QED. Such systems possess relatively simple spectra and some of their transitions can be measured with very high precision allowing for sensitive tests of both the magnetic and the electric sector of QED. The remarkable progress made in experimental determinations of Lamb shifts and bound-electron g factors (see e.g. Refs. [1, 2] and references therein) together with recent extensions and further developments of the calculation methods in bound-state QED of atomic systems [3, 4] facilitates independent precision determinations of phenomenological parameters, such as the electron mass m_e, the fine-structure constant α and electron g factors, or nuclear magnetic moments, nuclear radii and ion masses.

The most recent experimental determination of the magnetic moment of the bound electron in hydrogen-like oxygen [2] may exemplify the present situation: The experimental value for the g factor of the bound $1s$-electron in an $^{16}O^{7+}$ ion, $g_{1s}^{\rm exp} = 2.000\,047\,025\,4(15)(44)$, agrees within 1.1σ with the predicted value $g_{1s}^{\rm theory} = 2.000\,047\,020\,2(6)$ and thus provides a stringent test of bound-state QED to the level of 0.25%. Moreover, assuming the validity of the underlying theory allows for the determination of the most precise value for the electron mass $m_e = 0.000\,548\,579\,909\,6(4)$ u [2]. The experiments were performed with single H-like ions (with spin-zero nuclei) confined in a Penning trap measuring the ratio of the Larmor frequency ω_L of the electron and the cyclotron frequency ω_c of the ion, which is related to the electron g factor via

$$\frac{\omega_L}{\omega_c} = g\,\frac{|e|}{m_e}\,\frac{m_{\rm ion}}{q_{\rm ion}}\,. \qquad (1)$$

Here e denotes the elementary charge unite, $m_{\rm ion}$ and $q_{\rm ion}$ is the mass and the charge of the ion, respectively.

From experimental side further progress and extensions of the measurements, e.g., to Li-like ions and to H-like ions with nonzero nuclear spin is anticipated in the near future. A major advantage of comparing Li-like and H-like ions with the same nucleus lies in the fact that uncertainties due to nuclear effects can be significantly reduced in the specific difference g' between the corresponding g factors

$$g' = g_{(1s)^2 2s} - \xi g_{1s}\,. \qquad (2)$$

The parameter ξ is calculated numerically. In Ref. [5] we have provided most accurate calculations of various relativistic and QED corrections to the g factor of Li-like ions in the region of nuclear charge numbers $Z = 6 - 92$. The interelectronic-interaction correction of order $1/Z^2$ and higher obtained within the configuration-interaction

Table 1: Contributions to the ground-state g factor of Li-like calcium.

Dirac value (point nucleus)	1.996 426 011
Finite-nuclear size	0.000 000 014
Interelectronic interaction	0.000 454 45(14)
one-loop QED $\sim \alpha$	0.002 325 555(5)
one-loop QED $\sim \alpha^2$	-0.000 003 517(0)
Screened QED	-0.000 000 33(10)
Nuclear recoil	0.000 000 61(2)
Total	1.999 202 24(17)

Dirac-Fock method is combined with the $1/Z$-correction term derived rigorously from QED. Improved results for the one-electron QED corrections of first and second order in α together with screened QED corrections have been taken into account. The Mainz-GSI collaboration is aiming for the determination of the g factor, in particular, for Li-like calcium with anticipated experimental accuracy at the level of ppb. Corresponding data could be compared with recent predictions provided in [5] (see Table 1 as an example). Extensions of direct measurements of the electron g factor of heavy H-like ions with odd nuclei in the HITRAP facility at GSI seems very promising for tests of the magnetic sector of QED. Moreover, such results can be utilized for independent, precise determinations of nuclear properties, such as magnetic moments. Accordingly, a fully relativistic theory of the g factor of H-like ions with nuclear spin $I > 0$ has been developed [6]. The total magnetic moment of an ion state with total angular momentum F thus contains informations about the electronic and nuclear g factors, respectively. In [6] calculations for the g factor of ions in the ground state ($F = I \pm 1/2$) have been performed for a variety of ions. They account for corrections resulting from QED, nuclear recoil, finite-nuclear size, magnetic dipole, electric quadrupole and hyperfine interactions. To provide accurate theoretical results suitable for the analysis of corresponding data obtained in experiments with highly-charged ions at the GSI facilities represents an important goal of future theoretical investigations at the frontier of atomic and nuclear physics.

References

[1] A. Gumbaridze *et al.*, Phys. Rev. Lett. **92** (2004) 203004
[2] J. Verdú *et al.*, Phys. Rev. Lett. **92** (2004) 093002
[3] O. Yu. Andreev *et al.*, Phys. Rev. A **69** (2004) 062505
[4] V. M. Shabaev *et al.*, Phys. Rev. Lett. **93** (2004) 130405
[5] D. A. Glazov *et al.*, Phys. Rev. A **70** (2004) 062104
[6] D. L. Moskovkin *et al.*, Phys. Rev. A **70** (2004) 032105

Dynamical Schwinger effect in the focus of optical laser beams

D.B. Blaschke[1,2], A.V. Prozorkevich[3], R. Sauerbrey[4], and S.A. Smolyansky[3]

[1]Fakultät für Physik, Universität Bielefeld, D-33615 Bielefeld, Germany; [2]BLTP at JINR Dubna, RU-141980 Dubna, Russia; [3]Department of Physics, Saratov State University, RU-410026 Saratov, Russia ; [4]Friedrich-Schiller-Universität, Institut für Optik und Quantenelektronik, D-07743 Jena, Germany

The Schwinger effect of vacuum pair creation by a quasi-classical electric field although predicted long time ago has still not been experimentally verified since critical field strengths $E_{\rm cr} = m^2/e = 10^{16}$ V/m could not be reached. With the planned construction of X-ray free electron lasers producing field strengths close to the critical one, the possibility to prove the Schwinger effect attracts attention again. Here we consider the region of parameters already achievable with the operating SLAC and Jena Terawatt laser systems [1, 2] as well as the PHELIX laser [3] under construction at GSI, where $m\omega \ll eE \ll m^2$, with the result that optical lasers can generate a number of e^+e^- pairs large enough to allow their experimental observation.

For the theoretical analysis we use the kinetic equation approach, which allows to consider the dynamics of the creation process while taking into account the initial conditions [4]. This approach has been applied already to the periodical field case [5] with near-critical values of the field strength and X-ray frequencies. We consider here a simple model of the laser field, which can be formed in the focus of two counter-propagating laser beams: a harmonic linearly polarized field which acts during N periods. We solve the quantum kinetic equation numerically with the initial condition of a vanishing field and obtain the particle number density as a moment of the distribution function.

For a weak field $E \ll E_{cr}$, the e^+e^- plasma density oscillates with twice the field frequency. We obtain that the electric field $E \approx 7 \times 10^{-6} E_{\rm cr}$ produces $\approx 3 \cdot 10^5$ pairs in a volume of λ^3 averaged over one period of the laser field what corresponds to a particle density of 10^{18} cm^{-3}. This dense enough plasma exists during a laser pulse but vanishes almost completely after switching off the field. The residual density n_r corresponding to an integer number of field periods, is negligible in comparison with the mean density $\langle n \rangle$ per period. Under the above conditions the ratio of $\langle n \rangle / n_r$ is approximately $3 \cdot 10^{11}$. As a consequence, in spite of the fact that the residual density for the X-ray laser exceeds the one for the optical laser by a large factor, the situation is different regarding the mean density: the optical laser can produce more pairs in the volume of λ^3 than the X-ray one [6].

In order to prove the suggested effect experimentally, we discuss here two schemes. The first one is the two-photon annihilation of e^+e^- within the plasma volume. The corresponding γ quanta with the total energy ≈ 1 MeV can be registered in coincidence outside the focus of the counter-propagating laser beams. We have estimated the number of annihilation events per laser pulse $d\nu$ with the following parameters: pulse intensity $I = 10^{18}$ W/cm^2, pulse duration $\tau_L \sim 80$ fs, wavelength $\lambda = 795$ nm, cross size of laser beams $z_0 = 9$ μm [2]. The estimate results in ≈ 1 annihilation event per laser pulse, see Fig. 1. Another possible method to detect the formation of the quasiparticle plasma consists in the observation of the nonlinear plasma response on a weak monochromatic probe signal with intensity $I_{\rm pr}$. For example, the intensity of the third harmonic is of the order $I_3 \sim 10^{-4} I_{\rm pr}$ [7].

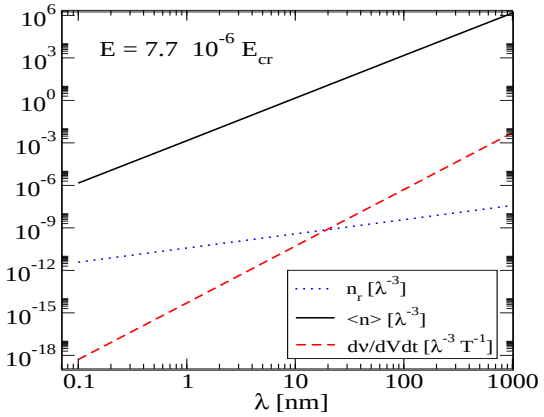

Figure 1: The laser wavelength dependence of the mean ($\langle n \rangle$) and residual (n_r) e^+e^- pair densities as well as the γ pair production rate per volume for the field strength $E = 7.7 \cdot 10^{-6} E_{\rm cr}$.

In conclusion, we have shown that the simplest model of the laser field predicts the creation of a dense quasiparticle plasma in the foci of the counter-propagating optical laser beams with parameters corresponding to presently operating systems [2, 1]. The plasma lives during a laser pulse and vanishes almost completely after switching off the field. The mean density does not depend on the frequency and reaches the values $10^{17} - 10^{18}$ cm^{-3} for field strengths $10^{10} - 10^{11}$ V/cm. One possible manifestation of this picture can be the pair of ≈ 1 MeV γ quanta emitted per laser pulse, another is the modulation of a probe laser beam with the time-dependent plasma density.

References

[1] C. Bula et al., Phys. Rev. Lett. **76**, 3116 (1996).
[2] B. Liesfeld, J. Bernhardt, K.-U. Amthor, H. Schwoerer, R. Sauerbrey, submitted to Appl. Phys. Lett.
[3] http://www-new.gsi.de/GSI-Future/cdr/
[4] S.M. Schmidt, D. Blaschke, G. Röpke, S.A. Smolyansky, A.V. Prozorkevich, and V.D. Toneev, Int. J. Mod. Phys. E **7**, 709 (1998).
[5] C.D. Roberts, S.M. Schmidt, and D.V. Vinnik, Phys. Rev. Lett., **89**, 153901 (2002).
[6] D.B. Blaschke, A.V. Prozorkevich, S.A. Smolyansky, A.V. Tarakanov, physics/0410114.
[7] D.B. Blaschke, A.V. Prozorkevich, R. Sauerbrey, S.A. Smolyansky, in preparation (2005).

Electron Cooling of Highly Charged Ions in Traps

B. Möllers, C. Toepffer, G. Zwicknagel
Institut für Theoretische Physik II, Universität Erlangen

Electron cooling in HITRAP [1] is an essential tool for providing cold ions required for planned precision tests of QED and experiments with low energetic highly charged ions or antiprotons. This method is well established in storage rings and is based on the energy loss of the ions due to Coulomb collisions with cold electrons. In Penning traps, like in HITRAP, the presence of a strong magnetic field presents a theoretical challenge. We thus developed several complementary analytical and numerical methods to calculate the cooling force [2], comprising linearized dielectric theory, a binary collision model [3], classical trajectory Monte Carlo (CTMC) calculations and particle-in-cell (PIC) simulations. Based on these results for the cooling force $\vec{F}(\vec{v}_i, T_e)$ or energy loss rate $dE_i/dt(\vec{v}_i, T_e) = \vec{F} \cdot \vec{v}_i$ we estimate cooling times from calculating the time evolution of the energy of the ions. The actual energy loss now depends on the actual ion velocity $\vec{v}_i$ and the electron temperature T_e. Since ions and electrons are trapped together, the temporal changes of T_e are important here. Hence three effects are taken into account for these calculations. The deceleration of the ion and its related energy loss, the heating of the electrons due to the energy transfer from the ions, and the cooling of the electrons by emission of synchrotron radiation [4]. This leads to the coupled differential equations for $\vec{v}_i(t)$ and $T_e(t)$ which are solved numerically:

$$\frac{d\vec{v}_i}{dt} = \frac{1}{M}\vec{F}(\vec{v}_i, T_e)$$

$$\frac{dT_e}{dt} = -\frac{2}{3k_B}\frac{n_i}{n_e}\frac{dE_i}{dt}(\vec{v}_i, T_e) - \frac{1}{\tau_e}(T_e - T_{e,0}) \quad .$$

M is the ion mass, n_i the ion density, n_e the electron density, $T_{e,0}$ the temperature to which the trap is cooled and τ_e the time constant for cooling of the electrons by the emission of synchrotron radiation.
Fig. 1 shows the ion energy $E_i = \frac{1}{2}Mv_i^2$ for U^{92+} ions as a function of time with $n_e = 10^7$ cm^{-3}, $B = 6$ T at a fixed electron temperature $T_e = T_{e,0} = 4$ K (that is for $n_i/n_e \to 0$) and different $\alpha := \sphericalangle(\vec{v}_i, \vec{B})$. The large variation of the cooling time with α results from the strong anisotropy of the cooling force $\vec{F}$ in the presence of the strong magnetic field. This is compared with the case $B = 0$, which yields the fastest cooling. If the heating of the electrons is taken into account (see Fig. 2 with $n_i/n_e = 10^{-4}$) this anisotropy is averaged out as a result of an intricate feedback between the electron temperature T_e (shown in the lower part of Fig. 2) and the force $\vec{F}(\vec{v}_i, T_e)$ on the ion. A similar qualitative behavior is also found for $n_i/n_e = 10^{-5}$ and 10^{-3} with cooling times 0.5 s and 4 s, respectively. Such a dependence on n_i/n_e and typical cooling times of the order of 1 s agree well with the previous findings of Ref.[4] where the influence of the magnetic field on dE_i/dt had been neglected. However, more quantitative comparison of the results of [4] with our calculations shows lower electron temperatures and cooling times which are longer by a factor $2-4$. - This work was supported by the BMBF (06ER128) and a GSI collaboration contract.

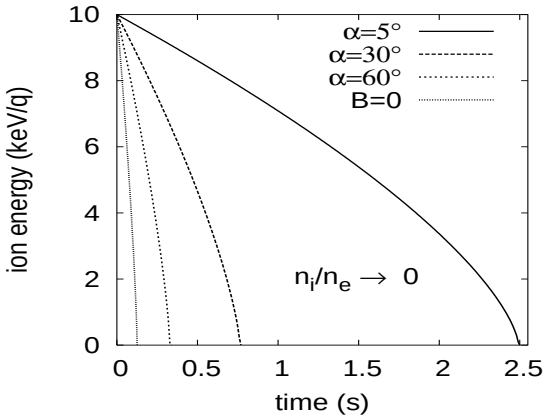

Fig.1: Temporal evolution of the energy of U^{92+} ions at a fixed electron temperature $T_e = 4$ K.

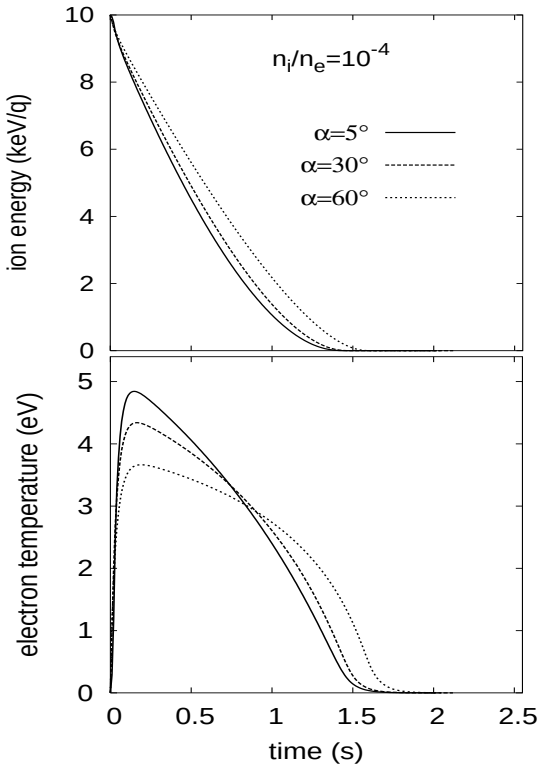

Fig.2: Time evolution of the ion energy and the electron temperature if electron heating is taken into account.

References

[1] W. Quint et al., Hyp. Int. **132** (2001) 457.
[2] B. Möllers et al., Nucl. Instr. Meth. B **205**, 285 (2003); Nucl. Instr. Meth. B **207**, 462 (2003); Nucl. Instr. Meth. A **532**, 279 (2004).
[3] C. Toepffer, Phys. Rev. A **66**, 022714 (2002).
[4] J. Bernard et al., Nucl.Instr.Meth. A **532**, 224 (2004)

PLPY-EXP

Plasma Physics

A fast 6-channel pyrometer for temperature measurement of HED matter generated by intense heavy ion beams

P. Ni[1], V.E. Fortov[3], V.K. Gryaznov[3], D.H.H. Hoffmann[1,2], A. Hug[1], M. Kulish[3], I. Lomonosov[3], Yu. Menzel[1], V. Mintsev[3], D. Nikolaev[3], N. Shilkin[3], A. Shutov[3], N. Tahir[2], V. Ternovoi[3], S. Udrea[1], D. Varentsov[1], and H. Wahl[2]

[1]TU Darmstadt; [2]GSI-Darmstadt; [3]IPCP-Chernogolovka

Recent experiments at the HHT area of the Plasma Physics group at the GSI were dedicated to investigation of heavy-ion-beam generated high-energy-density (HED) matter [1]. In contrast to traditional drivers like explosives, electrical discharges and powerful lasers, heavy ion beams can deposit energy into a sample material homogenously.

In the performed experiments, different metals (Pb, Fe, Sn, Cu) were heated by an intense uranium beam (350 AMeV, $2-4\cdot10^9$ particles, $150-230$ ns pulse duration) and the target's temperature was measured using a pyrometric method. The targets were foils oriented along the propagation of the beam with thickness ($\sim$200 μm) much smaller than the focal spot of the beam (1 mm). The free expansion of the foil was constrained by a pair of sapphire blocks. Under this conditions the target is optically thick and therefore has a Planck spectrum of thermal emission with a certain emissivity ($\epsilon(\lambda,T)$) of the surface:

$$I_{thermal}(\lambda,T)=\epsilon(\lambda,T)\cdot\frac{C_1}{\lambda^5}\cdot\frac{1}{e^{\frac{C_2}{\lambda T}}-1}.$$

We have designed and tested a special pyrometric setup that consists of a light collection system, a spectrum analyzer and a data recorder.

For optimal light collection we developed a special objective based on a pair of spherical mirrors (ten times more efficient than conventional glass objectives). The objective is mounted on a motorized holder driven by three linear translation stages with a 5 μm positioning accuracy.

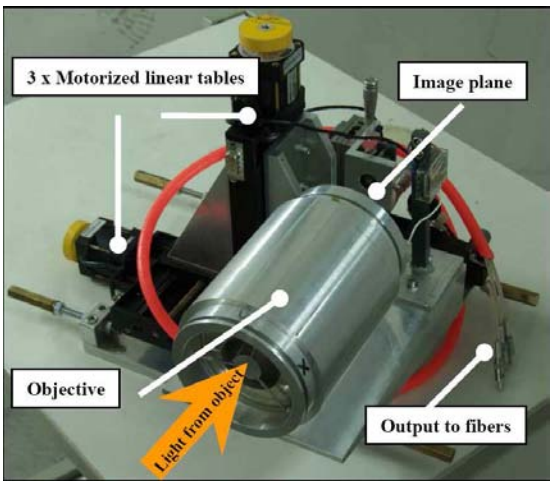

Figure 1: Light collection system.

The target's surface was 1:1 imaged on the entrance of an optical fiber (400 μm diameter, 100 m long) and transmitted to a remote spectrum analyzer. The 1:1 imaging in a broad spectral range is possible since the mirror system is achromatic.

The present intensity of uranium beams allows heating of metallic targets up to 6000 K with the maximum of thermal radiation in the visible and near infrared spectral regions. The spectrum is discriminated by interference filters (10 nm spectral width) centered at 550, 750, 850, 950, 1300 and 1500 nm. The scheme of light propagation inside the spectrum analyzer is shown in Figure 2. This analyzer

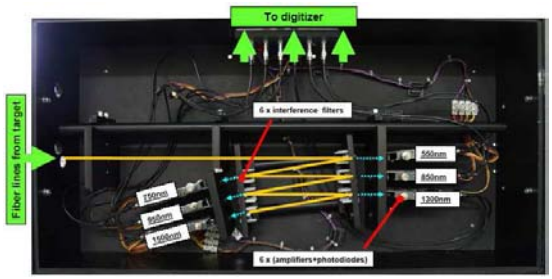

Figure 2: The spectrum analyzer.

has a higher efficiency in comparison to traditional schemes with beam splitters.

Filtered light is detected by fast photodiodes coupled to two-cascade, low noise, broadband amplifiers. The overall temporal resolution of the system is a few nanoseconds. Signals from detectors are recorded by a 12-channel digitizer (1 GHz bandwidth, 8 bit) operated by a specially written LabView software.

The pyrometer is absolutely calibrated using a tungsten ribbon calibration lamp from Osram. The absolute calibration allows immediate determination of so-called brightness (radiant) temperatures. For real objects, along with spectrum, knowledge of emissivity is necessary for precise determination of the true temperature. As the emissivity was not measured, it was approximated by gray body and linear dependance on wavelength models. Experimental signals $I_{experim}(\lambda_i)$ were fitted into a system of six equations using a model emissivity ϵ_{model}, and the temperature was one of the fitting parameters.

$$\{I_{experim}(\lambda_i)\}\rightarrow\{\epsilon_{model}(\lambda_i,T)\cdot\frac{C_1}{\lambda^5}\cdot\frac{1}{e^{\frac{C_2}{\lambda T}}-1}\},i=1,2,...6.$$

In the future, accuracy and sensitivity of the system will be improved by increasing the number of channels and by direct measurement of emissivity using reflectivity or polarimetry.

References

[1] Technical Proposal of the HEDgeHOB Collaboration.

Beam Emittance Measurement for Channel-based Ion Beam Transport

R. Knobloch[1], S. Neff[1], A. Tauschwitz[2], and D.H.H. Hoffmann[1,2]
[1]Technische Universität Darmstadt; [2]Gesellschaft für Schwerionenforschung

The transport of high-current beams is a crucial task in heavy-ion-beam-driven inertial fusion. Plasma-channel-based beam transport is a promising final transport concept which has been studied at the Gesellschaft für Schwerionenforschung and at the Lawrence Berkeley National Laboratory in recent years. Aspects of ion beam transport in plasma channels are studied with the Z4 beam transport experiment at GSI. In this experiment, plasma channels are formed by a high-voltage discharge in a background gas.

For any final beam transport scheme in a fusion reactor which includes drift space, it is important to know whether the beam quality decreases during beam transport. The most important measure of beam quality is the beam emittance. The particular challenge in a beam transport setup is an instantaneous measurement of the beam emittance, since all scanning measurements cannot be used to investigate changes during beam transport.

The beam is sent through the transport channel, then passes a gold pepper-pot foil of 35 m thickness and a drift space of several centimeters before it is made visible on a plastic scintillator which is photographed by a fast CCD camera. The integration of the emittance diagnostics into the setup is shown in Fig. 1.

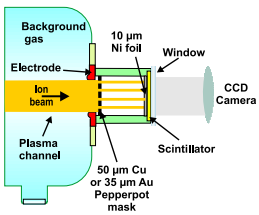

Figure 1: Emittance diagnostics setup

The drawback of the Al-coated BC-100 plastic scintillator used is that after several shots, the material starts to show burnout damage. Fig. 2 illustrates the change in the intensity profile of a pepper-pot spot due to scintillator burnout.

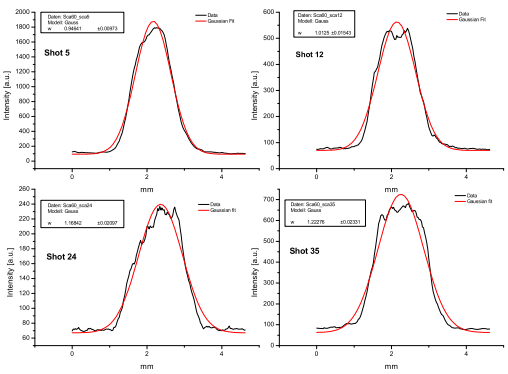

Figure 2: Scintillator burnout

The influence of burnout damage on the FWHM of a 2D Gaussian fit of the spot intensity profile, which was taken to be the spot width, had to be investigated. Results showed that the width of the fit is not very sensitive to the actual profile shape, and the effect is negligible in comparison to other errors. One of the largest sources of error in the setup is the location of the axis. The ion beam follows the discharge, which shifts slightly between shots. So, the location of the axis had to be determined individually from each picture by comparing the spots to a reference image and using linear regression to calculate the axis position. From measured spot widths and distances with respect to the axis, the emittance can be calculated [1]. A more exact formula is given in [2].

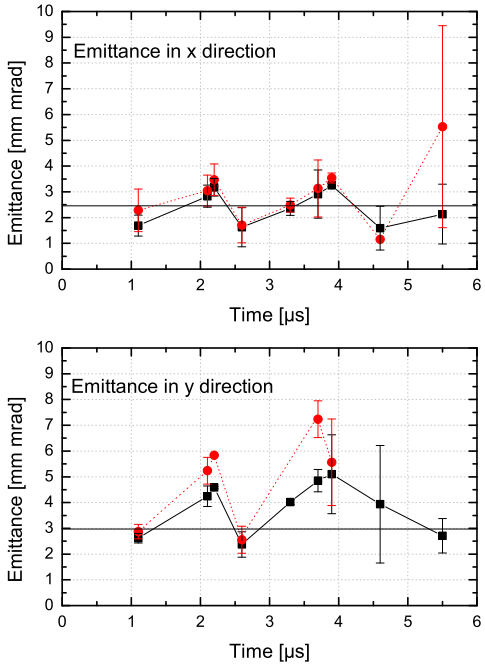

Figure 3: Measured emittance in x (upper panel) and y (lower panel). Solid lines and squares use the simple model from [1]; dashed lines and circles represent the more exact model from [2]. Horizontal lines indicate ”zero” emittance from UNILAC.

These emittance measurements were the first attempt at the Z4 setup to measure this important beam property instantaneously during beam transport through a plasma channel. The results show that the method is basically feasible and is able to produce results using only a single shot image and a reference. Within errors of about 25 %, the emittance was shown to be constant.

References

[1] J.G. Wang et al., *IEEE Transactions on Electron Devices* Vol. 37, No. 12, page 2622 (1990)
[2] J.G. Wang, D.X. Wang and M. Reiser, ”Beam Emittance Measurement by the Pepper-pot Method”, Nucl. Instr. and Methods in Physics Research A 307, 190-194 (1991)

CAST – The Solar Plasma as Laboratory for Axions

M. Kuster[1,2], T. Dafni[3,1], D.H.H. Hoffmann[1,3], J. Jacoby[4], and M. Kanapathipillai[3,1]
[1]Insitut für Kernphysik, TU Darmstadt, Germany; [2]Max-Planck-Institut für extraterrestrische Physik, Germany;
[3]GSI Darmstadt, Germany; [4]Universität Frankfurt, Germany

Our neighboring star the sun provides a deep insight into the physics of fusion, the physics of hot plasmas and is an excellent laboratory for astroparticle physics. As such the sun can be used to probe the existence of novel particles and dark matter candidates like the axion. The axion is a direct consequence (Weinberg, 1978; Wilczek, 1978) of the theoretical solution of the CP problem in strong interactions proposed by Peccei & Quinn (1977). Inside the core of the sun axions could be produced by coherent conversion of thermal photons interacting with the electromagnetic field of charged particles of the solar plasma (Primakoff effect). With the *CAST* experiment at *CERN*, we

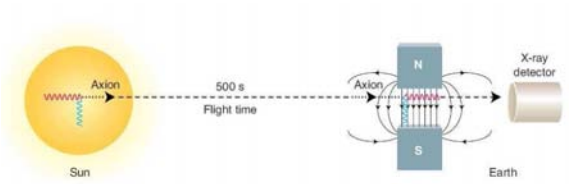

Figure 1: Physical principle of the CAST experiment (Zioutas et al., 2004b).

aim to detect such solar axions on earth by "converting" them back to X-ray photons inside a strong transversal magnetic field (inverse Primakoff effect, see Fig. 1). The conversion probability of axions to photons is proportional to the square of the strength of the magnetic field and its length. Thus, a strong magnetic field is essential to achieve a high sensitivity of the experiment.

The heart of CAST is a prototype LHC superconducting magnet providing a dipole magnetic field of $\approx 9\,\mathrm{T}$ in the interior of two parallel pipes over a distance of 9.26 m. On both ends of the magnet X-ray detectors are looking for a potential axion signal as an excess signal over detector background. A TPC detector covers two magnet bores on one end looking for axions during sunset. On the opposite side of the magnet, a micro mesh gas detector (Andriamonje et al., 2004) and an X-ray telescope with a pn-CCD detector are looking for axions at sunrise (Kuster et al., 2004). The magnet can be pointed towards the sun for about 1.5 h during sunrise and sunset, resulting in 3 h observation time per day. The remaining time is used for systematic background studies. The most sensitive detector system of *CAST* is the Wolter I type X-ray telescope which enhances the signal-to-background ratio by a factor of ≈ 100 by concentrating the potential signal flux on a small spot on the pn-CCD detector.

During the last two years *CAST* was taking data for about twelve months, six months during 2003 and during 2004. The analysis of the 2003 data reveals no significant excess signal over background and allows us to set a new upper limit on the axion to photon coupling of $g_{a\gamma\gamma}(95\,\%) < 1.16 \times 10^{-10}\,\mathrm{GeV}^{-1}$ (Zioutas et al., 2004a). Fig. 2 shows the corresponding combined upper limit of all three detector systems derived from the analysis of the

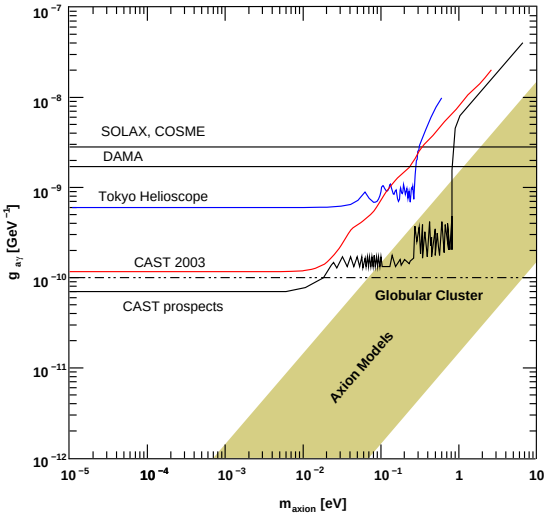

Figure 2: Upper limit (95 %) of the axion to photon coupling $g_{a\gamma\gamma}$ depending on the axion mass m_a derived from the data of 2003. The shaded area represents the parameter range of theoretical axion models. The results of earlier experiments *SOLAX*, *COSME*, *DAMA*, and the Tokyo helioscope are shown for comparison (Zioutas et al., 2004a). The best astrophysical limit based on evolutionary models of horizontal branch stars in globular clusters is indicated as "Globular Cluster".

2003 data. The analysis of the 2004 data is still in progress and will further improve the upper limit, such that we can surpass the best astrophysical limits in the *CAST* axion sensitive mass range ($m_a < 0.02\,\mathrm{eV}$, see Fig. 2). Due to coherence effects, the *CAST* helioscope in its current configuration is sensitive for axions with masses $m_a < 0.02\,\mathrm{eV}$. To extend the sensitivity to $m_a < 1.2\,\mathrm{eV}$ the refractive index of the conversion volume has to be changed. Then, the photon acquires an effective mass ($m_\gamma = m_\mathrm{a}$) and the momentum exchange during the Primakoff effect becomes negligible. This is forseen for the second phase of *CAST* starting mid of 2005, by filling the magnet pipes with an adequate buffer gas like ^{3}He or ^{4}He.

References

Andriamonje, S., et al., 2004, Nucl. Instrum. Methods Phys. Res., Sect. A, 518, 252
Kuster, M., et al., 2004, in Gravitational Wave and Particle Astrophysics Detectors, ed. J. Hough, G. H. Sanders, (Bellingham, WA: SPIE)
Peccei, R. D., & Quinn, H. R., 1977, Phys. Rev. Lett., 38, 1440
Weinberg, S., 1978, Phys. Rev. Lett., 40, 223
Wilczek, F., 1978, Phys. Rev. Lett., 40, 279
Zioutas, K., et al., 2004a, Phys. Rev. Lett., submitted
Zioutas, K., Hoffmann, D., Dennerl, K., & Papaevangelou, T., 2004b, Science, 306, 1485

Development of a dc magnetically confined plasma target for ion beam plasma interaction experiments

M. Iberler, R. Berezov, J. Jacoby, Ch. Teske

Inst. für Angewandte Physik, J.W.Goethe-Universität, D-60325 Frankfurt/Main, Germany

The propagation of a high-current ion beam in a background plasma is of considerable interest for many experiments. It has been shown, that the stopping power for heavy ions of a fully ionised plasma is up to forty times higher than of cold gases [1]. For this reason a new kind of gas discharge plasma target is now under investigation at Frankfurt University.

The particular embodiment of this new plasma target is based on an electrodeless configuration. The energy deposition into the plasma was done by cw-inductive coupling per antenna [2]. The fact that the plasma is a mixture of charged particles means it can be controlled and influenced by magnetic fields. Therefore a radial time independent quadrupole magnetic field was applied to confine the plasma. Due to the linear magnetic field gradient the confinement of the radio-frequency plasma is achieved by the stronger focusing than defocusing forces on the alternating electrons during the discharge [3]. Due to the interaction of the high frequency inductive coupling and the radial magnetic field the electron temperature increases steadily towards the centre of the discharge.

During this focusing effect of the magnetic field influenced by the electric fields of the rf-coil the ionisation and excitation of the atoms and ions are very effective and the current density is concentrated within a small area of the centre axis. Because of the magnetic minimum close to the centre axis the electrons will follow only the inductive coupled electrical field. In order to inhibit the movement of the charged particles along the axis two ring magnets are placed at the ends of the discharge functioning as a magnetic mirror. The inductive coupled plasma is run in a CW mode. The main section of this experimental set-up is a glass discharge tube of about 21 mm inner diameter wrapped with a radial field coil. The bias pressure of the discharge tube was in the range of 10^{-7} Pa and than filled with argon at a pressure in the range from 0.5-1.5 Pa. The next figure 1 shows a schematically drawing of the experimental set-up with the confined plasma.

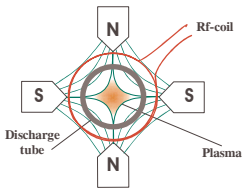

Fig.: 1 Schematic drawing of the used configuration.

With spectroscopic measurement we are studying the plasma parameters of argon depending on the radial magnetic quadrupole field, the gas pressure and the plasma power input. The measurements were performed with high magnetic fields between 0-1.5 T and at a rf-power input of 300 W.

The spectroscopic investigations were done with using three various field coils and by variation of the gas pressure for each. The differences between this used coils are in length, inductivity and windings. The inductivity various from 2.1 µH for the coil with 18 cm in length and 7 windings to 3.5 µH with 12 cm and 15 windings. With respect to the skin effect a 10 cm^2 copper wire was used.

To determine the plasma temperature and the ionisation degree the spectra of the argon plasma was analysed. For this purpose two different emission lines of excited and one time ionised Argon was used. Using [4] the electron temperature can be evaluated from the relative line intensities by applying the Saha equation. In case of the long field coil with the inductivity of 2.1 µH the measured maximum electron temperature was between 1.1-1.2 eV. Using the coil with the 3.5 µH the electron temperature was increasing almost 2.9 eV at a pressure of 1 Pa. The next figure shows the electron temperature dependent on the pressure.

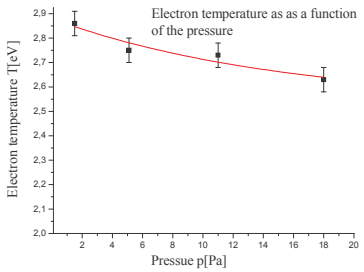

Figure 1: Electron temperature in dependent on the pressure of the argon plasma.

Now under progress are measurements for the determination of the electron density. For this purpose a 1 m spectrometer will be used.

Further investigations are proposed in the field of heavy ion interaction with the optimised plasma parameter. For this experiment a cylindrical time independent plasma target will be used for the ion beam target interaction to achieve a gas temperature in the range of several tens eV. This work was partially founded by the BMBF.

References

[1] J. Jacoby, D. Hoffmann, W. Laux, R. Müller, H. Wahl, K. Weyrich, E. Boggasch, B. Heimrich, C. Stöckl, H. Wetzler, S. Miyamoto, Phys. Rev. Lett., **74**, (1995), 1550.

[2] Peiyuan Zhu, R.W. Boswell, "A new argon-ion laser based on an electrodeless plasma", Journal of applied Physics, 68, No 5, September 1990.

[3] J. Christiansen et al., "High-frequency discharge gas-laser embedded in a magnetic multipole field", Patent pending, Aktenzeichen 199 30 755.5, München 1999.

[4] H. Griem. "Plasma Spectroscopy" *McGraw-Hill Book Company* 1964.

Heavy ion charge state and velocity dynamics during the stopping process

O. Rosmej[1], S. Pikuz[2], S. Korostiy[1], A. Blazevic[1], V. Efremov[2], A. Fertman[4], T. Mutin[3], D.H.H. Hoffmann [1, 4]

[1]GSI-Darmstadt, Germany; [2] Institute High Energy Density, Moscow [3] ITEP, Moscow; [4]TU-Darmstadt, Germany

The characteristic *K*-shell emition induced due to close collisions of heavy ions with target atoms was used to analyze the projectile stopping dynamics over more than 80% of the ion stopping path. The most important advantage of this method is that the information is collected directly from the interaction volume. From the projectile characteristic spectra one can conclude about the ion velocity and ion charge state dynamics along the ion stopping path. The line intensity distribution of $K\alpha$–satellites reflects the ion charge distribution. The variation of the line Doppler shift due to the ion deceleration in the target material was used to determine the ion velocity dynamics [2-4].

The stopping range of 11.4 MeV/u Ca ions in solid quartz (ρ = 2.23 g/cm^3) is of 170μm. Application of low density SiO_2 aerogel targets allows stretching the ion stopping range up to 100 times. It gives a possibility to visualize projectile and target radiation dynamics along the stopping range.

Comparison of the ion stopping process in porous and solid media was carried out recently (see GSI Report 2003). Experimentally it was shown that porous structure will not influence the projectile charge state distribution provided the time of flight of the ion inside the pore in vacuum is shorter than the time scale of the radiative- and Auger processes, which lead to the collision less relaxation of the projectile excited states.

In experiments reported below, new results on the interaction of 11.4 Me V/u Ca ions with SiO_2 aerogel target of 0.04 and 0.02 g/cm^3 volume density were obtained.

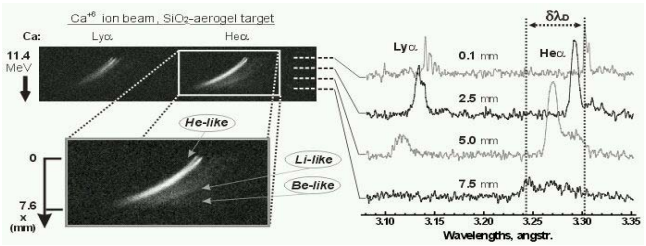

Fig.1 Ca projectile *K*-shell spectra. Vertical axis is the ion beam penetration depth (mm), horizontal axis – wavelength (A).

A much higher resolution of the ion charge and velocity dynamics as compared to the previous experiments was achieved due to application of aerogel targets with extreme low mean density. The x-ray emission from the ion beam - target interaction zone was registered by means of focusing spectrographs having a high spatial resolution (FSSR) [1, 2]. Spherically bent (R=150mm) crystals of mica and quartz were used as dispersive elements. Ca and Si $K\alpha$ - spectra in the ranges of (3.1 – 3.4) and (6.6 - 7.3) Å respectively resolved along the ion beam trajectory were measured. Figure1 shows the typical *K*-shell spectrum of highly ionized Ca projectile ions moving in solid matter. The stopping length of 11.4 MeV/u Ca in 0.04g/cm^3 aerogel target reaches 8.16 mm [SRIM]. We are able to register the ion *K*-shell radiation over 7.6 mm and therefore to analyze the projectile stopping dynamics over 80% of the ion pass with a spatial resolution of 50 μm. The length of the spectral lines at the detector (x-ray film) is a magnified length of the ion beam – target interaction zone [1, 2].

By observation of the projectile radiation perpendicular to the relativistic ion beam trajectory transversal Doppler red shift λ_D is dominating:

$\lambda_D = \lambda_0 / (1-\beta^2)^{1/2}$; $\beta = v/c$ (1),

Here λ_0 is a wave length of a radiative transition of the ion in rest; λ_D is a wave length of a radiative transition of the moving ion; v – the ion velocity; c – the light velocity.

The line shift is decreasing continuously along the ion path due to the ion energy loss. The spectral lines in the spatially resolved spectrum are tilted demonstrating the ion deceleration (see Fig. 1).

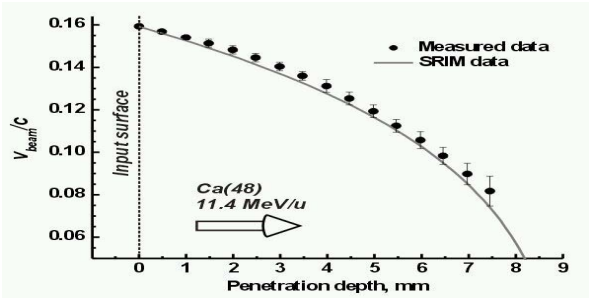

Fig. 2: The velocity dynamics of Ca ions with initial energy of 11.4 MeV/u versus ion penetration depth in 0.04g/cm^3 aerogel target.

Using the Doppler Shift Attenuation (DSA) method, ion velocity dynamics during the stopping process in solid media was analyzed. Figure 2 demonstrates the dependence of the ion velocity on the ion penetration depth in the aerogel target. Experimental results are in a good agreement with the calculated data [www.SRIM.org]. The *K*-shell projectile ion spectra show that the radiation of Ca^{+18} and Ca^{+19} ions is dominating down to the projectile energy of 3.5 MeV/u. The radiation of *Li*-like Ca (Ca^{+17}) can be registered at the energies lower than 7.5 MeV/u. At the end of the observed ion path (7.5mm), due to increase of the recombination cross sections at low energies, the intensity of Ly_α– transition in Ca^{+19} is vanishing and Be-like ions start to radiate. The quantitative analysis of the ion charge state dynamics demands the detailed description of the projectile bound electron population kinetics and is in the process. The experimental results on the ion velocity dynamics will be used for calculations of collision cross sections.

References:

[1] A.Ya. Faenov et al, Phys. Scripta, **50**, 333 (1994)
[2] O.N. Rosmej et al, NIM A **495**, 29 (2002)
[3] O.N. Rosmej et al, RSI, 74, No12, 5039 (2003)
[4] O.N. Rosmej et al, LPB, **23** (2005), in print

This work was supported by WTZ grand 02/001-6.98 and NATO grand PSTT CLG 979372

Laser produced chlorine plasma radiation studies for x-ray scattering experiments

M.S. Schollmeier[1], G. Rodríguez Prieto[1,2], F.B. Rosmej[3], G. Schaumann[1], A. Pelka[1], O.N. Rosmej[2], M. Roth[1], and D.H.H. Hoffmann[1,2]

[1]TU Darmstadt; [2]GSI Darmstadt; [3]PIIMA, Université de Provence et CNRS, Marseille

The scattering of x-rays on bound and free electrons in a dense plasma can be applied for the characterization of solid density and super-dense plasmas [1, 2]. This scattering results in a spectrum that is not symmetric due to the dynamic structure factors at each side of the central wavelength, related by $S(-\omega,k) \propto \exp(-\hbar\omega/k_BT_e)S(\omega,k)$. This is not important in the optical case ($\hbar\omega \ll k_BT_e$) but for x-rays. There is a Compton red-shift of scattered photons (0–90 eV) from the incident wavelength surrounded by Doppler-broadened Thomson scattering. Due to the extremely small Thomson scattering cross section of $6.65 \cdot 10^{-25}\,\mathrm{cm}^2$, a photon number about 10^{15} [3, 4] at energies of a few keV is needed for diagnostics. Simultaneously the spectral broadening $\Delta\lambda/\lambda$ of the probe radiation must be smaller than $4 \cdot 10^{-3}\sqrt{\mathrm{T}_e[\mathrm{eV}]}$ in order to resolve the Doppler broadening [5]. The He_α-line emission of medium-Z plasma produced with a high energy laser can fulfill both of these requirements. However, this radiation is not monochromatic but forms a narrow band due to the emission of dielectronic satellites. Therefore in x-ray scattering experiments the plasma source of x-rays needs to be diagnosed with a high spectral resolution. Unfortunately the highly reflecting HOPG-crystals [1, 2] that were used to disperse the scatter radiation do not have this high spectral resolution. Hence we have developed a method to calculate the signal that a HOPG spectrometer will measure from the spectrum mesured by a spectrometer with high spectral resolution.

The experiments were performed at the *nhelix* laser system installed at GSI [6] with a laser energy of 45 J. The targets were chlorine-doped samples and the Cl-He_α ($\lambda = 4.4444$Å, $E = 2.7$ keV) plasma radiation was simultaneously observed with a focusing spectrometer with spatial resolution (FSSR) [7] in fourth order and a HOPG-crystal spectrometer that was developed especially for these experiments. The spectral resolution of the HOPG-spectrometer could be increased due to the mosaic focusing effect [8]. In both spectrometers the x-rays were detected with Kodak DEF-5 films. The detailed analysis of the measured spectral lines was done with the development of a simple model for dielectronic recombination of helium-like ions and inner shell excitation of lithium-like ions that is based on ref. [9]. This model allows the estimation of the electron temperature from the line ratios of the optically thin lines jk and the higher order dielectronic satellites $1s2l3l' \longrightarrow 1s^23l'$. The necessary atomic data were calculated with the MZ-Code [10] including all satellites up to $1s2l4l'$.

The highly resolved measured spectrum of He-like Cl is shown in fig. 1(a) together with the fitted spectrum from the line calculation procedure. This fitting procedure indentifies the dielectronic satellite structure that is designated following the notation of A.H. Gabriel [11]. With the same fitting parameters but by changing the spectral resolution in the procedure the spectrum that the HOPG-spectrometer should have measured was calculated. This synthetic spectrum was then compared to the measured one. The comparison is shown in fig. 1(b). Despite slight differences the spectrum is well reproduced. The intercombination line y is not well reproduced due to the simple modelling that neglects density and transient effects.

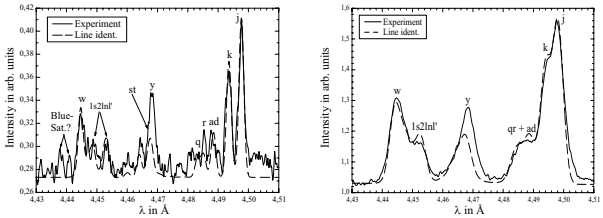

(a) Spectrum measured with FSSR spectrometer

(b) Spectrum measured with HOPG-spectrometer

Fig. 1: Measured spectra and calculated spectrum with the simple model. The line ratios of the dielectronic satellites j,k and higher order satellites $1s2lnl'$ allow the determination of the electron temperature to $T_e = 285$ eV.

With this method the red-shifted broadening of He_α line w due to the influence of dielectronic satellites can be determined experimentally and therefore shot-to-shot variations in the experiments can be taken into account. This asymmetric broadening on the red side should be taken into account in x-ray scattering experiments because there the Doppler-broadened Compton red shift is analysed.
The details of the methods describes here are written in ref. [12].

References

[1] S.H. Glenzer *et. al.*, Phys. Rev. Lett. **90**, 175002 (2003)
[2] G. Gregori *et. al.*, Phys. Plasmas **11**, 2754 (2004)
[3] O.L. Landen *et. al.*, JQSRT **71**, pp. 465-478 (2001)
[4] D. Riley and F.B. Rosmej, GSI-Report **2004-3**, 61 (2004)
[5] J. Sheffield, Plasma scattering of electromagnetic radiation (Academic Press, New York, 1975)
[6] G. Schaumann *et. al.*, this report
[7] A.Ya. Faenov *et. al.*, Phys. Scr. **50**, pp. 333-338 (1994)
[8] M. Sanchez del Rio *et. al.*, SPIE proceedings **3448**, 246 (1998)
[9] F.B. Rosmej, Europhys. Lett. **55**, 472 (2001)
[10] L.A. Vainshtein and U.I. Safronova, ADNDT **25**(4), 311 (1980)
[11] A.H. Gabriel, Mon. Not. R. astr. Soc. **160**, pp. 99-119 (1972)
[12] M.S. Schollmeier, diploma thesis, TU Darmstadt (2004)

Measurements of an Electron Beam Assisted Laser Ion Source

V. Orsic Muthig[1,3], Bianca Cudalbu[2], D.H.H. Hoffmann[3,4] , J.Jacoby[1], S. Krebs[4],
Gonzalo Rodriguez Prieto[3] U. Ratzinger[1], A. Tauschwitz[3]

[1]JWG-Univ. Frankfurt, Germany; [2]NILPRP, Magurele, Bucharest, Romania; [3]GSI, Germany; [4]TU Darmstadt, Germany;

In order to study the effects of space charge neutralization in a laser ion source (LIS) [1], a high current electron source [2] was combined with a LIS, as shown in Fig. 1.

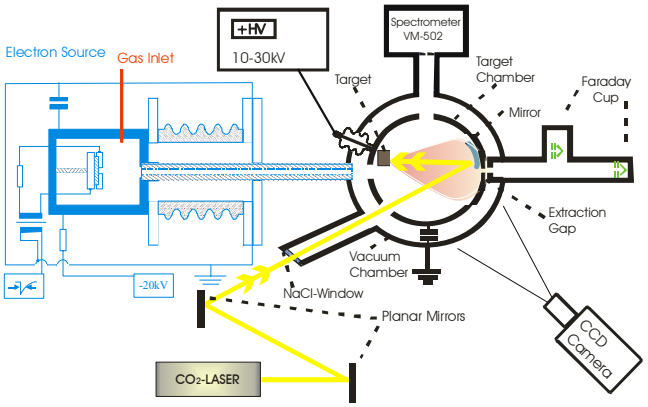

Fig. 1:Set-up of the neutralization experiment. The part of the figure depicted in blue represents the electron source.

Since the working pressure of the electron source is much higher (approx. 10^{-3} mbar) than the pressure needed in the ion source (approx. 10^{-6} mbar), a gas inlet into the hollow cathode of the electron source was built. This change in the experimental set-up, and increasing the length of the capillary tube (by a factor of two) connected to the hollow cathode, separates the vacuum systems of electron and ion source and thus allows the operation of the electron source connected to the ion source. Due to the highly decreased pressure at the end of the capillary tube, the electron source produces a current of 100 A only, which is a factor 10 below the current under best pressure conditions. The electron beam diameter increases slightly caused by the non-ideal pressure in the LIS.

The operation of the electron source leads to the following effects in the LIS:

- spark discharges between the extraction electrodes,
- a partial voltage break-down at the extraction.

To circumvent these problems, the total capacity connected to the extraction system was increased from 7.2 nF to 42 nF and the shape of the extraction electrodes was optimized to reduce voltage breakdown problems, (Fig. 2).

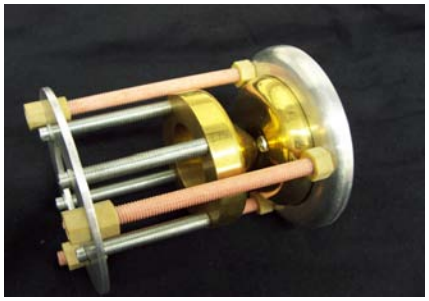

Fig. 2: Shape optimized extraction electrodes

The measurement of the electric current is performed with a faraday cup that cannot distinguish between electron and ion beam. The separation of these two beams is realized with the magnetic field of a permanent magnet which deflects the electron beam and leaves the ion beam mainly unaffected (Fig. 3).

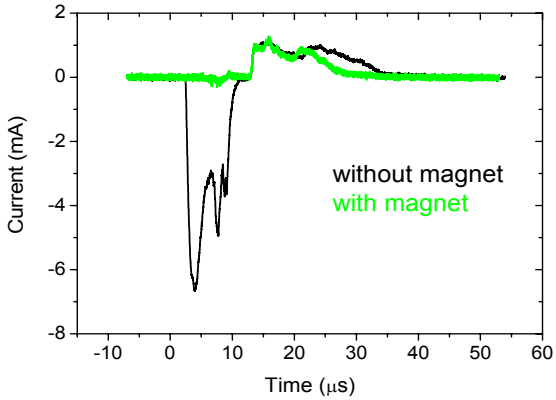

Fig. 3: Faraday cup measurements of both electron and ion beams with (green line) and without (black line) magnetic field.

The plasma expansion with (right part of Fig. 4) and without (left part of Fig. 4) electron beam was recorded with a gated CCD camera.

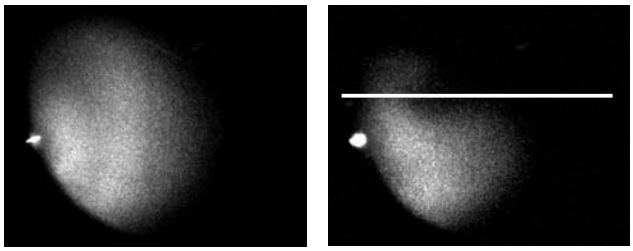

Fig. 4: Picture of the plasma cloud 6 µs after laser impact on the carbon target (left side without electron beam, right side with electron beam). The white line on the right side represents the axis of the electron beam, which has a maximum diameter of 2 cm.

In a spectroscopic measurement of the emitted plasma light in the wavelength region between 100 nm and 500 nm which was performed parallel and perpendicular to the direction of plasma expansion, no significant differences in line intensities of the charge states C^{1+}, C^{2+} and C^{3+} could be observed with or without using the electron source.

References

[1] V. Orsic Muthig *et al.* GSI-2003-1 Report, 136 (2003)
[2] V. Orsic Muthig *et al.* GSI-2004-3 Report, 23 (2004)

Microfield distribution in a strongly coupled two-component plasma

H. B. Nersisyan, C. Toepffer, and G. Zwicknagel
Institut für Theoretische Physik II, Universität Erlangen

The spectral line shapes of a radiator (atom or ion) immersed in a plasma are a valuable diagnostic tool and yield important information about the system [1]. Under certain assumptions [1, 2], the observed line shapes can be closely related to the electric microfield distribution (MFD) at the position of the radiator [2]. Since the pioneering work of Holtsmark [2], various theoretical approaches to determine the MFD with improved accuracy have been proposed (see, e.g., [3, 4] for reviews). Among them is the APEX treatment of Ref. [5], which involves a non-interacting quasiparticle representation of the screened ions, designed to yield the exact second moment of the MFD. Originally APEX has been developed for the MFD of a one-component plasmas (OCP) either of ions or electrons completely neglecting the influence of the attractive interactions between electrons and ions. We thus generalized APEX to a classical two-component plasma (TCP). For a TCP with spherically symmetric interactions between the particles and in thermal equilibrium the normalized MFD, $P(E)$, at a radiator with charge $Z_R e$ is given by

$$P(E) = \frac{2E}{\pi} \int_0^\infty \exp\left[-T(k)\right] \sin(kE)\, k dk,$$

$$T(k) = 4\pi k \sum_\alpha n_\alpha \int_0^\infty e_\alpha(r) \psi\left(kE_\alpha(r)\right) g_{\alpha R}(r) r^2 dr.$$

Here $\psi(x) = \frac{1}{x}\left(1 - \frac{\sin x}{x}\right)$ and n_α, $e_\alpha(r)$ and $E_\alpha(r)$ are the density, single-particle and effective fields of the species $\alpha = e, i$, respectively ($n = n_e + n_i$ is the total plasma density). $g_{\alpha R}(r)$ denotes the radial distribution functions (RDF) between radiator and plasma particles of species α. To calculate $P(E)$, the RDFs, $g_{\alpha R}$ and the effective fields, E_α, have to be known. In contrast to the original APEX, the effective fields are here derived from the $g_{\alpha R}$ within the potential of mean force approximation (PMFA) as

$$E_\alpha(r) = \frac{k_B T}{Z_R e} \frac{\partial}{\partial r} \ln g_{\alpha R}(r)\,,$$

where T is the plasma temperature. This automatically satisfies the exact second moment of $P(E)$ without any adjustable parameter. The required $g_{\alpha R}$ are calculated from the hyper-netted chain (HNC) equations for a TCP. To check the outlined APEX scheme we also determined $P(E)$ and $g_{\alpha R}$ by performing classical molecular-dynamics (MD) simulations. This has been done for a TCP with a bare Coulomb interaction between particles of the same species and an attractive ion-electron interaction which has been regularized at small distances using $V_{ei} \propto (1 - e^{-r/\delta})/r$. For all studied moderately coupled plasmas we found very good agreement between both the RDFs from MD and HNC and the MFD taken either from the MD or the APEX approach. As two examples we show the MDFs, $P(E)$, for a hydrogen TCP with coupling parameters $\Gamma_{ee} = \Gamma_{ii} = 1$ (Fig. 1) and for an Al^{+13}-e^- plasma with $\Gamma_{ee} = 0.1$ and $\Gamma_{ii} = 7.19$ (Fig. 2). The filled circles represent the microfield distributions from the MD simulations and the solid curves the results of the APEX with PMFA and the $g_{\alpha R}$ from HNC. The microfields are scaled in units of the ionic Holtsmark fields $E_0 = Ze/4\pi\varepsilon_0 a_i^2$ with $a_i = (4\pi n_i/3)^{-1/3}$, and $\delta = 0.4a$ has been used in both cases, where $a = (4\pi n/3)^{-1/3}$. For comparison we also plotted the Holtsmark MFD for a TCP (dotted) and the MFD obtained from MD simulations of the corresponding ionic OCP with Γ_{ii} (open circles). The attractive ion-electron interaction obviously shifts the MFD towards higher microfields. We are currently investigating the effect of this shift on the spectral line shape by solving the time-dependent Schrödinger equation for the radiating electron, as outlined in Ref. [3].–This work is supported by the GSI collaboration contract ER/TOE.

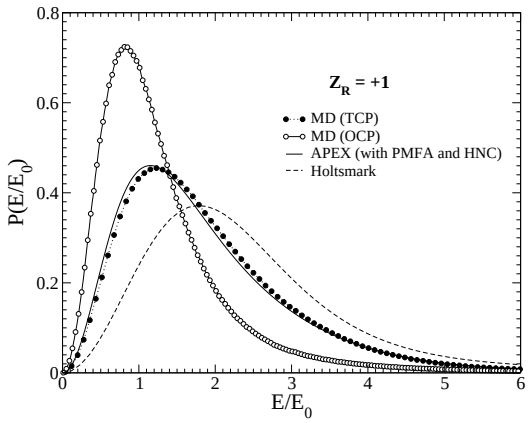

Figure 1

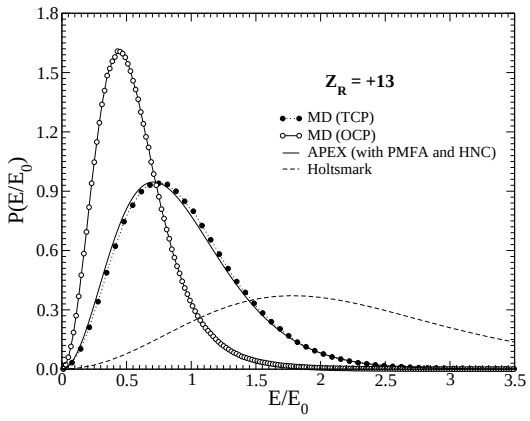

Figure 2

References

[1] H. R. Griem, *Spectral Line Broadning by Plasmas* (Academic Press, New York, 1974).
[2] J. Holtsmark, Ann. Phys. (Leipzig) **58** (1919) 577.
[3] J. Marten and C. Toepffer, Eur. Phys. J. D **29** (2004) 397.
[4] B. Talin *et al.*, Phys. Rev. E **65** (2002) 056406.
[5] C. A. Iglesias *et al.*, Phys. Rev. A **28** (1983) 1667.

Potential of the CERN Large Hadron Collider to Study High Energy Density States in Matter

N. A. Tahir[1], V. Kain[2], R. Schmidt[2], A. Shutov[3], I. V. Lomonosov[3], V. Gryaznov[3], V. E. Fortov[3], A. R. Piriz[4], M. Temporal[4], and D. H. H. Hoffmann[1,5]

[1]GSI Darmstadt; [2]CERN Switzerland; [3]IPCP Chernogolovka; [4]Univ. Castilla-La Mancha; [5]TU-Darmstadt

The motivation to construct the Large Hadron Collider (LHC) at CERN comes from fundamental problems in Particle Physics. The LHC is being installed in a tunnel with a circumference of 26.8 km that was previously used for the Large Electron Positron Collider (LEP). Two counter rotating proton beams will be made to circulate in separate beam pipes and will be accelerated to particle energies of 7 TeV. The protons in the two beams will then be made to collide at the center of mass energy of 14 TeV.

Each beam will consist of a bunch train with every bunch consisting of 1.15×10^{11} protons. The total number of bunches will be 2808, so that the total number of protons in each beam will be 3×10^{14}. The bunch length will be 0.5 ns and two neighboring bunches will be separated by 25 ns while the radial power profile in the beam spot will be Gaussian with a standard deviation of 0.2 mm. The total duration of the beam is of the order of 89 μs.

It is interesting to note that a very important "spinoff" of the LHC could be the studies of high-energy-density (HED) states in matter, because interaction of such powerful beams with solid matter would lead to creation of these exotic states. These include expanded as well as compressed hot liquid states, two-phase liquid-gas region, critical point region and strongly coupled plasma states including exotic phase transitions in nonideal plasmas.

In order to study the potential of using the LHC beams for this purpose, we carried out numerical simulations of thermodynamic and hydrodynamic response of a solid copper target that is irradiated with one of the LHC beams. The simulations have been carried out using a two-dimensional computer code BIG-2[1] which is based on a Godunov type numerical scheme. A multiphase semi-empirical EOS model[3] is used to treat different phases of the target material . Our simulations show that the first bunch deposits about 2.5 kJ/g specific energy in the target. The specific energy deposition increases as the subsequent bunches deliver their energy to the target.

It is well known that energetic heavy ions deposit their energy in the target as a result of Coulomb collisions, mainly with the target electrons. The 7 TeV protons, on the other hand, when incident on matter, will generate particle cascades in all directions and one needs to calculate the energy deposited by all these different particles in the target. For this purpose we have used the well known particle interaction and transport Monte Carlo code, FLUKA[2]. This code is capable of calculating all components of particle cascades in matter from TeV energies down to that of the thermal neutrons. The energy deposition profile calculated by the FLUKA code is used as input to the BIG-2 code. The target geometry for the FLUKA simulations is considered to be a cylinder of solid copper that is 5 m long and has 1 m radius. The energy deposition profile along the target axis per bunch (after 1 ns) is shown in Fig.1.

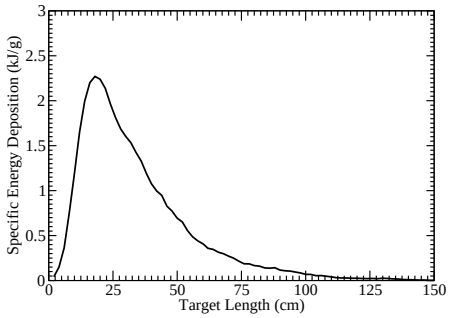

Figure 1: Specific energy deposited by one bunch along the target axis.

The longitudinal peak of energy deposition occurs at about 15 cm and the deposited energy is a factor 1250 lower than the peak value at about 1.5 m. Energy deposition profiles along the transverse direction at four different points along the length, namely, 8 cm, 16 cm, 24 cm and 36 cm are plotted in Fig.2.

For the BIG-2 calculations we consider a cylinder made of solid copper with a radius of 5 cm and the beam is incident along the axis. Due to the three dimensional nature of the energy deposition calculated by the FLUKA code, and the limitation that the BIG-2 code is two-dimensional, we simulate target heating and expansion in the transverse plane at different longitudinal positions, L. Here we only report results corresponding to L = 16 cm where the maxima of the energy deposition lies.

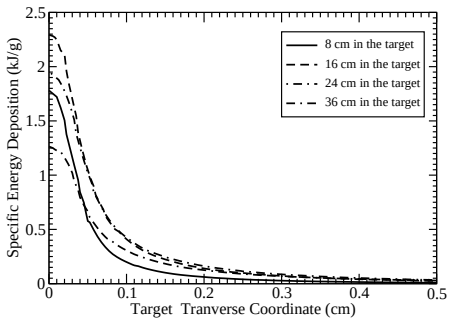

Figure 2: Specific energy vs transverse coordinate at different longitudinal positions.

In Fig. 3 we present the material state along the transverse plane of the target at L = 16 cm and at t = 500 ns. By this time a specific energy of 44 kJ/g has been deposited in the target that leads to a temperature of 5 eV and a pressure of 35 GPa. The high pressure drives a radi-

ally outgoing shock wave and as a consequence the density at the target center decreases to a value of 3.6 g/cm^3. It is seen that the material that lies within a radius of 4 mm has been transformed into an expanded hot liquid state while the melting front is seen moving outwards.

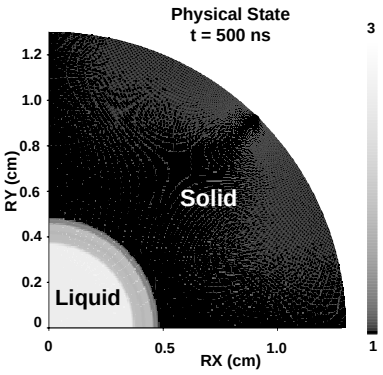

Figure 3: Material state at t = 500 ns

Figure 4 also shows the material physical state, but at t = 2.5 μs. It is within the inner 2 mm radius, a plasma is created and the plasma region is followed by a liquid region that extends up to a radius of 8 mm.

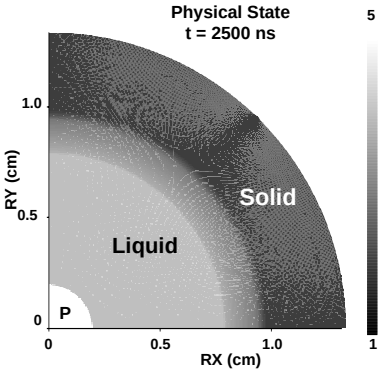

Figure 4: Material state at t = 2.5 μs

In Fig. 5 we plot the density and temperature at the target center vs time. In Figs. 6 we plot the plasma coupling parameter Γ in a copper plasma as a function of temperature and density, respectively. Calculations of the plasma coupling parameter have been performed using the code SAHA-IV[4] which is specially designed for calculations of thermodynamic properties of multicomponent plasma with strong interparticle interactions.

A comparison between Fig. 5 and Fig. 6 shows that at the central part of the target, a strongly coupled plasma with a plasma parameter of the order of 2-5 is created. An LHC beam will therefore be a very efficient tool to create states of an expanded hot liquid and strongly coupled plasmas with life times of the order of ten μs. We note that at t = 10 μs, only about 400 out of 2808 LHC bunches have been delivered. However, by this time the target density becomes extremely low, the rest of the bunches will encounter little mass and will therefore pass through this region of the target without any significant interaction and will penetrate deeper into the target. The time for investigation may therefore be limited to 10 μs, which is sufficiently long to carry out diagnostics.

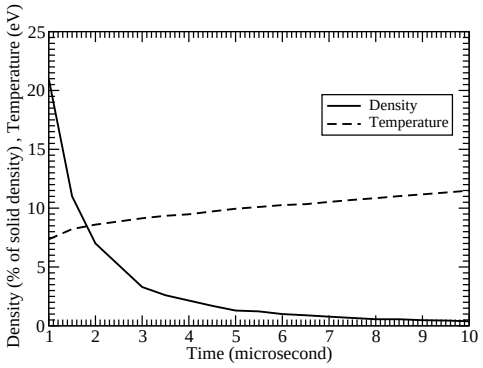

Figure 5: Density and temperature at the target center vs time

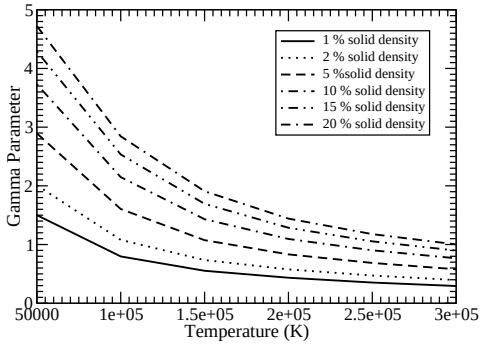

Figure 6: Plasma coupling parameter Γ as a function of temperatre and density

Diagnostics of such samples of HED matter will be a very challenging problem. A complete set of diagnostic tools will be needed to measure density, temperature and pressure of the sample to fully determine the EOS. The simulations show a temperature of the order of 10 eV that corresponds to a maximum of the Planck radiation of a wavelength of about 30 nm, that will make pyrometry in the vuv region a possibility to measure the temperature. Piezoelectric polymer stress gauges (PVDF) will immersed in the target can be used to measure the pressure. The density can be measured using X-ray backlighting and shadowgraphy technique as well as proton radiography.

References

[1] V.E Fortov *et al.,* Nucl. Sci. Eng. 123, 169 (1996).

[2] A.Fasso *et al.,* The physics models of FLUKA: status and recent development, CHEP 2003, LA Jolla, California, 2003

[3] A. V. Bushman and V. E. Fortov, Sov. Tech. Rev. B Therm. Phys. 1, 219 (1987).

[4] V.K.Gryaznov *et al.,* Zh.Exp.Teor.Fiz., 114, No.10, p.1242-1265, (1998).

Spatially resolved measurement of the electron density in laser produced plasmas

A. Pelka[1], A. Blazevic[2], A. Greiche[1], T. Hessling[1], D.H.H. Hoffmann[1,2], R. Knobloch[1], G. Rodriguez Prieto[1,2], M. Roth[1], G. Schaumann[1], and M. Schollmeier[1]

[1]TU Darmstadt; [2]GSI Darmstadt

For the interpretation of future experiments with laser produced plasmas it is of great importance to determine the plasma parameters such as electron density and temperature. For measuring the electron density laser interferometry has proved to be a good method in previous experiments. However most of the interesting phenomena in plasmas are limited to a very short timescale of about 5-100 ns. The setup which was used in past experiments was unable to supply sufficient time resolution due to a pulse length of the interferometry laser of 6 ns. In order to improve this it is also necessary to use a different interferometer type which is less dependent on the coherency length. Therefore a Wollaston Interferometer was implemented using a laser of 500 ps pulse length.

The experimental setup is scetched in Figure 1. An imaging lens is used to picture the position of the target onto the camera. The main element is a Wollaston prism, a polarizing beam splitter. In this the beam is separated into two beams under a small angle, which overlap in the plane of the camera and, taking into account the polarizer, create inteference patterns. These patterns depend on the shape of the wavefront which is changed if the beam propagates through plasma. Interpreting the so produced images allows a spatially resolved determination of the electron density. This is done by a computer program, which was especially written for this purpose. It offers automatic computation of the electron density and therefore allows to furthermore investigate the plasma expansion by changing the laser parameters with direct feedback form the experiments. The algorithm is based on a method known as *Abel inversion*[1], which implies the assumption of a cylinder symmetrical expansion of the plasma target. As the experiments have shown, this assumption is fulfilled within reasonable extent.

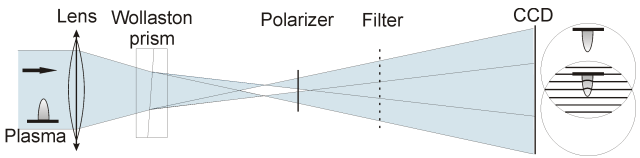

Figure 1: Wollaston Interferometer

The experiments were carried out using the recently enhanced nhelix system [2] in February 2005. This system offers a high energy laser beam with up to 120J for heating the plasma and an additional low energy beam with a relatively short pulse length of 500 ps, which was used for the interferometry. In order to resolve the probe beam from scattered light of the heating laser pulse the second harmonic frequency was used, since both lasers operate at the same wavelength. The delay between the two pulses can freely be varied using a delay generator to deliver the triggering pulses. This, combined with the new setup described above, supplied sufficient temporal and spatial resolution to allow measurements of the electron density at different times during the plasma expansion.

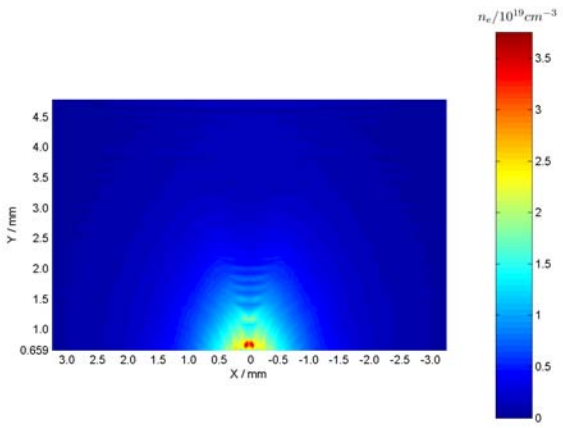

Figure 2: Electron density with $\Delta t_{pp} = 20ns$

Figure 2 shows a typical electron density which was computed from the measurements. The improved image quality compared to the images obtained from the Mach Zehnder Interferometer combined with the shorter laser pulse allows measurements at an earlier time and closer to the target. This expands the accessible range for the electron density by a factor of approximately 20.

In the near future the laser system PHELIX is planned to be replace the high energy beam of the nhelix system for plasma production. The highly improved Interferometer is a very flexible diagnostic tool which will easily be usable with that setup, since its functionality is completey independent of the beam line arrangement.

References

[1] Jahoda, F.C. et. al., *Methods of Experimental Physics*, Vol. 9B, Academic Press, New York (1971).

[2] Schaumann, G. et. al., *this report*

[3] Neumayer, P.; Seelig, W.; Cassou, K. et. al., *Transient collisionally excited X-ray laser in nickel-licke zirconium pumped with the PHELIX laser facility.* Applied Physics B-Lasers and Optics 78 (7-8), 957-959 (2004)

Studies of Strongly Coupled Plasmas at the Future FAIR Facility

N.A. Tahir[1], C. Deutsch[2], V.E. Fortov[3], V. Gryaznov[3], D. H. H. Hoffmann[1,4], I.V. Lomonosov[3], A. R. Piriz[5], A. Shutov[3], P. Spiller[1], M. Temporal[5], S. Udrea[4], and D. Varentsov[4]
[1]GSI Darmstadt; [2]LPGP Orsay; [3]IPCP Chernogolovka; [4]TU-Darmstadt; [5]UCLM Spain

Strongly coupled plasmas are ubiquitous in nature as they are found in stars, brown dwarfs and giant planets. A study of the physical properties of such plasmas in the laboratory is therefore of great importance to our understanding of the universe. Another very important problem associated with strongly coupled plasmas is the slowing down of charged particles in such systems. It has been theoretically predicted that stopping power of strongly coupled plasmas will be lower than that of ideal plasmas[1;2]. This could have very important implications on inertial confinement fusion target design.

Intense heavy ion beams are believed to be a very unique tool to create states of High-Energy-Density (HED) in matter including strongly coupled plasmas[3–5]. With the construction of the new heavy ion synchrotron, SIS100 at the future FAIR (Facility for Antiprotons and Ion Research) facility[6], the beam intensity will be increased by three orders of magnitude compared to that available at the existing facility. This will make it possible to carry out interesting experiments in a parameter space that previously was unaccessible. It is expected that the SIS100 will generate a uranium beam with an intensity, $N = 2 \times 10^{12}$ ions that will be delivered in a single bunch. A wide range of particle energy (0.4 – 2.7 GeV/u) will be available and depending on the energy, the bunch length will lie between 20–100 ns. Employing a two-dimensional hydrodynamic computer code, BIG-2[7], we have carried out numerical simulations of hydrodynamic and thermodynamic response of solid aluminum and lead targets that are irradiated with an ion beam with the above parameters. Our calculations show that one would be able to generate strongly coupled plasmas with a coupling parameter, Γ of up to of 6.

First in figures 1 and 2 we present the calculated Γ values for aluminum and lead respectively, vs density at different temperatures. These calculations have been done using the code SAHA-IV[8–10] which is specially designed for calculations of thermodynamic properties of multicomponent plasma with strong interparticle interactions. Calculational procedure is based on a chemical picture of the plasma[8;9]. Coulomb interaction of charged particles, short range repulsion of atoms and ions at close distances, degeneracy of free electrons, stages of ionization up to 20 were taken into account. Further details can be found in[10].

The beam-target geometry is shown in Fig. 3. We consider a solid cylindrical target whose one face is irradiated by ions whose range is larger than the cylinder length. The ion energy is therefore deposited uniformly along their trajectory and they emerge from the opposite face of the cylinder with a reduced energy. The beam radius which is the full width at half maximum (FWHM) of the Gaussian distribution of the beam intensity in the transverse direction, is smaller than the cylinder radius. A temperature of a few eV is generated in the deposition region that leads

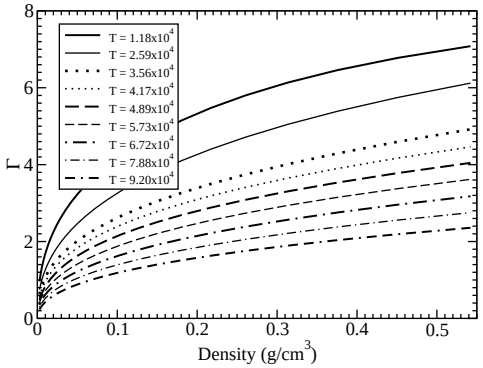

Figure 1: Plasma coupling parameter Γ vs density at different temperatures for aluminum[8–10].

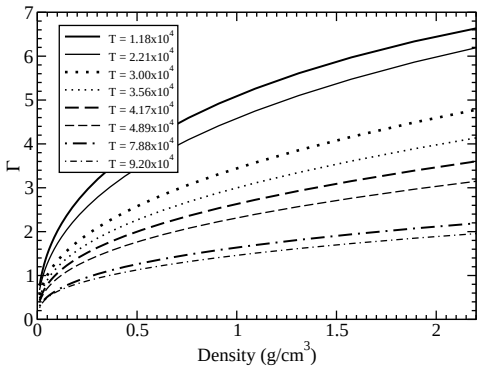

Figure 2: Plasma coupling parameter Γ vs density at different temperatures for lead[8–10].

to a high pressure. The high pressure launches a shock wave in the transverse direction that drives material outwards, thereby creating a sub solid density region that is converted to a high density, low temperature plasma. Such plasmas are classified as strongly coupled or non-ideal plasmas.

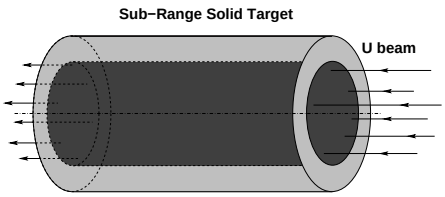

Figure 3: Beam-target geometry.

In Fig. 4 we plot density and temperature vs radius at the cylinder center at t = 1000 ns for a beam intensity of 2×10^{12} ions using a FWHM of 2 mm in case of an aluminum target. It is seen that the temperature has decreased to about 4×10^4K in the inner 1 mm radius of

the target while the density has been reduced to approximately 0.4 g/cm^3 due to expansion along the radial direction. According to the data shown in Fig. 1, this density and temperature regime corresponds to a Γ of the order of 3 for aluminum. In Fig. 5 we plot the same variables as in Fig. 4 at t = 1700 ns, but using a FWHM = 3 mm while keeping the rest of the beam parameters same. Since the temperature now is much lower than before, one achieves an aluminum plasma with a much higher Γ (about 6).

Next we consider a lead target and the results are presented in Figs. 6 and 7. In Fig. 6 we plot density and temperature vs radius at t = 5000 ns at the center of the cylinder using a beam intensity of 2×10^{12} ions with a FWHM = 2 mm. It is seen that the temperature is much higher than that in the corresponding case of aluminum shown in Fig. 4. Therefore one achieves a lower value of $\Gamma = 1$ in the present case. Figure 7 shows that using a larger beam spot with a FWHM of 3 mm, one gets a lower temperature that leads to a higher value of Γ of the order of 2.

It is interesting to note that the temperature achieved in low-Z materials using the same beam parameters is much lower than that in the high-Z materials. Therefore the Γ parameter in the range of the SIS100 beam parameters is higher in the former type of targets compared to the latter ones.

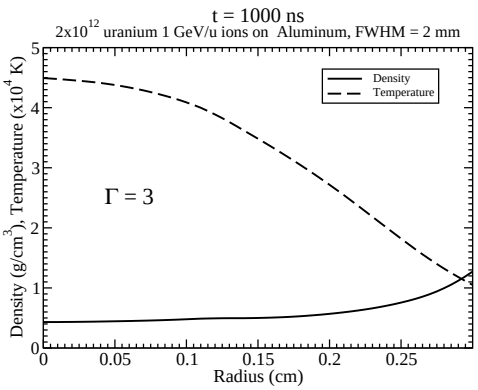

Figure 4: Density and temperature vs radius at the middle of the cylinder.

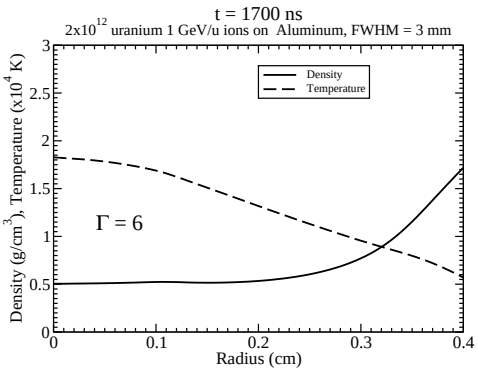

Figure 5: Density and temperature vs radius at the middle of the cylinder.

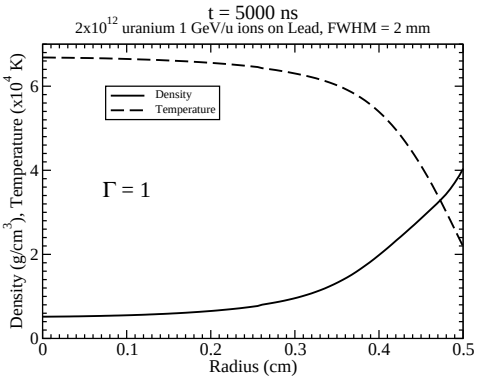

Figure 6: Density and temperature vs radius at the middle of the cylinder.

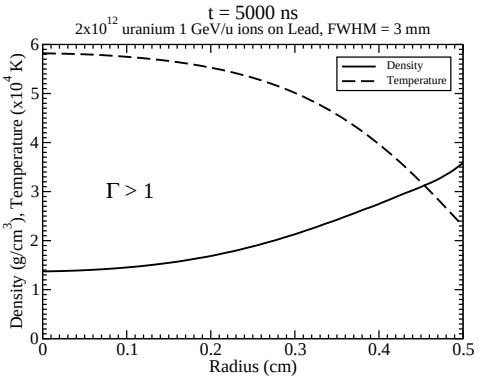

Figure 7: Density and temperature vs radius at the middle of the cylinder.

References

[1] D. Gericke and M. Schlanges, Phys. Rev. E (2002) 36406.

[2] G. Zwicknagel et al., Phys. Reports 309 (1999) 904.

[3] N.A. Tahir et al., Phys. Plasmas 7 (2000) 4379.

[4] N.A. Tahir et al., J. Phys. A: Math. Gen. 36 (2003) 6129.

[5] D.H.H. Hoffmann et al., Phys. Plasmas 9 (2002) 3651.

[6] W.F. Henning, Nucl. Inst. Meth. A 214 (2004) 211.

[7] V.E. Fortov et al., Nucl. Sci. Eng. 123 (1996) 169.

[8] V.K. Gryaznov et al., Thermophysical Properties of Working Media of Gas - Phase Nuclear Reactor, ed. by Ievlev V.M., Atomizdat, Moscow, 1980.

[9] W. Ebeling et al., Thermophysical Properties of Hot Dense Plasmas (Teubner, Stuttgart - Leipzig 1991).

[10] V.K. Gryaznov et al., Zh.Exp.Teor.Fiz., 114, No.10, p.1242-1265, (1998).

Study of Kink Instabilities in Plasma Channels

S. Neff[1], R. Knobloch[1], A. Tauschwitz[2], and D.H.H. Hoffmann[1,2]
[1]Technische Universität Darmstadt; [2]Gesellschaft für Schwerionenforschung

Heavy-ion beam transport in plasma channels is an option to transport high-current beams which are required in fusion reactor scenarios. The channel provides free electrons that space-charge and current neutralize the ion beams. In addition, the channel creates a large azimuthal magnetic field that prevents the beam ions from leaving the channel. A stable channel is necessary to guarantee good transport properties of the beam [1]. The most threatining instability in a plasma channel is the kink instability, that has helical structure and whose growth is in linear theory given by[2]

$$\xi(t) = \xi_0 \cdot \exp\left[\Gamma \cdot t + i \cdot (k \cdot z + \theta)\right] \qquad (1)$$

where ξ_0 is the initial amplitude of the perturbation, θ is the angle in cylindrical coordinates, and k is the wavenumber of the perturbation. The growth rate Γ depends on the discharge conditions and is largest for a channel in vacuum and significantly reduced by the ambient gas in our setup.

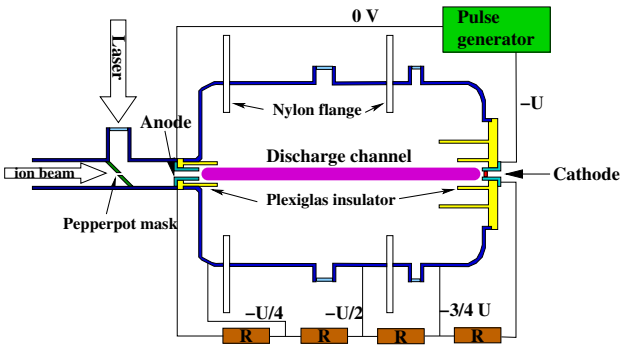

Figure 1: Schematic experimental setup

Figure 1 shows a sketch of our experiment at GSI that uses the UNILAC beam to study the ion beam transport properties of the channel [3]. The channels are created by a discharge in a $1\ \mathrm{m}$ long chamber that is $60\ \mathrm{cm}$ in diameter. Depending on the chamber gas, the channels are initiated either with a CO_2 laser (ammonia), or with the ion beam (xenon, krypton). The ion beam transport properties are studied with a setup using a pepperpot mask to shape the beam and a scintillator to detect it, whereas the evolution of the channel is studied with high-speed cameras which take side-view images of the channel.

The development of instabilities in our experiment was studied with a fast framing camera that takes eight consecutive pictures with minimum exposure times of $10\ \mathrm{ns}$. For normal operating conditions, that is at ambient chamber gas pressures of $0.5 - 10$ mbar, the channels in xenon, krypton, and ammonia are stable. A comprehensive search in ammonia revealed that the channels become unstable for gas densities above the equivalent of 15 mbar. In order to test the theory, the growth rate was determined for discharges in 22 mbar ammonia. The pictures of the framing camera were analyzed with a small computer program to determine the amplitude of the instability and the channel diameter.

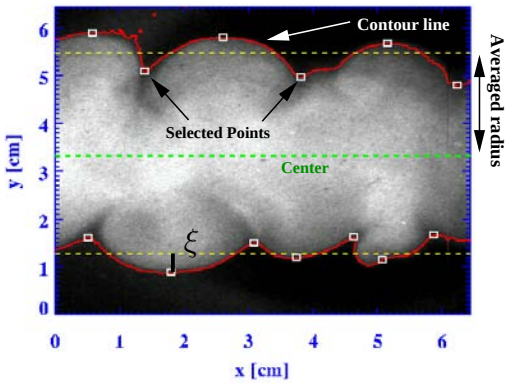

Figure 2: Analysis of the kink instability

The analysis of the channel images is illustrated in Figure 2. Based on the image, the program determines the channel boundary with a contour fit and calculates the central axis of the channel and the averaged boundary (indicated by dashed lines). In the next step, the user marks the extrema of the instability (marked with small boxes). From these data, the code calculates the averaged amplitude ξ and wavelength λ of the instability.

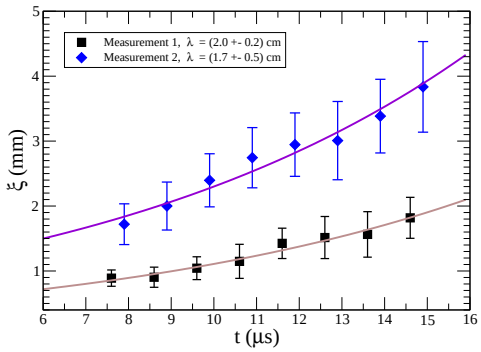

Figure 3: Measured amplitudes of the kink instability.

In Figure 3, the data from two growth rate measurements under identical discharge conditions are plotted. The measurements were carried out in 22 mbar ammonia, used a discharge voltage of $25\ \mathrm{kV}$, and started shortly after the time of the current maximum, which is at roughly $7\ \mu\mathrm{s}$ for this set of parameters. They are consistent with the exponential growth predicted by linear instability theory for the initial phase of the instability. The measured growth rates are of the order of $10^5/\mathrm{s}$ and thus two orders of magnitude smaller than predicted by a simple model [2]. The wavelength of the instability is roughly $2\ \mathrm{cm}$, whereas the model predicts growth at $4\ \mathrm{cm}$. All in all, the instabilities show the expected topological features, but the measured growth rates and wavelengths differ significantly from the model.

References

[1] D.V. Rose et. al., *Fusion Sc. & Techn.*, vol. 46, pp. 470–493
[2] W. Manheimer et. al., *Phys. Fluids*, vol. 16, pp. 1126-1134
[3] S. Neff et. al., *Proceedings EPAC 2004*,

Upgrade of the nhelix laser system at GSI

G. Schaumann[1], M.S. Schollmeier[1], A. Azima[5], A. Blažević[1], E. Brambrink[2], M. Geißel[3], T. Heßling[1], A. Pelka[1], P. Pirzadeh[1], M. Roth[1], and D.H.H. Hoffmann[1,4]

[1]Technische Universität Darmstadt, Germany; [2]Ecole Polytechnique, Paris, France; [3]Sandia National Labs, Albuquerque, USA; [4]GSI, Darmstadt, Germany; [5]DESY, Hamburg, Germany

The first high energy laser system that became operational at GSI is the "nanosecond high energy laser for heavy ion experiments" (nhelix). This system has recently been improved significantly. Due to major changes in the system layout, the quality in terms of temporal and spatial beam homogeneity was improved, while at the same time the output energy was raised up to 120 J. This could be achieved with the available number of amplifiers, which significantly brought down the cost for the upgrade. Moreover, a second front-end with shorter pulse length was integrated into the laser amplifier chain.

Therefore the nhelix system is now capable of delivering one beam with 120 J in 14 ns (ns-beam), while the second beam line is still under construction and is supposed to provide 5 J in 0.5 ns (sub ns-beam). While the power level of these two beams is of the same order of magnitude, their application at the plasma physics experiments is different. The high energy pulse with rather long pulse duration is primarily used to generate a high density plasma from thin solid state targets, while the second beam with short pulse length in comparison to the heating pulse and the timescale on which the hydrodynamic expansion of the plasma takes place, serves as a diagnostic tool. This more complex and versatile setup enables a great variety of experiments in the field of plasma physics, especially in combination with the PHELIX laser (Petawatt High Energy Laser for heavy Ion eXperiments), which is expected to deliver first light on the kJ level to the experimental area by the end of 2005 [1].

The actual laser configuration is one of the MOPA type (master oscillator-pulsed amplifier). A master oscillator (Nd:YAG) generates a low energy pulse for amplification, that is followed by rod amplifiers (silicate-glass), whose diameter increase stepwise up to 64 mm for the last amplifier. As the laser light fluence is well below the saturation level, the same amplifier can be used multiple times to increase the energy of a beam, e.g. in a double pass configuration, or one can even use the same amplifier to gain energy for pulses coming from different oscillators. The latter configuration has been realized with the first two amplifiers; see figure 3 for the outline of the nhelix laser system and with an overview of the main optical components.

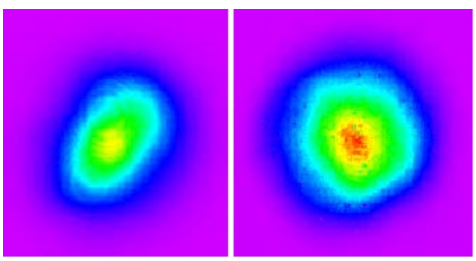

Figure 1: Beam shape of the long pulse frontend: Oscillator profile before and after the cylinder telescope.

The ns-oscillator is a commercial Coherent Powerlite 8000. Due to its non-ideal elliptical transversal profile the beam is reshaped with a custom made cylinder telescope. After passing this optical system, the laser beam is circularly shaped. The improvement in terms of the spatial intensity distribution is shown in figure 1 on the left hand side.

Both laser beams, the ns-beam as well as the sub-ns beam are launched into the first amplification section. The insertion is done with a thin film polarizer that transmits the ns-beam (p-polarized) and reflects the sub-ns beam which is impinging under the Brewster-angle with s-polarization. Since these beams are propagating parallel but with perpendicular polarization, they can be separated again with a polarizer. As the fluence is on the order of 1 J/cm^2 a thin film polarizer has to be used, which provides the highest available damage threshold while on the other hand it has a poor extinction ratio (200:1). A marginal misalignment - the two beams propagate under a small angle - allows to block the objectional energy, which has passed the polarizer, by the pinhole of the following spatial filter.

Before transferring the ns-beam to the next amplification section, it is first spatially reshaped with a soft polarizing aperture (SPA). This SPA consists of a birefringent plano-convex lens, a second plano-concave BK-7 lens to compensate for the optical power of the first lens and a thin film polarizer. The linear polarization of the incoming beam is rotated according to the thickness of the birefringent lens. Taking into account the polarizer, the total power

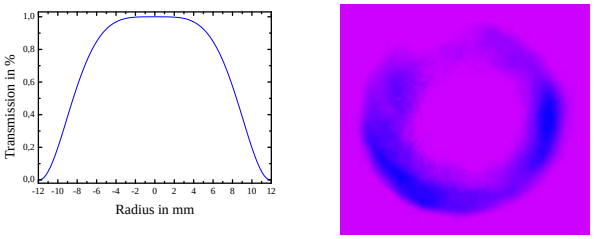

(a) Transmission of the soft polarizing aperture

(b) extracted energy

Fig. 2: Improved transversal beam profile of the long pulse frontend

transmission of the SPA is now a function of the beam radius,

$$T(r) = \cos^2\left(\frac{1}{2}\Delta n \frac{\pi}{\lambda}\frac{r^2}{R}\right)$$

where $\Delta n = 0,009$ denotes the difference between the refractive index of the ordinary and extraordinary wave;

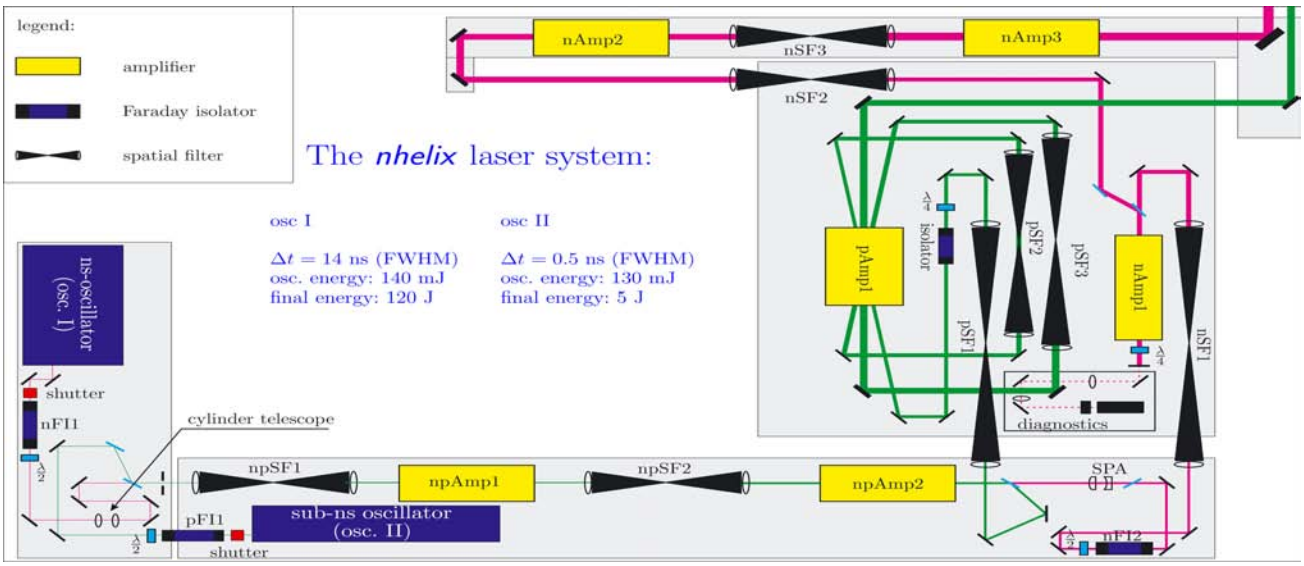

Figure 3: Outline of the *nhelix* laser system.

$\lambda = 1064\,nm$ is the laser wavelength, $R = 1197\,mm$ the radius of curvature of the birefringent lens and $r \approx 12\,mm$ is the so called zero transmission radius, which depends on Δn, λ and R. The calculated transmission is shown in figure 2(a) together with the part of the beam that is reflected at the polarizer. One can clearly see the ring shaped intensity distribution, while the asymmetry is due to the inhomogeneous intensity distribution of the incoming beam.
Since the gain in rod amplifiers increases with radius due to absorption of the pump light on its way to the center of the rod, an initially gaussian shaped intensity profile changes to a flat top like distribution along the amplifier chain. The SPA attenuates this effect, while it helps at the same time, to control diffraction at hard apertures in the laser chain. The overall extracted energy strongly depends on the input beam profile and was measured to be on the order of 20 percent. As the maximum laser energy which can be extracted from the system is not limited by a lack of pump power, but by the damage threshold of the optical components, the loss of energy at the beam shaping element could easily be compensated by slightly increasing the pump power of the amplifiers.

After reshaping the beam with the SPA it is relay imaged to the double pass amplifier. Due to thermal induced birefringence of the amplifying media and the limited extinction ration of the separating polarizer, there is always part of the radiation propagating backwards in the chain. To prevent damage, a Faraday isolator with $25\,mm$ clear aperture has been integrated. The pulse is then guided to the booster section with a $45\,mm$ and a $64\,mm$ amplifier. As long as the PHELIX laser beam is not yet available, the long pulse beam is used to produce a hot dense plasma, e.g. for energy loss experiments [2] with electron temperatures in the order of $200\,eV$ and electron densities up to solid state density. A small part of the sub-ns beam (some mJ) is coupled out and frequency doubled to probe the plasma by means of wollaston interferometry [3]. This diagnostic has recently been set up and provides a space resolved distribution of the free plasma electron density with time resolution given by the pulse length (0,5ns) of the probe beam. After the final amplification section for the sub-ns beam, which is realized as a geometrical tripple pass, the pulse is expected to deliver 5 J of energy. This high power (10GW) pulse can be focused on a medium-Z target that will serve as an x-ray backlighter [4]. However there are plans to use higher harmonics of this beam for collective Thomson scattering [5], [6]. This will lead to new insights into the physics of the expanding plasma and it will serve as an alternative temperature diagnostics. Together with the PHELIX laser that will deliver up to $1\,kJ$ laser energy in 1 ns, the new configuration of nhelix will act as a powerful diagnostic laser system.

References

[1] Neumayer P, Seelig W, Cassou K, et al., (2004). Transient collisionally excited X-ray laser in nickel-like zirconium pumped with the PHELIX laser facility. APPLIED PHYSICS B-LASERS AND OPTICS 78 (7-8): 957-959 MAY 2004
[2] M. Roth *et. al.*, Europhys. Lett. **50**, 28-34 (2000)
[3] A. Pelka *et. al.*, this report
[4] M.S. Schollmeier *et. al.*, this report
[5] S.H. Glenzer, Contrib. Plasma Phys. **40**(1-2), 36-45 (2000)
[6] S.H. Glenzer et. al., Phys. Plasmas **10**(6), 2433-2441 (2003); Phys. Rev. Lett. **90**(7), 175002 (2003)

MATS-RES

Materials Research with Heavy-Ions

Ion-induced high-pressure phase formation in pressurized zircon

M. Lang[1], U.A. Glasmacher[2], H. Keppler[3], F. Langenhorst[4], R. Neumann[1], D. Schardt[1], C. Trautmann[1], G.A. Wagner[2]

[1]Gesellschaft für Schwerionenforschung (GSI), Planckstr. 1, Darmstadt, Germany
[2]Forschungsstelle Archäometrie der Heidelberger Akademie der Wissenschaften am MPI für Kernphysik, Heidelberg, Germany
[3] Bayerisches Geoinstitut (BGI), Universität Bayreuth, Universitätsstr. 30, Bayreuth, Germany,
[4]Institut für Geowissenschaften der Universität Jena, Burgweg 11, Jena, Germany

Zircon ($ZrSiO_4$), as an abundant silicate of the Earth's crust, is distributed in many different rock types. Minerals of zircon may contain up to 5 wt% uranium and thorium and are therefore commonly used for dating of geological samples [1]. When exposing zircon at room temperature to a pressure above 20 GPa, it starts to convert into its high-pressure polymorph reidite having a scheelite structure [2]. At elevated temperatures of about 1100 K, this displacive phase transition occurs already at a lower pressure of about 8 GPa [3].

In a series of high-pressure irradiations of different materials, we exposed a natural zircon sample (France) enclosed in a diamond anvil cell to uranium ions from the SIS heavy-ion synchrotron. During the irradiation with $2x10^9$ ions/cm^2, the single crystal was kept at 14.2 GPa and room temperature. The ions, with a primary kinetic energy of 50 GeV, had a remaining energy of 13.8 GeV after passing through one of the diamond anvils, resulting in an energy loss of about 25 keV/nm at the sample site. After irradiation, the sample was inspected by means of Raman spectroscopy and transmission electron microscopy (TEM).

Fig. 1 displays two Raman spectra of our zircon sample, recorded before and after irradiation. After the high-pressure irradiation, several new bands are clearly observable, particularly at 810 and 840 cm^{-1}.

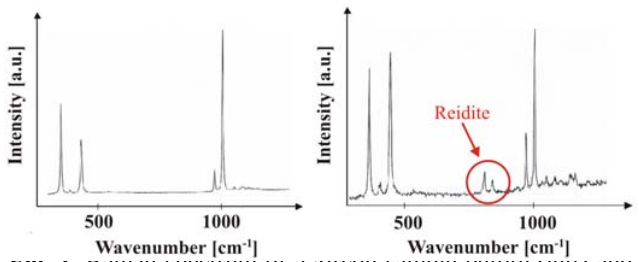

Fig. 1. Raman spectrum of a zircon sample before (left) and after (right) irradiation at 14.2 GPa. In addition to zircon bands, new bands of the high-pressure polymorph reidite are visible, particularly at 810 and 840 cm^{-1}.

These bands were also observed in previous Raman investigations and identified as bands of reidite [2]. The presence of reidite was also confirmed by the observation of characteristic rings in electron diffraction patterns. Fig. 2 depicts a TEM micrograph of the sample recorded after irradiation. The original single crystal was completely converted into an aggregate of zircon and randomly oriented irregular crystallites of reidite of size about 10 nm.

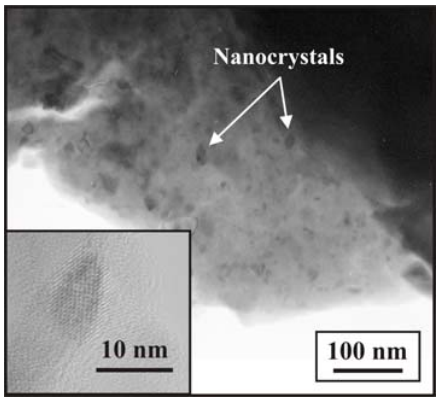

Fig. 2. TEM image of zircon after irradiation at 14.2 GPa. The ions induced a conversion of the pressurized sample into an aggregate of zircon and nanocrystals of reidite of size about 10 nm as indicated by the inset.

It is well known that heavy ions produce amorphous tracks of diameter ~8 nm within an otherwise crystalline zircon matrix [4]. Taking this into account, our study revealed that pressure considerably influences the kind and degree of ion-induced modifications. The irradiation at high pressure and room temperature caused the conversion of a substantial part of the sample into the stable high-pressure polymorph. This zircon-reidite transition took place at a pressure well below the pressure where the phase transition occurs spontaneously [2]. Furthermore, the initial single crystal was transformed into a polycrystalline aggregate by the ion bombardment. Since zircon may contain large amounts of uranium and thorium and is exposed to elevated-pressure conditions in the Earth's crust, the spontaneous fission of radioactive nuclei may initiate a conversion to reidite, similar to the results found in our investigations.

References

[1] G.A. Wagner, P. van den Haute, Fission Track Dating, Ferdinand Enke Verlag, Stuttgart, 1992.
[2] W. van Westrenen, M.R. Frank, J.M. Hanchar, Y. Fei, R.J. Finch, C.-S. Zha, Am. Mineral. 89 (2004) 197-203.
[3] S. Ono, K. Funakoshi, Y. Nakajima, Y. Tange, T. Katsura, Contrib. Mineral. Petrol. 147 (2004) 505-509.
[4] L.A. Bursill, G. Braunshausen, Philos. Mag. A 62 (1990) 395-420.

Ion-induced color centers in LiF at 15 K

K. Schwartz [1], M. Sorokin [2], C. Trautmann [1], R. Neumann [1], A. Volkov [2], K.-O. Voss [1]

[1] GSI, Darmstadt, Germany, [2] Russian Research Centre, Kurchatov Institute, Moscow, Russia

In the past, the results from low-temperature irradiations of alkali halides were essential for the basic understanding of the creation mechanism of primary color centers (F and H) and their interaction with various crystal defects [1,2]. At temperatures of a few Kelvin, the mobility of the primary color centers is strongly suppressed, thus enhancing annihilation and reducing aggregation processes.

To study color centers induced by swift heavy ions, we used a cryostat which is installed at the UNILAC beamline X0 and allows in-situ optical spectrometrometry (SD-2000, Ocean Optics). Optical density measurements can be performed from 0.01 up to 2.0 in the spectral range 200 – 850 nm. The sample is cooled down to the desired temperature and then irradiated up to a certain fluence. During interruptions of the ion beam, the sample holder is rotated in-situ allowing optical spectrometry.

First results were obtained for LiF crystals irradiated at 15 K and 300 K with ^{3}He (14.4 MeV), ^{12}C (57 MeV), ^{50}Ti (555 MeV), ^{95}Mo (1050 MeV), ^{197}Au (2180 MeV), and ^{238}U (2640 MeV) ions in the fluence range 5×10^{8} – 2×10^{12} ions/cm^{2}.

At 15 K, the optical spectra typically exhibit two absorption bands (Fig. 1): a prominent band at 241 nm due to F centers (electron centers) and a broad band with maximum absorption at ~345 nm. The broad band is ascribed to mainly H centers (hole centers) but also to V_K centers (self-trapped holes) and H centers modified by cation impurities (typical trace elements in LiF) [1]. The influence of these impurities is only dominant at low fluences. At 15 K, the creation of F_2 centers (445 nm) is absent for light ions (He, C, Ti) and strongly suppressed for heavy ions (U, Au, Mo). Note that without diffusion, the F_2-center formation is based on stochastic creation of two neighbouring F centers.

The presence of the H-center band is directly linked to the low temperature preventing defect diffusion. In agreement with irradiations using X rays [1], the H centers anneal above 100 K, because they become mobile and recombine either with F centers or transform into V_K and other hole centers (which are finally transformed into stable V_3 centers (114 nm) [3]). The survival of the H centers after the 15-K irradiation indicates that they are created in a track zone where the local heating did not surpass the critical annealing temperature of 100 K.

When warming up the crystals to room temperature (RT), the hole-center band disappears completely, and the intensity of the F-center band decreases. During annealing, some of the F centers aggregate into F_2 centers, evidenced by the small increase of the band at 445 nm (Fig. 1 b).

A quantitative comparison of the spectra shows that at 15 K, the F-center concentration of samples irradiated with heavy ions is similar as under RT irradiations (Fig. 1 b), whereas the exposure to light ions produces an F-center concentration smaller by a factor of 3-4. This difference is ascribed to the stopping power and thus to the different deposited energy density and local heating in the track. Higher temperatures in the ion track allow separation of the F and the H center (of the primary Frenkel pair) to a distance sufficiently large to avoid recombination. For light ions (low energy loss), the temperature increase seems to be absent or insignificant.

In conclusion, the irradiation temperature has a direct influence on thermally activated diffusion of primary defects and thus controls the final defect morphology. Details of the annihilation and recombination processes are influenced by the stopping power of the ions.

Additional low-temperature experiments are planned for other materials. First recent results on NaCl crystals showed similar defect creation phenomena as in LiF [4].

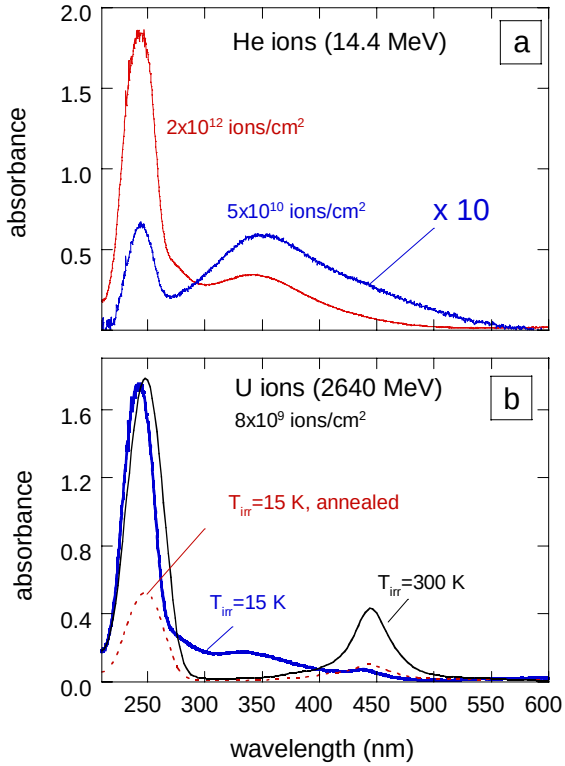

Fig. 1 Absorption spectra of LiF: (a) irradiation at 15 K with14.4-MeV ^{3}He ions at two different fluences and (b) irradiation with 2640-MeV ^{238}U ions at 300 K (solid line) and 15 K before (bold line) and after (dotted line) thermal annealing to 300 K.

References

[1] W. Känzig, J. Phys. Chem. Solids 17 (1960) 88

[2] H. Rabin and C.C. Klick, Phys. Rev. 117 (1960) 1005

[3] A.T. Davidson, K. Schwartz, J. Comins, A.G. Kozakiewicz, M. Toulemonde, and C. Trautmann, Phys. Rev. B 66 (2002) 214102.

[4] K. Schwartz, K.-O. Voss, A. E. Volkov, C. Trautmann, R. Neumann, M. Sorokin, F. Singh, to be published

Nanoscopic conducting ion tracks in diamond-like-carbon

J.-H. Zollondz [1,2], C. Trautmann [3], D. Schwen [1], A-K. Nix [1], J. Krauser [4], J. Berthold [5], B. Schultrich [5], H. Hofsäss [1]

[1] Georg-Albert-Universität, Göttingen, [2] Hahn-Meitner-Institut (HMI), Berlin; [3] Gesellschaft für Schwerionenforschung, Darmstadt, [4] Hochschule Harz, Wernigerode, [5] Fraunhofer Institut IWS, Dresden

In diamond-like-carbon films (DLC), energetic heavy ions create conducting tracks. Given by their small diameter of ~10 nm, these wires are interesting objects for various nanotechnological applications [1,2].

The DLC films were deposited on highly doped silicon substrates by either conventional ion-beam techniques (Univ. Göttingen) or by plasma deposition using the filtered arc method (IWS). In both cases, the energy of the deposited carbon particles has to be about 100 eV in order to form the compact tetrahedral (sp^3) structure by "subplantation". Such films are amorphous and contain up to 80% diamond-like sp^3 bonds. The thickness of the films used here was ~50 nm, but deposition of layers up to 1 µm is possible. The samples were irradiated at the UNILAC (GSI) with uranium projectiles of ~1GeV (decelerated from initially 2.7 GeV by a 50-µm thick Al degrader foil) and at the Ionenstrahllabor (HMI) with gold projectiles of 350 MeV and 600 MeV. The range of the beam was much larger than the film thickness.

The electrical properties of the conducting channels were studied by means of scanning probe microscopy (SPM) using a conducting tip. Fig. 1 shows a topographical SPM image and the simultaneously recorded current map. Individual tracks are recorded as hillocks of a few nm in height with an electrical conductivity which is increased up to four orders of magnitude compared to the intact matrix material. Compared to the rather homogeneous hillock size, the conductivity of different tracks varies significantly. The transformation from insulating diamond-like (sp^3 bonding) into conducting graphite-like (sp^2 bonding) carbon is ascribed to the high energy deposition along the path of the ions [3]. From earlier studies testing various amorphous-carbon (a-C) materials between graphite-like and diamond-like carbon, it is known that the ratio of the sp^3 to sp^2 bonding determines the electrical conductivity. The difference in conductivity between mainly sp^3 bonding (DLC) and mainly sp^2 bonding (graphite-like a-C) reaches up to twelve orders of magnitude [4].

We tested the current-voltage (I-V) characteristics of individual tracks with a conducing SPM tip. Fig. 2 presents the averaged current data as a function of the applied voltage

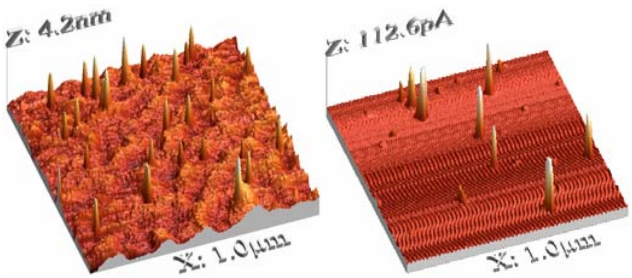

Fig. 1: Topography (left) and current mapping (right) of a DLC sample (80 % sp^3) after irradiation with 600 MeV Au ions (applied voltage: 500 mV)

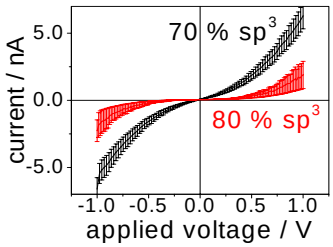

Fig. 2: Average of I-V characteristics of ~30 tracks in an area of 1µm^2 (cf. Fig.1) for two samples of different sp^3 content.

of all tracks within a square of 1µm × 1µm (compare Fig.1), showing that tracks in DLC films with a lower sp^3 content (70% compared to 80%) exhibit a higher conductivity.

When plotting the I-V curves of individual tracks, we find distinct groups (Fig. 3). For the sample with 70% sp^3 content, about 20% of the tracks show nearly ohmic behavior (steepest curve) whereas most tracks (80%) exhibit the typical characteristics of the Frenkel-Poole conductivity mechanism for a low barrier height [5]. For the sample with 80% sp^3, no ohmic curves are found. The majority of the tracks (~90%) show poor conductivity following the Frenkel-Poole mechanism with a large barrier height. Due to the higher number of sp^2 bonds in the pristine material, the ion-induced transformation in the tracks is obviously more effective. To date, the origin of the appearance of preferential I-V-characteristics is an open question, but we assume that the inhomogeneities in the DLC film and fluctuations of the material modified along a track play an important role [6].

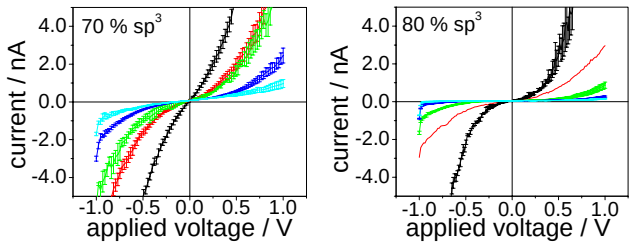

Fig. 3: Average of I-V-curves of preferential characteristics. 70 % sp^3 bonds in the virgin DLC (left), 80 % sp^3 (right).

References

[1] A. Weidinger, Europhysics News, 35/5 (2004) 152.

[2] J.-H. Zollondz, A. Weidinger, Nucl. Instr. and Meth. B 225 (2004) 178.

[3] M. Waiblinger et al., Appl. Phys. A 69 (1999) 239.

[4] E.B. Maiken, P. Taborek, J. Appl. Phys. 78 (2000) 4223.

[5] J. Frenkel, Phys. Rev. 54 (1938) 647.

[6] M. Toulemonde, C. Dufour and E. Paumier, Phys. Rev. B 46 (1992) 14362.

Orientation dependent mixing of Ta/Si interfaces

W.Berky, A.G.Balogh

Darmstadt University of Technology, Institute for Materials Science, Petersenstr.23, D-64287 Darmstadt, Germany

In addition to previous experiments concerning mixing effects at metal/metal and metal/ceramic interfaces pure tantalum was evaporated onto Si substrates with the orientations 111 and 100 by molecular beam epithaxy. The main goal of this study was to alter the silicon orientation to investigate the correlation between crystal structure and mixing parameters at the interface.

Ta/Si(111) and Ta/Si(100) samples were irradiated by different heavy ions at different energies, e.g. 500 keV Si, 1.85 MeV Ar^{+}, 45 and 50 keV C^{2+} and O^{2+}, in most cases at different ionic fluences and temperatures. Beam parameters were chosen to generate identical nuclear stopping powder values at the interface for both Si orientations.

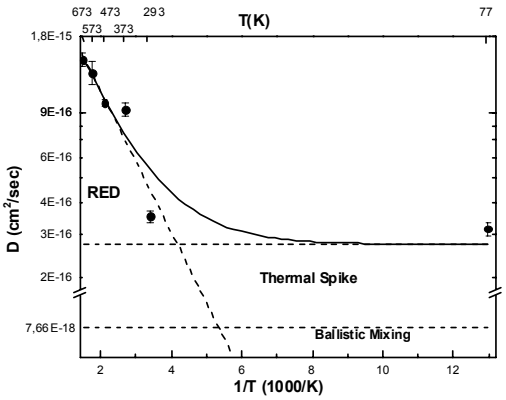

Figure 1: Arrhenius plot of the diffusion coefficient in the Ta/Si(111) system after irradiation with $4 \cdot 10^{16}$/cm^2 Si ions (500 keV)

Figure 1 shows the Arrhenius plot of the diffusion coefficient D at the Ta/Si (111) interface caused by irradiation with 500 keV silicon ions at a fluence of $4 \cdot 10^{16}$ Si/cm^2. The values of D clearly exceed those referring to pure ballistic mixing. An additional temperature independent component had to be taken into account. Additionally, a temperature-dependent mixing effect took place above room temperature. The migration enthalpy of this component was found to be Q=0.05 eV. This value is typical for radiation enhanced diffusion and clearly below the values referring to thermal diffusion.

Several beam parameters causing different stopping power values were used in order to investigate the formation of thermal spikes at the interface. According to the model of global thermal spikes (Ref. 2) the mixing rate k had to show a linear dependence on F_D^2 ($F_D \sim 0.6 \cdot s_N$) if global thermal spikes had been formed at the Ta/Si interface. Figure 2 illustrates this behaviour. We therefore assume the thermal spikes were created at the interface, causing an additional mixing effect independent of temperature as marked in figure 1.

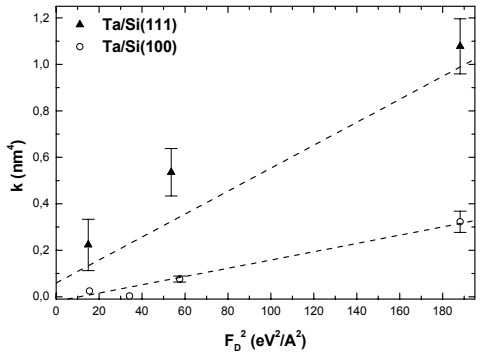

Figure 2: Comparison of mixing rate values in Ta/Si for both Si orientations

Figure 2 also shows the mixing rates found at the Ta/Si (100) interface after irradiation with the same ionic fluence and nearly identical beam parameters. We also found thermal spikes at this interface, but Ta/Si (100) only allowed considerably lower values of the mixing rate than Ta/Si (111).

SRIM [3] simulations showed that mixing effects at the Ta/Si interface primarily occurred due to diffusion of tantalum into silicon. Therefore we expected a considerable effect of the Si orientation of the mixing rate which was confirmed by experiment as shown in figure 2. The crystal structure of silicon offers longer diffusion channels in 111 direction than in 100 direction and this difference can be held responsible for the different mixing rates in both systems.

Acknowledgement

This work was financially supported by GSI.

References

[1] W. Berky, A. G. Balogh and R. G. Elliman: Heavy Ion Induced Intermixing at Ta/Si and Ta/SiO_2 Interfaces, NIM B 226 (2004) 309-319
[2] W.Bolse, Mat. Sci. and Eng. A 253, 194, 1998
[3] J.F. Ziegler, J.P. Biersack, U. Littmark, The Stopping and Range of Ions in Matter, vol. 4, eds., Pergamon, New York, 1985

Degradation of polyimide under the irradiation with swift heavy ions

D. Severin [1], W. Ensinger [1, 2], R. Neumann [3], C. Trautmann [3], G. Walter [3], I. Alig [4]

[1] University of Marburg, [2] TU Darmstadt, [3] GSI, Darmstadt, [4] DKI, Darmstadt, Germany

This study concentrates on radiation-induced ageing effects of polymers planned as insulating materials in the rapidly cycling superconducting magnets presently being developed for the FAIR facility. Although beam control and minimization of beam losses will be a major issue, the exposure of insulating parts (e.g. polyimide, polyetherimide, and glass-enforced epoxy-compounds) of various accelerator components to x-rays, gammas, neutrons, and scattered light or heavy particles may limit long-term operation.

We started to investigate degradation processes of commercial polyimide films (Kapton™, thickness 12, 25, and 50 µm) by irradiating them with various heavy ions at room temperature. The experiments were performed at the UNILAC with Ti, Mo, and Au of energy up to 11 MeV/u applying fluences between 1×10^{10} and 2×10^{12} ions/cm^2 under a maximum flux of 2×10^{8} ions/cm^2·s.

Although Kapton is known to be highly radiation resistant, pronounced material modifications were discovered by means of UV/Vis, infrared, and dielectric spectroscopy [1].

In the spectral range of UV/Vis, the wavelength of the absorption edge of irradiated foils shifts as a function of the applied fluence indicating carbonization and a decrease of the bandgap energy in agreement with studies using ions of lower energies [2]. Analyzing the derivative of the transmission spectra ($dT/d\lambda$) reveals that the wavelength at which $dT/d\lambda$ is maximum (dT_{max}) depends on the applied dose (Fig. 1a). The effect appears above a critical dose of about 1MGy for Au and Mo ions, and of a somewhat higher value for the lighter Ti projectiles (~2.7 MGy). The chemical degradation of several specific polymer groups exhibits a similar dose dependence. Fig. 1b shows as an example the decay of one of the imide bands (725 cm^{-1}) together with the band of the phenyl group (1169 cm^{-1}) as a representative for the rather stable aromatic polymer component [3]. Due to track overlapping, the evolution of the infrared and UV/Vis data of the three different ion species follows an exponential law, corresponding to a track radius of about 5, 4, and 2 nm for Au, Mo, and Ti ions, respectively.

The insulating property of irradiated Kapton foils was tested by dielectric spectroscopy performed at room temperature and in a frequency range from 1 MHz to 0.1 Hz using a frequency response analysis system (Solartron SI 1260 Impedance/Gain-Phase Analyzer and a Novo-control broadband dielectric converter). The conductivity of the irradiated Kapton foils was significantly increased, depending on the ion species and dose up to three orders of magnitude (Fig. 1c). The threshold behavior and subsequent exponential increase is in agreement with an insulator-conductor transition based on the creation of graphitic clusters along the ion tracks [4]. In contrast to the absorption data, the conductivity change does not directly scale with the dose of the different ions. To better understand these effects, additional measurements are in preparation.

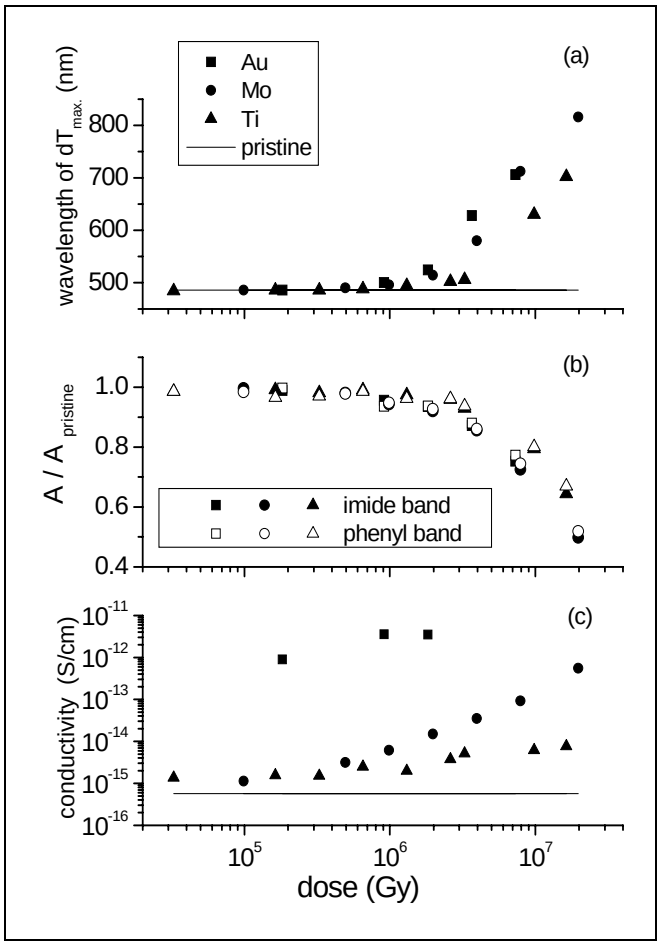

Fig. 1. Data from UV/Vis (a), infrared (b), and dielectric spectroscopy (c) as a function of irradiation dose for Ti, Mo, and Au ions: (a) wavelength of maximum transmission change dT_{max}, (b) band of imide ring (725 cm^{-1}) and of C-H rocking band of the phenyl group (1169 cm^{-1}), (c) electrical conductivity measured at 0.1 Hz.

In addition to the here presented activities, irradiation experiments at 15 K have been started at the GANIL accelerator facility (Caen, France), in order to test degradation and in particular the effect of outgassing processes at cryogenic operation temperatures of the future facility.

References

[1] D. Severin, W. Ensinger, R. Neumann, C. Trautmann, G. Walter, I. Alig, S. Dudkin, Nucl. Instr. and Meth. B (2005), in press.

[2] G. Compagnini, G. Foti, R. Reitano, G. Mondio, Appl. Phys. Lett. 57 (1990) 2546.

[3] T. Steckenreiter, E. Balanzat, H. Fuess, C. Trautmann, Nucl. Instr. and Meth. B 151 (1999) 161.

[4] J-M. Costantini, F. Couvreur, P. Salvetat, S. Bouffard, Nucl. Instr. and Meth. B 194 (2002) 132.

Polymer electrolyte fuel-cell membranes prepared by ion track technology

T. Yamaki[1], A. Hiroki[1], M. Asano[1], K.-O. Voss[2], R. Neumann[2], M. Yoshida[1]

[1]Japan Atomic Energy Research Institute, Takasaki, Gunma, Japan; [2]GSI, Darmstadt, Germany

Currently, there is increasing interest in polymer electrolyte fuel cells (PEFCs) for their wide applications in the fields of the transportation and portable power. The proton exchange membrane (PEM) is a vital component in the PEFCs; this membrane acts as a separator to prevent mixing of the reactant gases and as an electrolyte for transporting protons from the anode to the cathode. DuPont's Nafion is the PEM material most frequently used for this type of application because of its chemical stability and commercial availability. Since Nafion is quite expensive, much effort is being focused on the development of lower-cost membrane materials.

The Japan Atomic Energy Research Institute (JAERI) has recently developed new PEMs by γ-ray or electron-beam induced post grafting of styrene into crosslinked polytetrafluoroethylene films and subsequent sulfonation [1]. These membranes showed a large ion exchange capacity up to about 3 meq g^{-1} exceeding the performance of Nafion. However, the crucial problems still lie in undesired permeation (crossover) of hydrogen fuel through the membranes and insufficient durability above temperatures of 100ºC. The solution of both problems is indispensable to the high-output PEFCs for use in electric vehicles and household cogeneration systems.

To overcome these obstacles, we used swift heavy ions, instead of γ rays and electrons, for the preparation of ion exchange membranes. Irradiation with γ rays or electrons induces the uniform distribution of radicals leading to a homogeneously grafted copolymer. In contrast, high-energy heavy ions create latent tracks extending fully through a polymer foil. A heterogeneous grafting along these latent tracks is thus expected. The so-called heavy-ion grafting has been so far investigated since the first published work by Monnin and Blanford [2]. Nevertheless, the application of this kind of methodology to the development of PEM materials has not been explored. As shown in Fig. 1, the substrate matrix without any graft electrolyte chains mechanically prevents the excess swelling, thereby reducing fuel permeation, and also improves the thermal stability even though the membrane can maintain proton conductivity. It is likely that such materials become interesting because of their specific structure, especially in the domain of proton conducting pathways.

25-μm-thick poly(vinylidene fluoride) (PVDF) films were bombarded by heavy ions with kinetic energies of the order of MeV to GeV (6.3 MeV/n ^{16}O, 3.8 MeV/n ^{20}Ne, 3.5 MeV/n ^{129}Xe, 11.4 MeV/n ^{94}Mo, and 11.1 MeV/n ^{197}Au) from the TIARA cyclotron of JAERI and the UNILAC linear accelerator of the GSI. Just after irradiation, the films were exposed to air to produce peroxide groups initiating the grafting reactions. The peroxide grafting of styrene was then performed for 24 h at 60˚C.

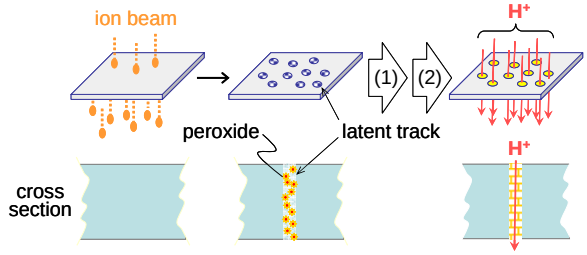

Fig. 1: The scheme for membrane preparation by a heavy-ion grafting method; (1) styrene grafting and (2) sulfonation.

The degree of grafting, defined as the percentage of weight increase after the grafting, is plotted against the absorbed dose in Fig. 2. The dose is related to the fluence, Φ_t, between 3.0×10^6 and 3.0×10^9 ions cm^{-2} by the following equation:

$$D\ [\mathrm{kGy}] = 1.6 \times 10^{-10}\ (\mathrm{d}E/\mathrm{d}x)_e\ [\mathrm{MeV\ cm^2\ mg^{-1}}] \times \Phi_t\ [\mathrm{ions\ cm^{-2}}],$$

where $(\mathrm{d}E/\mathrm{d}x)_e$ is the electronic stopping power. At doses < 1 kGy, the degree of grafting rose slowly. When the dose exceeded 1 kGy, a rapid increment of the grafting yield with increasing dose was observed. The points corresponding to PVDF films grafted using ion beams with different irradiation parameters (mass, velocity and fluence) fit exactly in the curve as if there was no difference in the type of irradiation. As a result, the degree of grafting was arbitrarily controlled in the range of 0 to 40%.

These grafted films were sulfonated in a chlorosulfonic acid solution to obtain the PEMs. The ratio of the sulfonic acid group to the styrene unit was found to be close to unity, suggesting that the membranes at all degrees of grafting were fully sulfonated. The membranes possessed ion exchange capacities reaching 2.2 meq/g, depending on the grafting yield.

Further studies are now in progress to optimize the experimental conditions for the development of high-performance PEMs.

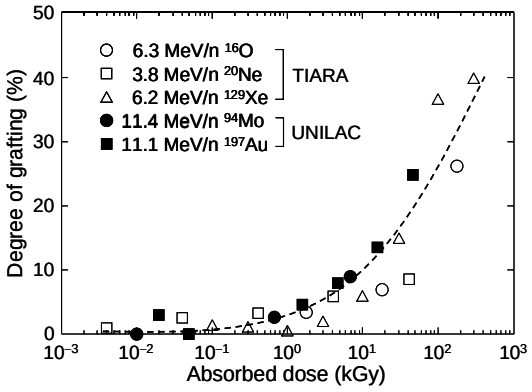

Fig. 2: Plot of the degree of grafting (at 24 h) vs. absorbed dose of ion beams with various irradiation parameters.

References

[1] T. Yamaki, K. Kobayashi, M. Asano, H. Kubota, M. Yoshida, Polymer 45 (2004) 6569.

[2] M. Monnin, G.E. Blanford, Science 181 (1973) 743.

Influence of ionic concentration on transport properties of single asymmetric nanopores in polymer films

B. Schiedt[1], R. Neumann[1], Z. Siwy[2, 3]

[1]*GSI, Planckstr. 1, D-64129 Darmstadt, Germany*
[2]*University of Florida, Gainesville, Fl 32611, USA*
[3]*Silesian University of Technology, 44-100 Gliwice, Poland*

It has been demonstrated that cone-shaped nanopores with charged surfaces are cation selective, and, for the same magnitude of applied voltage, show preferential cation flow from the narrow entrance to the wide opening of the cone [1].

Presently, there are two models which describe this non-linear current-voltage characteristic seen in polymer nanopores. The first model focuses on the presence of an electro-mechanical gate in the narrow end, or "tip" of the pore, which induces changes in pore diameter in response to an applied electric field [2], while the second points to the importance of electrostatic interactions between ions passing through the pore, and surface charges on the pore walls. This non-zero surface charge creates an internal electrostatic potential, with a profile dependent on pore shape. In a conical pore, this profile resembles an asymmetric "ratchet" tooth [3], which gives rise to an electrostatic trap for cations at the pore tip [4]. The depth of this trap differs with the polarity of the applied voltage, resulting in these conical nanopores having an asymmetric, diode-like current-voltage (I-V) characteristic. Also, the depth depends on the pore diameter, surface charge, as well as screening of these fixed surface charges by mobile ions (i.e. the thickness of the electrical double layer at the pore surface [3]). This double-layer thickness is influenced by electrolyte concentration, so if electrostatic interactions are responsible for the rectification effect, the current-voltage characteristic should depend strongly on this concentration parameter.

The single-pore membranes used here are prepared in PET of 12 µm thickness by asymmetric track-etching [1]. The resulting conical pores had narrow openings of 4-20 nm.

I-V curves of the conical nanopores were measured in aqueous KCl solutions of various concentrations ranging from 0.01 to 3 M. For lower salt concentrations, the electrical double layer at the pore walls is thicker, i.e. fewer counter-ions are screening the surface charges, whose effect is therefore more pronounced. So, one would expect that lowering the electrolyte concentration will enhance the rectification effect. Surprisingly, however, for PET pores the rectification increases with decreasing concentration only to 0.1 M KCl (Figure 1). As the concentration is decreased further, the degree of rectification drops again for the majority of the pores examined. The origin of this effect is not yet clear, but it seems to be related to the presence of polymer 'dangling' ends, since conical, negatively charged, Au nanotubes do not show this effect [4]. These dangling ends could act as an electro-mechanical gate, changing the pore diameter for different applied voltages, somewhat similar to the discrete conductance states between which PET pores fluctuate under certain conditions [2].

Also, our results have shown that the pores exhibit a non-classical conductance vs. electrolyte concentration

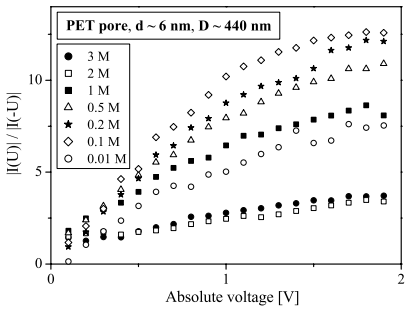

Fig. 1 Variation in the degree of rectification with concentration.

characteristic, having elevated conductances at low concentrations (Figure 2). We presume that it is related to surface conductivity, i.e. where a higher concentration of ions near the pore surfaces causes an increased conductance. In this case, negative surface charge attracts K^+ to the pore walls, forming the double layer. Thus at lower absolute concentrations, the relative concentration of K^+ ions in the pore (compared to that in the bulk) is much greater (i.e. the double layer is thicker, filling more of the pore). This higher relative concentration will give elevated conductances, compared to bulk estimates. Also, it is important to notice that the increase in pore conductance with electrolyte concentration is more pronounced for positive applied voltages, for which higher ion currents are observed.

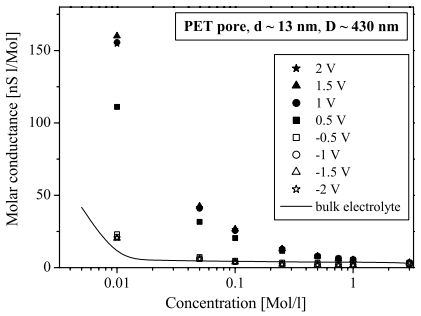

Fig. 2 Molar conductance compared to expected concentration values for a classical pore, based on bulk conductivities.

References

[1] P. Apel, Y.E. Korchev, Z. Siwy, R. Spohr, M. Yoshida, Nucl. Inst. and Meth. B 184 (2001) 337-346.

[2] Z. Siwy, Y. Gu, H.A. Spohr, D. Baur, A. Wolf-Reber, R. Spohr, P. Apel, Y.E. Korchev, Europhys. Lett. 60 (2002) 349-355.

[3] Z. Siwy and A. Fulinski, Phys. Rev. Lett. 89 (2002) 198103.

[4] Z. Siwy, E. Heins, C.C. Harrell, P. Kohli, C.R. Martin, J. Am. Chem. Soc. 126, 10850-10851 (2004).

Fabrication of perforated microcavities for cell cultures

S. Giselbrecht[1], E. Gottwald[1], C. Trautmann[3], R. Truckenmüller[2], K.F. Weibezahn[1] and A. Welle[1]

[1] Institute for Biological Interfaces (IBG), Forschungszentrum Karlsruhe, Germany, [2] Institute for Microstructure Technology (IMT), Forschungszentrum Karlsruhe, Germany, [3] Materials Research, GSI, Darmstadt, Germany

Today, a variety of processes is available for the production of two-dimensional and three-dimensional microstructured polymer components. The current state of the art, however, meets with considerable problems in particular when fabricating microporous cavities that are required for e.g. 3-dimensional cell cultures (Fig. 1). With a few exceptions, such as the fabrication of so-called microporous hollow fibers by extrusion and phase inversion processes, defined microperforation of already existing microcavities by laser-based or lithographic methods applied to individual, isolated structures is possible only when the structure is rotated and repositioned in the directed beam. For this, a high expenditure is required. Moreover, shadowing, diffraction, and scattering effects in components of high structural density limit a subsequent microperforation to a small proportion of the accessible areas. Here we are presenting a novel process based on the microthermoforming technique [1] in combination with the ion track technology, allowing a rapid and efficient fabrication of three-dimensional microporous components. In the macroscopic world, thermoforming is a major process applied in packaging industry. Thermoplastic semi-finished products are fixed at their edges, heated, and stretched to three-dimensional components in their viscoelastic state, as a result of which wall thickness is reduced [2]. Microthermoforming results from a special process, the so-called trapped sheet thermoforming. Here, the thin semi-finished film is fixed between the two metal plates of the forming tool that are pressed onto each other. By these plates, the polymer film is heated conductively to forming temperature. One-sided application of a pressurized gas causes the elastic film to be cast into the cavities of the microstructured mold that have been evacuated in advance. By cooling down the structure, the new shape of the film is frozen and the component can be demolded.

Fig. 1. Scheme of microcavity set as 3-dimensional containers for cell cultivation with perforated walls to improve supply with nutrients.

In analogy to macroscopic thermoforming of already textured or printed semi-finished products [2], microthermoforming may be used to turn films that have been surface or bulk modified (locally or globally) into three-dimensional microstructures. The polymer film is formed in its viscoelastic state and not in its melting phase, as it is the case in other conventional microreplication processes, e.g. microinjection molding. Due to permanent material cohesion, the previously generated properties of the film are maintained in principle, but distorted in geometry and possibly in location by stretching. Using the ion track technology has the particular advantage that the latent tracks generated by ion bombarding of flat polycarbonate film are not erased due to the moderate temperature at which microthermoforming is conducted. As a result, the individual process steps can be reordered, which is advantageous to the fabrication of microporous cavities. The flat, unstructured PC film may be irradiated over a large area with energetic ions at the parameters desired before it is subjected to three-dimensional structuring by microthermoforming. Following thermoforming, wet-chemical etching transforms the latent tracks in the walls of the microstructured body into pores. As in the planar case, the size and geometry of the pores is defined by the etching parameters. The stretching process, however, results in dose smearing and, hence, influences the etching rate. The pore density is affected proportionally to the stretching of the film.

As illustrated in Fig. 2, we successfully fabricated thin-walled, three-dimensional microcavities that are microperforated on all sides. In the future, these structures shall be used to produce highly adaptable, biomimetic container for the three-dimensional cultivation of cells, in which an optimum supply of the cell aggregates will be ensured by an all-side perfusion with medium.

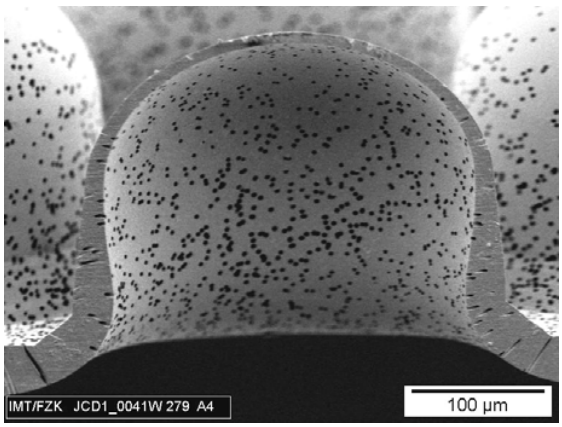

Fig. 2. Cross sectional view of an inverted microcavity perforated by means of ion track technology. In a first step a 50 µm thick polycarbonate film was exposed to 1460-MeV Xe (10^6 ions/cm^2). The irradiated film was processed by microthermoforming, and subsequently the ion tracks were transformed into pores by chemical etching in an aqueous solution of 5 Mol/L NaOH and 10% methanol (6h, 50°C).

References

[1] R. Truckenmüller, Z. Rummler, T. Schaller, W.K. Schomburg, in *Proc. Micromechanics Europe Workshop (MME)* 39-42 (Cork, Ireland, 2001)

[2] J.L. Throne, M. Heil, J. Beine, *Thermoformen* (Hanser, München; Wien, 1999).

IR-spectroscopy on single Bi nanowires

T.W. Cornelius[1], G. Fahsold[2], M.E. Toimil Molares[1], T. Kolb[2], R. Neumann[1], F. Kost[2], A. Pucci[2]
[1]Gesellschaft für Schwerionenforschung (GSI), Planckstr. 1, D-64291 Darmstadt, Germany
[2]Kirchhoff-Insitut für Physik (KIP), Heidelberg University, INF 227, D-69120 Heidelberg, Germany

Bismuth is a semimetal with very unusual properties. Bulk Bi exhibits a very small indirect band overlap (E_0 = 98 meV at 300 K). The electrons are located in three pockets at the L-point of the Brillouin zone while the hole bands are located at the T-point. The band structure of bulk Bi is sketched in Fig. 1. Direct transitions can occur in the vicinity of the L- and the T-point, where E_{G1} = 36 meV (290 cm^{-1}) and E_{G2} = 250 meV (2000 cm^{-1}) at T < 4 K. In addition, indirect transitions are possible from the L- to the T-point valence band [1, 2]. In the case of nanowires, the energy bands split into subbands if the diameter is in the range of the Fermi wavelength λ_F. For bismuth (λ_F ~ 40 nm), the splitting of the bands occurs already in nanowires with about 100 nm in diameter. The subbands are separated by an energy which is inversely proportional to the effective mass of the charge carriers m^* and the wire diameter d squared: $\Delta E \approx \hbar^2\pi^2/(m^*d^2)$. For Bi, m^* is very small (0.001 – 0.26 m_e), thus ΔE is large. Consequences of the subband splitting are: (1) the energies E_{G1}, E_{G2} and E_0 vary depending on the confinement of the wire. This implies changes, e.g. the onset of IR-optical transitions around the T-point should shift to higher energies for thinner nanowires. (2) Bi undergoes a transition from a semimetal to a semiconductor in thin nanowires.

Measuring absolute values of the electric resistance of single wires as a function of wire diameter [3] and performing infrared spectroscopy on single nanowires provide appropriate tools for investigating the electrical and optical properties of Bi nanowires.

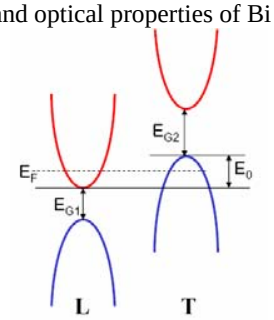

Fig. 1: Band structure of bulk bismuth

IR spectroscopy on single isolated Bi nanowires on Si/SiO_2 wafer was performed at the synchrotron light source ANKA (Forschungszentrum Karlsruhe). The advantage of examining spectra from individual wires is that we can exclude the influence of neighbouring wires occuring for nanowire arrays.

Bi nanowires with diameters between 50 and 300 nm were deposited in polycarbonate etched ion-track membranes [4]. After dissolution of the template, Bi nanowires were deposited on a Si/SiO_2 substrate and placed at the IR-microscope where single wires were located by using visible light. A scheme of the experimental setup and an optical micrograph of several single wires (d = 200 nm) are shown in Fig. 2.

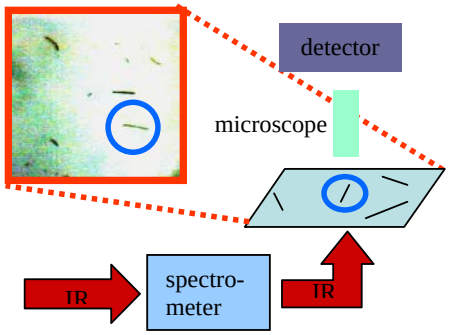

Fig. 2: Experimental setup and optical micrograph of single Bi wires on a Si/SiO_2 wafer.

Absorption spectra of single wires are displayed in Fig. 3. As the most pronounced feature, we find a strong onset of IR absorption (indicated by solid lines) which shifts from 1600 to 1700, 2900, and 3600 cm^{-1} for the 200, 160, 80, and 50-nm diameter wires, respectively. This is a clear signature of quantum confinement in these nanowires. We attribute this absorption to direct interband transitions in the vicinity of the T-point. The shift of the absorption edge reflects the increase of E_{G2} with decreasing nanowire diameter, which has not been shown in any previous experiment. The spectra for 80- and 50-nm show weak absorption at lower wavenumbers (marked by arrows) than the dominant absorption edge (see inset). Further experiments at ANKA are planned for probing this wavelength range for thin wires to attain signatures of indirect interband and intersubband transitions.

This work was supported in part by the DFG (Fa432/7-1). We acknowledge helpful discussions and technical support by the ANKA beamline scientists B. Gasharova and Y.-L. Mathis.

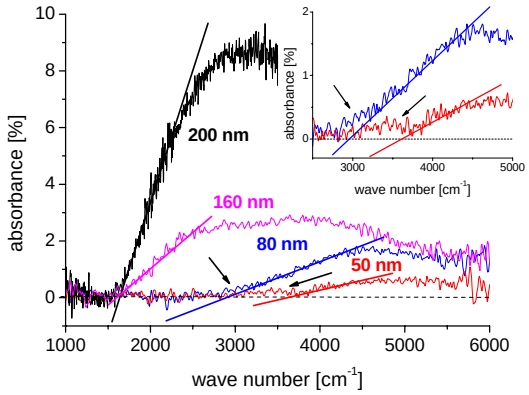

Fig. 3: IR absorption spectra of single Bi nanowires.

[1] R.T. Issaacson, G.A. Williams, *Phys Rev. 185* (1969) 682
[2] M.R. Black, Y.-M. Lin, S.B. Cronin, O. Rabin, M.S. Dresselhaus, *Phys. Rev. B 65* (2002) 195417
[3] M.E. Toimil Molares, N. Chtanko, T.W. Cornelius, D. Dobrev, I. Enculescu, R.H. Blick, R. Neumann, *Nanotechnology 15* (2004) S201
[4] T.W. Cornelius, J. Brötz, N. Chtanko, D. Dobrev, G. Miehe, R. Neumann, M.E. Toimil Molares, *Nanotechnology* (in print)

Synthesis of gold nanowires in nanoporous ion track membranes

J. Liu[1], S. Karim[2], J.L. Duan[1], M.E. Toimil Molares[3], T.W. Cornelius[3], D. Dobrev[3], H. J. Yao[1], Y. M. Sun[1], Z. G. Wang[1], R. Neumann[3]

[1] Institute of Modern Physics, CAS, Lanzhou, China, [2] University of Marburg, Germany, [3] GSI Darmstadt, Germany

Metallic nanowires are of great interest for future applications in fields such as optoelectronics and sensorics [1-3]. By electrochemical deposition in the nanopores of etched ion-track polymer membranes, single- and polycrystalline gold nanowires with diameters down to 20 nm have been produced in this work.

Polycarbonate foils of thickness 30 μm (Makrofol N, Bayer Leverkusen) were irradiated at the UNILAC (^{197}Au ions, E = 11.4 MeV/u), and subsequently etched in a 6N NaOH solution at 50 °C to obtain pores with diameters ranging from 20 to 150 nm. A thin gold film sputtered onto one side of the membrane and a gold cone served, respectively, as a cathode and anode during the growth of the wires. Both DC and pulsed deposition were employed at temperatures ranging between 50 and 65 °C. Two different electrolytes, potassium dicyanoaurate(I) ($KAu(CN)_2$) and ammonium gold(I) sulphite ($(NH_4)_3Au(SO_3)_2$) were employed.

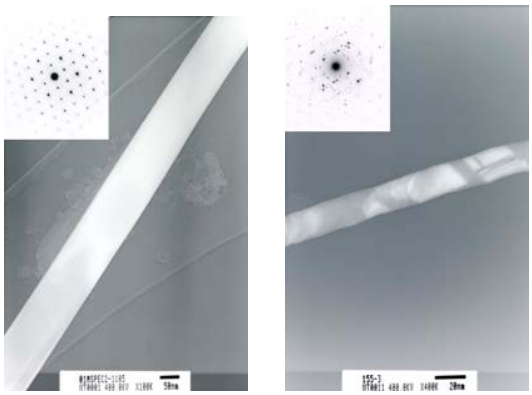

Fig.1. HRTEM images of (a) single- and (b) polycrystalline gold nanowires, with their SAED patterns (insets). Scale bars: (a) 50 nm, (b) 20 nm.

The crystalline structure of the nanowires deposited at different conditions was investigated by high-resolution transmission electron microscopy (HRTEM). Fig. 1 (left) shows a HRTEM micrograph of a Au nanowire deposited with the cyanide electrolyte using DC deposition (U = 900 mV) at 60 °C in an ultrasonic field. No grain boundaries were observed in nanowires grown under these conditions. The selected-area electron diffraction (SAED) pattern (inset) confirms the single-crystalline structure. In Fig. 1 (right), both HRTEM image and SAED pattern evidenced the polycrystalline structure of the Au wire, which is about 40 nm in diameter and was deposited using the ammonium-gold (I) sulphite electrolyte at U = 500 mV and 50 °C.

In all cases, the nanowires possessed a very homogeneous contour and a cylindrical shape. Fig. 2(a) shows a scanning electron microscopy (SEM) image of Au nanowires with diameter 50 nm after dissolution of the polycarbonate membrane in CH_2Cl_2.

SEM observations showed that the caps growing on top of the wires have different morphology, depending on the crystallinity of the nanowires. The caps grown on the top of poly-crystalline wires exhibit hemispherical shapes (Fig. 2b), while caps on the single-crystalline wires display faceted forms (Fig. 2c and 2d) [4].

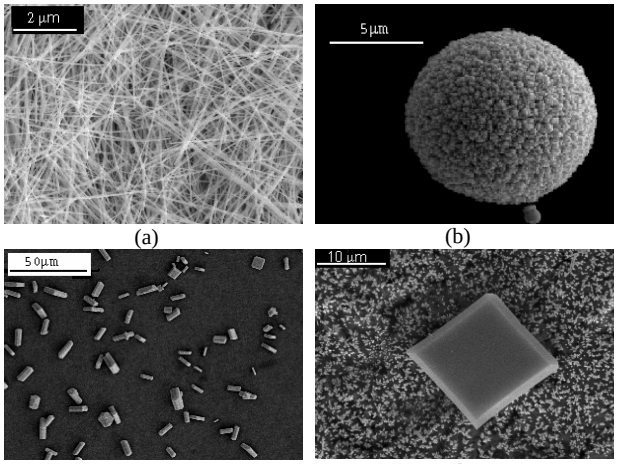

Fig. 2 SEM images of (a) Au nanowires with diameter 50 nm after dissolution of the polycarbonate foil, (b) a poly-crystalline cap obtained by deposition with ammonium-gold(I) sulphite electrolyte, (c,d) single-crystalline caps grown on the top of gold wires using pulsed deposition and cyanide electrolyte in ultrasonic field.

These results show that the crystalline structure of the nanowires depends mostly on the electrolyte, the cyanide solution favouring the growth of gold single-crystalline nanowires at both DC and pulsed deposition conditions. The sulphite electrolyte is unstable, forming colloidal gold particles. The depositions of these particles on the cathode serve as nucleation centers, thus leading to the formation of fine-grained, polycrystalline structures [5].

In conclusion, this study has provided the deposition conditions required for single- and poly-crystalline structures of gold nanowires.

[1] W.D. Williams and N.Giordano, Phys. Rev. B 33 (1986) 8146

[2] M.E. Toimil Molares, V. Buschmann, D. Dobrev, R. Neumann, R. Scholz, I.U. Schuchert and J. Vetter, Adv. Mater. 13 (2001) 62

[3] Y. Xia, P. Yang, Y. Sun, Y. Wu, B. Mayers, B. Gates, Y. Yin, F. Kim and H. Yan, Adv. Mater. 15 (2003) 353

[4] M.E. Toimil Molares, J. Brötz, V. Buschmann, D. Dobrev, R. Neumann, R. Scholz, I.U. Schuchert, C. Trautmann and J. Vetter, Nucl. Instr. and Meth. in Phys. Res. B 185 (2001) 192-197

[5] D. Dobrev, J. Vetter, N. Angert and R. Neumann, Electrochimica Acta 45 (2000) 3117

Silver single crystals and polymer membranes: Electrochemical filling of etched ion-track pores and free growth on the surface

D. Dobrev and R. Neumann

Gesellschaft für Schwerionenforschung (GSI), Planckstr. 1, 64291 Darmstadt, Germany

In previous works, we generated single-crystalline wires of various materials in pores of polycarbonate foils. We applied pulse-reverse electrodeposition based on an ultrasonic-field method developed for that case. The pores were created by irradiating the foils with U, Au, or Bi ions and chemically etching the narrow damage trails caused by the ions. Perfect single crystals were grown from copper [1], gold [2], iron [3], and bismuth [4].

In this work, we concentrate on silver single crystals overgrowing the pore orifices after filling the pores with silver. Foils with thicknesses 30-60 µm were irradiated with U ions with energy 11.4 MeV/u at the UNILAC of GSI. A fluence of 10^6 ions/cm^2 was used in all experiments. The ion tracks in the foils were transformed into channels with diameters 1.6-2 µm, using standard etching with NaOH. One side of the foils was made conductive by sputtering a thin Au layer. Usually, this layer is reinforced by electrodeposition of 20-30 µm Cu, which completely closes the pore orifices on this side and serves further as a cathode. However, the Ag deposition potential is more positive than that of Cu. In this case, to avoid a replacement deposition of Ag on Cu, the electrolytic cell should be filled with the electrolyte after preliminary polarization of the cathode. Especially for pulse-reverse deposition, it is more convenient to use a cathode of Ag or of a metal, whose potential is more positive. Therefore, the sputtered Au layer was electroplated with 2-3 µm Au from a $Na_3Au(SO_3)_2$ bath at 55 °C, applying a current density of 3 mA/cm^2. The thin Au layers always contain a substantial amount of cracks. For this reason, the Au film was additionally cladded with 10 µm Ag from an electrolyte containing 420g/l K_2AgI_3 at RT and a current density of 2 mA/cm^2. Finally, the cathode was strengthened by an electroplated Cu layer of 15-20 µm. The electroplating processes as well as the Ag deposition were carried out in an electrochemical cell described in detail in [5,2].

Using a Ag anode, Ag was deposited at RT from an electrolyte of 0.5 M $AgNO_3$ and 0.05 M free HNO_3. Potentiostatic pulses of 12 mV and reverse current of 8 mA/cm^2 at the active cathode (integral area of pore orifices) were used during deposition. Successive negative and positive pulses with lengths 5 and 1 s, respectively, were applied to the cathode. The Ag deposition was carried out in different stages. The single crystals start to grow in the pores before reaching the foil surface. If the deposition continues, they exit from the orifices. At a distinct stage, nearly hemispherical crystals can be formed on this surface. The deposits were imaged with a Philips XL30 SEM. Two growth stages visible after dissolving the polycarbonate foil with CH_2Cl_2 are presented in Fig. 1. A top view of a very perfect Ag single crystal, obtained on the polymer surface is shown in Fig. 2. It should be mentioned that when using potentiostatic pulses, the current density decreases significantly with enlarging crystal surface. A commercial program (© JCrystalsoft, 2003) was used to simulate the shape of the crystal in Fig. 2, the result being displayed in Fig. 3. This simulation permitted us to identify crystallographic planes, which are formed during the crystal growth. Obviously, crystals evince their growth habit. Only low-indexed, densest-packed (111), (100), and (110) planes correspond to equilibrium forms. Planes of type (210), (310), (431), and (522) are vicinal planes, which are much less dense-packed. The growth proceeds on such planes. They can change their form and size as well as completely disappear during further growth. Thus, a great variety of crystal forms can be generated at different stages of deposition.

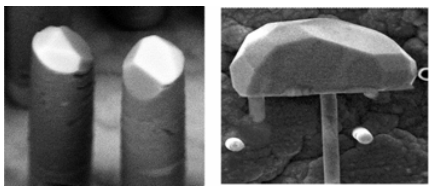

Fig. 1. Silver single-crystal before (left) and after (right) reaching the foil surface.

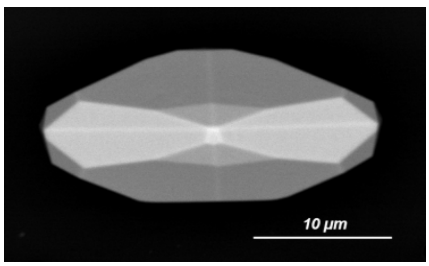

Fig. 2. Top view of a multi-faceted perfect Ag crystal.

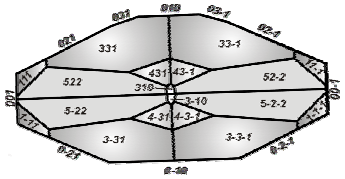

Fig. 3. Shape of the crystal in Fig. 2, simulated with the commercial program © JCrystalsoft, 2003.

References

1. D. Dobrev, J. Vetter, N. Angert, R. Neumann: Appl. Phys. A 69, 233 (1999).

2. D. Dobrev, J. Vetter, N. Angert, R. Neumann: Electrochimica Acta 45, 3117 (2000).

3. D. Dobrev, J. Vetter, N. Angert, R. Neumann: Appl. Phys. A 72, 729 (2001).

4. D. Dobrev, R. Neumann: GSI Sci. Rep. 2002, 147 (2003).

5. D. Dobrev, J. Vetter, N. Angert, Nucl. Instr. and Meth. B 149, 207 (1999).

RADBIOPH

Radiation Research and Biophysics with Heavy Ions

Radial ionisation distribution of heavy ions: Experimental results with OPAC and comparison with TRAX

G. Laczko, V. Dangendorf,, K. Tittelmeier, PTB Braunschweig
M. Krämer; D. Schardt, GSI Darmstadt

The difference in the relative biological efficiency (RBE) of ions of same linear energy transfer (LET) but different atomic number (Z) can be attributed to the difference in the radial ionisation distribution. We have performed systematic measurements of the spatial ionisation pattern of heavy ions of various Z but similar LET at GSI. The results are compared with track structure data obtained by the Monte Carlo code, TRAX [1]. The measurements were performed with a time projection chamber with optical readout (Optical Avalanche Chamber, OPAC) [2] which is able to quantitatively capture the spatial ionisation pattern of an ion traversing the chamber [3].

In the previous reports we have described the first results of measurements with C ions [3] and the modifications implemented in the TRAX code, in order to account for the specific properties of the OPAC interaction chamber [2]. In the meantime the optical system of OPAC was further improved and we are now able to obtain well focussed images in the whole field of view. Also a reduction of the stray light background by a factor of 13 as compared to the earlier measurements was obtained

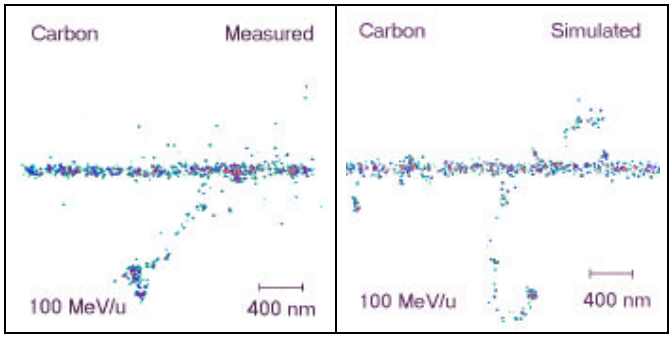

Fig.1: Carbon ion tracks, measured with OPAC and simulated with TRAX

With this instrument tracks of various kind of ions, from C to U, at energies ranging from the Bragg peak until 1500 MeV/u were measured to investigate the radial ionisation deposition from a few 10 nm till about 10 um radial distance. Since the radial dose distribution farther away from the track is determined by the stochastic appearance of fast δ-electrons for each ion energy and species a large number of tracks was measured to obtain sufficient statistics far away from the central track core. Fig 1 shows samples of measured and (TRAX-) simulated carbon tracks. The simulated track includes already part of the chamber response, like electron diffusion, peak broadening and gain variation of single electron images.

Even with the improved optical readout system, the event density there is determined by stray light from the central track region and by the geometrical broadening of the single electron images, which overlap in the central part and produce artificially high ionisation density in the vicinity of the track core. The stray light contribution in the remoter regions of the track was experimentally investigated with low energy α-particles, which have only short ranged delta electrons. Based on this the stray light in the images of the faster ions could be subtracted. The peak broadening was eliminated by an iterative unfolding algorithm which reduced the width of the peaks to a few pixels and simultaneously delivered the information on the number of electrons in each peak. With the purified experimental data the radial ionisation distributions were calculated and compared with corresponding TRAX simulations. Fig. 2. shows four examples.

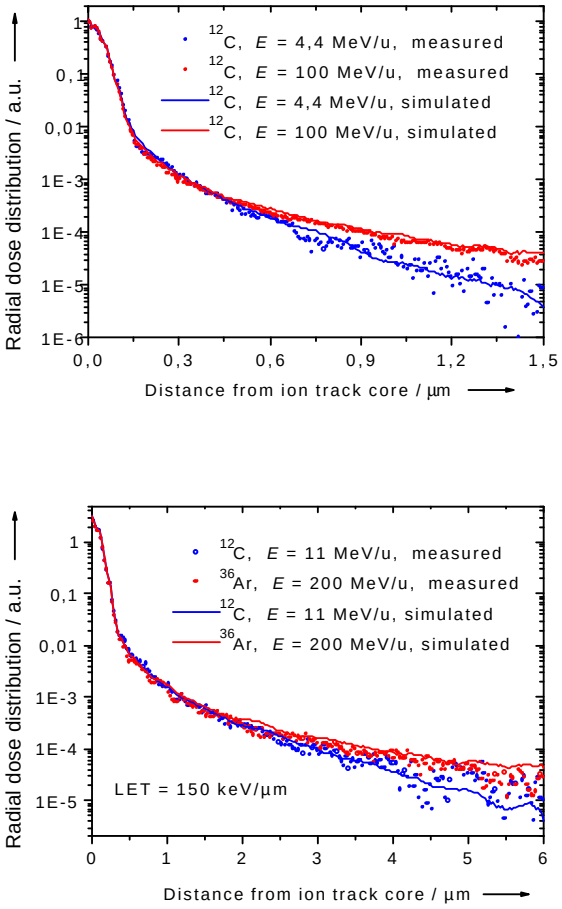

Fig.2. *Radial dose distributions for C and Ar ions at various energies.*

Fig 2 a compares carbon tracks of different energy. The total ionisation was normalised to the same integral. It can be observed that due to the lower average δ-electron energy for the slower ions the drop of the radial dose is faster for the slower ions. The same holds for Fig 2.b which compares Ar and C ions at the same LET.

All data show reasonably good agreement between simulation and experiment. For Ar it is slightly worse due to the known deficits of the models for the electron production of heavier ions used by TRAX. At energies below about 30 MeV/u the measurement results suffer from higher uncertainties. The reason for it is the fact, that these measurements were made with ions from SIS and their very high original energy had to be degraded by a water column to the required level. This method results in an energy straggling and only those ions can be accounted for, whose energy deposition in the chamber is inside a defined window. Thus, the amount of useful data in the low energy region is reduced and the energy of the ions is less well defined.

References:

[1] M. Krämer et al, GSI Sci. Rep. 2002, p 152
[2] G. Laczko et al., Nucl. Inst. and Meth. A, 53 (2004) p 216
[3] G. Laczko et al, GSI Sci. Rep. 2002 p 151

Toroidal electrostatic analyzer for double differential cross sections for low energy electron emission in solid foils

N.Lineva [1], S.Hagmann [1,2]

[1]GSI-Darmstadt; [2]Institut f. Kernphysik, Univ. Frankfurt

A quantitative study of the ionization density inside an ion track in a solid provides us a radial dose distribution which finally serves to determine the radiobiological efficiency for radiotherapy with heavy ions. However, a direct determination of double differential cross sections (DDCS) of electron emission after heavy ion impact is a complex task. Even in the thinnest technically feasible target foil electrons undergo numerous elastic and inelastic collisions before entering a spectrometer. This leads to a potentially severe loss of information on energy and emission direction of primary electrons. It is therefore of utmost importance to devise procedures, where the electron production process and subsequent transport of ionized electrons become separable. We will use target Auger electrons of well known energy to map inelastic collisions inside a solid and thus calculate the necessary scattering correction factors to derive the DDCS. To measure DDCS for low energy electrons we modified the electrostatic toroidal electron spectrometer to adapt it to a flexible set-up for various beam environments and target configurations. Its cross section is shown in Fig.1.

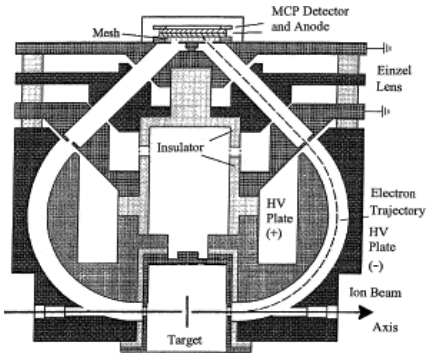

Fig.1. Cross section of electrostatic toroidal electron energy analyzer

Electrons emitted from the target are deflected in the electrostatic electron spectrometer by high voltage toroidal plates, energy analyzed and focused by a truncated cone lens onto a microchannelplate (MCP) detector equipped with a 2D position sensitive delay line anode. This permits identification of the position, where electrons hit the MCP, that determines direction of the electron emission from the target. The electron pass energy is determined by the spectrometer voltage and the geometrical spectrometer factor. Electrons with a kinetic energy up to 5 keV can be detected.

All electrooptical elements of the spectrometer possess rotation symmetry with respect to the axis through the center of the target and the center of the MCP detector. Therefore the complete range of emission angles from 0˚ to 360˚ is covered by the spectrometer.

A modified target wheel assembly for up to 8 different targets has been installed. The target chamber is equipped with a double μ-metal shield to reduce earth- and other stray magnetic fields to $B_{rest} \approx 2$mG. For testing purposes the system is equipped with an electron gun, which provides electron beams with energies from 100 to 3000eV. For shielding and collimation purposes a metallic tube on ground potential is situated in the entrance of projectile electrons into the spectrometer. Data acquisition is build with MBS. Data analysis program is based on Go4.

Fig.2 shows a radial velocity distribution of electrons emitted in collisions of projectile electrons e^- of 1keV energy with a carbon foil (thickness 7 μg/cm^2, ≈150 atom layers) and a gold foil (thickness μg/cm^2 ;≈ 100 atom layers). Polar coordinates are used. The radius reflects the electron velocity in atomic units. Indicated are angular position of the target axis (T)-(T) and the positions of four bridges in cylinder aperture (O) positioned in the target zone of the spectrometer.

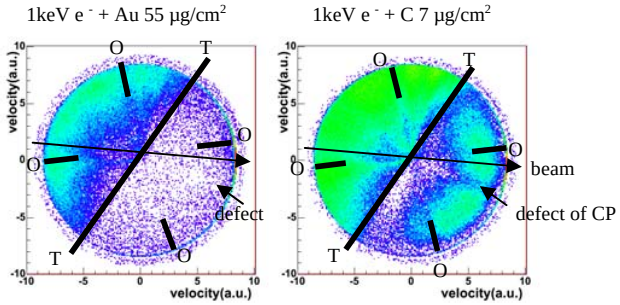

Fig. 2. Radial velocity distribution of electrons emitted in collisions of e^- beam with a gold (left side) and carbon foil.

On both figures one can see significant spots exactly in beam direction produced by projectile electrons traveling without energy loss through micropores in the targets with energy $E=E_0$. At the same time in the backward direction there are wide distributions produced by inelastically backscattered electrons with a velocity given by the radius vector (see, Fig. 2). The electron emission in the forward direction depends strongly on the material of the target. Whereas for carbon a significant fraction of the electrons passes through the foil with energy loss of about 300 to 700eV, for gold there are no e^- with $E<E_0$ in the forward direction. In the range from 0° to 360° there is a thin band at the projectile electron energy E_0. This is a near isotropic background electrons due to incomplete suppression of stray electrons.

Shadows from obstacles and the target frame are clearly seen. The decrease of the electron intensity in the backward direction at near 180º is related to the shielding tube, situated in the entrance hole of the spectrometer. One additional shadow on Fig.2 is caused by a defect on the MCP detector. Results of such test measurements are useful for the fine tuning of the toroidal spectrometer and the calibration of the MCP detector for planning beam times with the Unilac beam.

Studying DNA fragmentation with an Atomic Force Microscope

K. Psonka[1,2], E. Gudowska-Nowak[1,2], S. Brons[2], and G. Taucher-Scholz[2]
[1]Institute of Physics, Jagellonian University, Kraków; [2]GSI, Biophysik

Multiple damaged sites induced on the DNA molecule of the target cell are expected to be at the origin of the enhanced biological effectiveness of particle radiation compared to conventional ionising radiation [1]. However experimental evidence supporting this hypothesis is still scarce and most of the time only indirect. Therefore, Atomic Force Microscopy (AFM) of DNA damage induced by ionising radiation offers an interesting approach to directly visualise the action of ionising radiation on biological targets.

Previously we have reported on the development of an AFM analysis method to investigate the distribution of multiple double-strand breaks (DSBs) induced by X-rays and 3.5 $MeV\,u^{-1}$ Ni ions on plasmid DNA [4]. A home-made AFM operated in a *contact mode* has been used to investigate the DNA in a cationic solution deposited on freshly cleaved mica. Clear images could be recorded (figure 1), which allowed to extract fragment size distributions for different radiation qualities and to compare the average length of the induced fragments [2, 3].

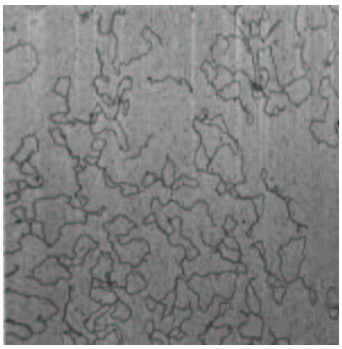

Figure 1: An exemplary picture of plasmid DNA scanned in contact mode.

However, the use of a home-built microscope operated in a *contact mode* imposes some restrictions, which seriously limit the scope of the information to be extracted by this method: First, the resolution and the signal to noise ratio are rather poor, implying an implicit detection limit for DNA fragments of about 100 nm. Secondly, the force executed on the sample by the permanent contact with the cantilever is rather high, making the method susceptible to artefacts (selective removal of loosely bound molecules, breaks induced during scanning). Also the analysis of more delicate systems, like complexes of repair proteins interacting with DNA, is not possible using such a setup.

Meanwhile the GSI Material Research Department has purchased a new, commercial AFM (MDT Solver P47), which provides the possibility to use various scanning modes. In particular the instrument is able to record images in a *tapping mode*, where the cantilever is not in a permanent contact with the sample, but vibrates at its resonance frequency above it. Upon approaching the sample, the tip briefly touches, or taps, the surface resulting in a decrease in oscillation amplitude. The feedback loop keeps this decrease at a preset value and a topographic image of the sample surface can be obtained. The destructive influence of lateral forces due to the relative movement of the tip with respect to the probe is virtually eliminated in this case, because the duration of the contact between tip and sample is so short. Figure 2 shows a picture taken from unirradiated plasmid DNA ΦX174 using this method: A drop of 10 μl DNA diluted in 28.6 mM $MgCl_2$ and 50 mM KCl was deposited on freshly cleaved mica treated before with 10 μl 28.6 mM $MgCl_2$. Prior to imaging the samples have been incubated for 5 min at room temperature and then dried in an exsiccator. The size of the scanned area in figure 2 is $3 \times 3\,\mu$m with a scanning step size of 6 nm.

Figure 2: An exemplary picture of plasmid DNA scanned in tapping mode.

The figure illustrates, that the approach to analyse fragmentation patterns of DNA using an AFM operated in a tapping mode is feasible and leads to images of at least comparable quality as the old method. We anticipate that, with the analysis being transferred to liquid and due optimisation of the scanning parameters, we will be able to achieve decisive improvements in spatial resolution and signal to noise ratio. Thereby we expect being able to study DNA fragmentation by heavy ions with much higher sensitivity than achieved so far. Due to the lower lateral forces exerted on the probe, we will also be able to study more delicate systems, as protein-DNA complexes. This would open a new realm of possible studies, as interaction of repair proteins with multiple damaged sites, and time resolved microscopy of DNA repair.

References

[1] J.F. Ward: Radiat. Res. **86**, 185-195 (1981).
[2] M. Heiß: Diploma thesis, Heidelberg university, 2000.
[3] K. Psonka: Master of science thesis, Krakow university, 2002.
[4] GSI Annual Report 2003, 158.

Quantification of DNA double strand breaks in cancer therapy related experiments with carbon ions

Y. Schweinfurth, B. Jakob, J. Rudolph, D. Fink and G. Taucher-Scholz

Biophysics, GSI Darmstadt, Germany

The aim of radiation tumour therapy is to destruct the tumour while sparing the healthy tissue to a large extend. The induction of DNA damage, especially the induction of DNA double strand breaks (DSBs) play a critical role in the emergence and treatment of cancer. In our study we used the molecular marker γH2AX as a system indicating the presence of DSBs. After induction of DSBs, the cell signals this by very rapid phosphorylation of the histone protein H2AX. The phosphorylation involves thousands of H2AX molecules in a megabase region flanking the break. DSBs can be visualise as foci using immunostaining of the phosphorylated form γH2AX [1].

In our experiments we simulated the situation during the irradiation of a tumour with carbon ions, using human fibroblast cells. We examined both the induction and the repair of DSBs in the extended Bragg-Peak and the entrance channel. We irradiated human skin fibroblasts (AG 1522) with high energy carbon ions in the way shown in Figure 1. Every position shown in Fig. 1, cointains 16 samples. For each time point, one sample was directly fixed and stained for γH2AX and one sample was extracted prior to fixation and stained for γH2AX and the protein p53. The DNA was counterstained with TO-PRO3.

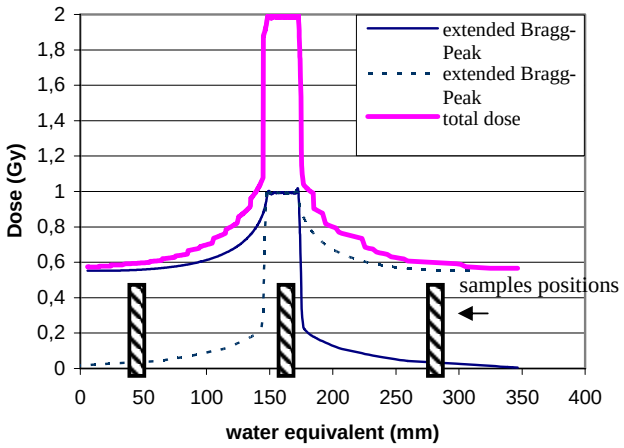

Figure 1: Experimental design.

The samples were placed at the marked positions. The irradiation was carried out first from one side with the shown dose distribution and than from the second side (180 ° turn) with the same dose distribution, similar to tumour treatment in patients.

Imaging was performed using a confocal laser scanning microscope (image size 1024x1024 pixel) with identical parameters for all samples. The image analysis was done with Scion (Scion Corp.). The confocal image stacks were transformed in maximum projections and these converted in binary images using adaptive thresholds. After visual inspection and counting of foci, we selected our parameters for a semiautomatic foci detection and counting. The cell nuclei were identified by the TO-PRO3 DNA staining. Using the nuclear area as a mask, we measured the mean intensity of the γH2AX staining in every nucleus and counted particles with a certain size (≥ 5 pixel) and intensity (≥ 3 fold of nuclear mean intensity).

The preliminary results are summarized in figure 2.

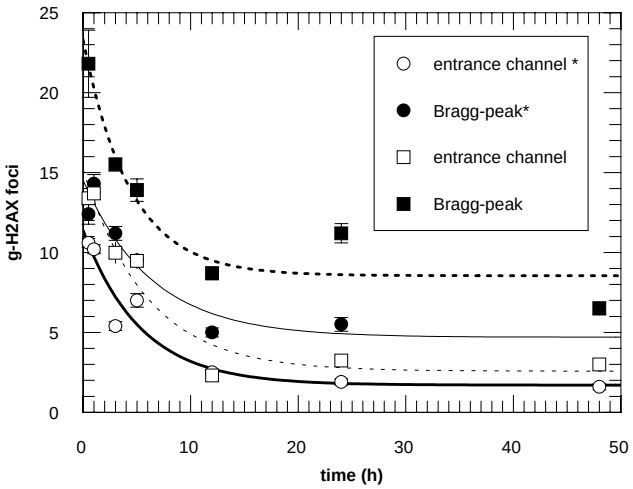

Figure 2. Time course of γH2AX Foci in AG cells.

Bragg-Peak and Entrance channel: stained for γH2AX ; Bragg-Peak * and Entrance channel *: extracted and stained for γH2AX and p53. Y-Axis: mean number of foci per nucleus ±StE (counted 110-140 nuclei/sample).

Our preliminary results showed a clear radiation dependent induction of DSBs in the Bragg-Peak as well as in the entrance channel as measured by γH2AX foci. At later time points γH2AX foci vanished indicating some form of repair. At the moment we are working on the optimization of our measurement and analysis method because of problems arising from unspecific background staining and overlapping of foci, leading to an underestimation especially at higher number of foci, as counted for the early time points. Main parameters influencing the results are the determination of a minimal focus area and intensity. For the better verification of the results we compare kinetics of the formation and loss of γH2AX foci at various doses with x ray and track segment experiments with higher LET ion irradiation at the UNILAC.

This type of experiment can help to understand the differences in DNA lesions formation and repair in the context of the heavy ion tumour therapy. Successful DSB repair may form a part of the basis of the observed differences of RBE values in the tumour (Bragg-Peak-repair) and the surrounding healthy tissue (entrance channel).

References:

[1] Modesti and Kanaar (2001), Curr Biol., 11 (6):R229-232

Quantitative analysis of DNA fragment distributions generated by densely ionising radiation

A. Fricke, M. Kühne and M. Löbrich

Fachrichtung Biophysik, Universität des Saarlandes, Germany

Radiation-induced DNA damage may be described both qualitatively and quantitatively by means of analytical and numerical models. The random breakage model (RBM) [1] is the most popular and the most simple model to describe DNA double strand break (DSB) distributions. Published experimental data on DNA fragmentation due to DSBs induced by sparsely ionising radiation are consistent with the RBM. Therfore this model appears to be a useful tool to analyse DNA fragmentation generated by X-rays and also, but much more limited, for high-LET radiation.

In the present study we investigated ionising radiation-induced double-stranded (ds) DNA fragment distributions in the size range between 20 kbp and 3 Mbp. A rapidly proliferating human tumor cell line, MGH-U1 cells, were used in synchronisation experiments to investigate DNA fragmentation in different cell cycle phases. Growing MGH-U1 cells were treated with the microtubule poison nocodazol for 16 h, resulting in an accumulation of approximately 70% of the cells with highly condensed chromatin at the G2/M border of the cell cyle (determined by flow cytometry analysis). Experiments with exponentially growing cells were done in parallel. After irradiation with carbon-, nickel- and zinc-ions at the UNILAC or with α-particles and X-rays in our laboratory, cells were trypsinised, embedded in agarose plugs and lysed. Two different electrophoretic conditions were applied for each sample to separate ds DNA fragments between 20 kbp and 3 Mbp. Southern hybridisation with whole-genome probes was used for analysis.

To investigate DNA fragment size distributions quantitatively, each lane of the Southern blot was divided by application software into different size intervals. The signal intensity is proportional to the amount of DNA mass in each size zone. The RBM was fitted to the dose-dependent amount of DNA in each zone and provided an estimate of the induction rate (Fig. 1). In Figure 2, these induction rates are blotted as a function of size (molecular weight).

In case of a random distribution of DSBs inside the genom, the induction rate would be expected to be independent

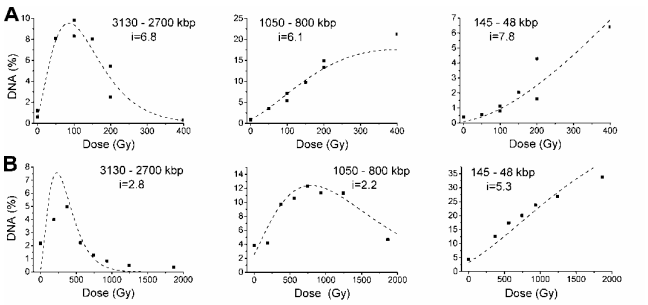

Fig. 1: Percentage of DNA mass as a function of radiation dose for X-ray (A) and Zn-ion (B) exposed exponential cell cultures inside several size zones.The dashed lines represent the simulated fragmentation pattern according to the RBM (i represents induction rate in DSBs per cell per Gbp).

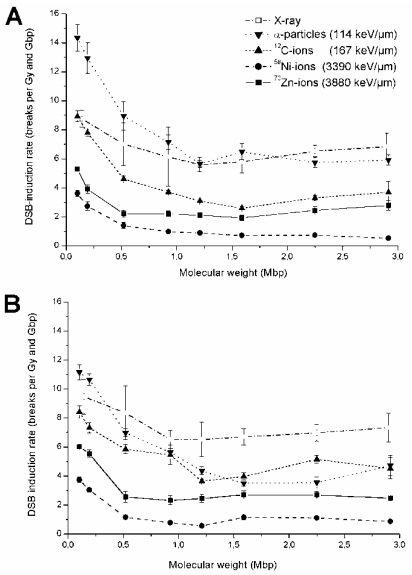

Fig. 2: DSB induction rates for different radiation qualities as a function of molecular weight in exponentially growing cells (A) and G2/M cell cultures (B). Error bars respresent uncertainties in fitting RBM in different size zones.

of the size zone used for analysis. However, figure 2 shows clearly a dependence of the induction rate on fragment size for all distributions generated by high-LET particles. A significant increase of the induction rate and thus a non-stochastical distribution of the ds DNA fragments is observed below 500 kbp. Because the deviation from non-randomness occurs at approximately the same size for all ions used, the physical properties of the radiation qualities appear to be less important for this effect than biological parameters e.g., the 3D organisation of the chromatin. This result is consistent with our qualitative analysis of DNA fragment distributions that suggested the generation of intra-track fragments with sizes of around 500 kbp independent of radiation quality [2]. Interestingly, even X-irradiated samples show some deviation from randomness below 500 kbp, possibly due to δ-electrons which have sufficient energy and LET to produce correlated breaks.

The variation of the induction rate with fragment size is nearly identical between cell cultures at the G2/M border (Fig. 2B) and exponentially growing cells (Fig. 2A). This indicates that the variation in higher-order chromatin structure, that is expected to occur through the cell cycle, is of minor importance for the DNA fragmentation in the size range of around 500 kbp.

References

[1] D. Blöcher, Int. J. Radiat. Biol. **57**, 7-12 (1990)

[2] A. Fricke and M. Löbrich, GSI sci. rep., 160 (2003)

Identification of TGF-b1-dependent signalling cascades mediating radiation-induced ATM activity

H. Peter Rodemann, Marcel Blaese
Division of Radiobiology and Molecular Environmental Research,
Dept. of Radiation Oncology, Univ. of Tuebingen

Over the recent years our laboratory could demonstrate that the radiation-induced terminal differentiation of the fibroblast cell system, i.e. the induced differentiation of progenitor fibroblasts to postmitotic highly collagen synthesizing fibrocytes, is the key event in the induction and manifestation of the fibrotic tissue remodelling mainly independent of the radiation quality used. Molecular biological studies into the basic mechanisms of radiation, i.e. photon and heavy ion radiation induced terminal fibroblast differentiation revealed that the cytokine TGF-β1 is a key mediator regulating radiation-induced differentiation [1-6].
As a consequence of both photon and heavy ion irradiation in the previous research period, it could be postulated that radiation (photon and heavy ion radiation) rather leads to the proteolytic activation of latent TGF-β1 (LTGF-β1) to the active form of this cytokine than to a stimulation of gene expression [7]. For practical reasons, this hypothesis was tested first in photon-irradiated cells by the use of a specific inhibitor of the protease furin, which is known to be a major component of the proteolytic activation process of LTGF-β1 to TGF-β1. Preincubation with the furin inhibitor CMK resulted in a significant decrease of the phosphorylation of Smad-2 and –3 proteins involved in the intracellular TGF-β1 receptor-dependent signal transduction. Although not yet analyzed, but based on the original data of significantly elevated and presumably TGF-β1-dependent terminal differentiation of fibroblasts exposed to heavy ion as compared to photons, it can be assumed that heavy ion irradiation will lead to a similar if not more pronounced activation of LTGF-β1 [7].

To enlight the underlying mechanisms in more detail, in the current project started in May 2004 different subclones of human fibroblasts and the p53 wild-type lung carcinoma cell line A549 genetically manipulated for the conditional expression (tet-on/tet-off) of various anti-sense constructs, i.e. α-TGF-β1, α-Smad2/3, α-Smad4 and α-Smad7 as well as α-furin, were established. Expression and functionality of the various antisense mRNAs was tested by conventional techniques and radiation response of stably transfected subclones was analyzed applying photon irradiation at different dose levels. So far, it could be demonstrated that clonogenic survival of stably transfected subclones of A549 cells presenting α-TGF-β1 as well as α-Smad2/3 is significantly altered as compared to the wild-type cells. Suppression of TGF-β1 by α-TGF-β1 as well as repression of Smad2/3 by α-Smad2/3 caused a significant increase in clonogenic survival at the different dose levels (2 and 4 Gy) analyzed. Currently, control experiments are performed to test the TGF-β1-dependent activation of ATM kinase in these A549 transfectants and the corresponding wild-type cells. At present the data indicate that blockage of the TGF-β1 signal transduction either at the level of the cytokine production or TGF-β1-dependent intracellular receptor signalling is able to downregulate radiation-induced ATM activity by nearly 50 %. These data indicate that ATM kinase is not only regulated in response to direct DNA damage (mainly DNA-DSB), but also through a TGF-β1-mediated process directly involved in regulating the cell cycle responses to radiation. These basic results obtained by conventional photon / x-ray irradiation prove the functionality of the cell systems created. Consequently, the direct comparison of radiation effects, i.e. heavy ions versus photons/x-rays, with respect to radiation-induced TGF-β1 activation and stimulation of the ATM-dependent cell cycle responses can now experimentally be approached. The results to be obtained will allow detailed insights into the principle mechanisms of cellular responses underlying radiation-induced normal tissue consequences.

REFERENCES

[1] Rodemann H.P., Binder A., Burger A., Güven N., Löffler H., Bamberg M.: The underlying cellular mechanism of fibrosis, 1996, Kidney Int., 49, 32-36 (1996).
[2] Burger A., Löffler H., Bamberg M., Rodemann HP.: Molecular and cellular basis of radiation fibrosis. Int. J. Radiat. Biol. 73:401-408 (1998).
[3] Hakenjos L, Bamberg M., Rodemann H.P.: TGFß1-mediated alterations of rat lung fibroblast differentiation resulting in the radiation-induced fibrotic phenotype. Int. J. Radiat. Biol. 76:503-509 (2000).
[4] Herskind C. and Rodemann H. P.: Spontaneous and radiation-induced differentiation of fibroblasts. Exp. Gerontol. 35:747-755 (2000).
[5] Fournier C., Scholz M., Kraft-Weyrather W., Rodemann H. P.,Kraft G.: Changes of fibrosis-related parameters after high and low LET irradiation of fibroblasts. Int. J. Radiat. Biol. 77(6):713-722 (2001).
[6] von Pfeil A., Hakenjos L., Herskind C., Dittmann K., Weller M., Rodemann H. P.: Irradiated homozygous TGF-β1 knockout fibroblasts show enhanced clonogenic survival as compared with TGF-β1 wild-type fibroblasts. Int: J. Radiat. Biol. 78(5):331-339 (2002).
[7] Haase O., Rodemann H. P.: Fibrosis and cytokine mechanisms: Relevant in hadron therapy? Radiother. Oncol. (2005) in press.

PCNA dependent accumulation of p21 at heavy ion induced DNA lesions

J. Rudolph, B. Jakob, Y. Schweinfurth, K. Kratz, C. Wiese*, G. Taucher-Scholz
Biophysik, GSI Darmstadt, Germany; *LBNL, Berkeley, CA, USA

The protein p21 is a well characterized cyclin dependent kinase inhibitor which is induced by TP53 after DNA damage and leads to cell cycle arrest in the G0/G1 phase [1]. We have shown previously that p21 accumulates at heavy ion induced DNA lesions, forming p21 foci [2]. This accumulation is shown to be independent of the TP53 pathway and of *de novo* protein synthesis and the p21 foci are most likely dynamic entities with p21 turnover [3]. Here, we try to elucidate the function of the accumulation of p21 at the heavy ion induced DNA lesions. We show that the accumulation of p21 at the DNA damaged sites is dependent on the interaction with the proliferating cell nuclear antigen, PCNA. PCNA is a protein which facilitates the loading of the DNA polymerases onto the DNA and increases their processivity; it is required for both replicating and repairing DNA.

As p21 has a PCNA binding site, we investigated whether the interaction of p21 with PCNA is essential for the foci formation at the DNA lesions. We transfected HeLa cells (cervical carcinoma cells) with a plasmid encoding either the p21 wild type protein or a mutated, phosphomimetic form of the p21 protein. The mutated form, referred to as T145D, mimics the phosphorylated form of p21 and is not able to bind to PCNA. Both plasmids were kindly provided by S. Dimmeler [4].

Remaining wild-type function of the ectopically expressed wtp21 and the mutated form of p21 was verified by coimmunoprecipitation. After transfection and cell lyses, p21 complexes were immunoprecipitated. This method allows the precipitation of a specific protein in complex with its interaction partners. The complex is separated by SDS-PAGE and the single compounds of the protein complex are identified by Western blot technique.

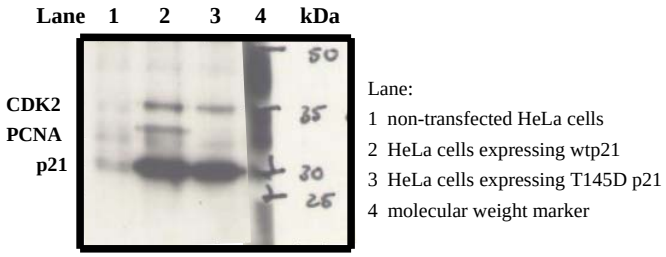

Fig.1 Western Blot analysis of the transfected HeLa cells. Immunoprecipitation from whole cell lysates was done with an anti-myc antibody targeting both against the myc-tagged ectopically expressed forms of p21.

Fig. 1 shows the Western blot analysis of the immunoprecipitated myc-tagged p21 form from whole HeLa cell lysates. The immunoprecipitate of the wtp21 expressing HeLa cells show a clear p21, PCNA and CDK2 band (Fig.1: lane 2). The T145D transfected cells however, only show the p21 and CDK2 bands and no PCNA band (Fig.1: lane 3). The non-transfected cells show very weak background signal (Fig.1: lane 1).

These results show that in HeLa cells the ectopically expressed wtp21 is able to interact with PCNA and CDK2 and that the phosphomimetic T145D p21 form does not interact with PCNA, although it interacts normally with CDK2 (Fig.1: lane 3).

To investigate whether the p21-PCNA interaction is needed for the accumulation of p21 at the damaged DNA sites, transfected HeLa cells were irradiated with Au ions at the UNILAC.

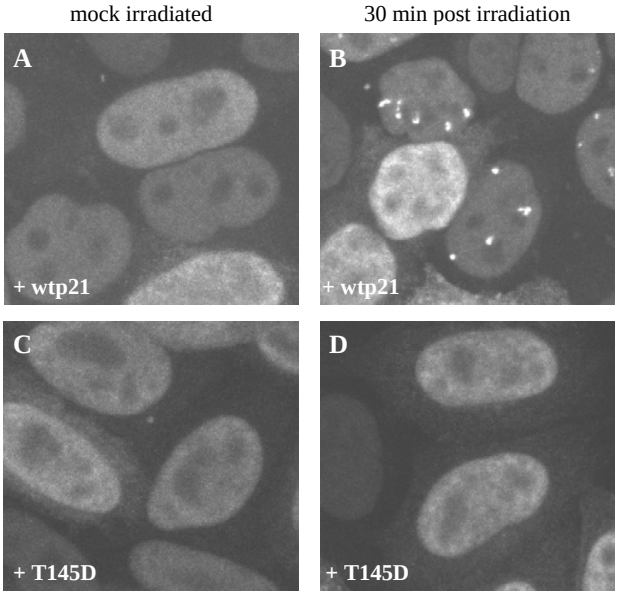

Fig.2: HeLa cells expressing either wtp21 (A, B) or T145D (C, D). A and C mock irradiated, B and D 30 min post irradiation with Au. Stained nucleus; clear focal accumulations of p21 in B (bright spots).

As seen in Fig.2, the ectopically expressed wtp21 accumulates at the heavy ion induced DNA lesions (Fig.2: B). However, the phosphomimetic form of p21, which is unable to interact with PCNA (Fig. 1: lane 3), does not form any p21 foci after irradiation with Au ions (Fig. 2: D). The same results were seen after irradiation with Ni, Zn and U ions.

Our results suggest that the accumulation of ectopically expressed p21 at heavy ion induced DNA lesions is dependent of the interaction with PCNA.

References

[1] El-Deiry et al., 1993; Cell
[2] Jakob et al., 2000; Radiat Res
[3] Rudolph, 2002; Diploma Thesis
[4] Rössig et al., 2001; Mol and Cell Biol

Cytogenetic studies for risk assessment of space radiation

R. Lee [1], P. Hessel [1], E. Nasonova [1,2], E. Gudowska-Nowak [1,3] and S. Ritter [1]

[1]GSI, Darmstadt, Germany; [2]JINR, Dubna, Russia; [3]Institute of Physics, UJ, Krakow, Poland

During space missions astronauts are exposed to doses of cosmic radiation that are higher than doses received on earth. Additionally, the radiation environment in space is different from that on earth. On earth, the natural and artificial radiation consists mainly of X-, γ-rays and α-emitters, while in space high energy particles from protons to iron ions predominate. Fe-ions are of major concern for radiation risk assessment, because they contribute significantly to the equivalent dose [1].

To examine the possible health hazards resulting from radiation exposure, chromosome aberrations in peripheral blood lymphocytes are measured [2]. According to the standard protocol, cells are fixed around 48 h and chromosome aberrations are scored [3]. However, heavy charged particles induce pronounced cell cycle delays that effect the time course of aberrations [4]. The purpose of the study was to assess the relationship between cell cycle delay and aberration yield in Fe-ion exposed lymphocytes.

Human blood lymphocytes were obtained from a healthy female donor. Cells were irradiated with 990 MeV/u Fe-ions at SIS (GSI) or 200 MeV/u Fe-ions at HIMAC (NIRS). Directly after exposure PHA and BrdU were added to the cultures to stimulate cell proliferation and to allow cell cycle discrimination, respectively. Cells were collected between 48 and 84 h after exposure. To accumulate mitotic cells colcemid was added to the samples 3 h before harvest. The yield of all types of chromosome aberrations which are detectable by fluorescence-plus-Giemsa staining was measured in first post-irradiation mitoses. For comparison, cells were exposed to X-rays. For further details see [4] and [5].

Analysis of the time-course of X-ray induced chromosomal damage (Fig.1, upper panel) revealed that the aberration yield was similar for lymphocytes collected at 48, 60 and 72 h. On the other hand, cytogenetic analysis revealed a different response for cells exposed to Fe-ions. Cells reaching the first mitosis 48 h after exposure to 990 MeV/u Fe-ions (Fig.1, middle panel) carried already more aberrations than those exposed to similar doses of X-rays. The yield increased with time and was at 72 h two times higher than at 48 h. Thereafter, the yields levelled off. In lymphocytes exposed to 200 MeV/u Fe-ions (Fig. 1, lower panel) few aberrations were detected at 48 h. However, cells that were delayed and entered the first mitosis at 72 h carried about seven times more aberrations than those collected at 48 h.

The difference in the time-course of X-ray and Fe-ion induced damage can be related to differences in the spatial energy deposition of both radiation qualities. The energy depositions of X-rays (low LET) are fairly uniformly distributed among cells leading to homogenous distributions of aberrations and cell-cycle delay times within the exposed cell population. In contrast, the exposure of cells to Fe-ions results in an inhomogenous energy deposition, which is determined by the stochastic distribution of particle hits per cell nucleus. As a consequence a broad range of chromosomal damage and delay times are produced.

In summary, our data show a pronounced delay of heavily damaged cells to enter mitosis. This observation argues against the use of the conventional metaphase assay to estimate the health risk of high LET radiation.

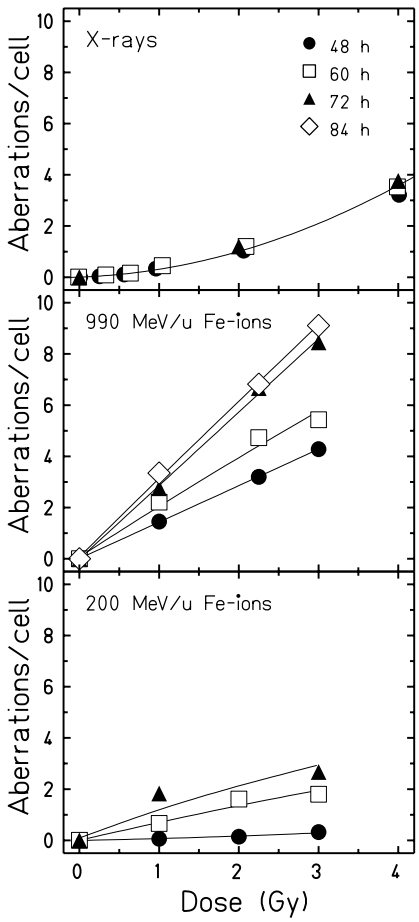

Fig.1. Time-course of chromosome aberrations in human lymphocytes at the first post-irradiation mitosis. Cells obtained from the same donor were irradiated with X-rays (upper panel), 990 MeV/u Fe-ions (LET = 155 keV/μm, middle panel) or 200 MeV/u Fe-ions (LET = 440 keV/μm, lower panel). Data were taken from [4] and [5].

This study was supported by BMBF (Bonn, grant 02S8203).

References

[1] Schimmerling et al., Adv. Space Res. **31**, 27-34 (2003)

[2] Bonassi and Au, Mutat. Res. **511**, 73-86 (2002)

[3] IAEA., Technical Reports Series No. 405. Vienna (2001)

[4] Ritter et al., J. Radiat. Res. **43 (Suppl.)**, S175-179 (2002)

[5] Lee et al., Adv. Space Res. (in press)

Chromosome aberrations in peripheral blood lymphocytes from patients with primary prostate cancer before radiotherapy

Hana Hofman-Hüther [1], Oliver Balzer [2] and Patricia Virsik-Köpp [2]

[1]Dept. Radiotherapy and Radiooncology; [2] Dept. Hygiene and Environmental Medicine
Medical Faculty, University of Goettingen, Germany

Spontaneous level of chromosome aberrations is considered to be indicative of inherent cancer predisposition, which plays an important role in cancer incidence. We have studied spontaneous chromosome aberrations in peripheral blood lymphocytes of patients with prostate cancer before their treatment with conventional therapy.

Twelve patients with Stage T1-T2 primary prostate cancer were included in this study. Four healthy male donors served as controls for comparison, and the yields of chromosome aberrations were compared between patients with prostate carcinoma and healthy donors.

Heparinized peripheral blood was obtained from healthy donors and patients before therapy. The whole blood samples were cultured in RPMI with 10% fetal calf serum, PHA and antibiotics in 5% CO_2 atmosphere at 37°C for 46, 48 and 50 hours. Colcemide was added for the last two hours. Metaphase cells were prepared according to the standard method and stored at 4°C.

Chromosome aberrations was analysed in their first mitosis by FISH technique involving whole chromosome hybridisation and DAPI staining.. The best culture time for hybridisation was chosen after FPG-staining (Giemsa-/Hoechst 33258-staining method). Whole chromosome probes for chromosomes no.2 and no.4 have been used simultaneously (dual paint FISH). Apparently simple exchanges and complex exchanges were scored.

Table 1: The yields of simple exchanges for healthy donors. Simple exchanges ($y_{s.e.}$) represent the sum of reciprocal translocation and dicentric chromosomes. The mean and the standard deviation are given for ($y_{s.e.}$) and the percentage of aberrant cells.

Donor	Age	Nikotin	N	N_0	$y_{s.e.}$	% aberant cell
P-K1	65	–	750	743	**0.004**	**0.6**
P-K2	69	–	966	942	**0.011**	**2.5**
P-K3	65	–	977	956	**0.008**	**1.6**
P-K4	64	+	972	959	**0.005**	**0.2**
mean ± s.d.					**0.007 ± 0.003**	**1.2 ± 0.9**

Complete and incomplete reciprocal translocations and dicentric chromosomes involving the "painted" chromosomes were scored under a fluorescent microscope in the first post-irradiation mitosis. The yields of both aberration types were added up and classified as simple exchanges. The yields of simple exchanges for healthy donors are given in table 1 and for patients in table 2. The percentage of aberrant metaphases are given in table 1 for the healthy donors and in table 2 for the patients, as well. For both we calculated the mean average and standard deviation.

All patients with prostate cancer displayed significantly increased spontaneous yields of simple exchanges and also increased percentage of aberrant metaphases in comparison with healthy donors. This observation has been reported already for the seminoma [1] or for breast cancer [2]. The old age of our patients should not play a decisive role. Bakshi et al. [3] observed higher spontaneous level of chromosome aberrations in young cancer patients, too.

Table 2: The yields of simple exchanges for patients with prostate cancer. Simple exchanges ($y_{s.e.}$) are the sum of reciprocal translocation and dicentric chromosomes. The mean average and the standard deviation are also calculated.

Patient	Age	Nikotin	N	N_0	$y_{s.e.}$	% aberant cell
P-16/0	71	–	744	706	**0.034**	**5.1**
P-15/0	64	–	838	783	**0.020**	**6.6**
P-14/0	79	–	510	490	**0.024**	**3.9**
P-13/0	62	–	324	308	**0.034**	**4.9**
P-12/0	66	–	879	845	**0.019**	**3.9**
P-11/0	77	–	797	757	**0.016**	**6.7**
P-10/0	71	+	534	515	**0.022**	**3.6**
P-8/0	72	–	716	687	**0.021**	**4.1**
P-7/0	76	–	529	496	**0.026**	**6.2**
P-5/0	69	–	272	257	**0.026**	**5.5**
P-4/0	79	–	626	593	**0.026**	**5.3**
P-1/0	75	–	506	480	**0.026**	**6.3**
mean ± s.d.					**0.025 ± 0.005**	**5.2 ± 1.1**

These results suggest that prostate carcinoma might involve genomic instability present already in lymphocytes of the patients and this must be investigated in a larger patient collective.

Acknowledgement: The authors thank BMBF for financial support of this study by a grant No.: 02S8203.

References:

[1] Schmidberger H. et al., Int.J. Radiation Oncology Biol. Phys., 2001

[2] Barrios L.. et al., Int.J. Radiation Oncology Biol. Phys., 1990

[3] Bakshi S.R. et al., Cancer Genet. Cytogenetic, 1999

Correlation between mitotic delay and aberration burden and their impact on the interpretation of chromosome data

E. Gudowska-Nowak [1,2], E. Nasonova [1,3], M. Scholz [1] and S. Ritter [1]

[1] GSI, Darmstadt, Germany, [2] Institute of Physics, Jagellonian University, Krakow, Poland, [3] JINR, Dubna, Russia,

Conventional cytogenetic studies rely on the scoring of chromosome aberrations in first cycle metaphases collected at a single sampling time after exposure. Yet, evidence is accumulating that cells arriving late at the first mitosis carry more aberrations than those arriving at earlier times. To examine in more detail the relationship between mitotic delay and the number of aberrations harboured by a cell previously published data on the time-course of chromosomal damage induced in G1 V79 cells by X-rays and 10.4 MeV/u Ar ions with LET=1226 keV/μm [1, 2] were supplemented and analysed. At each sampling time 100-400 first cycle metaphases were scored following Fluorescence-plus-Giemsa staining. Cells were grouped into subpopulations carrying 0, 1-2, 3-4, 5-6 or more aberrations. Then, based on the mitotic index the flux of each subgroup through mitosis was reconstructed [3,4] and the average entrance time to mitosis was estimated [4].

As clearly seen in fig. 1, the flux of V79 cells through the first mitosis is strongly affected by their aberration burden. For example, 12h after irradiation with 7.84 Gy Ar ions (fig. 1, lower panel) the highest proportion of cells entering the first mitosis consist of cells carrying 0 or 1-2 aberrations. However, at 18h the highest fractions of cells carry 3-4 or more aberrations, whereas undamaged cells or cells carrying 1-2 aberrations have almost completed the first mitosis. In contrast to populations exposed to particles, in X-irradiated cultures a higher synchrony in the first post-irradiation cycle is registered (fig. 1, upper panel). However, analogously to Ar ion exposure, the higher dose of X-rays shifts the peak of the flux of aberrant cells to later sampling times and the apparent delay in entrance time to mitosis becomes clearly visible for cells carrying more than 5 aberrations.

To quantify the relationship between the mitotic delay and the aberration burden of a cell, iterated fluxes for aberrant cells were used as probability densities for the entrance time to mitosis. For each subgroup of aberrant cells (fig. 1), the mean entrance time to mitosis was evaluated and plotted in figure 2 as a function of the average number of aberrations carried by cells. This plot clearly demonstrates a positive correlation between the aberration burden and the mitotic delay. Furthermore, when the X-ray and Ar ion data are fitted with a first-order polynomial, the same slope is obtained for all data sets suggesting that the increase in the delay time is independent of the LET. Finally, the data plotted in fig. 2 indicate that special attention has to be paid to the delay observed for subpopulations carrying no visible aberrations. In principle, for this group the delay should be 0h, but actually an average value of 1.15h is observed. This might elude to possible hidden aberrations, which are not detectable because they are too small or because they require refined staining techniques for visualization.

In summary, or data clearly demonstrate that the analysis of aberrations in metaphase cells at a single sampling time after exposure will result in over- or underestimation of the of the damage depending on the subpopulations of cells that reach mitosis at that time. Consequently, for reliable estimates improved protocols have to be developed to account for this effect.

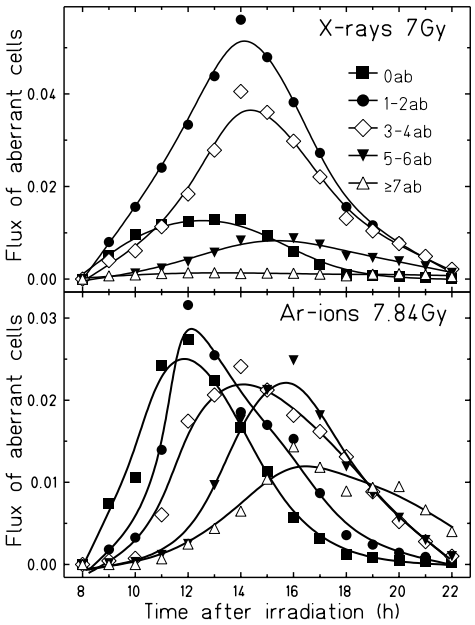

Fig. 1: Passage of undamaged and aberrant V79 cells through the first mitosis after exposure to 10.4 MeV/u Ar ions or X-rays. Note different amplitude of fluxes for both radiation types. For further details see Gudowska-Nowak et al. [4].

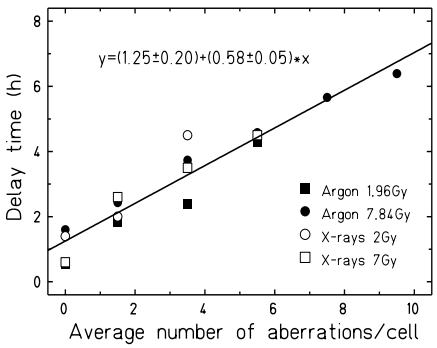

Fig. 2: Correlation between the average delay time in entering the first mitosis and the average number of aberrations carried by a cell after exposure of V79 cells to X-rays and 10.4 MeV/u Ar ions. The data are fitted by the least- squares procedure.

References:

[1] Ritter S. et al., Int. J. Radiat. Biol. 69, 155-166 (1996)
[2] Ritter S. et al., Int. J. Radiat. Biol. 76, 149-161 (2000)
[3] Scholz et al, Int. J. Radiat. Biol. 74, 325-331 (2000)
[4] Gudowska-Nowak et al., Int. J. Radiat. Biol. (in press)

This study was partly supported by BMBF (Bonn) under contract number 02S8203.

Telomerase activity of peripheral blood lymphocytes from radiotherapy patients

C. Herskind, A. Schwegler, D. Milanovic and F. Wenz

Dept. of Radiotherapy, Inst. of Clinical Radiology Mannheim, University of Heidelberg, Germany

Telomerase is a specialized enzyme capable of extending the long terminal hexanucleotide repeats $(5'\text{-TTAGGG-}3')_n$ forming the telomeric caps of chromosomes. Telomerase activity is present in stem cells and cancer cells but is absent from most somatic cells and, accordingly, a shortening of telomeres with increasing number of cell divisions has been found in most somatic cell types. In lymphocytes, however, a low level of telomerase activity has been found though this appears insufficient for maintaining telomere length. Furthermore, the telomerase activity of some hematopoietic cell lines has been shown to increase after low doses of radiation [1,2]. There is evidence that telomerase may play a role in the repair of DNA double strand breaks and in the formation of radiation-induced chromosome aberrations [3]. Therefore, it was hypothesized that telomerase activity may be increased in radiotherapy patients receiving large field irradiation involving a substantial fraction of circulating blood lymphocytes.

In a pilot study, we evaluated a quantitative PCR-ELISA assay (Roche) based on the Telomere Repeat Amplification Protocol (TRAP) for measuring telomerase activity in peripheral blood lymphocytes. The measured telomerase activity was corrected for background and assay variation by incorporating an inactivated sample and an internal oligonucleotide standard for each probe. Telomerase activity was measured in blood lymphocytes from six radiotherapy patients undergoing fractionated treatment with x-rays for prostate cancer (n=3; D=46-60 Gy), breast cancer (n=2; D=30-48 Gy), and cerebral metastases (n=1; D=15 Gy) as well as from three unirradiated healthy donors.

Preliminary results presented in fig. 1 showed that the telomerase activity of lymphocytes was at least three orders of magnitude lower than that of the TK6 lymphoblastoid cell line. No indication of an increased telomerase activity in radiotherapy patients and the normal donors was observed although the power was low owing to the small sample size. The mean value of the telomerase activity for the whole sample was not significantly different from zero owing to the fact that the activity in most samples was below the detection level. However, when the amount of lysate was increased far beyond the recommended quantitative range (10-3000 cell equivalents) as shown in fig. 2, the telomerase signal of the probe increased above that of the internal standard which was decreased owing to inhibitory factors in the lysate. This evidence strongly suggests that the telomerase activity may indeed be greater than zero. We are presently working to establish an assay with enhanced sensitivity in order to enable a more definitive test of our hypothesis.

Acknowledgement: This study was supported by the BMBF, Bonn (contract no. 02S8203).

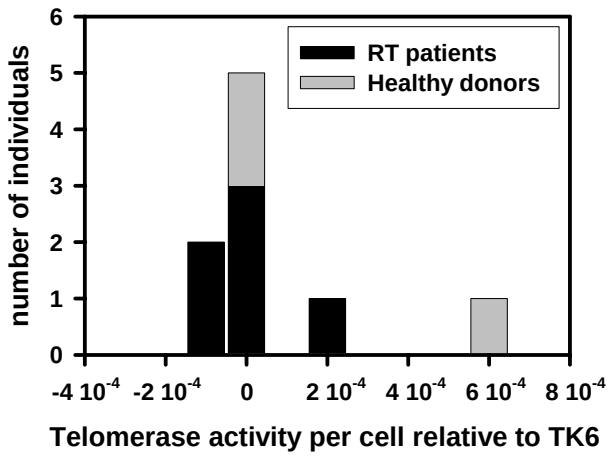

Figure 1. Distribution of telomerase activity in lymphocytes of six radiotherapy patients and three healthy donors relative to the activity of TK6 lymphoblastoid cells.

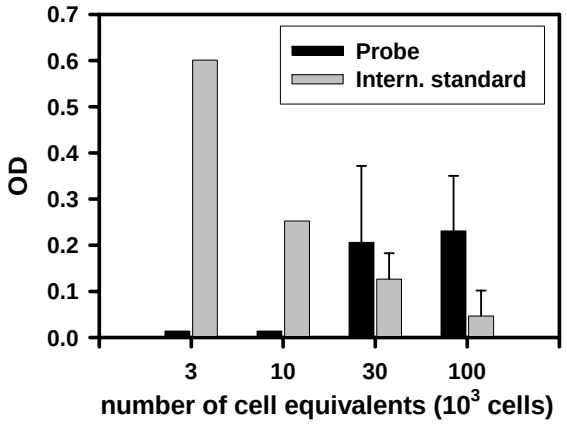

Figure 2. Telomerase signal (optical density, OD) obtained with the PRC-ELISA using different amounts of cell lysate from a single healthy donor compared with the internal standard of the assay.

References:

[1] Neuhof D, Ruess A, Wenz F, Weber K-J, Radiation Res. **155** (2001) 693-7

[2] Neuhof D, Auberger F, Ruess A, Wenz F, Weber K-J, Strahlenther. Onkol. **180** (2004) 52-6

[3] Sharma GS, Gupta A, Wang H, et al., Oncogene **22** (2003) 131-46

Live Cell Imaging of Heavy Ion Induced Radiation Responses - A Novel Microscope Setup at the UNILAC

B. Jakob [1], J. H. Rudolph [1], N. Gueven [2], M.F. Lavin [2] and G. Taucher-Scholz [1]

[1] GSI Biophysik, Germany ; [2] The Queensland Institute of Medical Research, Australia

Low energy ions generate extremely localized DNA damage within restricted regions of a cell nucleus. These local effects facilitate the study of dynamics of protein recruitment to DNA lesions. The spatial distribution of induced lesions can be indirectly visualized by immunocytochemical detection [1]. As this staining method can only be applied after fixation of the cells, it is only possible to obtain static images of single samples, making it difficult to address kinetic related questions.

To analyze fast protein translocations, we developed a remote controlled microscope system to obtain high-resolution fluorescence images of living cells during ion irradiation by utilizing GFP-tagged DNA repair proteins [2].

Time-lapse images of the GFP-coupled DNA repair protein aprataxin revealed accumulations within seconds at sites of ion hits indicating a very fast recruitment (Fig. 1).

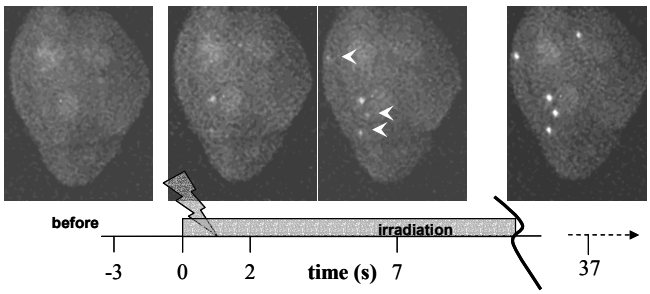

Fig.1: Selected images of EGFP-aprataxin expressing HeLa cells during irradiation with nickel ions (4.2 MeV/u). Appearance of radiation induced foci is marked by arrow heads [2].

Repositioning of the irradiated cells after fixation allowed a comparison of live cell observations with retrospective etching of ion tracks (Fig.2). This method served as tools for the identification of the spatial position of ion traversals.

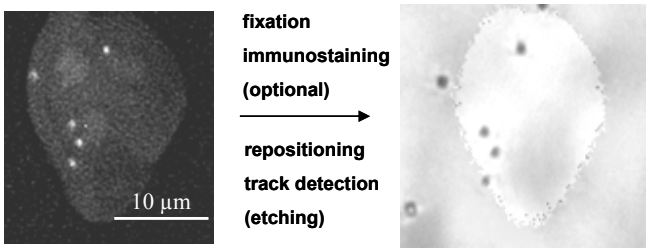

Fig.2: Comparison of traversal induced foci left and etched pits on CR39 serving as cell substrate and nuclear track detector (right) [2].

Using scratch replication labeling, we addressed a possible contribution of radiation-induced chromatin movements in the process of DNA damage recognition (Fig. 3 and 4). Following the position of chromatin speckles over time, only minor chromatin movement at sites of ion traversal was observed within the first few minutes of impact, not exceeding the motion observed in non hit regions.

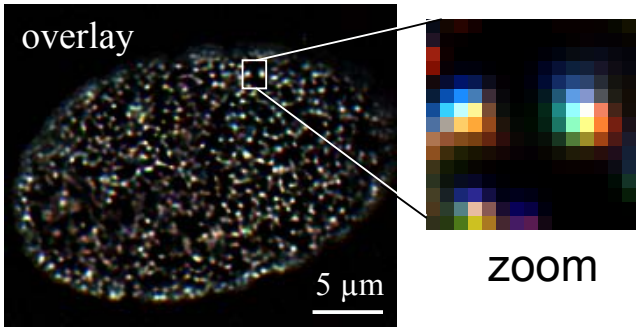

Fig.3: Image of a Cy3-dUTP replication labeled NHDF nucleus acquired during irradiation with carbon ions (9.6 MeV/u). Color-coded overlay of three images obtained during the irradiation experiment. White color indicates no migration. Color transition from red (before) to blue (3 min after) is a sign of movement. A typical displacement (~ 0.3 µm) of a subchromosomal focus can be seen in the magnification [2].

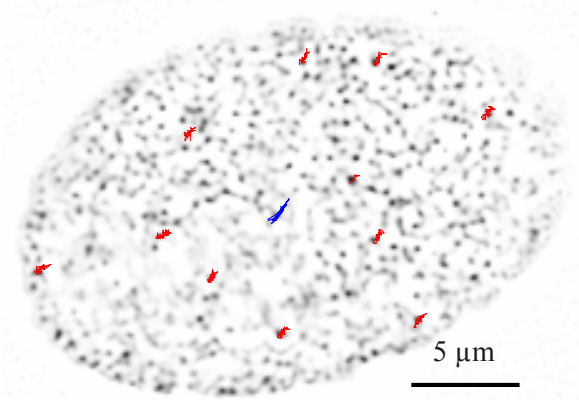

Fig. 4 Trajectories of the motion of selected, representative foci (red) taken from the experiment of Fig. 2 during the 5 min observation period. The trajectories are projected on the color inverted Cy3 pattern of the nucleus showing the small-scale, billowing movement [2].

Our results demonstrate that heavy ion radiation-induced changes in subnuclear structures can be used to determine the kinetics of early protein recruitment in living cells. Furthermore using the new device, we could show the early steps in DNA repair are not dependent on large scale chromatin movement exceeding 1 µm. As the complexity and density of DNA lesions is a function of the LET, we have here the possibility to adjust these parameters by the selection of the ion species and the energy used. We have now started studies comparing the influence of LET on the recruitment kinetics and, using different fluorescence tagged proteins, to investigate the spatiotemporal hierarchy of the damage sensing and signaling processes.

[1] Jakob et al. (2000) Rad. Res. **154**, 398-405

[2] Figures modified from: Jakob et al. Rad. Res. In press

Radiation Myelitis of the Rat Spinal Cord after Single and Fractionated Doses of Photons and Carbon Ions

Peter Peschke[1], Christian P. Karger[1], Michael Scholz[2], Jürgen Debus[1,3]
[1]DKFZ Heidelberg, Germany; [2]GSI Darmstadt, Germany,
[3]Dept. of Clinical Radiology, University of Heidelberg, Germany

Particle beams have achieved growing interest for tumor therapy. The beneficial beam dose profile characteristics, in combination with active beam-shaping (raster-scan system) and biologically based treatment planning, allow for highly effective conformal target irradiations. For long-term local tumor control of extraneural neoplasms and tumors of the central nervous system (CNS) high radiation doses are required. Contradictive to a successful treatment is often the risk of late complications due to the limited radiation tolerance of the CNS. Clinical studies at the GSI, in Darmstadt, are accompanied by a biological program to assess the relative biological effectiveness (RBE) of carbon ion irradiations relative to photons with special emphasis on late complications of the central nervous system (CNS).

Cellular mechanisms underlying radiation myelitis of the spinal cord are multifactorial and include vascular damage leading to hemorrhagic necrosis, demyelation progressing to white-matter necrosis as well as modifications of glial cells. Radiation-induced mitotic cell death is believed to be the cause for the reduction of surviving clonogens of either parenchymal or vascular cell populations. Both factors separately contribute to the development of radiation myelopathy and are dependent on the radiation dose applied and the age at irradiation. In humans, radiation myelopathy, with a risk of ~ 5% occurrence, is estimated to require a dose of 60 Gy of low LET-radiation delivered in conventional fractionation schemes with daily fractions of 1.8 to 2 Gy. At higher doses the risk of spinal cord damage increases steeply.

For heavy ions, which are known to possess an increased linear energy transfer (LET) only few experimental data are available. In the first studies at the GSI we have evaluated dose-response relationships for female Sprague Dawley rat spinal cord after 1, and 2 fractions of $^{12}C^{+6}$-ions in the plateau region and in the Bragg-peak. Carbon ion irradiation was performed at the heavy ion accelerator (SIS) of the Gesellschaft für Schwerionenforschung (GSI) in Darmstadt at an energy of 270 MeV/u. An intensity-controlled magnetic raster scanner, with active energy variation by the synchrotron, was used to generate the irradiation fields. For irradiation of the rat spinal cords, the Bragg-peak was spread out to 10 mm in the target volume by energy variation of the synchroton. Due to the horizontal direction of the ion beam the anesthesized animals had to be immobilized in a vertical (”hanging”) position, using a specially designed holding device with a capacity for 12 rats. Irradiation was performed subsequently for each animal by moving the immobilization device remotely to the respective position.

Photon irradiation was delivered by a linear accelerator (Siemens MPX, 15 MeV) with gantry angel at +90° for a horizontal beam. Positioning of the animals was identical to the carbon ion irradiation. Treatment fields were defined by a multileaf collimator with an aperture of 10 x 15 mm. Dose-rate was 500 cGy/min, under reference conditions. In all the experiments, the dose–response relationship for paralysis of fore or hind limbs up to 300 days after irradiation was used as biological endpoint.

Taken in consideration the results from the first part of the study, we can conclude that the latency period of myelopathy after Bragg-peak carbon ion irradiation is shorter than after plateau and photon irradiation. From the split dose experiments a clear fractionation effect was observed in the plateau phase, which allows more sparing of normal tissues. In contrast, no clinically relevant effect of fractionation was obtained when carbon ion irradiation was performed in the Bragg maximum.

After having established the technical set-up, the above described experiments were extended in the years 2001 and 2002 to 6 daily fractions of high energy carbon ions and photons, given to the upper cervical spinal cord of female Sprague Dawley rats.

To simulate the clinical situation, we initiated a three arm study applying 18 daily fractions of high energy carbon ions in the Bragg peak and the plateau phase, in comparison to photon irradiation in the years 2003 and 2004. For the 12-C plateau experiments, 10 groups of six animals each were treated with total doses ranging from 42 to 66 Gy with corresponding doses per fraction in the range of 2.33 to 3.67 Gy. The study arm with 12-C irradiations in the Bragg peak included 10 groups of six animals with total doses ranging from 16.5 to 26.5 Gy.

A critical issue in these extended fractionation studies was the development of a technique for safely anasthesizing the rats on multiple consecutive days. We achieved this by inhalation anesthesia using Ethrane®. This procedure was well tolerated. These experiments are ongoing. Animals without incidence of radiation-induced symptomatic myelopathy will be kept under observation through April 2005. Control experiments with photons have been finished and yielded an ED_{50} (effective dose where 50% of the animals exhibited damage probability) of 88.2 Gy.

These data will be used to derive radiobiological parameters such as RBE and alpha/beta ratios. In addition, these data will be used to explore the precision of the local effect model (LEM) for estimation of RBE values for late effects after carbon irradiation of neurological tissues such as the spinal cord.

Radiation Biology with ^{3}He

M.Müller, M.Krämer, W.K.Weyrather
GSI, Biophysik

In preparation for the therapy unit in Heidelberg radiation biological experiments with ^{3}He have been performed at the Unilac and the SIS. Clonogenic survival after irradiation with monoenergetic beams has been measured for CHO-K1 and V79 cells.The used energies were 167MeV/u and 64 MeV/u at the SIS, corresponding to a range of 15 cm and 8 cm respectively, and 5 energies between 0.87 MeV/u and 10.7 MeV/u on target at the Unilac representing the last mm and the Bragg peak region. CHO-K1 survival curves as a function of dose and compared to 250 kV x-rays are shown in figure 1. Figur 2 shows the RBE$_\alpha$ values calculated from these curves and compared to low energy proton measurements for the same cell line done at the MPIK tandem at Heidelberg [1]. In both cases the dose is calculated from the LET on target. A more exact consideration of the LET gradient over the cell nucleus for the lowest energies will lead to higher doses inside the cell and thus reduced values for the RBE maxima.

For a more realistic simulation of therapy conditions a stack with CHO cells in a medium filled container has been irradiated with a dose profile for a simulated tumor in 6cm to 10 cm depth.In figure 3 the physical (absorbed) dose, the measured and calculated survival and the measured RBE are shown. The physical dose is calculated from primary particles only. Nuclear fragmentation is neglected, thus the dose in the tumor volume is overestimated. Replacing high LET primary helium ions with lighter fragments with lower LET will lower the dose. This might explain the discrepancy between the calculation according to LEM and the measured survival in the tumor volume. The high survival in the entrance region with RBE values partly below one may also be influenced by repair processes due to the long time between iradiation and trypsination (up to two hours). This time was caused by the activation of the irradiated volume.

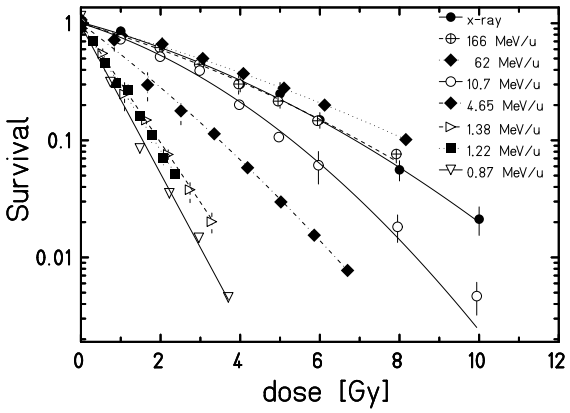

Figure 1: Survival as function of ^{3}He dose

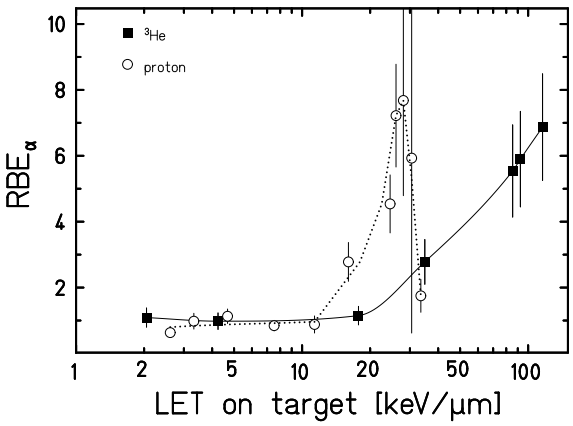

Figure 2: RBE$_\alpha$ values for ^{3}He compared to proton values from [1]

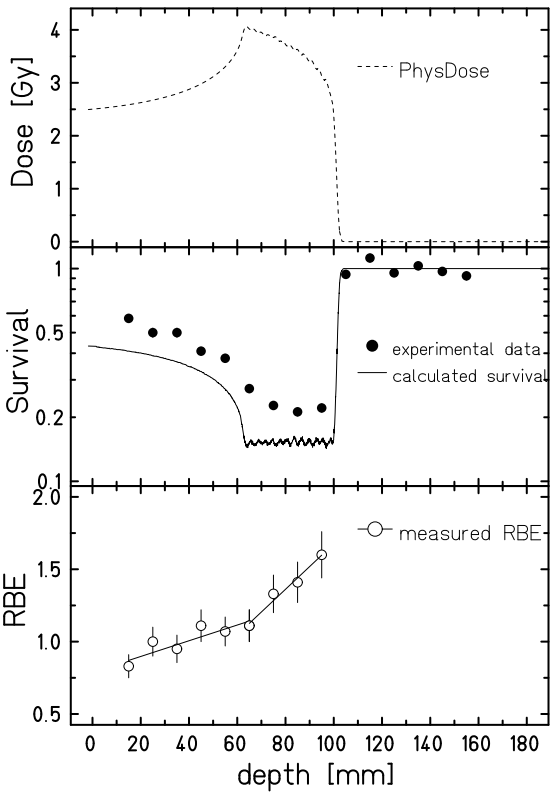

Figure 3: Dose, Survival and RBE. for the irradiation of an extended volume

References

[1] Progress Report 2003/2004 MPIK Heidelberg, in press

Mouse Gut Crypt Survivals after Single Irradiation with Carbon ions.

K. Ando[1], N. Takai[1], Y. Furusawa[1], Y. Matsumoto[1], A. Uzawa[1] and M. Scholz[2]
[1]NIRS, Heavy-ion Radiobiol. Res. Gr, Japan; [2]GSI, Biophysik, Germany

Purpose: To compare biological effectiveness of carbon ions between GSI and NIRS.

Materials and Methods: C3H/He female mice aged 10-14 week old were transported from NIRS to GSI. They were fed with pellets and drinking water. Shortly before irradiation, mice received an IP injection of 0.2 ml anesthesia (ketamine 13.79 mg/ml and xylazine 0.69 mg/ml in NaCl solution). Two (2) mice were placed in a jig specially designed for the gut irradiation experiment, and received carbon-ion radiation. Carbon ions with various mono-energies scanned mouse whole body so that mouse gut was irradiated by desired positions within a 6-CM width Spread-Out-Bragg peak. We selected 3 positions within the Spread-Out-Bragg peak; proximal, middle and distal positions were respectively at -20 mm of center, center and + 20 mm of center. Three and a half days after irradiation, mouse jejunum were removed and fixed in formalin. Cross section of jejunum were prepared as histology, and used to count crypts under light microscopy.

For NIRS experiments, materials and methods identical to GSI experiments were used except that a fixed energy of 290 MeV/u carbon ions were spread by a ridge filter to make a 6-CM width Spread-Out-Bragg peak.

Results: Three irradiation positions within the 6-CM width Spread-Out-Bragg peak are shown in Figure 1. Crypt survivals obtained by GSI carbon ions (Figure 2) shows 3 curves separated each other, meaning biological effectiveness of the 3 positions depends on position, which fits to what we expect in advance. Figure 3 shows comparison between GSI and NIRS. Survival curves well matched between GSI and NIRS, indicating biological effectiveness of therapeutic carbon ions is almost identical between GSI and NIRS.

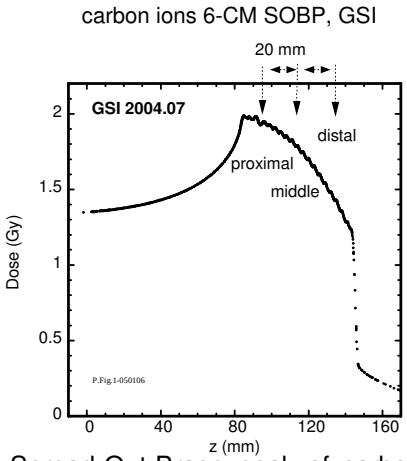

Fig.1 Spread-Out-Bragg peak of carbon ions and irradiation positions

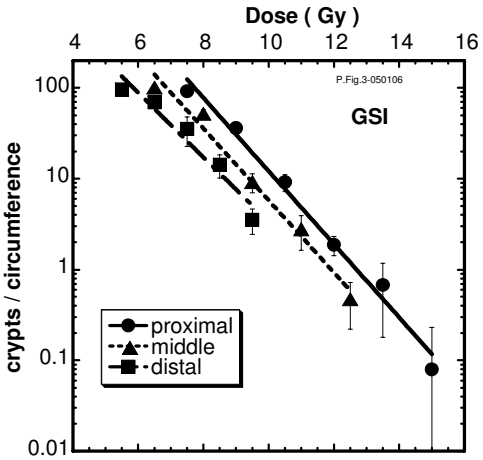

Fig.2 Gut crypt survivals irradiated by 3 positions within the SOBP

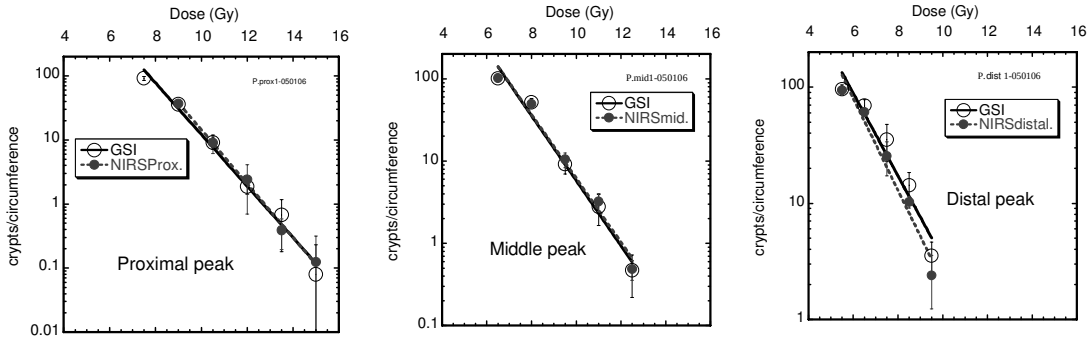

Fig.3 Comparison of crypt survivals between GSI and NIR. Left: proximal peak, Middle: middle peak, Right: distal peak

Neoplastic Transfomation Induced by Carbon Ions

Daniela Bettega[1], Francesca Botta[1], Paola Calzolari[1], Petra Hessel[2], and Wilma K. Weyrather[2]
[1]Dept.Physics, Univ. of Milan, Italy; [2]GSI, Biophysik

Induction of secondary tumors after radiation therapy cannot be neglected in case of the treatment of younger patients. Neoplastic transformation in vitro can be used as one indicator for risk assessment comparing different radiation types.

The human hybrid (Hela X skin fibroblast) cell line, developed by Stanbridge et al [1] and Redpath et al [2] and designated CGL1 has been used to compare carbon ion irradiation to conventional radiation [3]. Low LET experiments have been performed with 250 kV x-rays, which normally are used as reference radiation at GSI, and 15 MeV photons which are used in photon therapy.The photon experiments were performed at Milano. Figure 1 shows the comparison in survival and transformation induction. The 250 kV x-rays were more effective for both endpoints.The RBE at 10 % survival is 1.21, the effect on transformation induction is more expressed. Both experiments have been performed only once and will be repeated for better statistics. As further reference for the carbon experiments the 15 MV photons have been used.

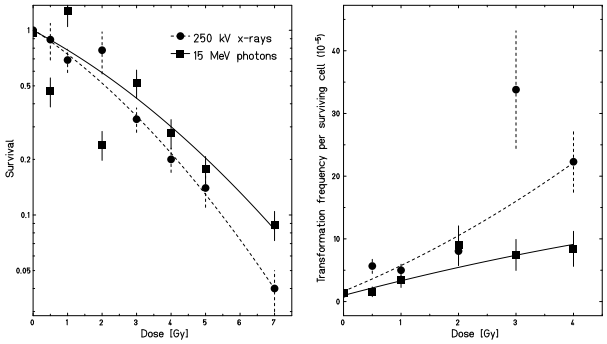

Figure 1: Survival (left) and transformation frequency (right) for 250 kV xrays and 15 MV photons

Experiments with carbon ions have been performed at 270 MeV/u (266.4 MeV/u on target, LET = 13.7 $keV/\mu m$) and 100 MeV/u (86.53 MeV/u on target, LET = 29.5 $keV/\mu m$). The results of two experiments for each energy are shown in figure 2.

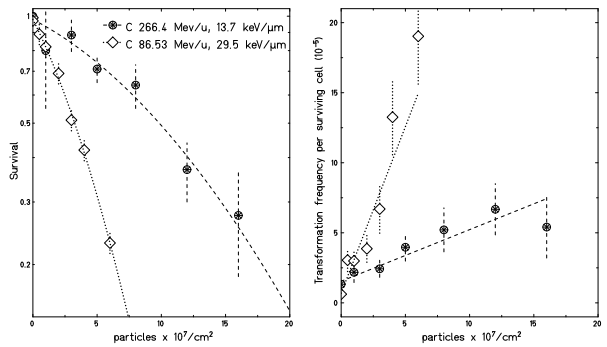

Figure 2: Survival and transformation frequency for 270 MeV/u and 100 MeV/u carbon ions

Figure 3 shows the results transferred to dose and compared to 15 MeV photons. The RBE for cell inactivation at 20% survival is 1.27 for 270 MeV/u and 1.65 for 100 MeV/u carbon ions. The rate of transformation frequency for 270 MeV/u carbon ions seems to be lower than for photons. For 100 MeV/u carbon ions it is higher for high doses. In all three cases the transformation induction is dose dependent.

For the risk assessment the transformation frequency per cell at risk (the number of irradiated cells) is more relevant than the frequency per surviving cell. Figure 4 shows that in this case the frequency is only slightly dose dependent and not very different for photons and 270 MeV/u carbon ions. As transformation induction and reproductive cell death are two competing processes, the transformation frequency per cell at risk decreases after a maximum. For higher doses the cell killing seems to be the more important part. At our measurements the maximum is at around 2 Gy. For the 100 MeV/u carbon ions the maximum value is approx. 1.6 times higher than for photons and 270 MeV/u carbon ions.

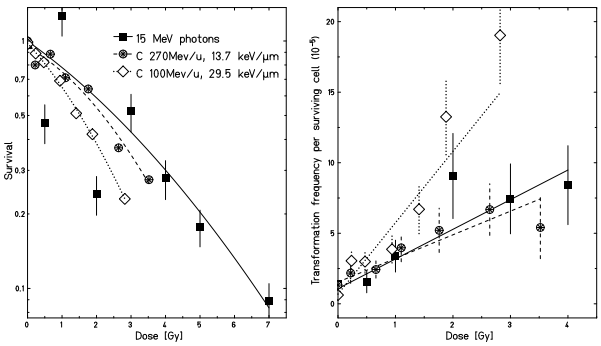

Figure 3: Survival and transformation as a function of dose. The same data as in fig.2 are used.

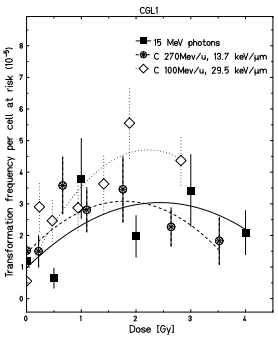

Figure 4: Transformation frequency for photons and carbon ions calculated for cell at risk

References

[1] Stanbridge et al , Science, 215, 252 (1982)
[2] Redpath et al, Radiat. Res. 110, 468 (1987)
[3] GSI Scientific Report 2003, 169 (2004)

Radiosensitivity of RAW 264.7 cells and primary human monocytes

S. Conrad[1], C. Fournier[2],S.Ritter[2] , K. Nixdorff[1]

[1]Institut für Mikrobiologie und Gentik, Darmstadt, Germany ; [2]GSI, Darmstadt, Germany

Monocytes and macrophages are essential components of the innate immune system because of their phagocytic activity and their ability to produce various proinflammatoriy cytokines as well as reactive oxygen and nitrogen species. Several investigators have studied the influence of radiation on peritonial macrophages [1], blood monocytes [2] and alveolar macrophages [3]. A general conclusion of these studies is that macrophages are more radioresistant than other cells because of their relatively differentiated cellular characteristics. In the present studies the RAW 274.7 murine macrophage cell line as a modell system and freshly isolated human primary monocytes were used.

To investigate the effects of ionizing radiation on the cells the MTT-test was used. In this test, the ability of mitochondrial dehydrogenases to reduce yellow tetrazolium-bromide to insoluble blue colored formazan was measured. A decrease in the amount of the formazan molecules reflects a decrease in the metabolic activity of the cells.

Monocytes and macrophages can be stimulated by lipopolysaccharides (LPS) from gram-negative bacteria. Such stimulated macrophages express detectable amounts of proinflammotory cytokines e.g. TNF-α and IL-1ß. The effects of radiation on the production of these cytokines were investigated in these studies. Figures 1 and 2 show the results of the MTT-test of irradiated RAW cells. The amount of formazan formed decreased only slightly, up to a dosis of 16Gy 250kV X-rays and 16Gy 11,7MeV/u carbon ions. Similar results were optained with X-ray irradiated cells [Fig.1] and in carbon ion irradiated cells [Fig.2]. LPS-stimulated RAW cells clearly show no decrease in their cell vitality, indicating that LPS has strong radioprotective effects on the macrophages. The measurement of TNF-α in the supernatant of the LPS-stimulated irradiated cells indicates differences in the type of irradiation. X-ray irradiated cells show no significant changes in the TNF-α level (data not shown) whereas carbon ion irradiated cells produced an increased amount of TNF-α [Figure 3].

Isolated human monocytes show similar reactions to 250kV x-rays as the RAW 264.7 cells in the MTT-test. They also show only a slight decrease in the level of formazan produced by the monocytes over a dosis from 0,5Gy to 16Gy 250kV X-rays [Fig.4.]. LPS-stimulated human monocytes show no decrease in the formazan level (data not shown). Also, there was no induction of TNF-α, IL-1ß or NO production of the unstimulated monocytes by the irradiation (data not shown). Further experiments with LPS activated human monocytes as well as B- and T-Lymphocytes are planned. These results clearly show the strong radioprotective effect of stimulation of the monocytes/macrophages, that are in themselves relativly radiorestsant in comparision with lymphocytes and fibroblasts.

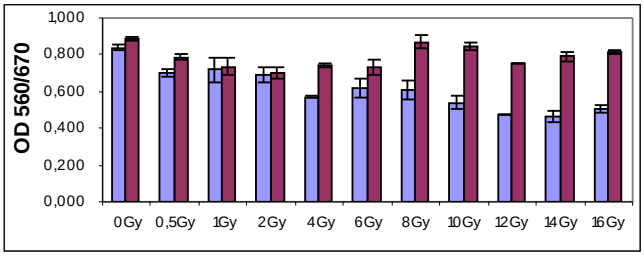

Fig.1. MTT-test; RAW 264.7 cells 24h after 250kV X-ray irradiation. Blue bars represent unstimulated cells; red bars represent stimulated cells (1µg/ml LPS). K= not irradiated cells

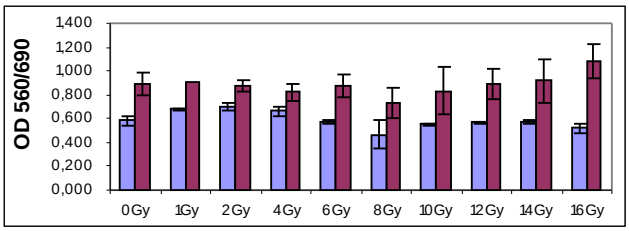

Fig.2. MTT-test; RAW 264.7 cells 24h after 11,7MeV/u carbon ion irradiation. Blue bars represent unstimulated cells; red bars indicates stimulated cells (1µg/ml LPS). K= not irradiated cells

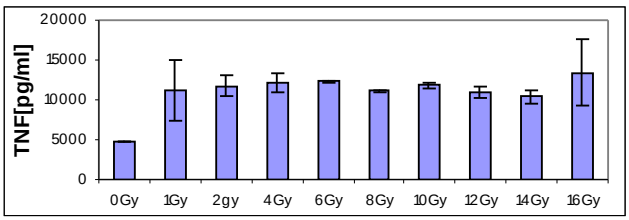

Fig.3. Measurement of TNF-α by ELISA in LPS-stimulated RAW 264.7 cells 24h after 11,7 MeV/u carbon ion irradiation. K= not irradiated cells

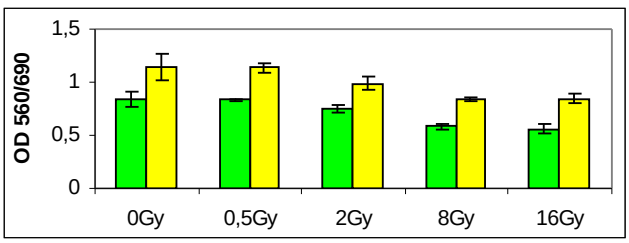

Fig.4. MTT-test, human monocytes after 250kV X-ray irradiation. Green bars = monocytes 24h after irradiation; yellow bars = monocytes 48h after irradiation.

1 Lambert et al. J. Immunol. 139:2834-2841 (1988)

2 D.K. Kwan Radiat. Res. 75: 556-562 (1978)

3 H-S. Lin Radiat. Res. 117: 70-78 (1982)

Acknowledgement: The authors thank the BMBF for financial support of this study by a grant No. 02S8203.

Advanced studies on the bystander response after exposure of human fibroblasts to low fluences and targeted irradiation with heavy ions

C. Fournier[1], F. Knauf[1], C. Sieben[1], G. Becker[1], M. Heiss[2,3], P. Barberet[2], B. Fischer[2], M. Scholz[1], S. Ritter[1] and G. Taucher-Scholz [1].

[1]GSI Biophysics and [2]GSI Material Research, Germany; [3] CENBG, France

Our studies on possibly radiation-induced effects in non-irradiated neighbouring cells are focused on human fibroblasts, which are known to be important mediators of side effects occurring during conventional radiotherapy.

Confluent monolayers of normal human fibroblast strains (mainly AG 1522 C) were used. Irradiation with low fluences of helium (LET 33 keV/µm) and carbon ions (LET 150 keV/µm) was carried out targeting 1% to 10% of the cells by at least one particle. Additionally, experiments with a heavy ion microbeam (helium, carbon and argon ions) developed at GSI have been carried out to irradiate single cells. At different times after exposure (up to 24h), the overall inductions of Connexin 43 (Cx43), one of the core proteins of gap junctions, and of the cell cycle regulator CDKN1A (p21) were assessed by Western Blot and Immunofluorescence. Between 48 and 72 h after exposure, the number of binucleated cells containing micronuclei (MN, after cytokinesis-block by cytochalasin B) and the amount of sister chromatid exchanges (SCE) were quantified.

Connexin 43 is discussed to be upregulated in response to irradiation [1,2]. Our experiments reveal an increased expression of Cx43 protein, for helium ions only when all cells are hit (see figure 1) and for carbon ions when at least 10% of the cells are hit (not shown). This is indicative for a cellular radiation response but not for a clear response of unirradiated bystander cells.

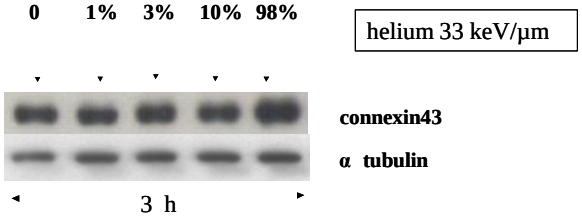

Figure 1: Western Blot analysis of Connexin 43 and tubulin (loading control) from cell lysates of AG1522C cells prepared 24 hours after irradiation with helium. The percentage of irradiated cell nuclei is indicated.

For carbon ions, a slight increment of the cell cycle regulator CDKN1A (p21) was observed, whereas for helium exposure no significant increase was found (not shown). In order to assess whether the observed induction of CDKN1A after carbon exposure is based on intercellular communication via gap junctions between adjacent cells, the accumulation of CDKN1A in nuclei in close proximity to irradiated cells was measured. Irradiation was carried out using a microbeam-facility (GSI, technical details in [4]). No clusters of cells bearing an increased CDKN1A protein amount after targeted irradiation of single cells was observed after exposure to helium, carbon and argon ions. The level of CDKN1A protein did not depend on the radial distance between bystander and irradiated cells of up to 200µm. The results did not indicate an induction of CDKN1A protein in unirradiated bystander cells via gap junctions. In order to compare the protein levels of nontargeted bystander cells to control cells under identical immunofluorescence-staining conditions, a special radiation chamber was developed. First tests have been carried out and the overall CDKN1A induction after targeted irradiation is under investigation.

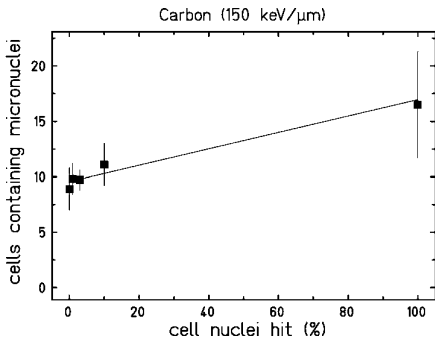

Figure 2: Fraction of AG1522C binucleated cells containing micronuclei stained 72 hours after exposure to carbon ions as a function the percentage of irradiated cell nuclei.

Furthermore, an elevated frequency of SCE- and MN-formation is reported following exposure to low fluences of α-particles [1, 3]. However, the exposure to low fluences of carbon ions did not result in an excess number of MN (see figure 2). We observed changes in the SCE frequency, but there was no clear correlation with fluence. Nevertheless, a delay in cell cycle progression of bystander cells compared to the control cells was observed during the SCE- and MN-assessments. This has to be investigated in further experiments.

In summary, the results obtained for a wide set of biological responses in human fibroblasts in response to carbon ion exposure are not indicative for bystander effects. Thus, an additional risk with regard to side effects related to a carbon-ion radiotherapy is not expected.

(Supported by BMBF 02S8203)

References

1 E. I. Azzam *et al.*, Oncogene 22, 7050-7057 (2003)

2 D. Glover *et al.*, Int. J. Radiat. Biol. 79, 955-964 (2003)

3 A. Deshpande *et al*, Radiat. Res. 145, 260-267 (1996)

4 M. Heiss *et al.*, Radiat. Res. 161, 98-99 (2004)

Cell cycle delay and premature differentiation in human fibroblasts after irradiation with high-LET carbon ions and X-rays

M. Winter[1], C. Fournier[1], P. Hessel[1], E. Nasonova[1,2], L. Melnikova[1,2], and S. Ritter[1]
[1]GSI, Darmstadt; [2]JINR, Dubna, Russia

Cell cycle delay, as observed in fibroblasts after irradiation, is discussed to contribute to genetic stability by providing time for repair and by removing damaged cells from the proliferating pool [1]. Radiation-induced accelerated terminal differentiation has been shown to occur in fibroblasts [2, 3], which may share common mechanisms with naturally occurring cellular senescence. In this study we investigated the influence of radiation quality on the extent of cell cycle delay and premature differentiation in human fibroblasts over a time scale of several weeks.

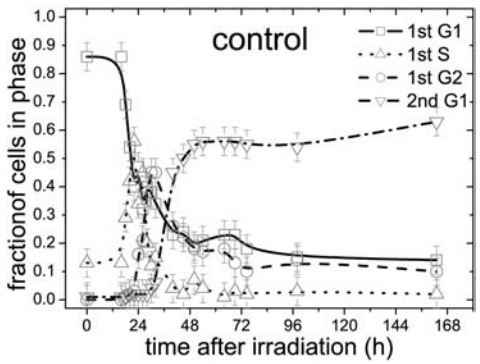

Fig. 1: *Cell cycle progression of unirradiated normal human skin fibroblasts. Cells progress sequentially through G1, S and G2 phases before cell division takes place and the cycle repeats.*

Density-inhibited, normal human fibroblasts (AG 1522) were irradiated with 9.8 MeV/u carbon ions (LET = 170 keV/µm) or 250 kV X-rays (LET = 2 keV/µm). The cells were reseeded after irradiation and cell cycle progression was analyzed during 166 hours by flow cytometry and S-phase BrdU-labelling.

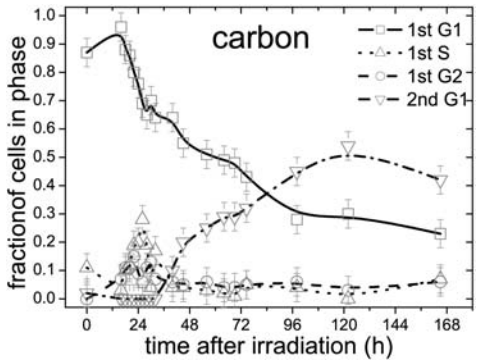

Fig. 2: *Cell cycle after 0.5 Gy ^{12}C ions ($1.8 \cdot 10^6$ cm^{-1}).*

Additionally, cells were subcultured every two weeks for more than 22 weeks after irradiation. The induced levels of cell cycle- (p53, p21) and senescence-related proteins (p16) were quantified by western blotting. In parallel, the differentiation pattern was assessed by measuring β-galactosidase activity and morphological features.

Compared to unirradiated controls (fig. 1), a dose and LET dependent delay of the cell cycle was observed during 166 hours after irradiation. The dose required to induce a similar fraction of delayed cells was about four times lower for carbon ions (fig. 2) than for X-rays (fig. 3), confirming results obtained with S-Phase labeling and mitotic index analysis (not shown). After adding fresh culture medium at 96 h a part of the irradiated and delayed cells did resume proliferation and left the first G1-phase. In spite of continued proliferation, levels of p53, p21 and p16 were elevated after carbon ions and X-irradiation. The increase of p53 and p21 was dose dependent. In case of high doses (4 Gy carbon, 16 Gy X-rays), p21 was continuously elevated up to 3 weeks while p16 was increased from 3 to at least 6 weeks after irradiation (not shown).

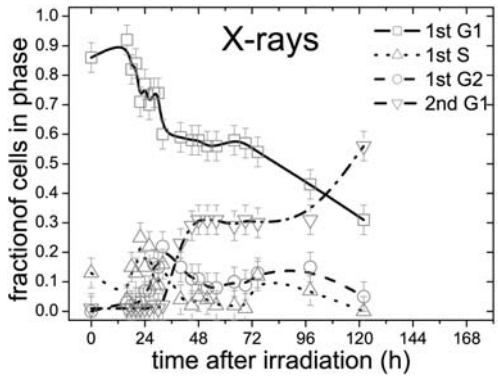

Fig. 3: *Cell cycle progression after 2 Gy X-rays.*

The observed delay of normal fibroblasts up to 168 h after irradiation is dose and LET dependent and occurs primarily in the first G1-phase. The fraction of delayed cells is decreased if fresh culture medium is added after irradiation. Further irradiation experiments have to be carried out in order to determine the ratio of permanently and transiently delayed cells. During weeks after exposure the delay is paralleled by premature differentiation and the expression of regulatory proteins. In particular, the increase of senescence related p16 after irradiation indicates a sharing of the pathways related to radiation induced and natural senescence that is relevant after both carbon ions and X-rays. These results are a further indication that DNA damage caused by carbon ions as well as X-rays leads to premature ageing of human skin fibroblasts.

Supported by BMBF 02S8203

References

[1] DiLeonardo A. et al., Genes Dev. 1994, 8(21), 2540 pp
[2] Rodemann H.P. et al., Scanning Microsc. 1991, 5(4), 113 pp
[3] Fournier, C. et al., Int. J. Radiat. Biol. 2001, 77(6), 713 pp
[4] Fournier, C. et al., Radiat. Res. 2004, 161(6), 675 pp

Cell Cyle Effects Contribute to Multicellular Radiosensitization

J. Topsch[1], W. Mueller-Klieser[1], M. Scholz[2] and G. Kraft[2]

[1]University of Mainz, Germany; [2]GSI Darmstadt, Germany

In the current project on effects of heavy ion irradiation in planar multilayer cell cultures, a "multicellular sensitization" was observed, i. e., multilayers were more radiosensitive than monolayers when treated under identical conditions [1]. This phenomenon was observed in multilayers, but also in multicell spheroids of SiHa and WiDr human tumor cells using plateau region or Bragg peak carbon ions or conventional x-rays for irradiation. The observation is in contrast to the "contact effect" or "multicellular resistance" commonly seen in small size multicellular tumor spheroids [2]. Interestingly, incubation of SiHa mono- and multilayers with the topoisomerase-II inhibitor etposide revealed a multicellular chemoresistance [1] which was in accordance with data from the literature [3]. Since the percentage of cells in the S-phase was much lower in multilayers than in monolayers, and since the proportion of G_0/G_1-phase cells showed the opposite behavior [1], we suspected this difference in cell cycle distribution to be, at least in parts, responsible for the multicellular radiosensitization. One approach to challenging this hypothesis was to seed monolayers in Petri dishes with a regular or a high cell density. Flow cytometry analysis of these cultures at day 5 after plating showed that the cell cycle distribution of dense monolayers was in between that of regular monolayers and multilayers (Tab. 1). Standardized colony forming assays were carried out on these three types of SiHa cell cultures with and without heavy ion irradiation. The resulting clonogenic survival curves are shown in Fig. 1. It can be clearly recognized that the multicellular radiosensitization in multilayers can be approximated by a similar effect in high density monolayers with heavy ion irradiation in both the plateau region (Fig. 1a) and in the extended Bragg peak (Fig. 1b). Corresponding experiments following an etoposide treatment resulted in survival curves of dense monolayers which are very similar to those of multilayers, and which indicated a multicellular chemoresistance under those conditions (data not shown). These findings suggest that cell cycle dependencies of radiation effects in multicellular culture systems have not been considered to a sufficient extent in a number of previous studies, and that they should be reconsidered in a comprehensive way. Furthermore, the data imply that the dependency on cell cycle phase of heavy ion irradiation still is to be investigated in a systematic manner.

Table 1: Cell cycle distribution in SiHa cells at day 5 in culture (values: means ± SD)

	G_0/G_1 (%)	G2/M (%)	S (%)
multilayers	81.1	6.2	12.7
monolayers (regular)	55.7 ± 6.4	10.2 ± 7.0	34.2 ± 1.4
monolayers: (high density)	67.4 ± 1.0	8.8 ± 0.5	23.8 ± 1.1

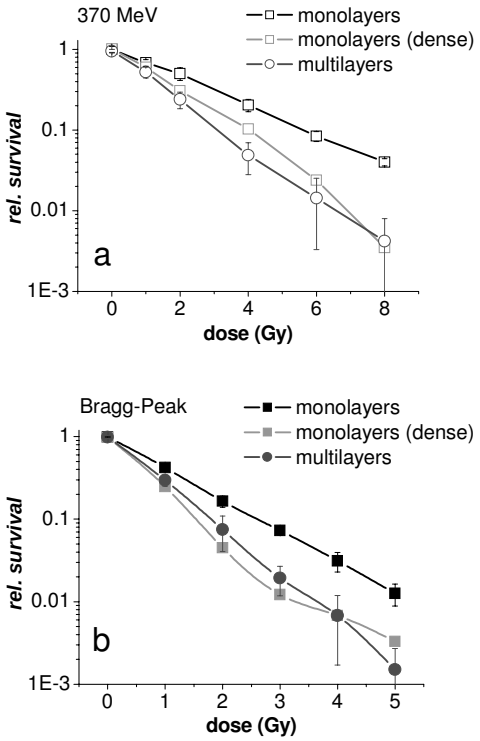

Fig. 1: Relative survival (mean ± SD) of human SiHa cervix carcinoma cells cultured as regular or dense monolayers or as multilayers and treated with heavy carbon ions
a. plateau region irradiation
b. Bragg peak irradiation

References

[1] Topsch, J., Mueller-Klieser, W., Scholz, M. and Kraft, G., GSI Scientific Report 2003, p. 167 (2004)

[2] Olive, P.L. and Durand, R.E., Cancer Metas. Rev. 13(2): 121-138 (1994)

[3] Francia, G., Man, S., Teicher, B., Grasso, L. and Kerbel, R.S., Mol. Cell Biol. 24(15): 6837-6849 (2004)

Application of the Local Effect Model to clinical data for carbon ion treatment of non small-cell lung cancer

M. Scholz[1], N. Matsufuji[2], and T. Kanai[2]
[1]GSI Darmstadt, Germany; [2]NIRS Chiba, Japan

Within the clinical studies performed with carbon ions at HIMAC, the excellent results for the treatment of non small-cell lung cancer [1] are of particular interest, because they allow a direct test of the predictive power of the local effect model concerning clinical data. The application of the local effect model was facilitated by a detailed analysis of the dose response curve obtained for conventional photon treatment of non small-cell lung cancer as described by Kanai et al. [2]. For that, the TCP-curves after photon irradiation were analyzed with respect to the heterogeneity of radiosensitivity parameters. According to this analysis, the shallow slope of the photon dose response curve is due to a significant patient-to-patient variation of the $alpha_X$-parameter; the distribution (Fig. 1) can be described by: $\overline{\alpha_X} = 0.331, \sigma(\alpha_X) = 0.18$ and $\overline{\alpha_X}/\beta_X = 5.585$.

These values correspond to a β_X-value of 0.06. For the application of the LEM the continuous distribution was replaced by a histogram with 10 different classes for α_X. The value of β_X was kept constant for the 10 subpopulations, in line with the general finding that variation of sensitivity is mostly related to variations in the α-term. The dose D_t, describing the transition to the linear part of the survival curve has been chosen according to the assumption, that the dose response curves for the different subpopulations are characterized by the same final slope. The radius of cell nuclei was assumed to be 5 μm.

Based on the parameters given above, cell survival curves were calculated using the local effect model for the mid of an 4cm extended Bragg peak of carbon ions. For a first estimate, the calculations were based on the primary carbon ions alone and fragmentation of the beam when passing through tissue has not yet been taken into account.

TCP curves were calculated for the different subpopulations using an initial cell number of Nc=3x109. According to the weighting factors for the fractions of different subpopulations, the effective TCP curve is then calculated and compared to the clinical data obtained at the HIMAC and the photon dose response curve. A remarkable good agreement is found when comparing the model prediction with the actual clinical outcome; the TCP50 as well as the extreme steepness of the TCP curve after carbon radiation are well reproduced. This steepness is in particular puzzling at a first glance, since it corresponds to an increasing RBE with increasing dose, whereas in general for in-vitro systems the opposite is observed.

According to the analysis described above, the steepness of the TCP curve after carbon irradiation can be attributed to the reduced variance of the sensitivity parameters after carbon compared to photon radiation. The reduced variance is a consequence of the systematics of α_X/β_X-ratios for the different subpopulations. When keeping the β_X-value constant, variation of the α_X-parameter results in a variation of the α_X/β_X-ratio. For

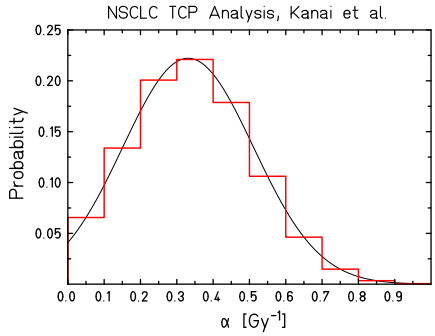

Figure 1: Distribution of α-parameters derived from the TCP-curves after photon treatment of non small-cell lung cancer patients

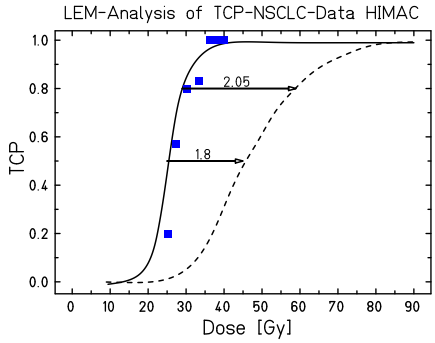

Figure 2: Comparison of the predicted TCP curve for carbon treatment of non small-cell lung cancer with the TCP-curve for photon radiation based on the distribution shown in Fig. 1

the highest α_X-values and thus the most sensitive tumors, the α_X/β_X-ratio is high and thus the RBE is expected to be small. In contrast, for the lowest α_X-values, corresponding to the resistant tumor population, the α_X/β_X-ratio is small, and expected RBE is very high. As a consequence, the range of sensitivities, expressed in terms of the α_X-parameter for ion irradiation, is smaller compared to the range for photon radiation.

This reduction of heterogeneity is specific for high-LET radiation. It can not be mimicked by giving e.g. correspondingly higher doses of proton (or photon) radiation, since protons show RBE values close to one in any case, regardless of the sensitivity against photon radiation. Therefore, protons will not show the pronounced differential RBE effect described above, which is required to obtain the reduction in heterogeneity.

[1] Miyamoto T. et al, Radiother. Oncol. **66** (2003), 127-140
[2] Kanai T. et al., manuscript in preparation

The feasibility of in-beam PET for therapeutic beams of ^{3}He

F. Fiedler[1], K. Parodi[1], and W. Enghardt[1]
[1]Forschungszentrum Rossendorf, Dresden

At the clinical heavy ion treatment facility, which is under construction in Heidelberg, beams of He will also be used for tumour irradiation. These will be monitored by means of in-beam PET for quality assurance. This requires a precise knowledge of the spatial distribution of beam induced positron emitters in the irradiated volume. For this an experiment at the Gesellschaft für Schwerionenforschung (GSI) with pencil-like ^{3}He-beams of 130.03 AMeV to 207.92 AMeV and mean intensities varying from $2.0 \cdot 10^8$ to $3.5 \cdot 10^8$ ions/s has been carried out. The data were taken in list-mode, the PET-measurement was performed over 10 min of irradiation and 20 min of decay. The beams were stopped in homogeneous thick targets consisting of PMMA ($C_5H_8O_2$, $9 \times 9 \times 20$ cm^3, $\rho = 1.18$ g cm^{-3}), graphite ($9 \times 9 \times 15$ cm^3, $\rho = 1.795$ g cm^{-3}) and solid water targets ($9{\times}9{\times}20(30)$ cm^3, $\rho = 1.0$ g cm^{-3}). These consist of water with gelatine resulting in a stoichiometric composition of $H_{66.2}O_{33.1}C_{0.7}$. The spatial distributions of the imaged β^+-activity are displayed in Fig. 1.

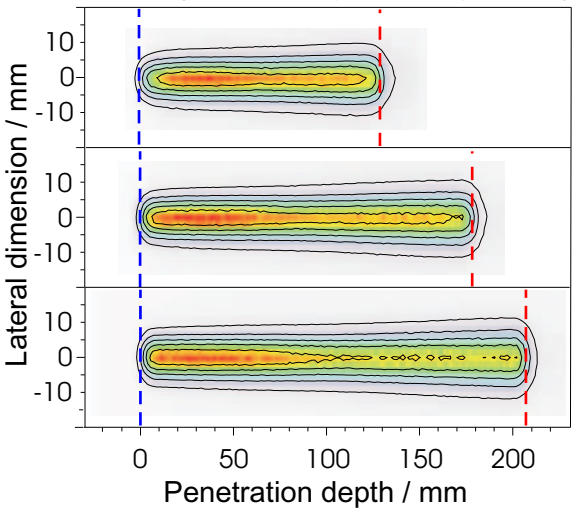

Figure 1: Spatial distributions of the β^+-activity induced by ^{3}He-beams in graphite (top), PMMA (middle) and water (bottom) at $E = 207.92$ AMeV. The blue lines indicate the front face of the target, the red lines mark the range of the ^{3}He.

These phantoms were placed in the center of the field of view of the PET-scanner at the experimental carbon ion therapy at GSI [1]. The absolute activity production rate [2] was found to be about three times larger than for carbon ions (3.2±0.4). It was shown for a spread-out Bragg peak (SOBP) irradiation of the PMMA phantom as well as for mono-energetic beams that range differences of about 0.9 mm can be resolved (Fig. 2). The lateral profile was found in a reasonable agreement with the calculations [3] (Fig. 3).

By means of the formula

$$\sigma(E) = \frac{N(E)}{R(E)\; n\; I(E)} \qquad (1)$$

cross sections for the formation of a specified isotope in thick targets of the given dimensions have been calculated, where $\sigma(E)$ is the cross section, N is the absolute number of produced positron emitters of one species, R is the range, n gives the atomic density and I is the number of incident ^{3}He-ions. Following this approach for the reaction ^{12}C(^{3}He, ^{3}He+n)^{11}C values of $\sigma(130.03\ A\text{MeV}) = (134 \pm 13)$ mb, $\sigma(166.05\ A\text{MeV}) = (127 \pm 13)$ mb, $\sigma(207.92\ A\text{MeV}) = (120 \pm 12)$ mb have been found by evaluating the graphite data, whereas analysing the water data for the production of ^{15}O $\sigma(130.03\ A\text{MeV}) = (140 \pm 14)$ mb, $\sigma(166.05\ A\text{MeV}) = (130 \pm 13)$ mb, $\sigma(207.92\ A\text{MeV}) = (116 \pm 12)$ mb and for ^{16}O(^{3}He, 4p+4n)^{11}C $\sigma(130.03\ A\text{MeV}) = (59 \pm 6)$ mb, $\sigma(166.05\ A\text{MeV}) = (52 \pm 5)$ mb, $\sigma(207.92\ A\text{MeV}) = (45 \pm 5)$ mb were determined.

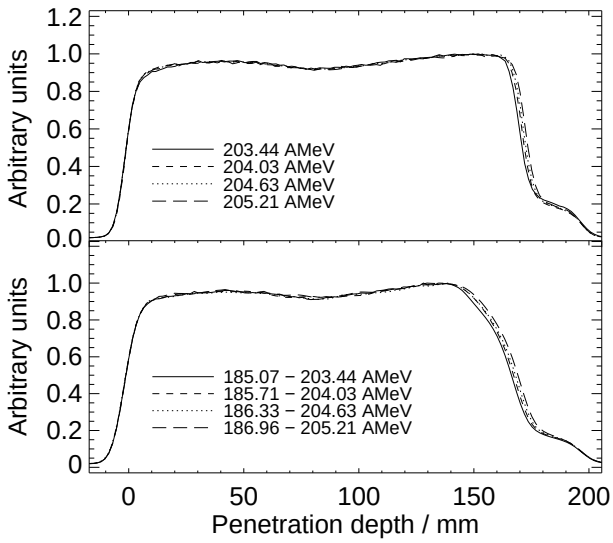

Figure 2: Measured depth profile of β^+-activity induced by mono-energetic (top) and SOBP irradiation (bottom), formed by eleven equally spaced energy steps stopped in PMMA.

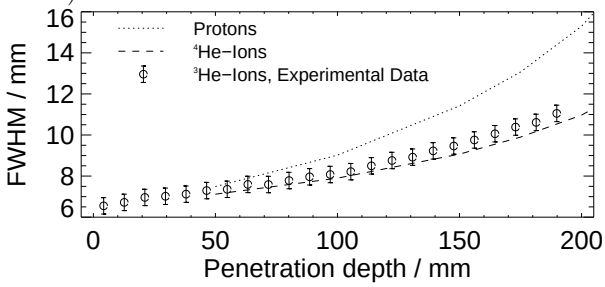

Figure 3: Comparison of the measured beam broadening in the water target with $E = 207.92$ AMeV with the calculations in [3], experimental data are corrected for the spatial resolution of the positron camera.

References

[1] W. Enghardt et al., Nucl. Instrum. Meth. A 525 (2004) 284
[2] K. Parodi, Wiss.-Tech. Ber. FZR-415 (2004)
[3] Th. Haberer, Ph.D. Thesis, GSI Report 94-09 (1994)

Suppression of Random Coincidences During In-Beam PET Measurements

P. Crespo[1], T. Barthel[1,2], H. Frais-Kölbl[3,4], E. Griesmayer[3,4],
K. Heidel[1], K. Parodi[1], J. Pawelke[1], and W. Enghardt[1]
[1]FZ Rossendorf, Germany; [2]Hochschule Mittweida, Germany; [3]MedAustron, Austria; [4]FOTEC, Austria

In-beam positron emission tomography (PET) is currently applied for in-situ monitoring of charged hadron radiotherapy [1]. However, in-beam PET data, measured at beams with a sub-μs-microstructure due to the accelerator radiofrequency (RF), are highly corrupted by random coincidences arising from prompt γ-rays following nuclear reactions as the projectiles penetrate the tissue [2,3]. Since conventional PET random-correction techniques fail, the clinical in-beam PET at the therapy facility at the Gesellschaft für Schwerionenforschung (GSI) Darmstadt merely reconstructs events registered in the pauses ($\sim$ 2-4 s) between the beam macropulses ($\leq$ 2 s) [1]. We have successfully tested at GSI two methods for suppressing the micropulse-induced random coincidences during beam extraction. Image statistics increased by about 90 %. Both methods, depicted in Fig. 1 (tested with Lucite phantoms only), synchronize the $\gamma\gamma$-coincidences measured by the positron camera with the time microstructure of the beam, either by using the RF-signal from the accelerator or the signal of a diamond detector placed in the beam path before the target [4].

The measured correlation between the $\gamma\gamma$ coincidences and the beam microstructure is shown in Fig. 2 for the RF measurements (diamond detector shows similar results). This correlation can first be seen in column 1: the shape of the $\gamma\gamma$ time spectrum is deteriorated by randoms and the $\gamma\gamma$-RF time spectrum shows a peak above a constant plateau, indicating the elevated and expected event flux during the microbunches [3]. After setting an energy window for the photon detectors (column 2), the peak-to-plateau ratio in the $\gamma\gamma$-RF time spectrum decreases more than one order of magnitude and the corresponding $\gamma\gamma$ time distribution presents the same shape and resolution as the spectra aquired during the extraction pauses [5]. Fig. 3 shows the depth profiles obtained by sorting events arriving within the microbunches from those outside it (B_2 and A_2 in Fig. 2, respectively).

The energy and triple-coincidence time correlated spectra (Fig. 2) and tomographic images of the β^+-activity induced by the beam in a plastic phantom (Fig. 3), first-measured during beam extraction, clearly confirm the feasibility of the proposed random suppression methods [5].

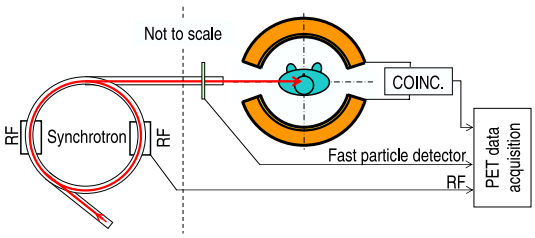

Figure 1: Methods proposed for in-beam PET random correction: every detected $\gamma\gamma$-coincidence is correlated with the incoming ion by using either a particle detector or the RF signal from the accelerator.

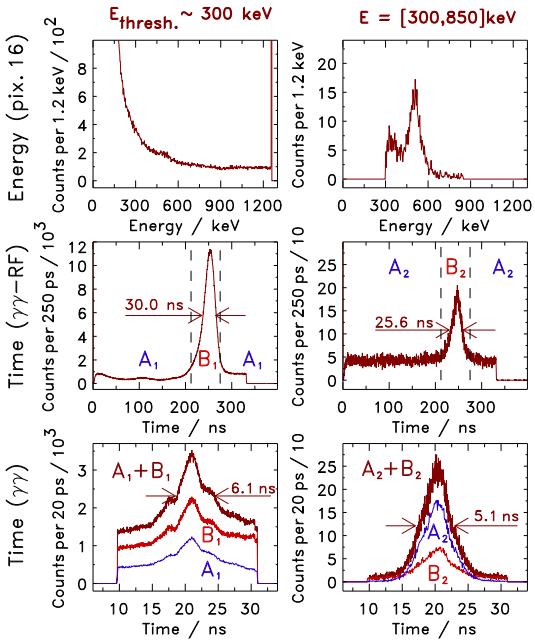

Figure 2: Results of $\gamma\gamma$-RF coincidence measurements during beam extraction. The $\gamma\gamma$ coincidence time spectra (bottom) result from different sorting conditions in the γ-ray energy spectra (top) and the $\gamma\gamma$-RF spectra (middle).

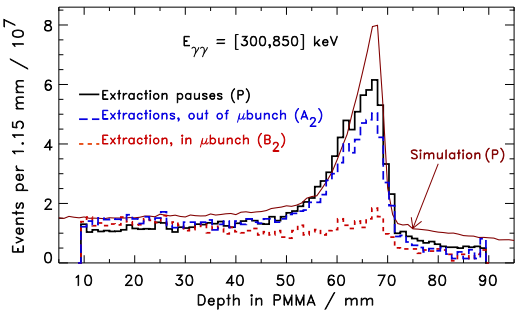

Figure 3: Depth profiles obtained with the $\gamma\gamma$-RF method. The simulation regards extraction pauses (P) only.

References

[1] W. Enghardt, P. Crespo et al., NIM A525 (2004) 284.
[2] J. Pawelke, W. Enghardt et al., IEEE Trans. Nucl. Sci. 44:4 (1997) 1492
[3] K. Parodi, P. Crespo et al., NIM A (2004), accepted.
[4] W. Enghardt, P. Crespo et al., Deutschen Patent- und Markenamt München (2004), pending.
[5] P. Crespo, T. Barthel et al., IEEE Trans. Nucl. Sci. (2004), submitted.

The time dependent influence of tissue stoichiometry and reaction cross sections on in-beam PET imaging of proton therapy

K. Parodi[1] and W. Enghardt[1]
[1]Forschungszentrum Rossendorf, Dresden

Following the positive clinical impact for carbon ion therapy [1] and the promising experiments with proton beams [2] at GSI, in-beam positron-emission-tomography (PET) will be used to monitor ion (p, He, C, O) treatment at the future hospital-based facility in Heidelberg. For protons, despite the lack of projectile fragments, millimetre precision for monitoring range and lateral field position was demonstrated in homogenous targets [2]. However, in contrast to heavy ions, the major role of target fragments challenges the accuracy of the modelling for prediction of irradiation-induced activity distributions, which is an essential requirement for therapy monitoring [1]. Although experiments in an inhomogeneous target were also performed, the sensitivity to tissue stoichiometry and reaction cross sections was studied in a more controlled way by time analysis of list mode data acquired during and after irradiation of PMMA ($C_5H_8O_2$) [2]. In this material, the dominant contribution to β^+-activity comes from (p, pn) reactions on C and O nuclei, the main constituents of living tissue. The resulting ^{11}C and ^{15}O isotopes have half-lives $T_{1/2}$ of 20.4 and 2.0 min, respectively. Several subsets of the measured data were reconstructed, corresponding to different ratios of ^{11}C to ^{15}O decays but, where possible, the same number of registered events. The shape of the activity depth profiles and the position $d_{50\%}$ of the 50 % distal fall-off, related to the range, is clearly sensitive to the selected time window (fig. 1a, b), due to the energy dependence of the cross sections for the involved reaction channels. For comparison, model predictions [2] using different cross sections from the experimental database [3] and the ICRU report [4], largely adopting calculations benchmarked against measurements, were examined. The resulting β^+-emitter profiles clearly differ (fig. 1c, d). The data from [3] were able to reproduce the

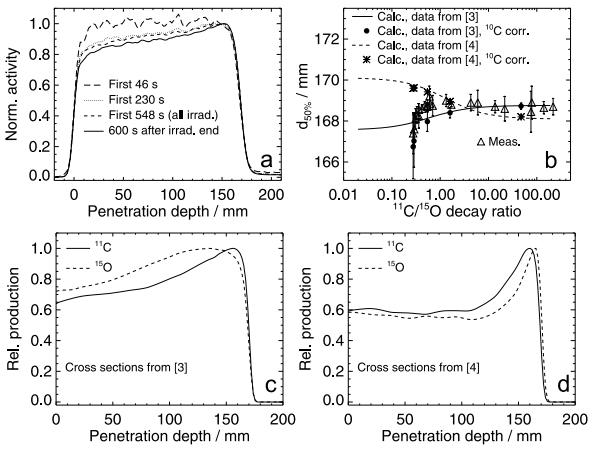

Figure 1: Activity profiles from data measured in different time windows at 173.13 MeV energy (a) and $d_{50\%}$ values (b) from more subsets of the same acquisition corresponding to the given ^{11}C/^{15}O decay ratio (triangles), compared to calculations based on predicted ^{11}C and ^{15}O profiles (c, d), without (lines) and with (symbols) corrections for ^{10}C (cf. text).

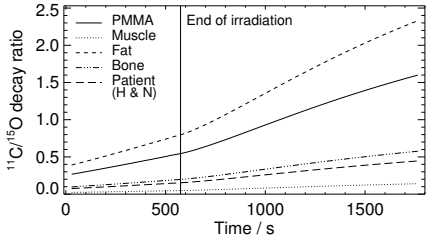

Figure 2: *Solid*: Estimated time-integrated ^{11}C/^{15}O decay ratio for 173.13 MeV protons in PMMA. *Others*: Extension to tissues and a typical head and neck (H&N) patient based on the C/O composition and only *(p,pn)* reactions [2]

trend of the measurement in dependence on the ^{11}C/^{15}O decay ratio. In fig. 1b, the larger deviation in the fall-off position for low ^{11}C/^{15}O was ascribed to the not negligible contribution of ^{10}C ($T_{1/2}$ = 19.3 s) in the first seconds of the irradiation. A correction [2] provided better agreement. In contrast, the data from [4] could not reproduce the experimental trend, even when correcting for ^{10}C. The results point out the high sentivity of in-beam PET monitoring to the time course of irradiation/acquisition as well as tissue stoichiometry and cross section data for protons. Similar considerations apply to light ions up to boron, producing insignificant amount of β^+-active projectile fragments. In view of applications to therapy, the time integrated ^{11}C/^{15}O decay ratio over a typical 10 min irradiation with the same time structure as for carbon ion therapy at GSI is shown in fig. 2. A rough extrapolation to materials of therapeutic interest is also given, though the corresponding $d_{50\%}$ differs from fig. 1b, due to different stopping properties. Moreover, isotopes from minor reaction channels (e.g. ^{10}C) have been already shown to have a time dependent, not negligible impact. Hence, in order to achieve the desired accuracy for therapy monitoring, at least in low perfused regions of interest, the time structure of the irradiation and PET acquisition has to be properly chosen to minimise uncertainties from the limited accuracy in the knowledge of tissue stoichiometry and cross sections. For dynamic beam delivery the optimal strategy should be investigated. Decreasing energy steps maximise the ^{11}C/^{15}O decay ratio at the most critical distal edge, minimising $d_{50\%}$ uncertainties, but increase probability of blurring due to perfusion. The stoichiometry problem less affects off-line PET at the cost of lower counting statistics, high sensitivity to perfusion and possible movement of the patient from the treatment position.

References

[1] W. Enghardt, P. Crespo, et al., Nucl. Instrum. Meth. A, 525 (2004) 284
[2] K. Parodi, Thesis, Wiss.-Tech. Ber. FZR-415 (2004)
[3] Nuclear Reaction Data Center Network, online at http://www.nndc.bnl.gov/exfor (2000)
[4] ICRU Report 63, March 2000

Treatment planning for the GSI radiotherapy

M. Krämer, A. Schmidt, GSI Darmstadt Biophysik

In 2004 our standard treatment planning software TRiP98 [1, 2, 3] was used in combination with the Voxelplan environment for the planning of all 40 patients treated. In a separate branch we pursued future developments, such as improvements on the beam model for ^{12}C, verifying beam models for lighter ions like ^{3}He, implementation of a faster calculation of biological effect, and last but not least realization of simultaneous biological optimization of multiple fields with reasonable computing resources.

Beam models for lighter ions

Lighter ions like helium potentially bridge the gap between the established therapeutical ion species protons and carbon. Lateral spread of helium beams does not increase with depth as much as for protons, and nuclear fragmentation is expected to be less than for carbon. The biological effectiveness is expected to be closer to protons than to carbon ions. Hence helium beams could be an alternative, when neither protons nor carbon ions are optimal. To be usable in clinical practice, however, a similar level of accuracy must be achieved for physical and biological beam modelling as established for carbon. First experiments showed encouraging results with ^{3}He [4, 5], but further refinements are needed to reduce the remaining discrepancies between experiment and TRiP98 calculation.

Faster calculation of biological effect

The "classical" version of biological effect calculation uses the full Local Effect Model [6], involving interpolation and sampling of particle spectra in huge databases. A complete patient plan takes on the order of half a day to calculate on our IBM Power4 hardware. To improve on this an alternative algorithm for biological effect calculation has been developed and integrated into dose calculation and optimization. It is based on a simplified version of the LEM for therapeutical dose levels. The simplified algorithm allows to operate with the first moments of particle spectra, rather than the spectra themselves. Clearly this is a big time saver, reducing computation times by one to two orders of magnitude for biological dose calculation and optimization, respectively. For typical patient plans the deviation from the classical algorithm is on the order of four percent, which would be acceptable for patient treatment. However, since the algorithm is based on an approximation, the limits of its applicability still have to be explored by systematic studies.

Simultaneous optimization of multiple fields

One of the remaining challenges for ion radiotherapy is the IMRT-style multiple field optimization, taking biological effects into account. Some of the necessary "infrastructure" was already implemented in 2003 [7]. However, calculation time still was too long, and could by no means be compensated for by just waiting for faster computer hardware to become available. The implementation of a faster biological effect algorithm, however, together with the inclusion of the RBE as a "driving force" in the Conjugated Gradient algorithm, now seem to allow the routine usage of multiple field optimization. As it turned out from several patient examples, a large number (several hundred) of iterations of the Gradient algorithm is necessary to achieve a satisfactory dose coverage of the target volume and simultaneous sparing of organs at risk.

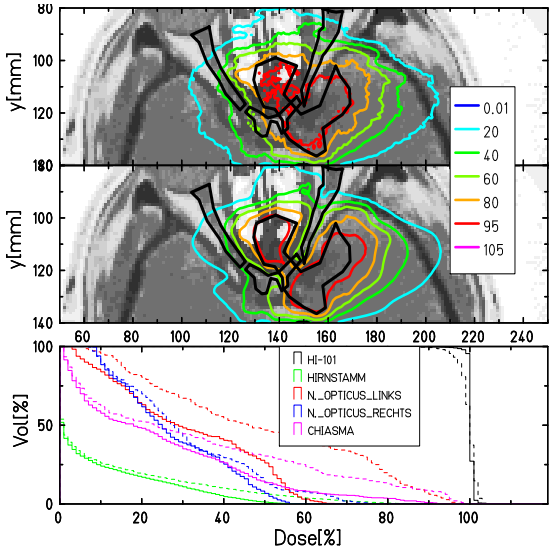

Figure 1: Biological dose distributions for separately (upper) and simultaneously (middle) optimized opposing fields. The insert indicates dose percentages. Lower picture: corresponding dose-volume histograms for separate (dashed) and simultaneous (solid) optimization.

Figure 1 compares two-field plans optimized separately and simultaneously, respectively. Dose-volume histograms show significantly increased target conformance. The maximum dose to critical structures can be reduced by 10 to 30 percentage points. Calculation times for a complete plan is still on the order of several hours, however, the results are much better, and with current Power4 and upcoming Power5 multi-processor machines a throughput of five to ten patient plans per day seems to be feasible. Since even plans with a modest number of raster points require dose-raster coupling matrices of 1 to 2 GByte size, it will be necessary to equip computers with at least 2 GByte of main memory per CPU and to switch to the 64bit version of the AIX operating system.

Our aim is to make available this novel irradiation scheme for GSI patient treatment in 2005.

References

[1] M. Krämer et al, Phys. Med. Biol., 45/11 (2000) 3299
[2] M. Krämer et al, Phys. Med. Biol., 45/11 (2000) 3319
[3] O. Jäkel et al., Phys. Med. Biol., 46/4 (2001) 1101
[4] S.Brons et al, this report
[5] W.Kraft-Weyrather et al, this report
[6] M.Scholz et al., Rad. Environ. Biophysics 36 (1997) 59
[7] GSI report 2003

Angular scattering of light ions in therapy planning at GSI

S. Brons[1], B. Hasch[1], P. Heeg[2], and M. Krämer[1]
[1]GSI, Darmstadt; [2]DKFZ, Heidelberg

Standard treatment planning for tumour therapy at GSI uses a Gaussian beam profile with a constant width throughout the target volume [1]. While this is a reasonable approximation for heavier projectiles, like ^{12}C, the broadening of the beam profile due to angular scattering of the beam particle and of its fragments can no longer be neglected for lighter beams, such as Helium or protons. In view of the routine use of lighter ions in tumour therapy at upcoming particle therapy centres, like at the Heidelberg facility HIT, it is therefore mandatory to upgrade and validate the physical beam model underlying the treatment planning software *TRiP* [1].

An algorithm incorporating the effect of angular scattering into *TRiP* has been presented some time ago [2]. Here we report on experiments performed with ^{3}He ions at GSI and their comparison to a research version of the planning software including these changes (labelled *TRiPbeam*), capable to calculate angular scattering and fragmentation for virtually any light beam particle.

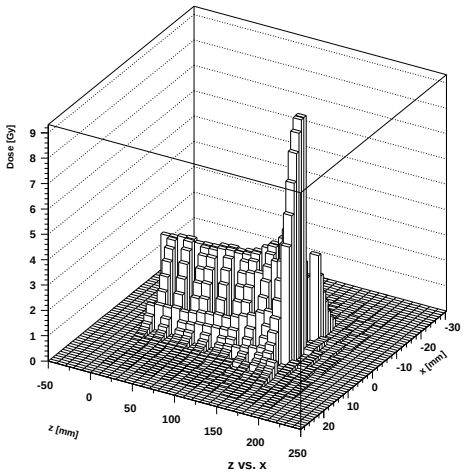

Figure 1: Measured lateral (x) dose distribution in water as a function of penetration depth (z) for ^{3}He.

Measurements were performed at *Cave M*, using a ^{3}He beam of 190 MeV u^{-1} with a FWHM of 8 mm at the isocentre. The beam was scanned in a vertical line of $\pm$40 mm height using the therapy scanning system, and stopped in a water phantom, which is routinely used to verify patient plans [3]. The dose deposited inside the phantom was measured using an array of 24 air-filled cylindrical ionisation chambers (inner diameter 2 mm), mounted in 6 rows of 4 chambers. The chambers can be moved through the water tank by means of a step motor system with a precision of 0.1 mm in all three space direction [3]. Using this setup lateral dose profiles have been recorded at different penetration depths, allowing to obtain a 2-dimensional representation of deposited dose in x versus z (figure 1), z being the beam axis and x the horizontal transverse coordinate.

The total dose distribution was then broken down into a series of slices of deposited dose laterally to the beam axis and fitted using an empirical parameterisation, consisting of the sum of 2 Gaussians. From the fits both the width and the integral of each component can be extracted and compared to the *TRiPbeam* prediction. This is shown in figure 2 and figure 3 for the contribution by the beam particle, which dominates the shape of the inner Gaussian. The figures illustrate that, taking into account the inherent beam dispersion of 2 $m$rad at *Cave M*, there is good agreement between measurement and calculation.

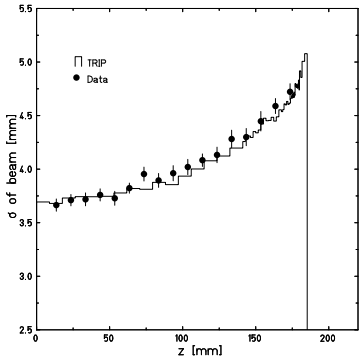

Figure 2: Measured beam width as a function of penetration depth z in water for ^{3}He compared to *TRiPbeam*.

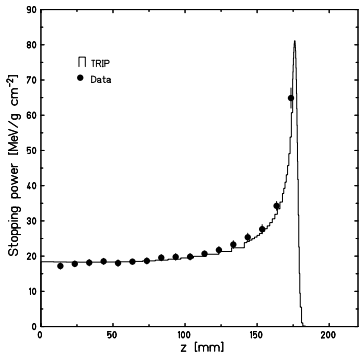

Figure 3: Measured ^{3}He stopping power as a function of penetration depth z in water compared to *TRiPbeam*.

These encouraging results show that the research version of the treatment planning software is already capable to produce reasonable dose distributions for ^{3}He. Further developments will focus on the proper inclusion of nuclear fragmentation [4].

References

[1] M. Krämer *et al.*: Phys. Med. Biol. **45**, 3299-317 (2000).
[2] U. Weber *et al.*: GSI ann. rep. 1998, 129-30.
[3] C. Karger *et al.*: Med. Phys. **26**, 2125-32 (1999).
[4] D. Schardt *et al.*: This report.

Dose Response of BANG Polymer-Gels to Carbon Ion Irradiation

Ulla Ramm[1], Belinda Spielberger[2], Jussi Moog[1], Frank Rudolf[1], Jörg Licher[1], Heinz-Dietrich Böttcher[1], and Gerhard Kraft[2]

[1]Universitätsklinikum, Klinik für Strahlentherapie und Onkologie, 60590 Frankfurt/Main, Germany; [2]Gesellschaft für Schwerionenforschung (GSI), 64291 Darmstadt, Germany

Magnetic resonance imaging (MRI) can be used to measure three-dimensional dose distribution produced by sparsely ionizing radiation absorbed in tissue-equivalent BANG polymer gels [1, 2].

As for high-LET radiation like the ^{12}C beam used in the radiotherapy project started at the GSI, Darmstadt, Germany saturation effects can be expected. Furthermore, ^{12}C beam in matter undergoes fragmentation and generates a mixed radiation field of various particles with different energies. Hence, systematic investigations on the dose response of BANG polymer gels to high LET heavy ion radiation relative to photon radiation were started.

For comparison with sparsely ionizing radiation irradiated BANG polymer gel samples (BANG, MGS Research Inc., Guilford, USA) were irradiated with 6 MV photons (LINAC SL25, Elekta, Universitätsklinikum, Frankfurt/Main, Germany). To determine the dose-response curve doses of up to 100 Gy were applied at a field size of 5 cm $*$ 5 cm .

The heavy ion experiments were performed with the raster scan facility in CAVE M at the GSI [3]. BANG polymer gels were irradiated with single beams of monoenergetic ^{12}C ions at a projectile energy of 205 MeVu^{-1}. The beams were scanned over areas of 3 cm $*$ 3 cm to ensure homogeneous distribution of the ions. The radiation doses varied from 5 to 100 Gy.

The MR images were measured at a 1.5 T whole body scanner (Magnetom, Siemens, Germany). A CP-CPMG phase cycling pulse sequence, that acquires 32 spin echoes, was used for MR imaging [4, 5]. Repetition time $TR = 2000$ ms and echo times $TE = 20$ ms up to 640 ms (echo spacing $\Delta TE = 20$ ms) were chosen. The transverse MR relaxation rate $R_2 = 1/T_2$ was taken as a measure of the radiation dose absorbed in the gel.

In Figure 1 the dose response curves of the relaxation rate for sparsely and densely ionizing radiation are shown. The polymer gel response on dose was taken as net relaxation rate: R_2 minus background $R_{2,0}$.

For 6 MV photon radiation up to a dose of $D \approx 20$ Gy the relaxation rate increases linearly, but saturates beyond. For that dose region the relaxation rates are mapped by fitting a linear function (*dashed line*). Due to the saturation of the polymerization process at higher doses, the measured relaxation rates become non-linear [2, 6].

For densely ionizing ^{12}C radiation the dose response curve is showing the same shape, but differs in its amount of changes in relaxation rates. This behaviour can be explained by the spatial energy deposition. For heavy carbon ions, in the particle track the ionization density is high and therefore saturation effects in the particle track are high too. This results in lower dose response of BANG gels.

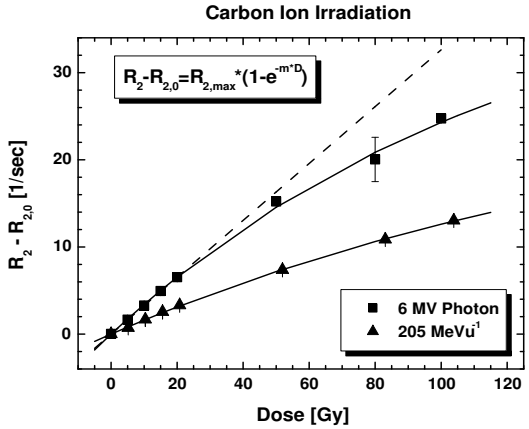

Figure 1: Dose response curve for BANG polymer-gel irradiated with 6 MV photons and 205 MeVu^{-1} ^{12}C ions. The data are fitted with a linear (*dashed line*), and an exponential function (*full line*): $R_2 - R_{2,0} = R_{2,max} \cdot (1 - e^{-mD})$).

BANG gel dosimetry is investigated in carbon ion irradiation. At present, the dose response of the BANG gel - depending on energy and atomic number of heavy ions - does not allow a direct dose measurement. However, once this dependence is determined by experimental data and extensive model calculations as suggested, MR imaging of tissue-equivalent aqueous polymer gel can be extended to the verification of three-dimensional dose distributions in high LET heavy ion radiotherapy.

References

[1] Gore, JC, Kang, YS and Schulz, RJ. Phys. Med. Biol. 1984; 29: 1189-1197.

[2] Maryanski, MJ, Gore, JC, Kennan, RP and Schulz, RJ. Magn. Res. Imag. 1993; 11: 253-258.

[3] Haberer, T, Becher, W, Schardt, D and Kraft, G. Nucl. Instr. and Meth. in Phys. Res. A 1993; 330: 296-305.

[4] Carr, HY and Purcell, EM. Phys. Rev. 1954; 94: 630-38.

[5] Meiboom, S and Gill, D. Rev. Sci. Instrum. 1958; 29: 688-91.

[6] Ramm, U, Weber, U, Bock, M, et al. Phys. Med. Biol. 2000; 45: N95-102.

Influence of respiratory motion on the dose distribution of a lung tumor

Christoph Bert [1], Eike Rietzel [1/2], Sven O. Grözinger [1], Thomas Haberer [1], and Gerhard Kraft [1]

[1]GSI, Biophysik, Darmstadt, Germany, [2]Massachusetts General Hospital, Boston, MA, USA

Currently at GSI only static tumors are treated with carbon ions. Treatment of moving targets in the thorax is not possible with the current system. Interplay effects between target motion and scanned beam application [1] result in inhomogeneous and imprecise dose deposition. To quantitatively investigate the impact of tumor motion on the dose distribution, the GSI treatment planning system TRiP [2] was extended. The planning process is based on time resolved computed tomographic data (4DCT), comparable to 10 conventional 3D CT scans evenly distributed within the approximately periodical breathing cycle of a patient [3].

Figure 1 shows coronal CT slices of a lung tumor patient. A standard carbon treatment plan was optimized on one of the CT datasets (end inhalation), corresponding iso-dose lines are shown in figure 1a. The high dose region encompasses the gross tumor volume (GTV) and the dose distribution is homogeneous .

Based on the 4DCT data sets, respiration parameters and beam intensity data, the dose distribution was calculated for various combinations of respiration period T and initial respiratory phase φ. Figures 1b/c show two examples of dose distributions received by a moving tumor. Respiratory motion results in areas with significant over- and underdosage up to ±15% of the prescribed dose within the GTV for both examples. In addition, areas outside of the PTV, receive therapeutical dose (figure 1b, 106%).

Figure 2 shows GTV dose-volume histograms for four different respiratory periods. All of them exhibit over- as well as underdosage.

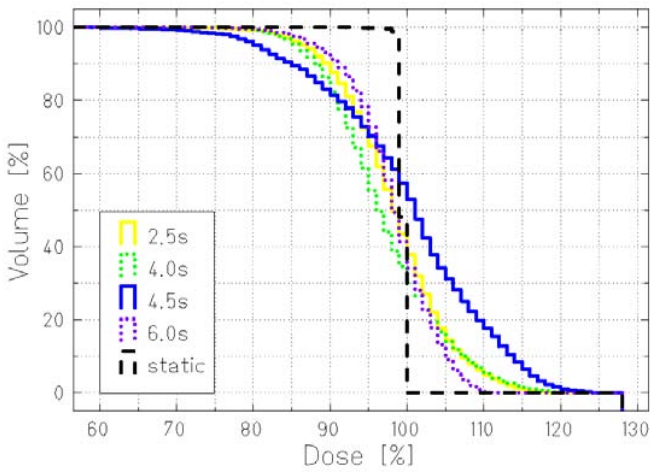

Figure 2 Dose volume histograms (DVH) of the GTV of the same patient as in figure 1. In the static case the entire volume is covered with the planned dose. In the presence of motion (φ=0°) the DVH is degraded with over-dose up to 120% and under-dose down to 70%.

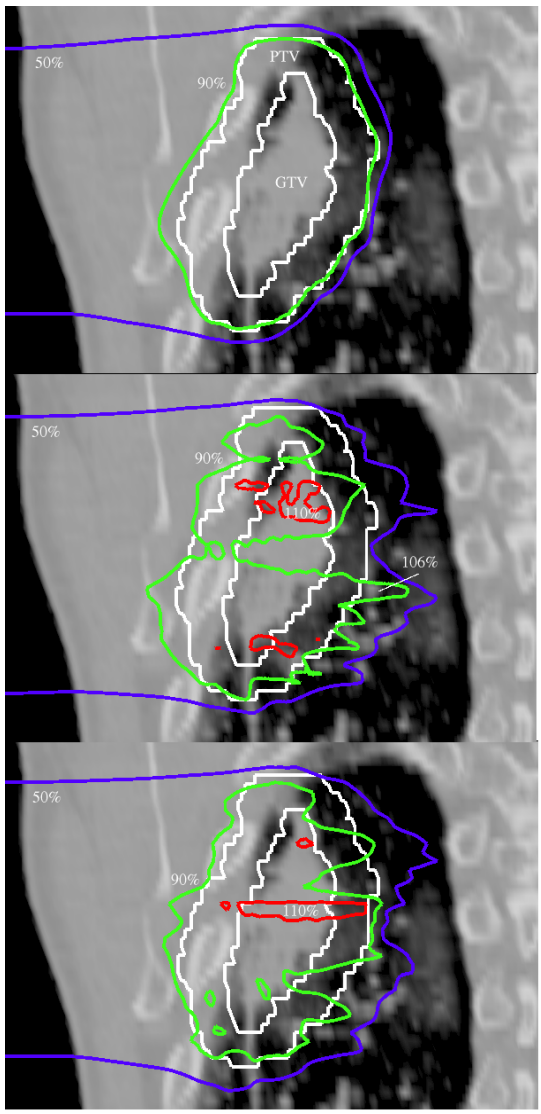

Figure 1 Coronal slice of a lung tumor patient with PTV and GTV. The iso-dose lines are at 50%, 90%, and 110% of the target dose. a) shows the static dose distribution planned on the reference 4DCT phase, b) for a moving tumor with T=4s, φ=0°, and c) for T=4.5s, φ=270°.

Because of the scanned beam application which in principle is sequential voxel by voxel, increased treatment planning margins do not guarantee appropriate coverage of the GTV in the presence of motion. We plan to adapt the beam position at the time of irradiation to compensate the target motion (3D-Online Motion Compensation [4]) based on online monitoring of the tumor position and 4DCT information.

References

[1] Haberer et al., NIM A330, 296-305, 1993
[2] Krämer et al., Phys.Med.Biol., 45, 3299-3317, 2000
[3] Rietzel et al., Int.J.Radiat.Oncol.Biol.Phys., 2005,in print
[4] Grözinger. PhD-thesis, TU Darmstadt, 2004

Intercomparison between NIRS and GSI Therapeutic 6 cm SOBP Carbon Beam with a Human Cancer Cell Line.

Y. Furusawa[1], M. Aoki[1], Y. Matsumoto[1], R Lee[1,2], S. Ritter[2], and M. Scholz[2]

[1]NIRS, Heavy-ion Radiobiol. Res. Gr., Japan; [2]GSI, Biophysik, Germany

Purpose: To compare biological effectiveness of 6 cm SOBP carbon ion therapy beams between GSI and NIRS.

Materials and Methods: HSG (Human salivary gland tumor original) cells were cultured in E-MEM medium supplemented 10% Fetal Bovine Serum and antibiotics in humidified air containing 5% CO_2 at 37ºC. The cells were seeded 1) at the concentration of $5x10^5$ cells per T25 flasks or 2) at the concentration of $1.5x10^5$ cells per 25 mm culture cover slip in a 35 mm Petri dish 1.5 days before irradiation. The cells on the slips were transferred at defined depth positions in the SOBP (center of the SOBP = middle, proximal, distal and distal end; 0, -25, +25, and +28 mmH_2O, respectively) of special made chambers so called CellStack (Fig. 1), and filled with the medium just before the irradiation.

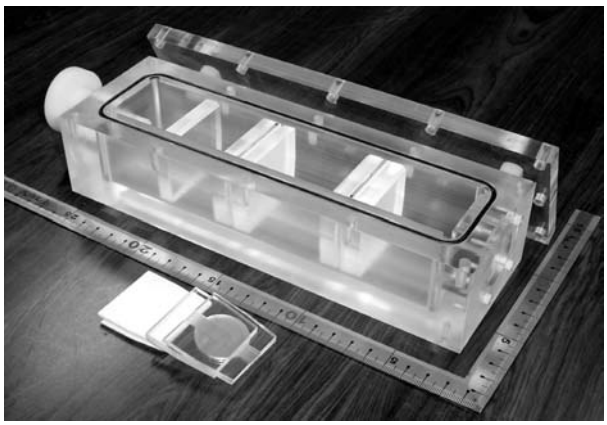

Fig. 1. CellStack irradiation chamber.

Cell exposure was performed at the Medical Cave in GSI and the Biology Irradiation Room at HIMAC in NIRS. The dose distribution at GSI was adjusted 1) as same as that at HIMAC for the primary intercomparison experiments, or 2) conformed the 4GyE dose distribution at GSI treatment planning for the second experiments. For the primary experiment, culture bottles were set in a polypropylene block, and the irradiation depth was adjusted as same as CellStack irradiation with polypropylene disks having different thicknesses (Fig.2) or the entrance of the beam.

Irradiated cells were harvested in medium by trypsinisation, counted the cell concentration, and diluted then seeded adequate number of cells in each three 60 mm Petri dish to obtain approximately 100 colonies. Colonies consists with more than 50 cells were counted as survivors after 13 days of post-incubation.

Results: Preliminary results showed a good agreement with HIMAC SOBP beam, and the biological dose distribution in the SOBP was within +/- 6.5% for all depth positions (proximal, middle, distal and distal end; Fig. 3) at 10 % survival level when the exposures were defined with the peak dose. The curve showed a highest efficiency at high dose region and a largest shoulder at the proximal position. That for distal or distal end showed smaller shoulder to indicate the contribution of higher LET beams.

Those data will be analyzed together with that for CellStack data that performed GSI style dose distribution performed Feburary 2005 at GSI and experiments performed at HIMAC.

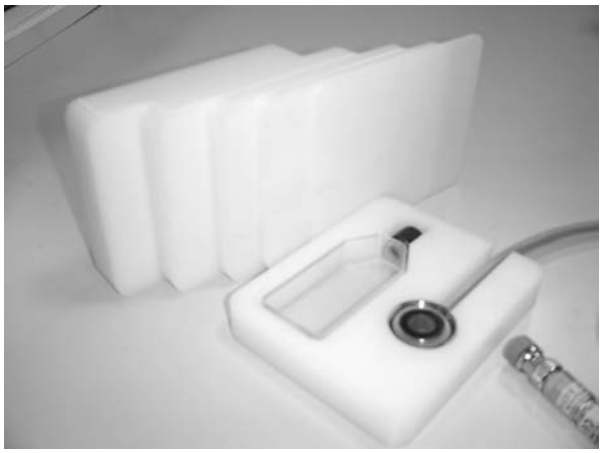

Fig.2. Irradiation materials for culture bottles

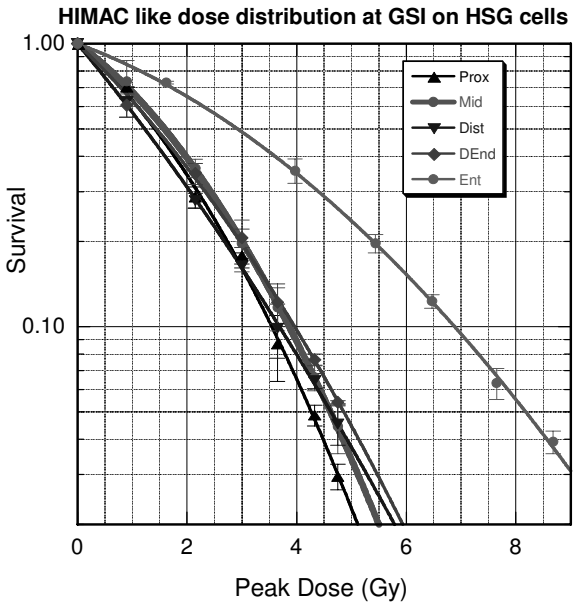

Fig.3. Survival curves of HSG cells exposed in T25 culture flasks with the HIMAC-like SOBP dose distribution at GSI at the proximal, middle, distal, distal end, and entrance positions.

Neutron dose angular distributions from high-energy ^{12}C ions stopping in various absorbers

H. Iwase, D. Schardt, and F. Gutermuth
GSI, Darmstadt

Using the irradiation system of the medical treatment unit (Cave M) at GSI, pencil-like beams of ^{12}C ions in the energy range of 100-400 MeV/u were stopped in thick targets of water, graphite, iron and lead placed at the reference point 100 cm behind the vacuum exit window. The beam intensity was monitored with a calibrated ionization chamber. Two kinds of neutron dosemeters, WENDI-II, a ^{3}He counter with polyethylene + tungsten moderator and BIOREM, a BF_3 counter with polyethylene moderator, were employed for the neutron dose measurements. The conversion factors of 3.2×10^9 counts/Sv for WENDI-II and 1.7×10^9 counts/Sv for BIOREM were determined with an ^{241}AmBe source. The REM-counters were placed at angles of 0, 5, 10, 20, 30, 60, 90, and 135° with respect to the beam axis. The distance from target center was 290 cm (0-30°), 250 cm (60°), 240 cm (90°) and 160 cm (135°). All data were normalized to a distance of 300 cm.

The measured angular distributions for a 12.8 cm thick water target are shown in Fig.1. The neutron dose per incident ion decreases rapidly between 0 and 20° and is most forward peaked for the highest beam energies.

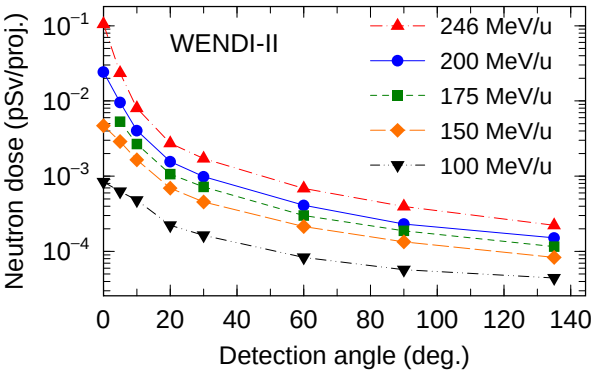

Figure 1: Neutron dose at 3m distance from a 12.8 cm thick water target (^{12}C primary beams)

Figure 2 shows a comparison of neutron doses measured with the REM-counters WENDI-II and BIOREM, and the neutron dose inferred from fluence measurements [1] with a BaF_2 scintillation detector for 200 MeV/u ^{12}C ions stopping in a 12.8 cm thick water target. The lower response of the BIOREM counter as compared to WENDI-II can be explained by the small sensitivity of BIOREM for neutrons above ~50 MeV, whereas WENDI-II has an improved energy response up to 5 GeV [2]. On the other hand, high-energy charged particles may increase the dose values of BIOREM at small angles. The BaF_2 fluence data, with a lower detection limit of 20 MeV, were converted into dose by convolution with the ambient dose equivalent h*(10) [3, 4]. The resulting dose angular distribution is in fair agreement with the WENDI-II data.

The neutron dose measured for various stopping materials (25.6 cm water, 20 cm graphite, 5 cm iron, and 5 cm lead) as a function of the incident ^{12}C energy is presented in Fig.3. The target thickness corresponds roughly to the range of 200 MeV/u ^{12}C ions in each material. At the highest energy the dose observed at 0° behind the water target is much higher than the dose behind the lead target. This is explained by the fact that the neutron production scales approximately with the mean number of nuclear interactions along the stopping path. Target dependences of neutron productions by 400 MeV/u ^{12}C were also investigated by Kurosawa et al. [5] and it gives similar tendency as the present results.

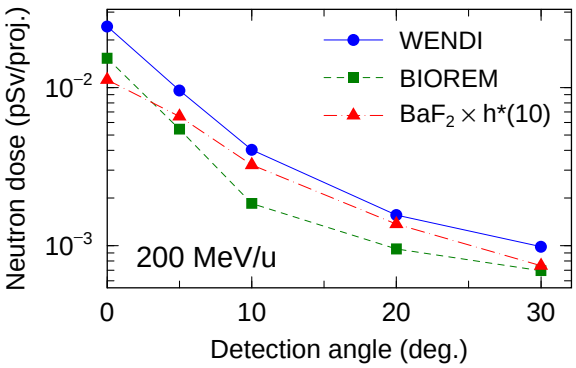

Figure 2: Comparison of neutron doses obtained from WENDI-II, BIOREM, and fluence measurements [1]

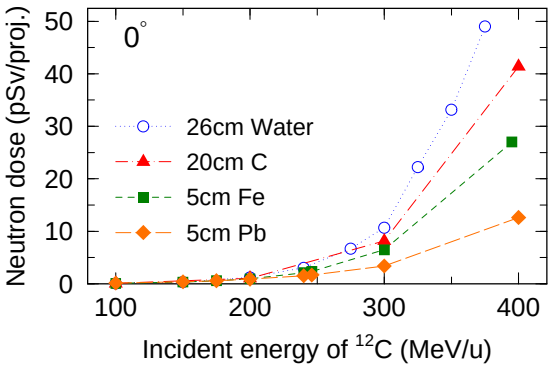

Figure 3: Neutron dose measured by WENDI-II at 0° from ^{12}C ions on various target

References

[1] K. Gunzert-Marx, Thesis, TU Damstadt, Nov. (2003)
[2] R. H. Olsher, et al., Health Phys. 79(2), 170 (2000)
[3] ICRU Report 66: Journal of the ICRU 1(3),(2001)
[4] ICRP 64: ICRP Publ. 74, Pergamon Press, (1996)
[5] T. Kurosawa, et al., Nucl. Sci. and Eng., 132, 30 (1999)

ACCS-OPD

Accelerator Operations and Development

Accelerator Operation Report

U. Scheeler, D. Wilms
GSI Darmstadt

This report describes the operation statistics of the accelerator facility in the year 2004. The data has been collected with the help of the program PROST [1]. Accelerator development and experiments are the topics of separate contributions [2], [3] and [4] to this annual report.

1. General overview

The year 2004 consisted out of four beam periods. Operating time started on January 14th with a beam period of about nine weeks. A power supply burnout of the extraction septa on January 24th led to an unintentional two week break of SIS operation. To ensure at least a minimum experimental program for the affected experiments, the beam time schedule for the rest of the first period was adapted.
The second operating block started after a three week shutdown at the end of March. It was scheduled to last until May 23rd. The High Current Injector was upgraded during the following shutdown, in the meantime the synchrotron tunnel was cleaned of smut and dirt caused by the fire in January. Accelerator structures, walls and ceiling had to be cleaned carefully. Operation started again on July 14th. The third beam period lasted until October 7th. The last beam period starts on October 27th with a length of 7 weeks.

Table 1: Overall beam time of the accelerator facility

	Total beam time 2004	Target time 2004	Target time 2003
UNILAC experiments	6644 h	5449 h	5100 h
SIS experiments	6384 h	5885 h	5775 h
ESR experiments		1225 h	682 h

Table 1 shows total beam time and achieved target time for different experimental areas. In 2004 accelerator operating time (number of working hours) decreased by 21 days compared to 2003, now amounting to 5952 hours. Nevertheless the reduced operation time has led to a higher amount of UNILAC target time. This result demonstrates the high level of time sharing operation at the UNILAC in 2004.
The available SIS operating time was at least 14 days longer than in 2003, although it had been reduced to 5560 h by the accident mentioned above. Therefore the higher amount of target time can be contributed to the increase in operating time. The growing usage of heavy ions like uranium, gold and bismuth led to a steep increase in scheduled ESR beam time. Beam was delivered to ESR for 1225 hours, a 100 % rise compared to 2003.
Altogether ion beams of 26 different isotopes from hydrogen to uranium were accelerated and delivered to 20 low energy experiments at UNILAC and 31 high energy experiments at SIS. As shown in Figure 1 UNILAC experiments mainly requested medium heavy elements, whereas light ions like Hydrogen, Carbon or Nitrogen and heavier elements were mostly used at SIS.

Figure 1: Accelerated isotopes in 2004

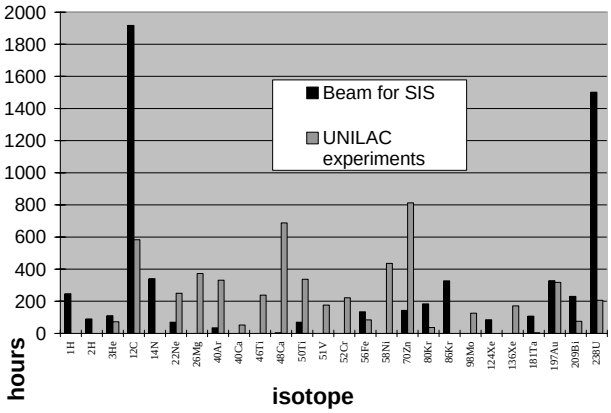

2. UNILAC Operation

The beam time for the UNILAC experiments is summarized in table 2. The column “fraction” contains the ratio between "number of hours for listed category" divided by "total amount of beam time" in percent. It indicates the efficiency of the accelerator operation.

Table 2: Beam delivered to UNILAC experiments in 2004

	(h)	Fraction
Target time for experiment runs	5449	82,0%
Beam for experiment tests	19	0,3%
Accelerator development	97	1,5%
Accelerator tune-up	394	5,9%
Ion source replacement	182	2,7%
Unscheduled down time	371	5,6%
Retuning	104	1,6%
Stand-by	28	0,4%
Total beam time	6644	

The increase in total beam time mainly led to a higher amount of target time since the amount of unscheduled downtime remained stable. Hence the percentage of beam time for experiments increased by 1.6% compared to 2003. The growing number of accelerated isotopes caused a greater amount of isotope changes which resulted in a higher amount of tuning time. In contrast, the time spent for accelerator development

declined in 2004, partly because the accelerator beam time at the end of the first beam period was canceled due to the SIS break.
A closer look at the unscheduled down time reveals that it can be attributed to failures of rf-amplifiers (110h), injectors (104h), computer control (5h), vacuum system (29h), magnet power supplies (40h), infrastructure (36h), and others (47h). The rf system down time originates mainly from instabilities in time sharing operation. Besides technical faults the increase of injectors down time results from difficult operation conditions due to the experiment request.

Table 3: UNILAC beam delivered to SIS in 2004

	(h)	Fraction
Beam available for SIS injection	6449	89,4%
Accelerator development	30	0,4%
Ion source replacement	81	1,1%
Accelerator tune-up	232	3,2%
Unscheduled down time	403	5,6%
Retuning	18	0,2%
Total beam time	7213	

Table 3 displays the beam time provided by the UNILAC for SIS injection. While beam availability is down by 1.8 % compared to 2003, time for tune up and down time are on the rise. A few times machines were reconfigured in parallel to running experiments after a change of the accelerated isotope.

Figure 2: Beam energies of the UNILAC experiments

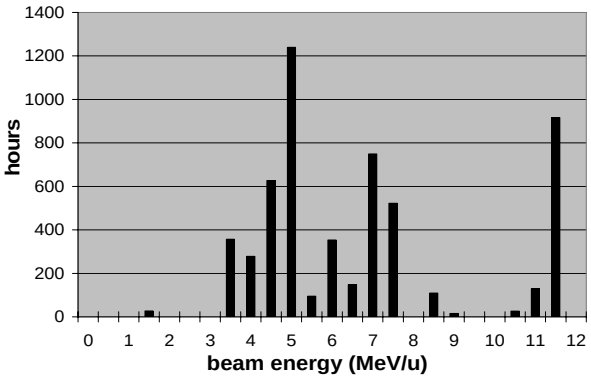

In Figure 2 the target time of the UNILAC experiments (without beam injected into SIS) is displayed versus beam energy. Beam energies in the range from 4 to 6 MeV/u mainly result from experiments for super heavy element synthesis, nuclear chemistry experiments took place at 7 MeV/u and energies at 11.4 MeV/u were used for material science, biology and plasma physics experiments.

3. SIS Operation

Operation statistics for SIS are shown in table 4. Compared to last year the total target time slightly increased. The decrease of beam time for the target area is compensated by an increase of beam delivered to the ESR. The fraction of beam time for the cancer therapy program remains nearly constant.
The main part of down time is related to problems with the high voltage power supply of the extraction septum. The 300-hour break caused by the fire in the ring tunnel is not included in the down time statistics. 101 hours of power supply down time can be divided into 60 hours for high voltage devices and 41 hours for magnet power supplies. Commissioning of new vacuum device control is responsible for reduction of vacuum down time from 56 (in 2003) to 33 hours in this year. Other categories of technical problems besides power supply and vacuum led to the following loss in beam time: infrastructure (15h), rf-amplifiers (5h), beam diagnostics (6h), controls (15) and others (59h).

Table 4: SIS operation time in 2004

	(h)	Fraction
Beam for target area	3360	52,6%
Therapy	1250	19,6%
Beam delivered to ESR	1225	19,2%
Beam for experiment tests	50	0,8%
Total target time	5885	92,2%
Accelerator development	100	1,6%
Accelerator tune-up	154	2,4%
Unscheduled down time	245	3,8%
Total beam time	6384	

Figure 3: Beam energies of the SIS experiments

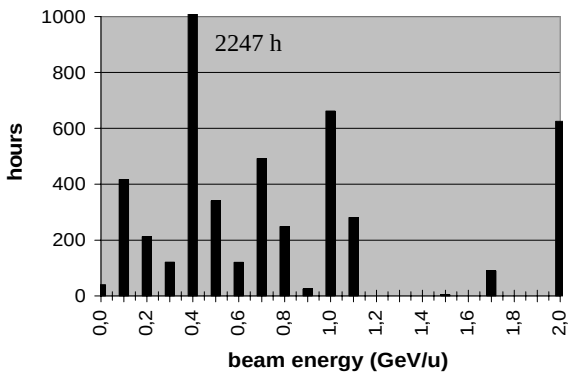

Figure 3 shows the beam time versus energy for the SIS experiments. The high amount of target time at energies about 400 MeV/u stems from the acceleration of 12C beam for cancer therapy. The 2 GeV/u beam was needed for pion production. As main users of gold, lead and uranium beams, the ESR got beam with energies up to 400 MeV/u and the fragment separator up to 1GeV/u.

References

[1] **PR**ogramm für **O**perating und **ST**atistik
[2] W. Barth et. al. UNILAC Status and Developments
[3] P. Spiller et. al. SIS Status Report
[4] M. Steck et. al. ESR Operation and Development

Ion Source Development and Operation

P. Spädtke, J. Bossler, M.Galonska, F. Heymach, R. Hollinger, R. Iannucci, R. Lang, K.D. Leible, K. Tinschert, GSI Darmstadt, R. Mayr, private consulting

ECR Ion Source (ECRIS)

Regular operation at the High Charge State Injector (HLI) was performed for: $^{1}H_2^+$ (8 days), $^{3}He^{1+}$ (11 days), $^{12}C^{2+}$ (100 days), $^{22}Ne^{5+}$ (16 days), $^{26}Mg^{5+}$ (16 days), $^{48}Ca^{7+}$ (19 days), $^{52}Cr^{7+}$ (11 days), $^{58}Ni^{9+}$ (15 days), $^{70}Zn^{10+}$ (29 days), $^{124}Xe^{18+}$ (7 days), and $^{136}Xe^{18+}$ (12 days).

Besides carbon $^{12}C^{2+}$ for therapy, $^{1}H_2^+$ and $^{58}Ni^{9+}$ all other ions were rare isotopes which had to be produced from highly enriched isotope material, most of them metals evaporated with the GSI standard oven.

The upgraded movable extraction system at the ECR injector test setup (EIS) was used in accel decel mode to perform extended studies on space charge compensation of the extracted ion beam and on the influence of backward accelerated electrons. The negatively biased screening electrode is mounted with a fixed gap width (≈ 7.5 mm) to the ground electrode. Both electrodes are movable in longitudinal direction from 16 mm to 37 mm distance between the plasma electrode aperture and the front plane of the screening electrode. This adjustment can be made during operation by remote control. Space charge compensation of the ion beam becomes increasingly important for the beam transport when the intensity rises by more than one order of magnitude as it is to be expected for the next generation of fully superconducting ECR ion sources [2],[1]. The effect of space charge compensation was demonstrated in simulation based exactly on experimental data.

Besides the challenging design of the magnet system and the cryostat of a superconducting ECRIS the extraction of ion beams of high intensity will be a crucial problem. In order to investigate such beams the CAPRICE ECRIS at the EIS was operated in a high density mode in order to extract considerably higher ion currents than in usual mode. Mainly to simplify the charge state distribution, and to achieve a higher extraction current, helium is provided to the plasma only. In case of the intense He beams the influence of the space charge compensation on the beam transport through the fixed acceptance of its LEBT was investigated. It could be shown that there is a linear dependence of the minimum screening voltage for space charge compensation on the extracted ion current but roughly independent from the extraction voltage. Accompanying computer simulations showed that good matching of plasma density and applied field strength is required to achieve a flat plasma boundary, which gave the best transmission at highest achievable intensity.

Both, computer simulations and experiments could show that variation of electrode distance at constant extraction voltage or variation of the extraction voltage at fixed electrode distance are equivalent for the formation of the plasma meniscus. For the beam transport, however, there is a different behavior due to the varying aspect ratio when changing the electrode distance. The present investigations indicate that high currents from ECRIS will be extractable with a decreased extraction distance, keeping the plasma boundary as flat as possible.

The modified accel decel extraction system of CAPRICE consists of the fixed plasma electrode, an intermediate screening electrode and the ground electrode.

The influence of the negative screening voltage could be clearly demonstrated. After reaching a specific negative potential (typically about -0.5 kV), the drain current of the positive voltage power supply drops and the analyzed current increases. Furthermore the intensity of visible light coming from the source is decreasing. These are clear indications of screening the electrons of the extracted beam from the positive source potential. Instead of being accelerated into the source plasma, these electrons will compensate the positive space charge created by the ions of the drifting beam.

In case of operation with an oven, which is inserted into the source on axis at the injection side (at the same position as the gas injection tube), the electrons which are accelerated from the beam to source potential cause an additional, undesired oven heating. The positive feedback of additional heating by the accelerated electron current with increasing density of neutrals and ions and therefore increasing electrons, can provoke an unstable operation especially for metals which are evaporated at low temperature as e. g. Ca. Generally, a complete decoupling of ion beam extraction and plasma generation would be desired. To make use of this blocking effect on the backwards accelerated electrons a simplified preliminary accel decel extraction system was also mounted at the ECRIS of the HLI. It was used in a ^{48}Ca beam time to prevent the parasitic oven heating by electrons. It could successfully improve the operating stability. Even the analyzed intensity $^{48}Ca^{7+}$ could be considerably enhanced.

Penning Ion Source (PIG)

Regular operation was performed for: $^{12}C^{1+,2+,3+}$ (27 days), $^{40}Ar^{2+}$ (7 days), $^{40}Ca^{3+}$ (5 days), $^{46,50}Ti^{2+}$ (25 days), $^{51}V^{2+}$ (10 days), $^{56}Fe^{2+}$ (8 days), $^{58}Ni^{3+}$ (6 days), $^{86}Kr^{2+}$ (7 days), $^{97}Mo^{4+}$ (7 days), $^{197}Au^{4+}$ (22 days), $^{209}Bi^{4+}$ (8 days), and $^{238}U^{4+,6+}$ (48 days).

Theoretical, experimental, and technical investigations to increase the available ion currents resulted in the design of an accel-decel extraction system. Due to financial restrictions the necessary upgrade of the regular ion sources for operating had to be postponed.

High Current Ion Sources (MUCIS, CHORDIS, MEVVA, VARIS)

Regular operation was performed for: $^{2}H_3^{1+}$ (22 days), $^{14}N_2^{1+}$ (17 days), $^{40}Ar^{1+}$ (5 days), $^{80}Kr^{2+}$ (10 days), $^{86}Kr^{2+}$ (13 days), $^{181}Ta^{3+}$ (14 days). Tantalum was provided the first time for regular beam time operation from a vacuum arc ion source. To decrease the radioactive weist

we propose $^{181}Ta^{3+}$ for accelerator experiments as substitute for $^{238}U^{4+}$. During the Ta beam time we made improvements under operating conditions, concerning reliability (use of electron welded cathode material, specific cathode preparation, specific finishing), beam noise (adding argon gas to the discharge) and intensity (using MEVVA instead of VARIS). After these improvements we could provide more then 10 emA of tantalum for injection into the HSI with good quality.

Computer Simulations

We continued computer simulations of the combined system extractor and post accelerator using the KOBRA3-INP code [3]. The characteristics of the ion beam extracted from one of the GSI high current ion sources MEVVA and VARIS in the injection beam line for the UNILAC was investigated. The results show that the losses of the extracted ion beam propagating through the beam line mainly occur in the drift space between the extraction system and the acceleration gap. The intensity of the ion beam behind the acceleration gap is not sensitive to the emission current density in the range of 180 mA/cm^2 to 230 mA/cm^2. Simulation also indicates that one of the optimized extraction systems is suitable for delivering an ion beam at higher emission current density, with lower beam emittance; and a 19-hole extraction system might be used to increase the intensity of the delivered ion beam compared to the regularly used 13-hole extraction system. Simulation also confirms that the shape of the aperture plays an important role in the beam formation. Simulation quantitatively supports the experimental result that the ion beam is space charge compensated along the drift sections; otherwise the transport would not be possible. Moreover, the experience obtained through this work will provide the base for optimizing the extraction system and the acceleration gap for the ion source [4] furthermore.

Emittance measurements at the HSST

The slit grid emittance measurement device from the PIG test bench has been temporally moved to the high current test bench HSST. Goal of the measurements was to compare the ion beam emittance for gaseous ion sources and vacuum arc ion sources. Up to now we assumed that the emittance of high current ion beams is given by the geometry of the multi aperture extraction system only. As shown with computer simulations we found different emittances for MUCIS and MEVVA ion sources because of the different generation processes. This could explain different transmission for the different ion sources in the LEBT section of the HSI during the regular beam time.
In a first step the emittance of an extracted argon ion beam from a CHORDIS has been measured. Here the commonly used 13-hole extraction system was installed. As expected and shown earlier the emittance of the ion beam is dominated by the geometry of the multi aperture extraction system. The divergence angles are in the range of 45 mrad, which reflects the cold plasma in multi cusp ion sources. Another important result is, that the plasma density is homogenous in front of the extraction area, although the magnetic field configuration of the plasma generator is a multi cusp pole. In some cases we observe a relatively high fraction of neutrals (up to 20 %) in the extracted beam. Charge exchange take place in the extraction system or close behind, where the residual gas pressure and ion density have reached their maximum. This has to be taken into account for further computer simulations. Emittance measurements for a VARIS generating a titanium ion beam show different results: the divergence angles are 75 mrad. Figure 1 (left) shows a measured emittance pattern of the titanium ion beam. The total emittance is 500 mm mrad, the effective emittance 950 mm mrad. The hole circle of the outer apertures defines the emittance pattern in space, which is 20 mm. Figure 1 (right) shows a simulated emittance pattern of the extracted ion beam. As a result the

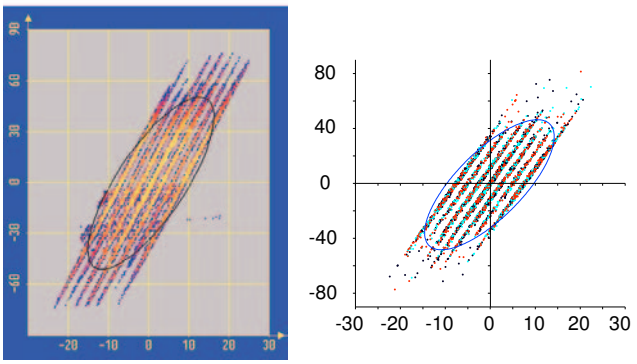

Figure 1: Left: Emittance pattern and KV ellipses of a titanium ion beam, extracted from a VARIS with multi aperture extraction system (13 holes, hor.: mm, vert.: mrad), right: Emittance pattern close behind the extraction system (2 cm downstream) of the simulated beam

rms emittance is a factor of 1.5 larger. Due to the explosive generation process of the ions, the ion temperature is much more higher compared to multi cusp ion sources with ion temperatures of tenth of eV. We measured ion temperatures for vacuum arc ion sources in the range of few eV [5]. In addition, vacuum arc ion sources show high longitudinal and transverse ion energies in the plasma. The longitudinal ion energy reduces the space charge forces in the extraction gap resulting in a higher extractable emission current density. Transversal energies as well as a high ion temperature increase the divergence angles of the ion beam. Large divergence angles lead to beam losses in the LEBT section, especially between extractor and post acceleration. We will improve the magnetic field configuration of the VARIS to ensure a more homogeneous plasma distribution close to the extraction system.

References

[1] RTD proposal: Innovative ECRIS; IHP-INF-99-1
[2] D. Leitner, SC-ECRIS VENUS with 28 GHz, Intl. Workshop on ECRIS, Berkeley, 2004
[3] INP, Junkernstrasse 99, 65205 Wiesbaden, Germany
[4] W. Xiang, GSI Scientific Report 2004-02
[5] M. Galonska, Rev. Sci. Instrum. 75 (5), 1592, 2004

UNILAC Status and Developments

W. Barth, L. Dahl, L. Groening, S. Richter, S. Yaramyshev

GSI Darmstadt

Status of Operation

During the beam time in 2003 a carbon beam from the ECR ion source was mainly accelerated via the high charge state injector (HLI) in the UNILAC for the SIS-injection like in the years before [1]. Several UNILAC experiments used the beam with high duty factor additionally. Additionally, the ECR source was in operation for the production of various isotopes (2H, ^{3}He, ^{22}Ne, ^{26}Mg, ^{40}Ar, ^{48}Ca, ^{52}Cr, ^{70}Zn, ^{124}Xe). Mainly experiments for the super heavy element synthesis (SHIP) and the nuclear chemistry requested beam time for the experimental hall. Additionally, ion beams from the ECR were injected into the SIS (Rising collaboration, ESR-experiments). The Penning ion source provided carbon, calcium, argon, titanium, vanadium, ferric, krypton and molybdenum beams with medium intensity, especially when the ECR was in use for the irradiation of patients. For heavy ions (^{197}Au, ^{207}Bi, ^{238}U) a beam from the PIG source was accelerated via HSI in the UNILAC with short pulses mostly for the injection into the SIS 18. Additionally $^{238}U^{4+}$ was used for HSI-RFQ-Tests. The MUCIS provided a high current beam for the re-commissioning of the HSI after shutdown 2 ($^{40}Ar^{1+}$) and for different high energy experiments with high intensities ($^{28}N_2$, ^{80}Kr, ^{84}Kr). The MEVVA ion source delivered only once a high intensity tantalum beam, accelerated via HSI in the UNILAC for SIS injection. Due to serious problems with the delivery of uranium cathodes no high current uranium beam operation was performed in 2004. Besides only 97 hours (209 hours in 2003) for accelerator tests were available, resulting in a reduced program for machine development.

Summary of machine experiments

A major concern with respect to the required uranium beam properties for FAIR is the brilliance (beam current divided by its emittance) of the beam injected into the SIS 18. Although the currents were increased considerably during the recent years, the transverse emittances still exceed the tolerable values by about a factor of two. Short machine experiments lasting few hours at the end of some beam time blocks indicated qualitatively that the UNILAC emittances might by reduced by changing the magnetic focusing strength along the Alvarez drift tube linac. However, to allow for quantitative conclusions dedicated experiments lasting several days are mandatory. Accordingly, a physics experiment was proposed officially to the Experiment-Ausschuß (EA) by the UNILAC- and by the High Current Beam Physics group [2]. The proposal is part of a funded FP6 activity and it was approved by the EA. This is the first dedicated accelerator experiment at GSI that was proposed to and approved by the EA to the same conditions as any other physics experiment. It is part of the FP6 contract with the EU and it will take place during the next long shutdown of the SIS18. Beam transmissions as well as beam emittances before and after the DTL will be measured as a function of the magnetic focusing strength along the DTL. Together with the proposed upgrade of the Alvarez quadrupole power supplies the experiment is expected to result in an increased uranium beam brilliance in order to get closer to the FAIR requirements.

Upgrade of the HSI-RFQ

During the shutdown in Mai-July 2004 the new mini-vanes of the HSI-RFQ had been manufactured and copper plated to improve the quality of its surface. The original design modulation of the rods was used, except the Input Radial Matcher (IRM) at the entrance of the RFQ. The IRM (≈ 12 cm long) was redesigned for the increase of transmission through the system consisting of the matching quadrupole quartet and the RFQ. As it was shown by simulations with the DYNAMION code, a slight change of the aperture leads to a 10 - 15 % increase of the transmission for high current U^{4+} beams. For precise numerical simulations all available experimental data were used, as results of the emittance measurements in the Low Energy beam Transport line (LEBT), the measured distribution of the magnetic field in the quadrupole lenses, the geometry of the mini-vanes "as fabricated", and the measured misalignments of the RFQ sections. The external electrical field in the IRM and in the regular part of the RFQ was precisely calculated taking the geometry of the mini-vanes and of the tank into account.

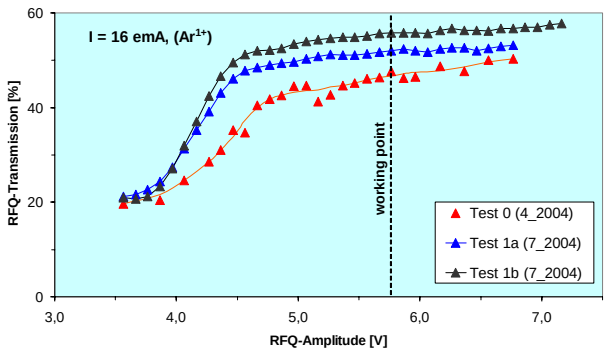

Fig. 1: Measured transmission for a high current argon beam before and after the upgrade of the RFQ-electrodes [3].

After the re-commissioning of the RFQ, the experiments with a high current argon beam (16 emA) and a low current uranium beam (< 0.5 emA) confirmed the results of simulations. For a low current U^{4+} beam a transmission of 100% was reached for the first time since the HSI-RFQ was commissioned in 1999; experiments with high current uranium beams were not carried out due to the lack of the required cathodes for the MEVVA ion source. In Fig. 1 the transmission for a 16 emA Ar^{1+} beam through the HSI-RFQ before

and after the upgrade is shown as a function of the inter-vane voltage.

The new IRM requires new matching parameters of the beam, leading to a smaller beam diameter and less perturbation of the beam emittance in the matching quadrupole lenses. Results of beam emittance measurements before the quadrupole lenses and at the entrance of the RFQ for the old and for the new matching conditions - measured during the shutdown - are presented in Fig. 2.

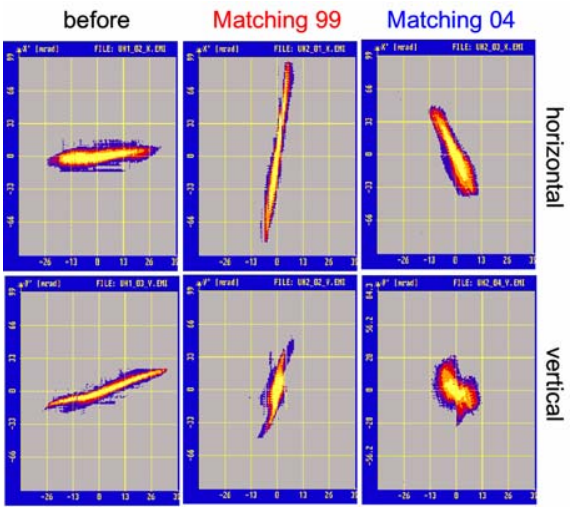

Fig. 2: Measured U^{4+} emittance before (left) and after the quadrupole quartet for the two matching cases. The transmission for the new matching (2004) is 15 % higher with respect to the former matching.

After five years of HSI-RFQ operation the electrode surface was damaged along the whole structure, requiring significant higher input rf-power during operation at the design limit. The electrodes were reproduced and additional copper plating was done. A dedicated procedure for the control of the copper-plating was proposed [4]. For each electrode precise measurements of the fabrication accuracy were done and on this base the size of the copper layer was calculated. After an exchange of the RFQ mini-vanes, the required rf-power for the acceleration of a $^{181}Ta^{3+}$ beam decreased from 650 kW to 380 kW. The old RFQ-electrodes (after disassembly) and the new electrodes (before assembly) are shown in Fig. 3.

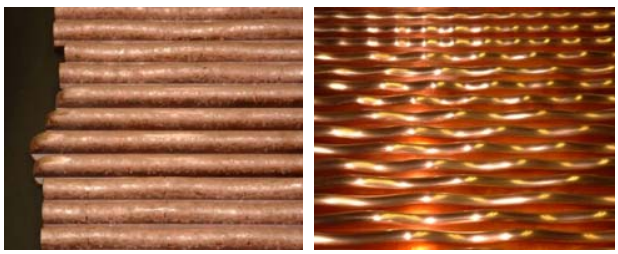

Fig. 3: Upgrade of the HSI-RFQ; Electrodes after five years of operation (left), new electrodes before assembly (right).

Longitudinal emittance measurements

The measurement of the longitudinal emittance is essential to perform 6d-matching to the SIS 18 especially for space charge dominated ion beams. The emittance measurement device [1] was additionally equipped with a luminescent screen. Now the energy- and phase-spread can be measured simultaneously within one pulse. A camera is able to provide a video signal transferred to the control room. Fig. 4 presents the influence of the rf-phase of a single gap resonator, placed approx. 22 m upstream. The dipoles in the transfer channel provide the dispersion and a 108 MHz chopper deflects the micro bunches vertically.

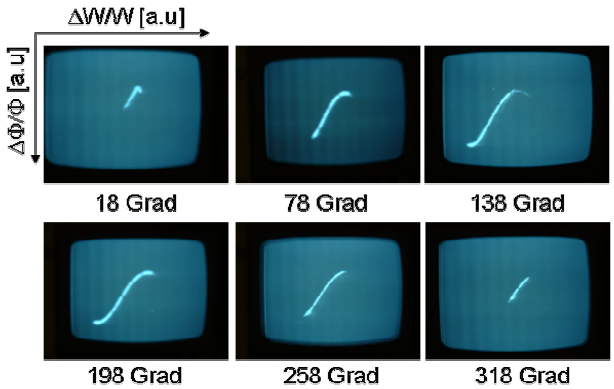

Fig. 4: Screenshots of the measured longitudinal emittance for different rf-phases of a single gap resonator (arbitrary units).

The different rf-phases result in the expected variation of the bunch length and energy spread. For the commissioning of the luminescent screen a low intensity (120 eμA) uranium beam with a typical pulse length of 200 μs was used. First investigations were also carried out with a intense Ta-beam of 2.5 emA in a 100 μs macro-pulse. To reduce the pulse power on the screen, the beam was attenuated through an iris in the transfer channel: the positioning and diminution of that iris is accurate to achieve the required attenuation allowing sufficient signal strength. In the near future the camera will be substituted by a digital camera with a frame grabber, allowing quantitative measurements of the longitudinal emittance.

References

[1] W. Barth, et. al., *UNILAC Status and Developments*, Annual Report 2003.

[2] I. Hofmann et al., *U212 Experimental study of high-intensity effects on beam quality in the DTL section of the UNILAC*, Approved proposal to the Experiment-Ausschuß of GSI, September 2004.

[3] W. Barth, et al., *Development of the UNILAC Towards a Megawatt Beam Injector*, Proc. of the XXII Linac Conf., Lübeck, Germany, (2004).

[4] S. Minaev et al., *Matching of the capacity distribution for the new HSI-RFQ electrodes by individual copper plating of all elements*, Note IAP-ACC-080604, Univ. Frankfurt, (2004).

SIS18 Status Report

P. Spiller [1], K. Blasche [1], U. Blell [1], O. Boine-Frankenheim [1], P. Forck [1], G. Franchetti [1], B. Franczak [1], I. Hofmann [1], P. Hülsmann [1], M. Kirk [1], H. Klingbeil [1], A. Krämer [1], P. Moritz [1], C. Omet, H. Ramakers [1], G. Breitenberger [1], H. Reich-Sprenger [1], U. Scheeler [1], P. Schütt [1] and D. Wilms [1]

[1]GSI Darmstadt, Germany

In the frame of a dedicated machine development run with N-ions, operation with high space charge tune shift was demonstrated. About 10^{11} N-ions could be injected leading to an incoherent tune shift of up to dQ_v=-0.2. By means of the new residual gas profile monitor, fast emittance blow-up was observed during the transition from the high current working point to the working point required for slow extraction.

Since the incoherent tune shift is getting more often an origin for beam losses at high current operation, the resonance diagram was subject of a number of machine experiments. A scanning method to determine strength and location of the resonances was developed. Several scans of the tune diagram around the standard working point have been performed [1].

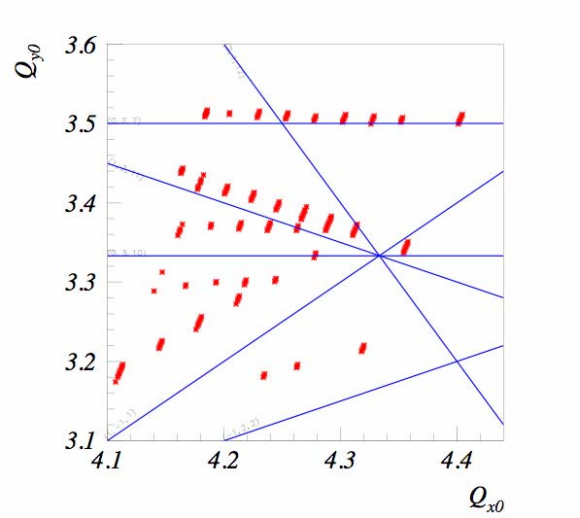

Figure 1: Resonance diagram of the SIS18. The lines mark the theoretical predictions and the dots indicate measured beam loss.

The installation of the set of new correction multipoles could be finished in 2004. Based on systematic resonance investigations, the correction coils will be applied to compensate the most relevant and limiting resonances.

In this context measurements on the influence of a longitudinal motion in an Rf bucket on the beam losses at high current operation were performed. First indications for enhanced losses caused by a trapping in resonances after Rf bunching were obtained. Since such phenomena may have an important impact on the SIS100 design, accompanying code developments and simulations are being conducted.

Due to a not optimal design of the high voltage frame of the residual gas profile monitor an asymmetric noise offset was generated a maximum voltage. The design of the high voltage frame was changed and the relevant components were replaced during a shut down. During a number of following machine experiments the new monitor was successfully commissioned and its capability for precise time resolved beam profile measurement was demonstrated.

A number of experiments requesting slow extraction suffered from a not satisfying microstructure at slow extraction during high intensity operation. The usual measures for smoothing the spill structure did not provide the required conditions. As a first step a system for a precise time structure analysis has been planned and will be taken into operation in 2005. Based on this system options for optimizations of the micro structure will be developed.

Machine experiments were performed with the goal to demonstrate the function of the new collimator concept realized in section S12. The residual gas pressure observed under the influence of the installed cryo pump and desorption gases from stopped beam on the collimator.

The design of the new bunch compression cavities was finished. The supply unit for the final amplifier was ordered and tested. The choice of the magnetic alloy core materials for the cavities has been made and cores for two Rf gaps were ordered. The final concept is to build two separate Rf compression systems, one equipped with amorphous and one equipped with nanocrystalline core material. The call for tender for the manufacturing of the first Rf compression system was carried out and the components were ordered.

The development of a new valve control was finished. The new system was installed and successfully commissioned.

A fail function of the high voltage supply unit of the electrostatic extraction septum caused a fire in the SIS tunnel. The soot and dust covered most of the accelerator components and the infrastructure in the SIS. With the help of external, specialized companies the synchrotron and most of the infrastructure had to be cleaned in two cleaning cycles.

References

[1] G. Franchetti, B. Franczak, and P. Schütt, GSI Note GSI-Acc-Note-2004-05-001

ESR Operation and Development

K. Beckert, P. Beller, B. Franzke, F. Nolden, U. Popp, A. Schwinn, M. Steck
GSI Darmstadt

1 Operation for Physics Experiments

Various physics programs have been continued employing stored cooled beams in the ESR. Highly charged ion beams were used at the injection energy, but quite often at lower energies achieved by deceleration in the ESR.

Amongst the ion beams used at the injection energy are hydrogen-like uranium ions for precision spectroscopy of dielectronic resonances. The U^{91+} beam at 400 MeV/u was cooled by the stochastic cooling system, whereas the electron beam of the electron cooler was detuned in velocity. The electron beam was operated as a target of free electrons with a variable relative velocity. Measurements of the beam quality (see 2.1) evidenced an increase of the beam emittance and momentum spread by a factor of two to three compared to the beam parameters achievable with electron cooling, which is still acceptable for the experiment.

For precision spectroscopy of the hyperfine splitting in the lithium-like charge state, Bi^{80+} ions at about 400 MeV/u were stored and cooled by electron cooling. A laser beam interacted with the ion beam in the electron cooling straight section. The alignment was optimized by special scrapers installed in the toroid magnets of the electron cooler.

For investigations of recombination between ions and electrons the electron beam provides a target of quasi-free electrons. The detections of x-rays emitted in the recombination process was achieved by installing high resolution germanium detectors at the entrance and exit of the cooling section. The Doppler effects were reduced by deceleration of the bare heavy ion beam to an energy of 23 MeV/u. Intensities of the decelerated ion beam of 2×10^7 were achieved reproducibly by deceleration during about 10 s without intermediate cooling.

As a new experimental installation the electron spectrometer after the internal gas jet target was commissioned. A dipole magnet allows the deflection of electrons exiting from the target with the velocity of the circulating ion beam into a beamline on the inner side of the ring. This beamline is equipped with elements for the transport of the electrons to special detectors. The distortion of the closed orbit of the ion beam due to the dipole magnet, deflecting the electrons into the beamline, must be corrected by the horizontal correctors installed in the ring dipole magnets. Proper correction of the orbit distortion and automated control of the correction elements allow a variation of deflection strength for the extracted electrons even with a stored ion beam. The correction scheme keeps the position and direction of the ion beam in the interaction point with the gas jet constant.

Another new set-up towards nuclear physics experiments at the internal target is a silicon strip detector for recoils which was installed in the scattering chamber of the internal target. Although this detector is only bakeable at moderate temperature (below 150°C), after its installation a pressure in the low 10^{-11} mbar range was achieved. First tests of the detector with the gas jet operated with methane, which provides highest target thickness of hydrogen, were successful.

A new calorimetric detector for x-rays was installed on a thin window of the internal target scattering chamber. It was commissioned with a beam of bare uranium ions.

The first experiments on laser cooling of C^{3+} were performed. The possibility of using electron cooling as precooling for laser cooling was described before [1]. A significant improvement could be observed for the lifetime of C^{3+} at 120 MeV/u. This is a result of careful inspection of the vacuum system, a few minor leaks could be closed. The lifetime was improved by more than an order of magnitude, it was 6 min compared to 20 s in the year before. This considerable improvement is mainly attributed to a reduction of heavier components in the residual gas, which have strongly increased cross section for the ionization of the circulating ion beam. For the laser cooling experiment a gentle bunching of the ion beam was required in order to provide a counteracting force for the ions which are decelerated by the laser. A sinusoidal rf of low amplitude (a few Volts) was applied to the longitudinal exciter of the BTF diagnostics system. This method gave more flexible control of the rf voltage and avoided the noise expected from the power amplifiers of the standard rf system. Results of the laser cooling experiment are described in a separate report [2].

2 Machine Development

2.1 Comparison of beam parameters with stochastic and electron cooling

It has been shown that stochastic cooling is fast for hot ion beams, whereas electron cooling is powerful when the ion beam has been cooled down [3]. For the typical electron current of 0.25 A the cooling time immediately after injection with electron cooling is in the order of 10 s, for stochastic cooling the cooling time is about an order of magnitude shorter. When the ion beam is cooled down, the stochastic cooling time basically does not change, electron cooling, however, provides cooling times in the millisecond range. This increased cooling rate results in lower equilibrium beam parameters which are finally limited by intrabeam scattering.

A comparison of the equilibrium beam parameters for stochastic and electron cooling is shown in Fig. 1. Values for 25 and 250 mA electron current are shown, stochastic cooling was optimized by reducing the rf power with increasing ion intensity in order to have optimum gain. Even with 25 mA electron current better beam quality is obtained than with stochastic cooling. The cooling rate in equilibrium with intrabeam scattering rate is consequently higher with electron cooling. The reduction of the electron current by a factor of ten, resulting in a cooling rate change by the same factor, demonstrates the weak dependence of the equilibrium values on the cooling rate. Stochastic cooling consequently provides even less cooling rate. The different cooling rates in transverse and longitudinal degree of freedom has two reasons. Stochastic cooling strengths in the longitudinal and transverse degree of freedom are decoupled and can be chosen independently, electron cooling provides most powerful cooling in the longitudinal degree of freedom.

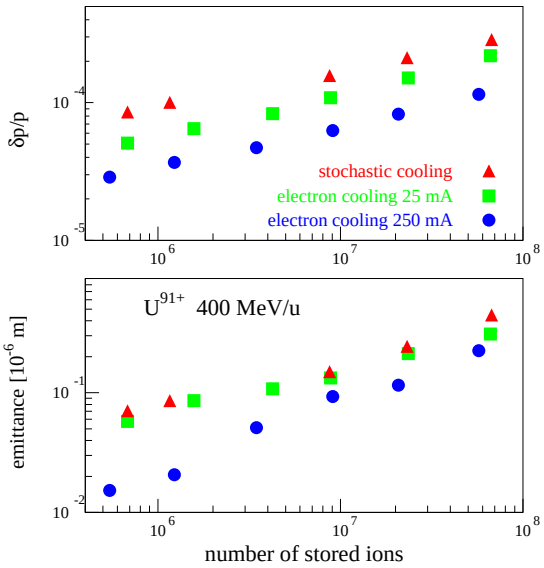

Figure 1: Comparison of momentum spread and horizontal emittance of a U^{91+} beam at 400 MeV/u cooled by stochastic cooling and by electron cooling with two electron currents.

2.2 *Cooling above transition energy*

Cooling of high energy beams in proposed accelerator projects will require cooling above transition energy. The isochronous mode of the ESR [4] allows operation of the ESR with a focussing setting with a transition energy $\gamma_t = 1.37$. By storing beams with relativistic factor γ exceeding the value of the transition energy, the ESR allows studies of the performance of cooling above transition energy.

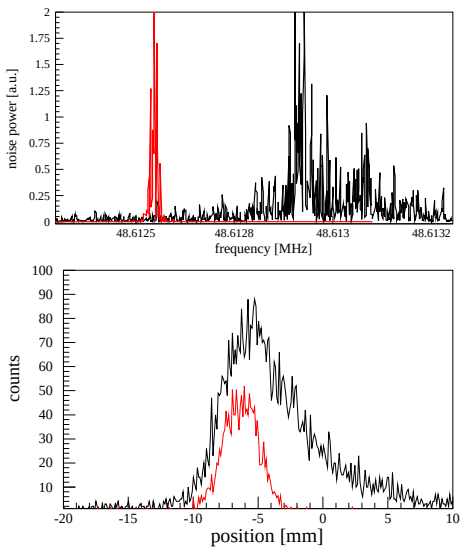

Figure 2: Distribution of a cooled Kr^{36+} beam above transition energy observed by Schottky noise analysis and with a beam profile monitor. With both methods the low energy particles are on the right hand side of the spectrum. Distributions are for two particle numbers, $N = 5 \times 10^5$ in red, $N = 1 \times 10^8$ in black.

For the experimental demonstration of cooling above transition energy a Kr^{36+} beam was injected with an energy of 380 MeV/u and electron cooling was applied. It was observed that with an electron current of 0.25 A the ion beam was cooled to the final equilibrium value in about 10 s, not significantly different from the cooling time for the same ion species in the ESR standard ion optical mode which has a transition energy $\gamma_t = 2.35$.

When the ion beam had been cooled down to a steady state, the beam profile was measured in the usual way with a residual gas ionization monitor and the frequency spread of the Schottky noise was analyzed. The measured transverse profiles and the longitudinal distribution showed no peculiarities for low ion beam intensities. At larger beam intensities strong longitudinal self bunching was observed on bunch probes installed for position measurement of a bunched beam. For intensities in the 10^8 range the Schottky spectra exhibited a strong tail due to low energy particles (Fig. 2). This low energy tail was also observed in the beam profile monitor. The dispersion function at the beam profile monitor location is about 40 m, in agreement with the measured extension of the low energy tail in the horizontal beam profile.

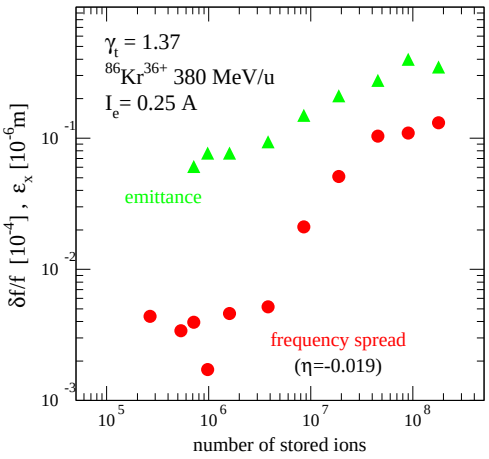

Figure 3: Momentum spread and horizontal emittance of the cooled Kr^{36+} beam stored with an energy exceeding the transition energy of the storage ring.

Analysis of the Schottky noise signal evidenced a nearly linear increase of the frequency spread with intensity for ion beam intensities exceeding 10^7 stored ions (Fig. 3). For higher beam intensities the frequency spread was proportional to the momentum spread (proportionality factor $\eta = -0.019$), but at low intensity the frequency spread was constant, due to the stability of the magnetic bending field. The beam emittance increased, similar to measurements in the standard mode, with the square root of the beam intensity. The strong increase of the momentum spread with intensity at higher intensities is attributed to the onset of microwave instabilities causing additional longitudinal heating of the ion beam. The measured frequency spread for higher intensities agrees well with the theoretical threshold value for microwave instabilities.

References

[1] M. Steck et al. GSI Scientific Report GSI 2004-1.
[2] U. Schramm et al., contribution to this report.
[3] M. Steck et al. GSI Scientific Report GSI 2003-1.
[4] M. Hausmann et al., Proc. of the 6^{th} Europ. Part. Acc. Conf., Stockholm, 1998, 511-513.

RF Development for the SIS12/18 Upgrade Program

H. Klingbeil[1], P. Hülsmann[1], G. Schreiber[1], P. Moritz[1], M. Kumm[1] and B. Zipfel[2]

[1]GSI Germany, [2]FH Fulda, Germany

1. Dual Harmonic Accelerating System

Fast acceleration of high intensity heavy ion and proton beams requires a new RF acceleration system. The two ferrite cavities operated at h=4, i.e. 0.86 to 5.8 MHz with a maximum amplitude of 16 kV per cavity do not provide a sufficient bucket area. Therefore, it is planned to install a new cavity with magnetic alloy cores (MA cavity) operated at h=2, i.e. 0.43 to 2.8 MHz with a maximum amplitude of 40 kV. At least one of the existing ferrite cavities shall serve as second harmonic cavity at h=4. In addition, the thereby generated double-harmonic bucket provides higher beam intensities by the generation of flattened bunch profiles with reduced incoherent tune shift.

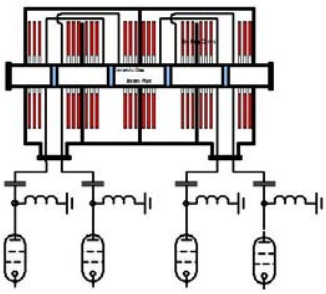

Fig. 1: Rough design of the h=2 cavity

It was proposed to build one double-gap MA cavity with a total length of 2.5 m for operation at h=2, i.e. f = 0.43 – 2.8 MHz, providing a total voltage of 40 kV. In the frame of this subproject, the MA cavity and the corresponding RF power stages and power supply units shall be delivered [1]. Detailed design studies will continue in 2005.

2. Bunch Compressor System

The design concept has been worked out in detail by the GSI RF group; the results are described in [2].

Both, the first final stage and the first supply unit have already been delivered. The commissioning is presently going on. The detailed design of the cavity is completed. The call for tender will be started at the beginning of 2005.

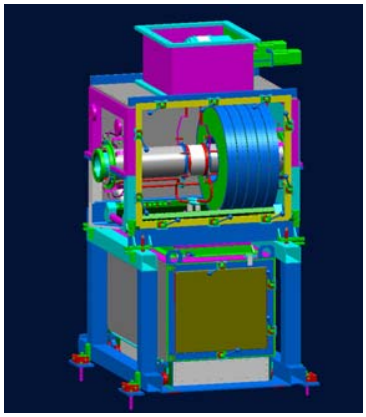

Fig. 2: Final 3D design for the bunch compressor

It is currently planned to install one bunch compressor cavity in the synchrotron ring during a long shutdown in 2006. This requires intensive tests and an optimization of the low-level RF electronics starting at the end of 2005.

3. Digital RF Control

A modular and scalable DSP system has been developed which can be used in different closed-loop control applications [3].

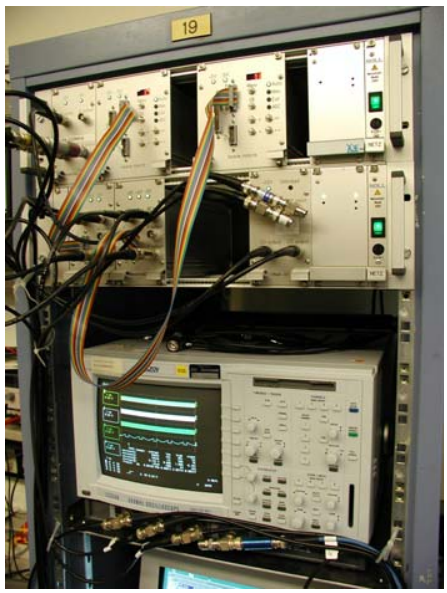

Fig. 3: DSP System for closed-loop RF control

It has already been shown that a cavity synchronization of two cavities is possible with this system if both cavities are running at the same frequency. An accuracy of ±3° has al-

ready been reached and the threshold for closing the control loop is below 100V gap voltage [4]. The concept for digital cavity synchronization also allows an operation at different harmonics. Therefore, the next steps will be to test the system at different harmonics and to allow an arbitrary synchronous phase ramp which is provided by the central control system. This shows that control system integration is a major task.

The first steps towards control system integration have already been initiated, and several hardware components like microcontroller units, FPGA interface cards and updated DDS modules are under development.

It has to be emphasized that the same concept will also be adopted for more advanced applications like beam phase control and for future synchrotrons like SIS100.

Due to the large development effort of this project, collaborations have been established. A collaboration with the Darmstadt University of Technology, Institute of Microelectronic Systems is currently concentrating on the question how much DSP functionality can be moved into FPGAs [5]. Another collaboration with the FH Fulda deals with system-oriented aspects of the low-level RF control system and with specific FPGA interfacing problems [6].

References

[1] P. Hülsmann, W. Vinzenz: "The h=2 Broadband Acceleration RF System for the SIS12/18 Upgrade at GSI", GSI-Acc-Note-2004-11-001, 09.11.2004.

[2] P. Hülsmann, G. Hutter, W. Vinzenz: "THE BUNCH COMPRESSOR SYSTEM FOR SIS18 AT GSI", EPAC 2004 proceedings.

[3] H. Klingbeil: "A fast DSP-Based Phase-Detector for Closed-Loop RF Control in Synchrotrons", accepted for publication in "IEEE Transactions on Instrumentation and Measurement" June 2005.

[4] H. Klingbeil: "Digitale Kavitätensynchronisation", Rev. 1.10, 27.05.2004.

[5] Statusbericht zum GSI-Projekt "Rekonfigurierbare Rechensysteme für digitale Hochfrequenzregelungen bei Schwerionenbeschleunigern", Berichtzeitraum: 01. Juli 2004 bis 23. Dezember 2004.

[6] Statusbericht zum GSI-Projekt Digitale HF-Regelung für den flexiblen Einsatz in Synchrotrons, Berichtszeitraum: 15. Juli 2004 bis 15. Januar 2005.

Numerical Calculation of Coupling Impedances in Kicker Modules for Non-Relativistic Particle Beams

B. Doliwa[31], H. De Gersem[1], T. Weiland[1], U. Blell[2], and O. Boine-Frankenheim[2]

[1]Technische Universität Darmstadt, Institut für Theorie Elektromagnetischer Felder; [2]Gesellschaft für Schwerionenforschung, Darmstadt

Within the design work of FAIR, beam-stability analyses play a important role. One relevant unknown is the beam response to the kicker modules. Here we report our numerical investigations of the respective longitudinal and transverse impedances, defined by

$$Z_{||}(\omega) = \frac{1}{q^2}\int \mathrm{d}^3x \boldsymbol{E}\cdot\boldsymbol{J}^*_{\mathrm{ext}}$$

$$Z_{x,y}(\omega) = \frac{\mathrm{i}}{q^2\Delta}\int \mathrm{d}^3x \rho_\perp\cdot(E_{x,y}\mp vB_{y,x}),$$

where the excitation current is given by

$$\boldsymbol{J}_{\mathrm{ext}}(x,y,z;\omega) = \hat{z}\rho_\perp(x,y)e^{-\mathrm{i}kz}, \qquad (1)$$

which is the fourier transform of an infinitely short bunch of particles travelling with velocity $v=\beta c$ along the positive z direction. We have set $k=\omega/v$ and $\rho_\perp(x,y)$ for the transverse charge distribution ($\int \mathrm{d}x\mathrm{d}y\rho_\perp(x,y)=q$), and Δ for the transverse displacement of the beam.

1 Computational approach

Our calculations are carried out in the framework of the Finite Integration Technique [1]. Upon discretization, one obtains a matrix counterpart of the continous wave equation,

$$\left(\tilde{\boldsymbol{C}}M_{\mu^{-1}}\boldsymbol{C}-\omega^2 M_\epsilon\right)\boldsymbol{e} = -\mathrm{i}\omega\boldsymbol{j}_{\mathrm{ext}}, \qquad (2)$$

where $\boldsymbol{e}$ and $\boldsymbol{j}_{\mathrm{ext}}$ are the discrete electric field and source current, respectively, M_ϵ, $M_{\mu^{-1}}$ the material parameters and $\tilde{\boldsymbol{C}}$, $\boldsymbol{C}$ represent the discrete curl. In the presence of ferrites, this system of linear equations becomes highly ill-conditioned due to the large jumps in (complex) permeability.

Open boundary conditions. Since the source current, Eq. 1, extends from $z=-\infty$ to $+\infty$ whereas our computational domain is finite, one has to apply suitable boundary conditions (see also [2]). Consider some accelerator component, residing in a vacuum cavity with attached beam pipe of smaller cross section than the cavity. Generally, the transitions from the pipe to the module have to be included into the computation, since steps of pipe cross sections contribute to the coupling impedance. For frequencies below beam-pipe cutoff, the fields excited within the cavity decay exponentially along the beam pipe. Thus, at some distance along the beam pipe, the perturbation resulting from the cavity can be neglected and fields can be considered stationary in the sense that $(\boldsymbol{E},\boldsymbol{B})_{\mathrm{pipe}}\propto\exp(-\mathrm{i}kz)$. Using this property, one can set up boundary conditions for the full 3D problem by solving for $(\boldsymbol{E},\boldsymbol{B})_{\mathrm{pipe}}$ in a 2D cross section of the beam pipe.

[3]Supported in part by DFG under contract GraKo 410 and GSI, Darmstadt.

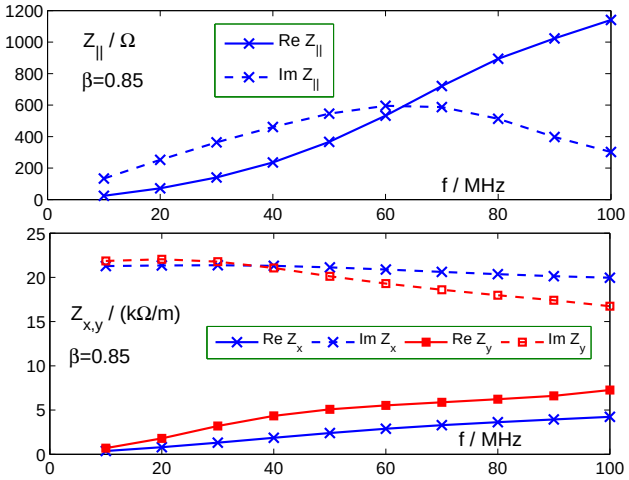

Figure 1: Top: longitudinal impedance. Bottom: horizontal (Z_x) and vertical (Z_y) impedance.

Optimized low-frequency solver. At low enough frequencies, the term $\omega^2 M_\epsilon \equiv b$ in Eq. 2 can be considered small compared with $\tilde{\boldsymbol{C}}M_{\mu^{-1}}\boldsymbol{C}\equiv B$ (i.e. $||bB^{-1}||<1$ in some matrix norm). As can be shown in the real case, the expansion of $(B-b)^{-1}$ in terms of bB^{-1} will be convergent as long as $\omega/2\pi$ is smaller than the lowest eigenfrequency of the cavity. The (pseudo-) inversion of the matrix B in each expansion term formally corresponds to solving a magnetostatic problem, for which powerful solution strategies are at hand, e.g. multigrid techniques. In this way one is able to deal with the bad conditioning arising from the ferrite material.

Software. Our calculations are carried out using CST MICROWAVE STUDIO® and MATLAB.

2 Results for the SIS-18 kicker

The model used in the calculations presented here is derived from the SIS-18 kicker construction plan. Since the impedances scale with the number of magnets, considering only one magnet is sufficient. Please note that the effect of the magnet winding and its connection to the pulse-forming network is not included in the results of Fig. 1. The investigation of these parts is under way.

References

[1] T. Weiland. *AEÜ-Int. J. Electron. Commun.*, 31(3):116, 1977.

[2] M. Balk, R. Schuhmann, and T. Weiland. *Proceedings of the IEEE AP-S/URSI 2003, Columbus, Ohio*, page 367, 2003.

Longitudinal Impedances and Shielding Effectiveness of a Resistive Beam Pipe[0]

A.M. Al-khateeb[1], O. Boine-Frankenheim[2], R.W. Hasse[2] and I. Hofmann[2]
[1]Department of Physics, Faculty of Science, Yarmouk University, Irbid, Jordan; [2]GSI Darmstadt

The longitudinal coupling impedance of a cylindrical beam pipe for arbitrary relativistic energy and mode frequency is obtained analytically for finite wall conductivity and finite wall thickness. Closed form expressions for the electromagnetic fields excited by a beam perturbation are derived analytically. In following previous work of Gluckstern[1], Piwinski[2], Zotter[3], and Wang and Kurennoi[4], general expressions for the resistive–wall impedance in the presence of a metallic shield and for the rf shielding effectiveness of the beam pipe have been obtained [5]. The results are applied to the GSI synchrotron SIS, where the thickness of the vacuum chamber in the dipole magnets is much smaller than the skin depth δ_s at injection energy.

The shielding by a beam pipe which is thin as compared to the skin depth is of relevance for the SIS 18 heavy ion synchrotron at GSI as well as for the design of the new SIS 100 as part of the FAIR project [6]. The SIS 18 magnets can be ramped with 10 T/s, the superconducting SIS 100 magnets shall be ramped with 4 T/s. In order to reduce Eddy current effects, the stainless steel beam pipe of SIS 18 is only 0.3 mm thick. The skin depth at injection (11.4 MeV/u) is 1 mm. For the stainless steel or titanium beam pipe in the new SIS 100 a thickness of a few 0.1 mm will be required [7]. Because SIS 100 will be a 'cold' machine, the heating of the thin pipe due to large image currents can be important.

In the following we apply our results to the SIS. In Fig. 1 we plot the real part of the resistive wall impedance as a function of d for SIS parameters. As expected, the thick wall limit can be used for $d > \delta_s$. For $\gamma = 2$ and $n = 1$ the skin depth is slightly larger than the wall thickness (0.3 mm) in the dipoles. For $d < \delta_s$ the real part of the impedance is proportional to $1/d$. For very small d below 1 μm the exact impedance decreases towards zero. For SIS parameters the resistive wall impedance divided by the harmonic number remains well below 10 Ω. The total (space charge and resistive wall) imaginary part of the wall impedance is plotted in Fig. 2. For $d \gtrsim 1$ μm the imaginary part is dominated by the space charge impedance. For smaller d the imaginary part of the total wall impedance tends towards the vacuum result.

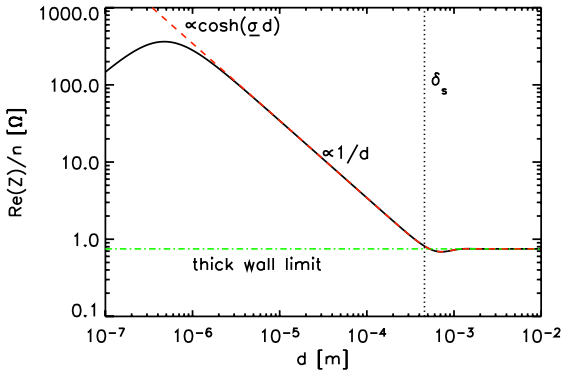

Figure 1: Real part (solid line) of the resistive wall impedance for $n = 1$ and $\gamma_0 = 2$ as a function of the wall thickness d (SIS 18).

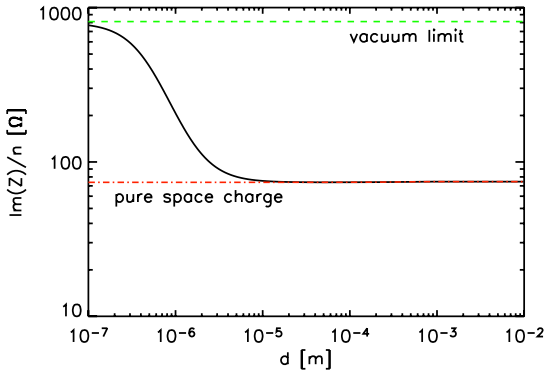

Figure 2: Absolute value of the imaginary part (solid line) of the total (space charge and resistive wall) impedance for $n = 1$ and $\gamma_0 = 2$ as a function of the wall thickness d (SIS 18).

References

[1] R. L. Gluckstern and A. V. Fedotov, Proc. Workshop on Instabilities of High Intensity Hadron Beams in Rings, ed. T. Roser and S. Y. Zhang, AIP Conf. Proc. 496, Melville, New York 1999 pp. 77-84; R. L. Gluckstern and B. Zotter, Phys. Rev. STAB **4**, 024402 (2001); R. L. Gluckstern, Analytical Methods for Calculating Coupling Impedances, CERN report 2000-011, p.9 (2000).

[2] A. Pivinski, IEEE Trans. Nucl. Sci. **24**, 1364 (1977).

[3] B. Zotter, Part. Accel. **1**, 311 (1970).

[4] T.-S. F. Wang and S. Kurennoy, Phys. Rev. STAB **4**, 104201 (2001); S.S. Kurennoi, Fiz. Elem. Chastits At. Yadra **24**, 878 (1993).

[5] A.M. Al-khateeb, O. Boine-Frankenheim, R.W. Hasse, I. Hofmann, Phys. Rev. E, in print

[6] An International Accelerator Facility for Beams of Ions and Antiprotons: Conceptual Design Report http://www.gsi.de/GSI-Future/cdr/.

[7] S. Wilfert and K. Keutel, *Die kryogenen Vakuumkammern der supraleitenden Magnete. der Synchrotrons SIS100/300*, internal report, GSI Darmstadt, 2004.

[8] A. W. Chao, Physics of Collective Beam Instabilities in High Energy Accelerators, Wiley, New York, (1993).

[0]Grant 4-2004 supported by the Council of Scientific Research of Yarmouk University, Irbid, Jordan

Measurements on the Energy Dependence of the Ion-Induced Desorption Yield of Selected Materials

Holger Kollmus[1], M. Bender[1], A. Krämer[1], M.C. Bellachioma[1], E. Mahner[2], L. Westerberg[3], E. Hedlund[4], O.B. Malyshev[5], and H. Reich-Sprenger[1]

[1]GSI Darmstadt; [2]CERN, Geneva, Switzerland; [3]The Svedberg Laboratory, Uppsala University, Uppsala, Sweden; [4]Department of Radiation Science, Uppsala University, Uppsala, Sweden; [5]CCLRC Daresbury Laboratory, Warrington, UK

1 Introduction

For the GSI Future Project FAIR a beam intensity of 10^{12} U^{28+} ions per second is planned to be extracted from the GSI heavy ion synchrotron SIS18. Measurements performed in 2001 showed that the beam lifetime of the ions in the synchrotron is decreasing with increasing number of injected particles [1]. This is caused by pressure rises due to ion beam-loss induced desorption: the primary beam hits, e.g., aperture limiting devices and gas is released. Along this way the number of charge exchanged particles –which get lost after the dipole magnets– will grow and will probably trigger vacuum instabilities. During last years experiments were performed to study desorption yields under high energy ion bombardment on various materials with different surface treatments in dedicated test stands at GSI [2] as well as at CERN [3,4]. In this paper we will discuss latest results measured at the SIS18 of GSI.

2 Experiment

The experimental setup, shown in Fig. 1, consists of three differential pumping stages and the experimental chamber containing the samples, mounted on a linear and rotational feedthrough. Additionally, the experimental chamber is equipped with a pressure (extractor) gauge and a residual gas analyzer (RGA) to measure the total pressure increase and the partial pressure distribution during ion bombardment. The differential pumping stages are necessary to reduce the high pressure from the beamline (10^{-7} mbar) to the experimental chamber (10^{-10} mbar). The test stand is separated from the accelerator by a sector valve and *in situ* baked to 300^0 C for 48h. The ion beam size on the targets can be adjusted using quadrupole magnets in the beam line. The focus is controlled by an Al_2O_3 fluorescence screen mounted on the target holder. The projectile ion current is measured using current transformers in the SIS18 and in the beamline to the experiment. All measurements presented here were performed at normal (perpendicular) incidence. We studied the effective desorption yields for 316LN stainless steel, for P506 stainless steel, OFE copper and 6082 aluminum at projectile ion energies of 15, 40, 100, 408 and 1000 MeV/u. For each measurement a new, unused target was selected to avoid uncertainties due to cleaning effects. The target thickness was chosen to be greater than the penetration depth of the projectile ions. In Fig. 2 a typical pressure evolution under ion bombardment is shown, recorded with the extractor ionization gauge calibrated for N_2. SIS18 was providing a mean number of 2.4 x 10^8 U^{73+} particles per hit every 3.9 sec. (7.2 x 10^7 particles/sec.). The corresponding pressure

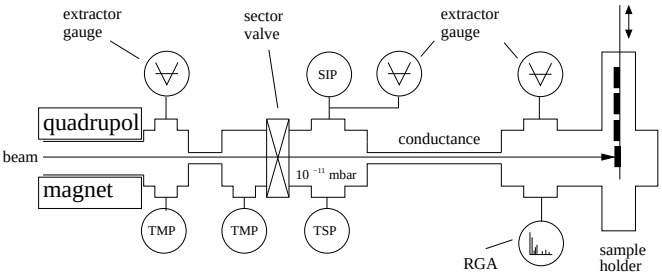

Figure 1: Schematic drawing of the ion-induced desorption experiment mounted in the HHT Cave of SIS18.

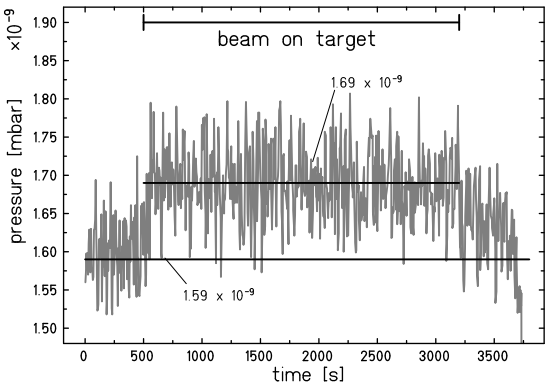

Figure 2: Total pressure development for 100 MeV/u U^{73+} ions hitting P506 stainless steel. The total pressure increase is about 1 x 10^{-10} mbar.

increase Δp was about 1 x 10^{-10} mbar. The partial ion currents for H_2, CH_4, CO and CO_2 were recorded simultaneously using the residual gas analyzer. Only a partial pressure increase for CO and CH_4 was detected on a H_2 dominated background. Using the ideal gas law one is able to determine the effective desorption yield η_{eff} using the formula

$$\eta_{eff} = \frac{\Delta p \cdot S}{\dot{N} \cdot k \cdot T} \quad (1)$$

where S is the pumping speed, $\dot{N}$ is the projectile ion flux, k the Boltzmann constant and T the temperature. "Effective" means, that all values might have the same systematic error, e.g., from the pressure measurement or from the pumping speed used in formula (1) (which depends on the partial pressure distribution).

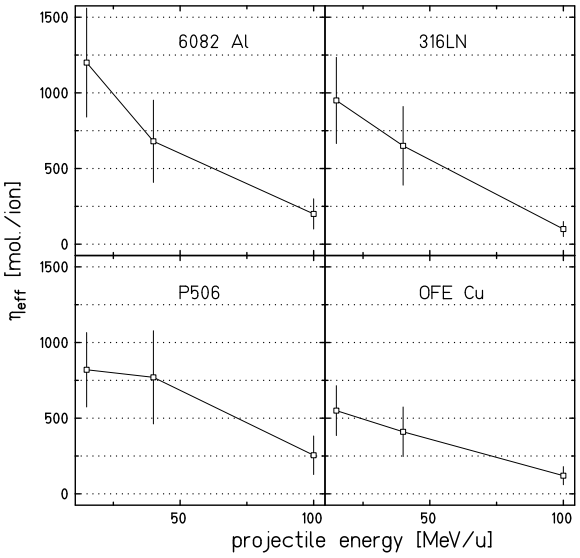

Figure 3: Effective desorption yield versus energy for the four different targets 316LN stainless steel, P506 stainless steel, OFE Cu and 6028 Al bombarded with U^{73+} under normal incidence. The error-bars are indicating relative errors between 30 % and 50 %.

3 Results & Discussion

The effective desorption yields for 6082 aluminum, 316LN stainless steel, P506 stainless steel and OFE copper, plotted as a function of the projectile energy, are shown in Fig. 3. All data points are derived from total pressure measurements done with the extractor gauge in the experimental chamber (see Fig. 1). One can clearly see that the desorption yield is dropping with increasing projectile energy in the regime investigated. As mentioned above, the pressure increase signal is comparable low. For this reason conservative (relative) errors between 30 % and 50 % are assumed. There are no data points available for 408 and 1000 MeV/u, since there was no gaugeable signal. An upper limit for the effective desorption yield for these energies can be given to be less than 200 particles per incident ion for all targets. This behavior might be explained by the energy loss dE/dx of the projectile inside the first nanometers of the material, displayed in Fig. 4. Here, the electronic energy loss of uranium ions in aluminum, stainless steel and copper is shown as a function of the incident energy. The energy regime investigated, is well above the Bragg-Peak and only electronic energy loss is relevant. Therefore the energy loss is also decreasing with increasing projectile energy. The desorption yield scales approximately with $(dE/dx)^2$. Concentrating on the 15 MeV/u value, one can also notice, that the highest desorption yield is recorded for aluminum and the lowest for Cu, whereas the stainless steel types 316LN and P506 are in between. Also this ranking might be explained by the different electronic energy losses of the materials investigated (compare. Fig. 4).

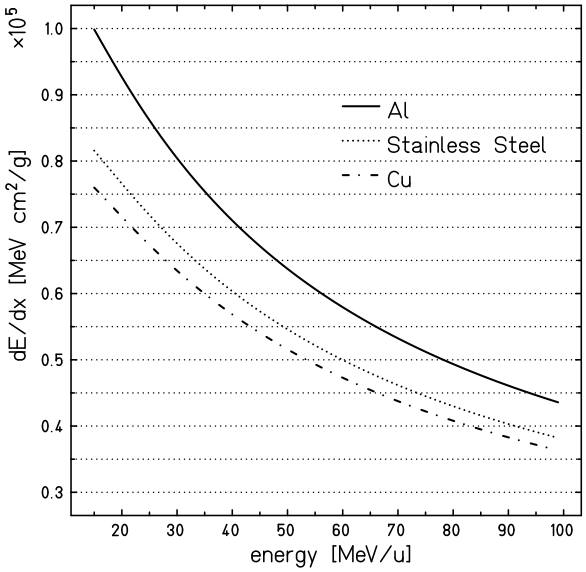

Figure 4: Electronic energy loss of U in Al, stainless steel and Cu for energies between 10 and 100 MeV/u calculated using the CMEE-Library [5]. All values are well above the Bragg-peak.

4 Outlook

The results presented here are showing for the first time a scaling of the ion-beam loss induced desorption yield with the electronic energy loss for normal incidence. In order to understand this behavior in more detail, we propose to repeat this experiment with a reduced base pressure and higher projectile current from the SIS18. This will allow us to get more pronounced signals with better accuracy and also data points for higher energies.

A dE/dx scaling of the ion-beam loss induced desorption enables new solution for the SIS18 desorption problem, e.g., by installing "anti-chambers" after the dipole magnets collecting the charge exchanged ions. Those collectors could be separated from the beam chamber by thin window foils, where the particles suffer nearly no energy loss.

5 Acknowledgments

We would like to thank the BES department of GSI for their help moving the experiment to the experimental area at SIS18 and the CERN workshop for the fabrication and cleaning of most samples and the target holder. We would also like to thank the GSI operating and the beam diagnostics group providing an excellent beam.

References

[1] A. Krämer *et al.*, EPAC2002, p. 2547 (2002)
[2] M. Bender *et al.* GSI Annual Report, p. 219 (2003)
[3] E. Mahner *et al.* EPAC2002, p. 2568 (2002)
[4] E. Mahner *et al.* PRST-AB6, 013201 (2003)
[5] CMEE-Library, http://www.txcorp.com

Deposition and characterization of non evaporable getter films

M.C.Bellachioma[1], J.Kurdal [2], H.Reich-Sprenger [2], R.Hollinger [2], J.Gavillet[3], and H. Hahn [1]

[1]Technische Universität Darmstadt, Germany; [2]GSI, Darmstadt, Germany, [3]CERN, Geneva, Switzerland

1. Introduction

Non-evaporable getter (NEG) film coatings were developed at CERN to provide linear pumping for vacuum chambers [1]. These NEG film coatings offer several advantages compared to the existing solutions. Since the whole inner surface of the vacuum chamber can be coated, a large increase of the pumping speed per unit length of chamber is obtained. Additionally, the very clean surface produced by activation reduces significantly both the beam induced desorption [2] and the secondary electron yields [3].

A new approach to the coating technique, the vacuum arc deposition, is proposed at GSI. Vacuum arc deposition might in fact be an interesting alternative to the magnetron sputtering. Its main advantages, compared to the standard sputtering process, are the highly ionized state of the evaporated material, the absence of gases to sustain the discharge (that not only eliminates the rare gas contamination from the film, but also reduces the possible contamination from the impurities present in the sputtering gas or eventually from leaks in the injection line), and the high energy (about 50 eV) of atoms reaching the substrate surface. Its main disadvantage is the production of microdroplets (or macroparticles) emitted from the region of the arc spot, consisting of molten cathode material with typical dimensions in the range from 0.1 to 5 microns [4].

2. Sample Production and Characterization

The coating parameters used to produce three different TiZrV thin films on SiOx substrate are presented in Table I.

Table I: *Coating parameters for vacuum arc deposition.*

Sample	Pulse duration	Pulse length	Pulse [A]	Coating duration
#1	1ms	1s	200	67min
#2	1ms	1s	200	120min
#3	1ms	1s	300	270min

The NEG activation process was studied applying the X-ray Photoelectron Spectroscopy. The thin film coatings were analysed by XPS, first in the as-received state and then after in situ heating for 1 hour at given temperature. In a previous study it was proven [5] that there is a strong correlation between coating composition and activation temperature. All the getters considered as easily activated, present a Ti-Zr-V film composition comprised in the coloured area of the "quality-composition map" shown in Figure 1, and they are characterized by a nanocrystalline structure. Two of the produced thin films (sample #1 and sample #2) are outside that area, while sample #3 shows a coating composition comparable to that of the Long Straight Section (LSS) produced at CERN by magnetron sputtering.

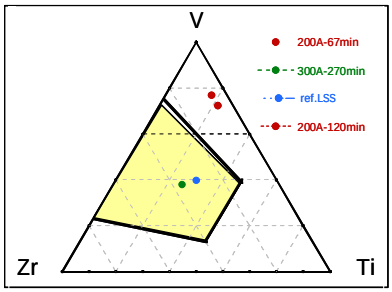

Figure 1: *Quality-composition map of Ti-Zr-V films*.

Figure 2 shows that while the samples #1 and #2 do not activate at the considered temperatures (no decrease of the O amount is observed during all the thermal cycle), the activation of the sample #3 is shifted to higher temperatures, compared to a reference LSS sample. In the XPS lines of the three metals (Ti, V and Zr), a corresponding state of reduction as for the standard LSS sample is obtained for a temperature shift of 100°C. It means that at 300°C this sample has reached the same activation of the metals as for a reference sample at 200ºC. The origin of this shift might be due to a difference in morphology (grain size) between the LSS sample and the arc-deposited sample. On the other hand, the presence of uncoated areas on the arc deposited samples modifies the measured O 1s quantity. As the Si compounds (under SiO_2 or SiO_4 forms) have higher decomposition temperatures, a non-negligible amount of the O detected arises from the glass: at 300ºC, as ~ 3 at.% of Si is detected, at least 6% of O concentration could be due to the glass. This could explain why at 300ºC, when the sample seems to be fully activated in the XPS lines of the three metals, the amount of O detected remains higher than in the reference case.

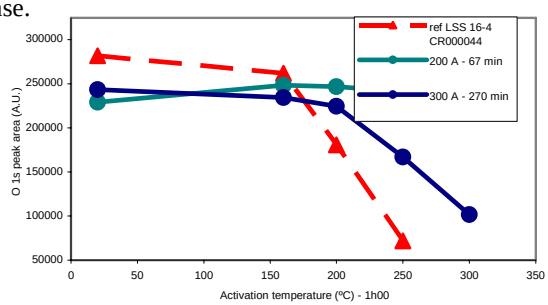

Figure 2: O1s peak area as a function of the activation temperature.

References

[1] C. Benvenuti et al., J.Vac.Sci.Technol., A16 p.148, 1998.

[2]P. Chiggiato and R. Kersevan, Vacuum 60 p.67, 2001.

[3]B. Henrist et al., Appl. Surf. Sci., 172 p.95, 2001.

[4]R. Russo et al., Proceedings of the 2004 European Particle Accelerators Conference, Luzern, Switzerland, 2004.

[5]A.E. Prodromides et al., Vacuum 60 p.35, 2001.

Benchmarking Linac Codes for the HIPPI Experiment at UNILAC

A. Franchi[1], R. Duperrier[2], G. Franchetti[1], F. Gerigk[3], L. Groening[1], I. Hofmann[1], A. Orzhekhovskaya[1], A. Sauer[4], D. Uriot[2], and S. Yaramyschev[1]

[1]GSI, Darmstadt, Germany; [2]CEA, Saclay, France; [3]CCLRC-RAL, UK; [4]IAP, Frankfurt, Germany

One of the main tasks of the beam dynamics working package of the European network "High Intensity Pulsed Proton Injector" (HIPPI) is the comparison and validation of 3D linac codes in the high current regime. Several codes are available and currently run for such simulations. Different approaches used to describe the space charge effects and different lattice modeling (expecially regarding the RF) may pose severe problems understanding the source of discrepancies when tracking simulations at high current are run. For this reason the code benchmarking has been divided in three steps.

The first is a "static" comparison of space charge calculations: common Gaussian ensembles of particles are given as input to the codes and the Poisson solvers are run without any tracking. The resulting space charge electric fields are compared with the analytical solution against different numerical parameters and boundary conditions. To investigate the effects of numerical errors on the single particle dynamics the instantaneous depressed tune is inferred using the previous calculated space charge electric fields and compared again with an analytical solution.

The second step consists of tracking simulation with a zero-current beam using a common Gaussian input distribution and the lattice of the UNILAC DTL section for comparison among codes. The scope of this test is dual: first the preparation of the input files for all the codes checking carefully that they describe the same structure; second the understanding of discrepancies arising from the different representation of physical elements implemented in the codes, especially for the RF.

In the last step tracking simulations will be run in the same conditions of the experiments planned for the beginning of 2006: measured beam current, profiles and emittances at the DTL entrance will be used to create input distributions that best fit these values and the results will be compared with profiles and emittances measured downstream at the DTL exit.

Five codes have been used so far: IMPACT [1], DYNAMION [2], TOUTATIS [3], PARMILA [4] and HALODYN [5]. Details about the program and the updated status of the benchmarking can be found in [6].

Fig. 1 shows the relative error of the computed "static" space charge electric field as function of the distance from the bunch center. The relative error shows for all codes an exponential drop within the bunch core, whereas outside some differences appear. It was observed [6] that these discrepancies are highly sensitive to mesh box size and the kind of boundary conditions chosen. Comparing the depressed single particle tune computed by codes with analytic analytic values, showed similar performances of the PIC codes: even for a severe tune depression of 0.7, the differences are bounded to about 30% [6].

Preliminary tracking simulations of the UNILAC DTL sections have been run using a zero-current beam to investigate the outcome of different lattice and RF modeling. SUPERFISH has been used to generate the TTF table for PARMILA and the RF (linear) maps for IMPACT. DYNAMION models the RF solving the Laplace equation in the gap region between two drift tubes, whereas HALODYN applies a thin kick at the gap center. The transverse sizes and emittances (not shown here) agree within 1%, while larger differences appear in the longitudinal emittance (Fig. 2): IMPACT does not show any growth (because of the linear map), which is of about 10% in the third tank for both HALODYN and PARMILA and reaches the 40% in DYNAMION. We plan to run in the future also IMPACT simulations using the Lorentz integrator instead of the linear transfer map.

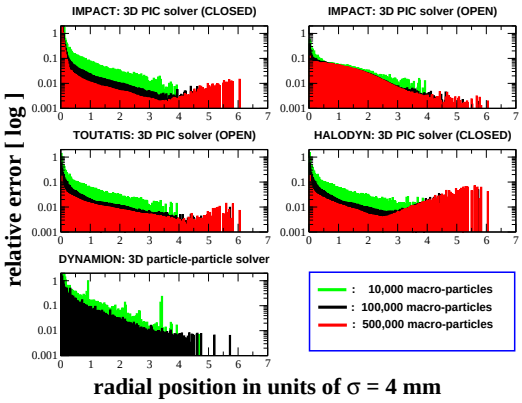

Figure 1: Static field error for DYNAMION and PIC codes with a grid resolution of 128^3 (129^3).

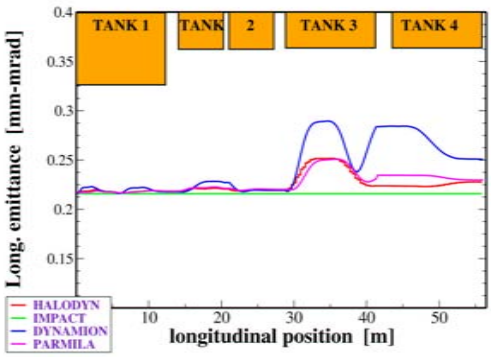

Figure 2: Longitudinal emittance profile at I=0.

References

[1] J. Qiang et al., Jo. of Comp. Phys., **163**, 2000, p. 434.
[2] A. Kolomiets et al., Proc. EPAC-98, pp. 1201–03.
[3] R. Duperrier, Phys. Rev. STAB, **3**, 2000, p.124201–06.
[4] J. H. Billen, *PARMILA*, LA-UR-98-4478, 2001.
[5] A. Franchi et al., Proc. LINAC-02, pp. 653–55
[6] A. Franchi et al., Proc. ICFA-HB04; http://www-linux.gsi.de/~franchi/HIPPI/code_benchmarking.html.

High Current Beams up to 150 keV at Frankfurt

A. Ushakov, M. Droba, N. Joshi, U. Ratzinger
Institut für Angewandte Physik der Johann Wolfgang Goethe-Universität, D-60054 Frankfurt am Main

For the production of 150 keV high current ion beams, IAP is constructing a 150 keV injector [1]. Figure 1 shows a schematic drawing of the terminal (top view). The terminal is connected to a 150 kV insulation transformer, which is able to transform up to 130 kW electric power from ground to high potential. A 150 kV / 300 mA power supply is providing the terminal voltage. This will allow the extraction of ion beams with currents close to 300 mA in dc mode. For pulsed source operations with the extraction of beam currents higher than 300 mA a buffer capacitor, with a capacity of 3 μF is connected in parallel with the high voltage power supply. The high voltage platform is equipped with power supplies, primarily for the operation of arc discharge sources. The terminal has two source positions allowing the installation of two beam lines, one for H^-- and proton beams and the other for heavy ion beams.

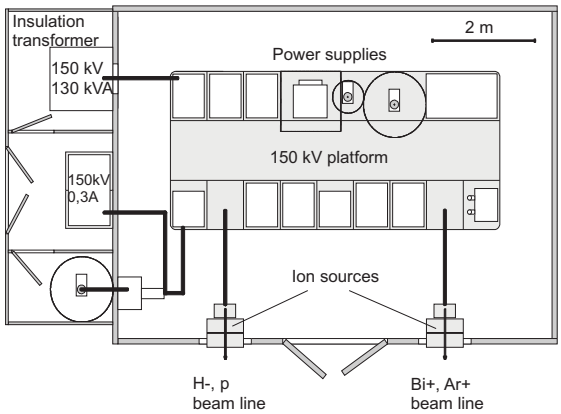

Figure 1: Schematic drawing of the high voltage terminal.

Table 1: Extraction system parameters.

Ion energy, keV	150
Proton beam current, mA	200
Plasma electrode aperture radius, mm	6
Pull electrode aperture radius, mm	7
Screening and ground aperture radii, mm	10
Distances between	
plasma and pull electrodes, mm	6.3
pull and screening electrodes, mm	31.3
screening and ground electrodes, mm	2.5

Figure 2 shows a schematic cross-sectional view of the ion source with extraction system. The tetrode extraction system has been designed for 200 mA proton beam. The potential of the plasma electrode is fixed to 150 kV. The potential of the screening electrode is about −10% of the plasma electrode potential. The extraction voltage (between plasma and pull electrode) should be variable in order to adjust the field to the extracted current (or plasma density). The extraction voltage is limited to

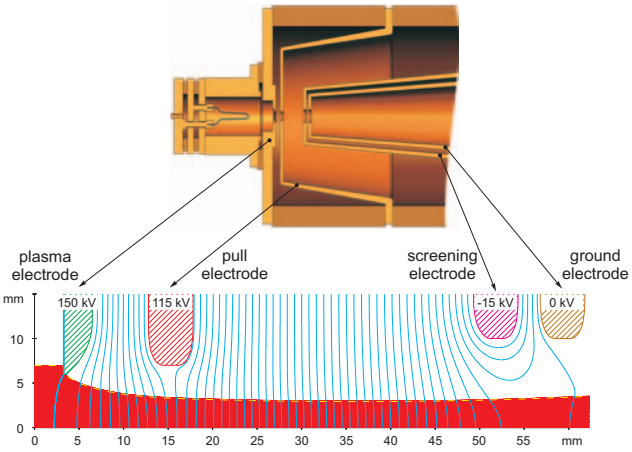

Figure 2: Schematic cross-sectional view of ion source with extraction system (top) and IGUN simulation of the 200 mA proton beam course (down).

35 kV due to the power supply. The electrode distances and their shapes have been optimized in order to minimize the electric fields on the electrode surfaces (maximum electric fields in vacuum are 5.6 kV/mm and 2 kV/cm in air, respectively) and to minimize the beam divergence angle and beam emittance. The 200 mA proton beam course for the 35 kV extracted voltage is shown in Fig. 2. The influence of the extracted voltage on beam divergence angle is presented in Fig. 3. Table 1 lists the geometry parameters of extraction system.

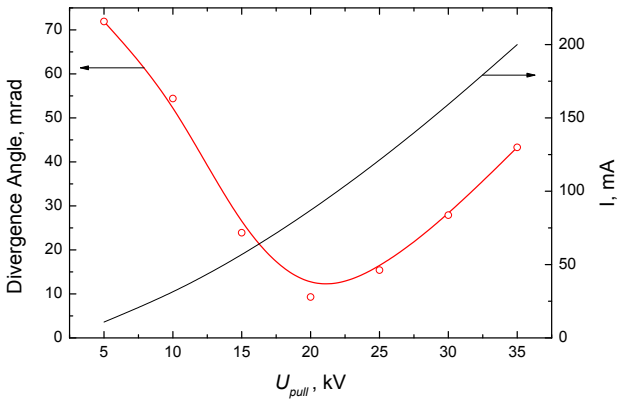

Figure 3: Beam divergence angle and extracted proton current vs potential difference between the plasma and pull electrode.

References

[1] M. Droba et al., High Current Ion Beams at Frankfurt University, in *Proceedings of EPAC 2004*, Lucerne, Switzerland, p. 1198, 2004.

INSTMETH

Instruments and Methods

Upgrade of the UNILAC Ion Beam Current Readout System

H. Brand [1], M. Laaroussi [2], A. Peters [1] and H. Reeg [1]

[1]GSI-Darmstadt, Planckstr. 1, 64291 Darmstadt, Germany; [2]FH-Darmstadt, Haardtring 100, 64259 Darmstadt, Germany

1. Introduction

The UNILAC accelerator produces heavy ion beam pulses with 50 Hz. The beam parameters (ion, energy, intensity etc.) can be changed from pulse to pulse. At 40 positions along the beam line the beam currents are measured synchronously with beam current transformers at 2 MS/s sampling rate. A user selectable subset of current waveforms can be visualised together with their corresponding digital frame pulses from the accelerator timing unit and integrated current and pulse length from the transformer electronics.

2. Old System

In the old system only two waveforms could be acquired and visualized at the same time by using multiplexers. The data acquisition and visualization was one monolithic program on a stand-alone PC. Since the hardware is not available any more and, with respect to FAIR, the requirements for a distributed and more flexible system became more important, it was decided to develop a new system.

3. Upgraded System

The new system, based on National Instruments Hardware and Software, was developed by the diplomacy student M. Laaroussi, supervised by the other authors.

3.1. Architecture

The overall architecture of the upgraded system is shown in Figure 1. A client-server approach was chosen to create a distributed system. The communication protocol is based on TCP/IP-socket connections. The server manages the client requests with a lower priority than the data acquisition which is running in a time critical thread. A FPGA board is used to read the pulse ID, integrated current and pulse length from the transformer electronics and to detect frames and triggers from the timing control unit.

3.2. Hardware

The client can be started on any computer with installed LabVIEW runtime engine and network connection. The Server is running on an embedded NI-PXI-8186 controller (2.2 GHz Pentium 4-M, 1GB RAM, 100 Mbit Ethernet). Up to 112 analog waveforms will be measured with 8-channel simultaneously sampling ADC cards NI-PXI-6133 (2.5 MS/s, 14 bit, 16/32 MB onboard memory). A NI-RIO-7811R FPGA board is used for digital IO.

3.3. Software

A dedicated LabVIEW Real-Time OS is used to implement the server and data acquisition loops. The FPGA module is used to program the NI-RIO board.

3.4. Application

The consumer-producer pattern is used to implement the client-server association. The client registers itself at the server for a subset of available data. If new data become available they are sent automatically to all registered clients.

The time critical data acquisition loop is implemented as state machine with well defined transitions for configuration, data acquisition and error handling. Commands and measured data are exchanged with the server loop by event driven communication.

The DAQ system is externally triggered by the timing control unit at 50 Hz. The onboard memory of the DAQ cards is sufficient to buffer complete 10 ms pulses so that the CPU is decoupled from the DAQ. The FPGA board is used to implement the transformer bus protocol and to measure the relative timestamps of the timing pulse edges.

4. Status & Outlook

A first functional test was performed successfully by simulating the missing transformer electronics and signals with another NI-RIO-7831 FPGA board and a NI-PXI-6070 MIO card. However, the system is not yet in the final stage and needs further improvement.

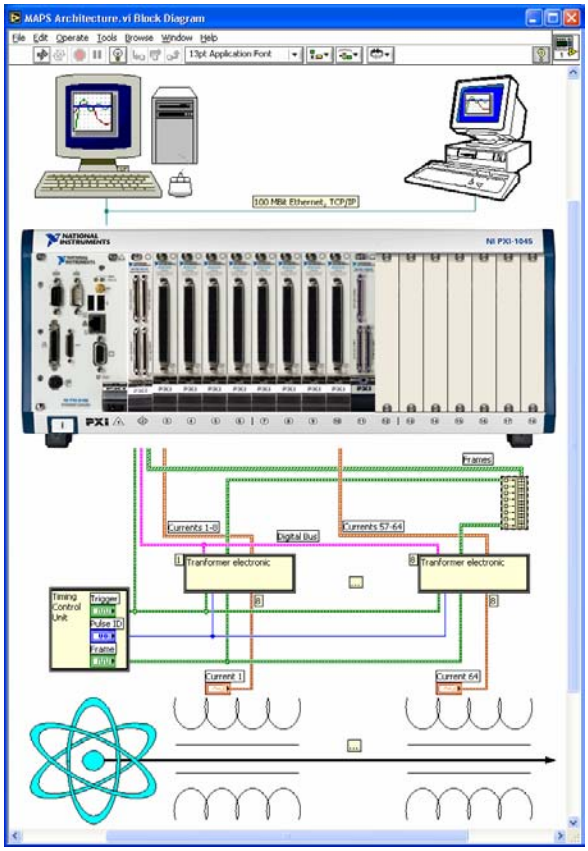

Figure 1: Architecture of the upgraded system.

New Evaporation Set-Up for Uranium Compound Targets

Willi Hartmann, Annett Hübner, Birgit Kindler, Bettina Lommel, Jutta Steiner
Gesellschaft für Schwerionenforschung (GSI), Planckstr. 1, 64291 Darmstadt, Germany

Introduction

In the past, thin uranium fluoride targets in the form of UF_4 on carbon backings were applied for heavy-ion experiments repeatedly. With this compound targets we had several problems: UF_4 had to be evaporated on thick carbon substrates of about 45 µg/cm². The targets were mechanically very fragile and showed heavy sputtering in the beam. The durability of the targets upon irradiation was generally unsatisfying.

For the heavy-element synthesis at GSI, targets of lead, bismuth and their compounds were applied successfully in cold-fusion reactions, where a low-Z projectile interacts with a target nucleus of lead or bismuth, respectively [1].

In recent experiments performed at Dubna [2] and at Berkeley [3] using recoil separators and at GSI using chemical separation [4], various types of ^{238}U targets were irradiated with ^{48}Ca beams with partly contradicting results.
At the GSI SHIP it is planned to study the same reaction early in 2005 [5]. For this experiment a great number of targets of ^{238}U in a good quality is needed. Because ^{238}U is the only target that can be prepared according to safety regulations in the current radioactive target laboratory at GSI, it is planned to use this material in an extended experimental program in the future. For the preparation of the necessary high quality targets a new evaporation apparatus was set up.

The target production has started in September 2004. A first test experiment with beams of ^{12}C and ^{51}V was completed in November 2004.

Requirements for the $^{238}UF_4$ production

Metallic uranium is not stable in air, as it oxidizes very quickly. Metallic uranium targets therefore require for a load lock at the recipient, a safe transport in a water-free and oxygen-free atmosphere and a load lock at the target chamber as well. Suitable uranium compounds as a substitute are UF_4 with a melting temperature of 960 °C, UO_2 of 2827 °C, and UC of 2300 °C. While UF_4 can be evaporated thermally, UO_2 and UC targets can only be produced with an electron beam gun or by magnetron sputtering. To evaporate expensive, enriched or radioactive material with an electron beam gun is not feasible because of the amount of material needed at a fairly low yield. So an evaporation set-up with a thermal evaporation for UF_4 and a magnetron for UO_2 and UC was needed. A substrate heating was wanted too, after the good experiences we had with compound targets on heated backings in the case of Pb and Bi compounds [4]. For the covering layer a resistance heating for carbon rods had to be included. For a target production in a radioactive laboratory a low-maintenance pumping system is sensible, so we went for a magnetically levitated turbo pump backed by an oil-free scroll pump. We decided for the modular high-vacuum coater TF 600© from BOC Edwards©. Equipment and vacuum chamber accessories were designed according to our requirements. Figure 1 shows the front-loading vacuum chamber with the evaporation wheel, the platinum crucible clamped to high-current feed throughs, and the substrate heater above.

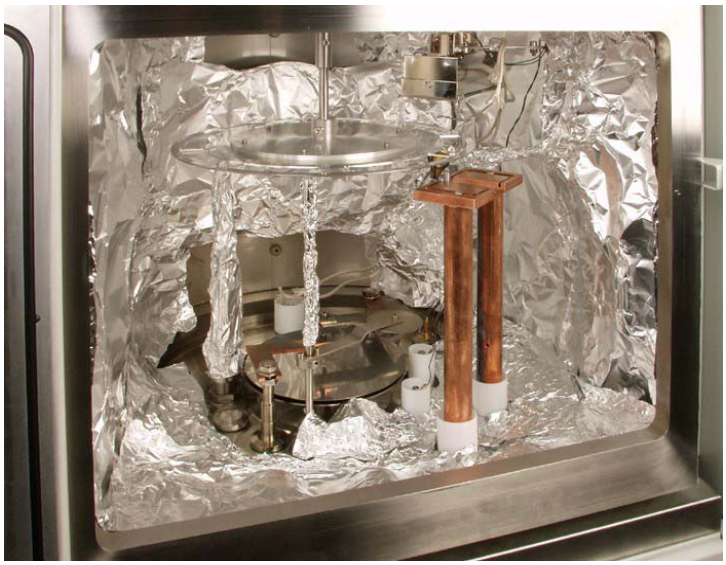

Figure 1: Open front-loading vacuum chamber of the high-vacuum coater TF 600© with the evaporation wheel, the platinum crucible clamped to high-current feed throughs, and the substrate heater above.

Radioactive laboratory

The old evaporator for the uranium was in use for about 15 years. Since then the safety standards concerning the handling as well as the disposal of radioactive contaminated material has changed a lot. Therefore the change of the evaporation set-up was done in close collaboration with the safety department. All the old equipment and the material and targets that could not be of further use were decontaminated as far as possible and the rest was disposed according to the current standard. Also the rest of the laboratory was decontaminated and cleaned thoroughly after the old machine was disassembled. A glove box and a cold roll for the handling, the preparation and the rolling of metallic uranium were also cleaned and the exhaust air was connected to the radioactive exhaust air.

For the protection of the operator during mounting and dismounting of the components before and after evaporation and particularly during cleaning of the

chamber a suction cabin was installed around the evaporation set-up with curtains in front of the recipient door, as shown in figure 2. The ventilation runs via filter into the radioactive outlet air. For a closed water cooling system, the cooling water for the machine is provided by a LAUDA© chiller WK1200©.

Figure 2: New high-vacuum coater TF 600© with the suction cabin installed in operation.

Experiment

We started with the thermal evaporation of UF_4 from a tantalum crucible on heated carbon backings with a thickness of 40 µg/cm². The evaporation started smoothly but after a while material often spurted out of the crucible, which damaged the targets. At the bottom of the crucible always remained remnant material which could only be evaporated by heating the crucible significantly higher. Probably there is a partial reaction of the fluoride with the tantalum crucible. As an alternative we evaporated the UF_4 from a platinum crucible. Though more power was needed to start the evaporation, the process itself ran much faster and without any splashing.

For both crucible materials we succeeded in depositing layers out of UF_4 with a thickness of 300 ± 30 µg/cm² according to the uranium. The targets were covered with a 10 µg/cm² carbon layer.

In a beam time in November 2004 at SHIP two UF_4 target wheels, one evaporated from the tantalum crucible and one from the platinum crucible, were tested with a ^{12}C beam and a ^{51}V beam. All targets were conditioned after mounting for the first time by increasing the beam intensity stepwise, as this is known to increase the life-time of fluoride targets in general. Since in 2005 a long beam time with a ^{48}Ca beam is scheduled, a vanadium beam was chosen as test beam for two reasons. Vanadium is a monoisotope so it was not necessary to use the ECR-ion source which can not be operated parallel to the therapy beam. That made it easier to get the beam time for a test. And V is a beam heavier than Ca so that we could feel safe for the production run if the targets survived the test.

Since the cross-section of the reaction $^{51}V + ^{238}U \rightarrow ^{289}115^*$ is fairly low we could not expect to see any evaporation residues. Therefore after one day of irradiation of the UF_4 wheel evaporated from the platinum crucible the beam was changed to a C beam which was readily available. With the reaction $^{12}C + ^{238}U \rightarrow ^{250}Cf^*$ the quality of the irradiated UF_4 targets was tested. The measured rate of reaction products was as expected for intact targets. After another day the target wheel was changed to the one evaporated from the tantalum crucible, this time beginning with the C beam. The same rate of evaporation residues was observed; again a proof that the irradiation did not change the targets, at least as far as the quality for the heavy-ion reactions is concerned. The two UF_4 wheels prepared from the different crucibles performed similar in the experiment, so we will go for the evaporation out of the platinum crucible as this process seems cleaner, more reliable and better to control.

Outlook

Since the UF_4 targets showed a good durability in the heavy-ion beam, we will prepare UF_4 targets on a heated carbon backing by thermal evaporation for a long beam time in 2005 for the reaction $^{48}Ca + ^{238}U$ to produce element 112 by hot-fusion reaction.

References

[1] S. Hofmann and G. Münzenberg, RMP **72**, No. 3, (2002) 733-767.

[2] Y. T. Oganessian et al., Phys. Rev. C **69**, 054607(9) (2004).

[3] K. E. Gregorich, http://www-w2k.gsi.de/future-she/

[4] H.W. Gäggeler et al. Nucl. Phys. **A734** (2004) 208.

[5] S. Hofmann et al., Search for SHE using the hot fusion reaction $^{48}Ca + ^{238}U$, GSI proposal 184, 2004.

[6] B. Kindler et al., Nucl. Inst. and Meth. A, to be published.

Neutron doses from a thick target bombardment with carbon ions

G. Fehrenbacher, F. Gutermuth, E. Kozlova, T. Radon, and D. Schardt
Gesellschaft für Schwerionenforschung, Darmstadt, Germany

Introduction

The shielding design at particle accelerators is especially affected by the secondary neutron radiation which is produced in nuclear interactions in the target and the first shielding layers. Since several decades physical models are continuously developed and improved which allow the mathematical description of the interaction of radiation with matter. As computer power is now available at reasonable costs and variance reduction techniques further improve the efficiency of numerical simulations shielding calculations employing the Monte-Carlo method are accomplished successfully more and more. However, there are not many computer codes available which are able to simulate the transport of heavy-ions (nucleus-nucleus interactions).

FLUKA [1, 2] is a Monte-Carlo code which combines the features which are essential for shielding calculations for heavy-ion particle accelerators: The ability to simulate interactions of both hadrons and leptons in the energy range from several keV to several TeV; a user interface for variance reduction techniques (biasing techniques); physical models for the transport of projectiles with N>1 (nucleus-nucleus interactions). In addition a routine has been programmed [3] which allows the direct conversion of fluence into the dose originating from the particles under consideration. Dose in this respect can be both, a quantity defined for radiation protection (e.g. effective dose) or for radiation measurement purposes (e.g. ambient dose equivalent). Using FLUKA together with the afore mentioned options dose profiles for accelerator buildings and structures can be calculated and the shielding design can be verified or optimized. Especially in situations were complex shielding geometries are investigated and multiple scattering can occur the Monte-Carlo approach outclasses simple mathematical models like Moyer's formula.

As in all simulations of physical processes the question arises, which accuracy can be expected from the models and codes used. A dedicated experiment measuring heavy-ion induced radiation doses in an experimental area at GSI shall address this question. A carbon ion beam with kinetic energy of 200 MeV per atomic mass unit is sent in Cave A at GSI. The beam is stopped in a 20 cm thick iron target and the neutron dose is measured at different locations inside the cave. A simulation of the experiment with FLUKA is done in parallel and the results are compared to the experimentally determined values.

1 Dose readings

Cave A is one of the experimental areas in the so-called target hall at GSI. The primary beam has been measured with a secondary electron transmission monitor. A thermoluminescent based neutron dose meter is used, which consists of a TLD element sensitive to thermal neutrons and a spherical moderator made of polyethylene. Several of these spheres are placed in Cave A for measuring the neutron dose at different locations (see figure 3). The moderator of every second sphere is equipped with an additional layer of lead improving the response of the system to neutrons with energies higher than 20 MeV.

2 FLUKA simulation

A full simulation of the experimental approach including the interaction of 200 MeV/amu carbon ions with a 20 cm thick iron target is performed with the heavy-ion version of FLUKA. Nucleus-nucleus interactions in this energy range are treated in the frame of the relativistic quantum molecular dynamics model (RQMD) in the version of H. Sorge [4]. The neutron dose (ambient dose equivalent) is scored over the total volume of the cave employing a user routine by S. Roesler and G. H. Stevenson [3] for converting the particle fluences into dose values. Figure 3 shows a plan-view of the cave with the dose color coded.

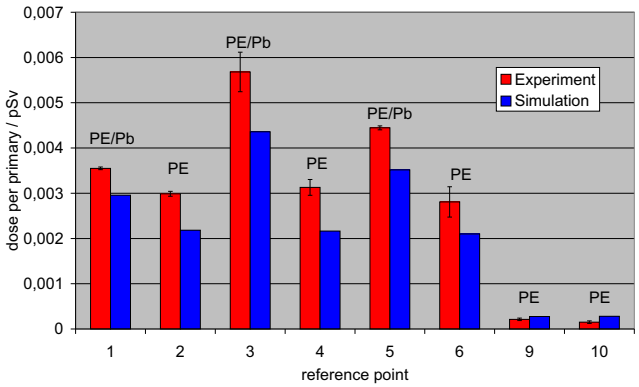

Figure 1: Reading of the thermoluminescent based neutron dose meter. The simulated values are derived from folding the differential neutron spectra with the response function of the detectors. Positions 7 and 8 have not been used.

3 Conclusion

The measurements of the doses in Cave A and the results of the radiation transport calculation performed with FLUKA are in good agreement. However, there are some differences: In forward direction the measured responses are up to 30 % and 45 % higher than the simulation for the spheres with lead and for the spheres without lead, respectively (see figure 1). If one compares the dose readings of the devices to the calculated value of the ambient dose equivalent for the 6 positions in downstream direction one can clearly observe an under-response of the spheres without the lead layer in the moderator (see figure 2). This can probably be explained by a substantial contribution of neutrons with energies higher than 20 MeV. The results also indicate that the additional layer of lead may indeed

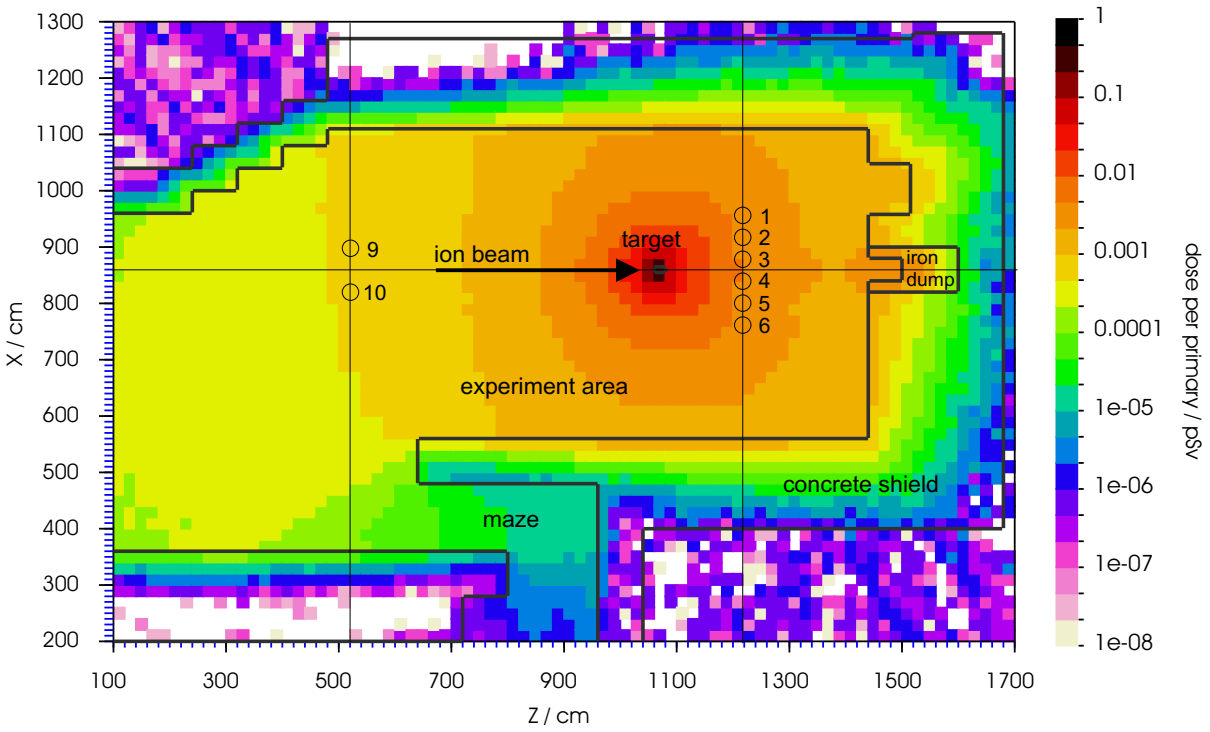

Figure 3: Dose map for a 200 MeV/amu carbon beam being stopped in an iron target in Cave A. Values have been determined using the Monte-Carlo code FLUKA [1, 2]. Doses have been measured at the positions marked with numbered circles.

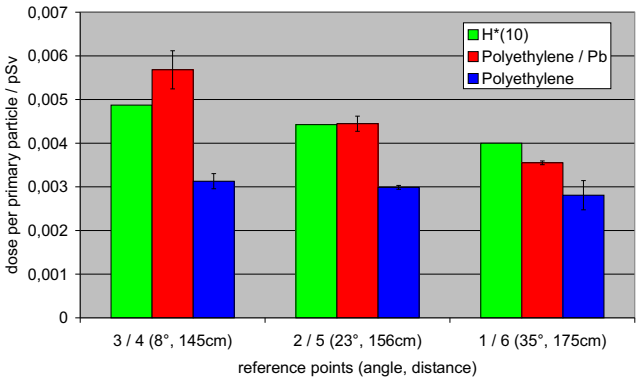

Figure 2: Dose readings of the thermoluminescent based dose meters versus the distance to the beam line. Values are shown for both types of moderators, with and without lead, in comparison to the value of the ambient dose equivalent from the FLUKA simulation.

lead to a slight overestimation of the ambient dose equivalent in some circumstances. This interpretation is supported by the course of the response function which has been determined previously [5]. Overall, the differences between the measurements and the Monte-Carlo simulation are not substantial and the experiment may be regarded as a verification of using FLUKA for dose calculations at heavy-ion accelerators. The radiation transport through thick shielding layers is not investigated in the frame of this work. This question remains to be addressed in another study.

References

[1] A. Fassò, A. Ferrari, and P. R. Sala. Electron-photon transport in FLUKA: status. *Proceedings of the MonteCarlo 2000 Conference, Lisbon, October 23–26 2000, A.Kling, F.Barao, M.Nakagawa, L.Tavora, P.Vaz - eds., Springer-Verlag Berlin*, pages 159–164, 2001.

[2] A. Fassò, A. Ferrari, J. Ranft, and P. R. Sala. FLUKA: Status and prospective for hadronic applications. *Proceedings of the MonteCarlo 2000 Conference, Lisbon, October 23–26 2000, A.Kling, F.Barao, M.Nakagawa, L.Tavora, P.Vaz - eds., Springer-Verlag Berlin*, pages 955–960, 2001.

[3] A. Fassò. Fluka user routine fluscw.f, Version for Fluka99 by S. Roesler and G. R. Stevenson, 18.4.2000. *Personal communication*, 2001.

[4] H. Sorge. Flavor production in Pb(160A GeV) on Pb collisions: Effect of color ropes and hadronic rescattering. *Physical Review C*, 52(6):3291–3314, 1995.

[5] F. Gutermuth, T. Radon, G. Fehrenbacher, and J. G. Festag. The response of various neutron dose meters considering the application at a high energy particle accelerator. *Kerntechnik*, 68(4):172–179, 2003.

An RFQ-based Ion Distribution System for Gas Cell Facilities

M. Petrick[1], W.R. Plaß[1], H. Geissel[1,2], M. Maier[2], C. Scheidenberger[2]

[1]II. Physikalisches Institut, Justus-Liebig-Universität Giessen; [2]GSI

At the FRS Ion-Catcher facility at GSI [1], exotic nuclei produced and separated in-flight at the FRS will be stopped in a gas cell, extracted and made available to low-energy precision experiments. For the transfer and distribution of the exotic nuclei to different experimental setups, a novel system has been designed, built and tested. It connects the extraction radio-frequency quadrupole (RFQ) of the gas-filled stopping cell with different experiments at the facility (Fig. 1). The ion distribution system is based on RFQs, which are known to feature very high transmission efficiencies for cooled ion beams. Novel elements in the system are curved RFQs, which allow to deliver the ions extracted from the gas cell to different directions. Three RFQs leading to different directions are mounted on a movable platform. By selecting the vertical position of this platform using a remote-controlled linear motion feed-through, the extraction RFQ can be connected with the experiment of choice.

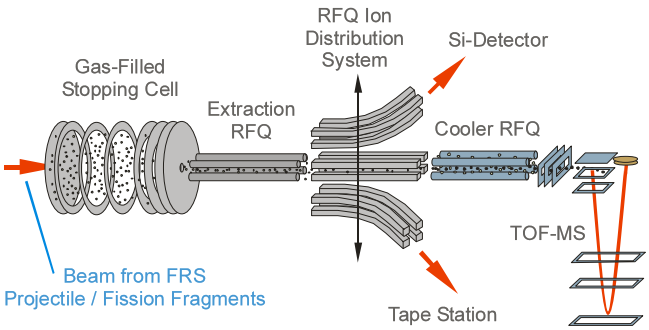

Figure 1: Schematic figure of the RFQ-based ion distribution system and its placement in the FRS Ion-Catcher facility.

Since RFQs are tolerant to high background pressures, the ion distribution system is located in a vacuum manifold, which can also serve as differential pumping stage behind the extraction RFQ of the gas cell. Thus ion distribution can occur simultaneous with differential pumping, leading to a simplified setup compared to an electrostatic ion guide system. The kinetic energy of ions in an RFQ can be of the order of eV or lower, thus no significant collisional reheating of the ion motion will occur. Furthermore, ion transport and injection to experiments that include RFQ systems themselves can be expected to be particularly efficient. An example for such an experiment is a time-of-flight mass spectrometer (TOF-MS) with orthogonal extraction [2], which will be used at the FRS Ion-Catcher. Because of their simplicity, RFQs also allow for quick transmission optimization and reliable operation.

Simulations have been used to investigate the performance of the ion distribution system. It has been found that very high transmission efficiencies approaching 100 % can be expected. The largest loss factor is the excitation of coherent ion oscillation transverse to the quadrupole axis in the curved sections of the RFQs. If the oscillation amplitude of this motion exceeds the size of the holes in the diaphragms at the exit of the device, ions can be lost. However, this effect occurs only for those ions, the kinetic energy of which is of the order of the depth of the pseudopotential well created by the confining RF fields. Thus it can be avoided by proper choice of the accelerating voltages in the setup.

The ion distribution system has been built and installed at the FRS Ion-Catcher facility. Preliminary efficiency tests have been made using a Cs ion source and a Faraday cup detector. The measured relative efficiencies vs. the RF voltage applied to the RFQs are shown in Fig. 2. They increase with RF amplitude and reach a plateau once the pseudopotential is large enough to guide the ions. Without an exit diaphragm, the efficiencies are comparable for straight and curved sections. For the curved section, the transmission decreases by about 20 % if a diaphragm with a hole of 3 mm diameter is installed. For the straight section, the transmission is almost unchanged by the diaphragm.

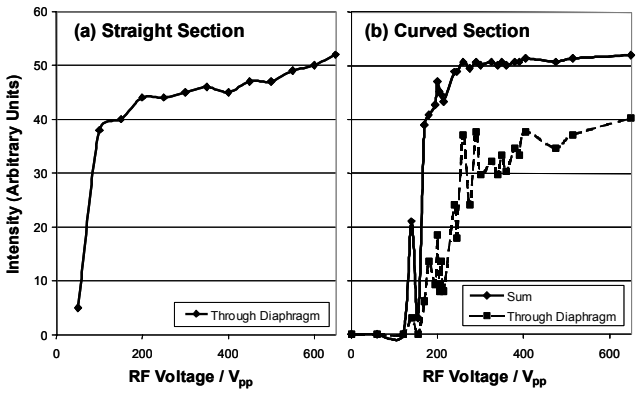

Figure 2: Measured transmission through the (a) straight and (b) curved sections of the distribution system for $^{133}Cs^{+}$ ions with a kinetic energy of 5 eV. For (b) the sum of the currents through and onto the diaphragm as well as the current through the diaphragm only is shown. The intensity scales for (a) and (b) are not necessarily identical.

Further improvements to the ion distribution system could include the addition of a linear RF trap for cooling, mass selection and identification of the ions. Also, the different exit RFQs of the system can be tailored towards the specific requirements of the different experiments at the FRS Ion-Catcher and e.g. provide bunched and post-accelerated ion beams if required. Furthermore, the addition of inlet RFQs for the introduction of test and calibration ions from off-line ion sources to the experiments connected to the distribution system is planned. Ultimately, the replacement of the mechanical selection of the beam direction by an electrical selection is envisaged. Clearly, the application of this novel design for an ion distribution system is not limited to the FRS Ion-Catcher, but could be advantageously implemented at other gas-cell facilities as well, e.g. at the SHIPTRAP facility.

References

[1] M. Maier et al., GSI Scientific Report 2004

[2] S. Eliseev, Doctoral Thesis, Giessen University, 2004.

Preparation of on-line tests of the Ion Catcher setup at the FRS

M. Maier[1], M. Petrick[2], G. Savard[3], C. Scheidenberger[1] , K.H. Behr[1], A. Brünle[1], J.A. Clark[3], Z. Di[2], S. Eliseev[1], H. Geissel[1,2], W. Hüller[1], M. Huyse[4], C. Karagiannis[1], Y. Kudryavtsev[4], T. Levand[3], Y. Litvinov[1], D. Morrissey[5], G. Münzenberg[1], P. Van Duppen[4], H. Weick[1], M. Winkler[1], W. Plass[2], M. Portillo[5], B. J. Zabransky[3]

[1]GSI Darmstadt, Germany; [2]JLU Giessen, Germany; [3]Argonne National Laboratory, USA; [4]KU Leuven, Belgium; [5]Michigan State University, USA

The FRS Ion Catcher is a system to efficiently stop in-flight separated exotic nuclei from the FRS in a helium-filled gas-cell, to separate them from the gas by means of differential pumping, to cool and guide them in a radio-frequency quadrupole (RFQ) system and finally deliver them to different experimental setups. The total transmission time is expected to be of the order of 10 ms [1] thus allowing for experiments with very short-lived nuclei. The areal weight of the gas cell is of the order of few mg/cm^2.

One essential prerequisite to stop in-flight separated exotic nuclei in thin gas layers of matter is a technique to reduce the momentum spread of the fragment beam [2]. This technique was developped and successfully tested with ^{56}Ni and ^{54}Co fragments [3] produced in a 3 g/cm^2 Al target with a 360 MeV/u ^{58}Ni beam. It was possible to reduce the range distribution of the ^{56}Ni to a width σ_R = 14 mg/cm^2, which is comparable to that of a stopped ^{58}Ni primary beam ($\sigma_R \approx 9$ mg/cm^2) from the SIS-18.

A key component of the FRS Ion Catcher setup is a sophisticated gas-cell of 1.25 m length with DC and RF fields, which has been developped at ANL [1]. It is being prepared for a first on-line test behind the FRS in February 2005. The areal weight of the helium-gas filling at a projected maximum pressure of 400 mbar is about 9 mg/cm. To test the performance, the cell was tested off-line with a ^{252}Cf source. The fission fragments are stopped inside the cell due to collisions with the buffer gas. A longitudinal DC potential drop is applied to swiftly transport the ions close to the exit nozzle where they are extracted, dragged by the gas flow. An additional RF field applied to the extraction cone repels the ions from the gas-cell surface. A silicon detector placed directly behind the extraction RFQ was used to count the β-decays from the fission fragments. Some results are shown in Figure 1 for different RF amplitudes and helium pressures. The data points show the expected behaviour, as the repelling force F is proportional to the applied amplitude U_{RF} and inversely proportional the pressure P_{He} of the gas: $F \sim U_{RF}/P_{He}$. By increasing the pressure more ions are stopped. By increasing the RF-field the extraction efficiency increases as well until reaching a plateau. Yet in order to prevent the ions from hitting the wall the required RF-amplitude increases as well. A maximum of these counteracting effects has been reached so far at a pressure of 150 mbar. This maximum is limited by the RF amplitude reachable on the gas-cell cone.

The overall setup (see Figure 2) consists of the stopping cell, an extraction RFQ, a novel RFQ-based ion distribution system [4]and several detectors (a solid state detector to count the activity of the fragments and a time-of-flight mass spectrometer with orthogonal extraction [5]). The setup, which can be controlled remotely, was built in a very compact and modular way in order to fit into the experimental area behind the FRS ("S4-area") and to keep moving times as short as possible.

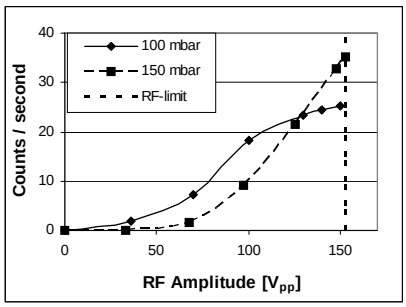

Figure 1 Measured yield of ^{252}Cf fission fragments behind the extraction RFQ versus the RF voltage applied to the cone of the cell.

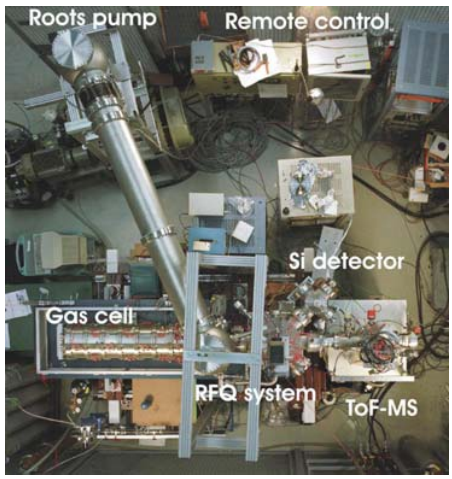

Figure 2 Top view of the FRS Ion Catcher.

The goals of the beamtime are to determine the overall efficiency of the system, to test the range focussing technique together with the gas-cell, explore possible intensity limitations due to space-charge effects, and to measure the extraction times for different operating conditions.

[1] G. Savard et al., Nucl. Instr. Meth. B204, 582 (2003).

[2] C. Scheidenberger et al.,N.Instr.Meth.B204,119 (2003).

[3] M. Maier, PhD Thesis, Univ. Girssen (2004).

[4] M. Petrick et al., contribution to this report.

[5] S. Eliseev, PhD Thesis, Univ. Giessen (2004).

Envisaged TASCA configuration

A. Semchenkov[1,2], W. Brüchle[1], E. Jäger[1], E. Schimpf[1], M. Schädel[1], A. Türler[2], A. Yakushev[2], K.E. Gregorich[3]
[1]GSI Darmstadt ;[2]TUM Garching; [3]LBNL Berkeley

The new **T**rans**A**ctinide **S**eparator and **C**hemistry **A**pparatus, **TASCA**, a new gas-filled recoil separator at the UNILAC, will use components of the former NASE [1]. As a typical reaction for design studies we took 5-6 MeV/u ^{48}Ca on a 0.5mg/cm^2 actinide target (^{238}U, ^{244}Pu). To find the best configuration, simulations were performed with the code TRANSPORT for a DQ_hQ_v (Fig1.), a DQ_vQ_h (Fig.2.), a Q_vDQ_h, and a $Q_vDQ_hQ_v$ (Fig.3.) structure (index **h** and **v** denotes focusing in horizontal and in vertical plane, respectively).

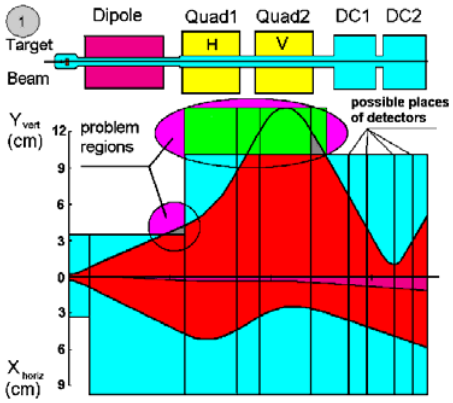

Fig.1. DQ_hQ_v simulations beam shape.

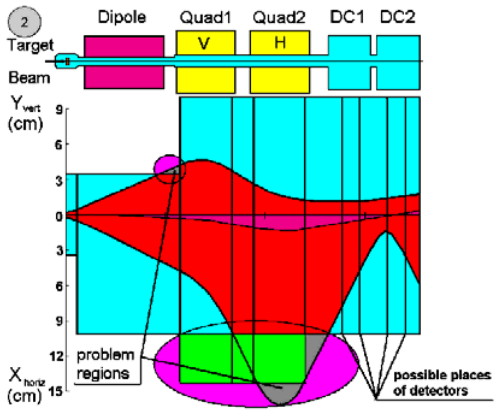

Fig.2. DQ_vQ_h simulations beam shape.

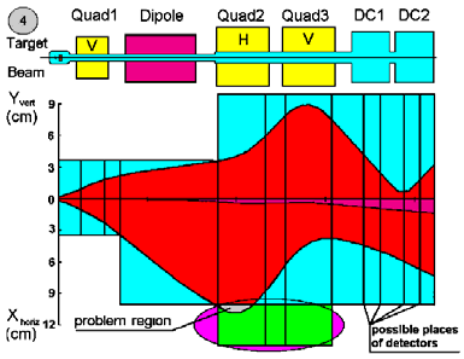

Fig.3. $Q_vDQ_hQ_v$ simulations beam shape.

We fixed the following ^{48}Ca beam parameters: Size x = y = ±2.5 mm, inclination x' = y' = 40 mrad and momentum dispersion ΔB=5%. Monte-Carlo simulations show [2] that 54% of all element 112 evaporation residues produced in the target are emitted within this angle and 92% within the assumed momentum bite. Therefore, a total transmission of about 50% seems reachable. The envelope of transmitted particles shows that, despite of losses at the end of the dipole magnet and in the Q_v vacuum chamber, we have the largest transmission in the DQ_hQ_v configuration and a 25 cm^2 image size; see Table 1. In the DQ_vQ_h arrangement products are lost in the dipole and the Q_1 vacuum chamber yielding a much lower transmission. However, a very small image size of 9 cm^2 is obtained. This can be advantageous when studying short lived isotopes. In a Q_vDQ_h configuration (not shown) a too large image size of 50 cm^2 is obtained. The $Q_vDQ_hQ_v$ set-up gives a horizontally and vertically well balanced shape, a large transmission, the largest dispersion and a 20 cm^2 image size. Figure 1 shows, that additional space from a new vacuum chamber, e.g. achievable with a rectangular tube inside the quadrupoles, would further increase the transmission of the DQ_hQ_v arrangement.

Instead of just using ± 40 mrad, final transmission calculation were made with those maximum beam inclinations which allow a full horizontal and vertical product acceptance with (i) the existing ("round") quadrupole vacuum chamber and (ii) "square" ones. Results are given in Table 1; for the square tubes normalized to a "round" solid angle. In essence, we opted for the DQ_hQ_v arrangement as a start for TASCA.

Table 1. Results of TRANSPORT simulations for different TASCA structures ("round" and "square" refer to different quadrupole vacuum chambers, x' and y' to the input inclination of the beam for simulations, and x'y' to the average inclination angle).

Structure	Dispersion	Acceptance	Trans.	Image size
DQ_hQ_v ("round")	0.7cm/ % L =3.5m	x'(y')=±80(±20)mrad, x'y'=±40mrad,	50%	S=25mm^2
DQ_hQ_v ("square")	0.7cm/% L =3.5m	x'(y')=±85(±30)mrad, x'y'=±50mrad,	55%	S=25mm^2
DQ_vQ_h ("round")	0.1cm/% L=3.5m	x'(y')=±20(±30)mrad, x'y'=±24mrad,	30%	S=9mm^2
DQ_vQ_h ("square")	0.1cm/% L=3.5m	x'(y')=±30(±30)mrad, x'y'=±30mrad,	36%	S=9mm^2
$Q_vDQ_hQ_v$ ("round")	1.1cm/% L=3.9 m	x(y)=±38(±40)mrad, x'y'=±39 mrad,	50%	S=20mm^2

References

[1] V. Ninov et al., Nucl. Instr. Meth. A 357 (1995) 486.
[2] K.E. Gregorich, private communication 2004.

3D magnetic measurements and field simulation of the TASCA C-magnet

T. Belyakova[1], V. Kukhtin[1], E. Lamzin[1], S. Sytchevsky[1], E. Jäger[2], E. Schimpf[2], M. Schädel[2], A. Semchenkov[2,3], G. Moritz[2], C. Mühle[2], F. Klos[2], A. Türler[3], A. Yakushev[3]
[1] Efremov Institute, St.Petersburg; [2]GSI Darmstadt; [3] TUM Garching

While preparing the new TASCA (**T**rans**A**ctinide **S**eparator and **C**hemistry **A**pparatus) project, 3D magnetic field measurements and simulations of the TASCA dipole magnet (C-type) were performed.

Measurements were carried out at GSI at coil currents of I=350, 600 and 700 A corresponding to magnetic field levels of B=1, 1.5 and 1.65 T, respectively. These 3D magnetic measurements, performed along the median and at planes ±25mm apart from it, will be used for trajectory simulations and magnet quality analysis.

The field calculations were made with the finite-element code KOMPOT [1,2]. KOMPOT simulates various 3D stationary field distributions. The code has rich graphic tools for building finite-element models and it can generate AutoCAD drawings. The postprocessor is capable of producing distributed and integral magnetic characteristics, for example, field maps or magnetic fluxes and EM forces for a given region. The graphical interface makes it possible to visualise calculated field distributions in any region of interest and compare it with measured GSI data.

The KOMPOT model developed for the TASCA C-magnet is presented in Fig. 1. The calculation model was reduced to one quarter of the magnet bordered by the median plane and the vertical symmetry plane. For both planes boundary conditions were given. The mesh had 128×63×59=475776 nodes. The mesh step in the working zone was taken as 6 mm along the horizontal axis and 4 mm along the vertical axis. 14 runs were carried out for the current varying from 50A to 700A with a 50A step. Fig. 2 and 3 illustrate field distributions at 700 A for typical cross sections.

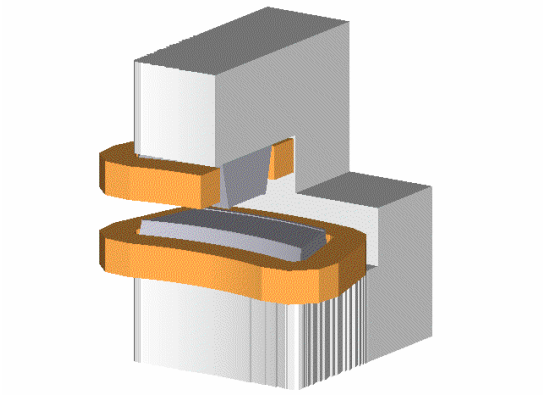

Fig.1. Computational model of the TASCA magnet

A comparison between measurements and simulations show a mismatch of less than 1%. Reasons are the unknown magnetic permeability curve for the existing magnet (a standard curve was used), some initial offset of the coordinate mesh of the measuring system from the magnet centre and non-symmetry of the real magnet assembly.

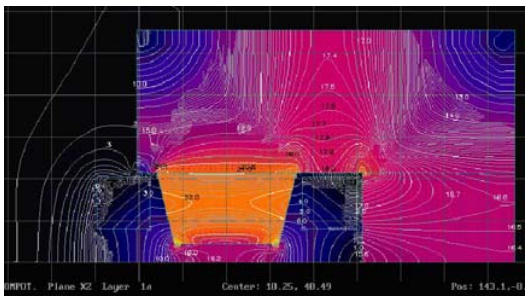

Fig.2. Induction [kG]. I=700amps. Vertical plane.

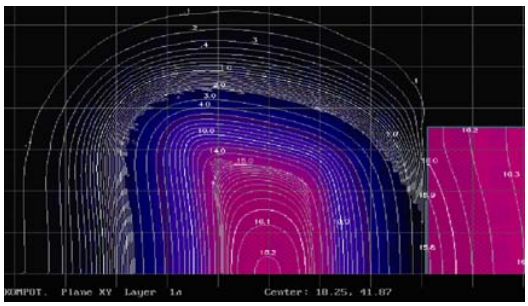

Fig.3. Induction [kG]. I=700amps. Median plane.

Computational model and magnetic measurement data allow us to calculate magnets with required magnetic field distributions. In addition, the synergism between model calculation and measurement will yield much better and much more economic results. Data of magnetic field simulations gives a possibility to have the 3D map of the field in the working area of the magnet for all required induction (current) region, which can be very useful for trajectory analysis.

As the next step we are calculating variants of pole pieces with anti-shims and new wider pole pieces in the frame of the existing coils in order to increase the maximum induction of the magnet and to provide a wide working area.

References

[1] A.Belov, et al., KOMPOT/M 1.0: computer code for 3D simulation of magnetostatic field in the analysis and synthesis of magnetic systems for electrophysical devices, RF Computer Program Register, Registration Certificate №2003612492, Moscow, Nov.12, 2003
[2] N.I.Doinikov, et al., On computation of 3-D magnetostatic fields of electrophysical apparatus magnet systems, IEEE Transact. On Magnetics, v.28, No.1, January 1992, pp.908–911

Performance and alignment studies of the HADES drift chambers

Y.C. Pachmayer[1], J. Markert[1], W. Koenig[2], S. Lang[1], C. Müntz[1], V. Pechenov[3], A. Rustamov[2], A. Schmah[2], H. Ströbele[1], J. Stroth[1], M. Sudol[1], C. Sturm[2], J. Wüstenfeld[1], and P. Zumbruch[2]
for the HADES Collaboration
[1]IKF, Univ. of Frankfurt; [2]GSI Darmstadt; [3]Univ. of Gießen

The spectroscopy of vector mesons in heavy ion collisions via their dielectron decay channel defines the decisive performance constraints on the HADES tracking system [1, 2]. An intrinsic spatial cell resolution of better than 140 μm along with the reduction of multiple scattering in detector materials and gas, high efficiency for detecting minimum ionizing particles and a large acceptance are mandatory. The tracking system consists of 24 low-mass (Aluminium field and cathode wires, Helium as carrier gas), trapezoidal drift chambers representing about 30 m^2 of active area. Presently 22 chambers are in place. High-precision tracking requires a detailed understanding of the chamber physics and performance by means of simulations [3] as well as the alignment of the detectors. Both can be experimentally assessed with cosmic rays [4].

The response of the drift chambers to charged particles has been modelled by GARFIELD simulations which reproduce to a high degree real data [3]. This agreement justifies the use of parameters in the calibration procedure which one extracted from simulation. Using both the track- and the electron drift-topology in the drift cell, the pulse shape can be correlated with the energy loss information for a given track. As a result, the normalized time-above-threshold $\Delta t \propto dE/dx$ is obtained and plotted as a function of the measured momentum in figure 1. The resolution (σ) of the normalized Δt is about 7 % (protons) and 12 % (π).

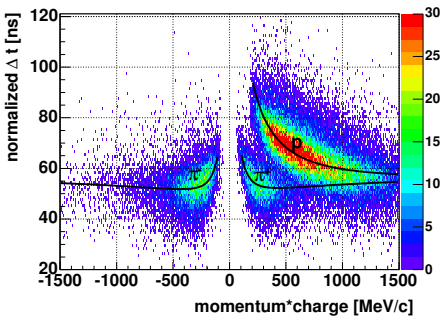

Figure 1: Normalized time-above-threshold $\Delta t \propto dE/dx$ plotted as a function of the measured momentum times the charge for the inner MDC segment (plane I and II). Lines indicate Bethe-Bloch parameterizations.

The separation of pions and protons at low momenta can be seen. Electrons cannot be distinguished from pions. These results provide confidence in the analysis power of the MDC's energy loss information, although the design of the chambers has been optimized for low-mass and not for particle identification.

Data taking triggered with cosmic ray muons is regularly carried out to study the chamber response and the relative detector alignment, because these muons are very similar to electrons with respect to their energy loss. Cosmic muons are triggered by the coincidence of the Time-Of-Flight detectors which sandwich the tracking system. Opposite sector trigger rates are 40-60 Hz, depending on the incident angle. Due to the geometrical trigger acceptance detailed investigations are reasonable only for the two outer drift chamber planes. As a result of the systematic performance studies the detection efficiency for cosmic muons has been determined to 98 % at the working point, for each of the six chamber layers [4]. The track reconstruction software tuned for tracks originating from the target region had to be modified for cosmic-ray muons. GEANT simulations show that the position of muon tracks can be determined to better than 0.3 mm (RMS) in two coordinates. Thus, tracking with cosmic rays enables to align chambers in opposite sectors with respect to each other. The distribution of position residuals from chamber hits in one sector relative to the track position projected from the chambers in the opposite sector is exemplified in figure 2 both for simulation and experimental data, transformed along the beam axis. For the given alignment parameters a displacement of about 5 mm results in this observable. The shape of the distributions further reflects the combined effects of the geometry, the spatial resolution of the chambers and tracking uncertainties.

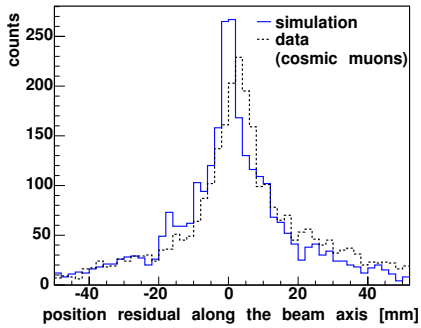

Figure 2: Position residual along the beam axis of opposite drift chambers for simulation (ideal geometry) and experimental data (cosmic muons), corresponding to about 18 hours of data taking with the cosmic ray trigger.

References

[1] C. Garabatos et al., NIM A 412 (1998) 38
[2] C. Müntz et al., NIM 535 (2004) 277
[3] J. Markert, PhD thesis, Univ. Frankfurt, 2005
[4] Y.C. Pachmayer, Dipl. thesis, Univ. Frankfurt, 2003

Response of a scintillating fibre detector to proton and pion beams at GSI

B. Seitz[a], M. Düren[a], M. Hartig[a], M. Hoek[a], T. Keri[a], S. Lu[a], L. Rubacek[a], W. Sommer[a], and H. Stenzel[a]

[a]II. Physikalisches Institut, Universität Giessen, 35392 Giessen, Germany

1 Introduction

The HERMES collaboration at DESY will install a new recoil detector surrounding its target region for the envisaged final two years of the HERA II running period aiming at detecting recoiling nucleons from hard exclusive scattering [1, 2].

Protons and Pions with momenta $p > 250$ MeV/c will be detected and identified by a two–barrel scintillating fibre tracker (SFT). It consists of two barrels made from 1 mm Kuraray SCSF-78 scintillating fibres each. A stereo angle of 10° between each two adjacent layers of each barrel allow space point reconstruction. The diameters of the barrels are 220 mm and 370 mm, respectively.

Beam tests of prototype modules for the SFT using particles in the relevant momentum range will be reported in this paper. Their applicability to the envisaged experiment will be evaluated.

2 Experimental Setup

The envisaged application in the HERMES Recoil detector requires protons and pions in the momentum range from 250 MeV/c to 1500 MeV/c to be detected and identified. A suitable test beam thus has to provide both particle species in the desired momentum range. At GSI secondary beams from heavy ions impinging on a production target are available. The momentum range and polarity of the beam can be chosen in the desired range.

The secondary beam is produced in the collision of a primary proton or heavy-ion beam from the SIS with a thick production target. The secondary particles –mainly protons and pions– are transported to the experimental area through the different beam-lines to the major SIS target hall. The 63 m long beam line leading to cave A was chosen for the experiments. The test experiment was carried out with primary beams of protons 2.2 GeV and ^{12}C ions at 2.2 AGeV incident energy. A borcabid (B_4C) production target of 30 g/cm^2 was employed[3].

The momentum and charge selection of the secondary beam was done by appropriate magnet configuration between the production target and the test beam area in Cave A. Central momenta of 300 MeV/c, 450 MeV/c, 600 MeV/c and 900 MeV/c were chosen.

The experimental set-up is depicted in Fig. 1. A MWPC is used to determine the point of impact on the module under test. The trigger is performed by a coincidence of the scintillators S1 and S2. The distance between S1 and S0 was used for an independent particle identification using time of flight. A small scintillator (S3) was added directly behind the scintillating fibre module for precise efficiency determination.

Four scintillating fibre modules were put behind each other in two pairs. Each pair consisted of a module parallel and a second module tilted by 10° to allow space point reconstruction. The spatial distance between the two pairs were 85 mm matching the distance of the two scintillating fibre barrels in the final application at HERMES.

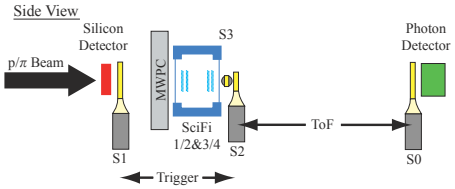

Figure 1: Setup of the recoil detector test experiment performed at GSI. Prototypes from all sub-detectors were exposed to a mixed proton/pion beam in the relevant momentum range. A ToF system and a MWPC served as independent reference detectors.

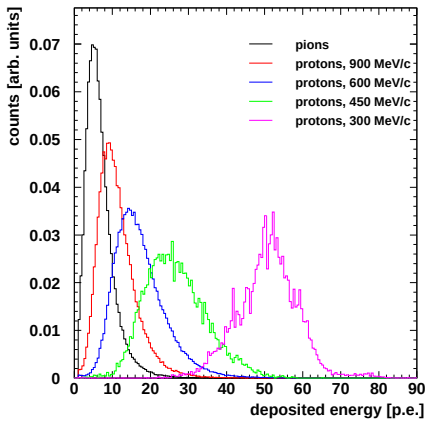

Figure 2: Energy response of leading fibres for pions and protons of various momenta. The energy response is averaged over all fibres of the first module under test.

3 Detector performance

Three crucial performance parameters were evaluated during the test beam periods at GSI. A clustering algorithm taking cross-talk into account was developed and used to extract the results shown in the following. Particle identification by ToF was applied whenever information on the particle species was needed. The energy response of leading fibres to protons and pions of the various momenta used is depicted in Fig.2. The response shown is averaged over all fibres of the first module under test.

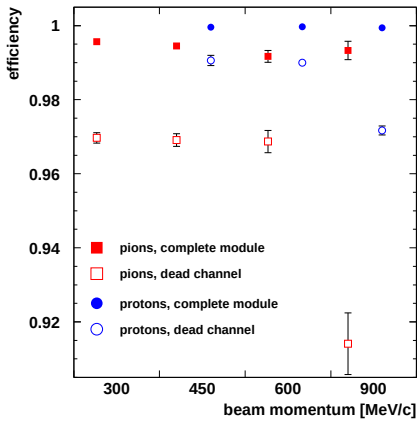

Figure 3: Efficiency of a single scintillating fibre module for proton and pion detection measured for four different momenta at the GSI test beam. The closed symbols show a completely working module, the open symbols the efficiency for a module with one dead channel. Data points corresponding to proton and pion signals are slightly shifted for better visibility.

Requiring a hit in the scintillator S3 whose geometrical dimensions are smaller than the dimensions of the scintillating fibre modules the efficiency of the scintillating fibres was evaluated. The results for the various momenta and particle species is depicted in Fig.3. For a completely working module the efficiency exceeds 98% for all particle species and momenta. A module with one dead channel shows the geometrical expected drop in efficiency.

In addition to providing space points, the scintillating fibre tracker will work for particle identification as well. The response of various modules will be combined using a log-likelihood scheme [4]. The results of this scheme are compared to particle identification in Fig.4. A clear separation between protons and pions using the information from the scintillating fibre modules is visible.

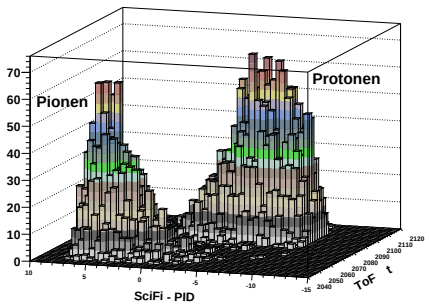

Figure 4: Particle identification with the SciFi test set-up vs. particle identification using the time–of-flight technique at the GSI test beam.

4 Summary

Prototype modules for the SFT of the HERMES recoil detector were tested using a mixed hadron beam of positive polarity at GSI. The central momenta of the beam were chosen between 300 MeV/c and 900 MeV/c matching the momentum range for the desired application. A full system test using four SFT modules in the final geometrical arrangement as well as the complete read-out chain was performed.

The signal from the scintillating fibres are collected using MAPMT Hamamatsu H-7548. A clustering algorithm was developed taking care of cross talk both on the PMT surface and also in the scintillating fibres and light guides[5]. Using this algorithm reliable track information and energy deposition could be extracted. The mean photoelectron yield for MIP is ≈ 7 p.e.. The efficiency of the detector for MIP using a threshold of 0.5 p.e. exceeds 98%. A position resolution of 300 μm was found including a contribution from the reference detector system. The particle discrimination properties reach the expected performance.

These results confirm the design specification for the SFT in the HERMES recoil detector system.

Acknowledgements

The hospitality and help from GSI is greatly acknowledged, in particular the invaluable help and assistance from the Cave A crew. We also like to thank the electronic and mechanical workshops in Giessen making this experiment possible. This work was supported by BMBF

References

[1] B. Seitz, Nucl. Instr. Meth. **A 535** (2004) 538
[2] B. Seitz, in Hadron Physics, Proc. Scottish Universities Summer Schools in Physics (SUSSP58), St. Andrews, eds. I.J.D. Mac Gregor and R. Kaiser, 2004
[3] J. Diaz *et al.*, Nucl. Instr. Meth. **A 478**(2002) 511
[4] W. Sommer, Diplomarbeit, Univ. Giessen 2003
[5] M. Hoek, in Hadron Physics, Proc. Scottish Universities Summer Schools in Physics (SUSSP58), St. Andrews, eds. I.J.D. Mac Gregor and R. Kaiser, 2004

Scintillating fiber detectors for high intensity pion beam at HADES

B. Spruck[1], L. M. Pant[1], J. Pietraszko[2], W. König[2], R. S. Simon[2], R. Novotny[1], V. Metag[1]
[1] II. Physikalisches Institut, Universität Gießen, [2] GSI Darmstadt

To cope with high intensity pion beams to the HADES cave a new detector system is needed to replace the present hodoscopes. A new beam tracking system, based on scintillating fibers, has been designed and brought into operation. The two detectors comprise 96 channels each. Four layers of round fibers of 1mm diameter and 60mm length are welded to clear light-guides of identical diameter and read-out via 16-fold multi anode photomultipliers. The active size of each detector amounts to $60 * 67\text{mm}^2$. A more detailed description can be found in [1,2]. In a test run with a π^- beam in May 2004 both detector allowed to track pions in the target region in horizontal and vertical position. In addition, two plastic scintillators were used for efficiency measurements. The efficiency of one fiber hodoscope has been determined to 98% with a time resolution of $\sigma < 300$ps performing slightly better than the prototypes. The momentum reconstruction of the pions was done by two of the existing pion hodoscopes (PH1&2) with 16 plastic rods each of 1cm width, positioned in the dispersive plane [3]. The setup is shown in figure 1.

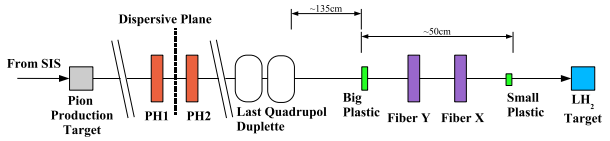

Figure 1: Schematic detector setup of the pion beamline.

The pions were produced by a beam of $3 * 10^{10}$ N-ions per burst of 2AGeV hitting a berylium production target. The HADES beamline was set to particles of 1.17GeV/c momentum with negativ polarity. The pions were focused onto the fiber hodoscopes instead of the HADES target. The measured rate was $8.5 * 10^5$ pions/spill with beam dimensions of 10.5mm in x and 8.4mm in y direction (FHWM). The x projection shows large tails on both sides, which would in an experiment hit the LH_2 target housing leading to large background.

Figure 3 shows that the horizontal distribution of the particles is momentum dependent. From the widths of the distributions it becomes evident that the focus in beam direction also depends on the momentum.

These results show that an improved beam focusing (with a 3rd quadrupol in the HADES cave) as well as an online monitoring system are mandatory. Such a system should be able to track pions and display their momentum dependent distribution in the target area. These informations can be used as additional trigger or veto signals.

Since the existing pion hodoscopes will not cope with the envisaged pion rate, new detectors are needed for the momentum reconstruction in the dispersive plane. Two more fiber hodoscopes, based on the present design, are under development. They will have a granularity of less than 2mm to reduce the countrate per channel by a factor of five and allow a determination of the pion momentum to 0.5%.

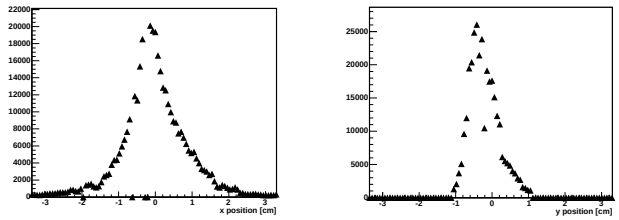

Figure 2: Beam profiles in x and y direction. Only the inner part of the y detector was read out.

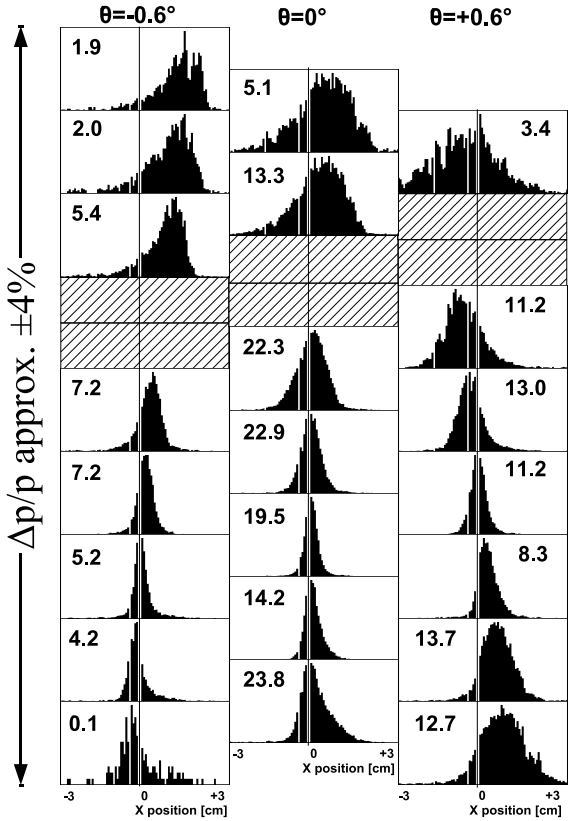

Figure 3: Momentum dependence of the spatial pion distribution in x. Numbers are relative intensities.

References

1. J. Díaz et al.: *Design and commissioning of the GSI pion beam*, Nucl. Instr. and Meth. A 478 (2002) 511.

2. M. Skoda et al.: *Development of a Scintillating Fiber Start Detector for HADES*, GSI Report 2002.

3. B. Spruck et al.: *Development of a Scintillating Fiber Detector for HADES*, GSI Report 2003.

Supported also by EU under RII3-CT-2004-506078 and BMBF 06GI146I.

Timing Multi-Gap Resistive-Plate Counters (MRPCs) in FOPI

A. Schüttauf, M. Ciobanu, H. Hardel, K.D.Hildenbrand, Y.J. Kim, K. Koch, M. Marquardt, R. Schulze, J. Weinert, V. Simion[1] and E. Cordier, N. Herrmann[2]

[1]GSI; [2]Physikalisches Institut, Universität Heidelberg

During the last year we finalized the hardware layout of the MRPCs [1][2] which we plan to implement in the FOPI setup as additional ToF detector shell featuring high granularity, good position and optimum time resolution [3][4]. Each counter has an active area of 900 x 46 mm^2; it consists of 10 glass plates (1 mm and 0.5 mm thick, respectively) with 8 gaps of 250 μm, placed in 2 symmetrical stacks above and below the readout anode. On the surface of the upper- and lowermost plate the cathodes are attached. The anode is a pc-board with 16 conductive strips, 1.94 mm wide, separated by gaps of 1 mm. To connect the Front-End-Electronics (FEE) with the MRPC, two SAMTEC multipin connectors are placed at both anode board ends as well as on the input stage of the FEE-card. For the connection a high-quality multi-coaxial 50 Ω-cable (0.8 mm ⌀) of 10 inch length is used.

In August 2004 we tested the performance of this detector type during a pion beam time of FOPI. A so-called supermodule [4] equiped with one detector (finally it will house 5 MRPCs of this type) was placed directly in the pion beam of 1.14 GeV/c momentum. As reference and trigger counters we used plastic scintillators read out by fast PMTs in front and behind the MRPC. Since this test took place during a running main experiment the counter was exposed to fairly high count rates of ∼1 kHz/cm^2; only for a short time the beam was turned down to the more realistic FOPI-ToF rate of ∼100 Hz/cm^2. In Fig. 1 we show a high voltage scan of time resolution and efficiency as well as the count rate dependence together with the influence of the calibration. The overall behavior of resolution and efficiency shows the known trend for both observables, a steep rise for the efficiency followed by a plateau and a slow decrease for the timing resolution towards its best value of σ_t ≤85 ps at ∼1 kHz/cm^2 (■). For the 10 times lower rate the time resolution improves to $\sigma_t \leq$ 75 ps (□); only two measurements are shown. The influence on the efficiency is not visible within the error bars; it stays at 99 % above 11.5 kV.

In addition we tested the influence of the correction of the integral non-linearities ("wiggles") of the TAC-ASIC chip in the readout electronics. The effect of this correction is shown in Fig. 1 by open triangles (△) for the low rate. They demonstrate the reachable limit in single hits, obtained after individual correction of all known electronic effects like slewing and wiggle dependencies. The resolution of σ_t ≤60 ps at 99 % efficiency for the full detector leads, by subtracting the electronic resolution of $\sigma_e \leq$ 35 ps, to σ_{rpc} ≤49 ps for the MRPC itself. Even if the average resolution in the planned full system of 150 MRPCs with 4800 electronic channels will be somewhat worse one can safely expect it will stay well below 100 ps for single and close to 100 ps in double hits, thus meeting the requirements of FOPI's physics program.

Fig. 2 finally displays the shape of the corrected time spectrum at the high rate of ∼1 kHz/cm^2; the non-gaussian tails are of the order of 3% and can be neglected for our purposes.

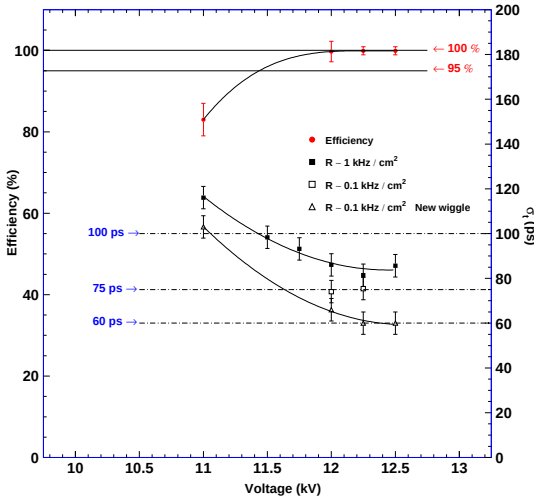

Figure 1: *HV dependence of efficiency and resolution.*

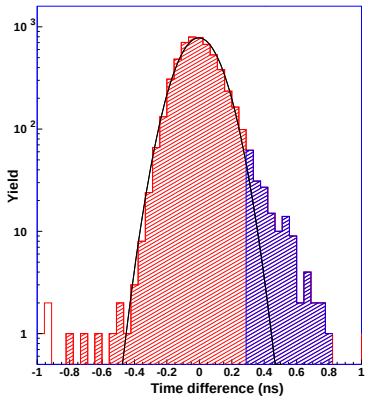

Figure 2: *MRPC time-spectrum after all corrections (the vertical line denotes a cut at 300 ps behind the maximum). The non-gaussian component is below 3%.*

References

[1] E.C. Zeballos et. al., *NIM A 374 (1996) 1322*
[2] P.Fonte et al., *NIM A 443 (2000) 201*
[3] M.Petrovici et. al., *NIM A 487 (2002) 337*
[4] A.Schüttauf et. al., *NIM A 533 (2004) 65*

A New Multi Channel Front-End Board for TOF Experiments with Excellent Timing Resolution

K.Koch, H.Hardel, R.Schulze, E.Badura, J.Hoffmann

GSI-Darmstadt, DVEE, Planckstr. 1, D-64291 Darmstadt, Germany

1. Introduction

A new integrated front-end electronics, based on a high resolution Time-to-Amplitude Converter ASIC chip (TAC), has been developed for time measurements in a time of flight experiment (RPC-detectors) of several thousand channels [1]. A sixteen channel board, named TACQUILA, with a time resolution of about 10ps RMS, has been built. It consists of a TAC stage and a 12 bit ADC for each channel followed by compact readout functionality[2].

To determine the charge of the detector pulses simultaneously to time measurement, an optional piggy-back board for TACQUILA with a QDC (Charge-to-Digital converter) has been designed.

As time reference for the common stop setup, additionally a precision 40 MHz clock system has been developed. It is realized in LVDS standard and is distributed to the front-end electronics in a cascade up to three steps. It shows a jitter of about 5ps RMS measured at the TAC chip.

2. The time-to-amplitude converter ASIC

As an essential part of the timing front-end electronics for many channels, a high resolution TAC-chip was developed at GSI in Darmstadt and implemented in a 0.8µm CMOS process at the IMS Fraunhofer Gesellschaft in Dresden [3].

The main features of the TAC are an outstanding linearity, low power consumption (~ 10mW), an available time range up to 35ns, a very good reproducibility of the properties of the chips and low cost for many channels.

The working principle of the chip is to ramp a voltage continuously from zero to an end value using the property of digital delay lines.

3. The TACQUILA board

The eight layers TACQUILA PCB with dimensions of about 95mm x 250mm carries sixteen identical channels for time measurement including control logic and data transfer capability (see Fig. 1). This compact board offers the chance to place it close to a detector facility with many channels. The incoming differential timing input signal is directly connected to a TAC and starts the measurement. With the next following leading edge of the common clock (40 MHz, LVDS) the measurement stops. In a next step the output voltage of the TAC will be converted by an ADC into a 12-bit digital value. An optional piggy-back card offers the possibility to determine the charge of very narrow pulses (few nano seconds) correlated to a TAC hit simultaneously and puts the results into the common data stream.

After an external trigger event occurred, all accumulated data from the ADC's will be written into a FIFO implemented in a FPGA on board. For data collection from many boards, up to 32 TACQUILA's could be daisy chained by a differential general purpose device bus (GSI-GTB) to a special GSI DSP board (SAM)[4].

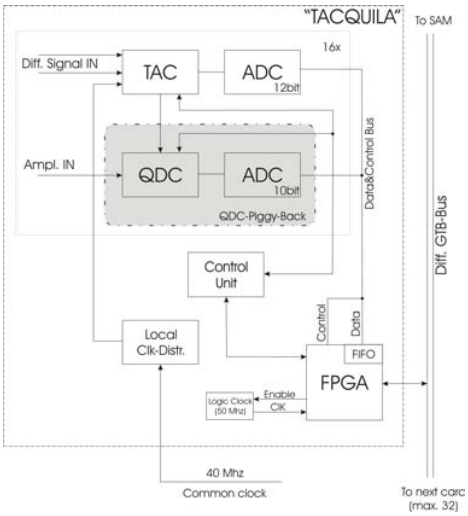

Fig. 1. Schematic of TACQUILA (The QDC-piggy-back is optional).

A typical result with a time resolution of two channels on one board is about 10ps RMS (see Fig. 2.). In comparison the time resolution between two arbitrary channels on separated boards is less than 20ps RMS.

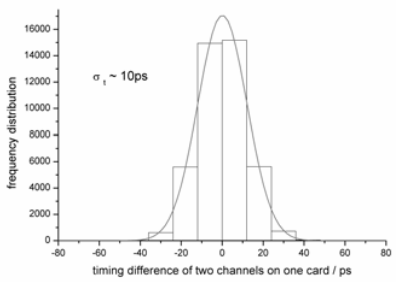

Fig. 2. Time resolution of TACQUILA

References

[1] A.Schüttauf et. al., "Timing Resistive Plate Counters (RPC) in FOPI", GSI Scientific Report, p. 231, 2003.

[2] K.Koch, H.Hardel, R.Schulze, E.Badura, J.Hoffmann, "A New TAC Based Multi Channel Front-End Electronics for TOF Experiments with Very High Time Resolution", accepted for publication in IEEE TNS

[3] R. Schulze, "Hochauflösender Zeit-Amplituden-Konverter", German Patent DE 19533414 C1, owner of the patent: Gesellschaft für Schwerionenforschung mbH (Germany), Jan. 1997

[4] E.Badura et. al., "Control System for Cancer Therapy with a Heavy Ion Beam at GSI", IEEE Trans. on NS, Vol. 47, No. 2, pp. 170-173, Apr. 2000.

Development of ADC multiplexer for SHIP

J. Hoffmann , N. Kurz, W. Ott,

GSI Darmstadt

The ADC multiplexer module AMUX has been developed to replace the existing RASMO based readout system of SHIP.

The NIM based AMUX module has the following features:

- readout and control of 4 spectroscopy ADCs
  - programmable coincidence/conversion time
  - synchronization with accelerator macro pulse
- counter/scaler function
  - max 40kHz / 16bit, readout after 1 sec of counting
- pattern unit function
  - 16 inputs, differential ECL, readout together with ADC readout
- programmable timer functions
  - fast timer: resolution 1 µs, 16 bit
  - slow timer: counts macro pulses, realized with DSP timer unit, 32 bit
- 8 channel control/trigger bus
  - synchronizing of ADC conversion
  - synchronizing of readout via GTB
  - distribution of time stamp for synchronization
- GTB access
  - Control of all amuxes from SAM3[1] over GTB
  - Fast data readout in TOKEN mode
- 4 character alphanumeric display
- 8 LEDs
- TMS320C6711 DSP for readout and control

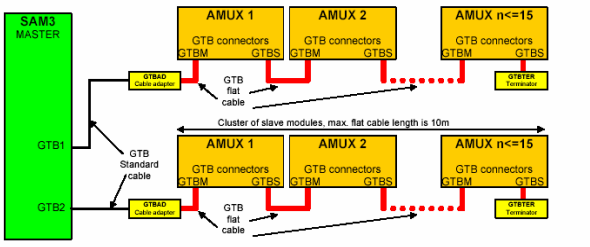

Fig 1: GTB connections of AMUX modules and SAM3

Up to 15 AMUX modules can be daisy chained on the GTB bus and connected to one of the two GTB ports of a SAM3 module, so in total 30 AMUX modules can be read out by one SAM3 module. The trigger bus connects all AMUX modules with the control port of the SAM3 and distributes timing and trigger information. After one of the ADC signals starts the coincidence time, all ADC signals that fall into the coincidence interval are accepted. At the end of the coincidence time the pattern registers are clocked and the conversion time of the ADCs starts. The end of the conversion time triggers an interrupt on the DSP, which starts the readout. The data is buffered in an event queue with a length of 400 events on the AMUX modules. The readout of the events to the SAM3 is done asynchronously by sending a readout token from the SAM3 to the AMUX modules via the GTB. The SAM3 is then read out with a VME processor running a MBS data acquisition system.

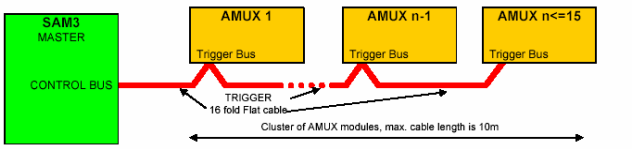

Fig 2: Trigger/Control bus connection

Due to the fact, that the functionality of the AMUX module is implemented with FPGA and DSP programs, the module can also be customized to other experimental setups.

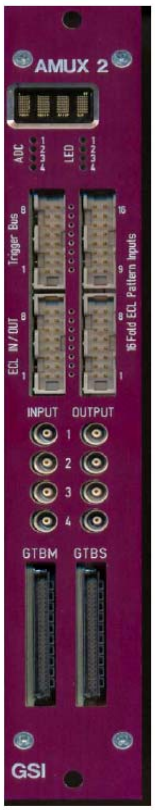

Fig 3 Front panel view of the AMUX module

References

[1] J. Hoffmann, W. Ott Development of new readout processor SAM3, GSI scientific report 2002

A high dynamic charge to frequency converter ASIC

H. Flemming[1] and E. Badura[1]
[1]Gesellschaft für Schwerionenforschung, DVEE

Since 1997 in the DVEE division a charge to frequency converter modul (QFW) has been developed to replace the older current digitiser moduls in ionisation chamber readout. This modul provided the benefit of a dynamic range of more than 7 decades without any range switching[1]. It consists of a small active PCB modul, that should be located close to the detector and a NIM modul providing four supply voltages for the activ PCB.

In 2004 the ASIC design group has started to design a full custom designed application specific integrated circuit (ASIC) with the same functionality. In the end of the year the prototypes came back from the foundary and now first test and measurement results are available.

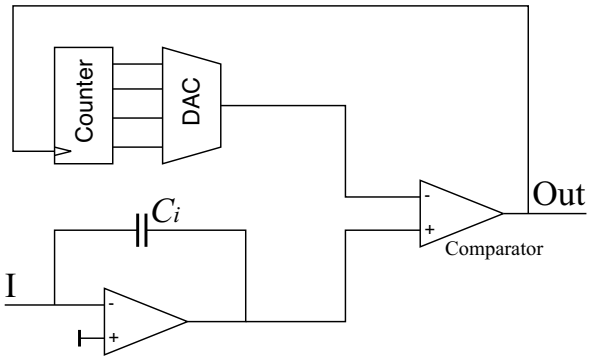

Figure 1: principle diagram of the converter

Figure 1 shows a principle diagram of the charge to frequency converter. The incoming charge is integrated on the capacitor C_i. The output voltage of the integrator is continously compared with a threshold voltage which is generated by a 4 bit digital to analog converter (DAC) getting the input data from a 4 bit counter. Each time the integrator output exceeds the threshold voltage the counter is incremented, so the threshold voltage is increased by one voltage step. When the counter reaches the maximum value a second integrator takes over the operation and the first one is cleared.

The charge, which is needed for each pulse is given by the step voltage of the DAC U_{LSB} and the integration capacitance C_i by $Q = U_{LSB} \cdot C_i$. The output frequency f increases linear with the input current I: $f = I/Q$.

With an integration capacitor C_i of 2.1 pF and a step voltage of 125 mV, the QFW-ASIC reaches a resolution of 0.265 pC. As the dynamic range at higher currents is limited by the maximum output frequency the comparator and counter can work with, C_i can be switched to a 21 pF capacitor. This expands the dynamic range to higher currents by one order of magnitude while the resolution decreases also by a factor of 10.

The charge to frequency converter is implemented in an 0.35 μm CMOS technology by AMS. In addition to two complete converter channels the voltage reference with 10-bit DACs for three reference voltages is implemented on a 3.28 by 3.38 mm^2 silicon die. It is bonded in a 64 pin QFP package and first measurements with these prototypes took place in the end of 2004.

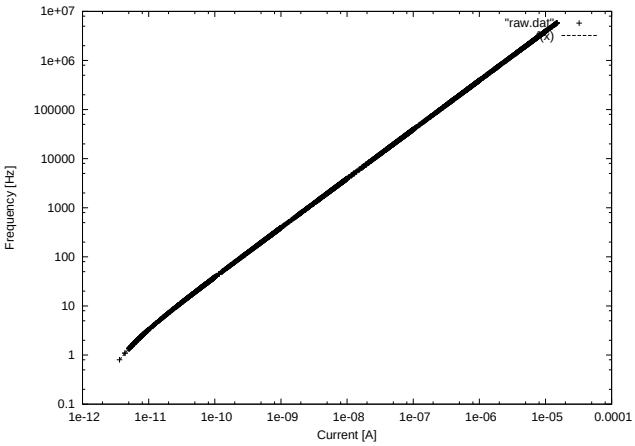

Figure 2: measured charactaristic of the QFW-ASIC

Figure 2 shows the current frequency characteristic of the converter in the range of 3 pA to 15 μA with 21 pF chosen as integration capacitance C_i. It shows an excellent linearity over the whole range. Only at very low currents is the effect of the leakage current visible. The relative deviation of the measured frequency from a linear dependancy is less than $\pm 1.5\%$ throughout the whole range. Between 20 pA and 15 μA it is even better than $\pm 0.5\%$.
In table 1 an overview over the most importend measured parameter leakage current I_L, maximum current I_{max} and frequency to current slope is given.

C_i	I_L	I_{max}	Slope
2.1 pF	1.65 pA	18 μA	3.924 MHz/μA
21 pF	1.60 pA	180 μA	392.6 kHz/μA

Table 1: measured parameter of the QFW-ASIC

The first prototype of the QFW-ASIC can handle negativ currents only. For a second prototype in 2005 it is planed to expand the converter circuit for currents of both polarities. Moreover, some minor changes in the layout to improve matching of different components are in progress.

References

[1] EU - Patent: EP 1 031 040 B1, E.Badura, Vorrichtung und Verfahren zum Umwandeln von Ladungsfluss in ein Frequenzsignal

Status of the *CS* framework

Dietrich Beck and Holger Brand

GSI-Darmstadt, DVEE, Planckstr. 1, D-64291 Darmstadt, Germany

1. Introduction

The *CS* (Control System) framework is object-oriented, multi-threaded, event-driven, distributed and provides SCADA (Supervisory Control And Data Acquisition) functionality [1]. Today, *CS* is in production at various facilities - SHIPTRAP [2], ISOLTRAP [3,4], LEBIT [5] and at another atomic physics experiment at GSI [6]. At PHELIX [7] and REXTRAP [8], the commissioning of *CS* based systems is in the final stage. For upcoming facilities like MATS [9] or HITRAP [10], the usage of *CS* is planned.

2. Recent developments

2.1. Object orientation

Until summer 2004, the toolkit ObjectVIEW [11] was used to allow for object oriented programming in LabVIEW. However, it became obvious that ObjectVIEW did not meet the requirements concerning performance and stability. Therefore, it was replaced by self-made tools that are well integrated into the *CS* framework – a class editor, a tool for inheritance as well as a utility to test classes and objects.

2.2. DIM integration

DIM (Distributed Information Management) is a transparent communication protocol based on TCP/IP and has been developed at CERN [12]. Its high performance and applicability to different operating systems (OS) make it very attractive. Moreover, DIM is the natural interface if one would like to integrate sub-systems into large control systems based on the JCOP framework [13], which is used for the large LHC experiments at CERN.

Although DIM supports C, C++, Fortran and Java, a port to LabVIEW was still missing. This was implemented at GSI during the last year [14]. Of course, a dedicated class *DIMIntProc* has been added to the *CS* framework.

2.3. Linux

Next to Windows, Linux is the common OS at GSI. Since National Instruments improved the LabVIEW support for Linux, the *CS* framework was ported to this OS in 2004. Various details differ between the two operating systems, but they are encapsulated in the code of *CS*. It is now possible to use the same LabVIEW sources on both platforms. Although more and more hardware drivers are available on Linux, the full functionality available with the Windows OS can not yet been achieved.

2.4. DomainConsole

DomainConsole is a program that runs on each node of a control system. Its main task is to start all processes that are required on each node, like a *CS* task or an OPC server. Moreover, it serves as a watchdog for the *CS* tasks in a distributed system. *DomainConsole* is configured via an ini-file with node specific sections. As an additional feature, one can monitor the CPU and memory usage of all nodes of a control system independently of their OS [14].

2.5. Performance

The performance of *CS* has improved considerably. On a 700MHz PIII, it takes about half a second to create a complex object. The time required to send an event to an object and to receive an answer is well below 1 ms. The stability of *CS* has improved as well. Even if a control system is reconfigured many times and sometimes suffers rude user interaction, the typical uptime is in the order of one week. On the one hand this should improve further; on the other hand this is sufficient for a typical on-line run of an experiment.

3. Conclusion

The year 2004 has been a major step for *CS*, which has improved considerably in reliability, performance and functionality.

We would like to thank the experiments who helped to improve *CS* by giving feedback and contributing software.

References

[1] D. Beck et al., Nucl. Instr. Meth. A 527 (2004) 567-579.

[2] J. Dilling et al., Hyp. Int. 127 (2000) 491-496.

[3] G. Bollen et al., Nucl. Instr. Meth. A 368 (1996) 675-697.

[4] F. Herfurth et al., Nucl. Instr. Meth. A 469 (2001) 254-275.

[5] S. Schwarz et al., Nucl. Instr. Meth.B 204 (2003) 507-511.

[6] S. Toleikis et al., GSI Scientific Report 2002 (2003) 86-87.

[7] E. W. Gaul et al., GSI Scientific Report 2002 (2003) 101-103.

[8] D. Habs et al., Hyp. Int. 129 (2000) 43-66.

[9] MATS Technical Proposal to FAIR (2005).

[10] T. Beier et al., HITRAP Technical Design Report (2003).

[11] R. Buhrke, "LabVIEW Technical Resource", Vol. 9 (2002) No. 3.

[12] C. Gaspar and M. Dönszelmann, Proc. *IEEE Eight Conference REAL TIME '93 on Computer Applications in Nuclear, Particle and Plasma Physics*, Vancouver, Canada, 8.-11. June 1993.

[13] http://www.cern.ch/itcobe/Projects/Framework.

[14] D. Beck et al., Proc. *Virtuelle Instrumente in der Praxis 2004*, VIP 2005, accepted.

Activities of the Experiment Control System (ECOS) Group

Harald Hahn and Uwe Thiemer

GSI-Darmstadt, DVEE, Planckstr. 1, D-64291 Darmstadt, Germany

1 Hard- and Software development for PHELIX control system

An important step during the year 2004 was the VDE certification of the "Phelix-Interlock-System" (PILS). This required changes on the lasers (build shutters in the path of ray) and the preamp-room, which must be safety controlled. The circuits of interlock system were expanded and the VDE inspection was successfully passed on May 11. The Phelix group has received a positive acceptance report from the VDE.

Over the year 2004 the control system was extended by monitoring and control plug-in modules, there are not integrated in the interlock system.

In the middle of the year we started first steps for the interlock revision of the Z6 experiment.

A main activity was the comparison of different safety bus systems. An overview on the comparison is available online at
http://www.gsi.de/informationen/wti/dvee/exp_kontrol/bus_Index.html.

A promising approach is the AS-i bus, which is qualified for experiment controls. In experiment control systems we have many changes over the time. AS-i allowed fast changes and can be expanded quickly.

The AS-i bus together with its extension "safety at work" was checked carefully. The standard control with Beckhoff-AS-i master and emergency stop with safety monitor were set up and tested. In addition, a test program for the master was developed with LabView.

A very important design tool for controls hardware is the CAE software E^3.series. It has a database interface to Microsoft's Access-db and we can optimize the structure of our requirements.

E^3 has a scripting interface based on Microsoft's Common Object Model (COM), which uses Visual Basic procedures.

This allows for the implementation of dedicated tools. One of these scripts is a datasheet-viewer. By this, the user of E^3 can select one component in the wiring diagram or in the control panel sheet and open the pdf-datasheet with one click.

A further possibility is to build an interface to 3D-CAD system "Solid Works". So one can place connectors, boards and assemblies in 19" crates, electrical control cabinets or sensors in rooms.

We have started this project to calculate automatically cable lengths and to have an design view.

2 Hard- and Software development for SHIPTRAP control system

The first version of the high voltage Switch (HV-Switch) is meanwhile successfully used by SHIPTRAP. Unfortunately, it does not meet the safety requirements from VDE. This required a redesign of all involved components und subsystems. As an example, the requirement of an easy galvanic isolation of the data transmission line to the control system resulted in the implementation of a serial interface based on a RS-485 network.

To be able to use some subsystems not only for the HV-Switch but also for other projects, the development was split into a project specific hardware and a second hardware platform that can be adopted by software to different projects.

The project specific HVAMP3 board has a maximum output voltage of +/- 180VDC and switches between two configurable voltages. The switching is triggered with an isolated TTL pulse.

A continuous temperature measurement of the fan and a fault save interlock input is provided to disable the high voltage output. A standard crate consists of six independent output channels. A maximum of ten creates can be connected via one RS-485 line. Optionally, the transmission line can be realized with fibre optics.

In a second project the temperature of an oven should be controlled and visualised independently of the connection to an over all control system. The temperature ranges from about 20°C to 800°C and has to be controlled in accordance to a second temperature measuring point. This is achieved with the same project independent control- and communication platform that is used in conjunction with the HV-Switch.

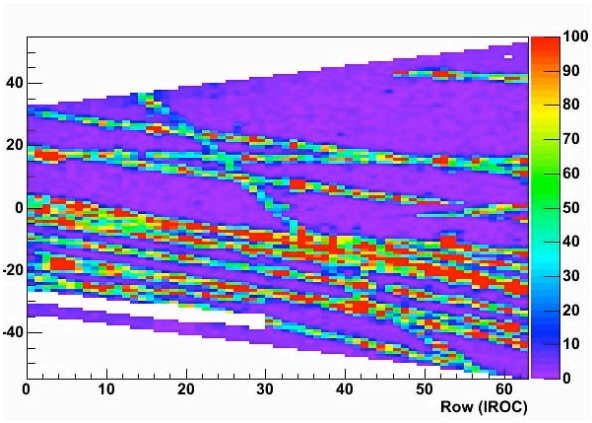

Figure 3 Cosmic ray multi-track event.

To study the response of the chamber with mono-energetic beam particles, the TPC test setup was installed in the CERN-PS T10 beam line. This allowed to evaluate the energy loss resolution with a high precision. By varying the extraction momentum a detailed study of the specific energy loss, dE/dx, in the newly proposed gas mixture – $NeCO_2N_2$ (90-10-5) – could be measured. A summary of the specific energy loss for different momenta and particles is shown in Figure 4 and compared with results from the ALEPH and Na49 experiments [4]. The corresponding energy resolution is $\sigma(dE/dx) \approx 5\text{-}6\%$ and thus comparable with the value specified in the TPC Technical Design Report[5

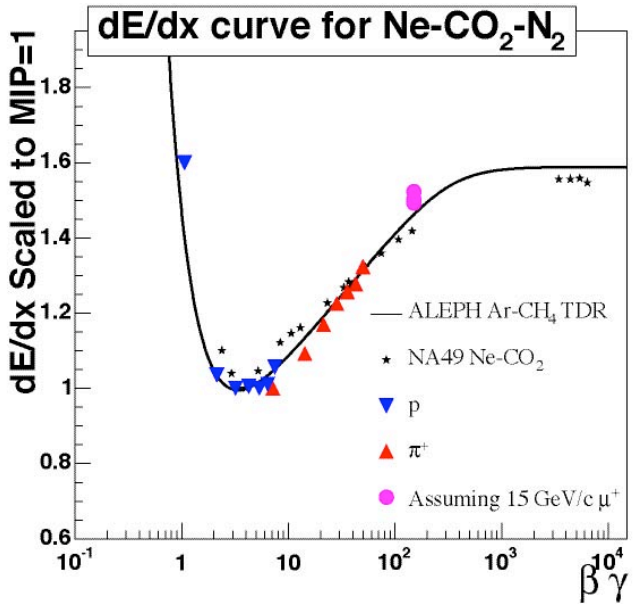

Figure 4 Comparison of dE/dx curve for the gas mixture $NeCO_2N_2$. with previous results.

References

1 U. Frankenfeld et al., "The ALICE TPC Readout Chamber: From prototypes to Series Production", ALICE-INT-2003-017;

H. Stelzer et al.; "The ALICE TPC Inner Readout Chamber: Results of Beam and Laser Tests", ALICE-INT-2002-030,

2 http://www-wnt.gsi.de/detlab/IROC.htm;
http://www-wnt.gsi.de/detlab/OROC.htm

3 C. Garabatos, Nucl. Inst. Meth. A535 (2004) 197

4 „Particle Identification in the NA49 TPCs", B. Lasiuk for NA49, Nucl. Inst. .Meth. A409 (1998) 402

5 Technical Design Report, CERN/LHCC 2000-001

Readout Chambers for the ALICE TPC

G. Augustinski[1], J. Bächler[2], P. Braun-Munzinger[1], P. Christiansen[2], H. Daues[1], U. Frankenfeld[1], J. Hehner[1], C. Garabatos[1], P. Glässel[3], R. Renfordt[4], H.R. Schmidt[1], S. Schwab[1], J. Stachel[1], H. Stelzer[1], D. Vranic[1], J. Wiechula[1], B. Windelband[2]

[1]GSI Darmstadt, [2]CERN, [3]University of Heidelberg, [3]University of Frankfurt

In 2007, the Large Hadron Collider (LHC) at CERN is scheduled to commence operations. ALICE is the only experiment at the LHC dedicated to the investigation of Pb-Pb collisions at 1248 TeV center-of-mass energy. The central tracking detector of ALICE is large TPC (V≈ 88 m^3). The two TPC readout planes ($Ø_{outer}$ = 530 cm) are divided into 18 sectors in ϕ. Each sector is radially subdivided in an inner and outer sector, each holding an Inner (IROC) and an Outer Readout Chambers (OROC) (cf. Figure 1).

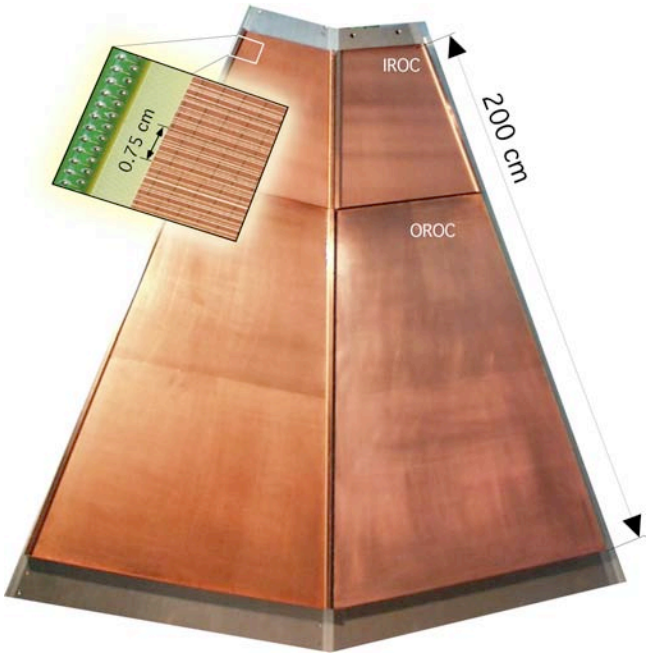

Figure 1 View of the pad side of two sectors of a TPC endplate. The magnification reveals the pad structure and the wire planes.

The design and construction of the TPC Read-Out Chambers is taken on by University of Heidelberg, Comenius University of Bratislava and GSI Darmstadt. The series production of, - in total 80 chambers -, had started in May 2001. It was completed, including quality control and functional tests [1] of all chambers by November 2004 [2].

Before and during production for each of the chambers were subjected to several tests:

All of the pad planes with 5.504 and 9.984 pads for IROC and OROC, respectively, have been checked with a semi-automatic device for a good contact to one and only one connector on the backside of the plane. About 5 % of the pad planes had to be rejected. The gluing of the pad plane onto the aluminium body and some machining has been done at the Physikalische Institute in Heidelberg. During production, several quality controls were applied to ensure the same performance for all the chambers. The planarity of the pad plane and its distance to the reference points on the backside was measured with a high-precision X-Y-Z measuring table. On each wire plane, the mechanical tension of each wire was measured and documented. The resistance of all the wire planes to each other and to ground was measured. The acceptance tests consisted of the check of the gas tightness, the determination of the gas gain by counting the pulses of a Fe^{55} source and measuring the anode current, a check of the homogeneity across the active area and, finally, a long term test, where the chamber was operated with a strong Fe-source at a gain of about 40.000 for 50 hours minimum. Figure 2 shows a summary of the gain measurement for the OROCs. About half of the chambers were test with a newly introduced gas mixture [3], which supplements the nominal mixture $NeCO_2$ (90-10) with 5% N_2.

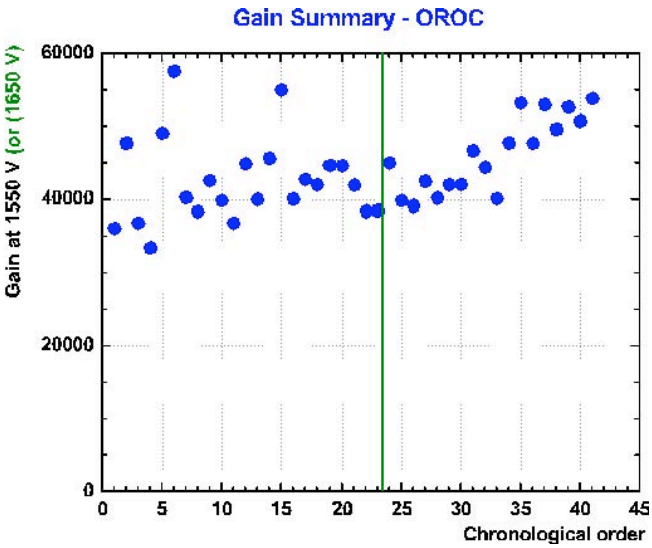

Figure 2 Compilation of the measured gain of all produced OROCs at 1550 V in a $NeCO_2$ gas mixture. The second half of the chambers (green line) were tested with an admixture of 5 % N_2 at 1650 V.

Within the TPC project a test facility was build at CERN to study in detail the performance of an IROC. The chamber was equipped with the final electronics (43 readout board à 128 channels). The data were read out by the ALICE DDL data transfer system. It should be pointed out that it was the first time that all components were available in a final version.

An example of a multi-track event as recorded by the online monitor is shown in Figure 3.

Testing of the PASA Chips of the ALICE TPC[B,G]

U. Bonnes, S. Lang, H. Oeschler and the ALICE Collaboration
Institut für Kernphysik, Darmstadt University of Technology, Germany

The "time projection chamber" (TPC) [1] as one of the main components of the ALICE detector has a cylindrical shape with a diameter of 5 m and a length of 5 m. It is composed of several individual TPC sectors. Altogether 570 000 read-out channels have to be equipped with electronics which requires 4500 "front-end cards" (FEC) each having 8 pre-amplification units (PASA) and 8 ALTRO chips. To improve the reliability of the boards, all PASA and ALTRO chips have been tested before loading the FECs. The completed FECs are then tested before assembling the TPC [2].

For testing the PASA chips, a test setup has been developed by the electronics workshop of our institute. It consists of a main board which is controlled by a PC. This board produces 16 variable signals (one "stimulus" per channel) which are sent to the PASA chip under test. The output signals of the PASA are read and digitized by 12-bit ADCs with 40 MHz simultaneously for all channels on the board. The results are transferred to a PC and a test software which has been written as part of a diploma thesis [3], calculates gain, noise, linearity, cross talk, shaping time, etc. This information allows to sort according to performance.

In total close to 50 000 PASA chips were tested. These tests were performed using a robot available at the University of Lund, used before to test the ALTRO chips. The robot was handling the insertion of the chips in the socket of the test board and the subsequent sorting. A crucial point are reliable contacts between the pins of the chips and the socket, achieved by a spring loaded socket. A mechanical device operated by compressed air and controlled by the PC released the socket for changing the chips.

The PASA chips have been sorted according to the following criteria: a chips is "bad", if the current exceeds the limits or if the performance is more than 20% off the expected values. Those chips were sorted out. For the use in the ALICE TPC further criteria have to be fulfilled:

- Amplification within ±5% of the nominal value.
- Shaping time within ±6% of the nominal value.
- Offset voltage of all channels within ±50 mV of the mean value.

Chips which passed the simple electrical test but with values outside the criteria given above, have been grouped as "out-of-tolerance". Figure 1 shows the distribution of the performance in gain and in peaking time together with the lines defining the chosen selection criteria. The peaking time is calculated from a Gamma-4 fit (see [2]) and is proportional to the shaping time.

The time for testing one chip was about 15 s for the various motions of the robot and about the same time was needed to run the test program using a 2.8 GHz PC. About two chips were tested within one minute. All ∼ 50 000 PASA chips were tested in five weeks.

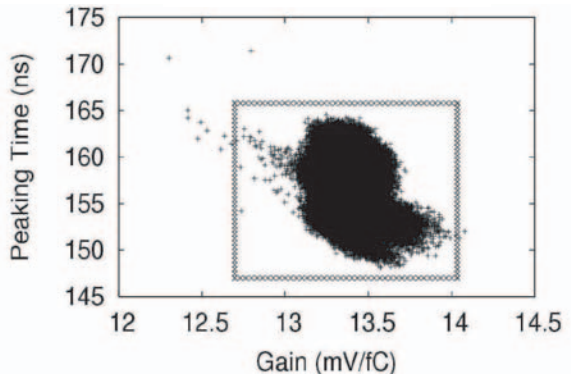

Figure 1: Distribution of gain versus peaking time and the selection criteria as line.

In total, about 2% of all chips are tested "bad", less than the manufacturer's estimate (AMS, Austria). 40 855 PASA chips fulfilled the chosen selection criteria and were used for loading the FECs now tested in Frankfurt [2].

The remaining 12.3% are functional but with at least one channel having characteristics outside the specifications. In most cases the chosen range of the offset voltage was exceeded. This parameter influences the dynamic range of the FECs. These PASA chips can easily be used when adapting the FECs slightly. For this reason, a second test run was performed for these "out-of-tolerance" chips and they were sorted into three classes with different ranges of offset voltages: Within a larger range of ±75 mV around the same mean value were 23% of the remaining chips. With a mean value being 1% lower than before and within a range of ±50 mV (same as for the first test) 54% were found. Finally 20% were sorted in a group with a 1% higher mean value and within a range of ±50 mV. For this second test two weeks were needed. 5500 additional PASA chips with known characteristics are now available for other applications.

The PASA preamplifier for the "transition-radiation-detector" (TRD) [4] is in many respects similar to the TPC PASA. With some changes, the developed main board and the software can be used here. However, the TRD PASAs have to be tested on the wafer. The adapter is built and the testing is in progress.

References

[1] ALICE TDR of the Time Projection Chamber, CERN/LHCC 2000-001.
[2] R. Renfordt et al., this annual report.
[3] S. Lang, diploma thesis, Darmstadt University of Technology, 2004.
[4] ALICE TDR of the Transition Radiation Detector, CERN/LHCC 2001-021.

Mass test of the front-end cards of the ALICE TPC*

R.Renfordt , W. Amend, N. Bialas, S. Kniege, E. Köhler, M. Marinova, W. Meuter, Th. Schwab, R. Stock and M. Urban and the ALICE Collaboration

J.W. Goethe University, Frankfurt/Main

The Time Projection Chamber (TPC) of the ALICE experiment is read out by 4356 front-end cards (FEC). The main components of the 8 layer boards are the 8 preamp/shaper chips (16 channels each) and the 8 ASICs for analog-to-digital conversion and signal processing. All chips went through an acceptance test before mounting on the board[1].

Space constraints on the TPC result in an elaborate mounting and dismounting procedure for the FECs. Therefore a rather stringent acceptance test is performed to avoid frequent exchange of cards.

In the first step of the acceptance test the front-end cards are exposed to 10 heating/cooling cycles with a minimum/maximum temperature of 28/100°C. This should expose weak soldering and bonding connections.

Then the 6 flat Kapton cables that connect later to the wire chambers of the TPC are inserted using a specially designed tool. Afterwards the cards are tested in a test stand (Fig. 1). Special care has been taken to ensure fast connection of the

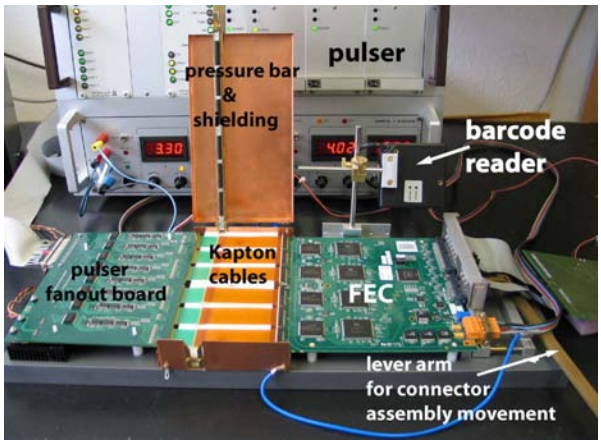

Fig. 1: Test stand for the front-end cards. The outputs of the pulser fanout board are connected to the inputs of the FECs by pressing the flat cables together with the pressure bar. On the right side the lever arm controlling the movement of the connector chariot is visible. For the identification of the board a barcode reader is installed.

cards to the input and output cables. The connection of the power and readout cables is performed by a simple movement of a chariot carrying all connectors. The connection of the inputs to the outputs of the pulser fanout card supplying individually controllable test signals for all 128 channels is achieved by simply pressing the output cables against the input cables of the FECs. Injecting charge - alternating between odd and even input channels - allows to detect shorts between adjacent channels. In addition relevant parameters of the analog circuit (noise, gain, shaping time and linearity) are extracted. All status and control registers as well as memory cells of the digital circuits are tested. The results of the tests are stored for each card in a database. The cards are identified by a barcode sticker which is read out by a barcode reader.

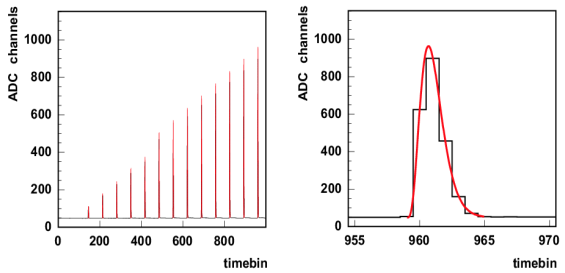

Fig. 2: Sequence of pulses with increasing charge (left side). Blow up of the highest peak together with a Gamma-4 fit (right side).

In Fig. 2 the response of a typical channel is shown for a sequence of increasing charge pulses over the full time range (left side) and an expanded view of the highest peak with a fit to a Gamma-4 function (right side). From this information the deviation from linearity is extracted by fitting a straight line to the response of the FEC (Fig. 3, left side). The deviation from a linear behaviour is shown on the right side of Fig. 3. Three different methods were used to extract the amplitudes: the maximum from the Gamma-4 fit, the time bin with the highest amplitude and the integral of the signal. Systematic differences between the different methods can be observed. Nevertheless the linearity is well within the required limit of 0.5%.

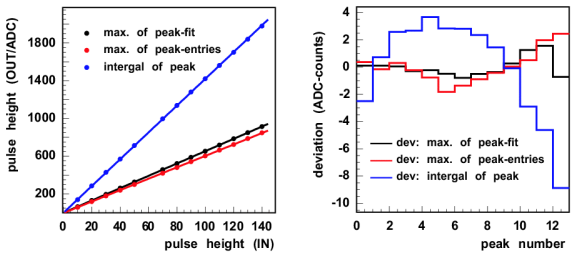

Fig. 3: Determination of linearity for a typical channel. Different methods to determine the amplitudes are compared (see text).

For the control of the pulser a digital I/O card (Natl. Instr. PCI-DIO-96) and for the readout of the FECs the ALICE RCU-1 (based on a commercial card from PLDA) or the ALICE RCU-2 card is used. A LabView program has been developed for control and readout. The parameters of the analog part are extracted from an intermediary data file using a ROOT macro. The computer controlled test takes about 1 minute. When taking into account the handling of the cards, the insertion of the Kapton cables and the mounting of the cooling plates on average 15 cards per hour can be tested. So far about 200 cards have been successfully tested in a trial run. The number of defective cards found was 7.

References

[1]U. Bonnes et al., this annual report

*Work supported by BMBF and GSI

A drift velocity monitor for the ALICE TPC

D. Antończyk[1], C. Garabatos[1], G. Augustinski[1], P. Braun-Munzinger[1], H. Daues[1], U. Frankenfeld[1], J. Hehner[1], H.R. Schmidt[1], H. Stelzer[1], D. Vranic[1] and J. Wiechula[2].

[1]GSI, [2]University of Frankfurt

The ALICE TPC [1] is an 88 m^3 detector which is planned to be operated with a Ne-CO_2-N_2 [90-10-5] gas[2]. The required relative uniformity of the drift velocity over time and space in the TPC is 10^{-4}, so that the foreseen momentum resolution can be achieved. However, the drift velocity of this optimised gas mixture is very sensitive to ambient fluctuations and, for example, it varies with the exact gas composition as much as -6.4% per percent change in CO_2 concentration. Therefore, precise monitoring of the temperature, pressure, gas composition and drift field will have to be ensured during the data taking periods. In addition, the drift velocity itself will be permanently monitored by a drift velocity monitor, known as Goofie, which underwent custom modifications in order to be operated at the specific ALICE conditions and to achieve a relative resolution of order 10^{-4}.

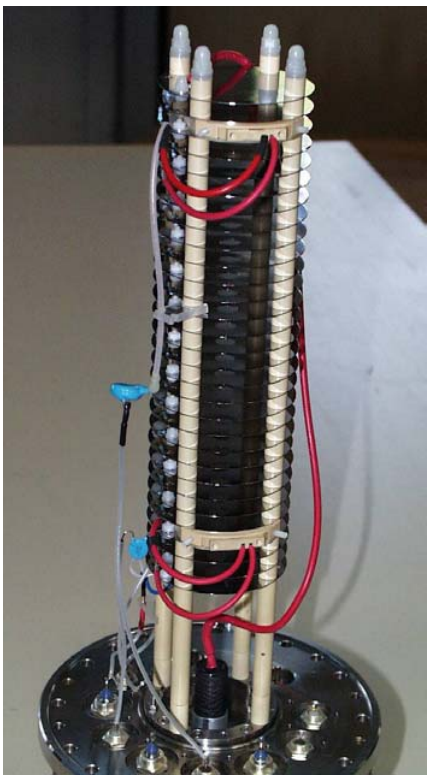

Fig. 1. Photograph of the drift velocity monitor. The field defining rings and the two trigger detectors mounted along the drift channel are visible.

The well-know principle of operation of the drift velocity monitor, shown in Fig. 1, is based on the measurement of the difference in drift time of electrons, produced in the gas by alpha-particle tracks, at two known distances from a so-called pick-up electrode. The electrons released in the gas drift down to the pick-up detector through a constant field drift channel defined by equally spaced ring electrodes. Two counters, facing each alpha source, provide a trigger signal, and the pulseheight spectrum in the pick-up is recorded as a function of time. The drift channel is operated at the unprecedented ALICE TPC field of 400 V/cm, for which measures against high voltage breakdown have been undertaken. In particular, the voltages of both the anode wire and the cathode tube of the trigger counters are taken from the nearest drift field electrodes. This prevents high fields to form near the counters, and limits the field distortions in the drift channel.

The monitor was operated in this fashion for several days and data were recorded in sets of about 20 minutes, during which the sum of all FADC signals received at the pick-up was accumulated. In addition, the temperature inside the monitor and the ambient pressure was recorded too. The gas enclosure may be water-cooled to provide good temperature uniformity in the ensemble, although this hasn't been used yet. The drift velocity is extracted from the position in time of the peaks corresponding to the signals coming from both the near and the far source. The electric field of the drift channel was also monitored and found to be constant during the measurements, and the gas mixture was premixed in order to avoid, at this stage, any possible fluctuation in the gas composition. The linear correlation between the drift velocity and the gas density (T/P) is shown in Fig. 2. After the subsequent correction, the precision in the drift velocity measurements is 3×10^{-4}. A better precision is expected to be achieved by actively cooling the monitor. In addition, the precise measurement of the gas gain will also be attempted.

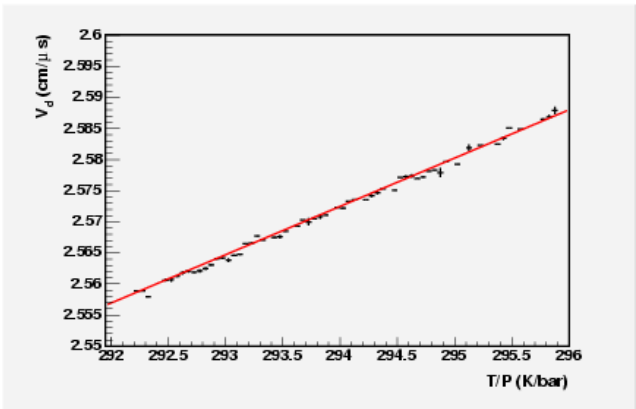

Fig. 2. Correlation between the measured drift velocity and the gas density.

References

[1] TPC Technical Design Report, CERN/LHCC 2000-001.

[2] C. Garabatos, *The ALICE TPC*, Nucl. Instr. and Meth. Phys. Res. A 535 (2004) 197.

Front-end electronic cooling and temperature monitoring of the Alice TPC

U. Frankenfeld [1], P. Braun-Munzinger [1], C. Garabatos [1], R. Renfordt [2], H.R. Schmidt [1], H. Stelzer [1], D. Vranic [1], J. Wiechula [1,2]

[1]GSI Darmstadt, [2]University of Frankfurt

The Time Projection Chamber (TPC) is the main tracking detector of the ALICE Experiment at the CERN Large Hadron Collider (LHC). A gas-filled, cylindrical volume of 88 m^3 composes the sensitive region of the TPC. The maximal drift length is 2.5 m. The readout chambers (ROC) are arranged in 18 trapezoidal sectors at both ends of the cylinder.

The electron drift velocity changes by ~0.3 %/K for the nominal gas mixture ($NeCO_2$ 90/10) and drift field (400 V/cm) [1]. This leads to the requirement for the temperature stability and homogeneity within the TPC drift volume of $\Delta T<0.1°C$ [2]. The main heat source is the Front-End Electronics of the detector itself, with a total heat dissipation of ~30 kW.

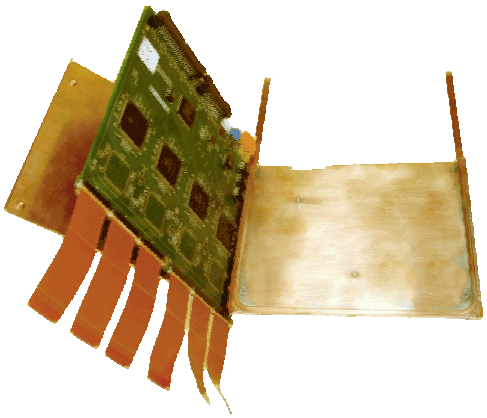

Figure 1: Cooling envelope of the front end electronic card.

The Front-End Cards (FEC) are covered with water-cooled copper plates (Figure 1). The cooling plates of one sector are connected to one cooling circuit which allows regulating the temperature for each sector individually. To remove residual heat not taken away by the FEC cooling the ROCs are connected to a common cooling circuit. To verify the cooling strategy tests with a readout chamber module and pre-series FECs in a thermal controlled environment have been carried out[3].

The pads signals from the detector are transferred to the inputs of the FECs via kapton cables. The cables have been chosen to minimize both the mechanical force and the heat transfer between the ROCs and the FECs.

Figure 2 shows the measured temperatures on the pad plane inside the TPC with and without the cables while switching off the power of the FECs. Approximately 25 % of the heat is transferred via the kapton cables. The relaxation time of the ROC is approx. 30 minutes.

Figure 3 demonstrates that the power dissipated by the FEC can be compensated by lowering the cooling water temperature. After the relaxation time of approx. one hour, here given by the chamber and the cooling system, there is no heat transfer to the pad plane measurable.

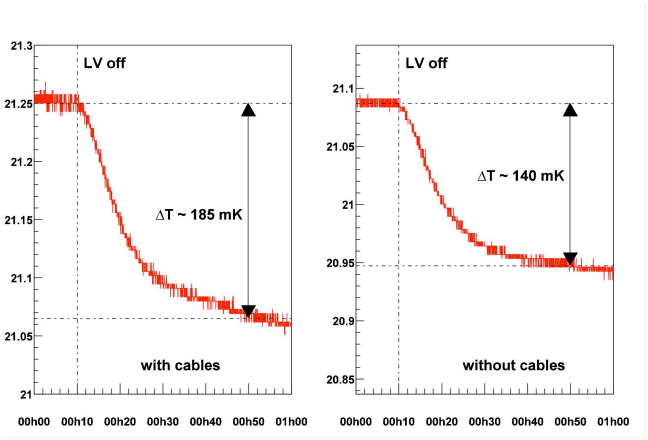

Figure 2: Measured heat transfer with and without the cables

To control the temperature stability within the TPC a temperature monitor system will be set up [4]. Altogether 432 sensors are mounted inside and outside of the gas volume of the TPC. Six sensors will be mounted on the ROCs in each sector, 144 on the field cage cylinder and 36 inside the TPC. At each sector one sensor will measure the cooling water inlet temperature and one the cooling outlet. The temperature monitoring system uses Pt-1000 sensors. To ensure a precision better than 0.1°C the sensors are calibrated against two certificated sensors at room temperature. Additional temperature sensors on the FECs (one sensor for each of the 4356 FECs) complete the monitoring system.

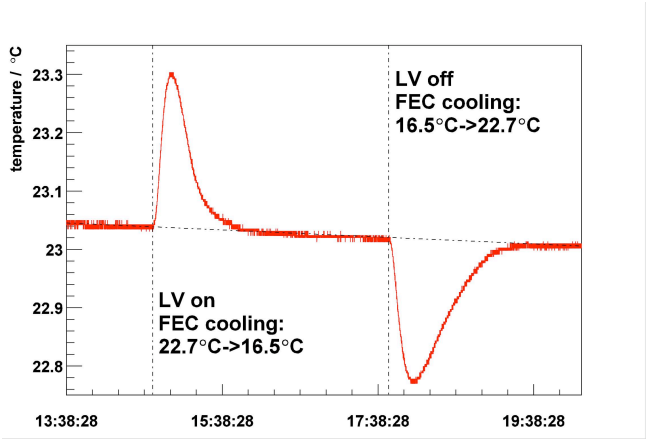

Figure 3: Compensation of the heat dissipation by the FECs with the cooling water temperature.

References

[1] Jens Wiechula, Diplomarbeit, 2004

[2] ALICE TPC TDR CERN/LHCC 2000–001

[3] ALICE-INT-2005-001

[4] ALICE-EN-2005-001

Simulation of the effect of clock jitter on the ALICE TPC Frontend electronics*

R. Bramm for the ALICE collaboration
Universität Frankfurt

Each digital clock has a finite jitter, which means that the time interval between two clock cycles is not exactly constant. The required clock accuracy is a compromise between the time accuracy of the measurement and the effort to build the clock. Since in this case, a clock is needed on each of the 4356 FECs (**F**ront**e**nd **C**ard) of the ALICE TPC, a complicated clock scheme is prohibited. A simulation was done to find out the required accuracy.
The starting point is the signal generated by the PASA (**P**rea**a**mp./**S**h**a**per), which has the shape of a semi-Gaussian function of fourth order:

$$f(t) = k\left(\frac{t-t_0}{\tau}\right)^4 \cdot e^{-4\frac{t-t_0}{\tau}} \quad t > 0, \qquad (1)$$

and $f(t < 0) = 0$ with the parameters t_0 as the starting time, the relaxation time τ and $k = Ae^4$ with the amplitude A.
The jitter is a Gaussian distributed noise generator with varying width σ which represents the assumed clock accuracy. The noise of the acquisition chain is a Gaussian distribution of the width of $\sigma = 0.6$. All parameters are shown in the table:

Par.	Min.	Max.	Comment
A	25	1000	18 Steps
t_0	-0.5	0.5	Flat random
τ	1.5	1.5	Fixed
Jitter	$\sigma = 0$ns	$\sigma = 2$ns	Gaussian random
Noise	$\sigma = 0.6$		Gaussian random

Three sets of samples have been calculated: only noise, only jitter, noise and jitter, which are then rounded to integer values to add the quantisation noise, and finally fitted separately using equation 1 as fit function. The starting parameters for the fit are the original values of the generated pulse. There are two important parameters of a pulse, the time position and the amplitude. The difference between the fit result

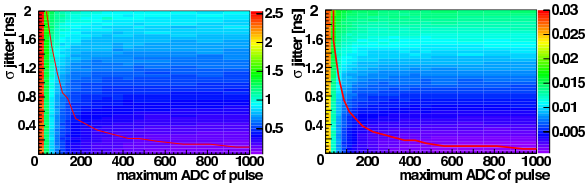

Figure 1: Error in the relative amplitude measurement (left) and time measurement in ADC (right) through all simulated amplitudes and jitter. The red line indicates the crossover in between the noise and the jitter as main error source.

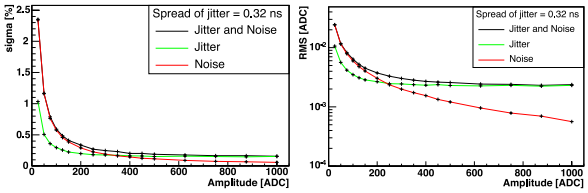

Figure 2: Relative error in the amplitude measurement (left) and in the time measurement (right) at the forseen clock accuracy of 0.3 ns

and the original values for amplitude and time are collected out of 2000 differing generated sets of pulses. From this distribution the RMS is calculated. For the amplitude difference, the distribution is fitted by a Gaussian to get more stable results. In figure 1 the error introduced when increasing the amount of jitter by widening the σ of the random generator and as function of the amplitude is shown.
In figure 2 the cut along the foreseen clock inaccuracy of 0.3 ns is shown. It is clearly visible, that in the domain of the most probable ADC values ($\approx$ 30 for a MIP (**M**inimum **I**onising **P**article)), the effect of the jitter plays a minor role compared to the influence of the noise.

* Work supported by BMBF and GSI

Pad plane production for the ALICE-TRD readout chambers

W. Sommer[1], C. Adler[2], W. Amend[1], H. Appelshäuser[1], C. Blume[1], D. Emschermann[2], S. Freuen[2], H. Hinke[1] and F. Kramer[1] for the ALICE-TRD collaboration

[1]Institut für Kernphysik, Universität Frankfurt a.M., Germany

[2]Physikalisches Institut, Universität Heidelberg, Germany

The ALICE detector is a dedicated heavy-ion experiment at the new Large-Hadron-Collider (LHC) at CERN. One of its major components is the Transition Radiation Detector (TRD). It consists of 540 readout chambers. Each chamber has a 5 cm thick radiator where the transition radiation is produced. Attached to the radiator is a gas chamber to detect the transition radiation and measure the ionisation produced by the traversing particle. The gas chamber has a 3 cm long drift region and a 0.7 cm amplification gap. The induced charge is collected at the back panel of the chamber which is covered by copper pads of size 1.2×9 cm^2. The copper pads are connected to the readout electronics via flat ribbon cables. Each cable connects 18 pads. 48 cables are soldered to the backside of each pad panel. All in all 1540 pad planes will be produced. The process of soldering consists of four major steps all conducted at the Institut für Kernphysik in Frankfurt:

- Application of tin-solder to the pads on the backside of the panel.
- Placing the ribbon cable.
- Soldering of the cables using a custom build soldering machine (see figure (1)).
- Quality control of the single connections.

Figure 1: Soldering ribbon cables to the pad plane.

Application of the tin-solder and the quality control turned out to be the crucial steps for the production. The tin-solder is applied to the pad plane by a dispenser, then the solder is distributed with a soldering iron. It takes some experience to apply the right amount of solder, insufficient amount of solder will lead to poor connections, while excessive amount of solder may cause shorts. To avoid poor connections which might pass the quality test but break afterwards, the amount of solder is chosen to be a bit more than necessary therefore the most dominant group of possible errors are shorts. The quality test is done using a custom-made device (see [1] for description) which measures the capacity of the copper pads. Shorts cause a significant higher capacity as two or more pads are connected while bad connections will lead to small capacities as the copper pads will not contribute.

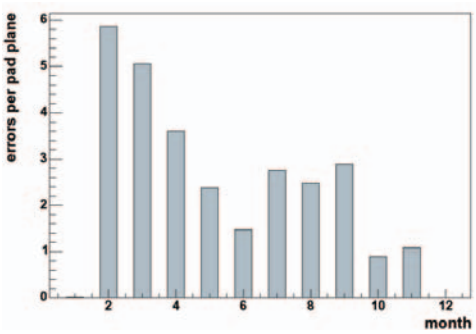

Figure 2: The evolution of errors per pad plane in 2004. More than 90% of the errors are shorts.

During the last year, the production developed in two ways: The amount of errors per produced pad plane reduced by a factor of two (see figure (2)) and the number of produced pad planes grew by a factor of 1.5 (see figure (3)) predominantly due to a better organisation of the production process and less time for repairs.

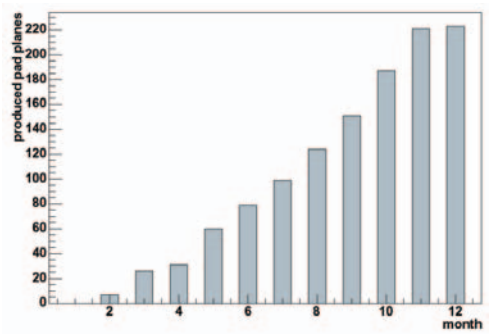

Figure 3: The number of produced pad planes in the year 2004. Due to the relocation of the institute the production was stopped in December.

In January 2005 three new student assistants started working on the production. Due to this fact and a larger production site at the new institute the amount of produced pad planes per month is expected to increase rapidly and will be enough to supply the different production sites for the chambers.

References

[1] T. Lehmann, *Vorbereitungen für die Qualitätstests der ALICE-TRD-Kammern*, Diplomarbeit, Universität Heidelberg (2004)

Development of a test-setup for ALICE TRD-PASA

H. K. Soltveit, V. Catanescu, J. Stachel
Physikalisches Institut, Heidelberg University

A very important part in the development of the PASA for the Transition Radiation Detector (TRD) of the ALICE experiment [1] is the test, to find out how well it agrees with the given specifications. The ALICE TRD PASA consist of 18 channels, and is fabricated with the AMS 0.35μm CMOS process. The area of the chip is 21 mm^2. The total amount of wafers to be tested is 97. As every wafer consists of 1275 dices, a total of 124 000 dices have to be tested. In this context a test-setup for mass-testing of the TRD-PASA is developed.

Figure 1: Overview of the mass test setup

A picture of this setup is shown in fig 1. It consist of the main PASA tester, the needle card (fig. 2), the needle card adapter (fig.3), a control panel, a wafer map, the chuck and a microscope for visual inspection. The wafer map is a virtual picture of the wafer where all the processed chips are marked. The main PASA tester is the same as used for the TPC mass tester [2]. A"universal" standard

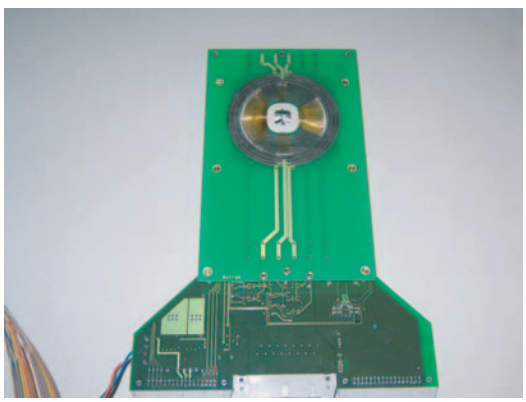

Figure 2: Needle card

needle-card available at ASIC laboratory in Heidelberg for the ATLAS project is used. This card has the possibility to electrically connect 144 test points, of which we need only 87. The needle card adapter consist of relays that are used to switch in the 5 extra channels that are there as compared to the 16 channels of the TPC-PASA. The needle card is the interface between the wafer and the main PASA test board and the PC.

The test software used for the mass test of the TRD-PASA is based on the test software successfully used for testing of the TPC PASA. Some software updates are necessary due to two extra input and five extra output pads, the in-chip test structure, the internally generated bias-network and the addition of a wafer stepper program. By a pre-defined data-stream from a programmed FPGA, the in-chip test circuit will be used to test the PASA through the three logic inputs: CLK (clock), DIN (serial data input), STR (strob).

We plan to measure the baseline variation, the conversion gain, the peaking time, the noise, the crosstalk, and the power consumption. As all the test data will be saved in one file, one can define the selection criteria to choose the best chips after the test is finished. The test preparation is ongoing. The anticipated test time per dice is about 30s. In addition the needle should be cleaned after every 300-400 dice. The anticipated testing time, including cleaning/reinstallation, gives a total of 170 working days of (8 h). The excpected yield will be in the area between 90-100%. After the testing is finished the wafers will be diced, soldered and glop-topped together with tested TRAP chips.

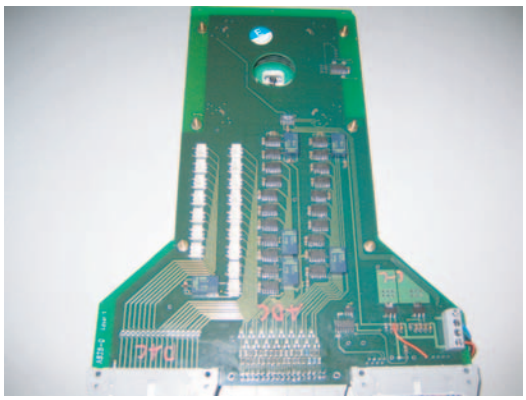

Figure 3: Needle card adapter

References

[1] H.K.Soltveit *et al.* GSI Annual Report 2003, p 244
[2] U.Bonnes *et al.* GSI Annual Report 2003, p 245

Final version of the tracklet processor chip (TRAP) for the ALICE TRD

V. Lindenstruth [1], R. Tielert [2], D. Muthers [2], Ch. Reichling [1], M. Gutfleisch [1], R. Schneider [1], J. de Cuveland [1], V. Angelov [1]

[1]Kirchhoff Institut für Physik, Ruprecht-Karls-Universität Heidelberg, Germany
[2]Fachbereich für Mikroelektronik, Universität Kaiserslautern, Germany

The ALICE TRD has about 1.2 million analog channels. The charges are converted to voltage pulses by a low noise low power preamplifier and shaping amplifier (PASA [1]) and digitized to 10 bits at 10 MSPS. The tracking information used for the trigger decision must be processed on the chamber in less than a microsecond and send to the Global Tracking Unit (GTU). To fulfill such requirements a mixed mode ASIC named TRAP has been developed. It contains 21 low power ADCs, configurable digital filters, preprocessor, four RISC CPUs with individual instruction memories and full custom quad-ported data memory (Fig. 1). The area

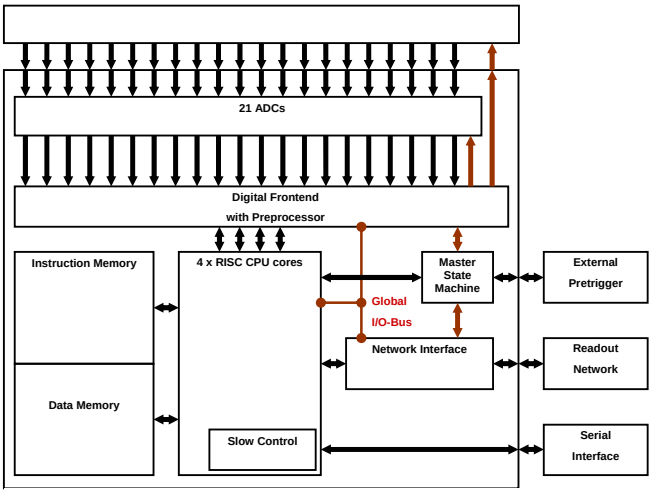

Figure 1, Block diagram of the TRAP chip

of a single ADC is 0.11µm^2 in 0.18µm CMOS due to its cyclic architecture. At 10 MSPS the typical ENOB of the ADC is 9.5 bits, measured with all ADCs and a CPU running (Fig. 2). The power consumption per ADC channel is 12mW at 10 MSPS. Between events this can be lowered without turning off the ADCs completely. In addition the TRAP chip is used to build up a tree structured network at 120 MHz DDR [2]. The data of the root node is send to a Global Tracking Unit (GTU) through a serial optical link at 2.4 GBps. The configuration of the TRAP chips is distributed via a slow control serial link using a small board with embedded Linux (DCS) and Ethernet interface.

The TRAP and PASA chips are bonded on a low cost MCM with a BGA footprint. There is a possibility to make a self test of the MCM using a test-generator inside the PASA chip. A detector prototype partially equipped with 139 MCMs and about 2300 analog channels was successfully tested in beam at CERN in fall 2004. All functional parts of the chip were found to operate as expected. In Fig. 3 an

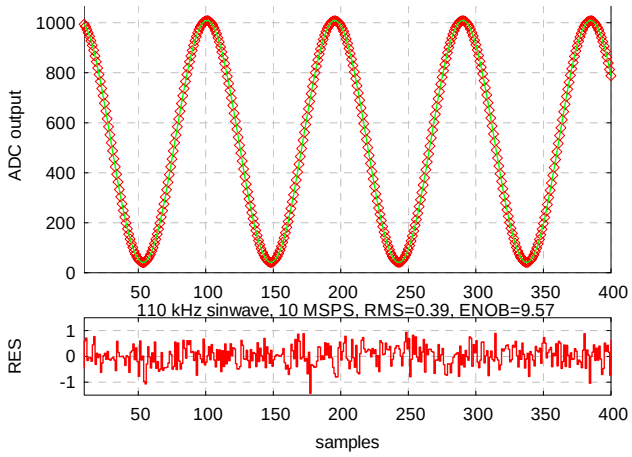

Figure 2, ADC test, readout done by the CPU

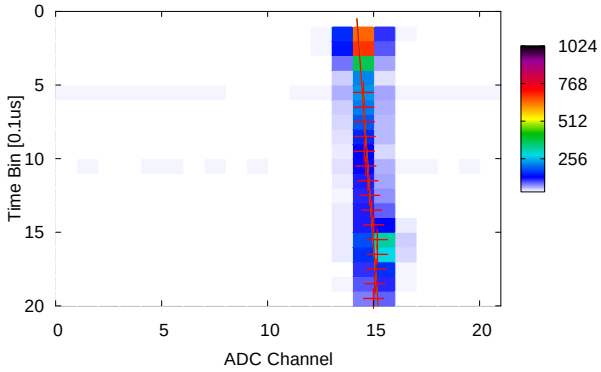

Figure 3, Online tracking of the TRAP chip.

example of the online tracking of the built-in preprocessor is shown.

A fully automated MCM tester was developed for the final production of about 100,000 MCMs starting 2005. It can control all input pads and read all output pads at nominal clock rate, control the supply voltages and measure the supply currents.

References

[1] GSI Scientific Report 2003, p. 244
[2] GSI Scientific Report 2002, p. 247

The new prototype of the ALICE TRD Readout Board

I. Rusanov, J. Stachel
Physics Institute, University of Heidelberg

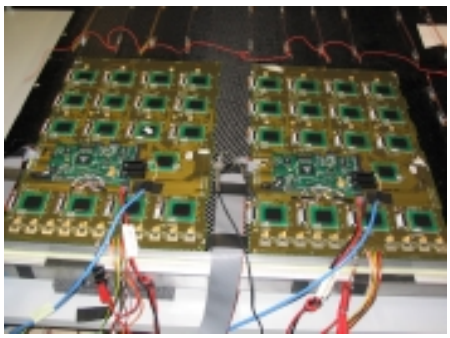

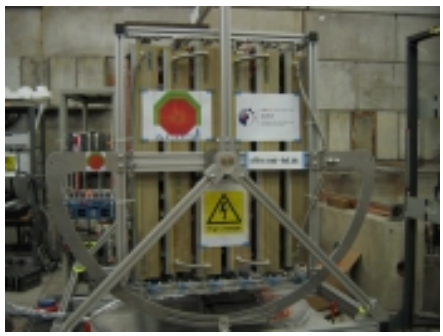

Fig.1. Readout boards on the TRD chamber and CERN test setup

One of the major component of the ALICE TRD front-end electronic is a readout board (ROB). General requirements of the ROB can be found in [1]. Here we briefly review the next prototype of the ROB (Fig. 1). This is a 6-layer board, which connects multichip modules (MCM) carrying 2 custom chips for 18 channels each: a charge sensitive amplifier (PASA) and a chip combining ADC and digital processing (TRAP). The readout board includes components, which are connected to 288 cathode pads of the drift chamber.

New power supply scheme. For the ALICE TRD one of the essential challenges is power dissipation. In this context it is essential to avoid the very high voltage drop on the voltage regulators, which are usually used in power supply lines of 1.8 V (TRAP and ADC's). Therefore in these power supply lines we use new type of ultra LDO voltage regulator (LP3882-1.8). The device operates with two input voltages (Vbias and Vin), which allows it to operate with voltage drop of 0.11 V. In the new power supply scheme there are 12 ultra LDO voltage regulators, arranged in three groups. Two of them include 5 voltage regulators. They are used for the supplying of the MCM modules, which produce data for the track reconstruction. The third group includes only two voltage regulators, which supply the MCMs where LVDS signals are merged in the read-out tree. With this new power supply scheme we can decrease the power dissipation in voltage regulators by 15 kW for the ALICE TRD detector.

The PCB layout. To minimize noise, one of the essential requirements for the readout board are good solid ground and power planes. Therefore the readout board has 4 power planes, on which are distributed 12 power supply voltages and 4 grounds (analogue – PASA and ADCs, digital – ADCs and TRAP). In the ALICE TRD we use ROBs with fixed positions of MCMs in 4 rows and 4 columns. In each column the grounds of ADCs (analog and digital) and TRAP ground are connected in one point below each MCM module. The PASA analogue ground is fully separated. The next connections between equivalent grounds of each column are done near to the power connector. On the ROB for each voltage regulator and power connector there are two possible places. Therefore the readout board has two joining points (current free) of equivalent grounds. Which one will be used as "common ground) of the ROB depends on its position on the chamber.

Another essential feature is to have very good decoupling capacitor groups. The decoupling capacitors should cover the full frequency range, in which our electronics work. Therefore there are on the readout board in each group of decoupling capacitors several capacitors with different values. The bypassing of TRAP power supply pins is done with capacitance values 270 pF, 6.8 nF, 0.1 μF and 4.7 μF. To improve the ADC's analogue power supply line (1.8 V) in each group of decoupling capacitors one resistor of 2.2 kΩ is added.

MCM module. Another issue in the improvement of the power delivery network of the readout board is minimizing of the parasitic inductances of each power supply line. To optimize this the PCB board of the MCM modules was redesigned. On its bottom layer the widths of each power supply trace were increased. Also, the number of supply and ground vias was increased.

With these changes a better balance between power supply and ground traces is obtained. The "stand alone" ROB contributes to the detector noise 500 e (0.5 LSB).

The new prototype of the readout board (ROB with DCS board) was used in ALICE TRD CERN beam time in November 2004.

References:

[1] ALICE TRD Technical Design Report. CERN/LHC 2001-021

First beam test with a real size, six layer, series production detector stack for the ALICE TRD

ALICE TRD Collaboration

The Transition Radiation Detector (TRD) of the ALICE experiment at LHC is designed to provide electron/pion identification and tracking of all charged particles [1]. The TRD will supplement the TPC electron/pion identification by a pion rejection factor of the order of 100 at momenta in excess of 1 GeV/c, allowing precision measurements of quarkonia. Sophisticated on-detector electronics [2] will allow to trigger on high-momentum electrons and on jets. The project has completed a successful period of design and prototype tests [1, 3] and is now in the production stage.

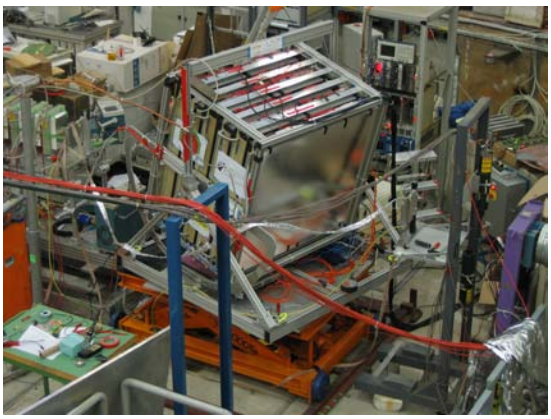

Figure 1: The TRD stack at the T9 beamline at CERN PS. The chambers are mounted in a frame allowing rotations of the detector with respect to the beam. The frame itself is installed on a lifting device.

A first beam test of a full size six-chamber detector stack of TRD was performed for two weeks at the CERN PS accelerator in October 2004. Measurements were carried out in an electron/pion beam with momenta of 1 to 10 GeV/c with the first chambers of the TRD series production. Fig. 1 shows a picture of the setup in the beam. Besides the TRD chambers, the setup was comprising of: beam trigger scintillators, a Pb-glass calorimeter and a Cherenkov detector for e/π identification and two Si-strip detectors for position reference.

Due to limited availability of readout board (ROB) prototypes, only one ROB was used for each detector layer. The detector signals from 288 detector pads are fed via flat cables into the 16 Multi Chip Modules (MCMs) on each ROB [4]. Each MCM consists of a Preamplifier/Shaper (PASA) and a digital Tracklet Preprocessor (TRAP) chip. The TRAP chip performs signal digitization (10-bit, 10 MHz sampling frequency), baseline subtraction, tail cancellation and tracklet fitting. For initialisation of the MCM chips and control of detector and electronics parameters, each ROB is equipped with a Detector Control System (DCS) mezzanine board. The DCS boards are compact standalone computing nodes running a Linux operating system, including Ethernet interface. Using the DIM protocol [5] for communication, the DCS boards are also delivering clock and trigger signals. For TRAP processor initialisation a broadcast is issued to all DCS boards which in turn send the binary operation code to all 68 CPUs on a readout board (four MIMD CPUs per TRAP chip) via a Slow Control Serial Network (SCSN) ring.

Once the data has been processed locally, it is sent through a 3-layer readout tree of MCMs, arriving via an ACEX card [6] in a readout computer. Here the data is converted into ALICE detector data link (DDL) format and travels via optical fiber into the DAQ system. The Data Acquisition (DAQ) system is based on ALICE DATE v4 [7]. We use two Local Data Concentrators (LDCs), one to readout the TRD stack, the second for the monitoring detectors. Event building is done on the Global Data Collector (GDC) and the data is then stored on a RAID disk server. The DAQ system is running at an average rate of 25 Hz at an event size of roughly 100 kBytes, limited only by the bandwidth of the ACEX card. More than 15 hosts were required during data taking to control and monitor the whole system. In order to facilitate the network configuration and for security reasons, the setup was operated in a private standalone Ethernet network. An on-line event display of a track in the TRD is shown in Fig. 2.

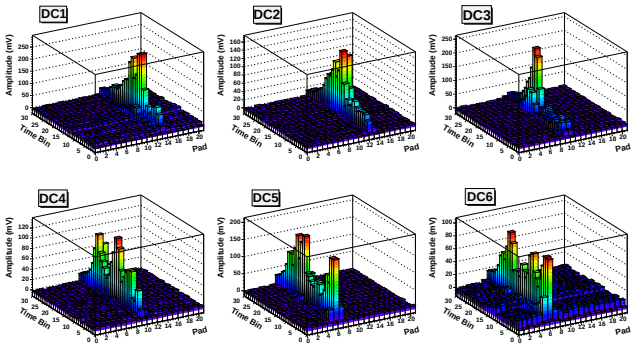

Figure 2: Event display of a track in the six chambers of the TRD.

In Fig. 3 we present the measured average signals as a function of drift time for pions and electrons, for the momentum of 4 GeV/c. The detector signal is spread over about 2 μs (the time zero is arbitrarily shifted). The peak at small drift times originates form the amplification region, while the plateau is from the drift region. For the electrons, the contribution of TR, which is preferentially absorbed at the entrance of the detector (corresponding to large drift times), is evident.

The distributions of measured integrated energy deposit in one layer of the detector are shown in Fig. 4 for pions and electrons of 2 and 6 GeV/c. The measured data are compared to calculations, which include ionization energy and, in case of electrons, transition radiation (TR).

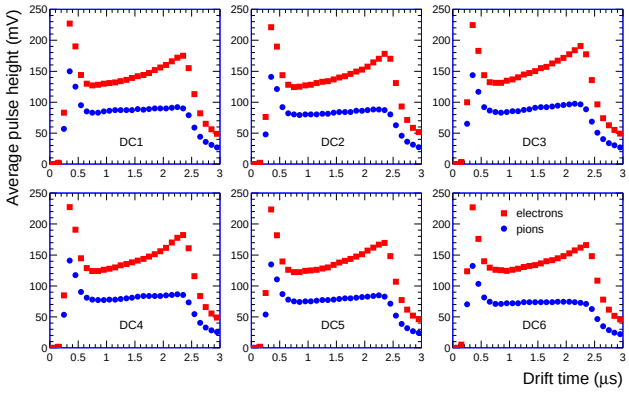

Figure 3: Average pulse heights for the 6 layers, for electrons and pions of 4 GeV/c.

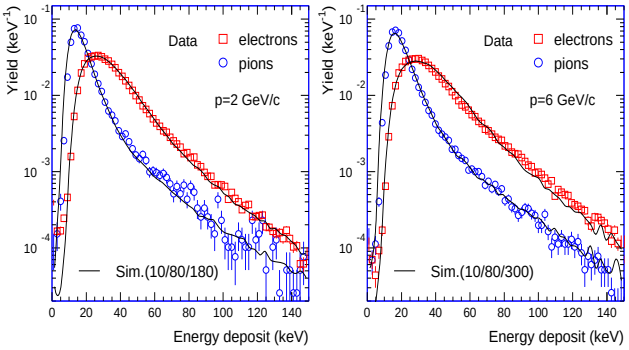

Figure 4: Integrated energy deposit spectra for one detector layer, for electrons and pions of 2 and 4 GeV/c. The lines are simulations.

The simulations were tuned to describe earlier measurements performed with prototypes [3] and describe well the present measurements.

In Fig. 5 we present the measured pion rejection (pion efficiency at 90% electron efficiency) as a function of momentum, using a simple likelihood method on total charge per layer (Fig. 4). The data obtained with the real size detectors is compared to data of smaller prototypes [3] measured in the same experiment. Compared to these reference detectors, the big chambers show a slightly worse pion rejection, which can be attributed to a smaller signal-to-noise value at which they were operated. In addition, the cross bar reinforcement of the radiators, used for the big chambers butnot for the small ones, may play a role too. The target pion rejection value is reached with this simple likelihood. Further improvements, using more sophisticated methods [3, 9], will provide a safety margin for the performance in the high-multiplicity events at LHC.

One of the special features of the readout pads geometry of the TRD chambers [1] is the alternating tilt of the pads relative to the beam axis (z). This improves the resolution in z direction, initially given only by the size of the long side of the pad (around 9 cm). For tracking within a single chamber (using the algorithm developed for the on-line straight-track reconstruction), this correlation is reduced to knowing the θ angle (along pads) of the track at the TRD entrance. In Fig. 6 we present the reconstructed angle for each layer, without and with the correction for the tilted pads, proving that the angle reconstruction method

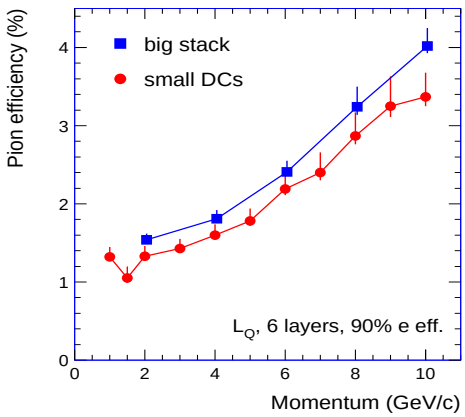

Figure 5: Momentum dependence of the pion efficiency.

works well. The difference between the reconstructed angle and the orientation of the stack (in ϕ-direction, i.e. across pads) is due to initial misalignment, and can be used as a reference for a further correction. Also shown in Fig. 6 is the distribution of the reconstructed angles, where it is demonstrated that resolutions below 0.5° are achieved. The analysis of the complete set of measurements, performed for a large range of angles (θ=0–25°, ϕ=0–20°), will validate the reconstruction algorithms and will allow detailed studies of position resolution performance [8].

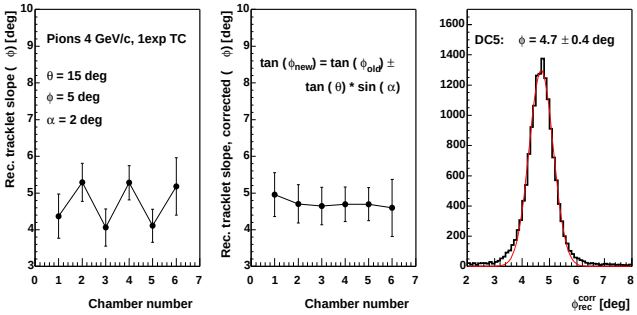

Figure 6: Layer dependence of the reconstructed angle, before and after correcting for the pad tilt, α.

In summary, the beam tests of real size detectors and final front-end electronics demonstrate that the envisaged design performance of the TRD can be achieved. Further analysis of the collected data will provide valuable inputs towards the preparation and final performance of the system in the ALICE setup.

References

[1] ALICE TRD Technical Design Report, CERN/LHCC 2001-021 (2001), `http://www-alice.gsi.de/trd`

[2] V. Lindenstruth, L. Musa, NIM A 522 (2004) 33.

[3] A. Andronic et al., NIM A 522 (2004) 40.

[4] I. Rusanov, J. Stachel, this Report.

[5] `http://dim.web.cern.ch/dim/`

[6] `http://www.kip.uni-heidelberg.de/ti/ACEXBoard/`

[7] `http://aldwww.cern.ch/`

[8] C. Adler et al., NIM A 540 (2005) 140.

[9] C. Baumann et al, GSI Sci. Rep. 2003, p. 66.

Transition Radiation Spectra measured with Prototypes of the ALICE TRD

A. Andronic, R. Bailhache, H. Appelshäuser, P. Braun-Munzinger,
O. Busch, C. Garabatos, C. Lippmann
GSI Darmstadt (for the ALICE TRD Collaboration)

In 2004 we carried out an extensive investigation of Transition Radiation (TR) properties using ALICE TRD prototype drift chambers. They are constructed similar to the final ALICE TRD chambers [1], but have a smaller active area. To back up and complement similar measurements from two years earlier [2], we now tested different radiator configurations and increased the beam momentum to 10 GeV/c. The measurements were performed at the T9 secondary beam line at the CERN PS. A dipole magnet was used to deflect the beam after passing through the radiator. We were thus able to separate the energy deposited by TR photons from ionization energy loss on the particle track. A pipe filled with helium was used to minimize absorption losses over the 1.3 m distance between the radiator and the drift chamber.

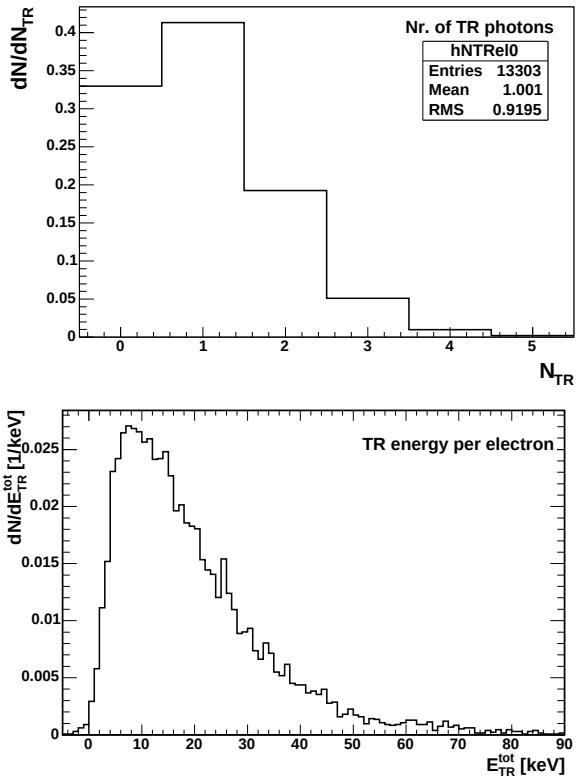

Figure 1: Top panel: Distribution of the number of photons detected in the drift chamber at a momentum of 8 GeV/c for the standard sandwich radiator. Bottom panel: Spectrum of TR energy deposited in the detector.

Fig. 1 shows the distribution of the number of photons detected in the drift chamber and the energy spectrum of these photons for electrons of momentum 8 GeV/c for the standard sandwich radiator of the final ALICE TRD chambers. The distribution of the number of photons is roughly Poissonian with a mean of one photon in the detector. Fig. 2 shows the mean number of photons detected in the drift chamber and the mean energy deposit per electron as a function of momentum for different radiator configurations: The standard sandwich radiator, a plexiglas dummy, a regular foil radiator and radiators composed of either pure fibers or pure foam (which are both components of the ALICE TRD sandwich radiator). Both the largest average number of photons and the highest energy deposit per electron are observed using the regular radiator. However, we also identify photons in the detector with only the dummy radiator. Their significant number can not be explained by bremsstrahlung. Whether this effect is due to a beam contamination or beam interaction with the helium pipe housing remains to be clarified.

The measurement of the properties of TR are essential also for comparison with and verification of simulation routines.

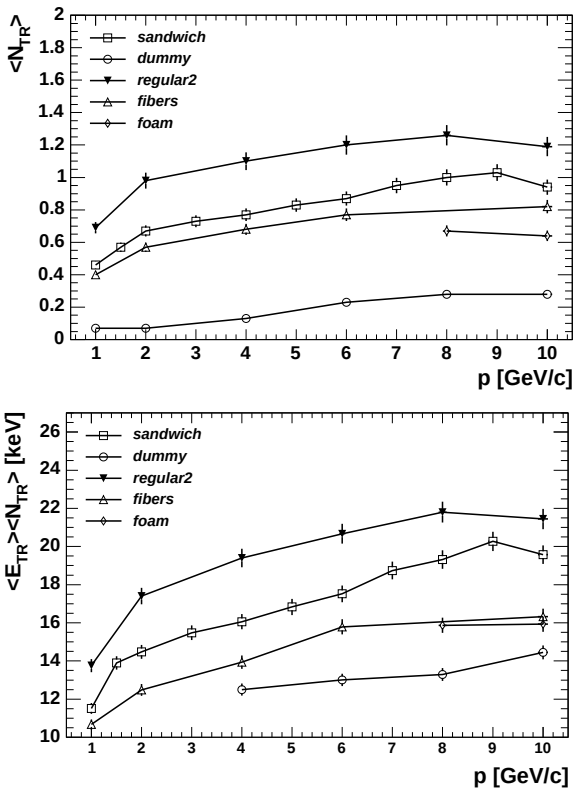

Figure 2: Mean number of photons detected in the drift chamber (top panel) and most probable energy deposit per photon (bottom panel) as a function of momentum for all radiator configurations.

References

[1] ALICE Transition Radiation Detector Technical Design Report, ALICE TDR 9, CERN/LHCC 2001-021.

[2] O. Busch et al., Nucl. Instr. Meth. Phys. Res. A 525 (2004) 153.

Data Flow Control System in a Real-Time Processing Farm

D. Atanasov, I. Kisel, V. Lindenstruth and G. Troeger

Kirchhoff Institute of Physics, Germany

Fast and efficient data transfer in computing farms requires data flow control to avoid network congestions. The developed congestion control system aims to allow transfer of 128 byte packets at the rate of more than 1 MHz in a commodity-of-the-shelf PC farm, implementing a torus type network topology [1].

The data flow control system consists of a centralized scheduling unit, the scheduler, interconnected with distributed transmitting nodes via a custom serial network called TagNet (Figure 1).

The scheduler's prime task is to choose the next destination a pending for processing data packet to be sent to. The choice must be done in such way that no congestions in the system may occur. The architecture of the scheduler is depicted in Figure 2. The scheduler core defines the very low latency of the Scheduler. It requests the Algorithm unit and the Source unit to provide next destination and source address correspondingly. This action is done in-between two successive data packet entries such that, upon receiving a new data packet, the scheduler is already prepared to serve it. Then it immediately triggers the TagNet Interface unit to transmit a tag that holds destination address as well as source address. The currently employed algorithm functions in a round-robin fashion thus preventing from sending two subsequent data packets to destinations residing in one and same torus column. This simple rule, in addition with the ability of the network fabric to buffer some data in every node, is sufficient to avoid congestion in the network. Once a remote computing node has finished processing current data, it sends its request for new job to a list of queued destinations. Maintenance of such a list in the scheduler allows the algorithm unit to retrieve next destination addresses.

Following the major characteristics of the processing farm, the scheduler is fast, scalable, and introduces very low latency.

The TagNet [2] is a unidirectional serial data channel used for transfer of tags between the scheduler and the transmitting nodes. The nature of the TagNet allows it to be adapted to different system sizes very easy. The TagNet plays a crucial role for the overall system operation. It is mostly characterized by simplicity and reliability, high speed and low price.

Every transmitting node is equipped with a TagNet Slave that, upon receiving a tag, initiates data transfer to a particular remote computing destination at a particular moment in time. Therefore, the TagNet Slave is an integral part of the data flow control system.

Given the high trigger rate, the data flow control system has been implemented completely in hardware. A multi-purpose PCI66/64 agent has been developed to accommodate the scheduler and the TagNet Slaves.

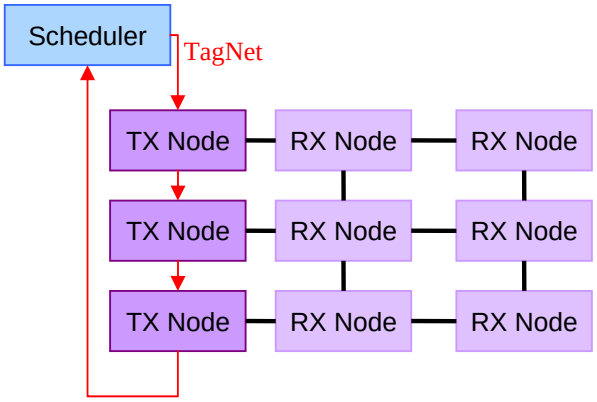

Figure 1: System Architecture

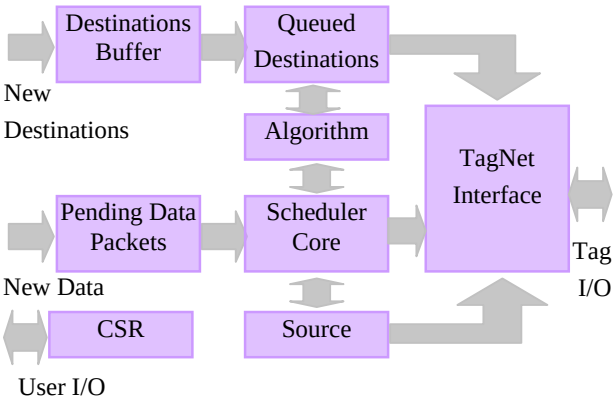

Figure 2: Scheduler Architecture

Current performance tests with a 2 by 8 torus prototype show that the system is capable of sending 128 byte packets at the rate of 1.7 MHz.

References

[1] A. Walsch, "Architecture and Prototype of a Real-Time Processor Farm Running at 1 MHz," *Inaugural Doctoral Thesis*, University of Mannheim, Sept. 2002

[2] H. Muller, F. Bal, S. Gonzalve, A. Guirao, and F. V. dos Santos, "TAGnet, a twisted pair protocol for event-coherent DMA transfers in trigger farms", *8th WS on Electronics for LHC*, Colmar, 2002

Hardware based Cluster Control System

G. Klein[1], V. Lindenstruth[1], R. Panse[1], and H. Tilsner[1]
[1]Kirchhoff Institute of Physics

1 Introduction

Future collider experiments like ALICE at the LHC at CERN or CBM at GSI will produce huge amounts of data, which have to be processed in a short period of time. For this task large computer farms with hundreds of PC will be used. These PC have to be installed and configured to run in a cluster network. Since every computer is prone to errors special care has to be taken in order to prevent the whole cluster stop working caused by a single failure of one computing node. The configuration, operation, and monitoring of such clusters are challenging task which are supported by the use of additional hardware, the so called Cluster Interface Agent.

2 Cluster Interface Agent

Several tools exists already to handle and manage computer clusters remotely. Most of these systems are software based and the available hardware solutions are limited to equipment of a certain vendor. Furthermore, software based control systems depend on the operating system and do not work if the operating system crashed. Therefore we have developed the Cluster Interface Agent (CIA) card. To be as flexible as possible this card is realized as a low profile PCI expansion card. The small form factor of the card allows its usage even in 2U server racks. Computing nodes equipped with this card allow for their total configuration remotely, including changing the BIOS settings which normally are not access-able via remote control. Access to the card is provided by a 10/100 Mbit/s network interface. This network interface can be part of a second network which is completely independent from the cluster network used to connect the computing nodes. This approach allows access to the computing nodes even if the network connection between the nodes break down. Figure 1 shows the applications running on a server node to access the CIA card. VNC[1], Java and a web interface are supported.

Figure 1: CIA Application.

Additionally features of the card are an USB and an infrared interface providing access to the card. The USB interface is also used for emulating USB devices to the host computer. This can be used to offer a boot device like an USB mass storage devices to the host system. The floppy interface integrated on the card simulates a floppy drive and supports legacy boot possibility. The ADC[2] of the card permits monitoring voltages or temperatures of the mainboard or of dedicated devices.

The main building block of the card is Alteras' Excalibur FPGA which contains an embedded hardcore processor on which Linux as operating system is running. The processor is an industry-standard ARM922T processor. It has a system performance of up to 200 MHz (210 Dhrystone MIPS). The main memory of the system is a 32 MB SDRAM. An 8 MB flash memory stores the root file system and the Linux kernel as well as the configuration data of the FPGA. Furthermore, the FPGA can be used to easily integrate additional hardware in order to adapt the CIA card to different hardware.

The CIA card functions as a video card and is registered as a default VGA card by the PCI bus. No additional video cards will be required for the computer system. The CIA card captures the video data and make them available via a VNC Server running on the ARM processor. Using a VNC viewer, the administrator can work on the node as sitting in front of it. The keyboard and mouse interaction sent from the VNC viewer will be translated via PCI cycles to the keyboard and mouse controller of the mainboard.

3 CIA Prototype

Figure 2: The CIA card prototype.

Figure 2 shows one of the first prototypes of the CIA board. The card was successfully tested and provides already a lot of features to control a computer system. The card has successfully emulated a monochrome graphic card and all kind of PCI cycles are supported. The BIOS setting was remotely configured by the aid of the VNC server running on the card. The temperature and the voltage was successfully measured. The boot device support is under development. Additionally, an infrared interface is planned for easy debugging and communicating facility.

References

[1] The ALICE Collaboration, "ALICE - Technical Design Report of the Trigger, Data Acquisition, High-Level Trigger, and Control System",CERN/LHCC/2003-062, January 2004.

[1]Virtual Network Computing

[2]analog digital converter

Design and Implementation of a Cluster Fault Tolerance System

Volker Lindenstruth [1], Lord Hess [1], Frank Pister [1]

[1] KIP Uni Heidelberg, Germany

In this article we briefly describe a cluster fault tolerance system which was designed and implemented at KIP.

In particular, we describe the basic components which are part of the system's framework. Also, a simple use case is given.

Motivation

Large computing clusters are becoming more and more popular in scientific computing. As the number of nodes in a cluster increases, the probability of a node failing increases accordingly. The system described here allows an administrator of such a cluster to automatically detect and correct faults on a node. The design goal of the system is to minimize the need for human intervention.

The system is implemented entirely in software which means that no additional or specialized hardware is needed.

We have chosen a rule based approach, giving an administrator a means to state complex error conditions and possible actions to handle those error conditions.

System Architecture

The system consists of three main parts which are sensors, actuators and a correlation engine, the last component providing the core functionality of the system.

A sensor is a source of data describing the state a node. For instance, it might be the current CPU load, the number of users currently logged in or the space available on a hard disk. In our framework we used a scalable monitoring system to implement the sensors and to transfer the relevant information.

The correlation engine may be configured by a set of rules describing all kinds of fault conditions which may occur on a node. These may be quite simple or may be arbitrarily complex involving several metrics provided by the sensors. XML was chosen as a convenient way to express the rules.

Actuators are executables which are started in case a fault condition (as given by one of the rules) occurs. Usually, these actuators are system binaries or scripts written by an administrator. The exit status of the actuators is reported to the monitoring system to provide a feed back and easier logging.

The structure of the system is shown Figure 1 below.

Implementation

C++ was used to implement the basic components defined above. The correlation engine uses a class hierarchy which may be used to express arbitrarily complex conditions describing the state of a node. Furthermore, there are classes for the actuators and for the sensors. We tried to keep the implementation as generic as possible, in order to be able to use different kinds of monitoring systems as source of sensor data.

Use case

Consider a typical UNIX-like systems on which several important daemons are running, e.g. crond, which are vital to the proper functioning of the node. These daemons may crash or might be terminated accidentally. Using our framework a rule may be established to check wether the daemon is running and to restart it in case it crashed. If the restart fails, other means to repair remain after a programmed number of retries.

Outlook

While the software described so far was node based, we are currently also developing a cluster wide fault tolerance system to support distributed applications. For that purpose we have designed an interface which allows an application to reschedule tasks, in case a node becomes unavailable due to an error or a network connection breaks.

Summary

We have designed and implemented a fault tolerance system which helps an administrator of a large cluster to keep nodes up and running by specifying a set of rules

Further information may be found on the KIP Grid homepage at http://www.kip.uni-heidelberg.de/ti/GRID

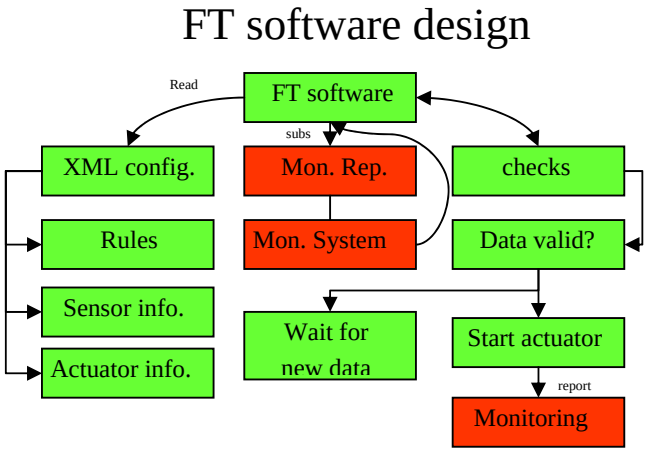

Figure 1

Single Board Computer for the ALICE DCS

D. Gottschalk[1], T. Krawutschke[2], V. Lindenstruth[1], and H. Tilsner[1]
[1]Kirchhoff Institut für Physik, University of Heidelberg; [2]University of Applied Science Cologne

The ALICE detectors requires a sophisticated control system for monitoring and control of the overall working conditions like voltages, temperatures, and pressures. This system has to be able to react to critical situations in order to avoid damages to the detector. In addition, the front-end electronic has to be initialised and configured (e.g. downloading pedestal values) depending on the actual running conditions. This entire functionality is performed by the Detector Control System (DCS) which consists of a number of hardware and software components. For the TPC, TRD, and PHOS detectors of ALICE the interface to the DCS is realized as a small autonomous single board computer.

Figure 1: ALICE DCS board.

1 Embedded System for DCS

Due to the manifold tasks of the DCS agent a flexible system is needed which can be easily adapted to changing requirements. On the DCS board this is accomplished by using Alteras' Excalibur FPGA with embedded ARM processor core on which the Linux operating system is running. In addition, the integrated, programmable FPGA allows the integration of specific functionality in a very flexible way and is being used to custom fit the device to the specific requirements of the detectors. The FPGA configuration and the program code for the CPU is stored in a Flash ROM from which the system is automatically configured after power-up. An ADC for digitizing analog signals coming from the detector, a SDRAM chip, and a FastEthernet PHY transceiver chip complete the system. Full control over all on-board configurable components, such as the FLASH memory or the FPGA, is ensured and mutual reconfiguration of the boards in case of failure is feasible with a JTAG chain. The system is able to react autonomously to critical situations in order to avoid damages of the detectors. Figure 1 shows a photo of the DCS board.

2 Software

Using Linux as operating system simplifies the development of application software since the well known GNU standard tools (compiler, debugger, and libraries) can be used. For instance, a web server was successfully ported and operated on the board. All programs necessary for starting the system and its operation are permanently stored on the Flash ROM. Therefore, the DCS single board computer can be operated stand-alone and it does not require a network connection in order to perform the basic control tasks. This feature is especially important in terms of safety requirements where a proper and secure operation of the detector has to be guaranteed even in cases where part of the higher levels of the control system are not working. During operation the Ethernet connection is required only for publishing measured data. It is also used in spy mode to access on-line data without affecting the main detectors data stream. This feature is very useful in particular during the debugging phase of the detectors and even during test measurements where performance is not essential. This functionality already proved as very useful during tests and conditioning of the TRD detector.

3 Ethernet as Field Bus

The communication with the DCS board requires a reliable field bus. One possible network technology which is discussed very actively in industry at the moment is Ethernet as field bus. One advantage of using Ethernet is its wide use and therefore the availability of cheap standard components. However, the proper function of Ethernet even in a harsh environment with electromagnetic background noise has to be ensured. Another complication arise due to the presence of strong magnetic fields since standard network devices use a transformer for signal coupling. In case of the DCS board this problem is solved by replacing the transformer with a small amplifier circuit which boosts the output signal of the physical layer chip. Measurements were done with a setup consisting of a DCS single board computer and a standard Ethernet switch with 50 m UTP CAT5 cable between the two devices and verified the proper function of the modification.

Although different commercial network interfaces for Ethernet exists a different approach was chosen for the DCS board. The Medium Access Controller (MAC) of the DCS board is realized as a very lightweight synthesizable module in VHDL, called Easynet. By the renouncement of collision detection this device uses only a minor fraction of the FPGA resources. Besides the benefit of eliminating external chips this approach allows in addition to complement the existing Ethernet protocol with quality of service functionality, allowing for the reservation of bandwidth and implementing high priority, reliable messages. Such functionality can be integrated and operated with existing commercial network components provided that all participating MACs adhere to such functionality.

High rate performance of fast gaseous detectors

A. Andronic[1], H. Appelshäuser[1], V. Babkin[2], P. Braun-Munzinger[1], S. Chernenko[2], D. Emschermann[3], C. Garabatos[1], V. Geger[2], V. Golovatiouk[2], J. Hehner[1], M. Hoppe[4], E. Jimenez[1], M. Kalisky[1], C. Lippmann[1], D. Miskowiecz[1], D. Moisa[5], M. Petris[5], M. Petrovici[5], A. Radu[1,5], V. Simion[5], R. Simon[1], H.-K. Soltveit[3], J. Stachel[3], H. Stelzer[1], F. Uhlig[1], A. Wilk[4], J.P. Wessels[4], Yu. Zanevsky[2], and V. Zryuev[2]

[1]GSI Darmstadt; [2]JINR Dubna; [3]University of Heidelberg; [4]University of Münster; [5]NIPNE Bucharest

Three different prototype MWPCs with a symmetric anode-cathode configuration were constructed, differing in anode pitch: 2 and 4 mm were used for the two chambers built at GSI (labelled GSI1 and GSI2 in the following plots), while 2.5 mm was used for the chamber built in Bucharest. The anode-cathode gap for these three chambers is 3 mm. The entrance window of 25 μm aluminized kapton simultaneously serves as gas barrier and cathode plane. The pad planes consist of a segmented cathode with 8 pads with an area of 6 cm^2 each. The width of one pad is 7.5 mm, the length 80 mm. Another MWPC, built in Dubna, has a different design, with a drift region of 8 mm and an amplification region of 4 mm, as seen in the left panel of Fig. 1. The anode wire pitch is in this case 2 mm, while the cathode wires are spaced by 0.5 mm. The size of the readout pads is 3×4 mm^2. For all chambers, the anode wires are made of gold-plated tungsten and have a diameter of 20 μm. The layout of the GEM chamber [1], also from the Dubna group, is shown in the right panel of Fig. 1. The detector has a drift gap of 3 mm and 3 amplification stages.

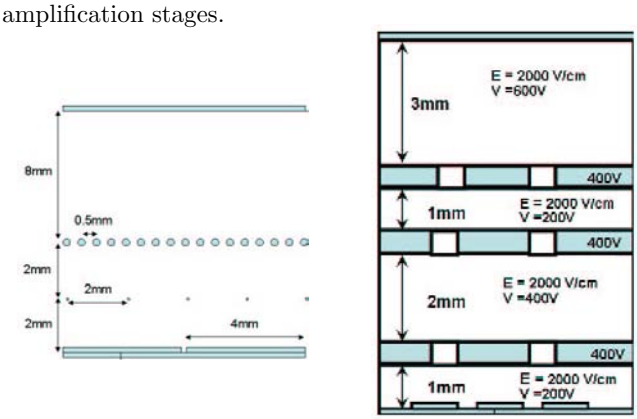

Figure 1: Layout of the MWPCs (left panel) and GEM (right panel) prototypes built in Dubna.

Custom-built charge-sensitive preamplifier/shapers are used to process the detector signals, which are digitized by an 8-bit nonlinear Flash ADC (FADC) system with 33 MHz sampling frequency, 0.6 V voltage swing and an adjustable baseline.

The prototypes have been tested with the Ar- and Xe-based gas mixtures (with 15% and 30% CO_2 as quencher) using a ^{55}Fe X-ray source of 5.9 keV and beams. In Fig. 2 the energy spectrum of ^{55}Fe measured for Ar,CO_2(15%), obtained with the MWPC built in Bucharest is shown. The energy resolution is σ=8.6%. The aim of the measurements performed at the secondary beam at SIS/GSI was to test the general detector performance of the different readout chambers under high rate conditions. The rate was chosen by varying the extraction time of the primary beam from 2 to 0.2 seconds.

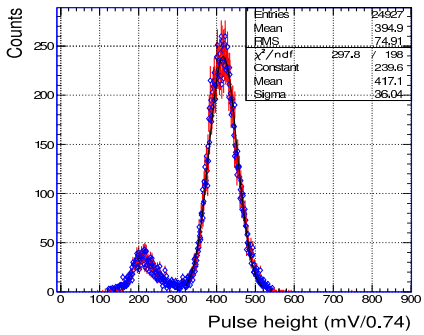

Figure 2: Energy spectrum of ^{55}Fe source measured with the Bucharest MWPC with the Ar,CO_2(15%) mixture.

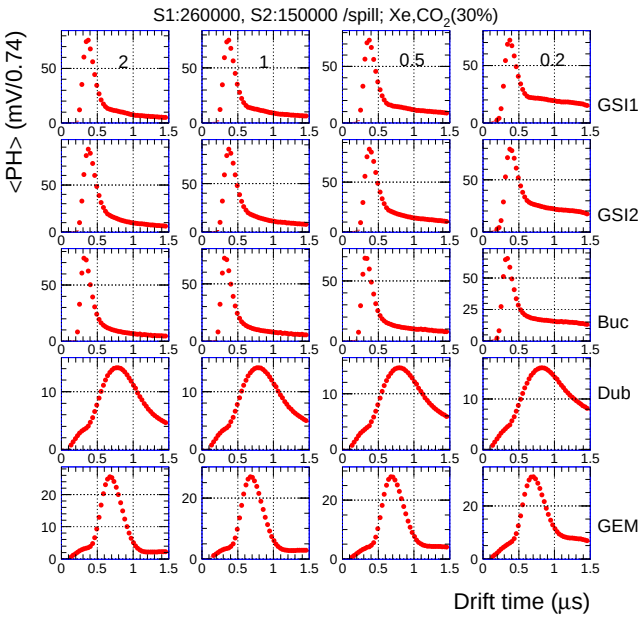

Figure 3: Average pulse height <PH> as a function of time for the different readout chambers (rows) and for different spill length (columns).

The time dependence of the average pulse height <PH> is shown in Fig. 3 for the gas mixture Xe,CO_2(70%/30%). From left to right the spill length is decreasing (increasing rate). From top to bottom the data for the different readout chambers are shown. The time zero has been shifted arbitrarily by about 0.2 μs to have a measurement

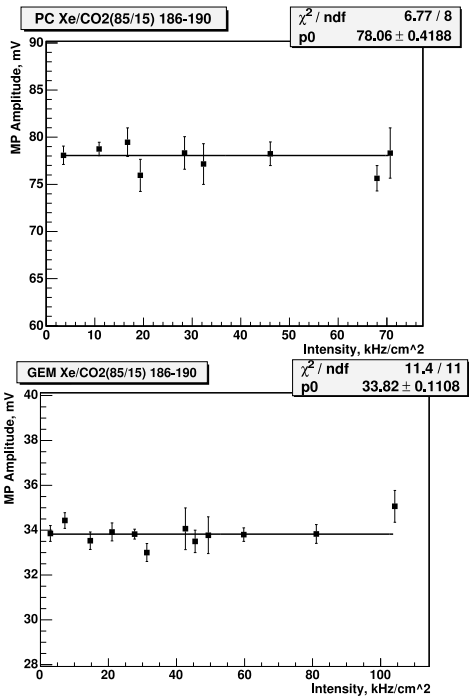

Figure 4: Rate dependence of the average signal for the MWPC (upper panel) and GEM (lower panel) detectors built in Dubna.

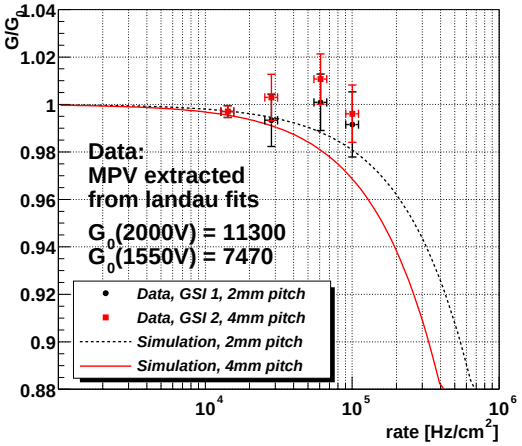

Figure 5: Relative detector gain as a function of rate for the two GSI chambers. The lines are simulations.

of the baseline. One can notice that the absolute magnitude of the peak is changing very little with increasing rate. However, the tails of the signals are larger with increasing beam rate, probably due to pile-up. The signals illustrated in Fig. 3 are summed over adjacent pads and integrated around the peak values to produce the energy deposit spectra. The resulting spectra are characterised by the most probable value (MPV) and by the width.

In Fig. 4 we present the results on rate dependence for the Dubna detectors. Both the MWPC and the GEM chambers show no degradation of the signal amplitudes for high rates. Apparently, the relatively long duration of the output pulses did not limit the count rate capability of Dubna MWPC. The results for the relative detector gain (derived from the MPV of the deposited charge distributions) as a function of rate are shown in Fig. 5 for the GSI detectors. These results correspond to the gas mixture Xe,CO_2(15%) with anode voltages of U_a=2.0 kV and 1.55 kV for GSI1 and GSI2, respectively. The gain values at low rate for these settings are 11300 for GSI1 and 7500 for GSI2. The lines are simulations taking into account the increasing space charge with increasing rate [2]. The measurements show no decrease of the gain with increasing rate, while the simulations indicate a gain drop of a few percent, depending on the anode wire pitch.

The rate dependence of position resolution performance is presented in Fig. 6, derived from the two GSI chambers data (assuming that both have the same resolution). The position is reconstructed in our chambers via charge sharing among adjacent pads. Resolutions of 260 μm are achieved at low rates, although the geometry of the present detector was not optimized for position resolution. A small degradation of the resolution is observed for higher rates, amounting to only 15 μm at 100 kHz/cm^2.

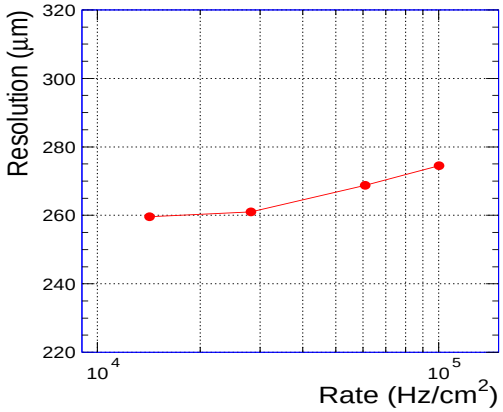

Figure 6: Position resolution as a function of rate for the GSI chambers.

In summary, the first exploratory beam measurements indicate that the performance of the detectors is not substantially degraded for rates up to 100 kHz/cm^2. This rate domain is of relevance for the CBM detector at FAIR [3], for which the TRD can be realized with MWPCs with pad readout of the type we have investigated. More quantitative statements will be derived from further analysis of the existing data, as well as from new measurements, which we foresee to realize in the course of the next years.

The authors from JINR Dubna would like to thank their collaborators from NC PHEP Minsk, Prof. N. Shumeiko, Prof. O. Dvornikov, and Dr. V. Tchekhovski for the development and construction of preamplifiers for Dubna chambers.

References

[1] G. Bencivenni et al., NIM A 488 (2002) 493.
[2] E. Mathieson and G.C. Smith, Nucl. Instr. Meth. A 316 (1992) 246.
[3] Letter of Intent for the CBM Experiment at FAIR, Darmstadt, January 2004.

Development of a Fast TRD Pre-Amplifier Shaper

Hans Kristian Soltveit, Johanna Stachel

Research and development for fast PASA suitable for MWPC-based detectors in future experiments (like TRD in CBM) has two challenges: i) low noise with short shaping time and high pulse rate. ii) low power consumption and small chip size. On the other hand, the use a state-of-the-art process that will bring less power and less area, and that will be the standard in few years is desireable. We have then decoupled the two open issues. First, one can check with a prototype that the requirements using standard technology (0.35 μm) can be fulfilled and tested with the prototype chambers give the expected physics performance. In a second step one needs to develop a completely new prototype in the state-of-the-art technology with close to final specifications (for example IBM 0.13 μm).

In order to achieve an overall noise of less than 1000 electrons per channel for a typical input capacitance of a total of 15-35 pF, the use of a low-noise circuit is required. A well proven topology to fulfil such a requirement is shown in fig. 1. Each channel consist of a low noise

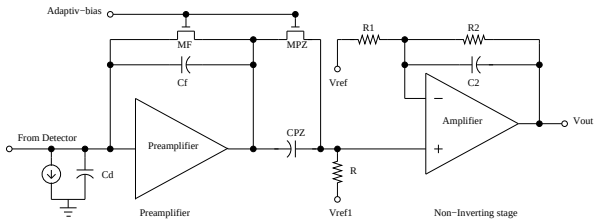

Figure 1: Schematics of the fast PASA done in 0.35μm technology

charge-sensitive amplifier, an active CR-RC pulse shaper, and a source follower buffer that can handle both polarities. The main noise contributor is the input transistor of the preamplifier that is based on the folded cascode topology. The cascode consist of a common-source stage followed by a common-gate stage. It combines two transistors (a wide input transistor and a narrower cascode transistor) to obtain: i) high transconductance and low noise of a wide transistor, ii) high output resistance and low output capacitance of a narrow transistor, and iii) reduced capacitance between output and input. In addition a Pole-Zero network is included to avoid undershoot that will strongly limit the counting rate behaviour. In the design a MOS transistor (MF) is used with a feedback capacitance Cf that is continously discharged with a decay time $td = Df \cdot Rds$ (MF). This continuously sensitive design is particularly suitable for a detector with high occupancy and high counting rate. To increase the gain and shape of the signal a shaper is built around a Miller OTA. By means of the external reference Vref, this part has in addition the capability of maximizing the dynamic range for a given polarity. The reference voltage is set closer to the positive rail so that its output swing towards the negative rail for positive input charges. For negative input charges the reference voltage is set closer to the negative rail such that its output swings toward the positive rail.

A first prototype using this design was submitted in October 2004 and has just been received back from foundry. First test has already been undertaken. Since the design was targeted for a slightly different type of detector the conversion gain is slightly higher (40mV/fC) in this prototype version compared to the requirement for the TRD. This can easily be lowered by adding a resistor of suitable size in series to the external reference voltage Vref . In this first prototype the peaking time is 30 ns (t0/100), and the FWHM is about 75 ns. It returns to the baseline after 270 ns. In terms of noise this circuit fulfil the requirement with an ENC of less than 850 electrons for an input capacitance of 35 pF. In terms of power consumption the circuit uses 8.5 mW/channel. The chip is fabricated in 0.35 μm standard CMOS technology, and has a pad pitch of 50 μm.

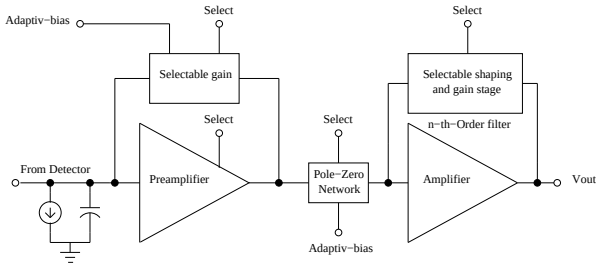

Figure 2: Schematics of the fast PASA under development in 0.13μm technology

The next step is to migrate from 0.35 μm technology to a smaller technology. A prototype development of a new circuit done in 0.13 μm IBM technology is already under way. The proposed schematic layout is shown in fig. 2. This circuit consist of a low noise, selectable gain, preamplifier that can detect both polarities. The choice of gain range in the preamplifier is made by switching the relevant range capacitors. The reason of choosing a selectable gain preamplifier is to provide a versatile preamplifier potentially suitable for several of the proposed CBM detectors (RICH, ECAL and TRD). The core preamplifier is based on the same topology as used in ALICE-TPC/TRD [1]. The change in decay time (due to change in gain range) also influence the P-Z network, that has to change to preserve to same relation to avoid undershoot. The shaper/gain circuit is also made selectable. The purpose of the selectable shaper/gain circuit is to amplify the input signal to the full scale voltage of the ADC ensuring that the maximum signal resolution is achieved. Several programmable shaper/gain topologies are under investigation to find the best candidate for the proposed detectors.

References

[1] H.K.Soltveit *et al.* GSI Annual Report 2003, p 244

Characterisation of Single-Crystal CVD-Diamond Detectors

E. Berdermann, M. Ciobanu, W. Hartmann, A. Martemiyanov, P. Moritz, M. Pomorski, M. Rebisz, B. Voss
GSI Darmstadt

Recently, the quality of intrinsic CVD Diamond (CVD-D) has tremendously been improved. The replacement of the previous used silicon substrates for growth by ultra-pure HPHT Single-Crystal (SC) {100}-oriented diamond provides homo-epitaxial grown material almost free of structural defects. Nevertheless, all substrates nominally {100}-oriented show a certain amount of off-angle declination from the perfect {100}-axis. If this off angle is > 2 degrees, growth is seriously influenced. We have started to investigate SC-CVDD for Heavy-Ion (HI) spectroscopy and ToF measurements with relativistic ions and protons, where PolyCrystalline CVD-D Detectors (PC-CVD-DD) fails[1].

1 Sample Preparation

The diamonds are cleaned in Sulfo-Chromic acid (CrO_3 + H_2SO_4, ˜ 0.5 h) aiming for oxidized diamond surfaces, free of rest impurities including carbide- or graphite phases, the latest being highly p-conductive. The resistivity of the films increases such a way by several orders of magnitude [2]. In order to remove previous metallization an Aqua Regia step is implemented before the samples become washed and dried with distillate water and pure nitrogen. Cleaned and oxidized diamonds remain in argon atmosphere until metallization.

The multilayer electrodes appear to be the most crucial step in the SC-CVD-DD fabrication. Contact effects arising from space charges that are present in the interface to the diamond depend on the type of rest-conductivity and quality of the material, both initially unknown. Cr/Au metallization on nominal intrinsic PC-D samples for instance, leads to the formation of a Schottky barrier of 3.8 eV of an intrinsic potential of 2.7 V [2]. A Schottky junction in an n-type semiconductor gives rise to an electron depletion layer and in a p-type semiconductor to a hole depletion layer, respectively. PC-CVDD has been characterized as n-type material [2]. It must be tested if better results are obtained applying both, one blocking- and one ohmic electrode (e.g. carbide forming Ti/Pt/Au) - analogous to the fabrication of silicon pin-diodes. Due to much lower quality of PC-CVD-DD, no influence to the detectors performance has been observed in the past testing a variety of evaporated or sputtered electrodes e.g. Cr/Au, Ti/Pt/Au or pure aluminium[1].

2 Electronic Properties of SC-CVDD Detectors

All data presented in this report are obtained from samples with Cr/Au (50/100 nm) sandwich dot electrodes, of diameter maintaining ˜ 0.5 mm surrounding non-metallic edge.

2.1 Dark-Current Characteristics at T = 300 K

Hysteretic measurements are performed under nitrogen flow in electrically shielded teflon boxes reducing ionization of gas volumes. Figure 1 shows the dark current behaviour tuning the bias of three SC-CVD-DDs measured with a Keithley electrometer. Except diamond D_4, all samples show lower break down field than a good as grown electronic grade PC detector [1]. This unexpected result indicates surface conductivity or contact effects, which cannot be distinguished with the present detector layout.

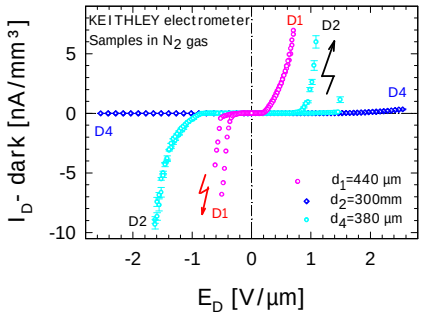

Figure 1: Hysteretic measurements of the normalized dark current in three SC-DDs (D_1, D_2, D_4) of various thickness and active areas of 2.5 (D_1) resp. 2.0 mm (D_2 and D_4) in diameter.

2.2 Charge Collection Properties

In the following characterisation procedure systematic data of sample D_2 (d_2 = 300µm) are presented.

2.2.1 Pulse Shape Analysis

Using short-range (12 µm) ^{241}Am alphas the drift of electrons and holes can be studied separately. Positive bias on the impinged electrode enables hole drift whereas negative bias electron drift only. The diamond signals are amplified with low-impedance broadband amplifiers (DBAII, GSI) and analyzed with a 3 GHz DSO. Figure 2 shows α-induced electron drift signals in D_2 (blue lines) and in a PC-DD (pink lines) at constant electric field E = -1 V/µm. The corresponding average signals are plotted in cyan and red. Note, that opposite to the extremely stable operation of the SC detector at positive bias (hole drift) the amplitudes of the electron signals are slightly decreasing with time. This observation indicates trapping in contacts or in the SC-D bulk.

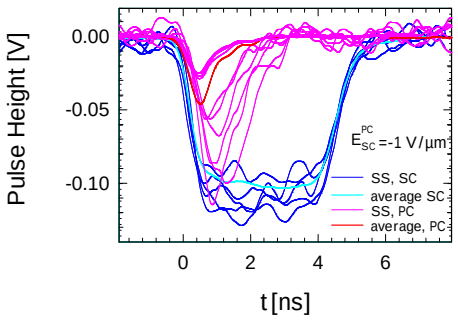

Figure 2: Electron drift signals in a SC- (blue/cyan) and in a PC- (pink/red) CVD-DD. The triangular shaped PC signals of various amplitudes (A^{avg} ˜ 0.4 A^{max}) mirror the inhomogeneous trapping of the generated charge, whereas the almost constant pulse height and width of the trapezoidal shaped SC signals indicate homogeneity of the detector material. The FWHM of the single pulses determines the transition time t_{TR} of the charge cloud generated from each α-particle to the opposite electrode.

Nevertheless, Figure 2 demonstrates impressively the improved quality of SC-CVDD. The signals have a similar rise time of ˜ 300 ps, as PC-DD, but reveal a much better S/N ratio. However, the picture shows either that in high-rate HI

timing applications PC-DDs may be still of advantage.
The development of electron (red)- and hole drift signals (blue) in SC-D with increasing electric field is illustrated in Figure 3. The peculiarities of the structures on top of the signals are not understood yet. They will be investigated later in more detail. Using the FWHM as the transition time t_{TR} the average carrier drift velocity $v(E_D) = d_D/t_{TR}(E_D)$ has been calculated and the results are plotted in Figure 4 versus the increasing electric field.

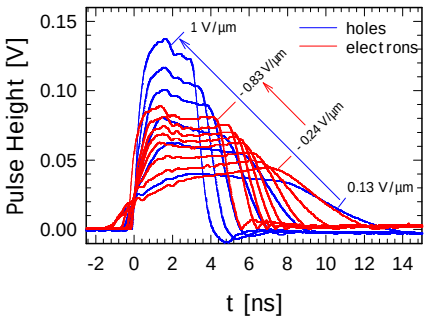

Figure 3: Development of average electron- and hole drift signals in SC-CVDD at increasing electric field E_D.

It is remarkable and in contradiction to the low-field values reported in the literature that at higher electric field holes drift faster than electrons confirming the suggestion of a DD revealing electron traps in the bulk or contact problems.

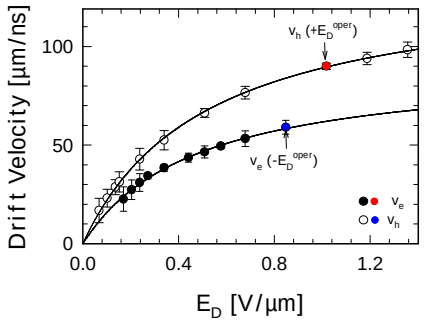

Figure 4: Electric field dependence of the drift velocity of the charge carriers. Opposite to the low-field values, in this SC-DD the holes at operation field are faster than the electrons.

2.2.2 Energy Resolution

The energy resolution measured with mono-energetic charged particles is a sensitive parameter to test homogeneity of solid-state detectors. We are using a mixed-nuclide alpha source with 5.1 MeV < $E^{\alpha}_{1,2,3}$ < 5.8 MeV and a silicon pin-diode as reference detector for these tests. The signals of both detectors are processed with a charge-sensitive preamplifier (CSTA2, TUD), a Tennelec shaping amplifier and a peak-sensing Silena 13 bit ADC.
The precision of the energy calibration is $\delta E = \pm 1$ keV and the α-resolution of the pin diode 14 keV. The SC-DD spectrum shown in Figure 5 is obtained at positive bias and has been calibrated using a linear fit to the measured ratios of the amplitudes in both detectors $R_{1,2,3} = A^{Si}(E_{1,2,3})/A^{D}(E_{1,2,3})$. The fit gives an $R^{avg} = 3.546 \pm 0.002$. An excellent energy resolution $\Delta E = 19$ keV corresponding to a $\Delta E/E = 0.003$ results for D_2. Considering the higher Fano factor expected for DDs, this value is almost as good as silicon resolution. Highest-quality PC-DDs have a $\Delta E/E = 0.65$ in best-case [1].

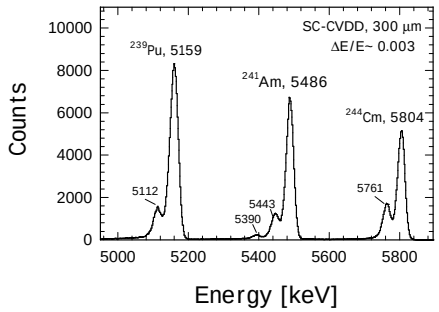

Figure 5: Mixed nuclide α-spectrum of a SC-DD detector. Due to a ΔE ~ 20 keV all satellite α-lines are distinguished.

Since R^{avg} can be also written as $R^{avg} = w^D/w^{Si}$, where w^D and w^{Si} are the energies needed to create an e-h pair in the respective material, a conversion factor $w^D = 12.84 \pm 0.01$ eV/e-h pair is extracted for this sample in contradiction to the usual assumed value of 13.4 eV/e-h. The precision of this value is determined by the uncertainty of the chosen w^{Si} (300K) = 3.62 ± 0.03 eV/e-h pair (ORTEC 1994).

2.2.3 Charge Collection Efficiency (CCE)

The charge collected for positive and negative bias from the 5.486 MeV line of a pure ^{241}Am source is plotted in Figure 6 versus the electric field. Full saturation at much lower fields than in PC-DDs is obtained[1]. The charge collected from electrons is slightly lower than that collected from holes (-2%) and saturates at higher field. The red dashed line indicates the whole charge expected if $w^D = 13.4$ eV/e-h. Obviously, this value is not valid for these data, which confirm perfectly the conversion factor of 12.84 eV/e-h for the case of loss-less charge drift (here, hole drift).

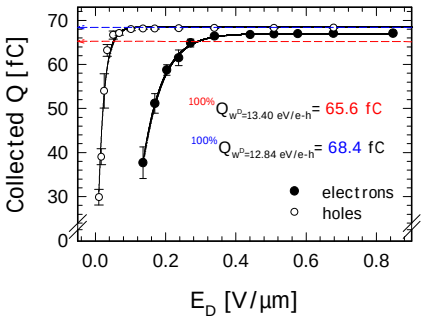

Figure 6: Collected charge measured with positive bias (hole drift) and negative bias (electron drift).

Concluding Remarks

The systematic data reported confirm the expectation that SC-DDs are suitable for HI spectroscopy and timing applications as well. A charge-sensitive but fast amplifier is in preparation for the tough case of MIP timing. The weak electron trapping in D_2 is not observable in data of recently delivered samples. The role of contacts is still confusing.

Acknowledgment

This work is supported by the EU, Project RII3-CT-2004-506078. We express our gratitude to Element Six, Ascot UK for generous provision of the SC-CVDD samples.

References

[1] E. Berdermann et al., GSI Ann. Reports 1997-2003
[2] C. Nebel, Habilitationsschrift, TUM 1998

The GSI Mass Storage System for Experiment Data

H. Göringer, M. Feyerabend
GSI Darmstadt

The GSI mass storage system with **A**utomatic **T**ape **L**ibrary (ATL) went into production at the beginning of 1997 and is available since that time 24 hours a day and 7 days a week. The system started with an IBM 3494 ATL and four IBM 3580 tape drives. Access was enabled by a GSI made client/ server system with the *adsmcli* command as user interface. For ATL and tape handling a commercial storage manager (ADSM) was used.

The requirements to the system increased considerably over the years. So the hardware had to be upgraded from time to time to keep track with the demands for more data capacity and I/O bandwidth. Accordingly also the software had to be enhanced continuously to satisfy the growing user requirements for more functionality. So besides the command interface also a programmer's interface (API) was implemented using the RFIO interface developed as a standard at CERN.

In 2001 an additional mass storage system with new hardware and software was designed in close collaboration with the GSI users. A new and ambitious concept with data movers (see figure 1) was developed and realized with a new StorageTek L700 ATL with Ultrium LTO tape drives. The new system uses the ADSM successor **T**ivoli **S**torage **M**anager (TSM) and provides a new command (*tsmcli)* as user interface. It went into production at the beginning of 2002. Until now its usage is mainly restricted to the largest GSI experiment collaborations (fopi, Hades, Alice).

The current status of **gstore**, the **G**SI mass **stor**ag**e** system is summarized in table 1:

	old (adsmcli)	new (tsmcli)
ATL	IBM 3494	StorageTek L700
stored data [TB]	47 (full)	32 (max 140) +10 bkp
tape drives	8 IBM 3590	9 x IBM LTO2 (SAN)
no. data movers	1 (adsmsv1)	8 (gsidm0x)
disk cache [TB]	1.1	3.2 (all DMs)
realized transfer	0.6 TB/d	2.5 TB/d (all DMs)

Table 1: Status gstore Hardware December 2004

The new mass storage system was designed according to the following requirements:

- Strict separation of control and data flow.
- Scalability in capacity and I/O bandwidth
- Independence from hardware and operating system
- Unique GSI name space

The first two items lead to a very flexible solution with tapes and data mover nodes connected via **S**torage **A**rea **N**etwork (SAN, see figure 1). This allows access from any data mover to any tape drive. Each data mover has a set of local disks used as read or write cache. Obviously more capacity and bandwidth can easily be realized by just adding more appropriate hardware. The third requirement is also fulfilled, as the TSM package supports all common ATL and tape hardware and runs on all relevant platforms.

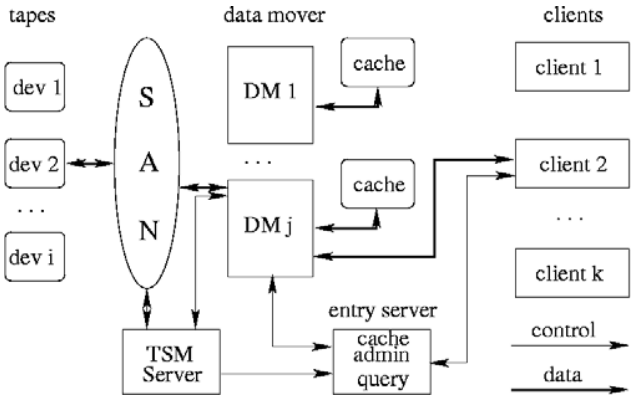

Figure 1: Overview new System (*tsmcli*)

A large data production on the GSI batch farm with several hundred jobs in parallel may provide a very big number of simultaneous read and write requests to the mass storage system. This can be handled efficiently only with a sufficiently large layer of read and write cache disks separating the users from the tape drives. The administration of the disk pools is also managed by the GSI software. For this purpose two servers for read and write cache were developed. Both have own metadata databases and are supported by a common slave server on each data mover. Their main tasks are

- to select data mover and file system for a given request,
- to lock/unlock files in use,
- to collect and utilize actual information about disk space and data mover load,
- to maintain some free disk space in read cache, and
- to archive asynchronously from write cache disk to tape.

Several disk pools with different attributes are available. In 2004 two write cache pools were implemented according to very different usage profiles:

- ***ArchivePool*:** prepared for highly parallel access from the batch farm
- ***DAQPool*:** accepting several continuous data streams from the data acquisition of running experiments

Since summer 2004 data collected in event builders can be written via RFIO interface directly into the *DAQPool* thus providing an on-line connection between running experiments and the GSI mass storage.

In 2005, new data movers running on Linux (instead of Windows) will be installed to increase the rare cache disk space. Then larger working sets can be provided on disk for longer times. The user interfaces of the old and new mass storage system will be merged and *adsmcli* / *tsmcli* will be replaced by one new command named "***gstore***". So users need no longer care in which ATL requested files are stored.

As conclusion gstore is able to manage very different usage profiles and - due to its scalable design - is well prepared for the requirements of the future.

Go4 analysis framework v2.9

J. Adamczewski, M. Al-Turany, D. Bertini, H.G. Essel, S. Linev

GSI

Status of Go4 and GOOSY

Since the first production release of Go4 in May 2002 all GOOSY based analysis programs have been replaced by Go4. SHIP, FRS, RISING, all atomic physics experiments and many sites outside GSI are using Go4. Go4 is available for free from the Web [1] under GPL. The feed back of the users and close cooperation resulted in considerable improvements for the Go4. The user accounts on VMS have been closed end of 2004. The era of GOOSY is over.

Go4 has been presented at all CHEP and Real time conferences [2] and ROOT workshops over the last years. Several workshops have been carried out at GSI. Go4 is well established as framework for small to medium sized analyses with excellent on-line features. It is also prepared for more complex analysis tasks.

The following sections describe briefly some major enhancements.

Macro support (CINT)

The GUI provides the execution of ROOT macros in the analysis task (between two events, if analysis is running). The analysis can completely run in CINT with or without GUI. All Go4 objects are accessible in macros. Macros could also be executed in compiled analysis programs to set up the analysis steps or set parameters and conditions. ROOT canvases created in analysis, i.e. by macro, can be sent to the GUI where they show up in the memory folder and can be displayed.

Analysis organisation

Simple analysis programs can now be written with minimum effort, i.e. a standard main program and one event processing class. On the other hand a complex Go4 analysis can be built by several steps, each with its own event IO and event processing. The steps can be configured from the GUI or by macro. The execution order is sequentially, but steps can be dis- or enabled arbitrarily. As shown in Fig.1 all event processors have access to event elements coming either from files or from previous steps. Mesh-like topologies can be constructed. However, the consistency of such meshes must be controlled at application level. Of course, partial IO is possible for all steps.

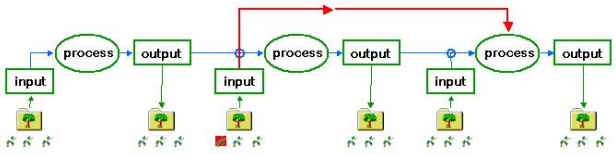

Figure 1: Chain of analysis steps.

On-line monitoring

The separation of analysis and GUI into two tasks provides asynchronous control of a running analysis. Objects like histograms or graphs can be monitored, i.e. periodically displayed in the GUI without interference with user activities. All objects displayed in the GUI can be updated from the analysis by a mouse click. Application specific GUIs can be added to the Go4 GUI. Such GUIs have full access to all objects of the analysis, also asynchronously.

Dynamic histogramming

Members of user event objects can be accumulated interactively in new histograms, optionally filtered by conditions. In the dynamic list editor such members can be dragged from the analysis browser. Dynamic list entries are shown in the analysis browser. By double click the editor is opened as shown in Fig.2.

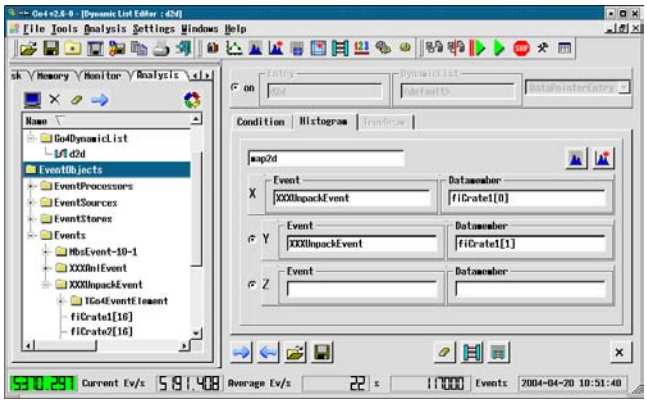

Figure 2: Dynamic list editor

Besides the event by event filling the dynamic histogramming can also be done out of a tree, either an optional memory back store or an output tree, by a ROOT tree draw executed every n events for the last n events.

Generic parameter editor

Go4 parameters are powerful tools because they not only store values but also can execute user functions in the (running) analysis. A double click on a parameter object in the browser opens the generic parameter editor shown in Fig.3.

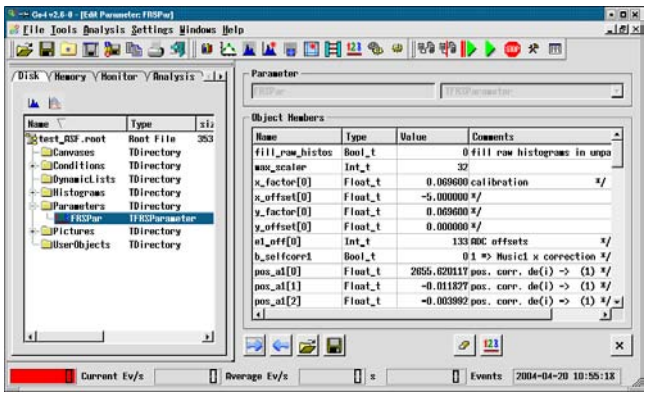

Figure 3: Generic parameter editor.

All fundamental type members of the (user) class are displayed and can be changed. With the update button the modified parameter object is sent to the analysis and an (user) update method is called. Depending on member values the user may then execute arbitrary methods of his class. Parameter objects are accessible globally.

Condition Handling

Usually condition parameters like boundaries are set interactively on histograms displaying the value(s) to be checked by the condition. To avoid setting on a wrong histogram the correct one can be attached to the condition: when the condition editor is opened this attached histogram is displayed automatically together with the condition. An even more powerful method is to add conditions to pictures (see below) together with histograms. The condition editor can then select a condition from the picture which is then displayed in the pad of the histogram., as shown in the upper right pad of the picture in Fig.4.

Pictures

Similar to GOOSY one can define picture objects keeping all information about histograms and their appearance in one view panel. An example is shown in Fig.4.

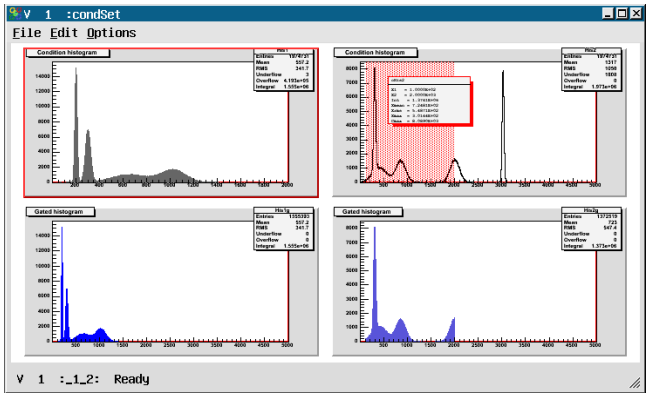

Figure 4: Picture view panel.

Go4 cursor modes

There was a strong request to have efficient markers for channels and regions. This is now provided by the marker modes shown in Fig.5. Entering the channel mode, for example, one gets per one mouse click a marker. The information of the marker can be configured. Markers can be stored and retrieved (content updated from actual histogram).

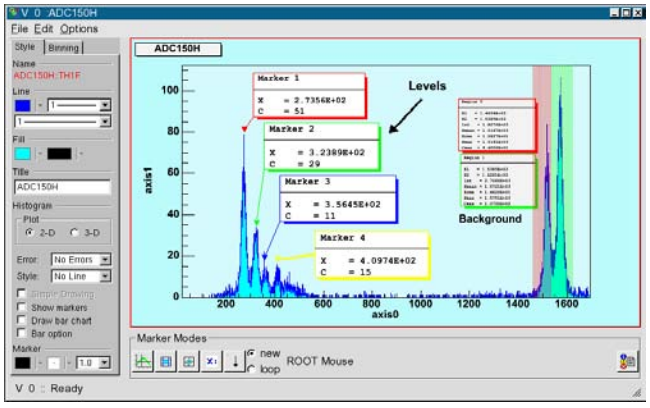

Figure 5: Go4 marker modes and embedded ROOT editor.

Note the embedded ROOT graphical editor on the left side.

Graphical user interface for fit package

There is now a GUI supporting the full functionality of the Go4 fit package. Fig.6 shows the peak finder and four gaussians found and fit. The fit parameters can be seen in another view. The whole fitter object can be stored/retrieved or used in macros.

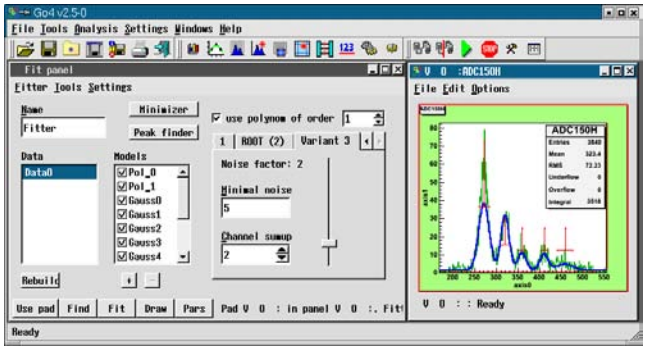

Figure 6: Fit GUI with peak finder and list of models.

Go4 hot start

After setting up a working context in the GUI, i.e. analysis program, histograms to be monitored, view panels, histograms in GUI memory, a hot start file can be generated. Starting the GUI with this file as argument the whole context will be restored, inclusively starting and setting up the analysis, opening view panels and moving histograms to monitor or memory. One has just to press the Start button to run.

Other useful new features

Of course, many bugs have been fixed. Big effort has been put into performance improvements for the analysis speed, the communication optimization and the interactive graphics operations.

A list of LMD files can be processed from a container file. In between the LMD files ROOT macros can be executed. At GSI, files can be directly opened via RFIO in the tape archive.

In the Go4 file browser remote files can be accessed through a ROOT file demon (XRootd), the Web (carrot), or the GSI tape archive (RFIO). Trees can be processed by the tree viewer. Multiple files can be opened. Objects from several files can be processed simultaneously.

Go4 settings can be stored in directories. This allows to run several Go4 analysis sessions simultaneously under one account with different set ups, as long as they run on different directories. This feature was required for experiment accounts.

Histograms can be exported in ASCII and Radware [3] format for further processing

Summary

The Go4 framework has been successfully established. Many collaborations in- and outside GSI are using it. The further development will be driven by new requirements. To provide tools for a more complex analysis some internal redesign might be necessary, i.e. the internal object management and mesh-like analysis structures. Especially the IO system should support in a convenient way all features the ROOT IO provides.

References

[1] http://go4.gsi.de

[2] J.Adamczewski et al., *Go4 online monitoring*, IEEE TNS Vol.51, No.3, June 2004, pp 565-570

[3] http://radware.phy.ornl.gov

Grid Activities at GSI

P. Malzacher, A. Manafov, R. Manteufel, V. Penso, C. Preuss, K. Schwarz

.

1 The EGEE project

GSI is part of the distributed Regional Operation Centre (ROC) of the new European Union project EGEE (Enabling Grids for E-SciencE [1]). Unlike it's predecessor project EDG [2] the focus is less on technical development but rather on the provision of production services to Grid users with the idea also to broaden the user base. Despite its strong focus on deployment of Grid software, the development of a new Grid middleware named gLite [3] is a core part of EGEE. A small testbed using the first prototype of gLite is already provided by the ARDA-group [4], with beginning participation of GSI and GridKa.

2 The LCG project

The common grid project of all LHC [5] experiments has reached production state by now and is used for the regular Data Challenges. This global production environment consists of approx. 10000 CPUs and a disk storage capacity of 5 PB distributed over more than 100 sites.

Since the LCG [6] software, in the version 2.3 the current production software of EGEE, is only provided for RedHat 7.3, now also for Scientific Linux, it has been necessary to port it to Debian before using it at GSI. To study the behaviour of the default LCG environment a stand-alone testbed has been set up running on Scientific Linux with OpenPBS (Torque). With the experience gained herewith it has been possible to setup a parallel LCG installation within the GSI environment. The LCG User Interface, from where people can interact with the system, is running on a standard Debian system being accessible from anywhere within GSI. To use GSI's batch farm the Computing Element (CE) which acts as an interface between the global Grid and the local batch system has been connected to LSF. Therefore Grid jobs can be sent from anywhere in the world to standard Debian Worker Nodes (WNs) at GSI. A classic Storage Element (SE) as well as a job monitoring system have also been installed. All these GSI capabilities are advertised in the global LCG information system and can be found on LCG web sites [7]. Additionally, recently it has been started to set up a Virtual Organisation (VO) server for the CBM experiment. Therefore a more recent Globus version (2.4) has been installed as well. Members of a VO are able to share the distributed resources provided by the Grid.

3 PROOF

With PROOF distributed datasets can be analysed in parallel by using the ROOT system. After having investigated the possibilites to set up a PROOF cluster [8], each user at GSI is given now the possibility to set up his own personal PROOF environment. Here the started PROOF server processes run under the personal userID in a dedicated high priority "proof" queue within the GSI batch farm. Authentication to the PROOF system is currently possible by using the userID/password combination of the user's GSI account. In testing state is the authentication via Globus based Grid certificates. By using the latter method a user's PROOF cluster could also be expanded to sites outside GSI.

4 AliEn

The first two stages of the ALICE Physics Data Challenge 04 (ADC04) in which ALICE deals with 10% of the amount of data as will arise during the time of the startup of the LHC has completed successfully. The whole production ran under the control of AliEn while using the global Grid resources connected to AliEn and LCG since it is possible to connect the complete LCG-grid as one of many CE's to AliEn. During the six months of Phase 1 and 2 in which data simulation, mixing of background and signal events as well as reconstruction took place an average of 600 jobs have been running concurrently consuming 1300 KSI2K of CPU power and filling a total of 300 TB of disk space. Phase 3 of the Data Challenge will be an individual analysis of the worldwide distributed data sets by Physicists using a combination of AliEn/gLite and PROOF. This concept has been demonstrated successfully on various conferences and is described in [8]. AliEn environments have been set up also for the GSI future experiment PANDA as well as for the SLAC experiment BaBar.

5 Outview

To be able to operate the current LCG and PROOF installations in production mode the development of a functioning support concept for future Grid users is necessary. Additionally the extension from the current batch system like Grid environments to interactive and distributed analysis systems has to be done. This is planned to be done within the framework of the D-Grid project [9].

References

[1] http://public.eu-egee.org/
[2] http://eu-dataGrid.web.cern.ch/eu-dataGrid/
[3] http://glite.web.cern.ch/glite/
[4] http://www.uscms.org/s&c/lcg/ARDA/
[5] http://lhc-new-homepage.web.cern.ch/lhc-new-homepage/
[6] http://lcg.web.cern.ch/LCG/ GSI Annual Report (2003) 237
[7] http://goc.grid.sinica.edu.tw/gstat/GSI-LCG2/
[8] GSI Annual Report (2003) 237
http://www-w2k.gsi.de/root/
[9] http://www.d-grid.de/

HICAT-HD

Hospital-based Ion Cancer Therapy Project in Heidelberg

Status Report of the HICAT/HIT-Project

H. Eickhoff and T. Haberer for the GSI Project Group of the HICAT-Facility

1) Abstract

Major progress of the Heidelberg Ion Cancer Treatment facility (HICAT /HIT=Heidelberg Ion Therapy) took place in 2004 .
After the orders for all technical systems of the accelerator had been launched to ten industrial firms in 2003, the construction and manufacturing process had been started; in parallel the building activities started near the end of 2003.
The tender for the treatment technique took place in March 2004; the contract between the clinics and Siemens-Med for this system was signed in Oct. 2004.
In parallel to these investment activities preparations for the operating phase took place.

2) Overall project status

a) Status of the building activities

Fig. 1 shows the first underground floor of the building, that houses the accelerator sections (Linac, Synchrotron, HEBT) and the 2 horizontal treatment areas (H-1, H-2), the Gantry and the 'quality assurance place' (Q-A) (for details of the facility see ref. [1]).

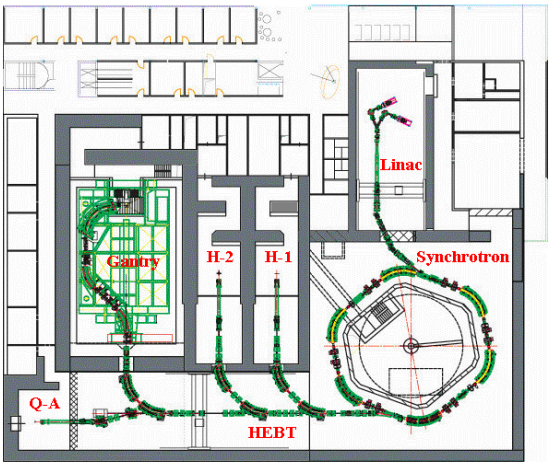

Fig. 1: Layout of the first underground floor, housing the accelerator complex

Fig. 2 shows the present status [2} of the building, performed by the firms STRABAG in cooperation with M+W Zander. As shown, the structure of the facility and the main areas can be clearly identified; concerning the schedule a delay of about 8 months took place, compared to the original one, that stated a finish of the accelerator areas in Feb. 2005; therefore at present the start of the accelerator assembly is scheduled for Oct. 2005. At this time, the building sections of the accelerator parts will be nearly completed, and the technical infrastructure (e.g. watercooling-systems, electric supply, assembly-tools), necessary for commissioning of the individual accelerator sections, will be installed.

Fig. 2: Status of the Building (Dec., 2004)

b) Status of the accelerator systems

The accelerator subsystems (magnets, power-supplies, etc.) were ordered in 2003 from about 10 international suppliers. The construction phase for most of these subsystems is nearly finished and the manufacturing process had been started; for most of the components the production will be finished in 2005. The delivery of magnets and vacuum components to GSI has been started. These components will be preassembled at GSI and stored on the GSI-area until the building is ready for starting the assembly work in Heidelberg from Oct., 2005.
Major achieved milestones are:

- The acceptance tests of the ECR ion sources, delivered by CANBERRA-EURYSIS have been started.
- At the IAP at Frankfurt University a proton beam could be successfully accelerated with the RFQ, that had been manufactured by this institute; further measurements of the beam properties, e.g. exact measurements of the acceleration energy, are under way.
- The IH-Linac-structure was finished at PINK (the supplier of the vacuum system); first RF-measurements were successful. The IH-quadrupole triplets, manufactured by DANFYSIK, will be delivered soon and the copperplating process of the IH-structure will start within the next two months.
- The specified beam diagnostic systems for the Linac-section were manufactured by GSI and the acceptance tests were successfully performed.
- The design of the controls system, ordered from ECKELMANN was finished; first control boards with test software were delivered to GSI.

- In December 2004 acceptance tests of Linac-magnets, supplied by SIGMAPHI, took place.
- The design of the synchrotron dipoles, ordered from TESLA, is finished. After the delivery to GSI will start in the first half of 2005 the magnetic measurements and shimming labour will be performed for all 6 dipoles.
- The construction and manufacturing of the 3 amplifier systems for the Linac RF-supply, ordered from THALES, is in progress.
- The complete synchrotron accelerating system was ordered from HITACHI; the factory acceptance test of this subsystem is foreseen for July 2005.

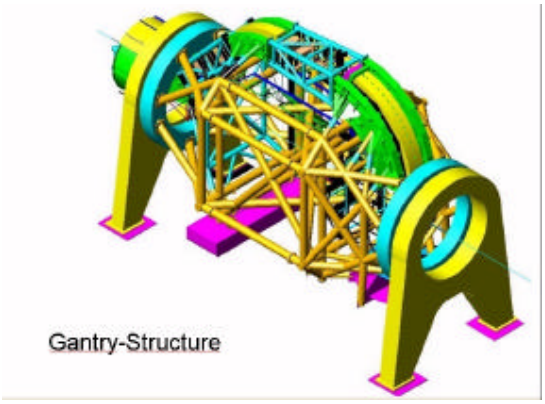

Fig. 3: Gantry structure (Courtesy of MAN Technology)

- The mechanical construction of the gantry-structure (see Fig. 3), ordered from MAN-MT is finished; the manufacturing process has started. The detailed construction of the gantry patient room, covering all aspects of the treatment components and subsystems, delivered by Siemens AG, has started.

c) Status of the irradiation technology systems

In March, 2004 the tender for the irradiation technology, i.e. the beam scanning controls and monitoring equipment, the patient positioners, the x-ray systems and the IT/workflow software platform, was launched. In Oct. 2004 the contract with Siemens AG, Medical Solutions as a general contractor was signed.
HICAT will be equipped both at the two horizontal treatment places and at the gantry treatment room with state of the art patient positioning and position verification modalities. The combination of a robotic patient positioner with large-area flat-panel x-ray imagers allows for a feedback procedure of the image analysis result. A fast matching algorithm calculates a multi-dimensional displacement vector of the actual setting relative to digital reconstructions derived from the planning CT that represents the basis of irradition course. Figure 4 shows the planned configuration of the medical equipment at the scanning ion gantry. Two flat-panel imagers mounted directly near the exit of the final large-aperture bending magnet, arranged under 60-degrees, are used to check the patient immobilization in the treatment position.

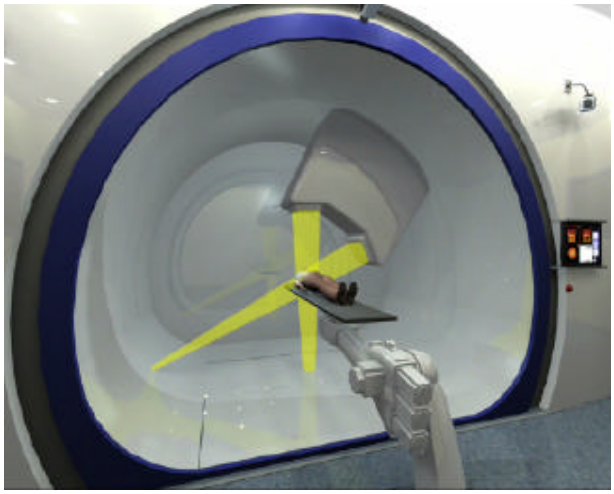

Fig.4: View into the nozzle region of the scanning ion gantry for a position verification x-ray exposure (the x ray-beams shaded in yellow). (Courtesy of Siemens AG, Medical Solutions)

3) Organization aspects

Besides the coordination and supervision labour of the various technical aspects also activities have started in preparation of the commissioning and operation phase of the facility. The Heidelberg Clinics have founded an operation department for the facility and employed first members of the technical operation staff; these members are presently trained at the GSI accelerator complex.
As the total facility is classified according to the medical device directive a certification organization ('notified body') was appointed by the Clinics to prepare the activities requested to achieve the patient treatment permission.
Tab. 1 shows the present project schedule with the major activities until the handing over to clinical operation.

Time (Year)	**Activities**
2005/6	assembly of the accelerator-systems
2006/7	overall commissioning
2007	patient treatments (horizontal places)
2008	patient treatments (gantry)

Tab. 1: Present overall Schedule

4) References

[1] H. Eickhoff et al., HICAT-The German Hospital-Based Light Ion Cancer Therapy Project; EPAC 2004
[2] Internet web-cam: www.arge-sit.de

ANNEXGSI

Annex to Publications and Activities at the GSI

Publications of the FAIR project

Compiled by K. Große

1. Reviewed publications

P-F001 Anselmino, M.; Barone, V.; Drago, A.; Nikolaev, N. N.: **Accessing transversity via J/ψ production in polarized $p \uparrow \bar{p} \uparrow$ interactions.** *Physics Letters B* **594**(1/2): 97–104. DOI:10.1016/j.physletb.2004.05.029

P-F002 Barnes, T.: **Exploring QCD: from LEAR to GSI.** *Nuclear instruments & methods in physics research, Section B, Beam interactions with materials and atoms* **214**: 44–49. [Low Energy Antiproton Physics (LEAP'03), Yamashita-park, Japan, 3 March - 7 March 2003] DOI:10.1016/S0168-583X(03)01759-2

P-F003 Dolinskii, A.*; Beller, P.*; Beckert, K.*; Franzke, B.*; Nolden, F.*; Steck, M.*: **Optimized lattice for the Collector Ring (CR).** *Nuclear instruments & methods in physics research, Section A, Accelerators, spectrometers, detectors and associated equipment* **532**(1): 483–487. [International Workshop on Beam Cooling and Related Topics, Lake Yamanaka, Yamanashi, Japan, 20030519/23] DOI:10.1016/j.nima.2004.06.083

P-F004 Efremov, A. V.; Goeke, K.; Schweitzer, P.: **Transversity distribution function in hard scattering of polarized protons and antiprotons in the PAX experiment.** *The European physical journal: C, Particles and fields* **35**(2): 207–210. DOI:10.1140/epjc/s2004-01854-9

P-F005 Henning, W.*: **RNB facilities in Europe - Present and future.** *Nuclear physics A, Nuclear and hadronic physics* **746**: 3C–8C. [Proceedings of the Sixth International Conference on Radioactive Nuclear Beams (RNB6) Argonne 20030922/26] DOI:10.1016/j.nuclphysa.2004.09.012

P-F006 Henning, W.*: **The GSI project: An international facility for ions and antiprotons.** *Nuclear physics A, Nuclear and hadronic physics* **734**: 654–660. [Proceedings of the Eighth International Conference On Nucleus-Nucleus Collisions] DOI:10.1016/S0375-9474(04)90359-4

P-F007 Henning, W. F.*: **The future GSI facility.** *Nuclear instruments & methods in physics research, Section B, Beam interactions with materials and atoms* **214**: 211–215. [Low Energy Antiproton Physics, Yamashita-park, Japan, 3 March - 7 March 2003] DOI:10.1016/S0168-583X(03)01761-0

P-F008 Koch, H.; PANDA Collaboration*: **Hadron physics with antiprotons.** *Nuclear instruments & methods in physics research, Section B, Beam interactions with materials and atoms* **214**: 50–55. [Low Energy Antiproton Physics (LEAP'03), Yamashita-park, Japan, 3 March - 7 March 2003] DOI:10.1016/S0168-583X(03)01771-3

P-F009 Lewandowski, B.; PANDA Collaboration*: **A fast and compact electromagnetic calorimeter for the PANDA detector at GSI.** *Nuclear instruments & methods in physics research, Section A, Accelerators, spectrometers, detectors and associated equipment* **537**(1-2): 349–352. [Proceedings of the 7th International Conference on Inorganic Scintillators and their Use in Scientific and Industrial Applications, Valencia, Spain, 08-12 September 2003] DOI:10.1016/j.nima.2004.08.041

P-F010 Maier-Komor, P.; Friese, J.; Gernhäuser, R.; Homolka, J.; Krücken, R.; Winkler, S.: **Investigation of deposition parameters for VUV reflective coatings on the HADES RICH mirrors.** *Nuclear instruments & methods in physics research, Section A, Accelerators, spectrometers, detectors and associated equipment* **521**(1): 35–42. DOI:10.1016/j.nima.2003.11.145

P-F011 Novotny, R. W.: **Fast and compact lead tungstate-based electromagnetic calorimeter for the PANDA detector at GSI.** *IEEE transactions on nuclear science* **51**(6): 3076–3080.

P-F012 Peters, K.: **Charmed hybrids in proton antiproton annihilation.** *Nuclear instruments & methods in physics research, Section B, Beam interactions with materials and atoms* **214**: 60–64. [Low Energy Antiproton Physics, LEAP'03, Yamashita-park, Japan, 3 March - 7 March] DOI:10.1016/j.nimb.2003.08.006

P-F013 Pochodzalla, J.: **Future experiments on hypernuclei and hyperatoms.** *Nuclear instruments & methods in physics research, Section B, Beam interactions with materials and atoms* **214**: 149–152. [Low Energy Antiproton Physics, LEAP'03, Yamashita-park, Japan, 3 March - 7 March] DOI:10.1016/j.nimb.2003.08.007

P-F014 Ritman, J.: **Conceptual design and simulation of the PANDA detector.** *Nuclear instruments & methods in physics research, Section B, Beam interactions with materials and atoms* **214**: 201–206. [Low Energy Antiproton Physics (LEAP'03), Yamashita-park, Japan, 3 March - 7 March 2003] DOI:10.1016/j.nimb.2003.08.011

P-F015 Saitoh, T. R.*; Pochodzalla, J.*; PANDA Collaboration*: **Hypernuclear physics projects with PANDA at GSI.** *Acta physica Polonica B, Particle physics and field theory, nuclear physics, theory of relativity* **35**(3): 1033–1041.

P-F016 Senger, P.*: **Exploring compressed baryonic matter - Nucleus-nucleus collisions at the future facility in Darmstadt.** *Acta physica Polonica B, Particle physics and field theory, nuclear physics, theory of relativity* **35**(3): 1131–1142.

P-F017 Senger, P.*: **Particle production in heavy-ion collisions.** *Progress in particle and nuclear physics* **53**(1): 1–23. DOI:10.1016/j.ppnp.2004.02.005

P-F018 Senger, P.*: **The compressed baryonic matter experiment at FAIR in Darmstadt.** *Journal of physics G, Nuclear and particle physics* **30**(8): S1087–S1090. DOI:10.1088/0954-3899/30/8/064

P-F019 Tahir, N. A.*; Udrea, S.; Deutsch, C.; Fortov, V. E.; Grandjouan, G.; Gryaznov, V.; Hoffmann, D. H. H.*; Hülsmann, P.*; Kirk, M.; Lomonosov, I. V.; Piriz, A. R.; Shutov, A.; Spiller, P.*; Temporal, M.; Varentsov, D.: **Target heating in high-energy-density matter experiments at the proposed GSI FAIR facility: Non-linear bunch rotation in SIS 100 and optimization of spot size and pulse length.** *Laser and particle beams* **22**(4): 485–493. DOI:10.1017/S0263034604040145

2. Further publications

P-F001nr Bogdanov, I.; Kozub, S.; Shcherbakov, P.; Tkachenko, L.; Fischer, E.*; Klos, F.*; Moritz, G.*; Muehle, C.*: **Study of Electrical Steel Magnetic Properties for Fast Cycling Magnets of SIS100 and SIS300 Rings**. In: CERN (Ed.): *EPAC 2004: A Europhysics Conference 5 to 9 July 2004, Lucerne Congress Centre Switzerland, www.epac04.ch*, Geneva: CERN, 2004. 9th European Particle Accelerator Conference, Lucerne, 05.07.2004-10.07.2004, 1741-1743p.

P-F002nr Bogdanov, I.; Kozub, S.; Shcherbakov, P.; Tkachenko, L.; Zintchenko, S.; Zubko, V.; Kaugerts, J.*; Moritz, G.*: **Study of the Quench Process in Fast-cycling Dipole for the SIS300 Ring**. In: CERN (Ed.): *EPAC 2004: A Europhysics Conference 5 to 9 July 2004, Lucerne Congress Centre Switzerland, www.epac04.ch*, Geneva: CERN, 2004. 9th European Particle Accelerator Conference, Lucerne, 05.07.2004-10.07.2004, 1744-1746p.

P-F003nr Chirila, C. C.; Joachain, C. J.; Kylstra, N. J.; Potvlige, R. M.: **Three-step processes with relativistic ions**. In: *12th International Laser Physics Workshop, Hamburg, 25.08.2003-29.08.2003*, 2004, 190-193p.

P-F004nr Dolinskii, A.*; Beckert, K.*; Beller, P.*; Franzke, B.*; Nolden, F.*; Steck, M.*: **Nonlinear Effects Studies for a Large Acceptance Collector Ring**. In: CERN (Ed.): *EPAC 2004: A Europhysics Conference 5 to 9 July 2004, Lucerne Congress Centre Switzerland, www.epac04.ch*, Geneva: CERN, 2004. 9th European Particle Accelerator Conference, Lucerne, 05.07.2004-10.07.2004, 1177-1179p.

P-F005nr Dolinskii, A.*; Boine-Frankenheim, O.*; Franzke, B.*; Steck, M.*; Bolshakov, A.; Zenkevich, P.; Olegovich, A.; Troubnikov, G.: **Simulation Results on Cooling Times and Equilibrium Parameters for Antiproton Beams at the HESR**. In: CERN (Ed.): *EPAC 2004: A Europhysics Conference 5 to 9 July 2004, Lucerne Congress Centre Switzerland, www.epac04.ch*, Geneva: CERN, 2004. 9th European Particle Accelerator Conference, Lucerne, 05.07.2004-10.07.2004, 1972-1974p.

P-F006nr Düren, M.: **Time-like Compton scattering and related exclusive processes in proton-antiproton annihilation at PANDA**. In: *Hadron Spectroscopy.* AIP Conference Proceedings 717 (1), Melville/New York, 2004, 827-831p. DOI:10.1063/1.1799802

P-F007nr Franchetti, G.*; Hofmann, I.*: **Beam Loss Modeling for the SIS100**. In: CERN (Ed.): *EPAC 2004: A Europhysics Conference 5 to 9 July 2004, Lucerne Congress Centre Switzerland, www.epac04.ch*, Geneva: CERN, 2004. 9th European Particle Accelerator Conference, Lucerne, 05.07.2004-10.07.2004, 1978-1980p.

P-F008nr Gianotti, P.: **Antiproton physics at GSI**. In: *Hadron Spectroscopy.* AIP Conference Proceedings Vol. 717 (1), Melville/New York, 2004, 525-532p. DOI:10.1063/1.1799757

P-F009nr Gorska, M.: **RISING status report**. In: *Hadron Spectroscopy.* AIP Conference Proceedings Vol. 701, Melville/New York, 2004, 143-148p. DOI:10.1063/1.1691699

P-F010nr Hasse, R.*; Boine-Frankenheim, O.*: **Comparison of Rate Equation Models for Equilibrium Beam Parameters**. In: CERN (Ed.): *EPAC 2004: A Europhysics Conference 5 to 9 July 2004, Lucerne Congress Centre Switzerland, www.epac04.ch*, Geneva: CERN, 2004. 9th European Particle Accelerator Conference, Lucerne, 05.07.2004-10.07.2004, 2544-2546p.

P-F011nr Henning, W.*: **FAIR - An International Accelerator Facility for Research with Ions and Antiprotons**. In: CERN (Ed.): *EPAC 2004: A Europhysics Conference 5 to 9 July 2004, Lucerne Congress Centre Switzerland, www.epac04.ch*, Geneva: CERN, 2004. 9th European Particle Accelerator Conference, Lucerne, 05.07.2004-10.07.2004, 50-53p.

P-F012nr Kauschke, M.; Schroeder, C. H.: **Cryogenic system for the new international accelerator facility for research with ions and antiprotons at GSI**. In: *Hadron Spectroscopy.* AIP Conference Proceedings Vol. 710 (1), Melville/New York, 2004, 363-370p. DOI:10.1063/1.1774704

P-F013nr Kovalenko, A.; Agapov, N.; Bartenev, V.; Donyagin, A.; Eliseeva, I.; Khodzhibagiyan, H.; Kuznetsov, G.; Smirnov, A.; Voevodin, M.; Fischer, E.*; Moritz, G.*: **Design and Study of a Superferric Model Dipole and Quadrupole Magnets for the GSI Fast-pulsed Synchrotron SIS100**. In: CERN (Ed.): *EPAC 2004: A Europhysics Conference 5 to 9 July 2004, Lucerne Congress Centre Switzerland, www.epac04.ch*, Geneva: CERN, 2004. 9th European Particle Accelerator Conference, Lucerne, 05.07.2004-10.07.2004, 1735-1737p.

P-F014nr Lundborg, A.: **Exotic charmonium hybrids at PANDA**. In: *Hadron Spectroscopy.* AIP Conference Proceedings Vol. 701, Melville/New York, 2004, 431-435p. DOI:10.1063/1.1799745

P-F015nr Moritz, G.*: **Fast Pulsed SC Magnets**. In: CERN (Ed.): *EPAC 2004: A Europhysics Conference 5 to 9 July 2004,*

Lucerne Congress Centre Switzerland, www.epac04.ch, Geneva: CERN, 2004. 9th European Particle Accelerator Conference, Lucerne, 05.07.2004-10.07.2004, 132-136p.

P-F016nr Mustafin, E.*; Moritz, G.*; Walter, G.*; Latysheva, L.; Sobolevskiy, N.: **Radiation Damage to the Elements of the Nuclotron-type Dipole of SIS100**. In: CERN (Ed.): *EPAC 2004: A Europhysics Conference 5 to 9 July 2004, Lucerne Congress Centre Switzerland, www.epac04.ch*, Geneva: CERN, 2004. 9th European Particle Accelerator Conference, Lucerne, 05.07.2004-10.07.2004, 1408-1410p.

P-F017nr Nesmiyan, I.*; Nolden, F.*: **Simulation Calculations of Stochastic Cooling for Existing and Planned GSI Facilities**. In: CERN (Ed.): *EPAC 2004: A Europhysics Conference 5 to 9 July 2004, Lucerne Congress Centre Switzerland, www.epac04.ch*, Geneva: CERN, 2004. 9th European Particle Accelerator Conference, Lucerne, 05.07.2004-10.07.2004, 2170-2172p.

P-F018nr Reich, H.; Christina, M.; Bender, M.*; Kollmus, H.*; Kraemer, A.; Kurdal, J.*; Spiller, P. J.*: **R&D Vacuum Issues of the Future GSI Accelerator Facilities**. In: CERN (Ed.): *EPAC 2004: A Europhysics Conference 5 to 9 July 2004, Lucerne Congress Centre Switzerland, www.epac04.ch*, Geneva: CERN, 2004. 9th European Particle Accelerator Conference, Lucerne, 05.07.2004-10.07.2004, 1657-1659p.

P-F019nr Steck, M.*; Beckert, K.*; Beller, P.*; Dolinskii, A.*; Franzke, B.*; Nolden, F.*; Parkhomchuk, V.; Borisovich, V.; Skrinsky, A.; Vostrikov, V.: **An Electron Cooling System for the Proposed HESR Antiproton Storage Ring**. In: CERN (Ed.): *EPAC 2004: A Europhysics Conference 5 to 9 July 2004, Lucerne Congress Centre Switzerland, www.epac04.ch*, Geneva: CERN, 2004. 9th European Particle Accelerator Conference, Lucerne, 05.07.2004-10.07.2004, 1969-1971p.

P-F020nr Tkachenko, L.; Bogdanov, I.; Kozub, S.; Shcherbakov, P.; Slabodchikov, P.; Sytnik, V.; Zubko, V.; Kaugerts, J.*; Moritz, G.*: **Comparison of Three Designs of Wide Aperture Dipole for SIS300 Ring**. In: CERN (Ed.): *EPAC 2004: A Europhysics Conference 5 to 9 July 2004, Lucerne Congress Centre Switzerland, www.epac04.ch*, Geneva: CERN, 2004. 9th European Particle Accelerator Conference, Lucerne, 05.07.2004-10.07.2004, 1747-1749p.

P-F021nr Tkachenko, L.; Bogdanov, I.; Kozub, S.; Shcherbakov, P.; Slabodchikov, P.; Zubko, V.; Moritz, G.*; Sytnikov, V.: **Methods for Reducing Cable Losses in Fast-Cycling Dipoles for the SIS300 Ring**. In: CERN (Ed.): *EPAC 2004: A Europhysics Conference 5 to 9 July 2004, Lucerne Congress Centre Switzerland, www.epac04.ch*, Geneva: CERN, 2004. 9th European Particle Accelerator Conference, Lucerne, 05.07.2004-10.07.2004, 1750-1752p.

P-F022nr Weick, H.: **The new Radioactive Ion Beam Facility at GSI**. In: Arnould, M.; Lewitowicz, M.; Münzeberg, G.*; Akimune, H.; Ohta, M.; Utsunaomiya, H.; Wada, T.; Yamagata, T. (Eds.): *Tours Symposium on Nuclear Physics, Tours 2003*. AIP Conference Proceedings Vol. 704, Melville/New York: AIP, 2004, 288-233p.

P-F023nr Widmann, E.*: **FLAIR: A Facility for Low-energy Antiproton and Ion Research**. In: Iori, I. (Ed.): *Proceedings of the XLII International Winter Meeting on Nuclear Physics*. Ricerca Scientifica ed Educazione Permanente; Suppl. 123, Milano: Dipartimento di Fisica, Università degli Studi di Milano, 2004. XLII International Winter Meeting on Nuclear Physics, Bormio, 26.01.2004-31.01.2004, 81-88p. DOI:10.1007/b98790

P-F024nr Zubko, V.; Bogdanov, I.; Kozub, S.; Shcherbakov, P.; Tkachenko, L.; Zintchenko, S.; Kauschke, M.*; Moritz, G.*: **Stability of Fast-cycling Dipole for SIS300 Ring**. In: CERN (Ed.): *EPAC 2004: A Europhysics Conference 5 to 9 July 2004, Lucerne Congress Centre Switzerland, www.epac04.ch*, Geneva: CERN, 2004. 9th European Particle Accelerator Conference, Lucerne, 05.07.2004-10.07.2004, 1756-1758p.

3. Preprints at arXive

X-F001 Agnello, M.; Ferro, F.; Iazzi, F.: **Production of double hypernuclei with high energy antiprotons at PANDA.** *ArXiv: hep-ex/0405061.*

Publications of the programme 'Physics of hadrons and nuclei'

Compiled by K. Große

This programme is part of the research field 'Structure of Matter' of the Helmholtz-Gemeinschaft
See <http://www.helmholtz.de/en/Research_Fields/Struktur_der_Materie.html>.

1. Reviewed publications

P-H001 Ackermann, D.*: **Reaction dynamics at the barrier for heavy compound systems.** *Heavy ion physics* **19**(1): 1–6.

P-H002 Ackermann, D.*; Antalic, S.; Axiotis, M.; Bazzacco, D.; Beghini, S.; Berek, G.; Corradi, L.; De Angelis, G.; Farnea, E.; Gadea, A.; Heßberger, F. P.*; Hofmann, S.*; Itkis, M. G.; Kniajeva, G. N.; Kozulin, E. M.; Latina, A.; Martinez, T.; Menegazzo, R.; Montagnoli, G.; Münzenberg, G.*; Oganessian, Y. T.; Alvarez, C. R.; Ruan, M.*; Sagaidak, R. N.*; Scarlassara, F.; Stefanini, A. M.; Szilner, S.; Trotta, M.; Ur, C.: **Reaction mechanism studies using the CN/ER spin distribution.** *The European physical journal A, Hadrons and nuclei* **20**(1): 151–152. DOI:10.1140/epja/i2002-10341-0

P-H003 Agakichiev, G.*; Appelshäuser, H.; Baur, R.; Bielcikova, J.; Braun-Munzinger, P.*; Cherlin, A.; Drees, A.; Esumi, S. I.; Filimonov, K.; Fraenkel, Z.; Fuchs, C.; Glässel, P.; Hering, G.*; Huovinen, P.; Lenkeit, B.; Marín, A.*; Messer, F.; Messer, M.; Milosevic, J.; Miśkowiec, D.*; Nix, O.; Panebrattsev, Y.; Petráček, V.; Pfeiffer, A.; Rak, J.; Ravinovich, I.; Razin, S.; Rehak, P.; Sako, H.*; Saveljic, N.; Schmitz, W.; Shimansky, S.; Socol, E.; Specht, H. J.; Stachel, J.*; Tilsner, H.; Tserruya, I.; Voigt, C.; Voloshin, S.; Weber, C.; Wessels, J. P.; Wurm, J. P.; Yurevich, V.; CERES Collaboration*: **Semihard scattering unraveled from collective dynamics by two-pion azimuthal correlations in 158A GeV/c Pb+Au collisions.** *Physical review letters* **92**(3): 032301. DOI:10.1103/PhysRevLett.92.032301

P-H004 Aggarwal, M. M.; Ahammed, Z.; Angelis, A. L. S.; Antonenko, V.; Arefiev, V.; Astakhov, V.; Avdeitchikov, V.; Awes, T. C.; Baba, P. V. K. S.; Badyal, S. K.; Bathe, S.; Batiounia, B.; Bernier, T.; Bhalla, K. B.; Bhatia, V. S.; Blume, C.*; Bucher, D.; Busching, H.; Carlén, L.; Chattopadhyay, S.; Decowski, M. P.; Delagrange, H.; Donni, P.; Dutta Majumdar, M. R.; El Chenawi, K.; Dubey, A. K.; Enosawa, K.; Fokin, S.; Frolov, V.; Ganti, M. S.; Garpman, S.; Gavrishchuk, O.; Geurts, F. J. M.; Ghosh, T. K.; Glasow, R.; Guskov, B.; Gustafsson, H. A.; Gutbrod, H. H.*; Hrivnacova, I.; Ippolitov, M.; Kalechofsky, H.; Karadjev, K.; Karpio, K.; Kolb, B. W.*; Kosarev, I.; Koutcheryaev, I.; Kugler, A.; Kulinich, P.; Kurata, M.; Lebedev, A.; Löhner, H.; Luquin, L.; Mahapatra, D. P.; Manko, V.; Martin, M.; Martínez, G.; Maximov, A.; Miake, Y.; Mishra, G. C.; Mohanty, B.; Mora, M.-J.; Morrison, D.; Moukhanova, T.; Mukhopadhyay, D. S.; Naef, H.; Nandi, B. K.; Nayak, S. K.; Nayak, T. K.; Nianine, A.; Nikitine, V.; Nikolaev, S.; Nilsson, P.; Nishimura, S.; Nomokonov, P.; Nystrand, J.; Oskarsson, A.; Otterlund, I.; Peitzmann, T.; Peressounko, D.; Petracek, V.; Phatak, S. C.; Pinganaud, W.; Plasil, F.; Purschke, M. L.; Rak, J.; Raniwala, R.; Raniwala, S.; Rao, N. K.; Retiere, F.; Reygers, K.; Roland, G.; Rosselet, L.; Roufanov, I.; Roy, C.; Rubio, J. M.; Sambyal, S. S.; Santo, R.; Sato, S.; Schlagheck, H.; Schmidt, H. R.*; Schutz, Y.; Shabratova, G.; Shah, T. H.; Sibiriak, I.; Siemiarczuk, T.; Silvermyr, D.; Sinha, B. C.; Slavine, N.; Söderström, K.; Sood, G.; Sørensen, S. P.; Stankus, P.; Stefanek, G.; Steinberg, P.; Stenlund, E.; Sumbera, M.; Svensson, T.; Tsvetkov, A.; Tykarski, L.; von der Pijll, E. C.; von Eijndhoven, N.; von Nieuwenhuizen, G. J.; Vinogradov, A.; Viyogi, Y. P.; Vodopianov, A.; Vörös, S.; Wyslouch, B.; Young, G. R.; WA98 Collaboration*: **Interferometry of direct photons in central ^{208}Pb+^{208}Pb collisions at 158A GeV.** *Physical review letters* **93**(2): 022301. DOI:10.1103/PhysRevLett.93.022301

P-H005 Al-Garni, S. D.*; Regan, P. H.; Walker, P. M.; Roeckl, E.*; Kirchner, R.*; Xu, F. R.; Batist, L.*; Blazhev, A.*; Borcea, R.*; Cullen, D. M.; Döring, J.*; El-Masri, H. M.; Narro, J. G.; Grawe, H.*; La Commara, M.; Mazzoechi, C.*; Mukha, I.*; Pearson, C. J.; Plettner, C.*; Schmidt, K.*; Schmidt-Ott, W. D.; Shimbara, Y.; Wheldon, C.*; Wood, R.; Wooding, S. C.*: **Evidence for a high-spin β-decaying isomer in ^{177}Lu.** *Physical review C, Nuclear physics* **69**(2): 024320. DOI:10.1103/PhysRevC.69.024320

P-H006 Algora, A.; Batist, L.; Borge, M. J. G.; Cano-Ott, D.; Collatz, R.*; Courtin, S.; Dessagne, P.; Fraile, L. M.; Gadea, A.; Gelletly, W.; Hellström, M.*; Janas, Z.; Jungclaus, A.; Kirchner, R.*; Karny, M.; Le Scornet, G.; Miehé, C.; Maréchal, F.; Moroz, F.; Nachér, E.; Poirier, E.; Roeckl, E.*; Rubio, B.; Rykaczewski, K.; Tain, J. L.; Tengblad, O.; Wittmann, V.; GSI-TAS Collaboration*: **Beta-decay studies using total absorption spectroscopy.** *The European physical journal A, Hadrons and nuclei* **20**(1): 199–202. DOI:10.1140/epja/i2002-10353-8

P-H007 Algora, A.; Nácher, E.; Rubio, B.; Cano-Ott, D.; Tain, J. L.; Gadea, A.; Agramunt, J.; Karny, M.; Janas, Z.; Rykaczewski, K.; Collatz, R.*; Hellström, M.*; Hu, Z.*; Kirchner, R.*; Roeckl, E.*; Shibata, M.*; Batist, L.; Moroz, F.; Wittmann, V.: **β decay of ^{148}Dy: Study of the Gamow-Teller giant state by means of total absorption spectroscopy.** *Physical review C, Nuclear physics* **70**(6): 064301. DOI:10.1103/PhysRevC.70.064301

P-H008 Alt, C.; Anticic, T.; Baatar, B.; Barna, D.; Bartke, J.; Behler, M.; Betev, L.; Bialkowska, H.; Billmeier, A.; Blume, C.*; Boimska, B.; Botje, M.; Bracinik, J.; Bramm, R.; Brun, R.; Bunčić, P.; Cerny, V.; Christakoglou, P.; Chvala, O.; Cramer, J. G.; Csato, P.; Darmenov, N.; Dimitrov, A.; Dinkelaker, P.;

Eckardt, V.; Filip, P.; Flierl, D.; Fodor, Z.; Foka, P.*; Freund, P.; Friese, V.*; Gál, J.; Gaździcki, M.; Georgopoulos, G.; Gładysz, E.; Grebieszkow, K.; Hegyi, S.; Höhne, C.; Kadija, K.; Karev, A.; Kliemant, M.; Kniege, S.; Kolesnikov, V. I.; Kollegger, T.; Kornas, E.; Korus, R.; Kowalski, M.; Kraus, I.*; Kreps, M.; van Leeuwen, M.; Lévai, P.; Litov, L.; Lungwitz, B.; Makariev, M.; Malakhov, A. I.; Markert, C.*; Mateev, M.; Mayes, B. W.; Melkumov, G. L.; Meurer, C.; Mischke, A.*; Mitrovski, M.; Molnar, J.; xMrówczyński, S.; Palla, G.; Panagiotou, A. D.; Panayotov, D.; Petridis, A.; Pikna, M.; Pinsky, L.; Pühlhofer, F.; Reid, J. G.; Renfordt, R.; Richard, A.; Roland, C.; Roland, G.; Rybczynski, M.; Rybicki, A.; Sandoval, A.*; Sann, H.*; Schmitz, N.; Seyboth, P.; Siklér, F.; Sitar, B.; Skrzypczak, E.; Stefanek, G.; Stock, R.; Ströbele, H.; Susa, T.; Szentpetery, I.; Sziklai, J.; Trainor, T. A.; Varga, D.; Vassiliou, M.; Veres, G. I.; Vesztergombi, G.; Vranic, D.*; Wetzler, A.; Włodarczyk, Z.; Yoo, I. K.; Zaranek, J.; Zimanyi, J.; NA49 Collaboration*: **Electric charge fluctuations in central Pb+Pb collisions at 20A, 30A, 40A, 80A, and 158A GeV.** *Physical review C, Nuclear physics* **70**(6): 064903. DOI:10.1103/PhysRevC.70.064903

P-H009 Alt, C.; Anticic, T.; Baatar, B.; Barna, D.; Bartke, J.; Betev, L.; Białkowska, H.; Billmeier, A.; Blume, C.*; Boimska, B.; Botje, M.; Bracinik, J.; Bramm, R.; Brun, R.; Bunčić, P.; Cerny, V.; Christakoglou, P.; Chvala, O.; Cramer, J. G.; Csató, P.; Darmenov, N.; Dimitrov, A.; Dinkelaker, P.; Eckardt, V.; Farantatos, G.; Filip, P.; Flierl, D.; Fodor, Z.; Foka, P.*; Freund, P.; Friese, V.*; Gál, J.; Gaździcki, M.; Georgopoulos, G.; Gładysz, E.; Hegyi, S.; Höhne, C.; Kadija, K.; Karev, A.; Kniege, S.; Kolesnikov, V. I.; Kollegger, T.; Korus, R.; Kowalski, M.; Kraus, I.*; Kreps, M.; van Leeuwen, M.; Lévai, P.; Litov, L.; Makariev, M.; Malakhov, A. I.; Markert, C.*; Mateev, M.; Mayes, B. W.; Melkumov, G. L.; Meurer, C.; Mischke, A.; Mitrovski, M.; Molnar, J.; Mr?ówczyński, S.; Pálla, G.; Panagiotou, A. D.; Panayotov, D.; Perl, K.; Petridis, A.; Pikna, M.; Pinsky, L.; Pühlhofer, F.; Reid, J. G.; Renfordt, R.; Retyk, W.; Roland, C.; Roland, G.; Rybczyński, M.; Rybicki, A.; Sandoval, A.*; Sann, H.*; Schmitz, N.; Seyboth, P.; Siklér, F.; Sitar, B.; Skrzypczak, E.; Stefanek, G.; Stock, R.; Ströbele, H.; Susa, T.; Szentpetery, I.; Sziklai, J.; Trainor, T. A.; Varga, D.; Vassiliou, M.; Veres, G. I.; Vesztergombi, G.; Vranić, D.*; Wetzler, A.; Włodarczyk, Z.; Yoo, I. K.*; Zaranek, J.; Zimányi, J.; NA49 Collaboration*: **Evidence for an exotic S =-2, Q =-2 baryon resonance in proton-proton collisions at the CERN SPS.** *Physical review letters* **92**(4): 042003. DOI:10.1103/PhysRevLett.92.042003 Also part of: Scientific Infrastructure.

P-H010 Alvarez-Pol, H. ; Alves, R.; Blanco, A.; Carolino, N.; Eschke, J.*; Ferreira-Marques, R.; Fonte, P.; Garzón, J. A.; Díaz, D. G.; Pereira, A.; Pietraszko, J.*; Pinhão, J.; Policarpo, A.; Stroth, J.*; HADES Collaboration*: **Performance of shielded timing RPCs in a ^{12}C fragmentation experiment.** *Nuclear instruments & methods in physics research, Section A, Accelerators, spectrometers, detectors and associated equipment* **533**(1): 79–85. [Proceedings of the Seventh International Workshop on Resistive Plate Chambers and Related Detectors, Clermont-Ferrand, France, 20031020/22] DOI:10.1016/j.nima.2004.07.005

P-H011 Alvarez-Pol, H.; Alves, R.; Blanco, A.; Carolino, N.; Eschke, J.*; Ferreira-Marques, R.; Fonte, P.; Garzón, J. A.; Díaz, D. G.; Pereira, A.; Pietraszko, J.*; Pinhão, J.; Policarpo, A.; Stroth, J.*: **A large area timing RPC prototype for ion collisions in the HADES spectrometer.** *Nuclear instruments & methods in physics research, Section A, Accelerators, spectrometers, detectors and associated equipment* **535**(1): 277–282. [Proceedings of the 10th International Vienna Conference on Instrumentation, Vienna, Austria, 20040216/21] DOI:10.1016/j.nima.2004.07.276

P-H012 Andreyev, A. N.; Ackermann, D.*; Heßberger, F. P.*; Heyde, K.; Hofmann, S.*; Huyse, M.; Karlgren, D.; Kojouharov, I.*; Kindler, B.*; Lommel, B.*; Münzenberg, G.*; Page, R. D.; de Vel, K. V.; Van Duppen, P.; Walters, W. B.; Wyss, R.: **Shape-changing particle decays of ^{185}Bi and structure of the lightest odd-mass Bi isotopes.** *Physical review C, Nuclear physics* **69**(5): 054308. DOI:10.1103/PhysRevC.69.054308

P-H013 Andreyev, A. N.; Ackermann, D.*; Heßberger, F. P.*; Hofmann, S.*; Huyse, M.; Münzenberg, G.*; Page, R. D.; Van de Vel, K.; Van Duppen, P.: **Conversion electron and beta decay spectroscopy at SHIP.** *Nuclear instruments & methods in physics research, Section A, Accelerators, spectrometers, detectors and associated equipment* **533**(3): 409–421. DOI:10.1016/j.nima.2004.07.204

P-H014 Andrianov, V. A.*; Bleile, A.*; Egelhof, P.*; Kraft, S.*; Kiseleva, A.*; Kiseleva, O.*; Meier, H. J.*; Meier, J. P.*: **Noise analysis for calorimetric low-temperature detectors for heavy ions.** *Nuclear instruments & methods in physics research, Section A, Accelerators, spectrometers, detectors and associated equipment* **520**(1): 84–86. [Proceedings of the 10th International Workshop on Low Temperature Detectors, Genoa, Italy, 7 - 11 July 2003] DOI:10.1016/j.nima.2003.11.227

P-H015 Andronic, A.*; ALICE TRD Collaboration: **Electron identification performance with ALICE TRD prototypes.** *Nuclear instruments & methods in physics research, Section A, Accelerators, spectrometers, detectors and associated equipment* **522**(1): 40–44. [TRDs for the Third Millenium. Proceedings of the 2nd Workshop on Advanced Transition Radiation Detectors for Accelerator and Space Applications, Bari, Italy, 4 - 7 September 2003] DOI:10.1016/j.nima.2004.01.015

P-H016 Andronic, A.*; Appelshäuser, H.; Blume, C.*; Braun-Munzinger, P.*; Bucher, D.; Busch, O.*; Cătănescu, V.; Ciobanu, M.*; Daues, H.*; Emschermann, D.; Fateev, O.; Foka, Y.*; Garabatos, C.*; Gunji, T.; Herrmann, N.; Inuzuka, M.; Kislov, E.; Lindenstruth, V.; Ludolphs, W.; Mahmoud, T.; Petracek, V.; Petrovici, M.; Rusanov, I.; Sandoval, A.*; Santo, R.; Schicker, R.; Simon, R. S.*; Smykov, L.; Soltveit, H. K.; Stachel, J.; Stelzer, H.; Tsiledakis, G.*; Vulpescu, B.; Wessels, J. P.; Windelband, B.; Xu, C.; Zaudtke, O.; Zanevsky, Y.; Yurevich, V.; ALICE Collaboration*: **Space charge in drift chambers operated with the Xe, CO_2(15%) mixture.** *Nuclear instruments & methods in physics research, Section A, Accelerators, spectrometers, detectors and associated equipment* **525**(3): 447–457. DOI:10.1016/j.nima.2004.01.076

P-H017 Andronic, A.*; Appelshäuser, H.; Blume, C.*; Braun-Munzinger, P.*; Bucher, D.; Busch, O.*; Cătănescu, V.; Ciobanu, M.*; Daues, H.*; Emschermann, D.; Fateev, O.; Foka, Y.*; Garabatos, C.*; Gunji, T.; Herrmann, N.; Inuzuka, M.; Kislov, E.; Lindenstruth, V.; Ludolphs, W.; Mahmoud, T.;

Petracek, V.; Petrovici, M.; Rusanov, I.; Sandoval, A.*; Santo, R.; Schicker, R.; Simon, R. S.*; Smykov, L.; Soltveit, H. K.; Stachel, J.; Stelzer, H.*; Tsiledakis, G.*; Vulpescu, B.; Wessels, J. P.; Windelband, B.; Xu, C.; Zaudtke, O.; Zanevsky, Y.; Yurevich, V.: **Energy loss of pions and electrons of 1-6 GeV/c in drift chambers operated with Xe,CO_2(15%).** *Nuclear instruments & methods in physics research, Section A, Accelerators, spectrometers, detectors and associated equipment* **519**(3): 508–517. DOI:10.1016/j.nima.2003.11.036

P-H018 Andronic, A.*; Biagi, S.; Braun-Munzinger, P.*; Garabatos, C.*; Tsiledakis, G.*: **Drift velocity and gain in argon- and xenon-based mixtures.** *Nuclear instruments & methods in physics research, Section A, Accelerators, spectrometers, detectors and associated equipment* **523**(3): 302–308. DOI:10.1016/j.nima.2003.11.426

P-H019 Antalic, S.; Cagarda, P.; Ackermann, D.*; Burkhard, H. G.*; Heßberger, F. P.*; Hofmann, S.*; Kindler, B.*; Kojouharova, J.; Lommel, B.*; Mann, R.*; Saro, S.; Schött, H. J.*: **Target cooling for high-current experiments at SHIP.** *Nuclear instruments & methods in physics research, Section A, Accelerators, spectrometers, detectors and associated equipment* **530**(3): 185–193. DOI:10.1016/j.nima.2004.04.217 Also part of: 'Large-scale facilities for research with photons, neutrons and ions'; Scientific Infrastructure.

P-H020 Anticic, T.; Baatar, B.; Barna, D.; Bartke, J.; Behler, M.; Betev, L.; Bialkowska, H.; Billmeier, A.; Blume, C.*; Boimska, B.; Botje, M.; Bracinik, J.; Bramm, R.; Brun, R.; Buňcić, P.; Cerny, V.; Christakoglou, P.; Chvala, O.; Cramer, J. G.; Csató, P.; Darmenov, N.; Dimitrov, A.; Dinkelaker, P.; Eckardt, V.; Filip, P.; Flierl, D.; Fodor, Z.; Foka, P.*; Freund, P.; Friese, V.*; Gál, J.; Gazdźicki, M.; Georgopoulos, G.; Gładysz, E.; Grebieszkow, K.; Hegyi, S.; Höhne, C.; Kadija, K.; Karev, A.; Kolesnikov, V. I.; Kollegger, T.; Korus, R.; Kowalski, M.; Kraus, I.*; Kreps, M.; van Leeuwen, M.; Levai, P.; Litov, L.; Makariev, M.; Malakhov, A. I.; Markert, C.*; Mateev, M.; Mayes, B. W.; Melkumov, G. L.; Meurer, C.; Mischke, A.*; Mitrovski, M.; Molnar, J.; Mrówczyński, S.; Pálla, G.; Panagiotou, A. D.; Panayotov, D.; Petridis, A.; Pikna, M.; Pinsky, L.; Pühlhofer, F.; Reid, J. G.; Renfordt, R.; Retyk, W.; Roland, C.; Roland, G.; Rybczyński, M.; Rybicki, A.; Sandoval, A.*; Sann, H.; Schmitz, N.; Seyboth, P.; Sikler, F.; Sitar, B.; Skrzypczak, E.; Stefanek, G.; Stock, R.; Strobele, H.*; Susa, T.; Szentpetery, I.; Sziklai, J.; Trainor, T. A.; Varga, D.; Vassiliou, M.; Veres, G. I.; Vesztergombi, G.; Vranić, D.*; Wetzler, A.; Włodarczyk, Z.; Yoo, I. K.; Zaranek, J.; Zimányi, J.: **Transverse momentum fluctuations in nuclear collisions at 158A GeV.** *Physical review C, Nuclear physics* **70**(3): 034902. DOI:10.1103/PhysRevC.70.034902

P-H021 Anticic, T.; Baatar, B.; Barna, D.; Bartke, J.; Behler, M.; Betev, L.; Białkowska, H.; Billimeier, A.; Blume, C.*; Boimska, B.; Botje, M.; Bracinik, J.; Bramm, R.; Brun, R.; Buncić, P.; Cerny, V.; Christakoglou, P.; Chvala, O.; Cooper, G. E.; Cramer, J. G.; Csato, P.; Dinkelaker, P.; Eckardt, V.; Filip, P.; Fischer, H. G.; Fodor, Z.; Foka, P.*; Freund, P.; Friese, V.*; Gál, J.; Gazdzicki, M.; Georgopoulos, G.; Gładysz, E.; Hegyi, S.; Höhne, C.; Jacobs, P.; Kadija, K.; Karev, A.; Kolesnikov, V. I.; Kollegger, T.; Korus, R.; Kowalski, M.; Kraus, I.*; Kreps, M.; van Leeuwen, M.; Levai, P.; Malakhov, A. I.; Markert, C.*; Mayes, B. W.; Melkumov, G. L.; Meurer, C.; Mischke, A.*; Mitrovski, M.; Molnár, J.; Mrówczyński, S.; Pálla, G.; Panagiotou, A. D.; Perl, K.; Petridis, A.; Pikna, M.; Pinsky, L.; Pühlhofer, F.; Reid, J. G.; Renfordt, R.; Retyk, W.; Roland, C.; Roland, G.; Rybczyński, M.; Rybicki, A.; Sandoval, A.*; Sann, H.*; Schmitz, N.; Seyboth, P.; Siklér, F.; Sitar, B.; Skrzypczak, E.; Stefanek, G.; Stock, R.; Ströbele, H.; Susa, T.; Szentpétery, I.; Sziklai, J.; Trainor, T. A.; Varga, D.; Vassiliou, M.; Veres, G. I.; Vesztergombi, G.; Vranić, D.*; Wenig, S.; Wetzler, A.; Włodarczyk, Z.; Xu, N.; Yoo, I. K.; Zaranek, J.; Zimányi, J.; NA49 Collaboration: **Energy and centrality dependence of deuteron and proton production in Pb+Pb collisions at relativistic energies.** *Physical review C, Nuclear physics* **69**(2): 024902. DOI:10.1103/PhysRevC.69.024902

P-H022 Anticic, T.; Baatar, B.; Barna, D.; Bartke, J.; Behler, M.; Betev, L.; Białkowska, H.; Billmeier, A.; Blume, C.*; Boimska, B.; Botje, M.; Bracinik, J.; Bramm, R.; Brun, R.; Buncić, P.; Cerny, V.; Christakoglou, P.; Chvala, O.; Cramer, J. G.; Csato, P.; Darmenov, N.; Dimitrov, A.; Dinkelaker, P.; Eckardt, V.; Filip, P.; Flierl, D.; Fodor, Z.; Foka, P.*; Freund, P.; Friese, V.*; Gál, J.; Gaździcki, M.; Georgopoulos, G.; Gładysz, E.; Hegyi, S.; Höhne, C.; Kadija, K.; Karev, A.; Kolesnikov, V. I.; Kollegger, T.; Kornas, E.; Korus, R.; Kowalski, M.; Kraus, I.*; Kreps, M.; van Leeuwen, M.; Levai, P.; Litov, L.; Makariev, M.; Malakhov, A. I.; Markert, C.*; Mateev, M.; Mayes, B. W.; Melkumov, G. L.; Meurer, C.; Mischke, A.*; Mitrovski, M.; Molnar, J.; Mrówczyński, S.; Pálla, G.; Panagiotou, A. D.; Panayotov, D.; Perl, K.; Petridis, A.; Pikna, M.; Pinsky, L.; Pühlhofer, F.; Reid, J. G.; Renfordt, R.; Retyk, W.; Roland, C.; Roland, G.; Rybczynski, M.; Rybicki, A.; Sandoval, A.*; Sann, H.*; Schmitz, N.; Seyboth, P.; Siklér, F.; Sitar, B.; Skrzypczak, E.; Stefanek, G.; Stock, R.; Ströbele, H.; Susa, T.; Szentpetery, I.; Sziklai, J.; Trainor, T. A.; Varga, D.; Vassiliou, M.; Veres, G. I.; Vesztergombi, G.; Vranić, D.*; Wetzler, A.; Włodarczyk, Z.; Yoo, I. K.; Zaranek, J.; Zimanyi, J.; NA49 Collaboration*: **Λ and $\bar{\Lambda}$ production in central Pb-Pb collisions at 40, 80, and 158A GeV.** *Physical review letters* **93**(2): 022302. DOI:10.1103/PhysRevLett.93.022302

P-H023 Appelshäuser, H.*: **Correlations and fluctuations.** *Journal of physics G, Nuclear and particle physics* **30**(8): S935–S942. DOI:10.1088/0954-3899/30/8/036

P-H024 Appelshäuser, H.*: **HBT interferometry at SPS and universal pion freeze-out.** *Acta physica Polonica B, Particle physics and field theory, nuclear physics, theory of relativity* **35**(1): 9–15.

P-H025 Appelshäuser, H.*; CERES Collaboration*: **Event-by-event fluctuations of the mean transverse momentum M_{PT} at SPS energies.** *Progress in particle and nuclear physics* **53**(1): 253–255. DOI:10.1016/j.ppnp.2004.02.022

P-H026 Armbruster, P.*; Benlliure, J.*; Bernas, M.; Boudard, A.; Casarejos, E.; Czajkowski, S.; Enqvist, T.*; Leray, S.; Napolitani, P.*; Pereira, J.; Rejmund, F.*; Ricciardi, M.-V.*; Schmidt, K. H.*; Stéphan, C.; Taieb, J.*; Tassan-Got, L.; Volant, C.: **Measurement of a complete set of nuclides, cross sections, and kinetic energies in spallation of ^{238}U 1A GeV with protons.** *Physical review letters* **93**(21): 212701. DOI:10.1103/PhysRevLett.93.212701

P-H027 Bałanda, A.; Jaskuła, M.; Kajetanowicz, M.; Kidoń, L.; Korcyl, K.; Kuhn, W.; Kulessa, R.; Malarz, A.; Otwinowski, J.; Petri, M.; Pietraszko, J.*; Prokopowicz, W.*; Przygoda, W.; Salabura, P.*; Skoczeń, A.; Szczybura, M.; Wajda, E.; Waluś, W.; Wisniowski, M.; Wójcik, T.; HADES Collaboration*: **The HADES pre-shower detector.** *Nuclear instruments & methods in physics research, Section A, Accelerators, spectrometers, detectors and associated equipment* **531**(3): 445–458. DOI:10.1016/j.nima.2004.05.082

P-H028 Bastid, N.; Dupieux, P.; Bendarag, A.; Barret, V.; Crochet, P.; Lopez, X.; Alard, J. P.; Andronic, A.*; Basrak, Z.; Benabderrahmane, M. L.; Čaplar, R.*; Cordier, E.; Dželalija, M.; Fodor, Z.; Gasparic, I.; Gobbi, A.*; Grishkin, Y.; Hartmann, O. N.*; Herrmann, N.*; Hildenbrand, K. D.*; Hong, B.; Kecskemeti, J.*; Kim, Y. J.*; Kirejczyk, M.; Koczon, P.*; Korolija, M.; Kotte, R.; Kress, T.*; Lebedev, A.; Leifels, Y.*; Mangiarotti, A.; Manko, V.; Merschmeyer, M.; Moisa, D.; Neubert, W.; Pelte, D.; Petrovici, M.; Rami, F.; Reisdorf, W.*; de Schauenburg, B.; Schuettauf, A.*; Seres, Z.; Sikora, B.; Sim, K. S.; Simion, V.*; Siwek-Wilczyńska, K.; Smolarkiewicz, M. M.; Smolyankin, V.; Soliwoda, I. J.; Stockmeier, M. R.; Stoicea, G.; Tyminski, Z.*; Wagner, P.; Wiśniewski, K.; Wohlfarth, D.; Xiao, Z.*; Yushmanov, I.; Zhilin, A.; FOPI Collaboration*: **Shape parameters of the participant source in Ru+Ru collisions at 400 A MeV.** *Nuclear physics A, Nuclear and hadronic physics* **742**(1): 29–54. DOI:10.1016/j.nuclphysa.2004.06.021

P-H029 Baur, G.; Typel, S.*: **Theory of the Trojan-Horse method.** *Progress of theoretical physics Supplement* (154): 333–340. Also part of: 'Large-scale facilities for research with photons, neutrons and ions'.

P-H030 Benlliure, J.; Audouin, L.; Bernas, M.; Casarejos, E.; Enqvist, T.*; Fernández, B.; Henzl, V.; Kelic, A.; Napolitani, P.*; Pereira, J.; Ricciardi, M. V.*; Schmidt, K. H.*; Taieb, J.: **Momentum distributions of projectile spectators: a new tool to investigate the equation of state of nuclear matter.** *Nuclear physics A, Nuclear and hadronic physics* **734**: 609–612. [Proceedings of the Eighth International Conference On Nucleus-Nucleus Collisions] DOI:10.1016/S0375-9474(04)90353-3

P-H031 Benlliure, J.; Schmidt, K. H.*: **Basic nuclear data for nuclear waste transmutation and radioactive nuclear beam production.** *Nuclear physics A, Nuclear and hadronic physics* **746**: 281C–287C. [Proceedings of the Sixth International Conference on Radioactive Nuclear Beams (RNB6) Argonne 20030922/26] DOI:10.1016/j.nuclphysa.2004.09.129

P-H032 Berdermann, E.* ; Ciobanu, M.*; Connell, S. H.; da Costa, A. M. O. D.; Fernandez-Hernando, L.; Oh, A.; Sellschop, J. P. F.: **Charged particle detectors made of single-crystal diamond.** *Physica status solidi A, Applied research* **201**(11): 2521–2528. DOI:10.1002/pssa.200405170 Also part of: Scientific Infrastructure.

P-H033 Blanco, A.; Carolino, N.; Correia, C. M. B. A.; Ferreira-Marques, R.; Fonte, P.; Gobbi, A.*; González-Díaz, D.; Lopes, M. I.; Lopes, L.; Macedo, M. P.; Mangiarotti, A.; Peskov, V.; Policarpo, A.: **Progress in timing Resistive Plate Chambers.** *Nuclear instruments & methods in physics research, Section A, Accelerators, spectrometers, detectors and associated equipment* **535**(1): 272–276. [Proceedings of the 10th International Vienna Conference on Instrumentation, Vienna, Austria, 20040216/21] DOI:10.1016/j.nima.2004.07.131

P-H034 Blank, B.; Savard, G.; Döring, J.*; Blazhev, A.*; Canchel, G.; Chartier, M.; Henderson, D.; Janas, Z.; Kirchner, R.*; Mukha, I.; Roeckl, E.*; Schmidt, K.; Zylicz, J.: **High-precision measurement of the half-life of ^{62}Ga.** *Physical review C, Nuclear physics* **69**(1): 015502. DOI:10.1103/PhysRevC.69.015502

P-H035 Blaschke, D.; Grigorian, H.; Voskresensky, D. N.*: **Cooling of neutron stars. Hadronic model.** *Astronomy & astrophysics* **424**(3): 979–992. DOI:10.1051/0004-6361:20040404

P-H036 Blazhev, A.*; Górska, M.*; Grawe, H.*; Nyberg, J.; Palacz, M.; Caurier, E.; Dorvaux, O.; Gadea, A.; Nowacki, F.; Andreoiu, C.; de Angelis, G.; Balabanski, D.; Beck, C.; Cederwall, B.; Curien, D.; Döring, J.*; Ekman, J.; Fahlander, C.; Lagergren, K.; Ljungvall, J.; Moszyński, M.; Norlin, L. O.; Plettner, C.*; Rudolph, D.; Sohler, D.; Spohr, K. M.; Thelen, O.; Weiszflog, M.; Wisell, M.; Wolińska, M.; Wolski, W.: **Observation of a core-excited E4 isomer in ^{98}Cd.** *Physical review C, Nuclear physics* **69**(6): 064304. DOI:10.1103/PhysRevC.69.064304

P-H037 Braun-Munzinger, P.*; Stachel, J.; Wetterich, C.: **Chemical freeze-out and the QCD phase transition temperature.** *Physics letters B* **596**(1): 61–69. DOI:10.1016/j.physletb.2004.05.081

P-H038 Busch, O.*; ALICE TRD Collaboration*: **Results from prototype tests for the ALICE TRD.** *Nuclear instruments & methods in physics research, Section A, Accelerators, spectrometers, detectors and associated equipment* **525**(1): 153–157. [Proceedings of the International Conference on Imaging Techniques in Subatomic Physics, Astrophysics, Medicine, Biology and Industry, Stockholm, Sweden, 24 - 27 June 2003] DOI:10.1016/j.nima.2004.03.039

P-H039 Busch, O.*; ALICE TRD Collaboration: **Transition radiation spectroscopy with prototypes of the ALICE TRD.** *Nuclear instruments & methods in physics research, Section A, Accelerators, spectrometers, detectors and associated equipment* **522**(1): 45–49. [TRDs for the Third Millenium. Proceedings of the 2nd Workshop on Advanced Transition Radiation Detectors for Accelerator and Space Applications, Bari, Italy, 4 - 7 September 2003] DOI:10.1016/j.nima.2004.01.016

P-H040 Caamaño, M.; Cortina-Gil, D.*; Sümmerer, K.*; Benlliure, J.; Casarejos, E.; Geissel, H.*; Münzenberg, G.*; Pereira, J.: **Production cross-sections and momentum distributions of fragments from neutron-deficient ^{36}Ar at 1.05 A GeV.** *Nuclear physics A, Nuclear and hadronic physics* **733**(3): 187–199. DOI:10.1016/j.nuclphysa.2004.01.070

P-H041 Carminati, F.; Foka, P.*; Giubellino, P.; Morsch, A.; Paic, G.; Revol, J.-P.; Safark, K.; Schutz, Y.; Wiedemann, U. A.; ALICE Collaboration*: **ALICE: Physics performance report, volume I.** *Journal of physics G, Nuclear and particle physics* **30**(11): 1517–1763. DOI:10.1088/0954-

3899/30/11/001

P-H042 Chulkov, L. V.*; S135 Collaboration*: **Heavy hydrogen isotopes ^{4}H and ^{5}H.** *Nuclear physics A, Nuclear and hadronic physics* **734**: 357–360. [Proceedings of the Eighth International Conference On Nucleus-Nucleus Collisions] DOI:10.1016/S0375-9474(04)90306-5

P-H043 Cortina, D.; Fernandez-Vazquez, J.; Aumann, T.*; Baumann, T.; Berlliure, J.; Borge, M. J. G.; Chulkov, L.*; Datta Pramanik, U. ; Forssén, C.; Fraile, L. M.; Geissel, H.*; Gerl, J.*; Hammache, F.*; Itahashi, K.; Janik, R.; Jonson, B.; Mandal, S.*; Markenroth, K.; Meister, M.; Mocko, M.; Münzenberg,G.; Ohtsubo, T.; Ozawa, A.; Prezado, Y.; Pribora, V.; Riisager, K.; Scheit, H.; Schneider, R.; Schrieder, G.; Simon, H.*; Sitar, B.; Stolz, A.; Strmen, P.; Sümmerer, K.*; Szarka, I.; Weick, H.*; GSI-E212 Collaboration*: **Nuclear structure of light exotic nuclei from break-up reactions.** *Nuclear physics A, Nuclear and hadronic physics* **746**: 479C–482C. [Proceedings of the Sixth International Conference on Radioactive Nuclear Beams (RNB6) Argonne 20030922/26] DOI:10.1016/j.nuclphysa.2004.09.153

P-H044 Cortina-Gil, D.; Fernandez-Vazquez, J.; Aumann, T.*; Baumann, T.; Benlliure, J.; Borge, M. J. G.; Chulkov, L. V.*; Datta Pramanik, U.*; Forssén, C.; Fraile, L. M.; Geissel, H.*; Gerl, J.*; Hammache, F.*; Itahashi, K.; Janik, R.; Jonson, B.; Mandal, S.*; Markenroth, K.; Meister, M.; Mocko, M.; Münzenberg, G.*; Ohtsubo, T.*; Ozawa, A.; Prezado, Y.; Pribora, V.*; Riisager, K.; Scheit, H.; Schneider, R.; Schrieder, G.; Simon, H.; Sitar, B.; Stolz, A.; Strmen, P.; Sümmerer, K.*; Szarka, I.; Weick, H.*: **Shell structure of the near-dripline nucleus ^{23}O.** *Physical review letters* **93**(6): 062501. DOI:10.1103/PhysRevLett.93.062501

P-H045 Davids, B.; Typel, S.*: **Reply to << Comment on 'Electromagnetic dissociation of ^{8}B and the astrophysical S factor for ^{7}Be(p,γ)^{8}B' >>.** *Physical review C, Nuclear physics* **70**(3): 039802. DOI:10.1103/PhysRevC.70.039802

P-H046 Denisov, V. Y.*: **Entrance-channel potentials in synthesis of the heaviest nuclei, muon catalysis of superheavy element formation.** *Heavy ion physics* **19**(1): 121–126.

P-H047 De Witte, H.; Andreyev, A. N.; Borzov, I. N.; Caurier, E.; Cederkäll, J.; De Smet, A.; Eeckhaudt, S.; Fedorov, D. V.; Fedosseev, V. N.; Franchoo, S.; Górska, M.; Grawe, H.*; Huber, G.; Huyse, M.; Janas, Z.; Koster, U.; Kurcewicz, W.; Kurpeta, J.; Płochocki, A.; Van de Vel, K.; Van Duppen, P.; Weissman, L.: **First observation of the β decay of neutron-rich ^{218}Bi by the pulsed-release technique and resonant laser ionization.** *Physical review C, Nuclear physics* **69**(4): 044305. DOI:10.1103/PhysRevC.69.044305

P-H048 Dilling, J.*; Herfurt, F.; Kellerbauer, A.; Audi, G.; Beck, D.*; Bollen, G.; Kluge, H.-J.*; Moore, R. B.; Scheidenberger, C.*; Schwarz, S.; Sikler, G.*; ISOLDE Collaboration*: **Direct mass measurements of neutron-deficient xenon isotopes using the ISOLTRAP mass spectrometer.** *The European physical journal A, Hadrons and nuclei* **22**(2): 163–171. DOI:10.1140/epja/i2004-10015-y Also part of: 'Large-scale facilities for research with photons, neutrons and ions'.

P-H049 Dzhioev, A.; Aouissat, Z.; Storozhenko, A.; Vdovin, A.; Wambach, J.: **Extended Holstein-Primakoff mapping for the next-to-leading order of the 1/N expansion at finite temperature.** *Physical review C, Nuclear physics* **69**(1): 014318. DOI:10.1103/PhysRevC.69.014318

P-H050 Eberhardt, K.; Schädel, M.*; Schimpf, E.*; Thörle, P.; Trautmann, N.: **Preparation of targets by electrodeposition for heavy element studies.** *Nuclear instruments & methods in physics research, Section A, Accelerators, spectrometers, detectors and associated equipment* **521**(1): 208–213. [Accelerator Target Technology for the 21st Century. Proceedings of the 21st World Conference of the International Nuclear Target Society, Argonne, IL, USA, 4 - 8 November 2002] DOI:10.1016/j.nima.2003.11.407

P-H051 Enders, J.; Guhr, T.; Heine, A.; von Neumann-Cosel, P.; Ponomarev, V. Y.; Richter, A.; Wambach, J.: **Spectral statistics and the fine structure of the electric pygmy dipole resonance in N=82 nuclei.** *Nuclear physics A, Nuclear and hadronic physics* **741**: 3–28. DOI:10.1016/j.nuclphysa.2004.05.014

P-H052 Ewald, G.*; Nörtershäuser, W.*; Dax, A.*; Götte, S.*; Kirchner, R.*; Kluge, H.-J.*; Kühl, T.*; Sanchez, R.*; Wojtaszek, A.*; Bushaw, B. A.; Drake, G. W. F.; Yan, Z. C.; Zimmermann, C.: **Nuclear charge radii of ^{8,9}Li determined by laser spectroscopy.** *Physical review letters* **93**(11): 113002. DOI:10.1103/PhysRevLett.93.113002 Also part of: 'Large-scale facilities for research with photons, neutrons and ions'.

P-H053 Förster, A.*; KaoS Collaboration*: **K^{+}- and K^{-} production in heavy-ion collisions at SIS energies.** *Journal of physics G, Nuclear and particle physics* **30**(1): S393–S400. DOI:10.1088/0954-3899/30/1/047

P-H054 Friese, V.; NA49 Collaboration*: **Strangeness from 20 A GeV to 158 A GeV.** *Journal of physics G, Nuclear and particle physics* **30**(1): S119–S128. DOI:10.1088/0954-3899/30/1/011

P-H055 Friman, B.*: **The physics of high baryon densities.** *Journal of physics G, Nuclear and particle physics* **30**(8): S895–S901. DOI:10.1088/0954-3899/30/8/031

P-H056 Gäggeler, H. W.; Brüchle, W.*; Düllmann, C. E.; Dressler, R.; Eberhardt, K.; Eichler, B.; Eichler, R.; Folden, C. M.; Ginter, T. N.; Glaus, F.; Gregorich, K. E.; Haenssler, F.; Hoffman, D. C.; Jäger, E.*; Jost, D. T.; Kirbach, U. W.; Kratz, J. V.; Nitsche, H.; Patin, J. B.; Pershina, V.*; Piguet, D.; Qin, Z.*; Rieth, U.; Schädel, M.*; Schimpf, E.*; Schausten, B.*; Soverna, S.; Sudowe, R.; Thörle, P.; Trautmann, N.; Turler, A.; Vahle, A.; Wilk, P. A.; Wirth, G.; Yakushev, A. B.; von Zweidorf, A.*: **Chemical and nuclear studies of hassium and element 112.** *Nuclear physics A, Nuclear and hadronic physics* **734**: 208–212. [Proceedings of the Eighth International Conference On Nucleus-Nucleus Collisions] DOI:10.1016/S0375-9474(04)90277-1

P-H057 Gaitanos, T.; Di Toro, A.; Typel, S.*; Baran, V.; Fuchs, C.; Greco, V.; Wolter, H. H.: **On the Lorentz structure of the symmetry energy.** *Nuclear physics A, Nuclear and hadronic physics* **732**: 24–48.

DOI:10.1016/j.nuclphysa.2003.12.001

P-H058 Gammino, S.; Ciavola, G.; Celona, L.; Ando, L.; Passarello, S.; Zhang, X. Z.; Spädtke, P.*; Winkler, M.*: **High intensity beams from electron cyclotron resonance ion sources: A study of efficient extraction and transport system (invited).** *Review of scientific instruments* **75**(5): 1637–1642. DOI:10.1063/1.1695647

P-H059 Garabatos, C.*: **The ALICE TPC.** *Nuclear instruments & methods in physics research, Section A, Accelerators, spectrometers, detectors and associated equipment* **535**(1): 197–200. [Proceedings of the 10th International Vienna Conference on Instrumentation, Vienna, Austria, 20040216/21] DOI:10.1016/j.nima.2004.07.127

P-H060 Garcia-Recio, C.; Lutz, M. F. M.*; Nieves, J.: **Quark mass dependence of s-wave baryon resonances.** *Physics letters B* **582**(1): 49–54. DOI:10.1016/j.physletb.2003.11.073

P-H061 Geissel, H.*; Litvinov, Y. A.*; Attallah, F.*; Beckert, K.*; Beller, P.*; Bosch, F.*; Boutin, D.*; Faestermann, T.; Falch, M.; Franzke, B.*; Hausmann, M.; Hellström, M.*; Kaza, E.*; Kerscher, T.; Klepper, O.*; Kluge, H.-J.*; Kozhuharov, C.*; Kratz, K- L.*; Litvinov, S. A.; Löbner, K. E. G.; Maier, L.; Matoš, M.*; Münzenberg, G.*; Nolden, F.*; Novikov, Y. N.; Ohtsubo, T.; Ostrowski, A.; Patyk, Z.; Pfeiffer, B.; Portillo, M*.; Radon, T.*; Scheidenberger, C.*; Shishkin, V.*; Stadlmann, J.*; Steck, M.*; Viera, D. J.; Weick, H.*; Winkler, M.*; Wollnik, H.; Yamaguchi, T.*: **New results with stored exotic nuclei at relativistic energies.** *Nuclear physics A, Nuclear and hadronic physics* **746**: 150C–155C. [Proceedings of the Sixth International Conference on Radioactive Nuclear Beams (RNB6) Argonne 20030922/26] DOI:10.1016/j.nuclphysa.2004.09.030 Also part of: 'Large-scale facilities for research with photons, neutrons and ions'; Scientific Infrastructure.

P-H062 Geissel, H.*; Münzenberg, G.*: **Experiments with exotic atoms and exotic nuclei at GSI, recent developments and future prospects.** *Heavy ion physics* **19**(1): 171–182.

P-H063 Georgiev, G.; Neyens, G.; Hass, M.; Balabanski, D. L.; Bingham, C.; Borcea, C.; Coulier, N.; Coussement, R.; Daugas, J. M.; de France, G.; Górska, M.*; Grawe, H.*; Grzywacz, R.; Lewitowicz, M.; Mach, H.; Matea, I.; de Oliveira Santos, F.; Page, R. D.; Pfützner, M.; Penionzhkevich, Y. E.; Podolyák, Z.; Regan, P. H.; Rykaczewski, K.; Sawicka, M.; Smirnova, N. A.; Sobolev, Y.; Stanoiu, M.; Teughels, S.; Vyvey, K.: **g-factors of isomeric states in the neutron-rich nuclei.** *The European physical journal A, Hadrons and nuclei* **20**(1): 93–94. DOI:10.1140/epja/i2002-10328-9

P-H064 Gerl, J.*; Ameil, F.; Kojouharov, I.*; Surowiec, A.: **High-resolution gamma backscatter imaging for technical applications.** *Nuclear instruments & methods in physics research, Section A, Accelerators, spectrometers, detectors and associated equipment* **525**(1): 328–331. [Proceedings of the International Conference on Imaging Techniques in Subatomic Physics, Astrophysics, Medicine, Biology and Industry, Stockholm, Sweden, 24 - 27 June 2003] DOI:10.1016/j.nima.2004.03.130

P-H065 Gladnishki, K. A.; Podolyak, Z.; Regan, P. H.; Gerl, J.*; Hellström, M.*; Kopatch, Y.*; Mandal, S.*; Górska, M.*; Page, R. D.; Wollersheim, H. J.*; Banu, A.*; Benzoni, G.; Boardman, H.; La Commara, M.; Ekman, J.; Fahlander, C.; Geissel, H.*; Grawe, H.*; Kaza, E.*; Korgul, A.; Matos, M.*; Mineva, M. N.; Pearson, C. J.; Plettner, C.*; Rudolph, D.; Scheidenberger, C.*; Schmidt, K. H.*; Shishkin, V.*; Sohler, D.; Sümmerer, K.*; Valiente-Dobon, J. J.; Walker, P. M.; Weick, H.*; Winkler, M.*; Yordanov, O.*: **Angular momentum population in the projectile fragmentation of ^{238}U at 750 MeV/nucleon.** *Physical review C, Nuclear physics* **69**(2): 024617. DOI:10.1103/PhysRevC.69.024617

P-H066 Golovkov, M. S.; Grigorenko, L. V.*; Fomichev, A. S.; Oganessian, Y. T.; Orlov, Y. I.; Rodin, A. M.; Sidorchuk, S. I.; Slepnev, R. S.; Stepantsov, S. V.; Ter-Akopian, G. M.; Wolski, R.: **Estimates of the ^{7}H width and lower decay energy limit.** *Physics letters B* **588**(3): 163–171. DOI:10.1016/j.physletb.2004.02.069

P-H067 Golovkov, M. S.; Grigorenko, L. V.; Fomichev, A. S.; Krupko, S. A.; Oganessian, Y. T.; Rodin, A. M.; Sidorchuk, S. I.; Slepnev, R. S.; Stepantsov, S. V.; Ter-Akopian, G. M.; Wolski, R.; Itkis, M. G.; Bogatchev, A. A.; Kondratiev, N. A.; Kozulin, E. M.; Korsheninnikov, A. A.; Nikolskii, E. Y.; Roussel-Chomaz, P.; Mittig, W.; Palit, R.*; Bouchat, V.; Kinnard, V.; Materna, T.; Hanappe, F.; Dorvaux, O.; Stuttgé, L.; Angulo, C.; Lapoux, V.; Raabe, R.; Nalpas, L.; Yukhimchuk, A. A.; Perevozchikov, V. V.; Vinogradov, Y. I.; Grishechkin, S. K.; Zlatoustovskiy, S. V.: **Observation of excited states in ^{5}H.** *Physical review letters* **93**(26): 262501. DOI:10.1103/PhysRevLett.93.262501

P-H068 Greenlees, P. T.; Andreyev, A. N.; Bastin, J.; Becker, F.*; Bouchez, E.; Butler, P. A.; Cocks, J. F. C.; Le Coz, Y.; Eskola, K.; Gerl, J.* ; Hauschild, K.; Helariutta, K.; Herzberg, R.-D.; Heßberger, F. P.*; Humphreys, R. D.; Hürstel, A.; Jenkins, D. G.; Jones, G. D.; Jones, P.; Julin, R.; Juutinen, S.; Kankaanpää, H.; Keenan, A.; Kettunen, H.; Khoo, T. L.; Korten, W.; Kuusiniemi, P.*; Leino, M.; Leppanen, A. P.; Muikku, M.; Nieminen, P.; Page, R. D.; Page, T.; Pakarinen, J.; Rahkila, P.; Reiter, P.; Schlegel, C.*; Scholey, C.; Theisen, C.; Uusitalo, J.; Van de Vel, K.; Wadsworth, R.; Wollersheim, H. J.*: **In-beam spectroscopy at the RITU gas-filled recoil separator.** *The European physical journal A, Hadrons and nuclei* **20**(1): 87–92. DOI:10.1140/epja/i2002-10327-x

P-H069 Grigorenko, L. V.*: **Experimental puzzle of ^{5}H.** *The European physical journal A, Hadrons and nuclei* **20**(3): 419–427. DOI:10.1140/epja/i2003-10159-2

P-H070 Grigorenko, L. V.*; Timofeyuk, N. K.; Zhukov, M. V.: **Broad states beyond the neutron drip line - Examples of H-5 and (4)n.** *The European physical journal A, Hadrons and nuclei* **19**(2): 187–201. DOI:10.1140/epja/i2003-10124-1

P-H071 Grüter, B.; Alkofer, R.; Maas, A.; Wambach, J.: **QCD propagators at non-vanishing temperatures.** *Progress in particle and nuclear physics* **53**(1): 343–345. DOI:10.1016/j.ppnp.2004.02.028

P-H072 Haba, H.; Tsukada, K.; Asai, M.; Toyoshima, A.; Akiyama, K.; Nishinaka, I.; Hirata, M.; Yaita, T.; Ichikawa, S. I.; Nagame, Y.; Yasuda, K. I.; Miyamoto, Y.; Kaneko, T.;

Goto, S. I.; Ono, S.; Hirai, T.; Kudo, H.; Shigekawa, M.; Shinohara, A.; Oura, Y.; Nakahara, H.; Sueki, K.; Kikunaga, H.; Kinoshita, N.; Tsuruga, N.; Yokoyama, A.; Sakama, M.; Enomoto, S.; Schädel, M.*; Brüchle, W.*; Kratz, J. V.: **Fluoride Complexation of Element 104, Rutherfordium.** *Journal of the American Chemical Society* **126**(16): 5219–5224.

P-H073 Heinz, A.; Schmidt, K.-H.*; Junghans, A. R.: **Shell stabilization and the survival of heavy compound nuclei.** *Nuclear physics A, Nuclear and hadronic physics* **746**: 483C–486C. [Proceedings of the Sixth International Conference on Radioactive Nuclear Beams (RNB6) Argonne 20030922/26] DOI:10.1016/j.nuclphysa.2004.09.124

P-H074 Henzlova, D.*; Ricciardi, M. V.*; Benlliure, J.; Botvina, A. S.*; Enquist, T.*; Kelic, A.*; Napolitani, P.*; Pereira, J.; Schmidt, K. H.*: **Investigation of the N/Z of the heavy fragmentation products - the isospin thermometer method.** *Progress in particle and nuclear physics* **53**(1): 97–100. DOI:10.1016/j.ppnp.2004.02.009

P-H075 Heßberger, F. P.*: **Nuclear structure investigations of heavy actinide and trans-actinide isotopes.** *Heavy ion physics* **19**(1): 133–138.

P-H076 Heßberger, F. P.*; Hofmann, S.*; Ackermann, D.*; Cagarda, P.*; Herzberg, R. D.; Kojouharov, I.*; Kuusiniemi, P.*; Leino, M.; Mann, R.*: **Alpha-gamma decay studies of ^{251,253}No and their daughter products ^{247,249}Fm.** *The European physical journal A, Hadrons and nuclei* **22**(3): 417–427. DOI:10.1140/epja/i2003-10238-4 Also part of: 'Large-scale facilities for research with photons, neutrons and ions'.

P-H077 Heßberger F. P.*; Hofmann, S.*; Kojouharov, I.*; Ackermann, D.*: **Decay properties of isomeric states in radium isotopes close to N=126.** *The European physical journal A, Hadrons and nuclei* **22**(2): 253–260. DOI:10.1140/epja/i2003-10233-9

P-H078 Hofmann, J.*; Lutz, M. F. M.*: **Open-charm meson resonances with negative strangeness.** *Nuclear physics A, Nuclear and hadronic physics* **733**(1): 142–152. DOI:10.1016/j.nuclphysa.2003.12.

P-H079 Hofmann, S.*: **Heavy element research at GSI - Recent results and perspectives.** *Heavy ion physics* **19**(1): 31–38.

P-H080 Hofmann, S.*; Heßberger, F. P.*; Ackermann, D.*; Antalic, S.; Cagarda, P.; Kindler, B.*; Kuusiniemi, P.; Leino, M.; Lommel, B.*; Malyshev, O. N.; Mann, R.; Münzenberg, G. M.*; Popeko, A. G.; Saro, S.; Streicher, B.; Yeremin, A.: **Properties of heavy nuclei measured at the GSI SHIP.** *Nuclear physics A, Nuclear and hadronic physics* **734**: 93–100. [Proceedings of the Eighth International Conference On Nucleus-Nucleus Collisions] DOI:10.1016/S0375-9474(04)90259-X Also part of: 'Large-scale facilities for research with photons, neutrons and ions'.

P-H081 Humphreys, R. D.; Butler, P. A.; Bastin, J. E.; Greenlees, P. T.; Hammond, N. J.; Herzberg, R. D.; Jenkins, D. G.; Jones, G. D.; Kankaanpää, H.; Keenan, A.; Kettunen, H.; Page, T.; Rahkila, P.; Scholey, C.; Uusitalo, J.; Amzal, N.; Brew, P. M. T.; Eskola, K.; Gerl, J.*; Hauschild, K.; Helariutta, K.; Heßberger, F. P.*; Hurstel, A.; Jones, P. M.; Julin, R.; Juutinen, S.; Khoo, T. L.; Korten, W.; Kuusiniemi, P.; Le Coz, Y.; Leino, M.; Leppanen, A. P.; Muikku, M.; Nieminen, P.; Ødegård, S. W.; Pakarinen, J.; Reiter, P.; Sletten, G.; Theisen, C.; Wollersheim, H. J.*: **In-beam electron spectroscopy of ^{226}U and ^{254}No.** *Physical review C, Nuclear physics* **69**(6): 064324. DOI:10.1103/PhysRevC.69.064324

P-H082 Ilievski, S.*; Aumann, T.*; Boretzky, K.; Elze, T. W.; Emling, H.*; Grünschloß, A.; Holeczek, J.; Holzmann, R.*; Kozhuharov, C.*; Kratz, J. V.; Kulessa, R.; Leistenschneider, A.; Lubkiewicz, E.; Ohtsuki, T.; Reiter, P.; Simon, H.; Stelzer, K.; Stroth, J.*; Sümmerer, K.*; Wajda, E.; Waluś, W.; LAND Collaboration*: **Evidence for multiphonon giant resonances in electromagnetic fission of ^{238}U.** *Physical review letters* **92**(11): 112502. DOI:10.1103/PhysRevLett.92.112502 Also part of: 'Large-scale facilities for research with photons, neutrons and ions'.

P-H083 INDRA ALADIN Collaborations*: **Multiplicity correlations of intermediate-mass fragments with pions and fast protons in ^{12}C+^{197}Au.** *The European physical journal A, Hadrons and nuclei* **21**(2): 293–301. DOI:10.1140/epja/i2003-10217-9

P-H084 Jurado, B.*; Schmitt, C.*; Schmidt, K. H.*; Benlliure, J.; Enqvist, T.*; Junghans, A. R*.; Kelić, A.*; Rejmund, F.*: **Transient effects in fission from new experimental signatures.** *Physical review letters* **93**(7): 072501. DOI:10.1103/PhysRevLett.93.072501

P-H085 Kanaki, K.; Dohrmann, F.; Enghardt, W.; Garabatos, C.; Grosse, E.; Hutsch, J.; Kampfer, B.; Kondyurin, A.; Kotte, R.; Müntz, C.*; Naumann, L.; Sadovsky, A.; Stroth, J.*; Sobiella, M.: **HADES tracking system: First in-beam experience.** *IEEE transactions on nuclear science* **51**(3): 939–942.

P-H086 Karamian, S. A.; Adam, J.; Chaloun, P.; Filossofov, D. V.; Henzl, V.*; Henzlova, D.*; Kalinnikov, V. G.; Korolev, N. A.; Lebedev, N. A.; Novgorodov, A. F.; Collins, C. B.; Popescu, I. I.; Ur, C. A.: **Yield of radionuclides and isomers produced in the fragmentation of ^{nat}W and ^{186}W (97%) targets with protons at 630, 420 and 270 MeV.** *Nuclear instruments & methods in physics research, Section A, Accelerators, spectrometers, detectors and associated equipment* **527**(3): 609–623. DOI:10.1016/j.nima.2004.03.185

P-H087 Karnaukhov, V. A.; Oeschler, H.; Avdeyev, S. P.; Rodionov, V. K.; Simomenko, A. V.; Kirakosyan, V. V.; Budzanowski, A.; Karcz, W.; Skwirczynska, I.; Kuzmin, E. A.; Norbeck, E.; Botvina, A. S.*: **Multifragmentation and nuclear phase transitions (liquid-fog and liquid-gas).** *Nuclear physics A, Nuclear and hadronic physics* **734**: 520–523. [Proceedings of the Eighth International Conference On Nucleus-Nucleus Collisions] DOI:10.1016/S0375-9474(04)90335-1

P-H088 Karny, M.; Batist, L.; Jenkins, D.; Kavatsyuk, M.*; Kavatsyuk, O.*; Kirchner, R.*; Korgul, A.; Roeckl, E.*; Zylicz, J.: **Excitation energy of the T=0 β-decaying 9$^+$ isomer in ^{70}Br.** *Physical review C, Nuclear physics* **70**(1): 014310. DOI:10.1103/PhysRevC.70.014310

P-H089 Kaye, R. A.; Grubor-Urosevic, O.; Tabor, S. L.; Döring, J.*; Sun, Y.; Palit, R.*; Sheikh, J. A.; Baldwin, T.; Campbell, D. B.; Chandler, C.; Cooper, M. W.; Gerbick, S. M.; Hoffman, C. R.; Pavan, J.; Riley, L. A.; Wiedeking, M.: **Collective excitations and shape changes in ^{80}Y.** *Physical review C, Nuclear physics* **69**(6): 064314. DOI:10.1103/PhysRevC.69.064314

P-H090 Kelić, A.*; Schmidt, K. H.*; Enqvist, T.*; Boudard, A.; Armbruster, P.*; Benlliure, J.; Bernas, M.; Czajkowski, S.; Legrain, R.; Leray, S.; Mustapha, B.; Pravikoff, M.; Rejmund, F.; Stéphan, C.; Taieb, J.; Tassan-Got, L.; Volant, C.; Włazlo, W.: **Isotopic and velocity distributions of $_{83}$Bi produced in charge-pickup reactions of Pb^{208}_{82} at 1A GeV.** *Physical review C, Nuclear physics* **70**(6): 064608. DOI:10.1103/PhysRevC.70.064608

P-H091 Kluge, H.-J.*; Blaum, K.*; Scheidenberger, C.*: **Mass measurement of radioactive isotopes.** *Nuclear instruments & methods in physics research, Section A, Accelerators, spectrometers, detectors and associated equipment* **532**(1): 48–55. [International Workshop on Beam Cooling and Related Topics, Lake Yamanaka, Yamanashi, Japan, 20030519/23] DOI:10.1016/j.nima.2004.06.029 Also part of: 'Large-scale facilities for research with photons, neutrons and ions'.

P-H092 Kolomeitsev, E. E.; Lutz, M. F. M.*: **On baryon resonances and chiral symmetry.** *Physics letters B* **585**(3): 243–252. DOI:10.1016/j.physletb.2004.01.066

P-H093 Kolomeitsev, E. E.; Lutz, M. F. M.*: **On heavy-light meson resonances and chiral symmetry.** *Physics letters B* **582**(1): 39–48. DOI:10.1016/j.physletb.2003.10.118

P-H094 Korpa, C. L.; Lutz, M. F. M.*: **Self consistent and covariant propagation of pions, nucleon and isobar resonances in cold nuclear matter.** *Nuclear physics A, Nuclear and hadronic physics* **742**(3): 305–321. DOI:10.1016/j.nuclphysa.2004.06.031

P-H095 Korten, W.; Bouchez, E.; Clément, E.; Chatillon, A.; Görgen, A.; Le Coz, Y.; Theisen, C.; Wilson, J.; Casandjian, J. M.; de France, G.; Sletten, G.; Czosnyka, T.; Iwanicki, J.; Zielinska, M.; Andreoiu, C.; Butler, P.; Herzberge, R. D.; Jenkins, D.; Jones, G.; Becker, F.*; Gerl, J.*; Catford, W.; Timis, C.: **Shape coexistence in Krypton isotopes studied through Coulomb excitation of radioactive Krypton ion beams.** *Nuclear physics A, Nuclear and hadronic physics* **746**: 90C–95C. [Proceedings of the Sixth International Conference on Radioactive Nuclear Beams (RNB6) Argonne 20030922/26] DOI:10.1016/j.nuclphysa.2004.09.125

P-H096 Kraft, S.*; Andrianov, V.*; Bleile, A.*; Egelhof, P.*; Golser, R.; Kiseleva, A.*; Kiselev, O.*; Kutschera, W.; Meier, J. P.*; Priller, A.; Shrivastava, A.*; Steier, P.; Vockenhuber, C.: **First application of calorimetric low-temperature detectors in accelerator mass spectrometry.** *Nuclear instruments & methods in physics research, Section A, Accelerators, spectrometers, detectors and associated equipment* **520**(1): 63–66. [Proceedings of the 10th International Workshop on Low Temperature Detectors, Genoa, Italy, 7 - 11 July 2003] DOI:10.1016/j.nima.2003.11.221

P-H097 Kraus, I.*; NA49 Collaboration*: **System size dependence of strangeness production at 158 A GeV.** *Journal of physics G, Nuclear and particle physics* **30**(1): S583–S588. DOI:10.1088/0954-3899/30/1/072

P-H098 Kronenberg, A.; Eberhardt, K.; Kratz, J. V.; Mohapatra, P. K.; Nähler, A.; Thörle, P.; Brüchle, W.*; Schädel, M.*; Türler, A.: **On-line anion exchange of rutherfordium in HF/HNO_3 and HF solutions.** *Radiochimica acta* **92**(7): 379–386. DOI:10.1524/ract.92.7.379.35753

P-H099 Kugler, A.; Agakichiev, H.*; Agodi, C.; Alvarez-Pardo, M.; Alvarez-Pol, H.; Badura, E.*; Balanda, A.; Ballester, F.; Bassi, A.; Bassini, R.; Bellia, G.; Bertini, D.*; Bielcik, J.*; Böhmer, M.; Boiano, C.; Bokemeyer, H.*; Boyard, J. L.; Brambilla, S.; Braun-Munzinger, P.*; Chernenko, S.; Coniglione, R.; Dahlinger, M.*; Daues, H.*; Diaz, R.; Dohrmann, F.; Duran, I.; Eberl, T.; Fabietti, L.; Fateev, O.; Fernandez, C.; Finocchiaro, P.; Friese, J.; Fröhlich, I.; Fuentes, B.; Garzon, J. A.; Genolini, B.; Gernhäuser, R.; Golubeva, M.; Gonzales, D.; Göringer, H.*; Grosse, E.; Guber, F.; Hehner, J.*; Hennino, T.; Hlavac, S.; Hoffmann, J.; Holzmann, R.*; Homolka, J.; Ierusalimov, A.; Iori, I.; Jaskula, M.; Kampfer, B.; Kanaki, K.; Karavichieva, T.; Kirschner, D.; Kidon, L.; Kienle, P.; Koenig, I.*; Koenig, W.*; Körner, H. J.; Kolb, B. W.*; Kopf, U.*; Kotte, R.; Kühn, W.; Kurtukian, T.; Krücken, R.; Kulessa, R.; Kurepin, A.; Lehnert, J.; Lins, E.; Magestro, D.*; Maier-Komor, P.; Maiolino, C.; Markert, J.; Metag, V.; Mousa, J.; Münch, M.; Müntz, C.*; Naumann, L.; Nekhaev, A.; Niebur, W.*; Ott, W.*; Novotny, R.; Otwinowski, J.; Panebratsev, Y.; Pechenov, V.; Petri, M.; Piattelli, P.; Pietraszko, J.; Pleskac, R.; Ploskon, M.; Przygoda, W.; Rabin, N.; Ramstein, B.; Reshetin, A.; Ritman, J.; Rosier, P.; Roy-Stephan, M.; Rustamov, A.*; Sabin, J.; Sadovski, A.; Sailer, B.; Salabura, P.; Sanchez, M.; Sapienza, P.; Senger, P.*; Schroeder, C.*; Shileev, K.; Shishov, P.; Simon, R.*; Smoliankin, V.; Smykov, L.; Spataro, S.; Stelzer, H.*; Ströbele, H.; Stroth, J. ; Sturm, C.*; Sudol, M.*; Taranenko, A.; Tlusty, P.; Toia, A.; Traxler, M.; Tsertos, H.; Turzo, I.; Vassiliev, D.; Vazquez, A.; Wagner, V.; Walus, W.; Winkler, S.; Wisniowski, M.; Wojcik, T.; Wüstenfeld, J.; Yahlali, N.; Zanevsky, Y.; Zeitelhack, K.; Zovinec, D.; Zumbruch, P.*: **Particle identification at HADES.** *Nuclear physics A, Nuclear and hadronic physics* **734**: 78–81. [Proceedings of the Eighth International Conference On Nucleus-Nucleus Collisions] DOI:10.1016/S0375-9474(04)90257-6 Also part of: Scientific Infrastructure.

P-H100 Kugler, A.; Agakishiev, H.*; Agodi, C.; Alvarez-Pol, H.; Balanda, A.; Bellia, G.; Bielčik, J.*; Böhmer, M.; Boyard, J.; Braun-Munzinger, P.*; Chernenko, S.; Christ, T.; Coniglione, R.; Djeridi, R.; Dohrmann, F.; Duran, I.; Eberl, T.; Fabbietti, L.; Fateev, O.; Finocchiaro, P.; Friese, J.; Fröhlich, I.; Garzon, J.; Gernhäuser, R.; Golubeva, M.; Gonzales-Dias, D.; Grosse, E.; Guber, F.; Hennino, T.; Hlavac, S.; Holzmann, R.*; Ierusalimov, A.; Iori, I.; Jaskula, M.; Jurkovi, M.; Kämpfer, B.; Kanaki, K.; Karavicheva, T.; Koenig, I.*; Koenig, W.*; Kolb, B.*; Kotte, R.; Kotulic-Bunta, J.; Krücken, R.; Kuhn, W.; Kulessa, R.; Kurepin, A.; Lang, S.*; Lehnert, J.; Maiolino, C.; Markert, J.; Metag, V.; Mousa, J.; Münch, M.; Müntz, C.; Naumann, L.; Novotny, R.; Novotny, J.; Otwinowski, J.; Pachmayer, Y.*; Pechenov, V.; Perez, T.; Pietraszko, J.*; Pleskač, R.; Pospíšil, V.; Przygoda, W.; Rabin, N.; Ramstein, B.; Reshetin, A.; Ritman, J.; Roy-Stephan, M.; Rustamov, A.*; Sadovski, A.; Sailer, B.; Salabura, P.;

Sanchez, M.; Sapienza, P.; Schmah, A.*; Simon, R.*; Smoliankin, V.; Smykov, L.; Spataro, S.; Spruck, B.; Ströbele, H.*; Stroth, J.*; Sturm, C.*; Sudol, M.*; Tlustý, P.; Toia, A.; Traxler, M.*; Tsertos, H.; Wagner, V.; Wiśniowski, M.; Wojcik, T.; Wüstenfeld, J.*; Zanevsky, Y.; Žovinec, D.; Zumbruch, P.*: **Charged hadrons and leptons identification at HADES.** *Acta physica Slovaca* **54**(4): 375–384.

P-H101 Kuusiniemi, P.*; Heßberger, F. P.*; Ackermann, D.*; Hofmann, S.*; Kojouharov, I.*: **Decay studies of $^{214-216}$Ac by α-γ-γ-coincidences.** *The European physical journal A, Hadrons and nuclei* **22**(3): 429–442. DOI:10.1140/epja/i2004-10101-2

P-H102 Le Fèvre, A.*; Ploszajczak, M.; Toneev, V. D.*; Auger, G.; Begemann-Blaich, M. L.*; Bellaize, N.; Bittiger, R.; Bocage, F.; Borderie, B.; Bougault, R.; Bouriquet, B.; Charvet, J. L.; Chbihi, A.; Dayras, R.; Durand, D.; Frankland, J. D.; Galichet, E.; Gourio, D.; Guinet, D.; Hudan, S.; Hurst, B.; Lautesse, P.; Lavaud, F.; Legrain, R.; Lopez, O.; Łukasik, J.*; Lynen, U.*; Müller, W. F. J.*; Nalpas, L.; Orth, H.*; Plagnol, E.; Rosato, E.; Saija, A.; Schwarz, C.*; Sfienti, C.*; Tamain, B.; Trautmann, W.*; Trzcinski, A.; Turzó, K.*; Vient, E.; Vigilante, M.; Volant, C., Zwiegliński, B.; Botvina, A. S.*; INDRA, ALADIN Collaborations*: **Statistical multifragmentation of non-spherical expanding sources in central heavy-ion collisions.** *Nuclear physics A, Nuclear and hadronic physics* **735**(1): 219–247. DOI:10.1016/j.nuclphysa.2004.01.133

P-H103 Leino, M.; Heßberger, F. P.*: **The nuclear structure of heavy-actinide and transactinide nuclei.** *Annual review of nuclear and particle science* **54**: 175–215. DOI:10.1146/annurev.nucl.53.041002.110332

P-H104 Lippmann, C.*: **Position resolution and electron identification with prototypes of the ALICE TRD.** *Nuclear instruments & methods in physics research, Section A, Accelerators, spectrometers, detectors and associated equipment* **535**(1): 457–460. [Proceedings of the 10th International Vienna Conference on Instrumentation, Vienna, Austria, 20040216/21] DOI:10.1016/j.nima.2004.07.191

P-H105 Lisetskiy, A. F.; Brown, B. A.; Horoi, M.; Grawe, H.*: **New T=1 effective interactions for the $f_{5/2}$ $p_{3/2}$ $p_{1/2}$ $g_{9/2}$ model space: Implications for valence-mirror symmetry and seniority isomers.** *Physical review C, Nuclear physics* **70**(4): 044314. DOI:10.1103/PhysRevC.70.044314

P-H106 Łukasik, J.*; Trautmann, W.*; Auger, G.; Begemann-Blaich, M. L.*; Bellaize, N.; Bittiger, R.*; Bocage, F.; Borderie, B.; Bougault, R.; Bouriquet, B.; Charvet, J. L.; Chbihi, A.; Dayras, R.; Durand, D.; Frankland, J. D.; Galichet, E.; Gourio, D.*; Guinet, D.; Hudan, S.; Hurst, B.; Lautesse, P.; Lavaud, F.; Le Fèvre, A.; Legrain, R.; Lopez, O.; Lynen, U.*; Müller, W. F. J.*; Nalpas, L.; Orth, H.*; Plagnol, E.; Rosato, E.; Saija, A.; Sfienti, C.*; Schwarz, C.*; Steckmeyer, J. C.; Tamain, B.; Trzciński, A.; Turzó, K.*; Vient, E.; Vigilante, M.; Volant, C.; Zwiegliński, B.; INDRA ALADIN Collaborations*: **INDRA@GSI: collective flow in Au plus Au collisions.** *Progress in particle and nuclear physics* **53**(1): 77–80. DOI:10.1016/j.ppnp.2004.02.013

P-H107 Lutz, M. F. M.*: **Chiral symmetry and strangeness at SIS energies.** *Progress in particle and nuclear physics* **53**(1): 125–136. DOI:10.1016/j.ppnp.2004.02.008

P-H108 Lutz, M. F. M.*: **Chiral symmetry, strangeness and nuclear matter.** *Acta physica Polonica B, Particle physics and field theory, nuclear physics, theory of relativity* **35**(3): 1105–1117.

P-H109 Lutz, M. F. M.*; Kolomeitsev, E. E.: **On charm baryon resonances and chiral symmetry.** *Nuclear physics A, Nuclear and hadronic physics* **730**(1): 110–120. DOI:10.1016/j.nuclphysa.2003.10.012

P-H110 Lutz, M. F. M.*; Kolomeitsev, E. E.: **On meson resonances and chiral symmetry.** *Nuclear physics A, Nuclear and hadronic physics* **730**(3): 392–416. DOI:10.1016/j.nuclphysa.2003.11.009

P-H111 Lutz, M. F. M.*; Kolomeitsev, E. E.; Korpa, C. L.: **Chiral symmetry, strangeness and resonances.** *Progress of theoretical physics Supplement* (156): 51–71.

P-H112 Maas, A.; Wambach, J.*; Gruter, B.; Alkofer, R.: **High-temperature limit of Landau-gauge Yang-Mills theory.** *The European physical journal: C, Particles and fields* **37**(3): 335–357. DOI:10.1140/epjc/s2004-02004-3

P-H113 Malyshev, O. N.; Yeremin, A. V.; Popeko, A. G.; Belozerov, A. V.; Chelnokov, M. L.; Chepigin, V. I.; Gorshkov, V. A.; Hofmann, S.*; Itkis, M. G.; Kabachenko, A. P.; Oganessian, Y. T.; Sagaidak, R. N.; Šaro,Š.; Shutov, A. V.; Svirikhin, A. I.: **In-beam separation and mass determination of superheavy nuclei. Part II.** *Nuclear instruments & methods in physics research, Section A, Accelerators, spectrometers, detectors and associated equipment* **516**(2): 529–538. DOI:10.1016/j.nima.2003.08.118

P-H114 Mangiarotti, A.; Fonte, P.; Gobbi, A.*: **Exactly solvable model for the time response function of RPCs.** *Nuclear instruments & methods in physics research, Section A, Accelerators, spectrometers, detectors and associated equipment* **533**(1): 16–21. [Proceedings of the Seventh International Workshop on Resistive Plate Chambers and Related Detectors, Clermont-Ferrand, France, 20031020/22] DOI:10.1016/j.nima.2004.06.121

P-H115 Marín, A.*; CERES Collaboration*: **New results from CERES.** *Journal of physics G, Nuclear and particle physics* **30**(8): S709–S716. DOI:10.1088/0954-3899/30/8/009

P-H116 Meister, M.*; Chulkov, L. V.*; Simon, H.; Aumann, T.*; Borge, M. J. G.; Elze, T. W.; Emling, H.*; Geissel, H.*; Hellström, M.; Jonson, B.; Kratz, J.; Kulessa, R.; Leifels, Y.*; Markenroth, K.; Münzenberg, G.*; Nickel, F.*; Nilsson, T.; Nyman, G.; Pribora, V.; Richter, A.; Riisager, K.; Scheidenberger, C.*; Schrieder, G.; Tengblad, O.: **Erratum to: 'Searching for the ^5H resonance in the t+n+n system' [Nucl. Phys. A 723 (2003) 13].** *Nuclear physics A, Nuclear and hadronic physics* **739**(3): 353–354. DOI:10.1016/j.nuclphysa.2004.04.115

P-H117 Meurer, C.*; NA49 Collaboration*: **Hyperon production in Pb plus Pb collisions at the CERN-SPS.** *Journal of physics G, Nuclear and particle physics* **30**(8):

S1325–S1328. DOI:10.1088/0954-3899/30/8/119

P-H118 Meurer, C.; NA49 Collaboration*: **Ξ_- and $\bar{\Xi}^+$ production in Pb+Pb collisions at 40 A GeV at CERN SPS.** *Journal of physics G, Nuclear and particle physics* **30**(1): S175–S180. DOI:10.1088/0954-3899/30/1/017

P-H119 Mischke, A.*; NA49 Collaboration*: **Λ and Φ production in heavy ion collisions.** *Progress in particle and nuclear physics* **53**(1): 265–267. DOI:10.1016/j.ppnp.2004.02.041

P-H120 Miura, Y.; Ajimura, S.; Fujii, Y.; Fukuda, T.; Hashimoto, A.; Hotchi, H.; Imai, K.; Imoto, W.; Kakiguchi, Y.; Kameoka, S.; Krutenkova, A.; Maruta, T.; Matsumura, A.; Miwa, K.; Miyoshi, T.; Mizunuma, K.; Nakamura, S. N.; Nagae, T.; Nomura, H.; Noumi, H.; Okayasu, Y.; Otaki, T.; Outa, H.; Saha, P. K.; Saitoh, T.*; Sato, Y.; Sekimoto, M.; Takahashi, T.; Tamura, H.; Tanida, K.; Toyoda, A.; Ukai, M.; Yamauchi, H.: **A recent experiment with Hyperball.** *Acta physica Polonica B, Particle physics and field theory, nuclear physics, theory of relativity* **35**(3): 1019–1031.

P-H121 Miura, Y.; Ajimura, S.; Fujii, Y.; Fukuda, T.; Hashimoto, O.; Hotchi, H.; Imai, K.; Imoto, W.; Kakguchi, Y.; Kameoka, S.; Krutenkova, A.; Maruta, T.; Matsumura, A.; Miwa, K.; Miyoshi, T.; Mizunuma, K.; Nakamura, S. N.; Nagae, T.; Nomura, H.; Noumi, H.; Okayasu, Y.; Otaki, T.; Outa, H.; Saha, P. K.; Saitoh, T.*; Sato, Y.; Sekimoto, I.; Takahashi, T.; Tamura, H.; Tanida, K.; Toyoda, A.; Ukai, M.; Yamauchi, H.: **g-factor of Λ in the hypernuclei studied from $B(M1)$ measurement.** *Progress of theoretical physics Supplement* (156): 160–162.

P-H122 Müntz, C.; Markert, J.; Agakichiev, G.; Alvarez-Pol, H.; Badura, E.*; Bielcik, J.*; Bokemeyer, H.*; Boyard, J. L.; Chepurnov, V.; Chernenko, S.; Daues, H.*; Dohrmann, F.; Enghardt, W.; Fateev, O.; Garabatos, C.*; Glonti, L.; Grosse, E.; Hehner, J.*; Heidel, K.; Hennino, T.; Hoffmann, J.*; Ierusalimov, A.; Kämpfer, B.; Kanaki, K.; Koenig, W.*; Kotte, R.; Naumann, L.; Ott, W.*; Pachmayer, Y. C.; Pechenov, V.; Pouthas, J.; Ramstein, B.; Rosenkranz, K.; Rosier, P.; Roy-Stephan, M.; Rustamov, A.*; Sadovski, A.; Smykov, L.; Sobiella, M.; Stelzer, H.*; Stroebele, H.; Stroth, J.*; Sturm, C.*; Sudol, M.*; Wüstenfeld, J.; Zanevsky, Y.; Zumbruch, P.*: **The HADES tracking system.** *Nuclear instruments & methods in physics research, Section A, Accelerators, spectrometers, detectors and associated equipment* **535**(1): 242–246. [Proceedings of the 10th International Vienna Conference on Instrumentation, Vienna, Austria, 20040216/21] DOI:10.1016/j.nima.2004.07.232

P-H123 Münzenberg, G.*: **Frontiers of nuclear structure research and the GSI experimental program.** *Nuclear physics A, Nuclear and hadronic physics* **734**: 395–402. [Proceedings of the Eighth International Conference On Nucleus-Nucleus Collisions] DOI:10.1016/S0375-9474(04)90313-2

P-H124 Münzenberg, G.*: **Storage-ring experiments with exotic nuclei: from mass measurements to the future.** *Progress in particle and nuclear physics* **53**(1): 351–362. DOI:10.1016/j.ppnp.2004.02.033

P-H125 Mukha, I.; Batist, L.; Becker, F.*; Blazhev, A.*; Brüchle, A.*; Döring, J.*; Górska, M.*; Grawe, H.*; Faestermann, T.; Hoffman, C.; Janas, Z.; Jungclaus, A.; Karny, M.; Kavatsyuk, M.*; Kavatsyuk, O.*; Kirchner, R.*; La Commara, M.; Mazzocchi, C.*; Plettner, C.*; Płochocki, A.; Roeckl, E.*; Romoli, M.; Schädel, M.*; Schwengner, R.; Tabor, S. L.; Wiedeking, M.; GSI ISOL Collaboration*: **Studies of β-delayed proton decays of N $\simeq$ to Z nuclei around ^{100}Sn at the GSI-ISOL facility.** *Nuclear physics A, Nuclear and hadronic physics* **746**: 66C–70C. [Proceedings of the Sixth International Conference on Radioactive Nuclear Beams (RNB6) Argonne 20030922/26] DOI:10.1016/j.nuclphysa.2004.09.065

P-H126 Mukha, I.*; Batist, L.; Roeckl, E.*; Grawe, H.*; Döring, J.*; Blazhev, A.*; Hoffman, C. R.; Janas, Z.; Kirchner, R.*; La Commara, M.; Dean, S.; Mazzocchi, C.*; Plettner, C.*; Tabor, S. L.; Wiedeking, M.: **β-delayed proton decay of a high-spin isomer in ^{94}Ag.** *Physical review C, Nuclear physics* **70**(4): 044311. DOI:10.1103/PhysRevC.70.044311

P-H127 Muntian, I.*; Patyk, Z.*; Sobiczewski, A.*: **Properties of heaviest nuclei within macro-micro approach.** *Heavy ion physics* **19**(1): 139–144.

P-H128 Murin, Y. A.; Carlén, L.; Jakobsson, B.; Yahlali, N.; Álvarez, M.; Ardid, M.; Díaz, J.; Bokemeyer, H.*; Koenig, W.*; Leinberger, U.*; Niebur, W.*; Novotny, R.; Schicker, R.*; Schön, W.*; Hartmann, O.*; Mittig, W.: **A scintillator based time-of-flight hodoscope with a new type of emitter follower divider.** *Nuclear instruments & methods in physics research, Section A, Accelerators, spectrometers, detectors and associated equipment* **533**(3): 361–369. DOI:10.1016/j.nima.2004.07.172

P-H129 Mutterer, M.; Kopatch, Y. N.*; Jessinger, P.; Gagarski, A. M.; Gonnenwein, F.; Von Kalben, J.; Khlebuikov, S. G.; Kojouharov, I.*; Lubkiewics, E.; Mezentseva, Z.; Nesvishevsky, V.; Petrov, C. A.; Schaffner, H.*; Scharma, H.; Schwalm, D.; Thirolf, P.; Trzaska, W. H.; Tyurin, G. P.; Wollersheim, H. J.*: **Recent experimental studies on particle-accompanied fission.** *Nuclear physics A, Nuclear and hadronic physics* **738**: 122–128. [Proceedings of the 8th International Conference on Clustering Aspects of Nuclear Structure and Dynamics] DOI:10.1016/j.nuclphysa.2004.04.020

P-H130 Mykulyak, A.*; Kapusta, M.; Lynen, U.*; Moszyński, M.; Müller, W. F. J.*; Orth, H.*; Schwarz, C.*; Szawlowski, M.; Trautmann, W.*; Trzciński, A.; Wolski, D.; Zwiegliński, B.: **Readout of plastic scintillators with cooled large-area avalanche photodiodes.** *Nuclear instruments & methods in physics research, Section A, Accelerators, spectrometers, detectors and associated equipment* **523**(3): 425–434. DOI:10.1016/j.nima.2004.01.003

P-H131 Napolitani, P.; Rejmund, F.; Tassan-Got, L.; Ricciardi, M. V.*; Kelic, A.*; Schmidt, K. H.*; Yordanov, O.*; Ignatyuk, A. V.; Villagrasa, C.: **Structural effects in the nuclide distributions of the residues of highly excited systems.** *International journal of modern physics E, Nuclear physics* **13**(1): 333–336. DOI:10.1142/S0218301304002144

P-H132 Napolitani, P.*; Schmidt, K. H.*; Botvina, A. S.*; Rejmund, F.; Tassan-Got, L.; Villagrasa, C.: **High-resolution velocity measurements on fully identified light nuclides produced in ^{56}Fe+hydrogen and ^{56}Fe+titanium systems.** *Physical review C, Nuclear physics* **70**(5): 054607.

DOI:10.1103/PhysRevC.70.054607

P-H133 Nayak, T. K.; WA98 Collaboration*: **Fluctuations as a signal of quark-gluon plasma: Present experimental results.** *Pramana - Journal of Physics* **62**(3): 623–625.

P-H134 Neff, T.*; Feldmeier, H.*: **Cluster structures within Fermionic Molecular Dynamics.** *Nuclear physics A, Nuclear and hadronic physics* **738**: 357–361. [Proceedings of the 8th International Conference on Clustering Aspects of Nuclear Structure and Dynamics] DOI:10.1016/j.nuclphysa.2004.04.061

P-H135 Nowak, M. A.; Rho, M.; Zahed, I.: **Chiral doubling of heavy-light hadrons: Babar 2317 MeV/c^2 and CLEO 2460 MeV/c^2 discoveries.** *Acta physica Polonica B, Particle physics and field theory, nuclear physics, theory of relativity* **35**(10): 2377–2391.

P-H136 Oganessian, Y. T.; Yeremin, A. V.; Popeko, A. G.; Malyshev, O. N.; Belozerov, A. V.; Buklanov, G. V.; Chelnokov, M. L.; Chepigin, V. I.; Gorshkov, V. A.; Hofmann, S.*; Itkis, M. G.; Kabachenko, A. P.; Kindler, B.*; Münzenberg, G.*; Sagaidak, R. N.; Šáro, Š.; Schött, H. J.*; Streicher, B.; Shutov, A. V; Svirikhin, A. I.; Vostokin, G. K.: **In-flight separation and mass selection of heavy evaporation residues..** *Nuclear physics A, Nuclear and hadronic physics* **734**: 196–199. [Proceedings of the Eighth International Conference On Nucleus-Nucleus Collisions] DOI:10.1016/S0375-9474(04)90274-6

P-H137 Oganessian, Y. T.; Yeremin, A. V.; Popeko, A. G.; Malyshev, O. N.; Belozerov, A. V.; Buklanov, G. V.; Chelnokov, M. L.; Chepigin, V. I.; Gorshkov, V. A.; Hofmann, S.*; Itkis, M. G.; Kabachenko, A. P.; Kindler, B.*; Münzenberg, G.*; Sagaidak, R. N.;Šáro, Š.; Schött, H. J.*; Štreicher, B.; Shutov, A. V.; Svirikhin, A. I.; Vostokin, G. K.: **Second experiment at VASSILISSA separator on the synthesis of the element 112.** *The European physical journal A, Hadrons and nuclei* **19**(1): 3–6. DOI:10.1140/epja/i2003-10113-4

P-H138 Okada, S.; Ajimura, S.; Aoki, K.; Banu, A.*; Bhang, H. C.; Fukuda, T.; Hashimoto, O.; Hwang, J. I.; Kameoka, S.; Kang, B. H.; Kim, E. H.; Kim, J. H.; Kim, M. J.; Maruta, T.; Miura, Y.; Miyake, Y.; Nagae, T.; Nakamura, M.; Nakamura, S. N.; Noumi, H.; Okayasu, Y.; Outa, H.; Park, H.; Saha, P. K.; Sato, Y.; Sekimoto, M.; Takahashi, T.; Tamura, H.; Tanida, K.; Toyoda, A.; Tsukada, K.; Watanabe, T.; Yim, H. J.: **Neutron and proton energy spectra from the non-mesonic weak decays of $^{5}_{\Lambda}$ He and $^{12}_{\Lambda}$C.** *Physics letters B* **597**(3): 249–256. DOI:10.1016/j.physletb.2004.07.031

P-H139 Ortega, R.; TAPS Collaboration*: **Constructing the nuclear caloric curve from thermal bremsstrahlung.** *Nuclear physics A, Nuclear and hadronic physics* **734**: 541–544. [Proceedings of the Eighth International Conference On Nucleus-Nucleus Collisions] DOI:10.1016/S0375-9474(04)90340-5

P-H140 Palit, R.*; Adrich, P.*; Aumann, T.*; Boretzky, K.*; Cortina, D.; Datta Pramanik, U.*; Elze, T. W.; Emling, H.*; Fallot, M.*; Geissel, H.*; Hellström, M.*; Jones, K. L.*; Khiem, L. H.; Kratz, J. V.; Kulessa, R.; Leistenschneider, A.; Münzenberg, G.*; Nociforo, C.*; Reiter, P.; Simon, H.*; Sümmerer, K.*; Walus, W.; LAND Collaboration*: **Coulomb breakup of secondary beams of neutron-rich nuclei.** *Nuclear physics A, Nuclear and hadronic physics* **738**: 45–51. [Proceedings of the 8th International Conference on Clustering Aspects of Nuclear Structure and Dynamics] DOI:10.1016/j.nuclphysa.2004.04.010

P-H141 Palit, R.*; Adrich, P.*; Aumann, T.*; Boretzky, K.; Cortina, D.*; Datta Pramanik, U.*; Elze, T. W.; Emling, H.*; Fallot, M.*; Geissel, H.*; Hellström, M.*; Jones, K. L.*; Khiem, L. H.; Kratz, J. V.; Kulessa, R.; Leifels, Y.*; Leistenschneider, A.; Münzenberg, G.*; Nociforo, C.; Reiter, P.; Simon, H.*; Sümmerer, K.*; Walus, W.: **Dipole excitations of neutron-proton asymmetric nuclei.** *Nuclear physics A, Nuclear and hadronic physics* **731**: 235–248. [Proceedings of the International Conference on Collective Motion in Nuclei under Extreme Conditions, Paris, France, 10 - 13 June 2003] DOI:10.1016/S0375-9474(04)90025-5

P-H142 Papakonstantinou, P.; Wambach, J.; Mavrommatis, E.; Ponomarev, V. Y.: **Nuclear vorticity and the low-energy nuclear response: towards the neutron drip line.** *Physics letters B* **604**(3): 157–162. DOI:10.1016/j.physletb.2004.10.053

P-H143 Parkhomenko, A.; Sobiczewski, A.*: **Proton one-quasiparticle states of heaviest nuclei.** *Acta physica Polonica B, Particle physics and field theory, nuclear physics, theory of relativity* **35**(10): 2447–2471.

P-H144 Parkhomenko, O.*; Muntian, I.*; Patyk, Z.*; Sobiczewski, A.*: **Neutron separation energy for heavy and superheavy nuclei.** *Heavy ion physics* **19**(1): 145–146.

P-H145 Pereira, J.; Armbruster, P.*; Benlliure, J.; Bernas, M.; Boudard, A.*; Casarejos, E.; Czajkowski, S.; Enqvist, T.*; Legrain, R.; Leray, S.; Mustapha, B.; Pravikoff, M.; Rejmund, F.; Schmidt, K. H.*; Stephan, C.; Taieb, J.; Tassan-Got, L.; Volant, C.; Wlazlo, W.: **Dynamics of spallation reactions investigated from production cross sections of residual nuclei in collisions induced by ^{238}U at 1 A · GeV on proton and deuterium.** *Nuclear physics A, Nuclear and hadronic physics* **734**: 221–224. [Proceedings of the Eighth International Conference On Nucleus-Nucleus Collisions] DOI:10.1016/S0375-9474(04)90280-1

P-H146 Peressounko, D.; WA98 Collaboration*: **Interferometry of direct photons in ^{208}Pb+ ^{208}Pb collisions at 158 A GeV.** *Journal of physics G, Nuclear and particle physics* **30**(8): S1065–S1068. DOI:10.1088/0954-3899/30/8/059

P-H147 Pershina, V.*: **Theoretical treatment of the complexation of element 106, Sg, in HF solutions.** *Radiochimica acta* **92**(8): 455–462. DOI:10.1524/ract.92.8.455.39279

P-H148 Pershina, V.* Bastug, T.; Sarpe-Tudoran, C.; Anton, J.; Fricke, B.: **Predictions of adsorption behaviour of the superheavy element 112.** *Nuclear physics A, Nuclear and hadronic physics* **734**: 200–203. [Proceedings of the Eighth International Conference On Nucleus-Nucleus Collisions] DOI:10.1016/S0375-9474(04)90275-8

P-H149 Plettner, C.*; Grawe, H.*; Mukha, I.*; Döring, J.*; Nowacki, F.; Batist, L.; Blazhev, A.*; Hoffman, C. R.; Janas,

Z.; Kirchner, R.*; La Commara, M.; Mazzocchi, C.*; Roeckl, E.*; Schwengner, R.; Tabor, S. L.; Wiedeking, M.: **On the β-decaying (21(+)) spin gap isomer in ^{94}Ag.** *Nuclear physics A, Nuclear and hadronic physics* **733**(1): 20–36. DOI:10.1016/j.nuclphysa.2003.12.014

P-H150 Rakers, S.; Bäumer, C.; van den Berg, A. M.; Davids, B.; Frekers, D.; De Frenne, D.; Fujita, Y.; Grewe, E. W.; Haefner, P.; Harakeh, M. N.; Hunyadi, M.; Jacobs, E.; Johansson, H.*; Junk, B. C.; Korff, A.; Negret, A.; Popescu, L.; Simon, H.*; Wörtche, H. J.: **Nuclear matrix elements for the ^{48}Ca two-neutrino double-β decay from high-resolution charge-exchange reactions.** *Physical review C, Nuclear physics* **70**(5): 054302. DOI:10.1103/PhysRevC.70.054302

P-H151 Regan, P. H.; Valiente-Dobón, J. J.; Wheldon, C.*; Wu, C. Y.; Smith, J. F.; Macchiavelli, A. O.; Cline, D.; Chakrawarthy, R. S.; Chapman, R.; Cromaz, M.; Fallon, P.; Freeman, S. J.; Görgen, A.; Gelletly, W.; Hayes, A.; Langdown, S. D.; Lee, I. Y.; Liang, X.; Pearson, C. J.; Podolyák, Z.; Teng, R.; Ward, D.; Warner, D. D.; Yamamoto, A. D.: **Production of exotic nuclear isomers in multi-nucleon transfer reactions.** *Laser Physics Letters* **1**(6): 317–324. DOI:10.1002/lapl.200410073

P-H152 Reisdorf, W.*: **Constraints on the equation of state of nuclear matter from nucleus-nucleus collisions.** *Nuclear physics A, Nuclear and hadronic physics* **734**: 565–572. [Proceedings of the Eighth International Conference On Nucleus-Nucleus Collisions] DOI:10.1016/S0375-9474(04)90345-4

P-H153 Reisdorf, W.*: **EOS information from heavy ion collisions between 0.1A and 2A GeV.** *Abstracts of papers American Chemical Society* **228**: U13–U13.

P-H154 Reisdorf, W.*; Andronic, A.*; Gobbi, A.*; Hartmann, O. N.*; Herrmann, N.; Hildenbrand, K. D.*; Kim, Y. J.*; Kirejczyk, M.*; Koczoń, P.*; Kress, T.*; Leifels, Y.*; Schüttauf, A.*; Tymiński, Z.*; Xiao, Z. G.*; Alard, J. P.; Barret, V.; Basrak, Z.; Bastid, N.; Benabderrahmane, M. L.; Čaplar, R.; Crochet, P.; Dupieux, P.; Dželalija, M.; Fodor, Z.; Grishkin, Y.; Hong, B.; Kecskemeti, J.; Korolija, M.; Kotte, R.; Lebedev, A.; Lopez, X.; Merschmeyer, M.; Mösner, J.; Neubert, W.; Pelte, D.; Petrovici, M.; Rami, F.; de Schauenburg, B.; Seres, Z.; Sikora, B.; Sim, K. S.; Simion, V.; Siwek-Wilczyńska, K.; Smolyankin, V.; Stockmeier, M.; Stoicea, G.; Wagner, P.; Wiśniewski, K.; Wohlfarth, D.; Yushmanov, I.; Zhilin, A.; FOPI Collaboration*: **Nuclear stopping from 0.09A to 1.93A GeV and its correlation to flow.** *Physical review letters* **92**(23): 232301. DOI:10.1103/PhysRevLett.92.232301

P-H155 Reisdorf, W.*; Rami, E.; de Schauenburg, B.; Leifels, Y.*; Alard, J. P.; Andronic, A.*; Barret, V.; Basrak, Z.; Bastid, N.; Benabderrahmane, M. L.; Čaplar, R.; Crochet, P.; Dupieux, P.; Dželalija, M.; Fodor, Z.; Gobbi, A.*; Grishkin, Y.; Hartmann, O. N.*; Herrmann, N.; Hildenbrand, K. D.*; Hong, B.; Kecskemeti, J.; Kim, Y. J.*; Kirejczyk, M.*; Koczoń, P.*; Korolija, M.; Kotte, R.; Kress, T.*; Lebedev, A.; Lopez, X.; Merschmeyer, M.; Mösner, J.; Neubert, W.; Pelte, D.; Petrovici, M.; Schüttauf, A.*; Seres, Z.; Sikora, B.*GAST; Sim, K. S.; Siwek-Wilczyńska, K.; Smolyankin, V.; Stockmeier, M.; Stoicea, G.; Tymiński, Z.*; Wagner, P.; Wiśniewski, K.; Wohlfarth, D.; Xiao, Z. G.*; Yushmanov, I.; Zhilin, A.; FOPI Collaboration*: **Droplet formation in expanding nuclear matter: a system-size dependent study.** *Physics letters B* **595**: 118–126. DOI:10.1016/j.physletb.2004.05.031

P-H156 Ricciardi, M. V.*; Ignatyuk, A. V.; Kelic, A.*; Napolitani, P.*; Rejmund, E.; Schmidt, K. H.*; Yordanov, O.*: **Complex nuclear-structure phenomena revealed from the nuclide production in fragmentation reactions.** *Nuclear physics A, Nuclear and hadronic physics* **733**(3): 299–318. DOI:10.1016/j.nuclphysa.2004.01.069

P-H157 Riek, F.*; Knoll, J.*: **Selfconsistent description of vector-mesons in matter.** *Nuclear physics A, Nuclear and hadronic physics* **740**(3): 287–308. DOI:10.1016/j.nuclphysa.2004.05.010

P-H158 Roth, R.; Neff, T.*; Hegert, H.; Feldmeier, H.*: **Nuclear structure based on correlated realistic nucleon-nucleon potentials.** *Nuclear physics A, Nuclear and hadronic physics* **745**(1): 3–33. DOI:10.1016/j.nuclphysa.2004.08.024

P-H159 Russkikh, V. N.*; Ivanov, Y. B.*; Nikonov, E. G.*; Nörenberg, W.*; Toneev, V. D.*: **Evolution of baryon-free matter produced in relativistic heavy-ion collisions.** *Physics of atomic nuclei* **67**(1): 199–208. DOI:10.1134/1.1644024

P-H160 Sako, H.*; Appelshäuser, H.*; CERES NA45 Collaboration*: **Event-by-event fluctuations at 40, 80 and 158 A GeV/c in Pb+Au collisions.** *Journal of physics G, Nuclear and particle physics* **30**(8): S1371–S1375. DOI:10.1088/0954-3899/30/8/130

P-H161 Salabura, P.*; Agakichiev, G.*; Agodi, C.; Alvarez-Pol, H.; Balanda, A.; Bellia, G.; Belver, D.; Bielcik, J.*; Böhmer, M.; Bokemeyer, H.*; Boyard, J.; Braun-Munzinger, P.*; Chepurnov, V.; Chernenko, S.; Christ, T.; Coniglione, R.; Diaz, J.; Djeridi, R.; Dohrmann, F.; Duran, I.; Eberl, T.; Emeljanov, V.; Fabbietti, L.; Fateev, O.; Fernandez, C.; Finocchiaro, P.; Friese, J.; Fröhlich, I.; Fuentes, B.; Garzon, J.; Gernhäuser, R.; Golubeva, M.; Gonzalez, D.; Grosse, E.; Guber, F.; Hennino, T.; Hlavac, S.; Hoffmann, J.*; Holzmann, R.*; Ierusalimov, A.; Iori, I.; Jaskula, M.; Jurkovic, M.; Kämpfer, B.; Kanaki, K.; Karavicheva, T.; Koenig, I.*; Koenig, W.*; Kolb, B.*; Kotte, R.; Kotulic-Bunta, J.; Krücken, R.; Kugler, A.; Kuhn, W.; Kulessa, R.; Kurepin, A.; Kurtukian-Nieto, T.; Lang, S.*; Lehner, J.; Maiolino, C.; Marn, J.; Markert, J.; Metag, V.; Montes, N.; Mousa, J.; Münch, M.; Müntz, C.; Naumann, L.; Novotny, J.; Otwinowski, J.; Pachmayer, Y.*; Panebratsev, Y.; Pechenov, V.; Perez, T.; Pietraszko, J.*; Pleskac, R.; Pospisil, V.; Przygoda, W.; Rabin, N.; Ramstein, B.; Reshetin, A.; Ritman, J.; Rodriguez-Prieto, G.; Roy-Stephan, M.; Rustamov, A.*; Sabin-Fernandez, J.; Sadovsky, A.; Sailer, B.; Sanchez, M.; Smolyankin, V.; Smykov, L.; Spataro, S.; Spruck, B.; Stroebele, H.; Stroth, J.*; Sturm, C.*; Sudol, M.*; Titov, A.; Tlusty, P.; Toia, A.; Traxler, M.*; Tsertos, H.; Vazquez, A.; Volkov, Y.; Wagner, V.; Walus, W.; Winkler, S.; Wisniowski, M.; Wojcik, T.; Wüstenfeld, J.; Zanevsky, Y.; Zumbruch, P.*; HADES Collaboration*: **Study of e^+, e^- production in elementary and nuclear collisions near the production threshold with HADES.** *Progress in particle and nuclear physics* **53**(1): 49–58. DOI:10.1016/j.ppnp.2004.02.037

P-H162 Salabura, P.*; HADES Collaboration*: **Studying in-medium hadron properties with HADES.** *Acta physica Polonica B, Particle physics and field theory, nuclear physics, theory of relativity* **35**(3): 1119–1129.

P-H163 Sawicka, M.; Matea, I.; Grawe, H.*; Grzywaczi, R.; Pfützner, M.; Lewitowicz, M.; Daugas, J. M.; Brown, B. A.; Lisetskiy, A.; Becker, F.*; Bélier, G.; Bingham, C.; Borcea, R.; Bouchez, E.; Buta, A.; Dragulescu, E.; de France, G.; Georgiev, G.; Giovinazzo, J.; Hammache, F.; Ibrahim, F.; Mayet, P.; Méot, V.; Negoita, F.; De Oliveira-Santos, F.; Perru, O.; Roig, O.; Rykaczewski, K.; Saint-Laurent, M. G.; Sauvestre, J. E.; Sorlin, O.; Stanoiu, M.; Stefan, I.; Stodel, C.; Theisen, C.; Verny, D.; Żylicz, J.: **Beta-decay of ^{71}Co and ^{73}Co.** *The European physical journal A, Hadrons and nuclei* **22**(3): 455–459. DOI:10.1140/epja/i2004-10047-3

P-H164 Sawicka, M.; Pfützner, M.; Grzywacz, R.; Daugas, J. M.; Matea, I.; Lewitowicz, M.; Grawe, H.*; Becker, F.*; Bélier, G.; Bingham, C.; Borcea, R.; Bouchez, E.; Buta, A.; Dragulescu, E.; Sauvestre, J. E.; Georgiev, G.; Giovinazzo, J.; Hammache, F.; Ibrahim, F.; Mayet, P.*; Méot, V.; Negoita, F.; de Oliveira Santos, F.; Perru, O.; Roig, O.; Rykaczewski, K. P.; Saint-Laurent, M. G.; Sorlin, O.; Stanoiu, M.; Stefan, I.; Stodel, C.; Theisen, C.; Verney, D.: **Evidence for an isomer in ^{76}Ni.** *The European physical journal A, Hadrons and nuclei* **20**(1): 109–110. DOI:10.1140/epja/i2002-10333-0

P-H165 Scheidenberger, C.*; Attallah, F.*; Beckert, K.*; Beller, P.*; Bosch, F.*; Boutin, D.*; Eickhoff, H.*; Faestermann, T.; Falch, M.; Franczak, B.*; Franzke, B.*; Geissel, H.*; Hausmann, M.*; Hellström, M.*; Kaza, E.*; Kerscher, T.; Klepper, O.*; Kluge, H.-J.*; Koyama, R.; Kozhuharov, C.*; Kratz, K. L.; Litvinov, Y. A.*; Löbner, K.; Maier, L.; Matos, M.*; Münzenberg, G.*; Nolden, F.*; Novikov, Y. N.*; Ohtsubo, T.; Ostrowski, A.; Ozawa, A.; Patyk, Z.; Pfeiffer, B.; Portillo, M.*; Quint, W.*; Radon, T.*; Shishkin, V.*; Stadlmann, J.*; Steck, M.*; Sümmerer, K.*; Suzuki, T.; Trzhaskovskaja, M. B.; Vieira, D. J.; Watanabe, S.; Weick, H.*; Winkler, M.*; Wollnik, H.; Yamaguchi, T.*: **Study of basic nuclear properties of highly-charged, unstable nuclei at the SIS-FRS-ESR complex.** *Heavy ion physics* **19**(1): 165–170. Also part of: 'Large-scale facilities for research with photons, neutrons and ions'.

P-H166 Scheidenberger, C.*; Pshenichnov, I. A.*; Sümmerer, K.*; Ventura, A.; Bondorf, J. P.; Botvina, A. S.*; Mishustin, I. N.; Boutin, D.*; Datz, S.; Geissel, H.*; Grafström, P.; Knudsen, H.; Krause, H. F.; Lommel, B.*; Møller, S. P.; Münzenberg, G.*; Schuch, R. H.; Uggerhøj, E.; Uggerhøj, U.; Vane, C. R.; Vilakazi, Z. Z.; Weick, H.*: **Charge-changing interactions of ultrarelativistic Pb nuclei.** *Physical review C, Nuclear physics* **70**(1): 014902. DOI:10.1103/PhysRevC.70.014902

P-H167 Schenke, B.; Greiner, C.*: **Statistical description with anisotropic momentum distributions for hadron production in nucleus-nucleus collisions.** *Journal of physics G, Nuclear and particle physics* **30**(5): 597–606. DOI:10.1088/0954-3899/30/5/004

P-H168 Schmitt, C.*; Jurado, B.*; Junghans, A. R.*; Schmidt, K. H.*; Benlliure, J.: **Modelling of dissipation in nuclear fission.** *International journal of modern physics E, Nuclear physics* **13**(1): 97–101. DOI:10.1142/S0218301304001783

P-H169 Schüttauf, A.*: **Timing RPCs in FOPI.** *Nuclear instruments & methods in physics research, Section A, Accelerators, spectrometers, detectors and associated equipment* **533**(1): 65–68. [Proceedings of the Seventh International Workshop on Resistive Plate Chambers and Related Detectors, Clermont-Ferrand, France, 20031020/22] DOI:10.1016/j.nima.2004.07.002

P-H170 Schwenk, A.; Friman, B.*: **Polarization contributions to the spin dependence of the effective interaction in neutron matter.** *Physical review letters* **92**(8): 082501. DOI:10.1103/PhysRevLett.92.082501

P-H171 Sfienti, C.; Baran, V.; De Napoli, M.; Imme, G.; Raciti, G.; Rapisarda, E.; Rascuna, S.; Spezzi, L.: **Temperature and density in heavy ion reactions at intermediate energies.** *Nuclear physics A, Nuclear and hadronic physics* **734**: 528–531. [Proceedings of the Eighth International Conference On Nucleus-Nucleus Collisions] DOI:10.1016/S0375-9474(04)90337-5

P-H172 Shevchenko, A.; Carter, J.; Fearick, R. W.; Fortsch, S. V.; Fujita, H.; Fujita, Y.; Kalmykov, Y.; Lacroix, D.; Lawrie, J. J.; von Neumann-Cosel, P.; Neveling, R.; Ponomarev, V. Y.; Richter, A.; Sideras-Haddad, E.; Smit, F. D.; Wambach, J.: **Fine structure in the energy region of the isoscalar giant quadrupole resonance: Characteristic scales from a wavelet analysis.** *Physical review letters* **93**(12): 122501. DOI:10.1103/PhysRevLett.93.122501

P-H173 Simon, H.*; Aumann, T.*; Borge, M. J. G.; Chulkov, L. V.*; Elze, T. W.; Emling, H.*; Forssen, C.; Geissel, H.*; Hellström, M.*; Jonson, B.; Kratz, J. V.; Kulessa, R.; Leifels, Y.*; Markenroth, K.; Meister, M.*; Münzenberg, G.*; Nickel, F.*; Nilsson, T.; Nyman, G.; Pribora, V.; Richter, A.; Rüsager, K.; Scheidenberger, C.*; Schrieder, G.*; Tengblad, O.; Zhukov, M. V.: **Two- and three-body correlations: breakup of halo nuclei.** *Nuclear physics A, Nuclear and hadronic physics* **734**: 323–326. [Proceedings of the Eighth International Conference On Nucleus-Nucleus Collisions] DOI:10.1016/S0375-9474(04)90299-0

P-H174 Sohler, D.; Timár, J.; Dombrádi, Z.; Cederkäll, J.; Huijnen, J.; Lipoglavšek, M.; Palacz, M.; Atac, A.; Fahlander, C.; Grawe, H.*; Johnson, A.; Kerek, A.; Klamra, W.; Kownacki, J.; Likar, A.; Norlin, L. O.; Nyberg, J.; Persson, J.; Seweryniak, D.; de Angelis, G.; Bednarczyk, P.; Foltescu, D.; Jerrestam, D.; Juutinen, S.; Makela, E.; de Poli, M.; Roth, H. A.; Shizuma, T.; Skeppstedt, O.; Sletten, G.; Tormänen, S.; Weiszflog, M.: **Band-terminating states in ^{101}Ag.** *Nuclear physics A, Nuclear and hadronic physics* **733**(1): 37–52.

P-H175 Stadlmann, J.*; Hausmann, M.*; Attallah, F.*; Beckert, K.*; Beller, P.*; Bosch, F.*; Eickhoff, H.*; Falch, M.; Franczak, B.*; Franzke, B.*; Geissel, H.*; Kerscher, T. H.; Klepper, O.*; Kluge, H.-J.*; Kozhuharov, C.*; Litvinov, Y. A.*; Löbner, K. E. G.; Matoš, M.*; Münzenberg, G.*; Nankov, N.*; Nolden, F.*; Novikov, Y. N.; Ohtsubo, T.*; Radon, T.*; Schatz, H.; Scheidenberger, C.*; Steck, M.*; Weick, H.*; Wollnik, H.: **Direct mass measurement of bare short-lived ^{44}V, ^{48}Mn, ^{41}Ti and ^{45}Cr ions with isochronous mass spectrometry.** *Physics letters B* **586**(1): 27–33.

DOI:10.1016/j.physletb.2004.02.014 Also part of: 'Large-scale facilities for research with photons, neutrons and ions'; Scientific Infrastructure.

P-H176 Stanoiu, M.; Azaiez, F.; Becker, F.; Belleguic, M.; Borcea, C.; Bourgeois, C.; Brown, B. A.; Dlouhý, Z.; Dombrádi, Z.; Fülöp, Z.; Grawe, H.; Grévy, S.; Ibrahim, F.; Kerek, A.; Krasznahorkay, A.; Lewitowicz, M.; Lukyanov, S.*; van der Marel, H.; Mayet, P.; Mrázek, J.; Mandal, S.; Guillemaud-Mueller, D.; Negoita, F.; Penionzhkevich, Y. E.*; Podolyák, Z.; Roussel-Chomaz, P.; Saint Laurent, M. G.; Savajols, H.; Sorlin, O.; Sletten, G.; Sohler, D.; Timár, J.; Timis, C.; Yamamoto, A.: **Study of drip line nuclei through two-step fragmentation.** *The European physical journal A, Hadrons and nuclei* **20**(1): 95–96. DOI:10.1140/epja/i2002-10329-8

P-H177 Stanoiu, M.; Azaiez, F.; Dombradi, Z.; Sorlin, O.; Brown, B. A.; Belleguic, M.; Sohler, D.; Saint Laurent, M. G.; Lopez-Jimenez, M. J.; Penionzhkevich, Y. E.; Sletten, G.; Achouri, N. L.; Angelique, J. C.; Becker, F.; Borcea, C.; Bourgeois, C.; Bracco, A.; Daugas, J. M.; Dlouhý, Z.; Donzaud, C.; Duprat, J.; Fülöp, Z.; Guillemaud-Mueller, D.; Grevý, S.; Ibrahim, F.; Kerek, A.; Krasznahorkay, A.; Lewitowicz, M.; Leenhardt, S.; Lukyanov, S.; Mayet, P.*; Mandal, S.*; van der Marel, H.; Mittig, W.; Mrázek, J.*; Negoita, F.; De Oliveira-Santos, F.; Podolyák, Z.; Pougheon, F.; Porquet, M. G.; Roussel-Chomaz, P.; Savajols, H.; Sobolev, Y.; Stodel, C.; Timár, J.; Yamamoto, A.: **N=14 and 16 shell gaps in neutron-rich oxygen isotopes.** *Physical review C, Nuclear physics* **69**(3): 034312. DOI:10.1103/PhysRevC.69.034312

P-H178 Stanoiu, M.; Azaiez, F.; Dombrádi, Z.; Sorlin, O.; Brown, B. A.; Belleguic, M.; Sohler, D.; Saint Laurent, M. G.; Penionzhkevich, Y. E.; Sletten, G.; Borcea, C.; Bourgeois, C.; Bracco, A.; Daugas, J. M.; Dlouhý, Z.; Donzaud, C.; Fülöp, Z.; Guillemaud-Mueller, D.; Grévy, S.; Ibrahim, F.; Kerek, A.; Krasznahorkay, A.; Lewitowicz, M.; Lukyanov, S.; Mayet, P*.; Mandal, S.*; Mittig, W.; Mrázek, J.; Negoita, F.; De Oliveira-Santos, F.; Podolyák, Z.; Pougheon, F.; Roussel-Chomaz, P.; Savajols, H.; Sobolev, Y.; Stodel, C.; Timar, J.; Yamamoto, A.: **Study of neutron rich carbon and oxygen nuclei up to drip line.** *Nuclear physics A, Nuclear and hadronic physics* **746**: 135C–139C. [Proceedings of the Sixth International Conference on Radioactive Nuclear Beams (RNB6) Argonne 20030922/26] DOI:10.1016/j.nuclphysa.2004.09.022

P-H179 Stiebing, E.; de Boer, F. W. N.; Fröhlich, O.; Bokemeyer, H.*; Müller, K. A.; Bethge, K.; van Klinken, J.: **A multi-detector array for high energy nuclear e^+e-^- pair spectroscopy.** *Journal of physics G, Nuclear and particle physics* **30**(2): 165–180. DOI:10.1088/0954-3899/30/2/014

P-H180 Stoicea, G.; Petrovici, M.*; Andronic, A.*; Herrmann, N.; Alard, J. P.; Basrak, Z.; Barret, V.; Bastid, N.; Čaplar, R.; Crochet, P.; Dupieux, P.; Dželalija, M.; Fodor, Z.; Hartmann, O.*; Hildenbrand, K. D.*; Hong, B.; Kecskemeti, J.; Kim, Y. J.; Kirejczyk, M.; Korolija, M.; Kotte, R.; Kress, T.; Lebedev, A.; Leifels, Y.*; Lopez, X.; Merschmeier, M.; Neubert, W.; Pelte, D.; Rami, F.; Reisdorf, W.*; Schüll, D.; Seres, Z.; Sikora, B.; Sim, K. S.; Simion, V.; Siwek-Wilczyńska, K.; Smolyankin, V.; Stockmeier, M.; Wiśniewski, K.*; Wohlfarth, D.; Yushmanov, I.; Zhilin, A.; Danielewicz, P.*; FOPI Collaboration*: **Azimuthal dependence of collective expansion for symmetric heavy-ion collisions.** *Physical review letters* **92**(7): 072303. DOI:10.1103/PhysRevLett.92.072303

P-H181 Sümmerer, K.*; S233 Collaboration: **Coulomb dissociation of high-energy radioactive beams: the case of ^8B.** *Nuclear physics A, Nuclear and hadronic physics* **746**: 544C–547C. [Proceedings of the Sixth International Conference on Radioactive Nuclear Beams (RNB6) Argonne 20030922/26] DOI:10.1016/j.nuclphysa.2004.09.087

P-H182 Sumikama, T.; Iwakoshi, T.; Nagatomo, T.; Ogura, M.; Nakashima, Y.; Fujiwara, H.; Matsuta, K.; Minamisono, T.; Mihara, M.; Fukuda, M.; Minamisono, K.; Yamaguchi, T.*: **Beta-ray angular distributions of spin aligned ^{8}Li and ^{8}B.** *Nuclear physics A, Nuclear and hadronic physics* **746**: 681C–684C. [Proceedings of the Sixth International Conference on Radioactive Nuclear Beams (RNB6) Argonne 20030922/26] DOI:10.1016/j.nuclphysa.2004.09.050

P-H183 Suzuki, K.; Fujita, M.; Geissel, H.*; Gilg, H.; Gillitzer, A.; Hayano, R. S.; Hirenzaki, S.; Itahashi, K.; Iwasaki, M.; Kienle, P.; Matos, M.; Münzenberg, G.*; Ohtsubo, T.; Sato, M.; Shindo, M.; Suzuki, T.; Weick, H.*; Winkler, M.*; Yamazaki, T.; Yoneyama, T.: **Precision spectroscopy of pionic 1s states of sn nuclei and evidence for partial restoration of chiral symmetry in the nuclear medium.** *Physical review letters* **92**(7): 072302. DOI:10.1103/PhysRevLett.92.072302

P-H184 Talanov, Y.; Adrian, H.; Basset, M.; Jakob, G.; Wirth, G.*: **Shift of the surface-barrier part of the irreversibility line due to columnar defects in $Bi_2Sr_2CaCu_2O_8$ thin films.** *Physica C, Superconductivity and its applications* **402**(1): 114–118. DOI:10.1016/j.physc.2003.09.068

P-H185 Toneev, V. D.*; Nikonov, E. G.*; Friman, B.*; Nörenberg, W.*; Redlich, K.: **Strangeness production in nuclear matter and expansion dynamics.** *The European physical journal: C, Particles and fields* **32**(3): 399–415. DOI:10.1140/epjc/s2003-01374-2

P-H186 Trimble, W.; Savard, G.; Blank, G.; Clark, J. A.; Buchinger, F.; Cocolios, T.; Crawford, J. E.; Frankel, A.; Greene, J. P.; Gulick, S.; Lee, J. K. P.; Levand, A.; Portillo, M.*; Sharma, K. S.; Wang, J. C.; Zabransky, B. J.; Zhou, Z.; S258 Collaboration*: **Development and first on-line tests of the RIA gas catcher prototype.** *Nuclear physics A, Nuclear and hadronic physics* **746**: 415C–418C. [Proceedings of the Sixth International Conference on Radioactive Nuclear Beams (RNB6) Argonne 20030922/26] DOI:10.1016/j.nuclphysa.2004.09.110

P-H187 Tumino, A.; Spitaleri, C.; Pappalardo, L.; Cherubini, S.; Del Zoppo, A.; La Cognata, M.; Musumarra, A.; Pellegriti, M. G.; Pizzone, R. G.; Rinollo, A.; Rolfs, C.; Romano, S.; Typel, S.*: **Indirect study of the astrophysically relevant ^{6}Li(p, α)^{3}He reaction by means of the Trojan Horse Method.** *Progress of theoretical physics Supplement* (154): 341–348.

P-H188 Tumino, A.; Spitaleri, C.; Pappalardo, L.; Cherubini, S.; Del Zoppo, A.; La Cognata, M.; Musumarra, A.; Pellegriti, M. G.; Pizzone, R. G.; Rinollo, A.; Romano, S.; Typel, S.*: **The Trojan-Horse Method applied to the $^6Li(p,\alpha)^3He$**

reaction down to astrophysical energies. *Nuclear physics A, Nuclear and hadronic physics* **734**: 639–642. [Proceedings of the Eighth International Conference On Nucleus-Nucleus Collisions] DOI:10.1016/S0375-9474(04)90357-0

P-H189 Typel, S.*; Baur, G.: **Effective-range approach and scaling laws for electromagnetic strength in neutron-halo nuclei.** *Physical review letters* **93**(14): 142502. DOI:10.1103/PhysRevLett.93.142502

P-H190 Ukai, M.; Ajimura, S.; Akikawa, H.; Alburger, D. E.; Banu, A.*; Chrien, R. E.; Franklin, G. B.; Franz, J.; Hashimoto, O.; Hayakawa, T.; Hotchi, H.; Imai, K.; Kishimoto, T.; May, M.; Millener, D. J.; Minami, S.; Miura, Y.; Miyoshi, T.; Mizunuma, K.; Nagae, T.; Nakamura, S. N.; Nakazawa, K.; Okayasu, Y.; Pile, P.; Quinn, B. P.; Rusek, A.; Sato, Y.; Sutter, R.; Takahashi, H.; Tang, L.; Tamura, H.; Tanida, K.; Yuan, L.; Zhou, S. H.; E930 01 Collaboration*: **Hypernuclear fine structure in $^{16}_{\Lambda}$O and the ΛN tensor interaction.** *Physical review letters* **93**(23): 232501. DOI:10.1103/PhysRevLett.93.232501

P-H191 Valiente-Dobón, J. J.; Regan, R. H.; Wheldon, C.*; Wu, C. Y.; Yoshinaga, N.; Higashiyama, K.; Smith, J. F.; Cline, D.; Chakrawarthy, R. S.; Chapman, R.; Cromaz, M.; Fallon, P.; Freeman, S. J.; Gorgen, A.; Gelletly, W.; Hayes, A.; Hua, H.; Langdown, S. D.; Lee, I. Y.; Liang, X.; Macchiavelli, A. O.; Pearson, C. J.; Podolyak, Z.; Sletten, G.; Teng, R.; Ward, D.; Warner, D. D.; Yamamoto, A. D.: **^{136}Ba studied via deep-inelastic collisions: Identification of the $(\nu h_{11/2})^{-2}_{10+}$ isomer.** *Physical review C, Nuclear physics* **69**(2): 024316. DOI:10.1103/PhysRevC.69.024316

P-H192 Van Roosbroeck, J.; Guénaut, C.; Audi, G.; Beck, D.*; Blaum, K.*; Bollen, G.; Cederkall, J.; Delahaye, P.; De Maesschalck, A.; De Witte, H.; Fedorov, D.; Fedoseyev, V. N.; Franchoo, S.; Fynbo, H. O. U.; Górska, M.*; Herfurth, F.; Heyde, K.; Huyse, M.; Kellerbauer, A.; Kluge, H.-J.*; Koster, U.; Kruglov, K.; Lunney, D.; Mishin, V. I.; Mueller, W. F.; Nagy, S.; Schwarz, S.; Schweikhard, L.; Smirnova, N. A.; Van de Vel, K.; Van Duppen, P.; Van Dyck, A.; Walters, W. B.; Weissman, L.; Yazidjian, C.*: **Unambiguous identification of three β-decaying isomers in ^{70}Cu.** *Physical review letters* **92**(11): 112501. DOI:10.1103/PhysRevLett.92.112501 Also part of: 'Large-scale facilities for research with photons, neutrons and ions'.

P-H193 Vidaña, I.*; Tolos, L.: **Superfluidity of Σ^- hyperons in β-stable neutron star matter.** *Physical review C, Nuclear physics* **70**(2): 028802. DOI:10.1103/PhysRevC.70.028802

P-H194 Volant, C.; Turzó, K.*; Trautmann, W.*; Auger, G.; Begemann-Blaich, M. L.*; Bittiger, R.*; Borderie, B.; Botvina, A. S.*; Bougault, R.; Bouriquet, B.; Charvet, J. L.; Chbihi, A.; Dayras, R.; Doré, D.; Durand, D.; Frankland, J. D.; Galichet, E.; Gourio, D.*; Guinet, D.; Hudan, S.; Immé, G.; Lautesse, P.; Lavaud, F.; Le Fèvre, A.*; Lopez, O.; Łukasik, J.*; Lynen, U.*; Müller, W. F. J.*; Nalpas, L.; Orth, H.*; Plagnol, E.; Raciti, G.; Rosato, E.; Saija, A.; Schwarz, C.*; Seidel, W.; Sfienti, C.*; Steckmeyer, J. C.; Tamain, B.; Trzciński, A.; Vient, E.; Vigilante, M.; Zwieglinski, B.; INDRA and ALADIN Collaborations*: **Intranuclear cascade+percolation+evaporation model applied to the $^{12}C + ^{197}Au$ system at 1 GeV/nucleon.** *Nuclear physics A, Nuclear and hadronic physics* **734**: 545–548. [Proceedings of the Eighth International Conference On Nucleus-Nucleus Collisions] DOI:10.1016/S0375-9474(04)90341-7

P-H195 von Oertzen, W.; Peter, I.*; Thummerer, S.; Bohlen, H. G.; Gebauer, B.; Gerl, J.*; Kaspar, M.*; Kozhoukharov, I.*; Kröll, T.; Rejmund, M.*; Wollersheim, H. J.*: **Selection of cold transfer and enhanced neutron-pair transfer in the $^{206}Pb + ^{117}$Sn reaction.** *The European physical journal A, Hadrons and nuclei* **20**(1): 153–156. DOI:10.1140/epja/i2002-10342-y

P-H196 von Zweidorf, A.*; Angert, R.*; Brüchle, W.*; Bürger, S.; Eberhardt, K.; Eichler, R.; Hummrich, H.; Jäger, E.*; Kling, H.-O.; Kratz, J. V.; Kuczewski, B.; Langrock, G.; Mendel, M.; Rieth, U.; Schädel, M.*; Schausten, B.*; Schimpf, E.*; Thorle, P.; Trautmann, N.; Tsukada, K.; Wiehl, N.; Wirth, G.*: **Evidence for the formation of sodium hassate(VIII).** *Radiochimica acta* **92**(12): 855–861. DOI:10.1524/ract.92.12.855.55112

P-H197 Voskresensky, D. N.*: **Fluctuations of the color-superconducting gap in hot and dense quark matter.** *Physical review C, Nuclear physics* **69**(6): 065209. DOI:10.1103/PhysRevC.69.065209

P-H198 Voskresensky, D. N.*: **Hadron liquid with a small baryon chemical potential at finite temperature.** *Nuclear physics A, Nuclear and hadronic physics* **744**: 378–444. DOI:10.1016/j.nuclphysa.2004.08.018

P-H199 Wheldon, C.*; Stuchbery, A. E.; Wilson, A. N.; Dracoulis, G. D.; Bruce, A. M.; Bark, R. A.; Byrne, A. P.; Prados-Estevez, F. M.; Lane, G. J.; Moon, C. B.; Orce, J. N.; Wood, R.: **Electromagnetic properties of pseudo-Nilsson bands in ^{185}Os.** *The European physical journal A, Hadrons and nuclei* **19**(3): 319–325. DOI:10.1140/epja/i2003-10131-2

P-H200 Wheldon, C.*; Valiente-Dobón, J. J.; Regan, P. H.; Pearson, C. J.; Wu, C. Y.; Smith, J. F.; Macchiavelli, A. O.; Cline, D.; Chakrawarthy, R. S.; Chapman, R.; Cromaz, M.; Fallon, P.; Freeman, S. J.; Görgen, A.; Gelletly, W.; Hayes, A.; Hua, H.; Langdown, S. D.; Lee, I. Y.; Liang, X.; Podolyák, Z.; Sletten, G.; Teng, R.; Ward, D.; Warner, D. D.; Yamamoto, A. D.: **Multi-quasi particle states in ^{184}W via multi-nucleon transfer.** *The European physical journal A, Hadrons and nuclei* **20**(3): 365–369. DOI:10.1140/epja/i2003-10189-8

P-H201 Wojtasiewicz, A.; Canchel, G.; Emsallem, A.; Gierlik, M.; Janas, Z.; Kisielinski, M.; Kurcewicz, W.; Kuppeta, J.; Lefort, H.; Lewandowski, S.; Penttila, H.; Plochocki, A.; Roeckl, E.*; Roussiere, B.; Sidor, S.; Syntfeldt, A.: **Investigation of a gas catcher/ion guide system at the Warsaw cyclotron.** *Nuclear physics A, Nuclear and hadronic physics* **746**: 663C–666C. [Proceedings of the Sixth International Conference on Radioactive Nuclear Beams (RNB6) Argonne 20030922/26] DOI:10.1016/j.nuclphysa.2004.09.047

P-H202 Wolf, G.; Lutz, M. F. M.*; Friman, B.*: **Vector mesons in nuclear matter.** *Heavy ion physics* **19**(3): 301–304.

2. Further publications

P-H001nr Agakishiev, G.; Agodi, C.; Alvarez-Pol, H.; et al.: **Dilepton Analysis im the HADES Sprectrometer for ^{12}C+^{12}C at 2AGeV**. In: Iori, I. (Ed.): *Proceedings of the XLII International Winter Meeting on Nuclear Physics*. Ricerca Scientifica ed Educazione Permanente; Suppl. 123, Milano: Dipartimento di Fisica, Università degli Studi di Milano, 2004. XLII International Winter Meeting on Nuclear Physics, Bormio, 26.01.2004-31.01.2004, 180-189p. DOI:10.1007/b98790

P-H002nr Al-Khalili, J.; Roeckl, E.: **The Euroschool Lectures on Physics with Exotic Beams Vol. I**. Lectures Notes in Physics; 651. Berlin, Heidelberg, New York: Springer, 2004. DOI:10.1007/b98790

P-H003nr Aumann, T.*: **Collective and Single-Particle Properties of Neutron-Rich Nuclei Investigated via Reactions of Relativistic Radioactive Beams**. In: Bracco, A.; Kalfas, C. (Eds.): *The Labyrinth in Nuclear Structure*. AIP Conf. Proc. Vol. 701, Melville/New York, 2004. EPS International Conf. on 'The Labyrinth in Nuclear Structure', Crete, 87.

P-H004nr Aumann, T.*: **The structure of exotic nuclei investigated via scattering experiments with fast fragmentation beams at GSI**. In: Suzuki, Y.; Ohya, S.; Matsuo, M.; Ohtsubo, T. (Eds.): *A New Era of Nuclear Structure Physics,*. International Symposium 'A New Era of Nuclear Structure Physics', Kurokawa Village, Niigata, 2004.

P-H005nr Cortina-Gil, D.; et al.: **Spectroscopy of Light Exotic Nuclei Using Nuclear Break-Up**. In: Bracco, A.; Kalfas, C. (Eds.): *The Labyrinth in Nuclear Structure*. AIP Conf. Proc. Vol. 701, Melville/New York, 2004. EPS International Conf. on 'The Labyrinth in Nuclear Structure', Crete, 112.

P-H006nr Denisov, V. Y.: **Superheavy element production, nucleus-nucleus potential and μ-catalysis**. In: Arnould, M.; Lewitowicz, M.; Münzeberg, G.*; Akimune, H.; Ohta, M.; Utsunaomiya, H.; Wada, T.; Yamagata, T. (Eds.): *Tours Symposium on Nuclear Physics, Tours 2003*. AIP Conference Proceedings Vol. 704, Melville/New York: AIP, 2004, 92-101p.

P-H007nr Feldmeier, H.*; Neff, T.*; Roth, R.: **Nuclear structure - ab initio**. In: Suzuki, Yasuyuki (Ed.): *A new era of nuclear structure physics : proceedings of the international symposium, Kurokawa Village, Niigata, Japan, 19 - 22 November 2003*, Singapore [u. a.]: World Scientific, 2004. International Symposium A New Era of Nuclear Structure Physics, Niigata, 11.11.2003-18.11.2003, 61.

P-H008nr Finocchiaro, P.; Salabura, P.*: **Dielectron Spectrometry with HADES.** *Nuclear Phyiscs News* **14**(3), 2004, 27-33p.

P-H009nr Hofmann, S.*; Münzenberg, G.*; Schädel, M.*: **On the Discovery of Superheavy Elements.** *Nuclear Physics News* **14**(4), 2004, 5-13p.

P-H010nr Hofmann, S.: **Properties of heavy nuclei measured at the GSI SHIP**. In: Arnould, M.; Lewitowicz, M.; Münzeberg, G.*; Akimune, H.; Ohta, M.; Utsunaomiya, H.; Wada, T.; Yamagata, T. (Eds.): *Tours Symposium on Nuclear Physics, Tours 2003*. AIP Conference Proceedings Vol. 704, Melville/New York: AIP, 2004, 21-30p.

P-H011nr Holzmann, R.*: **The Physics Program of the HADES Experiment at GSI**. In: Iori, I. (Ed.): *Proceedings of the XLII International Winter Meeting on Nuclear Physics*. Ricerca Scientifica ed Educazione Permanente; Suppl. 123, Milano: Dipartimento di Fisica, Università degli Studi di Milano, 2004. XLII International Winter Meeting on Nuclear Physics, Bormio, 26.01.2004-31.01.2004, 161-170p. DOI:10.1007/b98790

P-H012nr Ignayuk, F.: **Effects of nuclear structure in the transport coefficients of large-scale collective motion**. In: Arnould, M.; Lewitowicz, M.; Münzeberg, G.*; Akimune, H.; Ohta, M.; Utsunaomiya, H.; Wada, T.; Yamagata, T. (Eds.): *Tours Symposium on Nuclear Physics, Tours 2003*. AIP Conference Proceedings Vol. 704, Melville/New York: AIP, 2004, 120-129p.

P-H013nr Janas, Z.; Batist, L.*; Blazhev, A.; Brüchle, W.; Döring, J.; Gierlik, M.; Górsk, M.; Grawe, H.; Faestermann, T.*; Harissopulos, S.; Jungclaus, A.; Karny, M.; Kavatsyuk, M.; Kavatsyuk, O.; Krichner, R.; La Commara, M.; Mazzochi, C.; Mukha, I.; Płochocki, A.; Roeckl, E.; Romoli, M.; Schädel, M.; Schwengner, R.; Żylicz, J.: **Recent results from β-decay studies in the ^{100}Sn region**. In: Arnould, M.; Lewitowicz, M.; Münzeberg, G.*; Akimune, H.; Ohta, M.; Utsunaomiya, H.; Wada, T.; Yamagata, T. (Eds.): *Tours Symposium on Nuclear Physics, Tours 2003*. AIP Conference Proceedings Vol. 704, Melville/New York: AIP, 2004, 176-184p.

P-H014nr Junghans, A. R.; Schmidt, K.; Heinz, A. M.*; Ignatyuk, A. V.: **Shell Stabilization in Compound Nucleus Survival**. In: Arnould, M.; Lewitowicz, M.; Münzeberg, G.*; Akimune, H.; Ohta, M.; Utsunaomiya, H.; Wada, T.; Yamagata, T. (Eds.): *Tours Symposium on Nuclear Physics, Tours 2003*. AIP Conference Proceedings Vol. 704, Melville/New York: AIP, 2004, 102-110p.

P-H015nr Kelic, A.*: **Basic Research at GSI for the Transmutation of Nuclear Waste?** In: *Conference on 'Neutron Measurements, Evaluations and Applications -2', Bucharest, 20.10.2004-23.10.2004*, 2004.

P-H016nr Lisetsjiy, A.; Brown, B. A.; Horoi, M.; Grawe, H.: **Properties of $^{68-76}$Ni isotopes with new effective interaction**. In: Bjiker, R.; Casten, R. F.; Frank, A. (Eds.): *Proceedings of the International Conference in Microscopic Studies of Collective Phenomena Nuclear Physics, Large and Small, Morelos, Mexico, April 19-22*. AIP Conference Proceedings Vol. 726, Melville/New York: AIP, 2004, 231.

P-H017nr Lynen, U.*: **From IC to Music: Appreciating the contributions of Hans Sann**. In: Iori, I. (Ed.): *Proceedings of the XLII International Winter Meeting on Nuclear Physics*. Ricerca Scientifica ed Educazione Perma-

nente; Suppl. 123, Milano: Dipartimento di Fisica, Università degli Studi di Milano, 2004. XLII International Winter Meeting on Nuclear Physics, Bormio, 26.01.2004-31.01.2004, 1-7p. DOI:10.1007/b98790

P-H018nr Materna, T.; Bouchat, V.; Kinnard, V.; Hanappe, F.; Dorvaux, O.; Schmitt, C.; Stuttgé, L.; Siwek-Wilcyznska, K.; Aritomo, Y.; Bogatchev, A.; Prokhorova, E.; Ohta, M.: **Tracking dissipation in capture reactions**. In: Arnould, M.; Lewitowicz, M.; Münzeberg, G.*; Akimune, H.; Ohta, M.; Utsunaomiya, H.; Wada, T.; Yamagata, T. (Eds.): *Tours Symposium on Nuclear Physics, Tours 2003*. AIP Conference Proceedings Vol. 704, Melville/New York: AIP, 2004, 139-146p.

P-H019nr Nankov, N.*; Weick, H.*; Attallah, F.*; Eliseev, S.*; Geissel, H.*; Hausmann, M.; Hellström, M.; Kaza, E.; Litvinov, Y. A.*; Maier, M.*; Matos, M.; Ohtsubo, T.*; Savard, G.; Scheidenberger, C.*; Shishkin, V.*; Winkler, M.*; Zhou, Z.: **Slowing Down of Au Ions in Matter in the Energy Range 40-100 MeV/u and Energy Focusing of ^{56}Ni Fragments.** *Bulgarian Nuclear Society Transactions 9*, 2004, 199-203p.

P-H020nr Nociforo, C.*; et al.: **Coulomb Breakup of Neutron-Rich Oxygen Isotopes**. In: Bracco, A.; Kalfas, C. (Eds.): *The Labyrinth in Nuclear Structure*. AIP Conf. Proc. Vol. 701, Melville/New York, 2004. EPS International Conf. on 'The Labyrinth in Nuclear Structure', Crete, 174.

P-H021nr Pershina, V.: **The chemistry of superheavy elements and relativistic effects**. In: Schwerdtfeger, Peter (Ed.): *Relativistic electronic structure theory, Part 2: Applications*, Amsterdam: Elsevier, 2004, 1-80p.

P-H022nr Plaß, W.; Geissel, H.*: **Eine Reise mit SHIP zu den schwersten Atomkernen: Roentgenium – ein neues chemisches Element bekommt seinen Namen.** *Spiegel der Forschung: Wissenschaftsmagazin der JLU Giessen* **21**(1/2), 2004, 104-108p.

P-H023nr Ricciardi, M. V.*: **Complex nuclear-structure phenomena in the cooling down of highly excited nuclear systems**. In: *Conference on 'Phase transitions in strongly interacting matter', Prague, 23.08.2004-29.08.2004*, 2004.

P-H024nr Roeckl, E.*: **Decay Studies of N≃Z Nuclei**. In: Al-Khalili, J.; Roeckl, E. (Eds.): *The Euroschool Lectures on Physics with Exotic Beams*. Lectures Notes in Physics; 651, Berlin, Heidelberg, New York: Springer, 2004, 223-261p. DOI:10.1007/b98790

P-H025nr Schmidt, H. R.*: **The LHC Experiement ALICE-TPC Challenges at High Multiplicities**. In: Iori, I. (Ed.): *Proceedings of the XLII International Winter Meeting on Nuclear Physics*. Ricerca Scientifica ed Educazione Permanente; Suppl. 123, Milano: Dipartimento di Fisica, Università degli Studi di Milano, 2004. XLII International Winter Meeting on Nuclear Physics, Bormio, 26.01.2004-31.01.2004, 8-16p. DOI:10.1007/b98790

P-H026nr Schmidt, K.*: **Nuclear-data experimental programs at GSI**. In: *International Conference on Nuclear Data for Science and Technology, Santa Fe, 26.09.2004-01.10.2004*, 2004.

P-H027nr Schädel, M.*; Peter, I.*: **Grenzwertig!** In: Herrmann von Helmholtz-Gemeinschaft Deutscher Forschungszentren e.V. (Ed.): *Brains and Tools [Jahresheft 2004 der Helmholtz-Gemeinschaft]*, Berlin: Helmholtz-Gemeinschaft, 2004, 78-82p.

P-H028nr Takahashi, K.: **Nuclear Data for Low-Energy Astrophysics and Other applications – an Addendum**. In: Arnould, M.; Lewitowicz, M.; Münzeberg, G.*; Akimune, H.; Ohta, M.; Utsunaomiya, H.; Wada, T.; Yamagata, T. (Eds.): *Tours Symposium on Nuclear Physics, Tours 2003*. AIP Conference Proceedings Vol. 704, Melville/New York: AIP, 2004, 418-421p.

P-H029nr Tlustý, P.; Agakishiev, G.; Agodi, C.; et al.: **Hadron production in C+C collisions at 2 A GeV measured by the HADES sprectrometer**. In: Iori, I. (Ed.): *Proceedings of the XLII International Winter Meeting on Nuclear Physics*. Ricerca Scientifica ed Educazione Permanente; Suppl. 123, Milano: Dipartimento di Fisica, Università degli Studi di Milano, 2004. XLII International Winter Meeting on Nuclear Physics, Bormio, 26.01.2004-31.01.2004, 171-179p. DOI:10.1007/b98790

P-H030nr Trautmann, W.*; Le Févre, A.; Łukasik, J.; Indra and ALADIN Collaboration: **Complete survey of nuclides produced in spallation of ^{238}U+p at 1 GeV**. In: Bernas, M.; Ricciardi, V.; Taieb, J.; Armbruster, P.; Benlliure, J.; Boudard, A.; Casajeros, E.; Czajkowoski, S.; Enqvist, T.; Legrain, R.; Leray, S.; Mustapha, B.; Napolitani, P.; Pereira, J.; Rejmund, F.; Schmidt, K.-H.; Stéphan, C.; Tassan-Got, L.; Volant, C. (Eds.): *Proceedings of the XLII International Winter Meeting on Nuclear Physics*. Ricerca Scientifica ed Educazione Permanente; Suppl. 123, Milano: Dipartimento di Fisica, Università degli Studi di Milano, 2004. XLII International Winter Meeting on Nuclear Physics, Bormio, 26.01.2004-31.01.2004, 315-321p. DOI:10.1007/b98790

P-H031nr Trautmann, W.*; Le Févre, A.; Łukasik, J.; Indra and ALADIN Collaboration: **Isotopic distributions of spallation residues and energy dependencies - Results from the ^{208}Pb+p at 500AMeV experiment**. In: Audouin, L.; Tassan-Got, L.; Armbruster, P.; Benlliure, J.; Bernas, M.; Boudard, A.; Czajkowski, S.; Enqvist, T.; Fernandez, B.; Leray, S.; Rejmund, F.; Riccardi, M.-V.; Schmidt, K.-H.; Stéphan, C.; Taieb, J.; Volant, C.; Wlazło, W. (Eds.): *Proceedings of the XLII International Winter Meeting on Nuclear Physics*. Ricerca Scientifica ed Educazione Permanente; Suppl. 123, Milano: Dipartimento di Fisica, Università degli Studi di Milano, 2004. XLII International Winter Meeting on Nuclear Physics, Bormio, 26.01.2004-31.01.2004, 303-314p. DOI:10.1007/b98790

P-H032nr Trautmann, W.*; Le Févre, A.; Łukasik, J.; Indra and ALADIN Collaboration: **Multifragmentation with INDRAGSI: From the fermi to the participant-spectator domain**. In: Iori, I. (Ed.): *Proceedings of the XLII International Winter Meeting on Nuclear Physics*. Ricerca Scientifica ed Educazione Permanente; Suppl. 123, Milano: Dipartimento di Fisica, Università degli Studi di Milano, 2004. XLII International Winter Meeting on Nuclear Physics, Bormio,

26.01.2004-31.01.2004, 272-283p. DOI:10.1007/b98790

P-H033nr Villagrasa, C.; et al.: **Measurement of residual nucleus cross sections and recoil energies in p+Fe collisions at 300, 500, 750, 1000, and 1500 MeV**. In: *International Conference on Nuclear Data for Science and Technology, Santa Fe, 26.09.2004-01.10.2004*, 2004.

3. Preprints at arXive

X-H001 Aggarwal, M. M.; et al.; WA98 Collaboration*: **Azimuthal anisotropy of photon and charged particle emission in Pb-208 + Pb-208 collisions at 158-A-GeV/c.** *ArXiv: nucl-ex/0406022.*

X-H002 Aggarwal, M. M.; et al.; WA98 Collaboration*: **Centrality and transverse momentum dependence of collective flow in 158-A-GeV Pb + Pb collisions measured via inclusive photons.** *ArXiv: nucl-ex/0410045.*

X-H003 Alt, C.; et al.; NA49 Collaboration*: **Electric charge fluctuations in central Pb + Pb collisions at 20-AGeV, 30-AGeV, 40-AGeV, 80-AGeV and 158-AGeV.** *ArXiv: nucl-ex/0406013.*

X-H004 Alt, C.; et al.; NA49 Collaboration*: **Omega- and Antiomega+ production in central Pb + Pb collisions at 40-A-GeV and 158-A-GeV.** *ArXiv: nucl-ex/0409004.*

X-H005 Alt, C.; et al.; NA49 Collaboration*: **System size and centrality dependence of the balance function in A + A collisions at s(NN)**(1/2) = 17.2-GeV.** *ArXiv: hep-ex/0409031.*

X-H006 Alt, C.; et al.; NA49 Collaboration*: **System-size dependence of strangeness production in nucleus nucleus collisions at s(NN)**(1/2) = 17.3-GeV.** *ArXiv: nucl-ex/0406031.*

X-H007 Andronic, A.*; Biagi, S.; Braun-Munzinger, P.*; Garabatos, C. *; Tsiledakis, G.*; et al.: **Drift velocity and gain in argon and xenon based mixtures.** *ArXiv: physics/0402044.*

X-H008 Andronic, A.*; Braun-Munzinger, P.*; et al.: **Ultrarelativistic nucleus nucleus collisions and the quark-gluon plasma.** *ArXiv: hep-ph/0402291.*

X-H009 Andronic, A.*; et al.; ALICE Collaboration*: **Space charge in drift chambers operated with the Xe,CO-2(15%) mixture.** *ArXiv: physics/0402043.*

X-H010 Andronic, A.*; et al.; ALICE TRD Collaboration*: **Electron identification performance with ALICE TRD prototypes.** *ArXiv: physics/0402131.*

X-H011 Andronic, A.*; et al.; FOPI Collaboration*: **Excitation function of elliptic flow in Au + Au collisions and the nuclear matter equation of state.** *ArXiv: nucl-ex/0411024.*

X-H012 Appelshäuser, H.*; et al.: **Correlations and fluctuations.** *ArXiv: nucl-ex/0405005.*

X-H013 Appelshäuser, H.*; et al.; CERES Collaboration*: **Event-by-event fluctuations at SPS.** *ArXiv: nucl-ex/0409022.*

X-H014 Armbruster, P.*; et al.: **Measurement of a complete set of nuclides, cross-sections and kinetic energies in spallation of U-238 1-A-GeV with protons.** *ArXiv: nucl-ex/0406032.*

X-H015 Baur, G.; Hencken, K.; Trautmann, D.; Typel, S.*; et al.: **Recent Developments in Electromagnetic Excitation with Fast Heavy Ions.** *ArXiv: nucl-th/0402012.*

X-H016 Baur, G.; Typel, S.*; et al.: **Theory of the Trojan-Horse Method.** *ArXiv: nucl-th/0401054.*

X-H017 Blaschke, D.; Grigorian, H.; Khalatyan, A.; Voskresensky, D. N.; et al.: **Exploring the QCD phase diagram with compact stars.** *ArXiv: hep-ph/0409116.*

X-H018 Blaschke, D.; Grigorian, H.; Voskresensky, D. N.; et al.: **Cooling of neutron stars: Hadronic model.** *ArXiv: astro-ph/0403170.*

X-H019 Blaschke, D.; Voskresensky, D. N.; Grigorian, H.; et al.: **Cooling of neutron stars with color superconducting quark cores.** *ArXiv: astro-ph/0403171.*

X-H020 Bombaci, I.; Fabrocini, A.; Polls, A.; Vidana, I.*; et al.: **Spin-orbit and tensor interactions in homogeneous matter of nucleons: accuracy of modern many-body theories.** *ArXiv: nucl-th/0411057.*

X-H021 Busch, O.*; et al.; ALICE TRD Collaboration*: **Transition radiation spectroscopy with prototypes of the ALICE TRD.** *ArXiv: physics/0404106.*

X-H022 Dzhioev, A.; Wambach, J.*; Vdovin, A.; Aouissat, Z.; et al.: **Anharmonic O(N) oscillator model in next-to-leading order of the 1/N expansion.** *ArXiv: hep-ph/0407096.*

X-H023 Förster, A.*; et al.; KaoS Collaboration*: **Review of the results of the KaoS collaboration.** *ArXiv: nucl-ex/0411045.*

X-H024 Gazdzicki, M.; et al.; NA49 Collaboration*: **Report from NA49.** *ArXiv: nucl-ex/0403023.*

X-H025 Gruter, B.; Alkofer, R.; Maas, A.; Wambach, J.*; et al.: **Temperature dependence of gluon and ghost propagators in Landau-gauge Yang-Mills theory below the phase transition.** *ArXiv: hep-ph/0408282.*

X-H026 Jurado, B.; Schmitt, C.*; Schmidt, K. H.*; Benlliure, J.; Junghans, A. R.; et al.: **Manifestation of transient effects in fission induced by relativistic heavy-ion collisions.** *ArXiv: nucl-ex/0403004.*

X-H027 Jurado, B.; et al.: **New signatures on dissipation from fission induced by relativistic heavy-ion collisions.** *ArXiv: nucl-ex/0403006.*

X-H028 Jurado, B.; et al.: **Transient effects in fission evidenced from new experimental signatures.** *ArXiv: nucl-ex/0401013.*

X-H029 Kelic, A.*; et al.: **Isotopic and velocity distributions of Bi produced in charge-pickup reactions of ^{208}Pb.** *ArXiv: nucl-ex/0410004.*

X-H030 Kelic, A.*; et al.: **Isotopic and velocity distributions of Bi produced in charge-pickup reactions of 208Pb at 1 A GeV.** *ArXiv: nucl-ex/0407023.*

X-H031 Kniege, S.; et al.; NA49 Collaboration*: **beam energy.** *ArXiv: nucl-ex/0403034.*

X-H032 Kolomeitsev, E. E.; Voskresensky, D. N.; et al.: **Relativistic mean-field models with effective hadron masses and coupling constants, and rho- condensation.** *ArXiv: nucl-th/0410063.*

X-H033 Korpa, C. L.; Lutz, M. F. M.*; et al.: **Kaon and antikaon properties in cold nuclear medium.** *ArXiv: nucl-th/0404088.*

X-H034 Kotte, R.; et al.; FOPI Collaboration*: **Two-proton small-angle correlations in central heavy-ion collisions: A beam energy and system-size dependent study.** *ArXiv: nucl-ex/0409008.*

X-H035 Le Fèvre, A.*; et al.; INDRA Collaboration: **Isotopic Scaling and the Symmetry Energy in Spectator Fragmentation.** *ArXiv: nucl-ex/0409026.*

X-H036 Lisetskiy, A. F.; Brown, B. A.; Horoi, M.; Grawe, H.; et al.: **New T=1 effective interactions for the f5/2 p3/2 p1/2 g9/2 model space: Implications for valence-mirror symmetry and seniority isomers.** *ArXiv: nucl-th/0402082.*

X-H037 Lukasik, J.*; et al.: **Directed and elliptic flow in Au + Au at intermediate energies.** *ArXiv: nucl-ex/0410030.*

X-H038 Lutz, M. F. M.*; Garcia-Recio, C.; Kolomeitsev, E. E.; Nieves, J.; et al.: **Quark-mass dependence of baryon resonances.** *ArXiv: nucl-th/0401035.*

X-H039 Lutz, M. F. M.*; Kolomeitsev, E. E.; Korpa, C. L.; et al.: **Chiral symmetry, strangeness and resonances.** *ArXiv: nucl-th/0403065.*

X-H040 Lutz, M. F. M.*; Kolomeitsev, E. E.; et al.: **Chiral dynamics for exotic open-charm resonances.** *ArXiv: hep-ph/0406015.*

X-H041 Lutz, M. F. M.*; Kolomeitsev, E. E.; et al.: **Chiral symmetry and resonances in QCD.** *ArXiv: nucl-th/0402084.*

X-H042 Lutz, M. F. M.*; Soyeur, M.; et al.: **The associated photoproduction of positive kaons and pi0 Lambda or pi Sigma pairs in the region of the Sigma(1385) and Lambda(1405) resonances.** *ArXiv: nucl-th/0407115.*

X-H043 Maas, A.; Wambach, J.*; Gruter, B.; Alkofer, R.: **High-temperature limit of Landau-gauge Yang-Mills theory.** *ArXiv: hep-ph/0408074.*

X-H044 Maas, A.; Wambach, J.*; Gruter, B.; Alkofer, R.: **Residual confinement in high-temperature Yang-Mills theory.** *ArXiv: hep-ph/0408299.*

X-H045 Maas, A.; Wambach, J.*; Gruter, B.; Alkofer, R.; et al.: **Finite-temperature Yang-Mills theory in Landau gauge.** *ArXiv: hep-ph/0411289.*

X-H046 Maas, A.; Wambach, J.*; Gruter, B.; Alkofer, R.; et al.: **High-temperature limit of Landau-gauge Yang-Mills theory.** *ArXiv: hep-ph/0408074.*

X-H047 Meurer, C.; et al.; NA49 Collaboration*: **Hyperon production in Pb + Pb collisions at the CERN-SPS.** *ArXiv: nucl-ex/0406016.*

X-H048 Napolitani, P.; Schmidt, K. H.*; Botvina, A. S.*WISSENSCHAFTLER; Rejmund, F.; Tassan-Got, L.; Villagrasa, C.; et al.: **High-resolution velocity measurements on fully identified light nuclides produced in 56Fe + hydrogen and 56Fe + titanium systems.** *ArXiv: nucl-ex/0406006.*

X-H049 Papakonstantinou, P.; Mavrommatis, E.; Wambach, J.*; Ponomarev, V. Y.: **A microscopic investigation of the transition form factor in the region of collective multipole excitations of stable and unstable nuclei.** *ArXiv: nucl-th/0412079.*

X-H050 Papakonstantinou, P.; Wambach, J.*; Mavrommatis, E.; Ponomarev, V. Y.: **Nuclear vorticity and the low-energy nuclear response - Towards the neutron drip line.** *ArXiv: nucl-th/0411062.*

X-H051 Reisdorf, W.*; et al.; FOPI Collaboration*: **Droplet formation in expanding nuclear matter: A system-size dependent study.** *ArXiv: nucl-ex/0405014.*

X-H052 Reisdorf, W.*; et al.; FOPI Collaboration*: **Nuclear stopping from 0.09-A-GeV to 1.93-A-GeV and its correlation to flow.** *ArXiv: nucl-ex/0404037.*

X-H053 Riek, F.*; Knoll, J.*; et al.: **Self-consistent description of vector-mesons in matter.** *ArXiv: nucl-th/0402090.*

X-H054 Roland, C.; et al.; NA49 Collaboration*: **Event-by-event fluctuations of particle ratios in central Pb + Pb collisions at 20-A-GeV to 158-A-GeV.** *ArXiv: nucl-ex/0403035.*

X-H055 Roth, R.; Neff, T.*; Hergert, H.*; Feldmeier, H.*;

et al.: **Nuclear Structure based on Correlated Realistic Nucleon-Nucleon Potentials.** *ArXiv: nucl-th/0406021.*

X-H056 Rybczynski, M.; et al.; NA49 Collaboration*: **Multiplicity fluctuations in nuclear collisions at 158-A-GeV.** *ArXiv: nucl-ex/0409009.*

X-H057 Sako, H. *; Appelshaeuser, H. *; et al.; CERES/NA45 Collaboration*: **Event-by-event fluctuations at 40-A-GeV/c, 80-A-GeV/c, and 158-A-GeV/c in Pb + Au collisions.** *ArXiv: nucl-ex/0403037.*

X-H058 Schaefer, B. J.; Wambach, J.*: **The phase diagram of the quark meson model.** *ArXiv: nucl-th/0403039.*

X-H059 Schaefer, B. J.; Wambach, J.*; et al.: **The phase diagram of the quark meson model.** *ArXiv: nucl-th/0403039.*

X-H060 Schleifenbaum, W.; Maas, A.; Wambach, J.*; Alkofer, R.; et al.: **Infrared behaviour of the ghost gluon vertex in Landau gauge Yang-Mills theory.** *ArXiv: hep-ph/0411052.*

X-H061 Schleifenbaum, W.; Maas, A.; Wambach, J.*; Alkofer, R.; et al.: **The ghost-gluon vertex in Landau gauge Yang-Mills theory.** *ArXiv: hep-ph/0411060.*

X-H062 Sfienti, C.*; et al.; ALADiN2000 Collaboration: **Mass and isospin effects in multifragmentation.** *ArXiv: nucl-ex/0410044.*

X-H063 Sharma, M. M.; Farhan, A. R.; Münzenberg, G.*; et al.: **Alpha-decay properties of superheavy elements $Z = 113 - 125$ in the relativistic mean-field theory with vector self-coupling of ω meson.** *ArXiv: nucl-th/0409066.*

X-H064 Soyeur, M.; Lutz, M. F. M.*; et al.: **e+ e- pair production from nucleon targets in the resonance region.** *ArXiv: nucl-th/0402095.*

X-H065 Stoicea, G.; et al.; FOPI Collaboration*: **Azimuthal dependence of collective expansion for symmetric heavy ion collisions.** *ArXiv: nucl-ex/0401041.*

X-H066 Trautmann, W.*; Le Fèvre, A.*; Lukasik, J.*; et al.; INDRA collaboration: **Multifragmentation with Indra@GSI: From the Fermi to the Participant-Spectator Domain.** *ArXiv: nucl-ex/0404025.*

X-H067 Trautmann, W.*; et al.: **Multifragmentation and the liquid-gas phase transition: an experimental overview.** *ArXiv: nucl-ex/0411023.*

X-H068 Typel, S.*; Baur, G.; et al.: **Effective-range approach and scaling laws for electromagnetic strength in neutron-halo nuclei.** *ArXiv: nucl-th/0406068.*

X-H069 Typel, S.*; Baur, G.; et al.: **Electromagnetic strength of neutron and proton single-particle halo nuclei.** *ArXiv: nucl-th/0411069.*

X-H070 Uhlig, F.*; et al.: **Observation of different azimuthal emission patterns for K+ and of K- mesons in heavy ion collisions at 1-AGeV - 2-AGeV.** *ArXiv: nucl-ex/0411021.*

X-H071 Vidana, I.*; Bombaci, I.; Parenti, I.; et al.: **Quark deconfinement and neutrino trapping in compact stars.** *ArXiv: nucl-th/0411051.*

X-H072 Vidana, I.*; Tolos, L.; et al.: **Superfluidity of Sigma- hyperons in beta-stable neutron star matter.** *ArXiv: nucl-th/0405010.*

X-H073 Voskresensky, D. N.; et al.: **Hadron liquid with a small baryon chemical potential at finite temperature.** *ArXiv: hep-ph/0402020.*

Publications of the programme 'Large-scale facilities for research with photons, neutrons and ions'

Compiled by K. Große

This programme is part of the research field 'Structure of Matter' of the Helmholtz-Gemeinschaft
See <http://www.helmholtz.de/en/Research_Fields/Struktur_der_Materie.html>.

1. Reviewed publications

P-P001 Antalic, S.; Cagarda, P.; Ackermann, D.*; Burkhard, H. G.*; Heßberger, F. P.*; Hofmann, S.*; Kindler, B.*; Kojouharova, J.; Lommel, B.*; Mann, R.*; Saro, S.; Schött, H. J.*: **Target cooling for high-current experiments at SHIP.** *Nuclear instruments & methods in physics research, Section A, Accelerators, spectrometers, detectors and associated equipment* **530**(3): 185–193. DOI:10.1016/j.nima.2004.04.217 Also part of: 'Phyiscs of hadrons and nuclei'; Scientific Infrastructure.

P-P002 Ausloos, M.; Ivanova, K.; Siwy, Z.*: **Searching for self-similarity in switching time and turbulent cascades in ion transport through a biochannel. A time delay asymmetry.** *Physica A, Statistical mechanics and its applications* **336**(3): 319–333. DOI:10.1016/j.physa.2003.12.055

P-P003 Barak, J.; Haran, A.; Adler, E.; Azoulay, M.; Levinson, J.; Zentner, A.; David, D.; Fischer, B. E.*; Heiss, M.*; Betel, D.: **Use of light-lon-induced SEU in devices under reduced bias to evaluate their SEU cross section.** *IEEE transactions on nuclear science* **51**(6): 3486–3493. Also part of: 'Cancer research'.

P-P004 Basko, M. M.*; Schlegel, T.; Maruhn, J.: **On the symmetry of cylindrical implosions driven by a rotating beam of fast ions.** *Physics of plasmas* **11**(4): 1577–1588. DOI:10.1063/1.1650352

P-P005 Baur, G.; Typel, S.*: **Theory of the Trojan-Horse method.** *Progress of theoretical physics Supplement* (154): 333–340. Also part of: 'Phyiscs of hadrons and nuclei'.

P-P006 Beck, D.*; Blaum, K.*; Brand, H.*; Herfurth, F.*; Schwarz, S.: **A new control system for ISOLTRAP.** *Nuclear instruments & methods in physics research, Section A, Accelerators, spectrometers, detectors and associated equipment* **527**(3): 567–579. DOI:10.1016/j.nima.2004.02.043

P-P007 Beller, P.*; Beckert, K.*; Franzke, B.*; Kozhuharov, C.*; Nolden, F.*; Steck, M.*: **Observation of a reduction of recombination between ions and electrons.** *Nuclear instruments & methods in physics research, Section A, Accelerators, spectrometers, detectors and associated equipment* **532**(1): 427–432. DOI:10.1016/j.nima.2004.06.076

P-P008 Bercu, B.; Enculescu, I.*; Spohr, R.*: **Copper tubes prepared by electroless deposition in ion track templates.** *Nuclear instruments & methods in physics research, Section B, Beam interactions with materials and atoms* **225**(4): 497–502. DOI:10.1016/j.nimb.2004.06.011

P-P009 Bernard, J.; Alonso, J.; Beier, T.*; Block, M.*; Djekić, S.; Kluge, H.-J.*; Kozhuharov, C.*; Quint, W.*; Stahl, S.; Valenzuela, T.; Verdú, J.; Vogel, M.; Werth, G.: **Electron and positron cooling of highly charged ions in a cooler Penning trap.** *Nuclear instruments & methods in physics research, Section A, Accelerators, spectrometers, detectors and associated equipment* **532**(1): 224–228. DOI:10.1016/j.nima.2004.06.049

P-P010 Beyer, H. F.*; Stöhlker, T.*; Banas, D.; Liesen, D.*; Protić, D.; Beckert, K.*; Beller, P.*; Bojowald, J.; Bosch, F.*; Förster, E.; Franzke, B.*; Gumberidze, A.*; Hagmann, S.; Hoszowska, J.*; Indelicato, P.; Klepper, O.*; Kluge, H.-J.*; König, S.; Kozhuharov, C.*; Ma, X.*; Manil, B.; Mohos, I.; Oršić-Muthig, A.*; Nolden, F.*; Popp, U.*; Simionovici, A.; Sierpowski, D.; Spillmann, U.*; Stachura, Z.; Steck, M.*; Tachenov, S.*; Trassinelli, M.; Warczak, A.; Wehrhan, O.; Ziegler, E.: **FOCAL: X-ray optics for accurate spectroscopy.** *Spectro chimica acta, Part B, Atomic Spectroscopy* **59**(10): 1535–1542. [17th International Congress on X-Ray Optics and Microanalysis, Chamonix, Mont Blanc, France, 20030922/26] DOI:10.1016/j.sab.2004.03.023

P-P011 Blaum, K.*; Audi, G.; Beck, D.*; Bollen, G.; Guénaut, C.; Delahaye, P.; Herfurth, F.; Kellerbauer, A.; Kluge, H.-J.*; Lunney, D.; Rodríguez, D.*; Schwarz, S.; Schweikhard, L.; Weber, C.*; Yazidjian, C.*: **Recent results from the Penning trap mass spectrometer ISOLTRAP.** *Nuclear physics A, Nuclear and hadronic physics* **746**: 305C–310C. [Proceedings of the Sixth International Conference on Radioactive Nuclear Beams (RNB6) Argonne 20030922/26]

P-P012 Blaum, K.; Beck, D.*; Bollen, G.; Delahaye, P.; Guénaut, C.; Herfurth, F.*; Kellerbauer, A.; Kluge, H.-J.*; Lunney, D.; Schwarz, S.; Schweikhard, L.; Yazidjian, C.*: **Population inversion of nuclear states by a Penning trap mass spectrometer.** *Europhysics letters* **67**(4): 586–592. DOI:10.1209/epl/i2004-10089-5

P-P013 Brons, S.*; Psonka, K.; Heiß, M.*; Gudowska-Nowak, E.; Taucher-Scholz, G.*; Neumann, R.*: **Direct visualisation of heavy ion induced DNA fragmentation using atomic force Microscopy.** *Radiotherapy and oncology: journal of the European Society for Therapeutic Radiology and Oncology* **73**: S112–S114. Also part of: 'Cancer research'.

P-P014 Chtanko, N.*; Toimil Molares, M. E.*; Cornelius, T.*; Dobrev, D.*; Neumann, R.*: **Etched single-ion-track templates for single nanowire synthesis.** *The journal of physical chemistry B, Condensed matter, materials, surfaces, interfaces & biophysical chemistry* **108**(28): 9950–9954. DOI:10.1021/jp031368w

P-P015 Ciavola, G.; Celona, L.; Gammino, S.; Presti, M.; Ando, L.; Passarello, S.; Zhang, X. Z.; Consoli, F.; Chines, F.; Percolla, C.; Calzona, V., Winkler, M.*: **A version of the Trasco Intense Proton Source optimized for accelerator driven system purposes.** *Review of scientific instruments* **75**(5): 1453–1456. DOI:10.1063/1.1690459 Also part of: Accelerator resarch and development.

P-P016 Constantin, C.; Dewald, C.; Niemann, C.; Hoffmann, D. H. H*.; Udrea, S.; Varentsov, D.; Jacoby, V.*; Funk, U. N.; Neuner, U.*; Tauschwitz, A.*: **Cold compression of solid matter by intense heavy-ion-beam-generated pressure waves.** *Laser and particle beams* **22**(1): 59–63. DOI:10.1017/S0263034604221115

P-P017 Constantin, C.*; Niemann, C.*; Dewald, E.*; Udrea, S.*; Jacoby, J.*; Varentsov, D.*; Schwab, P.*; Wieser, J.*; Hoffmann, D. H. H.*: **Density measurements of heavy-ion-beam-induced stress waves in solid matter by a sensitive laser deflection technique.** *Review of scientific instruments* **75**(5): 1268–1273. DOI:10.1063/1.1711141

P-P018 Costantini, J. M.; Beuneu, F.; Gourier, D.; Trautmann, C.*; Calas, G.; Toulemonde, M.: **Colour centre production in yttria-stabilized zirconia by swift charged particle irradiations.** *Journal of physics Condensed matter* **16**(23): 3957–3971. DOI:10.1088/0953-8984/16/23/014

P-P019 Cowan, T. E.; Fuchs, J.; Ruhl, H.; Kemp, A.; Audebert, P.; Roth, M.*; Stephens, R.; Barton, I.; Blazevic, A.*; Brambrink, E.*; Cobble, J.; Fernández, J.; Gauthier, J. C.; Geissel, M.*; Hegelich, M.; Kaae, J.; Karsch, S.; Le Sage, G. P.; Letzring, S.; Manclossi, M.; Meyroneinc, S.; Newkirk, A.; Pépin, H.; Renard-LeGalloudec, N.: **Ultralow emittance, multi-MeV proton beams from a laser virtual-cathode plasma accelerator.** *Physical review letters* **92**(20): 204801. DOI:10.1103/PhysRevLett.92.204801

P-P020 Dilling, J.*; Herfurt, F.; Kellerbauer, A.; Audi, G.; Beck, D.*; Bollen, G.; Kluge, H.-J.*; Moore, R. B.; Scheidenberger, C.*; Schwarz, S.; Sikler, G.*; ISOLDE Collaboration*: **Direct mass measurements of neutron-deficient xenon isotopes using the ISOLTRAP mass spectrometer.** *The European physical journal A, Hadrons and nuclei* **22**(2): 163–171. DOI:10.1140/epja/i2004-10015-y Also part of: 'Phyiscs of hadrons and nuclei'.

P-P021 Dimopoulou, C.; Moshammer, R.; Fischer, D.; Höhr, C.; Dorn, A.; Fainstein, P. D.; Crespo López Urrutia, J. R.; Schröter, C. D.; Kollmus, H.*; Mann, R.*; Hagmann, S.*; Ullrich, J.: **Breakup of H_2 in singly ionizing collisions with fast protons: Channel-selective low-energy electron spectra.** *Physical review letters* **93**(12): 123203. DOI:10.1103/PhysRevLett.93.123203

P-P022 Djekic, S.; Alonso, J.*; Kluge, H.-J.*; Quint, W.*; Stahl, S.*; Valenzuela, T.; Verdú, J.; Vogel, M.; Werth, G.: **Temperature measurement of a single ion in a Penning trap.** *The European physical journal: D, Atomic, molecular and optical physics* **31**(3): 451–457. DOI:10.1140/epjd/e2004-00168-1

P-P023 Doron, R.; Arad, R.; Tsigutkin, K.; Osin, D.; Weingarten, A.; Starobinets, A.; Bernshtam, V. A.; Stambulchik, E.; Ralchenko, Y. V.; Maron, Y.; Fruchtman, A.; Fisher, A.; Huba, J. D.; Roth, M.: **Plasma dynamics in pulsed strong magnetic fields.** *Physics of plasmas* **11**(5): 2411–2418. DOI:10.1063/1.1651491

P-P024 DuBois, R. D.; Santos, A. C. F.; Stöhlker, T.*; Bosch, F.*; Bräuning-Demian, A.*; Gumberidze, A.*; Hagmann, S.*; Kozhuharov, C.*; Mann, R.*; Oršić-Muthig, A. O.*; Spillmann, U.*; Tachenov, S.*; Bart, W.*; Dahl, L.*; Franzke, B.*; Glatz, J.*; Gröning, L.*; Richter, S.*; Wilms, D.*; Ullmann, K.; Jagutzki, O.: **Electron loss from 1.4-MeV/u $U^{4,6,10+}$ ions colliding with Ne, N_2, and Ar targets.** *Physical review A, Atomic, molecular, and optical physics* **70**(3): 032712. DOI:10.1103/PhysRevA.70.032712

P-P025 El-Said, A. S.*; Cranney, M.*; Ishikawa, N.; Iwase, A.; Neumann, R.*; Schwartz, K.*; Toulemonde, M.; Trautmann, C.*: **Study of heavy-ion induced modifications in BaF_2 and LaF_3 single crystals.** *Nuclear instruments & methods in physics research, Section B, Beam interactions with materials and atoms* **218**: 492–497. DOI:10.1016/j.nimb.2003.12.057

P-P026 Ewald, G.*; Nörtershäuser, W.*; Dax, A.*; Götte, S.*; Kirchner, R.*; Kluge, H.-J.*; Kühl, T.*; Sanchez, R.*; Wojtaszek, A.*; Bushaw, B. A.; Drake, G. W. F.; Yan, Z. C.; Zimmermann, C.: **Nuclear charge radii of ^{8,9}Li determined by laser spectroscopy.** *Physical review letters* **93**(11): 113002. DOI:10.1103/PhysRevLett.93.113002 Also part of: 'Phyiscs of hadrons and nuclei'.

P-P027 Fulinski, A.; Kosinska, I. D.; Siwy, Z.*: **On the validity of continuous modelling of ion transport through nanochannels.** *Europhysics letters* **67**(4): 683–689. DOI:10.1209/epl/i2003-10304-y

P-P028 Götte, S.*; Knaak, K. M.*; Kotovski, N.; Kluge, H.- J.*; Ewald, G.; Wendt, K. D. A.: **Test of collinear spectroscopy for precise high-voltage determination.** *Review of scientific instruments* **75**(4): 1039–1050. DOI:10.1063/1.1651635

P-P029 Geissel, H.*; Litvinov, Y. A.*; Attallah, F.*; Beckert, K.*; Beller, P.*; Bosch, F.*; Boutin, D.*; Faestermann, T.; Falch, M.; Franzke, B.*; Hausmann, M.; Hellström, M.*; Kaza, E.*; Kerscher, T.; Klepper, O.*; Kluge, H.-J.*; Kozhuharov, C.*; Kratz, K- L.*; Litvinov, S. A.; Löbner, K. E. G.; Maier, L.; Matoš, M.*; Münzenberg, G.*; Nolden, F.*; Novikov, Y. N.; Ohtsubo, T.; Ostrowski, A.; Patyk, Z.; Pfeiffer, B.; Portillo, M*.; Radon, T.*; Scheidenberger, C.*; Shishkin, V.*; Stadlmann, J.*; Steck, M.*; Viera, D. J.; Weick, H.*; Winkler, M.*; Wollnik, H.; Yamaguchi, T.*: **New results with stored exotic nuclei at relativistic energies.** *Nuclear physics A, Nuclear and hadronic physics* **746**: 150C–155C. [Proceedings of the Sixth International Conference on Radioactive Nuclear Beams (RNB6) Argonne 20030922/26] DOI:10.1016/j.nuclphysa.2004.09.030 Also part of: 'Phyiscs of

hadrons and nuclei'; Scientific Infrastructure.

P-P030 Glasmacher, U. A.; Lang, M.*; Keppler, H.; Langenhorst, F.; Neumann, R.*; Schardt, D.*; Trautmann, C.*; Wagner, G. A.: **Heavy-ion irradiation of solids at extreme pressures: Ion track formation and high-pressure phases.** *Lithos* **73**(1): S43–S43. [Abstracts of the Tenth International Symposium on Experimental Mineralogy, Petrology and Geochemistry, Frankfurt am Main, Germany, 4 - 7 April 2004] DOI:10.1016/j.lithos.2004.02.003

P-P031 Gumberidze, A.*; Stöhlker, T.*; Banás, D.; Beckert, K.*; Beller, P.*; Beyer, H. F.*; Bosch, F.*; Cai, X.; Hagmann, S.*; Kozhuharov, C.*; Liesen, D.*; Nolden, F.*; Ma, X.; Mokler, P. H.*; Oršić-Muthig, A.*; Steck, M.*; Sierpowski, D.; Tashenov, S.*; Warczak, A.; Zou, Y.: **Electron-electron interaction in strong electromagnetic fields: The two-electron contribution to the ground-state energy in He-like uranium.** *Physical review letters* **92**(20): 203004. DOI:10.1103/PhysRevLett.92.203004

P-P032 Healy, K.*; Siwy, Z.*; Morrison, A. P.; Neumann, R.*: **Elastic and plastic deformation of individual conical polymer nanopores.** *Biophysical journal* **86**(1): 552A–552A.

P-P033 Heiss, M.*; Fischer, B. E.*; Cholewa, M.*: **Status of the GSI microbeam facility for cell irradiation with single ions.** *Radiation research* **161**(1): 98–99. DOI:10.1043/0033-7587(2004)161<0087:POTTIT>2.0.CO;2 Also part of: 'Cancer research'.

P-P034 Herfurth, F.*; Audi, C.; Beck, D.*; Blaum, K.*; Bollen, G.; Delahaye, P.; Guénaut, C.; Kellerbauer, A.; Kluge, H.-J.*; Lunney, D.; Rodríguez, D.*; Saxena, S.; Schwarz, S.; Schweikhard, L.; Sikler, G.*; Yazidjian, C.: **Masses along the rp-process path and large scale surveys on Cu, Ni and Ga with ISOLTRAP.** *Nuclear physics A, Nuclear and hadronic physics* **746**: 487C–492C. [Proceedings of the Sixth International Conference on Radioactive Nuclear Beams (RNB6) Argonne 20030922/26] DOI:10.1016/j.nuclphysa.2004.09.074

P-P035 Heßberger, F. P.*; Hofmann, S.*; Ackermann, D.*; Cagarda, P.*; Herzberg, R. D.; Kojouharov, I.*; Kuusiniemi, P.*; Leino, M.; Mann, R.*: **Alpha-gamma decay studies of ^{251,253}No and their daughter products ^{247,249}Fm.** *The European physical journal A, Hadrons and nuclei* **22**(3): 417–427. DOI:10.1140/epja/i2003-10238-4 Also part of: 'Phyiscs of hadrons and nuclei'.

P-P036 Hofmann, S.*; Heßberger, F. P.*; Ackermann, D.*; Antalic, S.; Cagarda, P.; Kindler, B.*; Kuusiniemi, P.; Leino, M.; Lommel, B.*; Malyshev, O. N.; Mann, R.; Münzenberg, G. M.*; Popeko, A. G.; Saro, S.; Streicher, B.; Yeremin, A.: **Properties of heavy nuclei measured at the GSI SHIP.** *Nuclear physics A, Nuclear and hadronic physics* **734**: 93–100. [Proceedings of the Eighth International Conference On Nucleus-Nucleus Collisions] DOI:10.1016/S0375-9474(04)90259-X Also part of: 'Phyiscs of hadrons and nuclei'.

P-P037 Ilievski, S.*; Aumann, T.*; Boretzky, K.; Elze, T. W.; Emling, H.*; Grünschloß, A.; Holeczek, J.; Holzmann, R.*; Kozhuharov, C.*; Kratz, J. V.; Kulessa, R.; Leistenschneider, A.; Lubkiewicz, E.; Ohtsuki, T.; Reiter, P.; Simon, H.; Stelzer, K.; Stroth, J.*; Sümmerer, K.*; Wajda, E.; Waluś, W.; LAND Collaboration*: **Evidence for multiphonon giant resonances in electromagnetic fission of ^{238}U.** *Physical review letters* **92**(11): 112502. DOI:10.1103/PhysRevLett.92.112502 Also part of: 'Phyiscs of hadrons and nuclei'.

P-P038 Kanapathipillai, M.; Mulser, P.; Hoffmann, D. H. H.; Schlegel, T.*; Maron, Y.; Sauerbrey, R.: **Net charge of a conducting microsphere embedded in a thermal plasma.** *Physics of plasmas* **11**(8): 3911–3914. DOI:10.1063/1.1769377

P-P039 Kellerbauer, A.; Audi, G.; Beck, D.*; Blaum, K.*; Bollen, G.; Brown, B. A.; Delahaye, P.; Guénaut, C.; Herfurth, F.*; Kluge, H.-J.*; Lunney, D.; Schwarz, S.; Schweikhard, L.; Yazidjian, C.*: **Direct mass measurements on the superallowed emitter ^{74}Rb and its daughter^{74} Kr: Isospin-symmetry-breaking correction for standard-model tests.** *Physical review letters* **93**(7): 072502. DOI:10.1103/PhysRevLett.93.072502

P-P040 Kellerbauer, A.; Audi, G.; Beck, D.*; Blaum, K.*; Bollen, G.; Delahaye, P.; Herfurth, F.; Kluge, H- J.*; Kolhinen, V.; Mukherjee, M.*; Rodríguez, D.*; Schwarz, S.: **Towards high-precision mass measurements on ^{74}Rb for a test of the CVC hypothesis and the unitarity of the CKM matrix.** *Nuclear physics A, Nuclear and hadronic physics* **746**: 635C–638C. [Proceedings of the Sixth International Conference on Radioactive Nuclear Beams (RNB6) Argonne 20030922/26] DOI:10.1016/j.nuclphysa.2004.09.099

P-P041 Kluge, H.-J.*; Blaum, K.: **Trapping radioactive ions.** *Nuclear physics A, Nuclear and hadronic physics* **746**: 200C–205C. [Proceedings of the Sixth International Conference on Radioactive Nuclear Beams (RNB6) Argonne 20030922/26] DOI:10.1016/j.nuclphysa.2004.09.034

P-P042 Kluge, H.-J.*; Blaum, K.*; Scheidenberger, C.*: **Mass measurement of radioactive isotopes.** *Nuclear instruments & methods in physics research, Section A, Accelerators, spectrometers, detectors and associated equipment* **532**(1): 48–55. [International Workshop on Beam Cooling and Related Topics, Lake Yamanaka, Yamanashi, Japan, 20030519/23] DOI:10.1016/j.nima.2004.06.029 Also part of: 'Phyiscs of hadrons and nuclei'.

P-P043 Knaak, K. M.*; Götte, S.*; Kluge, H.-J.*; Ewald, G.; Wendt, K. D. A.: **An evaluation procedure for scanning interferometer based wavemeters.** *Optics communications* **231**(1): 1–7. DOI:10.1016/j.optcom.2003.12.002

P-P044 Kretzschmar, M.; Götte, S.*; Ewald, G.; Knaak, K. M.; Wendt, K. D. A.; Kluge, H.-J.*: **Influence of the thermal motion on the line shape and position of resonances in collinear fast beam laser spectroscopy.** *Applied physics B, Lasers and optics* **79**(5): 623–627. DOI:10.1007/s00340-004-1608-1

P-P045 Lang, M.*; Glasmacher, U. A.; Moine, B.; Neumann, R.*; Wagner, G. A.: **Etch-pit morphology of tracks caused by swift heavy ions in natural dark mica.** *Nuclear instruments & methods in physics research, Section B, Beam interactions with materials and atoms* **218**: 466–471. [Proceedings of the Twelfth International Conference on Radiation Effects in Insulators, Gramado, Brazil, 31 August - 5 Septem-

ber 2003] DOI:10.1016/j.nimb.2004.01.009

P-P046 Lindroth, A.; Ames, F.; Beck, M.; Coeck, S.; Delaure, B.; Golovko, V. V.; Kozlov, V. Y.; Kraev, I. S.; Phalet, T.; Quint, W.*; Severijns, N.; Vereecke, B.; Versyck, S.; ISOLDE EUROTRAPS NIPNET Collaboration: **Fast controls for the WITCH Penning trap radioactive source experiment.** *Nuclear instruments & methods in physics research, Section A, Accelerators, spectrometers, detectors and associated equipment* **534**(3): 551–561. DOI:10.1016/j.nima.2004.06.175

P-P047 Litvinov, Y. A.*; Geissel, H.*; Novikov, Y. N.; Patyk, Z.; Radon, T.*; Scheidenberger, C.*; Attallah, F.*; Beckert, K.*; Bosch, F.*; Falch, M.; Franzke, B.*; Hausmann, M.; Kerscher, T.; Klepper, O.*; Kluge, H.-J.*; Kozhuharov, C.*; Löbner, K. E. G.; Münzenberg, G.*; Nolden, F.*; Steck, M.*; Wollnik, H.: **Precision experiments with time-resolved Schottky mass spectrometry.** *Nuclear physics A, Nuclear and hadronic physics* **734**: 473–476. [Proceedings of the Eighth International Conference On Nucleus-Nucleus Collisions] DOI:10.1016/S0375-9474(04)90328-4

P-P048 Mara, A.; Siwy, Z.*; Trautmann, C.*; Wan, J.; Kamme, F.: **An asymmetric polymer nanopore for single molecule detection.** *Nano letters* **4**(3): 497–501.

P-P049 Martin, C. R.; Siwy, Z. S.*; Heins, E.; Harrell, C.; Trautmann, C.*: **Voltage gating in synthetic single-nanotube membranes.** *Biophysical journal* **86**(1): 131A–131A.

P-P050 Metz, S.; Trautmann, C.*; Bertsch, A.; Renaud, P.: **Polyimide microfluidic devices with integrated nanoporous filtration areas manufactured by micromachining and ion track technology.** *Journal of micromechanics and microengineering* **14**(3): 324–331. DOI:10.1088/0960-1317/14/3/002

P-P051 Mokler, P. H.*; Dunford, R. W.: **Two-photon decay in heavy atoms and ions.** *Physica scripta* **69**(1): C1–C9.

P-P052 Mokler, P. H.*; Schäffer, H. W.*; Dunford, R. W.: **Two-photon decay of K-shell vacancies in silver atoms.** *Physical review A, Atomic, molecular, and optical physics* **70**(3): 032504. DOI:10.1103/PhysRevA.70.032504

P-P053 Morishita, Y.; Hutton, R.; Torii, H. A.; Komaki, K.; Brage, T.; Ando, K.; Ishii, K.; Kanai, Y.; Masuda, H.; Sekiguchi, M.; Rosmej, F. B.*; Yamazaki, Y.: **Direct observation of the initial-state distribution of the first electron transferred to slow highly charged ions interacting with a metal surface.** *Physical review A, Atomic, molecular, and optical physics* **70**(1): 012902. DOI:10.1103/PhysRevA.70.012902

P-P054 Moskovkin, D. L.; Oreshkina, N. S.; Shabaev, V. M.; Beier, T.*; Plunien, G.; Quint, W.*; Soff, G.*: **g factor of hydrogenlike ions with nonzero nuclear spin.** *Physical review A, Atomic, molecular, and optical physics* **70**(3): 032105. DOI:10.1103/PhysRevA.70.032105

P-P055 Mukherjee, M.*; Kellerbauer, A.; Beck, D.*; Blaum, K.*; Bollen, G.; Carrel, F.; Delahaye, P.; Dilling, J.; George, S.; Guénaut, C.; Herfurth, F.; Herlert, A.; Kluge, H.-J.*; Köster, U.; Lunney, D.; Schwarz, S.; Schweikhard, L.; Yazidjian, C.*: **The mass of ^{22}Mg.** *Physical review letters* **93**(15): 150801. DOI:10.1103/PhysRevLett.93.150801

P-P056 Neumayer, P.; Seelig, W.; Cassou, K.; Klisnick, A.; Ros, D.; Ursescu, D.*; Kuehl, T.*; Borneis, S.*; Gaul, E.*; Geithner, W.*; Haefner, C.*; Wiewior, P.: **Transient collisionally excited X-ray laser in nickel-like zirconium pumped with the PHELIX laser facility.** *Applied physics B, Lasers and optics* **78**(7): 957–959. DOI:10.1007/s00340-004-1450-5

P-P057 Nishimura, H.; Kawamura, T.*; Matsui, R.; Ochi, Y.; Okihara, S.; Sakabe, S.; Koike, F.; Johzaki, T.; Nagatomo, H.; Mima, K.; Uschmann, I.; Förster, E.: **Erratum to "K_α spectroscopy to study energy transport in ultrahigh-intensity laser produced plasmas" [Journal of Quantitative Spectroscopy and Radiative Transfer 81 (1-4) (2003) 327-337].** *Journal of quantitative spectroscopy & radiative transfer* **87**(2): 211–211. DOI:10.1016/j.jqsrt.2004.03.019

P-P058 Olson, R. E.; Watson, R. L.; Horvat, V.; Perumal, A. N.; Peng, Y.; Stöhlker, T.*: **Projectile electron loss and capture in MeV/u collisions of U^{28+} with ^{2}H, ^{2}N and Ar.** *Journal of physics B, Atomic, molecular and optical physics* **37**(22): 4539–4550. DOI:10.1088/0953-4075/37/22/012

P-P059 Osin, D.; Doron, R.; Arad, R.; Tsigutkin, K.; Starobinets, A.; Bernshtam, V.; Fisher, A.; Fruchtman, A.; Maron, Y.; Tauschwitz, A.*: **On the role of the plasma composition in the magnetic field evolution in plasma opening switches.** *IEEE transactions on plasma science* **32**(5): 1805–1811.

P-P060 Quint, W.*; Alonso, J.; Djekić, S.; Kluge, H.-J.*; Stahl, S.; Valenzuela, T.; Verdú, J.; Vogel, M.; Werth, G.: **Continuous Stern-Gerlach effect and the magnetic moment of the antiproton.** *Nuclear instruments & methods in physics research, Section B, Beam interactions with materials and atoms* **214**: 207–210. [Low Energy Antiproton Physics, Yamashita-park, Japan, 3 March - 7 March 2003] DOI:10.1016/j.nimb.2003.08.008

P-P061 Rodriguez, D.; Kolhinen, V. S.; Audi, G.; Aysto, J.; Beck, D.*; Blaum, K.*; Bollen, G.; Herfurth, F.*; Jokinen, A.; Kellerbauer, A.; Kluge, H.-J.*; Oinonen, M.; Schatz, H.; Sauvan, E.; Schwarz, S.: **Mass measurement on the rp-process waiting point ^{72}Kr.** *Physical review letters* **93**(16): 161104. DOI:10.1103/PhysRevLett.93.161104

P-P062 Scheidenberger, C.*; Attallah, F.*; Beckert, K.*; Beller, P.*; Bosch, F.*; Boutin, D.*; Eickhoff, H.*; Faestermann, T.; Falch, M.; Franczak, B.*; Franzke, B.*; Geissel, H.*; Hausmann, M.*; Hellström, M.*; Kaza, E.*; Kerscher, T.; Klepper, O.*; Kluge, H.-J.*; Koyama, R.; Kozhuharov, C.*; Kratz, K. L.; Litvinov, Y. A.*; Löbner, K.; Maier, L.; Matos, M.*; Münzenberg, G.*; Nolden, F.*; Novikov, Y. N.*; Ohtsubo, T.; Ostrowski, A.; Ozawa, A.; Patyk, Z.; Pfeiffer, B.; Portillo, M.*; Quint, W.*; Radon, T.*; Shishkin, V.*; Stadlmann, J.*; Steck, M.*; Sümmerer, K.*; Suzuki, T.; Trzhaskovskaja, M. B.; Vieira, D. J.; Watanabe, S.; Weick, H.*; Winkler, M.*; Wollnik, H.; Yamaguchi, T.*: **Study of basic nuclear properties of**

highly-charged, unstable nuclei at the SIS-FRS-ESR complex. *Heavy ion physics* **19**(1): 165–170. Also part of: 'Phyiscs of hadrons and nuclei'.

P-P063 Schwartz, K.*; Trautmann, C.*; El-Said, A. S.*; Neumann, R.*; Toulemonde, M.; Knolle, W.: **Color-center creation in LiF under irradiation with swift heavy ions: Dependence on energy loss and fluence.** *Physical review: B, Condensed matter and materials physics* **70**(18): 184104. DOI:10.1103/PhysRevB.70.184104

P-P064 Shevelko, V. P; Rosmej, O.*; Tawara, H.; Tolstikhina, I. Y.: **The target-density effect in electron-capture processes.** *Journal of physics B, Atomic, molecular and optical physics* **37**(1): 201–213. DOI:10.1088/0953-4075/37/1/012

P-P065 Silver, E.; Schnopper, H.; Austin, G.; Guth, G.; Murray, S.; Madden, N.; Landis, D.; Beeman, J.; Haller, E. E.; Stöhlker, T.*: **Using a microcalorimeter to measure the Lamb shift in hydrogenic gold and uranium on cooled, decelerated ion beams.** *Nuclear instruments & methods in physics research, Section A, Accelerators, spectrometers, detectors and associated equipment* **520**(1): 60–62. [Proceedings of the 10th International Workshop on Low Temperature Detectors, Genoa, Italy, 7 - 11 July 2003] DOI:10.1016/j.nima.2003.11.220

P-P066 Sima, M.; Enculescu, I.; Ioncea, A.; Visan, T.; Trautmann, C.*: **Manganese and copper doped CdS nanowire arrays preparation.** *Journal of optoelectronics and advanced materials* **6**(4): 1193–1198.

P-P067 Sima, M.; Enculescu, I.; Trautmann, C.*; Neumann, R.*: **Electrodeposition of CdTe nanorods in ion track membranes.** *Journal of optoelectronics and advanced materials* **6**(1): 121–125.

P-P068 Sima, M.; Enculescu, I.; Visan, T.; Spohr, R.*; Trautmann, C.*: **Electrochemical deposition of PBSe1-xTex nanorod arrays using ion track etched membranes as template.** *Molecular crystalls and liquid crystals* **418**: 749–755.

P-P069 Siwy, Z.*; Fulinski, A.: **A nanodevice for rectification and pumping ions.** *American journal of physics* **72**(5): 567–574. DOI:10.1119/1.1648328

P-P070 Siwy, Z. S.*; Fulinski, A.; Schiedt, B.*; Neumann, R.*; Trautmann, C.*: **Rectification, pumping and saturation of ion currents through asymmetric nanopores.** *Biophysical journal* **86**(1): 173A–173A.

P-P071 Stadlmann, J.*; Hausmann, M.*; Attallah, F.*; Beckert, K.*; Beller, P.*; Bosch, F.*; Eickhoff, H.*; Falch, M.; Franczak, B.*; Franzke, B.*; Geissel, H.*; Kerscher, T. H.; Klepper, O.*; Kluge, H.-J.*; Kozhuharov, C.*; Litvinov, Y. A.*; Löbner, K. E. G.; Matoš, M.*; Münzenberg, G.*; Nankov, N.*; Nolden, F.*; Novikov, Y. N.; Ohtsubo, T.*; Radon, T.*; Schatz, H.; Scheidenberger, C.*; Steck, M.*; Weick, H.*; Wollnik, H.: **Direct mass measurement of bare short-lived ^{44}V, ^{48}Mn, ^{41}Ti and ^{45}Cr ions with isochronous mass spectrometry.** *Physics letters B* **586**(1): 27–33. DOI:10.1016/j.physletb.2004.02.014 Also part of: 'Phyiscs of hadrons and nuclei'; Scientific Infrastructure.

P-P072 Teubner, U.; Eidmann, K.; Wagner, U.; Andiel, U.; Pisani, F.; Tsakiris, G. D.; Witte, K.; Meyer-ter-Vehn, J.; Schlegel, T.*; Forster, E.: **Harmonic emission from the rear side of thin overdense foils irradiated with intense ultrashort laser pulses.** *Physical review letters* **92**(18): 185001. DOI:10.1103/PhysRevLett.92.185001

P-P073 Toimil Molares, M. E. *; Balogh, A. G.; Cornelius, T. W.*; Neumann, R.*; Trautmann, C.*: **Fragmentation of nanowires driven by Rayleigh instability.** *Applied physics letters* **85**(22): 5337–5339. DOI:10.1063/1.1826237

P-P074 Toimil Molares, M. E.*; Chtanko, N.*; Cornelius, T. W.*; Dobrev, D.*; Enculescu, I.*; Blick, R. H.; Neumann, R.*: **Fabrication and contacting of single Bi nanowires.** *Nanotechnology* **15**(4): S201–S207. DOI:10.1088/0957-4484/15/4/015

P-P075 Toleikis, S.*; Manil, B.; Berdermann, E.*; Beyer, H. F.*; Bosch, F.*; Czanta, M.*; Dunford, R. W.; Gumberidze, A.*; Indelicato, P.; Kozhuharov, C.*; Liesen, D.*; Ma, X.*; Marrus, R.; Mokler, P. H.*; Schneider, D.; Simionovici, A.; Stachura, Z.; Stöhlker, T.*; Warczak, A.; Zou, Y.: **Lifetime of the 2(3)P(0) state of He-like Au-197.** *Physical review A, Atomic, molecular, and optical physics* **69**(2): 022507. DOI:10.1103/PhysRevA.69.022507 Also part of: Scientific Infrastructure.

P-P076 Tomaselli, M.*; Liu, L. C.; Fritzsche, S.; Kühl, T.*: **Dressed bosons theory for nuclear structure.** *Journal of physics G, Nuclear and particle physics* **30**(9): 999–1020. DOI:10.1088/0954-3899/30/9/005

P-P077 Tomaselli, M.*; Liu, L. C.; Fritzsche, S.; Kühl, T.*; Ursescu, D.*: **Cluster transformation coefficients in many-body nuclear physics.** *Nuclear physics A, Nuclear and hadronic physics* **738**: 216–220. [Proceedings of the 8th International Conference on Clustering Aspects of Nuclear Structure and Dynamics] DOI:10.1016/j.nuclphysa.2004.04.034

P-P078 Tomaselli, M.*; Liu, L. C.; Fritzsche, S.; Kühl, T.*; Ursescu, D.*; Neumayer, P.*; Wojtaszek, A.: **Charge radii of exotic nuclei: nuclear results versus isotopic shift calculations.** *Nuclear physics A, Nuclear and hadronic physics* **746**: 587C–590C. [Proceedings of the Sixth International Conference on Radioactive Nuclear Beams (RNB6) Argonne 20030922/26] DOI:10.1016/j.nuclphysa.2004.09.103

P-P079 Toulemonde, M.; Trautmann, C.*; Balanzat, E.; Hjort, K.; Weidinger, A.: **Track formation and fabrication of nanostructures with MeV-ion beams.** *Nuclear instruments & methods in physics research, Section B, Beam interactions with materials and atoms* **216**: 1–8. [Proceedings of the E-MRS 2003 Symposium E on Ion Beams for Nanoscale Surface Modifications, Strasbourg, France, 10 June - 13 June 2003] DOI:10.1016/j.nimb.2003.11.013

P-P080 Van Roosbroeck, J.; Guénaut, C.; Audi, G.; Beck, D.*; Blaum, K.*; Bollen, G.; Cederkall, J.; Delahaye, P.; De Maesschalck, A.; De Witte, H.; Fedorov, D.; Fedoseyev, V. N.; Franchoo, S.; Fynbo, H. O. U.; Górska, M.*; Herfurth, F.; Heyde, K.; Huyse, M.; Kellerbauer, A.; Kluge, H.-J.*; Koster,

U.; Kruglov, K.; Lunney, D.; Mishin, V. I.; Mueller, W. F.; Nagy, S.; Schwarz, S.; Schweikhard, L.; Smirnova, N. A.; Van de Vel, K.; Van Duppen, P.; Van Dyck, A.; Walters, W. B.; Weissman, L.; Yazidjian, C.*: **Unambiguous identification of three β-decaying isomers in ^{70}Cu.** *Physical review letters* **92**(11): 112501. DOI:10.1103/PhysRevLett.92.112501 Also part of: 'Phyiscs of hadrons and nuclei'.

P-P081 Vatulin, V. V.; Kunin, A. V.; Golubev, A. A.; Luk'yashin, V. É.; Turtikov, V. I.; Sharkov, B. Y.; Baldina, E. G.; Borisenko, N. G.; Gnutov, A. S.; Visar, J.*; Hoffmann, D. H. H.*; Jacobi, J.*: **Measurement of the total range and specific energy deposition of a beam of uranium ions in porous carbon targets.** *Atomic energy* **96**(4): 275–281. DOI:10.1023/B:ATEN.0000035998.92817.7c

P-P082 Verdú, J.; Djekić, S.*; Stahl, S.*; Valenzuela, T.; Vogel, M.; Werth, G.; Beier, T.*; Kluge, H.-J.*; Quint, W.*: **Electronic g factor of hydrogenlike oxygen $^{16}O^{7+}$.** *Physical review letters* **92**(9): 093002. DOI:10.1103/PhysRevLett.92.093002

P-P083 Wattellier, B.; Fuchs, J.; Zou, J. P.; Abdeli, K.; Haefner, C.*; Pepin, H.: **High-power short-pulse laser repetition rate improvement by adaptive wave front correction.** *Review of scientific instruments* **75**(12): 5186–5192. DOI:10.1063/1.1819379

P-P084 Wendt, K.; Blaum, K.*; Brück, K.; Geppert, C.; Kluge, H.-J.*; Mukherjee, M.*; Passler, G.; Schwarz, S.; Sirotzki, S.; Wies, K.: **A highly selective laser ion source for bunched, low emittance beam release.** *Nuclear physics A, Nuclear and hadronic physics* **746**: 47C–53C. [Proceedings of the Sixth International Conference on Radioactive Nuclear Beams (RNB6) Argonne 20030922/26] DOI:10.1016/j.nuclphysa.2004.09.067

P-P085 Zioutas, K.; Dennerl, K.; DiLella, L.; Hoffmann, D. H. H.; Jacoby, J.; Papaevangelou, T.: **Quiet-sun X-rays as signature for new particles.** *The astrophysical journal : an internat. review of spectroscopy and astronomical physics: Part 1* **607**(1): 575–579.

P-P086 Zioutas, K.; Hoffmann, D. H. H.; Dennerl, K.; Papaevangelou, T.: **What is dark matter made of?** *Science* **306**(5701): 1485–1487. DOI:10.1126/science.1102823

2. Further publications

P-I001nr Bergström, I.; Schuch, R.*; Blaum, K.*; Fritioff, T.: **Contributions to fundamental physics and constants using Penning traps**. In: Klapdor-Kleingrothaus, Hans V. (Ed.): *Beyond the desert 2003 : proceedings of the Fourth Tegernsee International Conference on Particle Physics Beyond the Standard Model, BEYOND 2003, Castle Ringberg, Tegernsee, Germany, 9 - 14 June 2003*. Springer proceedings in physics 92, Berlin, Heidelberg, New York, Hong Kong, London, Milan, Paris, Tokyo: Springer, 2004. International Conference on Particle Physics Beyond the Standard Model, Tegernsee.

P-I002nr Bethge, K.; Gruber, G.*; Stöhlker, T.*: **Physik der Atome und Moleküle: Eine Einführung**. Weinheim: Wiley-VCH, 2004. Second edition.

P-I003nr Blaum, K.*: **Exotische Kerne auf die Waage gestellt [Gustav-Hertz-Preis 2004].** *Physik Journal* **3**(8/9), 2004, 71-76p.

P-I004nr Brand, H.*; Beck, D.*; Gaul, E.; Geithner, W.; Götte, S.*; Kühl, T.*; Poppensieker, K.*; Roth, M.*; Thiemer, U.*; Kriznar, I.; Plesko, M.; Pucelj, A.; Sekoranja, M.; Verstovsek, I.: **The PHELIX Control System Based on UML Design Level Programming in LabVIEW**. In: Pohang Accelerator Laboratory (Ed.): *he IX International Conference on Accelerator and Large Experimental Physics Control Systems, Gyeongju, Korea from October 13 – 17, 2003*, Pohang: Pohang Accelerator Laboratory, 2004. International Conference on Accelerator and Large Experimental Physics Control Systems, Pohang, 13.10.2003-17.10.2003, 472-474p.

P-I005nr Gaiduk, P. I.; Trautmann, C.*; Toulemonde, M.; Nylandsed Larsen, A.: **Discountinous latent tracks in relaxed Si1-xGex alloy layers: a composite effect**. In: *Vesti Natsyyanal'nai Adaemiii Navuk Belarusi, Seryya Fizika-Matematychnykh Navuk*, 97-101p.

P-I006nr Mokler, P. H.*: **New Turbomolecular Pump with Central Opening for Free Axial Access.** *Vakuum in Forschung und Praxis* **16**, 2004, 89-91p.

P-I007nr Piriz, A. R.*; Temporal, M.*; Lopez Cela, J.; Grandjouan, N.; Tahir, N. A.*; Hoffmann, D. H. H.*: **Analysis of the Minimum Wobbler Rotation Frequency Required to Uniformly Irradiate a Heavy Ion Driven Cylindrical Target**. In: Hammel, B. A.; et al. (Eds.): *Inertial fusion sciences and applications 2003: state of the art 2003*, La Grange Park: American Nuclear Society, 2004. Third International Conference on Inertial Fusion Sciences and Applications, Monterey, 07.09.2003-12.09.2003, 907-9011p.

P-I008nr Roth, M.*; Azima, A.; Blazevic, A.*; Borneis, S.*; Brambrick, E.; Gaul, E.; Geisel, M.; Kuehl, T.*; Neumayer, P.*; Pirzadeh, P.*; Rosmej, F. B.; Rytter, M.; Schaumann, G.*; Schlegel, T.*; Tahir, N. A.*; Udrea, S.*; Varentsov, D.*; Hoffmann, D. H. H.*: **Research Using Intense Ion and Lase Beams at GSI**. In: Hammel, B. A.; et al. (Eds.): *Inertial fusion sciences and applications 2003 : state of the art 2003*, La Grange Park: American Nuclear Society, 2004. Third International Conference on Inertial Fusion Sciences and Applications, Monterey, 07.09.2003-12.09.2003, 907-9011p.

P-I009nr Stöhlker, T.*; Banas, D.*; Fritzsche, S.; Gumberidze, A.*; Kozhuharov, C.*; Ma, X.*; Orsic-Muthig, A.*; Spillmann, U.*; Sierpowski, D.*; Surzhykov, A.; Tachenov, S.*; Warczak, A.*: **Angular Correlation and Polarization Studies for**

Radiative Electron Capture into High-Z Ions. *Physica Scripta* **T110**, 2004, 384-388p.

P-I010nr Stöhlker, T.*; Banas, D.*; Fritzsche, S.; Gumberidze, A.*; Kozhuharov, C.*; Ma, X.*; Orsic-Muthig, A.*; Spillmann, U.*; Sierpowski, D.*; Surzhykov, A.; Tachenov, S.*; Warczak, A.*: **Angular Correlation and Polarization Studies for Radiative Electron Capture into High-Z Ions.** *Physica Scripta* **T110**, 2004, 384-388p. XXIII International Conference on Photonic, Electronic and Atomic Collisions, Stockholm University/ Aula Magna, Stockholm.

P-I011nr Tahir, N. A.*; Varentsov, D.*; Deutsch, C.; Filimonov, A.; Fortov, V. E.; Gryaznov, V.; Hoffmann, D. H. H.*; Kulish, M.*; Lomonosov, I. V.*; Mintsev, V.*; Nikolaev, D.*; Piriz, A. R.*; Shilkin, N.*; Shutov, A.*; Temporal, M.*; Ternovoi, V.*; Udrea, S.*; Utkin, A.: **Applications of Intense Heavy Ion Beams to Studies of Thermophysical Properties of High-Energy-Density Matter**. In: Hammel, B. A.; et al. (Eds.): *Inertial fusion sciences and applications 2003 : state of the art 2003*, La Grange Park: American Nuclear Society, 2004. Third International Conference on Inertial Fusion Sciences and Applications, Monterey, 07.09.2003-12.09.2003, 907-9011p.

P-I012nr Tomaselli, M.*; Liu, L. C.: **Study Nuclear Halo Structure with (e,e'p) and (e,e'd)**. In: *Probing Nucleons and Nuclei via the (e,e'p) Reaction*, Grenoble, 2004.

P-I013nr Verdú, J. L.; Alonso, J.; Djekic, S.*; Kluge, H.*; Quint, W.*; Valenzuela, T.; Vogel, M.; Werth, G.: **Determination of the g-factor of single hydrogen-like ions by mode coupling in a Penning trap.** *Physica Scripta* **T111**, 2004, 68.

Publications in 'Cancer research'

Compiled by K. Große

This programme is part of the research field 'Health' of the Helmholtz-Gemeinschaft
See <http://www.helmholtz.de/en/Research_Fields/Gesundheit.html>.

1. Reviewed publications

P-C001 Barak, J.; Haran, A.; Adler, E.; Azoulay, M.; Levinson, J.; Zentner, A.; David, D.; Fischer, B. E.*; Heiss, M.*; Betel, D.: **Use of light-Ion-induced SEU in devices under reduced bias to evaluate their SEU cross section.** *IEEE transactions on nuclear science* **51**(6): 3486–3493. Also part of: 'Large-scale facilities for research with photons, neutrons and ions'.

P-C002 Bert, C.*; Rietzel, E.*; Grözinger, S.*; Kramer, M.*; Haberer, T.*; Kraft, G.*: **4D treatment planning for organ motion compensated heavy-ion therapy.** *Medical physics* **31**(6): 1751–1751. [The AAPM 46th annual meeting program: 'Scientific Abstracts and Sessions'] DOI:10.1118/1.1776415

P-C003 Brons, S.*; Psonka, K.; Heiß, M.*; Gudowska-Nowak, E.; Taucher-Scholz, G.*; Neumann, R.*: **Direct visualisation of heavy ion induced DNA fragmentation using atomic force Microscopy.** *Radiotherapy and oncology: journal of the European Society for Therapeutic Radiology and Oncology* **73**: S112–S114. Also part of: 'Large-scale facilities for research with photons, neutrons and ions'.

P-C004 Fournier, C.*; Taucher-Scholz, G.*: **Radiation induced cell cycle arrest: an overview of specific effects following high-LET exposure.** *Radiotherapy and oncology: journal of the European Society for Therapeutic Radiology and Oncology* **73**: S119–S122.

P-C005 Fournier, C.*; Wiese, C.*; Taucher-Scholz, G.*: **Accumulation of the cell cycle regulators TP53 and CDKN1A (p21) in human fibroblasts after exposure to low- and high-LET radiation.** *Radiation research* **161**(6): 675–684.

P-C006 Grözinger, S. O.*; Li, Q.; Rietzel, E.*; Haberer, T.*; Kraft, G.*: **3D online compensation of target motion with scanned particle beam.** *Radiotherapy and oncology: journal of the European Society for Therapeutic Radiology and Oncology* **73**: S77–S79.

P-C007 Gudowska-Nowak, E.; Nasonova, E.; Ritter, S.*; Scholz, M.*: **Chromosome fragmentation after irradiation with C ions.** *Radiotherapy and oncology: journal of the European Society for Therapeutic Radiology and Oncology* **73**: S123–S126.

P-C008 Gueven, N.; Becherel, O. J.; Kijas, A. W.; Chen, P.; Howe, O.; Rudolph, J. H.*; Gatti, R.; Date, H.; Onodera, O.; Taucher-Scholz, G.*; Lavin, M. F.: **Aprataxin, a novel protein that protects against genotoxic stress.** *Human molecular genetics* **13**(10): 1081–1093. DOI:10.1093/hmg/ddh122

P-C009 Gunzert-Marx, K.*; Schardt, D.*; Simon, R. S.*: **Fast neutrons produced by nuclear fragmentation in treatment irradiations with ^{12}C beam.** *Radiation protection dosimetry* **110**(1): 595–600. DOI:10.1093/rpd/nch138

P-C010 Gunzert-Marx, K.*; Schardt, D.*; Simon, R. S.*: **The fast neutron component in treatment irradiations with C-12 beam.** *Radiotherapy and oncology: journal of the European Society for Therapeutic Radiology and Oncology* **73**: S92–S95.

P-C011 Haberer, T.; Debus, J.; Eickhoff, H.*; Jäkel, O.; Schulz-Ertner, D.; Weber, U.: **TheHeidelbergion therapy center.** *Radiotherapy and oncology: journal of the European Society for Therapeutic Radiology and Oncology* **73**: S186–S190.

P-C012 Heiss, M.*; Fischer, B. E.*; Cholewa, M.*: **Status of the GSI microbeam facility for cell irradiation with single ions.** *Radiation research* **161**(1): 98–99. DOI:10.1043/0033-7587(2004)161<0087:POTTIT>2.0.CO;2 Also part of: 'Large-scale facilities for research with photons, neutrons and ions'.

P-C013 Hofman-Hüther, H.; Scholz, M.*; Rave-Fränk, M.; Virsik-Köpp, V.: **Induction of reproductive cell death and chromosome aberrations in radioresistant tumour cells by carbon ions.** *International journal of radiation biology* **80**(6): 423–435.

P-C014 Jäkel, O.; Krämer, M.*; Schulz-Ertner, D.; Heeg, P.; Karger, C. P.; Didinger, B.; Nikoghosyan, A.; Debus, J.: **Treatment planning for carbon ion radiotherapy in Germany: Review of clinical trials and treatment planning studies.** *Radiotherapy and oncology: journal of the European Society for Therapeutic Radiology and Oncology* **73**: S86–S91.

P-C015 Jakob, B.*; Fournier, C.*; Scholz, M.*; Taucher-Scholz, G.*: **Cellular and subnuclear response of CDKN1A (p21) after low-fluence heavy-ion irradiation.** *Radiation research* **161**(1): 108–109. DOI:10.1043/0033-7587(2004)161<0087:POTTIT>2.0.CO;2

P-C016 Krämer, M.*; Jäkel, O.; Haberer, T.*; Rietzel, E.*; Schardt, D.*; Scholz, M.*; Wang, J. F.; Weber, U.*; Weyrather, W.*: **Treatment planning for scanned ion beams.** *Radiotherapy and oncology: journal of the European Society for Therapeutic Radiology and Oncology* **73**: S80–S85.

P-C017 Laczko, G.; Dangendorf, V.; Krämer, M.*; Schardt, D.*; Tittelmeier, K.: **High-resolution heavy ion track structure imaging.** *Nuclear instruments & methods in physics research, Section A, Accelerators, spectrometers, detectors and associated equipment* **535**(1): 216–220. [Proceedings of the 10th International Vienna Conference on Instrumentation, Vienna, Austria, 20040216/21] DOI:10.1016/j.nima.2004.07.125

P-C018 Li, Q.; Groezinger, S. O.*; Haberer, T.*; Rietzel, E.*; Kraft, G.*: **Online compensation for target motion with scanned particle beams: simulation environment.** *Physics in medicine and biology* **49**(14): 3029–3046. DOI:10.1088/0031-9155/49/14/001

P-C019 Narici, A.; Belli, F.; Bidoli, V.; Casolino, M.; De Pascale, M. P.; Di Fino, L.; Furano, G.; Modena, I.; Morselli, A.; Picozza, P.; Reali, E.; Rinaldi, A.; Ruggieri, D.; Sparvoli, R.; Zaconte, V.; Sannita, W. G.; Carozzo, S.; Licoccia, S.; Romagnoli, P.; Traversa, E.; Cotronei, V.; Vazquez, M.; Miller, J.; Salnitskii, V. P.; Shevchenko, O. I.; Petrov, V. P.; Trukhanov, K. A.; Galper, A.; Khodarovich, A.; Korotkov, M. G.; Popov, A.; Vavilov, N.; Avdeev, S.; Boezio, M.; Bonvicini, W.; Vacchi, A.; Zampa, N.; Mazzenga, G.; Ricci, M.; Spillantini, P.; Castellini, G.; Vittori, R.; Carlson, P.; Fuglesang, C.; Schardt, D.*: **The ALTEA/ALTEINO projects: studying functional effects of microgravity and cosmic radiation.** *Advances in space research* **33**(8): 1352–1357. DOI:10.1016/j.asr.2003.09.052

P-C020 Nasonova, E.; Füssel, K.*; Berger, S.*; Gudowska-Nowak, E.*; Ritter, S.*: **Cell cycle arrest and aberration yield in normal human fibroblasts. I. Effects of X-rays and 195MeVu^{-1}C ions.** *International journal of radiation biology* **80**(9): 621–634.

P-C021 Nasonova, E.*; Ritter, S.*: **Cytogenetic effects of densely ionising radiation in human lymphocytes: impact of cell cycle delays.** *Cytogenetic and genome research* **104**(1): 216–220. DOI:10.1159/000077492

P-C022 Pönisch, F.; Parodi, K.; Hasch, B. G.*; Enghardt, W.: **The modelling of positron emitter production and PET imaging during carbon ion therapy.** *Physics in medicine and biology* **49**(23): 5217–5232. DOI:10.1088/0031-9155/49/23/002

P-C023 Ramm, U.; Moog, J.; Spielberger, B.*; Bankamp, A.; Botcher, H. D.; Kraft, G.*: **Investigations of dose response of BANG (R) polymer-gels to carbon ion irradiation.** *Radiotherapy and oncology: journal of the European Society for Therapeutic Radiology and Oncology* **73**: S99–S101.

P-C024 Rietzel, E.*; Chen, G. T. Y.; Choi, N. C.; Willett, C. G.: **4D imaging and treatment planning.** *Radiotherapy and oncology: journal of the European Society for Therapeutic Radiology and Oncology* **73**: S140–S140.

P-C025 Rietzel, E.*; Rosenthal, S. J.; Gierga, D. P.; Willett, C. G.; Chen, G. T. Y.: **Moving targets: detection and tracking of internal organ motion for treatment planning and patient set-up.** *Radiotherapy and oncology: journal of the European Society for Therapeutic Radiology and Oncology* **73**: S68–S72.

P-C026 Sannita, W. G.; Acquaviva, M.; Ball, S. L.; Belli, F.; Bisti, S.; Bidoli, V.; Carozzo, S.; Casolino, M.; Cucinotta, F.; De Pascale, M. P.; Di Fino, L.; Di Marco, S.; Maccarone, R.; Martello, C.; Miller, J.; Narici, L.; Peachey, N. S.; Picozza, P.; Rinaldi, A.; Ruggieri, D.; Saturno, M.; Schardt, D.*; Vazquez, M.*: **Effects of heavy ions on visual function and electrophysiology of rodents: the ALTEA-MICE project.** *Advances in space research* **33**(8): 1347–1351. DOI:10.1016/j.asr.2003.11.007

P-C027 Scholz, M.*; Kraft, G.*: **The physical and radiobiological basis of the local effect model: A response to the commentary by R Katz.** *Radiation research* **161**(5): 612–620.

P-C028 Schulz-Ertner, D.; Nikoghosyan, A.; Didinger, B.; Debus, J.: **Carbon ion radiation therapy for chordomas and low grade chondrosarcomas - current status of the clinical trials at GSI.** *Radiotherapy and oncology: journal of the European Society for Therapeutic Radiology and Oncology* **73**: S51–56.

P-C029 Schulz-Ertner, D.; Nikoghosyan, A.*; Thilmann, C.*; Haberer, T.*; Jäkel, O.*; Karger, C.*; Kraft, G.*; Wannenmacher, M.; Debus, J.*: **Results of carbon ion radiotherapy in 152 patients.** *International journal of radiation oncology, biology, physics* **58**(2): 631–640. DOI:10.1016/j.ijrobp.2003.09.041

P-C030 Staab, A.; Zukowski, D.; Walenta, S.; Scholz, M.*; Mueller-Klieser, W.*: **Response of Chinese hamster V79 multicellular spheroids exposed to high-energy carbon ions.** *Radiation research* **161**(2): 219–227.

P-C031 Weyrather, W. K.*: **Introduction to radiobiological aspects of hadron therapy.** *Radiotherapy and oncology: journal of the European Society for Therapeutic Radiology and Oncology* **73**: S111–S111.

P-C032 Weyrather, W. K.*; Kraft, G.*: **RBE of carbon ions: Experimental data and the strategy of RBE calculation for treatment planning.** *Radiotherapy and oncology: journal of the European Society for Therapeutic Radiology and Oncology* **73**: S161–S169.

2. Further publications

P-C001nr Bethge, K.; Kraft, G.*; Kreisler, P.; Walter, G.*: **Medical Applications of Nuclear Physics**. Berlin, Heidelberg, New York, Hong Kong, London, Milan, Paris, Tokyo: Springer, 2004.

P-C002nr Weyrather, W. K.*: **Medical Applications of Accelerated Ions**. In: Al-Khalili, J.; Roeckl, E. (Eds.): *The Euroschool Lectures on Physics with Exotic Beams*. Lectures Notes in Physics; 651, Berlin, Heidelberg, New York: Springer, 2004, 469-490p. DOI:10.1007/b98790

P-C003nr Weyrather, W.*: **Tumortherapie mit schweren Ionen am Beispiel der GSI.** *Der mathematische und naturwissenschaftliche Unterricht* **57**(6), 2004, 328-333p. MNU-Kongress 2003, Frankfurt/M.

Publications in field of accelerator research and development

Compiled by K. Große

1. Reviewed publications

P-A001 Adamczewski, J.*; Al-Turany, M.*; Bertini, D.*; Essel, H. G.*; Kurz, N.*; Linev, S.*; Richter, M.*: **Go4 on-line monitoring.** *IEEE transactions on nuclear science* **51**(3): 565–570.

P-A002 Ageev, A.; Bogdanov, I.; Kozub, S.; Shcherbakov, P.; Slabodchikov, P.; Sytnik, V.; Tkachenko, L.; Zubko, V.; Kaugerts, J.; Moritz, G.*: **Development of superconducting dipole design for creation of fast-cycling magnetic fields.** *IEEE transactions on applied superconductivity* **14**(2): 295–299. DOI:10.1109/TASC.2004.829089

P-A003 Ciavola, G.; Celona, L.; Gammino, S.; Presti, M.; Ando, L.; Passarello, S.; Zhang, X. Z.; Consoli, F.; Chines, F.; Percolla, C.; Calzona, V., Winkler, M.*: **A version of the Trasco Intense Proton Source optimized for accelerator driven system purposes.** *Review of scientific instruments* **75**(5): 1453–1456. DOI:10.1063/1.1690459 Also part of: 'Large-scale facilities for research with photons, neutrons and ions'.

P-A004 Cimino, R.; Collins, I. R.; Furman, M. A.; Pivi, M.; Ruggiero, F.; Rumolo, G.*; Zimmermann, F.: **Can low-energy electrons affect high-energy physics accelerators?** *Physical review letters* **93**(1): 014801. DOI:10.1103/PhysRevLett.93.014801

P-A005 Franzke, B.*; Beller, P.*; Beckert, K.*; Dolinskii, A.*; Hülsmann, P.*; Nolden, F.*; Peschke, C.*; Steck, M.*: **Fast cooling of antiproton and radioactive ion beams in future storage rings at GSI.** *Nuclear instruments & methods in physics research, Section A, Accelerators, spectrometers, detectors and associated equipment* **532**(1): 97–104. [International Workshop on Beam Cooling and Related Topics, Lake Yamanaka, Yamanashi, Japan, 20030519/23] DOI:10.1016/j.nima.2004.06.100

P-A006 Galonska, M.*; Hollinger, R.*; Spädtke, P.*: **Charge sensitive evaluated ion and electron energy distributions of a vacuum arc plasma.** *Review of scientific instruments* **75**(5): 1592–1594. DOI:10.1063/1.1691518

P-A007 Hasse, R. W.*: **Coulomb strings in heavy ion storage rings: explanation and stability criteria.** *Nuclear instruments & methods in physics research, Section A, Accelerators, spectrometers, detectors and associated equipment* **532**(1): 382–387. DOI:10.1016/j.nima.2004.06.068

P-A008 Hasse, R. W.*; Boine-Frankenheim, O.*: **Scaling laws with current for equilibrium momentum spread and emittances from intrabeam scattering and electron cooling.** *Nuclear instruments & methods in physics research, Section A, Accelerators, spectrometers, detectors and associated equipment* **532**(1): 451–453. [International Workshop on Beam Cooling and Related Topics, Lake Yamanaka, Yamanashi, Japan, 20030519/23] DOI:10.1016/j.nima.2004.06.086

P-A009 Hollinger, R.*; Galonska, M.*; Spädtke, P.*: **Development of a vacuum arc ion source for injection of high current uranium ion beam into the UNILAC at GSI.** *Review of scientific instruments* **75**(5): 1595–1597. DOI:10.1063/1.1691516

P-A010 Hollinger, R.*; Spädtke, P.*: **Comparison of different extraction and acceleration systems for a high intense proton beam for the future proton linac at GSI.** *Review of scientific instruments* **75**(5): 1656–1658. DOI:10.1063/1.1702123

P-A011 Kalimov, A.; Fischer, E.*; Hess, G.*; Moritz, G.*; Muhle, C.*: **Investigation of the power losses in a laminated dipole magnet with superconducting coils.** *IEEE transactions on applied superconductivity* **14**(2): 267–270. DOI:10.1109/TASC.2004.829068

P-A012 Kalimov, A.; Moritz, G.*; Zeller, A.: **Design of a superferric dipole magnet with high field quality in the aperture.** *IEEE transactions on applied superconductivity* **14**(2): 271–274. DOI:10.1109/TASC.2004.829070

P-A013 Khodzhibagiyan, H. G.; Kovalenko, A. D.; Fischer, E.: **Some aspects of cable design for fast cycling superconducting synchrotron magnets.** *IEEE transactions on applied superconductivity* **14**(2): 1031–1034. DOI:10.1109/TASC.2004.830386

P-A014 Kindler, B.*; Hartmann, W.*; Klemm, J.*; Lommel, B.*; Steiner, J.*: **Preparation of targets by sputter deposition.** *Nuclear instruments & methods in physics research, Section A, Accelerators, spectrometers, detectors and associated equipment* **521**(1): 222–226. [Accelerator Target Technology for the 21st Century. Proceedings of the 21st World Conference of the International Nuclear Target Society, Argonne, IL, USA, 4 - 8 November 2002] DOI:10.1016/j.nima.2003.11.153

P-A015 Kovalenko, A. D.; Agapov, N. N.; Aksenov, V. G.; Karpunina, I. E.; Khodzhibagiyan, H. G.; Kuznetsov, G. L.; Voevodin, M. A.; Moritz, G.*; Fischer, E.*; Hess, G.*; Muehle, C.*: **Progress in the design and study of a superferric dipole magnet for the GSI fast-pulsed synchrotron SIS100.** *IEEE transactions on applied superconductivity* **14**(2): 321–324. DOI:10.1109/TASC.2004.829112

P-A016 Moritz, G.*; Pschorn, I.*; Klos, F.*; Weipert, M.*: **Geometric and magnetic measurements of the Gantry dipole for the HICAT medical accelerator.** *IEEE transactions on applied superconductivity* **14**(2): 612–615. DOI:10.1109/TASC.2004.830000

P-A017 Muehle, C.*; Langenbeck, B.*; Kalimov, A.; Klos, F.*; Moritz, G.*; Schlitt, B.*: **Magnets for the Heavy-Ion Cancer Therapy Accelerator facility (HICAT) for the clinic in Heidelberg.** *IEEE transactions on applied superconductivity* **14**(2): 461–464. DOI:10.1109/TASC.2004.829696

P-A018 Nolden, F.*; Beckert, K.*; Beller, P.*; Franzke, B.*; Peschke, C.*; Steck, M.*: **Experience and prospects of stochastic cooling of radioactive beams at GSI.** *Nuclear instruments & methods in physics research, Section A, Accelerators, spectrometers, detectors and associated equipment* **532**(1): 329–334. DOI:10.1016/j.nima.2004.06.062

P-A019 Peschke, C.*; Nolden, F.*; Balk, A.: **Planar pick-up electrodes for stochastic cooling.** *Nuclear instruments & methods in physics research, Section A, Accelerators, spectrometers, detectors and associated equipment* **532**(1): 459–464. [International Workshop on Beam Cooling and Related Topics, Lake Yamanaka, Yamanashi, Japan, 20030519/23] DOI:10.1016/j.nima.2004.06.082

P-A020 Qiang, J.; Ryne, R. D.; Hofmann, I.*: **Space-charge driven emittance growth in a 3D mismatched anisotropic beam.** *Physical review letters* **92**(17): 174801. DOI:10.1103/PhysRevLett.92.174801

P-A021 Rumolo, G.*; Tomas, R.: **Decoherence of a longitudinally kicked beam with chromaticity.** *Nuclear instruments & methods in physics research, Section A, Accelerators, spectrometers, detectors and associated equipment* **528**(3): 670–676. DOI:10.1016/j.nima.2004.03.206

P-A022 Spädtke, P.*: **Sophisticated computer simulation of ion beam extraction for different types of plasma generators.** *Review of scientific instruments* **75**(5): 1643–1645. DOI:10.1063/1.1695648

P-A023 Steck, M.*; Beller, P.*; Beckert, K.*; Franzke, B.*; Nolden, F.*: **Electron cooling experiments at the ESR.** *Nuclear instruments & methods in physics research, Section A, Accelerators, spectrometers, detectors and associated equipment* **532**(1): 357–365. DOI:10.1016/j.nima.2004.06.065

P-A024 Tinschert, K.*; Iannucci, R.*; Bossler, J.*; Lang, R.*: **Experimental studies of the afterglow mode with xenon in a CAPRICE ECRIS.** *Review of scientific instruments* **75**(5): 1407–1409. DOI:10.1063/1.1690472

P-A025 Wilson, A. N.; Anerella, M.; Ganetis, G.; Ghosh, A. K.; Joshi, P.; Marone, A.; Muehle, C.*; Muratore, J.; Schmazle, J.; Soika, R.; Thomas, R.; Wanderer, P.; Kaugerts, J.*; Moritz, G.*; Hassenzahl, W. V.: **Measured and calculated losses in model dipole for GSI's heavy ion synchrotron.** *IEEE transactions on applied superconductivity* **14**(2): 306–309. DOI:10.1109/TASC.2004.829096

P-A026 Zenkevich, P.; Dolinskii, A.*; Hofmann, I.*: **Dipole instability of a circulating beam due to the ion cloud in an electron cooling system.** *Nuclear instruments & methods in physics research, Section A, Accelerators, spectrometers, detectors and associated equipment* **532**(1): 454–458. [International Workshop on Beam Cooling and Related Topics, Lake Yamanaka, Yamanashi, Japan, 20030519/23] DOI:10.1016/j.nima.2004.06.092

2. Further publications

P-A001nr Barth, W.*; Dahl, L.*; Glatz, J.; Groening, L.*; Richter, S. G.*; Yaramishev, S.*: **Achievements of the High Current Beam Performance of the GSI Unilac**. In: CERN (Ed.): *EPAC 2004: A Europhysics Conference 5 to 9 July 2004, Lucerne Congress Centre Switzerland, www.epac04.ch*, Geneva: CERN, 2004. 9th European Particle Accelerator Conference, Lucerne, 05.07.2004-10.07.2004, 1171-1173p.

P-A002nr Bechtold, A.*; Otto, M.; Ratzinger, U.*; Schempp, A.; Vassilakis, E.; Schlitt, B.*: **Beam Test Stand of the RFQ-drifttube-combination for the Therapy Center in Heidelberg**. In: CERN (Ed.): *EPAC 2004: A Europhysics Conference 5 to 9 July 2004, Lucerne Congress Centre Switzerland, www.epac04.ch*, Geneva: CERN, 2004. 9th European Particle Accelerator Conference, Lucerne, 05.07.2004-10.07.2004, 2571-2573p.

P-A003nr Benedetto, E.; Schulte, D.; Zimmermann, F.; Rumolo, G.: **Simulated Emittance Growth due to Electron Cloud for SPS and LHC**. In: CERN (Ed.): *EPAC 2004: A Europhysics Conference 5 to 9 July 2004, Lucerne Congress Centre Switzerland, www.epac04.ch*, Geneva: CERN, 2004. 9th European Particle Accelerator Conference, Lucerne, 05.07.2004-10.07.2004, 1831-1833p.

P-A004nr Burkhardt, H.; Arduini, G.; Benedetto, E.; Métral, E.; Rumolo, G.: **Observation of a Fast Single Bunch Transverse Instability on Protons in the SPS**. In: CERN (Ed.): *EPAC 2004: A Europhysics Conference 5 to 9 July 2004, Lucerne Congress Centre Switzerland, www.epac04.ch*, Geneva: CERN, 2004. 9th European Particle Accelerator Conference, Lucerne, 05.07.2004-10.07.2004, 1843-1845p.

P-A005nr Burkhardt, H.; Manglunki, D.; Martini, M.; Roncarolo, F.; Rumolo, G.: **Investigation of Space Charge Effects and Intrabeam Scattering for Lead Ions in the SPS**. In: CERN (Ed.): *EPAC 2004: A Europhysics Conference 5 to 9 July 2004, Lucerne Congress Centre Switzerland, www.epac04.ch*, Geneva: CERN, 2004. 9th European Particle Accelerator Conference, Lucerne, 05.07.2004-10.07.2004, 1846-1848p.

P-A006nr Corsini, R.; Braun, H.; Carron, G.; Forstner, O.; Geschonke, G.; Jensen, E.; Rinolfi, L.; Schulte, D.; Tecker, F.; Thorndahl, L.; Groening, L.*; Bernard, M.; Bienvenu, G.; Garvey, T.; Roux, R.; Lefevre, T.; Koontz, R.; Miller, R.; Ruth, R.; Yeremian, A. D.; Ferrari, A.: **First Full Beam Loading**

Operation with the CTF3 Linac. In: CERN (Ed.): *EPAC 2004: A Europhysics Conference 5 to 9 July 2004, Lucerne Congress Centre Switzerland, www.epac04.ch*, Geneva: CERN, 2004. 9th European Particle Accelerator Conference, Lucerne, 05.07.2004-10.07.2004, 39-41p.

P-A007nr Dolinskii, A.*; Zenkevich, P.: **Transfer Matrix for a high energy cooling system.** *Problems of atomic science and technology (VANT), Kharkov, Ukraine* **44**(5), 2004, 155.

P-A008nr Eickhoff, H.*; Haberer, T.*; Schlitt, B.*; Weinrich, U.*: **HICAT - The German Hospital-Based Light Ion Cancer Therapy Project**. In: CERN (Ed.): *EPAC 2004: A Europhysics Conference 5 to 9 July 2004, Lucerne Congress Centre Switzerland, www.epac04.ch*, Geneva: CERN, 2004. 9th European Particle Accelerator Conference, Lucerne, 05.07.2004-10.07.2004, 290-294p.

P-A009nr Eickhoff, H.*; Haberer, T.*; Schlitt, B.*; Weinrich, U.*: **HICAT - The German Hospital-Based Light Ion Cancer Therapy Project**. In: CERN (Ed.): *EPAC 2004: A Europhysics Conference 5 to 9 July 2004, Lucerne Congress Centre Switzerland, www.epac04.ch*, Geneva: CERN, 2004. 9th European Particle Accelerator Conference, Lucerne, 05.07.2004-10.07.2004, 290-294p.

P-A010nr Fertman, A.*; Golubev, A.*; Prokuronov, M.; Sharkov, B.*; Fehrenbacher, G.*; Hasse, R.*; Hofmann, I.*; Mustafin, E.*; Schardt, D.*; Weyrich, K.*: **Measurement of Activation Induced by an Argon Beam in a Copper Target at the SIS18**. In: CERN (Ed.): *EPAC 2004: A Europhysics Conference 5 to 9 July 2004, Lucerne Congress Centre Switzerland, www.epac04.ch*, Geneva: CERN, 2004. 9th European Particle Accelerator Conference, Lucerne, 05.07.2004-10.07.2004, 1399-1401p.

P-A011nr Forck, P.*; Dorn, C.*; Herty, M.; Strehl, P.; Sharamentov, S.; Peplov, V.: **A Novel Device for Non-intersecting Bunch Shape Measurement at the High Current GSI-Linac**. In: CERN (Ed.): *EPAC 2004: A Europhysics Conference 5 to 9 July 2004, Lucerne Congress Centre Switzerland, www.epac04.ch*, Geneva: CERN, 2004. 9th European Particle Accelerator Conference, Lucerne, 05.07.2004-10.07.2004, 2541-2543p.

P-A012nr Franchetti, G.*; Hofmann, I.*; Aslaninejad, M.: **Linear Coupling Theory of High Intensity Beams**. In: CERN (Ed.): *EPAC 2004: A Europhysics Conference 5 to 9 July 2004, Lucerne Congress Centre Switzerland, www.epac04.ch*, Geneva: CERN, 2004. 9th European Particle Accelerator Conference, Lucerne, 05.07.2004-10.07.2004, 1981-1983p.

P-A013nr Franchetti, G.*; Orzhekovskaya, A.: **A Space Charge Algorithm for Ellipsoidal Bunches with Arbitrary Beam Size and Particle Distribution**. In: CERN (Ed.): *EPAC 2004: A Europhysics Conference 5 to 9 July 2004, Lucerne Congress Centre Switzerland, www.epac04.ch*, Geneva: CERN, 2004. 9th European Particle Accelerator Conference, Lucerne, 05.07.2004-10.07.2004, 1975-1977p.

P-A014nr Franchi, A.*; Beier, T.*; Kirk, M.*; Moritz, P.*; Rumolo, G.; Tomas, R.: **A Method to Measure the Skew Quadrupole Strengths in the SIS-18 using Two BPMs**. In: CERN (Ed.): *EPAC 2004: A Europhysics Conference 5 to 9 July 2004, Lucerne Congress Centre Switzerland, www.epac04.ch*, Geneva: CERN, 2004. 9th European Particle Accelerator Conference, Lucerne, 05.07.2004-10.07.2004, 1957-1959p.

P-A015nr Hofmann, I.*; Franchetti, G.*; Qiang, J.; D, R.: **Dynamical Effects of the Montague Resonance**. In: CERN (Ed.): *EPAC 2004: A Europhysics Conference 5 to 9 July 2004, Lucerne Congress Centre Switzerland, www.epac04.ch*, Geneva: CERN, 2004. 9th European Particle Accelerator Conference, Lucerne, 05.07.2004-10.07.2004, 1960-1962p.

P-A016nr Hülsmann, P.*; Hutter, G.*; Vinzenz, W.*: **The Bunch Compressor System for SIS18 at GSI**. In: CERN (Ed.): *EPAC 2004: A Europhysics Conference 5 to 9 July 2004, Lucerne Congress Centre Switzerland, www.epac04.ch*, Geneva: CERN, 2004. 9th European Particle Accelerator Conference, Lucerne, 05.07.2004-10.07.2004, 1165-1167p.

P-A017nr Iriso, U.; Blaskiewicz, M.; Cameron, P.; Drees, A.; Fischer, W.; Hseuh, H.; Lee, R.*; Peggs, S.; Smart, L.; Trbojevic, D.; Zhang, S. Y.; Rumolo, G.: **Analysis of Electron Cloud at RHIC**. In: CERN (Ed.): *EPAC 2004: A Europhysics Conference 5 to 9 July 2004, Lucerne Congress Centre Switzerland, www.epac04.ch*, Geneva: CERN, 2004. 9th European Particle Accelerator Conference, Lucerne, 05.07.2004-10.07.2004, 2239-2241p.

P-A018nr Kaspar, K.*; Guenter, H.; Winnefeld, T.*: **Studies on Maximum RF Voltages in Ferrite-tuned Accelerating Cavities**. In: CERN (Ed.): *EPAC 2004: A Europhysics Conference 5 to 9 July 2004, Lucerne Congress Centre Switzerland, www.epac04.ch*, Geneva: CERN, 2004. 9th European Particle Accelerator Conference, Lucerne, 05.07.2004-10.07.2004, 985-987p.

P-A019nr Kitegi, C. A.; Bechtold, A.*; Ratzinger, U.*; Schempp, A.; Beier, T.*; Dahl, L.*; Kozhuharov, C.*; Quint, W.*; Steck, M.*; Minaev, S.*: **Status of the HITRAP Decelerator Linac at GSI**. In: CERN (Ed.): *EPAC 2004: A Europhysics Conference 5 to 9 July 2004, Lucerne Congress Centre Switzerland, www.epac04.ch*, Geneva: CERN, 2004. 9th European Particle Accelerator Conference, Lucerne, 05.07.2004-10.07.2004, 1201-1203p.

P-A020nr Liakin, D.; Barabin, S.; Skachkov, V.; Forck, P.*; Giacomini, T.*; Vetrov, A.: **Development of a Permanent Magnet Residual Gas Profile Monitor With Fast Readout**. In: CERN (Ed.): *EPAC 2004: A Europhysics Conference 5 to 9 July 2004, Lucerne Congress Centre Switzerland, www.epac04.ch*, Geneva: CERN, 2004. 9th European Particle Accelerator Conference, Lucerne, 05.07.2004-10.07.2004, 2724-2726p.

P-A021nr Métral, E.; Carli, C.; Giovannozzi, M.; Martini, M.; Richard, R.; Franchetti, G.*; Hofmann, I.*; Qiang, J.; D, R.: **Intensity Dependent Emittance Transfer Studies at the CERN Proton Synchrotron**. In: CERN (Ed.): *EPAC 2004: A Europhysics Conference 5 to 9 July 2004, Lucerne Congress Centre Switzerland, www.epac04.ch*, Geneva: CERN, 2004. 9th European Particle Accelerator Conference, Lucerne, 05.07.2004-10.07.2004, 1894-1896p.

P-A022nr Neff, S.*; Knobloch, R.*; Niemann, C.; Penache, D.; Tauschwitz, A.*; Hoffmann, D.*; Darmstadt, T.; Yu, S.: **Heavy Ion Beam Transport in Plasma Channels**. In: CERN (Ed.): *EPAC 2004: A Europhysics Conference 5 to 9 July 2004, Lucerne Congress Centre Switzerland, www.epac04.ch*, Geneva: CERN, 2004. 9th European Particle Accelerator Conference, Lucerne, 05.07.2004-10.07.2004, 1183-1185p.

P-A023nr Nesmiyan, I.*; Nolden, F.*; Dolinskii, A.*; Schevchenko, V.: **Stochastic Cooling Simulation of Ion Beams**. In: *Scientific Papers of the institute for nuclear research*, 114.

P-A024nr Nesmiyan, I.*; Nolden, F.*; Schevchenko, V.: **Fokker-Planck Approach to Stochastic Momentum Cooling with Variable Diffusion**. In: *Bulletin of the University of Kiev. Series: Physics & Mathematics 4*, 429.

P-A025nr Nesmiyan, I.*; Nolden, F.*; Schevchenko, V.: **Simulation of Stochastic Momentum Cooling with a Notch Filter**. In: *Bulletin of the University of Kiev. Series: Physics & Mathematics 4*, 514.

P-A026nr Ohmi, K.; Toyama, T.; Rumolo, G.: **Simulation of Ep Instability for a Coasting Proton Beam in Circular Accelerators**. In: CERN (Ed.): *EPAC 2004: A Europhysics Conference 5 to 9 July 2004, Lucerne Congress Centre Switzerland, www.epac04.ch*, Geneva: CERN, 2004. 9th European Particle Accelerator Conference, Lucerne, 05.07.2004-10.07.2004, 2107-2109p.

P-A027nr Rumolo, G.; Bellodi, G.; Zimmermann, F.; Ohmi, K.: **Electron Cloud Build up in Coasting Beams**. In: CERN (Ed.): *EPAC 2004: A Europhysics Conference 5 to 9 July 2004, Lucerne Congress Centre Switzerland, www.epac04.ch*, Geneva: CERN, 2004. 9th European Particle Accelerator Conference, Lucerne, 05.07.2004-10.07.2004, 1963-1965p.

P-A028nr Schwickert, M.*; Peters, A.*: **Computer Controlled Beam Diagnostics for the HICAT Facility**. In: CERN (Ed.): *EPAC 2004: A Europhysics Conference 5 to 9 July 2004, Lucerne Congress Centre Switzerland, www.epac04.ch*, Geneva: CERN, 2004. 9th European Particle Accelerator Conference, Lucerne, 05.07.2004-10.07.2004, 2547-2549p.

P-A029nr Spiller, P. J.*; Blasche, K.*; Hülsmann, P.*; Kraemer, A.; Ramakers, H.*; Reich, H.: **High Intensity Uranium Operation in SIS18**. In: CERN (Ed.): *EPAC 2004: A Europhysics Conference 5 to 9 July 2004, Lucerne Congress Centre Switzerland, www.epac04.ch*, Geneva: CERN, 2004. 9th European Particle Accelerator Conference, Lucerne, 05.07.2004-10.07.2004, 1180-1182p.

P-A030nr Steck, M.*; Beckert, K.*; Beller, P.*; Franczak, B.*; Franzke, B.*; Nolden, F.*: **Improved Performance of the Heavy Ion Storage Ring ESR**. In: CERN (Ed.): *EPAC 2004: A Europhysics Conference 5 to 9 July 2004, Lucerne Congress Centre Switzerland, www.epac04.ch*, Geneva: CERN, 2004. 9th European Particle Accelerator Conference, Lucerne, 05.07.2004-10.07.2004, 1168-1170p.

P-A031nr Steck, M.*; Beckert, K.*; Beller, P.*; Franzke, B.*; Nolden, F.*: **Observation of Ultracold Heavy Ion Beams with Micrometer Size by Scraping**. In: CERN (Ed.): *EPAC 2004: A Europhysics Conference 5 to 9 July 2004, Lucerne Congress Centre Switzerland, www.epac04.ch*, Geneva: CERN, 2004. 9th European Particle Accelerator Conference, Lucerne, 05.07.2004-10.07.2004, 1966-1968p.

P-A032nr Tahir, N.*; Hoffmann, D.*; Goddard, B.; Kain, V.; Schmidt, R.; Fortov, V.; Lomonosov, I.*; Shutov, A.*; Piriz, R.*; Temporal, M.*: **Interaction of the CERN Large Hadron Collider (LHC) Beam with Solid Metallic Targets**. In: CERN (Ed.): *EPAC 2004: A Europhysics Conference 5 to 9 July 2004, Lucerne Congress Centre Switzerland, www.epac04.ch*, Geneva: CERN, 2004. 9th European Particle Accelerator Conference, Lucerne, 05.07.2004-10.07.2004, 641-643p.

P-A033nr Tomas, R.; Bai, M.; Fischer, W.; Franchi, A.*; Rumolo, G.: **Measurement of Multipole Strengths from RHIC BPM Data**. In: CERN (Ed.): *EPAC 2004: A Europhysics Conference 5 to 9 July 2004, Lucerne Congress Centre Switzerland, www.epac04.ch*, Geneva: CERN, 2004. 9th European Particle Accelerator Conference, Lucerne, 05.07.2004-10.07.2004, 2242-2244p.

P-A034nr Weinrich, U.*; Fuchs, R.*; Emde, P.: **The Heavy Ion Gantry of the HICAT-facility**. In: CERN (Ed.): *EPAC 2004: A Europhysics Conference 5 to 9 July 2004, Lucerne Congress Centre Switzerland, www.epac04.ch*, Geneva: CERN, 2004. 9th European Particle Accelerator Conference, Lucerne, 05.07.2004-10.07.2004, 2550-2552p.

P-A035nr Zimmermann, F.; Benedetto, E.; Ruggiero, F.; Schulte, D.; Blaskiewicz, M.; Wang, L.; Bellodi, G.; Rumolo, G.; Ohmi, K.; Su, S.; Furman, M.; Cai, Y.; Torino, M.; Decyk, V. K.; Mori, W.; Ghalam, A. F.; Katsouleas, T.: **Review and Comparison of Simulation Codes Modeling Electron-Cloud Build Up and Instabilities**. In: CERN (Ed.): *EPAC 2004: A Europhysics Conference 5 to 9 July 2004, Lucerne Congress Centre Switzerland, www.epac04.ch*, Geneva: CERN, 2004. 9th European Particle Accelerator Conference, Lucerne, 05.07.2004-10.07.2004, 2502-2504p.

Publications in the area of scientific infrastructure

Compiled by K. Große

1. Reviewed publications

P-I001 Agosteo, S.; Fehrenbacher, G.*; Silari, M.: **Attenuation curves in concrete of neutrons from 1 GeV/u C and U ions on a Fe target for the shielding design of RIB in-flight facilities.** *Nuclear instruments & methods in physics research, Section B, Beam interactions with materials and atoms* **226**(3): 231–242. DOI:10.1016/j.nimb.2004.06.038

P-I002 Alt, C.; Anticic, T.; Baatar, B.; Barna, D.; Bartke, J.; Betev, L.; Białkowska, H.; Billmeier, A.; Blume, C.*; Boimska, B.; Botje, M.; Bracinik, J.; Bramm, R.; Brun, R.; Bunčić, P.; Cerny, V.; Christakoglou, P.; Chvala, O.; Cramer, J. G.; Csató, P.; Darmenov, N.; Dimitrov, A.; Dinkelaker, P.; Eckardt, V.; Farantatos, G.; Filip, P.; Flierl, D.; Fodor, Z.; Foka, P.*; Freund, P.; Friese, V.*; Gál, J.; Gaździcki, M.; Georgopoulos, G.; Gładysz, E.; Hegyi, S.; Höhne, C.; Kadija, K.; Karev, A.; Kniege, S.; Kolesnikov, V. I.; Kollegger, T.; Korus, R.; Kowalski, M.; Kraus, I.*; Kreps, M.; van Leeuwen, M.; Lévai, P.; Litov, L.; Makariev, M.; Malakhov, A. I.; Markert, C.*; Mateev, M.; Mayes, B. W.; Melkumov, G. L.; Meurer, C.; Mischke, A.; Mitrovski, M.; Molnar, J.; Mr?ówczyński, S.; Pálla, G.; Panagiotou, A. D.; Panayotov, D.; Perl, K.; Petridis, A.; Pikna, M.; Pinsky, L.; Pühlhofer, F.; Reid, J. G.; Renfordt, R.; Retyk, W.; Roland, C.; Roland, G.; Rybczyński, M.; Rybicki, A.; Sandoval, A.*; Sann, H.*; Schmitz, N.; Seyboth, P.; Siklér, F.; Sitar, B.; Skrzypczak, E.; Stefanek, G.; Stock, R.; Ströbele, H.; Susa, T.; Szentpetery, I.; Sziklai, J.; Trainor, T. A.; Varga, D.; Vassiliou, M.; Veres, G. I.; Vesztergombi, G.; Vranić, D.*; Wetzler, A.; Włodarczyk, Z.; Yoo, I. K.*; Zaranek, J.; Zimányi, J.; NA49 Collaboration*: **Evidence for an exotic S =-2, Q =-2 baryon resonance in proton-proton collisions at the CERN SPS.** *Physical review letters* **92**(4): 042003. DOI:10.1103/PhysRevLett.92.042003 Also part of: 'Phyiscs of hadrons and nuclei'.

P-I003 Antalic, S.; Cagarda, P.; Ackermann, D.*; Burkhard, H. G.*; Heßberger, F. P.*; Hofmann, S.*; Kindler, B.*; Kojouharova, J.; Lommel, B.*; Mann, R.*; Saro, S.; Schött, H. J.*: **Target cooling for high-current experiments at SHIP.** *Nuclear instruments & methods in physics research, Section A, Accelerators, spectrometers, detectors and associated equipment* **530**(3): 185–193. DOI:10.1016/j.nima.2004.04.217 Also part of: 'Phyiscs of hadrons and nuclei'; 'Large-scale facilities for research with photons, neutrons and ions'.

P-I004 Berdermann, E.* ; Ciobanu, M.*; Connell, S. H.; da Costa, A. M. O. D.; Fernandez-Hernando, L.; Oh, A.; Sellschop, J. P. F.: **Charged particle detectors made of single-crystal diamond.** *Physica status solidi A, Applied research* **201**(11): 2521–2528. DOI:10.1002/pssa.200405170 Also part of: 'Phyiscs of hadrons and nuclei'.

P-I005 Bol, J.; Berdermann, E.*; deBoer, W.; Grigoriev, E.; Hauler, F.; Jungermann, L.: **Beam monitors for TESLA based on diamond strip detectors.** *IEEE transactions on nuclear science* **51**(6): 2999–3005.

P-I006 Dulinski, W.; Berst, J. D.; Besson, A.; Claus, G.; Colledani, C.; Deptuch, G.; Deveaux, M.*; Gay, A.; Grandjean, D.; Gornushkin, Y.; Himmi, A.; Hu, C.; Riester, J. L.; Valin, I.; Winter, M.: **CMOS monolithic active pixel sensors for minimum ionizing particle tracking using non-epitaxial silicon substrate.** *IEEE transactions on nuclear science* **51**(4): 1613–1617.

P-I007 Fehrenbacher, G.*; Festag, J. G.*: **Neutron dose distribution at the GSI fragment separator.** *Radiation protection dosimetry* **110**(1): 739–742. DOI:10.1093/rpd/nch210

P-I008 Geissel, H.*; Litvinov, Y. A.*; Attallah, F.*; Beckert, K.*; Beller, P.*; Bosch, F.*; Boutin, D.*; Faestermann, T.; Falch, M.; Franzke, B.*; Hausmann, M.; Hellström, M.*; Kaza, E.*; Kerscher, T.; Klepper, O.*; Kluge, H.-J.*; Kozhuharov, C.*; Kratz, K- L.*; Litvinov, S. A.; Löbner, K. E. G.; Maier, L.; Matoš, M.*; Münzenberg, G.*; Nolden, F.*; Novikov, Y. N.; Ohtsubo, T.; Ostrowski, A.; Patyk, Z.; Pfeiffer, B.; Portillo, M*.; Radon, T.*; Scheidenberger, C.*; Shishkin, V.*; Stadlmann, J.*; Steck, M.*; Viera, D. J.; Weick, H.*; Winkler, M.*; Wollnik, H.; Yamaguchi, T.*: **New results with stored exotic nuclei at relativistic energies.** *Nuclear physics A, Nuclear and hadronic physics* **746**: 150C–155C. [Proceedings of the Sixth International Conference on Radioactive Nuclear Beams (RNB6) Argonne 20030922/26] DOI:10.1016/j.nuclphysa.2004.09.030 Also part of: 'Phyiscs of hadrons and nuclei'; 'Large-scale facilities for research with photons, neutrons and ions'.

P-I009 Kugler, A.; Agakichiev, H.*; Agodi, C.; Alvarez-Pardo, M.; Alvarez-Pol, H.; Badura, E.*; Balanda, A.; Ballester, F.; Bassi, A.; Bassini, R.; Bellia, G.; Bertini, D.*; Bielcik, J.*; Böhmer, M.; Boiano, C.; Bokemeyer, H.*; Boyard, J. L.; Brambilla, S.; Braun-Munzinger, P.*; Chernenko, S.; Coniglione, R.; Dahlinger, M.*; Daues, H.*; Diaz, R.; Dohrmann, F.; Duran, I.; Eberl, T.; Fabietti, L.; Fateev, O.; Fernandez, C.; Finocchiaro, P.; Friese, J.; Fröhlich, I.; Fuentes, B.; Garzon, J. A.; Genolini, B.; Gernhäuser, R.; Golubeva, M.; Gonzales, D.; Göringer, H.*; Grosse, E.; Guber, F.; Hehner, J.*; Hennino, T.; Hlavac, S.; Hoffmann, J.; Holzmann, R.*; Homolka, J.; Ierusalimov, A.; Iori, I.; Jaskula, M.; Kampfer, B.; Kanaki, K.; Karavichieva, T.; Kirschner, D.; Kidon, L.; Kienle, P.; Koenig, I.*; Koenig, W.*; Körner, H. J.; Kolb, B. W.*; Kopf, U.*; Kotte, R.; Kühn, W.; Kurtukian, T.; Krücken, R.; Kulessa, R.; Kurepin, A.; Lehnert, J.; Lins, E.; Magestro, D.*; Maier-Komor, P.; Maiolino, C.; Markert, J.; Metag, V.; Mousa, J.; Münch, M.; Müntz, C.*; Naumann, L.; Nekhaev, A.; Niebur, W.*; Ott, W.*; Novotny, R.; Otwinowski, J.; Panebratsev, Y.; Pechenov, V.; Petri, M.; Piattelli, P.; Pietraszko, J.; Pleskac, R.; Ploskon, M.; Przygoda, W.; Rabin, N.; Ramstein, B.; Reshetin, A.; Ritman, J.; Rosier, P.; Roy-Stephan, M.; Rustamov, A.*; Sabin, J.; Sadovski, A.; Sailer, B.; Salabura, P.; Sanchez, M.; Sapienza, P.; Senger, P.*; Schroeder, C.*; Shileev, K.; Shishov, P.; Simon, R.*; Smoliankin, V.; Smykov, L.; Spataro, S.; Stelzer, H.*; Ströbele, H.; Stroth, J. ; Sturm, C.*; Sudol, M.*; Taranenko, A.; Tlusty, P.; Toia, A.; Traxler, M.; Tsertos,

H.; Turzo, I.; Vassiliev, D.; Vazquez, A.; Wagner, V.; Walus, W.; Winkler, S.; Wisniowski, M.; Wojcik, T.; Wüstenfeld, J.; Yahlali, N.; Zanevsky, Y.; Zeitelhack, K.; Zovinec, D.; Zumbruch, P.*: **Particle identification at HADES.** *Nuclear physics A, Nuclear and hadronic physics* **734**: 78–81. [Proceedings of the Eighth International Conference On Nucleus-Nucleus Collisions] DOI:10.1016/S0375-9474(04)90257-6 Also part of: 'Phyiscs of hadrons and nuclei'.

P-I010 Stadlmann, J.*; Hausmann, M.*; Attallah, F.*; Beckert, K.*; Beller, P.*; Bosch, F.*; Eickhoff, H.*; Falch, M.; Franczak, B.*; Franzke, B.*; Geissel, H.*; Kerscher, T. H.; Klepper, O.*; Kluge, H.-J.*; Kozhuharov, C.*; Litvinov, Y. A.*; Löbner, K. E. G.; Matoš, M.*; Münzenberg, G.*; Nankov, N.*; Nolden, F.*; Novikov, Y. N.; Ohtsubo, T.*; Radon, T.*; Schatz, H.; Scheidenberger, C.*; Steck, M.*; Weick, H.*; Wollnik, H.: **Direct mass measurement of bare short-lived ^{44}V, ^{48}Mn, ^{41}Ti and ^{45}Cr ions with isochronous mass spectrometry.** *Physics letters B* **586**(1): 27–33. DOI:10.1016/j.physletb.2004.02.014 Also part of: 'Phyiscs of hadrons and nuclei'; 'Large-scale facilities for research with photons, neutrons and ions'.

P-I011 Toleikis, S.*; Manil, B.; Berdermann, E.*; Beyer, H. F.*; Bosch, F.*; Czanta, M.*; Dunford, R. W.; Gumberidze, A.*; Indelicato, P.; Kozhuharov, C.*; Liesen, D.*; Ma, X.*; Marrus, R.; Mokler, P. H.*; Schneider, D.; Simionovici, A.; Stachura, Z.; Stöhlker, T.*; Warczak, A.; Zou, Y.: **Lifetime of the 2(3)P(0) state of He-like Au-197.** *Physical review A, Atomic, molecular, and optical physics* **69**(2): 022507. DOI:10.1103/PhysRevA.69.022507 Also part of: 'Large-scale facilities for research with photons, neutrons and ions'.

2. Further publications

P-S001nr Adam, W.; Berdermann, E.*; Bergonzo, P.; de Boer, W.; Bogani, F.; Borchi, E.; Brambilla, A.; Bruzzi, M.; Colledani, C.; Conway, J.; D'Angelo, P.; Dabrowski, W.; Delpierre, P.; Dulinski, W.; Doroshenko, J.; van Eijk, B.; Fallou, A.; Fischer, P.; Fizzotti, F.; Furetta, C.; Gan, K. K.; Ghodbane, N.; Grigoriev, E.; Hallewell, G.; Han, S.; Hartjes, F.; Hrubec, J.; Husson, D.; Kagan, H.; Kaplon, J.; Kass, R.; Keil, M.; Knoepfle, K. T.; Koeth, T.; Krammer, M.; Logiudice, A.; Lu, R.; Mac Lynne, L.; Manfredotti, C.; Meier, D.; Menichelli, D.; Meuser, S.; Mishina, D.; Moroni, L.; Noomen, J.; Ohl, A.; Pernicka1, M.; Perera, L.; Potenza, R.; Riester J. L.; Roe, S.; Rudge, A.; Sala, S.; Sampietro, M.; Schnetzer, S.; Sciortino, S.; Stelzer, H.*; Stone, R.; Sutera, C.; Trischuk, W.; Tromson, D.; Tuve, C.; Vincenzo, B.; Weilhammer, P.; Wermes, W.; Wetstein, M.; Zeuner, W.; Zoeller, M.: **New developments in CVD diamond for detector applications.** *European Physical Journal C - Particles and Fields* **33**, 2004, S1014-S1016p. DOI:10.1140/epjcd/s2004-03-1798-6

P-S002nr Bol, J.; Berdermann, E.*; de Boer, W.; Grigoriev, E.; Hauler, F.; Jungermann, L.: **Strahlmonitore für TESLA basierend auf Diamant-Streifendetektoren.** *Industrie Diamanten Rundschau* **38**, 2004, IV.

GSI as publisher

Compiled by U. Grundinger and K. Große

All publications of the GSI are available as full texts with public access in the GSI document system on the GSI's homepage.

GSI Accelerator Reports and Notes

GSI-Acc-Note-2004-01-001 Latycheva, L. N.; Mustafin, E. R.*: **Use of the Shield Code for Monte-Carlo Modeling of the Energy Deposition and the Fragmentation Spectra in the Elements of the SIS100 Dipole Magnet Irradiated by 1 GeV/u Uranium Ions**.

GSI-Acc-Note-2004-02-001 Cimino, R.; Collins, I. R.; Furmann, M. A.; Pivi, M.; Ruggiero, F.; Rumolo, G.; Zimmermann, F.: **Can low energy electrons affect high energy physics accelerators?** 2004.

GSI-Acc-Note-2004-03-001 Omet, C.*: **Auslegung eines Kollimatorsystems zur Kontrolle von Umladungsverlusten und Desorptionsgasen im SIS18**.

GSI-Acc-Note-2004-05-001 Franchetti, G.*; Franczak, B.*; Schütt, P.*: **A benchmarking experiment in SIS for dynamic aperture induced beam loss**.

GSI-Acc-Note-2004-06-001 Latyscheva, L. N.; Mustafin, E. R.*: **Modeling of energy deposition and fragment spectra in the construction elements of the SIS300 dipole magnet irradiated by 37 GeV/u uranium ions**.

GSI-Acc-Note-2003-07-001 Fertman, A.*; Golubev, A.*; Turtikov, V.*; Sharkov, B.*; Prokouronov, M.; Fehrenbacher, G.*; Hasse, R. W.*; Hoffmann, D. H. H.*; Hofmann, I.*; Mustafin, E.*; Schardt, D.*; Weyrich, K.*: **Experimental Investigation of the Radioactivity of Copper and Stainless Steel Induced by Irradiation with a Carbon Beam at 200, 300, 400 MeV/u**.

GSI-Acc-Note-2004-08-001 Hülsmann, P.*; Boine-Frankenheim, O.*; Klingbeil, H.*; Schreiber, G.*: **Considerations concerning the RF System of the accelerator chain SIS12/18 - SIS100 for the FAIR-project at GSI**.

GSI-Acc-Note-2004-09-001 Al-khateeb, A.; Boine-Frankenheim, O.*; Hasse, R.*; Hofmann, I.*: **Longitudinal Impedance and Shielding Effectiveness of a Resistive Beam Pipe for Arbitrary Energy and Frequency**.

GSI-Acc-Note-2003-10-002 Bolshakov, A.; Hofmann, I.*; Zenkevich, P.: **Equalization of Transverse Emittances of Extracted Beams in SIS-18 by use of Skew Quadrupoles**.

GSI-Acc-Note-2004-11-001 Huelsmann, P.; Vinzenz, W.*: **The h=2 Broadband Acceleration RF System for the SIS12/18 Upgrade at GSI**.

GSI-Acc-Report-2004-12-001 Omet, C.*; Spiller, P.*: **Loss Calculations for an Ion Beam under Dynamic Vacuum Conditions in a Circular Accelerator**.

GSI Reports and GSI Preprints

GSI-Report-2004-1 Grundinger, U. (Ed.)*: **GSI Scientific Report 2003**, 2004.

GSI-Report-2004-2 Xiang, W.; Spädtke, P.*; Hollinger, R.*; Galonska, M.*; Heymach, F.*: **Computer simulation of high current Uranium beams for the injection beam line of the UNILAC**, 2004.

GSI-Report-2004-3 Xiang, W.; Spädtke, P.*; Hollinger, R.*; Galonska, M.*; Heymach, F.*; Weyrich, K. (Ed.)*: **High Energy Density Physics with Intense Ion and Laser Beams (Annual Report 2003)**, 2004.

GSI-Report-2004-4 Ricciardi, M. V.*: **Estimate of the Intensities of the Radioactive Nucleides Produced at the Super-FRS at the Future GSI Facility**, 2004.

GSI-Preprint-2004-1 Mokler, P. H.*: **New Turbomolecular Pump with Central Opening for Free Axial Access**, 2004.

GSI-Preprint-2004-2 Scholz, M.*; Kraft, G.*: **The Physical and Radiobiological Basis of the Local Effect Model (LEM): A Response to the Commentary by R. Katz**, 2004.

GSI-Preprint-2004-3 Jurado, B.; Schmitt, C.; Schmidt, K.-H.*; Benlliure, J.; Enqvist, T.; Junghans, A. R.; Kelic, A.*; Rejmund, F.: **Transient effects in fission evidenced from new experimental signatures**, 2004.

GSI-Preprint-2004-4 van Roosbroeck, J.; Gunaut, C.; Audi, G.; Beck, D.*; Blaum, K.*; Bollen, G.; Cederkall, J.; Delahaye, P.; De Maesschalk, A.; De Witte, H.; Fedorov, D.; Fedoseyev, V. N.; Franchoo, S.; Fynbo, . H. O. U.; Gorska, M.*; Herfurth, F.*; Heyde, K.; Huyse, M.; Kellerbauer, A.; Kluge, H.-J.*; Köster, U.; Kruglov, K.; Lunney, D.; Mishin, V.; Mueller, W. F.; Nagy, S.; Schwarz, S.; Schweikhard, L.; Smirnova, N. A.; Van der Vel, K.; Van Duppen, P.; Van Dyck, A.; Walters, W. B.; Weissman, L.; Yazidjian, C.*: **Unambiguous Identification of Three Beta-Decaying Isomers in 70Cu**, 2004.

GSI-Preprint-2004-5 Gutermuth, F.*; Radon, T.*; Fehrenbacher, G.*; Siekmann, R.: **Test of the REM-counter WENDI-II from Eberline in different energy-dispersed neutron fields**, 2004.

GSI-Preprint-2004-6 Fehrenbacher, G.*; Wiegel, B.; Iwase, H.*; Radon, T.*; Schardt, D.*; Schuhmacher, H.; Wittstock, J.: **Spectrometry behind concrete shielding for neutrons produced by 400 MeV/u 12C ions impinging on a thick graphite target**, 2004.

GSI-Preprint-2004-7 Jurado, B.; Schmitt, C.; Schmidt, K.-H.*; Benlliure, J.; Junghans, A. R.: **A critical analysis of the modelling of dissipation in fission**, 2004.

GSI-Preprint-2004-8 Jurado, B.; Schmitt, C.; Schmidt, K.-H.*; Benlliure, J.; Junghans, A. R.: **Manifestation of transient effects in fission induced by relativistic heavy-ion collisions**, 2004.

GSI-Preprint-2004-9 Jurado, B.; Schmitt, C.; Schmidt, K.-H.*; Benlliure, J.; Enqvist, T.; Junghans, A. R.; Kelic, A.*; Rejmund, F.: **New signatures on dissipation from fission induced by relativistic heavy-ion collisions**, 2004.

GSI-Preprint-2004-10 Senger, P.*: **Particle Production in Heavy-Ion Collisions**, 2004.

GSI-Preprint-2004-11 Gumberidze, A.*; Stöhlker, T.*; Banas, D.*; Beckert, K.*; Beller, P.*; Beyer, H. F.*; Bosch, F.*; Cai, X.; Hagmann, S.*; Kozhuharov, C.*; Liesen, D.; Nolden, F.*; Ma, . X.; Mokler, P. H.*; Orsic-Muthig, A.*; Steck, M.*; Sierpowski, D.*; Tachenov, S.; Warzcak, A.; Zou, Y.: **Electron-electron interaction in strong electromagnetic fields : the two-electron contribution to the ground-state energy in He-like Uranium**, 2004.

GSI-Preprint-2004-12 Stöhlker, T.*; Banas, D.*; Fritzsche, S.; Gumberidze, A.*; Kozhuharov, C.*; Ma, X.*; Orsic-Muthig, A.*; Spillmann, U.*; Sierpowski, D.*; Surzhykov, A.; Tachenov, S.; Warzcak, A.: **Angular correlation and polarization studies for radiative electron capture ioto high-Z ions**, 2004.

GSI-Preprint-2004-13 Napolitani, P.; Schmidt, K.-H.*; Botvina, A. S.*; Rejmund, F.; Tassan-Got, L.; Villagrasa, C.: **High-resolution velocity measurements on fully identified light nuclides produced in 56-Fe + protons and 56-Fe + Titanium systems**, 2004. IPNO-DR-04-03.

GSI-Preprint-2004-14 Ewald, G.*; Nörtershäuser, W.*; Dax, A.*; Götte, S.*; Kirchner, R.*; Kluge, H.-J.*; Kühl, T.*; Sanchez, R.; Wojtaszek, A.; Bushaw, B. A.*; Drake, G. W. F.; Yan, Z.-C.; Zimmermann, C.: **TI:Nuclear charge radii of 8,9-Li determined by laser spectroscopy**, 2004.

GSI-Preprint-2004-15 Bosch, F.*: **Wie alt ist die Welt? Ältere und neue Vorstellungen der Physik zum Anfang des Universums**, 2004.

GSI-Preprint-2004-16 Rodriguez, D.; Kolhinen, V. S.; Audi, G.; Äystö, J.; Beck, D.*; Blaum, K.*; Bollen, G.; Herfurth, F.*; Jokinen, A.*; Kellerbauer, A.; Kluge, H.-J.*; Oinonen, M.; Schatz, H.; Sauvan, E.; Schwarz, S.: **Mass measurement on the rp-process witing point ^{72}Kr**, 2004.

GSI-Preprint-2004-17 Olson, R. E.; Watson, R. L.; Horvat, V.; Zaharakis, K. E.; DuBois, R. D.*; Stöhlker, T.*: **Electron stripping cross sections for fast, low charge state Uranium ions**, 2004.

GSI-Preprint-2004-18 Du Bois, R. D.; Santos, A. C. F.; Stöhlker, T.*; Bosch, F.*; Bräuning-Demian, A.*; Banas, D.*; Gumberidze, A.*; Hagmann, S.*; Kozhuharov, C.*; Mann, R.*; Orsic Muthig, A.; Spillmann, U.*; Tachenov, S.; Bart, W.; Dahl, L.*; Franzke, B.*; Glatz, J.; Gröning, L.; Richter, S.*; Wilms, D.*; Ullmann, K.; Jagutzki, O.: **Electron loss from 1.4 MeV/u U4,6,10+ ions colliding with Ne, N2, and Ar targets**, 2004.

GSI-Preprint-2004-19 Kelić, A.; Schmidt, K.-H.*; Enqvist, T.; Boudard, A.; Armbruster, P.*; Benlliure, J.; Bernas, M.; Czajkowski, S.; Legrain, R.; Leray, S.; Mustapha, B.; Pravikoff, M.; Rejmund, F.; Stéphan, C.; Taïeb, J.; Tassan-Got, L.; Volant, C.; Wlazło, . W.: **Isotopic and velocity distributions of ^{83}Bi produced in charge-pickup reactions of ^{208}Pb at 1 A GeV**, 2004.

GSI-Preprint-2004-20 Mukherjee, M.*; Kellerbauer, A.; Beck, D.*; Blaum, K.*; Bollen, G.; Carrel, F.; Delahaye, P.; Dilling, J.; George, S.; Guenaut, C.; Herfurth, F.*; Herlert, A.; Kluge, H.-J.*; Köster, U.; Lunney, D.; Schwarz, S.; Schweikhard, L.; Yazidjian, C.*: **The mass of ^{22}Mg**, 2004.

GSI-Preprint-2004-21 Armbruster, P.*; Benlliure, J.; Bernas, M.; Boudard, A.; Casarejos, E.; Czajkowski, S.; Enqvist, T.; Leray, S.; Napolitani, P.; Pereira, J.; Rejmund, F.; Ricciardi, M.-V.*; Schmidt, K.-H.*; Stéphan, C.; Taieb, J.; Tassan-Got, L.; Volant, C.: **Measurement of a Complete Set of Nuclides Cross-Sections and Kinetic Energies in Spallation of ^{238}U 1AGeV with Protons**, 2004.

Further publications

Buballa, M.; Knoll, J.*; Nörenberg, W.*; Schaefer, B.-J.; Wambach, J.*: **Probing Nuclei and Nucleons with Electrons and Photons. Proceedings of the International Workshop XXXII on Gross Properties of Nuclei and Nuclear Excitations, Hirschegg, Austria, January 11 - 17, 2004 [HIRSCHEGG 2004]** Darmstadt: GSI, 2004. <http://theory.gsi.de/hirschegg/>.

DESY (Ed.); GSI (Ed.): **Proceedings of LINAC 2004: XXII International Linear Accelerator Conference, Lübeck, Germany, August 16–20, 2004.** <http://www.linac2004.de/e8/index_eng.html>

Patents and patent applications

Compiled by K. Große

For more information see: <http://www.gsi.de/informationen/tt/index_e.html>

Granted patents and inventors

Haberer, T.; Ott, W.: **Feed-back control of a grid scanner.** US patent January 2004 (GSI No. P154).

Badura, E.: **Vorrichtung und Verfahren zum Umwandeln von Ladungsfluss.** Russian patent January 2004 (GSI No. P138).

Haberer, T.; Kraft, G.; Kraft-Weyrather, W.; Krämer, M.; Schardt, D.; Scholz, M.; Weber, U.; Eickhoff, H.; Dolinskii, A.; Franczak, B.; Krause, U.; Klabunde, J.; Dahl, L.; Pavlovic, M.; Ratzinger, U.; Schlitt, B.; Pawelke, J.; Hinz, R.; Enghardt, W.; together with FZR Dresden: **Ion Beam Therapy System and a method for operating the system.** US patent January 2004 (GSI No. P139).

Eickhoff, H.; Haberer, T.; Spiller, P.; Pavlovic, M.: **Beam scanning system for a heavy ion gantry.** US patent February 2004 (GSI No. P172).

Kraft, G.; Weber, U.: **Apparatus for irradiating tumour tissue.** US patent March 2004 (GSI No. P160).

Kraft, G.: **Ionenstrahlanlage zur Bestrahlung von Tumorgeweben.** US patent May 2004 (GSI No. P158).

Badura, E.; Eickhoff, H.; Haberer, T.; Poppensieker, K.; Schardt, D.: **Überprüfung der Strahlerzeugungs- und der Strahlbeschleunigungsmittel.** US patent June 2004 (GSI No. P151).

Müller, M.; Janik, J.: **Multi-Mode-Metall-Ionenquelle.** German patent June 2004 (GSI No. P182).

Badura, E.: **Vorrichtung und Verfahren zum Überwachen eines Signals.** Russian patent July 2004 (GSI No. P140).

Lang, R.: **Hochofen zur Festkörperverdampfung.** German patent July 2004 (GSI No. P181).

Mann, R.: **Örtliche Schichtdickenmessung an einer Probe.** German patent August 2004 (GSI No. P173).

Badura, E.; Becher, W.; Brand, H.; Essel, H.-G.; Haberer, T. Ott, W.; Poppensieker, K.: **Überprüfung einer Notabschaltung.** EU patent August 2004 (GSI No. P144).

Badura, E.; Eickhoff, H.; Haberer, T.; Poppensieker, K.: **Überprüfung der Strahlführung eines Ionenstrahl-Therapiesystems.** EU patent August 2004 (GSI No. P152).

Badura, E.; Eickhoff, H.; Haberer, T.; Poppensieker, K.; Schardt, D.: **Überprüfung der Strahlerzeugungs- und der Strahlbeschleunigungsmittel.** EU patent September 2004 (GSI No. P151).

Kraft, G.; Weber, U.: **Vorrichtung zur Bestrahlung eines Tumorgewebes.** EU patent September 2004 (GSI No. P160).

Badura, E.; Eickhoff, H.; Essel, H.-G.; Haberer, T.; Poppensieker, K.: **Verfahren zum Betreiben eines Ionenstrahl Therapiesystems.** EU patent October 2004 (GSI No. P146).

Hartmann, G.; Jäkel, O.; Karger, C.; Heeg, P.; DKFZ and University of Heidelberg: **Ionenstrahl Therapiesystem unter Überwachung der Bestrahlungsdosis.** EU patent October 2004 (GSI No. P150).

Dahl, L.; Schlitt, B.: **Apparatus for generating and selecting ions.** US patent October 2004 (GSI No. P168).

Brand, H.; Haberer, T.; Poppensieker, K.; Schardt, D.; Voss, B.: **Bestrahlungssteuereinheit eines Ionenstrahl-Therapiesystems.** EU patent November 2004 (GSI No. P143).

Badura, E.: **Vorrichtung und Verfahren zum Umwandeln von Ladungsfluss.** EU patent November 2004 (GSI No. P138).

Ratzinger, U.; Schlitt, B.: **Driftröhrenbeschleuniger zur Beschleunigung von Ionenpaketen.** German patent November 2004 (GSI No. P193).

Badura, E.: **Vorrichtung und Verfahren zum Überwachen eines Signals.** EU patent December 2004 (GSI No. P140).

Badura, E.; Brand, H.; Essel, H.-G.; Haberer, T.; Poppensieker, K.; Hoffmann, J. Ott, W.: **Vorrichtung und Verfahren zum Steuern einer Bestrahlungseinrichtung.** EU patent December 2004 (GSI No. P137).

Pavlovic, M.; Schardt, D.: **Gantry-System und Verfahren zum Betrieb des Systems.** EU patent December 2004 (GSI No. P142).

Patent applications and inventors

Fischer, B.; Khodzhibagiyan, H.; Kovalenko, A.; Moritz, G.: **Supraleitendes Kabel und Verfahren zur Herstellung desselben.** For EU patent, April 2004 (GSI No. P217).

Fehrenbacher, G.; Festag, J. G.; Gutermuth, F.; Radon, T.: **Passives Neutronendosimeter zur Umgebungsüberwachung.** For German patent, April 2004 (GSI No. P218).

Blasche, K.; Franczak, B.: **Beschleunigeranlage für eine Strahlentherapie mit Ionenstrahlen.** For German patent, May 2004 (GSI No. P219).

Naumann, R.; Poppensieker, K.: **Strahlschutzvorrichtung und Strahlzuteilungsverfahren für medizinische Teilchenbeschleuniger.** For German patent, May 2004 (GSI No. P220).

Grözinger, S. O.; Haberer, T.; Ott, W.; Poppensieker, K.: **Vorrichtung und Verfahren zur Kompensation von Bewegungen eines Zielvolumens während einer Ionenstrahl-Bestrahlung.** For German patent, June 2004 (GSI No. P221).

Blasche, K.; Franczak, B.: **Teilchenbeschleuniger für die Strahlentherapie mit Ionenstrahlen.** For German patent, June 2004 (GSI No. P222).

Giselbrecht, S.; Trautmann, C.; Truckemüller, R.: **Perforation von dreidimensionalen Mikrostrukturen.** For German patent, July 2004 (GSI No. P223).

Fehrenbacher, G.; Radon, T.: **Mehrschichtiger Strahlenschutzbaukörper.** For German patent, September 2004 (GSI No. P224).

Fehrenbacher, G.; Radon, T.: **Mehrschichtige Strahlenschutzwand und Strahlenschutzkammer.** For German patent, December 2004 (GSI No. P228).

Invited talks at conferences and at other institutions

Compiled by K. Große

T-E01 Ackermann, D.: **Beyond darmstadtium - status and perspectives of superheavy element research.** Callaway Gardens, Pine Mountain, Georgia, USA, The Fourth International Conference on Exotic Nuclei and Atomic Masses, September 2004.

T-E02 Ackermann, D.: **Heavy Ion Research at GSI on its way to FAIR.** Straßburg, Frankreich, SYMPOSIUM on Nuclear Physics around the Coulomb Barrier, September 2004.

T-E03 Ackermann, D.: **The Challenge of Super-Heavy Elements synthesis.** Straßburg, Frankreich, SYMPOSIUM on Nuclear Physics around the Coulomb Barrier, September 2004.

T-E04 Andronic, A.: **Statistical coalescence of charm - from SPS to LHC.** University of Clermont-Ferrand, International Workshop on Heavy Flavors in Heavy Ion Collisions at the LHC, December 2004.

T-E05 Andronic, A.: **The CBM Experiment at FAIR.** ICTP Trento, Workshop Creation and flow of baryons, May 2004.

T-E06 Angert, N.: **The FAIR Project- a New Facility for Antiproton and Ion Research.** CERN, Geneva, LHC - Seminar, June 2004.

T-E07 Appelshäuser, H.: **Correlations and fluctuations.** Oakland, Quark Matter 2004, January 2004.

T-E08 Aumann, T.: **Nuclear structure at the drip line.** Göteborg, Schweden, International Nuclear Physics Conference INPC2004, July 2004.

T-E09 Aumann, T.: **Prospects with rare isotope beams at the international facility for antiprotons and ion research (FAIR).** Paestum, Italien, 8th International Spring Seminar on Nuclear Physics: Key Topics in Nuclear Structure, May 2004.

T-E10 Aumann, T.: **Exotic nuclei at high energies.** Orsay, Frankreich, International Workshop on Physics with AGATA, March 2004.

T-E11 Aumann, T.: **Scattering experiments with high-energy radioactive beams.** Bhabha Atomic Research Centre, Mumbai, India, March 2004.

T-E12 Aumann, T.: **Spectroscopic Factors from Coulomb Breakup Measurements.** Trient, Italien, Workshop on Spectroscopic Factors, March 2004.

T-E13 Aumann, T.: **Electromagnetic dissociation of light exotic nuclei.** Hirschegg, Österreich, Hirschegg 2004: Probing Nuclei and Nucleons with Electrons and Photons, January 2004.

T-E14 Aumann, T.: **Untersuchungen von exotischen Kernen mit hochenergetischen Sekundärstrahlen.** Johannes Gutenberg Universität, Mainz, January 2004.

T-E15 Bathe, S.: **Production of direct Photons in Au+Au and p+p Collisions at $\sqrt{s_{NN}}$=200GeV.** UC Riverside/BNL Brookhaven, Physics, March 2004.

T-E16 Berdermann, E.: **Charged Particle Detectors made of Single-Crystal Diamond.** LUC, Diepenbeek-Hasselt (Belgium), IX International Workshop on Surface and Bulk Defects in CVD Diamond Films, February 2004.

T-E17 Blaum, K.: **Gewichtsprobleme anderer Art - Atome auf die Waage gestellt.** Volkshochschule/Fachhochschule Bingen, November 2004.

T-E18 Blaum, K.: **Gewichtsprobleme physikalischer Art - Eine Penningfalle als Waage für Atome.** Universität Mainz, Mainz, Fachbereich Physik, November 2004.

T-E19 Blaum, K.: **Vom Urkilogramm zu Präzisionsmassenmessungen.** Universität Mainz, Institut für Physik, Mainz, Arbeitskreis, November 2004.

T-E20 Blaum, K.: **Atomic physics with stored and cooled ions.** Lanzhou, China, Summer school, August 2004.

T-E21 Blaum, K.: **Exotische Kerne auf die Waage gestellt.** TU München, Sektion Physik, July 2004.

T-E22 Blaum, K.: **Mass measurements of exotic nuclides at 1E-8 precision with the Penning trap mass spectrometer ISOLTRAP.** Goeteborg, Sweden, INPC2004, June 2004.

T-E23 Blaum, K.: **Status and perspectives of Penning traps for high-precision mass measurements on exotic nuclides.** Giens, France, XIV Ganil Colloquium, June 2004.

T-E24 Blaum, K.: **Exotische Kerne auf die Waage gestellt.** Universität Bonn, Insitut für Physik, May 2004.

T-E25 Blaum, K.: **Unambigious identification of three beta-decaying isomers in Cu-70.** Poznan, LASER2004 Application of Lasers in Atomic Nuclei Research, May 2004.

T-E26 Blaum, K.: **Exotische Kerne auf die Waage gestellt.** München, DPG Fruehjahrstagung, March 2004.

T-E27 Block, M.: **Status and perspectives on mass measurements of heavy elements at SHIPTRAP.** LMU/Sektion Physik/München, LS Habs, November 2004.

T-E28 Borneis, S.: **Status of PHELIX Laser and First Experiments.** Sandia National Laboratory, Albuquerque, Z-Beamlet, November 2004.

T-E29 Borneis, S.: **Status of PHELIX Laser and First Experiments.** International Committee on Ultrahigh Intensity

Lasers; LLNL, International Conference on Ultrahigh Intensity Lasers, Tahoe City, California, October 2004.

T-E30 Borneis, S.: **Status of PHELIX Laser and First Experiments.** CCLRC, Rutherford Appleton Laboratory, Central Laser Facility, May 2004.

T-E31 Borneis, S.: **Status of PHELIX Laser and First Experiments.** FH Darmstadt, Physik, Lasertechnik, May 2004.

T-E32 Borneis, S.: **Status of PHELIX Laser and First Experiments.** University of Rochester, Laboratory for Laser Energetics, May 2004.

T-E33 Borneis, S.: **Status of PHELIX Laser and First Experiments.** München, DPG Frühjahrstagung, Hauptvortrag, March 2004.

T-E34 Borneis, S.: **Status of PHELIX Laser and First Experiments.** Lawrence Livermore National Laboratory, Laser Science and Technology, January 2004.

T-E35 Bosch, F.: **Wie alt ist die Welt.** Studienstiftung des Deutschen Volkes, Sommerakademie La Villa, Alta Badia (Südtirol), August 2004.

T-E36 Bosch, F.: **Nuclear Astrophysics at the Ion Storage-Cooler Ring ESR.** Triumf/Vancouver/Kanada, Summer Institute 2004, July 2004.

T-E37 Brandau, C.: **Photorekombination der schwersten Wenigelektronensysteme. Präzisionsspektroskopie im Dunkeln.** München, DPG-Frühjahrstagung, Hauptvortrag, March 2004.

T-E38 Braun-Munzinger, P.: **Der Urknall im Labor.** GSI Darmstadt, Saturday Morning Physics Vortrag, December 2004.

T-E39 Braun-Munzinger, P.: **Heavy Ion and Hadron Physics at GSI-Fair, Challenges for Lattice QCD.** Bielefeld, Workshop on Quantum Fields in the Era of Teraflop Computing, November 2004.

T-E40 Braun-Munzinger, P.: **The ALICE Experiment at the CERN LHC.** Bucharest, Talk at the Inauguration of the NIPNE Detector Lab., October 2004.

T-E41 Braun-Munzinger, P.: **Chemical Freeze-out and the QCD Phase Boundary.** Cape Town, South Africa, SQM, September 2004.

T-E42 Braun-Munzinger, P.: **Nuclear Collisions at Ultrarelativistic Energies and the QCD Phase transition.** Bejing, Invited Talk, September 2004.

T-E43 Braun-Munzinger, P.: **Nucleus-nucleus collisions, equilibration and the QCD phase boundary.** Tübingen, Seminar, June 2004.

T-E44 Braun-Munzinger, P.: **Physics at High Baryon Density and the GSI FAIR Project.** BNL, NSAC subcommittee on Relativistic Nuclear Collisions, June 2004.

T-E45 Braun-Munzinger, P.: **Ultra-relativistic nuclear collisions and the QCD phase boundary.** Goeteborg, INPC 2004, June 2004.

T-E46 Braun-Munzinger, P.: **Physics at High Baryon Density.** Skopelos, Greece, Workshop on, May 2004.

T-E47 Braun-Munzinger, P.: **Nucleus-Nucleus collisions and the QCD phase transition.** Helsinki, Colloquium, February 2004.

T-E48 Braun-Munzinger, P.: **Chemical freeze-out and the QCD phase transition.** GSI, Darmstadt, Nuclear Theory seminar, January 2004.

T-E49 Braun-Munzinger, P.: **What have we learned, what remains to be done?.** Oakland, Quark Matter, January 2004.

T-E50 Büsching, H.: **Neutral Pions with Large Transverse Momentum in Au+Au and d+Au Collisions at $\sqrt{s_{NN}}$=200GeV measurment by the PHENIX Experiment.** BNL Brookhaven, Physics, March 2004.

T-E51 Cornelius, T.: **Bismuth nanowires and confinement effects.** Kirchhoff-Institut für Physik, Universität Heidelberg, Oberflächenphysik und Infrarotspektroskopie, December 2004.

T-E52 Egelhof, P.: **Inverse Nuclear Reactions and Detectors.** Lanzhou, China, Int. Workshop on IMP/GSI collaborations, September 2004.

T-E53 Egelhof, P.: **Probing the Halo Structure of Exotic Nuclei by Elastic Proton Scattering in Inverse Kinematics.** Köln, Plenarvortrag, DPG Frühjahrstagung, March 2004.

T-E54 Emling, H.: **Rare-isotope beams next generation.** Wien, Österreich, Cutting Edge Technologies for Fundamental science, Life Science and Medical Applications, December 2004.

T-E55 Emling, H.: **Unstable neutron-rich nuclei studied in high-energy reactions with secondary beams.** Peterhof (St. Petersburg), Russland, International Symposium on Exotic Nuclei, July 2004.

T-E56 Emling, H.: **Single-particle structure of unstable nuclei experimental prospects with high-energy secondary beams.** Trient, Italien, Workshop on Spectroscopic Factors, ECT, March 2004.

T-E57 Feldmeier, H.: **Structure of Light Exotic Nuclei in Fermionic Molecular Dynamics.** St. Petersburg, International Symposium on Exotic Nuclei (EXON2004), July 2004.

T-E58 Feldmeier, H.: **About shells, clusters, and halos - Modern aspects of nuclear structure.** IPN, Orsay, May 2004.

T-E59 Forck, P.: **Methods of Beam Profile Measurements at High Current Hadron Accelerators by P. Forck and A. Peters.** Bensheim, ICFA-HB 2004, October 2004.

T-E60 Fournier, C.: **Biophysik und Strahlenmedizin -**

Ausgewaehlte Forschungsschwerpunkte der Arbeitsgruppe Biophysik der GSI. FH Darmstadt, Fb Biotechnologie, November 2004.

T-E61 Fournier, C.: **Les effets biologique du rayonnement des ions lourds.** Clermont-Ferrand, Frankreich, 20eme Journees des LARD, October 2004.

T-E62 Fournier, C.: **Studies on cell cycle arrest and premature differentiation in human fibroblasts after exposure to high and low fluences of heavy ions.** LBNL Berkeley, Life Science, August 2004.

T-E63 Friman, B.: **Renormalization group approach to the nuclear many-body problem.** Universtitaet Tuebingen, Institut für Theoretische Physik, November 2004.

T-E64 Friman, B.: **Non-central forces in nuclear matter.** ECTTrento, Novel approaches to the nuclear many-body problem, September 2004.

T-E65 Friman, B.: **Physics opportunities at FAIR@GSI.** BNL, NSAC subcommittee on Relativistic Nuclear Collisions, June 2004.

T-E66 Friman, B.: **Renormalization group approach to nuclear matter.** Universitat de Barcelona, Facultat de Fisica, March 2004.

T-E67 Friman, B.: **Renormalization group approach to nuclear matter.** Universitat de Valéncia, Institut de Fsica Corpuscular, March 2004.

T-E68 Geissel, H.: **Mass- and Lifetime Experiments of Stored Exotic Nuclei.** Darmstadt, Japanese-German Workshop, December 2004.

T-E69 Geissel, H.: **Experiments with Exotic Nuclei and Exotic Atoms.** Peking (China), Univ. of Peking, September 2004.

T-E70 Geissel, H.: **Experiments with the Present and Future Exotic Nuclear Beam Facilities.** Lanzhou (China), International Workshop on Collaboration of Physics Programs between IMP and GSI, September 2004.

T-E71 Geissel, H.: **Experiments with the Present and Future Exotic Nuclear Beam Facilities.** Lanzhou (China), International Workshop on Collaboration of Physics Programs between IMP and GSI, September 2004.

T-E72 Geissel, H.: **Precision Experiments with Exotic Atoms and Exotic Nuclei at Relativistic Energies.** Göteborg (Sweden), International Nuclear Physics Conference INPC-2004, July 2004.

T-E73 Geissel, H.: **Progress of Precision Experiments with Exotic Nuclei at GSI.** Peterhof, St. Petersburg (Russia), International Symposium on Exotic Nuclei, July 2004.

T-E74 Geissel, H.: **Experiments with Exotic Atoms and Exotic Nuclei at Relativistic Energies.** Edinburgh (United Kingdom), IOP, April 2004.

T-E75 Geissel, H.: **Production, Separation and Experiments with Exotic Nuclei at Relativistic En-ergies.** Workshop VISTAR, Rußbach (Austria), March 2004.

T-E76 Geissel, H.: **Nuclear Structure Experiments relevant for Nuclear Astrophysics.** Seattle (USA), Astrophysics conference JINA, January 2004.

T-E77 Geissel, H.: **Präzisionsmessungen mit exotischen Kernen bei relativistischen Energien.** Basel (Switzerland), Vorlesung Univ. Basel, January 2004.

T-E78 Grawe, H.: **Experimental evidence for exotic shell structure.** University of Tenessee, Knoxville TN (USA), September 2004.

T-E79 Grawe, H.: **Shell structure from ^{78}Ni to ^{100}Sn: Implications for nuclear astrophysics.** Pine Mountain GA (USA), ENAM 04, September 2004.

T-E80 Grawe, H.: **Shell structure from ^{100}Sn to ^{78}Ni: Implications for nuclear astrophysics.** Oslo, CMA workshop on Computational advances in the nuclear many-body problem, March 2004.

T-E81 Gumberidze, A.: **Atomic physics with highly-charged heavy ions at the GSI future facility: the scientific program of the sparc collaboration.** Debrecen, Fast Ion Atom Collisions, September 2004.

T-E82 Hartmann, O. N.: **Status of PANDA and HESR.** INFN, Sezione di Torino/Universit di Torino, Dip. di fisica generale 'A. Avogadro' (Italy), September 2004.

T-E83 Hebeler, K.: **Dynamical screening of non-Fermi liquid effects at finite temperature.** ECTTrento, Italy, Novel Approaches to the Nuclear Many-Body Problem: From Nuclei to Stellar Matter, September 2004.

T-E84 Hebeler, K.: **Fermi-liquid theory of quark matter at high densities.** Univ. Köln, DPG Frühjahrstagung, March 2004.

T-E85 Henning, W. F.: **The GSI Future Project.** CERN, Switzerland, Workshop on Beam Dynamics in Future Hadron Colliders and Rapidly Cycling High-Intensity Synchrotrons, November 2004.

T-E86 Henning, W. F.: **Challenges of the International FAIR Project.** Bensheim, Germany, ICFA-HB2004, 18-22.10.2004, October 2004.

T-E87 Henning, W. F.: **International Facility for Antiproton and Ion Research (FAIR).** Chicago, USA, OECD Workshop on Management Practices for Establishing Large International Scientific Research Faci, October 2004.

T-E88 Henning, W. F.: **Grundlagenforschung - Basis für Innovationen.** Innovationsforum der IHK Ostwürttemberg, Heidenheim, September 2004.

T-E89 Henning, W. F.: **The International FAIR Facility.** Sigtuna, Sweden, Workshop on future FAIR physics, 14./15.9.2004, September 2004.

T-E90 Henning, W. F.: **An International Accelerator Facility for Research with Ions and Antiprotons.** Lucerne, Switzerland, EPAC04, 5.-9.7.2004, July 2004.

T-E91 Henning, W. F.: **Das Zukunftsprojekt der GSI.** Gesamthochschule Kassel, Physikalisches Kolloquium, June 2004.

T-E92 Henning, W. F.: **Ups and Downs, and the Strange Charm of Roadmaps.** Göteborg, Sweden, INPC 2004, 27.6.-2.7.2004, June 2004.

T-E93 Henning, W. F.: **Die internationale Beschleunigeranlage für Ionen und Antiprotonen der GSI.** Univ. Dresden, Physik Kolloquium, May 2004.

T-E94 Henning, W. F.: **Internationales Beschleunigerzentrum für die Forschung mit Ionen- und Antiprotonenstrahlen - Perspektiven für die Wissenschaftsstadt Darmstadt -.** pro regio Darmstadt, April 2004.

T-E95 Henning, W. F.: **Das GSI-Zukunftsprojekt.** Neuenburg, Switzerland, Frühjahrstagung der Schweizerischen Physikalischen Gesellschaft (SPS), 3./4.3.2004, March 2004.

T-E96 Henning, W. F.: **GSI Today and Overview of the International Accelerator Facility for Beams of Ions and Anti Protons Tomorrow.** Delhi, India, International Workshop on India and the International Accelerator Facility at Darmstadt, 15./16.3.20, March 2004.

T-E97 Henning, W. F.: **Nustar Physics at the Future FRS Facility.** Milano Italy, Symposium on, March 2004.

T-E98 Herfurth, F.: **Further developments of traps.** KU Leuven, IKS, December 2004.

T-E99 Herfurth, F.: **Ion Beam Manipulation using Ion Traps.** Universität Frankfurt, Institut für angewandte Physik, November 2004.

T-E100 Herfurth, F.: **Mass Measurements - ISOLTRAP and HITRAP.** Universität Giessen, Physik - IONAS Gruppenseminar, November 2004.

T-E101 Herfurth, F.: **Mass Measurements - ISOLTRAP and HITRAP.** CSNSM Orsay/Paris, April 2004.

T-E102 Heßberger, F. P.: **Experimental Programme at SHIP on Synthesis and Investigation of Properties of the Heaviest Elements.** Midwinter Workshop, Univ. Jyväskylä, Finland, Dept. of Physics, January 2004.

T-E103 Hoffmann, D. H. H.: **Particle Beam Generation with Intense Laser Pulses and PHELIX Project- Perspectives for high energy density research with intense ion and laser beams.** Sydney, Australia, Int. Workshop: Fast High Density Plasma Blocks Driven by Picosecond Terawatt Lasers, December 2004.

T-E104 Hoffmann, D. H. H.: **Suche nach Dunkler Materie im Universum.** TU-Darmstadt, Saturday Morning Physics Lectures, December 2004.

T-E105 Hoffmann, D. H. H.: **Beam Plasma Interaction experiments en route to Inertial Fusion Energy.** Daejong, Korea, IAEA TCM Meeting on Elements of Fusion Power Plants, October 2004.

T-E106 Hoffmann, D. H. H.: **High Energy Density Physics with Intense Laser and Ion Beams.** GSI, Student Programme, October 2004.

T-E107 Hoffmann, D. H. H.: **Nuclear Fusion with Inertial Confinement.** IPP-Garching, Summer University of Plasma Physics, October 2004.

T-E108 Hoffmann, D. H. H.: **CERN Axion Solar Telescope - Status report.** CERN, SPS Committee, July 2004.

T-E109 Hoffmann, D. H. H.: **CERN Axion Solar Telescope - Suche nach Axionen von der Sonne.** TU-Karlsruhe, Physikalisches Kolloquium, July 2004.

T-E110 Hoffmann, D. H. H.: **Plasma Physics with intense ion and laser beams.** Univ. Tübingen, Physik: Int. Graduierten Kolleg Basel/Tübingen, July 2004.

T-E111 Hoffmann, D. H. H.: **Present and Future Perspectives for High Energy Density Physics with Intense Ion and Laser Beams.** CLRF, London, EPS Conf. Plasma Physics and Controlled Fusion, July 2004.

T-E112 Hoffmann, D. H. H.: **European Programme Overview and the German Perspective for Heavy Ion Inertial Fusion Energy Research.** Princeton, N.J., USA, Heavy Ion Inertial Fusion Symposium, June 2004.

T-E113 Hoffmann, D. H. H.: **High Energy Density Physics with Intense Heavy Ion and Laser Beams.** HMI-Berlin, Materialwiss.: Rutherfordseminar, June 2004.

T-E114 Hoffmann, D. H. H.: **Basic Physics for Inertial Fusion Energy andHigh Energy Density Physics with Intense Ion and Laser Beams.** Yong Pjong, Korea, Asian Pacific Laser Science Conference 2004, February 2004.

T-E115 Hoffmann, D. H. H.: **Experimental Sarch for Axions with the CERN Solar Telescope.** Hirschegg, Austria, Int. Workshop. on High Energy Density Matter Physics, February 2004.

T-E116 Hoffmann, D. H. H.: **High Energy Density and Inertial Fusion Research at GSI.** Korea Atomic Energy Research Institute KAERI, KAERI, February 2004.

T-E117 Hoffmann, D. H. H.: **The German perspective on Recent Progress of Inertial Fusion Energy Research.** Yong Pjong, Korea, Asian Pacific laser Science Conf. 2004, February 2004.

T-E118 Hoffmann, D. H. H.: **Experimentelle Suche nach Axionen, Licht und Dunkle Materie im Universum.** Univ. Bochum, Physikalisches Kolloquium, January 2004.

T-E119 Hofmann, S.: **Darmstadtium und die Superschweren Elemente.** Technische Universität Bergakademie

Freiberg/Sachsen, Vortragsveranstaltung zum 100. Todestag von Clemens Winkler, October 2004.

T-E120 Hofmann, S.: **Research of super-heavy elements and their chemistry.** Lanzhou, China, Int. Workshop on Collaboration of Physics Programs Between IMP and GSI, September 2004.

T-E121 Hofmann, S.: **Superheavy elements.** Beijing, China, Kolloquium, September 2004.

T-E122 Hofmann, S.: **Synthesis and properties of superheavy nuclei.** Beijing, China, Kolloquium, September 2004.

T-E123 Hofmann, S.: **Heavy element research at GSI.** Peterhof, Russland, Int. Symposium on Exotic Nuclei, July 2004.

T-E124 Hofmann, S.: **Prospects for the study of transactinides.** Caen, Frankreich, SPIRAL 2 Workshop, April 2004.

T-E125 Hofmann, S.: **Studies of SHE at high beam intensities.** Darmstadt, Workshop on The Future of Superheavy Element Research, February 2004.

T-E126 Hofmann, S.: **The future of super-heavy element research.** Darmstadt, Deutschland, NUSTAR Annual Meeting, February 2004.

T-E127 Holzmann, R.: **The HADES physics programme: an update.** XLII Bormio Meeting, Nuclear Physics, January 2004.

T-E128 Ivanov, Y.(GAST): **Nuclear Stopping Power in Three-Fluid Simulations of Relativistic Heavy-Ion Collisions.** ECTin Trento, May 2004.

T-E129 Kanapathipillai, M.: **Physics of collisionless absorption in solid targets and clusters (joint work with Prof. P. Mulser and Dr. D. Bauer; talk delivered by Prof. P. Mulser).** Kiel, Germany, International workshop on kinetic theory of non-ideal plasmas, September 2004.

T-E130 Kanapathipillai, M.: **Giant enhancement of inverse bremstrahlung in extended cluster media (joint work; poster presented by Prof. P.Mulser).** Arcetri, Florence, Italy., IV Congresso Fisica de Plasmi, January 2004.

T-E131 Kluge, H.-J.: **Atomphysik an Beschleunigern: heute (GSI) und morgen (FLAIR).** University of Bonn, November 2004.

T-E132 Kluge, H.-J.: **Highly-Charged Ions for Fundamental Tests and Constants.** Bonn, Hyperfine Interactions 2004 (HFI 2004), August 2004.

T-E133 Kluge, H.-J.: **Atomphysik mit hochgeladenen Ionen: Heute und morgen.** Hahn-Meitner Institut, Berlin, May 2004.

T-E134 Kluge, H.-J.: **Physics with a Multi-Megawatt Proton Source.** CERN, Geneva, Switzerland, May 2004.

T-E135 Kluge, H.-J.: **The scientific program of the FLAIR and SPARC community.** Nuclear Science Center, New Delhi, India, March 2004.

T-E136 Knoll, J.: **Fluid Dynamics, Multifragmentation and Flavor Kinetics.** FZ Rossendorf, Kern und Hadronenphysik, October 2004.

T-E137 Knoll, J.: **Verallgemeinerte Transportgleichungen für Teilchen und Resonanzen.** TU-Darmstadt, Physik, January 2004.

T-E138 Kollmus, H.: **Desorption Measurements at GSI.** Bensheim, ICFA 2004, October 2004.

T-E139 Kraft-Bermuth, S.: **Kalorimetrische Tieftemperaturdetektoren für Schwerionen und ihr erster Einsatz in der Beschleunigermassenspektrometrie.** Universität Mainz, July 2004.

T-E140 Kraft, G.: **Heilen mit Ionenstrahlen.** TU Darmstadt, Saturday Morning Physics, November 2004.

T-E141 Kraft, G.: **Musts for an accelerator for cancer therapy.** Kloster Banz/ Staffelstein, Workshop MPQ und Univ. Jena, November 2004.

T-E142 Kraft, G.: **Physikalische und strahlenbiologische Basis der Protonen- und Kohlenstofftherapie.** SSK Berlin, November 2004.

T-E143 Kraft, G.: **High LET Effects of Heavy Charged Particles.** Bloomington, Indiana, USA, PTCOG, October 2004.

T-E144 Kraft, G.: **Radiobiology for ion beam therapy.** ESBR 04 Budapest, August 2004.

T-E145 Kraft, G.: **The radiobiological basis of heavy ion tumor therapy.** NIRS/CHIBA, Japan, July 2004.

T-E146 Kraft, G.: **Recent developments in heavy ion radiation therapy.** Univ. Essen, March 2004.

T-E147 Kraft, G.: **Strategies of heavy ion therapy-the advantages of carbon beams.** Columbia University, New York, USA, College of Physicians and Surgeons, March 2004.

T-E148 Kraft, G.: **Strategies of heavy ion therapy-the advantages of carbon beams.** MSKCC Memorial Sloan Kettering Cancer Center, New York, USA, March 2004.

T-E149 Kraft, G.: **Strategies of heavy ion therapy-the advantages of carbon beams.** University of North Carolina, USA, School of Medicine, March 2004.

T-E150 Kraft, G.: **Strategies of heavy ion therapy-the advantages of carbon beams.** University of Pennsylvania, Philadelphia, USA, Hospital Systems, March 2004.

T-E151 Kühl, T.: **PHELIX - Physik mit Lasern und Schwerionen.** PTB Braunschweig, Helmholtz Kolloquium, June 2004.

T-E152 Kühl, T.: **PHELIX-A Petawatt High-Energie**

Laser for Heavy-Ion Experiments. Universität Poznan, Laser 2004, June 2004.

T-E153 Le Févre, A.: **Isotopic Scaling and the Symmetry Energy in Spectator Fragmentation.** GANIL - Caen (Frankreich), October 2004.

T-E154 Le Févre, A.: **Isotopic Effects in Multifragmentation.** Giens (Frankreich), XIVth Colloque GANIL, June 2004.

T-E155 Le Févre, A.: **Isotopic Effects in Multifragmentation.** IReS - Universit Louis Pasteur - Strasbourg (Frankreich), May 2004.

T-E156 Liesen, H.-D.: **Messungen der Lambverschiebung in wasserstoffähnlichen schweren Ionen.** Friedrich-Schiller-Universität Jena, Institut für Optik und Quantenelektronik, October 2004.

T-E157 Litvinov, Y.: **Recent Mass Measurements at ESR.** Darmstadt, Japanese-German Nuclear Structure and Astrophysics Workshop, December 2004.

T-E158 Litvinov, Y.: **Status and Prospects of Schottky Mass Spectrometry.** Darmstadt, ILIMA (Isomeric beams, Lifetimes and Mass measurements collaboration) Workshop (town meeting), September 2004.

T-E159 Litvinov, Y.: **Status and Prospects of Schottky Mass Spectrometry.** Darmstadt, ILIMA (Isomeric beams, Lifetimes and Mass measurements collaboration) Workshop (town meeting), September 2004.

T-E160 Litvinov, Y.: **Storage Ring Experiments.** Karlsruhe, Workshop on Experimental Nuclear Astrophysics, September 2004.

T-E161 Litvinov, Y.: **Mass Measurements of Stored Exotic Nuclei.** Darmstadt, NUSTAR Annual Meeting, February 2004.

T-E162 Lukasik, J.: **Collective flow from Fermi to relativistic energies in symmetric heavy ion collisions.** New London, NH, Gordon Research Conference on Nuclear Chemistry, June 2004.

T-E163 Lutz, M.: **Baryon resonances from chiral coupled-channel dynamics.** Ecole Polytechnique, The 10th International Conference on the Structure of Baryons, October 2004.

T-E164 Lutz, M.: **Open-charm meson resonances.** LNF workshop, The 2nd PANDA physics workshop, March 2004.

T-E165 Lutz, M.: **Chiral dynamics for exotic resonances.** YITP workshop, Multi-quark Hadrons: Four, Five and More?, February 2004.

T-E166 Lutz, M.: **Chirale Dynamik von Resonanzen in der QCD.** Schleching, Arbeitstreffen Kernphysik, February 2004.

T-E167 Magestro, D.: **Soft physics at RHIC.** Ohio State University, Physics, February 2004.

T-E168 Marin, A.: **New results from CERES.** Oakland, Quark Matter 2004, January 2004.

T-E169 Münzenberg, G.: **Frontiers of nuclear structure research at GSI some new developments.** Kurokawa Village, Niigata, Japan, A New Era of Nuclear Structure Physics, November 2004.

T-E170 Münzenberg, G.: **KP-II program (mid-term and future) and the NUSTAR-community at the GSI future facility FAIR.** Lanzhou, China, International Workshop on Collaboration of Physics Programs Between IMP and GSI, September 2004.

T-E171 Münzenberg, G.: **NUSTAR, Nuclear structure research within the GSI project objectives and organization.** Peterhof (St.Petersburg), Russland, International Symposium on Exotic Nuclei, July 2004.

T-E172 Münzenberg, G.: **In-flight separation, ion cooling and low statistics Precision experiments with exotic nuclei at relativistic energies.** Russbach, Österreich, 1st VISTARS Workshop on Nuclear Astrophysics, March 2004.

T-E173 Münzenberg, G.: **Medical Applications of Nuclear Methodsenergies.** Kuwait-City, Kuwait, Seminar, March 2004.

T-E174 Münzenberg, G.: **Superheavy Elements.** Kuwait-City, Kuwait, Seminar, March 2004.

T-E175 Neff, T.: **Cluster versus shell structure in FMD.** GSI Darmstadt, Japanese-German Nuclear Structure and Astrophysics Workshop, December 2004.

T-E176 Neff, T.: **Cluster and Shell-Structure in Light Nuclei.** Argonne National Lab, USA, Nuclei at the Limits, July 2004.

T-E177 Neff, T.: **Structure of light Nuclei in Fermionic Molecular Dynamics.** Michigan State University, East Lansing, p-shell Workshop, July 2004.

T-E178 Neff, T.: **Structure of light Nuclei in Fermionic Molecular Dynamics.** Göteborg, Internation Nuclear Physics Conference, June 2004.

T-E179 Neff, T.: **Nuclear Structure of light Nuclei in Fermionic Molecular Dynamics.** Köln, DPG Frühjahrstagung, March 2004.

T-E180 Neumann, R.: **Materials research with energetic heavy ions at GSI.** Japan Atomic Energy Research Institute Tokai (JAERI-Tokai), Department of Materials Science, October 2004.

T-E181 Neumann, R.: **Materials research with energetic heavy ions at GSI.** Nagasaki University, Nagasaki, Japan, Department of Materials Science and Engineering, October 2004.

T-E182 Neumann, R.: **Materials research with energetic heavy ions at GSI.** Osaka Prefecture University, Osaka,

Japan, Research Institute for Advanced Science and Technology, October 2004.

T-E183 Neumann, R.: **Materials research with energetic heavy ions at GSI.** Universtät Groningen, Niederlande, Kernfysisch Versneller Instituut, May 2004.

T-E184 Neumann, R.: **Recent results of heavy-ion irradiation of solids at GSI.** Uppsala, Workshop on Ion Track Technology, February 2004.

T-E185 Nörtershäuser, W.: **Elektronischer Lauschangriff auf Kerne - Laserspektroskopische Bestimmung von Ladungsradien an der Neutronen-Dripline.** Universität Mainz, Institut für Kernchemie, November 2004.

T-E186 Nörtershäuser, W.: **Electronic Eavesdropping on Nuclei: Whispers about the Charge Radii of Li-8,9,11.** TRIUMF, Vancouver, June 2004.

T-E187 Nörtershäuser, W.: **Electrons Spy on Nuclei - Detecting Whispers about the Charge Radii of Li-8,9,11.** Argonne National Laboratory, Physics Division, March 2004.

T-E188 Nörtershäuser, W.: **Electrons Spy on Nuclei - Detecting Whispers about the Charge Radii of Li-8,9,11.** Universität Giessen, Physik, January 2004.

T-E189 Pershina, V.: **Theoretical Predictions for the Chemical Identification of Superheavy Elements. Role of relativistic effects.** Peterhof, Russia, International Symposium on Exotic Nuclei, EXON 2004, July 2004.

T-E190 Peters, A.: **Non-Interfering Beam Diagnsotic Developments by A. Peters and P. Forck.** Lübeck, LINAC 2004, August 2004.

T-E191 Quint, W.: **HICAT- The German Hospital-Based Ion Cancer Therapy Project.** Varenna, Antiproton Meeting, October 2004.

T-E192 Quint, W.: **The HITRAP project at GSI.** GSI, Meeting of Wissenschaftlicher Rat, October 2004.

T-E193 Quint, W.: **High-precision measurements of the g-factor of highly charged ions: a new access to fundamental constants.** Vilnius, HCI2004, September 2004.

T-E194 Quint, W.: **Penning trap measurement of the magnetic moment of the antiproton.** Villars, CERN SPSC-Meeting, September 2004.

T-E195 Quint, W.: **The g-factor of the bound electron in hydrogen-like ions: a new determination of the electron mass.** Univ. Heidelberg, ANQ-Seminar, July 2004.

T-E196 Quint, W.: **FAIR - Facility for Antiproton and Ion Research.** Krakow, EU-Collaboration Meeting, June 2004.

T-E197 Quint, W.: **FLAIR - Die zukünftige GSI-Anlage für Experimente an Antiprotonen und hochgeladenen Ionen bei niedrigen Energien.** München, Atomphysik, DPG-Tagung, March 2004.

T-E198 Quint, W.: **FLAIR - Facility for Low-energy Antiproton and Ion Research.** Caen, TAS-Workshop on Trap-Assisted Spectroscopy, March 2004.

T-E199 Riek, F.: **Rho-Omega Mixing in Matter.** Univ. Koeln, DPG Tagung, March 2004.

T-E200 Ritter, S.: **Cytogenetic effects of space-relevant HZE-particles in human blood lymphocytes.** Paris, 35th Cospar Scientific Assembly, July 2004.

T-E201 Sako, H.: **Event-by-event fluctuations in 40, 80, and 158 A GeV/c Pb+Au collisions.** Oakland, Quark Matter 2004, January 2004.

T-E202 Schädel, M.: **SPIRAL II Related Aspects in the IN2P3-DMS/CEA - GSI French-German Collaboration Agreement.** GANIL/Caen/France, Workshop, April 2004.

T-E203 Schardt, D.: **Carbon ion radiotherapy.** Austrian Academy of Science, Wien, Symposium Cutting Edge Technologies CET-2004, December 2004.

T-E204 Schardt, D.: **Physikalische Charakterisierung von Ionenstrahlen für die Tumortherapy.** DKFZ Heidelberg, Medizinische Physik, May 2004.

T-E205 Schardt, D.: **The GSI contribution to hadrontherapy.** Erice (Italien), International School on Physics and Industry, April 2004.

T-E206 Schardt, D.: **Basic features of heavy-ion therapy.** Univ. Frankfurt, Theoretische Physik, February 2004.

T-E207 Scheidenberger, C.: **Antiprotonic exotic nuclei at FAIR.** Darmstadt, NIPNET, HITRAP Workshop at GSI, November 2004.

T-E208 Scheidenberger, C.: **Physics with exotic nuclei: nuclear structure and astrophysics.** Paris (Frankreich), NuPECC Meeting with Funding Agencies, November 2004.

T-E209 Scheidenberger, C.: **Experimente zu Grundzustands- und Zerfallseigenschaften hochgeladener Ionen mit gespeicherten exotischen Nukliden.** Johnannes-Gutenberg Universität Mainz, Kolloquium, July 2004.

T-E210 Scheidenberger, C.: **Präzisionsmassenspektrometrie mit einzelnen, kurzlebigen Ionen zur Untersuchung kernphysikalischer Schlüsselfragen.** Heidelberg, Deutschland, Bothe-Kolloquium, July 2004.

T-E211 Scheidenberger, C.: **The contribution of precision mass measurements to nuclear physics.** Göteborg (Schweden), INPC 2004, July 2004.

T-E212 Scheidenberger, C.: **Masses and beta-decay half-lives of highly-charged ions studied at FRS-ESR.** Saariselkä, Finnland, NIPNET Workshop on Precision Mass Measurements, April 2004.

T-E213 Scheidenberger, C.: **Direct mass measurement of**

exotic nuclei: past, present, future. Russbach, Österreich, 1st VISTARS Workshop, March 2004.

T-E214 Scheidenberger, C.: **Experiments at the Low-Energy Branch of the planned Super-FRS.** Darmstadt, Deutschland, Annual Meeting of the NUSTAR Collaboration, February 2004.

T-E215 Schmidt, K.: **Nuclear-data experimental programs at GSI.** Santa Fee (USA), International Conference on Nuclear Data for Science and Technology, September 2004.

T-E216 Schwartz, K.: **Heavy ion induced damange in ionic crystals.** Riga, Lithuania, International Conference Defects in Insulating Materials, July 2004.

T-E217 Schwarz, C.: **FAIR, the facility for antiprotons and ions research at GSI.** Charles University in Prague, Faculty of Mathematics and Physics, SPIN-Praha-2004, July 2004.

T-E218 Schwarz, C.: **PANDA a new detector for hadronic physics at GSI (FAIR).** IPN Orsay, Division de Recherche, June 2004.

T-E219 Senger, P.: **Das Zukunftsprojekt der GSI und seine Bedeutung für die Universität Frankfurt.** Physikalisches Kolloquium der Universität Frankfurt, Frankfurt, Germany, December 2004.

T-E220 Senger, P.: **The CBM Experiment at FAIR.** Colloquium at ITEP, Moscow, Russia, November 2004.

T-E221 Senger, P.: **The CBM experiment at FAIR.** International Workshop, Future of Nuclear Collisions at High Energies, Kielce, Poland, October 2004.

T-E222 Senger, P.: **Nuclear Matter Physics at GSI: past and future.** 21th workshop on electromagnetic interactions, Bosen, Germany, September 2004.

T-E223 Senger, P.: **The Compressed Baryonic Matter Experiment at FAIR in Darmstadt.** XVIIIth International Workshop, High Energy Physics and Quantum Field Theory, St. Petersburg, Russia, June 2004.

T-E224 Senger, P.: **Nucleus-nucleus collisions at FAIR in Darmstadt -The Compressed Baryonic Matter Experiment.** Colloquium at the Institute of Modern Physics, Lanzhou, China, April 2004.

T-E225 Senger, P.: **Nucleus-nucleus collisions at FAIR-The Compressed Baryonic Matter Experiment.** Scientific Opportunities and challenges, China and the international FAIR project, Beijing, China, April 2004.

T-E226 Senger, P.: **Nucleus-nucleus collisions at FAIR in Darmstadt -The Compressed Baryonic Matter Experiment.** Colloquium at the Bhabba Atomic Research Center, Bombay, India, March 2004.

T-E227 Senger, P.: **Nucleus-nucleus collisions at FAIR-The Compressed Baryonic Matter Experiment.** Indo-German meeting on the international FAIR project, Delhi, India, March 2004.

T-E228 Senger, P.: **Nucleus-nucleus collisions at the future facility in Darmstadt - Compressed Baryonic Matter at GSI.** International workshop on hot and dense matter in heavy-ion, Budapest, Hungary, March 2004.

T-E229 Sfienti, C.: **Mass and Isospin Effects in Multifragmentation.** Prague, Czech Republic, 18th Nuclear Physics Division Conference of the EPS, August 2004.

T-E230 Sfienti, C.: **Temperature and density in Heavy Ion Reaction at intermediate energies.** Bormio, Italy, XLII International Winter Meeting on Nuclear Physics, January 2004.

T-E231 Simon, H.: **Breakup of halo nuclei in complete kinematics.** Darmstadt, Japanese-German Nuclear Structure and Astrophysics Workshop, December 2004.

T-E232 Simon, H.: **Status and Perspectives for Studies of light unbound Systems at GSI/FAIR.** Giens (Frankreich), XIVth colloque GANIL, June 2004.

T-E233 Simon, H.: **Structure of few-nucleon systems near and beyond the dripline.** Köln, Frühjahrstagung DPG, March 2004.

T-E234 Simon, H.: **The Electron - Ion Collider Project at the new GSI facility.** Hirschegg (Österreich), Hirschegg 2004: Probing Nuclei and Nucleons with Electrons and Photons, January 2004.

T-E235 Spohr, R.: **Prospects of single-ion tracks.** Barcelona, 22nd International Conference on Nuclear Tracks in Solids, August 2004.

T-E236 Steck, M.: **Cooled Heavy Ions in the ESR Storage Ring.** Bensheim, ICFA 2004, October 2004.

T-E237 Stöhlker, T.: **Challenges for Atomic Physics with Highly-Charged Ions and Antiprotons at the GSI Future Facility.** Ahmedabad, National Conference on Atomic and Molecular Physics, December 2004.

T-E238 Stöhlker, T.: **Challenges for Atomic Physics with Highly-Charged Ions and Antiprotons at the GSI Future Facility.** National Science Center New Dehli, National Conference on Atomic and Molecular Physics, December 2004.

T-E239 Stöhlker, T.: **X-Ray Spectroscopy on Cooled Heavy Ions at Storage Rings.** National Science Center New Dehli, December 2004.

T-E240 Stöhlker, T.: **X-Ray Spectroscopy on Cooled Heavy Ions at Storage Rings.** TATA Institute of Fundamental Research, December 2004.

T-E241 Stöhlker, T.: **Atomic physics with highly-charged heavy ions at the GSI future facility: The scientific program of the SPARC collaboration.** Vilnus, International Conference on the Physics of Highly Charged Ions, September 2004.

T-E242 Stöhlker, T.: **The Physics of Highly Charged Heavy Ions Studied at Storage Rings.** Lanzhou, China, Summer school, August 2004.

T-E243 Stöhlker, T.: **X-Ray spectroscopy on cooled heavy ions at storage rings.** Rennes, 8th European Conference on Atomic and Molecular Physics, July 2004.

T-E244 Stöhlker, T.: **Application of Position Sensitive Solid State Detectors for X-ray Spectroscopy.** Krakow, EU-Collaboration Meeting, June 2004.

T-E245 Stöhlker, T.: **Challenges for Atomic Physics at the GSI Future Facility: The scientific program of the FLAIR and SPARC community.** Beijing, April 2004.

T-E246 Stöhlker, T.: **Atomic Physics Experiments on High-Z Ions: Position sensitive solidstate detectors.** LBNL Berkeley, January 2004.

T-E247 Stöhlker, T.: **Polarisations und Winkelverteilungsuntersuchungen zur Rekombination in hochenergetischen Elektron-Ion-Stößen.** Universität Giessen, Zweites Physikalisches Institut, January 2004.

T-E248 Stroth, J.: **Recent results of HADES.** Gießen (Germany), European Graduate School: Complex Systems of Hadrons and Nuclei, In-medium hadron physics workshop, November 2004.

T-E249 Stroth, J.: **The Physics of Dense Nuclear Matter.** Paris (France), NUPECC Expert Meeting, November 2004.

T-E250 Stroth, J.: **The Future at GSI and FAIR.** Paris (France), BARYONS 2004, October 2004.

T-E251 Stroth, J.: **Research at the future accelerator facility FAIR.** Lübek, LINAC 2004, August 2004.

T-E252 Stroth, J.: **The future international accelerator facility for heavy ions and anti-protons FAIR at GSI in Darmstadt.** TU München (Germany), Kernphysikalisches Seminar, July 2004.

T-E253 Stroth, J.: **Dielectron spectroscopy with HADES.** New London, Gordon Research Conference, June 2004.

T-E254 Stroth, J.: **Dielectrons as probes for the in-medium structure of hadrons.** Köln (Germany), DPG Frühjahrstagung, March 2004.

T-E255 Sümmerer, K.: **High-energy Coulomb dissociation experiments at GSI.** Trient (Italien), ECT Workshop Advances and Challenges in Nuclear Astrophysics, May 2004.

T-E256 Tahir, N. A.: **Studies of Thermophysical Properties of High-Energy-Density Matter Using Intense Heavy Ion Beams.** Bordeaux University 1, Bordeaux, December 2004.

T-E257 Tahir, N. A.: **Studies of Heavy Ion Induced High-Energy-Density States in Matter at the GSI Darmstadt SIS18 and Future FAIR Facility.** Sumposium on Heavy Ion Fusion, HIF04, Princeton, June 2004.

T-E258 Tahir, N. A.: **Impact of the Large Hadron Collider 7 TeV Proton Beam on a Solid Copper Target.** CERN, Geneva, February 2004.

T-E259 Taucher-Scholz, G.: **The use of track visualization for single-cell irradiation.** Universität Duisburg-Essen, Inst. für Med. Strahlenbiologie, December 2004.

T-E260 Taucher-Scholz, G.: **Research in Radiobiology with Swift Ions.** GANIL, Caen, LARIA, October 2004.

T-E261 Taucher-Scholz, G.: **Microscopic Track Visualization as a tool for low dose particle irradiation.** JAERI, Takasaki, Biotechnology Lab, August 2004.

T-E262 Taucher-Scholz, G.: **The Cellular Response to Low Dose Radiation.** Tohoko University, Sendai, Japan, Int. Workshop on Biological Responses to Low Dose Radiation, August 2004.

T-E263 Taucher-Scholz, G.: **Wie reagiert eine Zelle auf Bestrahlung.** LMU München, Inst. für Biomolekulare Optik, June 2004.

T-E264 Taucher-Scholz, G.: **Dynamics of DNA Damage Response Proteins.** University of Alberta, Banff, Canada, International workshop on radiation damage to DNA, May 2004.

T-E265 Taucher-Scholz, G.: **Literatur Ueberblick über Einzelzell Bestrahlung.** GSI Darmstadt, Workshop 'Strahlenbiologie am Mikrostrahl', March 2004.

T-E266 Taucher-Scholz, G.: **Effects of Radiation Quality on the Subnuclear Localization of Damage Response Proteins.** LBNL Berkeley, Life Science Division, February 2004.

T-E267 Tauschwitz, A.: **Assisted pinch final transport.** Sandia National Laboratories, Workshop on Heavy Ion Fusion Science Initiatives, February 2004.

T-E268 Tauschwitz, A.: **HEDP with heavy ion beams at GSI.** Sandia National Laboratories, Workshop on Heavy Ion Fusion Science Initiatives, February 2004.

T-E269 Toimil Molares, M. E.: **The template method: fabrication of nanostructures with novel properties.** Max-Plank Institut für Festkörperforschung/Stuttgart, Seminar am Nanoscale Science Department, December 2004.

T-E270 Toimil Molares, M. E.: **Single assymetric nanopores as chemical and biological sensors.** International Atomic Energy Agency, AEIA Headquarters Vienna, November 2004.

T-E271 Toimil Molares, M. E.: **Fabricating and contacting single nanowires using a template method.** Universität Konstanz/Fakultät für Physik, Seminar für Festkörperphysik und Clusterphysik, October 2004.

T-E272 Toimil Molares, M. E.: **Micro- and nanowires.** University of Arkansas/ Fayetteville (USA), College of Engineering, August 2004.

T-E273 Toimil Molares, M. E.: **Nanowires in multi- and single-pore track-etched membranes: electrochemical growth and properties.** New Hampshire (USA), Gordon Research Conference on Electrodeposition, August 2004.

T-E274 Toimil Molares, M. E.: **Copper and bismuth nanowires: fabrication, characterization and properties.** Universität Ulm, Sonderforschungsbereich, February 2004.

T-E275 Trautmann, C.: **Track formation and defect creation in different materials.** GSI Plasma Physics Seminar, Darmstadt, December 2004.

T-E276 Trautmann, W.: **Isotopic phenomena in nuclear multifragmentation.** A. Soltan Institute for Nuclear Studies, Warsaw, Poland, November 2004.

T-E277 Trautmann, W.: **Multifragmentation and the liquid-gas phase transition: an experimental overview.** Jagiellonian University, Kraków, Poland, M. Smoluchowski Institute of Physics, November 2004.

T-E278 Trautmann, C.: **Energetic heavy ions and solids; basic aspects and application in micro and nanoscience.** Inst. Nacional de Investigaciones Nucleares (ININ), Mexico, September 2004.

T-E279 Trautmann, C.: **How energetic heavy ions modify solids; Basic aspects and applications in micro and nanoscience.** Monterey, USA, 14th Intern. Conference on Ion Beam Modification of Materials (IBMM), September 2004.

T-E280 Trautmann, C.: **Material modification induced by MeV-GeV ions.** Erice, Italy, International School of Solid State Physics; Radiation Effects in Solids, July 2004.

T-E281 Trautmann, C.: **Nanostructuring and tumor therapy with swift heavy ions.** Erice, Italy, International School of Solid State Physics; Radiation Effects in Solids, July 2004.

T-E282 Trautmann, W.: **Isotopic scaling in spectator fragmentation and the symmetry term at low density.** New London, N.H., USA, Gordon Research Conference on Nuclear Chemistry, June 2004.

T-E283 Trautmann, W.: **Multifragmentation and the liquid-gas phase transition: an experimental overview.** Göteborg, Sweden, International Nuclear Physics Conference INPC2004, June 2004.

T-E284 Trautmann, W.: **Reaction studies with neutron rich beams.** GANIL, Caen, France, SPIRAL 2 Workshop, April 2004.

T-E285 Trautmann, W.: **Multifragmentation with INDRA@GSI: from Fermi energies to the participant-spectator domain.** Bormio, Italy, XLII International Winter Meeting on Nuclear Physics, January 2004.

T-E286 Typel, S.: **The Trojan-Horse Method in Nuclear Astrophysics.** GSI/Darmstadt, Japanese-German Nuclear Structure and Astrophysics Workshop, December 2004.

T-E287 Typel, S.: **Relativistic Mean Field Model with Momentum-Dependent Self Energies.** University of Washington/INT/Seattle, WA, USA, Workshop on Relativistic Density Functional Theory, September 2004.

T-E288 Typel, S.: **The Trojan-Horse Method for Nuclear Astrophysics.** Callaway Gardens/Pine Mountain, GA, USA, The Fourth International Conference on Exotic Nuclei and Atomic Masses, ENAM'04, September 2004.

T-E289 Typel, S.: **Electromagnetic Excitation of Halo Nuclei - Effective-Range Approach and Scaling Laws.** Forschungszentrum Juelich, Institut für Kernphysik, Seminar, May 2004.

T-E290 Typel, S.: **Indirect Methods for Nuclear Astrophysics.** GSI/KPII/Darmstadt, Seminar, May 2004.

T-E291 Typel, S.: **The Trojan-Horse Method for Nuclear Astrophysics.** ECT/Trento, Italien, Workshop on Advances and Challenges in Nuclear Astrophysics, May 2004.

T-E292 Typel, S.: **Final-State Effects in the Coulomb Breakup of Exotic Nuclei.** Universität Koeln, DPG-Fruehjahrstagung, FV Hadronen und Kerne, March 2004.

T-E293 Typel, S.: **Final-State Effects in the Electromagnetic Breakup of Exotic Nuclei.** ECT/Trento, Italien, Workshop on Spectrosopic Factors, March 2004.

T-E294 Typel, S.: **Indirect Methods for Nuclear Astrophysics.** Russbach, Oesterreich, 1st VISTARS Workshop on Nuclear Astrophysics, March 2004.

T-E295 Typel, S.: **Final-State Effects in the Electromagnetic Breakup of Exotic Nuclei.** Waldemar-Petersen-Haus/Hirschegg, Oesterreich, International Workshop XXXII on Gross Properties of Nuclei and Nuclear Excitations, January 2004.

T-E296 Ursescu, D.: **Transient collisionally excited Ni-like Zr X-ray laser at GSI-Darmstadt.** Uni-Frankfurt, HSB Gruppenseminars, May 2004.

T-E297 Vassiliev, Y.: **Measurment of the bb (bar) Production Cross Section in 920 GeV Fixed-Target Proton-Nucleus Collisions (Preliminary results of HERA-B).** DESY, Physics, April 2004.

T-E298 Wambach, J.: **Hadrons in Hot and Dense Matter.** Giessen, Workshop on In-Medium Hadron Physics, November 2004.

T-E299 Wambach, J.: **Neutronensterne.** TU-Darmstadt, Saturday Morning Physics, November 2004.

T-E300 Wambach, J.: **The Medium Modification of Hadrons.** Palaiseau, Baryons 2004, October 2004.

T-E301 Wambach, J.: **The Phase Diagram of Hadronic Matter from the Renormalization Group.** ECT-Trento, Novel Approaches to the Nuclear Many-Body Problem, September 2004.

T-E302 Weber, C.: **Penning Trap Mass Spectrometry at ISOLTRAP & SHIPTRAP.** CERN, Genf, Switzerland, ISOLDE Seminar, August 2004.

T-E303 Weyrather, W. K.: **Krebtherapie mit dem 'Ionen-TV'.** Max-Planck-Institut für Kernphysik Heidelberg, Physik am Samstagmorgen, November 2004.

T-E304 Weyrather, W. K.: **The basis of ion beam therapy in physics and radiobiological research.** GANIL Caen, Frankreich, Research and Applications in Radiobiology with Swift Ions, October 2004.

T-E305 Weyrather, W. K.: **Grundlagen der Strahlenbiologie und -medizin.** Staatliches Schulamt Darmstadt, Strahlenschutzlehrgang für Lehrer, September 2004.

T-E306 Weyrather, W. K.: **Particle Radiotherapy.** Fakultaet für klinische Medizin Mannheim, Kurs Radiotherapy/ Medical Imaging, August 2004.

T-E307 Weyrather, W. K.: **Tumortherapie mit Ionenstrahlen.** Univ. Innsbruck, Oesterreich, Radioonkologie, June 2004.

T-E308 Weyrather, W. K.: **Tumortherapie mit schweren Ionen.** Univ. Freiburg, Chemie und Umwelt, March 2004.

T-E309 Weyrather, W. K.: **Krebstherapie mit schweren Ionen.** Heinrich-Kleyer-Schule Frankfurt, Brueckenschlagen/Wissenschaft in Schulen, February 2004.

T-E310 Winkler, M.: **The new Rare Isotope Facility Super-FRS.** Darmstadt, Deutschland, Annual Meeting of the NUSTAR Collaboration, February 2004.

T-E311 Zeitträger, H.: **La terpia experimental con iones pesados Desde la investigación basica hasta la aplicación.** Universidad Austral, Buenos Aires (Argentina), November 2004.

T-E312 Zeitträger, H.: **Russian-German cooperation at GSI, an example of success and friendship.** Peterhof (Russia), International Symposium on Exotic Nuclei EXON 2004, July 2004.

Seminars and talks at GSI

Compiled by U. Grundinger

T-I001 Kollmus, H. (GSI, Darmstadt, Germany): **Messungen zur ionenstrahlinduzierten Desorption bei GSI.** January 8, 2004.

T-I002 Krämer, A. (GSI, Darmstadt, Germany): **Desorptionsmessungen zur Auslegung des Vakuumsystems.** January 8, 2004.

T-I003 Roth, M. (TU Darmstadt, Germany): **Experiments and Prospects of a Multi Terawatt Laser Installation at Z6.** January 13, 2004.

T-I004 Bloch, I. (University of Mainz, Germany): **Seeing the Particle Beneath the Waves – New Physics with Bose-Einstein Condensates in Optical Lattices.** January 13, 2004.

T-I005 Khouaja, A. (GANIL, Caen, France). **Reaction Cross Section and Reduced Strong Absorption Radii Measurements of Neutron-Rich Exotic Nuclei in the Vicinity of Closed Shells N=20 and N=28.** January 14, 2004.

T-I006 Tomaselli, M. (GSI Darmstadt, Germany): **Charge Radii of Exotic Nuclei: Nuclear Physics Versus Isotopic Shift (IS) Calculation.** January 14, 2004.

T-I007 Saitoh, T. R. (GSI, Darmstadt, Germany): **First Results from the RISING Project.** January 14, 2004.

T-I008 Schmidt, E. W. (University of Gießen, Germany): **A Compact Energy Analyser for Ion Thrusters.** January 20, 2004.

T-I009 Krausz, F. (TU Wien, Austria): **Attosecond Physics: Controlling and Tracing the Motion of Electrons in Atoms.** January 20, 2004.

T-I010 Nörtershäuser, W. (University of Tübingen, Germany): **Electrons Spy on Nuclei – Detecting Whispers about the Charge Radii of ^{8,9,11}Li.** January 21, 2004.

T-I011 Scheidenberger, C. (GSI Darmstadt, Germany): **Experiments at the LEB of the Super-FRS.** January 21, 2004.

T-I012 Hülsmann, P. (GSI, Darmstadt, Germany): **The Bunch-Compressor Project for SIS12/18: Theory and Technique.** January 21, 2004.

T-I013 Peters, A.; Forck, P. (GSI, Darmstadt, Germany): **Optischen Strahldiagnose.** January 22, 2004.

T-I014 Stachel, J. (University of Heidelberg, Germany): **Relativistic Nuclear Collisions and the QCD Phase Boundary.** January 27, 2004.

T-I015 Hoffmann, D. H. H. (GSI Darmstadt, Germany): **Dunkle Materie.** January 27, 2004.

T-I016 Heil, M. (FZ Karlsruhe, Germany): **Stellar Nucleosynthesis – s-Process.** January 28, 2004.

T-I017 Bachert, P. (DKFZ Heidelberg, Germany): **NMR in Biophysik und Radiologie.** January 28, 2004.

T-I018 Schwenk, A. (Ohio University, USA): **Neutron Star Physics from the Renormalization Group.** January 28, 2004.

T-I019 Roth, M. (TU Darmstadt, Germany): **High-Intensity Ion Beams from Relativistic Laser Plasmas – the next Generation of Ion Sources?** January 28, 2004.

T-I020 Bellachioma, C. (CERN, Geneva, Switzerland): **Thin Film Coatings for UHV Applications.** January 29, 2004.

T-I021 Magestro, D. (Ohio State University, USA): **Soft Physics at RHIC.** February 3, 2004.

T-I022 Klein, F. (University of Bonn, Germany): **Pentaquarks – Evidences and Questions.** February 3, 2004.

T-I023 Plaß, W. (University of Gießen, Germany): **Time-of-Flight Mass Spectrometry at SHIPTRAP.** February 4, 2004.

T-I024 Pereira, J. (Santiago de Compostela, Spain): **Spallation Reactions Investigated with High Precision Measurements at the FRS.** February 4, 2004.

T-I025 Weick, H. (GSI, Darmstadt, Germany): **The Super FRS.** February 5, 2004.

T-I026 Fisher, D. (Weizmann Institute, Israel): **Intraband and Interband Absorption of Femtosecond Laser Radiation in Metals.** February 10, 2004.

T-I027 Muronga, A. (University of Frankfurt, Germany): **Causal Theories of Relativistic Dissipative Fluid Dynamics for Nuclear Collisions.** February 11, 2004.

T-I028 Delahaye, P. (CERN Geneva, Switzerland): **Search for Tensor Currents in the Nuclear Beta Decay at LPC Caen.** February 11, 2004.

T-I029 Rumolo, G. (GSI, Darmstadt, Germany): **Introduction to Electron Cloud Effects and Application to the GSI Present and Future Machines.** February 12, 2004.

T-I030 Vidana, I. (GSI Darmstadt, Germany): **Implications of Quark Deconfinement for the Radius and the Limiting Mass of Compact Stars.** February 16, 2004.

T-I031 Polinder, H. (Nijmwegen, The Netherlands): **Strong Meson-Baryon Interactions.** February 18, 2004.

T-I032 Gröning, L. (GSI, Darmstadt, Germany): **Protonen-LINAC.** February 19, 2004.

T-I033 Langanke, K.-H. (University of Aarhus, Denmark): **Kernstruktur und Supernovae.** February 23, 2004.

T-I034 Hencken, M. (University of Basel, Switzerland): **Exploring Exotic Nuclei with Nuclear Reactions.** February 23, 2004.

T-I035 Takahashi, F. (JAERI, Tokai, Japan): **Development of High Energy Neutron Monitor for Radiation Protection at new High Intensity Proton Accelerator (J-PARC) in Tokai, Japan.** February 23, 2004.

T-I036 Schädel, M. (GSI Darmstadt, Germany): **Chemie an der Grenze des Periodensystems – Superschwere Elemente.** Im Rahmen des: Radioisotopenkurs der Universität Heidelberg und des Fortbildungszentrums für Technik und Umwelt am Forschungszentrum Karlsruhe. February 24, 2004.

T-I037 Vretenar, D. (University of Zagreb, Croatia): **Relativistic Mean-Field and QRPA Description of Exotic Nuclear Structure.** February 25, 2004.

T-I038 Mann, R. (GSI Darmstadt, Germany): **On-Line Target Diagnosis Using an Electron Beam.** March 3, 2004.

T-I039 Skokov, V. V. (Dubna, Russia): **Pair Creation in Strong Fields.** March 3, 2004.

T-I040 Stöhlker, T. (GSI, Darmstadt, Germany): **Untersuchungen zum Elektronen-Stripping.** March 4, 2004.

T-I041 Rezaeian, A. (Univ. of Manchester, Great Britain): **Hamiltonian Renormalization Flows; a New Approach.** March 5, 2004.

T-I042 Büsching, H. (BNL, Upton, USA): **Neutral Pions with Large Transverse Momentum in Au+Au and d+Au Collisions at $\sqrt{s_{NN}}$ = 200GeV Measured by the PHENIX Experiment.** March 5, 2004.

T-I043 Bathe, S. (UC Riverside/BNL, Upton, USA): **Production of Direct Photons in Au+Au and p+p Collisions at $\sqrt{s_{NN}}$ = 200GeV.** March 3, 2004.

T-I044 Damerau, H. (GSI, Darmstadt, Germany): **Barrier Bucket Studies for LHC and SPS.** March 18, 2004.

T-I045 Hayashigaki, A. (University of Regensburg, Germany): **High-pT Leading Hadron Suppression in Heavy-Ion Collisions.** March 25, 2004.

T-I046 Spiller, P. (GSI Darmstadt, Germany): **SIS18 – Entwicklungsschritte in Richtung Hochstrombooster.** March 25, 2004.

T-I047 Tolos, L. (University of Frankfurt, Germany): **The Properties of Antikaons in Hot and Dense Matter.** March 26, 2004.

T-I048 Sprenger, F. (MPI Heidelberg, Germany): **Das Heidelberger Elektronentarget am Speicherring TSR – auf dem Weg zum ultraklaten Elektronenstrahl.** April 1, 2004.

T-I049 Borneis, S. (GSI Darmstadt, Germany): **Status of PHELIX and First Experiments.** April 21, 2004.

T-I050 Haidenbauer, J. (FZ Jülich, Germany): **Investigations on the Hyperon-Nucleon Interaction.** April 21, 2004.

T-I051 Forck, P. (GSI Darmstadt, Germany): **Einführung in die Strahldiagnose.** April 23, 2004.

T-I052 Basko, M. (MPQ Garching, Germany / ITEP Moscow, Russia): **Coulomb Stopping of Fast Ions: beyond the Bohr-Bethe-Bloch Formulae.** April 27, 2004.

T-I053 Bushaw, B. A. (Pacific Northwest Nat. Lab., USA): **High Resolution Laser Spectroscopy of Stable Atomic Lithium.** April 28, 2004.

T-I054 Gattringer, C. (University of Regensburg, Germany): **Recent Lattice Results for the Excited Nucleons.** April 28, 2004.

T-I055 Marbs, A. (I3Mainz, FH Mainz, Germany): **Gewinnung von Objektgeometrien mittels 3D-Scannung und Photogrammetrie.** May 3, 2004.

T-I056 Fill, E. (MPQ Garching, Germany): **Röntgenlaser – Stand und Perspektiven.** May 4, 2004.

T-I057 Wetterich, C. (University of Heidelberg, Germany): **Dark Energy – a Cosmic Mystery.** May 4, 2004.

T-I058 Mann, R. (GSI Darmstadt, Germany): **On-Line Target Diagnosis using an Electron Beam.** May 5, 2004.

T-I059 Schützhold, R. (TU Dresden, Germany): **Analoga Schwarzer Löcher.** May 5, 2004.

T-I060 Nolden, F. (GSI Darmstadt, Germany): **Stochastische Kühlung: Prinzip und Anwendung bei der GSI und woanders.** May 6, 2004.

T-I061 Willeke, F. (DESY Hamburg, Germany): **The HERA Lepton-Proton Collider.** May 11, 2004.

T-I062 Hein, J. (University of Jena, Germany): **Stand und Zukunft der Hochintensitätslaser, Aspekte der Strecker-Kompressor-Problematik.** May 11, 2004.

T-I063 Lemmer, R. (Univ. of Johannesburg, South Africa): **The Lifetime of Kaonium.** May 12, 2004.

T-I064 Yerokhin, V. (Univ. of Paris, France): **Theoretical Investigations of QED Effects in Highly Charged Ions: Recent Developments and Perspectives.** May 12, 2004.

T-I065 Typel, S. (GSI Darmstadt, Germany): **Indirect Methods for Nuclear Astrophysics.** May 12, 2004.

T-I066 Gräf, H.-D.: (TU Darmstadt, Germany): **S-Dalinac – Status und Aktuelle Entwicklungen.** May 13, 2004.

T-I067 Faestermann, T. (TU München, Germany): **About Neutrons in Hiroshima and the Latest Close Supernova.** May 18, 2004.

T-I068 Maruhn, J. A. (University of Frankfurt, Germany): **Plasmatheorie im Umfeld der GSI.** May 18, 2004.

T-I069 Egelhof, P. (GSI Darmstadt, Germany): **Nuclear Structure Studies by Direct Reaction Experiments with Stored Radioactive Beams.** May 19, 2004.

T-I070 Hemalatha, M. (BARC, Mumbai, India): **The Study of Exotic Nuclei.** May 19, 2004.

T-I071 Wettig, T. (University of Regensburg, Germany): **QCDOC: a Massively Parallel Supercomputer on the 10 TFlops Scale for Lattice QCD and Other Applications.** May 19, 2004.

T-I072 Stadelmann, J. (GSI Darmstadt, Germany): **Isochrone Mass Measurements at the ESR.** May 19, 2004.

T-I073 Weinheimer, C. (University of Bonn, Germany): **The Direct Neutrino Mass Experiment KATRIN.** May 25, 2004.

T-I074 Grüner, P. (Accel. Lab., Univ. of München, Germany): **Simulations of Ion-Matter Interaction.** May 25, 2004.

T-I075 Jentschura, U. (University of Freiburg, Germany): **Quantenelektrodynamik und Fundamentalkonstanten.** May 26, 2004.

T-I076 Cleymans, J. (Univ. of Cape Town, South Africa): **Particle Ratios and the Phase Transition Curve.** May 26, 2004.

T-I077 Wei, X. (GSI Darmstadt, Germany): **Computer Simulation of High Current Uranium Beams for Injection Beamline at the UNILAC.** May 27, 2004.

T-I078 Schaefer, T. (North Carolina, USA): **Non-Fermi Liquid Effects in QCD at High Density.** May 27, 2004.

T-I079 Tkachenko, I. M. (Polytechn. Univ. of Valencia, Spain): **Properties of HED Coulomb Systems.** June 1, 2004.

T-I080 Sprenger, F. (MPI Heidelberg, Germany): **Das Heidelberger Elektronentarget am Speicherring TSR auf dem Weg zum ultrakalten Elektronenstrahl.** June 2, 2004.

T-I081 Welsch, C. (MPI-Kernphysik, Heidelberg, Germany): **Elektrostatische Speicherringe: Grundlagen und Projekte.** June 3, 2004.

T-I082 Kadal, M. (Troja Laser Physics, Center, Prague, Czech Republic): **Foam Traget and Double-Target Studies at PALS.** June 8, 2004.

T-I083 Jido, D. (Trento, Italy): **In-Medium Properties of N(1535) Probed by Eta-Mesic Nuclei.** June 9, 2004.

T-I084 Bräuning-Demian, A. (GSI Darmstadt, Germany): **New Physics with Old Atoms: SPARC's FLAIR at FAIR.** June 9, 2004.

T-I085 Brandau, C. (GSI Darmstadt, Germany): **Determination of Nuclear Ground State Properties with Large Atomic Cross Sections – Isotopic Shift Measurements by Means of Dielectronic Recombination.** June 9, 2004.

T-I086 Akaishi, Y. (KEK, Tokyo, Japan): **Deeply Bound Kaonic Nuclear States.** June 14, 2004.

T-I087 Geissel, H. (GSI): **The Super-FRS at FAIR.** June 14, 2004.

T-I088 Wambach, J. (TU Darmstadt, Germany): **Hot and Dense Hadronic Matter.** June 15, 2004.

T-I089 Verdu, J. (University of Mainz, Germany): **The Electronic g-Factor of Hydrogen-Like Oxygen.** June 16, 2004.

T-I090 Grisenti, R. (University of Frankfurt, Germany): **Single Filament Liquid He and H_2 Jet: a High Density Internal Target and Beyond.** June 16, 2004.

T-I091 Napolitani, P. (Orsay, France): **New Insights on the Onset of Thermal Multi-fragmentation.** June 16, 2004.

T-I092 Bacca, S. (Trento, Italy): **Inelastic Electromagnetic Reactions on Light Nuclei with the Lorentz Integral Transform Method.** June 16, 2004.

T-I093 Kollmus, H. (GSI Darmstadt, Germany): **Projektilionisation im Ion-Atom Stößen.** June 17, 2004.

T-I094 Rapp, R. (Texas A&M Univ., USA): **Thermal Photons in QCD.** June 21, 2004.

T-I095 Kern, K. (MPI Stuttgart, Germany): **Building the Quantum World Atom by Atom.** June 22, 2004.

T-I096 Gericke, D. (University of Greifswald, Germany): **Einfluss von Korrelationen auf die Relaxation dichter Plasmen.** June 22, 2004.

T-I097 Steinhögl, W. (Infineon): **Size-Effects in the Resistivity of Copper Nanostructures and its Implications on the Performance of Interconnect Systems.** June 22, 2004.

T-I098 Rapol, U. D. (Lab. Kastler Brossel, Univ. Paris, France): **Laser-Cooling and Trapping of Ytterbium Atoms.** June 23, 2004.

T-I099 Koide, T. (University of Frankfurt, Germany): **Enhancement of Critical Slowing Down around Tricitical Point in Chiral Phase Transitions.** June 23, 2004.

T-I100 Gorska, M. (GSI Darmstadt, Germany): **Nuclear Structure in the Vicinity of ^{100}Sn.** June 23, 2004.

T-I101 Urschütz, P. (CERN, Geneva, Switzerland): **Measurement and Compensation of Resonance Driving Terms**

at the CERN PS Booster Synchrotron. June 24, 2004.

T-I102 Ray, A. (Calcutta, India): **The Decay Rate of ^{7}Be in Different Media and its Implications.** June 24, 2004.

T-I103 Krämer, D. (BESSY, Berlin, Germany): **Innovative Synchrotron Light Sources at BESSY.** June 25, 2004.

T-I104 Spielmann, C. (University of Würzburg, Germany): **Generation durchstimmbarer Pulse im weichen Röntgenbereich.** June 29, 2004.

T-I105 Heil, W. (University of Mainz, Germany): **Search for the Electric Dipole Moment of the Neutron: Status of Experiments and Perspectives.** June 29, 2004.

T-I106 Äschbach-Hertig, W. (Univ. of Heidelberg, Germany): **Climate of the Past as a Basis for an Assessment of the Future.** June 29, 2004.

T-I107 Dauvergne, D. (IPN Lyon, France): **Crystal Channeling and Blocking Experiments with Highly Charged Ions.** June 30, 2004.

T-I108 Schreiber, G. (GSI Darmstadt, Germany): **Barrier Buckets – Technische Realisation, Anwendungen und erste Strahlexperimente an der GSI.** July 1, 2004.

T-I109 Adrian, H. (University of Mainz, Germany): **Die demographischen Ursachen des wirtschaftlichen Niedergangs Deutschlands.** July 6, 2004.

T-I110 Eidmann, K. (MPQ Garching, Germany): **Isochore Laser-Heizung und Emission von Harmonischen von der Rückseite überdichter Folien.** July 6, 2004.

T-I111 Borasoy, B. (TU München, Germany): **Nuclear Lattice Simulations with Chiral Effective Theory.** July 7, 2004.

T-I112 Schweikhard, L. (University of Greifswald, Germany): **Ion Trapping at Greifswald.** July 7, 2004.

T-I113 Shen, W. (Shanghai, P.R. of China): **Radioactive Ion Beam Physics in China.** July 7, 2004.

T-I114 Senger, P. (GSI Darmstadt, Germany): **CBM: The Study of Compressed Baryonic Matter.** July 7, 2004.

T-I115 Pisarski, R. (Niels Bohr Inst. and Brookhaven Nat. Lab.): **Deconfinement and the Gross-Witten Point.** July 12, 2004.

T-I116 Plönjes, E. (HASYLAB/DESY, Hamburg, Germany): **Stragegies for Experiments at SASE Free-Electron X-Ray Lasers.** July 13, 2004.

T-I117 Winterhalter, M. (Int. Univ. Bremen, Germany): **Porin: Structure, Function and Application.** July 13, 2004.

T-I118 Barth, K.; Schmidt, R. (CERN, Geneva, Switzerland): **Kryotechnik für Beschleuniger und Experimente am CERN. Der LHC-Beschleuniger und seine supraleitenden Magnete.** July 14, 2004.

T-I119 Reiter, P. (University of Köln, Germany): **Nuclear Structure of Transferium Nuclei – The Odd Case.** July 14, 2004.

T-I120 Koehler, S. (University of Arizona, USA): **Kadanoff-Baym Transport and Correlations.** July 14, 2004.

T-I121 Kambara, T. (RIKEN, Tokyo, Japan): **Acoustic Emission by Fast Heavy Ion Irradiation.** July 15, 2004.

T-I122 Klein, B. (University of Heidelberg, Germany): **Renormalization Group Treatment of the Quark-Meson Model: Effects in Finite Volume.** July 15, 2004.

T-I123 Fischer, W. (Brookhaven Nat. Lab., Upton, USA): **RHIC Operation with Gold and Polarized Protons, and Observation of Transverse Echoes.** July 15, 2004.

T-I124 Varentsov, D. (GSI Darmstadt, Germany): **Studies on High Energy Density Matter with Intense Heavy Ion Beams at GSI.** July 15, 2004.

T-I125 Mazzocco, M. (University of Padua, Italy): **Breakup and Elastic Scattering around the Coulomb Barrier in Reactions Involving Light Weakly Bound Nuclei.** July 21, 2004.

T-I126 Schenkel, T. (LBL Berkeley, USA): **Development of Spin Qubit Test Structures.** July 21, 2004.

T-I127 Hartmann, O. (GSI Darmstadt, Germany): **PANDA@FAIR – Hadron Physics with Antiprotons.** July 23, 2004.

T-I128 Fahsold, G. (KIP, University of Heidelberg, Germany): **Dynamic Charge Transport and Plasmon Properties of Metal Nanowires in the Infrared Range.** August 3, 2004.

T-I129 Petzenhauser, I. (Univ. Erlangen-Nürnberg, Germany): **Grundlagen und Anwend. von Pseudofunkenschaltern.** August 5, 2004.

T-I130 da Costa, A. (Schonland Res. Cent. for Nucl. Science Univ. of Witwatersrand, Johannesburg, South Africa): **Detector Test Measurements made on Two Type Ib HPHT Diamond Detectors with Different Crystal Qualities.** August 10, 2004.

T-I131 Minty, M. (DESY Hamburg, Germany): **Optimization of the Proton Accelerators at DESY.** August 10, 2004.

T-I132 Masunov, E. (MEPI, Moscow, Russia): **Using of Undulators for Low Energy Ion Linac.** August 26, 2004.

T-I133 Kong, H. J. (Korea Adv. Inst. of Scie. and Techn.): **New Laser Fusion Driver with Beam Combination Technique.** August 31, 2004.

T-I134 Franchi, A. (GSI Darmstadt, Germany): **Magnet Strength Measurement and Linear Coupling Correc-**

tion from BPM Data. September 16, 2004.

T-I135 Wahab, M. A. (JMI-Univ., New Delhi, India): **Molecular Dynamics Simulation of ZnS.** September 22, 2004.

T-I136 Mustafin, E. (GSI Darmstadt, Germany): **Beam Loss Induced Radiation Hazards in Heavy-Ion Accelerators.** September 23, 2004.

T-I137 Tripathi, A. (Nucl. Scie. Centre, New Delhi, India): **Studies of Electronic Sputtering; Surface Modifications and Angular Dependence.** September 23, 2004.

T-I138 Tatsumi, T. (Univ. of Kyoto, Japan): **Chiral Symmetry Restoration and Magnetic Properties of Quark Matter at Moderate Densities.** September 27, 2004.

T-I139 Hülsmann, P. (GSI Darmstadt, Germany): **Einführung in die Theorie des longitudinalen Phasenraums und ihre Anwendung am Beispiel des SIS 12/18 Upgrades.** October 7, 2004.

T-I140 Herfurth, F. (GSI Darmstadt, Germany): **High Precision Mass Measurements with ISOLTRAP.** October 14, 2004.

T-I141 Welch, D. R. (ATK Mission Res. Albuquerque, USA): **Neutralized Drift Compression and Adiabatic Discharge Focusing of Heavy Ion Beams.** October 19, 2004.

T-I142 Drukarev, E. (Petersburg Nucl. Phys. Inst., Russia): **Double Photoionization at High Energies.** October 20, 2004.

T-I143 Strieder, F. (University of Bochum, Germany): **^{12}C(alpha, gamma)^{16}O – 30 Years of Progress.** October 21, 2004.

T-I144 Witte, K. (MPQ, Garching, Germany): **Lasererzeugte, quasi-monoenergetische MeV Elektronenjets.** October 26, 2004.

T-I145 Mukha, I. (Leuven, Belgium): **Observation of Direct Proton Decay of High-Spin Isomer (21+) in ^{94}Ag.** October 28, 2004.

T-I146 Pfannmöller, J.: **Chiral Symmetry for Heavy-Light Mesons.** November 2, 2004.

T-I147 Schultheiß, E. (Fraunhofer-Inst. Dresden, Germany): **Moderne Verfahren der Elektronenstrahl- und Plasmatechnik – Das FEP in Dresden.** November 2, 2004.

T-I148 Eschke, J.; Spiller, P. (GSI, Darmstadt, Germany): **Status of FAIR – Steps towards the International Facility and Development of the Accelerator.** November 2, 2004.

T-I149 Tachenov, S. (GSI Darmstadt, Germany): **Hard X-Ray Polarimetry – Studies of the K-REC Transition into Highly Charges Ions.** November 3, 2004.

T-I150 Gies, H. (University of Heidelberg, Germany): **Renormalization Flow of Yang-Mills Theories.** November 3, 2004.

T-I151 Saito, T. (GSI Darmstadt, Germany): **Hyper Nuclei with Heavy Ion and RI Beam Induced Reactions at GSI.** November 4, 2004.

T-I152 Eloy, J.- F. (ESRF, Grenoble, France): **Advances in Ultra-Short Electromagnetic Pulses – Laser Coupled with Synchrotron Radiation Beams.** November 9, 2004.

T-I153 Crespo Lopez-Urrutia, J. R. (MPI für Kernphysik, Heidelberg, Germany): **Lifetimes of Metastable Electronic States Determined with an EBIT.** November 10, 2004.

T-I154 Oset, E. (University of Valencia, Spain): **Hadronic Aspects of Exotic Baryons: Pentaquark, Two Meson Baryon Components and Theta+Hypernuclei.** November 10, 2004.

T-I155 van Oers, W. T. H. (Dep. of Physics+Astronomy, University of Manitoba, Canada): **Weak Charge of the Proton: A Search for New Physics.** November 10, 2004.

T-I156 Herzberg, R.-D. (Univ. of Liverpool, Great Britain): **Alpha-, Beta-, Gamma-Spectroscopy of Superheavy Elements.** November 11, 2004.

T-I157 Janka, H.T. (MPI f. Astrophysik, Garching, Germany): **Neutrino-Powered Explosions: Supernovae and Gamma Ray Bursts.** November 16, 2004.

T-I158 Ledingham, K. (Univ. of Glasgow, United Kingdom): **Nuclear Phenomena Using a Near Petawatt Laser.** November 16, 2004.

T-I159 Polonyi, J. (Strasbourg, France): **Hydrodynamics of Quantum Liquids.** November 17, 2004.

T-I160 Sanchez, R. (GSI Darmstadt, Germany): **Electron Spy into the Nucleus – Revealing the Halo Structure of ^{11}Li.** November 17, 2004.

T-I161 Tachenov, S. (GSI Darmstadt, Germany): **Hard X-Ray Polarimetry-Studies of Radiative Recombination Transitions for Highly Charged Ions.** November 17, 2004.

T-I162 Kiselev, O. (University of Mainz, Germany): **Investigation of Nuclear Matter Distribution in Neutron-Rich Helium Isotopes.** November 18, 2004.

T-I163 Singh, P. (BHABHA Res. Centre, Mumbai, India): **Indian Accelerator Programme – An Overview.** November 18, 2004.

T-I164 Heil, W. (University of Mainz, Germany): **Search for an Electric Dipole Moment of the Neutron.** November 23, 2004.

T-I165 Müller, J. C. (MPI f. Kernphys., Heidelberg, Germany): **Few-Photon Electron-Positron Pair Creation in the Collision of a Relativistic Nucleus and an Intense X-Ray Laser Beam.** November 24, 2004.

T-I166 Schmiedeskamp, J. (Univ. of Mainz, Germany): **Production and Application of Polarised ^{3}He.** November 25, 2004.

T-I167 Reygers, K. (University of Münster, Germany): **The Search for the Quark-Gluon Plasma at RHIC.** November 30, 2004.

T-I168 Cribeiro, A. (GSI Darmstadt, Germany): **Resonances Described by Gamow Vector States in Fermionic Molecular Dynamics.** December 1, 2004.

T-I169 Geissel, H. (GSI): **The Super-FRS at FAIR.** December 2, 2004.

T-I170 Wambach, J. (TU Darmstadt, Germany): **Hot and Dense Hadronic Matter.** December 7, 2004.

T-I171 Lippert, T. (FZ Jülich, Germany): **String Breaking in Lattice Quantum Chromo-dynamics.** December 8, 2004.

T-I172 Grawe, H.: **Nuclear structure of proton- and neutron-rich medium mass nuclei.** December 16/18, 2004.

Workshops and meetings

Compiled by U. Grundinger

Workshops and meetings held at the GSI

February 11-13: **Compressed Baryonic Matter, CBM Meeting.**

February 17/18: **Workshop on The Future of Superheavy Element Research.**

February 18: **A Next Generation Experimental Setup for Studies of Reactions with Relativistic Radioactive Beams.**

February 19-21: **NUSTAR Annual Meeting.**

Febraury 30-31: **Microbream Workshop.**

March 15-16: **FLAIR Workshop.**

March 30- April 2: **Jahrestagung der Gesellschaft für Biologische Strahlenforschung (GBS).**

May 6: **Fachtagung Supraleitung – Innovation + Perspektiven für die Energieversorgung.**

June 1-3: **PANDA-Meeting.**

July 4-6: **1st NoRHDia Workshop Novel Radiation Hard CVD Diamond Detectors for Hadron Physics.**

July 7: **Workshop 'Strangeness@SIS'.** 10 years of KaoS at GSI

August 9- September 30: **International Student Programm.**

August 19-20: **Workshop Polarized Antiprotons at FAIR.**

August 27: **Workshop on Recoil Separator for Superheavy Element Chemistry '04**

October 13: **Workshop on 'Electron Scattering off Rare Isotopes'.**

September 29– October 2: **HADES-Meeting.**

October 6-8: **Compressed Baryonic Matter-Meeting.**

October 29-30: **Stored Particles Atomic Physics Research Coll.**

November 8-9: **Granzer Workshop.**

November 12-13: **Workshop 'Penning-Traps'.**

December 16-18: **Japanses-German Nuclear Structure and Astrophysics Workshop.**

Outside workshops and meetings organized by the GSI

January 11-17: **XXXII Int. Workshop on Gross Properties of Nuclei and Nuclear Excitations: Probing Nuclei and Nucleons with Electrons and Photons.** Hirschegg, Austria (TU Darmstadt and GSI)

February 1-6: **Int. Workshop on the Physics of High Energy Density in Matter.** Hirschegg, Austria (TU Darmstadt and GSI).

February 12-19: **Inelastic Scattering with Radioactive Ion Beams, Nuclei.** Groningen, The Netherlands (KVI and GSI)

August 16-20: **XII Int. Linear Accelerator Conf. (LINAC 2004).** Lübeck, Germany (DESY and GSI)

September 1-4: **Hadrons'03, Xth Int. Conf. on Hadron Spectroscopy.** Aschaffenburg, Germany (Univ, of Bochum and GSI)

September 16-18: **International Workshop on Collaboration of Physics Programs between IMP and GSI.** Lanzhou (China) (GSI and IMP)

October 18-22: **ICFA/HB2004, 33rd ICFA Adv. Beam Dynamics Workshop + High Intensity High Brightness Hadron Beams.** Bensheim, Germany (ICFA and GSI)

Teaching activities of GSI staff at universities

Compiled by K. Große

U-01 Ackermann, D.(WS 2003/04): **Interdis. Anw. Atom- und Kernphysik.** Joh. Gutenberg Universität Mainz (Physik), Seminar/seminar.

U-02 Beier, T.(WS 2004/05): **Rechenmethoden der Elektrodynamik.** TU Dresden (Physik), Vorlesung/lecture.

U-03 Beier, T.(SS 2004): **Rechenmethoden der Quantenmechanik.** TU Dresden (Physik), Vorlesung/lecture.

U-04 Blaum, K.(WS 2004/05): **Spektroskopie in Ionenfallen.** Universität Mainz (Physik), Vorlesung/lecture.

U-05 Blaum, K.(WS 2004/05): **Spektroskopie in Ionenfallen.** Universität Mainz (Physik), Übung/exercise.

U-06 Blaum, K.(WS 2004/05): **Zusatzvorlesung Physik für Chemiker.** Universität Mainz (Physik), Vorlesung/lecture.

U-07 Boine-Frankenheim, O.(SS 2004): **Einführung in die Beschleunigerphysik.** TU Darmstadt (Elektrotechnik, Physik), Vorlesung/lecture.

U-08 Bosch, F.(SS 2004): **Kern-und Elementarteilchenphysik II.** Universität Kassel (Naturwissenschaften (FB 18)), Vorlesung/lecture.

U-09 Bosch, F.(WS 2003/04): **Kern-und Elementarteilchenphysik I.** Universität Kassel (Naturwissenschaften (FB 18)), Vorlesung/lecture.

U-10 Egelhof, P.(WS 2004/05): **Experimentelle Atom- und Kernphysik.** Joh. Gutenberg Universität Mainz (Physik), Seminar/seminar.

U-11 Egelhof, P.(WS 2004/05): **Seminar zum Praktikum für Fortgeschrittene.** Joh. Gutenberg Universität Mainz (Physik), Seminar/seminar.

U-12 Egelhof, P.(SS 2004): **Experimentelle Atom- und Kernphysik.** Joh. Gutenberg Universität Mainz (Physik), Seminar/seminar.

U-13 Egelhof, P.(WS 2003/04): **Experimentelle Atom- und Kernphysik.** Joh.-Gutenberg - Universität Mainz (Physik), Seminar/seminar.

U-14 Egelhof, P.(WS 2003/04): **Interdisziplinäre Anwendungen der Atom- und Kernphysik.** Joh.-Gutenberg Universität Mainz (Physik), Seminar/seminar.

U-15 Egelhof, P.(WS 2003/04): **Seminar zum Praktikum für Fortgeschrittene.** Joh. Gutenberg Universität Mainz (Physik), Seminar/seminar.

U-16 Egelhof, P.(WS 2003/04): **Seminar zum Praktikum für Fortgeschrittene.** Joh.-Gutenberg Universität Mainz (Physik), Seminar/seminar.

U-17 Emling, H.(WS 2004/05): **Physik V (Kern- und Teilchenphysik).** Universität Heidelberg (Physik), Vorlesung/lecture.

U-18 Emling, H.(WS 2004/05): **Physik an der zukünftigen Beschleunigeranlage bei GSI.** Universität Heidelberg (Physik), Seminar/seminar.

U-19 Emling, H.(SS 2004): **Physik an der zukünftigen Beschleunigeranlage bei GSI.** Universität Heidelberg (Physik), Seminar/seminar.

U-20 Feldmeier, H.(WS 2004/05): **Informationstheorie und Quantenstatistik.** TU Darmstadt (Physik), Vorlesung/lecture.

U-21 Feldmeier, H.(WS 2003/04): **Informationstheorie und Quantenstatistik.** TU-Darmstadt (Physik), Vorlesung/lecture.

U-22 Forck, P.(WS 2004/05): **Beam Instrumentation and Diagnostics.**, Vorlesung/lecture.

U-23 Friman, B.; Braun-Munzinger, P.; Wambach, J.; Oeschler, H.(WS 2004/05): **Relativistische Schwerionenphysik.** TU Darmstadt (Physik), Seminar/seminar.

U-24 Friman, B.; Braun-Munzinger, P.(SS 2004): **QCD-Concepts and Experimental Tests.** TU Darmstadt (Physik), Vorlesung/lecture.

U-25 Friman, B.; Braun-Munzinger, P.; Oeschler, H.; Wambach, J.(WS 2003/04): **Relativistische Schwerionenphysik.** TU Darmstadt (Physik), Seminar/seminar.

U-26 Geissel, H.(WS 2004/05): **Exp. Meth. der Kernstr.forschung - Astrophysik.** Justus Liebig Universität Gießen (Physik), Vorlesung/lecture.

U-27 Geissel, H.(WS 2004/05): **Exp. Meth. der Kernstr.forschung - WW mit Materie.** Justus Liebig Universität Gießen (Physik), Vorlesung/lecture.

U-28 Geissel, H.(SS 2004): **Exp. Meth. der Kernstr.forschung - Astrophysik.** Justus Liebig Universität Gießen (Physik), Vorlesung/lecture.

U-29 Geissel, H.(WS 2003/04): **Exp. Meth. der Kernstr.forschung - Ionenoptik.** Justus Liebig Universität Gießen (Physik), Vorlesung/lecture.

U-30 Görnitz, T.; Korneck, F.; Trautmann, W.(SS 2004): **Moderne Physik.** Frankfurt (Physik), Vorlesung/lecture.

U-31 Hoffmann, D. H. H.(WS 2004/05): **Grundlagen der Trägheitsfusion.** TU-Darmstadt (FB05), Seminar/seminar.

U-32 Hoffmann, D. H. H.; Jacoby, R.; Richter, A.; Weiland, T.; Zilges, A.; Angert, N.; Ratzinger, U.; Schempp,

A.; Walcher, T. (WS 2004/05): **Graduiertenkolleg: Physik und Technik von Beschleunigern.** TU Darmstadt (FB05), Vorlesung/lecture.

U-33 Hoffmann, D. H. H.; Kinsep, A. (WS 2004/05): **Grundlagen nicht-lineare Plasmaphysik.** TU Darmstadt (FB05), Vorlesung/lecture.

U-34 Hoffmann, D. H. H.; Manakos, P.; Richter, A.; Wambach, J.(WS 2004/05): **Schwerionenphysik.** TU-Darmstadt (Physik), Seminar/seminar.

U-35 Hoffmann, D. H. H.; Richter, A.; Wambach, J.; Zilges, A. (WS 2004/05): **Saturday Morning Physics - Einführung in die Probleme der modernen Physik.** TU Darmstadt (FB05), Vorlesung/lecture.

U-36 Hoffmann, D. H. H.; Roth, M.(WS 2004/05): **High Energy Density in Matter.** TU-Darmstadt (FB05), Seminar/seminar.

U-37 Hoffmann, D. H. H.; Roth, M.(WS 2004/05): **Wechselwirkung intensiver Laser- und Ionenstrahlen mit Materie.** TU-Darmstadt (FB05), Seminar/seminar.

U-38 Hoffmann, D. H. H.; Roth, M.; Bock, R.(WS 2004/05): **Physik dichter Plasmen mit Schwerionen- und Laserstrahlen.** TU-Darmstadt (FB05), Seminar/seminar.

U-39 Hoffmann, D. H. H.; Tauschwitz, A.(WS 2004/05): **Dunkle Materie - Astroteilchenphysik.** TU Darmstadt (FB05), Seminar/seminar.

U-40 Hoffmann, D.(WS 2004/05): **Ions and Atoms in Plasmas - Introduction to Plasma Physics with Heavy Ions.** TU Darmstadt (FB05), Vorlesung/lecture.

U-41 Hoffmann, D. H. H.(SS 2004): **Einführung in die Plasmaphysik mit schweren Ionen.** TU-Darmstadt (FB05), Vorlesung/lecture.

U-42 Hoffmann, D. H. H.(SS 2004): **Experimentelle Projektarbeiten in der Plasmaphysik.** TU-Darmstadt (FB05), Praktikum/practical course.

U-43 Hoffmann, D. H. H.(SS 2004): **Grundlagen der Trägheitsfusion.** TU-Darmstadt (FB05), Seminar/seminar.

U-44 Hoffmann, D. H. H.(SS 2004): **Project work in plasma physics.**, Praktikum/practical course.

U-45 Hoffmann, D. H. H.; Jacoby, R.; Richter, A.; Weiland, T.; Zilges, A.; Angert, N.; Ratzinger, U.; Schempp, A.; Walcher, T. (SS 2004): **Graduiertenkolleg: Physik und Technik von Beschleunigern.** TU Darmstadt (FB05), Vorlesung/lecture.

U-46 Hoffmann, D. H. H.; Richter, A.; Zilges, A. (SS 2004): **Experimentelle Kernphysik.** TU Darmstadt (FB05), Seminar/seminar.

U-47 Hoffmann, D. H. H.; Roth, M.; Bock, R.(SS 2004): **Physik dichter Plasmen mit Schwerionen- und Laserstrahlen.** TU-Darmstadt (FB05), Seminar/seminar.

U-48 Hoffmann, D. H. H.; Roth, M.; Knoll, J.; Oeschler, H.(SS 2004): **International Student Program at GSI Research with heavy ions.** TU-Darmstadt (Physik), Vorlesung/lecture.

U-49 Kluge, H.-J.(WS 2004/05): **Modern Methods of Atomic and Molecular Physics.** Heidelberg (Physik), Vorlesung/lecture.

U-50 Kluge, H.-J.(WS 2004/05): **Moderne Methoden der Atomphysik.** Heidelberg (Physik), Vorlesung/lecture.

U-51 Kluge, H.-J.(WS 2003/04): **Modern Methods of Atomic and Molecular Physics.** Heidelberg (Physik), Vorlesung/lecture.

U-52 Knoll, J.(SS 2004): **Internationales Studentenprogramm (Organisator).** GSI (Physik), Praktikum/practical course.

U-53 Kraft, G.(WS 2004/05): **Physik von Zellen und zellulaeren Netzwerken.** TU Darmstadt (Biologie), Vorlesung/lecture.

U-54 Kraft, G.(SS 2004): **Physik für Biologen, mit Übungen.** TU Darmstadt (Physik), Vorlesung/lecture.

U-55 Kraft, G.(WS 2003/04): **Radiation Biophysics.** TU Darmstadt (Physik), Vorlesung/lecture.

U-56 Kraft, G.(WS 2003/04): **Zellulaere Biophysik.** TU Darmstadt (Bionik fachübergreifend), Vorlesung/lecture.

U-57 Kühl, T.(WS 2004/05): **Relativistische Laser-Plasmaphysik.** Johannes Gutenberg Universität Mainz (Physik), Vorlesung/lecture.

U-58 Kühl, T.; Bock, R.; Hoffmann, D.; Jacoby, J.; Maruhn, J.; Mulser, P.; Roth, M.; Schlegel, T.(WS 2004/05): **Physik dichter Plasmen mit Schwerionen- und Laserstrahlen.** Universität Mainz (Physik), Seminar/seminar.

U-59 Kühl, T.; Bock, R.; Hoffmann, D.; Jacoby, J.; Maruhn, J.; Mulser, P.; Roth, M.; Schlegel, T.(SS 2004): **Physik dichter Plasmen mit Schwerionen- und Laserstrahlen.** Universität Mainz (Physik), Seminar/seminar.

U-60 Kühl, T.(WS 2003/04): **Die Physik von Ultra-Hochintensitätslasern.** Johannes Gutenberg Universität Mainz (Physik), Vorlesung/lecture.

U-61 Kühl, T.; Bock, R.; Hoffmann, D.; Jacoby, J.; Maruhn, J.; Mulser, P.; Roth, M.; Schlegel, T.(WS 2003/04): **Physik dichter Plasmen mit Schwerionen- und Laserstrahlen.** Universität Mainz (Physik), Seminar/seminar.

U-62 Leifels, Y.(WS 2003/04): **Physik I.** Heidelberg (Physik), Übung/exercise.

U-63 Liesen, H.-D.(WS 2004/05): **Gruppenunterricht zur Physik III.** Universität Heidelberg (Physik), Übung/exercise.

U-64 Lutz, M.(SS 2004): **Introduction to effective field theories.** TU Darmstadt (Physik), Vorlesung/lecture.

U-65 Mokler, P.; Grün, N.; Müller, A.; Salzborn, E.; Schartner, K.; Scheid, W. (WS 2004/05): **Seminar über Atomphysik.** Universität Giessen (Atomphysik), Seminar/seminar.

U-66 Mokler, P.; Grün, N.; Müller, A.; Salzborn, E.; Schartner, K.; Scheid, W. (SS 2004): **Seminar über Atomphysik.** Universität Giessen (Atomphysik), Seminar/seminar.

U-67 Mokler, P.; Grün, N.; Müller, A.; Salzborn, E.; Schartner, K.; Scheid, W. (WS 2003/04): **Seminar über Atomphysik.** Universität Giessen (Atomphysik), Seminar/seminar.

U-68 Müller, W. F. J.(SS 2004): **Elektronik II: Digitale Elektronik.** Frankfurt (Physik), Vorlesung/lecture.

U-69 Müller, W. F. J.(SS 2004): **Elektronik-Praktikum für Physiker, Teil B: Digital-Elektronik.** Frankfurt (Physik), Praktikum/practical course.

U-70 Müller, W. F. J.(SS 2004): **Seminar zum Elektronik-Praktikum für Physiker; Teil B: Digital-Elektronik.** Frankfurt (Physik), Seminar/seminar.

U-71 Münzenberg, G.(WS 2004/05): **Experimentelle Atom- und Kernphysik.** Joh. Gutenberg Universität Mainz (Physik), Seminar/seminar.

U-72 Münzenberg, G.(WS 2004/05): **Seminar über aktuelle Themen aus Kosmochemie und Astrophysik.** Joh. Gutenberg Universität Mainz (Physik), Seminar/seminar.

U-73 Münzenberg, G.(SS 2004): **Experimentelle Atom- und Kernphysik.** Joh. Gutenberg Universität Mainz (Physik), Seminar/seminar.

U-74 Münzenberg, G.(SS 2004): **Seminar über aktuelle Fragen der Kosmochemie und Astrophysik.** Joh.Gutenberg Universität Mainz (Physik), Seminar/seminar.

U-75 Münzenberg, G.(WS 2003/04): **Experimentelle Atom- und Kernphysik.** Joh. Gutenberg Universität Mainz (Physik), Seminar/seminar.

U-76 Münzenberg, G.(WS 2003/04): **Interdisziplinäre Anwendungen der Atom- und Kernphysik.** Joh.-Gutenberg-Universität Mainz (Physik), Seminar/seminar.

U-77 Münzenberg, G.(WS 2003/04): **Seminar über aktuelle Themen aus Kosmochemie und Astrophysik.** Joh. Gutenberg Universität Mainz (Physik), Seminar/seminar.

U-78 Neumann, R.(WS 2004/05): **Hochauflösende Mikroskopie und Nanotechnologie II.** Universität Heidelberg (Fakultät für Physik und Astronomie), Vorlesung/lecture.

U-79 Neumann, R.(SS 2004): **Hochauflösende Mikroskopie und Nanotechnologie I.** Universität Heidelberg (Fakultät für Physik und Astronomie), Vorlesung/lecture.

U-80 Neumann, R.(WS 2003/04): **Materialforschung mit energiereicher Strahlung II.** Heidelberg (Physik), Vorlesung/lecture.

U-81 Quint, W.(WS 2004/05): **Atome und Felder.** Universität Heidelberg (Physik), Vorlesung/lecture.

U-82 Quint, W.(SS 2004): **Gruppenunterricht Physik II.** Universität Heidelberg (Physik), Übung/exercise.

U-83 Quint, W.(WS 2003/04): **Atome und Felder.** Universität Heidelberg (Physik), Vorlesung/lecture.

U-84 Rosmej, F. (WS 2003/04): **Atomare Kinetik.** Ruhr-Universität Bochum (Atom- und Plasmaphysik), Vorlesung/lecture.

U-85 Scheidenberger, C.(WS 2004/05): **Exp. Meth. der Kernstr.forschung - WW mit Materie.** Justus Liebig Universität Gießen (Physik), Vorlesung/lecture.

U-86 Scheidenberger, C.(SS 2004): **Exp. Meth. der Kernstr.forschung - Astrophysik.** Justus Liebig Universität Gießen (Physik), Vorlesung/lecture.

U-87 Scheidenberger, C.(WS 2003/04): **Exp. Meth. der Kernstr.forschung - Ionenoptik.** Justus Liebig Universität Gießen (Physik), Vorlesung/lecture.

U-88 Scholz, M.(WS 2004/05): **Radiologischer Kurs.** Univ. Heidelberg (Medizin), Vorlesung/lecture.

U-89 Scholz, M.(WS 2003/04): **Radiologischer Kurs/Strahlenbiologie.** Univ. Heidelberg (Medizin), Seminar/seminar.

U-90 Scholz, M.(WS 2003/04): **Radiologischer Kurs/Strahlenbiologie.** Univ. Heidelberg (Medizin), Vorlesung/lecture.

U-91 Schwarz, C.(WS 2004/05): **Praktikum für Fortgeschrittene im IKF.** Univ. Frankfurt (Institut für Kernphysik), Praktikum/practical course.

U-92 Schwarz, C.(SS 2004): **Praktikum für Fortgeschrittene im IKF.** Univ. Frankfurt (Institut für Kernphysik), Praktikum/practical course.

U-93 Schwarz, C.(WS 2003/04): **Experimentalphysik I.** Frankfurt (Physik), Übung/exercise.

U-94 Schwarz, C.(WS 2003/04): **Praktikum für Fortgeschrittene im IKF.** Frankfurt (Physik), Praktikum/practical course.

U-95 Senger, P.(WS 2004/05): **Ergänzungen zur Kernphysik 1.** University of Frankfurt (Physik), Vorlesung/lecture.

U-96 Senger, P.(WS 2003/04): **Ergänzungen zur Kernphysik 1.** University of Frankfurt (Physik), Vorlesung/lecture.

U-97 Senger, P.(WS 2003/04): **Hochenergiephysik.** Univ. Frankfurt (Physik), Seminar/seminar.

U-98 Stöhlker, T.(WS 2004/05): **Atomphysik I: Struktur und Dynamik von Ionen und Atomen.** Universität Frankfurt (Physik), Vorlesung/lecture.

U-99 Stöhlker, T.; Becker, R.; Hagmann, S.; Dreizler, R.;

Lüdde, H.; Schmidt-Böcking, H.(WS 2004/05): **Hauptseminar: Hochgeladene langsame Ionen - neue Aspekte in der Atomphysik.** Universität Frankfurt (Physik), Seminar/seminar.

U-100 Stöhlker, T.; Dörner, R.; Groenefeld, K.; Hagmann, S.; Schmidt-Böcking, H.; Stiebing, K. (WS 2004/05): **Atomphysik mit schweren Ionen.** Universität Frankfurt (Physik), Seminar/seminar.

U-101 Stöhlker, T.(SS 2004): **Atompyhsik IV: Hochgeladene Ionen in starken Laserfeldern.** Universität Frankfurt (Physik), Vorlesung/lecture.

U-102 Stöhlker, T.; Dörner, R.; Groenefeld, K.; Hagmann, S.; Schmidt-Böcking, H.; Stiebing, K. (SS 2004): **Atomphysik mit schweren Ionen.** Universität Frankfurt (Physik), Seminar/seminar.

U-103 Stöhlker, T.(WS 2003/04): **Atomphysik I: Struktur und Dynamik von Ionen und Atomen.** Universität Frankfurt (Physik), Vorlesung/lecture.

U-104 Stöhlker, T.; R. Becker, S. (WS 2003/04): **Hauptseminar: Hochgeladene langsame Ionen - neue Aspekte in der Atomphysik.** Universität Frankfurt (Physik), Seminar/seminar.

U-105 Stöhlker, T.; R. Dörner, K. (WS 2003/04): **Atomphysik mit schweren Ionen.** Universität Frankfurt (Physik), Seminar/seminar.

U-106 Trautmann, W.; Sfienti, C.(WS 2004/05): **Kernphysik für Studierende des Lehramtes.** Frankfurt (Physik), Vorlesung/lecture.

U-107 Trautmann, W.(WS 2003/04): **Kernphysik für Studierende des Lehramtes.** Frankfurt (Physik), Vorlesung/lecture.

U-108 Wambach, J.(WS 2004/05): **Rechenmethoden der Physik.** TU-Darmstadt (Physik), Vorlesung/lecture.

U-109 Wambach, J.(SS 2004): **Einfuehrung in die Theoretische Physik.** TU-Darmstadt (Physik), Vorlesung/lecture.

PhD, Master and Diploma Theses

Compiled by K. Große

A-01 Azima, A.: **Design und Aufbau eines Hochenergie-Lasersystems.** Diplomarbeit, Heidelberg, Univ. (Germany, Baden-Württemberg), 2004.

A-02 Brambrink, E.: **Untersuchungen der Eigenschaften lasererzeugter Ionenstrahlen.** Dissertation, Darmstadt, TU Darmstadt, Physik (Germany, Hessen), 2004.

A-03 Brosch, O.*: **A Kaon Trigger for FOPI: Development and Evaluation of a Trigger System for Strange Particles.** Dissertation, Heidelberg, Univ., Fakultät für Physik und Astronomie (Germany, Baden-Württemberg), 2004.

A-04 Cezanne, L.: **Softwareentwicklung zur Digitalisierung von Leuchttarget-Signalen.** Diplomarbeit, Wiesbaden, FH-Wiesbaden (Germany, Hessen), 2004.

A-05 Djekic, S.: **Implementation of new techniques for high precision g factor measurements.** Dissertation, Mainz, Universität (Germany, Rheinland-Pfalz), 2004.

A-06 Eberl, T.: **Untersuchung π^0-Mesonen induzierter e^+e^-Paare in C+C Stössen.** Dissertation, München, Technische Universität, Physik-Department E12 (Germany, Bayern), 2004.

A-07 El-Said, A.*: **Heavy ion-induced damage in ionic fluoride single crystals.** Dissertation, Heidelberg, Univ. (Germany, Baden-Württemberg), 2004.

A-08 Falter, T.: **Nuclear Reactions of High-Energy Protons, Photons, Leptons.** Dissertation, Gießen, Universität (Germany, Hessen), 2004.

A-09 Fleischer, P.: **Mean-Field Theory of Nuclear Collective Motion.** Dissertation, Erlangen, Universität (Germany, Bayern), 2004.

A-10 Fritsch, S.: **Chiral Dynamics and the Nuclear Many-Body Problem.** Dissertation, München, Technische Universität (Germany, Bayern), 2004.

A-11 Grözinger, S.*: **Volume Conformal Irradiation of Moving Target Volumes with Scanned Ion Beams.** Dissertation, Darmstadt, Techn. Univ, Fachbereich Physik, Institut für Kernphysik (IKP) (Germany, Hessen), 2004. GSI Diss-2004-03.

A-12 Gunzert-Marx, K.*: **Nachweis leichter Fragmente aus Schwerionenreaktionen mit einem BaF_2-Teleskop-Detektor: Messungen im Rahmen des Tumortherapieprojektes der GSI.** Dissertation, Darmstadt, Technische Universität, Fachbereich Physik, Institut für Kernphysik (IKP) (Germany, Hessen), 2004. GSI Diss-2004-02.

A-13 Haase, O.: **Strahleninduzierte Aktivierung von TGF-beta und Phosphorylierung von Smad-2 im Prozess der terminalen Differenzierung von Hautfibroblasten: Vergleich von Roentgen- und Schwerionenbestrahlung.** Dissertation, Tübingen, Univ. (Germany, Baden-Württemberg), 2004.

A-14 Hanauske, M.: **Eigenschaften von kompakten Sternen in QCD-motivierten Modellen.** Dissertation, Frankfurt, Univ. Frankfurt am Main (Germany, Hessen), 2004.

A-15 Heiß, M.*: **Entwicklung und Erprobung eines Aufbaus zur gezielten Bestrahlung einzelner biologischer Zellen an der Schwerionen-Mikrosonde der GSI.** Dissertation, Darmstadt, Technische Universität, Fachbereich Physik, Institut für Kernphysik (IKP) (Germany, Hessen), 2004. GSI Diss-2004-06.

A-16 Holtmann, S.: **Goldstone-mode effects and critical behaviour of QCD with 2 light quark flavours.** Dissertation, Universität Bielefeld (Germany, Nordrhein-Westfalen), 2004.

A-17 Häfner, C.*: **Entwicklung, Modellierung und Aufbau des 10 Joule-Vorverstärkers mit adaptiver Optik für den Pettawatt-Laser PHELIX.** Dissertation, Heidelberg, Ruprecht-Karls-Universität, Fakultät für Physik und Astronomie, Kirchhoff-Institut für Physik (Germany, Baden-Württemberg), 2004. GSI Diss-2004-04.

A-18 Jäger, B.: **Studies of Hadronic Spin Structure in Hard Scattering Processes at Next-to-Leading Order of QCD.** Dissertation, Universität Regensburg (Germany, Bayern), 2004.

A-19 Kalmykov, Y.: **Fine Structure of the Gamow-Teller Resonance in 90 Nb and 168 Tm Studied with the (3 He, t) Reaction at 0° .** Dissertation, Darmstadt, Technische Universität (Germany, Hessen), 2004.

A-20 Katayama, Y.: **Automatische Zellzahlbestimmung in Kolonien von Säugetierzellen zur Untersuchung der Wirkung niedriger Strahlendosen.** Diplom, Darmstadt, Technische Universität, Fachbereich Physik, Institut für Kernphysik (IKP) (Germany, Hessen), 2004.

A-21 Keil, C.: **Microscopic baryon-baryon interactions at finite density and hypernuclear structure.** Dissertation, Gießen, Universität (Germany, Hessen), 2004.

A-22 Kieslich, S.: **Präzisionsspektroskopie von doppelt angeregten Zuständen durch dielektronische Rekombination.** Dissertation, Universität Gießen (Germany, Hessen), 2004.

A-23 Kim, Y.: **Study of Nuclear Stopping in Isospin-Asymmetric Nuclear Collisions at 0.4 and 1.5A GeV.** Dissertation, Seoul, Univ. (Korea), 2004.

A-24 Kirchner, A.: **Untersuchungen zur tief-virtuellen Compton-Streuung.** Dissertation, Universität Regensburg (Germany, Bayern), 2004.

A-25 Knobloch, R.: **Beam Emittance Mesurements and Plasma Channel Properties for Channel-based Ion Beam transport.** Diplomarbeit, Darmstadt, Univ. (Germany, Hessen), 2004. A-26 Koval, P.: **Two–photon ionization of atomic inner–shells.** Dissertation, Kassel, Universität (Germany, Hessen), 2004.

A-27 Kraft-Bermuth, S.*: **Kalorimetrische Tieftemperaturdetektoren für niederenergetische (E $\leq$ 1 MeV/amu) Schwerionen und ihr erster Einsatz in der Beschleuniger-Massenspektroskopie zur Spurenanalyse von ^{236}U.** Dissertation, Mainz, Johannes-Gutenberg-Universität, Fachbereich Physik, Institut für Physik (Germany, Rheinland-Pfalz), 2004. GSI Diss-2004-08.

A-28 Kraus, I.: **Hyperonenproduktion in C+C und Si+Si Kollisionen bei 158 GeV pro Nukleon.** Dissertation, Universität Frankfurt/M, IKF (Germany, Hessen), 2004.

A-29 Lang, M.*: **The effect of pressure on ion track formation in minerals.** Dissertation, Heidelberg, Univ. (Germany, Baden-Württemberg), 2004.

A-30 Lopez, X.: **Production d'Etrangete dans les Collisions Ni+Ni a 1.93A GeV.** Dissertation, Clermont-Ferrand, Univ. (France), 2004.

A-31 Maas, A.: **The High-Temperature Phase of Yang-Mills Theory in Landau Gauge.** Dissertation, Darmstadt, Technische Universität (Germany, Hessen), 2004.

A-32 Mahmoud, .: **Optimization and Performance of the ALICE Detector.** Dissertation, Heidelberg, Universität (Germany, Baden-Württemberg), 2004.

A-33 Maier, M.*: **New applications for slowing down of high-energy heavy ion.** Dissertation, Gießen, Univ. (Germany, Hessen), 2004.

A-34 Martens, G.*: **Farbfelder und Quarkpotentiale im Chromo-Dielektrischen Modell.** Dissertation, Gießen, Universität (Germany, Hessen), 2004.

A-35 Matoš, M.: **Isochronous mass measurements of short-lived neutron rich nuclides at the FRS-ESR facilities.** Dissertation, Gießen, Justus-Liebig-Universität, Fachbereich 07 (Germany, Hessen), 2004.

A-36 Merschmeyer, M.: **Production and Flow of Neutral Strange Particles in Ni+Ni Collisions at 1.93A GeV.** Dissertation, Heidelberg, Univ. (Germany, Baden-Württemberg), 2004.

A-37 Mukherjee, M.*: **The mass of ^{22}Mg and a concept for a novel laser ion source trap.** Dissertation, Heidelberg, University, Combined Faculties for the Natural Sciences and for Mathematics (Germany, Baden-Württemberg), 2004. GSI Diss-2005-02.

A-38 Neumayr, J.: **The buffer-gas cell and the extraction RFQ for SHIPTRAP.** Dissertation, München, Ludwig-Maximilians-Universität, Fakultät für Physik (Germany, Bayern), 2004.

A-39 Orsic-Muthig, A.*: **Zustandsselektive Untersuchung der Elektroneneinfangprozesse in hochgeladenen Uranionen durch Nachweis der charakteristischen Projektilstrahlung.** Dissertation, Frankfurt, Johann Wolfgang Goethe-Universität (Germany, Hessen), 2004.

A-40 Parodi, K.: **On the feasibility of dose quantification with in-beam PET data in radiotherapy with 12C and proton beams.** Dissertation, Technische Universität Dresden, Fakultät Mathematik und Naturwissenschaften (Germany, Sachsen), 2004.

A-41 Prerauer, T.: **Darstellung eines internationalen Großprojektes in SAP© R/3©.** Diplom, Ludwigshafen, Fachhochschule Ludwigshafen am Rhein, Hochschule für Wirtschaft, Fachbereich für Betriebswirtschaftslehre I (Germany, Rheinland-Pfalz), 2004. GSI Dipl-2004-01.

A-42 Pschiwul, T.: **Untersuchungen zu dielektrischen und Transporteigenschaften von nichtidealen Zweikomponentenplasmen.** Dissertation, Erlangen, Universität (Germany, Bayern), 2004.

A-43 Roth, T.: **Medium modifications of antikaons in dense matter.** Dissertation, Darmstadt, Technische Universität (Germany, Hessen), 2004.

A-44 Ruppert, J.: **Selbstkonsistente Beschreibung stark wechselwirkender Materie bei endlichen Temperaturen.** Dissertation, Frankfurt, Univ. Frankfurt am Main (Germany, Hessen), 2004.

A-45 Salazar, T.: **Mode coupling for precise measurements of the electronic g-factor of hydrogen-like ions in Penning traps.** Dissertation, Mainz, Universität (Germany, Rheinland-Pfalz), 2004.

A-46 Sander, P.*: **Untersuchung von biologischen Faktoren, die den Zellzyklus-Verlauf und die Apoptoserate nach Bestrahlung beeinflussen.** Staatsexamen, Darmstadt, Technische Universität, Fachbereich Physik, Institut für Kernphysik (IKP) (Germany, Hessen), 2004.

A-47 Sarpe-Tudoran, C.: **Adsorption of element 112 on a Au suface.** Dissertation, Kassel, Universität (Germany, Hessen), 2004.

A-48 Schmitt, A.: **Spin-One Color Superconductivity in Cold and Dense Quark Matter.** Dissertation, Frankfurt, Univ. Frankfurt am Main (Germany, Hessen), 2004.

A-49 Schollmeier, M.: **Untersuchung schmalbandiger Linienstrahlung lasererzeugter Plasmen.** Diplomarbeit, Darmstadt, Univ. (Germany, Hessen), 2004. A-50 Schulze, T.: **Goldstone-Effekte und Skalenfunktionen in der QCD mit zwei leichten adjungierten Quark-Flavors.** Dissertation, Universität Bielefeld (Germany, Nordrhein-Westfalen), 2004.

A-51 Shukla, T.*: **Bunches with space charge for arbitrary rf wave forms.** Master, Indian Institute of Technology (IIT) (India), 2004.

A-52 Soverna, S.: **Attempt to chemically characterize element 112.** Dissertation, Bern, University (Switzerland), 2004.

A-53 Söldner, W.: **Chiral fermions in lattice QCD and random matrix theory.** Dissertation, Universität Regensburg (Germany, Bayern), 2004.

A-54 Thiel, U.: **Entwicklung eines vakuumtauglichen Szintillationszählers für Ionenstrahlenergien im MeV/u-Bereich.** Diplomarbeit, Wiesbaden, FH-Wiesbaden (Germany, Hessen), 2004.

A-55 Udrea, S.: **Elektrische Leitfähigkeit schwerioneninduzierter Plasmen.** Dissertation, Darmstadt, Univ. (Germany, Hessen), 2004.

A-56 Valenzuela, T.: **Mode coupling for precise measurements of the electronic g-factor of hydrogen-like ions in Penning traps.** Dissertation, Mainz, Universität (Germany, Rheinland-Pfalz), 2004.

A-57 Weber, C.*: **Konzeption eines kryogenen Penningfallenaufbaus für SHIPTRAP und Massenbestimmungen von Radionukliden um den Z = 82 - Schalenabschluss an ISOLTRAP.** Dissertation, Heidelberg, Universität (Germany, Baden-Württemberg), 2004.

A-58 Wilke, M.: **Zur numerischen Berechnung quasistationärer elektromagnetischer Felder im Zeitbereich.** Dissertation, Darmstadt, TU Darmstadt (Germany, Hessen), 2004.

A-59 Wojtaszek, A.: **Spektroskopia laserowa izotopw sodu i litu.** Dissertation, Warschau, Univ. (Poland), 2004.

A-60 Zantow, F.: **Lattice-Renormalization of the Polyakov Loop.** Dissertation, Universität Bielefeld (Germany, Nordrhein-Westfalen), 2004.

A-61 von Zweidorf, A.: **Gaschemische Untersuchungen in situ gebildeter flüchtiger Oxide des Rutheniums, Osmiums und Hassiums.** Dissertation, Universität Mainz (Germany, Rheinland-Pfalz), 2004.

Experiments performed at the GSI and map of the existing accelerator complex

Compiled by D. Miskowiec

Beam time coordinator in 2004: D. Miskowiec

1 shift means 8 hours main beamtime delivered from the accelerator.
Beam time sharing is not taken into account.

Experiments at the UNILAC

Pro-posal	Short title of the experiment	Spokesperson	Area	Ions	Shifts
U016	Parity violation	Hass	Y7	^{52}Cr	24
U074	Ion-laser interaction	Roth	Z6	^{40}Ar, ^{56}Fe	
U177	Ion optical properties of laser initiated ...	Neff	Z4	^{209}Bi	
U179	Nucl. structure investigation Z=103-105	Hessberger	Y7	^{50}Ti, ^{51}V	34
U182	Chemical properties of element 106	Kratz	X1	^{22}Ne	
U182	Element 106 and 108 chemistry	Kratz	X1	^{12}C, ^{80}Kr, ^{22}Ne	36
U184	Heavy elements	Hofmann	Y7, X4	^{136}Xe, ^{51}V, ^{12}C, ^{70}Zn, ^{46}Ti	109
U185	Gas phase chemistry ... 112 and 114	Gaeggeler	X1	^{48}Ca, ^{70}Zn	46
U189	Projectile spectroscopy	Rosmej	Z6	^{26}Mg, ^{48}Ca	35
U190	Stopping power measurements ...	Golubev	Z6	^{136}Xe, ^{12}C	
U198	Beta decay of 100Sn	Janas	Y5	^{58}Ni	
U201	Commissioning of SHIPTRAP	Quint	Y7	^{58}Ni	
U204	Measurement of ion-induced desorption	Kraemer	HHT	^{238}U	13
U205	Decay properties near Z=108 and N=162	Tuerler	X1	^{26}Mg, ^{40}Ar	33
U206	Towards the new region ...	Andreyev	Y7	^{46}Ti, ^{97}Mo	28
U207	Optical Spectroscopy of Nobelium	Backe	Y7	^{40}Ca, ^{40}Ar	15
U209	Nuclear Structure Investigations No, Lr	Hessberger	Y7	^{48}Ca	
U210	Missing alpha-emitters in the transuranium region	Novikov	X1	^{12}C	
UBIO	Biology	Scholz	X6	^{12}C, ^{197}Au, ^{3}He, ^{52}Cr, ^{58}Ni, ^{70}Zn, ^{80}Kr	
UMAT	Material science	Fischer / Trautmann	X0	^{12}C, ^{197}Au, ^{3}He, ^{40}Ar	
				^{197}Au, ^{238}U, ^{50}Ti, ^{51}V	20

Experiments at the SIS/ESR complex

Pro-posal	Short title of the experiment	Spokesperson	Area	Ions	Shift
E000	ESR machine development	Steck	ESR	^{238}U, ^{86}Kr, ^{70}Zn	4
E025	Laser spectroscopy of H- and Li-like ions	Kuehl	ESR	^{209}Bi	14
E035	Dielectronic Recombination DR (and RR)	Mueller	ESR	^{238}U	16
E043	Charge transfer from complex targets ...	Braeuning-Demian	X4	^{238}U	
E047	Electron spectrometer commissioning	Hagmann	ESR	^{238}U, ^{197}Au	14
E048	Exploring long-living K-isomers ...	Walker	FRS, ESR	^{238}U	17
E053	Laser cooling of C3+ ion beams ...	Schramm	ESR	$^{12}C3+$	17
E055	Direct mass measurement at FRS-ESR	Scheidenberger	ESR	^{238}U	17
E060	X-ray Study at the Electrion Cooler ...	Pajek	ESR	^{238}U	26
S134	2E1 decay in heavy systems	Mokler	HTA	^{209}Bi	
S200	HADES studies	Salabura	HAD	p	29
S214	Bound states of eta and omega mesons	Gillitzer	FRS	^{2}H	
S225	Life time measurements in He-like ions ...	Marrus	HTA	^{70}Zn	
S239	Anomalous effects in astronauts	Narici	HTA	^{50}Ti, ^{51}V, ^{12}C	
S243	Final focusing and HED matter	Varentsov	HHT	^{238}U, ^{14}N	
S248	Study of spallation mechanism	Ducret	HTB	^{12}C, ^{56}Fe	20
S249	Precise Measurement of Stopping Power	Golubev	HTA	^{238}U	
S250	Radii	Suzuki	FRS	^{80}Kr	
S251	Strangeness production	Herrmann/	HTB	^{238}U	
		Hildenbrand	HTB	p	
S255	EOS of HED matter	Varentsov	HHT	^{238}U	
S262	Pion beam development	Salabura	HAD	^{12}C	32
S262	Pion beam development	Simon	HAD,HTB	^{14}N	5
S266	Determination of the freeze-out temperature ...	Napolitani	FRS	^{214}Xe	10
S269	RISING	Reiter	FRS	^{12}C, ^{50}Ti, ^{51}V	
				^{238}U, ^{86}Kr	79
S271	Two-proton decay	Suemmerer	FRS	^{22}Ne	
S273	Strangeness Production w. Pion Beams	Herrmann	HTB	pions	34
S276	Investigation of the nuclear mean field ...	Henzl	FRS	^{197}Au	
S286	TRD tests	Garabatos	HTA	^{12}C	
SBIO	Biology	Scholz	HTM, HTA	^{12}C, ^{56}Fe	
SMAT	Material science	Trautmann	HTA	^{214}Xe, ^{56}Fe, ^{197}Au, ^{238}U	
STHE	Therapy studies	Haberer	HTM	3He	10

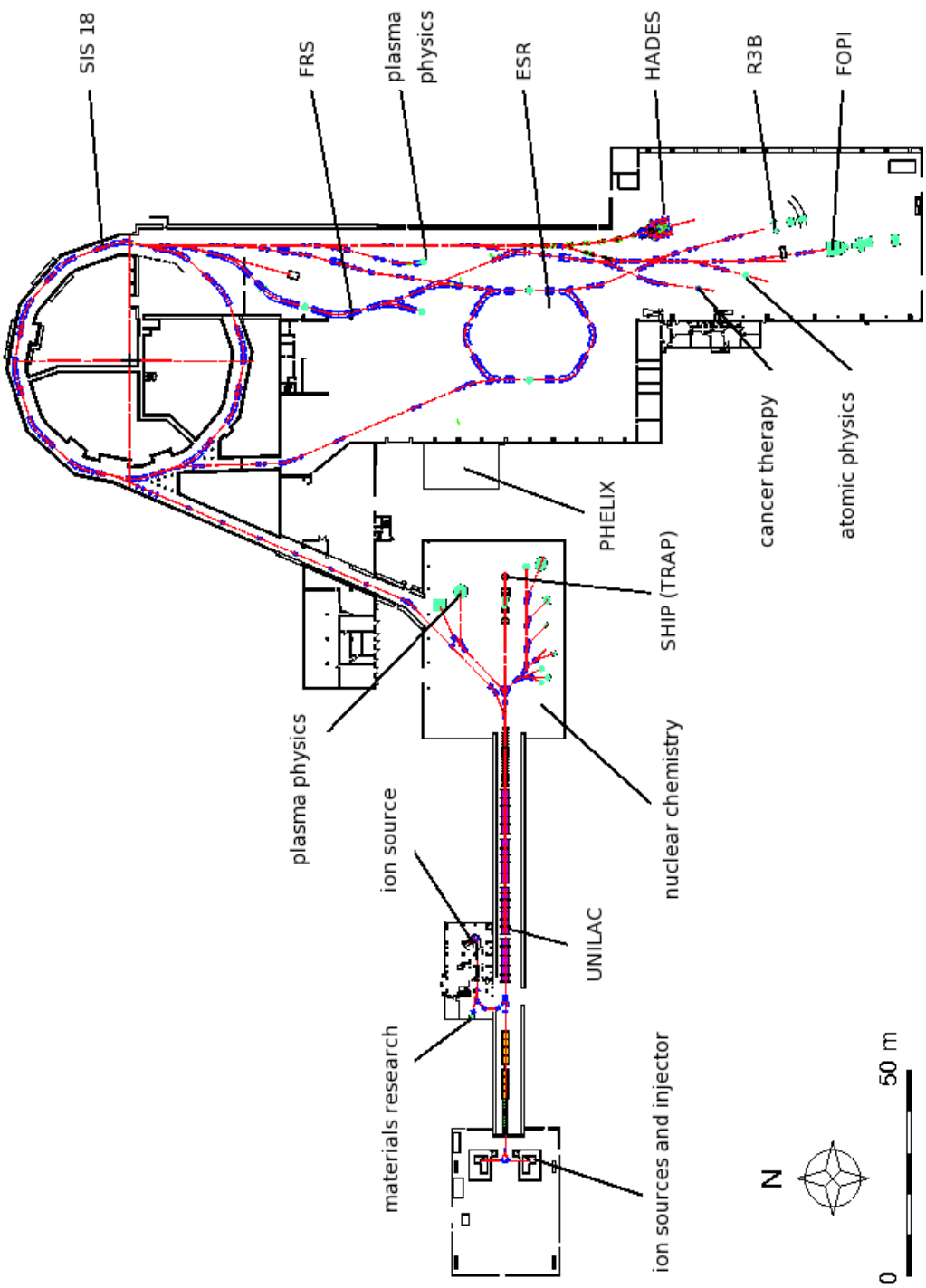
SIS 18
FRS
plasma physics
ESR
HADES
R3B
FOPI
cancer therapy
atomic physics
PHELIX
SHIP (TRAP)
nuclear chemistry
plasma physics
ion source
UNILAC
materials research
ion sources and injector
N
0
50 m

International and national collaborations of the GSI

Compiled by K. Große

The FAIR Collaborations

FAIR: The AIC Collaboration

Anti-proton Ion Collider
Spokesperson: R. Krücken, Munich (Germany)

Beller, P.[3]; Bosch, F.[3]; Cargnelli, M.[7]; Fabbietti, L.[8]; Faestermann, T.[8]; Franzke, B.[3]; Fuhrmann, H.[7]; Hayano, R. S.[9]; Hirtl, A.[7]; Homolka, J.[8]; Kienle, P.[8]; Kozhuharov, C.[3]; Krücken, R.[8]; Lenske, H.[5]; Litvinov, Y.[3]; Marton, J.[4]; Nolden, F.[3]; Ring, P.[8]; Shatunov, Y. M.[2]; Skrinsky, A. N.[2]; Suzuki, K.[8]; Vostrikov, V.[2]; Widmann, E.[9]; Wycech, S.[1]; Yamaguchi, T.[6]; Zmeskal, J.[7]

1 Andrzej Soltan Institute for Nuclear Studies Warsaw (Poland)
2 BINP Novosibirsk (Russia)
3 GSI Darmstadt (Germany)
4 IMEP Wien (Austria)
5 Justus-Liebig University Giessen (Germany)
6 Saitama University (Japan)
7 Stephan Meyer Institute Vienna (Austria)
8 TU Munich (Germany)

FAIR: The ASSIA Collaboration

A Study of Spin-dependent Interactions with Antiprotons
Spokesperson: R. Bertini (Italy)

Abazov, V.[1]; Alexeev, G.[1]; Alexeev, M.[2]; Amoroso, A.[2]; Angelov, N.[1]; Anselmino, M.[3]; Baginyan, S.[1]; Balestra, F.[2]; Baranov, V. A.[1]; Batusov, Y.[1]; Belolaptikov, I.[1]; Bertini, R.[2]; Bianchi, N.[11]; Bianconi, A.[4]; Birsa, R.[13]; Blokhintseva, T.[1]; Bonyushkina, A.[1]; Bradamante, F.[13]; Bressan, A.[13]; Bussa, M. P.[2]; Butenko, V.[1]; Colantoni, M. L.[5]; Corradini, M.[4]; Dalla Torre, S.[13]; De Sanctis, E.[11]; Demyanov, A.[1]; Denisov, O.[2]; Di Nezza, P.[11]; Drozdov, V.[1]; Erusalimtev, G.[1]; Fava, L.[5]; Ferrero, A.[2]; Ferrero, L.[2]; Finger, M.[6]; Finger, M.[7]; Frolov, V.[2]; Garfagnini, R.[2]; Giorgi, M.[13]; Gorchakov, O.[1]; Grasso, A.[2]; Grebenyuk, V.[1]; Hasch, D.[11]; Ivanov, V.[1]; Kalinin, A.[1]; Kalinnikov, V. A.[1]; Kharzheev, Y.[1]; Khomutov, N. V.[1]; Kirilov, A.[1]; Komissarov, E.[1]; Korenchenko, A. S.[1]; Kotzinian, A.[2]; Kovalenko, V.[1]; Kravchuk, N. P.[1]; Kuchinski, N. A.[1]; Lodi Rizzini, E.[4]; Lyashenko, V.[1]; Maggiora, A.[2]; Maggiora, M.[2]; Malyshev, V.[1]; Martin, A.[13]; Merekov, Y.[1]; Moiseenko, A. S.[1]; Muccaifora, V.[11]; Olchevski, A.[1]; Panyushkin, V.[1]; Panzieri, D.[5]; Piragino, G.[2]; Pontecorvo, G. B.[1]; Popov, A.[1]; Porokhovoy, S.[1]; Pryanichnikov, V.[1]; Ratclifffe, R. G.[12]; Rekalo, M. P.[10]; Rossi, P.[11]; Rozhdestvensky, A.[1]; Russakovich, N.[1]; Schiavon, P.[13]; Shevchenko, O.[1]; Shishkin, A.[1]; Sidorkin, V. A.[1]; Skachkov, N.[1]; Slunecka, M.[7]; Tchalyshev, V.[1]; Tessarotto, F.[13]; Tomasi, E.[8]; Tosello, F.[2]; Velicheva, E. P.[1]; Venturelli, L.[4]; Vertogradov, L.[1]; Virius, M.[9]; Zosi, G.[2]; Zurlo, N.[4]

1 Dzhelepov Laboratory of Nuclear Problems, JINR, Dubna (Russia)
2 Dipartimento di Fisca 'A. Avogadro' and INFN, Torino (Italy)
3 Dipartimento di Fisca Teorica and INFN, Torino (Italy)
4 Universita and INFN, Brescia (Italy)
5 Universita del Piemonte Orientale and INFN, Torino (Italy)
6 Czech Technical University, Prague (Czech Republic)
7 Charles University, Prague (Czech Republic)
8 DAPNIA, CEN Saclay (France)
9 Inst. of Scientific Instruments Academy of Sciences, Brno (Czech Republic)
10 NSC Kharkov Physical Technical Institute, Kharkov (Ukraine)
11 Laboratori Nazionali Frascati, INFN (Italy)
12 Universita dell' Insubria, Como and INFN, Milano (Italy)

FAIR: The BIOMAT Collaboration

The High-Energy Irradiation Facility for Biophysics and Materials Research
Spokespersons: M. Durante, Naples (Italy) S. Klaumünzer, Berlin (Germany)

Benyagoub, A.[5]; Bettega, D.[20]; Bolse, W.[25]; Bouffard, S.[5]; Chimi, Y.[26]; Cirio, R.[27]; Durante, M.[21]; Elsässer, T.[8]; Geissel, H.[8]; Glasmacher, U. A.[15]; Hagmann, S.[12]; Hoffmann, D. H. H.[9]; Ishikawa, N.[26]; Iwase, A.[22]; Iwase, H.[8]; Jin, G. M.[19]; Kambara, T.[29]; Keppler, H.[1]; Klaumünzer, S.[3]; Kraft, G.[8]; Krasavin, E.[11]; Lang, M.[8]; Langenhorst, F.[17]; Liu, J.[19]; Mewaldt, R.[23]; Miletich, R.[16]; Miller, J.[2]; Narici, L.[24]; Neumann, R.[8]; O'Sullivan, D.[10]; Okayasu, R.[7]; Picozza, P.[24]; Reitz, G.[18]; Ritter, S.[8]; Rothard, H.[5]; Schardt, D[8]; Schiwietz, G.[3]; Scholz, M.[8]; Schuhmacher, H.[4]; Sihver, L.[13]; Tahir, N.[8]; Ting, S. C. C.[6]; Toulemonde, M.[5]; Trautmann, C.[8]; Udrea, S.[9]; Valtonen, E.[28]; Varentzov, D.[9]; Wagner, G. A.[14]; Wang, Z. G.[19]

1 University of Bayreuth and Bayerische Akademie der Wissenschaften, Bayerisches Geoinstitut, Bayreuth (Germany)
2 Lawrence Berkeley Lab LBL, Berkeley (USA)
3 Hahn-Meitner-Institut HMI, Berlin (Germany)
4 Phys.-Techn. Bundesanstalt PTB, Braunschweig (Germany)
5 Centre Interdisciplinaire de Recherche Ions Laser CIRIL, Grand Acclrateur National d'Ions Lourds GANIL, Caen (France)
6 Massachusetts Institute of Technology MIT, Cambridge (USA)
7 National Institute of Radiation Science NIRS, Chiba (Japan)
8 GSI, Darmstadt (Germany)
9 University of Technology, Darmstadt (Germany)
10 Institute for Advanced Studies, Dublin (Ireland)
11 Joint Inst. f. Nucl. Research JINR, Dubna (Russia)
12 University of Frankfurt/Main (Germany)
13 Chalmers Univ. of Technology, Göteborg (Sweden)
14 Heidelberger Akademie der Wissenschaften, Heidelberg (Germany)
15 Max-Planck-Institut fr Kernphysik, Heidelberg (Germany)
16 University of Heidelberg, Heidelberg (Germany)
17 University of Jena, Jena (German)
18 Deutsches Inst. f. Luft-und Raumfahrt DLR, Köln (Germany)
19 Institute of Modern Physics, Chinese Academy of Sciences, Lanzhou (China)
20 University of Milano, Milano (Italy)
21 University of Naples, Naples (Italy)
22 Osaka Prefecture University, Osaka (Japan)
23 California Inst. of Technology CALTECH, Pasadena (USA)
24 University of Rome, Rome (Italy)
25 University of Stuttgart, Stuttgart (Germany)
26 Japan Atomic Energy Research Institute JAERI, Tokai (Japan)
27 Istituto Nazionale di Fisica Nucleare INFN, Torino (Italy)
28 University of Turku, Turku (Finland)

FAIR: The CBM Collaboration

The Condensed Baryonic Matter experiment
< http : //www.gsi.de/zukunftsprojekt/experimente/CBM/index_e.html >
Spokesperson: P. Senger, Darmstadt (Germany)

Adamova, D.[31]; Ahn, J. K.[30]; Aiftimiei, C.[2]; Akindinov, A.[21]; Akishin, P.[9]; Akishina, E.[9]; Al-Turany, M.[6]; Alyushin, M.[24]; Ammosov, V.[29]; Andronic, A.[6]; Angeles Lopez, M.[33]; Appelshäuser, H.[11]; Arefiev, A.[21]; Atanasov, D.[13]; Atkin, E.[24]; Badura, E.[6]; Baginyan, S.[9]; Baranova, N.[22]; Bashindjagyan, G.[22]; Basrak, Z.[42]; Belver, D.[33]; Benabderahmane, L. M.[12]; Berdermann, E.[6]; Berdnikov, Y.[38]; Bertini, D.[6]; Besson, A.[39]; Bezshyyko, O.[17]; Blaschke, D.[10]; Bocharov, Y.[24]; Bogdanovich, B.[24]; Bogolyubsky, M.[29]; Bolonin, A.[36]; Braun-Munzinger, P.[6]; Brenner, K.-H.[18]; Brzychczyk, J.[16]; Brüning, U.[18]; Bubak, A.[15]; Bucher, D.[25]; Burov, V.[10]; Cai, X.[41]; Čaplar, R.[42]; Catanescu, V.[2]; Chepurnov, V.[7]; Chernenko, S.[7]; Chubarov, M.[35]; Ciobanu, M.[6]; Cordier, E.[12]; Dželalija, M.[42]; Deak, F.[3]; Denes, E.[4]; Deppe, H.[6]; Deveaux, M.[6]; Dobulevich, V.[36]; Dohrmann, F.[32]; Dyatchenko, V.[29]; Emelianov, V.[24]; Eschke, J.[6]; Essel, H.[6]; Fateev, O.[7]; Ferreira Marques, R.[5]; Fischer, P.[18]; Flemming, H.[6]; Fodor, Z.[4]; Fonte, P.[5]; Friese, V.[6]; Gašparić, I.[42]; Galatyuk, T.[6]; Galkin, V.[27]; Garabatos, C.[6]; Garzon, J.[33]; Gaycken, G.[39]; Gläß, J.[18]; Golovatyuk, V.[7]; Golovin, A.[27]; Golubeva, M.[20]; Golutvin, A.[21]; Gomez, F.[33]; Gonzalez, D.[33]; Gousakov, Y.[8]; Grigalashvili, N.[8]; Grishkin, Y[21]; Grishuk, Y.[21]; Grosse, E.[32]; Grzeszczuk, A.[15]; Guber, F.[20]; Haspel, P.[18]; Heidel, K.[32]; Heini, S.[39]; Herrmann, N.[12]; Holzmann, R.[6]; Hong, B.[34]; Hoppe, M.[25]; Höhne, C.[6]; Ierusalimov, A.[7]; Igolkin, S.[36]; Ilyushenko, I.[24]; Ivanov, V.[37]; Ivanov, Va.[9]; Ivanov, Vi.[9]; Ivashkin, A.[20]; Izsak, R.[3]; Jimenes, E.[6]; Kadenko, I.[17]; Kalisky, M.[6]; Karabowicz, R.[16]; Karasev, G.[36]; Karasev, V.[35]; Karavichev, O.[20]; Karavicheva, T.[20]; Karmanov, D.[22]; Karpechev, E.[20]; Kazantsev, A.[23]; Kebschull, U.[13]; Kecskemeti, J.[4]; Kekelidze, G.[8]; Khanzadeev, A.[37]; Kharlov, Y.[29]; Khmelnikov, V.[29]; Kiš, M.[42]; Kim, D.-S.[30]; Kim, J.-Y[30]; Kim, Y. J.[34]; Kirejczyk, M.[40]; Kisel, I[13]; Kiselev, S.[21]; Kiseleva, A.[6]; Kiss, A.[3]; Kiss, T.[4]; Koch, K.[6]; Koczon, P.[6]; Kohlmeyer, B.[19]; Kolb, B.[6]; Korolev, M.[22]; Korolko, I.[21]; Kostenko, B.[9]; Kotte, R.[32]; Kowalski, S.[15]; Krasnuk, A.[24]; Krauze, M.[15]; Kresan, D.[17]; Kružić, G.[6]; Kryshen, E.[38]; Kugler, A.[31]; Kurepin, A.[20]; Kuznetsov, A.[29]; Kvaracheliya, T.[21]; Kämpfer, B.[32]; König, W.[6]; Ladygin, V.[7]; Lebedev, A.[21]; Leifels, Y.[6]; Leontiev, V.[29]; Lindenstruth, V.[13]; Linev, S.[6]; Lippmann, C.[6]; Litvinenko, E.[9]; Loshaev, S.[35]; Lucenko, V.[8]; Maevskaia, A.[20]; Maiatski, V.[21]; Majka, Z.[16]; Malakhov, A.[7]; Malyshev, S.[21]; Mangiarotti, A.[12]; Manko, V.[23]; Martemiyanov, A.[21]; Matulewicz, T.[40]; Matyushevsky, E.[7]; Merkin, M.[22]; Mikhailov, K.[21]; Mishin, S.[8]; Moisa, D.[2]; Mousa, J.[26]; Murin, Y.[35]; Muthers, D.[14]; Männer, R.[18]; Müller, W. F. J.[6]; Müntz, C.[11]; Nadtochii, A.[37]; Naumann, L.[32]; Niebur, W.[6]; Novotny, J.[31]; Obraztsov, V.[29]; Onishchenko, E.[24]; Ososkov, G.[9]; Ossetski, D.[27]; Peshekhonov, D.[8]; Peshekhonov, V.[8]; Peshenichnov, I.[20]; Petracek, V.[28]; Petris, M.[2]; Petrova, G.[36]; Petrovici, A.[2]; Petrovici, M.[2]; Plekhanov, E.[7]; Plujko, V.[17]; Plujschev, V.[35]; Policarpo, A.[5]; Polishchuk, B.[29]; Polozov, P.[21]; Popov, V.[24]; Pozdniakov, V.[7]; Prokudin, M.[21]; Rabin,

N.[21]; Raduta, A.[2]; Rami, F.[39]; Raportirenko, A.[9]; Rasin, V.[20]; Reshetin, A.[20]; Reygers, K.[25]; Riabov, Y.[37]; Rogachevsky, O.[7]; Ryazantsev, A.[29]; Rykalin, V.[29]; Ryzhikov, D.[27]; Ryzhinskiy, M.[38]; Röhrich, D.[1]; Sadovsky, S.[29]; Samsonov, V.[37]; Saveliev, V.[27]; Schindler, C.[19]; Schwarz, K.[6]; Schüttauf, A.[6]; Seleznev, E.[35]; Seliverstov, D.[37]; Semak, A.[29]; Senger, P.[6]; Shelikhov, V.[29]; Shevshenko, V.[17]; Sikora, B.[40]; Silaev, A.[24]; Sim, K. S.[34]; Simakov, A.[24]; Simon, R.[6]; Siwek-Wilczynska, K.[40]; Skoda, L.[28]; Slogsnat, D.[18]; Slusarczyk, L.[40]; Smirnitskiy, A.[21]; Smolyankin, V.[21]; Soldatov, A.[29]; Soloviev, A.[9]; Soos, C.[4]; Souffi-Kebbati, H.[39]; Sougonyaev, V.[29]; Staszel, P.[16]; Stavinsky, A.[21]; Steinle, C.[18]; Stephan, E.[15]; Stoicea, G.[2]; Stolin, V.[21]; Strekalovsky, O.[8]; Stroth, J.[11]; Ströbele, H.[11]; Sviridov, Y.[29]; Svischev, A.[36]; Szostak, P.[16]; Tielert, R.[14]; Tiflov, V.[20]; Tkachev, M.[36]; Tlusty, P.[31]; Toneev, V.[10]; Tontisirin, S.[14]; Topilskaya, N.[20]; Torralba, G.[13]; Tröger, G.[13]; Tsertos, H.[26]; Tsvetkov, A.[38]; Uhlig, F.[6]; Ullaland, K.[1]; Uzhinsky, V.[9]; Varava, V.[36]; Vasiliev, A.[36]; Vassiliev, I.[6]; Vesztergombi, G.[4]; Victorov, V.[29]; Viriasov, K.[8]; Volkov, Y.[24]; Voloshin, K.[21]; Vorobeva, A.[36]; Voronin, A.[22]; Wessels, J.[25]; Wilk, A.[25]; Winter, M.[39]; Wisniewski, K.[40]; Wohlfeld, D.[18]; Wu, T.[41]; Wurz, A.[18]; Yaritzin, V.[36]; Yin, Z. B.[41]; Yoo, I.-K.[30]; Yushmanov, I.[23]; Zaboudko, M.[27]; Zaets, V.[29]; Zagreev, B [21]; Zanevsky, Y.[7]; Zhalov, M.[37]; Zhilin, A.[21]; Zhou, D. C.[41]; Zipper, W.[15]; Zlobin, J.[8]; Zrelov, P.[9]; Zrjuev, V.[7]

1 Department of Physics and Technology, University of Bergen, Bergen (Norway)
2 National Institute for Physics and Nuclear Engineering, Bucharest (Romania)
3 Eötvös University, Budapest (Hungary))
4 KFKI Budapest (Hungary)
5 LIP, Coimbra (Portugal)
6 GSI, Darmstadt (Germany)
7 JINR-LHE, Dubna (Russia)
8 JINR-LPP Dubna (Russia)
9 JINR-LIT Dubna (Russia)
10 JINR-LTP Dubna (Russia) [1]
11 Institut für Kernphysik, Universität Frankfurt, Frankfurt (Germany)
12 2. Physikalisches Institut, Universität Heidelberg, Heidelberg (Germany)
13 Kirchhoff-Institut für Physik, Universität Heidelberg, Heidelberg (Germany)
14 Universität Kaiserslautern, Kaiserslautern (Germany) [1]
15 University of Silesia Katowice (Poland)
16 Jagiellonian University, Krakow (Poland)
17 National University of Kyiv, Kyiv (Ukraine)
18 Inst. of Computer Engineering, Universität Mannheim, Mannheim
19 Fachbereich Physik, Universität Marburg, Marburg (Germany)
20 Institute for Nuclear Research, Moscow (Russia)
21 ITEP Moscow (Russia)
22 SINP, Moscow State University, Moscow (Russia)
23 Kurchatov Institute Moscow (Russia)
24 MEPhi Moscow (Russia) [1]
25 Institut für Kernphysik, Universität Münster, Münster (Germany)
26 Cyprus University, Nikosia (Cyprus)
27 Obninsk State University of Atomic Energy, Obninsk (Russia)
28 Technical University, Prag (Czech Republic)
29 IHEP Protvino (Russia)
30 Pusan National University, Pusan (Korea)
31 Czech Academy of Sciences, Rez (Czech Republic)
32 FZR, Institut für Kern- und Hadronenphysik, Dresden (Germany)
33 University, Santiago de la Compostela (Spain)
34 Korea University, Seoul (Korea)
35 Khlopin Radium Institute (KRI), St. Petersburg (Russia)
36 CKBM, St. Petersburg (Russia)
37 PNPI St. Petersburg (Russia)
38 Petersburg State Polytechnic University, St. Petersburg (Russia)
39 IN2P3-CNRS/ULP (IRes), Strasbourg (France)
40 Warsaw University, Institute of Experimental Physics, Warsaw (Poland)
41 Institute of Particle Physics, Hua-zhong Normal University Wuhan (China) [1]

FAIR: The DESPEC Collaboration

Decay Spectroscopy
Spokesperson: B. Rubio, Valencia (Spain)

Algora, A.[6]; Angulo, C.[13]; Batist, L.[17]; Blank, B.[2]; Cata-Danil, G.[18]; Erduran, N.[8]; Faestermann, T.[20]; Gerl, J.[3]; Górska, M.[3]; Harissopulos, S.[7]; Huyse, M.[11]; Iordachescu, A.[16]; Johnson, A.[19]; Jokinen, A.[24]; Jolie, J.[22]; Jungclaus, A.[21]; Kettunen, H.[24]; Kratz, K.-L.[9]; Krücken, R.[20]; Leino, M.[24]; Maj, A.[5]; Nyberg, J.[27]; Page, R. D.[12]; Penttillae, H.[24]; Pfutzner, M.[28]; Plaß, W.[10]; Regan, P.[26]; Reiter, P.[22]; Rubio, B.[4]; Rudolph, D.[14]; Scheidenberger, C.[3]; Scholey, C.[24]; Simpson, J.[1]; Spohr, K.[25]; Uusitalo, J.[24]; Walker, P.[26]; Woods, P.[23]; Zamfir, V.[15] Äystö, J.[24]

1 CCLRC Daresbury (United Kingdom)
2 CEN Bordeaux-Gradignan (France)
3 GSI Darmstadt (Germany)
4 IFIC Valencia (Spain)
5 IFJ PAN Krakow (Poland)
6 Inst. of Nuclear Res. of the Hungarian Academy of Sciences (Hungary)
7 Institute of Nuclear Physics, NCSR 'Demokritos', Athens (Greece)
8 Istanbul University (Turkey)
9 Johannes Gutenberg University of Mainz (Germany)
10 Justus-Liebig University Giessen (Germany)
11 KU Leuven (Belgium)
12 Liverpool (United Kingdom)
13 Louvain-la-Neuve (Belgium)
14 Lund University (Sweden)
15 NIPNE Bucharest (Romania)
16 National Institute for Physics and Nuclear Engineering (Ro-

mania)
17 PNPI Gatchina (Russia)
18 Politechnical University of Bucharest (Romania)
19 Stockholm University (Sweden)
20 TU Munich (Germany)
21 UAM Madrid (Spain)
22 University of Cologne (Germany)
23 University of Edinburgh (United Kingdom)
24 University of Jyvaskyla (Finland)
25 University of Paisley (United Kingdom)
26 University of Surrey (United Kingdom)
27 Uppsala University (Sweden)

FAIR: The ELISe Collaboration

ELectron-Ion Scattering in a Storage Ring (eA collider)
<http://www.gsi.de/zukunftsprojekt/experimente/elise/>
Spokesperson: H. Simon, Darmstadt (Germany)

Al-Khalili, J.[23]; Amaro Soriano, J. E.[7]; Artukh, A.[10]; Aumann, T.[6]; Avdeichikov, V.[13]; Barton, C.[24]; Becker, F.[6]; Beller, P.[6]; Boretzky, K.[6]; Borge, M. J.[2]; Caballero, J. A.[17]; Catford, W.[23]; Chartier, M.[21]; Chulkov, L.[15]; Cullen, D.[22]; Distler, M. O.[11]; Dolinskii, A.[6]; Egelhof, P.[6]; Emling, H.[6]; Enders, J.[18]; Ershov, S. N.[10]; Fraile Prieto, L. M.[4]; Franzke, B.[6]; Garrido, E.[2]; Geissel, H.[6]; Grigorenko, L.[10]; Heinz, A.[25]; Hencken, K.[20]; Jenkins, D.[24]; Johansson, H.[6]; Johnson, R.[23]; Jonson, B.[3]; Jourdan, J.[20]; Kamerdzhiev, S. P.[9]; Kato, S.[26]; Kelic, A.[6]; Kester, O.[12]; Klygin, S.[10]; Koop, I. A.[1]; Korostelev, M. S.[1]; Krusche, B.[20]; Kurz, N.[6]; Lallena Rojo, A. M.[7]; Lemmon, R.[5]; Lisin, V. P.[8]; Litvinova, E. V.[16]; Logatchov, P. V.[1]; Merkel, H.[11]; Meshkov, I. N.[10]; Moya de Guera, E.[2]; Mushkarenkov, A. N.[8]; Müller, U.[11]; Münzenberg, G.[6]; Nedorezov, V.[8]; Nesterenko, I. N.[1]; Nilsson, T.[18]; Nolden, F.[6]; Nyman, G.[3]; Otboev, A. V.[1]; Parkhomchuk, V. V.[1]; Pavlov, V. M.[1]; Polonski, A. L.[8]; Rauscher, T.[20]; Richter, A.[18]; Rohe, D.[19]; Rudnev, N. V.[8]; Sarriguren, P.[2]; Schmidt, K.-H.[6]; Schrieder, G.[18]; Seleznev, I.[10]; Sereda, Y.[10]; Shatilov, D. N.[1]; Shatunov, Y. M.[1]; Shiyankov, S. V.[1]; Simon, H.[6]; Skrinsky, A. N.[1]; Steck, M.[6]; Stevenson, P.[23]; Suda, T.[14]; Syresin, E.[10]; Teterev, Y. G.[10]; Trautmann, D.[20]; Turinge, A. A.[8]; Udias-Moinelo, J.[4]; Valishev, A. A.[1]; Volkov, V. A.[15]; Vorontsov, A. N.[10]; Weick, H.[6]; Zilges, A.[18]

1 BINP Novosibirsk (Russia)
2 CSIC Madrid (Spain)
3 Chalmers University of Technology (Sweden)
4 Complutense University of Madrid (Spain)
5 Daresbury Laboratory (United Kingdom)
6 GSI Darmstadt (Germany)
7 Granada University (Spain)
8 INR Moscow (Russia)
9 IPPE Obninsk (Russia)
10 JINR Dubna (Russia)
11 Johannes Gutenberg University of Mainz (Germany)
12 Ludwig-Maximilians University of Munich (Germany)
13 Lund University (Sweden)
14 RIKEN (Japan)
15 RRC Kurchatov Institute Moscow (Russia)
16 SSC RF Obninsk (Russia)
17 Seville University (Spain)
18 TU Darmstadt (Germany)
19 University of Basel (Schweiz)
20 University of Basel (Switzerland)
21 University of Liverpool (United Kingdom)
22 University of Manchester (United Kingdom)
23 University of Surrey (United Kingdom)
24 University of York (United Kingdom)
25 Yale University (USA)

FAIR: The EXL Collaboration

Exotic nuclei studied in light-ion induced reactions at the NESR storage ring
<http://ns.ph.liv.ac.uk/∼mc/EXL/collaboration/EXL-collaboration.html>
Spokesperson: M. Chartier, Liverpool (United Kingdom)

Al-Khalili, J.[10]; Alamanos, N.[25]; Algora, A.[6]; Álvarez Rodríguez, R.[16]; Artukh, A. G.[7]; Auger, F.[25]; Aumann, T.[4]; Avdeichikov, V.[15]; Barton, C.[11]; Beaumel, D.[22]; Becker, F.[4]; Beckert, K.[4]; Beller, P.[4]; Blumenfeld, Y.[22]; Boretzky, K.[4]; Bortignon, P. F.[19]; Bracco, A.[19]; Böhmer, M.[21]; Carlén, L.[15]; Catford, W.[10]; Chartier, M.[14]; Chulkov, L.[20]; Coleman-Smith, P.[3]; Col, G.[19]; Cresswell, J.[14]; Csátlos, M.[6]; Datta Pramanik, U.[13]; Demonchy, C. E.[14]; Dolinski, A.[4]; Drouart, A.[25]; Egelhof, P.[4]; Ekström, C.[26]; Emling, H.[4]; Faestermann, T.[21]; Feldmeier, H.[4]; Fernandez Dominguez, B.[14]; Fernández Ramírez, C.[16]; Fraile, L.[17]; Franczak, B.[4]; Freer, M.[2]; Fujita, Y.[23]; Fulton, B.[11]; Garrido, E.[16]; Geissel, H.[4]; Gernhäuser, R.[21]; Gillibert, A.[25]; Gobulev, P.[15]; Grzonka, D.[12]; Gulyás, J.[6]; Gáski, Z.[6]; Hencken, K.[1]; Hunyadi, M.[6]; Ivanov, V.[9]; Jakobsson, B.[15]; Jenkins, D.[11]; Johnson, R.[10]; Jourdan, J.[1]; Kanungo, R.[27]; Khan, E.[22]; Khanzadeev, A.[9]; Kienle, P.[21]; Kiselev, O.[18]; Klygin, S. A.[7]; Korchagin, A. E.[7]; Kozhuharov, C.[4]; Krasznahorkay, A.[6]; Kratz, J. V.[18]; Krusche, B.[1]; Krücken, R.[21]; Laird, A.[11]; Lapoux, V.[25]; Lazarus, I.[3]; Lemmon, R.[3]; Letts, S.[3]; Litvinov, Y.[4]; Lépine-Szily, A.[24]; Lpez Herraiz, J.[17]; Maier, L.[21]; Meier, J. P.[4]; Moreno, O.[16]; Moya de Guerra, E.[16]; Nalpas, L.[25]; Neff, T.[4]; Nilsson, T.[5]; Nolden, F.[4]; Peschke, C.[4]; Pollacco, E.[25]; Polovnikov, S. V.[7]; Protic, D.[12]; Pucknell, V.[3]; Rathmann, F.[12]; Rauscher, T.[1]; Rohe, D.[1]; Rostchin, E.[9]; Sarriguren, P.[16]; Scarpaci, J. A.[22]; Schrieder, G.[5]; Sereda, Y. M.[7]; Simenel, C.[25]; Simon, H.[4]; Steck, M.[4]; Stevenson, P.[10]; Stroth, J.[8]; Stöhlker, T.[4]; Suzuki, K.[21]; Sümmerer, K.[4]; Tarasenkova, O.[9]; Teterev, Y.

G.[7]; Thielemann, F.[1]; Thompson, I.[10]; Thornhill, J.[14]; Typel, S.[4]; Udias, J.M.[17]; Vorontzov, A. N.[7]; Weick, H.[4]; Westerberg, L.[26]; Winkler, M.[4]

1 Universität Basel, (Switzerland)
2 University of Birmingham, (United Kingdom)
3 CLRC Daresbury Laboratory (United Kingdom)
4 Gesellschaft für Schwerionenforschung (Germany)
5 Technische Universität Darmstadt (Germany)
6 Institute of Nuclear Research (Hungary)
7 Joint Institute of Nuclear Research (Russia)
8 Universität Frankfurt (Germany)
9 St. Petersburg Nuclear Physics Institute and St. Petersburg State University (Russia)
10 University of Surrey (United Kingdom)
11 University of York (United Kingdom)
12 Institut für Kernphysik, Forschungszentrum Jülich (Germany)
13 Saha Institute of Nuclear Physics (India)
14 University of Liverpool (United Kingdom)
15 Lund University (Sweden)
16 Instituto de Estructura de la Materia (Spain)
17 Universidad Complutense (Spain)
18 Johannes Gutenberg Universität (Germany)
19 Universitá da Milano and INFN (Italy)
20 Russian Research Centre Kurchatov Institute (Russia)
21 Technische Universität München (Germany)
22 Institut de Physique Nucléaire (France)
23 Osaka University (Japan)
24 Universidade de São Paulo (Brasil)
25 CEA/DAPNIA (France)
26 The Svedberg Laboratory (Sweden)

FAIR: The EXO-pbar Collaboration

Exotic antiprotonic atoms
<http://www.gsi.de/NUSTAR/>
Spokesperson: M. Wada (Japan)

Äystö, J.[4]; Geissel, H.[2]; Ishida, Y.[1]; Jastrzebski, J.[5]; Jokinen, A.[4]; Kopecky, S.[4]; Kurcewicz, W.[5]; Moore, I.[4]; Nakai, K.[3]; Nakamura, T.[1]; Nieminen, A.[4]; Oshima, N.[1]; Quint, W.[2]; Scheidenberger, C.[2]; Takamine, A.[1]; Trzcińska, A.[5]; Wada, M.[1]; Winkler, M.[2]; Yamazaki, Y.[1]

1 Atomic Physics Laboratory RIKEN (Japan)
2 GSI Darmstadt (Germany)
3 Okada Sophia University, Tokyo (Japan)
4 Jyvaskyla University JYFL (Finland)

FAIR: The FLAIR Collaboration

A Facility for Low-energy Antiproton and Ion Research
< http://www-linux.gsi.de/∼flair/>
Spokesperson: E. Widmann (Austria)
Steering Commitee: M. Charlton (USA); H. Danared (Sweden); D. Grzonka (Germany); M. H. Holzscheiter (USA); H. Knudsen (Denmark); W. Quint (Germany); M. Steck (Germany); T. Stöhlker (Germany); G. Testera (Italy); A. Trzcinska (Poland); J. Walz (Germany); E. Widmann (Austria); Y. Yamazaki (Japan).

Andler, G.[41]; Bagge, L.[41]; Balashov, V. V.[29]; Barna, D.[37]; Bassalleck, B.[50]; Beier, T.[16]; Beyer, H.[16]; Blaum, K.[24]; Bloch, I.[24]; Block, M.[16]; Borneis, S.[16]; Bosch, F.[16]; Boucard, S.[38]; Bräuning-Demian, A.[16]; Bureyeva, L. A.[33]; Burgdoerfer, J.[28]; Cargnelli, M.[48]; Charlton, M.[11]; Corradini, M.[12]; Danared, H.[41]; Dax, A.[10]; Djekic, S.[24]; Dörner, R.[21]; Eikema, K.[39]; Engström, M.[41]; Franzke, B.[16]; Fuhrmann, H.[48]; Fujiwara, M.[49]; Gabrielse, G.[7]; George, S.[24]; Gillitzer, A.[15]; Gotta, D.[15]; Grieser, M.[40]; Grzonka, D.[15]; Hagmann, S.[16]; von Hahn, R.[40]; Hayano, R.[10]; Herfurth, F.[16]; Hessels, E.[6]; Hogervorst, W.[39]; Holzscheiter, M.[43]; Hori, M.[10]; Horvath, D.[37]; Ichioka, T.[40]; Indelicato, P.[38]; Ishikawa, T.[10]; Jastrzebski, J.[17]; Jentschura, U.[40]; Juhász, B.[30]; Kanai, Y.[1]; Karshenboim, S. G.[2]; Kellerbauer, A.[16]; Kienle, P.[48]; Kilian, K.[15]; Kingsberry, P.[50]; Kluge, H.-J.[16]; Knudsen, H.[3]; Kobets, A.[36]; Komaki, K.-I.[31]; Korotaev, Y.[36]; Kostelecky, A.[18]; Kozhuharov, C.[16]; Kuroda, N.[1]; Källberg, A.[41]; Kühl, T.[16]; Labzowsky, L. N.[8]; Le Bigot, E.-O.[38]; Leali, M.[12]; Lemell, C.[28]; Liesen, D.[16]; Liljeby, L.[41]; Lindroth, E.[4]; Lodi Rizzini, E.[12]; Löfgren, P.[41]; Maggiore, C.[43]; Mann, R.[16]; Marton, J.[48]; McCullough, R.[45]; Meshkov, I.[36]; Minaev, S.[26]; Mohri, A.[1]; Mokler, P.[16]; Moshammer, R.[40]; Müller, A.[22]; Mller, S. P.[27]; Nagata, Y.[1]; Name, V.[19]; Nefiodov, A. V.[47]; Nolden, F.[16]; Noordam, B.[14]; Nörtershäuser, W.[44]; Oelert, W.[15]; Orth, H.[16]; Pachucki, K.[34]; Paál, A.[41]; Pivin, P.[36]; Plunien, G.[25]; Quint, W.[16]; Ratzinger, U.[20]; Ray, A.[51]; Rensfelt, K.-G.[41]; Ritman, J.[15]; Saenz, A.[23]; Saito, H.[1]; Schempp, A.[20]; Schuch, R.[4]; Schuessler, H. A.[9]; Seleznev, I. A.[36]; Shabaev, V. M.[8]; Shibata, M.[1]; Sidorin, A.[36]; Simonsson, A.[41]; Skeppstedt, Ö.[41]; Smirnov, A. V.[36]; Stahl, S.[24]; Steck, M.[16]; Stöhlker, T.[16]; Syresin, E.[36]; T?kési, K.[30]; Takács, E.[5]; Testera, G.[35]; Tino, G. M.[13]; Tomaselli, M.[16]; Torii, H. A.[31]; Trubnikov, G.[36]; Trzcinska, A.[17]; Ubachs, W.[39]; Uggerhj, U.[3]; Ullrich, J.[40]; Venturelli, L.[12]; Verdú, J.[24]; Vogel, M.[24]; Wada , M.[1]; Walz, J.[42]; Weber, C.[24]; Welsch, C.[40]; Werth, G.[24]; Widmann, E.[48]; Wolf, A.[40]; Wycech, S.[46]; Yakovenko, S.[36]; Yamazaki, Y.[32]; Yoshida, S.[28]; Zmeskal, J.[48]; Zurlo, N.[12]

1 Atomic Physics Laboratory, RIKEN (Japan)
2 D.I. Mendeleev Institute for Metrology/VNIIM (Russia)
3 Department for Physics and Astronomy, Aarhus University (Denmark)
4 Department of Atomic Physics, Stockholm University (Sweden)
5 Department of Experimental Physics, University of Debrecen (Hungary)
6 Department of Physics and Astronomy, York University (Canada)
7 Department of Physics, Harvard University, Cambridge (U.S.A.)
8 Department of Physics, St. Petersburg State University (Russia)
9 Department of Physics, Texas A&M University, College Station (U.S.A.)
10 Department of Physics, University of Tokyo (Japan)
11 Department of Physics, University of Wales Swansea (United Kingdoms)
12 Dipartimento di Chimica e Fisica per l'Ingegneria e per i Materiali-Universita' di Brescia & INFN-Gruppo Collegato di Brescia (Italy)
13 Dipartimento di Fisica, Laboratorio LENS, INFN, Universita degli Studi di Firenze (Italy)
14 FOM Institute for Atomic and Molecular Physics (Netherlands)
15 Forschungszentrum Jülich (Germany)
16 GSI Darmstadt (Germany)
17 Heavy Ion Laboratory, Warsaw University (Poland)
18 Indiana University, Bloomington, (U.S.A.)
19 Institut (Land)
20 Institut für Angewandte Physik, Universität Frankfurt (Germany)
21 Institut für Kernphysik, Universität Frankfurt (Germany)
22 Institut für Kernphysik, Universität Giessen (Germany)
23 Institut für Physik, Humboldt-Universität zu Berlin (Germany)
24 Institut für Physik, Universität Mainz (Germany)
25 Institut für Theoretische Physik, Technische Universität Dresden (Germany)
26 Institute for Experimental and Theoretical Physics (Russia)
27 Institute for Storage Ring Facilities, Aarhus University (Denmark)
28 Institute for Theoretical Physics, Vienna University of Technology (Austria)
29 Institute of Nuclear Physics, Moscow State University (Russia)
30 Institute of Nuclear Research of the Hungarian Academy of Sciences/ATOMKI (Hungary)
31 Institute of Physics, University of Tokyo (Japan)
32 Institute of Physics, University of Tokyo, and Atomic Physics Laboratory, RIKEN (Japan)
33 Institute of Spectroscopy of the RAS (Russia)
34 Institute of Theoretical Physics, Warsaw University (Poland)
35 Istituto Nazionale di Fisica Nucleare (Italy)
36 JINR Dubna (Russia)
37 KFKI Research Institute for Particle and Nuclear Physics, Budapest (Hungary)
38 Laboratoire Kastler-Brossel, École Normale Supérieure et Université P. et M. Curie, Paris (France)
39 Laser Centre Vrije Universiteit, Faculty of Science (Netherlands)
40 MPI für Kernphysik/MPI-K (Germany)
41 Manne Siegbahn Laboratory/MSL (Sweden)
42 Max-Planck-Institut für Quantenoptik/MPQ (Germany)
43 Pbar Labs, LLC Santa Fe (U.S.A.)
44 Physikalisches Institut, Universität Tübingen (Germany)
45 Queens University (Russia)
46 Soltan Institute for Nuclear Studies (Poland)
47 St. Petersburg Nuclear Physics Institute (Russia)
48 Stefan Meyer Institut für subatomare Physki/SMI, Österreichische Akademie der Wissenschaften, Wien (Austria)
49 TRIUMF (Canada)
50 University of New Mexico, Albuquerque (U.S.A.)

FAIR: The HEDgeHOB Collaboration

High Energy Density Matter generated by Heavy-iOn Beams
Spokesperson: D. Varentsov, Darmstadt (Germany)

Adamyan, V.[29]; Adonin, A.[14]; Alcober Auban, J.[37]; Aleksandrova, I.[22]; Apfelbaum, E.[9]; Audebert, P.[19]; Ballester, D.[37]; Barigga, M.[38]; Basko, M.[12]; Batani, D.[39]; Benage, J. F.[23]; Blazevic, A.[7]; Bock, R.[7]; Borneis, S.[7]; Brambrink, E.[19]; Bret, A.[38]; Callahan, D.[21]; Caruso, A.[5]; Chtcherbakov, V.[22]; Constantin, C. G.[21]; Cortazar, O.[38]; Cowan, T.[40]; Davidson, R. C.[31]; Deutsch, C.[18]; Dewald, E. L.[21]; Dudin, S.[13]; Efremov, V.[8]; Faenov, A.[27]; Fernandez, J.[23]; Fertman, A.[12]; Fisher, V.[45]; Fortmann, C.[42]; Fortov, V.[13]; Friedman, A.[21]; Gauthier, J.-C.[43]; Geissel, M.[34]; Gericke, D.[3]; Glenzer, S.[21]; Golubev, A.[12]; Grandjouan, N.[19]; Gromov, A.[22]; Grubert, G.[3]; Gryaznov, V.[13]; Habs, D.[24]; Hegelich, M.[23]; Hoffmann, D. H.[35]; Iosilevski, I.[26]; Jacoby, J.[14]; Jungwirth, K.[30]; Juranek, H.[42]; Kain, V.[4]; Kalal, M.[2]; Kalinin, Y.[28]; Kanel, G.[13]; Khishchenko, K.[8]; Kietzmann, A.[42]; Kim, C. J.[16]; Kim, V.[13]; Kingsep, A. S.[28]; Knobloch, R.[35]; Kong, H.[15]; Konovalov, V.[26]; Koresheva, E.[22]; Koshelev, E.[22]; Krainov, V.[26]; Kuba, J.[2]; Kuhlbrodt, S.[42]; Kulish, M.[13]; Kupriashin, A.[22]; Kühl, T.[7]; Levashov, P.[8]; Li, R.[11]; Lim, C.[16]; Limpouch, J.[2]; Lisitsa, L.[28]; Logan, G.[20]; Lomonosov, I.[13]; Lopez-Cela, J.[38]; Lou, Q.[11]; Magunov, A.[27]; Maron, Y.[45]; Matveichev, A.[13]; Maynard, G.[18]; Mehlhorn, T. A.[34]; Merkuliev, Y.[22]; Meyer-ter-Vehn, J.[25]; Milyavskii, V.[8]; Minaev, S.[12]; Mintsev, V.[13]; Morozov, I.[8]; Murillo, M. S.[23]; Nardi, E.[45]; Nettelmann, N.[42]; Neumann, R.[7]; Ni, P.[35]; Niemann, C.[21]; Nikitenko, A.[22]; Nikolaev, D.[13]; Norman, G.[8]; Ogawa, M.[36]; Omar, B.[42]; Osipov, I.[22]; Pikuz, T.[27]; Piriz, A. R.[38]; Porter, J.[34]; Postnov, V.[13]; Povarnitsyn, M.[8]; Razorenov, S.[13]; Redmer, R.[42]; Reinholz, H.[42]; Riley, D.[32]; Romadinova, E.[26]; Rosmej, F. B.[44]; Rosmej, O.[7]; Roth, M.[35]; Roudskoy, I.[12]; Ruhl, H.[33]; Röpke, G.[42]; Sanchez-Duque, J.[38]; Sauerbrey, R.[6]; Schaumann, G.[35]; Schlanges, M.[3]; Schmidt, R.[4]; Schollmeier, M.[35]; Schurtz, G.[43]; Schwarz, V.[42]; Sharkov, B.[12]; Shen, B.[10]; Sheyko, A.[13]; Shilkin, N.[13]; Shutov, A.[13]; Skobelev, I.[27]; Smirnov, V.[28]; Son, E.[26]; Sosikov, V.[13]; Stamm, R.[44]; Starobinets, A.[45]; Suk, H.[17]; Sultanov, V.[13]; Tabak, M.[21]; Tahir, N. A.[7]; Tauschwitz, A.[14]; Tauschwitz, A.[7]; Temporal, M.[38]; Ternovoi, V.[13]; Thiele, R.[42]; Tikhonchuk, V.[43]; Timasheva, T.[22]; Tkachenko Gorski, I. M.[37];

Toepffer, C.[41]; Tolokonnikov, S.[22]; Trautmann, C.[7]; Tsigutkin, K.[45]; Turtikov, V.[12]; Udrea, S.[35]; Ullschmied, J.[30]; Utkin, A.[13]; Varentsov, D.[35]; Vorberger, J.[3]; Wahl, H.[7]; Weyrich, K.[7]; Wiewior, P.[40]; Wouchuk , J.[38]; Yu, W.[10]; Yuryev, D.[13]; Zaporoghets, Y.[13]; Zepf, M.[32]; Zhernokletov, M.[1]; Zhu, J.[10]; Zwicknagel, G.[41]

1 All-Russian Institute of Experimental Physics/VNIIEF (Russia)
2 Czech Technical University/CTU (Czech Republic)
3 Ernst-Moritz-Arndt-Universität Greifswald/UG (Germany)
4 European Organization for Nuclear Research/CERN (Switzerland)
5 Frascati Research Center/ENEA (Italy)
6 Friedrich-Schiller-Universität Jena/UJ (Germany)
7 Gesellschaft für Schwerionenforschung/GSI (Germany)
8 Institute for High Energy Densities RAS/IHED (Russia)
9 Institute for High Energy Densities of RAS/IHED (Russia)
10 Institute for Optics and Fine Mechanics, CAS/IOFM (China)
11 Institute for Optics and Fine Mechanics/IOFM, Chinese Academy of Sciens (China)
12 Institute for Theoretical and Experimental Physics/ITEP (Russia)
13 Institute of Problems of Chemical Physics RAS/IPCP (Russia)
14 Johann Wolfgang Goethe-Universität Frankfurt/UF (Germany)
15 Korea Advanced Institute of Science and Technology/KAIST (Korea)
16 Korea Atomic Energy Research Institute/KAERI (Korea)
17 Korea Electrotechnology Research Institute/KERI (Korea)
18 LPGP, CNRS-UMR8578, Université Paris XI/LPGP (France)
19 Laboratorie pour ltilisation des Lasers Intenses/LULI (France)
20 Lawrence Berkeley National Laboratory/LBNL (USA)
21 Lawrence Livermore National Laboratory/LLNL (USA)
22 Lebedev Physical Institute RAS/LPI (Russia)
23 Los Alamos National Laboratory/LANL (USA)
24 Ludwig-Maximilians-Universität München/LMU (Germany)
25 Max-Planck-Institut für Quantenoptik/MPQ (Germany)
26 Moscow Institute of Physics and Technology/MIPT (Russia)
27 Multi-charged Ion Spectra Data Center/MISDC of VNIIFTRI (Russia)
28 Nuclear Fusion Institute, Russian Research Center "Kurchatov Institute"/NFI (Russia)
29 Odessa National University/ONU (Ukraine)
30 PALS Research Center, IPP/PALS (Czech Republic)
31 Princeton University/PU (USA)
32 Queens University of Belfast/QUB (UK)
33 Ruhr Universität Bochum/RUB (Germany)
34 Sandia National Laboratories/SNL (USA)
35 Technische Universität Darmstadt/TUD (Germany)
36 Tokyo Institute of Technology/TIT (Japan)
37 Universidad Politecnica de Valencia/UPV (Spain)
38 Universidad de Castilla La Mancha/UCLM (Spain)
39 University of Milano/UM (Italy)
40 University of Nevada/UNR (USA)
41 Universität Erlangen/UE (Germany)
42 Universität Rostock/UR (Germany)
43 Université de Bordeaux/UB (France)
44 Université de Provence/UP (France)

FAIR: The HISPEC Collaboration

High resolution Spectroscopy
Spokesperson: Z. Podolyak, Surrey (United Kingdom)

Äystö, J.[49]; Ackermann, D.[8]; Al-Khalili, J.[57]; Algora, A.[14]; Angulo, C.[22]; Balabanski, D.[45]; Baur, G.[7]; Becker, F.[8]; Bednarczyk, P.[8]; Benlliure, J.[55]; Bentley, M.[21]; Borge, M. J.[5]; Borzov, I. N.[13]; Boston, A.[50]; Bucurescu, D.[11]; Cata-Danil, G.[32]; Cederwall, B.[33]; Chapman, R.[54]; Choudury, R. K.[15]; Crespo, R.[41]; Cullen, D.[51]; Dewald, A.[46]; Dombradi, Z.[1]; Dracoulis, G.[2]; Dudek, J.[16]; Erduran, N.[17]; Espino, J.[56]; Fahlander, C.[23]; Feldmeier, H.[8]; Fujita, Y.[30]; Gerl, J.[8]; Gloeckle, W.[34]; Gomez, J.[56]; Grebosz, J.[12]; Greenlees, P.[49]; Górska, M.[8]; Hass, M.[39]; Hencken, K.[42]; Huyse, M.[19]; Jenkins, D.[58]; Johnson, A.[35]; Jolie, J.[46]; Julin, R.[49]; Jungclaus, A.[40]; Korten, W.[4]; Kownacki, J.[60]; Krasznahorkay, A.[1]; Kreiner, A.[36]; Krücken, R.[38]; Labiche, M.[54]; Leino, M.[49]; Lemmon, R.[6]; Lenske, H.[18]; Mach, H.[59]; Maj, A.[12]; Mandal, S. K.[52]; Martel, I.[48]; Meczinski, W.[12]; Muralithar, S.[26]; Neyens, G.[19]; Nolan, P.[50]; Novikov, Y.[31]; Nyberg, J.[59]; Paul, E.[50]; Petrick, M.[18]; Petrovici, A.[27]; Podolyak, Z.[57]; Redondo, D.[37]; Regan, P.[57]; Reiter, P.[46]; Rubio, B.[10]; Rudolph, D.[23]; Saito, N.[8]; Saito, T.[8]; Scheidenberger, C.[8]; Scheit, H.[24]; Simpson, J.[3]; Sletten, G.[28]; Smith, A.[51]; Sohler, D.[1]; Speidel, K.-H.[44]; Spohr, K.[54]; Styczen, J.[29]; Tengblad, O.[5]; Vaagen, J.[43]; Van Duppen, P.[19]; Varley, B.[51]; Vitturi, A.[53]; Von Oertzen, W.[9]; Wadsworth, B.[58]; Walker, P.[57]; Woertche, H.[20]; Woods, P.[47]; Zamfir, V.[25]

1 ATOMKI Debrecen (Hungary)
2 Australian National University (Australia)
3 CCLRC Daresbury (United Kingdom)
4 CEA Saclay (France)
5 CSIC Madrid (Spain)
6 Daresbury Laboratory (United Kingdom)
7 FZ Jülich (Germany)
8 GSI Darmstadt (Germany)
9 HMI Berlin (Germany)
10 IFIC Valencia (Spain)
11 IFIN-HH Bucharest (Romania)
12 IFJ PAN Krakow (Poland)
13 IPPE (Belgium)
14 Inst. of Nuclear Res. of the Hungarian Academy of Sciences (Hungary)
15 Institute of Phyiscs Bhubaneswar (India)
16 IreS Strasbourg (France)
17 Istanbul University (Turkey)
18 Justus-Liebig University Giessen (Germany)
19 KU Leuven (Belgium)

20 KVI Groningen (The Netherlands)
21 Keele University (United Kingdom)
22 Louvain-la-Neuve (Belgium)
23 Lund University (Sweden)
24 Max-Planck-Institut für Kernphysik (Germany)
25 NIPNE Bucharest (Romania)
26 NSC (India)
27 National Institute for Physics and Nuclear Engineering (Romania)
28 Niels Bohr Institute (Denmark)
29 Niewodniczanski Institute of Nuclear Physics (Poland)
30 Osaka University (Japan)
31 PNPI Gatchina (Russia)
32 Politechnical University of Bucharest (Romania)
33 Royal Institute of Technology (Sweden)
34 Ruhr-University Bochum (Germany)
35 Stockholm University (Sweden)
36 TANDAR (Argentina)
37 TU Darmstadt (Germany)
38 TU Munich (Germany)
39 The Weizmann Institute of Science Rehovot (Israel)
40 UAM Madrid (Spain)
41 University Lisboa (Portugal)
42 University of Basel (Switzerland)
43 University of Bergen (Norway)
44 University of Bonn (Germany)
45 University of Camerino (Italy)
46 University of Cologne (Germany)
47 University of Edinburgh (United Kingdom)
48 University of Huelva (Spain)
49 University of Jyvaskyla (Finland)
50 University of Liverpool (United Kingdom)
51 University of Manchester (United Kingdom)
52 University of New Delhi (India)
53 University of Padova (Italy)
54 University of Paisley (United Kingdom)
55 University of Santiago de Compostela (Spain)
56 University of Sevilla (Spain)
57 University of Surrey (United Kingdom)
58 University of York (United Kingdom)
59 Uppsala University (Sweden)

FAIR: The ILIMA Collaboration

Isomeric Beams, Lifetimes and Masses
Spokesperson: Y. Novikov, Gatchina (Russia)

Audi, G.[2]; Badura, E.[3]; Beckert, K.[3]; Beller, P.[3]; Blaum, K.[5]; Bosch, F.[3]; Boutin, D.[3]; Bürvenich, T. J.[8]; Chen, L.[3]; Cullen, D.[14]; Di, Z.[6]; Dickel, T.[6]; Dolinskii, A.[3]; Faestermann, T.[13]; Fettouhi, A.[6]; Franczak, B.[3]; Franzke, B.[3]; Geissel, H.[3]; Hausmann, M.[7]; Herfurth, F.[3]; Hoffmann, J.[3]; Kienle, P.[13]; Kluge, H.-J.[3]; Knöbel, R.[6]; Kozhuharov, C.[3]; Kratz, K.-L.[5]; Kurz, N.[3]; Lalazissis, G.[1]; Litvinov, S. A.[3]; Litvinov, Y.[3]; Lunney, D.[2]; Madland, D. G.[7]; Maier, L.[13]; Mao, R.[4]; Matos, M.[9]; Moeller, P.[7]; Münzenberg, G.[3]; Nesmiyan, I.[3]; Nickel, F.[3]; Nolden, F.[3]; Novikov, Y.[10]; Ott, W.[3]; Ozawa, A.[11]; Patyk, Z.[17]; Petrick, M.[6]; Pfeiffer, B.[5]; Plaß, W.[6]; Podolyak, Z.[15]; Quint, W.[3]; Ring, P.[13]; Schatz, H.[9]; Scheidenberger, C.[3]; Seliverstov, D.[10]; Steck, M.[3]; Stoehlker, T.[3]; Sun, Z.[4]; Sümmerer, K.[3]; Takahashi, K.[16]; Typel, S.[3]; Vieira, D. J.[7]; Vorobjev, G.[10]; Walker, P.[15]; Weick, H.[3]; Winkler, M.[3]; Xiao, G.[4]; Yamaguchi, T.[12]

1 Aristotle University of Thessaloniki (Greece)
2 CSNSM Orsay (France)
3 GSI Darmstadt (Germany)
4 Institute of Modern Physics Lanzhou (China)
5 Johannes Gutenberg University of Mainz (Germany)
6 Justus-Liebig University Giessen (Germany)
7 LANL Los Alamos (USA)
8 MPI für Kernphysik (Germany)
9 NSCL/MSU (USA)
10 PNPI Gatchina (Russia)
11 RIKEN (Japan)
12 Saitama University (Japan)
13 TU Munich (Germany)
14 University of Manchester (United Kingdom)
15 University of Surrey (United Kingdom)
16 Université Libre de Bruxelles (Belgium)

FAIR: The LASPEC Collaboration

Laser Spectroscopy of short-lived isotopes at the FAIR Low Energy Beamline
Spokesperson: P. Campbell (United Kingdom)

Äystö, J.[2]; Billowes, J.[10]; Blaum, K.[5]; Bushaw, B.[12]; Campbell, P.[10]; Crespo Lopez-Urrutia, J.[8]; Dax, A.[9]; Habs, D.[7]; Heinz, S.[7]; Huber, G.[5]; Jokinen, A.[2]; Kessler, T.[2]; Kuehl, T.[6]; Le Blanc, F.[3]; Lunney, D.[3]; Moore, I.[2]; Neyens, G.[1]; Nieminen, A.[2]; Nörtershäuser, W.[6]; Scheidenberger, C.[6]; Schneider, D.[11]; Seliverstov, M.[5]; Swetz, M.[3]; Szerypo, J.[7]; Thirolf, P.[7]; Tomaselli, M.[6]; Ullrich, J.[8]; Wendt, K.[5]; Zimmermann, C.[4]

1 Katholieke Universiteit Leuven (Belgium)
2 University of Jyväskylä (Finland)
3 CSNSM Orsay (France)
4 Eberhard-Karls-University of Tübingen (Germany)
5 Johannes Gutenberg University of Mainz (Germany)
6 GSI Darmstadt (Germany)

7 Ludwig-Maximilians University of Munich (Germany)
8 MPI für Kernphysik (Germany)
9 CERN (Switzerland)
10 University of Manchester (United Kingdom)
11 Livermore National Laboratory (USA)

FAIR: The LEB Collaboration

Low Energy Branch
<http://www.gsi.de >
Spokesperson: C. Scheidenberger, Darmstadt (Germany)

Äystö, J.[74]; Ackermann, D.[14]; Al-Khalili, J.[84]; Algora, A.[21]; Angulo, C.[34]; Audi, G.[8]; Bachelet, C.[9]; Balabanski, D.[67]; Batist, L.[48]; Baur, G.[11]; Beck, D.[14]; Becker, F.[14]; Bednarczyk, P.[14]; Bender, M.[62]; Benlliure, J.[81]; Bentley, M.[30]; Billowes, J.[77]; Blank, B.[5]; Blaum, K.[26]; Bloch, I.[26]; Block, M.[14]; Bollen, G.[38]; Borge, M. J.[7]; Borzov, I. N.[20]; Boston, A.[76]; Bucurescu, D.[17]; Bushaw, B.[49]; Campbell, P.[77]; Cata-Danil, G.[50]; Cederwall, B.[53]; Chapman, R.[80]; Colonna, N.[19]; Crespo Lopez-Urrutia, J.[37]; Crespo, R.[63]; Cullen, D.[77]; Dax, A.[6]; Dewald, A.[68]; Djekic, S.[26]; Dombradi, Z.[1]; Dracoulis, G.[2]; Dudek, J.[23]; Erduran, N.[24]; Espino, J.[82]; Faestermann, T.[58]; Fahlander, C.[36]; Feldmeier, H.[14]; Ferrer, R.[76]; Fritioff, T.[83]; Fujita, Y.[47]; Geissel, H.[14]; George, S.[6]; Gerl, J.[14]; Gloeckle, W.[54]; Gomez, J.[82]; Grebosz, J.[18]; Greenlees, P.[75]; Gunsing, F.[4]; Guénaut, C.[8]; Górska, M.[14]; Habs, D.[35]; Harissopulos, S.[22]; Hass, M.[59]; Heenen, P. H.[61]; Heil, M.[13]; Heinz, S.[35]; Hencken, K.[64]; Herfurth, F.[14]; Herlert, A.[72]; Huyse, M.[28]; Iordachescu, A.[43]; Jastrzebski, J.[90]; Jenkins, D.[87]; Johnson, A.[55]; Jokinen, A.[74]; Jolie, J.[68]; Julin, R.[25]; Jungclaus, A.[60]; Junghans, A.[12]; Kellerbauer, A.[6]; Kester, O.[35]; Kettunen, H.[74]; Koehler, P.[46]; Kolhinen, V.[77]; Kopecky, S.[74]; Korten, W.[4]; Kownacki, J.[90]; Krasznahorkay, A.[1]; Kratz, K.-L.[26]; Kreim, S.[76]; Kreiner, A.[56]; Krücken, R.[58]; Kuehl, T.[14]; Kurcewicz, W.[90]; Labiche, M.[80]; Le Blanc, F.[8]; Leino, M.[75]; Lemmon, R.[10]; Lenske, H.[27]; Litvinov, Y.[14]; Lunney, D.[8]; Mach, H.[88]; Maj, A.[18]; Mandal, S.[69]; Martel, I.[73]; Marx, G. H.[14]; Matos, M.[42]; Meczinski, W.[18]; Mengoni, A.[6]; Moore, I.[74]; Muralithar, S.[41]; Nagai, Y.[51]; Nagy, S.[83]; Neyens, G.[28]; Nieminen, A.[74]; Nolan, P.[76]; Novikov, Y.[48]; Nyberg, J.[88]; Nörtershäuser, W.[14]; Page, R. D.[33]; Paul, E.[76]; Penttillae, H.[74]; Petrick, M.[27]; Petrovici, A.[43]; Pfutzner, M.[90]; Plaß, W.[27]; Podolyak, Z.[84]; Quint, W.[14]; Ray, A.[89]; Redondo, D.[57]; Regan, P.[84]; Reifarth, R.[31]; Reinhard, P.-G.[71]; Reiter, P.[68]; Rubio, B.[16]; Rudolph, D.[36]; Saito, N.[14]; Saito, T.[14]; Scheidenberger, C.[14]; Scheit, H.[39]; Schneider, D.[32]; Scholey, C.[74]; Schuch, R.[83]; Schwarz, S.[38]; Schweikhard, L.[72]; Sewtz, M.[9]; Simpson, J.[3]; Sletten, G.[44]; Smith, A.[77]; Sohler, D.[1]; Speidel, K.-H.[66]; Spohr, K.[80]; Stahl, S.[76]; Styczen, J.[45]; Swetz, M.[8]; Szerypo, J.[35]; Sümmerer, K.[14]; Tain, J. L.[16]; Tengblad, O.[7]; Thirolf, P.[35]; Tomaselli, M.[14]; Trzcinska, A.[90]; Ullrich, J.[37]; Uusitalo, J.[74]; Vaagen, J.[65]; Van Duppen, P.[28]; Varley, B.[77]; Verdu, J.[76]; Vitturi, A.[79]; Von Oertzen, W.[15]; Wada, M.[52]; Wadsworth, B.[87]; Walker, P.[84]; Weber, C.[26]; Widmann, E.[85]; Wiescher, M.[78]; Winkler, M.[14]; Woertche, H.[29]; Woods, P.[70]; Yamazaki, Y.[85]; Yazidjian, C.[6]; Zamfir, V.[40]; Zimmermann, C.[86]

1 ATOMKI Debrecen (Hungary)
2 Australian National University (Australia)
3 CCLRC Daresbury (United Kingdom)
4 CEA Saclay (France)
5 CEN Bordeaux-Gradignan (France)
6 CERN (Switzerland)
7 CSIC Madrid (Spain)
8 CSNSM Orsay (France)
9 CSNSM-IN2P3-CNRS (France)
10 Daresbury Laboratory (United Kingdom)
11 FZ Jülich (Germany)
12 FZ Rossendorf (Germany)
13 FZK (Germany)
14 GSI Darmstadt (Germany)
15 HMI Berlin (Germany)
16 IFIC Valencia (Spain)
17 IFIN-HH Bucharest (Romania)
18 IFJ PAN Krakow (Poland)
19 INFN Legnaro (Italy)
20 IPPE (Belgium)
21 Inst. of Nuclear Res. of the Hungarian Academy of Sciences (Hungary)
22 Institute of Nuclear Physics, NCSR 'Demokritos', Athens (Greece)
23 IreS Strasbourg (France)
24 Istanbul University (Turkey)
25 JYFL Jyvaskyla (Finland)
26 Johannes Gutenberg University of Mainz (Germany)
27 Justus-Liebig University Giessen (Germany)
28 KU Leuven (Belgium)
29 KVI Groningen (The Netherlands)
30 Keele University (United Kingdom)
31 LANL Los Alamos (USA)
32 Livermore National Laboratory (USA)
33 Liverpool (United Kingdom)
34 Louvain-la-Neuve (Belgium)
35 Ludwig-Maximilians University of Munich (Germany)
36 Lund University (Sweden)
37 MPI für Kernphysik (Germany)
38 MSU (USA)
39 Max-Planck-Institut für Kernphysik (Germany)
40 NIPNE Bucharest (Romania)
41 NSC (India)
42 NSCL/MSU (USA)
43 National Institute for Physics and Nuclear Engineering (Romania)
44 Niels Bohr Institute (Denmark)
45 Niewodniczanski Institute of Nuclear Physics (Poland)
46 ORNL Oak Ridge (USA)
47 Osaka University (Japan)
48 PNPI Gatchina (Russia)
49 Pacific Northwestr Laboratory (USA)
50 Politechnical University of Bucharest (Romania)
51 RCNP Osaka (Japan)
52 RIKEN (Japan)
53 Royal Institute of Technology (Sweden)

54 Ruhr-University Bochum (Germany)
55 Stockholm University (Sweden)
56 TANDAR (Argentina)
57 TU Darmstadt (Germany)
58 TU Munich (Germany)
59 The Weizmann Institute of Science Rehovot (Israel)
60 UAM Madrid (Spain)
61 UL Bruxelles (Belgium)
62 Universite Libre de Bruxelles (Belgium)
63 University Lisboa (Portugal)
64 University of Basel (Switzerland)
65 University of Bergen (Norway)
66 University of Bonn (Germany)
67 University of Camerino (Italy)
68 University of Cologne (Germany)
69 University of Delhi (India)
70 University of Edinburgh (United Kingdom)
71 University of Erlangen (Germany)
72 University of Greifswald (Germany)
73 University of Huelva (Spain)
74 University of Jyvaskyla (Finland)
75 University of Jyväskylä (Finland)
76 University of Liverpool (United Kingdom)
77 University of Manchester (United Kingdom)
78 University of Notre Dame (USA)
79 University of Padova (Italy)
80 University of Paisley (United Kingdom)
81 University of Santiago de Compostela (Spain)
82 University of Sevilla (Spain)
83 University of Stockholm (Sweden)
84 University of Surrey (United Kingdom)
85 University of Tokyo (Japan)
86 University of Tübingen (Germany)
87 University of York (United Kingdom)
88 Uppsala University (Sweden)
89 VECC Kolkata (India)

FAIR: The MATS Collaboration

Precision Measurement of vry short-lived nuclei using an Advanced Trapping System for highly-charged ions
Spokesperson: K. Blaum, Mainz (Germany)

Äystö, J.[17]; Audi, G.[2]; Bachelet, C.[3]; Beck, D.[4]; Bender, M.[14]; Blaum, K.[5]; Bloch, I.[5]; Block, M.[4]; Bollen, G.[10]; Crespo Lopez-Urrutia, J.[9]; Djekic, S.[5]; Ferrer, R.[17]; Fritioff, T.[18]; Geissel, H.[4]; George, S.[1]; Guénaut, C.[2]; Habs, D.[8]; Heenen, P. H.[13]; Heinz, S.[8]; Herfurth, F.[4]; Herlert, A.[16]; Jokinen, A.[17]; Kellerbauer, A.[1]; Kester, O.[8]; Kolhinen, V.[17]; Kreim, S.[17]; Litvinov, Y.[4]; Lunney, D.[2]; Marx, G. H.[4]; Matos, M.[11]; Moore, I.[17]; Nagy, S.[18]; Nieminen, A.[17]; Novikov, Y.[12]; Nörtershäuser, W.[4]; Plaß, W.[6]; Ray, A.[19]; Reinhard, P.-G.[15]; Scheidenberger, C.[4]; Schneider, D.[7]; Schuch, R.[18]; Schwarz, S.[10]; Schweikhard, L.[16]; Sewtz, M.[3]; Stahl, S.[17]; Szerypo, J.[8]; Thirolf, P.[8]; Ullrich, J.[9]; Verdu, J.[17]; Weber, C.[5]; Winkler, M.[4]; Yazidjian, C.[1]

1 CERN (Switzerland)
2 CSNSM Orsay (France)
3 CSNSM-IN2P3-CNRS (France)
4 GSI Darmstadt (Germany)
5 Johannes Gutenberg University of Mainz (Germany)
6 Justus-Liebig University Giessen (Germany)
7 Livermore National Laboratory (USA)
8 Ludwig-Maximilians University of Munich (Germany)
9 MPI für Kernphysik (Germany)
10 MSU (USA)
11 NSCL/MSU (USA)
12 PNPI Gatchina (Russia)
13 UL Bruxelles (Belgium)
14 Universite Libre de Bruxelles (Belgium)
15 University of Erlangen (Germany)
16 University of Greifswald (Germany)
17 University of Jyvaskyla (Finland)
18 University of Stockholm (Sweden)

FAIR: The NCap Collaboration

Neutron Capture Measurements
<http://www.gsi.de >
Spokesperson: M. Heil, Karlsruhe (Germany)

Audouin, L.[7]; Cano-Ott, D.[4]; Colonna, N.[2]; Gonzalez-Romero, E. M.[4]; Gunsing, F.[13]; Heil, M.[7]; Junghans, A.[6]; Koehler, P.[11]; Käppeler, F.[7]; Mastinu, P. F.[8]; Mengoni, A.[3]; Nagai, Y.[12]; Plag, R.[7]; Reifarth, R.[9]; Scheidenberger, C.[5]; Sümmerer, K.[5]; Tagliente, G.[1]; Tain, J. L.[14]; Walter, S.[7]; Wiescher, M.[10]

1 INFN Bari (Italy)
2 INFN Bologna (Itlay)
3 ENEA Bologna (Itlay)
4 CIEMAT Madrid (Spain)
5 GSI Darmstadt (Germany)
6 Forschungszentrum Rossendorf (Germany)
7 FZK Karlsruhe (Germany)
8 INFN Legnaro (Italy)
9 LANL Los Alamos (USA)
10 University of Notre Dame (USA)
11 ORNL Oak Ridge (USA)
12 RCNP Osaka (Japan)
13 CEA Saclay (France)

FAIR: The PANDA Collaboration

The Proton ANtiproton DArmstadt Experiment
<http://www.gsi.de/zukunftsprojekt/experimente/hesr-panda/index_e.html>
Spokesperson: U. Wiedner, Uppsala (Sweden)

Abazov, V. M.[10]; Achenbach, P.[23]; Agnello, M.[37]; Alberto, P.[24]; Alexeev, G.[10]; Alexeev, M.[36]; Aliotta, M.[11]; Amoroso, A.[36]; Annand, J.[19]; Ardashev, E.[31]; Arefiev, A.[10]; Arestov, Y.[31]; Ayzenshtat, G.[31]; Baldin, E.[28]; Balestra, F.[36]; Ballantini, R.[17]; Barabanov, M. Y.[10]; Bargholtz, C.[34]; Bassini, R.[24]; Batyunya, B. V.[10]; Belostotski, S.[32]; Bendiscioli, G.[30]; Bertini, R.[36]; Bettoni, D.[14]; Birsa, R.[38]; Boca, G.[30]; Bogoslovski, D.[10]; Boiano, C.[24]; Bokova, T. Y.[10]; Borisov, V. V.[10]; Borissov, A.[19]; Botta, E.[37]; Bradamante, F.[38]; Branford, D.[11]; Bressani, T.[37]; Brinkmann, K. -T.[9]; Britvich, G.[31]; Budilov, V. A.[10]; Bugaenko, Y. V.[10]; Bussa, M. P.[36]; Busso, L.[37]; Calén, H.[40]; Calabrese, R.[14]; Calvo, D.[37]; Cappellaro, F.[41]; Cargnelli, M.[43]; Cederwall, B.[33]; Chen, R.[22]; Chuiko, B.[31]; Clement, H.[39]; Colantoni, M. L.[35]; Döring, W.[18]; Dörner, R.[15]; Düren, M.[18]; Dalla, S.[38]; Dalpiaz, P.[14]; De Napoli, M.[6]; De, P.[37]; Denisov, O.[36]; Destefanis, M. G.[18]; Diaz, J. [42]; Dodokhov, V. Kh.[10]; Dormenev, V. I.[25]; Doroshkevitch, E.[39]; Drexler, P.[18]; Drobychev, G. Y.[25]; Drochner, M.[20]; Duan, L.[22]; Efremov, A. A.[10]; Ehrhardt, K.[39]; Ekström, C.[40]; Eyrich, W.[12]; Föhl, K.[11]; Fava, L.[35]; Fedorov, A. A.[25]; Fedorov, O. I.[10]; Feliciello, A.[37]; Ferrero, A.[36]; Ferrero, L.[36]; Ferro, F.[37]; Feshchenko, A. A.[10]; Filippi, A.[37]; Fontana, A.[30]; Fröhlich, I.[18]; Fransson, K.[40]; Freiesleben, H.[9]; Frekers, D.[27]; Frolov, V.[36]; Fuhrmann, H.[43]; Götzen, K.[3]; Galoyan, A. S.[10]; Garfagnini, R.[36]; Gast, W.[20]; Gavrilov, G.[32]; Genova, P.[30]; Gianotti, P.[16]; Gillitzer, A.[20]; Giorgi, M.[38]; Golischewski, A.[3]; Golovnya, S.[31]; Gonser, P. [39]; Gorokhov, S.[31]; Grasso, A.[36]; Grisenti, R.[15]; Grzonka, D.[20]; Guaraldo, C.[16]; Guidal, M.[29]; Guzik, Z.[44]; Höistad, B.[41]; Hartmann, O. N.[16]; Hawranek, P.[7]; Hejny, V.[20]; Held, T.[3]; Hennino, T.[29]; Hinterberger, F. [4]; Holeczek, J.[21]; Hu, Z. Li, W.[22]; Iazzi, F.[37]; Iliescu, M.[16]; Iori, I.[24]; Ireland, D.[19]; Ivanov, G.[10]; Jäkel, R. [9]; Jafarov, E.[10]; Johansson, T.[41]; Johnson, A. [33]; Kühn, W.[18]; Kaesz, M. [15]; Kaiser, R.[19]; Kamys, B.[7]; Kaplin, V. I.[10]; Karmokov, A.[10]; Kellie, J.[19]; Kemmerling, G.[20]; Ketzer, B.[26]; Kholodenko, A.[31]; Khoukaz, A.[27]; Kienle, P.[43]; Kirschner, D. G.[18]; Kisiel, J.[21]; Kisielinski, M.[44]; Kistryn, St.[7]; Kleines, H.[20]; Koch, H.[3]; Konorov, I.[26]; Kopf, B.[3]; Korneev, A. E.[25]; Korzhik, M. V.[25]; Koshurnikov, E. K.[10]; Kotulla, M.[1]; Kozlowski, T.[44]; Krusche, B.[1]; Kudaev, V. C.[10]; Kupsc, A.[40]; Kłos, B.[21]; Lühning, J.[8]; Lavezzi, L.[30]; Lehmann, A. [12]; Lehmann, I.[41]; Lewandowski, B.[3]; Lindberg, K.[34]; Lishin, V.[31]; Livingston, K.[19]; Lobanov, V. I.[10]; Lopatik, A. R.[25]; Lucherini, V.[16]; Lundborg, A.[41]; Luppi, E.[14]; Lynen, U.[8]; Mac, M.[29]; Macri, M.[17]; Maggiora, A.[36]; Maggiora, M.[36]; Magiera, A.[7]; Makarov, A. F.[10]; Makonyi, K.[18]; Malinina, L. V.[10]; Malyshev, V. L.[10]; Malyshev, V.[28]; Mann, A.[26]; Marcello, S.[37]; Marciniewski, P. [40]; Martin, A.[38]; Marton, J.[43]; Maslennikov, A.[28]; Mazza, G.[37]; McGeorge, C.[19]; Melnychuk, D.[44]; Metag, V.[18]; Mikhailov, K. V.[10]; Miklukho, O.[32]; Missevitch, O. V. [25]; Montagna, P.[30]; Morosov, B.[10]; Morra, O.[37]; Moskal, P.[7]; Mustafaev, G. A.[10]; Nakhushev, A. M.[10]; Nanova, M.[18]; Naryshkin, Y.[32]; Neubert, S.[26]; Nomokonov, P. V.[10]; Nordhage, Ö.[41]; Novotny, R.[18]; Nowak, H.[3]; Nyberg, J.[41]; Oelert, W.[20]; Oleks, I. A.[10]; Ong, S.[29]; Orth, H.[8]; Ottone, F.[18]; Pace, E.[16]; Panzarasa, A.[30]; Panzieri, D. [35]; Parakhin, V.[31]; Parodi, R.[17]; Paul, S.[26]; Peleganchyk, S.[28]; Peters, K.[8]; Petrascu, C.[16]; Pettersson, H.[41]; Pikalov, V.[31]; Piragino, G.[36]; Piskor-Ignatowicz, B.[7]; Piskor-Ignatowicz, C.[7]; Pismennaya, V.[10]; Pocheptsov, T. A.[10]; Pochodzalla, J.[23]; Polanski, A.[10]; Pontecorvo, G.[10]; Pontecorvo, G.[36]; Pospelov, G.[28]; Pouthas, J.[29]; Povtoreyko, A.[10]; Pozzo, A. [17]; Prasuhn, D.[20]; Protopopescu, D.[19]; Raciti, G.[6]; Ramstein, B.[29]; Rao, Y.-N.[41]; Rapisarda, E. [6]; Riboldi, S. [24]; Ritman, J.[20]; Rivetti, A.[37]; Rogov, Y. N.[10]; Rosier, P.[29]; Rosner, G. [19]; Rotondi, A.[30]; Rudy, Z.[7]; Rufanov, I. A.[10]; Ryabtsun, S.[10]; Sadygov, Z. Ya.[10]; Saitoh, T. R.[8]; Salabura, P.[7]; Salmin, R. A.[10]; Salvini, P. [30]; Salz, C.[18]; Samartsev, A. G.[10]; Sanchez-Lorente, A. [23]; Sapozhnikov, M. G.[10]; Sarantsev, A.[32]; Savriè, M. [14]; Schönning, K.[41]; Schadmand, S.[20]; Schiavon, P.[38]; Schmücker, H.[3]; Schmitt, L.[26]; Schneider, J.[18]; Schwarz, C.[8]; Seitz, B.[18]; Serbanut, G. -C.[18]; Sereda, T.[10]; Seth, K. [13]; Sfienti, C. [8]; Shabratova, G. S.[10]; Shelikhov, V.[31]; Shishkin, A. A.[10]; Shumeiko, N.[31]; Sibirtsev, A.[20]; Sirghi, D.[16]; Sirghi, F. [16]; Skachkov, N. B.[10]; Skachkova, A. N.[10]; Slowinski, B. [45]; Smyrski, J.[7]; Sokolov, A.[20]; Solin, A.[31]; Steinke, M.[3]; Stenzel, H.[18]; Stockmanns, T.[20]; Ströher, H.[20]; Strokovsky, E. A.[10]; Sukharev, A.[28]; Sun, Z.[22]; Täschner, A.[27]; Tegnér, P. E.[34]; Teshev, R. S.[10]; Tessarotto, F. [38]; Thöring, U. Thiel, M. [18]; Thörngren Engblom, P.[41]; Tikhomirov, V.[10]; Tikhonov, Y. [28]; Tokmenin, V. V.[10]; Tolbanov, O.[31]; Tosello, F.[36]; Tyazhev, A.[31]; Ucar, A.[20]; Ustenko, E. P.[10]; Uzhinsky, V. V.[10]; Van, J.[29]; Vikhrov, V. [32]; Vlasov, N. V.[10]; Vlasov, P.[20]; Vodopianov, A. S.[10]; Vorobiev, A. [31]; Wüstner, P. [20]; Watts, D.[11]; Weitzel, Q. [26]; Wessels, J. [27]; Wheadon, R. [37]; Widmann, E.[43]; Wieczorek, P.[3]; Wiedner, U.[41]; Wilms, A.[3]; Wintz, P.[20]; Wojciechowski, M. [7]; Wojtkowska, J.[44]; Woods, P. [11]; Xiao, G.[22]; Xiao, Z.[22]; Xie, J. J.[2]; Xu, H. [22]; Xu, H.[22]; Zaporozhets, S. A.[10]; Zartova, I. [34]; Zehr, F. [1]; Zenoni, A. [5]; Zerguerras, T. [29]; Zhong, J. [3]; Zhuravlev, N. I.[10]; Zinchenko, A. I. [10]; Zlomanczuk, J. [41]; Zmeskal, J. [43]; Zosi, G. [36]; Zou, B. S. [2]; Zwieglinski, B. [44]

1 Universität Basel (Switzerland)
2 Institute of High Energy Physics, Chinese Academy of Sciences, Beijing (China)
3 Universität Bochum, I. Institut für Experimentalphysik (Germany)
4 Helmholtz-Institut für Strahlen- und Kernphysik, Bonn (Germany)
5 Università di Brescia (Itlay)
6 Dipartimento di Fisica e Astronomia dell'Università di Catania and INFN, Sezione di Catania (Itlay)
7 Instytut Fizyki, Uniwersytet Jagiellonski, Cracow (Poland)
8 GSI, Darmstadt (Germany)
9 Technische Universität Dresden (Germany)
10 Veksler-Baldin Laboratory of High Energies (VBLHE), Joint Institute for Nuclear Research, Laboratory of Particle Physics (LPP), Laboratory of Information Technologies (LIT), Laboratory of Nuclear Problems (LNP), Dubna, Kabardian-Balkarian State University and Institute of Applied Mathematics and Automation, Nal'chik (Russia)
11 University of Edinburgh (United Kingdom)
12 Friedrich Alexander Universität Erlangen-Nürnberg (Germany)
13 Northwestern University, Evanston (U.S.A.)
14 Università di Ferrara and INFN, Sezione di Ferrara (Itlay)
15 Johann Wolfgang Goethe-Universität Frankfurt (Germany)
16 INFN-Laboratori Nazionali di Frascati (Itlay)

17 INFN, Sezione di Genova (Itlay)
18 Justus Liebig-Universität Gießen, II. Physikalisches Institut (Germany)
19 University of Glasgow (United Kingdom)
20 Institut für Kernphysik, Zentralinstitut für Elektronik, Forschungszentrum Jülich (Germany)
21 Uniwersytet Slaski, Katowice (Poland)
22 Institute of Modern Physics, the Chinese Academy of Science, Lanzhou (P.R. China)
23 Institut für Kernphysik, Johannes Gutenberg-Universität Mainz (Germany)
24 Politecnico di Milano, Physics Department, Università di Milano and INFN, Sezione di Milano (Itlay)
25 Research Institute for Nuclear Problems, Belarus State University, Minsk (Belarus)
26 Technische Universität München (Germany)
27 Westfälische Wilhelms-Universität Münster (Germany)
28 Budker Institute of Nuclear Physics (BINP), Novosibirsk (Russia)
29 Institut de Physique Nucléaire, Orsay (France)
30 Dipartimento di Fisica Nucleare e Teorica, Università di Pavia, INFN, Sezione di Pavia (Itlay)
31 Institute for High Energy Physics (IHEP), Protvino, Tomsk State University TSU (Russia), and National Center of Particle and High Energy Physics NCPHEP, Minsk (Belorussia)
32 Petersburg Nuclear Physics Institute of Academy of Science (PNPI), Gatchina, St. Petersburg (Russia)
33 Kungliga Tekniska Högskolan (KTH), Stockholm (Sweden)
34 Stockholms Universitet (Sweden)
35 Università del Piemonte Orientale Alessandria, Torino and INFN, Sezione di Torino (Itlay)
36 Dipartimento di Fisica Generale 'A. Avogadro', Università di Torino and INFN, Sezione di Torino (Itlay)
37 Dipartimento di Fisica Generale Università di Torino, Dipartimento di Fisica Sperimentale, Università di Torino, INFN, Sezione di Torino, IFSI, Sezione di Torino and Politecnico di Torino (Itlay)
38 INFN, Sezione di Trieste and Università di Trieste (Itlay)
39 Physikalisches Institut, Universität Tübingen (Germany)
40 The Svedberg Laboratory, Uppsala (Sweden)
41 Institutionen för Strålningsvetenskap, Uppsala Universitet (Sweden)
42 Universitat de Valencia, Dpto. de Física Atómica, Molecular y Nuclear (Spain)
43 Stefan Meyer Institut für Subatomare Physik, Österreichische Akademie der Wissenschaften, Vienna (Austria)
44 Soltan Institute for Nuclear Studies, Warsaw (Poland)

FAIR: The PAX Collaboration

The Condensed Baryonic Matter experiment
<http://www.fz-juelich.de/ikp/pax/home.html>
Spokespersons: P. Lenisa Hamburg (Germany) F. Rathmann Jülich (Germany)

Akopov, N.[29]; Anselmino, M.[8]; Avagyan, R.[29]; Avetisyan, A.[29]; Bagulya, A.[20]; Barone, V.[26]; Barsov, S.[22]; Baru, V.[14]; Belikov, N.[13]; Belostotski, S.[22]; Bianchi, N.[18]; Bisplinghoff, J.[10]; Boglione, M.[8]; Buttimore, N.[3]; Capiluppi, M.[18]; Chiladze, B.[17]; Chiladze, D.[11]; Chujko, B.[13]; Ciullo, G.[18]; Contalbrigo, M.[18]; Coriano, C.[26]; De Sanctis, E.[18]; Devitsin, E.[20]; Di Nezza, P.[18]; Drago, A.[18]; Dymov, S.[9]; Engels, R.[11]; Eversheim, D.[10]; Eyrich, W.[24]; Felden, O.[24]; Ferretti-Dalpiaz, P.[18]; Gasparyan, A.[14]; Gebel, R.[11]; Goeke, K.[12]; Grebenyuk, O.[22]; Grigoriev, K.[22]; Grishina, V.[14]; Haidenbauer, J.[11]; Hakopov, Z.[29]; Hanhart, C.[11]; Hasch, D.[18]; Hinterberger, F.[10]; Ivanov, O.[19]; Izotov, A.[22]; Jgoun, A.[22]; Jiang, Y.[4]; Kacharava, A.[23]; Kadagidze, N.[9]; Keshelashvili, I.[11]; Kharlov, Y.[13]; Komarov, V.[9]; Kondratyuk, L.[14]; Korotkov, V.[13]; Kozlov, V.[20]; Krauss, B.[23]; Kravtsov, P.[22]; Krewald, S.[11]; Krivokhizhin, V.[19]; Kudryavtsev, A.[14]; Kulikov, A.[9]; Kurbatov, V.[9]; Kurdadze, L.[21]; Lehmann, A.[24]; Lehrach, A.[11]; Lenisa, P.[18]; Leontiev, V.[9]; Liuti, S.[5]; Lomidze, N.[17]; Lorentz, B.[11]; Lu, H.[4]; Ma, B.[25]; Ma, W.[4]; Macharashvili, G.[9]; Manaenkov, S.[22]; Martin, S.[11]; Marukyan, H.[29]; Medvedev, V.[13]; Meissner, U.[11]; Merzliakov, S.[9]; Meshcheryakov, G.[29]; Metz, A.[12]; Mikirtytchiants, M.[22]; Mikirtytchiants, S.[22]; Miklukho, O.[22]; Montag, C.[2]; Muccifora, V.[18]; Mysnik, A.[13]; Nagaytsev, A.[28]; Naryshkin, Y.[22]; Nikolaev, N.[11]; Nioradze, M.[17]; Oganessyan, K.[18]; Peshekhonov, V.[19]; Prasuhn, D.[11]; Prokudin, A.[8]; Prudkoglyad, A.[13]; Rathmann, F.[11]; Reggiani, D.[23]; Rith, K.[23]; Rohdjess, H.[10]; Rossi, P.[18]; Ryckbosch, D.[7]; Sakhelashvili, T.[17]; Savin, I.[19]; Schleichert, R.[11]; Schweitzer, P.[12]; Scobel, W.[15]; Seidel, R.[23]; Semenov, P.[13]; Serdjuk, V.[9]; Seyfarth, H.[11]; Shaikhatdenov, B.[19]; Shen, J.[4]; Shevchenko, O.[19]; Sibirtsev, A.[11]; Stancari, M.[18]; Statera, M.[18]; Steffens, E.[23]; Stinzing, F.[23]; Stroeher, H.[11]; Tabidize, M.[17]; Tait, P.[23]; Taroian, S.[29]; Terkulov, A.[20]; Teryaev, O.[1]; Thorngren-Engblom, P.[6]; Trekov, I.[17]; Troshin, S.[13]; Trusov, S.[9]; Ukhanov, M.[13]; Urban, J.[16]; Uzikov, Y.[9]; Vassiliev, A.[22]; Volkov, A.[9]; Wise, T.[27]; Yarygin, G.[19]; Yaschenko, S.[23]; Ye, Y.[4]; Yin, Z.[4]; Zavertiaev, M.[20]; Zhang, Y.[4]; Zhdanov, A.[22]; Zhuravlev, N.[9]

1 Bogoliubov Laboratory of Theoritical Physics, Joint Institutefor Nuclear Research (Russia)Efremov, A.
2 Collider-Accelerator Department, Brookhaven National Laboratory (USA)
3 Department of Mathematics, University of Dublin (Ireland)
4 Department of Modern Physics, USTC (China)
5 Department of Physics, University of Virginia (USA)
6 Department of Radiation Sciences, Nuclear Physics Division,Uppsala University (Sweden)
7 Department of Subatomic and Radiation Physics, University ofGent (Belgium)
8 Dipartimento di Fisica Teorica, Universita di Torino and INFN (Italy)
9 Dzhelepov Laboratory of Nuclear Problems, Joint Institute forNuclear Research (Russia)
10 HISKP, Universität Bonn (Germany)
11 Institut für Kernphysik, Forschungszentrum Jülich (Germany)
12 Institut für Theoretische Physik II, Ruhr Universität Bochum (Germany)
13 Institute for High Energy Physics (Russia)
14 Institute for Theoretical and Experimental Physics (Russia)

15 Institute für Experimentalphysik, Universität Hamburg (Germany)
16 Institute of Experimental Physics, Slovak Academy of Sciences (Slovak Republic)
17 Institute of High Energy Physics and Informatization, TbilisiState University (Georgia)
18 Istituto Nazionale di Fisica Nucleare (Italy)
19 Laboratory of Particle Physics, Joint Institute for Nuclear-Research (Russia)
20 Lebedev Physical Institute (Russia)
21 Nuclear Physics Department, Tbilisi State University (Georgia)
22 Petersburg Nuclear Physics Institute (Russia)
23 Physikalisches Institut II, Universität Erlangen-Nürnberg (Germany)
24 Physikalisches Institut IV, Universität Erlangen-Nürnberg (Germany)
25 School of Physics, Peking University (China)
26 Universita' del Piemonte Orientale A. Avogadro (Italy)
27 University of Wisconsin (USA)
28 Veksler and Baldin Laboratory of High Energies, Joint Institutefor Nuclear Research (Russia)

FAIR: The R3B Collaboration

Reactions with Relativistic Radioactive Beams
<http://www-land.gsi.de/r3b/>
Spokesperson: T. Aumann Darmstadt (Germany)

Adrich, P.[17]; Al-Khalili, J.[56]; Algora, A.[26]; Alvarez, H.[53]; Aumann, T.[17]; Barton, C.[57]; Becker, F.[17]; Benlliure, J.[53]; Bhattacharya, S.[38]; Blumenfeld, Y.[24]; Boilley, D.[16]; Boretzky, K.[17]; Botvina, A.[22]; Boudard, A.[6]; Böhmer, M.[42]; Calvino, F.[43]; Casarejos, E.[53]; Catford, W.[56]; Chapman, R.[52]; Chartier, M.[50]; Chulkov, L.[37]; Coleman-Smith, P.[14]; Cortina, D.[53]; Csatlos, M.[2]; Cullen, D.[51]; Danilin, B.[37]; Datta Pramanik, U.[38]; Ducret, J.-E.[7]; Duran, I.[54]; Egelhof, P.[17]; Emling, H.[17]; Enders, J.[41]; Enqvist, T.[49]; Ershov, S. N.[27]; Faestermann, T.[42]; Fedorov, D.[3]; Feldmeier, H.[17]; Fernandez Dominguez, B.[50]; Fraile Prieto, L. M.[11]; Freeman, S.[51]; Freer, M.[4]; Friese, J.[42]; Fynbo, H.[44]; Gacsi, Z.[2]; Garrido, E.[8]; Gastineau, B.[12]; Geissel, H.[17]; Gelletly, W.[56]; Gerl, J.[17]; Gernhauser, R.[42]; Grigorenko, L.[27]; Grosse, E.[15]; Gulyas, J.[2]; Górska, M.[17]; Heinz, A.[58]; Hencken, K.[45]; Henzl, V.[17]; Henzlova, D.[17]; Hunyadi, M.[2]; Ignatyuk, A. V.[25]; Jensen, A.[3]; Johansson, H.[17]; Johnson, R.[56]; Jonson, B.[10]; Junghans, A.[15]; Kanungo, R.[40]; Kelic, A.[17]; Khan, E.[24]; Khanzadeev, A.[34]; Kisselev, O.[17]; Klimkiewicz, A.[17]; Kmiecik, M.[33]; Kojouharov, I.[17]; Krasznahorkay, A.[2]; Kratz, J. V.[29]; Kroell, T.[42]; Krücken, R.[42]; Kulessa, R.[28]; Kurz, N.[17]; Labiche, M.[52]; Langanke, K.-H.[44]; Lapoux, V.[6]; Lazarus, I.[5]; Le Gentil, E.[12]; Leifels, Y.[17]; Lemmon, R.[14]; Lenske, H.[30]; Lepine-Szily, A.[55]; Leray, S.[13]; Letts, S.[14]; Liang, X.[35]; Maj, A.[19]; Meister, M.[10]; Mittig, W.[16]; Müller, S.[20]; Müntz, C.[17]; Münzenberg, G.[17]; Neff, T.[17]; Nilsson, T.[41]; Nolan, P.[50]; Nolen, J.[1]; Nyman, G.[10]; Obradors, D.[8]; Oi, M.[39]; Pachalis, S.[50]; Palit, R.[48]; Pietri, S.[12]; Pivovarov, Y.[36]; Podolyak, Z.[56]; Pollacco, E.[6]; Pucknell, V.[14]; Regan, P.[56]; Reiter, P.[47]; Rejmund, F.[16]; Ricciardi, M. V.[17]; Richter, A.[41]; Riisager, K.[3]; Roussel-Chomaz, P.[16]; Rubio, B.[18]; Saito, T.[17]; Savajols, H.[16]; Scarpaci, J.-A.[24]; Scheit, H.[31]; Schmidt, K.-H.[17]; Schmitt, C.[23]; Schrieder, G.[41]; Sherrill, B.[32]; Simenel, C.[6]; Simon, H.[17]; Simpson, J.[5]; Spohr, K.[52]; Stevenson, P.[56]; Stroth, J.[17]; Sümmerer, K.[17]; Tain, J. L.[18]; Tengblad, O.[8]; Thompson, I.[39]; Tostevin, J. A.[56]; Trautmann, W.[17]; Typel, S.[17]; Udias-Moinelo, J.[11]; Vaagen, J.[46]; Volant, C.[6]; Wagner, A.[15]; Walus, W.[28]; Warner, D.[5]; Weick, H.[17]; Winkler, M.[17]; Zhang, Y.-H.[21]; Zhukov, M.[9]; Zieblinski, M.[28]; Zilges, A.[41]

1 ANL Argonne (USA)
2 ATOMKI Debrecen (Hungary)
3 Aarhus University (Denmark)
4 Birmingham University (United Kingdom)
5 CCLRC Daresbury (United Kingdom)
6 CEA Saclay (France)
7 CEA Saclay, DAPNIA/SPhN (France)
8 CSIC Madrid (Spain)
9 CTH/GU Gothenburg (Sweden)
10 Chalmers University of Technology (Sweden)
11 Complutense University of Madrid (Spain)
12 DAPNIA CEA Saclay (France)
13 DAPNIA/SPhN, CEA/Saclay (France)
14 Daresbury Laboratory (United Kingdom)
15 FZ Rossendorf (Germany)
16 GANIL (France)
17 GSI Darmstadt (Germany)
18 IFIC Valencia (Spain)
19 IFJ PAN Krakow (Poland)
20 IKP Darmstadt (Deutschland)
21 IMPCAS (China)
22 INR Moscow (Russia)
23 IPN Lyon (France)
24 IPN Orsay (France)
25 IPPE Obninsk (Russia)
26 Inst. of Nuclear Res. of the Hungarian Academy of Sciences (Hungary)
27 JINR Dubna (Russia)
28 Jagellonian University Krakow (Poland)
29 Johannes Gutenberg University of Mainz (Germany)
30 Justus-Liebig University Giessen (Germany)
31 Max-Planck-Institut für Kernphysik (Germany)
32 NSCL/MSU (USA)
33 Niewodniczanski Institute of Nuclear Physics (Poland)
34 PNPI Gatchina (Russia)
35 Paisly University (United Kingdom)
36 Polytechnic University of Tomsk (Russia)
37 RRC Kurchatov Institute Moscow (Russia)
38 Saha Institute of Nuclear Physics (India)
39 Surrey University (United Kingdom)
40 TRIUMF (Canada)
41 TU Darmstadt (Germany)
42 TU Munich (Germany)
43 UPC (Spain)
44 University of Aarhus (Denmark)
45 University of Basel (Switzerland)

46 University of Bergen (Norway)
47 University of Cologne (Germany)
48 University of Frankfurt (Germany)
49 University of Jyvaskyla (Finland)
50 University of Liverpool (United Kingdom)
51 University of Manchester (United Kingdom)
52 University of Paisley (United Kingdom)
53 University of Santiago de Compostela (Spain)
54 University of Santiago de Compostella (Spain)
55 University of Sao Paulo (Brasilia)
56 University of Surrey (United Kingdom)
57 University of York (United Kingdom)

FAIR: The SPARC Collaboration

Stored Particles Atomic Physics Collaboration
<http://www.gsi.de/zukunftsprojekt/experimente/sparc/index_e.html>
Spokesperson: R. Schuch, Stockholm (Sweden)

Afaneh, F.[58]; Ali, R.[58]; Andler, G.[79]; Andreev, O. Y.[34]; Andreev, O. Y.[67]; Anton, J.[38]; Artemyev, A.[67]; Aumayr, F.[3]; Backe, H.[37]; Bagge, L.[79]; Balashov, V.[71]; Banas, D.[60]; Baur, G.[27]; Beck, D.[29]; Becker, F.[29]; Beier, T.[29]; Beyer, H. F.[29]; Blaum, K.[80]; Block, M.[29]; Bosch, F.[29]; Braeuning-Demian, A.[29]; Brandau, C.[29]; Briggs, J.[28]; Bräuning, H.[30]; Bureyeva, L.[69]; Burgdoerfer, J.[2]; Cai, X.[10]; Chen, C.[9]; Chen, J.[13]; Ciortea, C.[65]; Cisneros, C.[59]; Currell, F.[84]; Danared, H.[79]; Dangendorf, V.[42]; Dauvergne, D.[23]; Dilling, J.[6]; Ding, D.[11]; Djekic, S.[37]; Dong, C.[15]; Dousse, J.-C.[81]; Drukarev, E.[72]; DuBois, R.[88]; Dumitriu, D. E.[65]; Dörner, R.[36]; Egelhof, P.[29]; Eichler, J.[46]; Emss, C.[92]; Engström, M.[79]; Enulescu, A.[65]; Fainstein, P. D.[1]; Fischer, D.[33]; Fleischmann, A.[40]; Fluerasu, D.[65]; Fogle, M.[89]; Fricke, B.[38]; Fritzsche, S.[38]; Förster, E.[48]; Gao, K.[14]; Garcia, G.[74]; Gaul, E.[93]; Goidenko, I.[67]; Gotta, D.[27]; Gumberidze, A.[29]; Gwinner, G.[4]; Habs, D.[32]; Hagmann, S.[36]; Hahn, T.[29]; Hanafy, H.[20]; Hencken, K.[82]; Herfurth, F.[29]; Herlert, A.[26]; Horbatsch, M.[5]; Huber, G.[37]; Hutton, R.[78]; Jakubassa-Amundsen, D.[43]; Jentschura, U.[28]; Kamber, E.[90]; Karpuk, S.[37]; Keitel, C. H.[33]; Kirchner, T.[39]; Kluge, H.-J.[29]; Kozhuharov, C.[29]; Krings, T.[27]; Källberg, A.[79]; Kühl, T.[29]; Labzowsky, L. N.[67]; Lamour, E.[24]; Lanzano, G.[56]; Le Bigot, E.-O.[25]; Lemell, C.[2]; Lestinsky, M.[33]; Liesen, D.[29]; Liljeby, L.[79]; Lindgren, I.[75]; Lindroth, E.[76]; Löfgren, P.[79]; Ma, X.[10]; Macek, J.[89]; Madsen, L. B.[19]; Madzunkov, S.[76]; Manchikanti, K.[51]; Manil, B.[21]; Mann, R.[29]; Manson, S.[87]; Marinkovic, B.[73]; Marx, G. H.[26]; Mathur, D.[51]; Matrasulov, D.[97]; Mitra, D.[55]; Mohamed, T.[20]; Mokler, P.[29]; Moshammer, R.[33]; Mukherjee, M.[29]; Müller, A.[30]; Nagy, S.[76]; Nandi, T.[53]; Nefiodov, A.[67]; Novotny, C.[37]; Nörtershäuser, W.[35]; Pachucki, K.[62]; Pajek, M.[60]; Pal'Chikov, V.[68]; Paál, A.[79]; Penescu, L. C.[65]; Peter, G.[77]; Pisk, K.[17]; Plunien, G.[34]; Potvliege, R.[83]; Presnyakov, L.[66]; Protic, D.[27]; Quint, W.[29]; Radu, A. T.[65]; Rahaman, S.[29]; Rakhimov, K.[97]; Rathmann, F.[27]; Reinhardt, S.[33]; Renner, O.[18]; Rensfelt, K.-G.[79]; Richard, P.[94]; Rothard, H.[21]; Rozet, J.-P.[24]; Rzadkiewicz, J.[64]; Röpke, G.[45]; Saathoff, G.[33]; Saenz, A.[47]; Safvan, C. P.[53]; Salomonson, S.[75]; Samek, S.[61]; Sanchez, R.[29]; Savin, D. W.[95]; Scheid, W.[31]; Schenkel, R.[86]; Schippers, S.[30]; Schmidt-Böcking, H.[36]; Schneider, D.[86]; Schramm, U.[32]; Schuch, R.[76]; Schulz, M.[88]; Schweikhard, L.[26]; Schützhold, R.[34]; Segal, D.[85]; Sepp, W.-D.[38]; Shabaev, V.[67]; Shevelko, V.[66]; Simionovici, A.[22]; Simon, H.[29]; Simonsson, A.[79]; Skeppstedt, Ö.[79]; Sliver, E.[91]; Soff, G.[34]; Sprenger, F.[33]; Stachura, Z.[63]; Stahl, S.[37]; Stiebing, K. E.[36]; Stöhlker, T.[29]; Sulik, B.[50]; Suri, B.[54]; Suric, T.[17]; Surzhykov, A.[38]; Tanis, J.[96]; Thompson, R.[85]; Tokesi, K.[50]; Toleikis, S.[86]; Tomasseli, M.[29]; Trautmann, D.[82]; Tribedi, L.[51]; Trotsenko, S.[29]; Ullrich, J.[33]; Varentsov, V.[70]; Verma, P.[52]; Vikor, G.[76]; Vogel, M.[37]; Volotka, A.[34]; Wang, J.[8]; Warczak, A.[61]; Weber, C.[29]; Wei, B.[10]; Welsch, C.[33]; Winter, H.[3]; Winters, D.[85]; Wolf, A.[33]; Ximeng, C.[12]; Yamazaki, Y.[57]; Yerokhin, V.[67]; Yoshida, S.[2]; Zeng, X.[7]; Zhang, F. S.[10]; Zhu, L.[13]; Zhu, X.[10]; Zilges, A.[41]; Zou, Y.[16]; Zouros, T.[49]; Zwicknagel, G.[44]

1 Centro Atomico Bariloche (Argentina)
2 Vienna University of Technolgy, Wien (Austria)
3 Institut für Allgemeine Physik, TU Wien (Austria)
4 University of Manitoba (Canada)
5 York University (Canada)
6 TRIUMF National Laboratory Vancouver (Canada)
7 China Institute of Atomic Energy, Beijing (China)
8 Institute of Applied Physics and Computational Mathematics, Beijing (China)
9 Institute of Modern Physics, Fudan University, Shanghai (China)
10 Institute of Modern Physics, Chinese Academy of Sciences, Lanzhou (China)
11 Institute of Atomic and Molecular Physics, Jilin University, Jilin (China)
12 Lanzhou University, Lanzhou (China)
13 University of Science and Technology of China, Hefei (China)
14 Wuhan Institute of Physics and Mathematics, Wuhan (China)
15 Physics Department, Northwest Normal University (China)
16 Applied Ion Beam Physics Laboratoy, Fudan University (China)
17 Ruder Boskovic Institute, Zagreb (Croatia)
18 Institute of Physics, Czech Academy of Sciences (Czech Republic)
19 Department of Physics and Astronomy, University of Aarhus (Denark)
20 Physics Department, Beni-Suef Faculty of Science (Egypt)
21 CIRIL Ganil (France)
22 Ecole Normale Superieure - Lyon (France)
23 Institut de Physique Nucléaire de Lyon (France)
24 Groupe de Physique des Solides (France)
25 Univ. P. & M. Curie et Ecole Normale Supérieure (France)
26 Ernst Moritz Arndt Universität Greifswald (Germany)
27 Forschungszentrum Jülich (Germany)
28 Freiburg University (Germany)
29 GSI, Darmstadt (Germany)
30 Institut für Atom- und Molekülphysik, Justus-Liebig-Universität Gießen (Germany)
31 Institut für Theoretische Physik der Universität Gießen (Germany)

32 Sektion Physik, LMU Munich (Germany)
33 Max-Planck-Institut für Kernphysik, Heidelberg (Germany)
34 Institut für Theoretische Physik, TU Dresden (Germany)
35 Tübingen University (Germany)
36 IKF, J.W.v.Goethe Universität Frankfurt am Main (Germany)
37 Institut für Physik, Universität Mainz (Germany)
38 Institut für Physik, Universität Kassel (Germany)
39 Institut für Theoretische Physik, TU Clausthal (Germany)
40 Kirchhoff-Institut für Physik, Universität Heidelberg (Germany)
41 TU Darmstadt (Germany)
42 Physikalisch-Technische Bundesanstalt (Germany)
43 Mathematics Institute, University of Munich (Germany)
44 Theoretische Physik, Universität Erlangen (Germany)
45 Institut für Physik, Universität Rostock (Germany)
46 Hahn-Meitner-Institut Berlin (Germany)
47 Humboldt-Universität zu Berlin (Germany)
48 Institute for Optics, Jena University (Germany)
49 University of Crete and IESL-FORTH (Greece)
50 Inst. of Nuclear Research (ATOMKI), Debrecen (Hungary)
51 Tata Institute of Fundamental Research (India)
52 Vaish College, Rohtak (India)
53 Nuclear Science Centre, New Delhi (India)
54 Bhabha Atomic Research Centre (India)
55 Saha Institute of Nuclear Physics (India)
56 Inst. Naz. Fisica Nucleare, Dip. di Fisica, Catania (Italy)
57 University of Tokyo & Atomic Physics Laboratory RIKEN, Wako (Japan)
58 Hashemite University (Jordan)
59 CCF Universidad Nacional Autónoma de México (Mexico)
60 Institute of Physics, Swietokrzyska Academy (Poland)
61 Institute of Physics, Jagiellonian University (Poland)
62 Institute of Theoretical Physics, Warsaw University (Poland)
63 Institute of Nuclear Physics of Polish Academy of Sciences (Poland)
64 The Soltan Institute For Nuclear Studies (Poland)
65 NIPNE National Institute for Physics and Nuclear Engineering (Romania)
66 Lebedev Physical Institute, Moscow (Russia)
67 Institute of Physics, St. Petersburg State University (Russia)
68 Institute of Metrology for Time and Space at VNIIFTRI (Russia)
69 Institute of Spectroscopy of the RAS (Russia)
70 V.G.Khlopin Radium Institute, St.Petersburg (Russia)
71 Institute of Nuclear Physics, Moscow State University (Russia)
72 Petersburg Nuclear Physics Institute (Russia)
73 Institute of Physics, Belgrade (Serbia and Montenegro)
74 CSIC (Spain)
75 Chalmers University of Technology and Goteborg University (Sweden)
76 Stockholm University (Sweden)
77 Mid-Sweden University (Sweden)
78 Lund University (Sweden)
79 Manne Siegbahn Laboratory MSL (Sweden)
80 CERN (Switzerland)
81 Department of Physics, University Fribourg (Switzerland)
82 Institut für Physik, Universität Basel (Switzerland)
83 Department of Physics, The University of Durham (United Kingdom)
84 Queen's University, Belfast (United Kingdom)
85 Imperial College (United Kingdom)
86 Lawrence Berkeley National Laboratory (USA)
87 Georgia State University (USA)
88 University of Missouri Rolla (USA)
89 Oak Ridge National Laboratory (USA)
90 Western Michigan University (USA)
91 Harvard-Smithsonian Center for Astrophysics (USA)
92 Brown University, Physics Department (USA)
93 Univeristy of Texas at Austin (USA)
94 Kansas State University (USA)
95 Columbia Astrophysics Laboratory, Columbia University (USA)
96 Western Michigan University (USA)

FAIR: The WDM Collaboration

Radiative Properties of Warm Dense Matter Produced by Intense Heavy Ion Beams
Spokesperson: B. Rosmej (France)

Abdallah Jr, J.[4]; Adonin, A.[14]; Aleksandrova, I. V.[12]; Basko, M.[10]; Beigman, I.[11]; Borneis, S.[19]; Chtcherbakov, V. I.[12]; Demura, A.[8]; Faenov, A. Y.[9]; Fertmann, A.[10]; Golubev, A. A.[10]; Gromov, A. I.[12]; Gtte, S.[19]; Hoffmann, D. H. H.[18]; Jacoby, J.[14]; Kapralov, V. G.[13]; Kizivetter, D. V[13]; Kluge, H.-J.[19]; Koresheva, E. R.[12]; Koshelev, E. L.[12]; Kostriukov, A. Y.[13]; Kuteev, B. V.[13]; Kühl, T.[19]; Lee, R. W.[5]; Lisitsa, V. S.[8]; Maruhn, J.[15]; Merkuliev, Y. A.[12]; Nagai, K.[6]; Nikitenko, A. I.[12]; Nishimura, H.[6]; Norimatsu, T.[6]; Onkels, E.[19]; Osipov, I. E.[12]; Pikuz, T. A.[9]; Redmer, R.[17]; Riley, D.[3]; Rosmej, F. B.[1]; Schlegel, T.[18]; Sergeev, V. Y.[13]; Sharkov, B.[10]; Stamm, R.[1]; Tauschwitz, A.[18]; Tauschwitz, Anna[15]; Timasheva, T. P.[12]; Tolokonnikov, S. M.[12]; Tolstikhina, I. Y.[11]; Turtikov, V.[10]; Ullrich, J.[16]; Vainshtein, L. A.[11]; Wahl, H.[18]; Weyrich, K.[18]; Yamazaki, Y.[7]; Zeitoun, P.[2]

1 Université de Provence, PIIM-DGP, Marseille (France)
2 LOA-ENSTA, Palaiseau (France)
3 Queens University, Belfast (United Kingdom)
4 LANL, Los Alamos (USA)
5 LLNL, Livermore (USA)
6 Institute of Laser Engineering, Osaka (Japan)
7 The Institute of Physical and Chemical Research RIKEN, Saitama (Japan)
8 Kurchatov Institute, Moscow (Russia)
9 MISDC VNIFFTRI, Mendeleevo (Russia)
10 ITEP, Moscow (Russia)
11 Lebedev Physical Institute, Laboratory of Optics, Moscow (Russia)
12 Lebedev Physical Institute,Thermonuclear Target Laboratory, Moscow (Russia)
13 State Polytechnic University of St. Petersburg, Plasma

Physics Laboratory, St. Petersburg (Russia)
14 Johann Wolfgang Goethe Universität, Institut für AP, Frankfurt (Germany)
15 Johann Wolfgang Goethe Universität, Institut für TP, Frankfurt (Germany)
16 Max-Planck Institut für Kernphysik, Heidelberg (Germany)
17 University of Rostock, Institute of Physics, Rostock (Germany)
18 GSI-Darmstadt, Plasmaphysik (Germany)

The SIS/ESR/UNILAC Collaborations

The ALADiN 2000 Collaboration

<http://www-kp3.gsi.de/www/kp3/aladinhome.html>
Spoekesperson: W. Trautmann, Darmstadt (Germany)

Adrich, P.[1]; Aumann, T.[1]; Bacri, C. O.[2]; Barczyk, T.[8]; Bassini, R.[6]; Boiano, C.[6]; Botvina, A. S.[1]; Boudard, A.[3]; Brzychczyk, J.[8]; Chbihi, A.[4]; Cibor, J.[9]; Czech, B.[9]; De Napoli, M.[5]; Ducret, J. -E.[3]; Emling, H.[1]; Frankland, J.[4]; Hellström, M.[1]; Henzlova, D.[1]; Immè, G.[5]; Iori, I.[6]; Johansson, H.[1]; Kezzar, K.[1]; Lafriakh, A.[2]; Le Gentil, E.[3]; Leifels, Y.[1]; Le Fèvre, A.[1]; Lynch, W. G.[10]; Lynen, U.[1]; Lühning, J.[1]; Majka, Z.[8]; Mocko, M.[10]; Mykulyak, A.[7]; Müller, W. F. J.[1]; Orth, H.[1]; Otte, A. N.[1]; Palit, R.[1]; Pawłowski, P.[9]; Pullia, A.[6]; Raciti, G.[5]; Rapisarda, E.[5]; Sann, H.[1]; Schwarz, C.[1]; Sfienti, C.[1]; Simon, H.[1]; Sümmerer, K.[1]; Trautmann, W.[1]; Tsang, M. B.[10]; Verde, G.[10]; Volant, C.[3]; Wallace, M.[10]; Weick, H.[1]; Wiechula, J.[1]; Wieloch, A.[8]; Zwieglinski, B.[7]; Łukasik, J.[1]

1 GSI, Darmstadt (Germany)
2 Institut de Physique Nucléaire, IN2P3-CNRS et Université, Orsay (France)
3 DAPNIA/SPhN, CEA/Saclay, Gif-sur-Yvette (France)
4 GANIL, CEA et IN2P3-CNRS, Caen (France)
5 Dipartimento di Fisica dell'Universitá and LNS-INFN, Catania (Italy)
6 Istituto di Scienze Fisiche, Università degli Studi and INFN, Milano (Italy)
7 A. Sołtan Institute for Nuclear Studies, Warsaw (Poland)
8 M. Smoluchowski Institute of Physics, Jagiellonian Univ., Kraków (Poland)
9 H. Niewodniczański Institute of Nuclear Physics, Pl-31342 Kraków (Poland)

The CHARMS Collaboration

Collaboration for High-Accuracy Experiments on Nuclear Reaction Mechanisms with the FRS
<http://www-w2k.gsi.de/charms>
Spokesperson: K.-H. Schmidt, Darmstadt (Germany)

Armbruster, P.[1]; Audouin, L.[3]; Bacri, C.-O.[3]; Benlliure, J.[2]; Bernas, M.[3]; Boilley, D.[8]; Botvina, A.[16]; Boudard, A.[4]; Casarejos, E.[2]; Danielewicz, P.[12]; Ducret, J.-E.[4]; Enqvist, T.[13]; Fernandez, B.[4]; Fernandez, M.[2]; Giot, L.[1]; Heinz, A.[11]; Helariutta, K.[14]; Henzl, V.[1]; Henzlova, D.[1]; Ignatyuk, A.[15]; Junghans, A.[9]; Jurado, B.[7]; Kelić, A.[1]; Krasa, A.[10]; Kugler, A.[10]; Kurtukian, T.[2]; Leray, S.[4]; Napolitani, P.[8]; Pereira, J.[2]; Pleskač, R.[1]; Rejmund, F.[8]; Ricciardi, M. V.[1]; Schmidt, K.-H.[1]; Schmitt, C.[6]; Shi, L.[12]; Stéphan, C.[3]; Taieb, J.[5]; Tassan-Got, L.[3]; Villagrasa, C.[4]; Volant, C.[4]; Wagner, A.[9]; Wagner, V.[10]; Yordanov, O.[1]

1 GSI, Darmstadt (Germany)
2 Univ. Santiago de Compostela, Sant. de Compostela (Spain)
3 IPN Orsay, Orsay (France)
4 DAPNIA/SPhN, CEA Saclay, Gif sur Yvette (France)
5 DEN/DM2S/SERMA/LENR, CEA Saclay, Gif sur Yvette (France)
6 IPNL, Université Lyon, Groupe Matiere Nucleaire, Villeurbanne (France)
7 CENBG, Le Haut Vigneau, Bordeaux-Gradignan (France)
8 GANIL, Caen (France)
9 Forschungszentrum Rossendorf, Dresden (Germany)
10 Nuclear Physics Institute, Rez (Czech Republic)
11 Wright Nuclear Structure Laboratory, Yale University, New Haven (USA)
12 National Superconducting Cyclotron Laboratory and Physics and Astronomy Department, Michigan State University, East Lansing (USA)
13 CUPP Project, Pyhsalmi (Finland)
14 University of Helsinki, Helsinki (Finland)
15 IPPE, Obninsk (Russia)

The FOPI Collaboration

4π Detector System for Charged Particles
<http://www-fopi.gsi.de/>
Spokesperson: N. Herrmann, Heidelberg (Germany)

Andronic, A.[1]; Barret, V.[2]; Basrak, Z.[3]; Bastid, N.[2]; Benabderrahmane, M. L.[4]; Caplar, R.[3]; Cordier, E.[4]; Crochet, P.[2]; Dupieux, P.[2]; Dzelalija, M.[3]; Gasparic, I.[3]; Grishkin, Y.[6]; Hartmann, O. N.[1]; Herrmann, N.[4]; Hildenbrand, K. D.[1]; Hong, B.[7]; Kang, D.[7]; Kecskemeti, J.[5]; Kim, Y. J.[7]; Kirejczyk, M.[4]; Koczon, P.[1]; Korolija, M.[3]; Kotte, R.[9]; Kowalczyk, M.[8]; Lebedev, A.[6]; Leifels, Y.[1]; Lopez, X.[2]; Manko, V.[11]; Matulewicz, T.[8]; Merschmeyer, M.[4]; Moisa, D.[10]; Petrovici, M.[10]; Rami, F.[2]; Reisdorf, W[1]; Schüttauf, A.[1]; Seres, Z.[5]; Sikora, B.[8]; Sim, K. S.[7]; Simion, V.[10]; Siwek-Wilczynska, K.[8]; Smolyankin, V.[6]; Stockmeier, M.[4]; Stoicea, G.[10]; Tyminski, Z.[8]; Wagner, P.[2]; Wisniewski, K.[8]; Wohlfarth, D.[9]; Xiao, Z. G.[1]; Yushmanov, I.[11]; Zhilin, A.[6]

1 GSI, Darmstadt (Germany)
2 Laboratoire de Physique Corpusculaire (LPC) / Université Blaise Pascal, Clermont-Ferrand (France)
3 Rudjer Boskovic Institute (RBI), Zagreb (Croatia)
4 Universität Heidelberg, I. Physikalisches Institut, Heidelberg (Germany.)
5 Central Research Institute of Physics (CRIP), Budapest (Hungary)
6 Institute for Theoretical and Experimental Physics (ITEP), Moscow (Russia)
7 Korea University, Depertment of Physics, Seoul (South Korea)
8 Institute of Experimental Physics, Nuclear Physics Division, Warsaw (Poland)
9 Forschungszentrum Rossendorf (FZR), Dresden (Germany)
10 National Institute for Physics and Nuclear Engineering (NIPNE), Bucharest (Romania)

The HADES Collaboration

High Acceptance Di-Electron Spectrometer
<http://www-hades.gsi.de/>
Spokesperson: P. Salabura, Cracow (Poland)

Agakishiev, G.[7]; Agodi, C.[2]; Alvarez-Pol, H.[19]; Balanda, A.[5]; Bassini, R.[10]; Bellia, G.[2]; Bellia, G.[3]; Belver, D.[19]; Bielcik, J.[6]; Blanco, A.[4]; Boiano, C.[10]; Bortolotti, A.[10]; Boyard, J. L.[16]; Brambilla, S.[10]; Braun-Munzinger, P.[6]; Böhmer, M.[14]; Cabanelas, P.[19]; Chernenko, S.[7]; Christ, T.[14]; Coniglione, R.[2]; Dahlinger, M.[6]; Djeridi, R.[9]; Dohrmann, F.[18]; Durán, I.[19]; Díaz, J.[20]; Eberl, T.[14]; Enghardt, W.[18]; Fabbietti, L.[14]; Fateev, O.[7]; Finocchiaro, P.[2]; Fonte, P. J. R.[4]; Friese, J.[14]; Fröhlich, I.[9]; Garzón, J. A.[19]; Gernhäuser, R.[14]; Golubeva, M.[12]; González-Díaz, D.[19]; Grosse, E.[18]; Guber, F.[12]; Heinz, T.[6]; Hennino, T.[16]; Hlavac, S.[1]; Hoffmann, J.[6]; Holzmann, R.[6]; Ierusalimov, A.[7]; Iori, I.[10]; Iori, I.[11]; Ivashkin, A.[12]; Jaskula, M.[5]; Jurkovic, M.[14]; Kajetanowicz, M.[5]; Kanaki, K.[18]; Karavicheva, T.[12]; Kirschner, D.[9]; Koenig, I.[6]; Koenig, W.[6]; Kolb, B. W.[6]; Kopf, U.[6]; Kotte, R.[18]; Kotulic-Bunta, J.[1]; Krücken, R.[14]; Kugler, A.[17]; Kulessa, R.[5]; Kämpfer, B.[18]; Kühn, W.[9]; Lang, S.[6]; Lehnert, J.[9]; Maier, L.[14]; Maier-Komor, P.[14]; Maiolino, C.[2]; Markert, J.[8]; Marín, J.[19]; Metag, V.[9]; Montes, N.[19]; Moriniere, E.[16]; Mousa, J.[15]; Münch, M.[6]; Müntz, C.[8]; Naumann, L.[18]; Novotny, J.[17]; Novotny, R.[9]; Ott, W.[6]; Otwinowski, J.[5]; Pachmayer, Y. C.[8]; Pant, L. M.[9]; Pechenov, V.[7]; Pietraszko, J.[6]; Pinhao, J. M. A.[4]; Pleskac, R.[17]; Pospísil, V.[17]; Przygoda, W.[5]; Pullia, A.[10]; Pullia, A.[11]; Pérez, T.[9]; Rabin, N.[13]; Ramstein, B.[16]; Riboldi, S.[10]; Ritman, J.[9]; Rosier, P.[16]; Roy-Stephan, M.[16]; Rustamov, A.[6]; Sadovsky, A.[18]; Sailer, B.[14]; Salabura, P.[5]; Sapienza, P.[2]; Schmah, A.[6]; Schroeder, C.[6]; Schwab, E,[6]; Schön, W.[6]; Senger, P.[6]; Simon, R.[6]; Smolyankin, V.[13]; Smykov, L.[7]; Spataro, S.[2]; Spruck, B.[9]; Stroebele, H.[8]; Stroth, J.[6]; Stroth, J.[8]; Sturm, C.[6]; Sudol, M.[6]; Sudol, M.[8]; Tiflov, T.[12]; Tlusty, P.[17]; Toia, A.[9]; Traxler, M.[6]; Tsertos, H.[15]; Turzo, I.[1]; Wagner, V.[17]; Walus, W.[5]; Willmott, C.[19]; Winkler, S.[14]; Wisniowski, M.[5]; Wojcik, T.[5]; Wüstenfeld, J.[8]; Zanevsky, Y.[7]; Zumbruch, P.[6]

1 Institute of Physics, Slovak Academy of Sciences, Bratislava (Slovakia)
2 Istituto Nazionale di Fisica Nucleare - Laboratori Nazionali del Sud, Catania (Italy)
3 Dipartimento di Fisica e Astronomia, Università di Catania, Catania (Italy)
4 LIP-Laboratório de Instrumentação e Física Experimental de Partículas, Departamento de Física da Universidade de Coimbra, Coimbra (Portugal)
5 Smoluchowski Institute of Physics, Jagiellonian University of Cracow, Cracow (Poland)
6 GSI Darmstadt (Germany)
7 Joint Institute of Nuclear Research, Dubna (Russia)
8 Institut für Kernphysik, Johann Wolfgang Goethe-Universität, Frankfurt (Germany)
9 II. Physikalisches Institut, Justus Liebig Universität Gießen, Gießen (Germany)
10 Istituto Nazionale di Fisica Nucleare, Sezione di Milano, Milano (Italy)
11 Dipartimento di Fisica, Università di Milano, Milano (Italy)
12 Institute for Nuclear Research, Russian Academy of Science, Moscow (Russia)
13 Institute of Theoretical and Experimental Physics, Moscow (Russia)
14 Physik Department E12, Technische Universität München, Garching (Germany)
15 Department of Physics, University of Cyprus, Nicosia (Cyprus)
16 Institut de Physique Nucléaire d'Orsay, CNRS/IN2P3, Orsay Cedex (France)

17 Nuclear Physics Institute, Academy of Sciences of Czech Republic, Rez (Czech Republic)
18 Institut für Kern- und Hadronenphysik, Forschungszentrum Rossendorf, Dresden (Germany)
19 Departamento de Física de Partículas, University of Santiago de Compostela. Santiago de Compostela (Spain)

The IKAR Collaboration

Alkhazov, G. D.[1]; Andronenko, M. N.[1]; Bleile, A.[2]; Dobrovolsky, A. V,[1]; Egelhof, P.[2]; Gavrilov, G. E.[1]; Geissel, H.[2]; Khanzadeev, A. V.[1]; Kisselev, O.[2]; Korolev, G. A.[1]; Meier, J. P.[2]; Mutterer, M.[3]; Münzenberg, G.[2]; Neumaier, S. R.[2]; Scheidenberger, C.[2]; Seliverstov, D. M.[1]; Vorobyov, A. A.[1]; Yatsoura, V. I.[1]

1 PNPI Petersburg (Russia)
2 GSI, Darmstadt (Germany)

The KaoS Collaboration

Kaon Spectrometer
<http://www-aix.gsi.de/%7Ekaos/html/kaoshome.html>

Dohrmann, F.[5]; Förster, A.[1]; Grosse, E.[5]; Koczon, P.[2]; Kohlmeyer, B.[4]; Lang, S.[1]; Naumann, L.[5]; Oeschler, H.[1]; Ploskon, M.[2]; Scheinast, W.[5]; Schmah, A.[1]; Schuck, T.[3]; Schwab, E.[2]; Senger, P.[2]; Ströbele, H.[3]; Sturm, C.[1]; Uhlig, F.[1]; Wagner, A.[5]; Walus, W.[6]

1 Technische Universität Darmstadt (Germany)
2 GSI (Germany)
3 Johann Goethe Universität Frankfurt (Germany)
4 Phillips Universität Marburg (Germany)
5 Forschungszentrum Rossendorf, Dresden (Germany)

The LAND-FRS Collaboration

Large Area Neutron time of flight Detector – Fragment Separator
Spokesperson: H. Emling, Darmstadt (Germany)

Adrich, P.[1]; Adrich, P.[4]; Aumann, T.[1]; Boretzky, K.[1]; Cortina-Gil, D.[5]; Datta Pramanik, U.[1]; Elze, T. W.[3]; Emling, H.[1]; Fallot, M.[1]; Geissel, H.[1]; Hellström, M.[1]; Ickert, G.[1]; Johansson, A.[1]; Jones, K. L.[1]; Kiselev, O.[2]; Klimkiewicz, A.[4]; Kratz, J. V.[2]; Kulessa, R.[4]; Leifels, Y.[1]; Nociforo, C.[2]; Palit, R.[3]; Simon, H.[1]; Surowka, G.[4]; Sümmerer, K.[1]; Walus, W.[4]

1 GSI Darmstadt (Germany)
2 Univ. Mainz (Germany)
3 Univ. Frankfurt (Germany)
4 Univ. Kraków (Poland)

The S174 Collaboration

Aksouh, F.[1]; Bleile, A.[1]; Bochkarev, O. V.[2]; Chulkov, L. V.[1]; Cortina-Gil, D.[1]; Dobrovolsky, A. V.[1]; Dobrovolsky, A. V.[3]; Egelhof, P.[1]; Geissel, H.[1]; Hellström, M.[1]; Isaev, N. B.[3]; Kiselev, O. A.[1]; Kiselev, O. A.[3]; Komkov, B. G.[3]; Moroz, F. V.[3]; Mutterer, M.[4]; Mylnikov, V. A.[3]; Münzenberg, G.[1]; Mátos, M.[1]; Neumaier, S. R.[1]; Pribora, V. N.[1]; Pribora, V. N.[2]; Seliverstov, D. M.[3]; Sergueev, L. O.[3]; Shrivastava, A.[1]; Sümmerer, K.[1]; Weick, H.[1]; Winkler, M.[1]; Yatsoura, V. I.[3]

1 GSI Darmstadt (Germany)
2 Kurchatov Institute, Moscow (Russia)
3 PNPI, St. Petersburg (Russia)

The SHIPTRAP Collaboration

<http://www.gsi.de/forschung/ap/projects/shiptrap/index.html>
Spokesperson: M. Block, Darmstadt (Germany)

Ackermann, D.[1]; Backe, H.[2]; Blaum, K.[2]; Block, M.[1]; Breitenfeld, M.[3]; Chauduri, A.[3]; Di, Z.[6]; Doemer, A.[4]; Dretzke, A.[2]; Eliseev, S.[1]; Ferrer, R.[2]; Geissel, H.[6]; Habs, D.[5]; Heinz, S.[5]; Herfurth, F.[1]; Hessberger, F. P.[1]; Hofmann, S.[1]; Horn, R.[2]; Kluge, H.-J.[1]; Kolhinen, V.[5]; Kunz, P.[2]; Lauth, W.[2]; Marx, G. H.[3]; Mukherjee, M.[1]; Münzenberg, G.[1]; Neumayr, J. B.[5]; Petrick, M.[6]; Plass, W.[6]; Quint, W.[1]; Rahaman, S.[1]; Rauth, C.[1]; Rodrguez, D.[7]; Scheidenberger, C.[6]; Schweikhard, L.[3]; Suhonen, M.[8]; Szerypo, J.[5]; Thirolf, P. G.[5]; Wang, Z.[6]; Weber, C.[2]

1 Gesellschaft für Schwerionenforschung, Darmstadt (Germany)
2 Institut für Physik, Johannes-Gutenberg-Universität, Mainz (Gerrmany)
3 Institut für Physik, Ernst-Moritz-Arndt-Universität, Greifswald (Germany)
4 Department of Physics & Astronomy, Michigan State University, East Lansing (USA)
5 Sektion Physik, Ludwig-Maximilians-Universität,Garching (Germany)
6 II. Physikalisches Institut, Justus-Liebig-Universität, Giessen (Germany)
7 LPC, ENSICAEN, Caen Cedex (France)

The EU Collaborations

Joint Research Projekt for I3HP/6th EU Framework: Development of High Speed Gas DEtector with Integrated Associated Elektronics

University of Bergen (Norway);
National Institute o fPhysics and Nuclear Engineering, Bucharest (Romania);
GSI Darmstadt (Germany);
CERN Geneva (Switzerland);
Deptment of Physics, University of Heidelberg (Germany);
Kirchhoff Institute, University of Heidelberg (Germany);
Institute for Nuclear Physics, University of Mnster (Germany);
SUBATECH, Nantes (France);
Joint Institute of Nuclear Research Dubna (Russia);
INVENTOR, Cracow (Poland);
optiprint, Rehetobel (Switzerland);
SCILAB, Oslo (Norway)

Joint Research Projekt for I3HP/6th EU Framework: Development of High Speed Data Acquistion and Trigger Systems

Contact persons:

Brenner, K. H.[2]; Brüning, U.[2]; Lindenstruth, V.[1]; Männer, R.[2]; Müller, W. J. F.[3]; Schnörr, C.[2]; Sikora, B.[5]; Vesztergombi, G.[4]; Zipper, W.[6]

1 Kirchhoff Institute for Physics, University of Heidelberg (Germany)
2 Institute of Computer Engineering, University of Mannheim (Germany)
3 GSI, Darmstadt (Germany)
4 FKKI Research Insitute for Particle and Nuclear Physics, Budapest (Hungary)
5 Institute of Exoperimental Physics, Warsaw University (Poland)

I3HP Networking Project: A European research network for the realization of the Compressed Baryonic Matter (CBM) Experiment at the future international accelerator facility in Darmstadt

Contact Persons:

Caplar, R.[19]; Dohrmann, F.[14]; Fonte, P.[3]; Garzon, J.[15]; Golutvin, A.[22]; Herrmann, N.[7]; Igolkin, S.[27]; Keszkemety, J.[2]; Kohlmeyer, B.[11]; Kugler, A.[13]; Kurepin, A.[23]; Lindenstruth, V.[8]; Majka, Z.[9]; Malakhov, A.[21]; Manko, V.[24]; Merkin, M.[25]; Murin, Y.[26]; Männer, R.[10]; Petrovici, M.[1]; Rami, F.[17]; Rekalo, M.[28]; Senger, P.[5]; Shevshenko, V.[20]; Sikora, B.[18]; Ströbele, H.[6]; Tsertos, H.[4]; Wessels, J.[12]; Zipper, W.[16]

1 Bucharest IPNE (Romania)
2 Budapest KFKI (Hungary)
3 Coimbra ISEC/LIP (Portugal)
4 Cyprus University, Nikosia (Cyprus)
5 GSI, Darmstadt (Germany)
6 Frankfurt University (Germany)
7 Heidelberg Univ. Phys. Inst. (Germany)
8 Heidelberg Univ. Kirchhoff Inst. (Germany)
9 Krakow Jagiellonian University (Poland)
10 Mannheim University (Germany)
11 Marburg University (Germany)
12 Mnster University (Germany)
13 Rez CAS (Czech Republic)
14 Rossendorf FZ (Germany)
15 Santiago de la Compostela Univ. (Spain)
16 Silesia University Katowice (Poland)
17 Strasbourg IReS (France)
18 Warsaw University (Poland)
19 Zagreb IRB (Croatia)
20 Kiev University (Ukraine)
21 Dubna LHE-JINR (Russia)
22 Moscow ITEP (Russia)
23 Moscow INR (Russia)
24 Moscow Kurchatov Inst. (Russia)
25 Moscow State University, SINP (Russia)
26 St. Petersburg KRI (Russia)
27 St. Petersburg, CKBM (Russia)

Joint Research Projekt for I3HP/6th EU Framework: NEWTOF New techniques for time-of-flight particle identification in nuclear collision experiments

Contact Persons:

Dohrmann, F.[4]; Eschke, J.[3]; Fonte, P.[2]; Garzon, J.[6]; Grosse, E.[4]; Herrmann, N.[5]; Hildenbrand, K.[3]; Petrovici, M.[1]; Schüttauf, A.[3]

1 IFIN Bucharest (Romania)
2 University of Coimbra (Portugal)
3 GSI Darmstadt (Germany)
4 Forschungszentrum Rossendorf (FZR) and TU Dresden (Germany)
5 Physikalisches Institut der Universität Heidelberg (Germany)

The NoRHDia Collaboration

Novel Radiation Hard CVD Diamond Detectors for Hadron Physics
<http://www-norhdia.gsi.de/>
Coordinator: E. Berdermann, Darmstadt (Germany)

Bassini, R.[1]; Berdermann, E.[2]; Bergonzo, P.[3]; Bol, J.[4]; de Boer, W.[4]; Bräuning-Demian, A.[2]; Caragheorgheopol, A.[5]; Ciobanu, M.[2]; Connell, S.[6]; Da Costa, A.[6]; Grigoriev, E.[4]; Hartmann, W.[2]; Iori, I.[1]; Kindler, B.[2]; Kutschera, W.[7]; Kuznetsova, E.[8]; Lange, W.[8]; Liechtenstein, V.[9]; Lohmann, W.[8]; Lommel, B.[2]; Macchiocci, D.[1]; Martemiyanov, A.[2]; Mikuz, M.[10]; Moritz, P.[2]; Morse, J.[11]; Nebel, C.[12]; Nesladek, M.[3]; Oh, A.[13]; Petris, M.[5]; Petrovici, M.[5]; Pomorski, M.[2]; Pullia, A.[1]; Rebisz, M.[2]; Roe, S.[13]; Voss, B.[2]; Weilhammer, P.[13]

1 INFN, Milano (Italy)
2 GSI Darmstadt (Germany)
3 LIST CEA Saclay, Paris (France)
4 Inst. f. Exp. Kernphysik, Karlsruhe (Germany)
5 IFIN-HH, Bucharest (Romania)
6 Wits University, Johannesburg (South Africa)
7 VERA Laboratory, Vienna (Austria)
8 DESY Zeuthen (Germany)
9 Kurchatov Institute, Moscow (Russia)
10 IJS, Ljubljana (Slovenia)
11 ESRF Grenoble (France)
12 AIST, Tsukuba (Japan)

Collaborations in the theoretical fields

The HGF Virtual Institute with German Universities 'Dense Hadronic Matter and QCD Phase Transitions'

<http://theory.gsi.de/Vir-Institute/>
Speakers: D. Blaschke D. Rischke

Blaschke, D.[6]; Cassing, W.[5]; Friman, B.[4]; Fäßler, A.[7]; Karsch, F.[1]; Rischke, D.[3]; Wambach, J.[2]

1 University of Bielefeld (Germany)
2 University of Darmstadt (Germany)
3 University of Frankfurt (Germany)
4 GSI (Germany)
5 University of Gießen (Germany)
6 University of Rostock (Germany)

The Collaboration for Correlation Dynamics in Nuclear Structure

<http://theory.gsi.de/∼fmd/>

Cribeiro, A.[1]; Feldmeier, H.[1]; Neff, T.[1]; Roth, R.[2]; Schnack, J.[3]

1 GSI and TU Darmstadt (Germany)
2 University of Oxford (Great Britain)

The TeraScale Supernova Initiative

<http://www.phy.ornl.gov/tsi/tsimain.htm>

Baker, P.[8]; Blodin, J.[6]; Bruenn, S. W.[3]; Dean, D.[1]; Dongarra, J.[5]; Eijkhout, V.[5]; Fuller, G.[4]; Haxton, W.[9]; Hayes, J.[4]; Langanke, K.[10]; Lattimer, J.[7]; Meyer, B.[2]; Mezzacappa, A.[1]; Prakash, M.[7]; Saied, F.[8]; Saylor, P.[8]; Strayer, M.[1]; Swesty, D.[7]; Toedte, R.[1]

1 Oak Ridge National Laboratory (USA)
2 Clemson University (USA)
3 Florida Atlantic University (USA)
4 University of California, San Diego (USA)
5 Univ. of Tennessee, Knoxville (USA)
6 North Carolina State University, New York (USA)
7 Stony Brook, New York (USA)
8 The National Center for Supercomputing Applications, University of Illinois at Urbana-Champaign (USA)
9 University of Washington (USA)

Network 6: Strongly Interacting Matter in Ultrarelativistic Heavy-Ion Collisions

'Study of Strongly Interacting Matter (Hadron Physics I3), 6th European framework programme
<http://www.infn.it/eu/i3hp/wel.html>

The Collaboration for Non-Equilibrium Strongly Interacting Dense Matter in Nucleus-Nucleus Collisions

<http://theory.gsi.de/Cooperations/DFG-RU/>

Bengt, K.[2]; Friman, L.[2]; Ivanov, Y. B.[1]; Nörenberg, W.[2]; Skokov, V.[3]; Toneev, V. D.[3]; Voskresensky, D.[4]

1 Kurchatov Institute, Moscow (Russia)
2 GSI (Germany)
3 JINR, Dubna (Russia)

The Lattice Forum of the German Nuclear Physics community

<http://www-zeuthen.desy.de/latfor/>

Universität Bern (Switzerland),
Humboldt-Universität zu Berlin (Germany),
FU Berlin (Germany),
ZIB Berlin (Germany),
Universität Bielefeld (Germany),
Ruhr-Universität Bochum (Germany),
GSI (Germany),
TU Darmstadt (Germany),
Universität Erlangen-Nürnberg (Germany),
J. W. Goethe Universität Frankfurt (Germany),
Universität Graz (Austria),
DESY (Germany),
FEST Heidelberg (Germany),
Universität Heidelberg (Germany),
Forschungszentrum Jülich (Germany),
Universität Leipzig (Germany),
Max-Planck-Institut für Physik München (Germany),
TU München (Germany),
Universität Münster (Germany),
Universität Regensburg (Germany),
Universität Rostock (Germany),
Universität Tübingen (Germany),
Universität Wuppertal (Germany),
Universität Wien (Austria),
DESY Zeuthen (Germany),
John von Neumann-Institute for Computing in Zeuthen (Germany)

Collaborations in the CERN context

The ALICE Collaboration

A Large Ion Collider Experiment at CERN LHC
<http://alice.web.cern.ch/Alice/AliceNew/collaboration/>
The collaborations contains 27 countries, 83 institutes, and about 1000 members. Here only the participants of the GSI are lsited.
Leader at the GSI: P. Braun-Munzinger

GSI Darmstadt (Germany)

Alessi-Rauch, D.; Andronic, A.; Antonczyk, D.; Appelshäuser, H.; Bailhache, R.; Beck, D.; Brand, H.; Braun-Munzinger, P.; Busch, O.; Ciobanu, M.; Dahlinger, M.; Daues, H.; Deveaux, M.; Foka, P.; Frankenfeld, U.; Garabatos, J. Gruwe, M.; Gutbrod, H.; Lippmann, C.; Malzacher, P.; Marin, A.; Maunder, R.; Miskowiec, D.; Müller, W. F. J.; Prybyla, A.; Radomsko, S.; Sandoval, A.; Schmidt, H. R.; Schwarz, K.; Sedykn, S.; Simon, R.; Soyk, D.; Stelzer, H.; Tsledakis, G.; Vranic, D.

The ALICE TRD Collaboration

The Transition Radiation Detector of the ALICE experiment at LHC
<http://www-alice.gsi.de/trd>
Project leader: J. Stachel, Heidelberg (Germany)

Adler, C.[6]; Aiftimiei, C.[2]; Amend, W.[8]; Andronic, A.[3]; Angelov, V.[5]; Appelshäuser, H.[8]; Bablok, S.[11]; Bailhache, R.[3]; Baumann, C.[9]; Blume, C.[8]; Braun-Munzinger, P.[3]; Bucher, D.[9]; Busch, O.[3]; Chepurnov, V.[4]; Chernenko, S.[4]; Christakoglou, P.[1]; Conner,

E. S.[11]; Cătănescu, V.[2]; de Cuveland, J.[5]; Daues, H.[3]; Emschermann, D.[6]; Fateev, O.[4]; Foka, Y.[3]; Freuen, S.[6]; Garabatos, C.[3]; Glasow, R.[9]; Gottschalk, D.[5]; Gottschlag, H.[9]; Grosse-Oetringhaus, J. F.[9]; Gunji, T.[10]; Gutfleisch, M.[5]; Hamagaki, H.[10]; Hartung, G.[7]; Hehner, J.[3]; Heine, N.[9]; Herrmann, N.[6]; Hinke, H.[8]; Hoppe, M.[9]; Höbbel, H.[5]; Kebschull, U.[5]; Keidel, R.[11]; Kislov, E.[4]; Kiworra, V.[5]; Klein-Bösing, C.[9]; Kofler, E.[11]; Krawutschke, T.[7]; Legrand, I.[2]; Lindenstruth, V.[5]; Lippmann, C.[3]; Mahmoud, T.[6]; Malzacher, P.[3]; Marin, A.[3]; Mercado, J.[6]; Miskowiec, D.[3]; Moisă, D.[2]; Morino, Y.[10]; Oyama, K.[6]; Panebratsev, Y.[4]; Petridis, A.[1]; Petriş, M.[2]; Petrovici, M.[2]; Radomski, S.[3]; Radu, A.[2]; Reichling, C.[5]; Reygers, K.[9]; Rusanov, I.[6]; Saito, S.[10]; Sandoval, A.[3]; Santo, R.[9]; Schiaua, C.[2]; Schicker, R.[6]; Schneider, R.[5]; Schwarz, K.[3]; Shukla, P.[6]; Simion, V.[2]; Simon, R. S.[3]; Soltveit, H. K.[6]; Sommer, W.[8]; Stachel, J.[6]; Stelzer, H.[3]; Stockmeyer, M. R.[6]; Stoicea, G.[2]; Tilsner, H.[5]; Tsiledakis, G.[3]; Vassiliou, M.[1]; Verhoeven, W.[9]; Vulpescu, B.[6]; Wessels, J. P.[9]; Wilk, A.[9]; Windelband, B.[6]; Yurevich, V.[4]; Zanevsky, Y.[4]

1 University of Athens (Greece)
2 NIPNE Bucharest (Romania)
3 GSI Darmstadt (Germany)
4 JINR Dubna (Russia)
5 Kirchhoff-Institut für Physik, University of Heidelberg (Germany)
6 Physikalisches Institut, University of Heidelberg (Germany)
7 Fachhochschule Köln (Germany)
8 Institut für Kernphysik, University of Frankfurt (Germany)
9 Institut für Kernphysik, University of Münster (Germany)
10 University of Tokyo (Japan)

The CERES Collaboration

Cherenkov Ring Electron Pair Spectrometer at the CERN SPS
<http://www.physi.uni-heidelberg.de/physi/ceres/>
Spokesperson: J. Stachel, Heidelberg (Germany)

Adamová, D.[7]; Agakichiev, G.[3]; Andronic, A.[3]; Antończyk, D.[3]; Appelshäuser, H.[4]; Belaga, V.[5]; Braun-Munzinger, P.[3]; Busch, O[3]; Cherlin, A.[9]; Damjanović, S.[4]; Drees, A.[8]; Esumi, S. I.[4]; Fomenko, K.[5]; Fraenkel, Z.[9]; Garabatos, C.[3]; Glässel, P.[4]; Gnaenski, A.[9]; Kalisky, M.[3]; Kushpil, V. [7]; Lenkeit, B.[2]; Ludolphs, W.[4]; Marín, A.[3]; Messer, F.[8]; Milov, A.[9]; Milošević, R.[4]; Miśkowiec, D.[3]; Ortega, R.[4]; Panebrattsev, Y.[5]; Petchenova, O.[5]; Petráček, V.[4]; Pfeiffer, A.[2]; Radomski, S.[3]; Rak, J.[3]; Ravinovich, I.[9]; Rehak, P.[1]; Sako, H.[3]; Schukraft, J.[2]; Sedykh, S.[3]; Shimansky, S.[5]; Slívová, J.[4]; Stachel, J.[4]; Šumbera, M.[7]; Tilsner, H.[4]; Tserruya, I.[9]; Tsiledakis, G.[3]; Wessels, J. P.[4]; Windelband, B.[4]; Wurm, J. P.[6]; Xie, W.[9]; Yurevich, S.[4]; Yurevich, V.[5]

1 BNL, Upton (U.S.A.)
2 CERN, Geneva (Switzerland)
3 GSI Darmstadt, (Germany)
4 Heidelberg University (Germany)
5 JINR Dubna (Russia)
6 MPI, Heidelberg (Germany)
7 NPI ASCR, Řež (Czech Republic)
8 SUNY at Stony Brook (U.S.A.)

The NA49 Collaboration

Large Acceptance Hadron Detector for an Investigation of Pb-induced Reactions at the CERN SPS
<http://na49info.cern.ch/>
Spokesperson: P. Seyboth

Alt, C.[9]; Anticic, T.[21]; Baatar, B.[8]; Barna, D.[4]; Bartke, J.[6]; Betev, L.[10]; Białkowska, H.[19]; Blume, C.[9]; Boimska, B.[19]; Botje, M.[1]; Bracinik, J.[3]; Bramm, R.[9]; Bunčić, P.[10]; Cerny, V.[3]; Christakoglou, P.[2]; Chvala, O.[14]; Cramer, J. G.[16]; Csató, P.[4]; Dinkelaker, P.[9]; Eckardt, W.[13]; Flierl, D.[9]; Fodor, Z.[4]; Foka, P.[7]; Friese, V.[7]; Gál, J.[4]; Gaździcki, M.[11]; Gaździcki, M.[9]; Georgopoulos, G.[2]; Grebieszkow, K.[20]; Gładysz, E.[6]; Höhne, C.[7]; Hegyi, S.[4]; Kadija, K.[21]; Karev, A.[13]; Kliemant, M.[9]; Kniege, S.[9]; Kolesnikov, V. I.[8]; Kornas, E.[6]; Korus, R.[11]; Kowalski, M.[6]; Kraus, I.[7]; Kreps, M.[3]; van Leeuwen, M.[1]; Lévai, P.[4]; Litov, L.[17]; Lungwitz, B.[9]; Makariev, M.[17]; Malakhov, A. I.[8]; Mateev, M.[17]; Melkumov, G. L.[8]; Mitrovski, M.[9]; Molnár, J.[4]; Mrówczyński, S.[11]; Nicolic, V.[21]; Pühlhofer, F.[12]; Pálla, G.[4]; Panagiotou, A. D.[2]; Panayotov, D.[17]; Petridis, A.[2]; Pikna, M.[3]; Prindle, D.[16]; Renfordt, R.[9]; Roland, C.[5]; Roland, G.[5]; Rybczyński, M.[11]; Rybicki, A.[10]; Rybicki, A.[6]; Sandoval, A.[7]; Schmitz, N.[13]; Schuster, T.[9]; Seyboth, P.[13]; Siklér, F.[4]; Sitar, B.[3]; Skrzypczak, E.[20]; Stefanek, G.[11]; Stock, R.[9]; Ströbele, H.[9]; Susa, T.[21]; Sziklai, J.[4]; Szymanski, P.[10]; Szymanski, P.[19]; Trubnikov, V.[19]; V. Genchev, V.[18]; Varga, D.[10]; Varga, D.[4]; Vassiliou, M.[2]; Veres, G. I.[4]; Veres, G. I.[5]; Vesztergombi, G.[4]; Vranić, D.[7]; Wetzler, A.[9]; Włodarczyk, Z. W.[11]; Yoo, I. K.[15]; Zimányi, J.[4]

1 NIKHEF, Amsterdam (Netherlands)
2 Department of Physics, University of Athens, Athens (Greece)
3 Comenius University, Bratislava (Slovakia)
4 KFKI Research Institute for Particle and Nuclear Physics, Budapest (Hungary)
5 MIT, Cambridge (USA)
6 Institute of Nuclear Physics, Cracow (Poland)

7 GSI, Darmstadt (Germany)
8 Joint Institute for Nuclear Research, Dubna (Russia)
9 Fachbereich Physik der Universität, Frankfurt (Germany)
10 CERN, Geneva (Switzerland)
11 Institute of Physics Świetokrzyska Academy, Kielce (Poland)
12 Fachbereich Physik der Universität, Marburg (Germany)
13 Max-Planck-Institut für Physik, Munich (Germany)
14 Institute of Particle and Nuclear Physics, Charles University, Prague (Czech
15 Department of Physics, Pusan National University, Pusan (Republic of Korea)
16 Nuclear Physics Laboratory, University of Washington, Seattle, WA (USA)
17 Atomic Physics Department, Sofia University St. Kliment Ohridski, Sofia (Bulgaria)
18 Institute for Nuclear Research and Nuclear Energy, Sofia (Bulgaria)
19 Institute for Nuclear Studies, Warsaw (Poland)
20 Institute for Experimental Physics, University of Warsaw, Warsaw (Poland)

The RD42 Collaboration

Development of Diamond Tracking Detectors for High Luminosity Experiments at the LHC RD42
<http://rd42.web.cern.ch/RD42/>
Spokespersons: H. Kagan Ohio (USA), P. Weilhammer Geneva (Switzerland)

Adam, W.[1]; Berdermann, E.[2]; Bergonzo, P.[3]; de Boer, W.[4]; Bogani, F.[5]; Borchi, E.[6]; Brambilla, A.[3]; Bruzzi, M.[6]; Colledani, C.[7]; Conway, J.[8]; D'Angelo, P.[9]; Dabrowski, W.[10]; Delpierre, P.[12]; Doroshenko, J.[8]; Dulinski, W.[7]; Fallou, A.[12]; Fischer, P.[22]; Fizotti, F.[15]; Furetta, C.[3]; Gan, K. K.[16]; Ghodbane, N.[12]; Grigoriev, E.[4]; Hallewell, G.[12]; Han, S.[16]; Hartjes, F.[13]; Hrubec, J.[1]; Husson, D.[7]; Kagan, H.[16]; Kaplon, J.[17]; Kass, R.[16]; Keil, M.[14]; Knöpfle, K. T.[18]; Koeth, T.[8]; Krammer, M.[1]; Logiudice, A.[15]; Lu, R.[15]; Mac Lynne, L.[8]; Manfredotti, C.[15]; Meier, D.[17]; Menichelli, D.[6]; Meuser, S.[14]; Mishina, M.[19]; Moroni, L.[9]; Noomen, J.[13]; Oh, A.[17]; Perera, L.[8]; Pernicka, M.[1]; Potenza, R.[23]; Riester, J. L.[7]; Roe, S.[17]; Rudge, A.[17]; Sala, J. S.[9]; Sampietro, M.[20]; Schnetzer, S.[8]; Sciortino, S.[6]; Stelzer, H.[2]; Stone, R.[8]; Sucera, C.[23]; Trishuk, W.[21]; Tromson, D.[3]; Tuve, C.[24]; van Eijk, B.[13]; Vincenzo, B.[23]; Weilhammer, P.[17]; Wermes, N.[14]; Wetstein, M.[7]; Zeuner, W.[11]; Zoeller, M.[16];

1 HEPHY, Vienna (Austria)
2 GSI, Darmstadt (Germany)
3 LIST CEA Saclay, Paris (France)
4 Inst. Exp. Kernphysik, Karlsruhe (Germany)
5 LENS, Florence (Italy)
6 Univ. of Florence, Florence (Italy)
7 LEPSI, IN2P3/CNRS-ULP, Strassbourg (France)
8 Rutgers University, New York (USA)
9 INFN, Milano (Italy)
10 UMM, Cracow (Poland)
11 II. Inst. für Exp. Physik, Hamburg (Germany)
12 CPPM, Marseille (France)
13 NIKHEF, Amsterdam (Netherlands)
14 Universität Bonn, Bonn (Germany)
15 Univ. of Torino Torino (Italy)
16 The Ohio State Univ., Columbus (USA)
17 CERN, Geneva (Switzerland)
18 MPI für Kernphysik, Heidelberg (Germany)
19 FNAL, Batavia (USA)
20 Polytechnico di Milano, Milano (Italy)
21 Univ. of Toronto Toronto (Canada)
22 Universität Mannheim, Mannheim (Germany)
23 University of Roma (Italy)

The WA98 Collaboration

Large Acceptance Photon and Hadron Spectrometer
<http://wa98.web.cern.ch/WA98/>
Spokesperson: T. C. Awes (USA)

Aggarwal, M. M.[1]; Agnihotri, A.[2]; Ahammed, Z.[3]; Angelis, A. L. S.[4]; Antonenko, V.[5]; Arefiev, V.[6]; Astakhov, V.[6]; Avdeitchikov, V.[6]; Awes, T. C.[7]; Baba, P. V. K. S.[8]; Badyal, S. K.[8]; Baldine, A.[6]; Barabach, L.[6]; Barlag, C.[9]; Bathe, S.[9]; Batiounia, B.[6]; Bernier, T.[10]; Bhalla, K. B.[2]; Bhatia, V. S.[1]; Blume, C.[9]; Bock, R.[11]; Bohne, E. M.[9]; Bucher, D.[9]; Buijs, A.[12]; Buis, E. -J.[12]; Böröcz, Z.[9]; Büsching, H.[9]; Carlen, L.[13]; Chalyshev, V.[6]; Chattopadhyay, S.[3]; Cherbatchev, R.[5]; Chujo, T.[14]; Claussen, A.[9]; Das, A. C.[3]; Decowski, M. P.[12]; Delagrange, H.[10]; Djordjadze, V.[6]; Donni, P.[4]; Doubovik, I.[5]; Dutt, S.[8]; Dutta Majumdar, M. R.[3]; El Chenawi, K.[13]; Eliseev, S.[15]; Enosawa, K.[14]; Foka, P.[4]; Fokin, S.[5]; Frolov, V.[6]; Ganti, M. S.[3]; Garpman, S.[13]; Gavrishchuk, O.[6]; Geurts, F. J. M.[12]; Ghosh, T. K.[16]; Glasow, R.[9]; Gupta, S. K.[2]; Guskov, B.[6]; Gustafsson, H. Å.[13]; Gutbrod, H. H.[10]; Higuchi, R.[14]; Hrivnacova, I.[15]; Ippolitov, M.[5]; Kalechofsky, H.[4]; Kamermans, R.[12]; Kampert, K. -H.[9]; Karadjev, K.[5]; Karpio, K.[17]; Kato, S.[14]; Kees, S.[19]; Kolb, B. W.[11]; Kosarev, I.[6]; Koutcheryaev, I.[5]; Krümpel, T.[9]; Kugler, A.[15]; Kulinich, P.[18]; Kurata, M.[14]; Kurita, K.[14]; Kuzmin, N.[6]; Langbein, I.[11]; Lebedev, A.[5]; Lee, Y. Y.[11]; Luquin, L.[10]; Löhner, H.[16]; Mahapatra, D. P.[19]; Manko, V.[5]; Martin, M.[4]; Martinez, G.[10]; Maximov, A.[6]; Mehdiyev, R.[6]; Mgebrichvili, G.[5]; Miake, Y.[14]; Mikhalev, D.[6]; Mir, Md. F.[8]; Mishra, G. C.[19]; Miyamoto, Y.[14]; Morrison, D.[20]; Mukhopadhyay, D. S.[3]; Myalkovski, V.[6]; Naef, H.[4]; Nandi, B. K.[19]; Nayak, S. K.[10]; Nayak, T. K.[3]; Neumaier, S.[11]; Nianine, A.[5]; Nikitine, V.[6]; Nikolaev, S.[5]; Nilsson, P.[13]; Nishimura, S.[14]; Nomokonov,

P.[6]; Nystrand, J.[13]; Obenshain, F. E.[20]; Oskarsson, A.[13]; Otterlund, I.[13]; Pachr, M.[15]; Parfenov, A.[6]; Pavliouk, S.[6]; Peitzmann, T.[9]; Petracek, V.[15]; Pinganaud, W.[10]; Plasil, F.[7]; Purschke, M. L.[11]; Rak, J.[15]; Ramamurthy, V. S.[19]; Raniwala, R.[2]; Raniwala, S.[2]; Rao, N. K.[8]; Retiere, F.[10]; Reygers, K.[9]; Roland, G.[18]; Rosselet, L.[4]; Roufanov, I.[6]; Roy, C.[10]; Rubio, J. M.[4]; Sako, H.[14]; Sambyal, S. S.[8]; Santo, R.[9]; Sato, S.[14]; Schlagheck, H.[9]; Schmidt, H. -R.[11]; Schutz, Y.[10]; Shabratova, G.[6]; Shah, T. H.[8]; Sibiriak, I.[5]; Siemiarczuk, T.[17]; Silvermyr, D.[13]; Sinha, B. C.[3]; Slavine, N.[6]; Solomey, N.[4]; Stankus, P.[7]; Stefanek, G.[17]; Steinberg, P.[18]; Stenlund, E.[13]; Stüken, D.[9]; Sumbera, M.[15]; Svensson, T.[13]; Söderström, K.[13]; Sørensen, S. P.[20]; Trivedi, M. D.[3]; Tsvetkov, A.[5]; Tykarski, L.[17]; Urbahn, J.[11]; v. Eijndhoven, N.[12]; v. Nieuwenhuizen, G. J.[18]; v. d. Pijll, E. C.[12]; Vinogradov, A.[5]; Viyogi, Y. P.[3]; Vodopianov, A.[6]; Vos, M. A.[12]; Vörös, S.[4]; Wyslouch, B.[18]; Yagi, K.[14]; Yokota, Y.[14]; Young, G. R.[7]

1 Univ. of Panjab, Chandigarh (India)
2 Univ. of Rajasthan, Jaipur (India)
3 VECC, Calcutta (India)
4 Univ. of Geneva (Switzerland)
5 Kurchatov Inst., Moscow (Russia)
6 JINR, Dubna (Russia)
7 ORNL, Oak Ridge National Laboratory (USA)
8 Univ. of Jammu, Jammu (India)
9 Univ. of Münster (Germany)
10 Subatech, Ecoles des Mines, Nantes (France)
11 GSI Darmstadt (Germany)
12 Univ. of Utrecht (The Netherlands)
13 Univ. of Lund, Lund, Sweden
14 Univ. of Tsukuba, Ibaraki (Japan)
15 Nucl. Physics Inst., Rez (Czech Republic)
16 KVI, Univ. of Groningen (The Netherlands)
17 Inst. of Nucl. Studies, Warsaw (Poland)
18 MIT, Cambridge (USA)
19 IOP, Bhubaneswar (India)
20 Univ. of Tennessee, Knoxville (USA)

Current scientific bodies and the organigram of the GSI

Compiled by K. Große

As at April 30, 2005

Supervisory Board/Aufsichtsrat:

Dr. B. Vierkorn-Rudolph [chair],
Bundesministerium für Bildung und Forschung, Bonn/Berlin (Germany),
as representative of the Federal Republic of Germany

Regierungsdirektor Dr. R. Koepke,
Bundesministerium für Bildung und Forschung, Bonn/Berlin (Germany),
as representative of the Federal Republic of Germany

Ministerialdirigent Dr. R. Bernhardt,
Hessisches Ministerium für Wissenschaft und Kunst, Wiesbaden (Germany),
as representative of the State Hessen in Germany

Prof. Dr. R. Klanner,
Universität Hamburg (Germay),
as representatives of the Scientific Council of the GSI

Scientific Directorate/Wissenschaftliches Direktorium WD:

Prof. Dr. W. F. Henning [chair]
Dr. N. Angert
Prof. Dr. P. Braun-Munzinger
Prof. Dr. H.-J. Kluge
Dr. A. Kurz/Dr. H. Zeitträger

Divisions and department leaders/Bereichs- und Abteilungsleiter:

Dr. H. Eickhoff, Dr. N. Angert,
Accelerator/Beschleunigerbereich

Prof. Dr. P. Braun-Munzinger,
Infrastructure/Infrastruktur

Prof. Dr. H.-J. Kluge,
Research/Forschungsbereich

Prof. Dr. H.-J. Kluge,
Atomic physics/Atomphysik

Prof. Dr. G. Kraft,
Biophysics/Biophysik

Prof. Dr. P. Braun-Munzinger,
Nuclear physics I/Kernphysik I

Prof. Dr. H. Emling,
Nuclear physics II/Kernphysik II

Prof. Dr. K. Peters,
Nuclear physics III/Kernphysik III

Prof. R. Neumann,
Materials research/Materialforschung

Prof. Dr. D. H. H. Hoffmann,
Plasma physics/Plasmaphysik

Prof. Dr. K. Langanke,
Theory: Nuclear structure and astrophysics/
Theorie: Kernstruktur- und Astrophysik

Prof. Dr. J. Wambach,
Theory: QCD and hadron physics/
Theorie: QCD und Hadronenphysik

Scientific Council/Wissenschaftlicher Rat WR:

<http://www.gsi.de/informationen/usres/EAC/wr/>

R. Klanner [chair], Universität Hamburg (Germany); N. Holtkamp, Oak Ridge National Laboratory (USA); M. H. R. Hutchinson, Rutherford Appleton Lab, Central Laser Facility, Oxfordshire (Great Britain); C. Leemann, Thomas Jefferson National Accelerator Facility, Newport News (USA); V. Metag, Justus-Liebig-Universität, Gießen (Germany); B. Mueller, Duke University, Durham (USA); H. Requardt, Siemens AG Medical Solutions, Erlangen (Germany); D. O. Riska, Helsinki Institute of Physics, University of Helsinki (Finnland); W.-D. Schlatter, CERN EP, Geneva (Switzerland); B. M. Sherrill, Michigan State University, East Lansing (USA); A. Shotter, TRIUMF, Vancouver (Canada); M. Soyeur, DSM/DAPNIA/SPhN, Gif-sur-Yvette (France)

Scientific Committee/Wissenschaftlicher Ausschuss WA:

<http://www-w2k.gsi.de/wa/scientific_committee.htm>

S. Richter [chair]; A. Bräuning-Demian; L. Dahl; H. Essel; B. Friman; S. Götte; W. F. Henning; I. Hofmann; B. Lommel; P. Malzacher; D. Miskowiec; G. Moritz; W. F. J. Müller; R. Neumann; H. Reich-Sprenger; C. Scheidenberger; M. Scholz; P. Senger; A. Tauschwitz; M. Traxler

GSI Programme Advisory Committee PAC/ Experimentausschuss EA:

H. W. E. M. Wilschut [chair], Kernfysisch Versneller Instituut, Groningen (Netherlands); J. Aichelin, SUBATECH, Nantes (France); A. Drees, SUNY Stony Brook (USA); R. Krücken, Technische Universität München, Physik-Department (Germany); K. Langanke, GSI and Technische Universität Darmstadt (Germany); M. Lewitowicz, GANIL, Caen (France); S. Paul, Technische Universität München, Physik-Department (Germany); T. Peitzmann, Utrecht University (Netherlands); G. Savard, Argonne National Lab, Physics Division (USA); B. Sharkov, Inst. of Theoretical and Experimental Physics, Moscow (Russia); J. Ullrich, MPI für Kernphysik, Heidelberg (Germany); E. Widmann, Stefan-Meyer-Institut für subatomare Physik, Österreichische Akademie der Wissenschaften, Wien (Austria)

GSI Programme Advisory Committee for Plasma Physics PPAC:

M. H. R. Hutchinson [chair], Rutherford Appleton Lab, Central Laser Facility, Oxfordshire (Great Britain); S. Jacquemot, Ecole Polytechnique, Palaiseau (France); G. Logan, Virtual National Laboratory for Heavy-Ion Fusion, Berkeley (USA); T. A. Mehlhorn, Sandia National Laboratories, New Mexico, Albuquerque (USA); R. Sauerbrey, Friedrich-Schiller-Universität Jena, Jena (Germany); B. Sharkov, Inst. of Theoretical and Experimental Physics, Moscow (Russia)

Scientific Coordinator:

K. D. Groß, GSI (Germany)

Committees of the FAIR Project

FAIR Project Coordinator:

H. H. Gutbrod, GSI (Germany)

The International Steering Committee for the Facility for Antiproton and Ion Research (ISC FAIR)

Chair: H. Schunk, BMBF (Germany)
Secretary: J. Eschke, GSI (Germany)
C. Alejaldre, Ministerio de Educación y Ciencia (Spain); M. Arajärvi, Councilor of Education, Ministry of Education and Science (Finland); L. Börjesson, Secretary General at the Swedish Research Council, Science and Engineering (Sweden); V. Fortov, Member Russian Academy of Science, Institute for High Energy Density (Russia); G. Fortuna, INFN - Laboratori Nazionali di Legnaro (Italy); D. Hurlin, Ministère de la Jeunesse, de l'Education et de la Recherche (France); R. Kulessa, University of Warsaw (Poland); D. Lajos Nagy, KFKI, Research Institute for Particle and Nuclear Physics (Hungary); H. Schunck, BMBF (Germany); J. Wood, Director Central Laboratory of Research Council CCLRC (United Kingdom); J. A. Zakrzewski, University of Warsaw (Poland)

Observer:
Hlavác, S.(Slovakia); D. Kovar, Associate Director Department of Energy (USA); D. Lajos Nagy, KFKI, Research Institute for Particle and Nuclear Physics (Hungary); Xie Ming, Academician of Chinese Academy of Sciences CAS (China); J.-L. Picqué, European Commission, DG Research (European Union); V. S. Ramamurthy, Secretary Department of Science and Technology DST (India); Meng Shuguang, Director of the Bureau of Basic Science of CAS (China)

The working group for Scientific and Technical Issues STI for the international Facility for Antiproton and Ion Research (FAIR) at GSI

Chair: H. Wenninger, CERN (Switzerland) [chair since March 2005]; S. Gales IN2P3 (France) [chair before March 2005]
Secretary: I. Augustin, GSI (Germany)
J. Äystö, University Jyväskylä (Finland); J. Benlliure, University Santiago de Compostella (Spain); P. Dalpiaz, INFN Ferrara (Italy); H. Danared, Manne Siegbahn Lab (Sweden); P. Fabbricatore, INFN Genova (Italy); S. Gales, IN2P3 (France); D. Goutte, GANIL (France); H. H. Gutbrod, GSI (Germany); W. F. Henning, GSI (Germany); T. Junquera, IN2P3 (France); D. O. Riska, University Helsinki (Finland); G. Rosner, University Glasgow (UK); B. Rubio, IFIC (Spain); P. Schroth, BMBF (Germany); B. Sharkov, ITEP (Russia); H. Ströher, FZ Jülich (Germany); D. Warner, CCLRC Daresbury (UK); U. Wiedner, University Uppsala (Sweden); W. Zhan, CAS (China)

The working group for Administrative and Funding Issues AFI for the international Facility for Antiproton and Ion Research (FAIR) at GSI

Chair: H.-F. Wagner, (Germany)
Secretary: T. Beier, GSI (Germany)
M. Arajärvi, Councilor of Education, Ministry of Education and Science (Finland); P. Bogdanov, Ministry of Atomic Energy (Russia); Y. Bravo, INFN (Italy); L. Eriksson, Swedish Research Council (Sweden); N. Godet, Ministère de la Jeunesse, de l'Education et de la Recherche Ministry of Research (France); J. Grapentin, GSI (Germany); C. Guaraldo, INFN-Frascati (Italy); S. Hieber, BMFT (Germany); A. Kurz, GSI (Germany); G. Mangel, HMWK (Germany); O. Patarakin, Ministry of Atomic Energy (Russia); R. Pellegrini, INFN-Frascati (Italy); E. Quingles Soteras, Ministry of Science and Technology (Spain); L. E. Ruiz, Ministry of Science and Technology (Spain); A. Scherbak, Ministry of Atomic Energy (Russia); D. Schildt, CCLRC (United Kingdom); Ö. Skeppstedt, Manne Siegbahn Laboratory (Sweden); B. Vierkorn-Rudolph, BMFT (Germany); H.-F. Wagner, (Germany), H. Zeitträger, GSI (Germany)

The Cost Review Group for Experiments CORE-E (FAIR)

Chair: W. Bartel, DESY (Germany)
H. G. Ritter, LBL (USA); J. Simpson, CCLRC (United Kingdom); A. Vacchi, INFN Trieste (Italy); I. Lazarus, CCLRC (United Kingdom); H. J. Hilke, CERN (Switzerland); P. Lazeyras, CERN (Switzerland)

Atomic, Plasma Physics and Applications Programme Advisory Committee FAIR APPA PAC

Chair: D. Schwalm, MPI Heidelberg, (Germany);
S. Atzeni, University of Rome (Italy); M. Basko, ITEP Moscow (Russia); G. W. F. Drake, University of Windsor (Canada); P. Indelicato, Univ. P. M. Curie Paris (France); G. Maynard, Univ. Paris-Sud (France); T. A. Mehlhorn, Sandia National Lab (USA); P. Norreys, RAL (United Kingdom)M R. Sauerbrey, University of Jena (Germany); B. Sharkov, ITEP (Russia); P. Spiller, GSI (Germany); M. Steck, GSI (Germany); D. Vernhet, GPS Paris (France); T. Yamazaki, RIBF-RIKEN (Japan)

Quantum Chromo Dynamics Programme Advisory Committee FAIR QCD PAC

Chair: E. Chiavassa, INFN Torino (Italy)
S. J. Brodsky, SLAC (USA); P. Dalpiaz, INFN Ferrara (Italy); D. Geesaman, Argonne National Lab (USA); H. A: Gustafsson, University of Lund (Sweden); S. Kox, LPSC Grenoble (France); R. Landua, CERN (Switzerland); A. Magnon, Saclay (France); R. Maier, FZ Jülich (Germany); B. Müller, Duke University (USA); J. Nelson, University of Birmingham (United Kingdom); E. Oset, IFIC (Spain); D. O. Riska, University of Helsinki (Finland); H. G. Ritter, LBL (USA); H. Ströher, FZ Jülich (Germany); I. Tserruya, Weizmann Institute Rehovot (Israel)

Nuclear Structure and Nuclear Astrophysics Programme Advisory Committee FAIR NUSTAR PAC

Chair: R. Casten, Yale (USA)
F. Azaiez, INP Orsay (France); P. Butler, CERN (Switzerland); B. Franzke, GSI (Germany); H. Grawe, GSI (Germany); R. Janssens, ANL (USA); S. Kubono, CNS LAB Riken (Japan); K. Kilian, FZ Jülich (Germany); H.-O. Meyer, University Indiana (USA); A. Poves, University Madrid (Spain); B. Rubio, IFIC (Spain); B. Sherril, MSU (USA); A. Shotter, TRIUMF (Canada); A. Villari, GANIL (France); D. Warner, CCLRC Daresbury (United Kingdom); H. Weick, GSI (Germany) M. Wiescher, University Notre Dame (USA)

The Technical Advisory Committee FAIR TAC

Chair: C. Yanlai, ANL (USA)
R. Garoby, CERN (Switzerland); M. Jacquemet, CEA Saclay (France); A. Müller, IPNO Orsay (France); J. Nolen, ANL (USA); S. Ozaki, BNL (USA); P. Fabbricatore, INFN Genova (Italy); S. Ivanov, IHEP (Russia); T. Junquera, IPNO Orsay (France); P. Willeke, DESY (Germany); Y. Yamazaki, KEK (Japan)

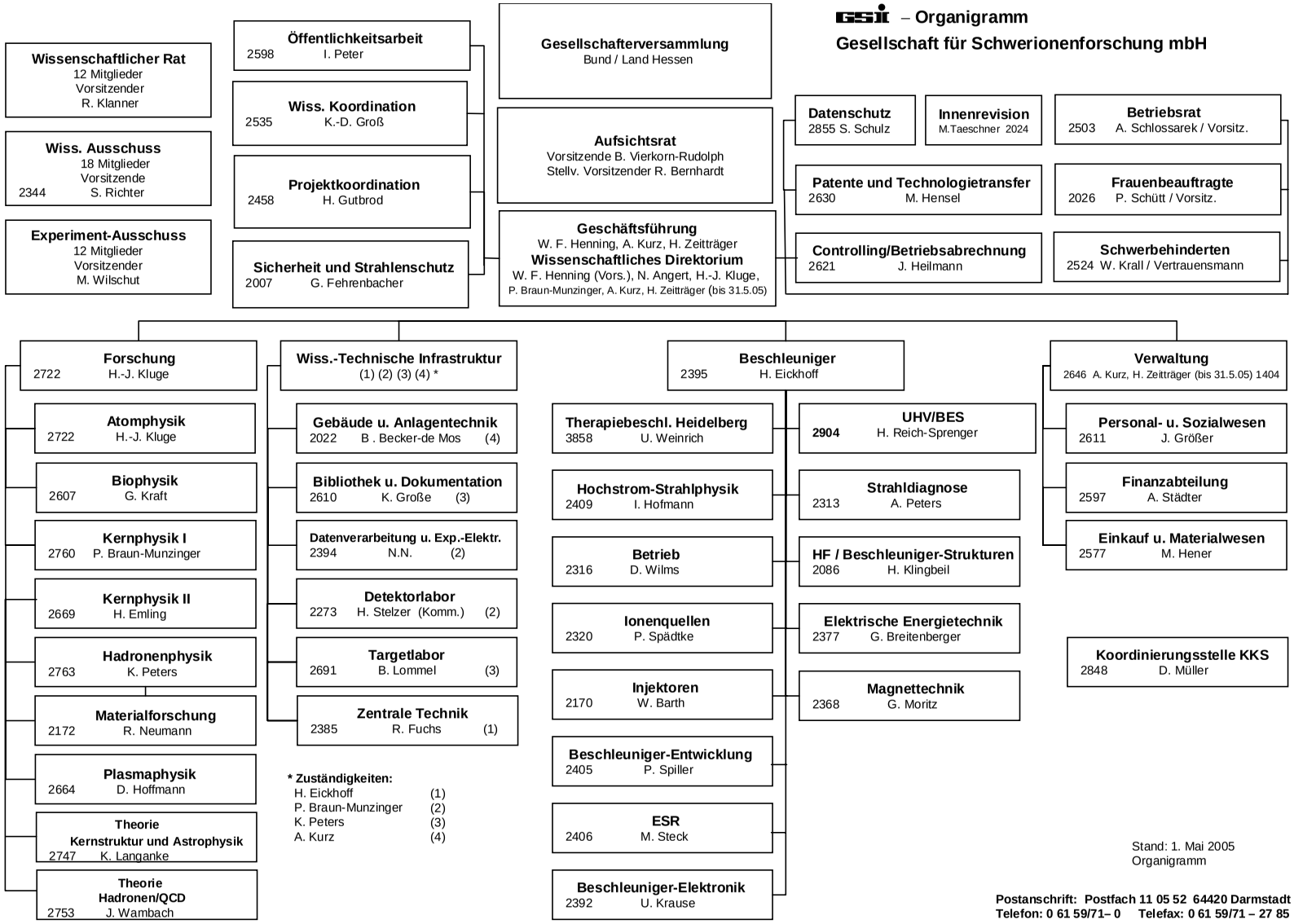
GSI – Organigramm
Gesellschaft für Schwerionenforschung mbH
Wissenschaftlicher Rat
12 Mitglieder
Vorsitzender
R. Klanner
Wiss. Ausschuss
18 Mitglieder
Vorsitzende
2344 S. Richter
Experiment-Ausschuss
12 Mitglieder
Vorsitzender
M. Wilschut
Öffentlichkeitsarbeit
2598 I. Peter
Wiss. Koordination
2535 K.-D. Groß
Projektkoordination
2458 H. Gutbrod
Sicherheit und Strahlenschutz
2007 G. Fehrenbacher
Gesellschafterversammlung
Bund / Land Hessen
Aufsichtsrat
Vorsitzende B. Vierkorn-Rudolph
Stellv. Vorsitzender R. Bernhardt
Geschäftsführung
W. F. Henning, A. Kurz, H. Zeitträger
Wissenschaftliches Direktorium
W. F. Henning (Vors.), N. Angert, H.-J. Kluge,
P. Braun-Munzinger, A. Kurz, H. Zeitträger (bis 31.5.05)
Datenschutz
2855 S. Schulz
Innenrevision
M.Taeschner 2024
Betriebsrat
2503 A. Schlossarek / Vorsitz.
Patente und Technologietransfer
2630 M. Hensel
Frauenbeauftragte
2026 P. Schütt / Vorsitz.
Controlling/Betriebsabrechnung
2621 J. Heilmann
Schwerbehinderten
2524 W. Krall / Vertrauensmann
Forschung
2722 H.-J. Kluge
Atomphysik
2722 H.-J. Kluge
Biophysik
2607 G. Kraft
Kernphysik I
2760 P. Braun-Munzinger
Kernphysik II
2669 H. Emling
Hadronenphysik
2763 K. Peters
Materialforschung
2172 R. Neumann
Plasmaphysik
2664 D. Hoffmann
Theorie
Kernstruktur und Astrophysik
2747 K. Langanke
Theorie
Hadronen/QCD
2753 J. Wambach
Wiss.-Technische Infrastruktur
(1) (2) (3) (4) *
Gebäude u. Anlagentechnik
2022 B . Becker-de Mos (4)
Bibliothek u. Dokumentation
2610 K. Große (3)
Datenverarbeitung u. Exp.-Elektr.
2394 N.N. (2)
Detektorlabor
2273 H. Stelzer (Komm.) (2)
Targetlabor
2691 B. Lommel (3)
Zentrale Technik
2385 R. Fuchs (1)
* Zuständigkeiten:
H. Eickhoff (1)
P. Braun-Munzinger (2)
K. Peters (3)
A. Kurz (4)
Beschleuniger
2395 H. Eickhoff
Therapiebeschl. Heidelberg
3858 U. Weinrich
Hochstrom-Strahlphysik
2409 I. Hofmann
Betrieb
2316 D. Wilms
Ionenquellen
2320 P. Spädtke
Injektoren
2170 W. Barth
Beschleuniger-Entwicklung
2405 P. Spiller
ESR
2406 M. Steck
Beschleuniger-Elektronik
2392 U. Krause
UHV/BES
2904 H. Reich-Sprenger
Strahldiagnose
2313 A. Peters
HF / Beschleuniger-Strukturen
2086 H. Klingbeil
Elektrische Energietechnik
2377 G. Breitenberger
Magnettechnik
2368 G. Moritz
Verwaltung
2646 A. Kurz, H. Zeitträger (bis 31.5.05) 1404
Personal- u. Sozialwesen
2611 J. Größer
Finanzabteilung
2597 A. Städter
Einkauf u. Materialwesen
2577 M. Hener
Koordinierungsstelle KKS
2848 D. Müller
Stand: 1. Mai 2005
Organigramm
Postanschrift: Postfach 11 05 52 64420 Darmstadt
Telefon: 0 61 59/71– 0 Telefax: 0 61 59/71 – 27 85

Index of Authors

Authors from the contributions, from the GSI serial publications (ANNEXGSI-07) and from the theses (ANNEXGSI-13) are listed here as well as the GSI authors from the publications (ANNEXGSI-01, ANNEXGSI-02, ANNEXGSI-03, ANNEXGSI-04, ANNEXGSI-05, ANNEXGSI-06).

Index of Collaborations

Collaborations from the contributions and from the publications (ANNEXGSI-01, ANNEXGSI-02, ANNEXGSI-03, ANNEXGSI-04, ANNEXGSI-05, ANNEXGSI-06) are listed here.

Form more information to the collaborations see ANNEXGSI-15.